

## Aggregation-Induced Emission: Together We Shine, United We Soar!

Ju Mei,<sup>†,‡,||</sup> Nelson L. C. Leung,<sup>†,‡,||</sup> Ryan T. K. Kwok,<sup>†,‡</sup> Jacky W. Y. Lam,<sup>†,‡</sup> and Ben Zhong Tang<sup>\*,†,‡,§</sup>

<sup>†</sup>HKUST-Shenzhen Research Institute, Hi-Tech Park, Nanshan, Shenzhen 518057, China

<sup>‡</sup>Department of Chemistry, HKUST Jockey Club Institute for Advanced Study, Institute of Molecular Functional Materials, Division of Biomedical Engineering, State Key Laboratory of Molecular Neuroscience, Division of Life Science, The Hong Kong University of Science and Technology, Clear Water Bay, Kowloon, Hong Kong, China

<sup>§</sup>Guangdong Innovative Research Team, SCUT-HKUST Joint Research Laboratory, State Key Laboratory of Luminescent Materials and Devices, South China University of Technology, Guangzhou 510640, China



### CONTENTS

1. Introduction	11718	5.2.1. Ions	11838
2. Working Mechanisms	11721	5.2.2. pH	11850
2.1. Restriction of Intramolecular Rotations (RIR)	11721	5.2.3. Gases	11852
2.2. Restriction of Intramolecular Vibrations (RIV)	11727	5.2.4. Explosives	11853
2.3. Restriction of Intramolecular Motions (RIM)	11729	5.2.5. Peroxides	11860
3. ACQ-to-AIE Transformation	11730	5.2.6. Hazardous Species	11861
3.1. Decorating ACQphores with AIEgens	11731	5.2.7. Fingerprints	11862
3.2. Replacing Parts of AIEgens with ACQphores	11733	5.2.8. Chirality	11863
3.3. New AIEgens Built from ACQphores	11736	5.2.9. Viscosity	11864
3.4. New AIEgens Incorporating Triphenylamine (TPA) Units	11738	5.2.10. Conformation	11866
4. AIEgen Systems	11739	5.2.11. Self-Assembly	11869
4.1. Hydrocarbon AIEgens	11740	5.2.12. Morphology	11873
4.2. Heteroatom-Containing AIEgens	11743	5.3. Optoelectronic Systems	11875
4.2.1. Pentacyclic Compounds	11743	5.3.1. Organic Light-Emitting Diodes (OLEDs)	11876
4.2.2. Boron Compounds	11745	5.3.2. Self-Assembly Systems	11885
4.2.3. Schiff Bases	11748	5.3.3. Organic Field-Effect Transistors (OFETs)	11887
4.2.4. Excited-State Intramolecular Proton Transfer (ESIPT) Systems	11749	5.3.4. Optical Waveguides	11889
4.2.5. Hydrogen-Bonding Systems	11751	5.3.5. Circularly Polarized Luminescence (CPL)	11891
4.2.6. Nitrile Compounds	11753	5.3.6. Liquid Crystals (LCs)	11893
4.2.7. Miscellaneous Systems	11756	5.3.7. Photovoltaics	11897
4.3. Macromolecular AIEgens	11760	5.4. Stimuli Responses	11898
4.3.1. Main-Chain Polymers	11760	5.4.1. Force	11898
4.3.2. Side-Chain Polymers	11761	5.4.2. Heat	11902
4.3.3. Initiator Systems	11763	5.4.3. pH	11903
4.3.4. Dendrimer Systems	11764	5.4.4. Vapor	11904
4.3.5. Hyperbranched Polymers	11766	5.4.5. Photon	11905
4.3.6. Metal-Organic Frameworks (MOFs)	11769	5.4.6. Multiplex	11906
4.4. Metal-Complex AIEgens	11771	6. Conclusions and Perspectives	11907
4.5. Unorthodox AIEgens	11778	Associated Content	11909
4.5.1. Molecular Systems	11779	Special Issue Paper	11909
4.5.2. Macromolecular Systems	11784	Author Information	11909
5. Technological Applications	11786	Corresponding Author	11909
5.1. Biological Probes	11786	Author Contributions	11909
5.1.1. Biomolecular Sensing	11786	Notes	11909
5.1.2. Biological Imaging	11810	Biographies	11909
5.2. Chemical Sensing	11838	Acknowledgments	11910
		References	11910

### 1. INTRODUCTION

Light is of essential importance to the universe and humankind. Light has been, and continues to be, one of the most fundamental and indispensable elements to life and society. To acknowledge

Received: May 5, 2015

Published: October 22, 2015



the great roles of light in scientific discoveries and technological innovations, the United Nations has proclaimed 2015 the International Year of Light and Light-based Technologies. During the long history of civilization, people have worked untiringly in the quest for knowledge of light. Whereas a wealth of information has been collected, much remains to be understood and explored.

Light is emitted from luminophores. The development of luminescent materials has allowed us to gain enormous knowledge that has undoubtedly promoted high-tech innovations and benefited the whole world. The breakthroughs in the understanding and applications of the light-emitting processes have opened new avenues to scientific advancement and societal development. This is exemplified by the Nobel Prize awarded to the work on the development of green fluorescent proteins (GFP), which has enabled us to “see” never before seen biochemical structures and processes to gain extraordinary knowledge and insights into biological pathways. Research on luminescent materials remains a principal focus and hot topic in the scientific community for its vast potential.

Luminescent materials can theoretically be used in every physical state, i.e., gaseous, liquid, and solid. For the vast majority of practical applications, however, luminophores are used as films and aggregates. For example, for optoelectronics applications in organic light-emitting diodes (OLEDs) and organic field-effect transistors (OFETs), luminophores are used as thin solid films and crystals. In the area of biomedical research, luminophores are often used in physiological environments or aqueous media. Although introduction of polar functional groups into molecular structures of the luminophores can help enhance their miscibility with water, the intrinsic hydrophobicity of their aromatic components (e.g., phenyl rings) still cause the formation of nanoaggregates with particle sizes so small that are invisible to the naked eyes. This is also true to the case where organic luminophores are utilized for ecosystem monitoring and environmental protection. For instance, organic luminescent chemosensors for assaying the toxic levels of hazardous species in drinking water, a salient field with an enormous impact on public health, frequently form nanoaggregates in the aqueous medium.

In the aggregate state, luminophores may show reduced, unchanged, or enhanced emission, in comparison to their dilute solutions. In many conventional systems, luminophores experience some effects of emission quenching, partially or completely. The phenomenon of aggregation-caused quenching (ACQ) has been documented for more than half a century since Förster's discovery of the concentration quenching effect in 1954.<sup>1</sup> Extensive studies on ACQ have afterwards been carried out, leading to the in-depth understanding of its photophysical processes and working mechanisms. It has been generally recognized that many aromatic luminophores suffer from the ACQ effect, according to the summary by Birks in his classic book on *Photophysics of Aromatic Molecules* in 1970.<sup>2</sup> Conventional luminophores often emit strongly as isolated molecules but meet with varying degrees of ACQ effect when they are aggregated or clustered. Once the luminophores aggregate, the molecules are located in the immediate vicinity. The aromatic rings of the adjoining luminophores, especially those with disc- or rod-like shapes, experience intense intermolecular  $\pi-\pi$  stacking interactions. The excited states of such aggregates often decay or relax back to the ground state via non-radiative channels, resulting in the emission quenching of the luminophores. The ACQ phenomenon is very common.<sup>2–4</sup> From the

viewpoint of real-world applications, it does harm than good in most cases.<sup>5–9</sup>

Perylene is a typical example illustrating the ACQ effect (Figure 1, left panel). When molecularly dissolved in a good

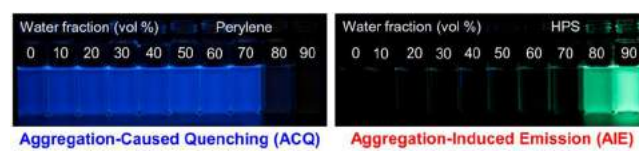


**Figure 1.** Fluorescence photographs of solutions or suspensions of (left) perylene (20  $\mu$ M) and (right) hexaphenylsilole (HPS; 20  $\mu$ M) in THF/water mixtures with different fractions of water ( $f_w$ ), with perylene and HPS showing typical ACQ and AIE effects, respectively.

solvent, e.g., pure tetrahydrofuran (THF), the dilute solution of perylene shows strong luminescence. With gradual increase in the fraction of poor solvent, e.g., fraction of water ( $f_w$ ), the emission of perylene becomes weakened. At  $f_w = 80$  vol %, its emission is significantly quenched. When  $f_w$  reaches 90 vol %, due to severe aggregate formation, its emission gets completely quenched. The planar polycyclic aromatic structure of perylene enables its molecules to pack in an ordered fashion in the aggregates. The involved  $\pi-\pi$  stacking interaction between the perylene molecules prompts the formation of such detrimental species as excimers, resulting in the observed ACQ effect.

Aggregation-induced emission (AIE) is another photophysical phenomenon associated with chromophore aggregation. The concept of AIE was coined by our group in 2001.<sup>10</sup> In the AIE process, non-emissive luminogens are induced to emit by the aggregate formation. (Whereas the emissive chromophores as molecular species are called “luminophores”, those non-emissive as molecules but emissive under appropriate conditions, e.g., as aggregates, are named “luminogens”.) The luminogens exhibiting AIE attributes are termed AIEgens, by analogue with the term of “mesogens” for the molecules showing mesomorphism under suitable conditions, e.g., at high temperatures, in the field of liquid crystal research. The AIE phenomenon is clearly depicted in Figure 1 with an archetype of AIEgen, hexaphenylsilole (HPS).<sup>10,11</sup> HPS is non-emissive when its molecules are genuinely dissolved in a good organic solvent, e.g., THF. Its emission is turned on when  $f_w$  reaches to ~80 vol %, as a result of heavy aggregation of the HPS molecules in the aqueous medium.

Another prototypical AIEgen is tetraphenylethene (TPE), which has been under extensive and intensive investigations (Figure 2).<sup>12–20</sup> The central olefin stator of the TPE molecule is surrounded by four peripheral aromatic rotors (phenyl rings). The isolated TPE molecules in a dilute solution emit almost no light. The dynamic rotations of the aromatic rotors against the olefinic stator around the single-bond axes non-radiatively dissipate the exciton energy. In the excited state, the central olefinic double bond can be opened, generating two diphenylmethylenes (DPM) units. The friction caused by their rotational or twisting motions against each other with the solvent media transforms the photonic energy to thermal energy, leading to radiationless relaxation of the excitons. Upon aggregate formation, the emission of TPE is induced or rejuvenated by the synergistic effects of the restricted intramolecular rotation (RIR) and the highly twisted molecular conformation that hampers the intermolecular  $\pi-\pi$  stacking interaction. The AIE activity of other propeller-shaped AIEgens such as HPS can all be ascribed to the RIR process.

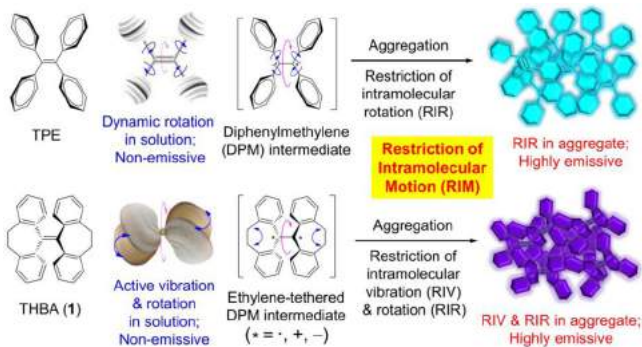


**Figure 2.** (Upper panel) Propeller-shaped luminogen of tetraphenylethene (TPE) is non-emissive when dissolved but becomes emissive when aggregated, due to the restriction to the intramolecular rotations (RIR) of its phenyl rotors (blue curved arrows) and diphenylmethylene (DPM) units generated by the photoinduced breakage of the olefinic double bond of its excitons (magenta curved arrows) in the aggregate state ( $*$  = radical, cation, and/or anion). (Lower panel) Shell-like luminogen of  $10,10',11,11'$ -tetrahydro- $5,5'$ -bidibenzol[*a,d*][7]-annulenylidene (THBA; 1), a TPE derivative, also shows AIE activity, due to the restriction to the intramolecular vibration (RIV) of its bendable vibrators (blue curved arrows) and rotatable ethylene-tethered DPM units (magenta curved arrows) in the aggregate state. Adapted and modified with permission from ref 12. Copyright 2014 Wiley-VCH Verlag GmbH & Co. KGaA.

For luminogens with vigorously vibrative moieties, their AIE effects can be interpreted by the mechanism of restriction of intramolecular vibration (RIV).<sup>12</sup> This is established on the basis of fundamental knowledge of physics that any movement consumes energy. For example, the AIE effect of  $10,10',11,11'$ -tetrahydro- $5,5'$ -bidibenzol[*a,d*][7]-annulenylidene (THBA; Figure 2, lower panel)<sup>12,21,22</sup> is partially attributed to the RIV process, because the active vibrational motions of the flexible parts in THBA play an important role in the radiationless dissipation of the exciton energy.<sup>12,22</sup>

Compared to AIE, the ACQ study has a much longer history.<sup>1</sup> As such, its working mechanism has been well understood.<sup>2</sup> Although luminophores with ACQ characteristics (ACQphores) have been utilized for practical applications, it is hard to explore their full potentials in the solid state. Since the solid of a luminophore is often inferior to its solution in performance, if its solution emission is not efficient, there is little prospect to find real applications for its solid. The AIE effect, however, changes this general belief: the traditionally viewed useless materials can be highly functional. The processes difficult to access by conventional ACQphores can now be readily realized by AIEgens. AIE has opened new avenues to an array of possibilities with great potential for high-tech innovations.<sup>12–20</sup> Unlike ACQphores that perform better as isolated species, AIEgens perfectly embody the philosophical idea of Aesop: “United we stand, divided we fall!” In other words, the power of unity is impeccably annotated by the unique AIE effect. In an AIE system, the aggregates shine brighter than their individual parts, following the general collective quantity–effect rule.

What kind of insights can we gain from AIE research? Studies of light emissions from isolated molecules of luminophores in dilute solutions have helped us grasp fundamental understanding of radiative processes.<sup>23–27</sup> The non-radiative processes of the molecular species, however, have been much less studied. To decipher AIE process, the first step is to learn emission quenching of single molecules of AIEgens by radiationless processes in the solution state. While photophysical processes

have usually been investigated in solutions,<sup>23–27</sup> emissions in the aggregate state are more relevant to real-world applications. Photophysical processes of luminophore aggregates, however, have not been well understood. Filling the gap of knowledge in these areas will help draw a complete figure of the photophysical processes. This is why AIE research is so important.

Study of AIE phenomena will widen and deepen our understanding of the fundamentals lying in the photophysical processes. It will help us learn more about the non-radiative pathways that lead to the non-emissive solution state and understand the underlying causes of the aggregate state that brings about radiative transition. The AIE study may potentially generate new theorems and models for luminescence processes. Just as the fundamental knowledge gained thus far has given rise to myriads of high-performance luminophores,<sup>12–20</sup> with a clearer and more developed picture of the photophysical processes, the AIE study offers a platform to access new areas that have never been explored before.

Once we understand the fundamentals, we can then design and create new luminogen systems and exploit their unique functions and utilities. The new knowledge gained through AIE research can be used as principles to rationally guide development of new processes and exploration of new applications. With deeper insights and better understanding into AIE processes, light emissions can be controlled for constructive purposes while averting destructive effects. Luminogens can be structurally tailored for specific high-tech applications with enhanced performances and reduced deficiencies, as opposed to relying on chance. With the understanding that active intramolecular motions can effectively dissipate exciton energy and that restriction of intramolecular motions (RIM) can activate radiative transition, numerous opportunities can be explored and many hitherto inaccessible areas will become accessible. Indeed, the application of AIE principle has triggered new developments in an array of fields, ranging from bioimaging, chemosensing, optoelectronics to stimuli-responsive systems (Figure 3).<sup>12–20</sup>

In principle, any approaches that can activate the RIM process can be utilized to develop new bio- and chemosensing systems.<sup>12</sup> AIEgens have been successfully used as fluorescence “turn-on” or “light-up” biosensors,<sup>16,19,28</sup> DNA visualizers,<sup>29</sup> and probes for biological processes such as protein fibrillation.<sup>30</sup> AIE effects have enabled specific imaging of organelles,<sup>12,31–33</sup> cells,<sup>12,19</sup> microorganisms,<sup>34</sup> and tissues<sup>12,35</sup> at molecular, cellular, and tissue levels. Highly luminescent nanoobjects, such as AIE dots, are now shining in the area of bioimaging.<sup>12,19</sup> Multifunctional systems constructed from AIEgens have also been developed for biomedical imaging, diagnosis, and therapy.<sup>12,19,36</sup> Diverse AIE-based chemosensing systems have been explored for a wide range of analytes, such as ions,<sup>37</sup> explosives,<sup>38</sup> and fingerprints,<sup>39</sup> the detection of which are of importance for environmental protection, water quality control, homeland security, and forensic investigation.

AIEgens have also been incorporated into many optoelectronic systems, because the AIE effect can completely circumvent the notorious ACQ effect experienced by conventional luminophores in the solid state. Taking advantage of the practically useful AIE effect, OLED devices,<sup>12</sup> optical waveguides,<sup>32</sup> circularly polarized luminescence (CPL) systems,<sup>40</sup> and liquid crystal displays<sup>41</sup> with efficient solid-state emissions have been successfully built. A large variety of AIEgens have been explored and developed into novel intelligent materials.<sup>12,42</sup> Such luminogens are susceptible to external stimuli, such as mechanical

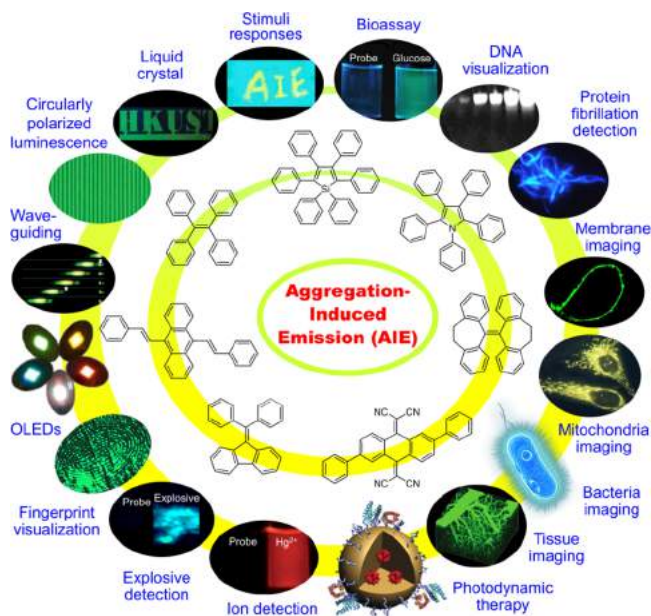


**Figure 3.** Typical examples of structural motifs of AIEgens and their technological applications. Adapted and modified with permission from refs 12 (Copyright 2014 Wiley-VCH Verlag GmbH & Co. KGaA, Weinheim), 28 (Copyright 2011 American Chemical Society), 29 (Copyright 2013 Wiley-VCH Verlag GmbH & Co. KGaA, Weinheim), 30 (Copyright 2012 American Chemical Society), 31 (Copyright 2014 American Chemical Society), 32 (Copyright 2013 Royal Society of Chemistry), 33 (Copyright 2013 Wiley), 34 (Copyright 2014 Wiley-VCH Verlag GmbH & Co. KGaA, Weinheim), 35 (Copyright 2013 Wiley-VCH Verlag GmbH & Co. KGaA, Weinheim), 36 (Copyright 2014 Royal Society of Chemistry), 37 (Copyright 2014 Wiley-VCH Verlag GmbH & Co. KGaA, Weinheim), 38 (Copyright 2014 American Chemical Society), 39 (Copyright 2012 Royal Society of Chemistry), 40 (Copyright 2012 Royal Society of Chemistry), 41 (Copyright 2014 Wiley-VCH Verlag GmbH & Co. KGaA, Weinheim), and 42 (Copyright 2013 Wiley-VCH Verlag GmbH & Co. KGaA, Weinheim).

force, temperature change, pH variation, toxic vapor, and photonic irradiation. A number of stimuli-responsive AIE-active smart materials with combined mechano-,<sup>20</sup> thermo-,<sup>43</sup> vapo-<sup>44</sup>, and photochromisms<sup>45</sup> have been designed and created.

Because of its fundamental importance and practical implications, AIE study has attracted many researchers with different academic and technological backgrounds to this fascinating wonderland. Since our first AIE paper published in 2001, the outputs of AIE research (the numbers of published papers and citations) have undergone exponential growths as indicated by the data retrieved from the *Web of Science* (Figure 4, upper panel). The numbers of annual publications and citations on AIE have already surpassed the 500 and 10 000 milestones, respectively, in 2014. As revealed by the Thomson Reuters Essential Science Indicators, AIE has been ranked no. 3 among the Top 100 Research Frontiers in the field of Chemistry and Materials Science in 2013 (Figure 4, lower panel), reflecting the increasing global interest towards the AIE research. As a result of this worldwide research enthusiasm, a very large number of scientific and technical papers have been published in recent years. For the benefit of the people who are working in the field or planning to enter the area, it is high time to prepare a comprehensive review article on the AIE research.

We intend to undertake the task herein. However, because there is an amazingly large amount of reported work, it is difficult, if not impossible, for us to discuss all the published results. While

we are forced to be selective, we still try to offer an integrated picture through the introduction and discussion of representative AIE systems in this review article. We will first carefully elaborate on the working principle of AIE and convey the mechanistic insights gained from the experimental measurements and theoretical simulations. We will then demonstrate how to transform traditional ACQphores into new AIEgens, followed by the presentation of a series of new AIEgens derived from the RIM principle, including the “typical” hydrocarbonic, heteroatomic, macromolecular, and organometallic systems as well as the “atypical” or unorthodox systems. Finally, we will recap the research efforts devoted towards the exploration of technological applications of the new AIEgens, ranging from biomedical imaging to chemical sensing to optoelectronic devices and finally to stimuli-responsive systems, through the judicious utilization of the AIE effect.

## 2. WORKING MECHANISMS

Decipherment of the underlying mechanisms for the AIE phenomena is of great importance to the quest for fundamental knowledge of photophysics, and just as crucial, it will guide our endeavors to design novel luminogens, explore practical applications, and promote technological innovations. Since the coinage of the AIE concept in 2001, researchers have shown persistent thirst for learning what are the real mechanistic causes for the AIE phenomena. A number of mechanistic pathways have been hypothesized, including conformational planarization, J-aggregate formation, *E/Z* isomerization, twisted intramolecular charge transfer (TICT), and ESIPT. None of them, however, can be fully supported by the experimental data or applicable to all the reported AIE systems. In our recent review article published in *Advanced Materials*,<sup>12</sup> we have carried out a study of mechanistic comparison, pieced together the scattered information on the manifold AIE mechanisms proposed by different research groups, and drawn a clear picture on the unique AIE processes. To avoid repetition, we herein will straightforwardly elucidate the experimental and theoretical works that have provided solid proof to the three main hypotheses for the mechanistic causes of the AIE effects, that is, RIR, RIV, and RIM.

### 2.1. Restriction of Intramolecular Rotations (RIR)

The RIR mechanism was proposed on the basis of careful and systematic study of an emblematic AIEgen, namely, HPS. The structure of HPS was closely examined.<sup>46</sup> In a single HPS molecule, the silole core is decorated with a total of six phenyl rings through single bonds, which makes the molecule conformationally flexible. Its crystal data given in Figure 5 show a number of structural characteristics commonly found in many other AIEgens. The HPS molecule takes a propeller-like conformation, as revealed by the large torsion angles between the peripheral phenyl rings and the central silacyclopentadiene or silole plane (Figure 5A). Owing to its highly twisted conformation caused by the steric repulsion between the neighboring phenyl rings, a dense face-to-face packing structure is not possible and as a result, the HPS molecules experience practically no  $\pi-\pi$  stacking interaction in the solid state (Figure 5B).

The long distances (9.363–10.043 Å) between the silole cores in the unit cell of HPS crystal manifest the lack of strong chromophore interactions (e.g.,  $\pi-\pi$  stacking interaction) that lead to radiationless relaxations and bothachromical shifts often seen in the crystals of the conventional luminophores or ACQphores. On the other hand, as shown in Figure 5C, massive

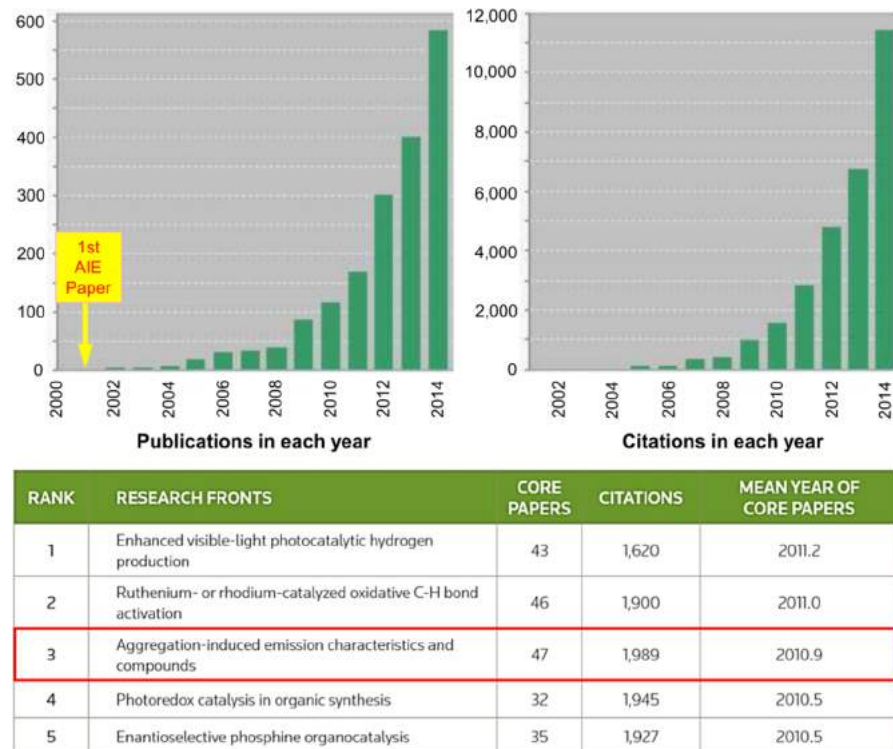


**Figure 4.** (Upper) Histograms showing the annual numbers of publications and citations on AIE in the past decade (data searched from *Web of Science* using the keywords of “aggregation-induced emission” on April 25, 2015). (Lower) The topic of “Aggregation-induced emission characteristics and compounds” ranked 3rd in the Top 100 Research Fronts in the field of Chemistry and Materials Science by Thomson Reuters in 2013. These materials are reproduced under a license from Thomson Reuters. You may not copy or re-distribute these materials in whole or in part without the prior written consent of Thomson Reuters.

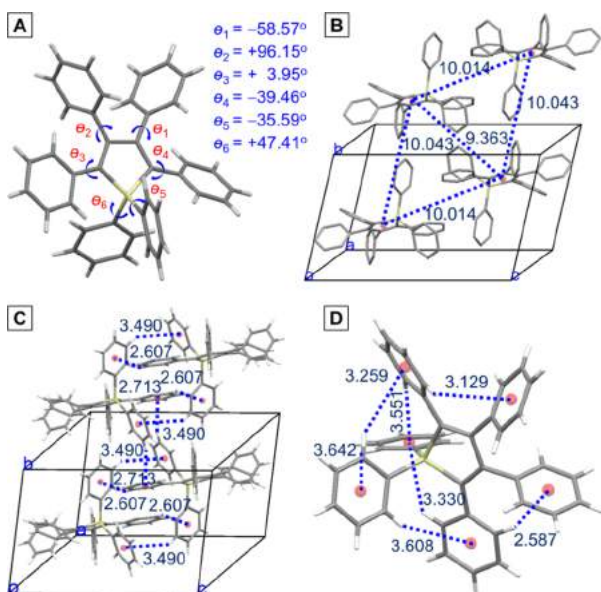


**Figure 5.** (A) Molecular conformation of HPS and its dihedral angles. (B) Unit cell of HPS crystal. (C) Intermolecular C–H $\cdots$  $\pi$  interactions in two crystal cells along axis  $b$ . (D) Intramolecular C–H $\cdots$  $\pi$  interactions in a single molecule. The crystal structures are retrieved free of charge from the Cambridge Crystallographic Data Centre (CCDC-195948) via [www.ccdc.cam.ac.uk](http://www.ccdc.cam.ac.uk).

intermolecular C–H $\cdots$  $\pi$  interactions exist between the adjacent HPS molecules. These non-covalent interactions help to hold the AIEgen molecules together, stabilize the crystal packing, and restrict the rotational motions of their phenyl rings. Further

analysis of the HPS crystal structure reveals the presence of multiple intramolecular C–H $\cdots$  $\pi$  interactions with short contact distances (2.587–3.642 Å; **Figure 5D**). Such kinds of intramolecular interactions and the non-planarity of the HPS molecules have a mutually beneficial relationship. Working together, the multiple inter- and intramolecular C–H $\cdots$  $\pi$  interactions synergistically constrains the HPS molecules in the crystal lattices and suppresses the rotations of their phenyl rings in the solid state.

The structural analysis of HPS helps to understand its photoluminescence (PL) behaviors. Its quantitative AIE effect is shown in **Figure 6A**.<sup>46</sup> HPS is very soluble in many common organic solvents, such as THF, chloroform, acetonitrile, and acetone, less soluble in methanol, and totally insoluble in water. Water is hence usually used as a non-solvent to induce aggregation of HPS molecules in a water-miscible solvent system. Dilute solution of HPS in acetone is non-emissive, with a negligibly low quantum yield of fluorescence ( $\Phi_F \sim 0.1\%$ ). The  $\Phi_F$  value shows insignificant change until  $f_w$  reaches  $\sim 50$  vol % but starts to increase swiftly afterwards. At  $f_w = 90$  vol %, the  $\Phi_F$  is boosted to 22%, which is  $\sim 220$ -fold higher than that of the acetone solution. The RIR mechanism is responsible for the AIE effect of HPS. In solution, its six phenyl rotors can dynamically rotate against the silole stator via the single-bond axes, which serves as a non-radiative pathway for the excitons to decay. In aggregates, such rotations are suppressed due to the physical constraint. The radiationless pathway is thus blocked, while the radiative channel is opened.

Using siloles and TPE derivatives as model AIEgens, the rationality of the RIR principle has been verified by a string of control experiments that are so designed as to externally and

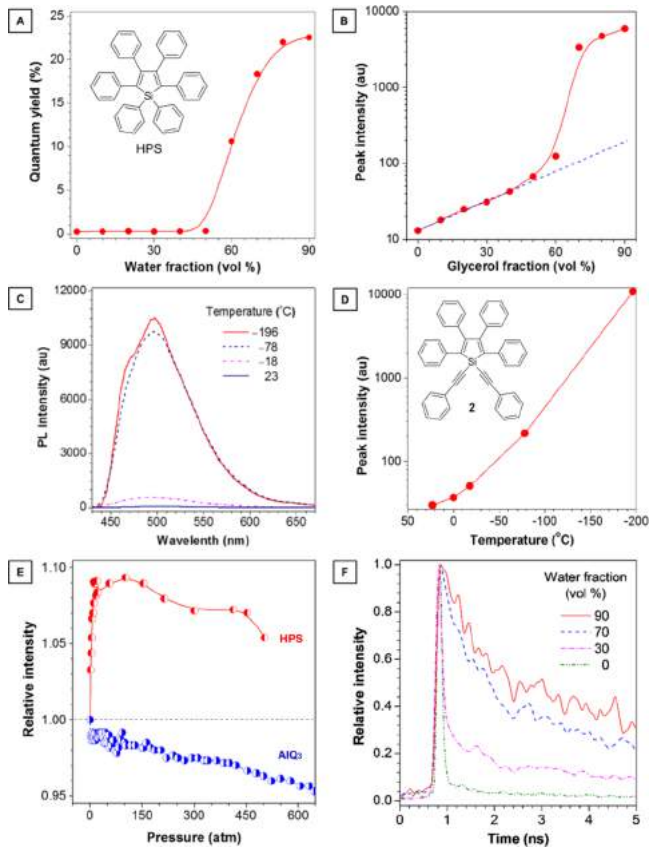


**Figure 6.** Plots of (A) fluorescence quantum yield of HPS vs water fraction in acetone/water mixtures and (B) its PL peak intensity vs glycerol fraction in glycerol/methanol mixtures; [HPS] = 10 μM. (C) PL spectra of 2 in 1,4-dioxane at different temperatures and (D) effect of temperature on its PL peak intensity; [2] = 10 μM. Panels A–D are reprinted from ref 46. Copyright 2003 American Chemical Society. (E) Effect of pressure on PL peak intensity of HPS film; data for AlQ<sub>3</sub> film shown for comparison. Reprinted with permission from ref 47. Copyright 2008 Royal Society of Chemistry. (F) Time-resolved fluorescence of HPS in DMF/water mixtures. Reprinted from ref 48. Copyright 2005 American Chemical Society.

internally manipulate the intramolecular rotations.<sup>46–68</sup> Examples of such manipulations are shown in Figure 6. Stronger emission is expected for AIEgens in more viscous media because high viscosity should slow down the intramolecular rotations. Considering that the viscosity of glycerol (934 cP at 25 °C) is three orders of magnitude higher than that of methanol (0.544 cP), the PL measurements of HPS were conducted in glycerol/methanol mixtures. With increasing viscosity of the mixture, the PL peak intensity of HPS linearly increases on the semilog scale for glycerol fractions ( $f_G$ ) in the range of 0–50 vol % at room temperature (Figure 6B). The luminescence enhancement in this  $f_G$  region should be primarily attributed to the viscosity effect, because the HPS molecules are soluble in these mixtures. In the glycerol/methanol mixtures with  $f_G > 50$  vol %, the sharp increase in the PL intensity is due to the formation of HPS nanoaggregates caused by the poor solubility of the silole molecules in the alcoholic mixtures with poor solvating power.

Since decreasing temperature, especially cryogenic cooling, can also retard the intramolecular rotations and fortify the RIR effect, the temperature effects on the light emissions were investigated for HPS as well as its derivative 2. When the dioxane

solutions of 2 are cooled, their emissions are monotonically but nonlinearly increased (Figure 6, panels C and D).<sup>46</sup> Dynamic NMR spectra were taken at different temperatures to further verify the RIR process. The very fast conformational exchanges caused by the vigorous intramolecular rotations at room temperature result in sharp NMR peaks. The peaks are broadened by cooling as the intramolecular rotations slow down at low temperature. A simple heating–cooling cycle of HPS in the solid state has been carried out to monitor the variation in the emission intensity. The emission of HPS is quickly diminished upon heating to its melting point and is clearly recovered after cooling back to room temperature. Increasing viscosity and reducing temperature both impede the intramolecular rotations, thus activating the radiative transitions and boosting the emission intensity.

Unlike viscosity and temperature, pressure exerts more complicated effects on the light emission process of HPS (Figure 6E).<sup>47</sup> Upon applying external pressure, the emission intensity of HPS rises swiftly to a plateau. However, further increasing pressure results in slightly and slowly reduced emission intensity. Theoretically, external pressurization imposes antagonistic effects on the luminescence process. Pressurization decreases the distance between the silole molecules. As a result, it reduces the freedom of the intramolecular rotations and enhances the light emission. On the other hand, it strengthens the intermolecular interactions and promotes the formation of such detrimental species as excimers that can weaken the light emission. The latter effect is found in the conventional luminophore systems as manifested by the result obtained from a thin solid film of tris(8-hydroxyquinolinato)-aluminum(III) (AlQ<sub>3</sub>). Its emission is weakened monotonously with increasing pressure, indicating that the pressurization enhances  $\pi$ – $\pi$  stacking interactions between the plate-like quinoline moieties.

Lifetime is a valuable parameter for evaluating the PL decay process. Time-resolved fluorescence has shed light on the AIE mechanism.<sup>48</sup> Adding water into the HPS solution not only enhances its emission but also causes a big change in its PL lifetime (Figure 6F). In DMF, a single-exponential relaxation of the excited states is observed: HPS primarily decays non-radiatively with a PL lifetime of ~40 ps. Upon addition of water, the excited states start to decay via two relaxation pathways. Increasing  $f_w$  of the DMF/water mixture leads to the formation of more nanoaggregates, resulting in a higher population of molecules that radiatively decay via a slower channel. At  $f_w = 90$  vol %, the excited states mainly decay by way of the slow channel and the lifetime for the slow component is lengthened to ~7 ns. When HPS is molecularly dissolved, the dynamic rotations of its phenyl rings quickly dissipate the exciton energy, resulting in the picosecond lifetime, whereas the aggregate formation restricts the phenyl ring rotations and spurs HPS to decay radiatively with the nanosecond lifetime. Lifetime measurements in the solutions with different viscosities and at varying temperatures have afforded results agreeing well with their PL intensity changes. The lifetime is lengthened with an increase in medium viscosity and a decrease in temperature. These observations reveal that (i) the rotational motions consume exciton energy and increase non-radiative decay rates, leading to a non-emissive state, and (ii) the restriction of the phenyl ring motions activates the radiative decay, thus switching on the luminescence process.

All the external control experiments described above strongly support the RIR mechanism and prove that the silole emission can be modulated by physical and engineering manipulations. To collect more supporting evidences, a series of structural

modifications have been done as internal control to examine whether the structural changes can affect rotational motions and tune the AIE activity.<sup>49–51</sup> Bulky isopropyl (*i*-Pr) groups are attached to the peripheral phenyl rings of HPS to see how the steric effect would influence its AIE behavior.<sup>49</sup> A group of HPS regioisomers with *i*-Pr substituents (3–5) have been synthesized to this end (Figure 7). The HPS functionalized with *i*-Pr groups

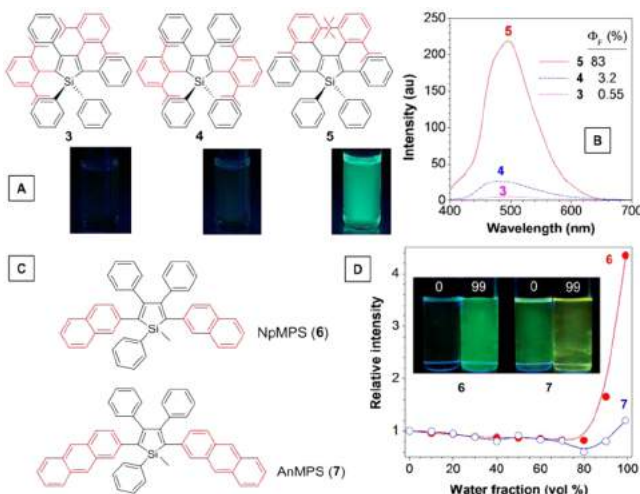


**Figure 7.** (A) Chemical structures and fluorescent photographs and (B) PL spectra of solutions of siloles 3–5 in acetone (10  $\mu$ M). Adapted from ref 49. Copyright 2005 American Chemical Society. (C) Chemical structures of siloles 6 and 7 and (D) plots of their fluorescence intensity vs water fraction in THF/water mixtures. Inset: Fluorescent photographs of 6 and 7 in THF/water mixtures ( $f_w = 0, 99$  vol %). Adapted with permission from ref 51. Copyright 2014 Royal Society of Chemistry.

at the 2,4-positions of its phenyl rings (3) is the least crowded, while the one with *i*-Pr groups at the 3,4-positions (5) is sterically most congested. Different from the HPS parent, 3–5 are fluorescent in solutions, although their emission efficiencies change dramatically with their regiostructures. The regioisomers emit blue-green luminescence in acetone with the increase in  $\Phi_F$  in the order of 5 > 4 > 3. Similar results are obtained in other solvent systems (e.g., THF), thus confirming the generality of the order of change in  $\Phi_F$ . The  $\Phi_F$  values of these regioisomers are generally higher than that of HPS, owing to the restraint on the intramolecular rotations in 3–5 by the elevated rotation barriers. The structural rigidification plays a decisive role in making 3–5 more emissive in solutions than their HPS parent.

In addition to steric effect, other effects such as electronic conjugation that may impose some influence on the RIR process have also been examined.<sup>50,51</sup> A series of silole derivatives with polycyclic aromatic substituents, i.e., naphthyl (6) and anthracyl (7) groups, at the 2,5-positions have been designed to extend the conjugation of the silole molecules (Figure 7C).<sup>51</sup> Slightly enhanced emission in solution state ( $\Phi_F = 2.4\%$ ) is observed for the naphthyl-substituted silole (6), while greatly intensified luminescence is displayed by the anthracyl-substituted silole (7) under identical conditions with a solution-state  $\Phi_F$  of 11.0%. The  $\Phi_F$  value of 6 in the film state is 37.0%, which is ~15-fold higher than its solution value. In sharp contrast, 7 shows a film-state  $\Phi_F$  (14.0%) barely enhanced as compared to that of its solution. Though the RIR process is activated and the radiative transition channels are opened in the aggregate state, the quenching effect due to the  $\pi$ – $\pi$  stacking interactions between the anthracene

rings is also activated. Hence, the solid film of 7 exhibits lower luminescence efficiency and larger red shift than that of 6. Clearly, the elongation in the electronic conjugation has antagonistic effects on the emissions of the AIEgen in the solution and aggregate states, thus resulting in a weak AIE effect.

Apart from the silole systems, a great deal of work has been done with other AIEgens, especially TPE derivatives, aiming at corroborating the RIR principle.<sup>52–60</sup> A variety of approaches to activate the RIR process have been smartly designed for this purpose. For instance, a new strategy to restrict intramolecular rotations of AIEgens based on host–guest inclusion has been developed.<sup>52</sup> TPE is tethered with a series of cyclodextrins (CDs) through esterification reaction between  $\alpha$ ,  $\beta$ , or  $\gamma$ -CD and monocarboxylic acid-substituted TPE, furnishing TPE-CD adducts. TPE in DMSO emits weakly at 470 nm out of the active intramolecular rotations of its phenyl rotors. The TPE decorated with the largest CD ring, i.e., TPE- $\gamma$ -CD, shows no obvious change in fluorescence intensity as compared to bare TPE. Drastically increased intensity, however, is observed for TPE- $\beta$ -CD (8 in Figure 8A), because  $\beta$ -CD is smaller in cavity

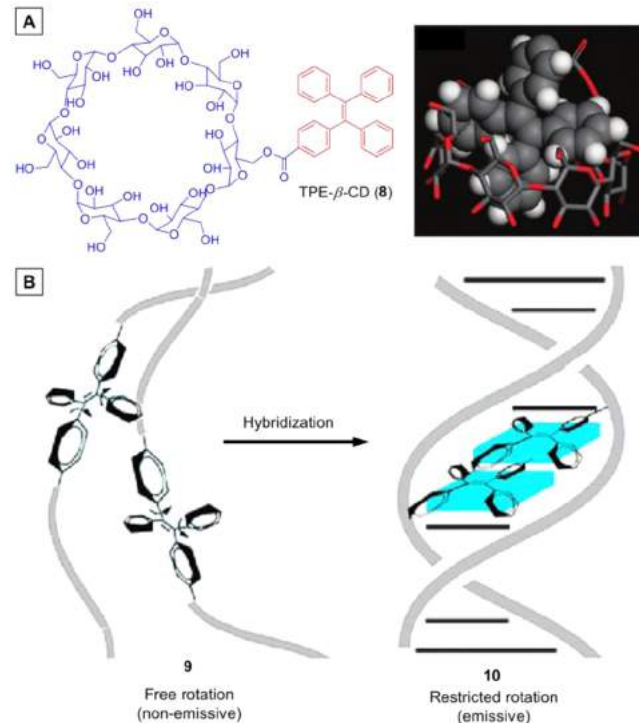


**Figure 8.** (A) Chemical and geometric structures of TPE- $\beta$ -CD. Reprinted with permission from ref 52. Copyright 2013 Royal Society of Chemistry. (B) Schematic illustration of activation of AIE effect by DNA hybridization process. Adapted with permission from ref 53. Copyright 2013 Royal Society of Chemistry. Adapted from ref 53 which was published by the Royal Society of Chemistry and licensed under the terms of the Creative Commons Attribution 3.0 Unported Licence via <http://creativecommons.org/licenses/by/3.0/>.

size. Following the decreasing trend in cavity size, TPE- $\alpha$ -CD exhibits the highest fluorescence efficiency in solution. The increase in the emission intensity is attributed to the strong host–guest interaction between the TPE unit and the CD cavity. In the small CD cavity, the intramolecular rotations of the phenyl rings and diphenylmethylene units become more restricted and the radiative relaxation becomes more efficient.

The RIR process can also be modulated by the DNA hybridization process.<sup>53</sup> Dialkynyl-substituted TPE (TPE-DA) units have been facilely incorporated into oligonucleotides to afford TPE-DNA bioconjugates. In the single-stranded form (e.g., **9** in Figure 8B), only a small increase in emission intensity is observed in the THF/water mixture with  $f_w = 95$  vol % when compared to pure TPE-DA. After DNA hybridization, notable emission enhancement relative to that of the single strand is observed for the double-stranded hybrid (**10**). Quantum yield in the hybrid can reach the value close to that of the TPE-DA aggregate. Upon hybridization, the TPE-DA units are sandwiched by the complementary DNA strands, resulting in supramolecular assembly due to the hydrogen bonds between the matching base pairs. This greatly increases the physical constraint experienced by the TPE moieties, which prevents the phenyl-ring rotations from dissipating the excited-state energy and hence promotes the radiative decay.

Enhancing the steric effect is an efficient means to activate the RIR process, as revealed by the work done on the substituted silole systems (i.e., **3–5**). Analogous studies have also been conducted in TPE systems.<sup>54,55</sup> The phenyl rings in TPE have been decorated with multiple methyl groups at the *o*-positions to examine how the intramolecular steric effects affect its photochemical properties.<sup>54</sup> The sterically crowded TPE derivative with four methyl (or tetramethyl) groups, i.e., TPE-TM (**11**), lost its AIE activity (Figure 9A), directly validating the RIR hypothesis. In THF solution, **11** gives a bright cyan emission with a  $\Phi_F$  of 64.0%, while almost no fluorescence is observed by the naked eye for TPE. The *o*-methyl groups efficiently suppress non-radiative decay that is active in dilute solution of TPE due to the rotational freedom of its phenyl rotors. For **11**, the bulkiness of the four methyl groups elevates rotational barriers on account of the large steric hindrance.

Another internal control of intramolecular rotations has been performed with TPE derivatives taking on folded *Z*-conformation.<sup>55</sup> TPE-BBP (**12**) with two biphenyl (BBP) substituents at the *p*-positions of TPE has been prepared as a control. TPE-BBP behaves like a typical AIEgen (Figure 9B). With BBP groups located at the *o*-positions of TPE, however, the folded luminogen (*Z*)-*o*-TPE-BBP (**13**) performs in a different manner (Figure 9C). Its  $\Phi_F$  value measured in a dilute THF solution is 45.0%, much higher than that of **12** (0.62%). As revealed by the crystal structure of **13**, its aryl rings highlighted in red in Figure 9C are located in a parallel pattern. As the rotations of such aryl rings are restricted due to the intramolecular through-space  $\pi$ -interaction and steric effect, the probability of the non-radiative decay of the excited states is reduced, leading to the reasonably efficient emission in the solution state. The aggregates of **13**, e.g., its solid film, show intensified emission ( $\Phi_F = 72.0\%$ ), as the rotations of the “free” phenyl rings (blue colored in Figure 9C) have been blocked by the spatial constraints.

Intramolecular rotations can also be hindered by coordination processes.<sup>56,57</sup> Tetrakis(bisurea)-decorated TPE (**14**) is only weakly emissive in the solution state but exhibits “turn-on” fluorescence over a broad concentration range upon complexation with anions such as sulfates and phosphates (Figure 10A).<sup>56</sup> Similar phenomenon has been observed in the coordination system based on another TPE derivative and cations.<sup>57</sup> Solvated tetra(4-pyridylphenyl)ethylene (**15**), for example, is non-emissive, while upon addition of  $Hg^{2+}$  cations, the fluorescence is turned on (Figure 10B). The conformational rigidification of **15** is realized through the coordination between  $Hg^{2+}$  ions and pyridine moieties in **15**. In these coordination-assisted

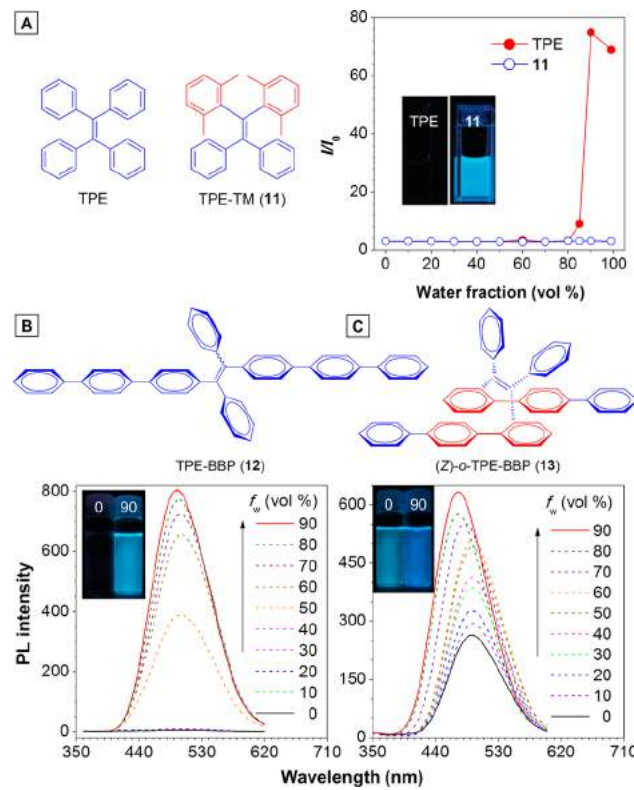


**Figure 9.** (A) Plots of  $I/I_0$  of TPE and TPE-TM (**11**) vs water fractions in THF/water mixtures (10  $\mu$ M), where  $I_0$  and  $I$  are the PL intensities in THF solution and a THF/water mixture, respectively. Inset: fluorescence photographs of TPE and **11** in THF solutions. Reprinted with permission from ref 54. Copyright 2014 Royal Society of Chemistry. PL spectra of (B) TPE-BBP (**12**) and (C) (*Z*)-*o*-TPE-BBP (**13**) in THF/water mixtures with different water fractions ( $f_w$ ). Inset: Photographs of (B) TPE-BBP and (C) (*Z*)-*o*-TPE-BBP in THF/water mixtures ( $f_w = 0, 90\%$ ) taken under the illumination of a UV lamp. Reprinted with permission from ref 55. Copyright 2013 Royal Society of Chemistry.

fluorescence “turn-on” systems, before ion-luminogen complexation, the intramolecular rotations actively consume exciton energy, resulting in non-emissive solutions. Once the coordination complexes are formed after the ion addition, the rotatory units in the ligands face higher rotational barriers and have less rotational freedom, hence triggering the light emission.

Locking the rotors by means of covalent bonding is the most straightforward and effective way to activate the RIR process.<sup>58–60</sup> The phenyl rings of TPE have been conveniently locked with “O” bridges (Figure 11A).<sup>58</sup> In TPE-O (**16**), one set of the phenyl rings are locked with an “O” bridge. Its solution  $\Phi_F$  rises to 4.6%, in comparison to TPE with a negligible  $\Phi_F$ . The solution  $\Phi_F$  for the TPE derivative with two pairs of phenyl rings locked (TPE-2O or **17**) is further increased to as high as 30.1%. By locking the phenyl rings with the O bridges, the covalent bonds suppress the rotational motions. The exciton energy cannot be depleted by the radiationless decay, thus making the molecule emissive even in isolated state. Both solution and crystalline states of **17** are emissive. It is neither AIE- nor ACQ-active. This is because **17** still adopts a twisted conformation preventing its molecules from close packing that forms detrimental species such as excimers.

AIEgens **18** and **22** shown in panels B and C of Figure 11 can be transformed into ACQphores by directly hooking up their aryl rotors.<sup>59,60</sup> The diphenylphenanthrene derivatives (**19–21**)

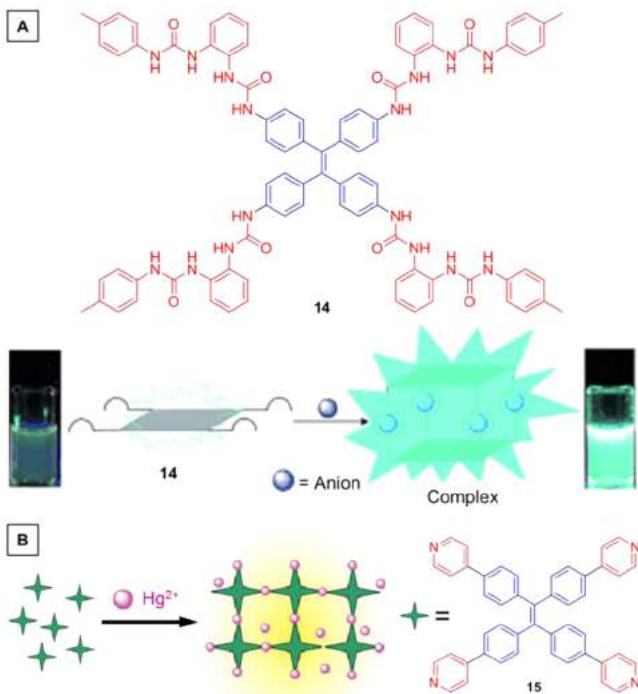


**Figure 10.** Schematic illustrations of coordination-induced restriction of intramolecular rotations based on luminogens (A) 14 (reprinted with permission from ref 56. Copyright 2014 Wiley-VCH Verlag GmbH & Co. KGaA) and (B) 15 (adapted with permission from ref 57. Copyright 2012 Royal Society of Chemistry).

obtained from UV-induced cyclization of 18 are AIE-inactive.<sup>59</sup> Their solution emissions are quenched in the aggregate state (Figure 11B). Similar to 16 and 17, the two remaining free phenyl rings in 19–21 cannot consume the exciton energy via rotational motions. Dibenzofulvene derivative 22 is an AIEgen. Dibenzofulvene derivative 22 is an AIEgen.

manifested by its faint and strong solution and aggregate emissions, respectively. Its locked form (23), however, shows obvious ACQ effect (Figure 11C).<sup>60</sup> It emits intensive and weak emissions in the solution ( $\Phi_F = 38.0\%$ ) and solid ( $\Phi_F = 5.5\%$ ) states, respectively. In the solution state, the intramolecular rotation of its remaining free phenyl ring is insufficient to consume the exciton energy non-radiatively. On the other hand, 23 becomes more planar in shape in the crystalline state. Such a conformation favors face-to-face stacking and  $\pi-\pi$  interaction, which quenches its emission in the aggregate state.

Various analytical tools such as terahertz time-domain spectroscopy (THz-TDS) have been used to gain experimental support to the RIR mechanism.<sup>61</sup> Electromagnetic radiation at frequencies of tetrahertz ( $10^{12}$  Hz, 4.1 meV) is low enough in energy to probe low-frequency intermolecular interactions and some low energy intramolecular motions. It is sensitive to the relaxation dynamics in condensed matter. The THz-TDS study in the solid state of TPE enables direct measurement to test the validity of the RIR hypothesis. TPE has been analyzed in a temperature range of 80–280 K. The measurement verifies that the phenyl ring rotations occur at the THz frequencies. TPE shows 38% higher absorption in the frequency range of 0.1–2.2 THz at 280 K. The overall higher absorption at the higher temperature than the lower temperature is in nice agreement with theoretical prediction.

Apart from experimental investigations, a series of theoretical studies in pursuit of decoding AIE mechanisms have also been carried out.<sup>62–68</sup> Shuai's team has played a leading role in this endeavor.<sup>63–67</sup> For example, Shuai et al. have done computational simulations of PL processes of DCDPP (24) and its locked-form DCPP (25; Figure 12).<sup>65,66</sup> Experimental results and theoretical calculations prove that 24 is an AIEgen, whereas 25 is an ACQphore.<sup>68</sup> As shown in Figure 12A, 24 shows increased PL efficiency with decreasing temperature in either the

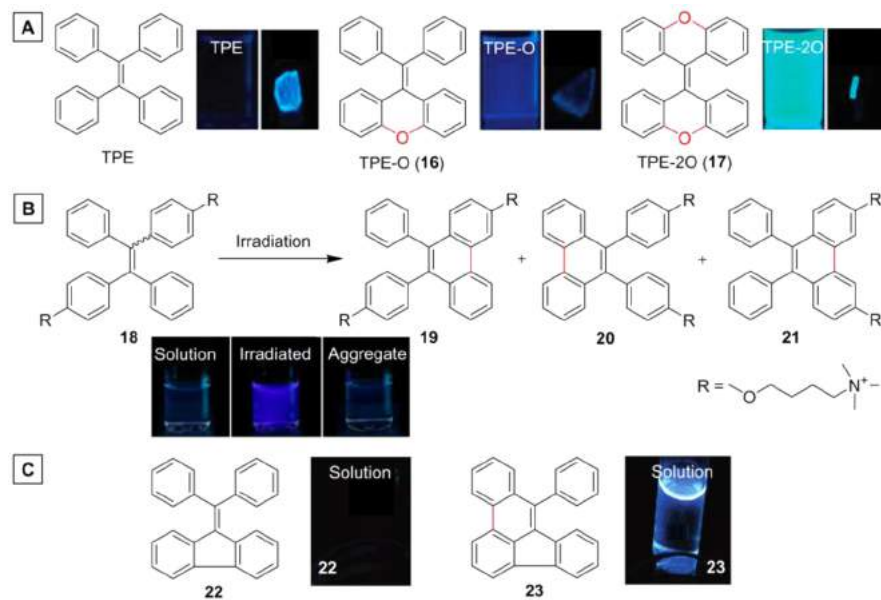


**Figure 11.** (A) Fluorescent photographs of solutions and crystals of TPE and its derivatives with “O” bridges (16 and 17). Reprinted with permission from ref 58. Copyright 2012 Royal Society of Chemistry. (B) Scheme for photocyclizations of TPE derivative 18 and fluorescent photographs of 18 before and after irradiation in solutions and the aggregates of its photocyclization products (19–21). Reprinted from ref 59. Copyright 2014 American Chemical Society. (C) Fluorescent photographs of AIEgen 22 and ACQphore 23 in solutions. Reprinted from ref 60. Copyright 2007 American Chemical Society.

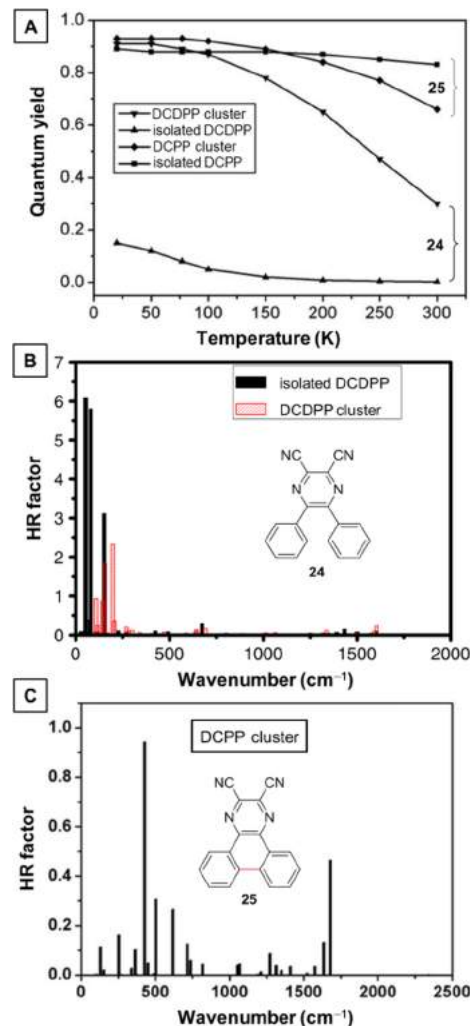


**Figure 12.** (A) Calculated fluorescence quantum yields of DCDPP (**24**) and DCPP (**25**) at different temperatures. Calculated Huang–Rhys (HR) factors vs normal mode wavenumbers for (B) isolated DCDPP and cluster and (C) DCPP cluster. Panels A and C are adapted with permission from ref 66. Copyright 2012 Wiley Periodicals, Inc. Panel B is reprinted with permission from ref 63. Copyright 2013 Elsevier B.V.

isolated or aggregated state. A much smaller temperature effect is observed in the case of **25**.

Taking a quantum mechanics and molecular mechanics (QM/MM) approach, the systems of **24** and **25** are modeled, which provides key insights into their photophysical behaviors in different states. Panels B and C of Figure 12 depict Huang–Rhys (HR) factors vs their normal modes. The HR factor describes the vibrational quanta that ultimately determine non-radiative relaxation rates.<sup>67</sup> In the case of isolated **24**, three modes with large HR factors exist in the low frequency region (55.76, 82.97, and 157.25 cm<sup>-1</sup>), signifying that a large amount of its excited-state energy is consumed by these normal modes (Figure 12B). Its cluster, however, shows significantly smaller HR factors in a somewhat higher frequency region, indicative of a substantial reduction in the excited-state energy dissipation via the low frequency vibrations, i.e., the phenyl ring twisting. In contrast, both isolated and clustered forms of **25** do not display low frequency normal modes featured by AIEgens but show much smaller HR factors in a much higher frequency region (e.g., 415.95 and 1582.06 cm<sup>-1</sup>; Figure 12C). The theoretical calculations thus offer clear support to the RIR principle.

To summarize this subsection, all the results expounded above, that is, the data obtained from external physical and engineering controls to internal chemical and structural modifications and from experimental measurements to theoretical calculations, have provided solid evidence to verify the RIR hypothesis for the rotatory AIEgen systems.

## 2.2. Restriction of Intramolecular Vibrations (RIV)

As the AIE study advances, new AIEgens are discovered, whose AIE processes cannot be explained by the RIR mechanism. THBA is such an example.<sup>21,22</sup> It has no rotatable units, as its phenyl rings are locked by a pair of ethylene tethers. However, it exhibits AIE activity: it is non-emissive in solution but highly luminescent as an aggregate (Figure 13). Rotational motions are

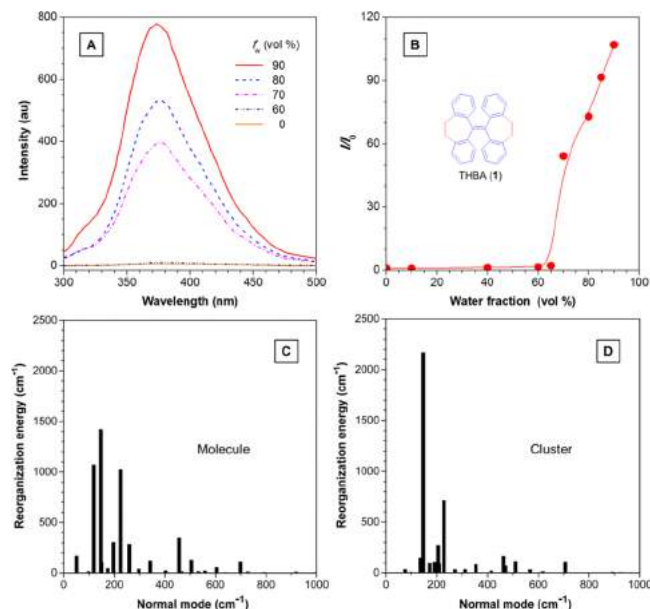


**Figure 13.** (A) PL spectra of THBA (**1**) in THF/water mixtures with different fractions of water ( $f_w$ ) and (B) change in PL intensity of **1** with water fraction ([**1**] = 20  $\mu$ M). Plots of reorganization energy vs normal mode wavenumbers for excited states of (C) molecular and (D) clustered species of **1**. Adapted with permission from ref 22. Copyright 2014 Wiley-VCH Verlag GmbH & Co. KGaA.

known to consume energy, and vibrational motions should work similarly. In the light of this, RIV is envisioned to be responsible for the AIE effect of THBA. Indeed, further investigations testify that the vibrational motions of the tethered phenyl rings are the source of the exciton energy consumption.<sup>22</sup> QM/MM modelling results depicted in Figure 13C clearly show that the isolated THBA has six normal modes that consume significant amounts of excited-state energy (each with a reorganization energy  $>200$  cm<sup>-1</sup>, resulting in a total energy of 5679 cm<sup>-1</sup>). In comparison, for THBA in the cluster, there are only three normal modes consuming significant amounts of excited-state energy ( $\sim 4016$  cm<sup>-1</sup>; Figure 13D). In the cluster, the combination of a decrease in the number of vibrational normal modes and a loss of  $\sim 30\%$  in the exciton energy consumption due to RIV enables THBA to decay radiatively, leading to the observed AIE effect.

The RIV hypothesis has been further validated by other AIEgen systems.<sup>69–72</sup> Iyoda et al. have reported a dibenzocyclooctatetraene-based AIEgen (**26**) which is non-emissive in the solution state but fluorescent in the crystalline state.<sup>70</sup> The AIEgen consists of three benzene units connected by two cyclooctatetraene (COT) cores (Figure 14A). Because of the

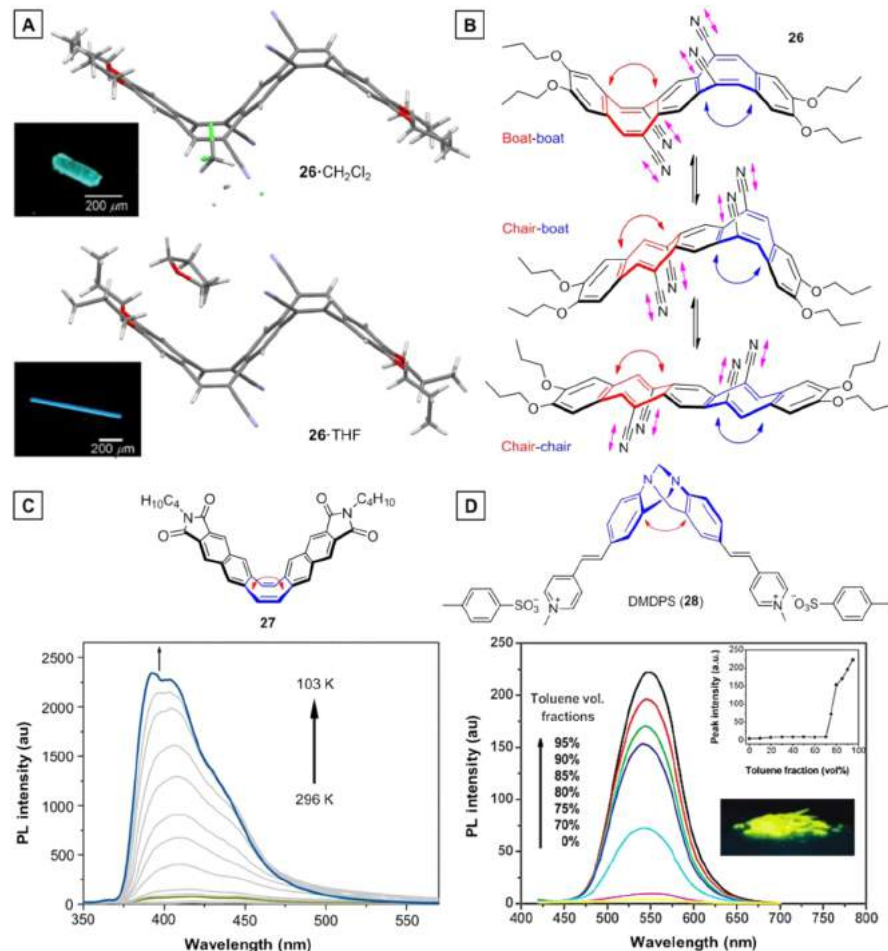


**Figure 14.** (A) Crystal structures and fluorescent photographs of **26**·CH<sub>2</sub>Cl<sub>2</sub> and **26**·THF. Crystal structures retrieved free of charge from the CCDC (773169 and 773170) via [www.ccdc.cam.ac.uk](http://www.ccdc.cam.ac.uk). Photographs reprinted with permission from ref 70. Copyright 2013 Wiley-VCH Verlag GmbH & Co. KGaA. (B) Possible vibrational motions and conformational changes of **26** in molecularly dispersed state. (C) Temperature-dependent PL spectra of **27** in 2-methyltetrahydrofuran;  $T = 103\text{--}296\text{ K}$ ,  $[27] = 1\text{ }\mu\text{M}$ . Reprinted with permission from ref 71. Copyright 2014 Wiley-VCH Verlag GmbH & Co. KGaA. (D) PL spectra of DMDPS (**28**) in acetonitrile/toluene mixtures ( $10\text{ }\mu\text{M}$ ). Insets: Change of PL peak intensity with fraction of toluene and fluorescent photograph of **28** in the solid state. Adapted from ref 72. Copyright 2007 American Chemical Society.

ring inversion or conformation variation of the COT core, **26** is structurally flexible. As a result, in the solution state, **26** can undergo various vibrational ring inversions, giving different boat/chair-shaped conformations (Figure 14B). Such intramolecular motions non-radiatively dissipate the excited-state energy, resulting in the non-emissive solution state. In the crystal state, the conformational changes of the COT units in **26** are restricted by the intermolecular steric effects and packing, hampering the intramolecular vibrations from occurring. The non-planar structure of **26** hinders the intermolecular  $\pi\text{-}\pi$  stacking interactions. These two effects collectively make the crystals of **26** luminescent, with an emission enhancement up to 710-fold higher than that of its solution. It is noted that the cyano (C≡N) unit can vigorously vibrate. The dynamic vibrations of the multiple cyano units in the solution of **26** and the RIV effect on the cyano vibration in its crystals due to the intermolecular C–H···N hydrogen bonds may have also contributed to its marked AIE activity.

Yamaguchi et al. have also reported a COT-cored AIEgen system (**27**).<sup>71</sup> As can be seen from Figure 14C, **27** is comprised of a flexible COT core connecting two naphthaleneimide groups. It exhibits a typical AIE effect, as reflected by the absence of emission from its solution and the profound fluorescence from its

aggregates. Moreover, **27** becomes increasingly more emissive when its solution in 2-methyltetrahydrofuran, a good solvent of **27** with a freezing point of 137 K, is progressively cooled from 296 to 103 K. Similar to **26**, the AIE effect of **27** is originated from the quenching of its solution-state luminescence caused mainly by the dynamic intramolecular vibrations of the COT ring that consumes the excited-state energy as well as the aggregate-state emission induced by the RIV process, although the difficulty for the multiple carbonyl groups in the naphthaleneimide wings of **27** to vibrate in the aggregates may have also made a contribution to its AIE activity.

Other non-COT systems, such as DMDPS (**28**), have also been found to be AIE active (Figure 14D).<sup>72</sup> Composed of a lambda ( $\Lambda$ )-shaped core and a styrylpyridinium unit on each side, DMDPS arguably has rotatable moieties responsible for its AIE activity. However, the styrylpyridinium units resemble stilbene in structure. This indicates that there exists strong electronic conjugation between the two aromatic rings linked by the ethenyl C=C bond, which can decrease rotational freedom and increase the rotational barrier, making it unlikely for RIR to be responsible for the AIE effect of DMDPS. Its  $\Lambda$ -shaped core, however, allows vibrational intramolecular motions to occur, which can consume exciton energy and quench its solution-state

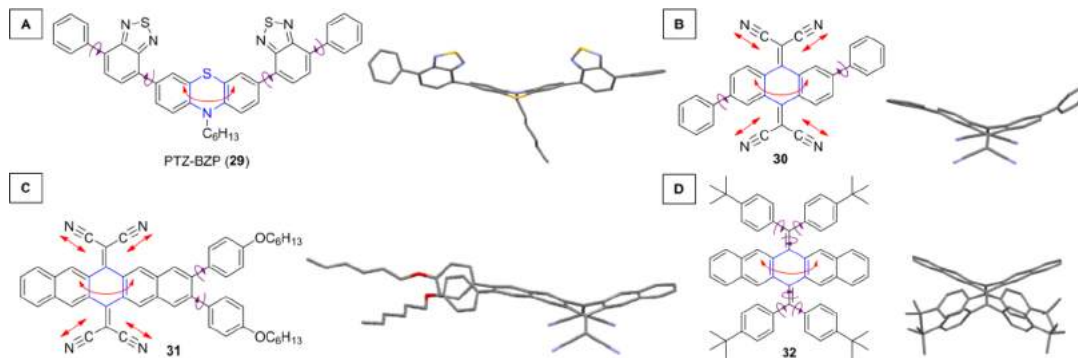


**Figure 15.** Examples of luminogens whose AIE activities are ascribed to the process of restriction of intramolecular motions (RIM). The structures are optimized by MMFF94 installed in Chem 3D.

emission. Aggregation hampers the vibrational motions, making DMDPS luminescent. Additionally, its twisted conformation or structural non-planarity is helpful for aggregate emission. It is noteworthy that 1,4-phenyl-di(*p*-ethenyl-*N*-methylpyridinium) ditosylate without the Λ-shaped Tröger's base structure shows no AIE activity. This offers further proof to the RIV mechanism for the AIE attribute of DMDPS.

The examples discussed above illuminate that in addition to rotations, vibrations (in-plane/out-of-plane bending, flapping, stretching, scissoring, wagging, twisting, rocking, etc.) can also expend excited-state energy. Mirroring the RIR principle, restricting these vibratory motions can also lead to the restoration of the luminescence process. The principle of RIV will greatly broaden the scope of AIE research, because it not only provides new insights to the photophysical fundamentals but also opens up new avenues to the design and development of new AIEgen systems as well as the exploration of their real-world, high-tech applications.

### 2.3. Restriction of Intramolecular Motions (RIM)

It has become clear that either RIR or RIV can lead to the AIE effect. Without doubt, if both RIR and RIV are involved in a system, the luminogen must be AIE active. In the AIEgen system, the working mechanism is RIM, where M (motion) includes R (rotation), and V (vibration). Some examples of such AIEgens are shown in Figure 15.

The first set of AIEgens that can be expounded using the principle of RIM contain a vibratable core and rotatable peripheries (Figure 15).<sup>73–76</sup> Phenothiazine derivative **29** takes on a nonplanar butterfly-like molecular conformation, as evidenced by the DFT-optimized ground-state geometry (B3LYP/6-31G-(d,p)).<sup>73</sup> It is non-luminescent in solution but emits bright red fluorescence in the THF/water mixtures with  $f_w \geq 70$  vol %, clearly showing an AIE effect. The phenothiazine core in **29** is decorated with rotatable benzothiadiazole and phenyl rings. The phenothiazine core shows a bent geometric configuration, as revealed by its optimized structure. In the isolated state, there are two major radiationless channels consuming its excited-state energy: (i) the rotational motions of the benzothiadiazole and phenyl rings and (ii) the vibrational motions of the phenothiazine core. The aggregate formation confines the intramolecular motions of the rotatable and vibratable units and thereby turns on the emission. The RIM process hence accounts for the AIE attribute of **29**.

The 11,11,12,12-tetracyano-9,10-anthraquinodimethane core of **30** is decorated with two phenyl rings at the 2- and 6-positions (Figure 15B).<sup>74</sup> This luminogen is non-emissive when dissolved in acetonitrile or acetonitrile/water mixtures with  $f_w \leq 60\%$ . When  $f_w$  is further increased, yellow light emission becomes

visible with an emission enhancement up to 33-fold. In the solution state, the rotational motions of the phenyl rings and the vibrational motions of the anthraquinodimethane core and the cyano units work in conjunction to dissipate the excited-state energy. As can be seen from the crystal structure of **30**, the central anthraquinodimethane core has a folded boat-like bent shape, allowing vibratory flapping motions to exhaust the exciton energy. With addition of poor solvent (e.g., water) into the solution of **30**, aggregation of its molecules occurs. The rotations of the phenyl rings as well as the vibrations of the anthraquinodimethane core and cyano units become restrained. The restriction is further reinforced by the intermolecular C–H···N hydrogen bonds, as evidenced by the short distances (2.6 Å) of the hydrogen bonds in the crystal structure.

Enlarging anthraquinodimethane to pentacenequinodimethane and decorating the larger core with phenyl rings result in the formation of **31**, which still retains AIE activity (Figure 15C).<sup>75</sup> The luminogen is non-fluorescent when dissolved in THF but becomes emissive when  $f_w \geq 70$  vol % in the THF/water mixtures. Its optimized molecular structure bears a strong conformational resemblance to that of **30**, adopting a highly twisted configuration with a bent core. This allows the flapping motions to aid in the exciton energy dissipation, along with the phenyl ring rotations and the cyano unit vibrations. The high water fractions in the aqueous mixtures cause the formation of nanoaggregates, as verified by SEM measurements. The physical constraint and the C–H···N hydrogen bonding of the malononitrile groups restrict the rotatory motions of the phenyl groups and the vibratory motions of the pentacenequinodimethane core and the cyano units, enabling RIM to take effect to turn on the light emission.

A pure hydrocarbonic luminogen (**32**) structurally similar to the examples discussed above also shows AIE behavior (Figure 15D).<sup>76</sup> The luminogen differs from the previous tetracyano systems, with the cyano groups on the central core being replaced by the isopropyl-substituted benzene rings. As can be seen from its crystal structure, the molecule of **32** is nonplanar with a highly bent central pentacenequinodimethane core and four remarkably twisted phenyl rings. Therefore, the vibratory motions of its pentacenequinodimethane core and the rotatory motions of its phenyl rings jointly consume its excited-state energy, bringing about non-radiative relaxation of its excited states in the isolated state. Even without C–H···N hydrogen bonds to enforce the structural rigidification, **32** is still able to show bright blue emission in the crystal state on account of the RIM process.

Besides the luminogens containing a bendable or vibratable core, a series of macrocycles have also been found to show AIE behaviors controlled by RIM processes.<sup>77–80</sup> Oxacalixarene **33** is

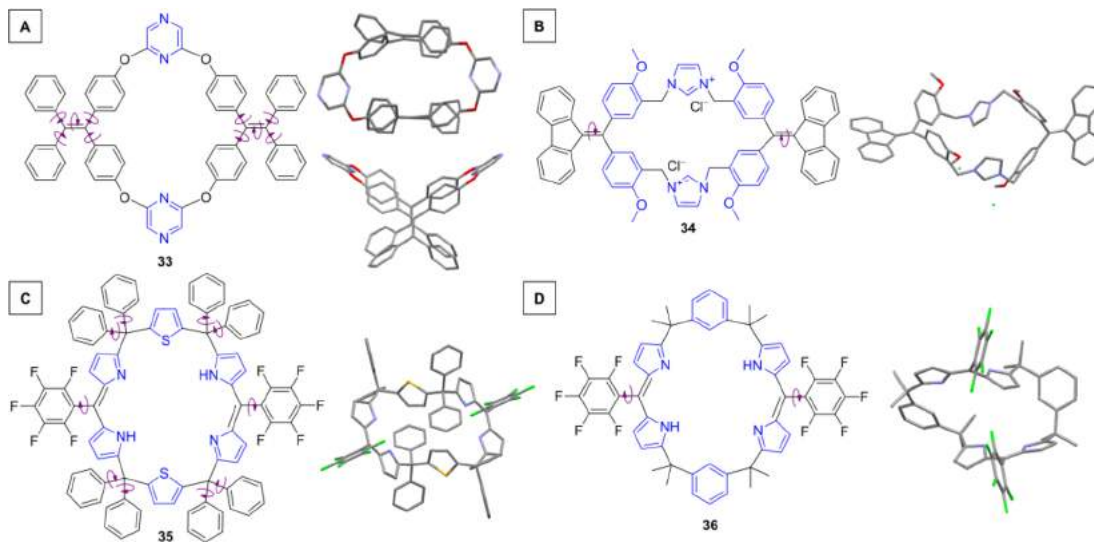


**Figure 16.** Examples of macrocyclic luminogen molecules whose AIE activities are ascribed to the RIM processes. Curved arrows indicate rotations, while the parts highlighted in blue color are the moieties that can vibrate. The crystal structures of 33 and 35 are obtained from refs 77 and 79. Copyright 2014 and 2013, American Chemical Society. The optimized structures of 34 and 36 are obtained by means of MMFF94 in Chem 3D.

an AIEgen with two TPE units bonded to two pyrazine groups at the 2,6-positions (Figure 16A).<sup>77</sup> It exhibits gradual emission enhancement with increasing water fraction in the THF/water mixture. The rotations of the phenyl and DPM rotors in the TPE moieties dissipate the excited-state energy non-radiatively. Careful inspection of its crystal structure reveals that the asymmetrically linked pyrazine units adopt slanted molecular conformations allowing flap-like vibratory motions hinging at the oxygen bridge to further consume exciton energy. By restricting the intramolecular motions through aggregate formation, luminescence is turned on. Imidazolium macrocycle 34 is composed of two diphenyldibenzofulvene moieties connected by two imidazolium units (Figure 16B).<sup>78</sup> With increasing glycerol fractions in the DMSO/glycerol mixtures, where glycerol is a poor solvent for 34 with high viscosity, emission is gradually turned on. The vibratory and rotatory motions of the imidazolium, phenyl, and fluorenyl units work together to increase non-radiative decay rates and result in weak luminescence. The restriction of these motions gives rise to the enhanced emission.

Macrocyclic calixthiaphyrin 35 (Figure 16C) exhibits aggregation-enhanced emission (AEE) effect upon increasing water fraction in the acetonitrile/water mixture.<sup>79</sup> The crystal structure of 35 offers clues to the hypothesis that its AEE nature is attributed to RIM. The multiple aromatic rings in 35 serve as the source of exciton energy consumption via a rotational pathway. The molecule contains multiple  $sp^3$  carbon hinges and pyrrolyl and thietyl units that can hardly rotate but vibrate, with the vibrational motions non-radiatively dissipating the exciton energy. As aggregates form with an increase in poor solvent fraction, RIM leads to the AEE effect. Even with a reduced number of phenyl rings, calixbenzophyrin 36 still shows AEE activity upon the formation of aggregates in acetonitrile/water mixtures (Figure 16D).<sup>80</sup> The intramolecular motions of its (pentafluoro)phenyl and pyrrolyl rings are restricted in the aggregates, thus making it AEE active.

The RIM mechanism is the unification of the RIR and RIV mechanisms. A simple, fundamental idea of RIM is that the RIR and RIV mechanisms are not mutually exclusive but instead can work together to bring about the AIE phenomenon. It seeks to explain and create a much more diverse family of AIEgens where

intramolecular motions can enhance non-radiative decay rates of isolated single molecules, whereas structural rigidification blocks these radiationless channels, directing relaxation of excitons through radiative channels.

### 3. ACQ-TO-AIE TRANSFORMATION

As mentioned in the **Introduction**, conventional luminophores are usually disc-like flat molecules that can emit efficiently when molecularly dissolved or dispersed in their good solvents. However, in the aggregate state, such molecules undergo compact packing and thus strong  $\pi$ - $\pi$  stacking interactions, further leading to the undesirable ACQ effect. There is indeed a vast selection of conventional luminophores. The mature research in the luminescence area has evidenced that many of these conventional dyes have valuable properties, but it is unfortunate that most of them can hardly get rid of the ACQ properties. The ACQ effect has been proven to be a thorny problem that is difficult to tackle with based on a great deal of endeavor paid on this issue. Various traditional strategies were used to solve the ACQ issue but always brought about undesired side effects that do harm to the useful properties of the luminophores.<sup>81–85</sup> A win-win situation where the ACQ effect is eradicated and meanwhile the functional properties of the luminogenic molecule are completely retained is hence of inestimable significance and highly desirable.

On the basis of our mechanistic understanding, it can be concluded that there are two key factors which determine the AIE property, one is the moieties that can undergo active intramolecular motions sufficiently dissipating excited-state energy in the isolated states, and the other is the twisted 3D structures in the aggregate states that effectively prevent detrimental  $\pi$ - $\pi$  stacking interactions. Thus, it is envisaged that integrating these AIE elements into the ACQ systems may work as an effective rationale to transform ACQ luminophores to AIEgens. Here, similar to AIEgens, ACQ luminophores will be referred to as ACQphores.

In the past few years, there has already emerged a lot of work transforming ACQphores into AIEgens that have maintained the desirable properties of the conventional luminophore and added the benefits of AIE property. The transference of the AIE

property onto conventional dyes would facilitate a huge growth in the AIEgenic systems, greatly diversifying existing AIEgens. This section has assembled a series of works done on ACQ-to-AIE transformations highlighting what has been accomplished and what insights can be gained. The multitude of works have been categorized into the following three main groups: (i) decorating ACQphores with AIE archetypes, (ii) replacing moieties of AIE archetypes with ACQ units, and (iii) creating new AIEgens from ACQphores based on the RIM principle.

### 3.1. Decorating ACQphores with AIEgens

One of the most straightforward ways to incorporate AIE elements into ACQphores is directly attaching well-known AIE archetypes onto ACQ cores. As an AIEgen itself is electronically conjugated, it can be anticipated that the meld of ACQ and AIE units at a molecular level would eliminate the ACQ effect and bestow the AIE effect on the new luminogen without sacrificing the desired peculiarity of the building blocks. Despite some reports with less optimistic results,<sup>86,87</sup> modular addition of AIE archetypes has been generally successful in the transformation of many conventional luminophores. On the basis of careful literature collection and collation, the examples exhibited in Figure 17 and Figure 18 have been selected out to systematically elaborate this strategy.

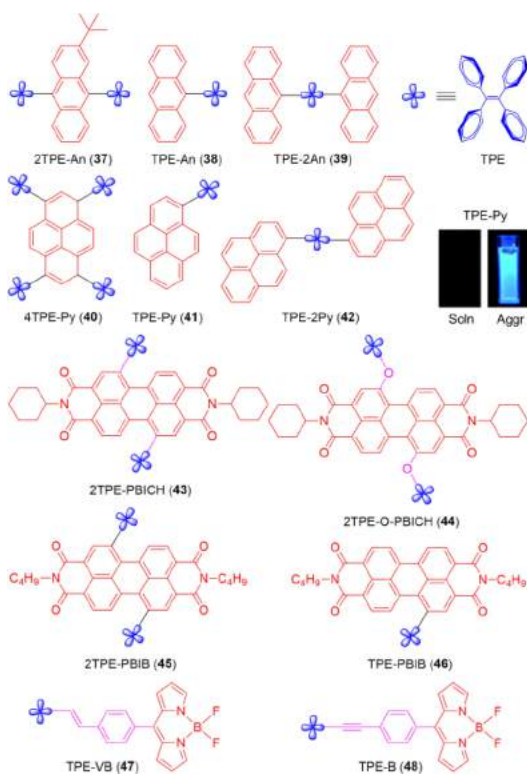


**Figure 17.** Examples of the transformation from ACQ to AIE by decorating ACQphores (anthracene, pyrene, perylene bisimide, and boron-dipyrrromethene) with AIEgen (e.g., TPE). The fluorescent photos are reprinted with permission from ref 91. Copyright 2010 Royal Society of Chemistry.

2TPE-An (37) is a good example to demonstrate ACQ-to-AIE conversion (Figure 17).<sup>88</sup> Anthracene derivatives have been extensively studied for OLED applications due to their photoluminescent, electroluminescent, and electrochemical properties.<sup>89</sup> However, the flat anthracene core suffers from the ACQ effect with a dramatic decrease in  $\Phi_F$  upon aggregation. Shu et al.

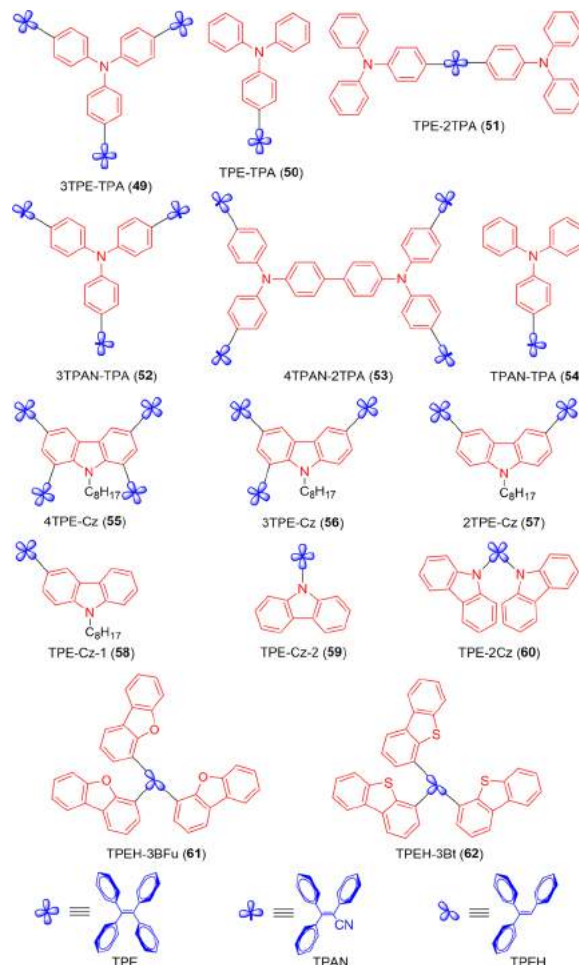


**Figure 18.** Examples of the transformation from ACQ to AIE by decorating ACQphores (triphenylamine, carbazole, dibenzob[b,d]furan and dibenzob[b,d]thiophene) with AIEgen [TPE, 2,3,3-triphenylacrylonitrile, and triphenyl ethylene (TPEH)].

tethered TPE moieties to both sides of the anthracene core, and the ACQphores is readily transformed into an AIEgen 2TPE-An (37).<sup>88</sup> Compared to pure anthracene which has a solution  $\Phi_F$  of 36.0%,<sup>90</sup> 37 displayed much weaker emission when dissolved in cyclohexane with a  $\Phi_F$  of 6.0% and greatly enhanced emission in the solid state. Being blended with poly(methyl methacrylate) (PMMA), the resulted film of 2TPE-An (37) shows a bright blue fluorescence with a  $\Phi_F$  up to 89.0%. In this successful ACQ-to-AIE transformation, the TPE units played two main roles: one is that the multiple phenyl rings on TPE moieties effectively dissipating the excited-state energy via intramolecular rotations when 2TPE-An (37) is molecularly dissolved. The propeller-shaped TPE moieties have increased the structural bulk and nonplanarity of the whole molecule and hence prevented  $\pi-\pi$  stacking interactions from forming in the aggregate state, and as a result, the intermolecular steric effects block the non-radiative decay channels resulting in the observed AIE effect. It was reported that 37 displayed fairly good performance when applied to a non-doped OLED device as an emitting layer.

In 37, the ratio in number of TPE unit(s) to anthracene is 2:1, which means the power of TPE should be very strong, so what will happen if the ratio is reduced? Would the reduced TPE proportion still have the capability to convert the ACQphore into an AIEgen? The positive answers have been given by TPE-An (38) and TPE-2An (39). With a 1:1 ratio between TPE and

anthracene, TPE-An (**38**) exhibits a typical character of AIE ([Figure 17](#)).<sup>91</sup> In THF, **38** only has a negligible  $\Phi_F$  of 0.12%, but it possesses an extremely high  $\Phi_F$  measured to be unity (100%) in the film state. With a further reduced ratio of 1:2, anthracene can still be completely converted to an AIEgen, i.e., TPE-2An (**39**), which retains very similar photophysical properties to **37** and **38**.<sup>92</sup> The  $\Phi_F$  of **39** is as low as 0.29% in solution but increases to unity in the film state. For both **38** and **39**, the structural flexibility and twisting instinct of aryl rings in TPE moiety endows the whole molecule with emission quenching in isolated states where the excited-state energy is consumed by active intramolecular motions. However, in the aggregate states, for one thing, the intramolecular motions are restricted to promote radiative decay; for another, the nonplanar 3D structure of TPE segment prevent the adjoining molecules especially the anthracene moieties from severe  $\pi-\pi$  stacking, further diminishing the possibility of emission quenching. Benefiting from the AIE feature, **38** and **39** also performed excellently when employed in OLED devices.<sup>92</sup>

The feasibility of this strategy for the ACQ-to-AIE transformation has been further verified by the work done on a diversity of ACQphores. Similar methodology has also been applied to pyrene, a typical and commonly used ACQphore.<sup>93</sup> An attempt was first taken to successfully deracinate the ACQ nature of pyrene by symmetrically embellishing it with four TPE peripherals to form the adduct 4TPE-Py (**40**) ([Figure 17](#)).<sup>94</sup> **40** is weakly emissive in the solution state and shows a large emission enhancement in the aggregate or solid state. Its film state was observed to have a satisfactory  $\Phi_F$  of 70.0%. Attempts to reduce the TPE-to-pyrene ratio while overcoming the ACQ effect were also successful. TPE-Py (**41**) and TPE-2Py (**42**), with a TPE-to-pyrene ratio of 1:1 and 1:2, respectively, both are AIE-active ([Figure 17](#)).<sup>91,92</sup> A rather low solution-state  $\Phi_F$  has been measured to be 0.22% and 0.37% for **41** and **42**, respectively. A film-state  $\Phi_F$  up to 100% has been determined for both **41** and **42**. The TPE component(s) in the TPE-pyrene adducts play analogous roles to those in the TPE-anthracene derivatives **37**–**39**. The TPE units indeed help both in the solution-state quenching and aggregate emission enhancement. In virtue of their efficient solid-state emission, the OLEDs constructed with these ACQphore-AIEgen adducts show superb EL performances.

In addition to hydrocarbonic systems (e.g., anthracene and pyrene), flat heteroatomic molecule perylene bisimide (PBI) is another well-known luminophore that can suffer ACQ.<sup>95,96</sup> Attaching TPE units to a PBI derivative on its 1,7-positions either through a single bond or via an oxygen linker creates adducts 2TPE-PBICH (**43**) and 2TPE-O-PBICH (**44**) with combined advantages of the two components: self-assembling capability (PBI) and AIE activity (TPE).<sup>97,98</sup> Moreover, extra value has been added by this means. In **43** and **44**, the TPE moieties serve as electron donors (D) and PBI act as an electron acceptor (A), and bright aggregate-state red fluorescence which is quite appealing to bioapplications is exhibited as a result of their AIE property and the D-A-D structure. Typical AIE curves were recorded with faint emission at water fractions below 50 vol % in their THF/water mixtures and progressively increasing emission as water fraction exceeds 50 vol %. The  $\Phi_F$  of **43** rises from 0.07% in solution to 6.3% in the film state. **44** shows similar properties with its solution-state  $\Phi_F$  of 0.03% while its film displays a  $\Phi_F$  of 13.0%. Dynamic intramolecular rotations of TPE moieties lead to non-radiative decay in the solution. In the aggregate state, their twisted conformation averts strong intermolecular  $\pi-\pi$  interactions, and meanwhile the RIM takes effect, collaboratively leading to efficient red fluorescence.

A more in-depth study has been carried out to further probe the effects of TPE decoration onto PBI derivatives by changing the number of TPEs attached to the PBI core.<sup>99</sup> With two TPE substituents, 2TPE-PBIB (**45**) holds very similar photophysical properties as compared to its structural analogue **43**. The two TPE moieties effectively consume excited-state energy endowing **45** with a non-emissive isolated state ( $\Phi_F = 0.07\%$ ). However, its analogue which is only decorated with one TPE unit on the 1-position, TPE-PBIB (**46**), is much more emissive with a PL property resembling the PBI core. Compared to its synthetic precursor, which possesses a Br substituent instead of the TPE moiety has a  $\Phi_F$  of 95.2%, **46** shows a solution-state  $\Phi_F$  of 2.2%. Such data indicates that the sole TPE moiety in **46** can only consume a majority of the excited-state energy instead of completely exhausting the energy, resulting in an emissive solution state. In the solid state, both **45** and **46** display strong red emission with  $\Phi_F$ s being 18.9% and 9.0%, respectively, due to TPE impairing of the  $\pi-\pi$  stacking interactions of the PBI cores and the restriction of the phenyl rings motions blocking non-radiative channels.

Cases become different as for the boron-dipyrromethene (BODIPY) systems ([Figure 17](#)). Attaching TPE to the BODIPY derivatives affords luminogens showing slightly complex photophysical behaviors.<sup>100</sup> As the BODIPY core itself is a strong electron-acceptor, integrating with an electron-donor will easily produce a D-A system with some particular photophysical properties.<sup>101–103</sup> The BODIPY derivative decorated with an electron-rich TPE via a vinyl bond, TPE-VB (**47**), shows both a TICT property and an AIE activity. When **47** is dissolved in THF, TICT emission at 640 nm is observed, but just increasing the water fraction to 10 vol % in the THF/water mixture makes the TICT emission become completely quenched. This emission quenching is likely due to both the polarity effect of the solvent system and the excited-state energy consumption by the intramolecular motions of the TPE unit. As the water fraction is further increased, aggregation occurs where RIM becomes predominant and leads to strong emission. Hence, **47** is apparently AIE-active. TPE-B (**48**), where the TPE moiety is attached to BODIPY via an ethynyl bond, shows a combination of ACQ-active locally excited (LE) emission and an AIE-active TICT emission. In THF, only the green LE emission at 529 nm is observed in **48**. As the  $f_w$  in its THF/water mixtures is increased, aggregation arises while the LE emission is continuously weakened, manifesting the typical ACQ activity. However, a new emission band peaking at 600 nm emerges at  $f_w$  of 68 vol % and higher. The emission intensity of this band is boosted as  $f_w$  is further increased, declaring the characteristic of AIE. The  $\Phi_F$ s have also been determined to give a quantitative picture. The  $\Phi_F$  values of **47** and **48** in THF solution are 0.3% and 0.1%, respectively, whereas their corresponding solid-state  $\Phi_F$  values are 27.0% and 7.5%, respectively. As it can be seen from the theoretical calculations, the LUMOs of **47** and **48** are mainly dominated by the BODIPY core, consistent with the observed photophysical properties. The results suggest that the intramolecular rotations of TPE may or may not be sufficient enough to fully consume energy of the LE state in the solution state, but AIE activity can still be granted in the aggregate state owing to the RIM effect and the diminished intermolecular  $\pi-\pi$  stacking interactions.

Tremendous efforts have been spent on the transformation of ACQ-active triphenylamine (TPA) into AIEgens.<sup>104–107</sup> A TPA core has been decorated with three and one TPE unit(s), respectively, to generate TPE-TPA adducts as 3TPE-TPA (**49**)<sup>104</sup>

and TPE-TPA (**50**).<sup>105</sup> Two TPA units have been attached to one TPE as well, furnishing TPE-2TPA (**51**; Figure 18).<sup>105</sup> All the three compounds retain integrated merits of the TPA and TPE units: the hole-transporting ability of TPA and the AIE activity of TPE. Compounds **49**, **50**, and **51** have small solution-state  $\Phi_{fs}$  of 0.42%, 0.38%, and 0.24%, respectively, and correspondingly their film-state  $\Phi_{fs}$  are as high as 92.0%, 100%, and 100%, respectively. With the increasing proportion of TPA to TPE, red-shifted emission maxima have been observed as 484, 486, and 505 nm for **49**, **50**, and **51**, respectively. This red-shift in emission could be explained either by the increasing electron-donating nature of the TPA moiety and/or by the expanded conjugation of the entire molecule. Besides using TPE as a building block, other AIEgens such as triphenylacrylonitrile (TPAN or **64**) can also be utilized to serve to the same purpose.<sup>42,106</sup> The ratio of TPAN to TPA can be systematically tuned from 3:1, 2:1, to 1:1, to create new adducts, 3TPAN-TPA (**52**),<sup>106</sup> 4TPAN-2TPA (**53**),<sup>106</sup> and TPAN-TPA (**54**; Figure 18).<sup>42</sup> **52**, **53**, and **54** are all AIE-active. In THF, their  $\Phi_{fs}$  are measured to be 0.23%, 0.48%, and 1.62%, respectively, and in the solid state,  $\Phi_{fs}$  are 33.2%, 38.2%, and 99.0%, respectively. The successful conversion from ACQ to AIE in these cases can be explained very similarly to the previous systems, where the phenyl ring motions of the attached AIEgens dissipate excited-state energy while their subsequent restriction turns on the emission. Thanks to their high solid-state emission and good hole-transporting capability, OLEDs with these materials functionalized as emitting layers and/or hole-transporting layers have shown outstanding performances, so as to be discussed in the Application section.<sup>104–106</sup>

Another typical nitrogen-containing ACQphore, carbazole, has also been systematically transformed by AIEgens, e.g., TPE.<sup>91,107,108</sup> Embellishing 9-octyl-9H-carbazole (Cz) with varying numbers of TPE blocks from four to one creates TPE-carbazole adducts, 4TPE-Cz (**55**), 3TPE-Cz (**56**), 2TPE-Cz (**57**), and TPE-Cz-1 (**58**; Figure 18).<sup>108</sup> Adducts **55**, **56**, **57**, and **58** are all AIE-active with solution-state  $\Phi_{fs}$  falling in the range of 0.18% to 0.37% and film-state  $\Phi_{fs}$  ranging from 44.6% to 61.1%. Although the  $\Phi_{fs}$  show no particular trend with the TPE proportion, there is a changing trend lying in the critical  $f_w$  where emission is switched on in the THF/water mixtures. The greater the number of TPE substituents is, the earlier the emission will be turned on: the critical  $f_w$ s are 60 vol % (4TPE-Cz), 60 vol % (3TPE-Cz), 65 vol % (2TPE-Cz), and 75 vol % (TPE-Cz-1). Such a trend is attributed to the fact that with increasing TPE substituents, solubility of these adducts in the THF/water mixtures is decreased and thus causes aggregation to occur earlier. The aggregates would then activate radiative decay through RIM process. There are further studies which convert carbazole into AIEgens by attaching TPE moiety at the nitrogen position while varying the TPE to carbazole ratio. Both TPE-Cz-2 (**59**)<sup>91</sup> and TPE-2Cz (**60**) are AIE-active (Figure 18).<sup>108</sup> It is observed that when TPE is attached to the nitrogen atom in **59** and **60**, their emission maxima are more blue-shifted than their analogues **55**–**58** where TPE group(s) is/are connected to the carbon atom(s) on the aromatic rings of carbazole. TPE-Cz-2 (**59**) and TPE-2Cz (**60**) display fluorescence peaking at 468 and 464 nm, respectively, while compounds **55**–**58** show maximum emission at a wavelength in the range of 483–488 nm, indicating that there is better electronic conjugation efficiency on the carbon connection. Because of the inherent nature of carbazole, compounds **55**–**58** and **60** demonstrated good EL properties in OLED applications.<sup>107,108</sup>

Changing the nitrogen atom of carbazole to oxygen or sulfur, the resulted dibenzofuran and dibenzothiophene are attached to AIEgenic triphenylethene (TPEH or **63**) to produce TPEH-3BFu (**61**) and TPEH-3Bt (**62**).<sup>109</sup> Both **61** and **62** weakly fluoresce in diluted solutions with a relatively small solution-state  $\Phi_f$  of 1.0% and 1.4%, respectively, while become quite emissive in the aggregate state with  $\Phi_{fs}$  of 19.0% and 22.0%, respectively. Even at a ratio of 1:3 (AIEgen to ACQphore), the intramolecular motions are able to hinder radiative decay in isolated states. It should be noted that in the cases like **61** and **62**, the small flat ACQphores themselves may act as rotors to aid the excited-state energy dissipation. Also, the nonplanarity of the **61** and **62** stemmed from TPE keeps them from intermolecular  $\pi$ – $\pi$  stacking, which together with RIM renders efficient emission in aggregate states.

Indeed a great deal of other work has also been done besides the works highlighted above,<sup>110–116</sup> all of which have successfully transformed the ACQphores into AIEgens. In this section, ACQ-to-AIE transformations through modular addition of AIEgens to ACQphores including anthracene, pyrene, PBI, BODIPY, TPA, carbazole, etc. have been systematically elaborated with special attention paid to the effect of the proportion of AIEgens in the AIEgen-ACQphore adducts as well as their linking modes on the ACQ-to-AIE transformation efficiency. The ACQphore-AIEgen adduct may become non-emissive in the solution state if the attached AIE moieties can effectively consume the excited-state energy. In some cases, if the ratio of the AIEgen to ACQphore is not high enough, the solution state of the adduct may show emission to varying degrees. It has been demonstrated that the twisted 3D structure of the archetypal AIEgens is able to isolate the adducts and impede detrimental intermolecular  $\pi$ – $\pi$  stacking interactions as well as the excimer formation in the aggregate state; meanwhile, the restriction of intramolecular motions would take effect as well, which jointly accounts for the enhanced emission. Just as expected, the resultant ACQphore-AIEgen adducts are often capable of integrating the advantages of the two components and giving rise to a beneficial synergy.

### 3.2. Replacing Parts of AIEgens with ACQphores

Apart from attaching AIEgens onto ACQphores, modifying archetypal AIE cores through the incorporation of ACQphoric units is believed to be another effective way to generate new AIE-active systems. This methodology seeks to maintain the existing AIE activity of the AIEgenic cores while integrating the functional properties of the ACQphores and eliminating their quenching effect.

In particular, noticing that displacing one phenyl ring of a TPE module does not lead to the loss of AIE activity, like TPEH (**63**) and TPAN (**64**), it can be anticipated that replacing one phenyl ring of TPE with ACQphores might be able to afford new AIEgens. Following this replacement policy, a considerable amount of work has been done with archetypal AIEgen, e.g., TPE. For example, using spirobifluorene to displace one aryl of TPE readily affords AIE-active TPE-SF (**65**) (Figure 19).<sup>108</sup> Inheriting a highly twisted conformation from the propeller-shaped TPE parent, the aggregate-state  $\pi$ – $\pi$  stacking interaction and emission quenching has been prevented. The phenyl ring motions quench the emission when solvated, while the aggregation blocks such motions and emission is turned on due to the RIM effect.

In the same way, TPA and carbazole have been utilized to create AIEgens **66**, **67**, and **68** (Figure 19).<sup>117</sup> The PL spectra of

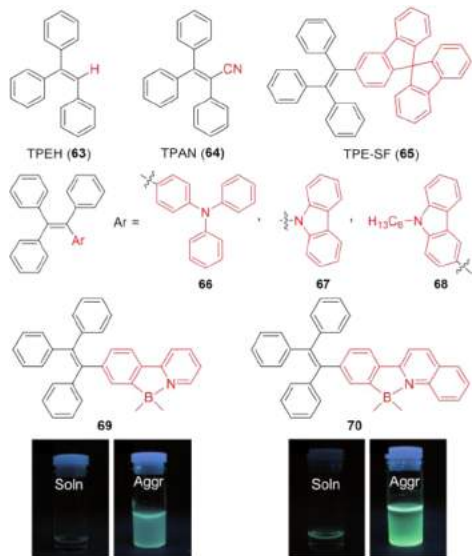


**Figure 19.** Examples of the transformation from ACQ to AIE by replacing one phenyl ring of AIEgens (e.g., TPE) with ACQphores (9,9'-spirobifluorene, triphenylamine, carbazole, pyridine-borane complex, and quinolone-borane complex). The fluorescent photos are reprinted with permission from ref 118. Copyright 2013 Wiley-VCH Verlag GmbH & Co. KGaA.

66–68 in dilute THF solutions display only noisy signals without observable emission maxima. The solution-state  $\Phi_F$ s are estimated to be approximately 1.2%, 0.7%, and 0.3%, respectively, for 66–68, which are much lower than those of TPA (13.0%)<sup>104</sup> and carbazole (37.0%).<sup>90</sup> Such results suggest that the triphenyvinyl group in 66–68 function as a PL quencher in the isolated state. The efficient aggregate-state emission of 66–68 has been clearly demonstrated by the film-state  $\Phi_F$ s ranging from 97.6%, 55.7% to 33.1%. It is worth mentioning that replacing one phenyl ring of TPE parent with a carbazole moiety no matter through carbon–nitrogen linking or carbon–carbon connection will definitely generate AIE-active carbazole derivatives. The AIE attribute of 66–68 together with the hole-transporting properties of TPA

and carbazole, endow compounds 66–68 with good EL properties.

ACQ-active boronic moieties, such as pyridine borane and quinolone borane, have also been used to replace the phenyl ring of TPE to produce 69 and 70 (Figure 19).<sup>118</sup> Both of them are very weakly non-emissive in dilute THF solution and the corresponding  $\Phi_F$ s are merely 0.4% and ~0.9%, owing to the active intramolecular rotational motions of the aryl rotors which dissipate the excited-state energy. High film-state  $\Phi_F$ s have been recorded as 98.0% and 99.0% for 69 and 70, respectively, suggesting their AIE activity. RIM process in conjunction with the nonplanar structures accounts for the efficient aggregate-state emission, as indicated by their crystal structures.

Just as the displacement of one phenyl ring in TPE could retain the AIE property, the replacement of two phenyl rings can also generate new AIEgens, e.g., diphenylfumaronitrile (71; Figure 20). Fluoranthene is a polycyclic aromatic hydrocarbon. Like other planar luminophores, it always meets with fluorescence quenching upon aggregation, showing a character of ACQ. Fluoranthene moieties were used to replace the moieties of TPE in the hope of overcoming the ACQ effect. An analogue of TPE, namely, compound 72, was consequently constructed (Figure 20).<sup>119</sup> As expected, 72 displays typical AIE behaviors showing significant emission enhancement in its THF/water mixtures with  $f_w > 60$  vol %. Distinctly different from the fluoranthene, whose solution-state  $\Phi_F$  is about 30.0%, the  $\Phi_F$  of 72 in THF is as low as ~0.7%. Intramolecular rotations of the peripheral fluoranthenyl and phenyl rings are likely responsible for the solution-state emission quenching. In aggregate state, the propeller-shaped configuration of 72 impairs the close  $\pi$ – $\pi$  stacking, which further impedes the excimer formation and the resulting fluorescence quenching. Thanks to its high solid-state  $\Phi_F$  (100%), OLEDs constructed with 72 as an emitter demonstrate a very good performance with a luminance up to 20 520 cd m<sup>-2</sup> and an efficiency of 10 cd A<sup>-1</sup>.

ACQ-active fluorene and its structurally similar analogues, including carbazole, dibenz[b,d]furan, and dibenz[b,d]thiophene, have also been used to replace two of the phenyl rings in a TPE unit affording a group of TPE analogues, 73, 74, 75, and 76,

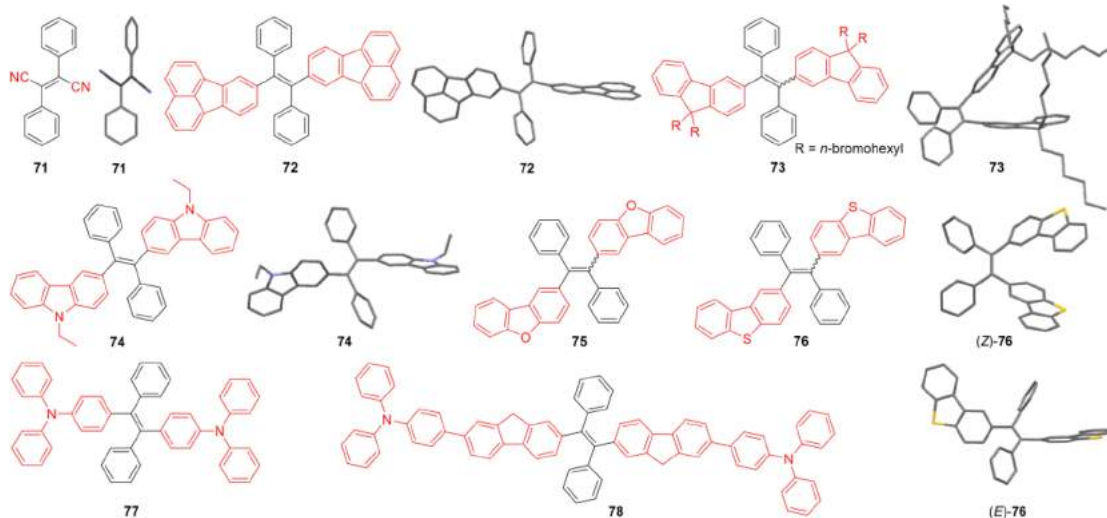


**Figure 20.** Examples of the transformation from ACQ to AIE by replacing two phenyl rings of AIEgens (TPE) with ACQphores (fluoranthene, fluorene, carbazole, dibenz[b,d]furan, dibenz[b,d]thiophene, and triphenylamine). The optimized molecular structures of 71–73 are obtained by means of MMFF94 in Chem 3D. The crystal structure of 74 is retrieved free of charge from CCDC (969370) via [www.ccdc.cam.ac.uk](http://www.ccdc.cam.ac.uk). While those of (Z)-76 and (E)-76 are provided by the authors of ref 122.

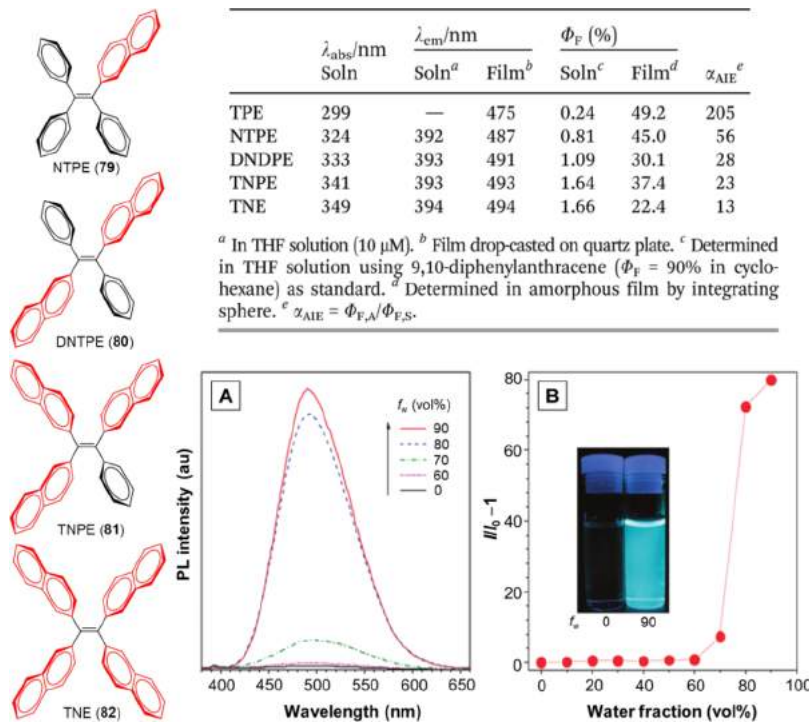


**Figure 21.** Systematically replacing the phenyl rings of TPE with naphthalene to afford new AIEgens. (A) PL spectra of TNE (82) in THF/water mixtures with different  $f_w$ . (B) Plot of  $I/I_0 - 1$  versus  $f_w$ , where  $I_0$  is the PL intensity in pure THF solution. Inset: Photos of TNE in THF/water mixtures ( $f_w = 0, 90$  vol %) under UV lamp illumination. Adapted with permission from ref 125. Copyright 2013 Royal Society of Chemistry.

respectively (Figure 20).<sup>120–122</sup> Similar to the aforementioned examples, compounds 73–76 are non-emissive in the solution state but highly emissive in the aggregate or solid state, evidently showing characteristics of AIE. TPA and its derivatives have also been incorporated into TPE forming AIE-active compounds 77 and 78.<sup>123,124</sup> Benefiting from the special electronic properties of the nitrogen, oxygen, and sulfur heteroatoms, AIEgens 74–78 show improved performances as compared to the ACQ moieties and the TPE parent when applied for OLED devices.

One important insight that can give an explanation to the AIE activity of the compounds shown in Figure 20 can be gained by examining their crystal structures. These molecules retain the twisted propeller-like shape of TPE. The twisting nature allows for rotational motion to occur in the solution state rendering the isolated molecule non-emissive. In the aggregate state, the twisted 3D structure prevents destructive intermolecular  $\pi-\pi$  stacking interactions allowing the molecules to be highly emissive when the intramolecular rotations are hindered by effects such as steric hindrance.

A systematic work has been carried out to replace phenyl ring(s) in TPE moiety with naphthalene ring(s) step by step, generating a series of new luminogens with AIE characteristics, where the naphthalene moieties also serve as rotors. The PL spectra of 82 in THF/water mixtures with different  $f_w$  and the corresponding plot of emission enhancement versus  $f_w$  are displayed in Figure 21A and 21B as an example to demonstrate the typical AIE behaviors of these naphthalene-based luminogenic systems. The photophysical properties of these naphthalene derivatives, naphthyltriphenylethene (NTPE or 79), dinaphthylidiphenylethene (DNDPE or 80), triphenylphenoxyethene (TNPE or 81), and tetranaphthylethene (TNE or 82) have been summarized in the table (inset of Figure 21).<sup>125</sup> It can be seen that with the gradual replacement of the phenyl rings by the naphthyl moieties, the increase in conjugation red shifts both the

absorption and emission of 79–82 (Figure 21). Although these four species are all AIE-active with very low  $\Phi_F$ s in solution state (0.81–1.66%) and significantly enhanced  $\Phi_F$ s in the aggregate/solid state, the emission enhancement ( $\alpha_{\text{AIE}}$ ) factor is inversely proportional to the number of naphthyl moieties.

The numerical parameter  $\alpha_{\text{AIE}}$  factor is defined as fluorescence quantum yield in the aggregate state ( $\Phi_{F,A}$ ) divided by the fluorescence quantum yield in the solution state ( $\Phi_{F,S}$ ). For TPE, the small phenyl rings allow rotational motions to more efficiently consume the excited state energy. In contrast, the ability of larger naphthyl groups to dissipate energy becomes diminished as exemplified by the slight raise in  $\Phi_{F,S}$  as the number of naphthyl groups increases. The  $\Phi_{F,S}$  values of 79–82 are a bit higher than that of TPE (0.24%) but much lower than that of naphthalene (23%). Moreover, with size double that of TPE, the planar naphthyl groups are more prone to form intermolecular  $\pi-\pi$  stacking. In the solid state, the naphthyl groups of neighboring molecules can partially overlap each other, giving rise to intense intermolecular interactions and reduced emission. As  $\Phi_{F,S}$  is increased and  $\Phi_{F,A}$  is decreased with the continual replacement of phenyl rings, TPE has the highest  $\alpha_{\text{AIE}}$  factor of 205 and TNE has the lowest of 13. This systematic work offers us a deeper understanding in the photophysical picture of AIE.

The versatility of creating new AIE derivatives by replacing phenyl rings of AIEgens with ACQphores has been further proved by other typical AIEgens such as diphenylfumaronitrile (71),<sup>126</sup> silole,<sup>127–129</sup> and 9,10-di((E)-styryl)anthracene (DSA).<sup>130</sup> For example, the two phenyl rings in 71 were replaced with TPA to generate a red-emissive AIEgen 83 (Figure 22), which has a solid-state  $\Phi_F$  of 42.5%.<sup>126</sup> TPA groups have also been incorporated into the silole core replacing the phenyl rings at the 2,5-positions and accordingly develops a good yellow solid emitter 84.<sup>127</sup> The addition of the TPA groups endows the silole with more efficient solid-state fluorescence as well as the extra hole-transporting

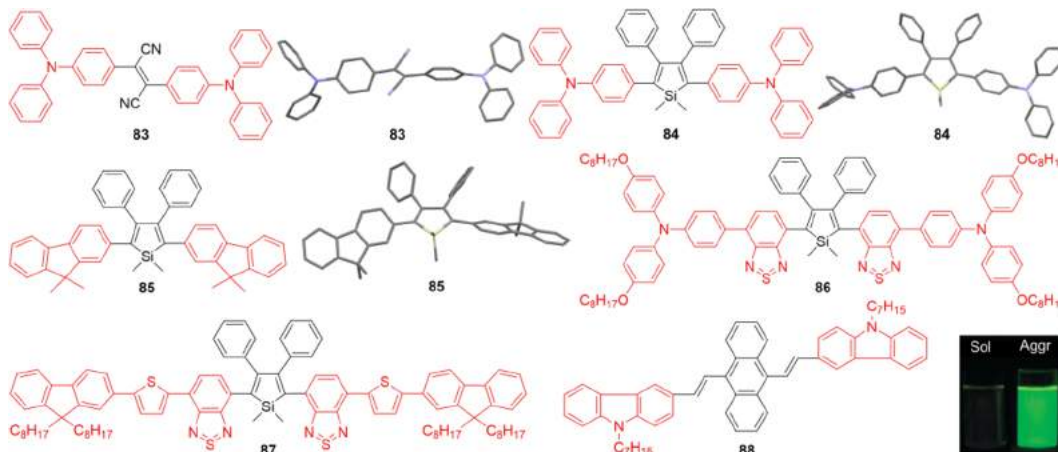


**Figure 22.** Examples of the transformation from ACQ to AIE by replacing the phenyl rings of AIEgens (diphenylfumaronitrile, dimethyltetraphenylsilole, 9,10-di((E)-styryl)anthracene) with ACQphores (triphenylamine, fluorene, carbazole, benzo[*c*][1,2,5]thiadiazole, etc.). Inset: Fluorescent photos of **88** in THF and THF/water mixture with  $f_w = 90$  vol %. Adapted with permission from ref 130. Copyright 2011 Royal Society of Chemistry. The optimized molecular structure of **83** is obtained by means of MMFF94 in Chem 3D. The crystal structures of **84** and **85** are retrieved free of charge from CCDC (842865 and 928433) via [www.ccdc.cam.ac.uk](http://www.ccdc.cam.ac.uk).

properties, which are highly desirable to OLEDs applications. Fluorene derivatives have also been attached to the silole core in the same fashion as **84** to afford AIEgen **85** that displays high luminance, current, and power efficiencies in OLED devices.<sup>128</sup> In compound **86**, benzothiadiazole was added between TPA peripheries and the silole core to further enlarge the conjugation and enhance the D-A effect in order to produce an AIEgen with deep red emission.<sup>129</sup> With an emission maximum at 635 nm, **86** has a low solution-state  $\Phi_F$  of  $\sim 0.6\%$  and a solid state  $\Phi_F$  of  $\sim 9.1\%$ . Further extension of the conjugation length meets with a reduction in gains as exemplified by **87**.<sup>129</sup> A less pronounced AIE effect was exhibited by **87** as compared to **86**. The solution-state and film-state  $\Phi_F$ s of **87** are about 1.0% and 2.1%, respectively. Besides the possible heavy atom effect of thiophene groups, the bulky and planar substituents on the silole ring which probably render a better  $\pi-\pi$  stacking also account for the low solid-state  $\Phi_F$ . Moreover, the larger conjugation and bulkier size of the substituents make the intramolecular rotations partially restricted even in solution, hence leading to a more emissive solution state. However, although the conjugation of **88** is also relatively large, it shows a typical AIE property with  $\Phi_F$  increasing from 0.5% in solution to 17.4% in aggregate state. The nonplanarity of **88** originated from the steric repulsion among the anthracene, vinyl groups, and carbazole groups play crucial roles in the AIE effect (Figure 22).<sup>130</sup>

As stated above, plentiful of research has been performed to see whether it is possible to create new AIEgens by means of replacing the moieties of existing AIEgens with ACQphores, the overwhelming majority of which has been very successful. It should be noted that there is a balance to be maintained, because systematic work has shown that too much change to the AIE core can ultimately reduce its AIE activity, either affecting solution state or solid state emission and sometimes even both.<sup>125,129,130</sup> In view of this, quite a few more issues need to be addressed before putting forward accurate instructions to this replacement strategy. For instance, how will the size and the shape of ACQphores affect the photophysical properties of the resulting luminogens? And what kind of influence will the conjugation and replacing sites impose on the photophysical behaviors? Hence, in some sense, what we have discussed here for one thing is to highlight the great jobs that have already been done, for the

other, is to stimulate more attention and ardour to this research subject.

### 3.3. New AIEgens Built from ACQphores

Simply speaking, the above two strategies for ACQ-to-AIE transformation are taking advantage of the features of AIEgens, especially their active intramolecular motion capability and the 3D nonplanar structures. On the basis of the AIE mechanism and the work mentioned earlier, it can be concluded that the essence of ACQ-to-AIE transformation strategies is to introduce sufficient motional elements and nonplanarity. In the light of this, it can be anticipated that any approach that matches this essence should be workable. Hence, creating new AIEgens from ACQphores and non-AIE elements is absolutely possible. There are more than enough examples that can be used for the demonstration. As exhibited in Figure 23 and Figure 24, a new set of AIE molecules have been generated by connecting aromatic stators and rotors together via rotatable single bonds. By means of such decoration, in the molecularly dissolved state, the excited-state energy can be dissipated through rotational motions and more importantly, while in the aggregate state, these motions will be hindered to direct excited-state decay through radiative means. What's more, the nonplanar structures originated from the twisting nature of the attached aromatic rings may prevent the resulting luminogens from close  $\pi-\pi$  stacking and avoid emission quenching in the aggregate state.

To start with, a single phenyl ring was attached to a small ACQphore, isothiazolo[5,4-*b*]pyridin-3(2H)-one, to produce **89** (Figure 23).<sup>131</sup> In its solution state, **89** displays almost no emission as the rotational motion of both the phenyl ring and the isothiazolo[5,4-*b*]pyridin-3(2H)-one group consume excited-state energy resulting in a non-emissive solution. In its aggregate state, strong blue emission is observed with an absolute  $\Phi_F$  of 28.0%, manifesting the AIE feature of **89**. The AIE effect can be ascribed to the RIM principle. Here, the simple addition of a rotatable phenyl ring drastically changes the photophysical properties of the ACQphore.

A similar system, **90**, has been constructed by embellishing quinoline with two rotatable phenyl rings (Figure 23).<sup>132</sup> With a solution-state  $\Phi_F$  of 0.3% and a solid-state  $\Phi_F$  of 3.2%, **90** has an  $\alpha_{AIE}$  factor of  $\sim 11$ . The two phenyl rings and quinolone efficiently expend energy through rotational motion in the excited

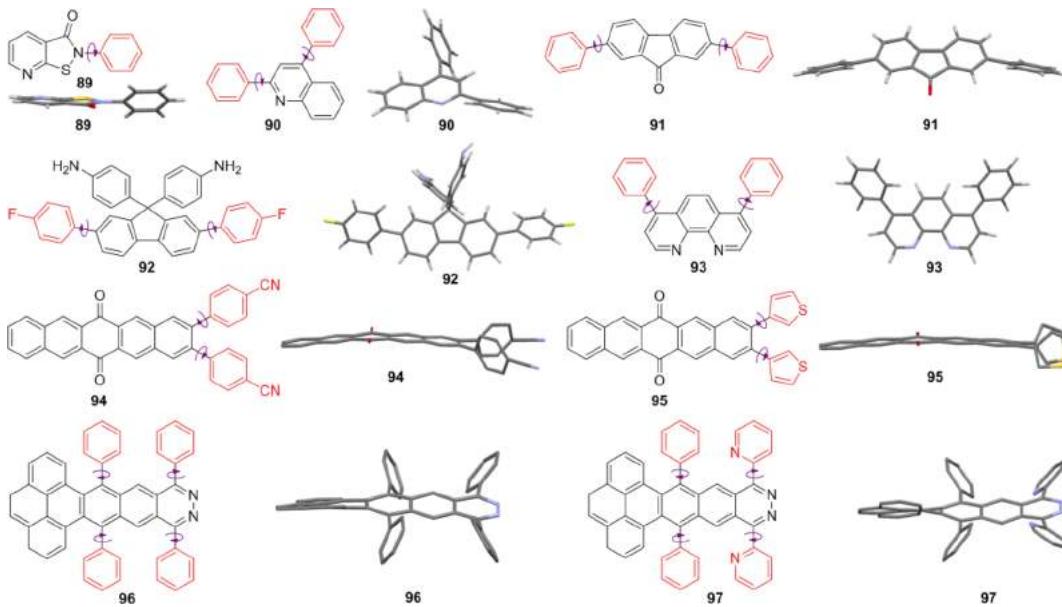


**Figure 23.** Examples of the transformation from ACQ to AIE by decorating ACQphores with aromatic rotors. The optimized molecular structures of 89, 90 and 93–95 are obtained by means of MMFF94 in Chem 3D. The crystal structure of 91 is obtained from the Supporting Information of ref 133 free of charge via <http://pubs.acs.org>. While those of 92, 96, and 97 are obtained free of charge from CCDC (960578, 985725 and 985726) via [www.ccdc.cam.ac.uk](http://www.ccdc.cam.ac.uk).

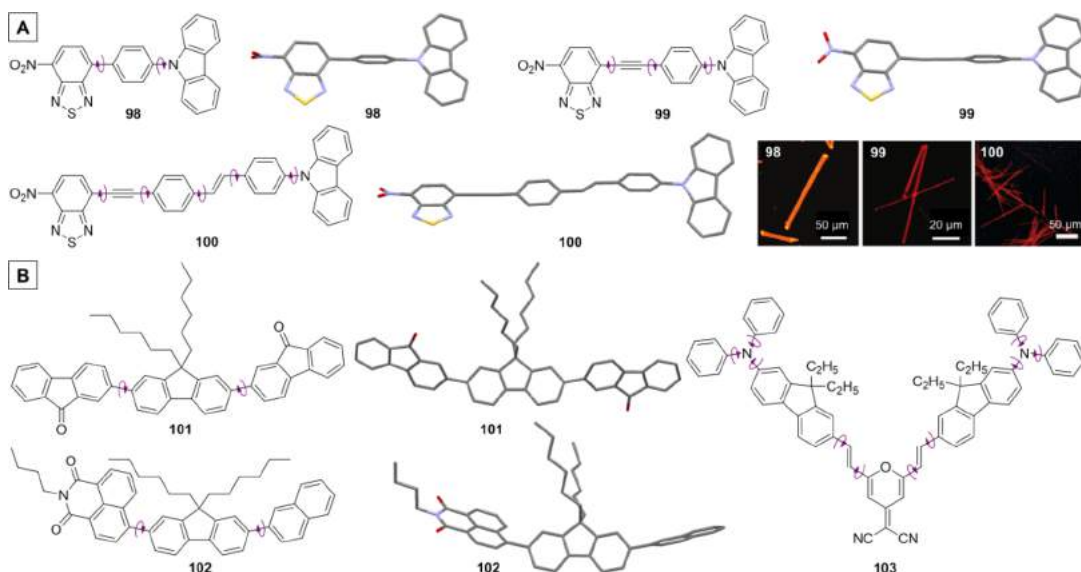


**Figure 24.** Examples of the transformation from ACQ to AIE by connecting (A) small or large (B) ACQphores together via single bonds. The fluorescent photographs for 98 and 99 are reprinted with permission from ref 138. Copyright 2013 Royal Society of Chemistry. While that of 100 is reprinted with permission from ref 139. Copyright 2012 Royal Society of Chemistry. The optimized molecular structures of 98, 101, and 102 are obtained by means of MMFF94 in Chem 3D. The crystal structures of 99 and 100 are retrieved free of charge from CCDC (865411 and 859087) via [www.ccdc.cam.ac.uk](http://www.ccdc.cam.ac.uk).

state; when these motions become blocked in the solid state, emission becomes visible. This is further verified by the addition of camphorsulfonic acid (CSA). CSA forms a complex with 90 and the rotation barriers are further increased as a result. The solution-state and solid-state  $\Phi_F$ s of the complex are accordingly increased to 1.3% and 11.5%, respectively. The addition of these phenyl rings effectively alters the quinoline core bestowing the AIE property.

Even for the ACQ-to-AIE conversion of larger ACQphores, the decoration with two aromatic rotors still works. For instance, two phenyl rings are attached to fluorenone to afford AIegen 91

(Figure 23).<sup>133</sup> With no discernible emission in the solution state ( $\Phi_F = 1.1\%$ ), compound 91 displays bright green emission in the crystalline state with a  $\Phi_F$  of 61.0%. Like the previous examples, the phenyl ring motions quench the solution-state emission, but in the aggregate state, the motions are restricted and the emission is increased.

Structurally similar to 91, luminophore 92 also exhibits AIE activity by joining a fluorene core with two fluobenzene rings and a pair of aminobenzene groups (Figure 23).<sup>134</sup> Because of its amine and fluorine substituents, 92 displays the combined behaviors of TICT and AIE in the THF/water mixtures with

varying  $f_w$ s. When molecularly dissolved, **92** shows a deep blue fluorescence, with the emission maximum at around 467 nm. With the increase in  $f_w$ , the increased polarity of the solvent system gradually stabilizes the TICT state and gives rise to a decrease and red-shift in emission. However, as the  $f_w$  reaches a critical point where aggregation occurs, the aggregates restrict the rotational motions and thus emission is restored and hypochromic-shifted. This type of photophysical behavior is very typical in systems with strong D-A interaction. Moreover, the twisted structure stemmed from the rotatable fluobenzene and anilino groups prevents the formation of intermolecular  $\pi-\pi$  stacking interactions, which working together with the RIM effect leads to a solid-state  $\Phi_F$  of 36.0%. With a further enlarged ACQ core, AIEgen **93** consists of a phenanthroline core decorated with two phenyl groups (Figure 23).<sup>135</sup> **93** hardly luminesces in the solution state but shows gradually enhanced fluorescence with the increase in poor solvent fraction. Analogous to the previous examples, the introduction of the phenyl rings has allowed the compound to become AIE-active.

Bulky aromatic conjugated cores, such as pentacene derivatives, have also been endowed with AIE properties by the attachment of rotatable aromatic rings.<sup>75,136,137</sup> Pentacene-6,13-dione has been decorated with benzonitrile and thiophene groups to generate AIE-active **94** and **95**, respectively (Figure 23).<sup>75,136</sup> **94** and **95** both display very weak emission in the solution state, as the rotational motions dissipate excitation energy. As the fraction of their poor solvent, i.e., water, is increased, emission is gradually intensified. The rotational motions become hindered and emission is thus triggered by RIR. Compounds **96** and **97** are constructed by using four rotatory aromatic groups to embellish a much bulkier pentacene derivative (Figure 23). Both **96** and **97** are AIE-active.<sup>137</sup> Because of the proximity of the two phenyl rings and the pyrene core, the resulting steric repulsion forces the core of **96** or **97** to adopt a distorted conformation as shown by the crystal structures. The motions of the four aromatic rings quench the solution-state emission. When these motions become impaired in the aggregate state, radiative decay becomes the major channel for excited-state relaxation. Meanwhile, the highly twisted 3D structure also helps to the emission in the aggregate state, in view of its role in impeding  $\pi-\pi$  stacking and excimer formation.

Apart from the strategy of attaching rotatory aromatic rings to ACQphores, single-bonded linking of ACQphores has also been employed to achieve ACQ-to-AIE transformation. Nitryl, benzothiadiazole, phenyl, and carbazole are singly bonded to afford **98**, **99**, and **100**, which display typical AIE activities (Figure 24A).<sup>138,139</sup> These compounds are highly fluorescent in their crystalline states but non-emissive in their solution state. From their crystal structures, it is visible that various aromatic species tilt out of plane with respect to each other. The twisted nonplanar conformation indicates relatively loose conjugation between the aromatic moieties. It allows for rotational motions to occur when the moieties are unconstrained, ultimately aiding in the emission quenching in the solution state. In contrast, in the solid state, the RIR comes into play and triggers the emission. By bonding these electron-withdrawing and electron-donating aromatic moieties together via single bonds, AIEgens with orange or even red emissions can easily be obtained.

Larger aromatic moieties can also be singly linked together via single bonds to form new AIE molecules (Figure 24B).<sup>140–142</sup> For example, a fluorene core and two fluorenone moieties have been bonded together to yield **101**. Similarly, a fluorene core, a naphthyl, and a naphthalimide moiety have also been connected together to generate **102**.<sup>140,141</sup> In like manner, **103** has been

created by joining a malononitrile pyran moiety, fluorenyl, and diphenylamine together.<sup>142</sup> In these molecules, all the main components can be taken as rotors. All these three luminogens display both TICT and AIE properties. They are emissive in the solution state, but with the increase of water fraction, emission becomes significantly reduced until a critical point where the luminophores begin to aggregate together. At this critical point, the RIM process causes excited-state energy to be relaxed via radiative pathways, leading to the enhanced emission. The solid-state  $\Phi_F$ s of **101** and **102** are measured to be 78.0% and 73.0%, respectively. These high  $\Phi_F$ s can be attributed to the RIM effect and their highly twisted conformations which hinder intermolecular  $\pi-\pi$  stacking and detrimental species from forming. Although compound **103** is AIE-active, because of its larger conjugated core, it holds a lower aggregate-state  $\Phi_F$  of 15.0% in the THF/water mixture with  $f_w = 90$  vol %. It should be noted that the twisted nature of the diphenylamine group aids in preventing further decrease in the  $\Phi_F$  in the aggregate state by suppressing intermolecular  $\pi-\pi$  stacking.

In this subsection, successful examples of new AIEgens created through the connection of rotatable moieties via single bonds have been expounded. Although not every luminophore constructed exploiting this approach becomes AIE-active,<sup>137,143</sup> it remains a highly promising strategy for it makes full use of the mechanistic understanding of AIE.

### 3.4. New AIEgens Incorporating Triphenylamine (TPA) Units

Building from the previous principle, a lot of work incorporating the TPA moiety into the construction of new AIEgens has been conducted recently. The three phenyl rotors and the nonplanar structure of TPA make it an ideal building block for AIEgens. The rotational motions of the phenyl rings in TPA aid in dissipating excited-state energy in the solution state and assist in RIR in the solid state. Its twisted structure helps reduce the formation of destructive intermolecular  $\pi-\pi$  stacking interactions. In virtue of its electron-rich (electron-donating) nature, the addition of electron-deficient (electron-accepting) moieties can easily generate molecules with D-A structure, thus giving rise to some special properties such as solvatofluorochromism and two-photon absorption or two-photon excited fluorescence.

Blue AIEgen **104**, green AIEgen **105**, and yellow AIEgen **106** can easily be generated by integrating TPA with imidazolium, pyrimidine, and malononitrile groups, respectively (Figure 25).<sup>144–146</sup> The multiple rotors of **104**, **105**, and **106** help dissipate excited-state energy via rotational motions, and upon aggregation these motions become constrained and emission is consequently turned on. As suggested by the crystal structure of **104** and the optimized structures of **105** and **106**, the lack of planarity in these molecules due to the single-bonded connection of the aromatic constituents help prevent undesirable  $\pi-\pi$  stacking interactions, making them show efficient aggregate-state emission.

Red emission can be achieved when TPA is combined with BODIPY derivatives forming **107** and **108** (Figure 25).<sup>147</sup> Owing to the strong electronic interaction between the TPA donor and the BODIPY acceptor, both **107** and **108** display TICT plus AIE properties. Although both **107** and **108** are already luminescent when dissolved in THF, the LE emission is abruptly reduced with the slightly increased  $f_w$  due to the polarity effect. Above the critical  $f_w$  at which point aggregation occurs, AIE is observed when the rotatable aromatic rings become restricted. Alternatively, two red AIEgens have been created by joining diketopyrrolopyrrole and benzoselenodiazole with TPA unit(s) to form **109** and **110**, respectively (Figure 25).<sup>148,149</sup> AIEgen **109** shows no observable luminescence when dissolved in THF, and

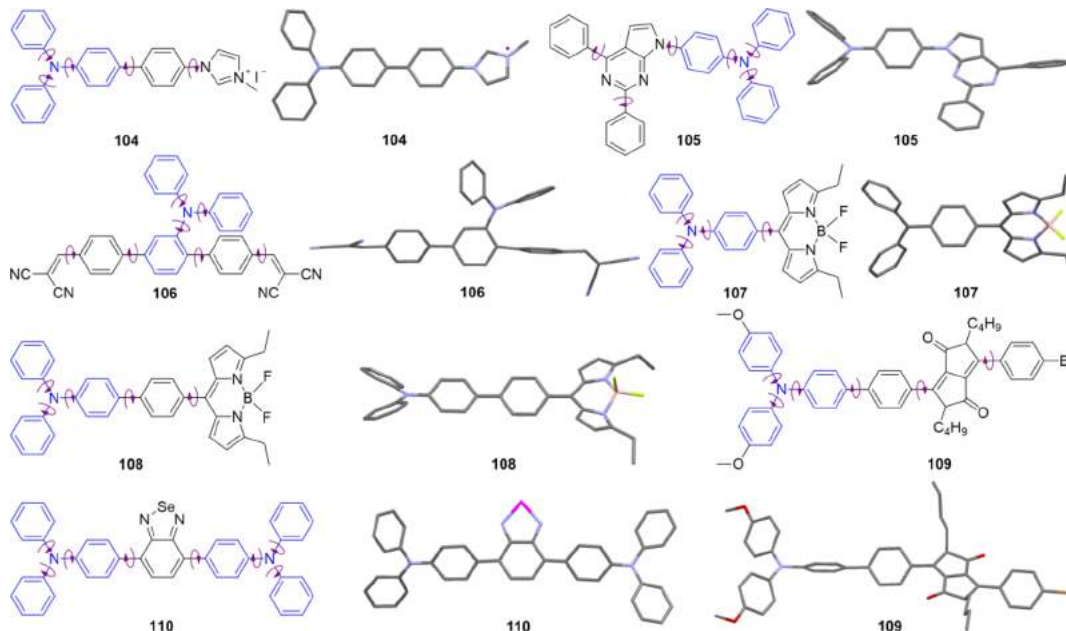


**Figure 25.** Examples of the transformation from ACQ to AIE by connecting triphenylamines together with other  $\pi$  moieties through single bonds. The optimized molecular structures of **104**, **105**, **106**, and **108–110** are obtained by means of MMFF94 in Chem 3D. The crystal structure of **107** is obtained and reprinted from the Supporting Information of ref 147. Copyright 2009 American Chemical Society.

red emission is gradually enhanced with the increase in  $f_w$ . Compound **110** is TICT + AIE-active: it is already emissive when dissolved in THF, and the red emission is weakened as the  $f_w$  increases but is restored when aggregate formation restricts the intramolecular motions. As previously mentioned, the twisted conformation of TPA moieties in these systems inhibits  $\pi$ - $\pi$  stacking interactions and thus prevents the emission quenching in the aggregate state.

Furthermore, a number of starburst multibranched TPA systems with D- $\pi$ -A- $\pi$ -D architectures have been reported to be AIE-active.<sup>150–154</sup> Through vinyl linkages from a dicyanobenzene core, TPA units act as branching points for diphenyl amine or phenothiazine to form TPA quadrupolar derivatives **111a** and **111b**, respectively (Figure 26).<sup>150</sup> With a similar approach, starburst TPA derivatives **112a** and **112b** have been constructed (Figure 26).<sup>151</sup> These four compounds are nearly non-emissive when dissolved in THF, but bright red emissions are observed in the aggregate state, displaying typical AIE behaviors. Because of the interconnectivity of the multi D-A system, these molecules also exhibit large two-photon absorption (2PA) cross section values along with efficient two-photon excited fluorescence (TPEF) in the aggregate state, making them promising materials for biophotonic applications.<sup>150,151</sup>

This section has highlighted new AIEgens that have incorporated TPA motif(s) into their molecular structures, taking full advantage of the multiple phenyl rings and the twisted 3D structure of the TPA unit. Not only could TPA aid in endowing the molecules with AIE activity, making use of its electron-donating nature, luminogens with varying emission colors covering the whole visible range could be easily obtained. By further extending and connecting TPA to multiple electron donors and acceptors, molecules with large 2PA cross sections and even TPEF can be achieved by the molecular designs. The use of TPA exemplifies how AIEgens could be created while integrating desirable properties from ACQphores.



**Figure 26.** Examples of the transformation from ACQ to AIE by connecting triphenylamines together with other  $\pi$  moieties through single bonds to afford new AIEgens with starburst structures and two-photon excited fluorescence.

#### 4. AIEGEN SYSTEMS

With the increasing research interest in AIE, not only has the understanding of the mechanism advanced greatly, but the development of new AIEgens has also significantly progressed. From pure hydrocarbons to heteroatomic compounds, from small molecules to macromolecules, from organic to inorganic- or metallic-organic, the variety of AIEgens has maintained a continual growth. Indeed, the AIE property is evidently compatible with other photophysical effects like TICT and ESIPT.

This section aims to showcase structures of new AIEgens and discuss different AIE systems grouped together. Closely examining a variety of new AIEgens will aid in the illustration of the AIE process and hopefully inspire the syntheses of more AIEgens.

#### 4.1. Hydrocarbon AIEgens

Pure hydrocarbon systems remain an important class of AIEgens for a variety of reasons. Without the presence of heteroatoms, their properties, e.g., chemical, electro, photophysical, are relatively easier to study, thus providing simpler systems for structure-property relationship analyses and mechanism decipherment. Moreover, these systems can also function as building blocks for the construction of functional AIEgens. Taking TPE as an example, it is the best-known hydrocarbonic AIEgen and has been extensively used for mechanistic studies, AIE macromolecules construction as well as the ACQ-to-AIE transformation. As demonstrated in section 3, the crucial factors for AIE activity are the motional moieties and structural nonplanarity. Herein, with simple hydrocarbonic models, this viewpoint can be further checked and expatiated. This section will go over a variety of recently developed pure hydrocarbon systems, highlighting their structural characteristics and uncovering the working principles of their AIE effect.

Shimizu et al. have reported a series of new AIEgens based on hexa-1,3,5-trienes cores decorated with aryl rings at the peripheries, among which, compounds **113** and **114** are considered as representatives for their simplest structures (Figure 27).<sup>155</sup>

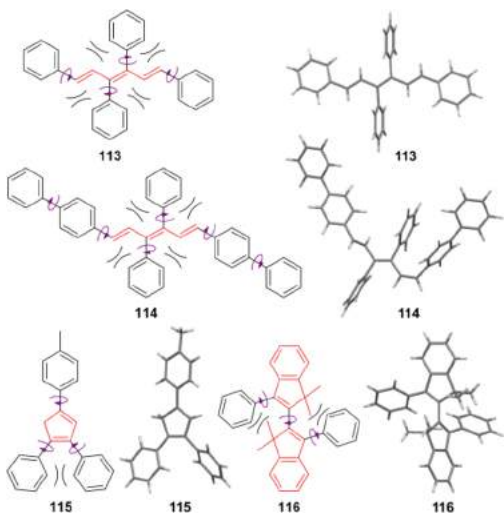


**Figure 27.** Examples of arylenevinylene-based (**113** and **114**), cyclopentadiene-based (**115**) and indenyl-based (**116**) AIEgens. The bracket symbols indicate the existence of the steric repulsion interactions. The crystal structures of **113**, **115** and **116** are retrieved free of charge from CCDC (619193, 894150 and 762612) via [www.ccdc.cam.ac.uk](http://www.ccdc.cam.ac.uk). The optimized molecular structure of **114** is obtained by means of MMFF94 in Chem 3D.

Both **113** and **114** display no observable emission when dissolved in chloroform, but their intense solid-state emissions are observed with  $\Phi_F$ s of 25.0% and 33.0%, respectively. By analyzing the chemical and crystal structure of **113**, it becomes clear why these molecules are AIE-active. As revealed by the crystal structure, the highly conjugated central hexa-1,3,5-trienes fragment in **113** is almost planar with dihedral angles  $<2^\circ$ , and the horizontally substituted phenyl rings slightly tilt out of plane with dihedral angles of  $15.16^\circ$  and  $15.77^\circ$ . However, the

two vertical phenyl rings of **113** adopt an almost orthogonal conformation with respect to the conjugated core with dihedral angles falling in the range of  $82.31^\circ$  and  $99.82^\circ$ . This orthogonal conformation is due to the steric repulsion interactions of the hydrogen atoms at the *ortho*-position of these phenyl rings with the neighboring hydrogen atoms on the hexa-1,3,5-trienes core. Due to a much weaker conjugation with the central core, these vertically positioned phenyl rings can easily rotate to consume excited-state energy when in the isolated state. Although the horizontally positioned phenyl rings are much more conjugated with the hexa-1,3,5-trienes moiety, they can still twist around the single bonds, assisting in the excited-state energy dissipation and the subsequent emission quenching in the isolated state. In the aggregate state, the orthogonal phenyl rings together with the slightly twisted horizontal phenyl rings impair detrimental  $\pi-\pi$  stacking interactions, which work jointly with the RIR process to turn on the emission. The structural analogue **114** contains two more phenyl rings as compared to **113** and is also AIE-active for similar reasons. The optimized structure of **114** suggests that it has bulky molecular size and highly twisted spatial configuration. On the basis of these hydrocarbonic backbones, a series of heteroatom-decorated molecules have been synthesized. The resulting molecules also retain the AIE activity.

Besides the above-discussed linear aromatic systems composed of bridged polyene units, AIE systems in which the  $C=C$  double bonds are locked by five-membered rings such as cyclopentadiene (e.g., **115**) and indenyl groups (e.g., **116**), have also been developed (Figure 27).<sup>156–159</sup> Comprised of three aryl moieties and one cyclopentadiene ring, **115** is very weakly fluorescent in solution with a  $\Phi_F$  of 1.5%, while the  $\Phi_F$  rises to 35.0% in its crystalline state, displaying a 23-fold enhancement.<sup>156</sup> Undoubtedly, the RIR effect of the three phenyl species in **115** plays the most significant role in the AIE process; meanwhile, the twisted 3D structure also plays a part. The proximity of the neighboring phenyl ring on the cyclopentadiene core imposes steric hindrance onto each of the rings forcing them to twist out of plane. This nonplanar configuration, as well as the  $sp^3$  carbons of the cyclic core and the methyl group, collaboratively separate the molecules and hinder close  $\pi-\pi$  stacking, which as a result prevent fluorescence quenching in aggregate states. Using **115** as a backbone, a variety of AIEgens can be readily derived.<sup>157,158</sup>

Luminogen **116** reported by Tian et al. is a hydrocarbonic system with two indenyl moieties connected together by a rotatable single bond (Figure 27).<sup>159</sup> This biindenyl derivative emits weakly detectable photoluminescence when dissolved in  $CH_3CN$  and shows a marked emission enhancement up to 255 times when  $f_w = 70$  vol % in the  $CH_3CN$ /water mixture. Notably, a  $\Phi_F$  as high as 76.0% has been detected in its crystalline state. The rotations of the phenyl and indene moieties work together to consume excited-state energy so that only a weak PL signal is detected when **116** is dissolved or isolated. When these rotatory motions are restricted, for example, by crystal packing, excited-state decay is driven into radiative channels causing the emission enhancement. As depicted in Figure 27, the nonplanar conformation arises from intramolecular steric hindrance and a repulsion effect also contributes to the efficient aggregate-state emission. Similar to the previous compounds, a series of modifications have been made using **116** as a building block and the resulting derivatives have also been reported to be AIE-active.<sup>159</sup>

As suggested by the examples shown in Figure 27, the steric interaction affects molecular conformation, crystal packing, intermolecular interactions, as well as the luminescence behavior, hence judiciously taking advantage of the steric effect could help

to create new luminogenic systems. A number of AIEgens have been constructed with pure aromatic or aryl elements. For instance, benzene has been fully decorated with six phenyl rings to form hexaphenylbenzene (HPB, **117**), which shows an AEE character (Figure 28A).<sup>160</sup> The fluorescence of HPB (**117**) in

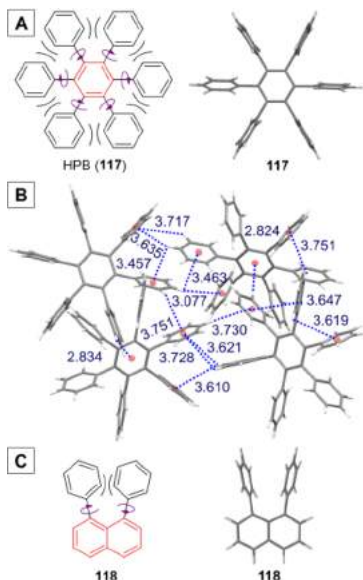


**Figure 28.** Examples of hydrocarbon AIEgens which are constructed by taking advantage of RIR principle and steric interactions. (B) Packing mode and multiple C–H···π interactions in a single crystal cell of HPB (**117**). The bracket symbols indicate the existence of the steric repulsion interactions. The crystal structure of **117** is retrieved free of charge from CCDC (177146) via [www.ccdc.cam.ac.uk](http://www.ccdc.cam.ac.uk). While that of **118** is obtained from the Supporting Information of ref 161 free of charge via <http://www.sciencedirect.com>. Copyright 2011 Elsevier.

solution is weak but detectable. In the THF/water mixture with  $f_w = 80$  vol %, its emission is intensified by 12-fold. The rotational motions of its six phenyl rings render its solution state only weakly emissive. However, the multiple phenyl rings in HPB cannot rotate as freely as those in HPS and TPE due to the steric repulsion between the adjoining phenyl groups. The steric crowdedness imposes restriction on the intramolecular rotations of these phenyl rings even when it is in isolated states, thus making its emission observable in solutions. In the aggregate state, the RIR effect comes into play. As can be seen from its crystal packing (Figure 28B), a large number of intra- and intermolecular C–H···π interactions aid in rigidifying the molecules, stabilizing the packing, hindering phenyl ring motions, and thus enhance the emission. It should also be noted that the six phenyl rings take almost orthogonal orientations to the central benzene core as the steric interactions prevent these rings from adopting a planar conformation with the benzene core. The propeller-like shape of HPB obstructs the close π–π stacking and the excimer formation and hence impedes the emission quenching. Because the orthogonality of the system weakens the overall conjugation, HPB (**117**) emits in a short-wavelength (UV) range with an emission maximum at 334 nm. A series of HPB derivatives have been synthesized which not only show AIE/AEE properties, but their emissions have been tuned to fall in the visible spectrum.<sup>160</sup>

The luminescence behavior of **118** is similar to that of HPB. Enlarging the aromatic core (stator) from benzene to naphthyl, the phenyl rings (rotors)-decorated naphthalene derivative **118** is also found to be AEE-active (Figure 28C).<sup>161</sup> With a relatively

low  $\Phi_F$  of 3.2% when dissolved in cyclohexane, a 7.8-fold enhancement in its  $\Phi_F$  is observed when the  $f_w$  is increased to 90 vol % in the THF/water mixture. Its AEE activity can be easily interpreted by the RIR principle: phenyl ring motions help dissipate excited-state energy in the solution state; aggregation constrains these intramolecular motions forcing the excited-state molecules to radiatively decay. Moreover, this U-shaped lumiphore is nonplanar with the substituted phenyl rings twisted out of the naphthalene plane, which helps to avoid aggregate-state emission quenching. With **118** as a framework, a multitude of new AIEgens have been developed as well.<sup>161</sup>

9,10-Di(*E*-styryl)anthracene (DSA, **119**) is generated by decorating the both sides of an anthracene core with styryl moieties (Figure 29A).<sup>162</sup> The luminogen is practically non-fluorescent

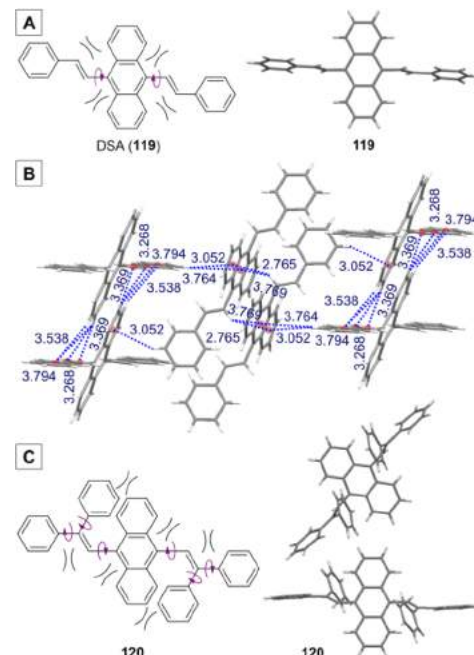


**Figure 29.** Molecular and crystal structures of 9,10-di(*E*-styryl)-anthracene (DSA, **119**) and its derivative (**120**). (B) Packing mode and multiple C–H···π interactions in a single crystal cell of DSA. The bracket symbols indicate the existence of the steric repulsion interactions. The crystal structures of **119** and **120** are retrieved free of charge from CCDC (688692 and 936040) via [www.ccdc.cam.ac.uk](http://www.ccdc.cam.ac.uk).

when it is dissolved in THF. The  $\Phi_F$  value of the crystal of DSA (**119**) is 50.8%, which is much higher than that of its THF solution (0.4%). It thus behaves like a typical AIEgen. Examination on its crystal structure gives us a deep insight into its AIE mechanism. Because of the steric repulsion interactions between the hydrogen atoms on the anthracene core and the styryl moieties, the vinyl linkages take an almost orthogonal conformation relative to the anthracene core, greatly diminishing conjugation between the two segments (Figure 29A). As a result, the styryl arms become much more able to rotate and thus can consume excited-state energy when DSA exists as an isolated species. As shown in Figure 29B, in its crystal packing, the orthogonal styryl arms prevent the anthracene cores from forming π–π stacking which could decrease the emission. A large number of different C–H···π interactions rigidify the highly twisted conformation and restrain the free rotation of the styryl arms, rendering an activated RIR process which is responsible for the 127-fold emission enhancement in the crystal state. In view of its

simple structure and typical AIE behavior, DSA has been used as the backbone to a multitude of structural modifications allowing its derivatives to be applied into a number of different areas, as to be discussed in the [Technological Applications](#) section.

On the basis of the DSA (**119**) core, a simple structural modification yields luminogen **120** ([Figure 29C](#)).<sup>163</sup> With an extra phenyl group on each styryl unit, the whole molecule becomes more twisted and bulkier. As proved by the crystal structure of **120**, similar to DSA, owing to the multiple steric interactions, the side arms take orthogonal orientations with minimal conjugation to the central anthracene core. Furthermore, the phenyl rings on the arms also adopt twisted orientations. This structural feature suggests that the RIM process is at work in this system. Because both of these effects reduce conjugation, intramolecular motions become relatively easier, permitting the excited-state energy to be non-radiatively dissipated in isolated states. However, the intramolecular motions are limited by the steric crowdedness in **120** even when the molecules are well isolated, therefore leading to a relatively emissive solution state with a  $\Phi_F$  of 17.0%. In its crystal form, the  $\Phi_F$  rises to as high as 60.0%, suggesting the AEE property. The further activated RIM process blocks the non-radiative channels, the butterfly-like molecular shape of **120** impedes the intermolecular  $\pi-\pi$  stacking, and the light emission is hence enhanced in the aggregate state.

AIEgens are not confined to those with small phenyl rotors. For example, AIE-active luminophore **121** is comprised of two anthracyl units linked to the central phenyl ring through single bonds with vinylene groups as bridges ([Figure 30A](#)).<sup>164</sup> Since the two 9-vinylanthracene arms are attached on the 1,2-positions of the benzene core, the intense steric repulsion interactions compel the large anthracyl groups to take highly twisted conformations relative to the vinyl linkages with torsion angles ranging from 53.20° to 73.55°. This twisted structure feature weakens the overall electronic conjugation and permits free rotations of the rotors in isolated states, resulting in an almost non-emissive state in ethanol ( $\Phi_F < 1.0\%$ ). With the addition of >20 vol % of water into ethanol, aggregates form and large emission enhancement arises. The solid-state  $\Phi_F$  of **121** is 12.0%, much higher than that of its solution state. The 1,3- and 1,4-isomers of **121** (the 1,2-isomer) have been studied to provide more evidence to the RIM mechanism. Contrary to **121**, its 1,3- and 1,4-isomers are both ACQ-active. The small steric interactions and large conjugation in the 1,3- and 1,4-isomers render the molecules more planar and rigid in conformation and hence more difficult to rotate in solution. The strong  $\pi-\pi$  stacking interaction between the anthracyl units as verified by the crystal structure accounts for the emission turn-off in the aggregate state. In sharp contrast, there is no typical  $\pi-\pi$  stacking interaction in **121**, and its crystal packing shows multiple intra- and intermolecular C–H··· $\pi$  interactions which assist the RIM process to cause the emission enhancement ([Figure 30B](#)).

Two 9-vinylanthracene moieties are linked to a biphenyl core via single bonds to create another pure aromatic luminogen **122** ([Figure 30C](#)).<sup>165</sup> **122** is reported to be AEE-active. Its AEE activity is mainly owing to the steric interactions between the anthracyl group and the vinyl linkage. The steric repulsion prevents a planar conjugated conformation, making the anthracyl groups adopt nearly orthogonal orientations relative to the divinylbiphenyl moiety with the dihedral angles of 84.26° and 94.53°, as can be seen from its crystal structure. This disruption in the electronic conjugation allows the anthracyl moieties to

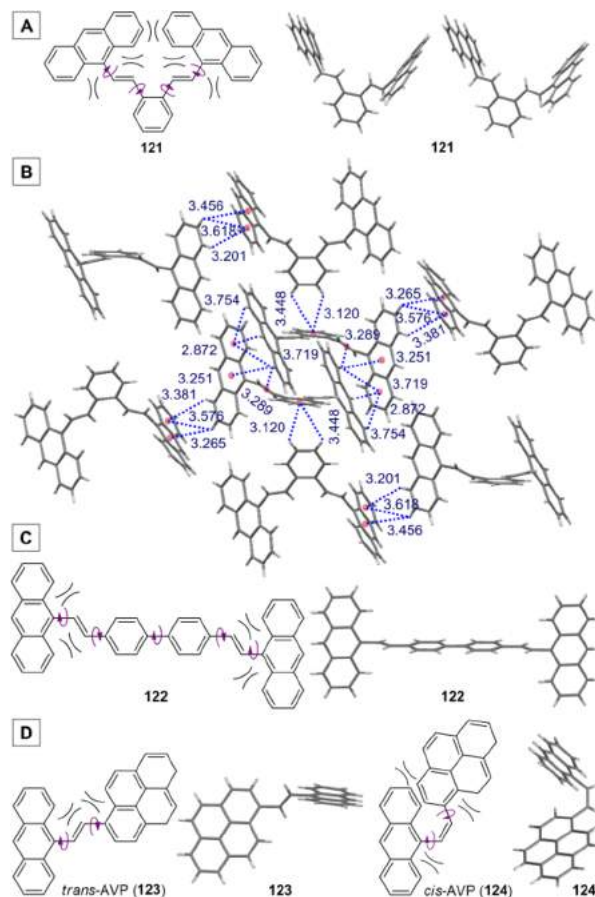


**Figure 30.** Examples of 9-vinylanthracene-based AIEgens which are constructed by taking advantage of RIR principle and steric interactions. (B) Packing mode and multiple C–H··· $\pi$  interactions in a single crystal cell of **121**. The bracket symbols indicate the existence of the steric repulsion interactions. The crystal structures of **121**–**124** are retrieved free of charge from CCDC (848984, 844123, 845768, and 832521) via [www.ccdc.cam.ac.uk](http://www.ccdc.cam.ac.uk).

rotate, dissipating energy in the excited state and weakening the emission in the solution state. On the other hand, the good conjugation of the divinylbiphenyl segment and the bulky size of the anthracene units partially rigidify the molecular conformation and constrain the intramolecular motions, which leads to an incomplete emission quenching even in the isolated state. In the solid state, the strong and multiple C–H··· $\pi$  interactions further stiffen the molecular structure, giving rise to the observed emission enhancement.

Another set of 9-vinylanthracene-based AIEgens have been developed by Li et al. (**123** and **124**; [Figure 30D](#)).<sup>166</sup> The structure of 1-[9-anthracenyl]vinyl]pyrene (AVP) is featured with an anthracene group linked to a pyrene unit via single bonds with a vinyl bridge. The cis/trans isomers of AVP both show AEE properties. The *trans*-AVP (**123**) is slightly less congested than the *cis*-AVP (**124**; [Figure 30D](#)). Similar to **121**, the steric interactions play a crucial role in their AEE behaviors. Both the anthracyl group and pyrene moiety of *trans*-AVP (**123**) experience large steric strain/repulsion with the vinyl linkage, causing it to take a highly twisted conformation. Both of the two bulky rotors are twisted out of the vinylene plane with torsion angles of ~113° (anthracyl) and ~30° (pyrene), respectively. Such a nonplanar structure favors intramolecular rotations and weakens the solution-state light emission. The anthracyl and

pyrene in **124** are tilted out of the vinylene plane with torsion angles of  $\sim 61^\circ$  and  $\sim 47^\circ$ , respectively. The *cis*-AVP (**124**) undergoes an even greater steric congestion and repulsion due to the proximity of the large pyrene and anthracene moieties. The freedom of rotations in **123** and **124** is limited due to the large size of the rotors (anthracyl and pyrene) as well as the large steric crowdedness. Therefore, their excited-state energy cannot be completely dissipated via non-radiative pathways even in the isolated state, as proved by their relatively high solution-state  $\Phi_F$ s. The  $\Phi_F$  values of *trans*-AVP (**123**) and *cis*-AVP (**124**) in solution are 15.0% and 17.0%, respectively. In the aggregate state, the intramolecular rotations are restricted, the  $\pi-\pi$  stacking is hindered, and the light emission is hence intensified. The solid-state  $\Phi_F$ s of **123** and **124** are 54.0% and 36.0%, respectively, manifesting the AEE effect.

The AIE activity of the afore-mentioned hydrocarbonic systems could predominantly be explained by the RIR principle. Here are a few examples whose AIE activity is related to principles of RIV and RIM.<sup>167,76</sup> Triphenylene (**125**) is a typical arene which is highly planar and well conjugated (Figure 31).<sup>168</sup> In the

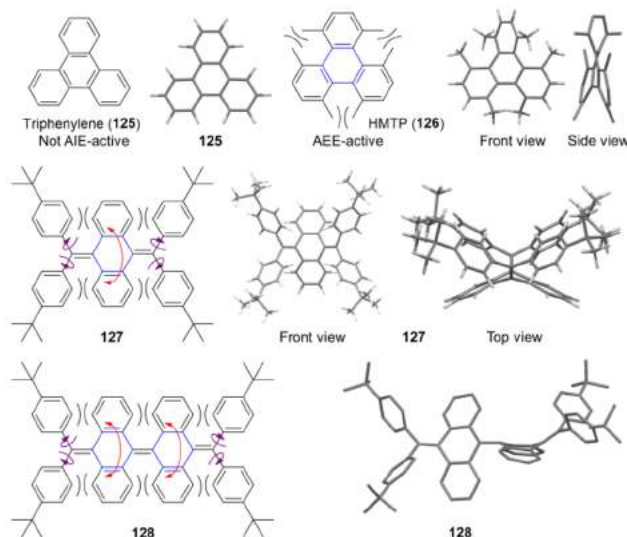


**Figure 31.** Examples of hydrocarbon AIEgens which were constructed by taking advantage of the RIV/RIM principles and steric effect. The optimized molecular structures of **125–128** are obtained by means of MMFF94 in Chem 3D.

THF solution, its photoluminescence exhibits concentration dependence that the emission maximum red shifts with the increase in concentration or aggregation formation, which implies the existence of intermolecular  $\pi-\pi$  stacking. **125** is luminescent with a  $\Phi_F$  of 6.0% in THF solution and becomes a bit more emissive in film and powder with  $\Phi_F$ s of 13.0% and 12.0% accompanied by a large bathochromic-shift in emission. In this sense, **125** is neither AIE-active nor ACQ-active. However, by introducing six methyl groups into the triphenylene core, a distinct derivative hexamethyltriphenylene (HMT, **126**) is readily generated. The steric repulsion interactions between the methyl groups greatly affect the molecular conformation and photophysical properties.<sup>167</sup> When dissolved in THF, HMT (**126**) has a  $\Phi_F$  of 5.0%. While in the solid state, the  $\Phi_F$  rises to 31.0%, definitely exhibiting an AEE activity. The methyl groups distort the once planar conformation and disrupt the original good conjugation, permitting the molecule to much more easily vibrate. These vibrational motions efficiently consume the

excited-state energy as reflected by its solution-state  $\Phi_F$ . In the solid state, the twisted structure and the methyl groups prevent the  $\pi-\pi$  stacking interactions between the molecules which would otherwise quench the emission, and meanwhile the RIV is activated and the light emission is thus enhanced.

A series of interesting molecules whose AIE attributes result from the principle of RIM have been reported recently.<sup>76,169</sup> A pair of diphenylmethylene moieties are connected by one or two dihydroanthracene cores to afford polyaromatic rings systems **127** and **128**, respectively (Figure 31). These luminogens show undetectable solution-state  $\Phi_F$ s. In the solid state, noticeable light emissions are observed for **127** and **128**, with  $\Phi_F$ s of 9.9% and 9.2%, respectively. As can be seen from their crystal structures, the dihydroanthracene cores in **127** and **128** adopt bent and nonplanar configurations, suggesting the vibrational motions in the isolated states. Such a highly twisted structure could be of lower energy due to the steric effects of the phenyl moieties. Their AIE properties can be attributed to both RIR of the peripheral aryl rings and RIV of the dihydroanthracene core(s).

A variety of hydrocarbonic systems have been highlighted in this section: starting from phenyl rings decorating conjugated linear to cyclic cores, then from smaller to larger aromatic cores and rotors, and finally from systems that are AIE-active because of RIR principle to those due to RIV and RIM processes. We expounded their AIE behaviors and uncovered their working principles, in hope of further inspiring the creation of new AIE hydrocarbon systems.

#### 4.2. Heteroatom-Containing AIEgens

The hydrocarbonic AIEgens enjoy simplicity in structure and accessibility in synthesis. They can function as excellent models for the mechanistic study of AIE effects. The categories of the pure hydrocarbon systems, however, are limited. Incorporation of heteroatoms into AIEgens will definitely enrich the variety of AIE systems and expand the scope of AIE research. Because of the large variety of heteroatoms and the great structural diversity of the resulting heteroatomic AIEgens, this section will be split into smaller subsections so that it might be easier to compare similar AIEgenic systems. First, pentacyclics, AIEgens that bear a structural similarity to silole will be discussed, followed by boronic species in the second subsection. Then the AIEgens derived from Schiff bases and those also displaying ESIPT properties will be subsequently demonstrated. In the fifth subsection, AIEgens with hydrogen bonds will be elucidated. Since quite a few AIEgens contain the nitrile functional group, they will be grouped together and set forth in the sixth section. Finally, other heteroatomic AIEgens that cannot fit into the above classifications will be discussed.

**4.2.1. Pentacyclic Compounds.** Heteroatom-bridged cyclopentadienes which are often referred to as heteroles have drawn extensive attention, due to their unique electronic structures and optoelectronic characteristics. Many heteroles are found to be AIE-active, such as silacyclopentadienes (silole), one of the most well-studied AIEgens.

The heavier group-14 congeners of siloles, e.g., germoles, have also been reported to be AIE-active.<sup>170–172</sup> Germoles **129a** and **129b**, with the 1,1-positions of the germanium-bridged pentacyclic cores, respectively, substituted by methyl groups and phenyl groups, have very low solution  $\Phi_F$ s of 0.14% and 0.29% in THF, respectively. As compared to the light emission of isolated state, 21- and 32-fold emission enhancement in the aggregate state are observed for **129a** and **129b**, respectively (Figure 32).<sup>170,171</sup> More recently, another AIE-active

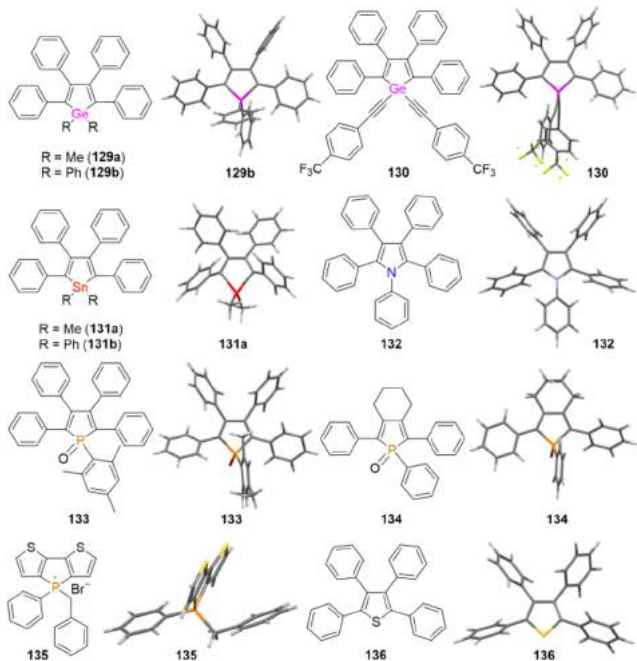


**Figure 32.** Representative examples of AIEgens with pentacyclic cores containing main group elements. The crystal structures of **129b**, **130**, **133**, and **134** are retrieved free of charge from CCDC (268956, 857430, 767155 and 721628) via [www.ccdc.cam.ac.uk](http://www.ccdc.cam.ac.uk). The optimized molecular structures of **131a**, **132**, **135**, and **136** are obtained by means of MMFF94 in Chem 3D.

1,1-disubstituted 2,3,4,5-tetraphenylgermole, i.e., **130**, has been developed by Braddock-Wilking et al. (Figure 32).<sup>172</sup> In the aggregate state, the  $\Phi_F$  of **130** is increased to 26.0%, 65 times higher than that of the acetone solution. Their single crystal structures have highly distorted configurations with the substituted phenyl rings twisted out of the pentacyclic cores. Similar to its silole counterparts, the AIE activity of these germoles can be interpreted by the principle of RIR. The rotations of the phenyl rings on the germole ring cores quickly relax the excited state via non-radiative channels. Upon aggregation, the activation of RIR and the lack of intermolecular  $\pi-\pi$  stacking interaction give rise to the enhanced emission.

Stannoles are much heavier group-14 congeners of siloles and germoles. A family of stannoles with AIE features have also been reported.<sup>171</sup> For instance, structurally similar to **129**, **131** contains a tin atom in the cyclopentadiene core instead of germanium (Figure 32). **131a** and **131b** have slightly smaller solution-state  $\Phi_F$  values (0.03% for **131a**; 0.11% for **131b**) than their germole counterparts (**129**). However, they are also slightly less emissive in the aggregate state: **131a** exhibits a 7-fold emission enhancement and **131b** displays an 11-fold increase. Analogous to their silole and germole counterparts, their AIE effects are rationalized to originate from the RIR process and the absence of intermolecular  $\pi-\pi$  stacking. The general reduction in emission intensity of the stannoles has been attributed to the heavy-atom effect of the tin atom.

Other than the group-14 elements-containing pentacyclic systems, heteroles with group-15 elements have also been explored. The pyrrole derivative with multiple aryl substituents (**132**) shows typical AIE activity (Figure 32).<sup>173</sup> When dissolved in THF, minimal photoluminescence is detected. As the water fraction is increased in its THF/water mixtures, pronounced emission enhancement could be observed. As revealed by the

analysis of its crystal structure and packing, **132** adopts a propeller-shaped conformation commonly observed in AIEgens. This prevents  $\pi-\pi$  stacking from occurring and renders the molecules to stay brightly emissive in the solid state. Multiple C–H··· $\pi$  interactions could also be observed in the crystal packing which aids in RIR allowing it to be AIE-active.

Phosphole oxide derivatives containing multiple phenyl groups show typical AIE phenomenon, as reported by some Japanese research teams.<sup>174–176</sup> It is observed that when phosphole oxide **133** (Figure 32) was dissolved in good solvent, e.g., THF, the fluorescence is almost negligible, but in the crystalline state, it strongly luminesces with a greenish yellow light with a  $\Phi_F$  as high as 91.0%.<sup>174</sup> Quite similar to the aforementioned systems, the RIR effect of the phenyl substituents and the nonexistence of  $\pi-\pi$  stacking interaction account for its AIE activity. Another phosphole oxide **134**, the 3,4-dialkylated analogue of **133**, also displays the AIE feature.<sup>175</sup> With less phenyl substituents, **134** is slightly more emissive in THF solution ( $\Phi_F = 0.12\%$ ), and enhanced emission is observed in the aggregate state ( $\Phi_F = 0.35\%$ ). In the crystalline state, the  $\Phi_F$  is greatly boosted to 33.0%. Compared to **133**, it is understandable why **134** has a stronger solution-state emission: although the vibrational motions of the alkyl group in **134** can consume some of the excited-state energy along with the rotations of the remaining phenyl rings, it is not as effective as the rotational motions of the phenyl rings at the 3,4-positions of **133**. The vibrational motions of the cycloalkyl moiety also affect the solid-state emission of **134**. Intramolecular rotations of phenyl rings are easily restricted; in contrast, vibrational motions of cycloalkyl require less free volume to occur and thus cannot be completely constrained by aggregation, leading to a less emissive solid state of **134**.

Baumgartner et al. reported a structurally interesting phosphole derivative **135** which possesses an AEE attribute (Figure 32).<sup>177</sup> Different from **133** and **134**, **135** has a larger phosphole core with two thiophene groups being fused together. Also, the number of rotors is further decreased. In dichloromethane (DCM) solution, **135** is luminescent with a  $\Phi_F$  of 6.0%, and the  $\Phi_F$  value surges to 60.0% in the solid state. The AEE activity of **135** has been ascribed to the rotational motions of the phenyl and benzyl moieties. Moreover, the highly distorted 3D conformation also plays an important role in the efficient aggregate-state emission for it obstructs the intermolecular  $\pi-\pi$  stacking and the resulting excimer formation which would quench the emission.

The group-16 congener of siloles, i.e., tetraphenyl-substituted thiophene (**136**), is also AIE-active (Figure 32).<sup>178</sup> When dissolved in THF, **136** only shows faint fluorescence with a  $\Phi_F$  measured to be 0.23%. In its THF/water mixture with an  $f_w$  of 90 vol %, as the result of aggregation, **136** becomes intensively luminescent with a  $\Phi_F$  of 41.0%, exhibiting a 177-fold emission enhancement. Because of the propeller-shaped conformation adopted by its phenyl rings, the molecules of **136** experience no intermolecular  $\pi-\pi$  stacking interaction in the aggregate state and the C–H··· $\pi$  interactions stiffen the conformation, favoring the RIR process and permitting the emission to be turned on.

Tellurophenes are attracting growing research interest with respect to the development of novel optoelectronic materials owing to their lower optical band gaps, higher LUMO levels, and potentially higher charge carrier mobility as compared to their thiophene counterparts.<sup>179</sup> Recently, Shankar and Rivard et al. have discovered that the previously known boronic ester (pinacolboronate) capped tellurophene **137** amazingly features remarkable AIE characteristics (Figure 33).<sup>180</sup> As exhibited in the

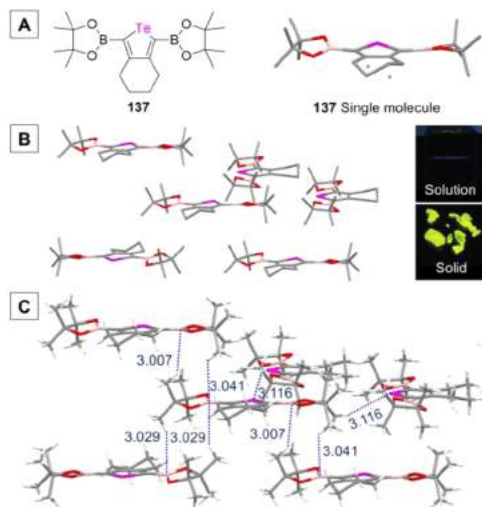


**Figure 33.** Aggregation-induced phosphorescence from tellurophenes. (A) The chemical structure and crystal structure of **137**. (B) Molecular orientation and (C) the intermolecular short-distance contacts. Inset: Photographs of **137** in solution and solid states taken under UV light (365 nm). Adapted with permission from ref 180. Copyright 2014 Wiley-VCH Verlag GmbH & Co. KGaA. The crystal structure of **137** is retrieved free of charge from CCDC (984482) via [www.ccdc.cam.ac.uk](http://www.ccdc.cam.ac.uk).

inset of Figure 33, when this tellurophene is dissolved in organic solvents like THF, the resulting solutions are practically non-emissive, while its solid shows intense green luminescence ( $\lambda_{\text{em}} = 535 \text{ nm}$ ). Moreover, the THF/water mixtures of **137** even with an  $f_w$  up to 70 vol % still do not show obvious luminescence. With  $f_w = 80 \text{ vol } \%$ , **137** starts to emit, and the emission intensity significantly rises with the increase in  $f_w$ . Such an observation is a hallmark of the AIE effect. Emissive films of **137** are able to be fabricated in PMMA (containing 1–10 wt % **137**) or directly be casted from THF solution. A luminescence quantum yield of 11.5% as well as a weighted average lifetime of  $166 \mu\text{s}$  has been found for the neat films of **137**, signifying the phosphorescent nature of the light emission. Furthermore, the large Stokes shift (170 nm) observed in **137** provides extra support for the presence of phosphorescence. It is believed that the empty p-orbitals within the pinacolboronate units are likely involved in the phosphorescence emission of **137**. The main mechanism of its AIE activity can be primarily pinpointed to the RIM process involving RIR of the pinacolboronate arms and RIV of the cycloalkyl and pinacolboronate moieties. When dissolved in THF, the rotatable pinacolboronate species and the vibratable cycloalkyl and pinacolboronate segments hold great motional freedom, allowing them to efficiently quench the emission. As the molecules of **137** begin to aggregate together, the intramolecular rotations of pinacolboronate arms become constrained, but the conformational changes of the cyclohexane ring and pinacolboronate units can still serve as a channel to consume the excited-state energy. These two processes work together to help explain why no emission emerges until  $f_w = 80 \text{ vol } \%$ . In addition to the activated RIM process, the bulky size of the pinacolboronate moieties and the twisted conformation of **137** also contribute to the strong solid-state emission (Figure 33A). They keep the central tellurophene moieties separated from each other (5.5 Å) preventing intermolecular  $\pi-\pi$  interactions as well as the Te...Te that might quench the solid-state phosphorescence (Figure 33B). Moreover, as exhibited in Figure 33C, massive intermolecular short-distance contacts such as C-H...B and C-H...Te

interactions play an important role in stabilizing the crystal packing and rigidifying the molecular conformation, which benefits the RIM process and the resulting radiative decay of the excited-state energy. It is worth mentioning that **137** is a rare example of main-group-element-based (group-16) emitters that possess a feature of aggregation-induced phosphorescence (AIP). Also, the studies on **137** have implied that even the intramolecular motions of nonaromatic moieties (rotors and vibrators) can also act as consumption pathways of excited-state energy.

Indeed mimicking the chemical structures of the AIE-active siloles has been proven to be a feasible approach to the construction of new AIEgens. Replacing the silicon atom with group-14, 15, or 16 elements have resulted in a diverse array of AIEgens. The photophysics of these AIEgens are often analogous to their silole counterparts whose AIE activity can primarily be explained by the principle of RIR/RIM.

**4.2.2. Boron Compounds.** Because of the unique electronic nature and chemical characteristics of boron, organoboron species always possess highly useful properties, especially the optoelectronic properties. The aforementioned **137** has already reflected the specialty of boron species. Furthermore, taking advantage of its electron-deficient nature, for example, various D-A systems with special chemical and photophysical properties can be readily created by incorporating different electron-rich functional groups. However, conventional organoboron systems are often afflicted by the ACQ effect, which limits their practical applications. Delightfully, the novel AIE phenomenon has casted a new light on the organoboron research. With the RIM principle as a guideline, a large amount of work has been done to develop new AIEgens that make the best of the boronic nature and virtues of AIE. This subsection will expound the boronic AIEgens in the sequence of carborane, dimesitylborane, boron diketonate, boron ketoiminate, and boron diiminate derivatives.

Chujo et al. have reported a variety of *o*-carborane species which enjoy AIE properties.<sup>181–183</sup> *o*-Carborane, an icosahedral boron cluster compound, is comprised of three-center, two-electron bonds and subsequent three dimensional delocalization of skeleton electrons (three-dimensional aromaticity). What's more, it possesses a well-known highly polarizable  $\sigma$ -aromatic character and electron-withdrawing property through C-substitution. It hence can be envisaged that the introduction of *o*-carborane units into AIE systems will bring about benefits for both areas. For example, by attaching diphenylethynyl groups to the 1,2-position of *o*-carborane, AIEgen **138** is formed (Figure 34).<sup>181</sup> Its negligible  $\Phi_F$  (< 0.02%) in THF can be ascribable to the rotational motions of the aromatic moieties. The crystal structure of **138** indicates that the phenyl rings are not well conjugated, making the molecules take on a twisted conformation that lowers the rotation energy barrier. When aggregated, the activated RIR and the absence of intermolecular  $\pi-\pi$  stacking interactions restore the emission and raise the  $\Phi_F$  to 12.0%.

Another example of AIE system containing *o*-carborane was recently reported by Inagi et al.<sup>184</sup> They created an *o*-carborane-triphenylamine dyad (**139**) with special electrochemical properties owing to the redox response of the triphenylamine (TPA) and *o*-carborane moieties (Figure 34). Different from **138**, the emission maximum of which is at 485 nm, by linking electron-donating TPA to electron-accepting *o*-carborane, the resulting D-A structure (**139**) emits a much redder fluorescence with the emission maximum at 570 nm. Almost no fluorescence is noticeable ( $\Phi_F = 0.7\%$ ) when **139** is dissolved in THF; however, stronger emission ( $\Phi_F = 5.0\%$ ) is induced by the formation of aggregates in the THF/water mixture with  $f_w = 99 \text{ vol } \%$ .

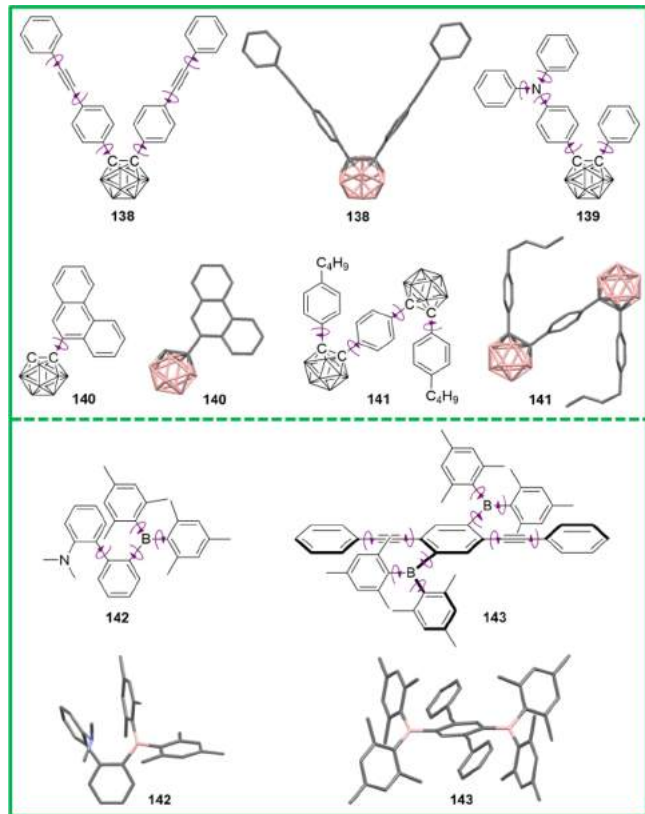


**Figure 34.** *o*-Carborane- (138–141) and dimesitylborane-based (142, 143) new AIEgens, which were designed based on RIR principle. The crystal structure of 138 is obtained and reprinted from the Supporting Information of ref 181. Copyright 2009 American Chemical Society. While those of 140–143 are retrieved free of charge from CCDC (771728, 943436, 833238, and 709030) via [www.ccdc.cam.ac.uk](http://www.ccdc.cam.ac.uk).

Similarly, the AIE effect of 139 results from the RIR process and nonplanar configuration.

Even when *o*-carborane is connected to a substantially larger aromatic system, e.g., phanthrene, via a single bond, the resultant 140 was still found to be AIE-active (Figure 34).<sup>185</sup> The emission from its dilute THF solution is very weak. However, its luminescence dramatically goes up with the  $\Phi_F$  rising to 24.0% when  $f_w = 99$  vol %. 140 is a particularly interesting AIEgen as the carborane or phanthrene moiety can be viewed as both a rotor and a stator, unlike the previously discussed disubstituted carborane derivatives where the carborane moiety mainly acts as a stator core. On the one hand, the small “round” carborane moiety could rotate rather freely at a high frequency and consequently dissipate the excited-state energy. On the other hand, the structurally larger phanthrene moiety may consume more energy in a single instance of rotation on account of a larger moment of inertia. In fact, these situations may even work together to quench the emission in the isolated state. Nevertheless, once the RIR is activated, the emission will be triggered.

141 is an AIEgen that is composed of two *o*-carborane units joined together and decorated with phenyl moieties (Figure 34).<sup>186</sup> Virtually non-emissive when dissolved in THF, 141 displays bright luminescence in the aggregate and solid states, i.e., powder or film. Because of through-space charge transfer from the outer phenyl moieties to the central phenyl core, the emission wavelength of the system could be tuned by modifying the other phenyl units which ultimately affects the HOMO/LUMO band gap.

In addition to *o*-carborane systems, a few luminogens with bulky dimesitylborane moieties in their structures have also been reported to be AIE/AEE-active.<sup>187,188</sup> Compound 142 shows an AEE activity: its  $\Phi_F$  rises from 27.0% in a THF solution to 86.0% in the neat film (Figure 34).<sup>187</sup> It is believed that the RIR process plays an essential role in its AEE characteristics as revealed by its structure feature. Even though 142 adopts a highly twisted structure affecting conjugation between the  $\pi$  systems, because of a strong intramolecular charge transfer (ICT) effect between the nitrogen and boron atoms, the emission maximum of 142 is at 521 nm. The crystal structure also shows evidence of strong N–B interaction, which imposes steric effects onto the phenyl moieties. This aids in explaining why the molecule is already emissive when dissolved in solution. In this case, the great steric crowdedness rigidifies the molecules and hinders intramolecular rotations from efficiently consuming excited-state energy.

Two dimesitylborane groups were attached to a bis(phenylethynyl)benzene core to generate 143 (Figure 34).<sup>188</sup> This luminogen has a  $\Phi_F$  of 16.0% in a benzene solution and its spin-coated film is significantly more emissive with a  $\Phi_F$  of 43.0%. Although there are multiple rotatable phenyl moieties in 143, only the AEE effect is observed. It is because the steric effects between the mesitylene units partially restricted their rotations and hence the excited-state energy cannot be completely extinguished even in isolated states. Undoubtedly, in the aggregate state, the intramolecular rotations are further constrained, leading to an intensified emission.

Recently, some boron diketonates have shown AIE activity.<sup>189,190</sup> Difluoroboron diketonate 144 exhibits an array of interesting luminescence properties, such as mechanochromism, thermochromism, and chronochromism (Figure 35).<sup>189</sup> Moreover, owing to its D-A nature, 144 displays solvatofluorochromism properties, with emission red-shifting as solvent polarity increasing. When dissolved in  $\text{CH}_3\text{CN}$ , 144 is nearly non-luminescent due to the cooperative effects of the high solvent polarity and active intramolecular motions. When aggregated in its  $\text{CH}_3\text{CN}$ /water mixtures or in the solid state, 144 becomes highly emissive exemplifying AIE behavior. Notably, as suggested by its crystal structure, the central difluorodioxaborininium is not completely planar; instead, the  $\text{BF}_2$  moiety is warped out of the central core, indicating vigor vibrational motions of the  $\text{BF}_2$  in the isolated state. Therefore, the AIE feature of 144 should be ascribed to the RIM process. In the aggregate state, the rotations of the aryls and the vibrations of the  $\text{BF}_2$  segment are restricted, and the emission is hence turned on. Other four-coordinate organoboron compounds, like diphenylboron diketonate 145, have been designed and synthesized by Zhang’s team. 145 shows crystallization-induced emission (CIE; Figure 35).<sup>190</sup> CIE is a special case of AIE. The CIE-active luminogen is non-emissive in the isolated state and amorphous state but is only induced to luminesce in the crystalline state.<sup>191</sup> 145 emits weakly in its DCM solution with an observable  $\Phi_F$  of 2.0%. Intriguingly, even freezing the solution cannot obviously intensify the fluorescence. However, the near-infrared (NIR) emissive crystals of 145 exhibit a  $\Phi_F$  as high as 30.0%. For the CIE systems, the amorphous aggregates cannot effectively restrict the intramolecular motions resulting in a non-emissive amorphous aggregate state. However, the compact packing together with the short-distance contacts such as C–H $\cdots$  $\pi$  interactions in the crystalline state are able to effectively constrain these motions, blocking the non-radiative channels and rendering the crystals to become emissive.

Apart from the boron diketonates, there has also been a variety of boron-containing AIEgens derived from ketoiminate.<sup>192–197</sup>

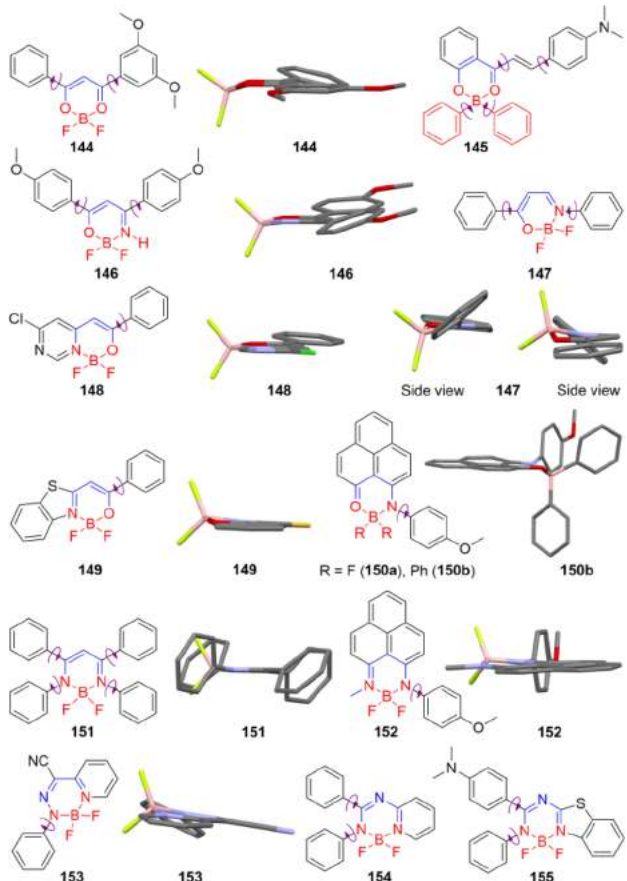


**Figure 35.** Boron-containing heterocyclic AIEgens, varying from dioxaborininium (diketonate) complexes (**144**, **145**), boron ketoimimates (**146**, **147**), oxazaborininium complexes (**148**–**150**), boron diimides (**151**, **152**) to  $\text{BF}_2$ -hydrazone (BODIHY) complexes (**153**–**155**). All of them were constructed based on the RIM principle. The vibrational parts are highlighted in red, and the purple arrows indicate the intramolecular rotations. The crystal structures of **144** and **147** are obtained and reprinted from the Supporting Information of ref 189 (Copyright 2014 American Chemical Society) and ref 193 (Copyright 2014 American Chemical Society). While those of **146**, **148**, **149**, and **150b**–**153** are retrieved free of charge from CCDC (905566, 931994, 890426, 965229, 991936, 965230, and 841443) via [www.ccdc.cam.ac.uk](http://www.ccdc.cam.ac.uk).

A pair of difluoroboron ketoimimates (**146** and **147**) with AIE characteristics have been reported by Chujo and coworkers.<sup>192,193</sup> The difluoroboron ketoimimate **146** (Figure 35) with two anisole units substituting the 4- and 6-positions of the central ring is obviously AIE-active: it is non-emissive in THF ( $\Phi_F = 1.0\%$ ) and highly fluorescent in the aggregate state ( $\Phi_F = 76.0\%$ ).<sup>192</sup> Similar AIE phenomenon has been observed for **147** (Figure 35).<sup>193</sup> The 1- and 4-positions of the central six-membered ring are decorated with two phenyl groups. Interestingly, the original precursor enaminoketone (before complexation with difluoroboron) behaves as an ACQphore, weakly fluorescent in THF ( $\Phi_F = 1.0\%$ ) but almost non-luminescent in the solid state ( $\Phi_F < 1.0\%$ ). As revealed by the crystal structure, enaminoketone is highly planar in molecular shape, making it easy to form excimers that decrease the emission. Furthermore, the carbonyl unit also goes against the emission. After complexation, the resulting **147** shows marked AIE activity: its  $\Phi_F$  value in THF is 1.0%, while in the solid state the  $\Phi_F$  is boosted to 33.0%. Analysis of its crystal structure reveals that the molecule no longer takes on a planar conformation but instead it becomes

highly distorted with twisted phenyl rings and a nonplanar central ring. This structural feature indicates that the phenyl ring rotations and the vibrational motions of the central ring (highlighted in red) could occur more easily due to the weakened conjugation caused by the twisted conformation. This could explain the non-emissive solution state. In the aggregate state, the RIM process is activated, the intermolecular  $\pi$ – $\pi$  stacking interactions are hindered by the highly nonplanar 3D configuration, and the luminescence is therefore switched on.

Kubota et al. observed that some difluoroboron ketoimimates even with a larger conjugated core and decorated by only one phenyl ring could still be AIE/AEE-active.<sup>194,195</sup> Luminogen **148** (Figure 35), with a pyrimidine iminoenolate core, has a low  $\Phi_F$  of 2.0% in DCM. Its  $\Phi_F$  rises to 13.0% in the solid state, exhibiting an AEE behavior.<sup>194</sup> Benzothiazole-based difluoroboron ketoimimate **149** (Figure 35) is nearly non-emissive when dissolved in hexane ( $\Phi_F < 1.0\%$ ) but brightly luminesces in the solid state ( $\Phi_F = 26.0\%$ ), suggesting a typical AIE activity.<sup>195</sup> For both of these luminogens, RIM is verified to be the main cause for their AEE/AIE effect. The intramolecular rotations of the aryl rings and the vibrations of the central boron-bridged ring account for the inefficient emission in the solution state. It is observed that in the crystal state, these molecules form dimeric species which further helps to prevent rotational motions from consuming excited-state energy. Moreover, the distorted molecular conformation obstructs the intermolecular  $\pi$ – $\pi$  stacking interactions, benefiting the aggregate-state light emission.

With a larger and more conjugated core as compared to **146**–**149**, phenalenyl ketoimimates decorated with difluoroboron (**150a**) or diphenylboron (**150b**) have been reported to be AIE-active (Figure 35).<sup>196,197</sup> The  $\Phi_F$  values of **150a**, the difluoroboron compound, in THF and solid state are 0.7% and 8.0%, respectively.<sup>196</sup> In comparison, the diphenylboron complex **150b** possesses a  $\Phi_F$  of 0.2% in THF solution and 51.0% in the film state.<sup>197</sup> For **150a**, there is only one unconstrained aryl moiety that can rotate to consume the excited-state energy. It is hard to believe that the intramolecular rotation of a single rotor could quench the solution-state emission to that large extent, hence it can be envisaged that there should be some other motion modes contributing to the energy consumption. Closer examination on its crystal structure provides some clues to this assumption. The boron-bridged part (highlighted in red in Figure 35) is tilted out of the phenalene plane, indicating that this segment is able to experience dynamic vibrations that help to consume the excited-state energy. RIM thus plays a crucial role in the AIE properties of **150a** and **150b**. The two extra phenyl rings in **150b** further decrease the solution-state luminescence. Furthermore, the solid-state  $\Phi_F$  value of **150a** is remarkably smaller than of its analogue **150b**. Analysis of their crystal packing modes sheds light on this difference. Severe and intense  $\pi$ – $\pi$  stacking interactions amongst neighboring molecules have been observed in **150a**, which result in the formation of destructive species such as excimers and cause decrease in the solid-state emission. In contrast, due to the bulky nature of the two phenyl rings bonded to the boron atom of **150b**, the intermolecular  $\pi$ – $\pi$  stacking is disrupted, enabling it to luminesce much more efficiently in aggregate state.

Besides diketonates and ketoimimates, boron diimides have been reported to show AIE activity.<sup>197–200</sup> Tetraphenyl-decorated difluoroboron diimide **151** shows low  $\Phi_F$ s in good solvent (<1.0% in THF) and in the amorphous state (2.0%), but exhibits higher  $\Phi_F$  in the crystalline state (23.0%).<sup>198</sup> The large increase in the  $\Phi_F$  of the crystal state is indicative of the CIE

activity. The CIE phenomenon of **151** is fairly straightforward to explain: the intramolecular rotations dissipate excited-state energy in the isolated state. Although aggregation can hamper the phenyl ring rotations, as evidenced by the small  $\Phi_F$  value, rotational motions have not been totally restricted. After crystallization, the molecules are further stiffened and the intramolecular motions become more constrained, the non-radiative decay is further blocked and the emission is hence enhanced.

AIEgen **152** and compound **150a** are quite analogous in structure but slightly different in the photophysical properties (Figure 35).<sup>197</sup> Even with a big phenalenyl core, this difluoroboron diiminate is also almost non-emissive in THF with a  $\Phi_F$  as low as 0.8%, which is quite close to that of **150a**. However, **152** emits an intense yellow light in the film state with a  $\Phi_F$  up to 89.0%, which is 10 times higher than that of **150a**. The relatively weak solid-state emission of **150a** had been previously explained by the presence of  $\pi-\pi$  stacking interactions. However, such interactions also exist in the crystal packing of **152** which has an unusually high solid-state  $\Phi_F$ . In the AIEgens **150a** and **152**, the existence of the ketoiminate/diiminate allows for vibratory motions that aid in the dissipation of excited-state energy.<sup>201</sup> For **152**, intermolecular distances are slightly shorter than those of **150a**; this small difference might be the keystone that controls the solid-state luminescence efficiency. The tighter packing may be able to sufficiently restrict the vibrational motions, whereas the looser packing in **150a** still allows for excited-state energy to be consumed by intramolecular motions. In **150a**, the  $\pi-\pi$  stacking interactions are more extensive and in three dimensions, whereas in **152**, they are only extended in the direction of axis *a*. More importantly, the  $\pi-\pi$  stacking interactions play a destructive role in **150a**. On the contrary, they are constructive for **152** for they help to rigidify the molecules and constrain the intramolecular motions.

With extra nitrogen atoms in the diiminate core, boron diiminate derivatives such as borondifluorohydrazone (BODI-HY) complexes are found to be AIE/AEE-active. **153** is such an example (Figure 35).<sup>199</sup> When dissolved in DCM, **153** weakly luminesces with a relatively low  $\Phi_F$  of 6.0%, but in the aggregate state, strong fluorescence is observed with the  $\Phi_F$  as high as 52.0%. Its AEE activity can be demonstrated by the principle of RIM. In the dissolved/isolated state, the intramolecular rotational motions of the phenyl ring and the vibrational motions of the diiminate core dissipate the excited-state energy. While in the aggregate state, the physical constraint and intermolecular interactions impair these intramolecular motions, and the distorted molecular structure prevents the harmful  $\pi-\pi$  stacking interactions, enabling the excited-state molecules to relax radiatively.

In addition to the diiminate compound **153** which was synthesized from a hydrazone precursor, a large group of AIE-active diiminates were synthesized from amidine-based starting reagents.<sup>200</sup> Two examples from this family of AIEgens are **154** and **155** (Figure 35). Incorporating a pyridine moiety to phenyl-decorated amidine affords compound **154**. With a  $\Phi_F$  less than 1.0% in DCM, **154** becomes brightly blue emissive in the solid state ( $\Phi_F = 13.0\%$ ,  $\lambda_{em} = 428$  nm). The AIE phenomenon is also observed for compound **155** which is generated by replacing the pyridine ligand with a benzothiazole moiety. Also, **155** is non-fluorescent in DCM ( $\Phi_F < 1.0\%$ ) but is induced to emit a strong greenish emission in the solid state ( $\Phi_F = 17.0\%$ ,  $\lambda_{em} = 501$  nm). Similar to their analogues discussed above, the RIM process together with their nonplanar conformation accounts for the AIE characteristics of **154** and **155**. Additionally, the emission color of this AIE family can be easily tuned from blue to red by the

variation in the ring fused with the diiminate core. There has been continuously growing interest in creating new boron AIEgens. By means of simply incorporating rotatable moieties and/or vibratable units into the chemical structure, a large array of brightly emissive AIEgens can be easily achieved. By making use of boron's electron-withdrawing nature, strong solid-state emitters whose emissions cover the whole visible spectrum also become accessible by introducing varying electron-donating groups into the molecule.

**4.2.3. Schiff Bases.** AIE-active Schiff bases are a newly emerging class of AIEgens. With its straightforward chemistry, it is easy for Schiff bases to link rotatable moieties via single bonds, making them promising candidates for AIE research. This section seeks to highlight a few examples of AIEgens that take advantage of Schiff base chemistry.

Compound **156** is a Schiff base derivative synthesized from hydrazine and an aldehyde-substituted aza-crown-ether (Figure 36).<sup>202</sup>

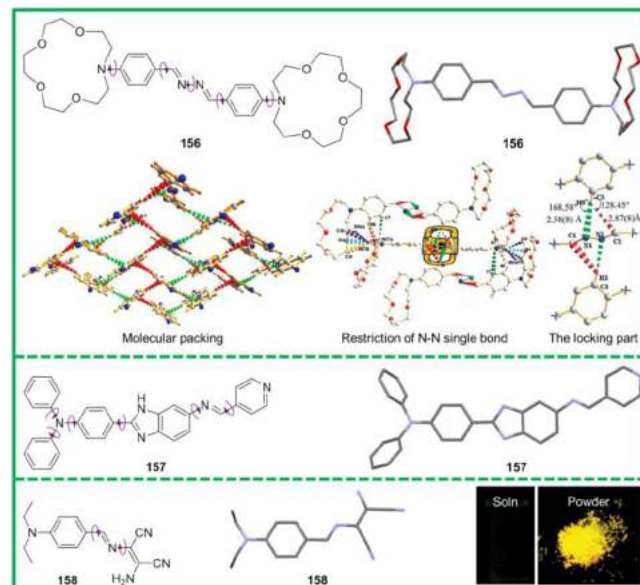


**Figure 36.** Representative examples of Schiff base derived AIEgens designed according to RIR principle. The molecular packing diagram of **156** is adapted with permission from ref 202. Copyright 2012 Royal Society of Chemistry. The fluorescent photographs for **158** are reprinted with permission from ref 204. Copyright 2013 Royal Society of Chemistry. The crystal structures of **156** and **157** are retrieved free of charge from CCDC (848148 and 941787) via [www.ccdc.cam.ac.uk](http://www.ccdc.cam.ac.uk). While that of **158** is obtained with permission from the Supporting Information of ref 204. Copyright 2013 Royal Society of Chemistry.

The structure of **156** is featured with two conjugated moieties linked by a rotatable N–N single bond instead of a C–C bond and rotatable flexible substituents (bulky aza-crown-ether units). In dilute THF solution, **156** only faintly luminesces with a  $\Phi_F$  as low as 0.09%. In the aggregate state, an 88.9-fold increase in emission has been observed, implying its AIE activity. Its AIE activity is in connection with the aza-crown-ether moieties. When the aza-crown-ethers are displaced by diethyl amines, the AIE property is lost. As can be seen from its crystal structure, the aza-crown-ethers are found to play two important roles in the AIE effect. In the isolated state, the rotations and vibrations of the big aza-crown-ether rings work collaboratively with the rotation of phenyl rings to dissipate the excited-state energy. In the aggregate state, for one thing, the bulky character of the aza-crown-ethers prevents intermolecular  $\pi-\pi$  stacking interactions

and the resulting emission quenching. For another, the aza-crown-ethers also direct the molecules to pack in a way that aids in rigidification. The rigidification occurs at two sites: the first one is between two neighboring ether moieties and a phenyl ring unit; the second one is between the central conjugated segment ( $-C=N-N=C-$ ) and its two neighboring phenyl rings. With the help of multiple strong C–H $\cdots\pi$ , C–H $\cdots$ O, and C–H $\cdots$ N interactions, the rotations of the aza-crown-ethers and the N–N bond are restricted and the radiative pathways are hence activated, resulting in the enhanced emission. Yang and Zhou et al. recently reported a Schiff base derivative **157** which contains a TPA unit and heterocycles (Figure 36).<sup>203</sup> It shows a typical AIE phenomenon: it is almost non-emissive when dissolved in THF ( $\Phi_F < 0.1\%$ ); however, upon water addition, the molecules of **157** start to form aggregates and the fluorescence is boosted. A 37-fold increase in the PL intensity was recorded when  $f_w = 80$  vol %. The crystal packing of **157** indicates that there are no  $\pi$  $\cdots\pi$  interactions between neighboring molecules but instead a large number of strong C–H $\cdots\pi$  interactions exist within the range of 2.848 and 3.299 Å. The absence of  $\pi$  $\cdots\pi$  interactions and activation of RIR are rationalized to be the causes of the AIE effect.

Diaminomaleonitrile-functionalized Schiff base, i.e. **158**, exhibits interesting photophysical properties (Figure 36).<sup>204</sup> First of all, **158** shows an AEE activity. In the solution state, **158** is weakly luminescent. In its THF/water mixtures, as water fraction is increased, the molecules are aggregated and the emission is gradually enhanced. Unlike most archetypal AIEgens which often have a twisted propeller-like structure (e.g. HPS and TPE), **158** is a highly planar molecule and such a structure feature brings about unique photophysical properties. In the amorphous state, the less ordered packing and intermolecular interactions such as steric effects allow the activation of RIR and thus switch on fluorescence. However, in the crystal state, the molecules experience severe  $\pi$  $\cdots\pi$  stacking interactions between neighboring molecules resulting in a weakly emissive crystalline state ( $\Phi_F = 3.8\%$ ). Because of the coexistence of amino groups (electron-donating) and cyano groups (electron-withdrawing), **158** possesses a TICT property, exhibiting notable solvatofluorochromism.

Owing to its simplicity, Schiff base chemistry is proved to be a useful tool for the creation of new AIE molecules. The examples of Schiff base AIEgens are not limited to the molecules shown above. In fact, the Schiff base AIEgens that involve some special photophysical processes, i.e., ESIPT, will be discussed in the following subsection.

**4.2.4. Excited-State Intramolecular Proton Transfer (ESIPT) Systems.** ESIPT is a phototautomerization process which proceeds extremely fast at a subpicosecond time scale. The main characteristics of this photophysical process include the formation of intramolecular hydrogen-bonding and the large Stokes shift without self-absorption.<sup>205–208</sup> In the light of the beneficial effects that the ESIPT process imposes on the photophysical fundamentals, plenty of research has been conducted not only to understand but also to harness the process.<sup>209–212</sup> Indeed there have been a large number of successful cases in which compounds that exhibit ESIPT properties have been designed for various practical applications such as photostabilizers,<sup>209</sup> laser dyes,<sup>210</sup> luminescent materials,<sup>211</sup> and molecular probes.<sup>212,213</sup> Integrating AIE with ESIPT will definitely bring about great benefits such as new properties, novel functions, as well as new ideas to both sides. So far, a number of AIE-active ESIPT luminogens have been designed and synthesized, which truly show the magic power of the amalgamation. However, prior to the elucidation of these AIE-

active ESIPT systems, some basic but important insights or knowledge of ESIPT should be gained.

In most ESIPT systems, the proton donors are hydroxyl groups and the proton acceptors are usually nitrogen atoms. If the ESIPT process is inhibited, the enol (E) form undergoes E–E $^*$ –E transitions after excitation, showing a normal emission with a small Stokes shift. Once the ESIPT is allowed, a fast four-level cyclic proton-transfer process (E–E $^*$ –K $^*$ –K) mediated by the intramolecular hydrogen-bonding occurs immediately upon photoexcitation (Figure 37A). The excited enol state (E $^*$ )

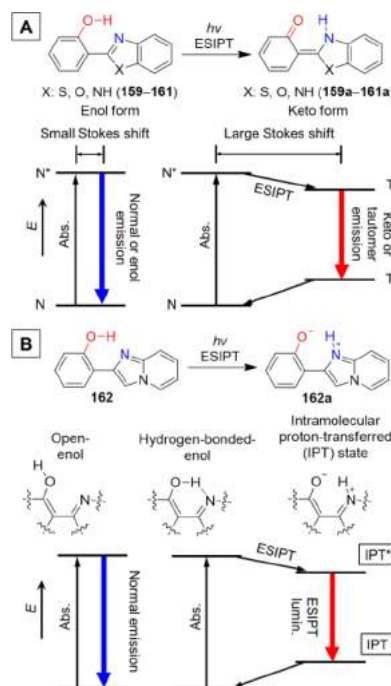


Figure 37. Two kinds of typical ESIPT systems and their corresponding schematic illustration.

tautomerize ( $k_{\text{ESIPT}} > 10^{12} \text{ s}^{-1}$ ) very quickly to the energetically lower excited keto state (K $^*$ ).<sup>214</sup> The energy band gap between the excited keto (K $^*$ ) state and ground state (K) is much narrower than that of the non-ESIPT state. As a result, the ESIPT process (enol-keto tautomerism) generates red-shifted emission with a large Stokes shift. The ESIPT processes of 2-(2'-hydroxyphenyl)benzoazoles (159–161) where the enol-forms tautomerize to their keto forms (159a–161a) in the excited state are illustrated in Figure 37A.<sup>212,215,216</sup> From the structural point of view, the possible conformational flexibility of 159a–161a should arise from the vibrational motions of the 2,3-dihydrobenzoazole moieties. It means that if such ESIPT systems are AIE-active, the emission quenching in the isolated state should be ascribed to the dynamic intramolecular motions. In other words, the AIE attributes of ESIPT compounds are also associated with the RIM processes. Specific examples will be described hereinafter.

As the ESIPT research advanced, it has been found that the ESIPT emissions of quite a few dyes can hardly be interpreted by the principle illustrated in Figure 37A, because their molecular structures do not permit them to adopt keto forms during the ESIPT process. 2-(2'-Hydroxyphenyl)benzimidazole (162) is such an example, whose rational keto structure cannot even be drawn. As depicted in Figure 37B, the stable open-enol form (162) can only change into the intramolecular proton-transferred

(IPT) state (**162a**) with the hydrogen-bonded enol form as an intermediate. In other words, the proton on the hydroxyl group of **162** is transferred to the nitrogen atom in the excited state through intramolecular hydrogen-bonds, affording a charged state (**162a**). Similar to the enol-keto ESIPT systems, in the cases of molecules like **162**, the four-level cyclic proton-transfer process (E–E\*–IPT\*–IPT) would result in a much larger Stokes shift compared with the normal emission. In the zwitterionic charged benzoimidazole (**162a**), the phenolate and imidazo[1,2-*a*]-pyridin-1-ium moiety are connected by a single bond. Such a structural feature renders the two parts freely rotate, serving as a non-radiative channel to extinguish the excited state. More examples of this type of ESIPT compounds can be referred to the works published by Araki's group.<sup>217–219</sup>

In either case, ESIPT has been demonstrated to be compatible with the AIE process. A wide range of ESIPT-active AIEgens developed from Schiff bases fall in the first category shown in Figure 37A. However, there are much fewer AIEgens pertaining to the second type of ESIPT systems. Fortunately, **162** is AIE-active, providing us a good model to elaborate the AIE behavior of an ESIPT compound.<sup>217</sup> When excited at 330 nm, **162** in good solvents weakly fluoresces in the visible region with low  $\Phi_F$  ranging from 1.0% to 8.0%. Blue fluorescence at 375 nm, orange fluorescence at 567 nm with a large Stokes shift, and both blue and orange luminescence at 377 and 602 nm are observed in protic ethanol, nonpolar cyclohexane, and THF, respectively. In the ethanol solution, only normal or enol emission can be seen, because the intramolecular hydrogen-bonding is replaced by the intermolecular hydrogen-bonding between **162** and solvent molecules. As a consequence, the intramolecular rotations of **162** become slightly restricted. In apolar cyclohexane, there exists little interaction between **162** and the nonpolar solvent. The luminophore therefore undergoes an ESIPT process mediated by the intramolecular hydrogen-bonding and completely changes to the IPT form. As mentioned above, this IPT form is flexible in structure and its dynamic intramolecular motions consume most of the excited-state energy, leading to a weak light emission in cyclohexane. Because of the moderate polarity of THF, the two tautomers are in equilibrium. The two PL peaks shown by **162** in aprotic solvent like THF are hence ascribed to the emissions of its enol and IPT forms. No matter which form **162** takes, the solution emission is weak. The single-bonded moieties (rotors) can rotate easily and the radiative decay is thus effectively blocked. When it comes to the aggregate or solid state, even in the amorphous state, **162** becomes a strong emitter with  $\Phi_F$  varying from 37.0% to 50.0%, clearly demonstrating its AIE activity. The RIM or RIR is rationalized to be the main working principle of the AIE effect of this kind of ESIPT luminogens.

Compound **163**, namely, salicylaldehyde azine, is a symmetric simple Schiff base enjoying both ESIPT property and AIE activity (Figure 38).<sup>220</sup> No obvious light emission is observed from the dilute ethanol solution of **163** ( $\Phi_F = 0.2\%$ ). Adding non-solvent like water into such ethanol solution causes the aggregate formation. Luminescence emerges and goes up with the increase in  $f_w$ . In protic ethanol, the hydroxyl groups of the solvent molecules compete with those of **163** to form intermolecular hydrogen-bonds. No matter what kind of hydrogen-bonding is formed, this luminogen can undergo active intramolecular motions in the excited state. In the case of intermolecular hydrogen-bonds, the rotatory segments in **163** can rotate not only around the N–N axis but also the C–C axes as well. While in the form of intramolecular hydrogen-bonding, the ESIPT process will take effect and gives rise to the keto form (**163-keto**)

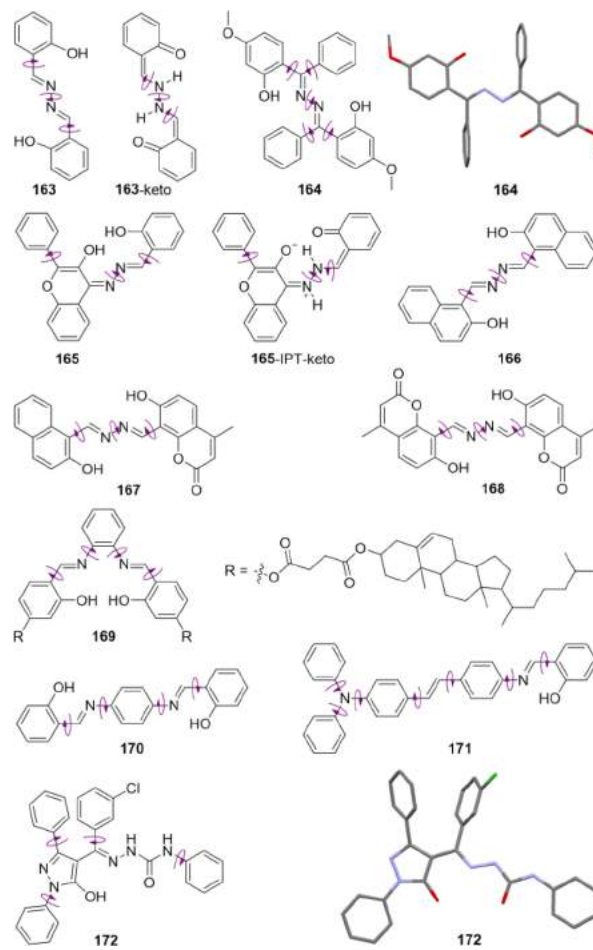


**Figure 38.** Representative examples of AIE-active ESIPT compounds derived from Schiff bases. The crystal structure of **164** is obtained and reprinted from the Supporting Information of ref 221. Copyright 2013 American Chemical Society. The optimized molecular structure of **172** is obtained by means of MMFF94 in Chem 3D.

in the excited state. For **163-keto**, the vigorous intramolecular rotations of the aromatic parts around the N–N and C–N axes non-radiatively exhaust the excited-state energy. All these intramolecular rotational modes jointly dissipate excited-state energy granting a non-emissive solution state. Whereas the molecules in the aggregate state are rigidified by the intramolecular hydrogen-bonding and the physical constraints. The RIR process is thereupon activated to endow **163** with efficient emission. It should be noted that the ESIPT and AIE are two individual and compatible processes. AIE originates from RIM and results in enhanced emission, while ESIPT stems from intramolecular hydrogen-bonding mediating proton transfer in the excited state and leads to a large Stokes shift in the emission.

Decorating **163** with different groups can readily afford a family of AIE-active ESIPT luminogens with diverse emission colors and various functionalities. Luminogen **164** is a member of such a family (Figure 38).<sup>221</sup> With one extra phenyl ring on each C=N moiety, **164** is almost non-luminescent in the solution state while brightly emissive in the aggregate/solid state. Quite similar to its analogue **163**, the intramolecular motions especially the rotations are responsible for the non-emissive solution state. When molecularly dispersed, no matter **164** is in the form of enol or keto, intramolecular rotations around the single bonds (enol form, N–N and C–C; keto form, N–N, C–N, and C–C)

effectively dissipate the excited-state energy. These energy-consuming motions become restricted both in the aggregate and solid states due to the physical constraint as well as the intramolecular hydrogen-bonding interactions, thus allowing radiative decay and efficient luminescence. Moreover, the two additional phenyl rings are twisted out of the central plane, which contributes to the enhanced emission in aggregate state for it has hampered the intermolecular  $\pi-\pi$  stacking interactions. In addition to the symmetric salicylaldehyde azine derivatives (e.g., 163 and 164), asymmetric Schiff bases such as 165 are also found to possess AIE characteristics. In 165, one intramolecular hydrogen-bonding locus is on the 2-(iminomethyl)phenol segment and the other is on the 4-imino-2-phenyl-4H-chromen-3-ol moiety derived from 3-hydroxyflavone (Figure 38).<sup>222</sup> It is notable that 165 is an example that the two typical ESIPT modes discussed in Figure 37 are incarnated in one compound. Under appropriate conditions, 165 will undergo ESIPT processes affording 165-IPT-keto in the excited state, where the original 4-imino-2-phenyl-4H-chromen-3-ol part takes a IPT form and the 2-(iminomethyl)phenol unit is in a keto form. As previously mentioned, no matter whether the ESIPT process is activated or not, the AIE properties of ESIPT systems should be attributed to the RIM principle. Specifically speaking, for 165, the absence of solution-state emission results from the active intramolecular rotations around the axes of single bonds (enol, C–C and N–N; IPT-keto form, C–C, N–N, and C–N). The high luminescence efficiency in the aggregate state is thus ascribed to the activated RIR process and the distorted molecular conformation.

Replacing the phenol rings in 163 with hydroxy naphthyl groups creates a new simple ESIPT luminophore featured with AEE characteristics (166; Figure 38).<sup>223</sup> In the same way, displacing one or both of the naphthyl moieties in 166 with 4-methyl-coumarin derives the ESIPT compounds 167 and 168 (Figure 38), respectively, which are similarly AIE-active.<sup>224</sup> The  $\Phi_F$  values of 166 in pure DMF and the aggregate state are, respectively, 5.7% and 27.0%, indicative of an AEE activity. The nanoaggregates of 167 and 168 emit strong orange and red luminescence, respectively. The occurrence of the ESIPT processes is demonstrated by the large Stokes shifts ( $\sim$ 240 nm for 167 and  $\sim$ 270 nm for 168). Their aggregate-state  $\Phi_F$ s are as high as 54.6% and 82.7%. In sharp contrast, when molecularly dissolved in DMSO, both 167 and 168 are very weakly fluorescent with  $\Phi_F$ s that can hardly be detected. Analogous to 163 and 164, the AEE/AIE effects of 166–168 are rationalized to be caused by the RIM processes. In the molecularly isolated states, the rotatory moieties in these luminogens actively rotate around the C–C and N–N (enol) or C–C and N–N and C–N axes (keto), extinguishing the excited-state energy and leading to the non-radiative relaxation. In the aggregate or solid state, the molecules are stiffened and the intramolecular motions are impeded, the radiative decay pathways are switched on. With the aromatic moieties changing from phenyl, naphthyl to 4-methylcoumarin, the emission color of the resulting ESIPT compounds can be fine-tuned from green (163) to yellow (166) and even to orange (167) or red (168). The red-shift in the emission wavelength is probably due to the enlarged conjugation and the strengthened D-A effect.

The above examples are Schiff base derivatives, each of which has two intramolecular hydrogen-bonding sites joined together via a rotatable N–N single bond. The following two examples are those having their salicylideneamine moieties separated by a phenyl ring, with the connection either at the *ortho*- (169) or

*para*-positions (170) of the benzene ring (Figure 38).<sup>225–227</sup> The salicylideneaniline-based organogelator 169 is nearly non-emissive in the solution state with a  $\Phi_F$  as low as  $\sim$ 0.01%, but the gelation of 169 owing to its cholesterol groups induces a bright yellow fluorescence. The  $\Phi_F$  of the gel is approximately 7.7%, much higher than that of the solution.<sup>225</sup> Similarly, *N,N'*-bis(salicylidene)-*p*-phenylenediamine 170 is scarcely luminescent in THF, while its emission is greatly brightened by the aggregation. The  $\Phi_F$  is up to 33.0% in the THF/water mixture with  $f_w = 90$  vol %.<sup>226</sup> Although these ESIPT systems do not have rotatable N–N single bonds like 163–168, they do have C–C and/or C–N single bonds that allow rotational motions to consume excited-state energy. As the various rotations in 169 and 170 efficiently dissipate the excited-state energy, these ESIPT compounds are non-emissive in the dissolved state. When gelation of 169 and aggregation of 170 occur, RIR processes come into play, rendering them emissive. In addition, functionalizing the 170 on the salicylideneamine moieties with different electron-donors can facilely tune the emission colors of these AIE-active ESIPT luminogens.<sup>227</sup>

The salicylideneamine unit, as a pretty serviceable ESIPT building block, has been attached to diverse other moieties in order to generate new AIE-active ESIPT compounds.<sup>228,229</sup> TPA-based Schiff base 171 (Figure 38) has also been found to show the AIE property. Ascribable to the multiple intramolecular rotations around the C–C and C–N axes that dissipate the excited-state energy, 171 has a low  $\Phi_F$  of 0.4% in the THF solution. The  $\Phi_F$  rises to 5.2% in the solid state as the RIM process causes the excited-state molecules to relax radiatively.

Pyrazolone phenylsemicarbazone derivative 172 (Figure 38) shows an AIE attribute as well as an ESIPT activity.<sup>230</sup> Very weak fluorescence was detected for the dilute ethanol solution of 172. Intramolecular motions such as the multiple phenyl ring rotations in 172 (no matter enol or keto form) deplete the excitation energy, giving rise to a weakly-emissive state. In the aggregate state, such intramolecular motions are obstructed, making the molecules radiatively relax to the ground state and resulting in an emission enhancement of 24-fold. It is worth mentioning that the highly distorted configuration of 172 also makes contributions to the efficient aggregate-state emission.

As suggested above, the large variety of AIE-active ESIPT luminogens has demonstrated the compatibility of AIE with other processes and systems. These works further diversify the AIE family, providing a feasible and flexible pathway for the molecular design of more AIEgens. By combining the advantages of AIE and ESIPT processes, it becomes much simpler and easier to prepare efficient solid-state emitters with a large Stokes shift in their emission overcoming self-absorption quenching.

**4.2.5. Hydrogen-Bonding Systems.** As an important non-covalent force, hydrogen-bonding (H-bonding) has been recognized to be of significance in the field of photophysics research. In the previous section, intramolecular H-bonding has already displayed its ability to aid in the rigidification of the AIE molecules to either turn on or enhance emission. In the same way, intermolecular hydrogen-bonding can and has been used to aid the processes of RIR, RIV, and RIM. It helps minimize the non-radiative energy losses and maximize the probability of radiative relaxations. This section will highlight the luminogens that have hydrogen-bonding designed into the molecular structures to facilitate the AIE processes.

Phenylbenzoxazole-based compound 173, namely, *N*-(4-(benzo[*d*]oxazol-2-yl)-phenyl)-4-*tert*-butyl benzamide, is a simple and representative example that contains hydrogen-bonding by

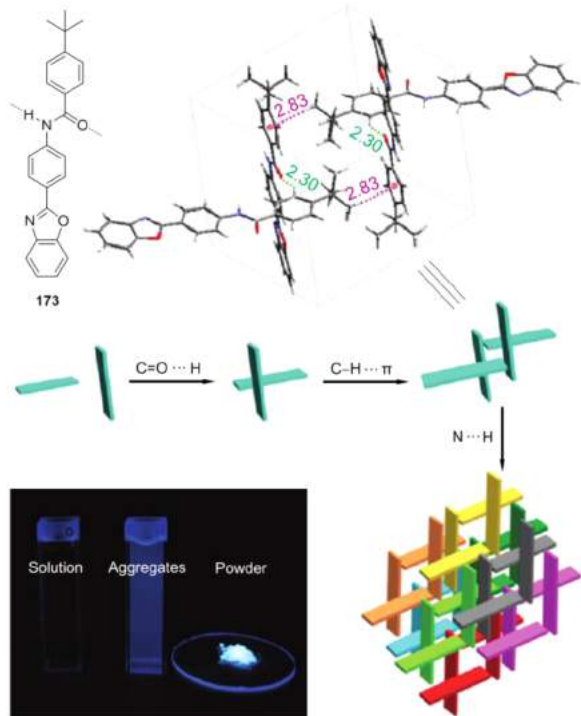


**Figure 39.** AIE-active hydrogen-bonding-containing compound *N*-(4-(benzo[*d*]oxazol-2-yl)-phenyl)-4-*tert*-butylbenzamide (173). Adapted with from ref 231. Copyright 2012 American Chemical Society.

incorporating an amide moiety into its structure (Figure 39).<sup>231</sup> When dissolved in THF, the light emission from this solution is rather weak ( $\Phi_F = 0.2\%$ ) as the molecules are well dispersed and dynamic intramolecular rotations effectively dissipate the excited-state energy. With the addition of water, a poor solvent to 173, the molecules aggregate together and the hydrogen-bonding between molecules starts to form. From its crystal structure it can be seen that there are four 173 molecules per unit cell, exhibiting cross stacking by means of two kinds of interactions, i.e., the H-bonding associated with the carbonyl groups and C–H...π interactions. A pair of molecules are initially held together by a C=O...H bond with a distance of 2.30 Å and stacked in an edge-to-edge mode forming an X-shaped dimer. Two such X-dimers are then edge-to-face connected with each other via strong C–H...π bonds with a distance as short as 2.83 Å, forming a #-shaped tetramer in a unit cell. These #-aggregates are further interconnected by intermolecular N...H interactions between the nitrogen atom on the oxazole ring and hydrogen atoms of the aryl ring or amide on the neighboring molecules, expanding into a 3D network. The distances of the N...H interactions are as short as 2.49, 2.34, and 2.60 Å. These short-distance intermolecular interactions together with the physical constraints resulting from aggregation stiffen the molecular conformation and restrict the intramolecular motions and thus switch on the luminescence. The nanoaggregates in the THF/water mixture are emissive while the fluorescence from the powder state is significantly more intense ( $\Phi_F = 50.3\%$ ). This could be ascribed to two reasons: for one thing, the water molecules might compete to form hydrogen-bonds with the luminogenic molecules weakening the restriction on the intramolecular motions; for another, the loose and irregular packing in the aggregates is less in favor of the formation of H-bonding. In contrast, there is no interference affecting the RIM

process in the solid powder, which makes the fluorescence greatly enhanced.

Dendritic compound 174 is composed of a *p*-terphenylene core decorated with two amide moieties and poly(benzyl ether) dendrons (Figure 40).<sup>232</sup> When molecularly dissolved, the

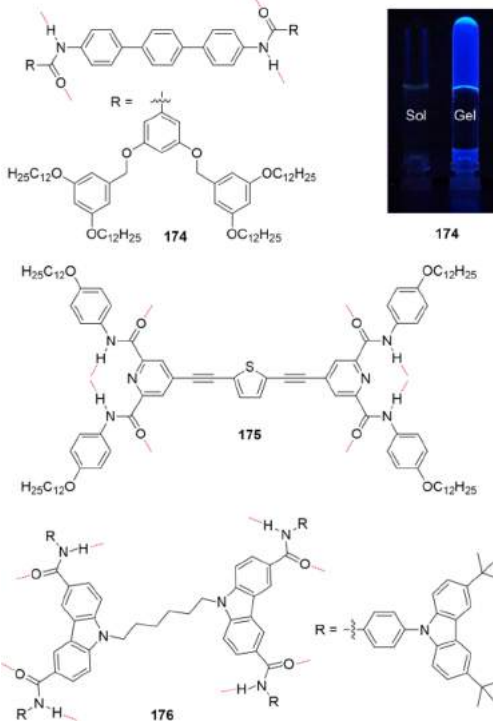


**Figure 40.** Representative AIE-active systems containing multiple hydrogen bonds based on amide groups. Inset: Fluorescent photographs of 174 in solution and gel states. Adapted from ref 232. Copyright 2009 American Chemical Society.

multiple rotatable phenyl rings exhaust the excited-state energy so that 174 becomes non-luminescent. This compound could also gelatinize in many organic solvents due to a cooperative effect of the hydrogen-bonding between the amide groups and van der Waals forces. The gel state is observed to be 800 times more fluorescent than its solution state. The AIE feature of this luminogen can be well explained by the RIR principle. The introduction of more amide bonds is anticipated to further aid the gelation and reinforce the molecular rigidification that helps to activate the AIE processes.<sup>233,234</sup> Along with rotatable moieties, each of 175 and 176 has four amide groups in the molecular structure (Figure 40). They are non-emissive when dissolved in good solvents. Multiple hydrogen-bonding between amide groups as well as van der Waals interactions play a vital role in the gelation processes. In the gel state, these two compounds become strong emitters with 175 showing yellow fluorescence and 176 emitting blue luminescence. Their AIE properties are also ascribable to the RIR principle.

In addition to the amide groups, other H-bonding motifs such as carboxyl, amine, imide, and sulfonyl groups have also been utilized to construct H-bonding-containing AIE systems.<sup>235,236,238</sup> In fact, niflumic acid (177; Figure 41A), a well-known pharmaceutical drug widely used in the biological and medical chemistry areas and especially effective in the muscular and joint pain,<sup>236</sup> has been identified to be an AIEgen by Yan et al.<sup>235</sup> The carboxylic and imine groups in its structure allow for

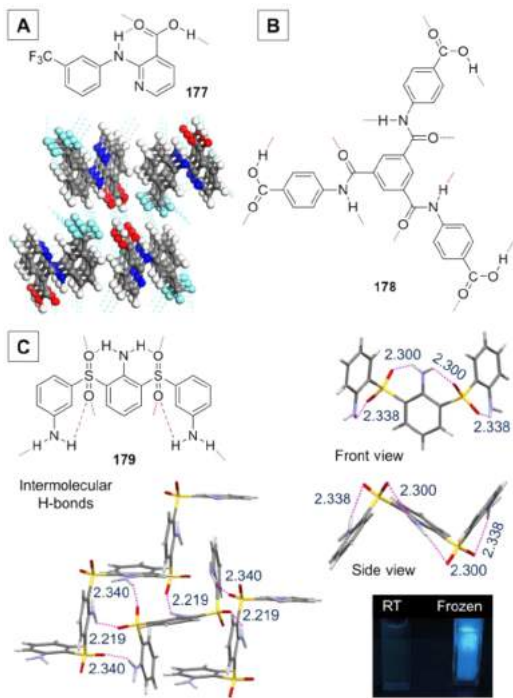


**Figure 41.** Representative AIE-active systems containing multiple hydrogen bonds based on the synergistic effect of (A) carboxyl/imine, (B) carboxyl/amide, (C) sulfonyl/amine groups. The molecular structure of **177** is reprinted from ref 235. Copyright 2014 American Chemical Society. The fluorescent photographs for **179** are reprinted with permission from ref 238. Copyright 2014 Wiley-VCH Verlag GmbH & Co. KGaA. The crystal structure of **179** is retrieved free of charge from CCDC (951163) via [www.ccdc.cam.ac.uk](http://www.ccdc.cam.ac.uk).

the formation of both intramolecular and intermolecular hydrogen-bonds. **177** dissolved in THF possesses a  $\Phi_F$  as low as 0.03%, while the  $\Phi_F$  increases to 4.26% in the solid state, exhibiting dramatic emission enhancement. The hydrogen-bonds aid in rigidifying the molecular conformation and constraining the intramolecular motions and further contribute to the efficient luminescence of **177** in the aggregate state.

AIE systems that incorporate both amide and carboxylic groups as H-bonding motifs to stiffen the molecular conformation and exert constraints on intramolecular motions have been reported as well. Taking the 1,3,5-benzene tricarboxamide-based hydrogelator **178** as example, no fluorescence is shown when it is fully dissolved (Figure 41B).<sup>237</sup> Strong multiple hydrogen bonds between the neighboring molecules make it easy for **178** to gelatinize. In the gel state, the multiple and massive intramolecular forces impose great restrictions on the intramolecular motions that once quenched the solution-state emission. As a result, the H-bonding-assisted RIR process turns on the light emission of this multiarmed luminogen.

The compound **179** highlighted in Figure 41C is of particular interest. **179** is only faintly luminescent in dilute DMSO solution ( $\Phi_F = 0.2\%$ ), but in the aggregate state or when its solution is frozen, blue emission becomes visible and gets intensified (Figure 41C).<sup>238</sup> The  $\Phi_F$  of **179** in powder state is up to 15.0%, manifesting its evident AIE activity. As evidenced by its molecular structure, it is not difficult to understand its weakly-emissive nature in solution state: multiple rotational motions around single bonds are possible when DMSO molecules separate the luminogenic molecules and interfere with the hydrogen-bonding formation. In comparison, in the aggregate state, the

intra- and intermolecular H-bonding between the sulfonyl and amine groups are readily formed. With the aid of these short-distanced interactions (2.219–2.340 Å), the molecules of **179** are highly rigidified, the RIR process is activated, and the luminescence is thus switched on.

By means of introducing H-bonding motifs or building blocks into the molecular structures, the resulting hydrogen-bonding interactions can be utilized to promote the AIE processes of luminogenic compounds. Both intra- and inter-molecular H-bonds can serve as effective means to stiffen the conformation and contribute to the RIM processes. Such kind of work makes AIEngens promising candidates for various luminescent gelation systems that can be used to serve diverse purposes.<sup>231–235,237,238</sup>

**4.2.6. Nitrile Compounds.** Owing to its structural simplicity and high polarizability, the nitrile or cyano group has been extensively applied as a functional unit in the design of advanced optoelectronic materials. By making use of the nitrile groups, a great number of AIEngens have been developed. The nitrile group, although not as large as the phenyl ring, is still able to bring on steric effects like crowdedness to the neighboring moieties and gives rise to twisted conformation because of its rigid structure.<sup>239</sup> Thanks to this feature, there have already been a lot of fumaronitrile and cyanostilbene-based AIEngens.<sup>240–242</sup> Another advantage of the nitrile group is its electron-withdrawing nature, which makes it easy to create simple D-A systems with desired photoluminescent properties through judicious molecular design. For instance, by taking advantage of its electron-donating property and twisted molecular structure, TPA has been increasingly often combined with nitrile groups to create AIEngens with D-A structures and special photophysical properties such as long-wavelength emission, solvatochromism, etc.<sup>243,244</sup> This section will examine how the nitrile groups have been utilized to create new AIEngens and elucidate their AIE mechanisms as well.

One of the examples that merge TPA moieties and cyanostilbene groups together to afford new AIEngens is sketched in Figure 42 (i.e., **180**).<sup>245</sup> It has been found that both steric and electronic effects of a nitrile group affect the emission process of an AIEngen. **180** possesses a D-A structure and multiple rotatory moieties. As a result of such a structural feature, **180** displays typical TICT plus AIE behaviors. It is weakly emissive when molecularly isolated in THF ( $\Phi_F = 2.0\%$ ). As the  $f_w$  increases in the THF/water mixtures, the polarity of the solvent system becomes higher and a clear drop in the emission intensity is thereby a result. When the  $f_w$  reaches the critical point where the molecules of **180** begin to aggregate together due to poor solubility, the emission starts to be intensified. The weak fluorescence in the solvated state can be ascribed to the rotational motions of phenyl rings. Intermolecular steric effects and multiple intensive H-bonds like C–H···N and C–H···π cooperatively impair these motions, rendering the excited states to radiatively decay in the aggregate or solid state. **180** holds a  $\Phi_F$  of 33.0% and 31.0% in the powder and crystal state, respectively. The twisted molecular conformation originated from the steric hindrance between the neighboring phenyl rings and the nitrile moiety obstructs the intermolecular π–π stacking and thus prevents the emission quenching in the aggregate state.

New AIEngens created by joining the TPA skeletons together with cyano acrylamide (e.g., **181**) or malononitrile (e.g., **182**) moieties have recently been reported (Figure 42).<sup>246,247</sup> Both **181** and **182** are weakly emissive when dissolved in good solvents like THF and DMF, because the intramolecular rotations actively dissipate the excited-state energy. With a high enough fraction of

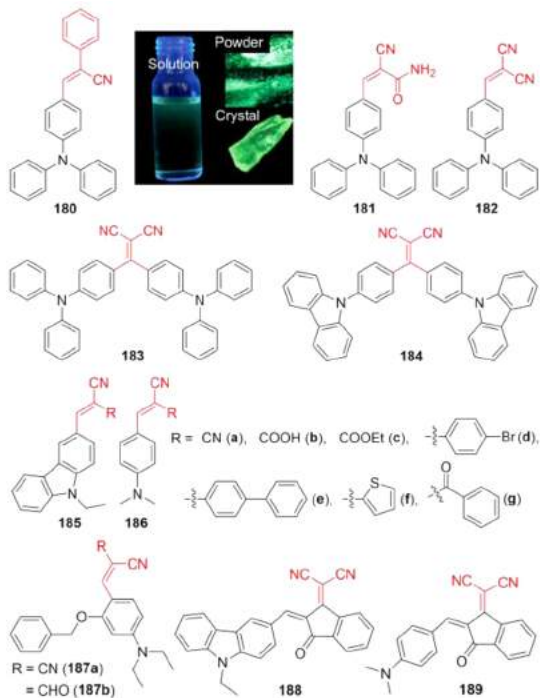


**Figure 42.** Cyano-substituted AIE plus TICT systems. The fluorescent photographs are reprinted with permission from ref 245. Copyright 2013 Royal Society of Chemistry.

poor solvent, the dye molecules aggregate together, the luminescence is readily turned on as a consequence of RIM processes. Careful inspection on the crystal structure of **181** has provided a deeper insight into the reasons for the efficient aggregate-state emission. **181** takes on a highly distorted conformation to fit in the crystalline lattice, hindering the detrimental excimer formation. The C—O···H and two types of N—H···O interactions between adjacent molecules with a distance of 2.177 Å, 2.409, and 2.702 Å, respectively, lock and rigidify the molecular conformation and hence increase the  $\Phi_F$ .<sup>246</sup> The AIE effect of **182** is likewise caused by the RIM process together with the twisted configuration as well as the multiple intermolecular interactions.<sup>247</sup> Luminogen **181**, which is decorated with cyano acrylamide, displays a green fluorescence, while stronger electron-withdrawing malononitrile-embellished compound **182** shows a yellow-orange emission.

Attaching one malononitrile group with two identical electron-donating moieties, e.g., TPA and carbazole units, generates luminogens **183** and **184** (Figure 42).<sup>248</sup> Both of them exhibit TICT properties and AIE features. Although their THF solutions are fluorescent, when water is added to these solutions, the increase in polarity of the mixtures causes them to become much less emissive. When the solubility of the luminogens becomes too poor due to the high water fraction, the aggregates begin to form and the activated RIR process thus induces the light emission. The  $\Phi_F$ s of **183** and **184** in the solid state are 11.5% and 16.0%, respectively. Benefiting from their AIE properties and large D-π-A structures, both **183** and **184** exhibit large two-photon absorption cross sections as well as the corresponding two-photon excited fluorescence (TPEF).

Systematic works have been done on a group of nitriles, each of which is decorated with an electron-donating skeleton like carbazole (**185**) or dimethylaniline (**186**; Figure 42).<sup>249</sup> All these luminogens show typical AIE and TICT properties.

The malononitrile-functionalized carbazole derivative (**185a**) and dimethylaniline (**186a**) are representatives of such a system. Because of the proximity of the nitrile group to the phenyl ring attached to the double bond, the steric repulsion makes it not possible for the molecules to adopt a planar configuration. The resulting twisted structure reduces the rotation energy barrier facilitating the rotational motions to occur in the solution state. Consequently, neither **185a** nor **186a** luminesces strongly in the solution state, with the corresponding  $\Phi_F$ s as low as 0.29% and 0.71%, respectively. However, in the THF/water mixtures with  $f_w = 90$  vol %, the nanoaggregates form owing to poor solubility. Greatly enhanced emission is displayed with  $\Phi_F$ s rising to 12.1% for **185a** and 44.0% for **186a**. In the nanoaggregates, the intramolecular motions get constrained causing the molecules to relax via radiative pathways. The distorted nature of the molecules also reduces the intermolecular π-π interactions that would have resulted in emission quenching. By changing the R group of **185** and **186** from CN (**185a** and **186a**) to COOH (**185b** and **186b**), COOEt (**185c** and **186c**), bromobenzene (**185d** and **186d**), biphenyl (**185e** and **186e**), thiophene (**185f** and **186f**), or benzaldehyde (**185g** and **186g**), the emission wavelength could be tuned while retaining the AIE activities of the cores (Figure 42).<sup>249</sup> The AIE effect for the **185** and **186** systems is associated with the twisted structure that results from the steric hindrance between the aromatic core and one of the branches from the double bond. The substitution of different groups does not affect the AIE property because these moieties maintain the steric effect imposed onto the aromatic core. The tuning of the emission wavelength is achieved by manipulating the D-A effect. While keeping the electron-donating groups constant as the carbazole or dimethylaniline, the electron-withdrawing segment of the luminogen is gradually modified with various substitutions. In this way, a full spectrum of solid-state emitters has been generated, from blue all the way to red.

Structurally similar to the previously-discussed compound **186a**, **187a** consists of a [4-(diethylamino)benzylidene]malononitrile core decorated with a benzyloxy group (Figure 42).<sup>250</sup> This luminogen also displays AIE characteristics. It strongly emits in the aggregate state, with a  $\Phi_F$  of 11.0% in the crystal state, although it is almost non-emissive when well dissolved in good solvents ( $\Phi_F < 0.1\%$ ). By replacing one of the nitrile groups with an aldehyde moiety, AIE-active luminogen **187b** is formed. **187b** possesses very similar photophysical properties as its predecessor: in contrast to its negligible solution-state  $\Phi_F$ s (< 0.1%), its  $\Phi_F$  in the crystal state rises to 13.0%. The crystal analyses of **187a** and **187b** both indicate that their molecular conformations have been greatly rigidified by the multiple intermolecular interactions such as C—H···π, C—H···N, and/or C—H···O, and the intramolecular motions have hence been hindered. Their AIE mechanisms are thus rationalized to be the RIR principle. One of the greatest advantages of nitrile-containing systems is their facility and feasibility with regard to the construction of long-wavelength emitters. Luminogens **188** and **189** are perfect examples to demonstrate this.<sup>249</sup> Malononitrile group is fully substituted by a large conjugated (Z)-9-ethyl-9H-carbazol-3-yl-methylene-indenone or (Z)-dimethylanaminobenzylidene-indenone, readily generating compound **188** or **189**. In virtue of their large electronic conjugations and strong D-A effects, these two luminogens exhibit near-infrared fluorescence in the aggregate state. Moreover, their molecules are distorted in conformation as a result of the steric repulsion effects between the CN groups and their adjoining aromatic rings. Such a structure feature endows them with free intramolecular

motions in the isolated state and obstructs the intermolecular  $\pi-\pi$  stacking interactions in the aggregate state. Therefore, **188** or **189** are induced to intensely fluoresce by the aggregation, indicative of their AIE attributes.

AIE phenomena have also been found in a number of other fully-substituted malononitrile derivatives. For example, quinoline-malononitrile derivatives **190** and **191** show marked AIE characteristics (Figure 43A).<sup>251</sup> In each of these molecules, the

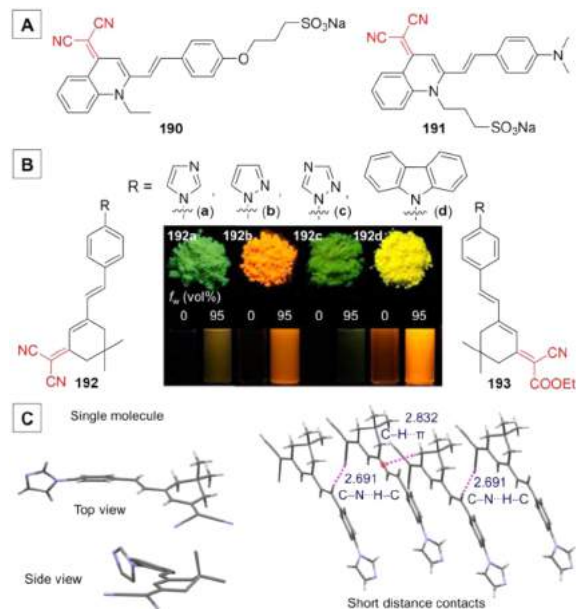


**Figure 43.** AIE-active quinoline-malononitrile compounds (**190**, **191**) and cyano substituted isophorone derivatives (**192**, **193**). (C) The crystal structures of **192a**. The insets in part B are the fluorescent images of compound **192a**–**192d** in the solid state and ethanol/water mixtures with  $f_w = 0$  and 95 vol %, respectively. The fluorescent photos for **192** are reprinted from ref 252. Copyright 2013 American Chemical Society. The crystal structure of **192a** is retrieved free of charge from CCDC (916477) via [www.ccdc.cam.ac.uk](http://www.ccdc.cam.ac.uk).

quinoline-malononitrile core serves as an AIE-active building block. When the sulfonate group is incorporated on the donor functional group position in the backbone, the resulting luminogen **190** is water immiscible but AIE-active. No emission from **190** is noticeable when it is dissolved in THF ( $\Phi_F = 0.2\%$ ) or ethanol ( $\Phi_F = 1.5\%$ ). The addition of water into such a solution gradually intensifies the fluorescence, exhibiting an enhancement in  $\Phi_F$  up to 96-fold when  $f_w = 99$  vol % in the THF/water mixture. In sharp contrast, when the sulfonate group is directly attached to the quinoline-malononitrile core, the afforded compound **191** is quite soluble in water. **191** is thus non-emissive when dissolved in water with a  $\Phi_F$  as low as 0.1%. Its aggregates in water/ethanol mixtures show a maximum  $\Phi_F$  of 27.5% resulting in a  $\alpha_{AIE}$  value as high as 275. The excellent AIE activity and efficient red emission as well as the superb water miscibility of **191** make it a perfect candidate for biological applications such as label-free and light-up fluorescent assay of proteins. The AIE features of **190** and **191** can be explained by the RIM principle: the intramolecular motions consume excited-state energy through non-radiative relaxations in the isolated state; on the other hand, steric constraints and intermolecular interactions such as C–H··· $\pi$  and C–H···N prevent such motions from taking effect, permitting the molecules to relax via radiative channels in the aggregate state.

Recently, quite a few cyano-substituted isophorone derivatives have been reported to be AIEgens.<sup>252–254</sup> Zhou's research team has conducted a systematic work to investigate the substitution effect of the dicyanoisophorone (**192**)<sup>252</sup> and cyano-ester isophorone derivatives (**193**) (Figure 43B).<sup>253</sup> The isophorone-based core of compound **192** is decorated with malononitrile while the one of **193** is functionalized with a cyano-carboxylate moiety. By changing the R group with a variety of nitrogen-containing heterocyclic rings, diverse AIEgens are facilely created. The molecular packing modes, electronic structures and photophysical properties are directed by the variation in the terminal substituent (Figure 43B and 43C). The electron-donating heterocyclic groups together with the electron-withdrawing malononitrile or the ethyl 2-cyanoacrylate moiety endow the luminogens with D-A structures and the emission colors hence become tunable. Crystallographic analyses of these isophorone derivatives reveal that the existence of various short-distance contacts like intermolecular hydrogen-bonding interactions between the adjacent molecules constrains the intramolecular vibrations and rotations, and the luminogens **192** and **193** are hence enabled to fluoresce intensely in the aggregate state. Take **192a** for example. As revealed by Figure 43C, **192a** adopts a twisted configuration. Packed together with the aid of multiple intermolecular C–H··· $\pi$  and C–H···N–C interactions, the molecules of **192a** are greatly stiffened, and the RIM process comes into play, resulting in the emission turn-on in the aggregate state. In addition, the absence of destructive  $\pi-\pi$  interactions shown by the crystal packing impedes the emission quenching.

There have also been a few reports of attaching nitrile groups to large conjugated cores with the aim of producing red to NIR AIEgens.<sup>255–257</sup> Cruciform structured **194** is embellished with a total of six nitrile groups in order to guarantee a strong electron-withdrawing effect and further augment the D-A effect to push the emission into the red region (Figure 44).<sup>255</sup> When dissolved

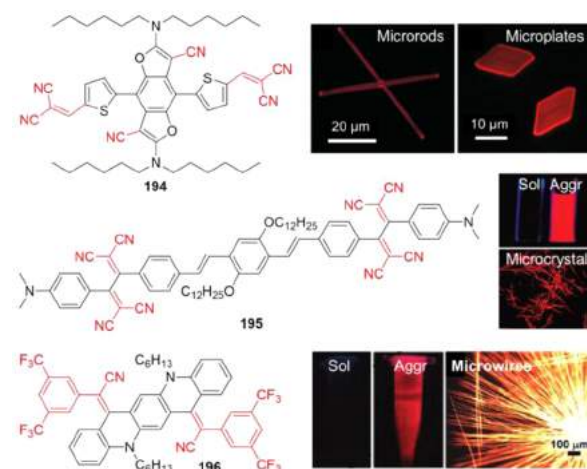


**Figure 44.** Cyano-containing AIEgens with large  $\pi$ -conjugation and red emission as well as self-assembling properties. The fluorescent photos for **194**, **195**, and **196** are reprinted with permission from refs 255, 256, and 257, respectively, Copyright 2014 Wiley-VCH Verlag GmbH & Co. KGaA, Copyright 2008 American Chemical Society, and Copyright 2012 American Chemical Society.

in THF or DCM, **194** shows negligible fluorescence. The increase of poor solvent fraction causes aggregates to form, which is confirmed by the dynamic light scattering (DLS) technique. The aggregates and crystals of **194** emit strong red fluorescence, with

the microcrystals exhibiting a  $\Phi_F$  of 16.0%. The crystal structure suggests that the thiophenyl malononitrile arms adopt a twisted orientation with respect to its benzodifuran core. Such a distorted conformation originates from the steric repulsion between the nitrile groups on the benzodifuran core and the thiophene moieties, which allows the arms to rotate more easily in the isolated state. As a result, the active rotational motions of these arms aid to reduce solution-state emission. In the aggregate state, the molecules are packed in a lamellar-like layered fashion with the alkyl chains interdigitated between the molecular layers. Instead of  $\pi-\pi$  interactions, there exist multiple intermolecular interactions like C–H…N (2.362 Å) and C–N… $\pi$  (3.242 Å), restricting these intramolecular motions and enabling the luminogen to become efficiently luminescent.

An oligo(*p*-phenylenevinylene) core is decorated with four fully-substituted malononitrile groups and two terminal dimethylamine groups, generating the intramolecular charge-transfer compound **195**. This luminogen shows strong red emission in the aggregate state (Figure 44).<sup>256</sup> Strong steric repulsion effects between the malononitrile groups and their neighboring phenyl rings cause this molecule to take on a twisted nonplanar conformation. Such a twisted orientation reduces the overall conjugation and thus permits the rotatory parts to rotate much more easily. Therefore, when it is dissolved in THF, **195** does not show obvious fluorescence. When the intramolecular rotational motions become blocked in the aggregate state, the excited states relax radiatively and the AIE effect is thus observed.

**196** is an acceptor-donor-acceptor (A-D-A)-type quinoacridine derivative, another intramolecular charge transfer compound, with the central alkyl-substituted quinoacridine as an electron-donating core and the two 2-(3,5-bis(trifluoromethyl)phenyl)acetonitrile moieties serving as electron-accepting units (Figure 44).<sup>257</sup> From its molecular structure and the understandings gained from previously-discussed molecules, it can be seen that the phenyl rings are tilted out of the central plane and the quinoacridine core is evidently bent. The distorted nature of this luminogen brings about two effects. Firstly, when **196** is dissolved in THF, the phenyl rings can rotate easily and the central quinoacridine can actively vibrate, consuming the excited-state energy to result in a non-emissive solution state. Secondly, the twisted structure impairs strong intermolecular  $\pi-\pi$  stacking interactions and further prevents the emission quenching in the aggregate state. Upon aggregation, the intramolecular motions are constrained, which works collaboratively with the lack of  $\pi-\pi$  stacking interactions to give rise to the efficient aggregate-state luminescence.

Researchers have made full use of the nitrile groups to further enrich the heteroatom-containing AIEgens. The electron-accepting nature of the nitrile moieties has been well utilized to facilely tune the emission colors by virtue of variation in the electron-donating groups based on D-A interactions. Simple integration of alkylamines, carbazoles, or TPA groups with nitrile units has shown the ease of generating new AIEgens. The nitrile group facilitates the generation of twisted structures which are propitious to the AIE properties. Their rigidity forces the neighboring moieties (e.g., phenyl groups) to take distorted conformations, weakening the electronic conjugations. It effectively reduces the energy barriers for the intramolecular motions and therefore allows them to reduce the emission when the luminescent molecules are unconstrained. Meanwhile, the twisted configurations in the aggregate state hinder strong intermolecular  $\pi-\pi$  stacking interactions which often cause ACQ effect in the conventional systems.

**4.2.7. Miscellaneous Systems.** Last but definitely not least, this section introduces heteroatom systems that do not fall under the above six subcategories. There are a large number of such systems, however, what we can do is to screen out the most representative ones and deliver the main points. In terms of their structural similarity and their working principles, the selected examples have been divided into three major groups for better demonstration. These AIEgens are varying from structurally simple molecules decorated with rotors to complicated systems possessing multiple motional moieties, with the conjugated center changing from small linear to large cyclic aromatic cores. The AIE mechanisms of the majority of these systems are ascribed to the RIR principle. However, some heteroatom-containing AIE systems dominated by RIM principle will also be discussed here.

The first set of heteroatom systems highlighted in this section are derived from a well-known and widely-used phosphorus compound, namely, triphenylphosphine (TPP, **197**; Figure 45).<sup>258</sup>

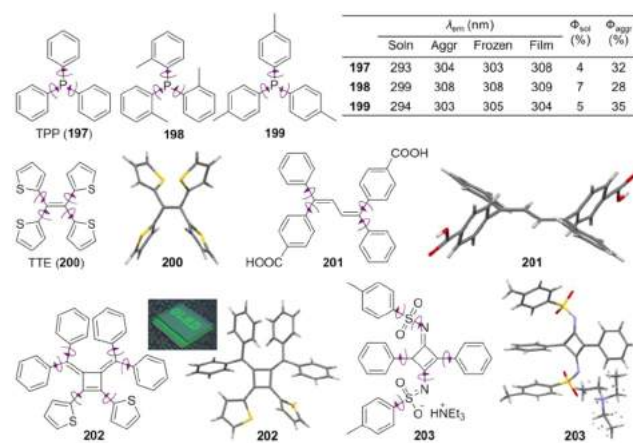


**Figure 45.** Heteroatomic AIEgens with relatively small central stators (i.e., phosphorus atoms, ethene, butadiene, and cyclobutadiene) and multiple rotors. Inset: Schematic illustration of the OLED built on **202**. Adapted with permission from ref 261. Copyright 2014 Royal Society of Chemistry. The optimized structure of **200** is obtained by means of MMFF94 in Chem 3D. The crystal structures of **201–203** are retrieved free of charge from CCDC (933576, 973432, and 822410) via [www.ccdc.cam.ac.uk](http://www.ccdc.cam.ac.uk).

Very surprisingly, it has been recently reported that the “old” compound TPP and its derivatives display “novel” photophysical properties, i.e., typical AEE properties. Because of the relatively small electronic conjugation of this system, TPP emits in the UV region with the emission maximum falling in the range of 293–308 nm depending on the conditions. In the solution state, its  $\Phi_F$  is only recorded to be 4.0%, while the  $\Phi_F$  raises to 32.0% in the aggregate state. The TPP derivatives like **198** and **199** show similar photophysical properties with the aggregate-state  $\Phi_F$ s of 28.0% and 35.0%, respectively (Figure 45). All these three compounds are propeller-like in shape. Their AEE activities can be easily attributed to the RIR principle: the three rotors in each luminogen dissipate the excited-state energy when the luminogens are dissolved or molecularly isolated, rendering them only weakly emissive. In the aggregate state, the activated RIR process permits effective radiative decay of the excited-state energy. It is notable that the AEE attributes of these derivatives are affected by the steric hindrance. For example, with the methyl groups substituted on the *ortho*-positions of the phenyl rings, the steric crowdedness partially constrains the intramolecular

rotations even when the luminogenic molecules are isolated species, endowing compound **198** with a higher solution-state  $\Phi_F$  in comparison to **197** and **199**.

Quite similar to TPE in structure, tetra(2-thienyl)ethene (TTE or **200**; Figure 45) has been reported to be AIE-active.<sup>259</sup> Like TPE, whose ethene core is decorated with four phenyl rotors, the central vinyl group of TTE is embellished with four thiophene rings which can freely rotate around the single bonds in the isolated state and make the molecule highly twisted in the aggregate state. TTE is nearly non-luminescent in dilute solutions. Interestingly, no light emission is detected for the concentrated or even saturated DCM solution of TTE. In sharp contrast, it emits much stronger in rigid matrixes or the solid state. The crystals of TTE luminesce at 420 nm with a  $\Phi_F$  of 6.0%. Its AIE behavior is analogous to TPE. The thienyl rings dissipate the excited-state energy via active intramolecular rotational motions. In the aggregate or solid state, such intramolecular motions become obstructed and the excitation energy is mainly released via light emission. It is believed that the peculiar electronic properties of the thiophene groups will bring about extra benefits to the AIE research.

As suggested by the RIR principle, no matter how large the stator it is, so long as there are sufficient and powerful enough rotatory parts attached, the resulting luminogen should retain the AIE property. Compound **201** is such an example. With four phenyl rotors decorating a larger butadiene core, **201** displays a  $\alpha_{AIE}$  value of 55, clearly indicating the AIE attribute (Figure 45).<sup>260</sup> When dissolved in THF solution, a  $\Phi_F$  of only 1.28% was observed. In the solid state, the  $\Phi_F$  was measured to be as high as 69.6%. Because of its multiple rotatable single bond connections and twisted phenyl ring orientations which facilitate the rotational twisting, the intramolecular motions efficiently and non-radiatively extinguish the excited-state energy. On the other hand, owing to the activated RIR process, **201** experiences evident emission enhancement in the aggregate state. Additionally, the highly distorted conformation impairs the intermolecular  $\pi-\pi$  stacking and the emission quenching is thereby avoided in the aggregate state.

Besides linear conjugated cored-AIEgens, AIE systems can also be constructed with cyclic conjugated cores (stators) decorated with aryl moieties (rotors).<sup>261,262</sup> **202** is an AIEgen built from a cyclobutene core attached with six aromatic rings.<sup>261</sup> The pairs of phenyl rings are highly twisted as a result of steric repulsion effects. The ultimate effect of these structure features leads to low rotation barriers which enable the rotational motions to easily and efficiently consume the excited-state energy via non-radiative channels, resulting in a  $\Phi_F$  of <0.5% in the solution state. In the aggregate state, a more than 590-fold increase in the PL intensity was observed and its solid state shows a  $\Phi_F$  of 29.0%. Its AIE activity can be interpreted with the RIR principle: when the intramolecular rotations become restricted, the molecules in the excited state can no longer return to their ground states via non-radiative channels but instead are forced to relax radiatively. Undoubtedly, the propeller-like molecular configuration also plays a role in the efficient aggregate-state luminescence.

Another cyclobutene-based system which is decorated with multiple rotatory moieties (**203**; Figure 45) has also been found to show typical AIE behaviors.<sup>262</sup> When dissolved in chloroform, no noticeable photoluminescence of **203** is detected. Under this situation, the phenyl rings attached to the cyclobutene core and the sulfonyl groups actively rotate around the C–C, C–N, S–C, and S–N single bonds in the excited state, making the molecules quickly relax back to the ground state without luminescence. As evidenced by its crystal structure, the absence of strong

intermolecular  $\pi-\pi$  stacking interactions originates from the highly twisted conformation of **203**. When the molecules aggregate together, the intramolecular rotational motions of the peripheral phenyl rings become restricted. Without these motions that exhaust the excited-state energy, the excited molecules decay radiatively resulting in the observed AIE phenomenon. Upon addition of hexane into its chloroform solution, the luminescence is gradually intensified. Significant emission enhancement is observed in the solid state.

In addition to the above systems, a multitude of AIEgens have been created by decorating aromatic cores with rotatable rings. The benzene core in **204** is embellished with two piperidine rings and a pair of phenylmethanone groups (Figure 46).<sup>263</sup>

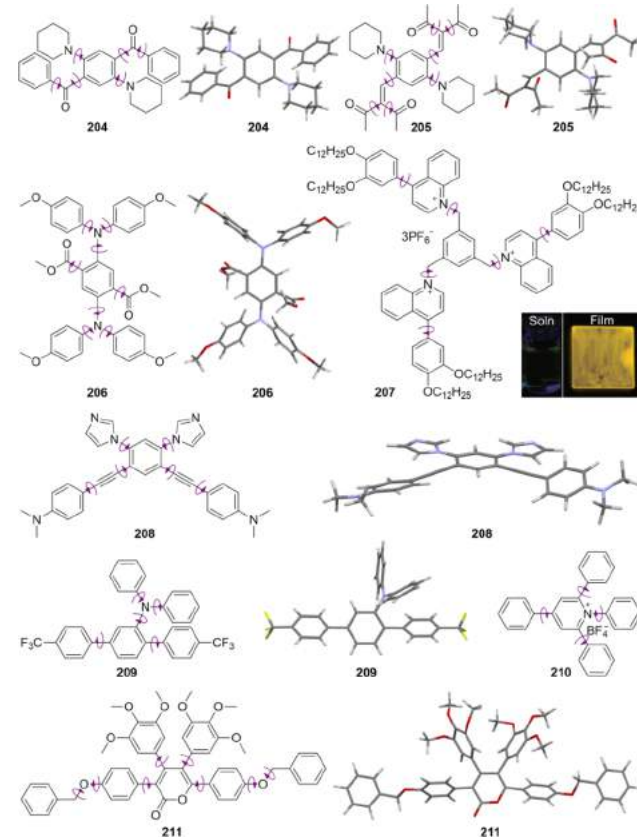


**Figure 46.** Heteroatomic AIEgens with relatively larger central stators (i.e., benzene, pyridine, and pyranone) and multiple rotors. The fluorescent photographs of **207** are reprinted with permission from ref 265. Copyright 2014 The Chemical Society of Japan. The crystal structures of **204** and **209** are retrieved free of charge from CCDC (801002 and 805836) via [www.ccdc.cam.ac.uk](http://www.ccdc.cam.ac.uk). The optimized structures of **205**, **206**, **208**, and **211** are obtained by means of MMFF94 in Chem 3D.

The crystal structure of **204** suggests that the phenone groups are not perfectly conjugated with the benzene core as evidenced by the twisted conformation. This reduces the rotation barriers enabling the piperidine and phenylmethanone groups to rotate easily and efficiently, which quenches the emission in the solution state. In the crystal state, the motions of the rotors become more tightly constrained. In this way, the molecules of **204** relax radiatively with its  $\Phi_F$  rising to 38.0%.

With a similar piperidine-decorated benzene core, **205** shown in Figure 46 is also AIE-active.<sup>264</sup> Analogous to **204**, the 3-methylenepentane-2,4-dione side arms adopt twisted conformations

weakening the conjugation. This facilitates the intramolecular motions in the solution state where the excited-state energy is quickly consumed resulting in a relatively low  $\Phi_F$  of 9.0%. In the crystal state, the intramolecular motions become obstructed due to small intermolecular distances, leading to a large gain in the emission intensity ( $\Phi_F = 43.0\%$ ). Owing to the strong D-A effect between the piperidine and 3-methylenepentane-2,4-dione groups, **205** shows an intense red crystal-state emission with a  $\lambda_{em} = 638$  nm.

Another D-A system with a pair of diphenylamine groups and two ester moieties attached to a benzene core has also been found to feature AIE characteristics (**206**; Figure 46).<sup>263</sup> Its crystal structure demonstrates that these peripheral rotatable moieties also adopt a nonplanar orientation with respect to the central benzene core. For one thing, the intramolecular motions such as phenyl rotations can occur more readily to consume the excited-state energy, causing the molecules to become non-emissive in the solution state. For another, the nonplanar configuration impedes the strong  $\pi-\pi$  stacking interactions and further prevents the luminescence quenching in the aggregate state. As a result of the RIR process, the powder form of **206** displays strong fluorescence at 568 nm with the  $\Phi_F = 63.0\%$ .

Other benzene-cored AIEgens have also been obtained by decorating the central core with various aromatic rotors in addition to phenyl rings. The donor-acceptor (D-A)-type luminogen **207** is composed of multiple quinolinium and phenyl moieties which work together to dissipate the excited-state energy in the solution state, yielding a  $\Phi_F$  of  $\sim 1.2\%$  (Figure 46).<sup>265</sup> **207** emits strong yellow fluorescence in the solid state with the  $\Phi_F$  rising to 12.6%. The imidazole groups along with the *N,N*-dimethylaniline rings in the cruciform luminogen **208** can also serve as active rotors to dissipate the excited-state energy (Figure 46).<sup>266</sup> In dilute solution, **208** is weakly fluorescent as the rotors may experience a relatively high rotation barrier because of good conjugation of the whole molecule. The  $\Phi_F$  increases to 33.0% in the solid state, exhibiting a maximum of 12-fold emission enhancement as compared to that of the solution state. Such an AEE effect is rationalized to be ascribed to the RIR principle. The *para*-terphenyl laterally substituted with a diphenylamino group (**209**; Figure 46) is a strong solid-state emitter with an excellent  $\Phi_F$  as high as 99.0%.<sup>267</sup> Because of the strong D-A effects in their molecular structures, **209** together with **207** and **208** all exhibit both TICT and AIE properties. When dissolved in a nonpolar solvent like benzene, **209** is moderately emissive, exhibiting a LE emission. Its crystal analysis shows that none of the phenyl rings adopts a planar orientation with respect to each other. Such a highly distorted conformation is partially due to the steric effects between the diphenylamino group and its adjacent phenyl rings. More importantly, this twisted state weakens the electronic conjugation, allowing the phenyl rings to rotate more easily to diminish the excited-state energy. Furthermore, the twisted conformation prevents the intermolecular  $\pi-\pi$  stacking which commonly reduces the solid-state emission and thus endows **209** with a near unity quantum yield in the film state.

Other relatively large central stators besides benzene, such as pyridine and pyranone rings, have also been utilized to construct new AIE systems (Figure 46).<sup>268,269</sup> The pyridinium core (stator) of **210** is decorated with four phenyl rotors whose rotational motions aid in the non-radiative consumption of its excited-state energy in the solution state.<sup>268</sup> Increasing the water fraction in its DMSO/water mixtures induces the molecules to aggregate together, which gradually restricts the intramolecular rotations and steadily enhances the fluorescence. Pyranone-cored

AIEgen **211** is embellished with a total of six phenyl rings.<sup>269</sup> These phenyl rings efficiently rotate and in this way the excitation energy is non-radiatively consumed in the solution state. The  $\Phi_F$  for the solution state is measured to be 0.07%. In the aggregate state, a maximum  $\Phi_F$  of 17.0% has been detected. As suggested by its crystal structure, the aryl rings directly attached to the central stator experience large steric hindrances because of the proximity of them. The steric repulsion effects in turn make the phenyl rings twisted out of the pyranone plane. The twisted nonplanar conformation allows the phenyl rings to rotate more easily to efficiently consume the excited-state energy in the solution state and prevent the intermolecular  $\pi-\pi$  stacking-induced quenching in the aggregate state.

Quinoxaline, a larger aromatic core, has been attached with a pair of anthracenyl groups and two phenyl rings, generating the D-A-D-type luminogen **212** (Figure 47).<sup>270</sup> The bulky

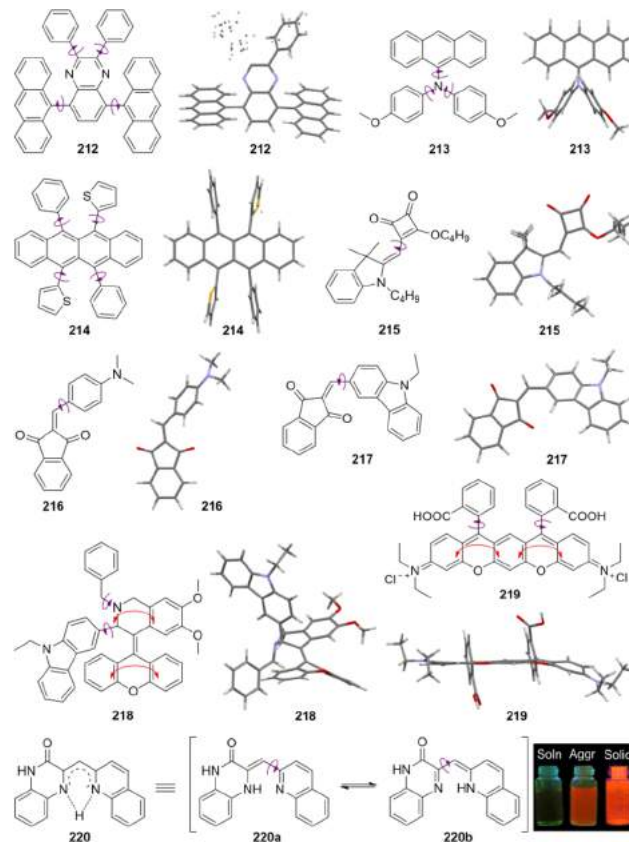


**Figure 47.** Heteroatomic AIEgens with larger central stators and multiple relatively large rotors. The RIM principle accounts for the AIE property of compounds **218–220**. The crystal structures of **212**, **214**, **215**, and **218** are retrieved free of charge from CCDC (927591, 917691, 696949 and 899105) via [www.ccdc.cam.ac.uk](http://www.ccdc.cam.ac.uk). The optimized structures of **213**, **216**, **217**, and **219** are obtained by means of MMFF94 in Chem 3D. The fluorescent photographs of **220** are reprinted with permission from ref 277. Copyright 2014 Royal Society of Chemistry.

anthracenyl moieties function mainly in two vital ways: (i) they rotate to consume the excited-state energy in the isolated state, and (ii) meanwhile, their large size imposes strong steric hindrance onto the adjacent phenyl rings in **212** and thereby renders a highly flexible and twisted structure. As compared with the phenyl rings, the anthracenyl groups are larger in size and harder to rotate. In other words, the anthracenyl group rotates at a smaller frequency than the phenyl ring. However, the energy

dissipated by each rotation of an anthracenyl moiety might be larger than that of the phenyl ring, so that the total energy dissipated by the intramolecular rotations of the anthracenyl groups are still quite considerable. As evidenced by the experimental and theoretical results, the twisted skeleton plays an essential role in the AEE property of **212**, because it hinders the face-to-face coplanar arrangement and prevents the resulting strong intermolecular  $\pi-\pi$  stacking interactions as well as the fluorescence quenching.

The triarylamine derivative **213** is another example of AIEgens with an anthracenyl element (Figure 47).<sup>271</sup> Luminogen **213** can be taken as an analogue of TPA where one of the phenyl rings is replaced with an anthracene unit. The anthracenyl moiety can be mainly viewed as a large stator; however, in some sense it can also act as a bulky rotor. The bulky anthracene group prevents the phenyl rings from taking a planar conjugated form. The almost orthogonal orientation of the phenyl rings with respect to the anthracene plane evidenced in the crystal state suggests that there is little conjugation between the aryl rings and hence the aryl rings are allowed to rotate easily. **213** is ambipolar with a weak electron-accepting anthracene unit attached to an electron-donating dianisylamine moiety. As a result of the modest D-A effect and the capability to undergo vigorous intramolecular rotations, **213** shows the combined TICT and AIE effects. It emits weak fluorescence at 612 nm when dissolved in acetonitrile and shows very strong luminescence at 570 nm in the aggregate state with  $f_w = 90$  vol % in the acetonitrile/water mixture. Weak red-shifted solution-state emission and strong blue-shifted aggregate-state emission are the signature behaviors of TICT plus AIE systems. When the molecules aggregate together due to poor solubility as a result of high water content, the effective polarity experienced by the luminogenic molecules in the micro-environment is reduced, which blue shifts the light emission. The aggregation also activates the RIR process so that the AIE effect arises.

Further enlarging the aromatic core to tetracene and attaching it with phenyl and thiophene substituents has facilely created an AIE-active rubrene derivative **214** (Figure 47).<sup>272</sup> The aryl rings actively rotate when **214** is dissolved in THF and thus consume the excited-state energy, further leading to a negligible emission. Adding water to the THF solution causes the molecules of **214** to aggregate. The aggregation hampers the rotational motions by means of the abundant inter- and intramolecular short-distance contacts such as C–H $\cdots\pi$  and C–H $\cdots$ S, forcing the excited molecules to relax radiatively to the ground state. A more than 40-fold emission enhancement is observed in the aggregate state, and the solid state shows a red fluorescence with a  $\Phi_F$  of 7.0%. Notably, the 3D nonplanar conformation also contributes to the AIE effect in view of its role in the prevention of intermolecular  $\pi-\pi$  stacking.

Attaching a semi-squarylium moiety to an indoline core generates the AIEgen **215** (Figure 47).<sup>273</sup> The solution state of **215** shows a weak blue light emission at around 460 nm ( $\Phi_F < 1.0\%$ ). The addition of poor solvent gradually intensifies a much red-shifted photoluminescence with two peaks at around 535 and 560 nm. The emission enhancement can be attributed to the formation of aggregates as evidenced by Tyndall scattering. The solid state of **215** displays a much higher  $\Phi_F$  value of 21.0%. The weak blue solution-state luminescence could be ascribed to a twisted and less conjugated configuration. With large structural flexibility, rotational motions could consume the excited-state energy to decrease the emission efficiency in the isolated state. The crystal analysis indicates that the molecules of **215**

experience strong intermolecular interactions such as C–H $\cdots$ O, C–H $\cdots\pi$ , as well as  $\pi-\pi$  interactions between two carbonyl groups. These interactions rigidify and planarize the molecules, which collaboratively make the RIR process take effect, turn on the emission, and red shift the fluorescence.

Two indenedione derivatives, one of which is decorated with a dimethylaniline (**216**) and the other one with a carbazole unit (**217**), have been reported to show the AIE characteristics (Figure 47).<sup>249</sup> **216** holds a solution-state  $\Phi_F$  of 1.0% and an aggregate-state  $\Phi_F$  of 12.0%. Similarly, **217** shows negligible fluorescence in the solution state ( $\Phi_F = 0.6\%$ ) but displays a large increase in the emission intensity in the aggregate state ( $\Phi_F = 20.0\%$ ). The ketone moieties impose steric effects onto the neighboring aryl rings, weakening the electronic conjugation by twisting the aryl ring orientations. The distorted molecular configuration permits the aryl rings to rotate more easily, affording a non-emissive solution state. The RIR process activated by aggregation gives rise to the enhanced aggregate-state emission.

Tetrasubstituted olefinic xanthene derivative **218** contains multiple rotatable moieties as well as a vibratable xanthene group (Figure 47).<sup>274</sup> Unlike most of the previously-discussed luminogens whose AIE properties are predominantly ascribable to the RIR principle, **218** is an example of heteroatomic luminophores whose AIE effect is dominated by the RIM principle. It is fairly easy to understand that the rotations of the carbazole and benzyl units non-radiatively consume the excited-state energy. The xanthene moiety, as indicated by the crystal structure, is bent in shape, allowing flapping motions to dissipate the excited-state energy as well. The cooperation of rotations and vibrations renders **218** to be essentially non-luminescent in acetonitrile. The molecular packing of **218** in the crystal is stabilized by the intermolecular C–H $\cdots$ O hydrogen-bonding with a distance of 2.529 Å, which stiffens the molecular conformation and locks the intramolecular motions. The combination of RIR and RIV processes (i.e., RIM process) induces the radiative relaxation, thus making **218** emit intense green fluorescence.

The aminobenzopyrano-xanthene derivative **219** (Figure 47) shows an AIE attribute, overcoming the ACQ effect which is commonly experienced by typical xanthene dyes (e.g., rhodamine).<sup>275,276</sup> When dissolved in THF, no discernable luminescence of **219** is detected. When increasing the water fraction in its THF/water mixtures, the red emission becomes stronger and stronger. The non-emissive solution state can be explained by the intramolecular motions induced efficient dissipation of the excited-state energy via non-radiative pathways. The crystal analysis also reveals that the aminobenzopyrano-xanthene core adopts a twisted conformation. It may be possible that the bending of this core also dissipates the excited-state energy together with the rotational motions. The addition of water causes the molecules to aggregate, which imposes physical constraints onto the molecules and rigidifies their conformations. Such a rigidification prevents the intramolecular motions from consuming the excited-state energy and thus switches on the emission and gives rise to the AIE effect. Moreover, the two carboxylic benzene moieties of **219** are bulky enough to obstruct the face-to-face intermolecular  $\pi-\pi$  stacking of the xanthene units, which is in favor of an efficient emission in the aggregate state.

The (Z)-3-(quinolin-2-ylmethylene)-3,4-dihydroquinoxalin-2(1H)-one derivative **220** is a new AIEgen created by connecting dihydroquinoxalinone and quinoline moieties together (Figure 47).<sup>277</sup> When **220** is dissolved in pure THF, negligible

emission is detected ( $\Phi_F = 0.34\%$ ). In its THF/water mixture at  $f_w = 90$  vol %, a 40-fold emission increase is observed when compared to that of the pure THF solution. The almost non-emissive solution state is ascribed to the dynamic intramolecular motions, such as the rotations around the single bond and the vibrations of the dihydroquinoxalinone moiety. When the molecules of **220** become rigidified in the aggregate or solid state, fluorescence emerges as the excited-state energy is no longer extinguished by intramolecular motions. Even in the aggregate state, the ESIPT is still permissible. This luminogen consists of two tautomers, namely, **220a** and **220b**. DFT calculation shows that **220a** is more thermodynamically stable than **220b** in the ground state, indicating that the ESIPT process occurs and generates **220b** when **220a** reaches the excited state, which results in a red-shifted luminescence.

Attaching simple rotors to a linear, cyclic, or bulky conjugated core can readily afford a variety of AIE-active luminogens. Because the AIE property is highly compatible with a large array of molecular systems and photophysical processes, it is possible to make use of the chemical properties of heteroatoms to further diversify and functionalize AIEgens. By introducing electron-donating and accepting moieties into the molecular systems, it becomes possible to join TICT and AIE processes together enabling emission wavelengths to be easily tuned. Incorporating tautomeric systems can readily afford AIE-active ESIPT compounds with red-shifted emission and reduced detrimental effects of self-absorption. There are now more and more systems demonstrating the possibility to branch out the AIE scope from RIR-induced emission to RIV- or RIM-dominated AIE systems. The small molecules highlighted in these sections as a whole only begin to show the immense potential and infinite variety of AIEgens. In the following section, some AIE-active macromolecular systems will be expounded.

#### 4.3. Macromolecular AIEgens

With great success in developing small molecular AIEgens, considerable progress has also been achieved regarding the exploration of macromolecular AIE systems. As a matter of fact, macromolecular materials possess quite a few advantages over small molecule materials. For instance, there are numerous possibilities to tune the molecular structure, topology, and morphology as well as functionalities of the macromolecular systems, which are hard to realize in small molecule systems. Moreover, on the other hand, small molecular luminogens often need to be processed by expensive techniques and tedious procedures such as vacuum vapor deposition. Such processing disadvantages can be surmounted by means of synthesizing macromolecules, which can be facilely fabricated into large-area film via simple processes like spin-coating or static-casting. Additionally, the covalently bonding of the repeating units in macromolecules often endows the resulting materials with decent mechanical strengths. AIE macromolecules thus can serve as a great platform for the creation of novel functional materials that incorporate the desired properties of both AIEgens as well as polymeric systems. Since a comprehensive review has been recently published regarding macromolecules with AIE characteristics,<sup>15</sup> herein the present review article will only focus on some representative works that help to exemplify and demonstrate typical macromolecular AIEgens. This section will introduce various types of AIE macromolecules as well as their synthetic methods. AIE-active macromolecules that have incorporated AIEgens into their backbones (i.e. main-chain) will be elucidated first and then systems that attach AIEgens as

pendant moieties (i.e. side-chain) will also be discussed. Afterwards, there will be some examples showcasing the intriguing AIE-active macromolecular luminogens that are constructed by merely using AIEgens as initiators. AIE-active dendrimers as well as hyperbranched AIE systems will be elaborated as well. Finally, special macromolecular systems such as metal-organic frameworks (MOFs) systems demonstrating AIE activity will be introduced.

**4.3.1. Main-Chain Polymers.** The core design strategy of AIE-active macromolecules is to incorporate typical AIEgens, such as TPE, HPS and DSA, into the polymer architectures. One of the most direct methods for the generation of a linear AIE polymer is to link the AIEgen-containing monomers together. Pure TPE-based full-conjugated polymer is produced in high yields and moderate molecular weights by joining the TPE units together via Suzuki coupling (**221**; Figure 48).<sup>278</sup> **221** inherits

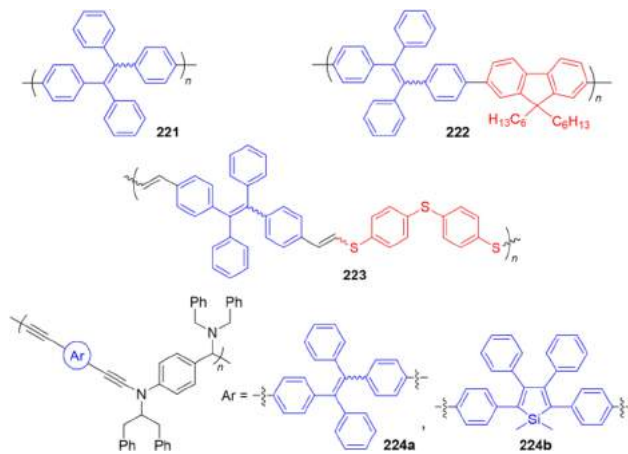


Figure 48. Representative examples of AIE-active linear polymers with AIEgens in the backbones.

the AIE attribute from its TPE monomer. When dissolved in pure THF, **221** emits at 506 nm albeit in a very low intensity with a  $\Phi_F$  of 1.2%. When the polymeric molecules are induced to aggregate by increasing the  $f_w$  of its THF/water mixtures, the fluorescence intensity shows a general tendency to increase. Emission intensity at  $f_w = 90$  vol % displays a 68-fold enhancement over its pure THF solution, showing a  $\Phi_F$  of 28.0%. Whereas TPE emits at around 470 nm, **221** fluoresces at 506 nm due to the extended electronic conjugation. This polymer bears two interesting properties owing to its TPE backbone. For one thing, the polymer is highly soluble in solution, and for another, **221** is also strongly emissive in the aggregate and solid states. As is often the case, planar aromatic systems always form multiple  $\pi-\pi$  interactions resulting in poor solubility and emission quenching. In contrast, the highly twisted nature of the TPE modules prevents strong  $\pi-\pi$  stacking interactions between the aromatic rings, endowing the polymer not only with good solubility but also efficient luminescence.

Another common approach to achieve linear AIE-active macromolecular systems is to copolymerize AIEgens with other conventional luminophores or monomers.<sup>279–281</sup> For example, as a building block, TPE has been copolymerized with fluorene via Suzuki coupling reaction in a molar feeding ratio of 1:1 (TPE to fluorene) to generate a conjugated polymer **222** (Figure 48).<sup>281</sup> This polymer weakly fluoresces in solutions ( $\Phi_F = 1.4\%$ ) but emits much more strongly as the aggregate formation ( $\Phi_F = 27.0\%$ ), suggesting an AEE feature. It is notable

that 222 in the solution state is more emissive than those  $\pi$ -conjugated TPE-containing small molecules. This effect results from the reinforced rigidity of the TPE moieties in the  $\pi$ -conjugated polymeric skeletons. The intramolecular rotations, however, are not completely restricted in the solution state, and meanwhile the polymer backbone tends to take on a twisted conformation, inhibiting the intermolecular  $\pi-\pi$  stacking interactions. Since fluorene is a typical conventional fluorophore, the ratio of the AIE units to the fluorene groups should be of crucial importance to the photophysical properties of the resulting AIEgen-ACQphore polymeric conjugates. Using the TPE-fluorene conjugated polymers analogous to 222 as models, Shi and Dong et al. have carefully tuned the bis(6-bromo-hexyloxy)-TPE to fluorene with the aim to systematically probe how the photophysical properties of the resultant polymers would be affected by the TPE-to-fluorene ratio in the polymer backbones.<sup>280</sup> A general trend of increase could be seen in their solution-state  $\Phi_F$  as the ratio of TPE is decreased. Initially, the increase is quite slow, with the  $\Phi_F$  gradually changing from 1.6% to 5.1% as the fraction of TPE moieties varying from 100% to 20%. However, when the proportion of TPE in the backbone decreases to 10%, the solution-state  $\Phi_F$  value sharply and quickly rises to 26.9% and finally reaches unity with a TPE ratio of zero (i.e. pure poly-carbazole). Consistent with the discussion in the “ACQ-to-AIE Transformation” section (cf. section 3), TPE and possibly other AIEgens can act as a source to dissipate the excited-state energy in the isolated state. The greater the proportion of TPE is, the larger the reduction in solution-state  $\Phi_F$  will be. In the aggregate state, the  $\Phi_F$  value has no defined correlation with the TPE ratio. When the TPE fraction is 20% or greater, the polymers exhibit  $\Phi_F$ s falling in the range of 28.3%–42.6%. However, at a TPE fraction of 10%, the  $\Phi_F$  abruptly drops to 18.7%. The pure poly-carbazole (TPE fraction of 0%) only holds a film-state  $\Phi_F$  as low as 1.6%, indicative of the typical ACQ behaviors. These results clarify that the incorporation of a sufficient amount of AIEgens with twisted structures like TPE into the conventional conjugated polymers can effectively prevent destructive intermolecular  $\pi-\pi$  stacking interactions as well as the resulting ACQ effect.

Various polymerization reactions have been adopted to introduce AIE properties into polymeric systems.<sup>15</sup> Apart from Suzuki coupling reactions, AIEgens have also been incorporated into the polymer backbones via some newly developed polymerization methods.<sup>282,283</sup> Polymer 223 is one of such examples. For this poly(vinylene sulfide), TPE was readily copolymerized into the backbone through a catalyst-free thiol-yne click reaction (Figure 48).<sup>282</sup> 223 is practically non-luminescent when dissolved in its good solvents like THF. However, when adding water into its THF solution, a weak visible emission can be observed at  $f_w = 30$  vol % and the fluorescence continues to be boosted as the  $f_w$  increases. When the  $f_w$  reaches 90 vol %, the THF/water mixture exhibits a maximum emission enhancement of 66-fold in comparison with its pure THF solution. Making use of this facile and powerful “thiol-yne” click polymerization, other soluble and regioregular functional polymers with AIE characteristics can be easily generated under very mild conditions.

Another new type of alkyne polymerization which has been developed to construct functional macromolecules with well-defined structures has been utilized to create AIE-active polymeric systems as well. These three-component polycoupling reactions of dialkynes, dialdehydes, and amines catalyzed by indium(III) chloride in *o*-xylene at 140 °C have successfully polymerized TPE (224a) and dimethyltetraphenylsilole (224b)

into polymeric backbones with high molecular weights and high yields (Figure 48).<sup>283</sup> Both polymers 224a and 224b display very weak solution-state emission with the  $\Phi_F$  of 1.5% and 2.9%, respectively. While in the solid state, 224a possesses larger  $\alpha_{AIE}$  value of 9.5 as well as higher  $\Phi_F$  of 14.3%. The silole-based copolymer 224b only has a  $\alpha_{AIE}$  value of 4 with a solid-state  $\Phi_F$  of 11.6%. Clearly, these polymers are AIE-active. In this case, the TPE and dimethyltetraphenylsilole units in 224a and 224b linked together by covalent bonds have been partially constrained and hence their rotations are partially hindered, making the polymers somewhat luminescent in solutions. While in the aggregate or solid state, the RIR process is further activated and intensifies the light emission to a larger extent. Demonstratively, such work provides good examples on how to build highly emissive polymers with superb spectral stability in the aggregate state.

Incorporating AIEgens into the polymeric backbones or main chains via homopolymerization or copolymerization has been verified to be able to confer AIE/AEE activity on the polymers. It is probably because the AIEgen can efficiently and non-radiatively dissipate the excited-state energy via intramolecular motions rendering the polymers to become non-emissive. Whereas in the aggregate state, the intramolecular motions become restricted and the radiative decay channels are opened to turn on the luminescence. Meanwhile, the distorted 3D configurations of the AIEgens also play an important part in the efficient aggregate-state emission for it obstructs the intermolecular  $\pi-\pi$  stacking interactions of the fluorophores in the polymer main chains as well as the resulting emission quenching. Studies have also shown that the degree of AIE can be tuned by varying the proportion of AIEgen in the copolymers. In this way, the optimized AIEgen fraction in the AIEgen-ACQphore conjugated polymers can be obtained. Such kind of work is of instructive significance in the transformation of the ACQ-active polymers into AIE macromolecules.

**4.3.2. Side-Chain Polymers.** Besides the above-discussed AIE-active linear polymers that have integrated AIEgens into their backbones, researchers have also successfully created polymeric AIEgens in a variety of other ways. This subsection will showcase AIE polymers synthesized with archetypal or novel AIEgens as pendant moieties as well as the methods applied to achieve them.

The well-known reversible addition-fragmentation chain transfer (RAFT) polymerization, a kind of living radical polymerization for vinyl compounds, has been used to synthesize TPE-pendant homopolymer 225 (Figure 49).<sup>284</sup> Taking advantage of the RAFT polymerization, the researchers are able to control the number of repeating units in the polymer chain. The resulting polymers, although different in molecular weight, all show the AIE characteristics. Nearly no light emission is detected from their THF solutions. However, their aggregates suspended in the THF/water mixtures are quite luminescent and the emission intensities are boosted with the increase in the  $f_w$ . Owing to the hydrophobic nature of the polymer skeleton, the addition of water causes the polymers to assemble themselves into nanoparticles. In this way, whereas phenyl ring rotations are capable of dissipating excited-state energy rendering the polymers to be non-emissive in the isolated state, the aggregation greatly restricts the intramolecular rotations forcing the excited-state luminophores to decay radiatively. It was observed that the polymers with longer chain lengths exhibited higher  $\Phi_F$ s in the aggregate state. With a longer chain, the hydrophobicity of the polymer is increased and their solubility in the THF/water mixtures is decreased. And thus the



**Figure 49.** Representative examples of AIE-active linear polymers with AIEgens as side groups. Inset: Plot of emission intensity of **228** at 558 nm versus  $f_w$  in the aqueous mixture and the fluorescent photographs of **228** in the THF/water mixtures with  $f_w = 0$  and 90 vol %. Adapted from ref 286. Copyright 2009 American Chemical Society.

polymers are caused to aggregate more tightly to more severely constrain the intramolecular rotations, resulting in an increased  $\Phi_F$ . In virtue of their good dispersibility, stability, and biocompatibility, these AIE polymeric nanoparticles have been incorporated into bioimaging applications such as the staining and imaging of HeLa cells.<sup>284</sup>

New AIEgen tetraphenylthiophene (**136**) can also be introduced into a vinyl polymer as a side-chain pendant via radical polymerization. The resulting homopolymer **226** is AEE-active (Figure 49).<sup>285</sup> Weak fluorescence is detected for the dilute solution of **226** and stronger luminescence is induced by the addition of water into the THF solution. Quantificationally, **226** possesses a low solution-state  $\Phi_F$  of 4.4% and a much higher  $\Phi_F$  of 37.0% and 55.0% in the aggregate and solid states, respectively. The phenyl ring rotations actively consume the excited-state energy when the polymer is dissolved in good solvents. As the solubility in the THF/water mixture is decreased by increasing the water fraction, the polymer molecules begin to aggregate. The aggregation hinders the intramolecular rotational motions, blocks the non-radiative relaxation pathways, and ultimately makes the polymer emissive. Thanks to the pendent thiophene moieties, the polymer **226** displays promising electroluminescence (EL) properties when used as the emitting layer in the OLEDs.<sup>285</sup>

Another new AIEgen diphenylquinoline (**90**) has also been used as a pendent moiety to generate the vinyl polymer **227**, which is structurally similar to **226** (Figure 49). In pure THF, **227** shows a  $\Phi_F$  of 2.1% while the  $\Phi_F$  rises to 4.3% in its solid state, indicating an AEE property. The covalent bonding draws the fluorophores together and imposes constraints on them, permitting part of the excited-state energy to be dissipated via the

radiative channels in the isolated state. Although the restriction of intramolecular rotations becomes stronger in the solid state, the relatively low and only slightly enhanced  $\Phi_F$  signifies that there are still significant rotations non-radiatively consuming the excited-state energy. The addition of camphorsulfonic acid (CSA), however, greatly affects the photophysical properties of this polymer. The CSA molecules form complexations with the diphenylquinoline units in **227**. The bulky nature of the CSA molecules is able to hinder the intramolecular rotations even in the solution state, resulting in  $\Phi_{FS}$  up to 11.6% and 66.7% in the solution and solid state, respectively. The CSA complexation serves as an additional proof to the RIR mechanism of the AEE property of **227**.

**225–227** are all polyolefins with flexible nonconjugated main chains. Besides them, even polyacetylenes which possess rigid and well-conjugated backbones have also been functionalized with AIEgens as their side groups to create AIE-active conjugated polymers, such as **228** (Figure 49).<sup>286</sup> The polymerization of acetylene monomers with aminated TPE units at their terminals using organo-rhodium as catalysts generates TPE-functionalized luminogen **228** with an *E* conformation. In the aggregate state, the polymer **228** emits bright yellow fluorescence with the maximum at 558 nm. The luminescence detected from its THF/water mixture with  $f_w = 90$  vol % is more than 56-fold stronger than the negligible emission of its THF solution. A typical AIE curve has been recorded for **228** in the THF/water mixtures. The light emission is intensified with increasing  $f_w$  in the mixtures. In **228**, the polymer backbone and the TPE pendants are separated by flexible alkyl spacers, hence providing enough freedom for the TPE moieties to undergo active intramolecular rotations and facilitate the emission quenching in the isolated state. Upon aggregation, such intramolecular motions become restricted and the RIR process is hence induced to take effect, rendering the polymer highly emissive. Thanks to the intense emission of the nanoaggregates, **228** has been reported to be able to detect explosive like picric acid (PA) with a high quenching constant ( $K_{SV}$ ) and a superamplification effect.<sup>286</sup>

In the above examples, the AIEgens are originally part of the monomers. AIE-active polymers can also be obtained by means of post-functionalization. Using the poly(allylamine) as a backbone, TPE units are grafted onto the polymer chain via a Schiff base reaction to produce **229** (Figure 49).<sup>287</sup> The AIE attribute of TPE has undoubtedly been retained by this polymer. Moreover, **229** was found to form micelles in the mixture of methanol/water (1:4 in volume) at pH = 6. The hydrophobic nature of the TPE moieties makes them buried inside the micelles while the hydrophilic amine groups forms an outer shell. The micellization of the polymer would cause the TPE moieties to experience enhanced physical constraints and induce strong emission in the nanoparticles, making them potential candidates for luminescence sensors and optoelectronic applications.

Designed with a conjugated ACQ backbone, polymer **230** (Figure 49) has been synthesized by copolymerizing carbazole monomers with TPE-decorated carbazoles in a 1:1 ratio via nickel-catalyzed Yamamoto coupling under microwave heating.<sup>288</sup> The intramolecular rotations of TPE moieties are able to effectively consume the excited-state energy when the polymer is dissolved in THF, resulting in an almost non-emissive solution state. Its THF/water mixtures show an almost linear increase in emission intensity with the water fractions. **230** in THF only has a  $\Phi_F$  of 0.8%, while its solid film exhibits a  $\Phi_F$  of 21.0%, demonstrating an  $\alpha_{AIE}$  value of 26. It means that the presence of the TPE moieties allows the polymer to surmount the ACQ

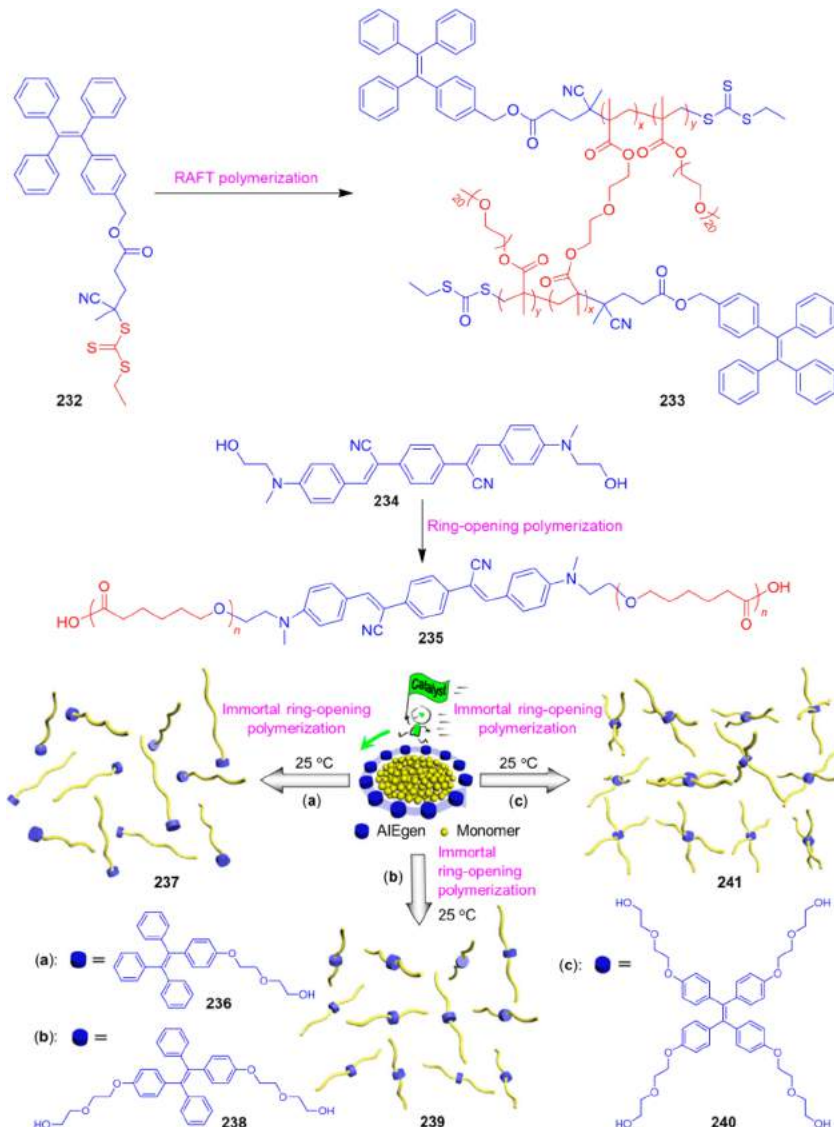


**Figure 50.** Representative examples of using AIEgens functionalized initiators to construct AIE-active polymers. The reaction scheme for 237, 239, and 241 is adapted from ref 293. Copyright 2014 American Chemical Society.

effect of its carbazole backbone, which is possibly attributed to the fact that TPE units hinder the destructive  $\pi-\pi$  stacking interactions because of its bulky and twisted structure. Meanwhile, the aggregation constrains the intramolecular motions and activates the RIR process, enabling 230 to become a strong solid-state emitter. The effective PL quenching of 230 towards trinitrobenzene vapor and solution has been demonstrated as well.

AIE/AEE polymers have also been created from natural biopolymers, such as TPE-decorated chitosan (231; Figure 49).<sup>289,290</sup> The polymer was synthesized by reaction between the TPE-functionalized isothiocyanate and the deacetylated primary amine of the chitosan (CS) backbone. The TPE-CS bioconjugates are soluble in acidic media. Weak luminescence is observed from 231 when it is dissolved in good solvents. When a TPE unit is bound to a chitosan backbone, the intramolecular rotations of its phenyl rings become more difficult than the unbound “free” TPEs. Hence, the RIR process is activated even in the solution state. Owing to the strengthened RIR effect, both the natural aggregates and specially synthesized nanoparticles (NPs) of 231 show much stronger light emission than the solutions. In the form of aggregates or nanoparticles, the TPE

moieties experience much greater steric hindrance because of the internal crowded microenvironment. The biocompatibility of the chitosan backbone and the AIE feature of 231 have enabled the aggregates and NPs to be successfully applied for cell imaging.<sup>289,290</sup>

The incorporation of AIEgens as pendant moieties of macromolecules not only exemplifies the flexibility of enduing polymers with AIE activity but also combines the properties of the polymer backbones and the pendent AIEgens to further improve their functionalities. Their enhanced processability, improved solubility, as well as the capability to form uniform nanoparticles bring about near-endless possibilities to the field of AIE and macromolecules.

**4.3.3. Initiator Systems.** A fascinating way to generate AIE-active polymers has been demonstrated through the utilization of the AIEgen-derived initiators.<sup>291–293</sup> For example, TPE was used to create 232, an AIE-active chain transfer agent (Figure 50).<sup>291</sup> By means of RAFT polymerization, 232 initiates the copolymerization of the hydrophilic monomer poly(ethylene glycol) monomethyl ether methacrylate and diethylene glycol dimethacrylate (the cross-linker) to afford the cross-linked

polymer **233** (Figure 50). Because of its amphipathy originated from the hydrophilic PEG and hydrophobic TPE moieties, this cross-linked polymer self-assembles in aqueous media to form nanoparticles. The hydrophilic PEG segments cover the nanoparticle surface with the hydrophobic TPE units being buried inside. The TPE moieties are compacted together in the cores, which restricts the phenyl ring rotations and makes the nanoparticles display bright fluorescence. Owing to the biocompatibility of the PEG surface and the ultra-stable dispersibility, the fluorescent polymeric nanoparticles made from **233** has been successfully used for cell imaging.

Other initiators based on AIEgens besides TPE have also been reported recently, such as the cyanostilbene derivative **234** (Figure 50).<sup>292</sup> Similar to the other AIE-active cyanostilbenes, the dynamic intramolecular motions accounts for the inefficient isolated-state emission of **234**. Whereas in the aggregate state, the RIR process aided by the physical constraints as well as the massive short-distance contacts such as C—H···N, C—H···O, and C—H···π is responsible for the enhanced emission. With two hydroxyl end groups, **234** is able to initiate the ring-opening polymerization of 6-hexanolactone monomers, yielding polymer **235** (Figure 50). The initiator **234** is very weakly emissive when dissolved in THF and as a result the obtained polymer **235** also shows quite weak fluorescence in THF. In contrast, in the THF/water mixtures, as the  $f_w$  is increased, the polymer begins to aggregate due to the poor solubility. The aggregation induces stronger and stronger steric hindrance onto the AIE molecules and further imposes restrictions on the phenyl ring rotations, resulting in continuous emission enhancement with the increasing  $f_w$ . In other words, **235** is a macromolecular AIEgen built from an AIE-active initiator.

In the above example, the two hydroxyl groups of the initiator **234** serve as active sites and take part in the polymerization. Other hydroxyl-modified AIEgens could also serve the same purpose. Cui and Liu et al. have carried out a systematic work to carefully examine how the vibration in the number of functional end groups in an AIEgen-derived initiator would affect the structures and properties of the resulting polymers.<sup>293</sup> Using TPE as the AIE core, the number of hydroxyl groups is fine-tuned from 1 to 2 and finally to 4, creating the corresponding AIE-active compounds **236**, **238**, and **240** (Figure 50). In the polymerization process, these hydroxyl-functionalized AIEgens are acting as the chain transfer agents and firstly bind to the active rare-earth metal catalysts via the rapid-reversible metathesis reaction. The resulting complexes further initiate the immortal ring-opening polymerizations of cyclic esters at 25 °C. Notably, the *in situ* generated initiators display similar performance to the purified ones, indicating that the formation of the active species is rapid and selective. The AIE fragments are incorporated into the polymer chains at specific sites, generating polyesters with linear, block, or star-shaped microstructures. In this way, the initiator based on **236** ultimately produces polymer **237**, a polyester end-capped with a TPE moiety. **238** results in **239**, which is a polymer consisting of two polyester chain segments connected by a TPE core. And the initiator derived from **240** gives rise to **241**, a four-armed and star-shaped polyester with a TPE unit in the center. All these three polymers (**237**, **239**, and **241**) display evident AIE activities. Even **241**, which has four polyester branches decorated onto each TPE unit still shows virtually no luminescence when dissolved in THF. It suggests that the polyester branches cannot sufficiently hinder the phenyl ring rotations to turn on the solution-state emission. As the  $f_w$  is increased in the THF/water mixtures, the emission intensity gradually rises until  $f_w = 40$  vol %.

Beyond this point, the fluorescence intensity is swiftly boosted. **241** is also able to be uniformly coated onto a glass substrate by spin-coating, facilely yielding a strongly luminescent solid film under UV excitation. Such a novel strategy avoids complicated synthesis of catalyst/monomers and the usage of toxic metal reagents and thus has been proven to be a straightforward and efficient approach to access AIE-active and/or biodegradable functional polymers.

What has been demonstrated here is that by means of judicious design, even introducing only a single AIE molecule into a polymer chain would still possibly afford an AIE-active polymer. Moreover, the resultant polymers can retain the characteristics of AIE no matter if the AIE motif is labelled at the end or in the middle of linear polymers (e.g., **237** and **239**) or in the core of star polymers (e.g., **241**). In the prior sections, AIE polymers, no matter of homo- or co-polymers could be synthesized purely with AIEgen-containing monomers or be obtained via post-functionalization of the existing polymers with AIEgens. Research has shown that now an even smaller proportion of AIEgen in a polymer chain is also able to confer the AIE feature onto the whole polymer. The significance of such work lies in that it provides more choices to the researchers on making full use of AIE to create diverse functional materials that can be better catered to specific applications.

**4.3.4. Dendrimer Systems.** Dendrimers are hierarchically branched macromolecules with multiple chains and branching units emanating from a single core. Owing to their unique features such as three-dimensional, regular, and multifunctional architectures, dendrimers have drawn extensive attention in diverse research areas, including pharmaceutical chemistry, supramolecular assembly, nanotechnology, and catalysis study.<sup>294–297</sup> In light of the special conformation feature of dendrimers and the unique emission character of AIEgens, a family of novel dendritic AIE systems have been constructed in pursuit of developing more functional materials.<sup>175,232,298–302</sup> These fantastic dendrimers show very weak or even no emission in the solution state but become brightly emissive in the aggregate state. The mechanistic cause of their AIE properties can be interpreted by the RIM principle: the dynamic intramolecular motions extinguish their excited-state energy in solution and the restriction of these motions allows the excited-state energy to be dissipated through the emerging radiative pathways in the aggregate state. In terms of their synthetic strategies and structural characteristics, currently there are mainly two kinds of AIE-active dendrimers. One class of them are made by functionalizing an AIE core with multiple branching or dendritic arms and the other group are fabricated by decorating the dendrimers with AIE moieties on their peripheries. In fact, the two types of AIE dendrimers depicted in Figure 51 have also reflected the most general preparation methods for dendrimers: the convergent (**242**) and divergent (**243**) synthetic approaches.

Dendritic phosphole oxides **242-G1**–**242-G3** prepared through the convergent strategy from the corresponding benzyl bromides are representatives of the first group of AIE dendrimers (Figure 51).<sup>175</sup> The phosphole oxide core **242-G0** is a typical AIEgen showing negligible fluorescence in the solution state ( $\Phi_F = 0.12\%$ ). It experiences a 5.2-fold emission enhancement in the aggregate state as compared to its THF solution. For each successive generation of the dendrimer, a pair of benzyloxy groups branch out from each of the previous aryl ring. Among all these generations, **242-G1** displays the highest increment ( $I/I_0 = 66$ ) in the aggregate state ( $I$ ) versus its THF solution ( $I_0$ ).

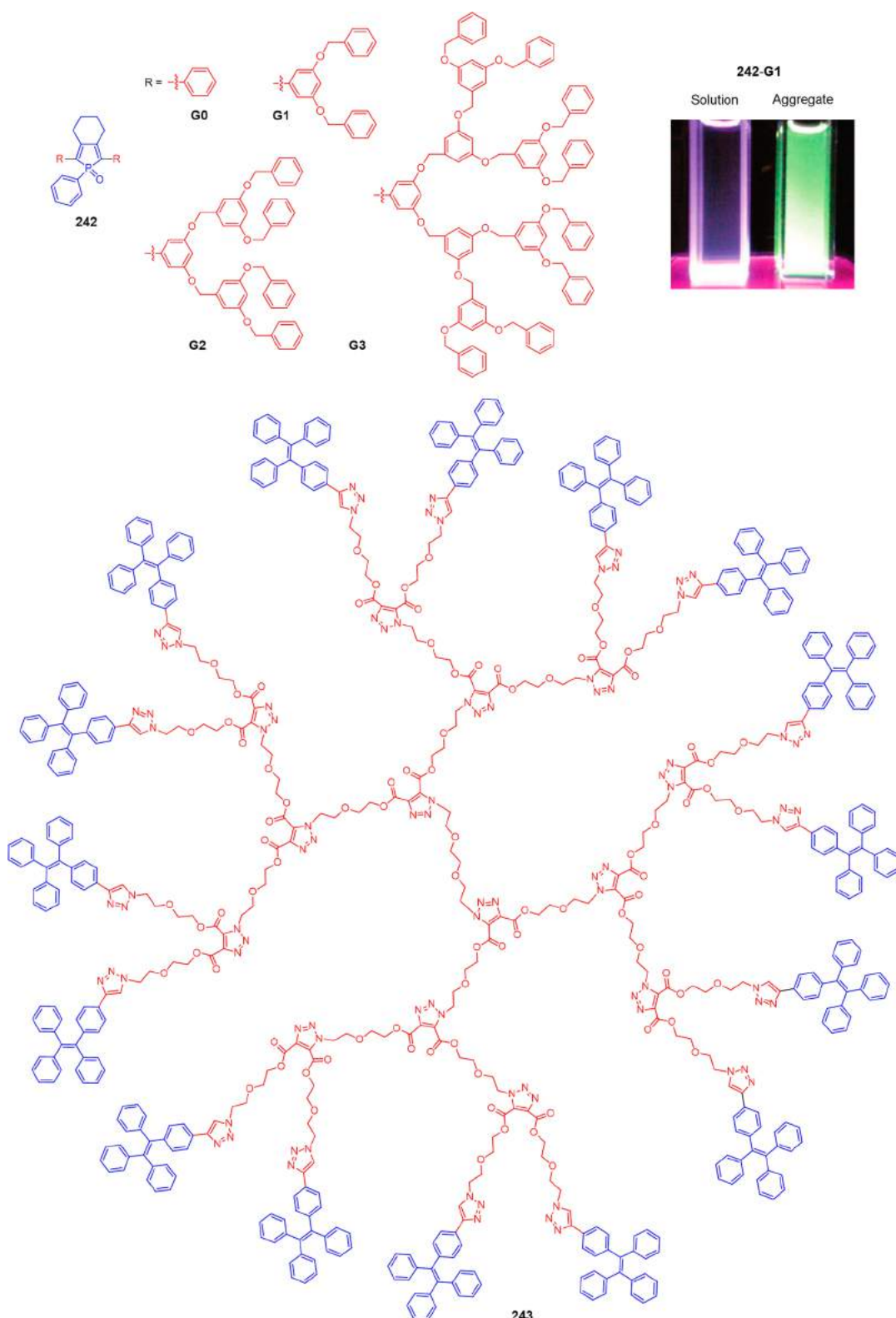


**Figure 51.** Chemical structures of AIE-active dendritic compounds. Inset: Fluorescence photographs of 242-G1 in THF and the THF–water mixture with 90 vol % water fraction. Reprinted with permission from ref 175. Copyright 2009 Royal Society of Chemistry.

The emission enhancements of the following generations show a dramatic decrease with the value of  $I/I_0$  dropping to 25 and 8 for 242-G2 and 242-G3, respectively. The smallest enhancement in the fluorescence of 242-G0 as well as its minimum AIE effect is likely due to the fact that the intramolecular motions have not been strongly restricted even in the aggregate state. On the other

hand, 242-G1 experiences pretty free intramolecular motions in the solution state but great restriction on the intramolecular motions in the aggregate state, enabling it to show the most significant AIE effect. As the generation increases (e.g., 242-G2 and 242-G3), more dendrons are attached to the core, resulting in larger steric crowdedness that makes the intramolecular

motions difficult even in the isolated state. This leads to a higher solution-state emission and a smaller difference in the emission intensity between the solution and aggregate states, hence reducing the AIE effect.

Besides the AIE-active phosphole oxide, other fluorophores have also been utilized as cores to build dendritic AIE systems. TPE-containing dendrimers were prepared by Zhang's group through a similar synthetic strategy to that of 242.<sup>298</sup> G0 of the resulting dendrimer shows no discernible emission in its THF solution. As the generation grows, the solution-state emission is intensified from nil (G0) to weak (G1 and G2) and further to strong (G3 and G4). The change in the  $\Phi_{fs}$  shows a similar trend. The  $\Phi_f$  of G4 in the THF solution is 23-fold higher than that of G1. The TPE cores might be encapsulated by the bulky peripheral dendrons and be shielded from the solvent molecules, and meanwhile, the intramolecular rotations are depressed by such physical constraint. In consequence, the light emission is turned on even in solution. Furthermore, the addition of water into the THF solution of G4 further enhances its fluorescence. Amazingly, even attaching dendrons to a non-AIEgen core can still generate AIE-active dendrimers, such as a group of dumbbell-shaped dendrimers with a *p*-terphenylene core.<sup>232</sup> The G1 of this category of dendrimers is 174, which has been specifically discussed in Section 4.2.5.

Among the second category of AIE-active dendrimers, there are some examples that the TPE modules have been used to decorate the peripheries of the dendrimer branches.<sup>299,300</sup> Attaching TPE units onto a nonconjugated ethylene oxide dendritic core through click reaction creates a series of AIE dendrimers up to generation three, among which, G3 (243) is shown in Figure 51 as a representative.<sup>299</sup> The ethylene oxide-containing dendritic cores have been synthesized via the efficient and rapid divergent approach by means of catalyst-free click chemistry.<sup>303</sup> The terminal azide groups of the dendritic cores could readily undergo a copper alkyne-azide coupling (CuAAC) reaction with the alkynyl AIEgens. The AIEgen-functionalized dendrimers are designed for the purpose of probing the dendritic architecture and examining the dendritic peripheral crowding. Since the AIE effect is quite sensitive to steric hindrance, the AIE feature of TPE moieties is used as a tool to check whether the steric effects (e.g., crowdedness) experienced by the peripherals increase as the generations grows. First of all, all generations of the dendrimers from G0 to G3 are AIE-active. Each of them is almost non-luminescent or weakly emissive when dissolved in THF, but all are intensely emissive in their THF/water mixtures with sufficient water content. There is a clear trend lying in this family of dendrimer that less and less water is needed for the mixtures to start emitting as the dendrimer generation increases from 0 to 3. In other words, as the generation grows, the critical  $f_w$  at which point the light emission is first observed is decreased. For G0, the critical  $f_w$  is 70 vol %, while the critical water percentages for G1, G2, and G3 are 50 vol %, 30 vol %, and 15 vol %, respectively. This change indicates that lower generations require a larger proportion of poor solvent to cause the formation of fluorophores aggregation where the dendrimers experience enough steric hindrance to restrict the intramolecular motions of TPE units and induce the luminescence. In contrast, higher generations possess lower tolerance to water and become more prone to aggregation. The peripheral TPE moieties of 243 likely have already experienced steric hindrance from neighboring TPE units to some degree even when 243 is in the isolated state. Although these interactions are not strong enough to allow for efficient emission, the amount of additional force required to

cause AIE effect would be less than that of the other generations. So that even at  $f_w = 15$  vol %, the mild decrease in solvated power is able to alter the conformation of the dendrimer causing the TPE units to experience enough restriction to begin fluorescing. The other group of dendrimers introduced in this work are embellished by TPE moieties with longer spacers. Even with the same dendritic core, the "long" series does not show such a trend between the generations. The difference originates from the rotational freedom provided by the extra ethylene oxide spacers. Such a difference between the "short" and "long" ones is indicative of the fact that AIE technique is sensitive enough to distinguish small or subtle changes in the macromolecular architectures and conformations.

Another analogous work has been reported almost at the same time with the above one. A series of poly(amidoamine) (PAMAM) dendrimers peripherally decorated with TPE moieties were synthesized (D0–D4) to investigate the conformational fluctuation induced by the external stimuli.<sup>300</sup> The higher generation dendrimers (D2–D4) take on compact conformations due to the congested packing periphery in a selective solvent. The intramolecular motions of TPE segments are consequently restrained to result in intense luminescence from isolated dendritic molecules. The fluorescence intensity can be modulated by altering the PAMAM conformation via changing the temperature, solvent composition, and pH value. It is noteworthy that the "breathing" conformation changes under temperature regulation give rise to dark-bright switching of the dendrimer. These systematic studies have offered a deeper fundamental understanding of the AIE dendrimers, which will pave the way towards applications such as biomimetic systems and sensors.

In addition to the examples highlighted here, there are quite a few other intriguing dendritic systems with AIE attributes. For instance, the benzenetricarboxamide-cored triphenylamine dendrimers reported by Ho and coworkers are H-bonding-containing systems, each of which is composed of an electron-deficient aromatic core and an electron-rich peripheral shell.<sup>301</sup> Remarkable AIE phenomenon has been observed in this series of dendrimers. Conjugated AIE dendrimers with a twisted 9,10-divinylanthracene core which is symmetrically decorated with multibranched TPA-based dendrons via alkene linkers has been developed by Tian's group.<sup>302</sup> The AIE property of this kind of dendrimers is dedicated by the 9,10-divinylanthracene unit which has been recognized as an archetypal AIEgen. Moreover, the arylamines serve as efficient electron-donors as well as branching centers, providing strong interbranching coupling and enhanced two-photon absorption. Because of the AIE attribute and high solid-state  $\Phi_{fs}$ , the nanoaggregates and thin films of these dendrimers show intense two-photon excited fluorescence with a large Stokes shift, indicating their potential for nonlinear optical applications.

**4.3.5. Hyperbranched Polymers.** Hyperbranched macromolecular systems possess similar architectures and properties as dendrimers but enjoy much simpler syntheses. Moreover, owing to their unique features such as one-pot synthesis, good solubility, low viscosity, three-dimensional structure, as well as multiple reactive terminal groups, etc., hyperbranched polymers have drawn great research enthusiasm.<sup>304,305</sup> In consideration of the particularities of hyperbranched polymers and AIEgens, systems fusing these two elements together are definitely of great interest and fairly appealing. To this end, enormous efforts have been made to the syntheses and studies of AIE-active hyperbranched polymers. Through incorporation of different AIEgens

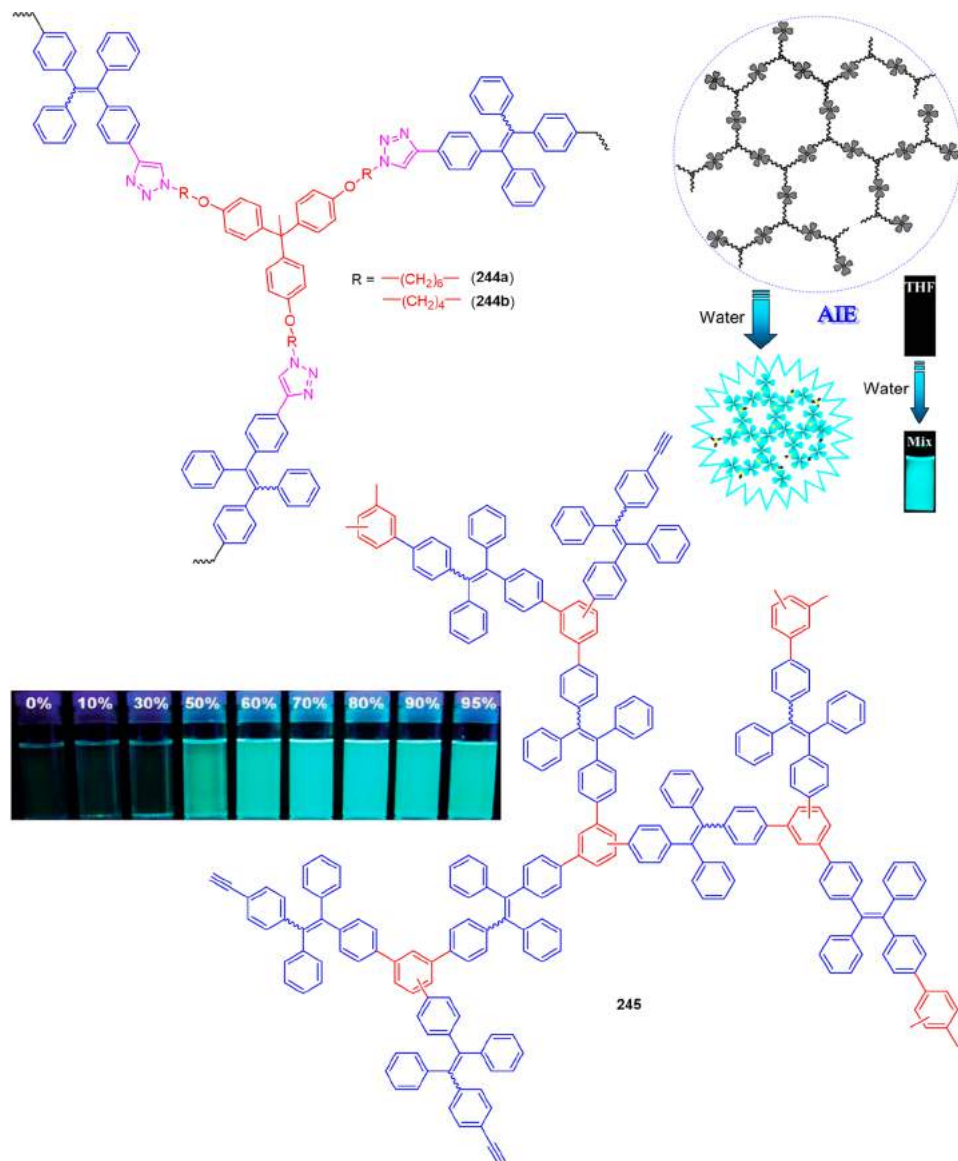


**Figure 52.** Representative AIE-active hyperbranched polymers (**244** and **245**). Insets: Schematic illustration of the AIE process of **244** and fluorescence photographs of **245** in the THF–water mixture with different water fractions. The scheme and fluorescent photographs for **244** are reprinted with permission from ref 309. Copyright 2011 Royal Society of Chemistry. The fluorescent photographs for **245** are reprinted with permission from ref 310. Copyright 2012 Royal Society of Chemistry.

into the polymeric skeletons via smartly designed synthetic routes, a large variety of AIE-active hyperbranched systems have been achieved. Even conjugated hyperbranched luminogenic systems which are often thought to facilitate exciton quenching have also been endowed with AIE properties. By bestowing AIE activity onto hyperbranched polymers, the resulting functional materials have shown great promise towards applications such as explosive detection, optical limiting, polymer-based LEDs, and so on. The methods that have been utilized to synthesize or construct AIE hyperbranched polymers as well as their resultant properties will be elaborated in this section.

As discussed above, the rigid and crowded architectures of the polymers always exert some restriction on the intramolecular motions of the AIE moieties even in the isolated state, making the polymers emissive and further reducing the overall AIE effect. Hyperbranched polymers are intrinsically crowded in their molecular structures and thus it is really difficult to obtain a hyperbranched polymer which is non-emissive in solution but

strongly luminesces in the aggregate state. Numerous endeavors had been made on this challenging project but ended up with limited success until 2011.<sup>306–308</sup> Our group put forward a smart strategy on the molecular design of AIE-active hyperbranched polymers, which hewed out a path to this research field. Spring-like flexible spacers were introduced into the hyperbranched architectures to endow the obtained polymers with greatly extended conformation in solution and tightly compressed configuration in the aggregate state. In this way, the AIE feature can be counted on according to the RIM mechanism. Specifically speaking, triazines with varying spacer lengths were designed and integrated into the hyperbranched structures by the well-established CuAAC click polymerization with the diyne-modified TPE derivative, readily furnishing 1,4-regioregular hyperbranched polytriazoles **244a** and **244b** (Figure 52).<sup>309</sup> These polymers are well soluble in most of the common organic solvents. The PL spectra of **244a** and **244b** are nearly flat lines parallel to the abscissa in THF solution with negligible  $\Phi_F$  values

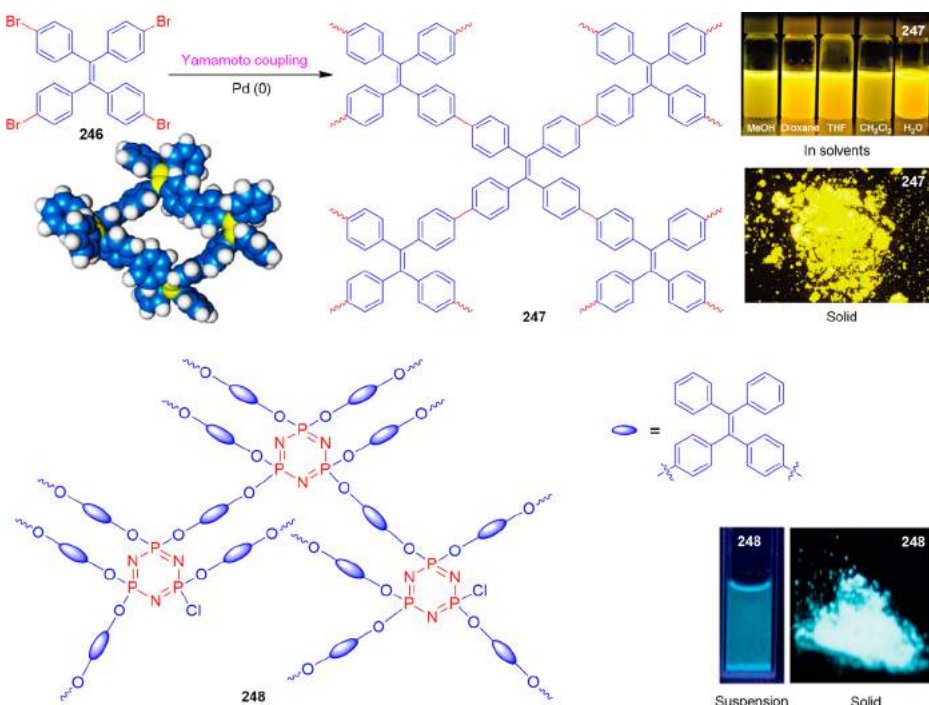


**Figure 53.** Representative conjugated microporous organic polymer (**247**) and inorganic–organic hybrid microporous polymer (**248**) constructed from AIEgens. Insets: (left panel) Closed tetragonal skeleton of **247** segments simulated by DFT calculations at the B3LYP 6-31G\* level (phenyl, blue; ethene, yellow; H, white) and (right panel) fluorescence photos of **247** in MeOH, dioxane, THF, CH<sub>2</sub>Cl<sub>2</sub>, H<sub>2</sub>O as well as its solid powder. Reprinted from ref 311. Copyright 2011 American Chemical Society. Fluorescence photos of **248** in suspension and solid-state (the lower right corner). Reprinted with permission from 314. Copyright 2011 Royal Society of Chemistry.

(0.11% and 0.14%, respectively), manifesting that they are practically non-emissive in the isolated state. The photoluminescence is continuously boosted with gradual addition of water, suggesting the AIE characteristics of these two polymers. The  $\Phi_F$  values of **244a** and **244b** in their THF/water mixtures with the  $f_w = 90$  vol % reach 38.3% and 32.3%, respectively. Their spin-coated films show  $\Phi_F$  values up to 100%. Such remarkable AIE features of **244a** and **244b** are ascribed to their innovative spring-like architectures. The function of the alkyl spacers is to introduce flexibility into this luminogenic hyperbranched system. When molecularly isolated in good solvents, these alkyl arms (springs) are fully stretched and enlarge the distances between the TPE moieties ensuring enough freedom for the intramolecular motions like phenyl rings rotations to quench the light emission. When aggregated in the THF/water mixtures with a large amount of water, the flexible and hydrophobic polymer branches become agglomerate and the bulky spheres are induced to compress into smaller ones. The reduced space freedom severely constrains the intramolecular motions of the phenyl rings, which forces the TPE units in the excited state to relax radiatively resulting in AIE effect. It is worth mentioning that the flexible alkyl chains also enable **244a** and **244b** to possess good film-forming ability as well as the high optical transparency in their film states, rendering them promising for photonic applications.

Besides the nonconjugated hyperbranched polymeric systems like **244**, conjugated hyperbranched polymers are also possible to feature AIE/AEE characteristics. As exhibited in Figure 52, **245** is such an example. It was synthesized through the TaBr<sub>5</sub>-catalyzed cyclotrimerization of a diyne-functionalized TPE derivative.<sup>310</sup> With a molecular weight ( $M_w$ ) up to 157 800, the TPE moieties in this hyperbranched system (**245**) are connected with

1,3,5- and 1,2,4-linkages. When **245** is dissolved in THF, weak luminescence is observed with a  $\Phi_F$  measured to be ~3.1%. The weak emission is attributed to the molecular architecture of **245**: although there is void space inside the polymer, the proximity of adjoining TPE moieties has already imposed some extent of steric hindrance on the aryl rings. Part of the excited-state energy cannot be non-radiatively consumed by the intramolecular motions, affording an emissive solution state albeit not strong. It provides indirect evidence to the fact that the flexibility in architecture is of vital importance to the successful design of AIE-active hyperbranched polymers. In its THF/water mixture with 90 vol % of water, bright fluorescence peaked at 501 nm is observed with a  $\Phi_F$  of 45.4%, revealing the AEE behavior of **245**. Because of the hydrophobic nature of this polymer, the increase in water percentage likely causes the macromolecules to adopt more compressed and compact conformations to reduce the surface area in contact with the water molecules. Such compression induces strong restriction on the phenyl ring rotations, causing the polymer to become brightly emissive. The luminescence of this hyperbranched AIE polymer could be efficiently quenched by PA with large quenching constants, demonstrating its promising potential for explosive detection. In addition, **245** also exhibits excellent optical limiting properties which are useful for dampening high energy laser pulses.

As a versatile building block, the easy-to-prepare and ready-to-functionalize AIEgen TPE was used to construct a fully-conjugated hyperbranched polymer with a distinct architecture. With the brominated TPE derivative **246** as a single component, a rigid and highly ordered hyperbranched network **247** has been derived via the Yamamoto coupling reaction (Figure 53).<sup>311</sup> Because of the high connectivity and interlocking nature of the structure, phenyl ring rotations are already significantly

suppressed, rendering the polymer highly emissive even when it is molecularly dissolved in a variety of solvents. As compared to the previous system (**245**,  $\lambda_{\text{em}} = 501 \text{ nm}$ ) and its linear analogues, the conjugation experienced by the TPE moieties in **247** is much larger as its maximum emission is red-shifted to the wavelength up to 551 nm with a  $\Phi_F$  as high as 40.0%. The similarly high  $\Phi_F$  values of **247** under different conditions further indicate that each TPE unit in this interwoven skeleton is effectively interlocked by the covalent bonds from four different directions. Furthermore, the twisted 3D configuration of the TPE units renders a microporous network with large surfaces areas to **247**. Nitrogen sorption isotherm measurements performed at 77 K exhibit reversible curves with a Brunauer–Emmett–Teller (BET) surface area up to  $1665 \text{ m}^2 \text{ g}^{-1}$ . Positive “conjugated microporous polymer (CMP)” effects such as the extension in  $\pi$ -conjugation, facilitation in exciton migration, as well as the enhancement in luminescence have been observed in this interweaving scaffold. Such a work has provided a validation to the RIR principle. A large variety of other fluorescent microporous polymers have been developed via synthetic methods varying from Suzuki coupling polycondensations to oxidative coupling polymerizations with diverse building blocks.<sup>312,313</sup>

In addition to the pure organic hyperbranched AIE systems, fluorescent inorganic–organic hybrid microporous polymeric systems have also been exploited. For instance, one-step polycondensation between the TPE derivative 4,4'-(2,2-diphenylethene-1,1-diyl)diphenol and chlorinated cyclotriphosphazene under basic conditions has effectively generated a cross-linked hyperbranched polymer **248** (Figure 53).<sup>314</sup> Large-scale product can be facilely obtained in this way. This polymer is neither soluble in water nor in common organic solvents, such as THF, chloroform, acetonitrile, and methanol. As displayed in the inset of Figure 53, this hyperbranched hybrid is evidently emissive ( $\Phi_F = 9.9\%$ ,  $\lambda_{\text{em}} = 462 \text{ nm}$ ) when suspended in a THF/water mixture with the  $f_w = 90 \text{ vol } \%$ . Even brighter luminescence has been observed from its solids with the maximum at 485 nm. The fluorescence of this system stems from the TPE units, whose emission is turned on by the RIR process. The fluorescence of **248** can be effectively quenched by both 2,4,6-trinitrotoluene (TNT) and PA on the basis of electron transfer from **248** to the explosive species, making it a promising candidate for the sensitive detection of explosives. As the above examples have shown, the architecture of the hyperbranched polymers incorporating AIEgens can greatly affect the overall photophysical properties of the system. If enough spatial freedom is given to the AIEgen, the intramolecular motions will be able to quench the emission in the isolated state. In contrast, when the intramolecular motions of the AIE moieties become restricted due to the structural crowdedness or the architecture rigidness, the isolated-state emission will be brightened and the AIE effect of the whole polymer will hence be reduced.

**4.3.6. Metal-Organic Frameworks (MOFs).** MOFs are a category of organic-inorganic hybrids which are constructed from inorganic metal-containing nodes and organic linkers bearing large internal surface areas, diverse structures, as well as versatile functions.<sup>315,316</sup> They are promising functional materials that can be used for catalysts, gas separation/storage, OLEDs, and luminescent sensors, etc., and thus the study on MOFs has been recognized to be a “hot” topic in various research areas over the past few years. Inspired by the intriguing properties of MOFs, AIEgens especially TPE derivatives, have recently been utilized to synthesize luminescent MOFs. A few examples will be

showcased in this subsection, and special attention will be paid on their molecular design, architecture, as well as their properties.

One of the AIE-active ligands first used to construct MOFs is tetrakis(4-carboxyphenyl)ethene, a TPE derivative decorated with four carboxyl groups (**249**; Figure 54A).<sup>317</sup> The

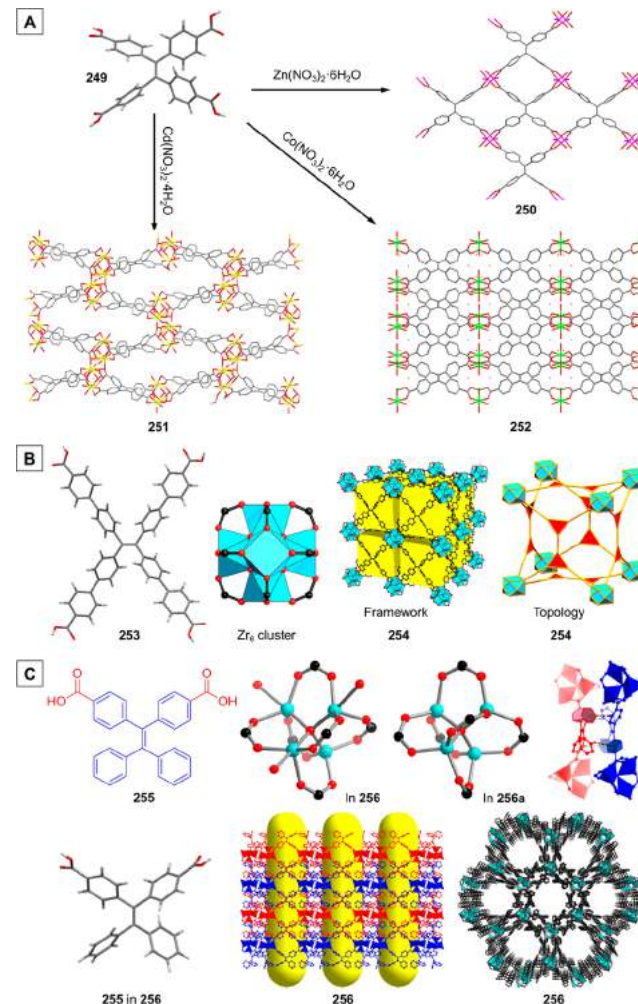


**Figure 54.** Representative examples of metal-organic frameworks (**250–252**, **254**, and **256**) constructed by using carboxyl functionalized TPE derivatives (**249**, **253**, and **255**). Panel B is adapted from ref 319. Copyright 2014 American Chemical Society. Panel C is adapted from ref 320. Copyright 2014 American Chemical Society. The crystal structures of **250**, **252**, and **253** are retrieved free of charge from CCDC (946152, 833060 and 991702) via [www.ccdc.cam.ac.uk](http://www.ccdc.cam.ac.uk). While those of **251** and **255** are obtained and reprinted from the Supporting Information of ref 317 and ref 320. Copyright 2011 and 2014, respectively, American Chemical Society.

coordination of **249** with  $d_{10}$  metal cations can generate various luminescent MOFs. For example, **249** was reacted with  $\text{Zn}(\text{NO}_3)_2 \cdot 6\text{H}_2\text{O}$  in a mixture of DMF and ethanol at  $75^\circ\text{C}$ , affording the rigid two-dimensional MOF **250**, as evidenced by its X-ray crystal analysis. In **250**, paddlewheel shaped  $\text{Zn}_2(\text{O}_2\text{C}-)_4$  secondary building units are bridged by the deprotonated **249** ligands. The fluorophore can also be immobilized in other rigid MOF matrixes under similar reaction conditions. The reaction between the ligand **249** and metal source  $\text{Cd}(\text{NO}_3)_2 \cdot 4\text{H}_2\text{O}$  produced **251**, a neutral three-dimensional framework made from tetranuclear  $\text{Cd}_4$  units bridged by the deprotonated **249** ligands, as shown in Figure 54A. Both **250**

and **251** are luminescent, with emission maxima at 480 and 455 nm, respectively, which are akin to the value observed for **249** (480 nm). Moreover, these two MOFs show biexponential fluorescence decay comprised of one short subnanosecond term and a longer term, with values in line with those closely-packed molecular aggregates. The **249** cores are identified to be the sources of luminescence in **250** and **251**. Coordinative immobilization of AIE-active cores inside the rigid MOF matrixes which hinder the intramolecular motions turns on the fluorescence. Anchoring AIEgens to metal ions within a robust matrix is hence supposed to be an alternative pathway to restrict the intramolecular motions. In a like manner, a novel (4,8)-connected *scu* [ $\text{Co}(\text{249})_{0.5}(\text{H}_2\text{O})_2\cdot 0.5\text{H}_2\text{O}$ ] framework **252** has been constructed by using a predesigned octahedral node of **249** (Figure 54A).<sup>318</sup> Red needle crystals of **252** were obtained via the hydrothermal reaction between the  $\text{Co}(\text{NO}_3)_2\cdot 6\text{H}_2\text{O}$  and **249**. In the coordination polymer **252**, the  $\text{Co}^{2+}$  ions are bridged by the ligands to form a complicated 3D network. Each  $\text{Co}^{2+}$  is octahedrally coordinated to four carboxylate oxygen atoms from four molecules of **249** as well as two water molecules. Although the photophysical properties of **252** were not clearly mentioned in the original paper, in view of the similarity in their structures and compositions, it can be envisaged that **252** should also show similar photophysical behaviors as **250** and **251**.

Another example where the luminogenic linkers are rigidified by the coordination with metal ions is depicted in Figure 54B. The novel TPE-based zirconium MOF is built by Zhou and Omary et al., using a new extended TPE-based linker **253**.<sup>319</sup> The ligand itself is AIE-active, exhibiting bright yellow emission at 545 nm with a  $\Phi_F$  of 30.0% in the solid state. Crystallizing **253** with Zr(IV) furnished a porous and robust tetravalent zirconium 3D MOF **254**. As revealed by the crystal structure analysis, each **253** unit is connected to four  $\text{Zr}_6$  clusters (Figure 54B). Every  $\text{Zr}_6$  cluster links 18 other  $\text{Zr}_6$  clusters through 12 **253** units. The framework of **254** only contains one type of cubic cage, in which the eight  $\text{Zr}_6$  clusters occupy the vertices and the six **253** moieties cover the faces. Such cavities are packed in a primitive cubic lattice. From the topological viewpoint, the  $\text{Zr}_6$  cluster acts as a 12-connected node and the **253** units serve as 3,3-connected nodes, making the porous coordination network of **254** adopt a rare 3,3,3,12-c 4 nodal net. **254** shows significant emission enhancement as compared to its ligand **253**, with a solid-state  $\Phi_F$  reaching  $99.9 \pm 0.5\%$  under Ar atmosphere. In addition, the MOF exhibits a deep-blue fluorescence at 470 nm, representing a blue-shift of  $\sim 3600 \text{ cm}^{-1}$  compared to the linker precursor. The remarkably high  $\Phi_F$  of **254** is mainly attributed to the immobilization of the **253** linkers via strong coordination to Zr(IV). The formation of a rigid MOF rigidifies the structure of fluorescent linkers, hampers the intramolecular motions and thus diminishes the non-radiative energy loss. Unlike the free conformation of **253**, a prominent change in molecular conformation was observed for the twisted **253** linkers in **254**. The minimum angle between adjacent carboxylate groups of the linker is enlarged from approximately  $65^\circ$  to  $86^\circ$ . In the precursor, the benzene rings in each biphenyl arm adopt much more coplanar orientations expanding the electronic conjugation of the whole molecule, which results in the observed yellow emission. However, in the MOF, after binding to the  $\text{Zr}_6$  clusters, the delocalized conjugation of the linker is broken by the more nonplanar conformation, giving rise to a widened energy gap between HOMO and LUMO. The reduction in conjugation is primarily responsible for the large blue-shift in the emission. The DFT calculations performed on the free and constrained **253**

have clearly and quantitatively demonstrated this mechanism. Notably, the origin of these unusual photoluminescence properties is ascribed to the twisted linker conformation, intramolecular hindrance, as well as the framework rigidity.

Besides the tetradentate ligands, dicarboxylic TPE derivative **255** has also been used to synthesize luminescent MOFs.<sup>320</sup> Solvothermal reactions between **255** and  $\text{Zn}(\text{NO}_3)_2\cdot 6\text{H}_2\text{O}$  in *N,N*-diethylformamide (DEF) produced the colorless and transparent single crystals of **256** with a hexagon plate shape. **256** is a layered 2D MOF with outstanding properties (Figure 54C). Single-crystal X-ray analysis of as-prepared **256** suggests that **255** ligands are expanded by tetravalent  $\text{Zn}_4\text{O}$  secondary building units (SBUs) composed of a central  $\text{O}^{2-}$  bonded to four  $\text{Zn}^{2+}$  (Figure 54C). In each SBU, three  $\text{Zn}^{2+}$  ions are capped by the carboxylate groups from **255** and coordinated water molecules, while the fourth  $\text{Zn}^{2+}$  is only coordinated to the ligand. **255** ligands are connected by the tetravalent SBUs to form staggered Kagomé-type 2D sheets, which stack together to afford the overall framework. These sheets are held together by the intermolecular C–H···π interactions between TPE units. Wide hexagonal channels with a deducting van der Waals radius of  $\sim 15 \text{ \AA}$  are formed by a ring of six **255** ligands connected by six tetravalent SBUs. A single crystal of **256** was evacuated to remove the trapped solvent molecules such as water molecules, giving the activated analogue **256a**. The space group and all the structural properties keep unchanged before and after treatment, indicative of the framework's robustness. With these large channels, the **256a** possesses BET and Langmuir specific surface areas of 1234 to  $1389 \text{ m}^2 \text{ g}^{-1}$ , respectively, with a total pore volume of  $0.79 \text{ cm}^3 \text{ g}^{-1}$ . The crystal of ligand **255** has a  $\Phi_F$  as high as 79.0% whereas the solvent-free MOF **256a** shows a  $\Phi_F$  of only 15.0%. Unlike the previously-mentioned ligands (**249** and **253**), **255** has two dangling phenyl rings without carboxylate groups that remain unrestricted even after the formation of MOFs. The as-synthesized **256** displays a slightly higher  $\Phi_F$  (17.0%) and a 19 nm red-shift in the emission maximum as compared to the solvent-free **256a**. Encouraged by this, **256a** was applied for the chemosensing of volatile organic compounds (VOCs). As the VOCs fill the hexagonal channels, the  $\Phi_F$  of the MOF-VOCs complex is increased to varying extents depending on the guest molecules. The highest  $\Phi_F$  up to 49.0% is achieved in the benzene-treated MOF system. Meanwhile, the VOCs can either blue- or red-shift the emission maximum with a variation falling in the range of –28 to 18 nm. The combination of emission enhancement and the shift in the emission maximum grants **256a** the ability to sense various VOCs.

The examples illustrated in this section have shown how the rigidity of the MOF matrix restricts the intramolecular motions of AIEgens and turns on their emission and how the porous matrix of the MOF allows for not only gas adsorption but also fluorescence turn-on response towards VOCs. In fact, apart from carboxyl groups, other functional moieties such as imidazolyl and pyridyl groups which could readily coordinate with metal ions have also been attached to the TPE units to create building blocks for the construction of luminescent MOFs and other supramolecular systems.<sup>321,322</sup> The research of MOFs integrating with AIE properties is still in its infancy stage but has already shown the charm as a fantastic field of research. In this sense, any work related to this appealing area will definitely receive great attention and have a great impact.

#### 4.4. Metal-Complex AIEgens

As defined by Wikipedia, metal complexes or coordination complexes refer to chemical compounds containing at least one bond (i.e. coordination bond) between atoms of an organic ligand and a metal center. From this viewpoint, the MOFs are in nature one type of metal complex. However, more specifically, they are coordination networks or coordination polymers that are porous. In consideration of this correlation and difference between MOFs and metal complexes as well as their own peculiarities, we put MOFs under the category of macromolecules and summarize the small metal complexes here in an individual section right after the discussion of MOFs. Metal complexes have found practical uses in stoichiometric and catalytic processes as well as optoelectronics (e.g., LEDs). However, similar to many organic systems, light emissions of metallic-organic luminophores also often meet with ACQ problems. Delightedly, AIE effects have been observed in a number of metal complexes.<sup>12–14</sup> So far, metal-containing AIE systems are believed to be a rapidly growing variety of AIEgens. The incorporation of transition metals has made it possible to take advantages of the electronic properties of the metal species such as the transitions of triplet excited states to easily access phosphorescence. Combining the AIE effect with metal complexes has bred a great number of novel luminogens with highly efficient aggregate-state emissions that span the whole visible spectrum and even approach the NIR region. These successes have paved the way towards the development and exploration of more diverse, efficient, and beneficial luminescent systems.

In this section, many different AIE-active metal complexes will be covered, including systems based on single metal centers as well as those with multi-metallic coordination centers. The discussion will be conducted generally in the order of the coordination number of the metal center (i.e. coordination center), from 2 (Au, Ag, Cu) to 4 (Cu, Zn, Pd, Pt) then to 6 (Ru, Re, Ir) and finally to 8 (Os). The compounds are primarily grouped together in terms of their metal centers. For those metallic systems that only involve a few examples, compounds with the same coordination numbers in their metal centers will be put together for the sake of systematic study. We will expound their photophysical properties and highlight the mechanistic causes of their AIE behaviors to draw out new insights and understandings.

Xie et al. reported an interesting finding that the Au(I)-thiolate complexes show strong luminescence induced by the formation of aggregation.<sup>323,324</sup> Glutathione (GSH) was used as the model thiolated ligand for the synthesis of oligomeric Au(I)-thiolate complexes. **257** was produced via a two-step procedure (Figure 55A).<sup>324</sup> The first step is the reduction from Au(III) to Au(I) by GSH and the subsequent coordination of Au(I) to the thiol group to form insoluble aggregates of Au(I)-thiolate complexes. The second step is the NaOH-initiated dissolution of the aforesaid aggregates and the oligomerization of the Au(I)-thiolate complexes. Good solubility of **257** in the aqueous medium with pH = 7.0 is imparted by the negative charge on the GSH (isoelectric point of pH 2.85).<sup>325</sup> As can be seen from Figure 55A, the oligomeric Au(I)-thiolate complexes **257** are almost non-luminescent in aqueous solution. With the addition of ethanol into water, the emission gradually becomes visible at 75 vol % ethanol fraction ( $f_e$ ) and continues to rise as the  $f_e$  increases. The large amount of ethanol disrupts the hydration shell of complex **257**, resulting in the charge neutralization and the consequent aggregation of the complexes. Such aggregation also promotes the intra- and intercomplex aurophilic interactions

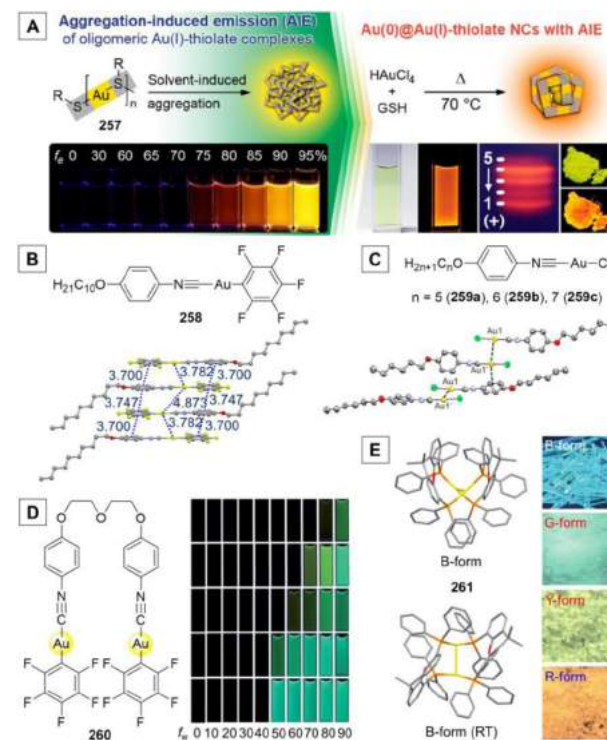


**Figure 55.** Representative examples of AIE-active gold complexes. (A) The chemical structure, AIE effect, and synthetic route of oligomeric Au(I)-thiolate complexes **257** and the Au(0)@Au(I)-thiolate core-shell NCs. Reprinted from ref 324. Copyright 2012 American Chemical Society. (B and C) Gold(I) complexes and their intermolecular interactions. Panel B is adapted with permission from ref 326. Copyright 2013 Royal Society of Chemistry. Panel C is adapted with permission from ref 327. Copyright 2014 Royal Society of Chemistry. (D) Structure of a stimuli-responsive gold(I) complex and its AIE behaviors in different solvent mixtures. Reprinted with permission from ref 328. Copyright 2014 Royal Society of Chemistry. (E) A stimuli-responsive double-stranded digold(I) helicate and fluorescence photographs of its different polymorphs. Reprinted with permission from ref 330. Copyright 2014 Royal Society of Chemistry. The crystal structures of B-form and B-form (RT) for **261** are retrieved free of charge from CCDC (942202 and 980610) via [www.ccdc.cam.ac.uk](http://www.ccdc.cam.ac.uk).

between the closed-shell metal centers. Meanwhile, the formation of Au(I)…Au(I) interactions (aurophilic bonds) in turn provides the impetus for aggregation, and as a result, denser and more rigid aggregates are formed. The average sizes of the **257** aggregates measured by DLS show that as the  $f_e$  increases from 75 vol % to 95 vol %, the sizes decrease, further supporting the above hypothesis. As the aggregates are compacted by the decrease in solubility, the steric hindrance experienced by the Au(I)-thiolate complexes is strengthened and the non-radiative relaxation caused by the intramolecular motions becomes blocked, ultimately turning on the emission. Any means that causes the formation of aggregates has been verified to be capable of inducing strong emission of the Au(I)-thiolate complexes. Furthermore, the discovery of the AIE properties of **257** has encouraged the authors to develop a novel strategy to synthesize highly luminescent Au-thiolate nanoclusters (NCs) in water. The controlled aggregation of Au(I)-thiolate complexes was induced on the in-situ generated Au(0) cores to form Au(0)@Au(I)-thiolate core-shell NCs where strong luminescence comes from the AIE of Au(I)-thiolate complexes on the NC surface. By means of this simple one-pot synthesis, Au-thiolate NCs with a

$\Phi_F$  of 15.0% which is orders of magnitude higher than that of the conventional Au-thiolate NCs have been achieved.

A series of AIE-active organogold(I) complexes have been synthesized by reacting gold species with isocyanobenzene derivatives.<sup>326–328</sup> Organogold(I) compound **258** with a 1-(decyloxy)-4-isocyanobenzene bridge features AIE characteristics and has attracted great interest (Figure 55B). Very weak photoluminescence is observed from its dilute ethanol solution. However, when the  $f_w$  in its ethanol/water mixtures exceeds 30 vol %, deep blue emission ( $\lambda_{em} = 402$  nm, 425 nm) emerges and is gradually intensified with a maximum enhancement of ~80-fold ( $f_w = 40$  vol %).<sup>326</sup> When the  $f_w$  changes from 40 vol % to 50 vol %, the deep blue emission decreases as a yellow-green band (559 nm) arises. Further increasing the  $f_w$  gradually diminishes the band at 559 nm. This phenomenon can be understood by examining its thermochromic crystal. The original crystal grown by slowly diffusing *n*-hexane into the DCM solution of **258** shows bright blue fluorescence ( $\lambda_{em} = 407$  nm, 428 nm). Gentle heating of the crystal to around 59 °C causes the blue emission to drop while a broad emission band at 530 nm is observed. Further cooling restores the initial blue emission. As depicted in Figure 55B, the X-ray analysis of the crystal at room temperature reveals that molecules of **258** are weakly self-associated, with an Au···Au distance of 3.782 Å. These self-associated molecules are situated in such a way that they form extended loose chains with neighboring Au···Au distances of 4.83 Å. As these distances are larger than the generally accepted intermolecular Au···Au interactions of 2.7–3.3 Å,<sup>329</sup> no obvious intermolecular aurophilic interactions is indicated. The molecular packing is promoted by the weak  $\pi$ – $\pi$  interactions (3.700 and 3.747 Å) as well as the intermolecular C–H···F contacts. Therefore, the observed blue emission of **258** can be assigned to the monomeric emission that originates from the RIM-dominated AIE effect. The red-shifted emission is likely caused by the intermolecular Au···Au interactions and  $\pi$ – $\pi$  interactions which also aid in the diminishing of emission.

Tsutsumi et al. have recently reported another set of AIE-active gold(I) isocyanobenzene derivatives **259a**–**259c**.<sup>327</sup> These gold(I) complexes were designed to have rodlike structures with the variation in the alkyl chain ranging from pentyl to heptyl (**259a**–**259c**; Figure 55C). All these three coordination compounds exhibit obvious AIE behaviors. The complexes brightly fluoresce in the crystalline phases with the  $\Phi_F$ s of 18.0%, 5.0%, and 11.0% for **259a**, **259b**, and **259c**, respectively. In sharp contrast, no light or very weak fluorescence is emitted by their dilute ( $10^{-6}$  mol L<sup>−1</sup>) or concentrated solutions ( $10^{-4}$  mol L<sup>−1</sup>), respectively. As suggested by the crystal structures (**259b** shown in Figure 55C as a representative example), multiple Au···Au interactions as well as the intermolecular Au··· $\pi$  contacts exist in the crystals, which stabilize the molecular packing and stiffen the molecular conformations and hence activate the RIM process, turning on the luminescence. In addition, these three complexes also possess intriguing LC properties, owing to which, a reversible “on–off” switching of the luminescence controlled by the phase transition between LC and isotropic phases is achieved for each complex.

A series of diisocyanobenzene-based dinuclear gold(I) complexes which differ only in the ether bridge linking the two identical arms have been synthesized by Yin and Liu et al.<sup>328</sup> Compound **260** with diethylene glycol as a linkage is depicted in Figure 55D as a representative of such a system. **260** is non-emissive in a variety of organic solvents such as THF, acetonitrile, acetone, DMF, and DMSO but can be gradually induced to luminesce by adding poor solvent like water into its solutions.

For example, the acetone/water mixtures of **260** with  $f_w \leq 50$  vol % show negligible luminescence with the emission maximum at around 414 nm. However, yellow emission ( $\lambda_{em} = 559$  nm) is observed in the acetone/water mixture with a  $f_w > 60$  vol % and its intensity is rapidly intensified with the further addition of water. A 538-fold emission enhancement is observed at  $f_w = 90$  vol %, indicative of the AIE activity. Such an AIE effect is attributed to the RIR process caused by the strengthened physical constraints in the aggregate/solid state. Moreover, **260** shows a mechanochromic behavior that its green luminescence can be reversibly switched between “dark (off)” and “bright (on)” states by mechanical stimuli.

Another reported stimuli-responsive dinuclear gold(I) complex is shown Figure 55E as **261**. Complex **261** is assembled from gold(I) atoms and phenyl-substituted diphosphine ligands derived from a xanthene-type backbone (L).<sup>330</sup> This double-stranded  $[\text{Au}_2\text{L}_2]^{2+}$  helicate virtually shows no luminescence when dissolved in DCM. The AIE activity of this  $[\text{Au}_2\text{L}_2]^{2+}$  helicate has been evaluated by adding diethyl ether into its DCM solution. The increase in the fraction of diethyl ether causes the helicates to aggregate and even form ordered assemblies. At 60 vol % diethyl ether fraction, the luminescence is enhanced by 13-fold with the maximum at 430 nm. When the fraction of diethyl ether is increased to 70 vol %, the emission is red-shifted to 462 and 495 nm, and the intensity is boosted by 55-fold as compared to that in pure DCM. Increasing the diethyl ether fraction further bathochromically shifts the emission but decreases the intensity. Blue-green ( $\lambda_{em} = 515$  nm) and yellow ( $\lambda_{em} = 560$  nm) emitting species of **261** emerge in the mixture with diethyl ether fraction equal to 80 vol % and 90 vol %, respectively. When the diethyl ether content reaches 99.5 vol %, the PL spectrum suggests the presence of red-emitting ( $\lambda_{em} = 616$  nm) species. This metallosupramolecule is a unique AIE system that possesses various polymorphs with emission colors covering the whole visible spectral region (blue, bluish green, yellow, and red). The RIM principle is rationalized to be the main cause of the AIE feature of **261**. In addition to the phenyl substituents whose rotations dissipate the excited-state energy, as indicated by the slightly bent conformations exhibited in the crystal structures, the xanthene moieties are flexible in the isolated state and hence could vibrate to aid in the consumption of the excitation energy. There are a large number of intra- and intermolecular non-covalent interactions (e.g., C–H··· $\pi$ , C–H···O, and N–O··· $\pi$  interactions) locking and rigidifying the twisted conformation of the double-stranded  $[\text{Au}_2\text{L}_2]^{2+}$  helicate, which turn on the aggregate-state emission of **261**. The enhanced  $\pi$ -stacking between its aromatic units induce the red-shift in the solid-state luminescence. It can be concluded that the conformational flexibility of this dinuclear helicate gives rise to a diversity of molecular conformations and packing arrangements that result in different solid-state emission colors. Interestingly, the solid-state luminescence of this helicate can be reversibly switched from blue to red by external (e.g., mechanical and chemical) stimuli.

Owing to the instability of their single crystals as well as the difficulty in their syntheses, studies on Ag NCs are still in a preliminary stage relative to those carried out on Au NCs. Nevertheless, a work on the thiolated Ag NCs which are analogous to the above-discussed thiolated AuNCs has recently been reported by Wang's research Team.<sup>331</sup> Ag NCs were obtained via a “one-pot” synthetic procedure by subjecting the aqueous mixture of *D*-penicillamine and  $\text{AgNO}_3$  to the microwave irradiation for 3 min. The Ag NCs are generated through

strong Ag–S coordination bonds. The white solids of Ag NCs emit strong luminescence under UV excitation, with a photoluminescence quantum yield ( $\Phi_{PL}$ ) as high as 25.6%. It is noteworthy that the light emission from Ag NCs is phosphorescent, as indicated by the average lifetime of  $\sim 83.9\ \mu s$ . The AIE feature of this Ag(I) complex was studied by the solvent-induced aggregation. The Ag NC aggregates are formed with the increasing  $f_c$  and simultaneously the luminescence is gradually intensified. Such aggregates could be redissolved in water, along with the disappearance of emission. In the aggregate state, stronger Ag…Ag and hydrogen bond interactions are involved to restrict the intramolecular motions, which impairs the excited-state energy loss through non-radiative decay channels and thus induces a remarkable enhancement in the emission efficiency. Self-assembly of the Ag NCs gives access to intriguing photophysical properties as well as the multicolor emissions.

Being situated in the same group (Group-11) with gold and silver in the periodic table, copper (Cu) also possesses the capability to serve as a coordination center for metal nanoclusters (NCs). However, the difficulty in the control of ultrafine size and the susceptibility to oxidation upon exposure to air make the preparation of Cu NCs a challenging task. Fortunately, Wang's group has developed a facile, one-pot and "green" strategy for the synthesis of stable thiolated CuNCs (Figure 56A).<sup>332</sup> The Cu

decays associated with the transition of triplet excited states. The intramolecular motions of moieties like *D*-penicillamine may play an essential role in the observed AIE effect. When the Cu NCs are well dissolved or isolated, the vibratory intramolecular motions of **262** could efficiently dissipate the excited-state energy so that no emission is observed. In the solid or aggregate state, the intramolecular motions become blocked due to the steric hindrances as well as non-covalent intermolecular interactions such as hydrogen-bonding between the carboxyl groups, leading to the strikingly enhanced emission. As can be seen from Figure 56A, the Cu NCs can be easily coated onto a variety of substrates including glass, silicon, and cotton. The resulting aggregates all exhibit intense red emission. Furthermore, the Cu NCs can be used as luminescent ink. The words written on the commercially available paper cannot be seen in daylight but becomes visible under UV excitation (see the red luminescent "copper nanoclusters" in Figure 56A).

As a matter of fact, unlike the Au(I) which predominately possesses dicoordination, for Cu(I), the tetracoordination is usually more common than dicoordination. In addition to the CuNCs, the AIE phenomena have also been observed in the tetracoordinated Cu(I) complexes, such as **263a**–**263d** (Figure 56B).<sup>333</sup> **263a**–**263d** are a set of binuclear mixed-ligand Cu(I) complexes chelated by two 3,8-dibromo-1,10-phenanthroline units and a pair of bridging diphosphine ligands with varying alkyl-chain lengths. All these four complexes strongly luminesce in the solid state. The intramolecular rotations of the four diphenyl phosphine moieties and the vibrational motions of the dibromo-1,10-phenanthroline groups work collaboratively to exhaust the excited state and quench the emission, when the complexes are well dissolved in good solvents such as DCM. When the molecules aggregate together as a result of the weakened solvated power of the solvent mixture, the RIM process is activated and the AIE effect is hence exhibited. For example, when the poor solvent hexane is added to the DCM solution of **263b**, the emission becomes observable when the  $f_h$  reaches 72 vol %. The intensity continues to rise afterwards with the further increased  $f_h$ . The luminescence lifetimes of these complexes range from 2.51 to 9.26  $\mu s$ , indicative of the phosphorescence characteristics. These AIE-active phosphorescent compounds have also been successfully applied for living cell imaging.

Zn(II) is among the metallic centers that usually possess tetracoordination. A systematic work has been performed by Su's team to study the photophysical properties of tetracoordinated Zn(II) Schiff base complexes such as **264a** and **264b** (Figure 57).<sup>334</sup> Both of them are weakly emissive when dissolved in DCM with  $\Phi_{PLS}$  of 3.0%. In the aggregate or solid state, they exhibit large increases in their emission intensities, suggesting their AEE activities. The powders of **264a** and **264b** possess  $\Phi_{PLS}$  measured to be 16.7% and 21.4%, respectively. In order to verify the fact that the AEE properties are attributed to the rotatable aromatic moieties (R groups, TPA and phenyl carbazole units) attached on the chelated N atoms, a derivative with ethyl moieties as the R groups has also been synthesized and studied. In this case, even having the same core part with **264a** and **264b**, this derivative shows photophysical properties opposite to those of **264a** and **264b**. It strongly luminesces in the solution state but displays almost no emission in the aggregate state. The AEE attributes of **264a** and **264b** thus are associated with their rotatable aromatic R groups. The intramolecular rotations of these moieties greatly dissipate the excited-state energy when the molecules are dissolved, resulting in the inefficient emission.

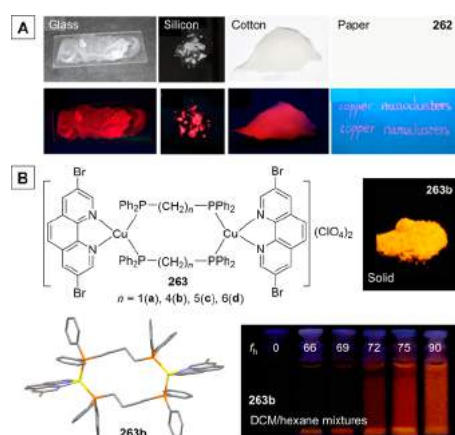


**Figure 56.** Representative AIE-active copper complexes. (A) Photographs of the copper nanoclusters (Cu NCs, **262**) aqueous solution deposited on the surface of glass, silicon, cotton, and commercially available paper under the irradiation of daylight (top) and UV light (bottom). The words "copper nanoclusters" were written using **262** as ink in pen. Reprinted with permission from ref 332. Copyright 2013 Royal Society of Chemistry. (B) Chemical structures of Cu(I) complexes (**263**) and crystal structure of **263b**. Inset: Photographs of **263b** in solid state and the mixtures of DCM/hexane with different hexane fractions ( $f_h$ ) under UV light (365 nm). Reprinted from ref 333. Copyright 2014 American Chemical Society. The crystal structure of **263b** is retrieved free of charge from CCDC (951447) via [www.ccdc.cam.ac.uk](http://www.ccdc.cam.ac.uk).

NCs **262** are synthesized by reacting  $Cu(NO_3)_2$  with *D*-penicillamine. The *D*-penicillamine moieties anchor on the surface of Cu NCs with their sulfur atoms attached to the copper cores through coordination bonds (i.e. Cu–S bonding). Due to the carboxyl end group of the *D*-penicillamine, the Cu NCs are soluble at high pH ( $> 6.2$ ) showing no light emission. At a pH lower than 6.2, the NCs precipitate out of the solution and display strong luminescence peaked at 640 nm when excited ( $\Phi_{PL} = 14.1\%$ ). In the solid state, the Cu NCs hold a  $\Phi_{PL}$  of 16.6% and an average lifetime of 150.6  $\mu s$ , declaring the radiative

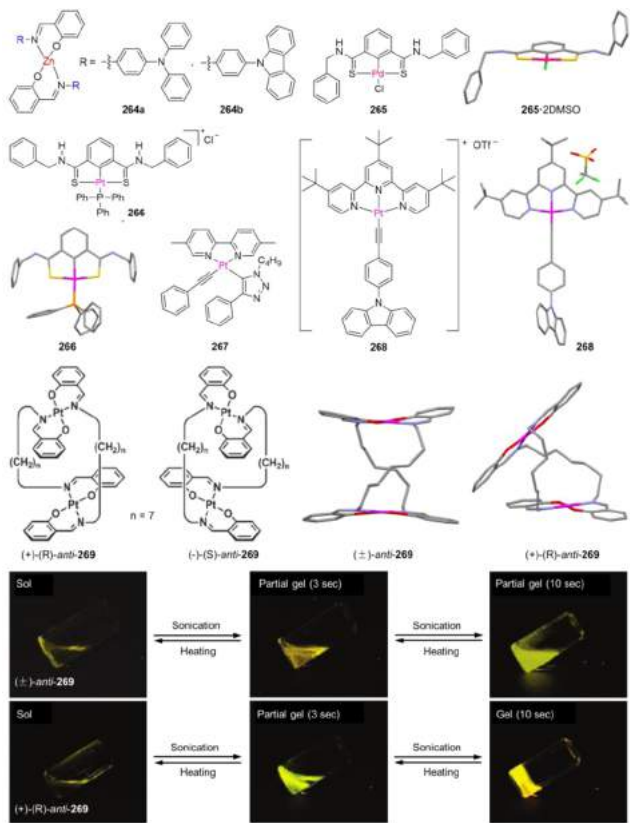


**Figure 57.** AIE-active systems possessing four coordination numbers, i.e., Zn(II) Schiff base complexes (**264**), thioamide-based pincer palladium complex (**265**), thioamide-based cationic pincer platinum(II) complex (**266**), platinum(II)-alkynyl-pyridine complexes (**267**, **268**), and chiral binuclear platinum complexes (**269**). Insets: Photographs of emission switches between solution and gel state of ( $\pm$ )-anti-**269** and (+)-(R)-anti-**269** via sonication and heating cycles. The crystal structures of **265**, **266**, **268**, ( $\pm$ )-anti-**269** and (+)-(R)-anti-**269** are retrieved free of charge from CCDC (794887, 957173, 771466, 860557 and 860558) via [www.ccdc.cam.ac.uk](http://www.ccdc.cam.ac.uk). The fluorescent photographs for ( $\pm$ )-anti-**269** and (+)-(R)-anti-**269** are adapted from ref 339. Copyright 2011 American Chemical Society.

In contrast, in the aggregate state, the rotational motions of these groups become hindered, consequently enhancing the light emission. Meanwhile, the bulky and nonplanar R groups on **264a** and **264b** prevent undesirable intermolecular interactions which would quench the luminescence.

The thioamide-based pincer Pd(II) complex **265** demonstrates interesting photophysical properties which provide an insight into the understanding of the AIE effect (Figure 57).<sup>335</sup> The complex is non-emissive both in solution and powder state, with  $\Phi_{PL}$  values less than 0.1%. Out of its five crystal polymorphs, three exhibit bright greenish yellow luminescence, signifying a typical CIE behavior. However, the remaining two polymorphs show very weak emission. It is found that the molecular arrangement and packing modes of the polymorphs are affected by the solvent used to cultivate the crystals. The crystal polymorph with the highest  $\Phi_{PL}$  of ~4.9% was grown from its DMSO solution (**265**-2DMSO; Figure 57). The variation in the emission efficiency of the polymorphs is closely associated with the density of the molecular packing. Looser arrangements in these polymorphs allow for the intramolecular rotations and vibrations to diminish the emission. The high density in the molecular packing impedes these motions at the excited state,

resulting in the suppression of non-radiative decay channels. Therefore, densely packed crystals of **265** (e.g., **265**-2DMSO) with hydrogen bonds show bright luminescence at room temperature.

A variety of Pt(II) complexes featuring AIE characteristics have been reported, one of which also bears a thioamide-based pincer similar to the complex **265**.<sup>336</sup> Moreover, this cationic Pt(II) complex **266** is decorated with a triphenylphosphine unit (Figure 57). The rotational motions of the phenyl and benzyl moieties together with the vibrational motions of the metal-bridged moieties contribute to its negligible emission when dissolved in chloroform. At  $f_h = 90$  vol % in its chloroform/hexane mixtures, the emission intensity of **266** is 46 times higher than that of its chloroform solution. The X-ray crystallographic analysis of **266** suggests the absence of  $d^8-d^8$  metal–metal interactions because of the long Pt–Pt distance between the adjacent molecules (9.66 Å). The observed emission enhancement is thus attributed to the RIM effect: the intramolecular motions are restricted by the physical constraints and the intermolecular hydrogen-bonding as well as the ionic interactions with the counteranions, leading to the activation of radiative pathways and hence making the Pt(II) complex emissive. Furthermore, the microsecond lifetimes indicate that the luminescence of **266** is phosphorescent.

AIE phenomena have also been observed in some asymmetric Pt(II) complexes. For instance, the unsymmetric bipyridine-Pt(II)-alkynyl complex **267** synthesized via a post-click reaction exhibits notable enhancements in its phosphorescence emission upon aggregation.<sup>337</sup> Complex **267** shows rather weak emission in THF. The emission intensity is gradually boosted as the  $f_w$  is increased in its THF/water mixtures. Luminescence with a  $\Phi_{PL}$  of 19.0% is recorded for the neat film of **267**, which is much higher than the one measured in DCM ( $\Phi_{PL} = 3.0\%$ ). Large emission enhancement of this system can also be achieved under low temperature (e.g., 77 K) or by doping the complex into rigid matrixes. The photophysical behaviors of **267** are relevant to the intramolecular motions of the appended phenyl and triazole moieties. The rotations of these rings when the complex is well isolated consume the excited-state energy and promote the non-radiative decay pathways; while in the aggregate or solid state, the activated RIR process causes the excited states to relax via radiative channels, giving rise to the intense phosphorescence.

The Pt(II) center in **268** is chelated by a terpyridine unit and an alkynyl group functionalized with a phenyl-carbazole moiety (Figure 57). Evidently, **268** is another Pt(II)-alkynyl-pyridine complex showing an array of interesting photophysical properties.<sup>338</sup> Firstly, the complex demonstrates an AIE activity: when it is dissolved in acetonitrile, almost no luminescence could be observed; while increasing the volume percentage of PBS buffer in its acetonitrile/PBS buffer mixtures causes the complex to aggregate and results in dramatic enhancement in the emission intensity. The AIE feature of **268** can be predominately attributed to the RIR principle. The rotations of the phenyl and carbazolyl groups dissipate the excited-state energy, rendering **268** non-emissive in the isolated state. But when these motions are depressed in the aggregate state, the non-radiative pathways are blocked while the radiative channels are activated. Making use of its AIE activity, intense electrogenerated chemiluminescence with  $S_2O_8^{2-}$  as a coreactant in the acetonitrile/water mixture is induced to arise. The  $S_2O_8^{2-}$  is reduced into  $SO_4^{2-}$ , and during this reaction process, **268** is energetically pushed into the excited state. The observed resultant chemiluminescence is related to the AIE effect of **268**, because the reaction was carried out in the PBS

buffer solution with 25 vol % of acetonitrile. In such a mixture, the nanoaggregates are formed due to the poor solubility, causing the excited-state energy to be decayed radiatively.

Binuclear Pt(II) complexes **269** show ultrasound-induced gelation and marked AIE effect in their phosphorescence emission (Figure 57).<sup>339</sup> The chiral clothespin-shaped *trans*-bis(salicylaldiminato)Pt(II) complexes (+)-(R)-*anti*-**269** and (-)-(S)-*anti*-**269**, which are linked by heptyl spacers, emit weakly in solutions. The ultrasound-induced gels of the racemic ( $\pm$ )-*anti*-**269** and optically pure enantiomer (+)-(R)-*anti*-**269** exhibit intense yellow luminescence peaked at 554 nm. These emissive states can readily be returned back to non-emissive states via the heating process. As can be seen from Figure 57, such an on–off switching of the luminescence is repeatable, because the emission arises from simple conformational changes of the complexes. The ultrasound-generated gel of (+)-(R)-*anti*-**269** possesses emission lifetimes of 21 and 502 ns (75:25 in ratio), indicating that the yellow emission is phosphorescent in nature. Furthermore, the quantum yield of the gel of (+)-(R)-*anti*-**269** at 77 K is determined to be 34.0%. In comparison, the gel of ( $\pm$ )-*anti*-**269** induced by the ultrasound displays a relatively weaker emission. The emission enhancements of the gels are attributed to the enhanced rigidity in the gel fiber which reduces the motional freedom of the individual monomers. By suppressing the intramolecular motions which are dissipation sources of the excited-state energy, strong phosphorescence could be seen. (+)-(R)-*anti*-**269** is likely to form much more rigid gel fibers with its optically pure units experiencing more intermolecular  $\pi$ – $\pi$  stacking interactions, benefiting their efficient aggregate-state emissions.

Enormous interest has been drawn to Ru(II) polypyridyl complexes owing to their potentials in various applications.<sup>340</sup> Since many Ru(II) polypyridyl complexes suffer from the ACQ problem, the development of **270** which holds the AIE property is of great significance (Figure 58).<sup>341</sup> The central Ru(II) of **270** is coordinated with two bipyridine ligands and a pyrazinyl triazine diamine moiety, possessing a distorted octahedral coordination sphere. When excited at 441 nm, the dilute solution of **270** only exhibits a fairly weak luminescence ( $\lambda_{\text{em}} = 613 \text{ nm}$ ) with the  $\Phi_{\text{PL}}$  as low as 0.1%. The addition of a large amount of toluene (toluene fraction = 90 vol %), a poor solvent, into the acetonitrile solution causes the complex molecules to aggregate together and turns on the bright red emission. The crystals of the complex are also brightly emissive with the emission maximum measured to be 656 nm. The analysis of its crystal structure clearly shows the C–H···N interaction between the uncoordinated nitrogen atom of the pyrazine and a hydrogen atom of the pyridine ring. Since all the rotatory moieties in **270** are locked by the coordination bonds between the ligands and metallic center, the possible pathway of the excited-state energy consumption for this complex should be the vibrational motions of the bipyridine and pyrazinyl triazine diamine moieties. This also explains why such a large toluene fraction is needed before AIE is observed. The vibrational motions can be effectively restricted only if the aggregates are very tightly packed together.

A series of dinuclear Re(I) complexes have been found to demonstrate AIE activities.<sup>342,343</sup> As displayed in Figure 58, the

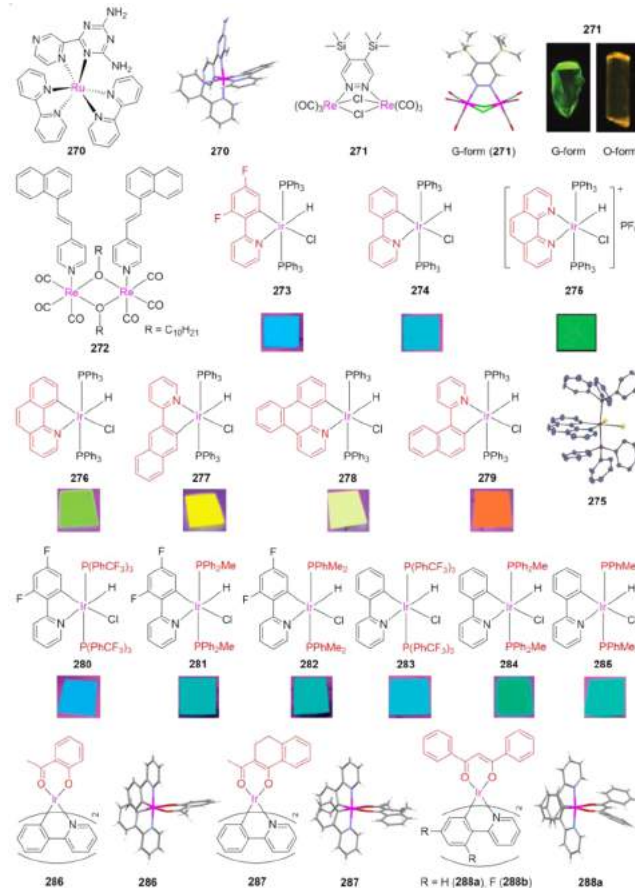


**Figure 58.** AIE-active systems possessing six coordination numbers, i.e., ruthenium(II) polypyridyl complex (**270**), binuclear rhenium complexes (**271**, **272**), iridium(III) complexes with variation in the cyclometalated and phosphine ligands (**273**–**285**), iridium(III) complexes varied in “O” bridged ligands (**286**–**288a**). Insets: Photographs of polymorphic crystals of **271** (Reprinted from ref 342. Copyright 2010 American Chemical Society.) and **273**–**285** in the solid state. The fluorescent photos of **273**, **274**, and **276**–**285** are reprinted with permission from ref 344. Copyright 2014 Royal Society of Chemistry. The fluorescent image and crystal structure of **275** are reprinted with permission from ref 44. Copyright 2014 Wiley-VCH Verlag GmbH & Co. KGaA. The crystal structures of **270**, **271** (G-form), and **286**–**288a** are retrieved free of charge from CCDC (773019, 785595, 699183, 699180 and 610633) via [www.ccdc.cam.ac.uk](http://www.ccdc.cam.ac.uk).

dinuclear Re(I) complex **271** has two brightly emissive crystal polymorphs, one of which is green emissive (534 nm, G-form) and the other is orange emissive (570 nm, O-form).<sup>342</sup> The G-form and O-form hold  $\Phi_{\text{PL}}$ s of 56.0% and 52.0%, respectively, which are almost one magnitude higher than the  $\Phi_{\text{PL}}$  detected in its toluene solution (6.0%). The low solution-state emission efficiency is supposed to result from the rotational motions of the two  $\text{Me}_3\text{Si}$  groups as well as the vibrational motions of moieties around the metal centers. These intramolecular motions become constrained upon crystallization, giving rise to the strong phosphorescence emission in the microsecond range. Additionally, bulky substituents that prevent detrimental intermolecular  $\pi$ – $\pi$  stacking interactions also make some contribution to the efficient emission in the aggregate or solid state.

Another six-coordinated rhenium(I)-tricarbonyl-based metal complex (i.e. **272**) has also been reported to be AIE-active. As shown in Figure 58, this alkoxy-bridged binuclear Re(I) complex **272** bears two long alkyl chains and a pair of

4-(1-naphthylvinyl)pyridine ligands.<sup>343</sup> When dissolved in good solvents such as DCM, the complex only weakly luminesces. However, the emission intensity is strikingly increased by almost 500-fold with the addition of poor solvent like acetonitrile. The naphthylvinylpyridine groups dynamically rotate when the complex is well dissolved, which consumes the excited-state energy, accounting for its weak solution-state emission. With the addition of acetonitrile, the nonpolar nature of the complex causes the molecules to form nanoaggregates. Upon aggregation, the rotation freedom of the naphthylvinylpyridine moieties is deprived, the non-radiative relaxation channels are blocked, and the light emission thus becomes enhanced.

Iridium(III) complexes are one of the largest families of metal-containing AIEgens that have been studied so far.<sup>44,344–347</sup> Owing to the extensive study, a wide variety of AIE-active Ir(III) complexes have been developed. Systematic investigations have been carried out to examine the influences on the photophysical properties exerted by the ligands. A large series of AIE/AEE-active monocometalated Ir(III) complexes (273–279; Figure 58) with simple and common frameworks but varying ligands have thus been prepared, with their photophysical properties being systematically studied.<sup>344,44</sup> All of them take on distorted octahedral coordination geometries as revealed by their single crystal X-ray analyses. These six-coordinated complexes display pretty weak emission when dissolved in solution with the  $\Phi_{PLS}$  ranging from 0.01% to 0.9%. In sharp contrast, their luminescence emissions are enormously intensified with the solid-state  $\Phi_{PLS}$  falling in the range of 8.0% to 54.8%. The marked AIE effects of these complexes are mainly associated with their triphenylphosphine groups. The intramolecular rotations of phenyl rings in triphenylphosphine units actively consume the excited-state energy, leading to the weakly emissive solution states. Meanwhile, the 5-membered cyclometalates might undergo some sort of vibrational motions which help the dissipation of excited-state energy. In the solid state, these motions can no longer efficiently work to quench the emission due to the steric hindrances increased by the shorter intermolecular distances. As a result, large emission enhancement can be observed. It is noteworthy that the fine tuning of the emission wavelength throughout the visible range (from blue to red) can be achieved by suitable combinations of chromophoric cyclometalates and non-chromophoric triphenylphosphine ligands. Furthermore, the Ir(III) complexes 273 and 274 were individually further modified by altering the phosphine ligands from tris(4-(trifluoromethyl)phenyl)phosphine to methylidiphenylphosphine and then to dimethylphenylphosphine, affording a group of analogues (280–285; Figure 58).<sup>344,44</sup> The complexes in this series are also AIE-active: non-emissive when dissolved but highly luminescent when aggregated or in the solid state. For both sets of Ir(III) complexes, either embellished with 2-(2,4-difluorophenyl)pyridine (273, 280–282) or 2-phenylpyridine (274, 283–285) groups, the emission maxima of solid-state emissions are slightly shifted depending on the ligand with the following trend:  $P(PhCF_3)_3 < PPh_3 < PPh_2Me < PPhMe_2$ . The AIE features of Ir(III) complexes with less aryl rings in their phosphine ligands (e.g., 282 and 285) provide more evidences to the assumption that the vibrational motions of the cyclometalates should also play a role in the emission quenching of solution states.

Within the family of AIE-active Ir(III) complexes, there have also been many reported phosphorescent systems decorated with 2-phenylpyridine and diketonate ligands (286, 287 and 288a–288b; Figure 58).<sup>345–347</sup> Both 286 and 287 show negligible

luminescence in the solution state with  $\Phi_{PLS} < 0.1\%$ , but their powder forms display  $\Phi_{PLS}$  measured to be 4.3% and 6.6%, respectively, suggestive of rather large enhancements.<sup>345</sup> Without rotatable moieties, it is likely that the vibratory intramolecular motions of the ligands are the main causes of emission quenching in the solution state, which is similar to the case of complex 270. Crystal analyses of 286 and 287 reveal the existence of weak and angled  $\pi-\pi$  interactions between the 2-phenylpyridine units as well as strong C–H… $\pi$  interactions, which work together to restrict or fix the vibrational motions of the ligands, giving rise to the observed intensified light emissions. Both 288a and 288b are functionalized with 1,3-diphenyl-1,3-propanedione units via coordination bonds, but 288b differs from 288a by having 2-(2,4-difluorophenyl)pyridine ligands instead of 2-phenylpyridine units (288a).<sup>346,348</sup> 288a is practically non-emissive in solution while 288b is weakly luminescent in chloroform ( $\Phi_{PL} = 3.0\%$ ). In addition to the vibrations of the ligands, the rotations of the extra phenyl rings also promote the non-radiative dissipation of the excited-state energy. 288a holds a solid-state  $\Phi_{PL}$  reported to be 7.6%, greater than those of 286 and 287. The higher  $\Phi_{PL}$  can be interpreted by the fact that the intramolecular rotations of phenyl moieties are more easily restricted than the vibrational motions. In other words, in the solid state, the intramolecular motions of 288a are restricted to a larger extent as compared to those of 286 and 287.

In addition to the diketonate ligands, ketoiminate ligands have also been used to construct cyclometalated Ir(III) complexes with AIE characteristics, such as 289 and 290 (Figure 59).<sup>346,349</sup> These two complexes have a common ketoiminate ligand but differ from each other by bearing either 2-phenylpyridine (289) or phenylpyrazole ligands (290). In solution, only negligible luminescence is observed, while in the solid state, 289 and 290 possess  $\Phi_{PLS}$  of 7.9% and 4.4%, respectively. The RIM processes account for the emission enhancements of 289 and 290 in the aggregate or solid state as compared to their solution states. Without the intramolecular motions which extinguish the excited-state energy, the excited complexes are forced to relax radiatively.

Cyclometalated Ir(III) complex 291 is embellished with phenylpyrazole-based ligands in addition to a triazolylpyridine ligand (Figure 59).<sup>350</sup> An indole unit is attached to the triazole moiety via a butyl linker. This cationic Ir(III) complex shows no discernible luminescence in the solution state with a  $\Phi_{PL}$  close to zero that cannot be detected but displays a strong emission in the solid state with a  $\Phi_{PL}$  up to 23.6%. Its intense cyan solid-state emission has been attributed to the restriction of non-radiative pathways, such as the vibrational motions of ligands as well as the rotational motions of the ancillary indole group. Structurally similar to 291, cyclometalated Ir(III) complex 292 contains two 2-phenylpyridine ligands and one triazolylpyridine moiety (Figure 59).<sup>351</sup> The butyl spacer in 292 tethers a phenothiazine moiety to the triazole group. 292 exhibits similar photophysical properties as its analogue 291. This Ir(III) complex emits negligible luminescence when dissolved in acetone, with a  $\Phi_{PL}$  estimated to be 0%. The complex keeps exhibiting minimal fluorescence while increasing the volume of poor solvent, e.g., water, in its acetone/water mixtures until the  $f_w$  reaches 90 vol %. A 60-fold increment in the emission intensity as compared to its pure acetone solution has been detected under this situation. In the solid state, its emission enjoys a  $\Phi_{PL}$  of 15.0% with a lifetime of about 0.20  $\mu s$ , indicative of an AIP effect. In like manner, the AIP activity of 292 is ascribed to the RIM principle. In solutions, the intramolecular motions of the ligands of 292 annihilate the

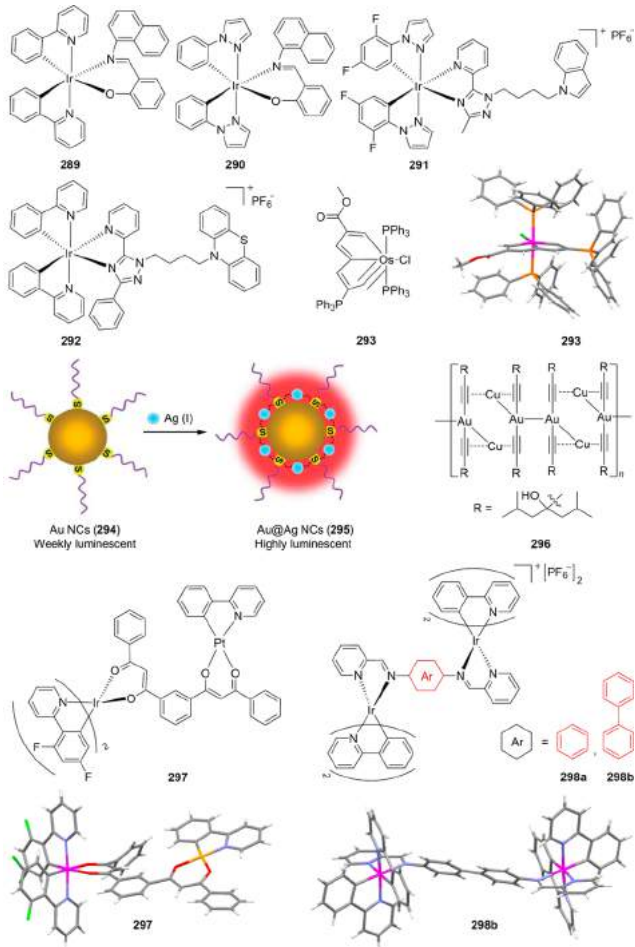


**Figure 59.** Iridium(III) complexes with variation in the cyclometalated ligands (289–292). Chemical and crystal structure of osmapentalyne (293). Lighting up thiolated Au@Ag nanoclusters (295) via AIE. Adapted with permission from ref 353. Copyright 2013 Royal Society of Chemistry. Au–Cu-alkynyl complexes (296) with AIP. Chemical and crystal structure of iridium(III)–platinum(II) heterodinuclear complex linked by a bis( $\beta$ -diketonato) bridging ligand (297) and ionic homodinuclear Ir(III) Schiff base complexes (298). The crystal structures of 293, 297, and 298b are retrieved free of charge from CCDC (820684, 756977 and 970289) via [www.ccdc.cam.ac.uk](http://www.ccdc.cam.ac.uk).

excited-state energy via non-radiative relaxation pathways in the isolated state. Nevertheless, in the aggregate state, their intramolecular motions become impaired and the phosphorescence is hence switched on.

Marvellously, the AIE/AEE effect has also been observed in a novel eight-coordinated osmapentalyne 293 (Figure 59).<sup>352</sup> The original high ring-strain of the pentalyne moiety has been reduced by the osmium core, generating the smallest angles observed so far in a carbyne carbon ( $129.5^\circ$ ). In addition to the reduction of the ring strain, another advantage of incorporating the osmium center lies in the conversion of the Hückel antiaromaticity into Craig-type Möbius aromaticity in the metal-lapentalynes. 293 is composed of an osmapentalyne core attached with triphenylphosphine groups. This metal-aromatic compounds displays unusual optical properties such as near-infrared luminescence ( $\lambda_{\text{em}} = 780 \text{ nm}$ ) with particularly large Stokes shift (320 nm), long lifetimes (0.1–1  $\mu\text{s}$ ), as well as the AEE activity. When 293 is dissolved in ethanol, a weak luminescence with a  $\Phi_{\text{PL}}$  of 1.2% is detected. The emission intensity

of 293 is continually boosted in the ethanol/water mixtures with the increase in  $f_w$ . The maximum  $\Phi_{\text{PL}}$  is measured to be 4.6% when  $f_w = 95$  vol %. In the dilute ethanol solution, the rotations of the multiple phenyl rings exhaust the excited-state energy, giving rise to a lower  $\Phi_{\text{PL}}$ . The addition of water, which is a poor solvent of 293, makes the complex aggregate together. The aggregation imposes additional steric effects onto the molecules of 293 which prevent the rotational motions from diminishing emission, resulting in the rise in  $\Phi_{\text{PL}}$ . Moreover, as suggested by the crystal structure exhibited in Figure 59, the detrimental intermolecular  $\pi$ – $\pi$  stacking of the luminophores is precluded sterically by the bulky ligands as well as the highly distorted 3D conformation of 293, which is also responsible for the bright emission in the aggregate state.

Besides the highly luminescent core-shell Au(0)@Au(I)-thiolate NCs, Xie's group has also made full use of AIE to construct bimetallic Au@Ag nanoclusters (295; Figure 59) with intense luminescence.<sup>353</sup> These novel nanoclusters are expected to have synergistic effects in their properties, especially photochemical performances compared with their mono-metallic analogues. The GSH-protected Au NCs (294) exhibited only very weak emission ( $\lambda_{\text{em}} \sim 800 \text{ nm}$ ) with a  $\Phi_{\text{PL}}$  as low as 0.37% in aqueous solution. The solution of as-prepared 294, which was originally greenish brown in color, immediately changes to brown upon the addition of Ag(I) ions, indicating the generation of Au@Ag NCs. The red luminescence is lighted up in the reaction system in approximately 15 min, which is in stark contrast to the weak emission of the parental nanoclusters 294. The Au@Ag NCs 295 holds an increased  $\Phi_{\text{PL}}$  of  $\sim 6.8\%$ . Among its various lifetime components, the one with the largest percentage of 56% holds a lifetime of 2.21  $\mu\text{s}$ . The microsecond-scale lifetimes indicate that the luminescence of 295 is phosphorescence via metal-centered triplet states, which arises from the AIE of Au(I)/Ag(I)-thiolate complexes on the NC surface. The weak isolated-state emission of the parental Au NCs (294) is similar to that of the GSH-ligand Au(I) complexes (e.g., 257). When the NCs are well dissolved in solution, the vibrational motions of the GSH arms likely consume the excited-state energy, which is exacerbated by the long lifetime of 294. The prolonged excited state originating from the intersystem crossing to the triplet states offers sufficient time for the vibrations of the GSH arms to exhaust the excited-state energy. As the thiol group of the GSH is already bound to the Au NC surface, the added Ag(I) ions likely interact with the multiple functional groups of the GSH arms such as the carboxyl, carbonyl, and amine groups. The Ag(I) ions link the small Au(I)-thiolate motifs on the parental NC surface, forming a grid network or large Au(I)/Ag(I)-thiolate motifs around the whole NC surface, which restrict their motions like vibrations. Blocking these non-radiative decay channels allows the excited molecules of 295 to relax via the release of phosphorescence.

In addition to the bimetallic Au(I)/Ag(I) system 295, an AIE-active bimetallic Au/Cu phosphorescent system has been reported as well (296; Figure 59).<sup>354</sup> This complex molecules are aggregated in the solid state, affording a polymeric topology. As depicted in Figure 59, for this Au–Cu–alkynyl complex 296, the roughly linear infinite chains are constructed from tetranuclear  $[\text{Au}_2\text{Cu}_2(\text{C}_2\text{R})_4]$  building blocks, which are linked via the unsupported aurophilic bonding interactions, e.g., Au–Au interactions. Each  $\{\text{Au}_2\text{Cu}_2\}$  motif displays effective Au–Cu bonding within the distances of 2.86–2.93 Å. Apart from the metallophilic attractions and  $\pi$ –C≡C–Cu bridging coordination of the alkynyl ligands, the  $[\text{Au}_2\text{Cu}_2(\text{C}_2\text{R})_4]$  segments are

stabilized by O–H···O hydrogen bonds. As a result of such a polymeric structure, unlike its pretty faint emission in solution, the light emitted by **296** in the solid state is very strong with a phosphorescence quantum yield ( $\Phi_{\text{ph}}$ ) up to 50.0% and a lifetime of 0.91  $\mu\text{s}$ . The AIP activity of **296** is likely associated with the bulky 2,6-dimethyl-4-heptanoyl groups on the alkyne ligands. In solution, the vibrational motions of these moieties dissipate the excited-state energy over the long triplet state. Upon aggregation in the solid state, these moieties impose steric hindrances on their neighboring groups and in turn experience such steric repulsion from the adjacent moieties, which is evidenced by the single crystal analysis of **296**. The RIV process enables the excited states to decay through radiative channels. This hypothesis is supported by the investigations on its structural analogue with a much smaller isopropanoyl alkyne ligand. Even in the solid state, these isopropanoyl groups experience much larger motional freedom that allows the intramolecular vibrations to effectively consume the excited-state energy, resulting in a rather low  $\Phi_{\text{PL}}$  of 1.0%.

Heterodinuclear Ir(III)–Pt(II) complex **297** bridged by a bis( $\beta$ -diketonato) ligand exhibits evident AEE activity (Figure 59).<sup>347</sup> The complex **297** in the solution state only possesses a low  $\Phi_{\text{PL}}$  detected to be 2.3%, with an emission maximum at 615 nm. The rotatable phenyl moieties might play a significant role in suppressing the solution-state emission, with their rotations actively and efficiently consuming the excited-state energy via non-radiative pathways. Similar to the other AIE/AEE-active Ir(III) and Pt(II) complexes, vibrational motions of moieties like phenylpyridine units may also contribute to the weak solution-state luminescence. In the solid state, intense light emission with an orange-red color ( $\lambda_{\text{em}} = 597 \text{ nm}$ ) can be observed. As verified by the crystal packing structures of **297**, steric effects experienced by the phenyl rings hinder their motions. In addition,  $\pi$ – $\pi$  interactions between the adjacent phenylpyridine rings exist in the crystal packing. Nevertheless, the detrimental 3D  $\pi$ – $\pi$  stacking network has been interrupted by the multiple intermolecular interactions such as C–H··· $\pi$ , C–H···F, etc. Therefore, in this specific case, like the C–H··· $\pi$ , C–H···F interactions, the  $\pi$ – $\pi$  interactions play a constructive role in the rigidification of molecular conformations as well as the RIM process, benefiting the light emission.

Similar to the previous heterodinuclear complex, the ionic homodinuclear Ir(III) Schiff base complexes **298a** and **298b** display marked AIP effects (Figure 59).<sup>355</sup> The two Ir(III) cores in each complex are coordinated by four cyclometalated ligands and one ancillary ligand, making the complexes adopt distorted octahedral geometries. The aryl spacer in the bridging diimine ligand of **298a** is a phenyl group while the one of **298b** is a biphenyl unit. The bridging diimine ligands are designed to electronically couple the two Ir(III) centers as well as aid in the AIE processes. Indeed, the rotations of the aryl spacers together with the vibrations of the phenylpyridine ligands and diimine fragments give rise to solution states that show negligible luminescence. In contrast, the neat film of **298a** emits a bright light with the maximum at 644 nm and retains a high  $\Phi_{\text{PL}}$  of 37.3%. For **298b**, strong luminescence peaked at 692 nm with a  $\Phi_{\text{PL}}$  measured to be 26.4% is shown. From the crystal structures of these complexes, intermolecular  $\pi$ – $\pi$  interactions rather than  $\pi$ – $\pi$  stacking between adjacent pyridine rings are observed. Analogue to **297**, these  $\pi$ – $\pi$  interactions and the short-distance intermolecular C–H··· $\pi$  contacts rigidify the conformations of the complex molecules and further constrain the intramolecular motions, rendering them highly emissive in the solid state.

Constructing AIE systems from metal complexes provides a simple and feasible strategy for the development of a large variety of strongly fluorescent or even phosphorescent materials in the aggregate or solid state. The various systems highlighted here spanning from metallic nanoclusters to metal centers decorated with rotatable aryl moieties and/or vibratable ligands have been obtained via different approaches, fully demonstrating the feasibility of the aforesaid strategy. All of these systems have further proven that intramolecular motions consume the excited-state energy resulting in weak solution-state emission, but once these non-radiative channels are hindered by steric effects and/or intermolecular interactions, the AIE or AEE will be observed. This is even more significant in the phosphorescent systems, which have more elongated lifetimes due to the triplet excited states. The long lifetimes make the compounds more susceptible to non-radiative quenching. Indeed it has been elaborated that in some of the more tightly packed crystals, phosphorescence intensities are stronger than those of systems with looser crystal packing. The research on these metal complex-based AIE systems paves the way towards the development of new metal complexes and functional luminescent systems.

#### 4.5. Unorthodox AIEgens

For organic compounds, one of the most important prerequisites for their luminescence is the large enough electronic conjugation. Just as the numerous examples which we have discussed in the previous sections, all the  $\pi$ -systems are covalently bonded to render sufficient conjugations. For instance, in TPE and THBA (**1**) which are among the most representative AIEgens, the phenyl rings and the vinyl rods are connected via single bonds to afford large  $\pi$ -conjugated systems (yellow circles highlighted in Figure 60A). Such kind of through-bond electronic conjugation

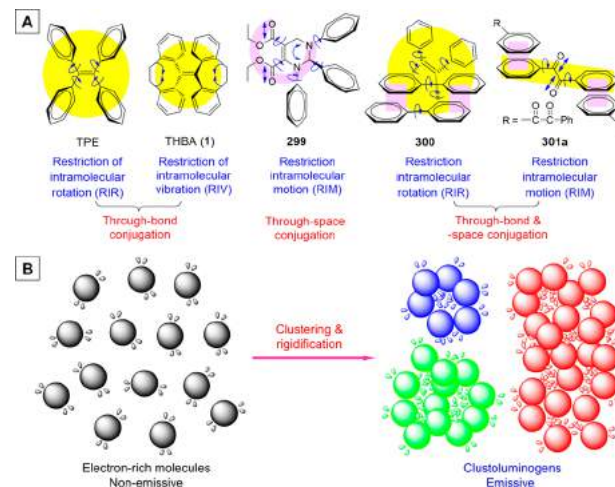


**Figure 60.** (A) Major conjugation modes for light-emitting systems and their AIE mechanisms. Reprinted from ref 356 which was published by Elsevier Ltd. and distributed under the terms of the Creative Commons Attribution-NonCommercial-No Derivatives License (CC BY NC ND) via <http://creativecommons.org/licenses/by-nc-nd/4.0/>. Copyright 2015 The Author(s). (B) Diagrammatic representation of proposed working mechanisms for the luminescence emission and AIE behaviors of some unorthodox systems which possess intermolecular through-space conjugations. Adapted with permission from ref 12. Copyright 2014 Wiley-VCH Verlag GmbH & Co. KGaA.

forms the structural basis of the most of luminogens. For TPE and THBA (**1**), their AIE effects are believed to arise from RIR and RIV, respectively. Therefore, in other words, for such

"conventional" AIE systems, the through-bond conjugation theory has answered why they can luminesce, and the RIM principle including RIR and RIV has provided an explanation to their AIE behaviors.

However, recently there is a growing class of unorthodox systems that do not possess conventional chromophores or through-bond conjugations but still have been found to exhibit a marked AIE effect.<sup>12,15,356</sup> Compound **299**, namely, (*R*)-diethyl-1,2,3-triphenyl-1,2,3,6-tetrahydropyrimidine-4,5-dicarboxylate, for example, is practically non-emissive in solution but luminesces brightly as crystals.<sup>357</sup> Examination on its crystal packing reveals that the electron-rich oxygen and nitrogen atoms with lone pairs are spatially arranged in close proximity. Such a through-space electronic interaction yields a conjugated chromophore or luminogen (pink crescent in Figure 60A). In the solution state, for one thing, the dynamic rotations of the aryl and ester units as well as the active vibrations of the tetrahydropyrimidine ring and carbonyl bonds consume the excited-state energy via non-radiative decay channels. For another, the active intramolecular motions may also separate the electron-rich moieties and hence impair the formation of through-space conjugation. These two effects collectively impede the light emission of **299** in the isolated state. The crystals of **299** emit efficiently, thanks to the RIM process in the ordered aggregates which guarantees the through-space electronic conjugation and simultaneously blocks the non-radiative decay pathways.

Besides the systems which individually own a through-bond or through-space conjugation, AIEgens possessing both conjugation modes have been exploited.<sup>55,358</sup> The TPE derivative with a folded conformation, namely, compound **300**, is such an example. As displayed in Figure 60A, the phenyl rings and vinyl rod in **300** are organized into a large  $\pi$ -electronic conjugation system through single bonds (yellow circle). Moreover, this unique folded molecular structure favors intramolecular  $\pi$ - $\pi$  interaction, generating an electronic delocalization system via the intramolecular through-space  $\pi$ -conjugation (pink rectangle in Figure 60A). These two kinds of electronic conjugations endue **300** with AIE attribute associated with RIR process.<sup>55</sup>

In addition to fluorescent systems such as **299** and **300**, similar electronic communication fashion has also been observed in some phosphorescent systems. The ketone-containing compounds are promising phosphorescence emitters, because carbonyl excitons are known to undergo efficient intersystem crossing from singlet state to triplet state. Some luminogens which contain single and multiple carbonyl groups have recently been found to exhibit crystallization-induced phosphorescence (CIP) at room temperature.<sup>358</sup> Benzyl (**301a**), for example, emits intense phosphorescence in its crystalline state, as a result of the efficient intersystem crossing promoted by the multiple carbonyl fragments. As can be seen from Figure 60A, there exist intramolecular through-bond electronic interaction in a single benzil molecule (yellow rectangle) and intermolecular through-space  $\pi$ -conjugation between different benzil molecules (pink rectangle). In the solution state, the phosphorescence of benzil is quenched by the dynamic carbonyl vibrations and phenyl rotations. The crystals of **301a** phosphoresce efficiently, owing to the RIM process activated by crystallization.

For some unorthodox luminogens, where intramolecular through-space conjugation can hardly form, the only alternative to yield a large conjugation might be intermolecular through-space electronic interaction. A working mechanism for the luminescence of this type of non-conventional system (including both fluorescence and phosphorescence) is proposed as illustrated

in Figure 60B. When molecularly dispersed, the electron-rich compounds are non-emissive, due to the lack of chromophores with extended electronic conjugations and the luminescence quenching by rotational and vibrational motions of the groups carrying the rambling and ramshackle lone-pair electrons. Once the aggregation occurs, the molecular conformations become rigidified. In the aggregates, the electron-rich atoms may form clusters of various sizes, where their electron clouds are overlapped and shared, thus generating the intermolecular through-space conjugation. The resulting "clustoluminogens" have smaller energy gaps and more extended electronic conjugations compared to the isolated molecules. In the meantime, the RIM process is activated, considerably blocking the non-radiative deactivation channels, thereby rendering the clustoluminogens emissive. The larger the cluster, the brighter and redder the luminescence would be. This kind of light emission may therefore be termed as rigidification-induced emission (RIE).<sup>12</sup> As a matter of fact, since the RIM process is in essence structural rigidification, the AIE can be named as RIE from a wider point of view. A number of natural products, including chitosan, dextran, glycogen, glucose, xylose, and galactose, have been found to show the RIE effect (*vide infra*), proving the generality of this phenomenon. RIE may offer a new clue to the underlying causes for the autoluminescence in biological systems.

In this section, the main effort will be directed to the description of the AIE/luminescence behaviors of non-conventional systems as well as the discussion on their working mechanisms. In view of their structural characteristics, the unorthodox luminophores highlighted herein will be divided into two sub-categories as molecular and macromolecular systems.

**4.5.1. Molecular Systems.** Direct synthesis via a facile urea-catalyzed chemoselective five-component reaction under mild conditions has produced an array of C-6 unsubstituted tetrahydropyrimidines with AIE characteristics.<sup>357</sup> Among them, the above-mentioned **299** is a good example to demonstrate the through-space electronic conjugation (*vide ut supra*). **299** has very limited electronic  $\pi$ -conjugation formed through bonds and yet its crystal polymorphs are strongly blue or green emissive (Figure 61A).<sup>357</sup> The B-form of **299** emits blue luminescence with the maximum at 434 nm and the  $\Phi_F$  up to 52.0%. The G-form is a green-emissive polymorph of **299**, which luminesces maximally at 484 nm with a  $\Phi_F$  as high as 55.0%. On the contrary, the solutions of **299** are virtually non-emissive with the  $\Phi_F$  values rather close to zero. Careful analyses on their crystal structures have offered more evidence to the through-space conjugation and the RIM principle. Parallel analyses have been performed on both the B- and G-form; however, to avoid repetition, only the structural information on the B-form is exhibited in Figure 61A. From a traditional viewpoint, there is little conjugation throughout the molecule, because only one of the carbonyl  $\pi$  systems extends to the  $\pi$  cloud of the C=C double bond. This makes the strong and relatively long-wavelength emission of **299** very unusual. Nevertheless, further investigation on the crystal structure has revealed that multiple intramolecular lone-pair interactions become possible because of the short distances between the neighboring heteroatoms. Comparing the B-form and G-form, the distances of these intramolecular lone-pair interactions are shorter in the G-form. To be precise, the O–O distances in the B-form are in the range of 2.241–2.816 Å, whereas in the G-form, the distances between adjacent O atoms range from 2.238 to 2.770 Å. And the O–N and N–N distances in B-form are 3.010 and 2.397 Å while those in G-form are 2.906 and 2.407 Å, respectively. These multiple and strong

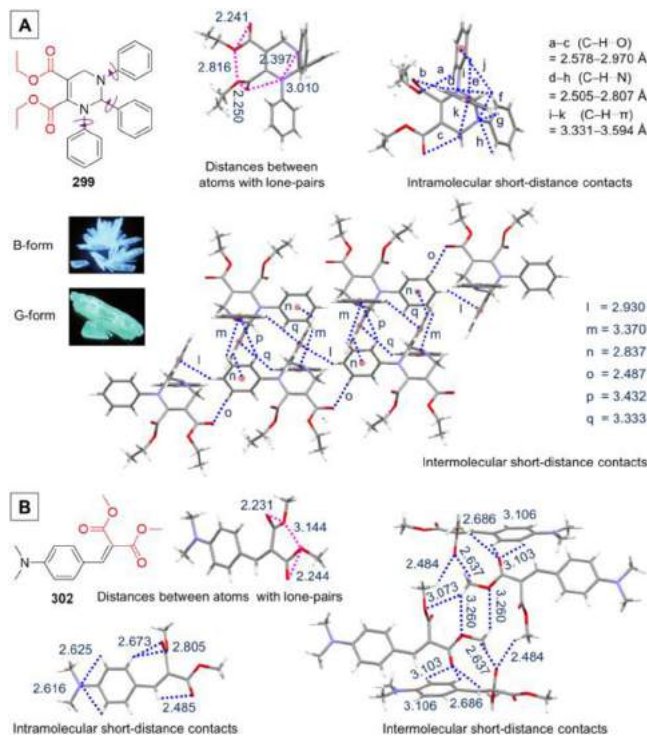


**Figure 61.** Representative unorthodox AIE/CIE systems (**299**, **302**) which are rich in ester groups. Insets: Fluorescent photographs of **299** in B- and G-form. Reprinted with permission from ref 357. Copyright 2013 Wiley-VCH Verlag GmbH & Co. KGaA. The crystal structure of **299** is retrieved free of charge from CCDC (818027) via [www.ccdc.cam.ac.uk](http://www.ccdc.cam.ac.uk). While that of **302** is obtained from the Supporting Information of ref 359. Copyright 2011 Royal Society of Chemistry.

short-distance electronic interactions afford electronic conjugations that are large enough for blue/green emissions. Furthermore, the multiple inter- and intramolecular interactions such as C–H···O, C–H···N, and C–H···π (2.487–3.594 Å) in the B- and G-forms not only conformationally rigidify the molecules and activate the RIM process but also stabilize the formation of intramolecular interactions between lone pairs. The electron clouds of these heteroatoms extend conjugation through space, lowering the energy gap. On the basis of these experimental results and analysis, it can be concluded that the shorter the distances between the nearby lone pairs, the redder and stronger the luminescence would be.

Bearing a similar ester moiety, 4-dimethylamino-2-benzylidene malonic acid dimethyl ester **302** (Figure 61B) shows a typical CIE behavior.<sup>359</sup> When it is molecularly isolated in the toluene solution, negligible emission with a  $\Phi_F$  lower than 0.1% has been measured. Amorphous films of **302** exhibit very faint greenish blue luminescence at room temperature. For the crystals of **302**, strong emission peaked at 468 nm with a  $\Phi_F$  of 38.0% is observed. Analogue to **299**, there exists multiple through-space electronic interactions between the lone pairs within the distance range of 2.231–3.144 Å, which favors the formation of a large π-conjugation. The enormous intra- and intermolecular short-distance contacts (2.484–3.106 Å) in the crystal stiffen the molecular conformations to stabilize the through-space electronic conjugation and meanwhile activate the RIM process to turn on the emission. In sharp contrast, in the solution or amorphous state, without such constraints, the assortment of intramolecular motions around single bonds work together to efficiently diminish the emission. In addition, the absence of

through-space electronic interactions also helps to reduce the noncrystalline luminescence.

CIE/CEE phenomena have also been observed in other molecules which are rich in ester groups.<sup>360,361</sup> A group of CIE/CEE-active diphenylmethane derivatives have been developed by Silva et al.<sup>360</sup> **303** is a member of this family, which is comprised of two ethyl salicylates connected by a methylene spacer (Figure 62A). It displays a  $\Phi_F$  of only 2.0% in THF. On the

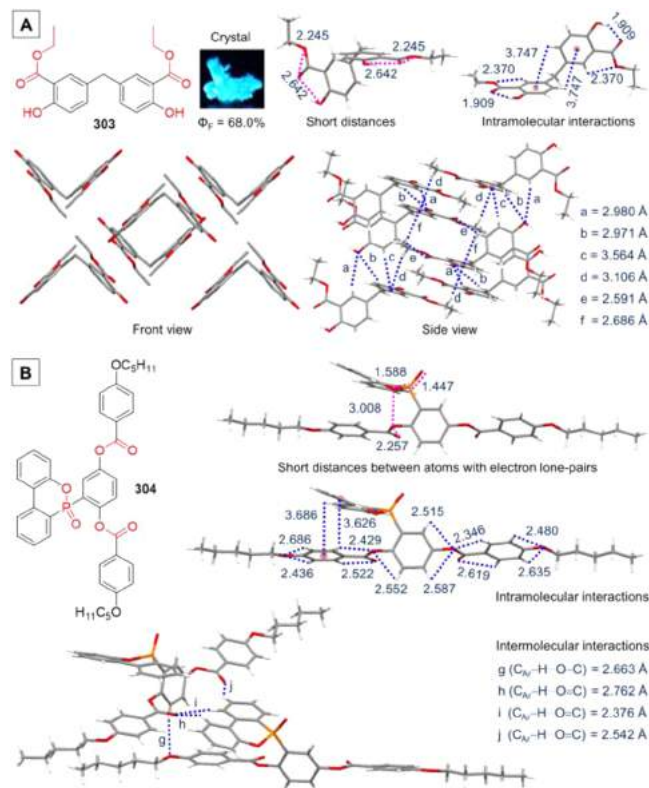


**Figure 62.** CIE-active unorthodox systems with ester/hydroxyl (**303**) and ester/phosphinate groups (**304**). Inset: Fluorescent photograph of the crystal of **303**. Reprinted with permission from ref 360. Copyright 2013 Elsevier Ltd. The crystal structure of **303** is retrieved free of charge from CCDC (938828) via [www.ccdc.cam.ac.uk](http://www.ccdc.cam.ac.uk). While that of **304** is provided by the authors of ref 361 and adapted from ref 361. Copyright 2009 American Chemical Society.

contrary, its crystals become strongly emissive at 465 nm with a drastically increased  $\Phi_F$  up to 68.0%. The weak emission in THF is owing to the active intramolecular rotational motions which dissipate the excited-state energy as well as the lack of extended conjugation. It is worth mentioning that due to the intramolecular hydrogen-bonding (O–H···O) which can still exist in THF, the molecular conformation is partially stiffened, causing **303** to luminesce. As aforementioned, although the efficiency is low, **303** does emit in THF. As can be seen from Figure 62A, the adjoining oxygen atoms with lone pairs are spatially organized in close proximity in the highly ordered crystals of **303**, with the O–O distances falling in the range of 2.245–2.642 Å. The through-space electronic interaction affords a conjugation sufficient for luminescence. Moreover, upon crystallization, the molecules of **303** are severely rigidified by the synergistic intra- and intermolecular interactions such as O–H···O, C–H···O, and C–H···π contacts (1.909–3.747 Å). These non-covalent forces not only restrict the intramolecular motions but also stabilize the

through-space electronic interactions between the neighboring lone pairs on the oxygen atoms.

Heterocyclic compound **304** is another ester-rich CEE-active species (Figure 62B).<sup>361</sup> In addition to the ester groups, **304** also contains an oxaphosphaphenanthreneoxide moiety. As indicated by the crystal structure, the distances between the adjacent heteroatoms on the same side of the central benzene range from 1.447 to 3.008 Å. It suggests that there exists a through-space  $\pi$  delocalization, but on the other hand, such a conjugation is neither large enough nor strong enough, which hence only gives rise to the weak luminescence peaked at 361 nm with a  $\Phi_F$  of about 2.1% (the crystalline aggregates in the mixture of acetonitrile/water with  $f_w = 80$  vol %). With a flexible molecular structure in solution, the dynamic intramolecular motions hamper the through-space interactions between the lone pairs, for another, they efficiently consume the excited-state energy, collectively resulting in emission quenching. The intramolecular motions are restricted by a lot of intra- and intermolecular  $C_{Ar}-H\cdots O-C$ ,  $C_{Ar}-H\cdots O=C$ , and  $C-H\cdots \pi$  interactions in the crystalline state, leading to the formation of through-space electronic conjugation and the enhancement in emission intensity. It is noteworthy that without such a through-space conjugation, there would be no luminescence at all, which has been verified by the model compound which does not have the oxaphosphaphenanthreneoxide ring.

A number of maleimide systems, which are rich in heteroatoms, have been reported to be AIE/AEE-active.<sup>362,363</sup> **305** is a prototype of these maleimide-based AIEgens (Figure 63A).<sup>363</sup> The THF solution of **305** shows weak luminescence with a maximum at 424 nm, possessing a  $\Phi_F$  of 2.4%. With the addition of water, the emission intensity keeps unchanged until the  $f_w$  exceeds 70 vol %. Further addition of water greatly intensifies the luminescence and red shifts the emission maximum to 500 nm. The THF/water mixture of **305** with  $f_w = 90$  vol % exhibits a  $\Phi_F$  of 45.0%, which is much higher than that in THF solution. Similar to the solution behavior of **303**, the molecular conformation of **305** might also get partially rigidified by the intramolecular hydrogen-bonding ( $N-H\cdots O=C$ ) in THF. It permits the formation of a weak and small through-space  $\pi$ -conjugation and results in a weak blue solution-state emission. When aggregated or crystallized, the conformation of **305** is further stiffened by the strong and multiple intra- and intermolecular hydrogen-bonding ( $N-H\cdots O=C$  and  $C-H\cdots O=C$ ; 2.121–2.453 Å) as well as the intermolecular  $C-H\cdots \pi$  (2.713–3.710 Å) and  $C-H\cdots N$  (2.643–3.297 Å) interactions. The distances between the adjacent heteroatoms are as short as 2.324, 2.327, and 2.801 Å. In this way, the strong and extended through-space electronic conjugation is generated and stabilized. In the meantime, the RIM process is further reinforced, and the luminescence is hence enhanced and red shifted.

As mentioned above, the hydrogen-bonding interactions play significant roles in the photophysical properties of compounds like **305**. For 2-(phenylamino)benzoic acid **306**, hydrogen-bonding interactions even play a more tremendous role in its photoluminescent behaviors (Figure 63B).<sup>364</sup> The molecules isolated in chloroform solution only show very weak emission with a low  $\Phi_F$  of 1.0%, but **306** displays bright blue luminescence ( $\lambda_{em} \sim 430$  nm) when crystallized, holding a  $\Phi_F$  of 35.4%. The crystal structure reveals a network of strong hydrogen-bonding interactions. Thanks to the multiple intramolecular hydrogen-bonding, the electron-rich oxygen and nitrogen atoms are almost coplanar and closely arranged in short distances (2.220, 2.649, and 2.662 Å), facilitating the formation of extended conjugation

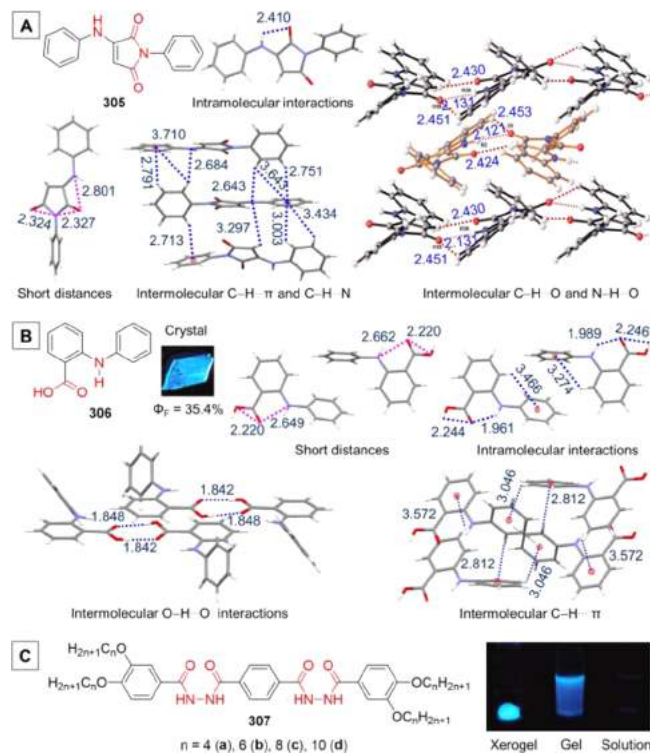


**Figure 63.** Unorthodox AIE systems with hydrogen-bonding interactions (305–307). The illustration for the intermolecular interactions in the crystal of **305** is adapted with permission from ref 363. Copyright 2013 Royal Society of Chemistry. Insets: Fluorescent photographs of crystal of **306**, the xerogel, gel, and solution of **307**. Reprinted with permissions from ref 364 and 365. Copyright 2009 Royal Society of Chemistry (306). Copyright 2010 American Chemical Society (307). The crystal structures of **305** and **306** are retrieved free of charge from CCDC (938824 and 709893) via [www.ccdc.cam.ac.uk](http://www.ccdc.cam.ac.uk).

through electronic interaction between lone pairs. Intermolecular hydrogen-bonds between carboxyl groups ( $O-H\cdots O$ ; 1.842 and 1.848 Å) dimerize a pair of molecules of **306**. The molecular conformation is further rigidified through intramolecular  $O-H\cdots O$  (2.244, 2.246 Å) and  $N-H\cdots O$  (1.961, 1.989 Å) hydrogen-bonds together with intra- and intermolecular  $C-H\cdots \pi$  interactions (2.812–3.572 Å). These interactions collectively stabilize the through-space electronic conjugation and restrict the intramolecular motions, thereby resulting in the efficient aggregate-state luminescence.

A series of hydrazine derivatives **307a**–**307d** can form organogels and xerogels as a result of multiple intermolecular hydrogen-bonds with greatly enhanced emissions (Figure 63C).<sup>365</sup> Each of these low-molecular-mass organic gelators is bearing two hydrazine linkages and end-capped by phenyl moieties with alkoxy chain lengths varying from four (**307a**), six (**307b**), eight (**307c**) to ten (**307d**). All these four species display quite weak emissions in chloroform with  $\Phi_F$ s between 0.13% and 0.17%. In contrast, emission increments over 100-fold as compared to those of solutions have been recorded for the xerogels of **307a**–**307d**, which possess  $\Phi_F$ s ranging from 18.0% to 22.0%. It is worthwhile to note that accompanying with the emission enhancement, there are remarkable red-shifts in the emission maxima from about 371 and 392 nm to 438 nm. Although no crystal data was provided, on the basis of the information obtained from the examples discussed above, it could still be believed that in the gel state, the hydrazine units in each compound might form through-bond and through-space electronic conjugations due to the multiple

hydrogen-bonding interactions. Such conjugations are further reinforced by the formation of intermolecular hydrogen-bonds, and meanwhile, RIM process comes into play, giving rise to the strong emission.

A large variety of heteroatom-rich organic compounds have been reported to display strong room-temperature phosphorescence (RTP) in the solid or crystal state.<sup>358,366–370</sup> A series of molecular asterisks with persulfurated benzene cores fall in this category (Figure 64). The R groups are *para*- (308), *meta*- (309), and *ortho*-substituted (310) on the peripheral benzene rings.<sup>366</sup>

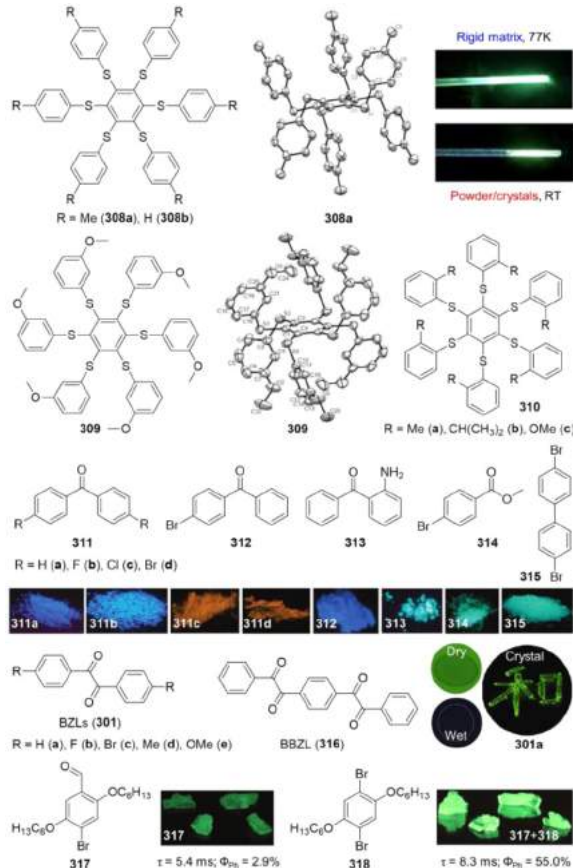


**Figure 64.** Representative small AIE systems with room-temperature phosphorescence. Insets: Photographs of 308a, crystal of 311a–311d, 312–315, 301a, 317, and 317/318 taken under UV light. The photos of 308a and the crystal structures for 308a and 309 are reprinted with permission from ref 366. Copyright 2014 Elsevier Ltd. The photos for 311a–311d and 312–315 are reprinted from ref 367. Copyright 2010 American Chemical Society. The ones for 301a are reprinted with permission from ref 358. Copyright 2013 Science China Press and Springer-Verlag Berlin Heidelberg. While those for 317 and 317/318 are reprinted with permission from ref 368. Copyright 2011 Rights Managed by Nature Publishing Group.

or *ortho*-substituted (310) on the peripheral benzene rings.<sup>366</sup> All these compounds are non-luminescent in solutions at room temperature. They can be phosphorescent only if their molecular conformations are sufficiently rigidified. For instance, these compounds brilliantly phosphoresce in the solid phase at room temperature or in a rigid matrix at low temperatures with  $\Phi_{\text{Phs}}$  of 6.0%–100.0%. Their phosphorescence lifetimes are ranging from 3.0 to 15.8  $\mu\text{s}$ . Without a rigid environment to restrict the intramolecular motions, the excited-state energy would be easily exhausted through non-radiative channels. This is because the long lifetime of triplet decay is much more susceptible to the

intramolecular motions that would lead to energy loss. Moreover, as implied by the crystal structures, the electron-rich sulfur atoms in each compound are proximately coplanar and close to each other, favoring the formation of through-space  $\pi$ -conjugation. It explains why they can emit at such long wavelengths ( $\lambda_{\text{em}} = 487$ –526 nm). Such a through-space electronic conjugation also needs to be stabilized by the rigid environments. In light of this, the large difference lying in the solid-state  $\Phi_{\text{Phs}}$  of these compounds becomes easy to understand. Among compounds 308–310, 308 holds the highest  $\Phi_{\text{Ph}}$ , with the  $\Phi_{\text{Phs}}$  of 308a and 308b up to unity (100.0%) and 60.0%, respectively. The crystal structure of 308a exhibited in Figure 64 shows the conformations of its six highly bulky substituents. The toluene arms alternate between up and down orientations, which prevent the intermolecular  $\pi$ – $\pi$  stacking interactions. In the crystalline state, the phenyl ring rotations and vibrations of the sulfide bridges are severely constrained, rendering a strong emission. Comparing the distances between the persulfurated benzene cores, the molecules of 308a are packed in a distance of 8.078 Å, while the molecules in 308b are arranged in further distances of 10.274 Å. The increase of intermolecular distances reduces the steric hindrance experienced by the molecules. This small reduction in rigidity results in a huge decrease in the emission efficiency. The variations in  $\Phi_{\text{Phs}}$  of the other counterparts follow this law.

Other pure organic luminogens featuring CIP property at room temperature include carbonyl-rich and/or halogenated species like 311–315 (Figure 64).<sup>367</sup> These compounds show no luminescence when they are dissolved in good solvents, adsorbed on thin-layer chromatography (TLC) plates, and doped into polymer matrixes. In these isolated states, intramolecular motions effectively annihilate their triplet excitons through non-radiative decay pathways. As can be seen from Figure 64, the benzophenone derivatives (311–313), methyl 4-bromobenzoate (314) and 4,4'-dibromobiphenyl (315) show different colors in their phosphorescent emissions varying from blue to green to orange. Benzophenone 311a has a solution-state  $\Phi_{\text{Ph}}$  of only 0.001%, but its crystals possess a  $\Phi_{\text{Ph}}$  of 15.9%. The crystals of the halogenated benzophenone derivatives 311b, 311c, and 311d show  $\Phi_{\text{Phs}}$  of 39.7%, 8.3%, and 12.0%, respectively, which are much higher than those of their solutions (0.003%–0.565%). The phosphorescence of these halogenated compounds are red shifted with the increasingly heavier atoms (i.e.,  $\lambda_{\text{em}}:$  311b < 311c < 311d). A similar CIP effect has also been observed in other benzophenone derivatives, such as 312 and 313, the  $\Phi_{\text{Phs}}$  of which are 6.7% and 8.6%, respectively. Methyl 4-bromobenzoate (314) and 4,4'-dibromobiphenyl (315) holds a  $\Phi_{\text{Ph}}$  of 5.9% and 13.9%, respectively. These high  $\Phi_{\text{Phs}}$  are first and foremost a result of the strengthened rigidity in molecular conformations due to crystallization. The crystal packing of these compounds has evidenced the existence of extensive strong intermolecular interactions, such as C–H···O, N–H···O, and C–H··· $\pi$  hydrogen bonds, C–H···X (X = F, Cl, or Br) halogen bonds, and C–Br···C–Br interconnects. All of these short-distance contacts collaboratively restrict the intramolecular motions, leading to the turn-on in phosphorescence. As suggested by the crystal structures, intermolecular through-space  $\pi$ -conjugations between the phenyl rings occur in these luminogens, which also benefit the efficient light emission. The phosphorescence lifetimes of these molecules range from 19.2  $\mu\text{s}$  (e.g., 311c) to 4.8 ms (e.g., 311d).

Quite similar to the benzophenone derivatives, a series of benzil derivatives (301a–301e and 316; Figure 64) have also

been found to be CIP-active at room temperature.<sup>358</sup> These compounds are virtually non-emissive even in the oxygen-free solvents or the amorphous state. Brilliant green phosphorescence of **301a** with  $\lambda_{\text{em}} = 521$  nm is observed upon crystallization or when the solutions are cooled to 77 K. As shown by the crystal analysis of **301a**, multiple C–H $\cdots$ O hydrogen bonds in the range of 2.416–2.483 Å as well as the intermolecular through-space conjugation hold the molecules together to yield highly rigid conformations. This rigidification prevents intramolecular motions such as phenyl rotations and carbonyl vibrations from actively consuming the excited-state energy, resulting in efficient phosphorescence with a mean lifetime of 0.142 ms. In the isolated state or amorphous state where the molecules are packed in a much less rigid mode compared with those in the crystal state, the intramolecular motions continuously deplete the excitation energy during the long lifetime of the excited state, rendering **301a** non-luminescent. Other benzil derivatives, i.e., **301b**–**301e**, behave similarly, being non-emissive in the solution/amorphous state but strongly phosphorescent in the crystal state ( $\lambda_{\text{em}} = 500$ –526 nm). With additional carbonyl groups, **316** exhibits much red-shifted phosphorescence ( $\lambda_{\text{em}} = 584$  nm) due to the extended conjugation length.

By combining the factors such as carbonyl group(s), heavy atom effect, as well as the hydrogen/halogen-bonding interaction(s), Kim et al. have recently developed an array of organic systems showing the room-temperature CIP effect based on bromobenzaldehyde cores.<sup>368–370</sup> **317** is a 4-bromobenzaldehyde derivative decorated with two hexyloxy chains (Figure 64).<sup>368</sup> In solution, **317** only emits very weak blue fluorescence peaked at 420 nm with a  $\Phi_F$  as low as 0.5% and a lifetime of 0.5 ns. Non-radiative decay through intramolecular motions and the lack of effective C=O $\cdots$ Br contacts work jointly to give rise to the weak fluorescence. In the crystalline state, green phosphorescence with the emission maximum at 500 nm is readily observed for **317**, with a  $\Phi_{\text{Ph}}$  of 2.9% and a lifetime of 5.4 ms. Examining the crystal structure has revealed that close and ordered C=O $\cdots$ Br interactions exist between the carbonyl groups and the bromines of the adjacent molecules. The C=O $\cdots$ Br bond is in the angle of 126° with a distance of 2.86 Å. The short-distance O $\cdots$ Br interaction was reported to promote spin-orbit coupling aiding in the intersystem crossing from the singlet to triplet excited state and possibly from the triplet to singlet excited state as well. These short-distance interactions also impede intramolecular motions such as the carbonyl vibrations and thus reduce non-radiative energy loss in the excited state. More interestingly, when **317** is co-crystallized with **318**, namely, 2,5-dihexyloxy-1,4-dibromobenzene (Figure 64), a bihalogenated analogue to **317**, the  $\Phi_{\text{Ph}}$  of the resulting mixed crystals is dramatically increased to  $55.0 \pm 3.0\%$  and the lifetime is prolonged to 8.3 ms. The crystals are grown from a mixture of **317** and **318** with  $\sim 1$  wt % of **317**. **317** is likely locked within a sea of **318** molecules and are tightly packed together due to strong Br $\cdots$ Br and C=O $\cdots$ Br halogen interactions. Such a rigid crystalline matrix plays an important role in the observed phosphorescence enhancement.

In addition to crystallization, other means that can rigidify the conformations, such as doping the chromophores into rigid matrixes or amorphous solids, have also been utilized to achieve RTP of metal-free organic materials.<sup>369–371</sup> For instance, Kim's group has further used **317** as a model luminogen to develop novel organic phosphors.<sup>359,370</sup> By means of embedding **317** in the amorphous polymer matrix such as poly(methyl methacrylate) (PMMA; Figure 65A), the vibrational dissipation of the

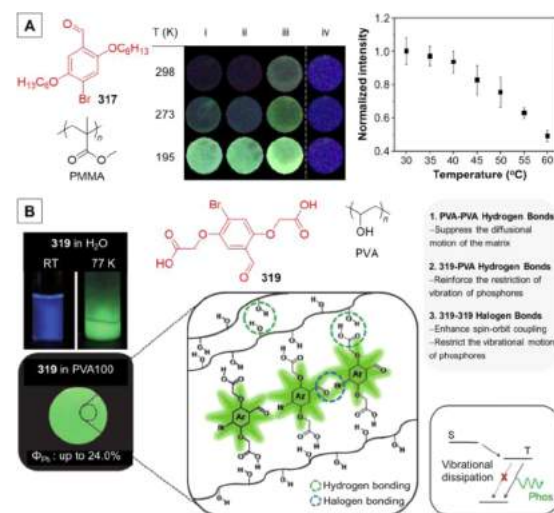


**Figure 65.** Fabrication of RTP emitters by doping metal-free organic materials (**317**, **319**) into rigid matrixes (PMMA, PVA). Insets: (A) Phosphorescence emission of **317** embedded in (i) aPMMA, (ii) sPMMA, and (iii) iPMMA at different temperatures. (iv) Blue fluorescence emission of pure **317**. Adapted from ref 369. Copyright 2013 American Chemical Society. (B) (left) Images of (upper) aqueous solution of **319** at room temperature and at 77 K and (lower) **319** embedded in PVA100 under UV light. (right) Schematic illustration of phosphorescence process in the **319**-PVA composite. Adapted with permission from ref 370. Copyright 2014 Wiley-VCH Verlag GmbH & Co. KGaA.

triplet excited states has been successfully suppressed.<sup>369</sup> These PMMA-blended films show green phosphorescence ( $\lambda_{\text{em}} = 520$  nm), which is in sharp contrast to the fluorescent neat films of **317** ( $\lambda_{\text{em}} = 425$  nm). Since the phosphorescence of the PMMA-blended films results from the suppression of the vibrations by the glassy PMMA matrix, theoretically, the more rigid the polymer matrix, the stronger the phosphorescence would be. The tacticity of the polymer chain should thus greatly affect the  $\Phi_{\text{Ph}}$ s of the blended films, because it is a structural parameter for the stereoregularity. **317** in the atactic PMMA (aPMMA) and syndiotactic PMMA (sPMMA) matrixes exhibits only weak phosphorescence, whereas **317** in the isotactic PMMA (iPMMA) show an approximate 10-fold increase in the phosphorescence at room temperature. The increase in the isotacticity of the polymer matrix from 0% to 100% results in the  $\Phi_{\text{Ph}}$  change from 0.7% to 7.5%. When the temperature is decreased to 195 K, green phosphorescence of these PMMA-blended films is intensified regardless of the tacticity of the polymer matrix, which can be seen from Figure 65A. For the films of pure **317**, the decrease in temperature, however, only mildly enhances its blue fluorescence, signifying that the polymer matrix is the source of rigidification that reduces the vibrational relaxations and promotes the phosphorescence. Although bright RTP can be realized in purely organic crystalline materials, these organic phosphors still have limitations to practical applications due to the stringent requirement of high quality crystal formation. The processability of polymers makes them more suitable for real-world applications, which has also been verified by this work. Since the glass transition point of iPMMA is 55 °C, the phosphorescence intensity of luminogen **317** doped in iPMMA decreases nearly linearly as the temperature increases from 30 °C to 60 °C (Figure 65A). This temperature responsive behavior affords a sensitive, inert, and cheap temperature sensor based on a metal-free organic phosphorescence emitter. Temperature

sensing in microfluidic device using 317 embedded in iPMMA has been realized as well, which is promising for biomedical applications owing to the biocompatibility of each component.

As previously pointed out, the crucial factors for the construction of efficient RTP systems based on purely organic components are the promotion of singlet-to-triplet and triplet-to-singlet intersystem crossing as well as the suppression of the non-radiative relaxations from the triplet state to the ground state. Inspired by the successful attempts achieved in the 317 system, Kim and coworkers have designed a new organic phosphor 319 which consists of a bromobenzaldehyde core and two carboxylic acid side chains (Figure 65B).<sup>370</sup> 319 is used as a dopant. The bromobenzaldehyde unit is supposed to offer a structural basis for the strong halogen-bonding in the assembly to facilitate the intersystem crossings as well as the triplet-exciton generation. The carboxylic acid pendants are expected to enable the formation of strong hydrogen bonds between the phosphor and the amorphous matrix, in order to suppress the vibrations/diffusions of the phosphors and matrix. In view of its hydrogen-bonding capability, poly(vinyl alcohol) (PVA) has been selected as an amorphous polymer matrix to establish a new RTP system with 319. Blue fluorescence peaked at 460 nm with a  $\Phi_F$  of 11.5% and a lifetime of 2.18 ns has been detected for the aqueous solution of 319 under ambient conditions. When the solution is cooled to 77 K, strong green phosphorescence at 510 nm is observed, with a long lifetime of 5.9 ms. Even without intermolecular interactions, the frozen solution at this cryogenic temperature significantly impairs the vibrational dissipation of triplets and thus permits phosphorescence emission. 319-embedded PVA films exhibit strong green phosphorescence (530 nm) with the  $\Phi_{ph}$  up to 24.0% and a lifetime of 4.7 ms even at room temperature. The strong phosphorescence observed in the amorphous films is due to the strong intermolecular hydrogen and halogen bonds. Firstly, a large number of hydrogen bonds between PVA polymer chains generate a highly rigid matrix which greatly hinders the intramolecular motions. Secondly, the hydrogen-bonding between PVA and 319 locks the luminogens within the matrix and reinforces the restriction of the vibrations of phosphors. In addition, the intermolecular halogen bonds between the luminogens not only further rigidify the molecular conformations but also enhance the spin-orbit coupling and stabilize the triplet excited states. Intriguingly, the phosphorescence of 319-PVA can be readily converted into blue fluorescence when water is dropped onto the 319-PVA blended film. The water molecules not only break the PVA-PVA and 319-PVA hydrogen bonds but also disrupt the 319–319 halogen-bonding interactions which are conducive for phosphorescence. The dissolved luminophores become fluorescing rather than phosphorescing. The phosphorescence-to-fluorescence switching of this system makes it a ratiometric water sensor which can be utilized as water indicator for fuel/organic solvents and residual-water detector in the root-canal treatment in dentistry, etc.

The various small molecular systems presented here are rich in heteroatoms that are in close proximity to each other often resulting in luminescence in the visible spectrum range. Some electron-rich purely organic systems even show RTP upon crystallization or in the highly rigid amorphous polymer matrixes. The rigidification of the molecular conformation by strong intermolecular interactions such as hydrogen bonds and/or halogen bonding or physical constraints accounts for the resulting RTP. Macromolecular unorthodox AIE systems will be introduced and discussed in the next section.

**4.5.2. Macromolecular Systems.** It is amazing that rice is luminescent! This incredible fact has recently been uncovered by our group.<sup>372</sup> As exhibited in Figure 66, rice emits a bright blue

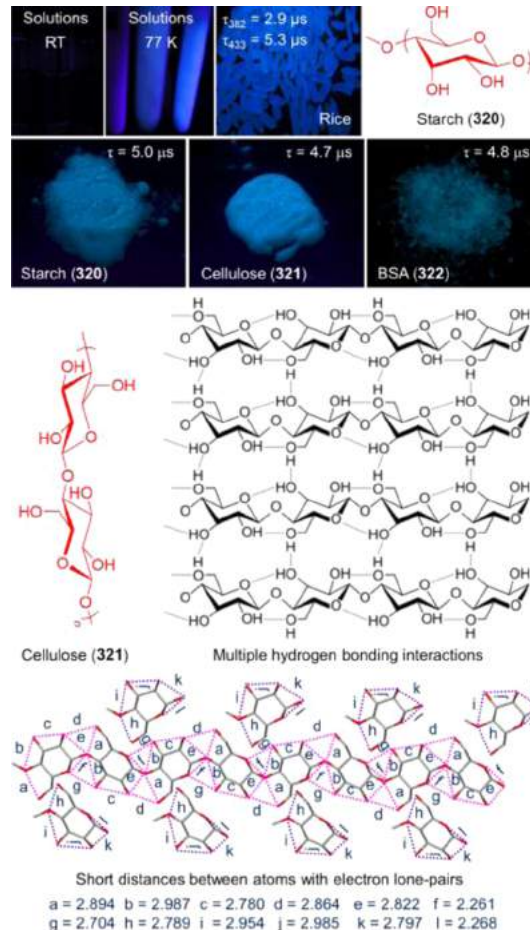


**Figure 66.** Pure organic non-conventional luminescent compounds showing RTP. Insets: Photograph of the solutions of (left) starch, (middle) cellulose, and (right) bovine serum albumin (BSA) taken at room temperature and 77 K, and the rice and the solid powders of starch, cellulose, and BSA taken under UV light illumination. Adapted with permission from ref 372. Copyright 2013 Science China Press and Springer-Verlag Berlin Heidelberg.

light with a peak and a shoulder at 382 and 433 nm, respectively, upon UV excitation. The long lifetimes corresponding to these emission species are 1.72 ns/2.9  $\mu$ s and 1.78 ns/5.3  $\mu$ s, suggesting the dual fluorescence and phosphorescence from the rice. It is intriguing that rice can emit such efficient RTP. As mentioned above, intermolecular interactions are effective to reduce the vibrational dissipations of the excitons and hence conducive to light emission. Strong and multiple hydrogen bonds existing in rice due to the presence of oxygen atoms and hydroxyl groups should play a role in its emission. Moreover, the semi-crystalline morphology of rice also helps to decrease the thermal deactivation and promote the luminescence, because the crystallization acts as a physical means to fix the chain conformations. In addition, the covalent bonding in the polymer framework is supposed to play an important part in both the light emission and RTP effect of rice.

Since the major component of rice is starch, the photophysical properties of starch (320) were checked as well. The aqueous solution of starch is non-luminescent and even when the solution

is dropped onto a TLC plate, it is still non-emissive. However, when the solution is cooled to 77 K, blue luminescence arises. Intriguingly, starch powder emits brightly even at room temperature. As a carbohydrate similar to starch, cellulose (321), which is comprised of a large number of glucose units jointed by glycosidic bonds, shows analogous luminescent behaviors. Such fascinating emission behaviors have also been found in other natural products such as proteins. BSA, a frequently-used protein for experimental research, was chosen as an example. It has been found that BSA (322) also behaves similarly to starch and cellulose. The solid powders of starch (320), cellulose (321), and BSA (322) display RTP emissions with the major peak maxima at 470, 427, and 418 nm, respectively. Their phosphorescence lifetimes are 5.0, 4.7, and 4.8  $\mu$ s, respectively (Figure 66). Closer examinations of their powder X-ray diffraction patterns reveal that these natural polymers, especially BSA, are more amorphous than crystalline.<sup>372</sup> It suggests that in the polymeric systems, crystallization is not an indispensable prerequisite for the RTP effect, although crystallization can enhance the RTP efficiency. It also indicates that the covalent bonds connecting the repeating units in the polymer backbones serve as essential pathways to the rigidification of the molecular conformation and the stabilization of the triplet states.

All these three natural polymers contain no conventional chromophore, so the question comes out that what is/are the source(s) of the emissions? As mentioned in the illustration of Figure 60B, the mechanism for the luminescence of this type of non-conventional system has been proposed. Electron-rich units like oxygen and nitrogen atoms are abundant in these polymers. When molecularly isolated, cellulose is non-emissive, because there is no chromophore with sufficient electronic conjugation and meanwhile, the rotations and vibrations of the groups carrying rambling and ramshackle lone pairs non-radiatively annihilate the excited states. Upon aggregation, the structural rigidification immediately takes place. In the aggregates, the electron-rich atoms form clustoluminogens with smaller energy gaps and more extended electronic conjugations. Take cellulose for example. The crystal packing of cellulose (321) reveals the existence of through-space electronic conjugation between the adjoining oxygen atoms. The electron-rich oxygen atoms are closely arranged within short distances (2.261–2.987 Å), which facilitate the electronic interactions between their lone pairs as well as the formation of clustoluminogens. The numerous hydrogen-bonding interactions and the tight crystal packing as well as the covalent bonding of the repeating units make a concerted effort to stiffen the molecular structure, stabilize the clustoluminogens and restrict the intramolecular motions. As a result, the emission is switched on.

Some other natural polymers such as chitosan (323) and dextran (324) (Figure 67A), which are structurally similar to starch and cellulose, also exhibit RTP in the solid state, especially the crystalline state.<sup>372</sup> It is believed that the electron-rich species such as oxygen and nitrogen units are accountable for their luminescence. Moreover, the tremendous intermolecular interactions and the physical constraints among polymer chains also play vital roles in their efficient RTP emissions, for these effects stabilize the through-space electronic conjugations and activate the RIM process which blocks the non-radiative relaxation channels and promotes the radiative decay.

Apart from the above phosphorescent polymer systems without conventional chromophores, there are quite a few unorthodox polymeric fluorophores.<sup>373,374</sup> A family of dynamic glycopolymers made from polycondensation though reversible

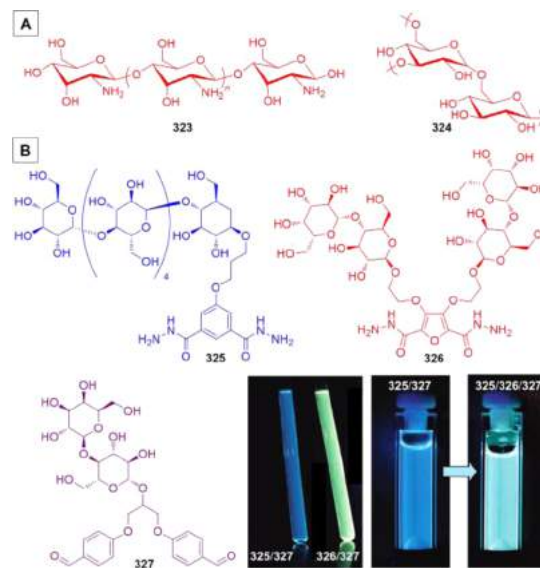


**Figure 67.** (A) Other natural products showing RTP (323, 324). (B) Chemical structures of the bis-hydrazides 325, 326, the dialdehydes 327. Insets: Fluorescence photographs of (left) the typical dynamic glycopolymers prepared by polycondensation of bis-hydrazides and dialdehyde, and (right) samples of polymer 325/327 before and after chemical exchange with 326. Reprinted from ref 373. Copyright 2010 American Chemical Society.

acylhydrazone formation between the oligosaccharide-attached bis-hydrazides 325 or 326 and dialdehyde 327 have been reported to show strong emission (Figure 67B).<sup>373</sup> Polycondensation between 325 and 327 produces the dynamer 325/327, a blue fluorescent (457 nm) glycopolymer. In like manner, dynamer 326/327 with bluish green fluorescence peaked at 499 nm is generated by the polymerization reaction between 326 and 327. Furthermore, because of the reversibility of the acylhydrazone bonds in these glycodynamers, covalent exchange reactions of one monomeric component by another can easily take place, which results in the modification of polymer constitution and photophysical properties of the glycodynamers. The exchange reaction between 325/327 and 326 can be monitored by fluorescence spectroscopy. With the addition of 326 into the sample of 325/327, the emission maximum shifts from blue to green (insets in Figure 67B), due to the transformation of the polymer constitution from 325/327 into 325/326/327. These polymers have been reported to be AIE-active. For 325/327, the fluorescence intensity decreases dramatically upon the addition of DMSO into its aqueous solution, probably owing to the destabilization of the tightly packed micellar structure. Whereas, in the aggregate state, the numerous saccharide moieties of the glycopolymers give rise to the tremendous hydrogen bonding interactions amongst repeating units within and between the polymer chains, resulting in highly rigid conformations. As a consequence, the intramolecular motions are effectively restricted and the through-space  $\pi$ -conjugation is reinforced, therefore leading to the strong fluorescence.

The small and macromolecular unorthodox systems elaborated in this large section become highly luminescent when their conformations are rigidified by the cryogenic cooling, crystallization (ordered packing), non-covalent interactions, host blending, polymer doping, covalent-bonding, and so on. Although without classical chromophores in their structures, they always possess abundant electron-rich heteroatoms which could form clustoluminogens via through-space lone pair

interactions. Once the clustoluminogens or extended electronic conjugations are generated and the RIM processes come into play, the light emission would be turned on or enhanced. Although the increasing interest in unorthodox luminogens have shone more insights into this class of luminescent materials, further and more work is still needed to gain a deeper understanding into their working mechanisms of luminescence. Their unique structures produce fascinating photophysical properties, promoting even more research. With continual research, the knowledge and understanding gained from studies on these special systems can be used to further advance other luminescent systems.

## 5. TECHNOLOGICAL APPLICATIONS

Since the AIE concept was first put forward in 2001, tremendous research interests from both academic and technological areas have been attracted to this territory and have brought about enormous varieties of AIEgens with diversified functionalities as discussed above.<sup>12–20,356</sup> These AIE materials have in turn brought forth plentiful technological innovations. In some sense, the scope of technological applications based on AIEgens is boundless, limited probably only by our imagination. In principle, the AIE materials can be utilized in any case where the RIM process is involved. The AIE effect provides exhilarating possibilities for empoldering new sensing systems that operate in a luminescence turn-on fashion. As efficient solid emitters with good thermal- and photo-stabilities, AIEgens definitely fill the bill and are promising materials for the fabrication of high-performance optoelectronic devices. To date, numerous efforts have been devoted to the utilities of AIE materials in a wide variety of high-tech areas. In this section, we will systematically and roundly discuss the so-far achieved success in AIE-involved applications, with an emphasis on the work reported after the publication of our first review in 2009.<sup>13</sup>

### 5.1. Biological Probes

Biological area itself is a vast and appealing research field. There are uncountable species which are vital to living things need to be detected and numerous events that need to be unveiled and monitored. Luminescence as a technique is a perfect choice for the applications in biological areas, in the light of its rich advantages such as superior sensitivity, high selectivity, fast response, low background noise, simplicity, and so on. More importantly, luminescence offers direct visualization tools, which enable on-site and noninvasive array of bioanalytes at the molecular level in real-time and provide useful insights into complicated biological structures and processes.<sup>27,375,376</sup> Luminescent technique becomes “one of the most important tools” for contemporary bioscience because it can “watch processes that were previously invisible”, as said by the Nobel Foundation. It explains why two Nobel Prizes in Chemistry were awarded to the scientists that contributed to the area of luminescent techniques in a short time (2008 and 2014). A variety of luminescent materials, including organic dyes, quantum dots (QDs), inorganic or organic nanoparticles (NPs), and fluorescent proteins (FPs) have been developed and utilized in biological sensory and imaging applications.<sup>377–379</sup> QDs are highly emissive and photostable but most of them are inherently cytotoxic since they typically comprise heavy metals and chalcogens (e.g., CdSe and PbS).<sup>380,381</sup> The surfactants used in the fabrication of polymeric and silica NPs such as sodium dodecyl sulfate (SDS) are harmful to living cells.<sup>382,383</sup> FPs have attracted much attention because they can be genetically

encoded to the targets of interest, but the use of FPs requires complicated transfection processes and their large molecular sizes may interfere with the conformation and dynamics of the targets.<sup>384</sup> Most of the conventional luminophores suffer from the ACQ effect, which prohibits them from being used at high concentrations and further results in compromised sensitivity. Diametrically opposed to these conventional luminophores, AIEgens are nearly non-luminescent in the isolated state but luminesce strongly in the aggregate/clustered state. Light-up/turn-on probes could be facilely engineered and they possess higher resistance to photobleaching and superior reliability relative to those conventional turn-off probes.<sup>19</sup> Moreover, the low background is another merit of AIE-based bioprobes, which makes them tempting options for continuous monitoring of biological processes with high sensitivities and resolution, dispensing with repeated washing procedures. In biological areas, AIEgens are mainly used as probes for the sensing of biogenic species or as stains/contrast agents for the imaging of cells and organisms or they are even integrated with other functions for diagnosis and/or therapy, in view of this, this section will be split into two smaller sections as biomolecular sensing and biological imaging.

**5.1.1. Biomolecular Sensing.** Biogenic species detection and quantification is of crucial importance to life science, biotechnology, healthcare of human beings (e.g., clinical diagnostic examinations, treatment monitoring), fermentation industry, as well as food and pharmaceutical industries, etc. AIE has been proven to be a powerful approach for sensitive and specific biosensing. Taking advantage of the AIE effect, diverse sensing systems can be facilely established for a wide range of analytes varying from small biogenic molecules (e.g., monosaccharides, biothiols, amino acids, amines, adenosine triphosphate) to biomacromolecules (e.g., polysaccharides, DNAs, proteins, enzymes, lipids). This section will be a showcase for these multifarious and excellent AIE-based sensing systems, starting with the ones tailored for biogenic small molecules and followed by those for biomacromolecules.

**5.1.1.1. Small Biogenic Molecules.** Glucose is an important biomolecule as a basic necessity of living organism and a pervasive fuel for biological processes. The abnormal levels of glucose in body fluids such as human blood or urine signifies biological dysfunctions.<sup>385</sup> In light of the biological importance of glucose,<sup>386</sup> many AIEgens have been tailored to create highly sensitive and selective systems for glucose detection.<sup>387,388</sup> TPE moieties have been linked to an amphiphilic copolymer, affording brightly fluorescent micelles.<sup>388</sup> By means of combining the cascaded enzymatic oxidation of D-glucose with glucose-oxidase (GOx) and the chemical oxidation of I<sup>-</sup> (a fluorescence quencher) by H<sub>2</sub>O<sub>2</sub>, the fluorescent micelles can be used for the selective detection of D-glucose in aqueous solution with a detection limit of 2.29 μM. However, this AIE biosensor works in a turn-off mode. Although the selectivity is good and the sensitivity is acceptable, this approach is indirect and needs a few extra co-reagents.

L-Tyrosine-functionalized TPE derivative 328a (Figure 68) has been developed into a fluorescence turn-on biosensing system with fast response and high specificity.<sup>389</sup> 328a is composed of a TPE core and four L-tyrosine units at the periphery. The TPE core serves as a signaling motif and the tyrosine units bestow water solubility and enzymatic coupling reactivity on the probe. TPE-Tyr (328a) is molecularly dispersed in aqueous solution and hence experiences no restriction on the intramolecular motions of its phenyl and tyrosine units, rendering it

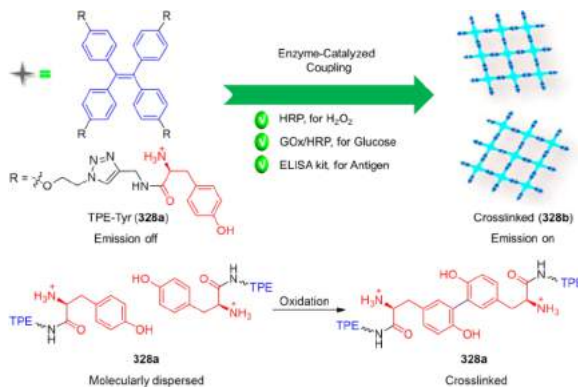


**Figure 68.** Schematic illustration of the fabrication of a fluorometric off-on multianalyte biosensor for  $\text{H}_2\text{O}_2$ , glucose, and specific antigens via enzyme-catalyzed coupling and crosslinking of L-tyrosine (Tyr)-functionalized TPE, TPE-Tyr (328a), and the corresponding AIE in aqueous media. Reprinted with permission from ref 389. Copyright 2014 American Chemical Society.

faintly or even non-emissive. The tyrosine units of nearby 328a molecules can undergo intermolecular cross-linking via phenol polymerization by using horseradish peroxidase (HRP) as a catalyst in the presence of  $\text{H}_2\text{O}_2$ . In this way, 328a can be polymerized into a large crosslinked network where the TPE units are connected by dityrosine linkages (328b). The cross-linked aggregates imposes strong constraints onto the TPE units as a result of the rigidity of the structure, thereby activating the RIM process and switching on the fluorescence of the TPE motifs. Making use of this  $\text{H}_2\text{O}_2$  responsive system, glucose can be detected by utilizing the enzymatic oxidation reaction between glucose and GOx to generate a source of  $\text{H}_2\text{O}_2$ . Indeed, when glucose is added into a solution of 328a with HRP and GOx, the fluorescence is immediately turned on. As GOx oxidizes glucose,  $\text{H}_2\text{O}_2$  is generated in situ which is further consumed by the HRP-catalyzed crosslinking polymerization forming 328b. A detection limit of  $\sim 10 \mu\text{M}$  for glucose has been achieved. This method also guarantees the satisfactory sensing selectivity in virtue of the enzymatic selectivity of GOx to glucose. No discernible emission is observed from the aqueous mixture of 328a and GOx/HRP, upon the addition of D-fructose, D-galactose, or D-mannose. Furthermore, HRP is commonly used in enzyme-linked immunosorbent assay (ELISA) and immuno-histochemistry. The 328a probe is also competent to be integrated into a commercial ELISA kit and act as an optional fluorogenic substrate for HRP, showing a superb detection sensitivity ( $\sim 2.0 \text{ ng mL}^{-1}$ ) to human carcinoembryonic antigen, a well-known biomarker for carcinoma (Figure 68).

Although the above-mentioned glucose sensing systems show good selectivity, they are indirect and cannot work without co-reagents such as enzymes and/or quencher. Delightedly, direct sensing of glucose species has been achieved by incorporating boronic acid functional group into AIEgens.<sup>390,28</sup> Phenylboronic acid is an alcohol-affinitive moiety that can reversibly react with diols in aqueous media and hence can be employed as synthetic receptors for carbohydrates.<sup>391–394</sup> For example, TPE is easily functionalized with two boronic acid groups generating 329 (Figure 69A).<sup>28</sup> The obtained TPE-diboronic acid adduct 329 is immiscible with neutral water and its suspended aggregates show bright blue emission (pH 4.34). However, when the pH of the buffer is raised to  $>8.61$ , the emission begins to decrease and becomes fairly weak at  $\text{pH} \geq 9.74$ . As the  $\text{pK}_a$  of the phenylboronic acid is  $\sim 9$ , the high pH of the buffer solution ionizes 329

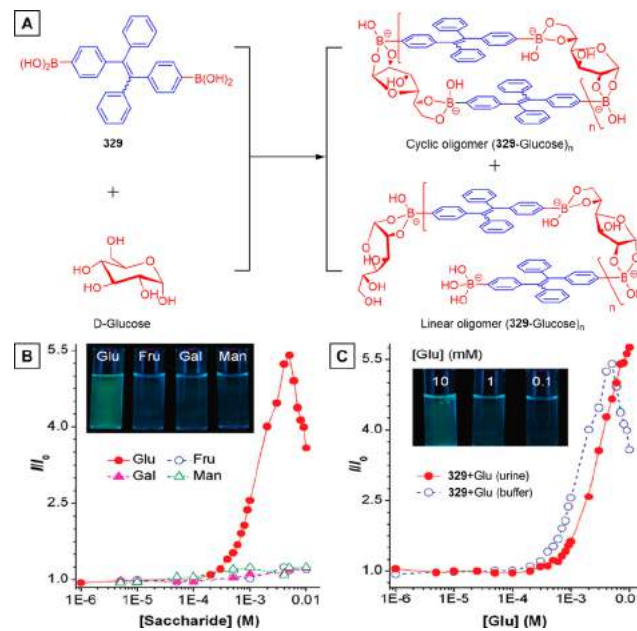


**Figure 69.** (A) Proposed mechanism for the process of glucose-specific sensing by the AIE probe 329. (B) The fluorescent responses of 329 ( $50 \mu\text{M}$ ) to different saccharides in a carbonate buffer containing 2 vol % DMSO (pH 10.5). Inset: Photographs of solutions of 329 in carbonate buffers containing 5 mM saccharide taken under UV illumination. (C) Variations in the fluorescence intensities ( $I$ ) of mixtures of 329 ( $50 \mu\text{M}$ ) with glucose in artificial urine (red line) and buffer (blue line).  $I_0$  is the intensity in the absence of saccharide. Inset: Photographs of mixtures of 329 ( $50 \mu\text{M}$ ) in the artificial urines containing different amounts of glucose taken under UV illumination. Reprinted from ref 28. Copyright 2011 American Chemical Society.

and makes it soluble. Under such circumstances, the emission of 329 is quenched by dynamic intramolecular motions of TPE fragments. Turn-on detection of glucose is achieved by adding glucose into a carbonate-buffered solution of 329 (pH 10.5). The *cis*-1,2-diol and *cis*-5,6-diol units of the glucose react with the boronate moieties of 329 affording either cyclic or linear oligomers (Figure 69A). The oligomer formation restricts the phenyl ring motions of the TPE units and thus switches on the emission. The emission intensity is boosted along with the concentration of glucose (Figure 69B). The oligomerization reaction is not solely specific to glucose; instead it can also take place with fructose, galactose, and mannose. However, the emission increments from these analogues are minimal when compared to the 5.4-fold increase caused by the addition of glucose. The selective emission enhancement is ascribed to the existence of a pair of *cis*-diol moieties at both the 1,2- and 5,6-positions of glucose which ensures the occurrence of oligomerization of 329 with glucose. In contrast, fructose, galactose, and mannose only possess a single *cis*-diol to react with 329. As a result, 329 is end-capped with two monosaccharide units which are no longer reactive to boronic acid. The intramolecular motions of TPE units in such small adducts are not sufficiently restricted and still able to efficiently dissipate the excited-state energy via non-radiative channels, hence resulting in the small emission enhancement. Therefore, it is evidently that the key structural feature of glucose (1,2- and 5,6-positioned *cis*-diol units) confers a glucose-specific response on 329. 329 is verified to be a promising biosensor for the specific detection of urinary glucose. As can be seen from Figure 69C, it shows good response to the glucose with increasing concentration.

Biological thiols such as cysteine (Cys) and GSH play vital roles in numerous biological and physiological processes such as homeostasis, detoxification, and protein function and so on. Biothiols are also decisive in maintaining the appropriate oxidation-reduction states of proteins, cells, and organisms. The abnormal levels of these biothiols are indicative of a number of diseases, such as liver damage, skin lesions, slow growth, neurodegenerative diseases, cancers, and acquired immunodeficiency syndrome (AIDS).<sup>395–399</sup> Homocysteine (Hcy), as another primary biothiol, is structurally similar to Cys but functions differently. A high level of Hcy in the blood ( $>15 \mu\text{M}$  in serum) is a significant risk factor for cardiovascular diseases and it is also linked to a wide range of diseases, including neuropsychiatric, fractures, renal dysfunction, and Alzheimer's disease, etc.<sup>400,401</sup> Selective and sensitive detection and discrimination of biothiols is thus of great significance. To this end, quite a few strategies have been established, including high-performance liquid chromatography,<sup>402</sup> gas chromatography-mass spectrometry,<sup>403</sup> capillary electrophoresis separations coupled with different detection methods, electrochemical assays,<sup>404</sup> and optical detection.<sup>405,406</sup> Amongst all these approaches, fluorescent assays are the most appealing one for inherent merits such as visual sensing and real-time *in situ* responses. By making use of thiol chemistry, a varied set of luminescent systems built from AIE molecules have been developed. As summarized in Figure 70 and Figure 71, the luminescence of these sensing

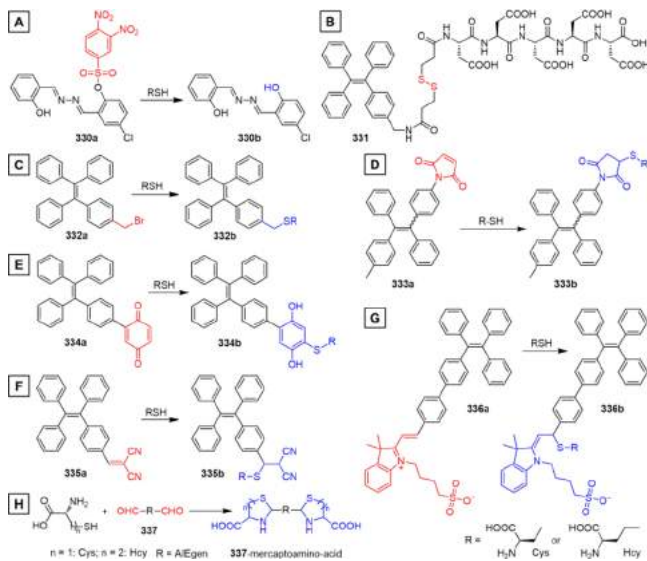


**Figure 70.** Summary of AIEgens that were used for thiol detection based on different mechanisms. The recognition moieties are highlighted in red.

systems can be controlled either by thiol-induced dissociations or via nucleophilic reactions. A variety of AIEgens has been designed for biothiol detection based on the cleavage of sulfonate or disulfide bond by thiols.<sup>407,408</sup> For example, Tong et al. have made use of the sulfonate cleavage to develop a novel AIEgen-based turn-on fluorescent probe, 2-(2',4'-dinitrobenzenesulfonyl)-5-chlorosalicylaldehydeazine (DNBS-CSA or 330a).<sup>407</sup> In this system, 5-chlorosalicylaldehyde azine (CSA or 330b) with ESIPT property serves as a signaling AIEgen, while 2,4-dinitrobenzenesulfonyl (DNBS) is incorporated both as a recognition moiety to thiols and an effective quencher of the AIEgen (Figure 70A). As implied by the PL measurement of 330b in the DMSO/10 mM phosphate buffer saline (PBS) mixture with different DMSO

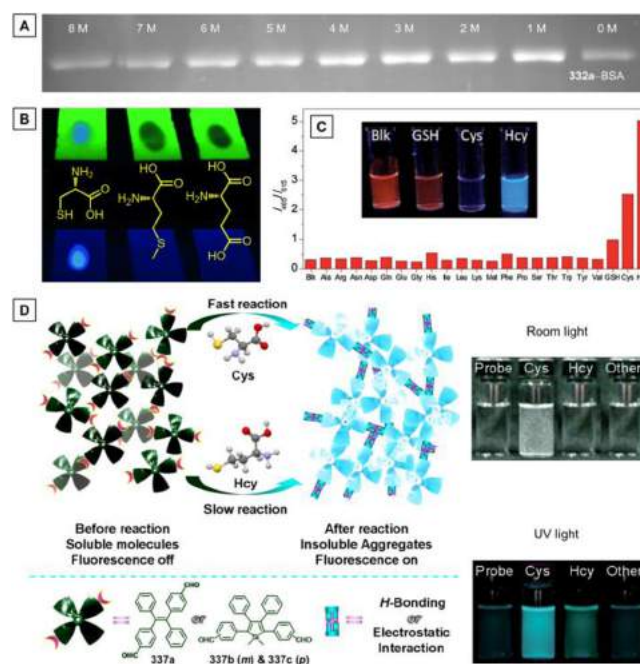


**Figure 71.** (A) SDS-PAGE fluorescence image of 332a labeled BSA in the presence of different concentrations of urea. Reprinted from ref 410. Copyright 2013 American Chemical Society. (B) Thiol-specific biomolecular probing by AIEgen 333a on a TLC plate through the thiol–ene click mechanism. Reprinted with permission from ref 411. Copyright 2010 Wiley-VCH Verlag GmbH & Co. KGaA. (C) Emission ratio  $I_{465}/I_{615}$  of 336a in the absence or presence of different amino acids or GSH in pH buffer. [336a] = 10  $\mu\text{M}$ ;  $\lambda_{\text{ex}} = 380 \text{ nm}$ . Inset: Photos of 10  $\mu\text{M}$  336a in blank buffer or 100 mM GSH, Cys, and Hcy (from left to right) under a handheld UV lamp. Reprinted with permission from ref 415. Copyright 2014 Royal Society of Chemistry. (D) Schematic illustration of discrimination of Cys and Hcy with dialdehyde-functionalized AIEgens such as TPE (337a) and siloles (337b and 337c). Insets: Photos of 25  $\mu\text{M}$  337b in blank buffer or 2.5 mM Cys, Hcy, and other amino acids (from left to right) taken under (upper) ambient light and (lower) UV light. Reprinted with permission from ref 416. Copyright 2013 Wiley-VCH Verlag GmbH & Co. KGaA.

fractions, 330b is non-fluorescent in DMSO because of the good solubility, and its emission is boosted up when the DMSO fraction is less than 70 vol % as a result of aggregation-activated RIM. However, 330a is nearly non-emissive in the detection medium (10 mM PBS buffer at pH 7.4 containing 30 vol % DMSO), which results from the quenching effect of the DNBS moiety. With a very low background, the fluorescence of the mixture is readily turned on by the addition of thiols, such as cysteine, glutathione, 3-mercaptopropionic acid, and 2-amino-benzenethiol, as the dinitrobenzenesulfonyl group is cleaved to release 330b (Figure 70A). As mentioned above, 330b should aggregate in the detection medium, resulting in strong yellow emission (558 nm). Furthermore, benefiting from the AIE effect, such thiol detection can be performed on test paper. As the detection is thiol-specific, no emission enhancement is observed with the addition of amino acids without thiol group(s).

Comprising a peptide with five carboxyl groups, TPE-peptide conjugate 331 is highly hydrophilic (Figure 70B).<sup>408</sup> Therefore, when 331 is applied as a thiol probe in aqueous solution, the background signal can be easily eliminated with a small amount of organic solvent. As the disulfide linkage is thiol-specific and cleavable, with the existence of thiol species such as GSH, 331 can be cleaved to arouse changes in water solubility, giving rise to

obvious fluorescence turn-on. GSH was selected as a representative thiol analyte to examine the capability of **331** as a thiol probe. Varying concentrations of GSH from 5 to 1000  $\mu\text{M}$  were added to solutions of **331** in DMSO/water (v/v = 1/199) and the fluorescence gradually increases owing to the cleavage of the disulfide bond and the resulting residue aggregation in the detection medium. The linear line obtained by plotting the fluorescence intensity at 465 nm against the GSH concentration suggests the potential of utilizing the probe for GSH quantification with a detection limit of 4.26  $\mu\text{M}$ . By attaching a targeting moiety onto the terminal of peptide chain, this system has been further adopted to realize targeted intracellular thiol imaging and monitor intracellular thiol levels in cancer cells.<sup>409</sup>

Alkyl halide groups that are thiol-reactive can be used to construct thiol probes. By incorporating the bromomethyl unit, the simple TPE derivative **332a** has been designed for thiol detection based on the nucleophilic reaction between the thiol group and the bromomethyl moiety (Figure 70C).<sup>410</sup> **332a** has been further employed as a fluorescent probe to specifically stain Cys-containing proteins in SDS-PAGE. **332a** is only weakly emissive even in the aggregate state due to the heavy atom effect of the bromide. With the addition of a thiol species such as dithiothreitol (DTT), the substitution reaction occurs, removing the bromide and yielding sulfoether **332b** (Figure 70C). Strong emission is restored as a result of the elimination of the internal heavy atom effect. Such a fluorescence turn-on response of **332a** to thiols makes it able to be used to label the proteins in SDS-PAGE with improved signal-to-noise ratio. When the samples of BSA, a thiol-containing protein, are subjected to labeling with increasing concentration of **332a** in the SDS-PAGE, the fluorescence intensity of labeled BSA is enhanced accordingly. Since the thiol groups often take the form of a disulfide linkage in proteins, urea was applied to denature the proteins to allow for effective labeling. The concentration of urea typically used for protein denaturation is 8 M. As exhibited in Figure 71A, BSA samples are all labelled successfully with **332a** when treated with varying concentrations of urea at 50 °C for 3 h with agitation prior to labeling. The very small difference lying in the fluorescence intensities of the lanes labelled in the presence of 8 and 0 M urea indicates that even without using any denaturants, BSA could be denatured by high-temperature pretreatment.

To enlarge the signal-to-noise ratio of a sensing system, one of the most effective ways is to minimize the background or noise. Among all the methods, quencher incorporation is a good way to reduce the noise, which has already been validated by the detection system based on **330a**. Moreover, besides ESIPT compounds (e.g., **330b**), other AIEgens can also be used for this purpose. Quenching moieties render the AIEgen non-emissive. If the quenchers on the AIEgens are reacted with the thiol groups, the emissions of AIEgens would be restored in the aggregate state.<sup>411,412</sup> For example, TPE was decorated with a maleimide (MI) group, creating a TPE-MI adduct **333a** which is almost non-luminescent either in solution or the aggregate state (Figure 70D).<sup>411</sup> The luminescence of **333a** is quenched by the MI group via the exciton annihilation process associated with the  $n-\pi$  conjugation between the carbonyl units and C=C groups. Thiol units react with the MI group through "thiol–ene" click reaction readily generating **333b** (Figure 70D), breaking the  $n-\pi$  electronic conjugation, and strong emission is thus rejuvenated. Because of the solid-state quenching and click reactivity, **333a** can be spotted onto TLC plates as solid strips for thiol detection (Figure 71B). The addition of thiol species triggers the **333b**

formation reaction and the fluorescence is accordingly switched on. The reaction is specific to thiol groups and no fluorescent response from the TLC plates can be observed after being treated with amino acids lacking thiol groups. Using this method, a detection limit of 1 ng/mL (~1 ppb) of cysteine could be detected even by the naked eyes. This light-up probe is thereby handy, specific, and sensitive. The **333a** nanoaggregates perform quite well as a fluorescent marker for mapping thiol distribution in living cells. With judicious design, **333a** has been further encapsulated into polymeric micelles to form redox-responsive nanoparticles.<sup>412</sup> The fluorescence of such nanoparticles is boosted by the increasing amount of GSH. These nanoparticles provide an evident contrast between the intracellular compartments and the extracellular matrix in cells and thereby promising for differentiation of cellular redox environment.

Similar to **333a** in design principle, **334a** has been developed by attaching the quenching moiety benzoquinone to a TPE unit (Figure 70E).<sup>413</sup> Photoinduced intramolecular charge-transfer from TPE segment to the benzoquinone moiety results in no observable luminescence even in the aggregate or solid state. Exploiting this property, thiol detection can be carried out with the suspension of **334a** in THF/water mixture (v/v = 5/95), where **334a** molecules form nanoaggregates but are still non-emissive. A thiol group reacts with the benzoquinone moiety to afford **334b** via a thiol–ene addition, transforming the benzoquinone into a hydroquinone unit and completely eliminating the effect of photoinduced intramolecular charge-transfer. Instantaneous biothiol detection can thus be achieved by this simple fluorescent probe (**334a**). Using Cys as a representative thiol analyte, the fluorescent response of **334a** to Cys is recorded by the fluorescence spectrometry. At a near stoichiometric point, the fluorescence emission is turned on with an abrupt increase in PL intensity from ~7 to ~200 (up to 29-fold enhancement). Analogous to **333a**, **334a** is also a highly sensitive thiol-specific probe, which can be used for strip-test (on TLC plates) with naked-eye observable response.

The above systems are based on thiol chemistry. Although they usually possess high selectivity for all thiol-based molecules, response to some specific thiol species remains a challenge. However, by integrating the sensitive nature of AIE process with smart experimental design, discriminative detection of thiol compound(s) has been made possible.<sup>414–417</sup> Selective GSH turn-on detection has been achieved by using a malononitrile-decorated TPE derivative **335a** as a probe (Figure 70F).<sup>414</sup> The detection is implemented based on thiol–ene click chemistry, therefore, all thiol compounds such as GSH, Cys, and Hcy, can react with **335a** to form thioether **335b** (Figure 70F). However, it has been observed that the thiol species greatly affect the solubility of resulting **335b** in the detection medium. By tuning the type of solvents and solvents ratio of the detection medium, it is possible to optimize the detection conditions and find a critical point where the emission can only be selectively turned on by GSH. In the water/ethanol mixture (v/v = 68/32), **335a** is very weakly emissive, indicating a molecularly dispersed state. As expected, no emission enhancement is observed upon the addition of Cys, Hcy, or other amino acids. But when GSH is added, strong emission at 520 nm is detected. The high selectivity of this GSH sensing system has been rationalized to originate from the poor solubility of the resulting GSH-probe adduct in this medium which causes aggregation formation and activates the RIM process to switch on the fluorescence. Since GSSG can be cleaved by the glutathione reductase and produces free GSH, the ensemble of **335a** and GSSG has thus been

employed as a label-free sensor for enzymatic activity assay of glutathione reductase.

Discrimination of Hcy, Cys, and GSH has been achieved by using a hemicyanine TPE-based dye **336a** (Figure 70G).<sup>415</sup> In an aqueous buffer solution with pH = 8, the probe **336a** shows a red emission peaked at 615 nm (Figure 71C). Upon the addition of Cys or Hcy, a ratiometric fluorescence change is clearly visible: when the concentration of Cys or Hcy is increased, the emission band at 615 nm begins to decrease and a new emission band at 465 nm rises. The blue emission can be attributed to the nucleophilic addition of the thiol species which yields **336b** and breaks the electronic conjugation between the indole moiety and the TPE-based core. As **336a** is destroyed through the reaction, its red emission band is gradually weakened and meanwhile the blue emission of **336b** emerges and holds a dominant position, making the ratio of the blue and red emission ( $I_{465}/I_{615}$ ) gradually go up. When GSH is added to the detection medium of **336a**, the red emission is slightly weakened. Nevertheless, when the same amount of Cys is introduced into the detection medium, the fluorescence is changed from red to weak blue. Under parallel conditions, Hcy arouses the most marked fluorescent response. Intense blue emission has been observed for the detection medium containing **336a** and Hcy (Figure 71C). The discriminative responses of **336a** to Hcy, Cys, and GSH are associated with two main factors: one is the reactivity difference of these thiols and the other is the solubility difference of their resultant adducts. It is believed that Hcy, Cys, and GSH all can react with **336a**; however, the reactivity decreases as the steric hindrance around the thiol group increases. In addition, upon reaction with biothiol, the positively charged nitrogen on probe **336a** is neutralized, which will increase the hydrophobicity of the resulting product. Since Hcy is the most hydrophobic among these three biothiols, the resultant adduct has the highest tendency to aggregate in the aqueous medium. As a result of RIM process, the blue emission of the adduct is switched on. The collective effect renders the **336a**-Hcy the most emissive.

Apart from the above-discussed sensing systems which are based on the reactions between the recognition groups and thiol groups, detection systems taking advantage of both the amino groups and thiol groups on the mercaptoamino acids have also been developed.<sup>416,417</sup> The well-known cyclization of the aldehyde group with amino and thiol groups forming thiazinane/thiazolidine is a classical reaction that has been widely used for Cys/Hcy detection. In pursuit of new sensing systems, a series of dialdehyde-functionalized AIEgens (**337**) have been designed and synthesized (Figure 70H and Figure 71D). The formation of thiazinane/thiazolidine through the chemical reaction of aldehydes on **337** and the amino and thiol groups of Cys/Hcy determines the selective recognition of Cys and Hcy over other amino acids and glucose (Figure 70H). More importantly, no matter the AIEgen here is TPE (**337a**) or silole (**337b** and **337c**) derivative, similar discriminatory detections of Cys over Hcy can be achieved. Take **337b** for example. **337b** is very weakly emissive ( $\lambda_{\text{em}} = 479 \text{ nm}$ ) in the mixture of DMSO/HEPES buffer (pH 7.4) with an optimized volume ratio as 6/4. Upon the addition of Cys, the emission peak is evidently blue-shifted to 424 nm as a result of the formation of a thiazoline derivative, and simultaneously, the fluorescence intensity is rapidly and dramatically intensified because of the lower solubility of the resulting adduct **337b**-Cys. Meanwhile, white solids precipitate from the detection medium within several minutes (Figure 71D). The intermolecular hydrogen-bonding between the carboxylic and thiazolidine groups accounts for the poor solubility. On the

other hand, **337b** shows similar response to Hcy, but in a much longer time scale (~3 days at room temperature). The discrimination between Cys and Hcy comes from the difference in reaction kinetics of **337** with Cys and Hcy, thereby the fluorescence responses show different time courses and intensity enhancements. It is worth noting that the response performance of these dialdehyde-substituted AIEgens (**337a**–**337c**) can be modulated by the molecular structures and the hydrophobicity. With *meta*-substituted aldehyde groups, **337b** shows better performance than its *para*-isomer **337c**, because the less conjugated *meta*-substituted aldehydes are more reactive than their *para*-counterparts. Whereas, dialdehyde-substituted TPE derivative (**337a**) outshines the other two probes (**337b** and **337c**) in performance with faster response, larger fluorescence enhancement, higher sensitivity, and better specificity and selectivity. This is attributed to the most hydrophobic and rigid molecular structure of **337a** among all these three dialdehyde-decorated AIEgens, which results in the poorest solubility of the resultant adducts and further triggers the most significant fluorescence turn-on effect.

With the beneficial AIE strategy, basic amino acids, such as arginine and lysine, can also be detected as well (Figure 72A).<sup>418</sup>

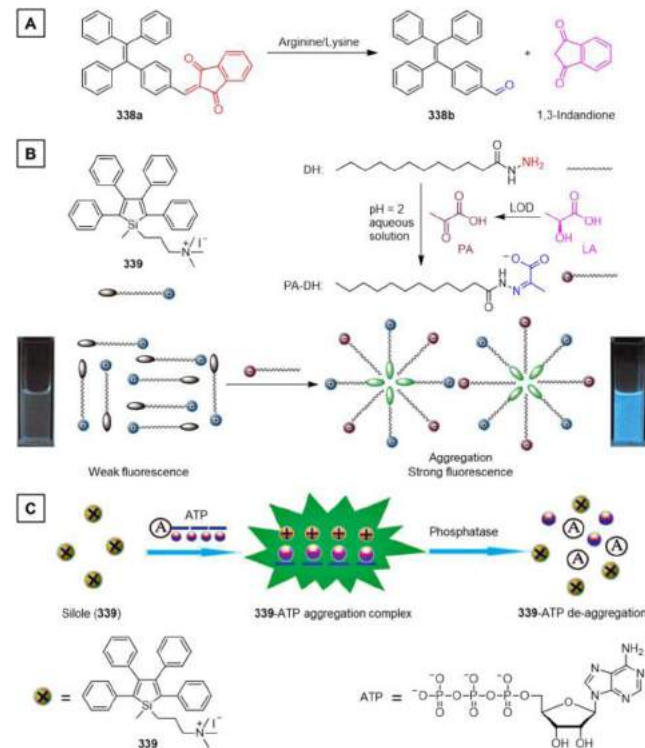


**Figure 72.** (A) Schematic illustration of the principle of the fluorescent response of **338a** to alkaline amino acids in THF/water mixture (3/7 in volume). (B) The design rationale for the fluorescence turn-on detection of LA by taking advantage of the AIE feature of **339**. Adapted from ref 419. Copyright 2012 American Chemical Society. (C) Continuous on-site label-free ATP fluorometric assay based on AIE effect of **339**. Insets: Fluorescent photos of the corresponding ensemble solution in the (left) absence and (right) presence of LA. Reprinted from ref 420. Copyright 2009 American Chemical Society.

1,3-indandione-functionalized TPE (**338a**) has been applied as a probe in virtue of the C=C double bond which has been activated by two adjacent carbonyl groups. The AIE activity and the D-A effect as well as the extended electronic conjugation

makes **338a** emit strong orange fluorescence peaked at 595 nm in the aggregate state. The activated olefin bond is susceptible to hydrolysis reaction in the presence of base under mild conditions. Arginine and lysine are alkaline amino acids among the 20 essential amino acids with isoelectric points of 10.76 and 9.74, respectively. In the light of this, it can be anticipated that **338a** would show some response to arginine and lysine. A mixture of THF/water ( $v/v = 3/7$ ) has been set as the detection medium. At this point, the molecules of **338a** begin to aggregate, leading to the decent emission and meanwhile the mutual-contact between the probe and analyte is still allowable for sufficient reaction. As expected, the fluorescent enhancement starts promptly upon the addition of arginine into the probe-containing detection medium. The fluorescence intensity displays a monotonous signal with the extension of reaction time. **338a** responds to lysine in a similar way. As depicted in Figure 72A, the  $\text{OH}^-$  released by the basic amino acids could attack the activated  $\text{C}=\text{C}$  double bond and cleave **338a** into **338b** and 1,3-indandione. Such a cleavage breaks the electronic conjugation between TPE and 1,3-indandione moieties, which further causes a color change both in out-appearance and fluorescence. Although the product **338b** is also an AIEgen, no emission was observed in the reaction mixture. The reason for this is that the better solubility of **338b** in the detection medium than **338a** prevents the RIR process from coming into play and hence gives rise to a turn-off fluorescent response. Such a work further demonstrates the flexibility of AIE strategy.

By means of simple design in the molecular structure of the AIEgen-based probes and/or experimental conditions, the performance as well as the response mode (e.g., turn-on/light-up, turn-off, ratiometric, etc.) can be easily modulated. L-Lactic acid (LA) is one of the most important metabolites in clinical areas and the food industry. The detection of LA is of great importance to clinical assay for the diagnosis of numerous diseases such as hypoxia, poor perfusion of tissue, acute circulatory shock, and liver failure and so on. As for food industry, the sensing of LA is crucial for that it is related to the freshness, stability, and storage quality of various food products. Considering these significances, Zhang and his coworkers have established a fluorescence turn-on assay for LA in aqueous solution by taking advantage of the cascade enzymatic and chemical reactions as well as the AIE feature of silole compound (**339**; Figure 72B).<sup>419</sup> **339** is a silole species decorated with a positively charged ammonium group which endows the probe with enhanced solubility in aqueous solution. **339** is thus very weakly fluorescent in the mixture of water/DMSO ( $v/v = 98/2$ ). As can be seen from Figure 72B, oxidation of LA catalyzed by lactate oxidase (LOD) generates pyruvic acid (PA) which is capable of reacting with dodecanoic hydrazine (DH) to yield the corresponding Schiff base (PA-DH). Such an amphiphilic PA-DH motif forms coaggregates with silole **339** via hydrophobic and electrostatic interactions in aqueous solution. Consequently, the fluorescence of silole **339** is switched on as a result of the activated AIE process. The relative fluorescence intensity ( $I/I_0$ ) of silole **339** at 480 nm in the detection system is plotted versus concentration of LA, which exhibits an almost linear increase in fluorescence increment with the concentration of lactic acid in the range of 0–40  $\mu\text{M}$  with the detection limit as low as 9.2  $\mu\text{M}$ . Thanks to the AIE effect, this fluorometric turn-on sensing of LA features the following superiorities: (1) the probe and reagents are simple and easy to gain; (2) the detection is performed under mild conditions; (3) the sensitivity is good and

no obvious interference from saccharides, amino acids, and ascorbic acids was observed.

Electrostatic interactions between AIEgens and analytes have also been exploited to realize fluorescence turn-on/light-up assays of other small biospecies such as adenosine triphosphate (ATP).<sup>420</sup> ATP has been acknowledged as “energy currency” in most animate beings for its pivotal roles in most enzymatic activities. The ATP concentration and its dissipative rate are believed to closely relevant to various diseases including ischemia, Parkinson’s disease, hypoxia, and hypoglycemia. Therefore, simple, sensitive and selective sensing systems for the real-time monitoring of ATP and its consumption are highly desirable. On the basis of its AIE attribute, positively charged silole **339** has been employed as such a superb probe for continuous on-site label-free ATP fluorometric assay that satisfies all the requirements (Figure 72C).<sup>420</sup> In buffer solution, **339** is proximately dissolved at a concentration of 60  $\mu\text{M}$ , it is thereby only weakly fluorescent due to its active intramolecular motions. Adding ATP, a highly negatively charged compound, to the aqueous buffer solution of **339** induces strong emission and significant enhancement as compared to the control sample without ATP. The ATP molecules form assemblies with the molecules of **339** via electrostatic interactions. Consequently, the formed **339**-ATP complex strongly restricts the intramolecular motions of the phenyl rings in the silole units and triggers the strong emission. A linear relationship between the relative fluorescence intensity and concentration of ATP has been obtained from 0 to 7  $\mu\text{M}$ . The detection limit of ATP by this protocol has been estimated to be approximately 69 nM. Furthermore, the fluorescence response is only specific to the addition of ATP; minimal change in emission is observed when **339** coexists with other phosphate-containing species like ADP, AMP, and pyrophosphate. It suggests that the electrostatic interactions and hydrophobic interactions are pretty essential to the aggregation of **339**. A well-studied enzyme, calf intestine alkaline phosphatase (CIAP), was utilized as the model to evaluate the application of **339** as a label-free probe for *in situ* and continuous monitoring of the enzymatic consumption of ATP. As shown in Figure 72C, the CIAP hydrolyzes the ATP, leading to the de-aggregation of the **339**-ATP complex. As a consequence, the silole molecules are released from the physical constraints, and the free dynamic intramolecular motions thereby promote the non-radiative decay pathways. Apart from silole systems, other positively-charged AIEgens, such as the guanidinium-tethered TPE, have also been used as light-up probes for the ATP assay. Similarly, this guanidinium-tethered TPE probe realizes the selective fluorometric turn-on detection of ATP through the self-assembly between the probe molecules and ATP moieties via electrostatic attractions, with nonlinear fluorescence response and high signal-to-noise ratio.<sup>421</sup>

A general approach towards fluorescent sensing has been established by Liu and Zhang et al. through the use of charge-generation polymers (CGPs) and subsequent triggered complexation with water-soluble AIEgens.<sup>422</sup> As elucidated in Figure 73, bearing carbamate-masked amine functional pendants, the CGPs in this work is able to undergo transition from the initially neutral state to a charged state when triggered by a specific analyte of interest. The charge-generation process of these amine-caged CGPs is integrated with the induced-aggregation of a TPE derivative carrying four anionic carboxyl groups (**340**), affording CGPs-based fluorescent probes with improved sensitivity and designing flexibility. In the presence of a triggering analyte, electrostatic complexation between **340** and the newly generated

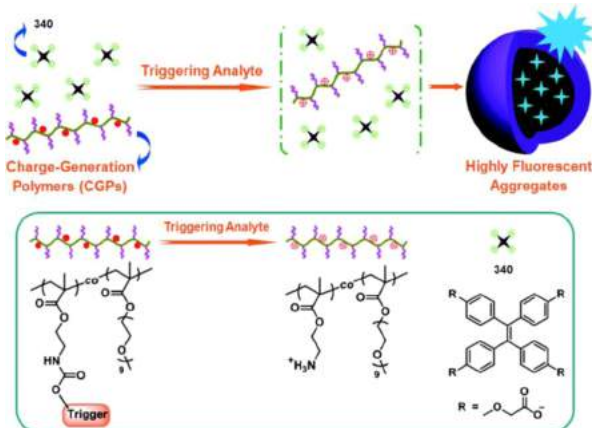


**Figure 73.** Schematic illustration of the general strategy to construct fluorogenic probes from CGPs and AIEgens through triggered complexation. Reprinted with permission from ref 422. Copyright 2012 Wiley-VCH Verlag GmbH & Co. KGaA.

cationic polyelectrolytes greatly restricts the phenyl ring motions of the TPE units and turns on the light emission. Thanks to the versatile design and facile preparation of analyte-triggerable CGPs, this conceptual approach is anticipated to offer a general strategy towards the construction of a wide range of fluorogenic probes with diverse functions. Biologically relevant species, i.e.,  $\text{H}_2\text{O}_2$  and thiols have served as proof-of-concept examples. For example, the addition of  $\text{H}_2\text{O}_2$  triggers the generation of the positively charged polymer via the deprotection of carbamate caging motifs and the detachment of 4,4,5,5-tetramethyl-1,3,2-dioxaborolane segments from the polymer chains. Electrostatic interactions between the positively charged polyelectrolyte and the negatively charged 340 elicit aggregate formation and switch on the fluorescence of 340. A detection limit of  $30 \mu\text{M}$  is achieved for  $\text{H}_2\text{O}_2$ . This system has been further applied to glucose detection by utilizing GOx to generate  $\text{H}_2\text{O}_2$ . Diverse other analyte-specific carbamate-based amine-caging motifs can be introduced into the CGP design for the fabrication of more elaborate sensing systems.

Through smart design in molecular structures and/or experimental conditions, other small biogenic molecules, such as biogenic amines,<sup>423</sup> dicarboxylate,<sup>424</sup> and NADPH,<sup>425</sup> have also been selectively detected via AIEgen-based probing systems in a turn-on manner. In view of the extraordinary performance of AIE luminogens/process in the sensing of small biospecies, it can be expected that they would flourish in the detection of other larger biogenic species.

**5.1.1.2. Natural Macromolecules.** As previously demonstrated, a highly successful strategy to employ AIEgens for luminescent sensing or detection is making use of electrostatic interactions which brings two species with opposite charges together and causes aggregation. Such a detection system is simple-to-construct, easy-to-operate, and flexible-to-modify. Moreover, in biological media, numerous biomolecules such as polysaccharides, DNA, and phospholipids exist in the form of charged species. This fact even makes the electrostatic attraction strategy more popular with sensing of biospecies. For instance, heparin is recognized as one of the most negatively charged biological molecules. As a highly sulfated polysaccharide, heparin plays an important part in the regulation of various physiological processes and inflammatory processes.<sup>426</sup> It has been extensively applied as an anticoagulant to prevent thrombosis during surgery or therapy.<sup>427</sup> Furthermore, overdose of heparin can cause some

side effects, and hence the detection and monitor the level of heparin are of great significance.<sup>428,429</sup> It is for this reason that there have been a large variety of cationic AIEgens developed and utilized as heparin sensors to date. Specifically, positively charged ammonium or pyridine groups have been incorporated into AIEgens for the design and establishment of small molecular<sup>430–432</sup> or polymeric<sup>433–437</sup> heparin probes.

Tong et al. fabricated a fluorescence turn-on probe on the basis of the AIE-active ESIPT compound 341 for facile, sensitive, and selective detection of heparin (Figure 74A).<sup>430</sup> The salicylalde-

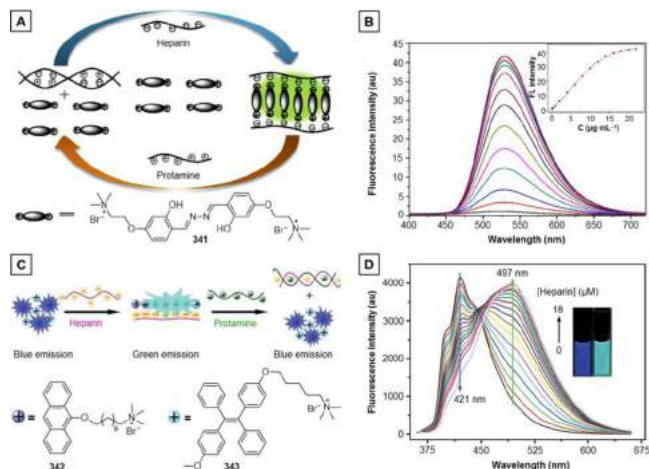


**Figure 74.** (A) Design principle of the fluorescence turn-on detection of heparin based on AIE characteristics of 341. (B) Fluorescence spectra of 341 ( $30 \mu\text{M}$ ) in  $10 \text{ mM}$  Tris–HCl buffer solution,  $\text{pH} = 7.0$ ) in the presence of different amounts of heparin (from 0 to  $22 \mu\text{g}/\text{mL}$ ),  $\lambda_{\text{ex}} = 391 \text{ nm}$ . Adapted with permission from ref 430. Copyright 2013 Elsevier B. V. (C) Illustration of the design rationale for the fluorescence ratiometric detection of heparin based on the combination of the ACQ feature of compound 342 and the AIE feature of 343, and the potential application to study the interaction between heparin and protamine. (D) The fluorescence spectra of the ensemble of 342 ( $12.0 \mu\text{M}$ ) and 343 ( $13.2 \mu\text{M}$ ) in HEPES buffer ( $5.0 \text{ mM}$ ,  $\text{pH} = 7.4$ ) solution after the addition of different amounts of heparin (from 0 to  $18.0 \mu\text{M}$ ). Inset: Fluorescent photos of the ensemble of 342 and 343 in HEPES buffer solution in the (left) absence and (right) presence of heparin ( $16.0 \mu\text{M}$ ) under UV ( $365 \text{ nm}$ ) illumination. Adapted with permission from ref 432. Copyright 2011 Royal Society of Chemistry.

hyde azine 341 is decorated with two positively charged tertiary amine groups which can bind to the negatively charged heparin via charge–charge interaction. The probe 341 in Tris–HCl buffer solution at  $\text{pH} 7.0$  is only very weakly emissive, whereas its emission grows rapidly at  $530 \text{ nm}$  with the addition of heparin (Figure 74B), resulting from the aggregation induced by electrostatic interaction. The electrostatic complexation between 341 and heparin activates the RIM process and thereby switches on the emission of 341. When the concentration of heparin reaches  $22 \mu\text{g mL}^{-1}$ , approximately 40-fold enhancement in fluorescence has been detected. With a good linear range from  $0.2$  to  $14 \mu\text{g mL}^{-1}$ , the system has a detection limit of  $57.6 \text{ ng mL}^{-1}$  and a response time as short as 2 min. The addition of highly cationic protamine competitively binds with heparin, and a decrease in emission is subsequently observed. As protamine disassembles the 341/heparin complex, the intramolecular motions of 341 are restored and the excitation energy becomes non-radiatively decayed, leading to fluorescence quenching.

To further enlarge the signal-to-noise ratio and improve the selectivity of AIE-based heparin detection, a ratiometric

fluorescence system was designed by coupling the ACQ nature of the anthracene derivative (**342**) with the AIE feature of the TPE derivative (**343**; Figure 74C).<sup>432</sup> A tertiary amine group was attached onto both **342** and **343** in order to enhance their solubility in an aqueous medium suitable for heparin detection and endow the probes with a strong affinity towards the heparin molecules. In HEPES buffer, **342** shows strong deep blue fluorescence peaked at 421 nm while **343** is minimally emissive because the molecules are well dissolved. Upon the addition of heparin, the dye molecules are drawn towards the negatively charged polymeric molecules by electrostatic attractions and forms heteroaggregates with heparin molecules, initiating two individual phenomena: the ACQ effect of **342** comes into play making the emission band at 421 nm decrease; in contrast, in the meantime, the AIE effect of **343** is activated by the aggregation and a new emission band at 497 nm appears and grows (Figure 74D). Accordingly, the fluorescence intensity ratio at 497 and 421 nm ( $I_{497}/I_{421}$ ) changes with the addition of heparin, which allows for the ratiometric fluorescent detection of heparin with a detection limit as low as 20 nM and a good linear range from 0 to 15  $\mu$ M. Such a method enables heparin to be discriminated from its analogues such as hyaluronic acid (HA) and dextran. The original blue emission could be restored by the addition of protamine which releases the molecules of both **342** and **343** from the heparin/dye complexes. The displacement allows the **342** molecules to become well separated in solution and regain its strong emission, while the active rotational motions of the phenyl rings in released **343** molecules open the non-radiative pathways to reduce the emission band at 497 nm.

As we all know, electrostatic attraction is neither directional nor specific, in principle, anionic species can interact with cations in any direction without saturation and vice versa. In view of this, for those simply designed probes which utilize electrostatic attraction as a working mechanism, high selectivity can hardly be counted on. To surmount this problem, our group has smartly developed an effective approach for selective and sensitive heparin detection.<sup>120</sup> We have briefly introduced the variant of TPE and fluorenyl, namely, **73**, in section 3.2, as a typical ACQ-to-AIE example created by replacing two phenyl rings of the TPE core with the *n*-bromoethyl substituted fluorenyl units. To gain the water solubility and make this AIEgen competent for heparin detection in aqueous media, **73** was transformed into **344** by quaternization. **344** is still weakly fluorescent in the buffer solution due to the slight aggregation caused by its bulky hydrophobic core. Its fluorescence emission is gradually intensified by the addition of heparin. Since such a cationic probe can respond to any molecule carrying negative charges, varying levels of emission enhancement have been observed upon the addition of heparin and its negatively charged analogues such as chondroitin sulfate (ChS) and HA.

In order to improve the selectivity and sensitivity, graphene oxide (GO) was integrated with this AIE-based probe **344**. There are two modes of operation to achieve this end: one is to add the GO into the buffer solution of the **344**/analyte complex (Figure 75A) and the other is to mix the GO with **344** first and then add the analyte. In the former mode, the added GO cannot disassemble the complex of **344** and heparin for the strong binding affinity of heparin to **344**. The strong emission from **344/heparin** can thereby be preserved. While for the analyte with lower charge density such as ChS and HA, GO dissociates the **344**/analyte complex, releases the probe, weakens the fluorescence and hence enhances the selectivity of the heparin detection. In this sense, GO acts as a “touchstone” which testifies

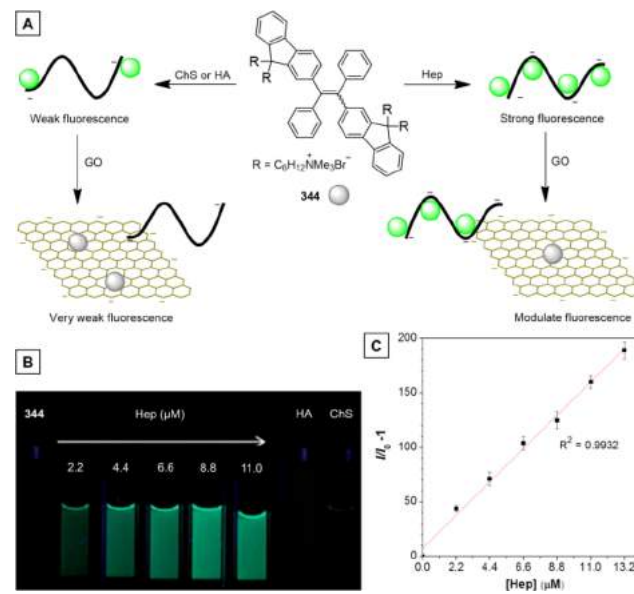


**Figure 75.** (A) Schematic illustration of heparin and its analogues detection with **344**/GO. (B) Fluorescence photos of **344**/GO in PBS buffer in the absence and presence of HA, ChS, or Hep taken under 365 nm UV illumination using a hand-held UV lamp. Concentration: 12  $\mu$ M (**344**), 11  $\mu$ M (HA and ChS), 2.2–11  $\mu$ M (Hep), 48 mg mL<sup>-1</sup> (GO). (C) Calibration curve for Hep quantitation, where  $I$  and  $I_0$  is the PL intensity of **344**/GO in the presence and absence of Hep, respectively. Concentration: 12  $\mu$ M (**344**); 48 mg mL<sup>-1</sup> (GO); excitation wavelength: 365 nm. Adapted with permission from ref 120. Copyright 2014 Royal Society of Chemistry.

the authenticity of the recognition. In the latter mode, GO is a fluorescence quencher to eliminate the background and enlarge the signal-to-background ratio. When GO is added into the buffer solution of **344**, it will tightly bind with the molecules of **344** via electrostatic interaction and possible  $\pi$ – $\pi$  interaction, resulting in greatly weakened fluorescence (Figure 75B). The mixture begins to fluoresce when heparin is added, because the heparin detaches the probe molecules from the surface of GO and forms electrostatic complex with them. The complexation activates the RIM process and switches on the green fluorescence. The addition of ChS and HA cannot “light up” the emission of probe, because their electrostatic attraction power is not strong enough to seize the **344** molecules from GO (Figure 75B). Visual discrimination of heparin from its analogues can be realized in these two modes. A linear response in the range of 0–13.2  $\mu$ M with a detection limit estimated to be as low as 10 nM has been achieved by this “light-up” probing system, as indicated by the plot of  $(I/I_0 - 1)$  versus the heparin concentration (Figure 75C). Such a detection range makes the **344**/GO ensemble a promising probe for heparin level monitoring during surgery and therapy (2–11  $\mu$ M).<sup>438</sup>

Together with proteins, nucleic acids including DNA and RNA are the most important biological macromolecules, essential for all known forms of life. They are found in abundance in all living things, where they function in encoding, transmitting, and expressing genetic information. The detection of nucleic acids is of great importance in genetic engineering, forensics, and bioinformatics in terms of its crucial roles in various physiological processes. In this regard, numerous efforts have been made towards applying AIE molecules/process as fluorescent techniques for DNA recognition,<sup>439–442</sup> labelling,<sup>443</sup> quantification,<sup>444</sup> visualization,<sup>29</sup> and monitoring of conformational

changes.<sup>445,446</sup> As demonstrated by the research done, AIE is a powerful tool and AIE-based probes have excelled the conventional fluorometric DNA probing systems in many respects. For example, fluorescently labelled DNA strands with the degree of labeling (DOL) up to the theoretic limit can be synthesized by enzymatically incorporating AIEgen-labeled nucleotide [*S*-(3-aminoallyl)-2'-deoxyuridine-5'-triphosphate; dUTP] via nick translation, random priming, or polymerase chain reaction (PCR).<sup>443</sup> Unlike the FITC-labeled DNA which encountered fluorescence quenching when the fraction of dye-dUTP is over 0.9, with the aid of AIE property, no self-quenching in fluorescence is observed for the AIEgen-labelled DNA strands even with a DOL 10 times higher than that was ever reported. Such highly fluorescent DNAs can be further used as probes for various bioassays such as gene detection.

A single-stranded DNA (ssDNA) with guanine (G)-rich repeat sequences can adopt a square-planar arrangement of the G units with the help of Hoogsteen hydrogen bonds. The face-to-face stacking of G-quartets can form a secondary four-stranded structure called G-quadruplex, which is further stabilized by the monovalent cations (e.g., K<sup>+</sup>) located in the centers of G tetrads.<sup>447–449</sup> It has been reported that G-quadruplex formation can affect gene expression and inhibit telomerase activity in cancer cells,<sup>450–452</sup> and hence probing of G-quadruplex structures is of vital importance to the quartet-specific medication design<sup>453</sup> and telomere-aimed anticancer therapy.<sup>454</sup> In particular, a series of studies have been carried out to examine how AIEgens could monitor/probe the formation of the DNA G-quadruplex.<sup>445,446,455</sup> Our group initiated this research project and has played a major role in this regard. TPE derivative **345** (Figure 76A) decorated with triethylammonium groups has shown strong affinity towards DNA as well as the ability to monitor the formation of the G-quadruplex.<sup>445</sup> Strong electrostatic interactions between cationic **345** and negatively charged G-rich DNA strand restrict the intramolecular motions of **345** blocking non-radiative decay channels and strong emission is turned on. Upon the formation of the G-quadruplex induced by the addition of K<sup>+</sup> into the **345**/DNA complex, the fluorescence intensity show negligible change while the emission maximum is red-shifted by 20 nm, resulting in a quadruplex-specific emission peak at 492 nm. Therefore, the AIE-based “label-free” probe distinguishes the G-quadruplex formed by d[G<sub>3</sub>(T<sub>2</sub>AG<sub>3</sub>)<sub>3</sub>] (i.e., HG21), a mimic of human telomeric DNA, from the random coil and duplex structures.

To elucidate the structural effects on the binding of the AIE molecules with the G-quadruplexes, a series of TPE derivatives with different lengths of side arms (**346**) and alkyl units of the ammonium groups (**347**), and different numbers of side arms (**348**) have been systematically designed.<sup>446</sup> These AIEgens are individually mixed with the congeners of HG21 with varying sequences. Although the oligonucleotides used in this study are all G-rich DNA strands, as demonstrated in Figure 76B, varying degrees of emission enhancements are observed for the mixture of **345** and G-quadruplex forming sequences such as pure guanine sequence dG<sub>12</sub> (PG12), a thrombin-binding aptamer d[G<sub>2</sub>T<sub>2</sub>G<sub>2</sub>TGTG<sub>2</sub>T<sub>2</sub>G<sub>2</sub>] (AP15), *oxytricha* telomeric repeat mimic d[G<sub>4</sub>(T<sub>4</sub>G<sub>4</sub>)<sub>3</sub>] (Ox28), and HG21. In the presence of K<sup>+</sup> ions and G-rich DNA strands, **345** shows the most remarkable light-up response to the G-quadruplex formed by HG21 with an approximately 20 nm red-shift in the emission maximum. Such a unique response allows for naked-eye differentiation of the quadruplex structure formed by the human telomeric sequence from the other quadruplex structures. **346** shows a larger

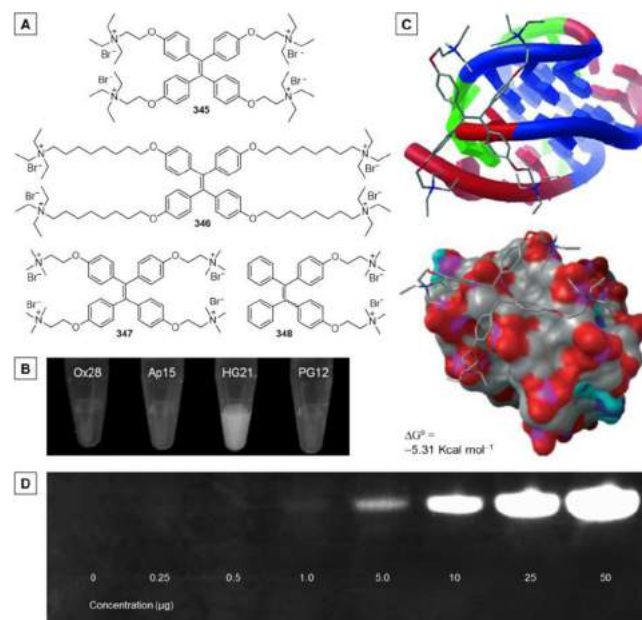


**Figure 76.** (A) Chemical structures of AIEgens (345–348) which were used for the purpose of elucidating the structural effects on the binding of the fluorogens with the G-quadruplexes. (B) Photographs of **345** solutions in the presence of different G-quadruplexes taken under UV illumination (365 nm). (C) Docking arrangement of **345** on human telomeric G-quadruplex folded by HG26 in the presence of K<sup>+</sup> (Protein data bank entry of the NMR-refined DNA structure: 2HY9). Adapted with permission from ref 446. Copyright 2010 Wiley-VCH Verlag GmbH & Co. KGaA. (D) Staining of oligonucleotides in PAGE by **345**. Concentration of dyes: 10 μM. Staining time: 30 min. Reprinted with permission from ref 29. Copyright 2013 Wiley-VCH Verlag GmbH & Co. KGaA.

emission enhancement towards ssDNA (i.e. HG21) than **345**. However, the fluorescence of the mixture of **346** and HG21 is greatly quenched upon the addition of K<sup>+</sup> ions, because **346** becomes better dissolved with the aid of K<sup>+</sup> ions and the dissociation of the **346**/HG21 complex gives rise to the fluorescence reduction. Similarly, **347** with less sterically shielded ammonium groups experiences stronger interactions with HG21 and exhibits a boosted emission when HG21 is added. Nevertheless, **347** becomes more soluble in the buffer solution after the formation of the G-quadruplex. The emission of the mixture of **347** and HG21 is also quenched in the presence of K<sup>+</sup> ions as the fluorogenic molecules become detached. **348** possessing only half the trimethylammonium groups of **347** undergoes much weaker electrostatic attraction with DNA sequences in both the single strand and G-quadruplex structure and hence can hardly show marked fluorescence response to these species.

In the pursuit of understanding two main issues: how the AIE molecule (e.g., **345**) binds to the quadruplex and how the binding interactions influence the photophysical behaviors of the AIEgen. Since the folding structure of the HG26/K<sup>+</sup> G-quadruplex in solution is not available, in terms of the similarity in their folding structures, the NMR-refined HG26/K<sup>+</sup> G-quadruplex structure was chosen as an alternative computational model for the docking simulation (Figure 76C). The **345** molecules dock on the surface of the folding structure of the DNA strands (G-quadruplex), with the aromatic core being stacked on the deoxyribose regions of DNA backbone via carbohydrate–π interactions. The side arms are located above

the grooves formed by phosphates and deoxyribooses, with the alkyl groups of the ammonium groups extruding into the valley between the neighboring phosphate ions. Such a docking structure clearly illustrates that the molecular conformations of **345** molecules are greatly rigidified and the intramolecular motions are hindered, hence rendering them highly emissive upon binding with HG21. In the meantime, to achieve an optimal binding configuration, in the **345**/HG21/K<sup>+</sup> system, the phenyl rings of **345** probably have been adjusted to smaller torsion angles which lead to stronger emission. The binding energy of **345** with HG21/K<sup>+</sup> quadruplex is calculated to be  $-5.31\text{ kcal/mol}$ , close to the experimental value ( $-6.2\text{ kcal/mol}$ ). In comparison, the docking energies of **345** on other G-quadruplexes are much smaller, suggestive of unfavorable docking.

Taking advantage of the strong affinity of these quaternized AIEgens to DNA which results in fluorescence turn-on, **345** and **347** have been used for detection and fluorescent staining of nucleic acid in aqueous solution and PAGE (Figure 76D).<sup>29</sup> The fluorescent visualization and quantitation can be achieved either by prestaining the DNA solution prior to casting or by poststaining the gel in a solution of the probe after electrophoresis, which allows for greater flexibility in the staining process. Because of the strong binding ability and the AIE nature of the probes, large signal-to-background ratio in the visualization is easily achieved: excess dye molecules which are weakly adsorbed onto the gel surface are easily removed (low background or noise) and strong emission enhancement occurs after binding to the DNA molecules (strong signal). In this way, even  $1\text{ }\mu\text{g}$  of DNA in electrophoretic gels can be visualized by AIEgen **345**. Moreover, the AIEgens have been proved cytocompatible without interfering with the viability of the living cells by the MTT assay.

Furthermore, encouraged by the “light-up” behavior to DNA and excellent biocompatibility of these AIEgens, **345** and **347** have been applied for cell imaging. However, they cannot permeate to the cell nucleus and thus have been developed as DNA counterstains for chromosome labeling in fixed cells.<sup>29</sup> The blue fluorescence of these AIE stains readily and selectively lights up the DNA-rich regions such as the chromosomes and the nuclei in the animal or plant cells. The cationic nature of the trimethylammonium groups is only weakly shielded by the methyl moieties which drives them to bind with the negatively charged chromosomal DNA via electrostatic forces and thus significant emission enhancement is observed due to the restriction of intramolecular motions of the AIEgens. Excellent photostability of **345** and **347** originating from their AIE characteristics endues them the ability to visualize the DNA under harsh conditions. Fast and easy visualization of cell mitotic process can be realized by **345**. As exhibited in Figure 77, at the interphase of cell mitosis, intact nuclei are captured and visualized by **345** with relatively strong blue light. When the cells enter their prophase, the nuclear membrane disintegrates and releases the chromosomes into the surrounding cytoplasm. The chromosomes align along the center plane in the metaphase and the molecules of agglomerate on the chromosomes, thereby rendering them even more emissive. The sister chromatids begin to migrate toward the opposite poles of the cells during anaphase, and as a result of looser aggregation, the fluorescence is less bright than that in the metaphase. At telophase, the chromosomes start to cluster together and the formation of a new nuclear membrane is hence facilitated. Since **345** and **347** can easily penetrate cells with compromised plasma membranes but will not cross the nuclear membrane of live cells, such features endow them with potential

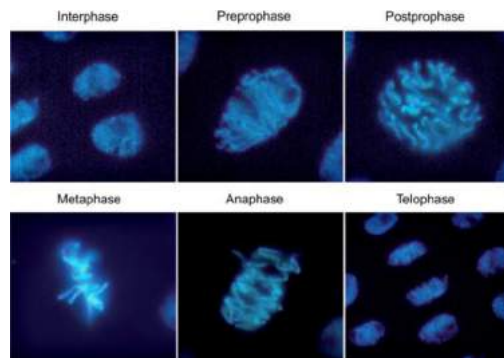


**Figure 77.** Fluorescence images of cells from onion root tips at different stages of the cell cycle stained by **347**.  $[347] = 50\text{ }\mu\text{M}$ . Reprinted with permission from ref 29. Copyright 2013 Wiley-VCH Verlag GmbH & Co. KGaA.

utilization for simple and quantitative one-step dead-cell indication or live/dead cell differentiation.

With the aim of developing fluorescent probes which are simple, universal, and highly sensitive for the detection of nucleic acids in gel matrixes, Yang and coworkers designed and synthesized the amino-functionalized TPE derivative **349** (Figure 78A).<sup>456</sup> This pair of amino arms on **349** are expected to induce strong hydrogen-bonding interactions between the probe molecules and the phosphate backbone of DNA strands or oligonucleotides and thus enable the turn-on detection of nucleic acids in both solution and gel matrixes. In particular, upon equal addition of nucleic acid, the fluorescence of the probe with a *cis* configuration (*Z*-isomer) experiences a larger emission enhancement (i.e. higher sensitivity) than that of the *trans* isomer (*E*-isomer). In aqueous solution, (*Z*)-**349** displays a 143-fold fluorescence enhancement when the concentration of oligonucleotides (30 nucleotides long) reaches  $0.5\text{ }\mu\text{M}$ , whereas the increment for *E*-**349** is 8-fold. This significant disparity has been attributed to the different binding affinities of these two isomers to the nucleic acids. The *cis* configuration binds to DNA with a higher affinity which results in greater intramolecular motion restriction. In contrast, the weaker binding in the *trans* isomer does not completely lock the intramolecular motions and hence cannot efficiently block the non-radiative decay channels, so a weaker enhancement is observed. For oligonucleotides with lengths of 20 and 30 nucleotides, (*Z*)-**349** has a detection limit of only  $10\text{ ng}$ . The limit of detection is even lower for double-stranded DNA (dsDNAs) which has more binding sites for the probe molecules. As estimated from the bands in polyacrylamide gels, ultralow detection limits of  $2.5\text{ ng}$  and even  $1.0\text{ ng}$  have been achieved for dsDNA with 35 base pairs and 75–300 base pairs, respectively, which are superior to the commonly used commercial fluorescent markers such as ethidium bromide (EB), making **349** promising for practical applications.

In addition to electrostatic and hydrogen-bonding interactions, with regard to the detection of nucleic acids, other means such as coordination interactions can also be employed as pathways to induce rigidification and/or aggregation of the probe molecules and switch on their luminescence during the detection course.<sup>440</sup> Despite this, the probes used are frequently built upon electrostatic interactions in view of the simplicity and universality. Similar to the sensing systems of heparin, AIEgens are embellished with quaternary ammonium groups and pyridinium units to enhance their solubility in aqueous media and meanwhile to gain positive charges which could bind to DNA species

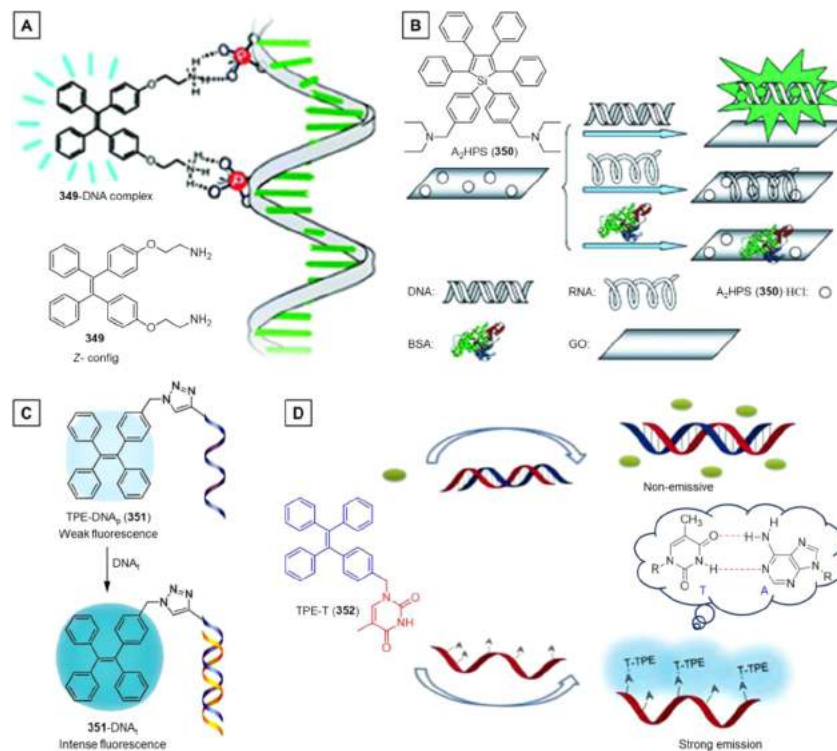


**Figure 78.** (A) Highly sensitive nucleic acid stain based on amino-modified TPE (349). Reprinted with permission from ref 456. Copyright 2014 Royal Society of Chemistry. (B) Strategy for dramatically enhancing the selectivity of AIEgen (350-HCl) towards biomacromolecules with the aid of GO. Reprinted with permission from ref 459. Copyright 2012 Wiley-VCH Verlag GmbH & Co. KGaA. (C) Schematic illustration of the application of TPE-DNA conjugate 351 in nucleic acid hybridization detection. DNA<sub>p</sub> and DNA<sub>t</sub> stand for the DNA probe and the target complementary DNA, respectively. Adapted with permission from ref 461. Copyright 2013 Royal Society of Chemistry. (D) Detection of adenine-rich single stranded DNA based on thymine-substituted TPE (TPE-T or 352) with AIE characteristics. Adapted with permission from ref 462. Copyright 2014 Royal Society of Chemistry.

and activate the AIE process through electrostatic interactions.<sup>439,441,442,444–446,455–459</sup> As mentioned in the discussion of the heparin assay, without special design either in the probe structure or experimental conditions, the sensing systems built on electrostatic strategy can hardly possess good selectivity. In order to improve the selectivity and sensitivity of the electrostatic complexation-induced fluorescence turn-on/light-up detection of DNA, GO has been intelligently incorporated into the detection system.<sup>458,459</sup>

For example, by simply modifying the molecular structure of HPS, its diethylaminomethyl-functionalized derivative A<sub>2</sub>HPS (350; Figure 78B) has been yielded and further protonated into ammonium salts (350-HCl) in the acidic aqueous media.<sup>459,460</sup> Cationic 350-HCl is soluble in aqueous buffer and its fluorescence can be lit up by negatively charged species such as DNA, RNA, and proteins without selectivity. However, with the aid of GO, the situation has been turned around.<sup>459</sup> Prior to detection, 350-HCl was mixed with GO in aqueous solution, and the dye molecules could be absorbed on GO via electrostatic as well as possible  $\pi$ - $\pi$  interactions, leading to a non-emissive state. As shown in Figure 78B, discriminatory detection of a specific analyte can be realized because the stable 350-HCl/GO complex functions as an “inspector” to check the binding affinity of the analyte to 350-HCl. The molecules of 350-HCl will strongly interact with the analyte that can displace the probe from GO surface. The oppositely charged probe and analyte will form electrostatic complexes with intense green luminescence as a result of the exemption from GO quenching and the activated RIM process. On the other hand, if the added analyte is not

powerful enough to dissociate the 350-HCl/GO complex, even though there is aggregation, no significant “turn-on” response would be a result, probably due to the quenching effect imposed by GO. Upon the addition of calf thymus DNA (ctDNA), the fluorescence was observed to proportionally increase with the increasing concentration of ctDNA. An 80-fold enhancement in fluorescence intensity has been recorded when the concentration of ctDNA reached 200  $\mu\text{g mL}^{-1}$ . A linear correlation between the emission enhancement ( $I/I_0 - 1$ ) and concentration of ctDNA was observed in the range of 0–80  $\mu\text{g mL}^{-1}$ , which is suitable for the quantification of ctDNA. Minimal or negligible fluorescence enhancement was observed when various other analytes such as RNA, proteins, or enzymes were added to the mixture of 350-HCl/GO. The complex of 350-HCl and GO is also able to sensitively and selectively detect ctDNA even in the presence of other biomacromolecules. The improvement in selectivity also benefits the sensitivity and endows the methodology with a detection limit as low as 2.3  $\mu\text{g mL}^{-1}$  towards ctDNA, indicative of the effectiveness of such a GO strategy.

Specific nucleic acid detection has also been achieved by labeling an AIEgen with a single-stranded oligonucleotide.<sup>461</sup> In this manner, this AIEgen-DNA bioconjugate shows specific response to the complementary DNA in solution via the hybridization reaction, considering that the nucleic acid hybridization is one of the most specific biochemical reactions taking place at the molecular level with high fidelity and efficiency. Through a simple “click” reaction, TPE was conjugated to a specific oligonucleotide sequence to afford the probe TPE-DNA<sub>p</sub> (351; Figure 78C). In 351, the TPE unit functions to modulate off/on

fluorescence upon analyte binding, and the oligonucleotide sequence endows the probe with water-solubility and also serves as a recognition moiety to specifically hybridize with its complementary strand. **351** is only very weakly fluorescent in DMSO/water ( $v/v = 1/199$ ) mixture, but the addition of the complementary sequence, the targeted DNA ( $DNA_t$ ) sequence, arouses the bright fluorescence, exhibiting a fluorescence turn-on effect. Interestingly, if the DNA sequence had one or two mismatch base(s), the emission enhancement are much lower than that of the perfectly matched **351**- $DNA_t$ . The addition of a completely random DNA sequence only induces minimal emission enhancement, suggesting the high selectivity/specificity of this probe (**351**). Furthermore, a detection limit of  $0.3 \mu\text{M}$   $DNA_t$  has been obtained with a probe-to- $DNA_t$  ratio of 10 to 1. This light-up DNA probe features quite a few advantages: it is simple to synthesize, low in cost, selective, readily available to a wide range of oligonucleotide sequences, and showing high fidelity in target recognition.

It can be learnt from the above example that by means of judicious design in the molecular structure of AIEgens, fluorescence “turn-on” probes for a particular ssDNA can be constructed with ease. More specifically, by simply decorating TPE with a thymine motif, TPE-T (**352**; Figure 78D) have been created as a DNA probe which can be used for the probing of adenine-rich ssDNA.<sup>462</sup> The selectivity and specificity of this probe (**352**) comes from the complementation between the thymine and adenine base pairs. TPE-T (**352**) molecules bind to adenine-rich DNA sequences mainly via duplex hydrogen-bonding interactions. Probe **352** is an AIEgen with an  $f_w$  threshold of 68 vol %, above which the aggregation occurs and the fluorescence is turned on. Accordingly, the ethanol/water mixture with  $f_w = 64$  vol % has been set as the detection medium, where the fluorescence of **352** is triggered by the addition of adenine-rich ssDNA. The light-up fluorescence results from the RIM process induced by the formation of hydrogen bonds between **352** molecules and adenine units in the ssDNA. In sharp contrast, dsDNA (calf thymus DNA) cannot switch on the fluorescence in the detection medium owing to the lack of available hydrogen-binding sites. As revealed by the fluorescent titration experiment, **352** is so sensitive that the adenine-rich ssDNA (AA) with a concentration as low as 100 nM can even be detected with observable fluorescent signal. A linear fluorescent response to the concentration in the range of  $1.3\text{--}1.9 \mu\text{M}$  has been exhibited by the plot of relative fluorescence ( $I/I_0$ ) at 450 nm against the concentration of AA. Moreover, nearly no change in the fluorescence of **352** is observed when the ssDNA without adenine is added, even at a very high concentration, which demonstrates the superb specificity of **352** to adenine-containing ssDNA. It can be envisaged that replacing the thymine moiety in **352** with other nucleobases such as adenine (A), guanine (G), and cytosine (C) will generate various new probes which are sensitive and selective to their corresponding complementary bases.

Proteins are large biological molecules, or biomacromolecules, comprised of one or more amino acid residues. Proteins function in a vast array of biological or physiological processes occurring in living organisms, including catalyzing metabolic reactions (enzyme), replicating DNA, responding to stimuli, and transporting molecules. The sequence of amino acids of a protein primarily distinguishes it from one another and usually results in folding of the protein into a specific three-dimensional structure that determines the activity of this protein. Most proteins fold into unique 3D structures and the shape into which a protein

naturally folds is called the native conformation. The conformation change of a protein is closely relevant to its activity and some physiological events, and the monitoring of conformational transitions of proteins is thereby of great significance to research regarding proteomics and pharmaceuticals, etc. Specifically, protein folding and unfolding are pretty important to its secretion, membrane-bound, and cellular functions.<sup>463–467</sup> Study of conformation transitions of proteins is an interesting and important topic because it can provide mechanistic insights into the folding and unfolding processes of biopolymers. Despite that intermediate states have been suspected to be involved in the unfolding and refolding processes, they can hardly be detected due to the complexity of these processes as well as lack of appropriate probes. AIEgens are usually sensitive to the vibration in microenvironments, so that even subtle changes could induce appreciable response in their luminescence, making them perfect choices for the conformational transition monitoring. In light of this, water-soluble AIEgens such as TPE derivative **353** and DSA derivative **354** have been utilized to visualize and monitor the protein unfolding process in the presence of a denaturant (Figure 79A).<sup>468–470</sup>

The general mechanism proposed for the fluorescent probing of the guanidine hydrochloride (GndHCl)-induced protein unfolding process has been demonstrated in Figure 79A. Originally, the ionized AIEgens **353** and **354** are virtually non-emissive in buffer solutions where they are well dissolved. The addition of protein like human serum albumin (HSA) or erythropoietin (EPO) triggers the fluorescence of **353** or **354**. The AIEgens are trapped in the hydrophobic cavities of proteins in their native folded structure, which restricts the intramolecular motions of the AIE molecules and strong emission is thus observed. GndHCl is a commonly used bulky ionic cosolvent for protein research, which can weaken hydrophobic interaction and interfere with association of charged solutes. With the addition of different amounts of GndHCl, a three-step unfolding process with the protein conformation transforming from native folding structure to random coil state can easily be observed with the aid of AIEgen **353** or **354**.

Take the system of **354** and EPO for example. As depicted in Figure 79A,B, with the concentration of added GndHCl in the range of 0–1.0 M, the first transition (Step 1) appears and the fluorescence intensity drops sharply to  $2/3$  of the initial state.<sup>469</sup> The sharp dropping in the fluorescence intensity suggests that the tertiary structures are rearranged, the domains are separated, and the interdomain hydrophobic pockets are opened, freeing a large portion of the molecules of **354** into the aqueous medium. The second transition (Step 2) emerges in the GndHCl concentration range of 1.0–1.8 M. The emission intensity keeps practically invariant. During this course, as indicated by the circular dichroism (CD) results, parts of the secondary structures of the protein have been damaged. However, this intermediate state may offer more hydrophobic sites for the dye molecules to be captured. The interdomain contacts might become looser after domain separation, which facilitates the entering of dye molecules into the buried hydrophobic patches. The intramolecular motions of the AIEgens are greatly hindered by this kind of encapsulation, and this is the reason for why the intensity stays unchanged in Step 2. Afterwards, the fluorescence intensity decrease monotonously along with the addition of GndHCl (Step 3) and the emission gets completely quenched when the GndHCl concentration exceeds 4.0 M. In this stage, the hydrophobic pockets in the protein are completely destroyed and the secondary structures as well as the strand helicity are all

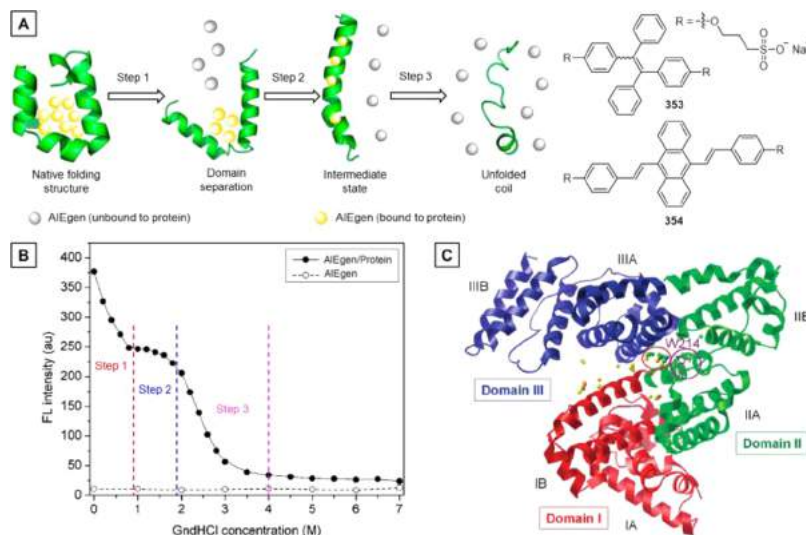


**Figure 79.** (A) Design and application of AIEgens for visualization and monitoring of conformation transitions of proteins. (B) Change of the fluorescent intensity of 354 at 522 nm with different concentrations of GndHCl in the presence or absence of erythropoietin (EPO). [354] = 0.4  $\mu$ M; [EPO] = 0.85  $\mu$ M;  $\lambda_{\text{ex}} = 404$  nm. Adapted from ref 469. Copyright 2013 American Chemical Society. (C) Summary of the 50 conformations of 353 docked on human serum albumin (HSA), whose domains are denoted by different colors, with red, green, and blue for domains I, II, and III, respectively. Each of the docked conformation of 353 is represented by a sphere placed at the average position of the coordinates of all the atoms in that conformation. The tryptophan residue in domain II (W214) is marked by a purple circle. 353 shows a high preference (22 out of 50) to the hydrophobic cavity (circled by red color) adjacent to the W214 residue. Adapted from ref 468. Copyright 2010 American Chemical Society.

lost. The molecules of 354 are completely released into the aqueous solution, making the fluorescence faint. Figure 79B shows the typical changes in the emission intensity of 354 with the addition of GndHCl in the presence or absence of the EPO.<sup>469</sup> It can be seen that the three different stages of the protein unfolding schematically illustrated in Figure 79A can be clearly identified by the changes in fluorescence intensity. Indeed, similar unfolding processes have also been observed in other protein systems such as HSA with AIEgens like 353.<sup>468</sup>

Furthermore, to gain deeper insights into the binding mode as well as better understandings on the favorable interactions between the AIE probe and protein, computational modeling has been conducted for each probe-protein pair. Taking 353 and HSA for example, the computational simulations exhibited in Figure 79C reveal that the hydrophobic pocket which is surrounded by subdomains IIIA, IB, and IIA and adjacent to a tryptophan residue (W214) is a favorable location for the AIE probe to bind to.<sup>468</sup> Out of the 50 calculated docked conformations of 353 on HSA, there are 22 conformations located in this cavity, indicating a high probability of occurrence of AIE molecules in this structural region. Careful examination on the simulated structures offers more details. It has been found that the 353 molecule inserts into the interdomain cleft formed by the  $\alpha$ -helices from subdomains IIA (green helix) and IIIA (blue helix). The TPE core of 353 docks on the  $\alpha$ -helix through hydrophobic interaction while the peripheral sulfonate arms interact with the polar patches inside the pocket of the HSA folding structure, which suggests that the hydrophobic interaction is the main driving force for the binding of AIEgen to protein.

In addition to the visualization and monitoring of the conformation change of a single protein during folding, unfolding (denaturation), and refolding, AIEgens have been reported to be able to sense the protein aggregation such as protein fibrillation.<sup>30,471,472</sup> An excessive accumulation of the amyloid fibrils which are insoluble protein aggregates in organs and tissues can give rise to biological dysfunctions and bring about

pathologic symptoms.<sup>473–477</sup> Amyloid fibrils have been acknowledged as the hallmarks of a great variety of well-known diseases or disorders such as Alzheimer's disease, type II diabetes, Parkinson's and Huntington's disease, spongiform encephalopathy, cardiac arrhythmias, atherosclerosis, polyneuropathy, and others.<sup>478–481</sup> Undoubtedly, sensitive probing of protein aggregates and the monitoring of amyloid fibrillation kinetics have great diagnostic implications and are of therapeutic value. Insulin is an excellent model for protein amyloidogenesis, in terms of its capability to readily undergo the fibrillogenesis process.<sup>482</sup> The understanding of insulin aggregation is of great importance to amyloidogenesis modeling and to the improvement of delivery systems for diabetes treatment. The AIE effect is an ideal tool with regard to the study of protein fibrillogenesis, considering both of them are associated with the aggregation process. A water-miscible AIEgen can function as a superb probe for amyloid detection and monitoring for the following reasons: (i) minimal background can be guaranteed by the non-emissive solution state of AIEgen, (ii) the aromatic core may promote its docking on the hydrophobic surface of insulin aggregates, thereby triggering the RIM process and turning on its luminescence, and (iii) its luminescence intensity can be boosted to varying extents in different phases or stages of amyloid fibrillation process, hence enabling the evaluation of amyloidogenesis dynamics.

Encouraged by its good water miscibility as well as outstanding performance in the monitoring of conformational transitions of protein, sulfonated TPE derivative 353 has been chosen as a model compound to explore the potential applications of AIEgens for amyloidogenesis study.<sup>30</sup> As can be seen from Figure 80A, 353 stays almost non-luminescent in a PBS buffer solution ( $\text{pH} = 7$ ) after the addition of native insulin. In contrast, when a small amount of fibrillar insulin is added into the buffer solution of 353, the fluorescence is immediately turned on. The solutions of 353 in the presence of native and fibrillar forms of insulin are undistinguishable under ambient lighting as they are both colorless and transparent. With UV illumination, these

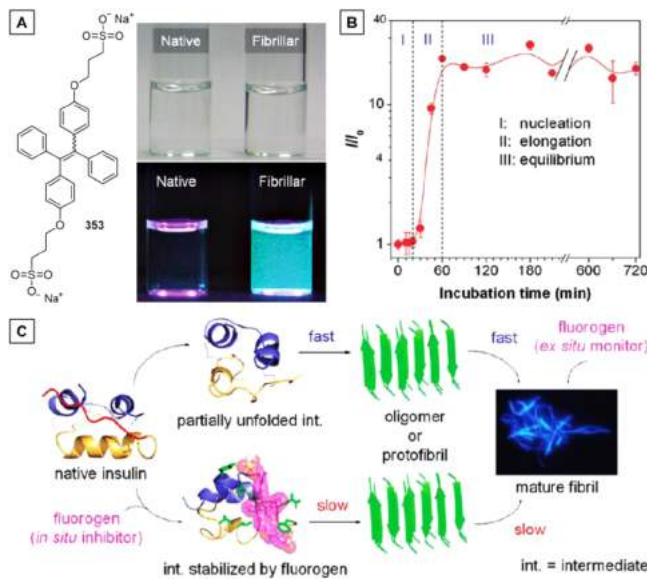


**Figure 80.** (A) Photographs of mixtures of 353 with native and fibrillar forms of insulin taken under (upper panel) normal lighting and (lower panel) illumination with a UV light of 365 nm. (B) Insulin fibrillogenesis process monitored by 353 bioprobe. PL measurements were performed in a pH 7 buffer at  $[353] = 5 \mu\text{M}$ ,  $[\text{insulin}] = 5 \mu\text{M}$ , and  $\lambda_{\text{ex}} = 350 \text{ nm}$ . (C) Proposed mechanistic diagrams for the dual functions of 353 as ex-situ monitor and in-situ inhibitor in the process of insulin amyloidogenesis. Adapted from ref 30. Copyright 2012 American Chemical Society.

two forms of insulin can easily discriminate, for the mixture containing fibrillar insulin fluoresces with a strong green light, whereas the one with native insulin emits almost no light. The distinct emission behaviors of 353 in the presence of the native and fibrillar forms of insulin can be explained by the fact that insulin in its native form has an isoelectric point of pH 5.6, which renders the insulin negatively charged in the buffer solution of pH 7. The electrostatic repulsion between insulin and the sulfonated probe hampers the binding of 353 to insulin, leading to the minimal emission change. The insulin fibrils are comprised of extended  $\beta$ -strand structures which are assembled via hydrophobic interactions. Containing multiple phenyl rings, 353 can dock on the surface of the  $\beta$ -strand structure through hydrophobic interaction, resulting in the restriction of the intramolecular motions and ultimately causing the probe to luminesce.

Inspired by the difference lying in the responses of 353 to native and fibrillar forms of insulin, 353 has been further utilized to monitor the kinetic process of amyloid fibrosis (Figure 80B). Three separate phases can be observed when the probe is added to insulin samples after being allowed to fibrillate. Three distinct steps are involved in the insulin amyloidogenesis process: (i) the initial phase ( $<20 \text{ min}$ ) experiences minimal fluorescence enhancement as nucleation occurs, (ii) emission appears and a large increase in fluorescence intensity is then observed as of the fibrils elongate, and (iii) finally the amyloidogenesis process reaches the final equilibrium stage as indicated by the tiny change of the already strongly fluorescent mixture. Insulin in its native form does not inhibit the intramolecular motions of 353. When fibrils begin to form, interactions between the protofibrils and the probe can restrict the aforesaid motions to induce fluorescence by blocking the non-radiative channels. On the basis of these results, 353 has been proven to be an excellent ex-situ

bioprobe for insulin fibrils detection and amyloidogenesis kinetics monitoring.

More intriguingly, when 353 is applied as an in-situ probe, a significant delay in the nucleation phase is observed. Moreover, the presence of 353 in situ also decelerated the growth rate in the elongation phase, and thereby the overall fibrillogenesis is greatly slowed down. The incubation period of fibrillogenesis is lengthened with the increase in the concentration of 353 in the mixture. When the dose of 353 comes to  $500 \mu\text{M}$ , the insulin fibrillogenesis is totally suppressed, for no obvious fluorescent change is observed even after 1 week's incubation. An indispensable step in the process of insulin fibrillation is the partial unfolding of native protein. It can be speculated that 353 might bind to such a partially unfolded insulin structure, prolonged the nucleation step, and slowed down the fibril formation. The *in-situ* inhibition of the nucleation process and deceleration of the fibril formation was further studied to examine its underlying mechanism via MD simulations and docking calculations (Figure 80C). A total of 100 000 docking poses were calculated by varying the docking conformation of the probe as well as protein structures to analyze the inhibition. The calculations reveal that 353 binds more preferably to the partially unfolded insulin as compared to the native insulin. Close inspection of the docking conformations with the lowest energies declares that hydrophobic interactions between the phenyl rings of 353 and hydrophobic residues of insulin including leucine, valine, phenylalanine, and tyrosine stabilizes the 353-insulin conjugate. The B-chain helix (B11–B19) of insulin is partially unfolded under fibril-forming conditions, encouraging the binding of 353. Since this B-chain is involved in the nucleation phase of protein fibrillogenesis, the binding of 353 to this segment thereby may hinder the nucleus formation and inhibits the further assembly into fibrillar aggregates (Figure 80C). Considering that 353 does not bind to the native insulin, it may not interfere with the biological functions of the protein. As an *ex-situ* fluorescent probe for the monitoring of the protein fibrillation process, 353 is free from self-quenching and resistant to photobleaching, while as an anti-amyloid *in-situ* inhibitor, it possesses a high suppression efficiency. 353 and other analogous AIEgens are thus promising candidates as new diagnostic reagents and therapeutic drugs for monitoring and treatment of the diseases relevant to conformational disorders of proteins.

In the previously discussed examples, based on the state (aggregation)-dependent fluorescence, AIEgens can be employed as a convenient tool for the sensing of biomolecular species, in which they aggregate via interactions, resulting in the display of intense luminescence. For protein detection, the interactive forces between the luminogens and biomolecules are mainly electrostatic and hydrophobic interactions in nature, which are unspecific and lead to a relatively limited selectivity of the probing systems. AIE strategy for biosensing has already been superior in many respects to those working in a conventional fashion. However, to be an advanced fluorescence turn-on detection tool suited for real-sample assay, a modification in probe design and/or sensing conditions is required to further promote the selectivity and sensitivity to analytes. By taking advantage of some naturally occurring but specific binding processes, a large array of selective protein probing systems have been cleverly developed. Amongst these processes, the notable carbohydrate–protein binding has drawn extensive attention for the carbohydrate–protein interactions mediate a wide variety of biological events, such as cell recognition and differentiation (host–pathogen recognition), cell adhesion and growth, signal transduction between cells, cancer metastasis, inflammation, and

viral or bacterial infections.<sup>483–486</sup> The specificity and affinity of these carbohydrate–protein interactions rest strongly with multivalency (multiple binding), owing to the well-known “cluster glycoside effect”.<sup>487–489</sup> A variety of optical-sensing methods for carbohydrate-binding proteins, lectins, bacteria, and viruses have been reported.<sup>490–494</sup> The carbohydrate–protein interactions reflect a collective behavior or effect, so does the AIE effect. In terms of this, the AIE effect and carbohydrate–protein interactions should fit each other like a hand in a glove. In other words, the AIE effect is an ideal means for the evaluation of carbohydrate–protein interactions and in turn, the carbohydrate–protein interactions facilitate the AIE-based protein detection and ensure the selectivity, which have been testified by the large series of AIE-active probes constructed on the basis of the carbohydrate–protein interactions.<sup>495–499</sup>

The general design and working mechanisms of the light-up protein detection systems which integrate the AIE effect with carbohydrate–protein interactions and enzymatic hydrolyses have been schematically illustrated in Figure 81. For such

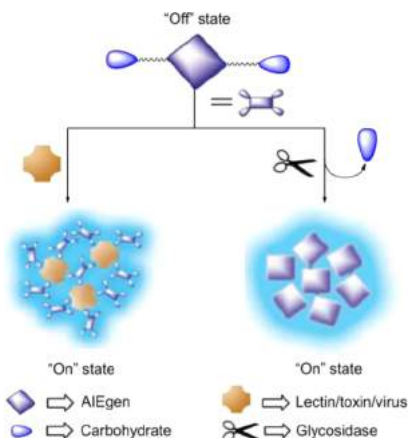


**Figure 81.** Schematic illustration of the general strategy of taking advantage of carbohydrate functionalized AIEgens to specifically detect proteins such as lectin, toxin or virus via specific carbohydrate–protein interactions and enzymatic hydrolyses. Adapted with permission from ref 495. Copyright 2010 Royal Society of Chemistry.

systems, the essential step is to construct a carbohydrate-bearing AIEgen. The incorporation of the sugar (carbohydrate) moieties not only endows the AIEgen with water-solubility and biocompatibility but also provides neutral ligands to bind specific proteins or undergo selective enzymatic reactions. Sugar-bearing AIEgen is almost non-luminescent in its dilute aqueous solution when molecularly dissolved (i.e. “off” state). Thanks to the AIE effect, strong luminescence would be switched on when the aggregation arises from the addition of specific protein species (i.e. “on” state). There are two main pathways to induce or derive the aggregation in these protein detection systems: one is carbohydrate–protein binding that draws the probe and analyte molecules together and the other one is glycosidase (enzyme)-induced hydrolysis which causes the change in water solubility.

On the basis of the aforementioned rationale, diverse AIE-active probes varying both in AIE core and carbohydrate peripheries have been designed and established for the specific detection of carbohydrate-binding species such as lectin, toxin, virus, and so on.<sup>495–499</sup> More specifically, AIE probes have been designed to detect concanavalin A (Con A), a well-studied lectin which is frequently used to model protein–carbohydrate interactions. Since Con A has a homotetrameric structure with

four binding sites that are specific to  $\alpha$ -D-mannosyl and  $\alpha$ -D-glucosyl residues, an AIE core, such as TPE, has been decorated with multivalent  $\alpha$ -D-mannosyl residues to produce highly sensitive probes for Con A. Addition of Con A to the originally non-emissive solutions of such probes triggers bright luminescence. Strong protein–carbohydrate interactions between Con A and the mannosyl moieties pull the Con A and probe molecules together to form heteroaggregates which restrict the intramolecular motions of the AIE cores leading to fluorescence turn-on. With an optimal design in the molecular structure of the mannose-TPE bioconjugate, highly selective Con A sensing with a detection limit as low as 20 nM (Con A) has been achieved by this methodology.<sup>496</sup> Altering the carbohydrate motif can give rise to more protein detection systems utilizing other protein–carbohydrate interactions, such as the detection of peanut agglutinin with a lactose-functionalized silole.<sup>497</sup>

With this powerful strategy based upon the alliance of AIE and carbohydrate–protein interactions, protein species closely related to diseases, such as cholera toxin<sup>498</sup> and influenza virus,<sup>499</sup> can be selectively and sensitively recognized in a turn-on fashion. Cholera is an acute infection of the intestine, with symptoms as a large amount of watery diarrhea and vomiting, which can lead to severe dehydration and electrolyte imbalance or even death.<sup>500</sup> Cholera, toxin released by the bacterium *vibrio cholerae*, is the primary virulence factor of cholera. The AB<sub>5</sub> hexameric architected toxin is composed of five identical B-subunits which selectively bind to a pentasaccharide. The first step towards contracting cholera is the attachment of cholera toxin B-subunit to the intestinal cells with the aid of the pentasaccharide recognition. Because this B-subunit is known to bind to lactose through the recognition of the terminal galactose moiety, a lactose-functionalized TPE derivative has been designed and synthesized by a copper(I) catalyzed “click” reaction between the tetrapropargyl-attached TPE and azido-decorated lactose. Such a lactose-functionalized TPE derivative selectively shows fluorescence turn-on response to cholera toxin as a result of the carbohydrate–protein interaction activated RIM process. Likewise, a TPE derivative decorated with 6'-sialyllactosyl residues can work as a fluorescence “turn-on” sensor towards detection of influenza virus.<sup>499</sup> It is because the influenza virus is known to bind to sialyl sugar chain receptors located on the cell membranes of the host. Influenza virus possesses trimeric hemagglutinin molecules at a high density (1000 molecules per virus), which can bind to 6'-sialyllactosyl moieties via carbohydrate–protein interactions. These interactions allow the TPE derivative to bind to the surface of influenza viruses, which freezes the intramolecular motions of the TPE units and thus turns on the light emission. A detection limit where the concentration of influenza virus is  $10^5$  plaque-forming unit (PFU)  $100 \mu\text{L}^{-1}$  is achieved, indicating the great potential of AIEgen-carbohydrate probe to be used for diagnosis of the influenza virus.

The fluorescent light-up sensing systems discussed above are on the basis of the aggregation induced by carbohydrate–protein interactions between the AIEgen-carbohydrate conjugates and the proteins. The other approach shown in Figure 81 has been exemplified by the protein detection system with the  $\beta$ -cellobiosyl-carrying TPE derivative as a probe.<sup>495</sup>  $\beta$ -cellobiosyl is a certain substrate for  $\beta$ -glucosidase and will undergo hydrolysis with the aid of an enzyme. Upon the addition of  $\beta$ -glucosidase, water-soluble  $\beta$ -cellobiosyl-carrying TPE derivative is converted into water-insoluble TPE derivatives by enzymatic hydrolysis and form insoluble aggregates, and in the

meantime, the emission-off state is switched to luminescence-on state with a 9-fold fluorescence enhancement (Figure 81). Considering this, a unique and versatile platform for the selective detection of a specific enzyme like glycosidase has been provided by this work.

As protein–carbohydrate-directed interactions are able to arouse the emission of an AIEgen in specific protein detection as a result of RIM, protein/peptide–protein interactions also can be made use of to serve for the same purpose. Integrin  $\alpha_5\beta_3$  plays a crucial role in the regulation of tumor growth and metastasis, and it is overexpressed on tumor cells of different origins, with the levels of expressions closely relevant to the aggressiveness of the diseases.<sup>501–505</sup> Integrin  $\alpha_5\beta_3$  is thereby a unique protein biomarker for early diagnosis and treatment of rapidly growing solid tumors and it is also a receptor for the extracellular matrix protein with exposed arginine–glycine–aspartic acid (RGD) sequence. In the light of the high specificity and affinity of cyclic RGD tripeptides (cRGD) to integrin  $\alpha_5\beta_3$ , two cRGD units have been integrated with the tetraphenylsilole (TPS) moiety, an archetypal AIEgen, via a facile “click” reaction to create the AIEgen-peptide bioconjugate TPS-2cRGD (355; Figure 82) for

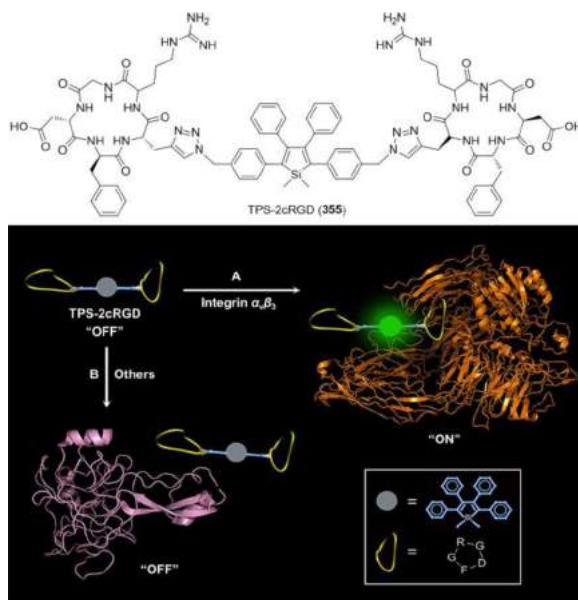


**Figure 82.** Discrimination of (A) integrin  $\alpha_5\beta_3$  from (B) other proteins via specific cRGD–integrin interaction using AIEgen 355 as a bioprobe. Reprinted with permission from ref 506. Copyright 2012 Royal Society of Chemistry.

the specific sensing of integrin  $\alpha_5\beta_3$ .<sup>506</sup> As schematically illustrated in Figure 82, the incorporation of cRGD into the AIE system brings about two major benefits. First, these water-soluble peptide units render the probe (355) to be well dissolved in the aqueous media, so that the AIE core experiences enough freedom to undergo active intramolecular motions to non-radiatively annihilate the excited states. In this manner, the probe can maintain an “off” state even in a complicated environment, which guarantees the minimum background interference for a light-up probe with large signal-to-noise ratio and high sensitivity. Second, the cRGD endows the AIEgen with the ability to specifically respond to the integrin  $\alpha_5\beta_3$ . The resultant TPS-2cRGD (355) is miscible with water, exhibiting nearly no luminescence in aqueous buffer. Two scenarios can be displayed by the addition of a protein into the aqueous solution of 355.

Scenario A refers to the addition of integrin  $\alpha_5\beta_3$ , where the strong binding between 355 and integrin  $\alpha_5\beta_3$  severely suppresses the intramolecular motions of TPS moieties, inducing fluorescence switch-on of 355. If the added protein cannot specifically interact with 355, the detection medium remains in the dark state without any response (scenario B). An almost perfect linear ( $R^2 = 0.999$ ) line can be achieved in the range of  $0\text{--}50 \mu\text{g mL}^{-1}$ , as revealed by the plot of the net changes in the fluorescence intensity against the integrin concentration, indicative of the possibility of applying 355 for integrin quantification. Moreover, 355 gives a detection limit of  $0.5 \mu\text{g mL}^{-1}$  integrin  $\alpha_5\beta_3$ . The fluorescence response of 355 is also highly specific to integrin  $\alpha_5\beta_3$ , for the emission enhancement induced by integrin  $\alpha_5\beta_3$  is  $\sim 10$ - to 182-fold larger than those induced by the addition of other biomacromolecules such as DNA, Con A, heparinase, trypsin, BSA, and so on.

In addition to the conformational transition monitoring and visualization and special protein detection via carbohydrate–protein or peptide–protein interactions, a lot of research efforts have been devoted to the detection, visualization, and quantification of the common proteins<sup>507,508</sup> such as casein,<sup>509</sup> BSA,<sup>286,510–512</sup> and HSA<sup>468</sup> based on AIE approaches. Although these proteins are not as unique as the aforementioned ones like insulin, Con A, and integrin  $\alpha_5\beta_3$ , the assays of them are still of biological and physiological importance. For example, HSA is the most abundant protein in the circulatory systems and plays various roles in the human body, including regulating water balance, transporting substances such as hormones, fatty acids, and maintaining osmotic pressure, etc. A low blood HSA level may indicate liver diseases (e.g., cirrhosis and chronic hepatitis), kidney diseases (e.g., nephrotic syndrome) and among others. A higher albumin level in urine is regarded as albuminuria. The development of effective methods for urinary protein detection and quantification is thus of clinical value.

To this end, AIEgens have been explored as fluorescent probes for HSA quantification, such as the TPE derivative 353 (Figure 83A).<sup>468</sup> The fluorescence of the solution of 353 can be triggered even by a small amount of HSA. The emission intensity at 475 nm keeps rising with the increasing concentration of HSA. The fluorescence is rapidly intensified in the lower HSA concentration range and levels off to a plateau when the HSA concentration exceeds  $1 \mu\text{M}$ . As the concentration of HSA increases in an aqueous buffer solution of 353, more and more molecules of 353 enter the hydrophobic pockets of HSA and the non-radiatively decay channels of 353 become blocked as a result of the restricted intramolecular motions of the probe. 353 exhibits a broad linear working range from 0 to  $100 \text{nM}$  ( $R^2 = 0.995$ ) with the detection limit as low as  $1 \text{nM}$ . HSA quantitation in artificial urine has been conducted to examine the feasibility of applying 353 for protein assay in body fluids. Similar or even identical binding isotherm to that in PBS has been recorded. The superior sensitivity and excellent selectivity of 353 to albumin proteins including HSA and BSA remain unperturbed in the artificial urine. Owing to its AIE property and high affinity to HSA, 353 has also been successfully applied to visualize HSA via fluorescent staining in PAGE (Figure 83B). The PAGE image obtained for 353 and HSA exhibits a much higher contrast than that from the colorimetric staining with Coomassie Brilliant Blue (CBB), a common staining reagent. Even a trace amount of HSA can be seen in the PAGE with the aid of 353. In addition to the sensitivity, fluorescent staining with 353 is both rapid and simple in comparison to the conventional staining with SYPRO Ruby, CBB, or silver as stains. Gel staining of HSA can be achieved with

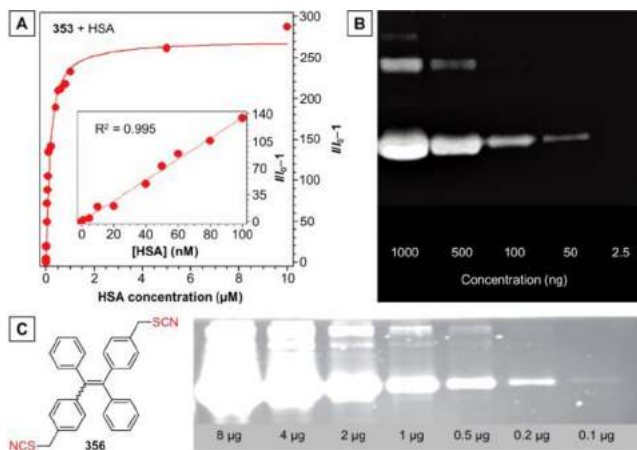


**Figure 83.** (A) Quantitation and (B) visualization of HSA by a TPE derivative with AIE feature (353). Adapted from ref 468. Copyright 2010 American Chemical Society. (A) Change in the FL intensity at 475 nm with HSA concentration. Inset: Linear region of the binding isotherm of 353 to HSA.  $[353] = 5 \mu\text{M}$ ;  $\lambda_{\text{ex}} = 350 \text{ nm}$ . (B) PAGE analyses of HSA using 353 as the staining reagents through non-covalent interactions. (C) SDS-PAGE fluorescence image of amine-reactive AIEgen 356 poststained BSA with various loaded amounts. Reprinted with permission from ref 513. Copyright 2012 Royal Society of Chemistry.

353 in as short as 5 min. Since excess dye is not fluorescent unless bound to HSA, neither careful timing nor a destaining step is needed for the staining with 353. A similar work has been carried out by Ouyang's group with another water-soluble AIEgen, i.e., sulfonated DSA.<sup>508</sup> This probe shows a very high sensitivity ( $0.78 \text{ ng } \mu\text{L}^{-1}$ ) to ferritin in PAGE. Thanks to their AIE feature, all these AIEgens offer rapid, sensitive, economic, and effective assays to proteins.

Besides the fluorescent staining of protein in PAGE via non-covalent interactions such as hydrophobic interaction, covalent staining of protein in gels can also be realized with specially designed AIEgens. For example, amine-reactive isothiocyanate-functionalized TPE derivative 356 has been designed as a staining agent for protein visualization in PAGE, whose fluorescence is lit up by the covalent-binding between the probe and protein molecules (Figure 83C).<sup>513</sup> Considering that nearly all kinds of proteins have reactive amine groups, 356 is applicable to stain a broad range of proteins. BSA is chosen as a representative protein to testify the staining ability of 356. The AIEgen 356 can be used to visualize protein in SDS-PAGE either in a prestaining mode via mixing the dye with the protein solution prior to the denaturation step or in a poststaining manner by immersing the polyacrylamide gel into a solution of 356. In either case, the isothiocyanate group on 356 will react to free amine moieties on the protein, which restricts the phenyl ring rotations of the TPE units and thus turns on the emission. In prestaining, as compared to CBB staining, 356 shows a comparable detection limit ( $0.2 \mu\text{g}$ ) but a much shorter staining time. Working in a poststaining fashion, 356 performs even better with a detection limit as low as  $0.1 \mu\text{g}$ . Both the prestaining and poststaining methods exhibit a broad linear detection range. An additional benefit of employing this amine-reactive AIE probe is that no fixation is required, so the transferring of labelled proteins to nitrocellulose membranes for further analysis is enabled. It is noteworthy that the AIE property of 356 keeps it from  $F/P$  ratio restriction, allowing the use of relatively high

concentration of fluorophore in both covalent prestaining and poststaining methods.

Mirroring the detection of negatively charged biomacromolecules like heparin, DNA, and some proteins with cationic AIE probes, negatively charged AIEgens have been designed to sense positively charged proteins/peptides in a fluorescence light-up manner (Figure 84).<sup>514,515</sup> For example, AIEgen 357 is a sulfonate group-embellished TPE derivative, which emits negligible fluorescence when dissolved in the PBS buffer solution with  $\text{pH} = 8.5$ ; however, the addition of a positively charged peptide composed of six arginine units, Arg<sub>6</sub>, triggers the fluorescence via the electrostatic complexation with the probe. The intramolecular motions of 357 in the heteroaggregates are greatly hindered and the non-radiative relaxation pathways are blocked, leading to the emission turn-on. A steady linear increase ( $R = 0.9996$ ) in emission intensity has been displayed with the concentration of Arg<sub>6</sub> in the range of  $0\text{--}10 \mu\text{M}$ .<sup>514</sup> Since Arg<sub>6</sub> is a substrate for trypsin, the most important digestive enzyme generated by the pancreas,<sup>516</sup> the strongly fluorescent complex of 357 and Arg<sub>6</sub> can be further used as a label-free probe for the continuous fluorometric assay of trypsin and inhibitor screening in a fluorescence "turn-off" mode. The decreased fluorescence results from the hydrolysis of the Arg<sub>6</sub> motif as well as the subsequent deaggregation of the 357/Arg<sub>6</sub> complex.

A similar fluorescence turn-on system for protein assay was reported with the salicylaldehyde azine derivative 358, an AIE-active ESIPT compound comprising a carboxylate group.<sup>515</sup> This water-miscible AIEgen has been applied for the fluorescence turn-on detection of protamine based on the AIE effect induced by the electrostatic interactions between the highly cationic protamine and anionic 358 (Figure 84). Under optimal detection conditions, a large Stokes shift of about 198 nm could be observed due to the ESIPT property of 358. The fluorescence increment at 538 nm is linearly correlated to the concentration of protamine in the range of  $0.6\text{--}18 \mu\text{g mL}^{-1}$  with a relative coefficient ( $R^2$ ) as high as 0.9996 and a detection limit as low as  $43 \text{ ng mL}^{-1}$ . Such a method has been successfully used for protamine quantification in diluted horse serum. As heparin is the most negatively charged biological macromolecule, which could strongly bind with protamine through electrostatic interaction, the addition of heparin into the mixture of 358 and protamine induces dramatic decrease in the fluorescence intensity. It is attributable to the fact that the competitive electrostatic binding between heparin and protamine destroys the 358/protamine complex and releases the dye molecules into the aqueous medium, where 358 can undergo free intramolecular motions rendering the excited states to be non-radiatively annihilated (Figure 84). In this sense, 358 could also be employed as a fluorescence turn-off probe to investigate the interactions between protamine and heparin. Apart from the examples highlighted here, there are still a great number of probe sensing systems constructed with AIE effect and electrostatic interactions.<sup>286,459,510,511</sup> It is worth mentioning that the GO strategy has also been utilized to improve the sensitivity of AIEgens in the protein detections based upon electrostatic interactions.<sup>511</sup>

It is noticeable that a great deal of research interest has recently been put in establishing detection systems which are made from AIEgens, for the sensing and assay of enzymes, an important class of proteins. Enzymes are biomacromolecules that accelerate or catalyze bio/chemical reactions and most enzymes are proteins in essence. It is accepted that enzymes play pivotal roles in almost all metabolic processes, for enzymes ensure their rates of

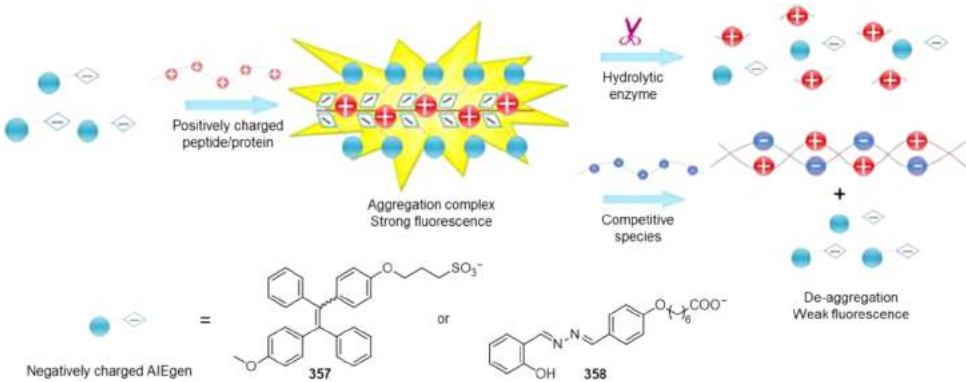


**Figure 84.** Schematic illustration of the general strategy of taking advantage of negatively charged AIEgens (e.g., 357 and 358) to detect positively charged peptide/proteins like Arg<sub>6</sub> or protamine via electrostatic interactions. Adapted with permission from ref 515. Copyright 2010 Royal Society of Chemistry.

occurrence and determine their pathways. The assay of enzymes is thus of obvious value to biological research and has diagnostic and therapeutic implications. In view of the specialty of enzymes, we sort out the research related to enzymes from the large family of protein studies and separately discuss them here. As shown in Figure 85, there are three major design principles established for

and thus results in fluorescence turn-on/enhancement. It is worth noting that the enzymes can be detected by this rationale include but are not limited only to the model shown in Figure 85. More specifically, some enzymes transform their substrates into cationic species while some others turn their substrates into anionic species; however, all of these enzymes can be assayed in this way with an oppositely charged AIEgen. Moreover, the electrostatic strategy with regard to enzyme detection is also not restricted to the pathway/process depicted in Figure 85; instead, any enzyme assay process involving electrostatic interactions should fall into this category.

The work done by Wu et al. has perfectly exemplified the first model highlighted in Figure 85.<sup>517</sup> They constructed a two-component one-step fluorescent assay for histone deacetylase (HDAC) by utilizing a water-soluble hyperbranched polyester decorated with the acetylated lysine groups [H40-Lys(Ac)] and sulfonated TPE 353. HDAC triggers the deacetylation of H40-Lys(Ac) and hence turns the electroneutral polymer into the positively charged one. As a result, the electrostatic complexation between the cationic polymer and anionic AIEgen takes place, thereby making the intramolecular motions of 353 subjected to great restriction and ultimately switching on the fluorescence. Such a sensing system shows a very low detection limit of 25 ng mL<sup>-1</sup>. Also, the assay of HDAC in serum has been achieved in terms of their high sensitivity and superb specificity. Zhang's group has employed a similar electrostatic strategy to develop a fluorometric turn-on assay for monoamine oxidase B (MAO-B) based on cationic AIEgen 339, heptylamine and HSO<sup>3-</sup>.<sup>518</sup> The anionic species, which form electrostatic complexes with 339, are generated by the cascaded enzymatic and chemical reactions among MAO-B, heptylamine, and HSO<sup>3-</sup>. This fluorometric turn-on assay can be carried out continuously in aqueous media with a detection limit as low as 0.25 μg mL<sup>-1</sup>. In addition, some other enzymes such as hyaluronidase can also be detected by coupling the AIE effect with electrostatic interactions, and the assay system works in a turn-off mode similar to the trypsin example shown in Figure 84, demonstrating the flexibility of the AIE-based electrostatic strategy.<sup>519</sup>

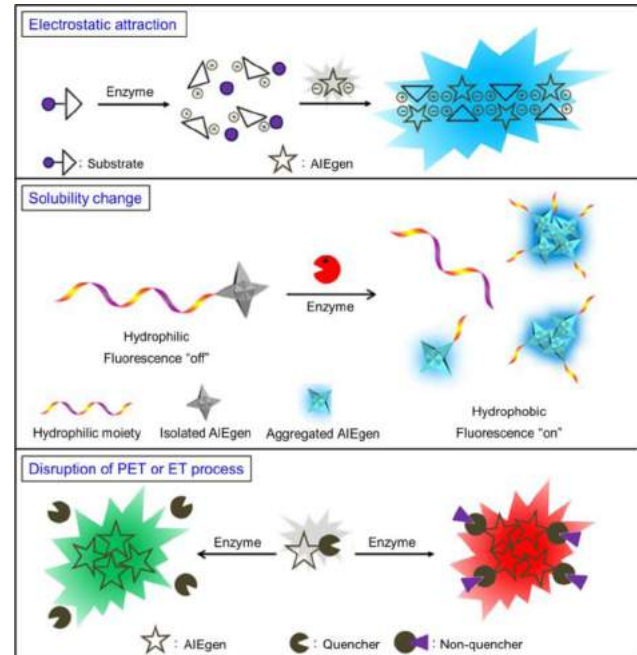


**Figure 85.** Schematic representation of the most frequently used principles for the design of luminescence light-up enzyme detection systems on the basis of the AIE effect. Abbreviations: PET stands for photoinduced electron transfer; ET means energy transfer. The scheme for "Solubility change" is adapted from ref 534. Copyright 2012 American Chemical Society.

fluorescence light-up enzyme assay. By capitalizing on the specificity of the enzymatic activity, highly selective sensing systems for enzymes can be achieved with ease. The first general design is based upon electrostatic attraction. When the substrate molecules are directly or indirectly converted into charged species by enzyme, the newly generated products will bind to the oppositely charged AIEgen via electrostatic interactions and form complexes.<sup>517,518</sup> The complexation activates the RIM process

The second design rationale is on the basis of the solubility change of the AIE probe upon the interaction with enzyme, and it can hence be referred to as the solubility change strategy. Hydrophilic motif(s) is/are attached onto a hydrophobic AIEgen to confer the hydrophilicity on the probing system so that the probe is almost non-emissive in the aqueous buffer solution with a very low background. Just as important, these hydrophilic

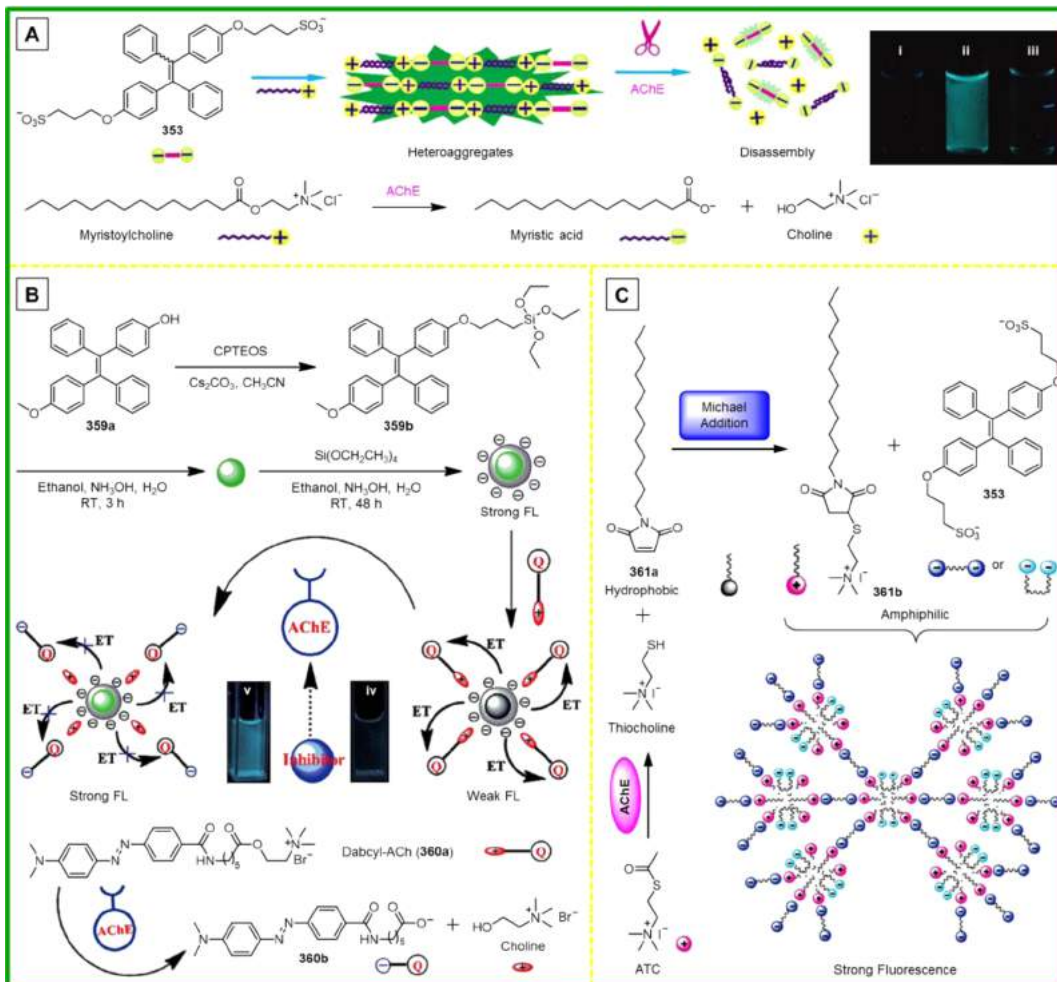


**Figure 86.** Representative examples of utilizing AIEgens for the fluorometric assay of acetylcholinesterase (AChE). (A) Continuous fluorometric assay for AChE and inhibitor screening based on the AIE effect of 353 and electrostatic attraction. Insets: Fluorescent photographs of (i) 353, (ii) the ensemble of 353 and myristoylcholine, and (iii) the ensemble of 353 and myristoylcholine in the presence of AChE. Adapted from ref 521. Copyright 2009 American Chemical Society. (B) The synthetic approaches for compound 359b and the emissive silica particles, illustration of the mechanism for the application of emissive silica particles for AChE activity assay and inhibitor screening, and the chemical structure of 360a (dabocyl-ACh) and its hydrolysis product catalyzed by AChE. Adapted with permission from ref 522. Copyright 2012 Royal Society of Chemistry. (C) Cascade reactions among ATC, AChE, and 361a and illustration of the aggregation of 353 in the presence of 361b. Adapted from ref 523. Copyright 2009 American Chemical Society.

moieties should be specially designed for a particular enzyme, so the enzyme is able to specifically cut off these groups and release the hydrophobic AIE core into the aqueous media. Consequently, such hydrophobic AIE moieties will readily aggregate together resulting in the AIE response. There have been quite a few enzyme assay systems built on the solubility change strategy. The most representative ones of them will be elucidated in the following discussion. The third design principle is based upon the disruption of non-radiative decay processes such as photo-induced electron transfer (PET) and energy transfer (ET). By means of adding quenching species into the probing medium or decorating AIEgens with quenching moieties, the detection background is eliminated and meanwhile the AIE probes will be in the “off” state until the addition of enzymes that can annihilate the quenching effect. The quenching compound/moiety is chosen as the substrate of a certain enzyme, so that if the added enzyme can cleave the quenchers away from the AIEgens or converts them into non-quenchers, the emission of the AIE probes will then be recovered. Such a strategy makes it possible to realize light-up/turn-on detection even in the aggregate state.

On the basis of these three primary design principles and variations derived from these ideas, numerous fluorometric assay systems for multifarious enzymes have been created.

To be systematic, typical studies for the same enzyme are summarized together into one or two figures. For example, the representative fluorescent detection systems for acetylcholinesterase (AChE) are exhibited in Figure 86. AChE is a hydrolase that hydrolyzes the acetylcholine, a central neurotransmitter, and thereby it is highly important in the regulation of the neural response system. In particular, evidences have indicated that low levels of acetylcholine as a result of its hydrolysis by AChE can accelerate the process of amyloidogenesis, which is strongly associated with the development of Alzheimer’s disease.<sup>520</sup> As clinical treatment for Alzheimer’s disease is operated by inhibiting AChE, there is a high demand for simple, sensitive, and reliable assay for the activity evaluation and quantification of AChE. A convenient and continuous fluorometric assay for AChE has been demonstrated in a system which consists of a water-soluble AIEgen 353 and myristoylcholine (Figure 86A).<sup>521</sup> Myristoylcholine plays two important roles in this fluorometric

assay system. First, it is an amphiphilic compound with positive charge and accordingly the molecules of myristoylcholine can form heteroaggregates with the negatively charged AIEgen 353 via electrostatic interactions. Second, it is a substrate for AChE and can be hydrolyzed into myristic acid and choline. The inset of Figure 86A shows that 353 in a PBS buffer solution is non-emissive (Figure 86A: inset i). Once the electrostatic complexation occurs between 353 and myristoylcholine, the RIM process of 353 is activated, the non-radiative relaxation is hindered, and the light emission is thus switched on (Figure 86A: inset ii). After the addition of AChE, myristoylcholine is converted into myristic acid and choline by hydrolysis. As a result, the complex of AIEgen 353 and myristoylcholine is disintegrated, due to the Coulombic repulsive interaction between 353 and the hydrolysis product of myristoylcholine (i.e., myristic acid). The molecules of 353 become unconstrained again to undergo active intramolecular motions and consequently a dramatic decrease in emission is recorded (Figure 86A: inset iii). Therefore, on the basis of the AIE feature of 353, continuous fluorometric monitoring of AChE activity becomes possible, and AChE with concentration as low as 0.5 U/mL can be assayed. Considering its simplicity, sensitivity, and selectivity, this assay method could also be used for inhibitor screening for AChE. In the presence of a tacrine, an inhibitor of AChE, fluorescence decrease of the ensemble of 353 and myristoylcholine containing AChE is drastically slowed. The rate in the fluorescence decrease could thus be utilized to evaluate the inhibition efficiency.

In the above work, the AChE is assayed through altering or disassembling the electrostatic complexation between the AIE probe and substrate molecules via enzymatic reaction to cause the fluorescence change (quenching). On the basis of it, Zhang's group further developed another continuous fluorometric assay system, which exhibits fluorescence turn-on response to AChE as a result of the disruption of the energy transfer (ET) process (Figure 86B).<sup>522</sup> Silane-decorated 359b is obtained by the reaction between hydroxyl-substituted TPE (359a) and 3-chloropropyltriethoxysilane (CPTEOS) in the presence of Cs<sub>2</sub>CO<sub>3</sub>. Co-hydrolysis of 359b and tetraethoxysilane (TEOS) produces uniform core-shell silica particles with average diameters of 40 nm. Since the TPE moieties are encapsulated in the silica particles, their intramolecular motions are thereby greatly suppressed and the radiative relaxation channels are opened. With a negative zeta ( $\zeta$ ) potential when pH > 5, the silica particles are well dispersed in a PBS buffer solution (pH = 8.5). The original strong emission of the silica particles is significantly weakened (Figure 86B: inset iv) upon the addition dabcyl-ACh (360a). 360a is comprised of positively charged choline moiety and a dabcyl [4-(dimethylamino)-4'-carboxy-azobenzene] chromophore. In this way, cationic 360a is adsorbed onto the negatively charged surface of the silica particles. This proximity facilitates the ET between TPE molecules and the dabcyl chromophores, and thus the fluorescence is quenched. Just as important, 360a is also a substrate for AChE. The addition of AChE into the weakly fluorescent mixture of silica particles and 360a restores the emission of the silica particles (Figure 86B: inset v). It is because that 360a is hydrolyzed into choline and a negatively charged residue (360b). Whereas electrostatic attraction pulls the nanoparticles to bind with 360a, electrostatic repulsion between anionic 360b and negatively charged silica particles pushes them away from the particles. As a result, the distance-dependent ET process is disrupted, and the fluorescence of the trapped TPE moieties is restored. The ensemble of

the TPE-loaded silica particles and 360a can therefore be used as a fluorescence light-up assay system for AChE. The detection limit achieved by this assay for AChE is as low as 0.2 U mL<sup>-1</sup>. Emission enhancement is greatly reduced in the presence of known inhibitors such as neostigmine and tacrine, suggesting its ability to screen inhibitors for AChE.

Zhang's research team has conducted a systematic work in the construction of AChE assay systems by altering the experimental design and changing the substrate. They have realized another turn-on assay of AChE based upon the AIE effect of 353 and the electrostatic interaction between the probe and co-reagents (Figure 86C).<sup>523</sup> This probing system based on a series of cascade reactions among AChE, acetylthiocholine iodide (ATC), and 1-dodecyl-1H-pyrrole-2,5-dione (361a) has resulted in an even more sensitive assay of AChE. A transparent solution of AIEgen 353 (20  $\mu$ M), ATC (30  $\mu$ M), and 361a (30  $\mu$ M) in the mixture of 10 mM HEPES buffer solution/THF (v/v = 1000/3) shows very weak fluorescence. Being well dissolved, AIEgen 353 experiences active intramolecular motions, allowing its excited states to non-radiatively relax. The addition of AChE hydrolyzes its substrate ATC into thiocholine which subsequently undergoes Michael addition with 361a to yield an amphiphilic compound 361b (Figure 86C). Strong electrostatic interactions occur between the cationic 361b and anionic 353, which generate the aggregates, ultimately rigidify the TPE moieties, block the non-radiative decay channels, and trigger the fluorescence. With this ensemble of 353, ATC and 361a as an assay system, AChE with concentration as low as 0.005 U mL<sup>-1</sup> can be analyzed, indicative of its high sensitivity. Since the hydrolysis of 361a catalyzed by AChE can be retarded by inhibitors such as neostigmine, the degree of fluorescence enhancement of the ensemble of 353, ATC, 361a, and AChE is accordingly decreased after the addition of inhibitor, rendering the system to be able to effectively screen the inhibitors of AChE.

Considering the great importance of alkaline phosphatase (ALP), a large array of assay systems based on AIE effect have also been created for the sensing and activity study of this class of hydrolase enzyme.<sup>524–528</sup> ALP widely exists in various organs of mammals including bone, liver, placenta, and intestine, and it has been acknowledged as an important biomarker for clinical diagnostics.<sup>529</sup> The elevated levels of ALP in the blood serum is usually associated with a vast variety of diseases such as biliary obstruction, bone diseases (e.g., osteoblastic bone tumors, osteomalacia), leukemia, lymphoma, sarcoidosis, hyperthyroidism, liver diseases, breast and ovarian cancer, and diabetes, and so on.<sup>530,531</sup> Generally speaking, the strategies established for ALP assay are mainly on the basis of its ability to hydrolyze phosphate groups into hydroxyl groups from many types of biomolecules or chemicals. For example, a simple one-step light-up ALP fluorometric assay with the use of TPE derivative 362a has been reported by Liu and Tang et al. (Figure 87A).<sup>527</sup> This AIE probe (362a) is obtained by functionalizing the TPE core with two phosphate terminal groups which play a dual role in the detection. For one thing, it endows the probe with good water-solubility to render 362a in an emission "off" state in a Tris buffer solution (pH 8.0). In light of the negligible background, a high signal-to-background ratio can be achieved. For another, the phosphate groups act as the specific substrates for ALP. With the addition of ALP, the enzyme recognizes and cleaves the phosphate groups on 362a to yield a highly hydrophobic product 362b (Figure 87A). As ALP produces more and more 362b, the hydrophobicity of 362b causes the molecules to aggregate together and the fluorescence of the insoluble

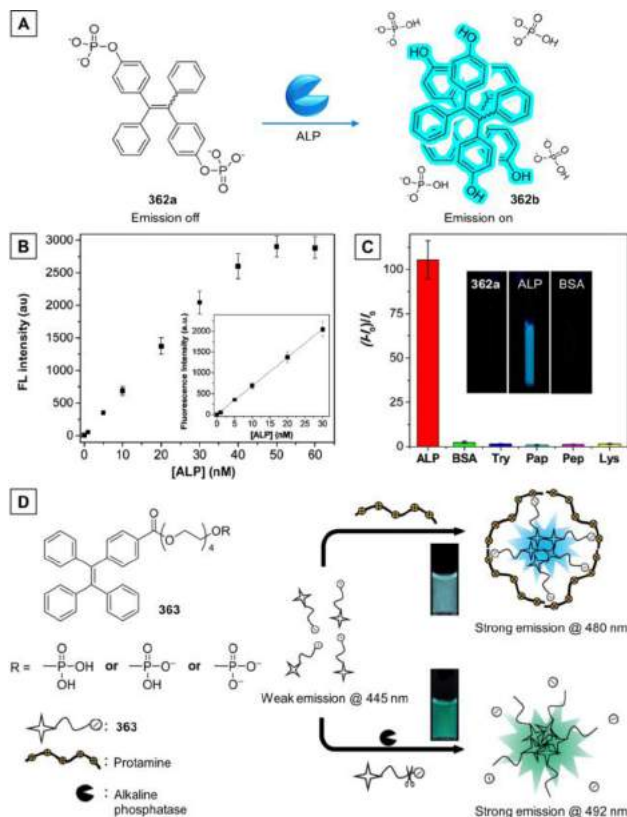


**Figure 87.** (A) Illustration of design principle of ALP assay based on a phosphate functionalized TPE (362a). (B) Plots of fluorescence intensity of  $10 \mu\text{M}$  362a in Tris buffer (10 nM, pH 8.0). Inset: linear fitting of the curve at ALP concentrations in ranges of 0–30 nM. (C) Bar graph of  $(I - I_0)/I_0$  of 362a incubated with different proteins in Tris buffer (10 nM, pH 8.0). Insets: The photographs of 362a before and after incubated with ALP and BSA in Tris buffer, respectively, taken under UV lamp illumination. Adapted from ref 527. Copyright 2013 American Chemical Society. (D) Schematic illustration of sensing mechanisms of 363 in protamine detection and ALP activity assay. Reprinted with permission from ref 528. Copyright 2014 Royal Society of Chemistry.

aggregates is lit up as a result of the activation of RIM process. Making use of the enhanced fluorescence, a specific fluorescence turn-on probe for ALP sensing and enzyme activity studies is constructed. A linear increase in emission intensity is observed with respect to the concentration of ALP in the range of  $3\text{--}526 \text{ U L}^{-1}$  (Figure 87B). The detection limit has been estimated to be  $0.2 \text{ U L}^{-1}$  or  $11.4 \text{ pM}$  in Tris buffer solution. Moreover, the probe 362a also performs well in diluted serum, exhibiting a linear response range up to the ALP concentration of  $175 \text{ U L}^{-1}$  or  $10 \text{ nM}$  (normal level of serum ALP:  $30\text{--}135 \text{ U L}^{-1}$ ). It suggests the potential of 362a to be applied for the clinical assay of ALP in real samples. In addition, 362a is highly selective to ALP among a group of proteins with only minimal response being shown in the presence of other proteins or enzymes (Figure 87C).

Through elaborate design, dual-mode fluorescence “turn-on” probe has also been developed by Tang and Liu et al. on the basis of the AIE feature of 363 (Figure 87D), which is able to quantify protamine and evaluate ALP activity in two different working modes.<sup>528</sup> The tetraethylene glycol and phosphate groups on 363 endue the probe with good water-solubility and this phosphorylated TPE derivative is thereby only weakly emissive with an emission maximum at 445 nm in pure water or a Tris-HCl buffer solution (pH 9.6). Owing to the amphiphilicity of

363, micellar aggregates of the probe molecules and protamine will form via the electrostatic interaction between the negatively charged phosphate group of 363 and the positively charged protamine, where the RIM process of 363 is triggered, and the fluorescence is consequently turned on with the emission peak red-shifted to 480 nm. For protamine, a linear response in the fluorescence ( $I/I_0$  versus protamine concentration) is observed in the concentration range of  $0\text{--}1000 \text{ ng mL}^{-1}$  with the detection limit as low as  $12 \text{ ng mL}^{-1}$ . On the other hand, in the presence of ALP, the fluorescence emission peak is red-shifted to 492 nm and significantly intensified. The ALP hydrolyzes and cleaves the phosphate group on 363, releasing the insoluble TPE residues into the buffer solution again. The insoluble products then aggregate together and give rise to a strong emission with a maximum at 492 nm as a consequence of the activated RIM process. The linear light-up fluorescent response of 363 enables the quantification of ALP within the concentration range of  $10\text{--}200 \text{ mU mL}^{-1}$ , which covers the normal physiological level of ALP in human serum. Such a fluorescence response (emission enhancement at 492 nm) of 363 is highly specific to ALP, in sharp contrast, minimal emission enhancement is observed for other enzymes such as esterase, deoxyribonuclease, AChE, and trypsin. There are still quite a few other AIE-based probes developed for the ALP assay by other research teams on the basis of the solubility change of AIE fluorophore which induced by the dephosphorylation.<sup>526</sup>

Caspases are a family of cysteine proteases that are critically important in the initiation and execution of apoptosis (programmed cell death), necrosis, and inflammation.<sup>532,533</sup> Some caspases are also required in the immune system for the maturation of lymphocytes. Among these enzymes, caspase-3 has been regarded as a crucial mediator of cell apoptosis, making it an appealing and unambiguous target for apoptosis imaging. The development of simple, noninvasive, and specific probes with high signal-to-noise ratio for assay of caspase as well as real-time monitoring of cell apoptosis is thus highly desirable and very significant for the evaluation of apoptosis-related drugs and treatments. A string of AIEgens have been systematically designed to this end, serving as caspase-specific probes.<sup>534–536</sup> Constructed on the basis of the solubility change strategy discussed in Figure 85 (vide supra), these probing systems all work in a fluorescence light-up manner with high signal-to-noise ratios. Fluorescence turn-on response is easily achieved by functionalizing a hydrophobic AIEgen with hydrophilic peptide sequence(s) which is/are caspase-specific.

For instance, probe 364 is a TPE-peptide bioconjugate obtained by embellishing the hydrophobic TPE moiety with a hydrophilic acetyl-protected N-terminal Asp-Glu-Val-Asp-Lys (Ac-DEVDK) peptide via Cu(I)-catalyzed “click” reaction.<sup>534</sup> The peptide Asp-Glu-Val-Asp (DEVD) plays two important roles. One is to confer the hydrophilicity on the probe to render 364 in an emission “off” state in aqueous detection media without caspase. And the other function of DEVD is to serve as a caspase substrate, which will be hydrolyzed in the presence of the enzyme, releasing the hydrophobic AIE core and ultimately triggering the fluorescence. In sharp contrast to the weak intrinsic emission of 364 in the buffer solution, significant emission increase (up to 75-fold) is observed in the presence of caspase-3/-7. The enzymes cut the DEVD peptide from the probe 364, leaving the TPE-lysine conjugate (TPE-K), which is much more hydrophobic than its precursor and prone to aggregate together. The phenyl ring motions of the TPE fragments are greatly hindered by the self-aggregation of the hydrophobic TPE-K in

buffer solution, resulting in the observed strong fluorescence. In the absence of caspase-3/7, no matter which protein or enzyme is added, no fluorescence change is observed (Figure 88),

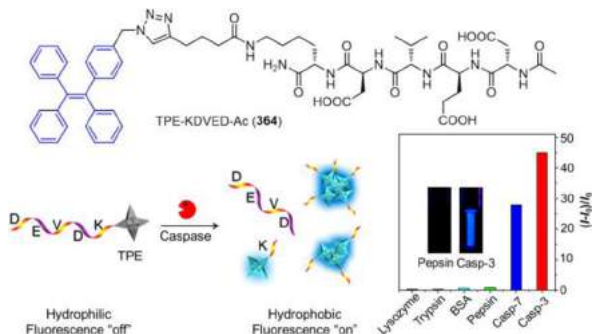


**Figure 88.** Chemical structure of 364 and design rationale as well as specific light-up response of 364 to caspase. Adapted from ref 534. Copyright 2012 American Chemical Society.

indicating that 364 is specifically recognized and hydrolyzed by caspases. Furthermore, enhancement in fluorescence is greatly reduced when caspase-3/-7 coexists with its inhibitor 5-[*(S*)-(+)-2-(methoxymethyl)pyrrolidino]sulfonylisatin, and the reduction degree depends on the dose of inhibitor. It is ascribable to the fact that with the enzyme activity inhibited, the DEVD peptide on the probe 364 cannot be cleaved and no aggregation would occur, leading to the decrease or absence of fluorescence change.

As we all know, the molecular structure including chemical structure and spatial structure of a probe plays a decisive role in its sensing/probing performance. In other words, the number of the substituted recognizing moieties, the substitution position of these recognizing units as well as the geometric configuration can greatly affect the probe's workability, sensitivity, and specificity/selectivity, etc. Usually, even a small alteration in the probe's structure will cause big change in its performance. Taking the stereoisomers, which are identical in chemical structure (molecular formula and sequence of bonded atoms) but different in 3D atomic orientations, for example, their study is significant to the enzymatic studies, drug discoveries, evaluation of drug efficacy, etc., because the active sites of enzymes usually rest with subtle geometric configurations of substrates. It means that the design of probes for enzyme assay should also take the steric effects into consideration. Liu's group has collaboratively worked with our research group on the development of effective caspase probes with AIE characteristics. Given all the above considerations, they have conducted a careful study to examine how the stereoeffect of the AIE probes affect their response to enzymes like caspase. As the aforesaid probe (364) is a mono-substituted TPE derivative, the *E/Z* isomers are not involved. Dual DEVD-labeled TPE derivatives (TPE-2DEVD; 365) are thereby designed and synthesized via "click" reaction to explore the effect of stereoisomeric probes and their different interaction with caspase (Figure 89A).<sup>537</sup> The introduction of DEVD peptide sequence greatly facilitates the separation of the two isomers owing to the difference in hydrophobicity and size. Facile HPLC separation has successfully isolated the *E* and *Z* isomers of 365, making it possible to carry out comparative study of their photophysical properties as well as their sensing abilities.

Like 364, both isomers, i.e., *E*-365 and *Z*-365, are AIE-active, as indicated by the undetectable fluorescence signals exhibited in Figure 89B. Upon treatment with caspase-3 for 30 min, evident

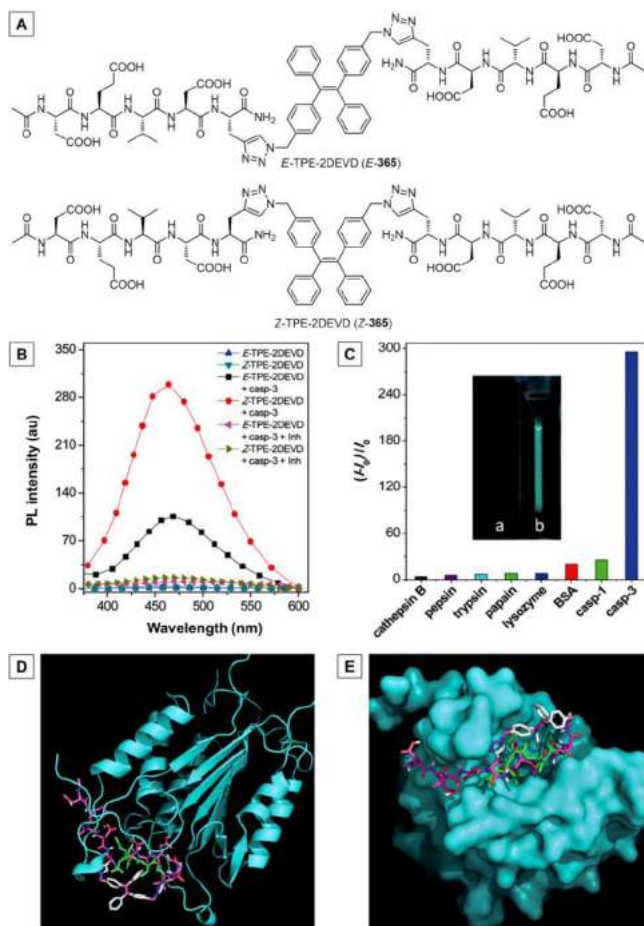


**Figure 89.** Distinct optical and kinetic responses from *E/Z* isomers of caspase probes (365) with AIE characteristics. (A) Chemical structures of *E/Z* isomers of 365 constructed by "click" chemistry. (B) PL spectra of *E*- and *Z*-365 before and after incubation with caspase-3 in the presence and absence of inhibitor Z-DEVD-FMK in DMSO/HEPES buffer (*v/v* = 1/199). (C) Plot of  $(I - I_0)/I_0$  versus different proteins, where  $I$  and  $I_0$  are the PL intensities at protein concentrations of 100 and 0 nM, respectively.  $[Z\text{-}365] = 10 \mu\text{M}$ . The inset shows the photographs of *Z*-365 in the presence of (a) cathepsin B and (b) caspase-3 at 100 nM, respectively, upon UV light illumination. (D and E) Molecular docking of *E*-365 and inhibitor DEVD-CHO in the active site of caspase-3. Caspase-3, *E*-365, and DEVD-CHO are shown in sky blue, multiple colors and green, respectively. (D) Overlay structures of *E*-365 and DEVD-CHO binding to the active site pocket of caspase-3. (E) Superimposition of *E*-365 bound to caspase-3. Adapted with permission from ref 537. Copyright 2014 Royal Society of Chemistry.

fluorescence enhancements over the background are recorded for both probes. In the presence of caspase-3, the probe solutions containing Z-DEVD-FMK, a common and irreversible inhibitor of caspase-3, do not display intense fluorescence signals. Such an obvious suppression in fluorescence response verifies the specific reaction between the probes and caspase-3. The intensified light emission of the probing systems results from the aggregation of the cleavage residue of *E*-365 or *Z*-365, which is proved by the large particle-sizes (266–278 nm). It is worth noting that the fluorescence arises from cleavage/hydrolysis of *Z*-365 is apparently stronger than that of *E*-365. An array of experiments and analyses have been carried out to clarify the origin of the distinctively different fluorescence responses from these two isomers. It has been found that the difference in fluorescence responses comes from the fluorescent properties of

the released residues. The cleavage product of Z-365 is more hydrophobic and brighter with higher  $\Phi_F$  in 1× PBS buffer (11.0%) as compared to that of its E-counterpart (5.0%). Furthermore, the enzymatic kinetic of caspase-3 has been investigated with these two probes. Both E-365 and Z-365 display a gradual increase in fluorescence along with time. However, E-365 reaches the equilibrium in a much shorter time (~5 min) in comparison with Z-365 (~20 min). This result suggests that the caspase-3 has a more efficient interaction with E-365 that gives rise to the accelerated reaction rate. Such a hypothesis has also been proved by the reverse phase HPLC–MS, and it suggests that the spatial arrangement between the probe and enzyme does exert an impact on the reaction kinetics.

In the light of its better light-up response (i.e., higher light-up ratio), Z-365 has been utilized to perform the enzymatic assays with different concentrations of caspase-3 in the range from 0 to 200 nM. The detection limit was estimated to be 0.68 nM. As depicted in Figure 89C, being treated with different proteins, such as cathepsin B, pepsin, trypsin, papain, lysozyme, BSA, as well as caspase-1 under parallel conditions, Z-365 shows the greatest fluorescence change to caspase-3 with a signal-to-noise ratio as high as ~258, among all the other proteins, substantiating the high specificity of this probe to caspase-3. In addition, a deeper insight into the binding mode of these two isomers with caspase-3 has been gained via the molecular-docking studies with the X-ray structure of caspase-3. As revealed by the software-generated results shown in Figure 89D, the most optimal binding models were the *trans* (E) form of 365, suggesting that the E-365 matches and binds well in the active site of caspase-3. Additionally, one of the DEVD peptides in E-365 coincides fairly well with the notable caspase-3 inhibitor, DEVD-CHO. It provides further evidence to the fact that E-365 is the better binding substrate for caspase-3 and favors faster hydrolysis. This piece of study not only establishes effective probes and facile strategies for caspase assay but also offers useful information on the structure–property relationship of the AIEgens, which is undoubtedly instructive to the design of more AIE-based bioprobes with excellent performance.

With the solubility change principle displayed in Figure 85, other types of hydrolase enzymes can also be fluorometrically assayed by AIE-based probing systems. For example, a fluorescence “light-up” carboxylesterase probe derived from TPE has been developed by Li and Chen et al.<sup>538</sup> As a family of isoenzymes common in mammalian organs, carboxylesterases play critical roles in catalyzing the hydrolysis of carboxyl esters for detoxification of narcotics or chemical toxin clearance, and thus their assays will benefit various biochemical studies.<sup>539–542</sup> TPE derivative bearing four carboxylic ester groups is weakly fluorescent due to its relative good solubility in the aqueous solution with pH = 7.4. The specific cleavage of the carboxylic ester bonds by carboxylesterase generates a much more hydrophobic TPE residue that self-assembles into supramolecular microfibers, thereby triggering the fluorescence as a result of the activated RIM process. Apart from its “turn-on” response and high specificity, this probe is also highly sensitive towards carboxylesterase with a detection limit as low as 29 pM, which is much lower than those obtained in other fluorescent assay systems of carboxylesterase. Such a work further provides an extra proof to the feasibility and universality of the solubility change strategy.

Lysosomal enzymes are closely correlated with intracellular digestion of various carbohydrates, proteins, and lipids, and the functional deficiencies of these enzymes would bring about a

number of inherited lysosomal storage disorders (LSDs).<sup>543</sup> The deficiency of lysosomal esterase, for example, would cause Wolman disease.<sup>544</sup> Given that early diagnosis and therapy is crucial to the efficacious treatment of LSDs, the development of self-quenching-free and fluorescence light-up probes for lysosomal enzymes is of great importance. Liu and coworkers have reported such a superb probe that satisfies all the requirements for the specific detection of lysosomal esterase (Figure 90).<sup>545</sup> Although the probe is also built on the basis of

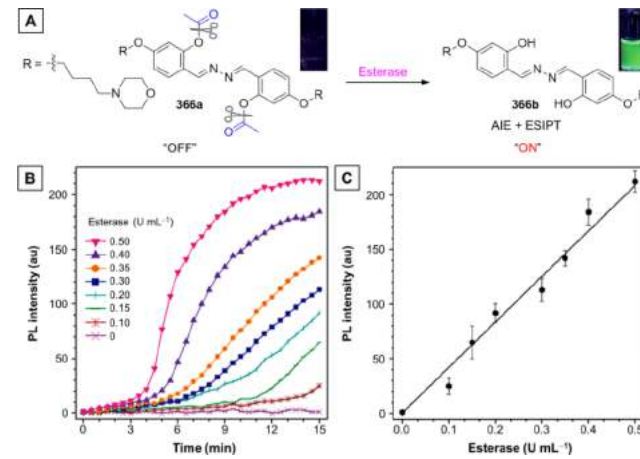


**Figure 90.** (A) Design of probe 366a for specific detection of lysosomal esterase. (B) Plot of fluorescence intensity of 366a (10  $\mu$ M) versus the reaction time in the presence of esterase with different concentrations. (C) Plot of the fluorescence intensity against the esterase concentration in the range of 0–0.50 U  $\text{mL}^{-1}$ . The measurements were performed in 10 mM PBS (pH 7.4). Adapted with permission from ref 545. Copyright 2014 Royal Society of Chemistry.

AIE effect, the design of it is quite different from those of the enzyme-specific AIE probes discussed above which requires very high hydrophilicity to guarantee a low background signal. The hydrophobic probe 366a is designed by integrating AIE with ESIPT and constructed by conjugating the salicylalazine fluorophore with esterase reactive acetoxy groups and lysosome-targeting morpholines (Figure 90A). The substitution of the hydroxyl groups with the esterase-specific substrate acetoxy groups blocks the ESIPT process and quenches the salicylalazine fluorescence, owing to the destruction of intramolecular hydrogen-bonding and the active intramolecular motions like rotation of the N–N bond. When the acetyl moieties are cleaved by esterase, the fluorescence of the corresponding product 366b would be lit up. The reconstructed intramolecular hydrogen-bonding is responsible for the “turn-on” response. It not only activates the ESIPT process but also rigidifies the molecular conformation, resulting in the activation of RIM process as well as the AIE process.

On the basis of this working mechanism (Figure 90A), 366a does show a good performance in esterase assay (Figure 90B,C). No discernible fluorescence is observed for 366a even in aqueous media; however, strong emission peaked at 532 nm emerges when sufficient amount of esterase is added into the detection medium. The fluorescence kinetic curves of the probing system upon incubation with esterase at different concentrations exhibited in Figure 90B reveal that the higher the concentration of esterase, the faster the cleavage rate and the stronger the fluorescence would be. For esterase at 0.50 U  $\text{mL}^{-1}$ , the fluorescence increase arrives at a plateau in 15 min with the curve

sigmoidal in shape because of the two-step sequential hydrolysis from **366a** to **366b**. As shown in Figure 90C, the fluorescence intensity linearly increases when the esterase concentration is in the range of 0.10–0.50 U mL<sup>-1</sup>. The detection limit is determined to be  $2.4 \times 10^{-3}$  U mL<sup>-1</sup>. The fluorescence enhancement of the assay system induced by esterase is 70–200 times higher than those caused by the interference substances, such as inorganic salts, vitamin C, reactive oxygen species (ROS), and proteins, confirming the high selectivity of **366a** to esterase. This enzyme assay system displays a number of superiorities including no self-quenching at high concentration, excellent signal-to-background ratio, large Stokes shift (176 nm), high specificity to esterase, low cytotoxicity, and lysosome-specific targeting ability. In the light of these, it has also been applied for *in situ* monitoring of lysosomal esterase activity in living cells, which will be discussed later in the following section.

Methyl parathion hydrolase (MPH) is an enzyme that catalyzes the conversion of methyl parathion (MP) to *p*-nitrophenol (*p*NP).<sup>546</sup> MPH can potentially be employed for the detoxification and/or detection of organophosphorous compounds in the environment.<sup>547</sup> More importantly, its application as an enzyme label has been recently demonstrated, which is drawing more and more attention. Since a good signal generating system is very essential to the improvement of the detecting sensitivity of an enzyme label, enormous endeavors have been directed in this regard but met with limited success. AIE strategy has been reported to bring new hope to this area, for an effective signal generating system for MPH has been established on the basis of it (Figure 91).<sup>548</sup> In this reporter system for MPH, the

mode with high selectivity and sensitivity. A detection limit of  $1 \times 10^{-5}$   $\mu\text{g mL}^{-1}$  or  $2.85 \times 10^{-13}$  M (the concentration of MPH) can be achieved, which is  $10^5$  times more sensitive than that given by the spectrophotometric approaches. A comparative study has been performed without MP, **350** displays a smaller fluorescent response and a much lower selectivity to MPH, suggesting the important role of MP in the light-on response as well as the selectivity of this assay system. This work has well exemplified the third strategy shown in Figure 85.

Lipids are a group of naturally occurring biomolecules that widely exist in living things. A large portion of the genes (~5%) in eukaryotic cells are dedicated to the synthesis of lipids in terms of their indispensable functions.<sup>549</sup> For example, they are vital to the constitution of cell membranes, energy storage, signal transduction, and molecular recognition.<sup>549,550</sup> As a unique diphosphatidylglycerol lipid, cardiolipin (CL) is exclusively found in the inner membrane of mitochondria and is comprised of four unsaturated acyl chains and a negatively charged polar head (Figure 92A).<sup>551</sup> CL plays key roles in various biological and physiological processes, such as oxidative phosphorylation, mitochondria-mediated respiration, and apoptosis.<sup>551–555</sup> The abnormalities in the level of CL is closely relevant to a vast range of diseases including Barth syndrome, heart ischemia, reperfusion, gliomas, cardiac hypertrophy and failure, Tangier disease, Parkinson's diseases, AIDS, and cancers.<sup>556–558</sup> Development of effective methods for the detection and quantitation of CL is thus of great significance.

10-Nonyl acridine orange (NAO) is the only fluorescent dye at present available for CL detection; however, its performance is far from satisfactory in terms of selectivity and sensitivity. By virtue of AIE strategy, a superior fluorescent probe (i.e., **347**) has been developed by our group for the CL sensing (Figure 92).<sup>559</sup> As previously mentioned, **347** is well soluble in aqueous media with the help of the quaternary ammonium moieties, and thus it shows nearly no emission in buffer. In the presence of CL-containing vesicles which were fabricated by the mixture of 1,1',2,2'-tetraoleoylcarniolipin (TOCL; Figure 92A) and 1,2-dioleoyl-sn-glycero-4-phosphocholine (DOPC), a stabilizer to the vesicles, the fluorescence of **347** is switched on. In contrast, coexisting with CL-free vesicles which were constituted solely by DOPC, the fluorescence remains very weak (Figure 92A). The response of **347** to other major lipids found on mitochondrial membranes, such as 1,2-dipalmitoleoyl-sn-glycero-3-phosphoethanolamine (DPPE), L- $\alpha$ -phosphatidyl-L-nositol (soy PI), 1,2-dioleoyl-sn-glycero-3-phospho-L-serine (DOPS), and N-hexanoyl-D-sphingomyelin (SM), has been examined to further evaluate the specificity of **347** toward CL and gain an insight into the working principle of this probing system. All these lipid-containing vesicles were fabricated at the exact percentage as mitochondrial membrane. As can be seen from Figure 92B, the fluorescence of **347** is selectively switched on with the TOCL-containing vesicles, whereas no pronounced fluorescence change is induced by other vesicles with the lipids at their physiological concentrations. This result together with a series of other experiments and analyses have corroborated that **347** binds to CL mainly via electrostatic attraction, which restricts its intramolecular motions and triggers the light emission. Although DOPS and PI are anionic lipids, with only one charge on each molecule and a small percentage (1% and 2%) in the total mitochondrial membrane lipids, their interference to the CL (~20%) detection is minimal. Since even other charged biomolecules can hardly affect the selectivity of this probe, **347** is workable in the complicated CL-containing vesicles which

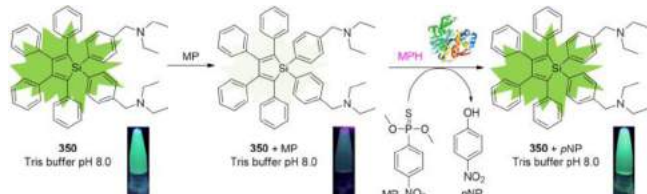


**Figure 91.** Principle of detecting methyl parathion hydrolase (MPH) with the **350**–MP complex as a probe. The fluorescent probe gives an emission at 490 nm in a Tris buffer at a pH of 8; upon addition of the enzymatic substrate methyl parathion (MP), the emission of the **350** is quenched, resulting in a low fluorescence background; upon further addition of the MPH, the quenched emission of the **350** recovered at 490 nm due to the turnover of the MP to *p*-nitrophenol (*p*NP) whose quenching effect was smaller than that of the MP. The recovered emission intensity was dependent on the amount of MPH. Adapted with permission from ref 548. Copyright 2014 Royal Society of Chemistry.

amino-functionalized HPS, i.e., A<sub>2</sub>HPS (**350**), serves as a signaling moiety whose fluorescence can be modulated between the “on” and “off” state by stimuli, whereas MP is a substrate for MPH and also a quencher to **350**. A unique fluorescence response of the ensemble towards MPH has been achieved. Owing to its hydrophobicity and AIE activity, A<sub>2</sub>HPS (**350**) shows a brilliant green emission in the Tris buffer (pH 8.0), but its emission is subsequently quenched by the addition of MP. This ensures a very low background for the detection of MPH. Upon reaction with MPH, MP is turned into *p*NP, a much weaker quencher to **350** as compared with MP. The initially quenched fluorescence emission is hence recovered (Figure 91). The restored fluorescence intensity exhibits a dependence on the concentration of MPH. At a fixed amount of **350** and MP, the amount of MPH can be reported by this system in a “turn-on”

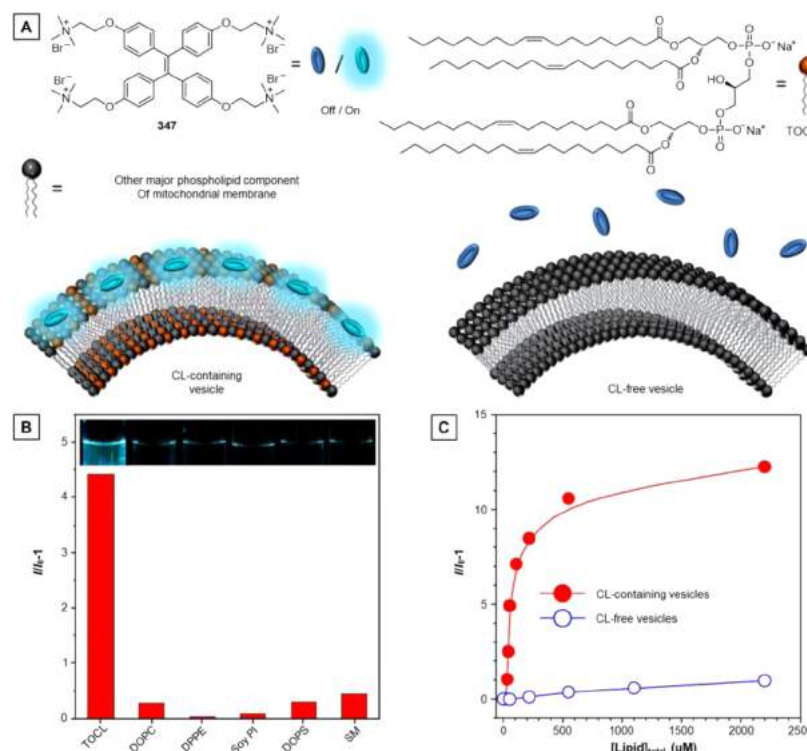


**Figure 92.** (A) Chemical structure of 347 and 1,1',2,2'-tetraoleoylcardiolipin (TOCL) and the working principle for the cardiolipin (CL) detection. (B) Change in fluorescence intensity of 347 with vesicles of different lipid contents (left to right, 20% TOCL, 100% DOPC, 40% DPPE, 2% soy PI, 1% DOPS, and 2% SM; the rest of each type of vesicle is filled by DOPC). Insets: Fluorescence photographs of 347 solutions in the presence of these vesicles. (C) Plot of the fluorescence enhancement ( $I/I_0 - 1$ ) of 347 at 480 nm with CL-containing and CL-free vesicles. Adapted from ref 559. Copyright 2014 American Chemical Society.

were prepared by mimicking the mitochondrial membranes. Whereas the response of the turn-off sensor NAO is greatly interfered by the other lipid compounds, both the selectivity and sensitivity are unsatisfactory. The fluorescence of 347 is dramatically intensified with the increase in the total lipid concentration of the CL-containing vesicles, which is quite different from the behavior of 347 with CL-free ones (Figure 92C). The fluorescence enhancement ( $I/I_0 - 1$ ) of 347 at 480 nm shows a linear response to the concentration of CL in the range of 0–10  $\mu\text{M}$ , indicative of its potential for quantitative analysis of CL in real samples.

This biomolecular sensing section has provided a great number of examples to prove the extraordinary charm of AIE as a powerful approach for sensitive and specific detection of biospecies. This unique sensing strategy is highly flexible, for it can not only work in turn-on/light-up mode but also function in a turn-off fashion, relying on the design in molecular structure of probes and experimental conditions. No matter in which fashion, the AIE effect benefits the performance of the sensing systems. The AIE approach is also widely applicable, because it can be employed to almost all biogenic species, no matter they are small or large, charged or neutral, active or inactive. The sensing systems built on AIE effect are highly effective, for they are usually easy-to-prepare, simple-to-operate, fast responsive, and highly sensitive. The last but not the least, AIE probing systems can be multifunctional, for example, they can recognize, quantify, monitor, and visualize the analyte and sometimes can even inhibit some destructive processes such as amyloid fibrillation. In a word, AIE offers numerous advantages, boundless opportunities, as well as infinite development space to the area of biosensing.

**5.1.2. Biological Imaging.** Biological imaging may refer to any imaging technique used in biology, but since most of the time, it is used for medical purpose and hence the term as “biomedical imaging” is derived. Usually, these two terms can alternate each other. More specifically, biological imaging is the technique and process that creates visual representation of the interior of a cell, tissue, or body for biological or clinical analysis and medical intervention. It is reported that biomedical imaging technologies occupy a significant portion of the health budgets of all developed economies, and most people have the need of advanced imaging during their life, making biological imaging research an appealing and vigorous area. There are various imaging modalities including fluorescence imaging, bioluminescence imaging, magnetic resonance imaging (MRI), optoacoustic imaging, photoacoustic imaging, ultrasound imaging, X-ray radiography, positron emission tomography (computed tomography; CT). Amongst these imaging techniques, fluorescence imaging is attracting more and more research interest owing to their advantages lying in the large variety of fluorescent reagents, strong labelling capability, intense output signal, high temporal and spatial resolution, low cost, and wide applicability. For fluorescence imaging, the most essential issue is the development of highly performed fluorescence imaging reagents, i.e., fluorogens. The commonly used fluorescence imaging reagents include organic dyes and proteins (e.g., green fluorescent protein) and inorganic quantum dots (QDs). However, the molar absorptivity and photobleaching resistance of currently available organic dyes or protein-based fluorescence imaging reagents are low. Moreover, the ACQ effect of conventional fluorogens also prevents them from being good players in biological imaging. Inorganic QDs are always suffering from high

cytotoxicity in oxidative environment. The high luminosity of AIEgens in the aggregate state and the distinct feature that AIEgens become stronger emitters at higher concentrations make them promising candidate reagents for fluorescence imaging applications. It has been found that the AIE-involved imaging systems show superior features to conventional organic dyes and QDs, such as large absorptivity, high brightness, excellent biocompatibility, free of random blinking, and strong photobleaching resistance.<sup>12,15,19</sup> These merits have enabled the use of AIEgens in fluorescent imaging at the subcellular, cellular, and/or tissue levels in a noninvasive and high contrast manner. Given that there are multitudinous examples, we summarize them in a clear and simple fashion and divide them into five categories in terms of constitution and function. The discussion will begin with the imaging systems comprised of small organic AIEgens (organic NPs), followed by those made from polymeric AIEgens (polymeric NPs), and then the unique systems named as “AIE dots”, and the AIE imaging systems constructed with silica matrix (silica NPs), and end with the systems showing dual or multiple functions. Note that the AIE-involved imaging systems presented here are referred to as “NPs”, which means the imaging reagents exist in the form of nanoparticles in biological systems.

**5.1.2.1. Organic Nanoparticles (NPs).** Organic NPs here refer to the fluorescent imaging systems purely based on small AIE molecules without any additional reagents. There have been a vast variety of such systems which are constructed on the basis of diverse AIEgens and used for organelle/cell imaging and tracing. For example, compound **8** is a TPE-CD conjugate.<sup>52</sup> Although it is already emissive in good solvent due to the restriction on the intramolecular motions of TPE motif imposed by the CD moiety (*vide supra*, Figure 8), it inherits high emission efficiency from TPE in the aggregate state. When incubated with HeLa cell in aqueous media, fluorogen **8** spontaneously aggregates into blue-emissive NPs. The NPs of **8** can penetrate the cell membrane and function as a fluorescent visualizer for intracellular imaging, which specifically stain the cytoplasm of the HeLa cells with high contrast (Figure 93A).<sup>52</sup> Aminated silole derivative **367** is an AIEgen with a high solid-state quantum yield of 36.5%.<sup>560</sup> The aggregation of **367** naturally occurs in the aqueous media, furnishing NPs with an average diameter of around 220 nm. The NPs of **367** are electrically neutral and cytocompatible and thus can be internalized into cells with high efficiency via a physical process. Interestingly, the NPs of **367** selectively stain the cytoplasmic regions of living HeLa cell with brilliant green fluorescence (Figure 93B). The cytophilic nature of these nanoaggregates and their hydrophobic interactions with membrane-enclosed organelles ensure their high retention ability inside the living cells. The leak-free lodging of these NPs prevents them from penetrating into the co-cultured human embryonic kidney (HEK) 293T cells, rendering them promising for the application in the discrimination of cancerous and normal cells. Moreover, the excellent cellular retention together with the high brightness of the NPs has enabled long-term cell tracking up to four passages and the visual monitoring of cell growth. The AIE organic NPs outshine the commercial Cell Tracker and MitoTracker bioprobes, considering that **367** can be used at high concentrations in subcellular/cellular imaging with long cellular retention. Inspired by the dual fluorescence (green and red) of TPE-B (**48**) in the aggregate state, in like manner, it has been incubated with HeLa cells in aqueous media.<sup>100</sup> Intriguingly, the NPs of **48** also specifically stain the cytoplasm of living HeLa cells with dual-colour output signals. Under blue or green excitation channels, the image exhibits bright green

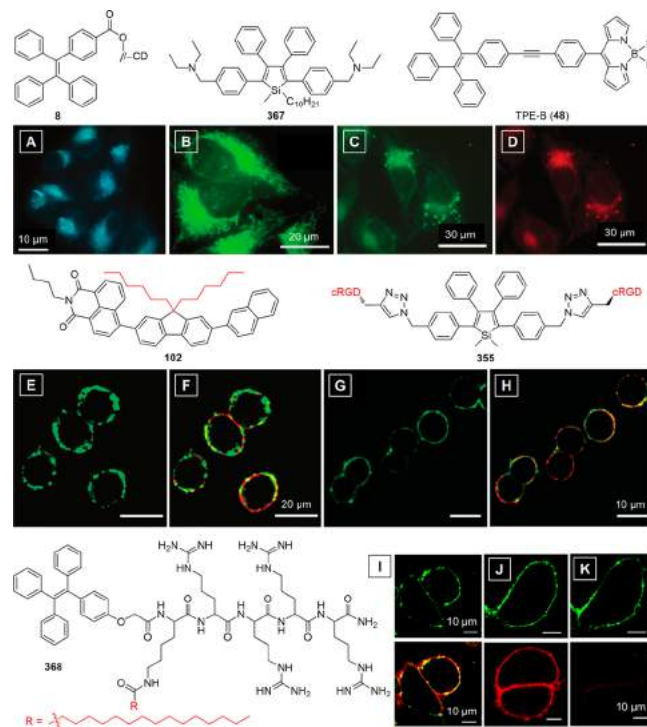


**Figure 93.** Representative AIEgens used for cytoplasm imaging (A–D, compounds **8**, **367**, and **48**) and cell membrane tracking (E–K, compounds **102**, **355**, and **368**). Fluorescent images of the HeLa cells stained by (A) **8**, (B) **367**, and (C and D) **48**. Panel A is reprinted with permission from ref 52. Copyright 2013 Royal Society of Chemistry. Panel B is reprinted with permission from ref 560. Copyright 2011 Wiley-VCH Verlag GmbH & Co. KGaA. Panels C and D are reprinted with permission from ref 100. Copyright 2012 Royal Society of Chemistry. (E) Confocal luminescence image of living HepG-2 cells stained by **102** and (F) its overlay image with the one obtained from DiI stained cells. Reprinted with permission from ref 141. Copyright 2013 Royal Society of Chemistry. (G) Fluorescent images of the HT-29 cells stained by **355**, and (H) its overlay images with the one obtained by staining the cells with membrane tracker. Reprinted from ref 506. Copyright 2012 American Chemical Society. (I) (upper panel) CLSM image of living MCF-7 cells stained by **368** and (lower panel) its merged image with the one obtained from DiI stained cells. CLSM images of living MCF-7 cells treated with (upper) **368** or (lower) DiI with increasing scanning time from (J) 0 min to (K) 9 min. Adapted from ref 31. Copyright 2014 American Chemical Society.

(Figure 93C) or red fluorescence (Figure 93D). Because of the hydrophobic nature of **48**, these NPs probably enter the living cells through endocytosis, where the NPs are enclosed by the cell membrane forming small vesicles, internalized by the cells and ultimately released to the cytoplasm.

Besides the cytoplasm-selective AIE NPs, quite a few other organic NPs based on AIEgens bear specific imaging/tracking ability to the cell membrane. The cell membrane (also known as cytoplasmic membrane or plasma membrane) is a biological membrane that segregates the interior of a cell from the outside environment. It protects the cell from the surroundings with its selective permeability, by regulating substances that enter and exit the cells.<sup>561</sup> Cell membranes are involved in a variety of cellular processes, including cell adhesion, ion conductivity, nutrient transport, and cell signaling.<sup>562</sup> Given the subcellular resolution under fluorescent microscopy, visualizing the membrane-related events is of great significance to biomedical research.<sup>563–566</sup> Currently, there are only a few commercial

organic fluorogens available for cell membrane monitoring, such as DiI<sup>567</sup> and DiO.<sup>568</sup> Thereby, the development of membrane-specific fluorescent probes is rather challenging but quite important. Recently, AIEgens emerge as new alternatives to these conventional dyes.

For instance, the organic dye **102** featuring TICT plus AIE characteristics could specifically adhere to and track the cell membrane (**Figure 93E**).<sup>141</sup> Owing to its hydrophobicity, AIEgen **102** spontaneously aggregates and forms NPs with an average particle diameter measured to be ~150 nm in aqueous media. In the light of the superb fluorescence efficiency ( $\Phi_F$  up to 73.0%) and low cytotoxicity, the NPs of **102** have been employed for cell imaging. After being incubated with living HepG-2 cells, the NPs selectively visualize the membrane region with intense green emission. In contrast, the cytoplasm and nucleus merely show very faint fluorescence signal (**Figure 93E**), indicating an extremely high signal-to-noise ratio. As shown in **Figure 93F**, the imaging region in **Figure 93E** overlaps well with the one obtained by DiI (red), suggesting that **102** is a good fluorescence imaging agent that can exclusively stain the cell membrane. Parallel investigations on the photostability of the NPs of **102** and DiI have been conducted in PBS solution. Because of the AIE feature, the NPs of **102** are much more photostable than the conventional organic dye. Thanks to the excellent photostability and strong adhesion to the membrane, NPs of **102** can specifically trace a cell membrane for as long as 4 days. As previously discussed, AIE-active silole-CRGD conjugate, i.e., **355**, is a light-up probe specific for integrin  $\alpha_v\beta_3$ .<sup>506</sup> Since integrin  $\alpha_v\beta_3$  is overexpressed on tumor/cancer cells, it is anticipated that **355** could specifically bind to the cellular membranes with overexpressed integrin  $\alpha_v\beta_3$ . Colon cancer cell HT-29 is a cell line that overexpresses integrin  $\alpha_v\beta_3$ . As can be seen from **Figure 93G**, when HT-29 cells are incubated with **355**, obvious fluorescence signal has been detected in the cell membrane region. Moreover, the excellent overlap between the fluorescent images of **355** (**Figure 93G**) and the commercial membrane tracker confirms the occurrence of specific binding on the cell membrane (**Figure 93H**).

As can be learnt from the molecular structures of DiI, DiO as well as **102**, the lipophilic structure is fairly critical to the membrane-specific probes, because it enables the probes to become embedded into cell membranes. Bearing this idea in mind, Liang and Zou et al. have smartly designed and constructed a cell membrane tracker based on a TPE derivative (**368**; **Figure 93I–K**).<sup>31</sup> The amphiphatic AIEgen **368** consists of three major components, namely, the TPE unit, the tetra-peptide sequence comprised of four arginine residues, and palmitic acid. These components serve as a fluorescence motif for signaling, positively charged hydrophilic moiety to target membrane, and lipophilic moiety for membrane insertion, respectively. It is worth mentioning that the hydrophobic TPE also contributes to the lipophilicity of the whole molecule. After being incubated with living MCF-7 cells in aqueous media, the amphiphatic **368** clusters into nanoscopic aggregates and lights up the cytoplasmic membranes (**Figure 93I**, green) due to the activated RIR process. No discernible fluorescence signal is observed in the nucleus and cytoplasm. By merging the regions imaged by the NPs of **368** and DiI, the green signal from **368** was found to co-localize with the red DiI signal (**Figure 93I**, red), suggesting that **368** is specific to the cell membrane. The photostability of **368** NPs and DiI was comparatively studied by continuous laser irradiation using confocal laser scanning microscopy (CLSM). The dramatic difference in their photostability is clearly exhibited in **Figure 93J,K**.

These results reveal that the AIE feature enables **368** to outperform the commercial dye DiI. In terms of its outstanding specificity to cell membrane, low cytotoxicity, and excellent photostability, **368** can be a potential alternative to DiI. Additionally, **368** can be utilized as a two-photon bioprobe for cell membrane tracking. When excited with a 700 nm two-photon microscopy in scanning lambda mode, intense fluorescence can be emitted from the cell membrane region of **368**-labelled HUVEC cells, which renders another advantage over conventional cell membrane imaging probes to **368**.

Mitochondrion, a membrane-bound organelle found in nearly all eukaryotes, plays pivotal roles in cell life and death.<sup>569</sup> These organelles are also described as “the powerhouse of the cell” because the most prominent functions of mitochondria are to produce the energy currency of the cell, i.e., ATP.<sup>570</sup> Moreover, mitochondria are involved in various metabolic tasks such as signaling through mitochondrial ROS, cellular differentiation, regulating cell cycle, growth, and death (e.g., mitochondria-mediated apoptosis).<sup>571,572</sup> They vary in number, location, and morphology according to cell type, cell-cycle stage, and intracellular metabolic state. Mitochondria have been implicated in several human diseases, such as mitochondrial disorders, cardiac dysfunction, and heart failure.<sup>573,574</sup> Especially, the morphology of mitochondria can be affected by cell functions and thus can reflect cell health.<sup>575</sup> The morphology is controlled by a set of proteins, mutations of which will lead to a number of diseases like degenerative diseases (e.g., Parkinson’s and Alzheimer’s diseases).<sup>576</sup> It has been recently reported that the proteins which participate in apoptosis can influence the morphology of mitochondria.<sup>575,577</sup> Specifically visualizing the mitochondria and tracking their dynamic morphological change is hence of remarkable biomedical value and may offer some insights for the study of apoptosis and degenerative conditions. Fluorescent probes are powerful tools for the monitoring of the morphological changes if they can exclusively illuminate cellular mitochondria. Specificity and photostability are the most important prerequisites to an efficient fluorescent probe used for the studying of dynamic changes in mitochondrial morphology. However, the conventional probes developed for mitochondria staining and tracking are less satisfactory in terms of photostability.<sup>578</sup> Very dilute working concentrations of these dyes are used in the imaging process, and such a few dye molecules can be quickly photobleached under a harsh laser beam excitation. The photostability cannot be improved through increasing the dye concentration because of the intrinsic ACQ effect. On the other hand, AIE may provide an effective solution to this problem, because the emission of an AIEgen is intensified along with the increase in concentration. Given these facts, a series of AIEgens with emission color ranging from blue to red are specially designed as photostable and specific fluorescent probes for mitochondrial imaging and tracking.<sup>32,579–581</sup>

For instance, the simple integration of archetypal AIEgen (e.g., TPE) with triphenylphosphonium (TPP), a well-accepted functional unit that facilitates the entrance of probe into mitochondria with the aid of its lipophilicity and electrophoretic force, has afforded a mitochondria-specific light-up probe **369** (**Figure 94A** and **94B**).<sup>580</sup> **369** inherits the AIE feature from its TPE parent and strongly fluoresces in the aggregate state. It spontaneously aggregates into NPs with an average size of 144 nm in aqueous solution containing 0.1% DMSO, the identical conditions for cell staining, suggesting that **369** will work in a nanoaggregation mode rather than as a molecular probe in the imaging process. The NPs of **369** has been testified to have low

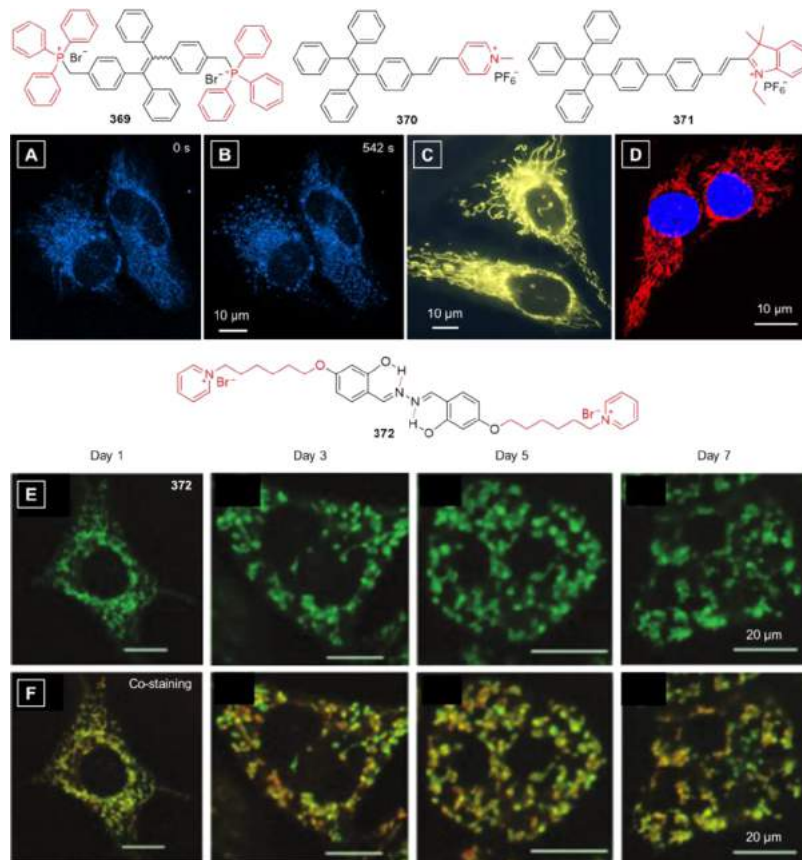


**Figure 94.** Fluorescent images of carbonyl cyanide *m*-chlorophenylhydrazone (CCCP, 20  $\mu$ M) treated living HeLa cells stained with **369** (5  $\mu$ M) with increasing scan time from (A) 0 s to (B) 542 s. Reprinted from ref 580. Copyright 2013 American Chemical Society. Fluorescent images of the HeLa cells stained by (C) **370** and (D) **371**. Reprinted with permission from ref 33. Copyright 2013 John Wiley and Sons. (E) Fluorescent imaging of differentiating brown adipose cells stained with **372** (5  $\mu$ M) and (F) their merged images with those stained by MitoTracker red FM (50 nM). Scale bar = 20  $\mu$ m. These images were obtained using a confocal microscope. Adapted with permission from ref 581. Copyright 2014 Royal Society of Chemistry.

cytotoxicity and applied for mitochondrial staining in living HeLa cells. The NPs of **369** specifically enter and light up the mitochondrial region, rendering the reticulum structures of mitochondria clearly visible with bright blue fluorescence (Figure 94A). The specificity has been further verified by the comparison with the image obtained from the commercial mitochondria probe MitoTracker red FM (MT). The photostability of **369** NPs and MT have been comparatively studied and apparent difference has been shown. The signal loss of **369** NPs in cells is less than 20% during 50 scans with total irradiation time of  $\sim$ 7 min, whereas the fluorescence signal of MT almost disappears after only 6 scans with a remained signal intensity <25%. The nanoaggregates formation is very crucial to this imaging agent. For one thing, it facilitates the diffusion of the dye cross the cell membrane to accumulate in the mitochondrial region. For another, it activates the AIE process and ensures the high brightness. When exposed to excitation light, the NPs protect the most part of the dye inside the particles from photobleaching or photo-oxidation and hence guarantee the photostability. With these emissive and photostable NPs, the dynamics of mitochondrial morphology can be monitored. Carbonyl cyanide *m*-chlorophenylhydrazone (CCCP) is used to induce mitochondrial morphology change. When exposed to CCCP, the gradual transformation from reticulum-like mitochondria (Figure 94A) to small dispersed fragments (Figure 94B) has been clearly visualized by the **369** NPs. With high specificity, superb photostability, and appreciable tolerance to micro-environmental change, **369** is undoubtedly a promising imaging

agent for mitochondrial targeting and morphological change tracking.

Encouraged by the exciting work done with **369**, our group has dedicated more efforts to the enrichment of mitochondria-specific AIE probes as well as the improvement of their performance. With smart molecular design, even without TPP moiety, AIEgens like **370** and **371** can still work as light-up probes specific to mitochondria (Figure 94C,D).<sup>32,33</sup> The specificity/selectivity should be ascribed to their unique structures. Each of these two AIEgens is composed of a large lipophilic/hydrophobic moiety donated by TPE motif and other  $\pi$ -conjugate groups, together with a positively charged head. Therefore, with analogous structural characteristics and AIE feature, these two fluorophores could function as well as **369** in a similar manner. Moreover, with well-extended electronic conjugation and strong D-A effect, the nanoaggregates of **370** and **371** in mitochondria emit yellow and red fluorescence, respectively. It is noteworthy that the images of mitochondria stained by **370** and **371** show even higher resolution than that of **369**. The possible reason for this observation might be that the autofluorescence from the cells is avoided due to the mismatch in the excitation wavelength. Such kind of studies not only expand the variety of preeminent mitochondria visualizers but also provide more insight into their molecular design. Enlightened by this research, a general principle can be put forward that if a fluorogen possesses the AIE attribute, sufficient hydrophobicity and cationic moiety, its excellent performance as a mitochondria-specific probe can be anticipated.

Recently, another interesting work related to specific mitochondrial imaging has been jointly carried out by Liu's team and our group.<sup>581</sup> Salicylalazine, a typical AIE-active ESIPT compound, has been decorated with two positively charged pyridinium groups, generating the new fluorescent probe 372. The two hexyloxy spacers together with the central salicylalazine core ensure the lipophilicity of the probe. In this way, 372 can be mitochondria-specific owing to its hydrophobic and cationic nature. The molecules of 372 form nanoaggregates or NPs in aqueous media. Benefiting from the AIE and ESIPT features, the NPs of 372 are highly emissive without self-quenching instead with a large Stokes shift (176 nm). They are also much less cytotoxic than MT and hence can be used for living cell imaging. The live brown preadipose cells were chosen as a model for mitochondria tracking considering their distinguishing features in structure and functions. The brown adipose cells can dissipate energy as heat.<sup>582</sup> In the light of this, increasing interest has been attracted towards understanding the differentiation process of brown adipose cells, which are vital to the treatment of obesity-related diseases.<sup>582,583</sup> A critical feature of brown adipose cells during differentiation is that their mitochondrial content and activity will increase to satisfy the larger metabolic demands. Delightfully, with the aid of the noninvasive fluorescent probe 372, the changes in number, morphology, as well as sub-cellular localizations of mitochondria can be observed with ease (Figure 94E,F). During the differentiation process, the overall cellular shape changes from fibroblastic to spherical. At days 1 and 3, the mitochondria retain the tubular and reticular structures. At days 5 and 7 of differentiation, the mitochondria hold a punctate morphology. The specific imaging of 372 for mitochondria has been confirmed by the comparative study with MT (Figure 94F). This AIE probe (372) for mitochondria imaging enjoys a lot of superiorities, such as simple synthesis, high cell permeability, excellent signal-to-background ratio, good cellular retention ability, as well as strong resistance to photobleaching, enabling it to identify the differentiation stages of brown adipose cells in a fast and convenient fashion.

In addition to mitochondrion, lysosome is another membrane-bound cell organelle found in most animal cells. Lysosomes are spherical vesicles containing hydrolytic enzymes capable of breaking down almost all kinds of biomolecules. They thus serve as the waste disposal sites of cells and are also responsible for cellular homeostasis, plasma membrane repair, cell signaling, and energy metabolism, thereby closely relevant to health and diseases.<sup>584</sup> Their sizes vary upon their functional activity and hence visualizing their morphology, mapping their distribution and locations, tracing their movements in living cells have great biological implications. As mentioned in the above section, 366a is a light-up probe for lysosomal esterase.<sup>545</sup> Since it has been equipped with two lysosome-targeting morpholine units, 366a is envisioned to be able to monitor the lysosomal esterase in living cells. Owing to its hydrophobic nature, 366a exists as NPs in the cell-culture media and so does its hydrolysis product 366b, the source of fluorescence signal. A discrete labeling pattern that matches the distribution of lysosomes is obtained from living MCF-7 incubated with 366a (Figure 95A). Such a pattern overlaps well with the LysoTracker Red costaining (Figure 95B), revealing the high specificity of 366a for lysosomes. It has been verified that the morpholine groups play a critical role in the selective lysosome targeting. The control fluorophore without morpholine units cannot be efficiently internalized into the cells, which results in weak fluorescence signal, low contrast, and no specificity. Moreover, the NPs of 366a are very photostable

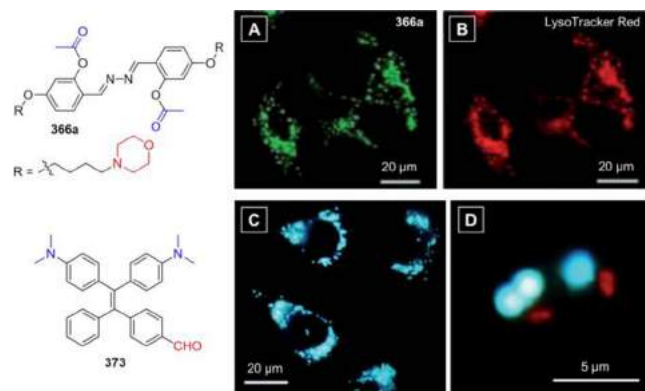


**Figure 95.** Confocal images of MCF-7 cells stained with (A) 1  $\mu$ M 366a and (B) 50 nM LysoTracker Red. Reprinted with permission from ref 545. Copyright 2014 Royal Society of Chemistry. (C) Fluorescent images of liver LO2 cells stained with 373 (10  $\mu$ M) after incubation in the presence of 50  $\mu$ M oleic acid for 6 h. Staining time: 15 min. (D) Fluorescent images of green algae stained with 373 (2.5  $\mu$ M) in the presence of 20 vol % DMSO at 40 °C for 10 min. The blue emission is from the lipid droplets; the red emission is from the chloroplast. Reprinted with permission from ref 600. Copyright 2014 Royal Society of Chemistry.

during the continuous laser scanning with a signal loss less than 20% in 8 min, which is much smaller than that of the LysoTracker Red (~70%). The NPs of 366a also have the ability to be used for in-situ monitoring of lysosomal esterase activity and real-time imaging of lysosome. It is accepted that figuring out the spatial and temporal distribution of lysosomes is conducive to the diagnosis of lysosomal storage diseases.<sup>585</sup> With this superb probe (366a), the lysosome movements even slight ones can be tracked and visualized.

Lipid droplets (LDs) are lipid-rich cellular organelles that regulate the storage and hydrolysis of neutral lipids and are found largely in the adipose tissue.<sup>586–588</sup> LDs are regarded as highly dynamic organelles that play a very important role in the regulation of intracellular lipid storage and metabolism, membrane formation and maintenance, protein binding and degradation, signal transduction.<sup>589–593</sup> Their regulation functions and level have a close association with inflammatory responses and metabolic disorders, such as obesity, cancer, fatty liver disease, type II diabetes, hyperlipidemia, and atherosclerosis.<sup>594</sup> Besides its biomedical significance, the LD is a type of alternative biofuel for sustainable energy.<sup>595</sup> Fluorescence techniques are effectual means to study LDs in living cells and tissues in virtue of their advantages such as high sensitivity, visibility, and adjustability in the design of bioprobes.<sup>27</sup> Enlightened by the D-A structural features of the developed LD dyes such as Nile red and Seoul-Fluor-based fluorogens,<sup>596–599</sup> a TPE derivative, namely, 373, bearing alkylamino (D) and carbonyl (A) groups has been designed and synthesized, in pursuit of a new imaging agent for LDs.<sup>600</sup> Owing to the D–A effect and AIE activity, 373 emits orange fluorescence in the aggregate state. Similarly, 373 also self-aggregates in the aqueous media, giving brilliantly emissive nanoscale particles. These NPs are biocompatible and thus then used to successively stain HeLa cells, liver LO2 cells, and green algae to access their capability of LD-specific imaging. As indicated by the experimental results, the NPs of 373 spontaneously enter the living HeLa cells and liver LO2 cells (Figure 95C) and selectively light up the spherical LDs within a short time (~10–15 min). 373 is a lipophilic fluorogen prone to accumulate in the hydrophobic LDs, which accounts for the

specificity. It is notable that the fluorescence from the labelled LD is blue, whereas 373 is orange emissive in aqueous media. This is ascribable to the solvatochromism property of 373 as well as the less polar environment in LDs. Oleic acid is a known stimulator to the production of LD in cells. Exposing the liver LO2 cells to increased concentrations of oleic acids can trigger the generation of more LDs. Such a process can be visualized and tracked by 373 with high resolution and high signal-to-background ratio (Figure 95C), suggesting its potential application for in vitro transhepatic biopsy to aid the diagnosis of early-stage liver diseases. Algae are potential environment-friendly alternatives to fossil fuels. The content of lipids is an important evaluation criterion of their value. 373 was further used for the LDs imaging in algae with the green algae *Nannochloropsis sp.* as a model. A certain amount of DMSO was added into culture media to facilitate the diffusion of 373 into the algae. When green algae was co-incubated with 2.5  $\mu\text{M}$  373 at 40 °C for 10 min in the presence of 20 vol % DMSO, a clear image with the lipid content identified by the greenish blue fluorescence of the probe can be easily acquired (Figure 95D). Note that the red emission from the chloroplast can be distinguished from the LDs. The size of LDs is reflected by the diameter of green emission region, and in the meantime, the total lipid content in the LD body could be correlated with the overall brightness of the image, demonstrating the feasibility of utilizing 373 for facile and high-throughput screening of algae species with high lipid (bio-fuel) contents.

In addition to the selective imaging of cytoplasm and organelles, the monitoring of some specific cellular/intracellular processes and events can also be realized by taking advantage of AIE effect and/or AIEgens. As the smallest units and “building blocks” of life, cells are highly organized.<sup>601</sup> Proper conditions are required for cellular compartments to play their routine functions. Abnormal variation in the intracellular environments will affect cellular behaviors and pathological conditions. Take the intracellular pH ( $\text{pH}_i$ ) for example.  $\text{pH}_i$  plays critical roles in the regulation of many cellular behaviors, such as proliferation and apoptosis as well as enzyme activity and protein degradation.<sup>602</sup> The normal range of  $\text{pH}_i$  is from 4.7 in lysosome to 8.0 in mitochondria. Mutation in the  $\text{pH}_i$  may result in dysfunction of the organelles, and the anomalous  $\text{pH}_i$  is thus an indicator of many well-known diseases including cancer, stroke, and Alzheimer’s diseases. Considering the significance of sensing and monitoring pH changes inside living cells, great effort has been devoted to this subject. Although probes with decent performance have been achieved, full-range  $\text{pH}_i$  sensing remains challenging. Recently, our group has designed an AIEgen (i.e. 336a) comprised of TPE and cyanine moieties, which shows ratiometric fluorescence response to the thiol species, as a result of nucleophilic addition reaction.<sup>415</sup> As revealed by the retro-structural analysis, there are three reactive sites lying in the vinyl-indolium segment of 336a, which are open for nucleophilic addition (Figure 96). Since  $\text{OH}^-$  can also act as a nucleophile, it is unsurprisingly that 336a gives a significant ratiometric response in fluorescence to the pH change.<sup>603</sup> As the detailed mechanism will be explicated later in the **Chemical Sensing Section**, herein we will just briefly summarize the main results and focus on the introduction of its biological application as a probe for  $\text{pH}_i$  sensing.<sup>604</sup> 336a features large Stokes shift (> 185 nm) and AIE characteristics, which together with the well-defined reactivity of 336a with  $\text{OH}^-/\text{H}^+$  endow it with the capability to sense  $\text{pH}_i$  in a wide range, the broadest to date.

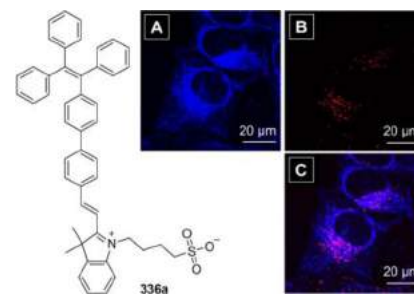


**Figure 96.** Confocal images of HeLa cells incubated with 336a for 2 h under excitation of (A) 405 and (B) 488 nm. (C) Image merged from those in panels A and B. [336a] = 10  $\mu\text{M}$ . Adapted from ref 604. Copyright 2013 American Chemical Society.

336a exhibits red fluorescence with strong-to-medium and weak-to-nil intensities at pH 5–7 and pH 7–10, respectively, and nil-to-strong blue fluorescence at pH 10–14. More importantly, in the physiological range (pH 5.0–7.4), the fluorescence intensity of 336a changes with pH in a linear fashion, making it a promising fluorescent  $\text{pH}_i$  indicator. 336a has been found to be biocompatible and cell-permeable. After entering a live cell, the nanoaggregates of 336a distribute in the cytoplasm and accumulate in certain organelles to give the fluorescence signal due to its AIE attribute (Figure 96A–C). As shown in Figure 96A, the majority of the cytoplasmic region stained by 336a emits strong blue fluorescence upon excitation at 405 nm. Red fluorescence signals can be collected in a pattern different from that of the blue ones, when excited at 488 nm (Figure 96B,C). Whereas the regions with intense blue fluorescence are more alkalescent, the red signals are from the acidic organelles such as lysosomes (Figure 96C). Because of the interaction with the lipid components in cells, the red-to-blue emission transition point shifts from extracellular pH 10 to the intracellular physiological pH range. As the ratio of the blue-to-red signals from 336a corresponds to the local pH, mapping of  $\text{pH}_i$  in the cytoplasm can be achieved, implying that 336a has a great potential for high-resolution and high-throughput analysis of intracellular environments.

As mentioned above, detection and sensing of the intracellular/cellular environments and events are of great importance. Cancer, for example, is hardly detectable in clinics until it is beyond control. However, during the development process of cancer or some diseases, there will be some special signaling substances released as markers. Therefore, signature information crucial for early diagnosis, susceptibility assessment, and metastasis prediction can be unveiled by detecting and tracing various molecular changes in living systems.<sup>605–607</sup> Despite that numerous research efforts have been invested to this end, given the increasing challenges in the sensitive, dynamic and multiparameter detection of cancer-related molecular events in complicated biosystems, there is still a long way to go before achieving that ambitious goal. However, a bright future of this research theme can be envisioned in the light of the extraordinary performance of the AIEgens in the biological area.<sup>12,15,19,608,609</sup> For instance, Zhang et al. have recently reported an AIE probe (i.e. 374) consisting of TPE and a specific peptide IHGHIIISVG (referred to as AP2H), which can be used for the direct detection and imaging of cancer cells by targeting tumor-related markers (Figure 97).<sup>609</sup> In 374, AP2H serves as a recognition moiety in view of its specific binding to the hydrophilic extracellular loop (EL2, PYRDDVMSVN) of lysosomal protein transmembrane 4 beta (LAPTM4B),<sup>610</sup> which is a

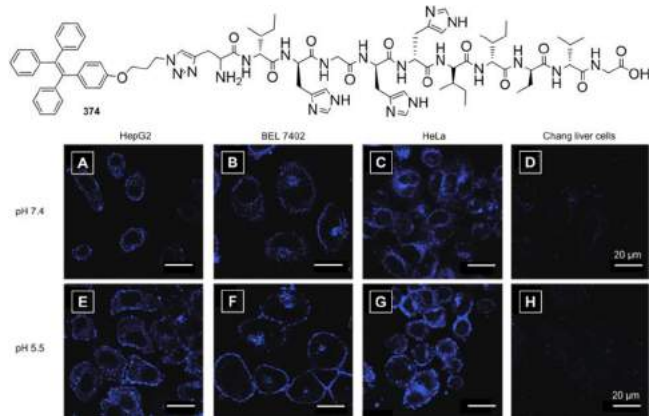


**Figure 97.** Discrimination of the expression level of LAPTm4B protein in different cells by 374. CLSM images of (A, E) HepG2 cells, (B, F) BEL 7402 cells, (C, G) HeLa cells, and (D, H) Chang liver cells incubated with 374 in neutral (pH 7.4) and acidic (pH 5.5) environments, respectively; scale bars: 20  $\mu$ m. Reprinted with permission from ref 609. Copyright 2014 Wiley-VCH Verlag GmbH & Co. KGaA.

unique tumor biomarker overexpressed in most solid tumors, including liver, lung, breast, cervix, and ovary.<sup>611</sup> The abnormal appearance and distribution of LAPTm4B is supposed to be an indicator for cancer susceptibility, prognosis, and the optimization of chemotherapy.<sup>612–614</sup> The target-activatable probe 374 is nearly non-emissive after incubation with normal cells. In contrast, when incubated with 374 for 60 min, the human liver carcinoma HepG2 cells, a type of LAPTm4B-overexpressed live cancer cells, are clearly visualized with blue fluorescence under CLSM (Figure 97A). Thanks to the AIE feature of 374, high-contrast staining of the cancer cellular membrane was achieved dispensing with the washing step. The binding process of 374 to the LAPTm4B protein on cancer cells has been imaged and monitored: as incubation prolonged, blue fluorescence signal emerges and gets intensified. The spatial distribution of the LAPTm4B protein in different cells has been investigated with another human hepatocellular carcinoma cell line, BEL 7402. The distribution of blue fluorescence in 374-stained BEL 7402 (Figure 97B) is different from the unevenly scattered signals observed for HepG2 cells (Figure 97A), reflecting the different ubiquitylation status of LAPTm4B protein in these cells. Note that the intracellular fluorescence signals in the image of BEL 7402 indicate the intracellular delivery of the probe and reflect the movement of LAPTm4B from the cellular membrane to the cytoplasmic regions of the live cancer cells. In other words, the spatiotemporal distribution of this cancer marker and its dynamic process in live cells can be monitored by AIEgen 374.

A low extracellular pH value is a hallmark of solid tumors at both very early and advanced stages, and it is closely correlated with tumor growth and development.<sup>615–617</sup> Thereby, sensing of tumor-related acidosis is important to cancer cell imaging and the delivery of therapeutic drugs. To assess the capability of 374 to distinguish acidic microenvironments, four different types of cells were incubated with 374 in neutral (pH 7.4) and acidic (pH 5.5) media, respectively. HepG2, BEL7402, and HeLa cells, which come from different solid tumor sources (hepatoblastoma, adult hepatocyte, and cervix, respectively), are all lit up by 374 (Figure 97). In comparison, Chang liver cells from a normal human liver exhibit no observable fluorescence in either neutral or acidic media due to the lack of LAPTm4B protein (Figure 97D,H).

Stronger fluorescence signals are given by all these three types of cancer cells under acidic conditions (Figure 97E–G), which is attributed to the stronger binding of AP2H on 374 to the LAPTm4B protein in the environment with lower pH. In this way, both the expression level of the LAPTm4B protein and the characteristic low-pH microenvironment of the tumor cells can be simultaneously evaluated by 374 with the aid of its AIE character and the histidine residues in AP2H. In virtue of these advantages as well as its low cytotoxicity and high photostability, this dual-responsive bioprobe is hence promising for the *in vivo* recognition and imaging of tumor cells.

Apoptosis, also referred to as programmed cell death, is an important cellular event that always occurs in multicellular organisms.<sup>618,619</sup> Apoptosis is a critical and active regulatory pathway of cell growth and proliferation. Deregulated cell apoptosis can ultimately cause many diseases, including cancers, neurodegenerative diseases, autoimmune diseases, atherosclerosis, myocardial infarction.<sup>533,620</sup> Real-time imaging and monitoring of the progress of apoptosis in living organisms is thus not only of diagnostic value but also has therapeutic significance to apoptosis-related diseases.<sup>621</sup> As mentioned in Section 5.1.1.2, caspase especially caspase-3 is an well-accepted key mediator of cell apoptosis and becomes a well-defined biomarker for apoptosis imaging. Since TPE-peptide conjugate 364 has been developed and shows light-up response to caspase-3/-7 in aqueous media, the potential of this probe (364) for live-cell imaging of caspase-3 activation (i.e. cell apoptosis) was further explored by Liu and Tang et al. (Figure 98A–C).<sup>534</sup> As indicated by the MTT assay, 364 enjoys low cytotoxicity. After incubation with 364 for 2 h at 37 °C, MCF-7 cells were treated with the commonly-used apoptosis inducer, staurosporine (STS, 1  $\mu$ M). With 1 h incubation, intense fluorescence signals are collected, indicating the intracellular delivery of the imaging probe. In contrast, under identical experimental conditions, extremely low fluorescence signals have been shown by the normal and uninduced cells, suggestive of the caspase-specific activation of 364. Undeniably, 364 is a light-up probe with a high signal-to-background ratio suitable for caspase-3 activity detection and apoptosis imaging in live cells. Real-time imaging experiments were further carried out to monitor the cell apoptosis process. After being incubated with 364 (5  $\mu$ M) for 2 h at 37 °C, MCF-7 cells were treated with STS (1  $\mu$ M) and monitored with fluorescence microscopy. The dark background in the images exhibited in Figure 98A–C suggests that the probe is non-fluorescent in the cell culture media. As the incubation time elapses, the fluorescence is gradually intensified with the proceeding of cellular apoptosis (Figure 98A–C), which reaches the maximum at 90 min (Figure 98C), manifesting that 364 possesses the capability for real-time monitoring of cell apoptosis. Furthermore, the AIE activity of 364 allows it to be utilized for *in situ* screening and quantification of apoptosis-inducing agents in living cells.

In the light of the simplicity, low cost, and high efficiency of 364 as a live cell apoptosis imaging probe, it can be envisaged that further tuning of the emission of AIEgens to the longer wavelength region would facilitate the development of specific bioprobes for *in vivo* imaging of cell apoptosis and drug screening. It is because that *in vivo* imaging usually favors fluorogens with large Stokes shifts and long-wavelength absorption and emission in order to eliminate or minimize the autofluorescence from biosubstrates. In consideration of this, AIEgens-peptide conjugates analogous to 364 but with longer emission wavelengths have been designed, such as TPE-Py-DVED-Ac

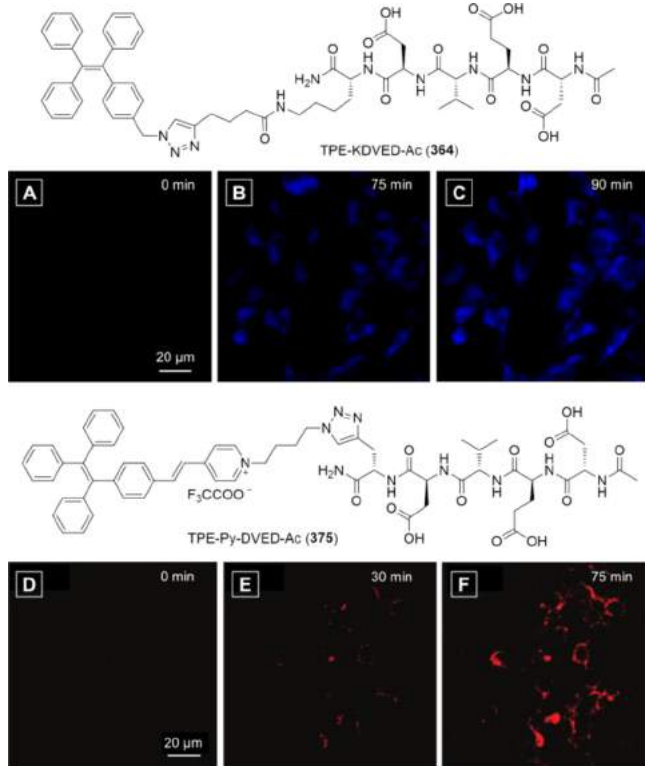


**Figure 98.** Real-time fluorescence images showing the cell apoptotic process of MCF-7 cells with (A–C) TPE-KDVED-Ac (364) and (D–F) TPE-Py-DVED-Ac (375) at room temperature. Staurosporine (STS, 1  $\mu$ M for 364 and 3  $\mu$ M for 375, respectively) was used to induce cell apoptosis. The images A–C were acquired using a fluorescence microscope (Nikon) equipped with a DAPI filter. Reprinted from ref 534. Copyright 2012 American Chemical Society. The images D–F were acquired with CLSM under excitations at 405 nm using optical filters with band passes of 575–635 nm. All images have the same scale bar (20  $\mu$ m). Reprinted from ref 535 published by the Royal Society of Chemistry and licensed under a Creative Commons Attribution 3.0 Unported Licence via <http://creativecommons.org/licenses/by/3.0/>.

(375).<sup>535</sup> Similarly, 375 has been constructed by conjugating a hydrophilic N-terminal acetyl protected and C-terminal alkyne-modified Asp-Glu-Val-Asp (Ac-DEVD) peptide with a hydrophobic azide-decorated TPE-pyridinium fluorophore via Cu(I) catalyzed “click” reaction. Owing to the extended electronic conjugation as well as the D-A or electron push-pull effect, orange red emission has been achieved for 375, which is in some sense, more advantageous to bioimaging. With a similar molecular structure and AIE feature, 375 behaves in a like manner to 364: it is soluble and thus almost non-fluorescent in aqueous media; strong fluorescence is turned on once 375 is specifically hydrolyzed by active caspase-3/7 at the C-terminal of Asp (D), as a result of the poor solubility and self-aggregation of the TPE residues. 375 is also biocompatible and can be used for live-cell imaging of caspase-3 activation. Both the normal and apoptotic MCF-7 cells which were pretreated with 375 have been imaged by the confocal microscopy. The un-induced cells display very low fluorescence signals, indicating the low background from the probe and little/no caspase-3 activity. In sharp contrast, intense fluorescence signals have been collected for the STS-treated MCF-7 cells with high resolution and contrast. Real-time monitoring of cellular apoptosis has also been realized with 375 (Figure 98D–F). The fluorescence gradually increases along with the cellular apoptotic progress and arrives to

the maximum in 75 min (Figure 98F). This AIEgen can also work as a light-up probe for the *in situ* screening of drug or apoptosis-inducing agents in living cells. Thanks to its AIE character and orange-red fluorescence, the probe can be employed for *in vivo* apoptosis imaging and work in a turn-on mode. After intratumoral injection of 375, the normal tissue or tumors without STS treatment show very weak fluorescence signal. Like the *in vitro* imaging, gradually increasing fluorescence signals are observed from the tumors treated with 375 and STS, due to the induced apoptosis.

As can be seen from the above two examples, real-time apoptosis imaging at the single cellular level indeed can aid in the diagnosis and drug-screening for diseases associated with apoptosis. Since the deregulation of apoptosis can lead to cancers and induce responses to anticancer treatments, real-time apoptosis imaging of cancer at the cellular level can offer new opportunities in the early prognosis and progress tracing of cancers as well as the efficacy estimation of anti-cancer agents. Therefore, effective and sensitive probes with the capability of real-time apoptosis imaging in target cancer cells are in urgent demand. To simultaneously satisfy the requirements of cancer-targeting ability and apoptosis-specific imaging, an asymmetric AIEgen, namely, 376, has been designed on the basis of the above discussed apoptosis imaging agents (364 and 375) and the integrin  $\alpha_v\beta_3$ -targeting probe (355).<sup>536</sup> From the structural and functional point of view, 376 consists of three major parts, namely, the TPS unit, cyclic Arg-Gly-Asp (cRGD) peptide sequence, and the Ac-DEVD peptide which, respectively, serve as signaling, cancer-targeting, and apoptosis/caspase-3 recognition motifs (Figure 99A). This asymmetric probe is virtually

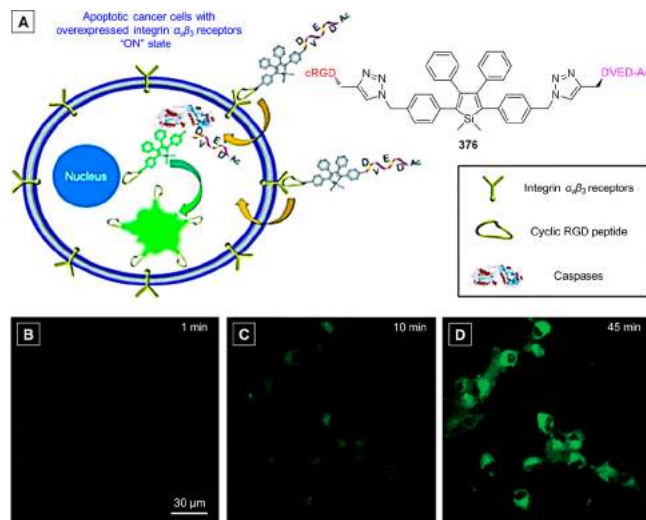


**Figure 99.** (A) Molecular structure of 376 and the principle of apoptosis imaging in target cancer cell based on 376. (B–D) Real-time CLSM images displaying the apoptotic progress of 376-stained U87MG cells upon STS-induced apoptosis at room temperature. [376] = 5  $\mu$ M, [STS] = 1  $\mu$ M. All images share the same scale bar. Adapted with permission from ref 536. Copyright 2013 Royal Society of Chemistry.

non-emissive in aqueous media. Caspase-3 significantly switches on the probe fluorescence due to the cleavage of DEVD moiety via caspase-catalyzed hydrolysis and the subsequent aggregation of the released TPS-cRGD residues, which activates the RIM process of TPS and populates the radiative relaxation channels.

Such a fluorescence light-up probe has been successfully utilized for real-time targeted imaging of cancer cell apoptosis

with the integrin  $\alpha_v\beta_3$  receptor-overexpressed U87MG human glioblastoma cells as an example (Figure 99B–D). The working principle of this asymmetric probe is schematically illustrated in Figure 99A. By virtue of the specific and efficient binding between cRGD and integrin  $\alpha_v\beta_3$  receptors, 376 is preferably internalized by integrin  $\alpha_v\beta_3$  receptor-overexpressed cancer cells over other cells with low receptor expression on the cell membrane. Considering that 376 is highly water-soluble, it is speculated that the intracellular 376 up-taken by healthy cancer cells without apoptosis can still maintain the fluorescence “off” state. On the other hand, when the AIEgen is internalized into apoptotic cancer cells, the activated caspase should exclusively cut off the Ac-DEVD moiety from 376, releasing the amphiphilic TPS-cRGD fragment which will light up the cells upon binding to cell components or form nanoaggregates in situ. The binding is also conducive to the retention of AIE probe inside the cancer cells, which ensure the good contrast for the real-time imaging of apoptosis progress. All the experimental results are perfectly consistent with the above hypothesis. The real-time CLSM images for STS-treated U87MG cells recorded within 1 h duration are shown in Figure 99B–D. The green fluorescence gradually gets more intense over time along with the progress of apoptosis, and the saturation is reached at 45 min. These results substantiate that this AIE probe is capable of real-time imaging and monitoring cancer cell apoptosis in a specific and sensitive manner. Additionally, this probe is also safe in terms of low cytotoxicity. It is worth mentioning that the cRGD plays dual functions in the imaging, namely, the targeting effect and improving sensitivity by offering a low background signal. Such systematic works from 364 to 375 and then to 376 are thus of guiding significance to the molecular design for more apoptosis imaging agents based on AIEgens.

The study on microorganisms is an important research subject called microbiology. Microorganisms are crucial to human beings and environments, as they fulfill a vast variety of roles in the areas spanning from ecological equilibrium maintaining, environmental monitoring and treatment, medical hygiene, and food processing to pharmaceutical industry.<sup>622,623</sup> Bacteria constitute a large domain of prokaryotic microorganisms and have been widely used in waste processing and bioremediation, pesticides, and pharmaceuticals, etc. Long-term tracing of bacteria as well as monitoring of their viability have great implications in the quality assessment of water and food under storage or use, disinfection efficiency evaluation, and pharmacokinetics and pharmacodynamics investigation of antibacterials.<sup>624</sup> Amongst the methods developed for the bacteria viability evaluation, fluorescence-based techniques are superior in virtue of their high sensitivity, easy operation, and rapid response. A number of fluorescent dyes have been exploited for bacteria assay, among which propidium iodide (PI) is the most extensively used imaging agent. However, PI suffers from high cytotoxicity and poor photostability, making it unsuited to be used in long-term tracking study. In addition to its glucose sensing ability, our group have uncovered another important function of 329 as a fluorescent visualizer for the discrimination of live and dead bacteria (Figure 100A–C).<sup>34</sup> In contrast to PI, 329 is highly fluorescent, photostable, and very friendly to bacteria, rendering it well-suited for long-term bacterial viability tracing.

After incubation with 329 for 0.5–3 h, no fluorescence is given by live bacteria (Figure 100B), while intense emission is observed from dead bacteria (Figure 100C). The staining mechanism of 329 for dead bacteria which has been verified by a series of experiments is schematically demonstrated in Figure 100A.

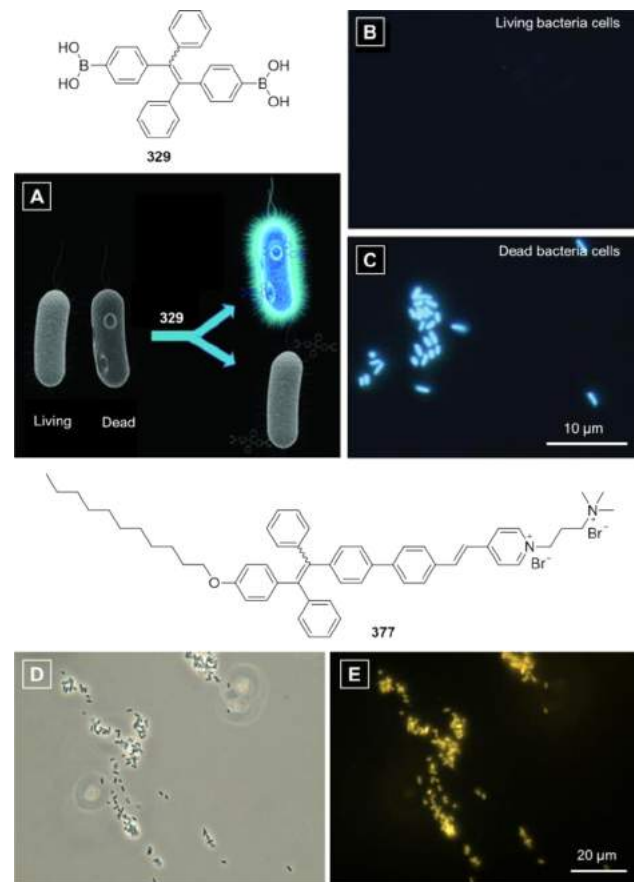


**Figure 100.** (A) Molecular structure of 329 and the schematic illustration of the discrimination of dead/live bacteria by 329. Fluorescent images of (B) living and (C) dead *E. coli* stained with 329 for 0.5 h. [329] = 100  $\mu$ M. Chemical structure of AIegen 377 which could stain both living and dead bacteria. Adapted with permission from ref 34. Copyright 2014 Wiley-VCH Verlag GmbH & Co. KGaA. (D) Bright-field and (E) fluorescent images of living *E. coli* stained with 377. [377] = 10  $\mu$ M. The images in parts D and E were provided by the authors of ref 625a. Copyright 2015 Wiley-VCH Verlag GmbH & Co. KGaA.

The AIegen 329 is a cell-impermeable bacteria stain that binds to the groove of double-stranded DNA. For the live bacteria, their membranes are intact and 329 cannot enter the bacterial cells to interact with the intracellular DNA strands. In comparison, for the dead bacteria, their membranes are broken and the access for 329 to the protoplasm is opened, which exposes their DNA strands to the molecules of 329 for interactive binding. The 329 molecules bound onto the dead bacteria strongly fluoresce due to the triggered RIR process. With excellent photostability and negligible cytotoxicity over a long period of time, long-term viability assay for bacteria has been achieved with 329. The application of 329 for simple screening of bactericides has been demonstrated as well. The efficacy of bactericides can be directly reflected by the fluorescence of 329. If a bactericide is ineffective, even treated with this bactericide at a high concentration, the bacteria are still alive as indicated by the extremely low fluorescence of 329. In turn, if a bactericide is effective to the bacteria, even with a small amount of such bactericide, the fluorescence of 329 is turned on, suggesting that the bacteria are killed.

Apart from the blue light-emitting AIegen 329, AIE imaging agents with other emission colors, such as yellow, orange, and

red, have also been developed for bacterial imaging.<sup>625a</sup> Take 377 for example. 377 is a cationic TPE derivatives carrying a styrylpyridinium moiety as well as a long alkyl chain. Thanks to the enlarged electronic conjugation and D-A effect, 377 emits yellow fluorescence in the aggregate state. 377 can be readily dissolved in buffer solution with very faint emission. After incubating with 377 at 37 °C for 10 min, the bacteria are already visible with strong yellow emission under fluorescence microscopy (Figure 100E), indicative of its fast imaging capability. As the probe visualizes bacteria in a fluorescence turn-on manner by activation of RIR process, no washing step is required to remove the unbounded dye. Additionally, it can be seen from Figure 100E,D that the bacterial image achieved with 377 enjoys a very low background emission and high signal-to-background ratio. This probe is fairly stable under ambient conditions and hence it can be used for long-term tracing of bacteria. Unlike 329, 377 can not only stain dead bacteria but also live ones.<sup>625a</sup> The reasons for this live-bacteria imaging ability probably lie in the unique molecular structure of 377. Its cationic nature may facilitate the interaction with bacteria. Meanwhile the amphiphilic feature originating from the hydrophobic alkyl chain and aromatic rings and the two hydrophilic amines may help 377 to intercalate into the membrane of the bacteria and enhance the membrane permeability by disturbing the phosphatidyl lipid arrangement of the membrane. Collectively, no matter whether molecules of 377 bind to the cell components or form nanoaggregates, the RIR process will be activated and the bacteria will be lit up. Furthermore, through judicious design, the AIE-based imaging system can even be endowed with bacterial killing ability and hence can be used as a bactericide for elimination of bacteria.<sup>625,626</sup>

In this subsection, a large group of small AIEgens have been tailored for diverse specific-imaging objects varying from cell components (e.g., cytoplasm, membrane, mitochondria, lysosomes, lipid droplets), intracellular environments (e.g., pH<sub>i</sub>), cellular events (e.g., expression of tumor markers and apoptosis), and then to bacteria. These AIEgen-based small imaging agents usually take the form of nanoaggregates or NPs in biological systems and work as light-up visualizers in a sensitive and specific manner with low cytotoxicity, appreciable photostability, and high signal-to-noise ratio.

**5.1.2.2. Polymeric NPs.** Polymeric fluorescent NPs have attracted increasing interest for their superb photo- and physical stability, good biocompatibility, potential biodegradability, flexible synthesis, and facile surface functionalization. As a consequence, these remarkable advantages allow them to become an important class of fluorescent agents for biological imaging. Since aggregation of organic luminophores is a naturally occurring process during nanoparticle fabrications, AIEgens are ideal emitters to construct highly fluorescent nanoparticles without emission quenching. The polymeric fluorescent NPs with AIEgens as the fluorescence sources are even more attractive for they integrate the advantages of these two structural elements. As there are several review articles published recently,<sup>627,628</sup> which summarized the AIE-based polymeric fluorescent NPs from different viewpoints, to avoid repetition, this part only covers the most recent progress, with a few representative examples. In terms of the fabrication methodologies, there are two main categories of polymeric AIE NPs. In this part, we will focus on the polymeric NPs where the AIEgens are covalently incorporated into the polymer chains. The other type of polymeric NPs where the AIEgens are encapsulated into polymeric matrixes via non-covalent interactions will be

elaborated in the following subsection and referred to as “AIE dots” in view of their uniqueness.

Directly conjugating AIEgens to biocompatible polymers (e.g., chitosan) could yield AIEgen-polymer conjugates.<sup>289,290,629,630</sup> As discussed in Section 4.3.2, our research team synthesized a TPE-chitosan conjugate (i.e. 231) via a coupling reaction between an isothiocyanate-decorated TPE derivative and chitosan (Figure 101A).<sup>289</sup> The resultant conjugate 231 enjoys

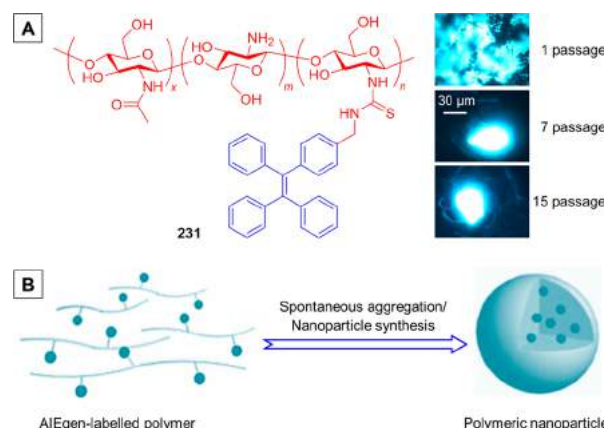


**Figure 101.** (A) Molecular structure of a bioconjugate (231) of TPE and chitosan and fluorescent images of the HeLa cells stained by the aggregates of the 231 with a labeling degree of 7.86 mol % at different passages taken at magnifications of  $\times 1000$ . Reprinted from ref 289. Copyright 2013 American Chemical Society. (B) Schematic illustration of the fabrication of polymeric NPs with AIEgen labelled polymers such as 231 via spontaneous aggregation or NP preparation methods. Adapted with permission from ref 290. Copyright 2013 Wiley-VCH Verlag GmbH & Co. KGaA.

a character of AIE and the fluorescence of 231 powders is intensified with the increased TPE-labeling degree. The high degree of fluorogen-labeling exerts a beneficial effect on the fluorescence of luminophore-polymer conjugates, which is unachievable for traditional ACQphores.<sup>289,631,632</sup> The spontaneously-formed aggregates of 231 in the cell-culture media can be internalized into HeLa cells and retained in the cells for 15 passages (Figure 101A). The extraordinary long-term cell tracing ability is ascribed to the fact that the internalized large aggregates of 231 are preserved in one cell, instead of being equally split to two daughter cells in each cell division cycle. The leakage-free retention of the internalized AIE aggregates also makes them able to differentiate specific cancerous cells from normal cells. It is noticeable that the aggregates of 231 are microscopic and nonuniform, which leaves some room for improvement in terms of cellular uptake of fluorogen. To this end, our group further fabricated the NPs of 231 by means of simple ionic gelation method under mild conditions.<sup>290</sup> The obtained NPs are uniform in size, spherical in shape, monodispersed, and positively charged on the surface. These NPs are fairly cyocompatible and highly fluorescent in suspension. Such NPs can be efficiently internalized into cytoplasm via endocytosis and retained inside live cells, thus they are able to undertake the long-term cell imaging task. In this way, a general platform for fabricating AIEgen-based polymeric NPs has been established. As depicted in Figure 101B, by virtue of spontaneous aggregation (including self-assembly) or nanoparticle synthesis methodologies, AIE polymeric NPs can be easily fabricated from AIEgen-labeled polymers.

As we all know, chitosan is a natural carbohydrate polymer, which is abundant, biocompatible, and biodegradable. Considering this, apart from the above work, there have quite a few other AIEgen-chitosan conjugates been constructed by taking advantage of the merits of AIEgens and chitosan.<sup>629,630</sup> For example, Wei and Zhang et al. have prepared another TPE-chitosan conjugate via a Schiff base reaction between an aldehyde-modified TPE derivative and a carboxymethyl chitosan.<sup>629</sup> By converting the dynamic Schiff base into a stable C–N bond with NaBH<sub>4</sub>, the resulting amphiphilic conjugate is able to self-assemble into uniform NPs with diameter in the range of 200–400 nm. These highly emissive NPs are well dispersed in water and biocompatible and display efficient living cell internalization. In addition to isothiocyanate and aldehyde groups, carboxyl groups can also be incorporated into AIE cores to generate reactive AIEgens which can further label the amine-bearing polymers. For instance, a biopolymeric amphiphile has been yielded via the amidation between a hydrophilic glycol chitosan backbone and an AIE-active carboxyl-tricyanostilbene derivative.<sup>630</sup> Fluorescent AIE NPs with NIR emission have been prepared through the self-assembly of such biopolymeric amphiphiles and further used for NIR bioimaging with enhanced fluorescence signal and better spectral coincidence with the *in vivo* transparent window. Certainly, besides chitosan, other polymeric backbones can also be used for the same purpose. In principle, with specific modification, any AIEgen can be conjugated to a polymer chain and serve as a fluorescence unit of the subsequent polymeric NPs (Figure 101B).

*In situ* polymerizing AIEgen into a polymer chain is another effective methodology to generate covalently-bonded AIE-polymer which might be able to form NPs under certain conditions.<sup>291,433,633–643</sup> Recently, Wei's group has fabricated a number of fluorescent polymeric NPs on the basis of polymerizable AIEgens.<sup>291,633–643</sup> They made use of diverse AIEgens and various polymerization methods including emulsion polymerization,<sup>634,642</sup> RAFT polymerization,<sup>291,636,637</sup> anhydride ring-opening polymerization,<sup>638,639,641–643</sup> and cross-linked polymerization,<sup>637,640,641,643</sup> to create a series of amphiphilic AIE polymers. The self-assembly of these amphiphilic polymers in aqueous solution functions as a general driving force for the formation of fluorescent polymeric NPs. During the self-assembly procedure, hydrophobic moieties including AIEgens are encapsulated in the core, which is covered by a shell formed with the hydrophilic fragments. The hydrophilic outer shells endow the NPs with high water dispersibility. The polymeric NPs produced through *in situ* polymerization possess advantages such as compact structure without fluorophore leakage or surface coating detachment in harsh biological environments. Moreover, these NPs display appreciable cytocompatibility and satisfactory cellular uptake efficiency.

Taking 378, as an example, with this polymerizable AIEgen, different polymeric NPs can be fabricated by varying polymerization pathways and/or nanoparticle synthesis methods (Figure 102A). In the emulsion polymerization strategy, 378 bearing a terminal vinyl group can be facilely copolymerized with styrene and acrylic acid and incorporated into the polymeric NPs.<sup>634</sup> Owing to its hydrophobic nature, 378 tends to aggregate in the core of polymeric NPs with the hydrophobic styrene segments. The hydrophilic acrylic acid parts, on the other hand, are covered on the core and serve as a hydrophilic shell. The obtained polymeric NPs intensely fluoresce and disperse well in aqueous media. Furthermore, these polymeric NPs possess spherical morphology, uniform size, as well as good biocompatibility,

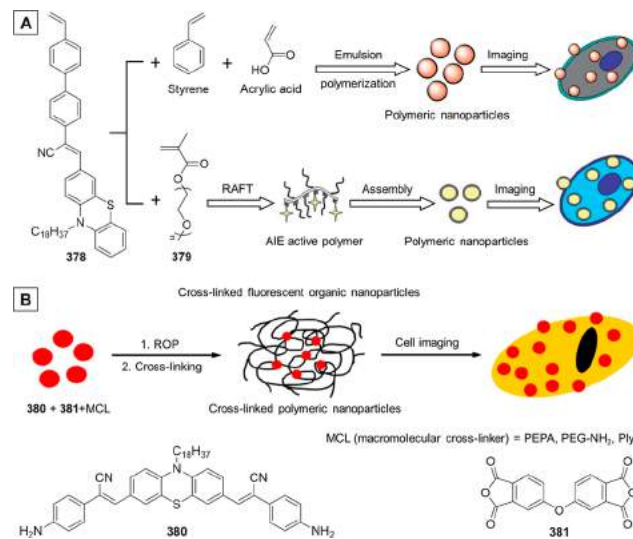


**Figure 102.** (A) Schematic illustration of the preparation of polymeric NPs on the basis of 378 and their cell imaging applications. Adapted with permission from ref 634 and 635. Copyright 2013 Royal Society of Chemistry. (B) Schematic illustration of the preparation of cross-linked polymeric NPs through room temperature anhydride ring-opening polymerization and consecutive cross-linking with macromolecular cross-linkers such as polyethylene polyamine (PEPA), amino polyethylene glycol (PEG-NH<sub>2</sub>), and polylysine (Ply) based on the AIEgen (380) and subsequent cell imaging applications of these obtained polymeric NPs. Adapted with permission from ref 641. Copyright 2013 Elsevier B.V.

rendering them promising for cell imaging. RAFT is a powerful polymerization method that is applicable to a wide range of monomers and can yield polymers with controlled molecular weights and very narrow polydispersities. Hence RAFT has been employed into the fabrication of 378-based polymeric NPs by Wei's group.<sup>635</sup> Polyethylene glycols (PEGs) are a class of amphiphilic polymers known for their good compatibility, low immunogenicity, and high water solubility; therefore, PEGs have been accepted as a good choice for bioapplications. In light of this, poly(ethylene glycol) monomethacrylate (379) was used as a monomer to undergo copolymerization with 378 based on the designed degree of polymerization through RAFT polymerization (Figure 102A). The resulting amphiphilic copolymers readily self-assembled into AIE-based polymeric NPs in physiological solutions. The afforded polymeric NPs show high water dispersibility, strong fluorescence, and superb biocompatibility and hence can be used as a fluorescent visualizer for cell imaging. Because of the controllability of RAFT polymerization, various monomers with different functional groups and polymerizable AIEgens with different optical properties could also be conveniently introduced into polymeric NPs,<sup>637</sup> and thus multifunctional imaging and theranostic platforms are likely to be obtained.

In addition to emulsion and RAFT polymerization, ring-opening polymerization is another method frequently used by Wei's group. A series of amino-functionalized AIEgens have been introduced into the polymer chains via ring-opening copolymerization with anhydride monomers.<sup>638,639,641,643</sup> For example, as depicted in Figure 102B, AIEgen 380 with two amino terminal groups has been facilely incorporated into stable cross-linked polymeric NPs through anhydride (e.g., 381) ring-opening polymerization and consecutive cross-linking with a macromolecular cross-linker such as polyethylene polyamine (PEPA),<sup>641</sup> amino polyethylene glycol (PEG-NH<sub>2</sub>),<sup>639</sup> and polylysine (Ply).<sup>642</sup>

In aqueous solution, the resultant cross-linked amphiphilic copolymers are all prone to self-assemble into uniform spherical NPs with diameters falling in the range of 100–400 nm. These polymeric NPs emit strong red fluorescence originating from the AIE feature of **380** and exhibit uniform spherical morphology, high water dispersibility, excellent biocompatibility, and efficient cellular internalization. Additionally, Tian et al. reported a type of AIE-active DSA-based polymeric NPs, which are fabricated from the self-assembly of amphiphilic polymers with DSA at the side chain.<sup>644</sup> Therefore, *in situ* polymerization of AIEgens with polymerizable functional groups becomes a universal strategy to customize AIE NPs with manifold functionalities through introduction of desired reactive monomers.

The examples highlighted in this section represent two strategies towards covalent incorporation of AIEgens into polymeric NPs, namely, polymer conjugation and *in situ* polymerization. The obtained AIE-based polymeric NPs usually enjoy good stability, compact structures, high water dispersibility, and excellent biocompatibility, etc. Although they are useful strategies for the construction of polymeric NPs, multiple synthetic steps are needed for AIEgen modification or functionalization prior to polymerization, which complicates the procedures and increases the cost of the AIE NP fabrication. The size distribution and the surface of these NPs also have a requirement for optimization before they could be utilized for more specific applications.

**5.1.2.3. AIE Dots.** Broadly speaking, AIE dots refer to any nanoobjects that contain elements of AIE, or in other words, they can be the aforesaid AIE-based organic NPs, polymeric NPs, or silica NPs (section 5.1.2.4).<sup>19</sup> Nevertheless, in this review, AIE dots are specified as a type of polymeric NPs where the AIEgens are non-covalently incorporated into polymer matrixes via physical encapsulation. These special kind of polymer-encapsulated fluorescent NPs are chiefly developed by Liu and Tang et al. and become the most attractive AIE-based NPs for their extraordinary performance in biological applications ranging from *in vitro* and *in vivo* imaging at cellular and/or tissue levels to dual-modal imaging or theranostic reagents. In this part, we will primarily discuss their imaging utilities and set aside their dual-modal imaging or theranostic applications for the discussion in section 5.1.2.5.

As the AIE dots are prepared by direct encapsulation of AIEgens using biocompatible polymers, theoretically the combination of the numerous AIEgens and biocompatible polymers would derive uncountable AIE dots. In the light of this, we sort out the existing AIE dots into several groups according to the encapsulation polymer matrix: lipid-PEG NPs, natural polymers-based NPs, and amphiphilic polymers-based NPs. The lipid-PEG, often refers to 1,2-distearoyl-*sn*-glycero-3-phosphoethanolamine-*N*-[methoxyl-(polyethylene glycol)] (DSPE-PEG), is a frequently used encapsulation matrix, and the AIE dots based on this polymer can be referred to as DSPE-PEG NPs. Liu's team and our group have jointly developed a nanoprecipitation strategy with this polymer matrix and the general fabrication procedure is schematically shown in Figure 103.<sup>645,646</sup> To fabricate the surface-functionalized AIE dots, DSPE-PEG<sub>2000</sub> and its derivative with reactive moieties such as maleimide and amine groups (activated DSPE-PEG<sub>2000</sub>) were used as polymeric matrices. A homogenous THF solution containing AIEgen, DSPE-PEG<sub>2000</sub> and activated DSPE-PEG<sub>2000</sub> was added into Milli-Q water followed by ultrasound sonication using a microtip probe sonicator. Upon THF/water mixing, the hydrophobic DSPE domains and the AIEgen intertwine with each other to form the core, and meanwhile the hydrophilic PEG chains extend toward

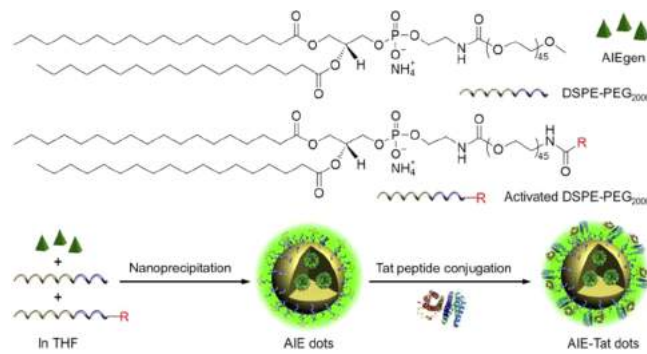


**Figure 103.** Schematic illustration of AIE-Tat dots formation. Adapted with permission from ref 645. Copyright 2014 Elsevier Ltd.

aqueous phase to prevent the AIE nanoparticle from aggregation and render the dots with abundant surface reactive groups. The existence of PEG shell minimizes their nonspecific interaction with biological species and also provides reactive groups for further chemical modification or biological conjugation. The AIE dots were further conjugated with a cell-penetrating peptide derived from HIV-1 transactivator of transcription (Tat) protein via reaction between the surface reactive moiety and terminal reactive groups of the peptide. The free peptides were removed by dialysis against Milli-Q water and the resultant AIE dots suspension was further purified by filtration through a 0.2  $\mu\text{m}$  syringe driven filter. AIE-Tat dots were collected and stored at 4 °C for further use. Such a lipid-PEG formulation and universal procedure has been actively employed in encapsulating versatile AIEgens to afford stable fluorescent dots due to their good biocompatibility and easy preparation.<sup>126,645–648</sup> Before using for imaging, the AIE-Tat dots were fully characterized by a series of experiments. Their average hydrodynamic size and size distribution were measured by DLS technique. The morphology was observed with a high resolution-transmission electron microscopy (HR-TEM). Moreover, the colloidal stability assessment, photophysical properties measurements and single-dot imaging of these AIE-Tat dots were performed as well.

2TPE-BT (i.e., **382**) consists of two electron-donating TPE units at the periphery and an electron-accepting 2,1,3-benzothiadiazole moiety as the core (Figure 104A). This D-A structured fluorophore shows a combined effect of TICT and AIE in the THF/water mixtures with different water fractions.<sup>35</sup> **382** was loaded into the DSPE-PEG<sub>2000</sub> and maleimide DSPE-PEG<sub>2000</sub> matrixes according to the above-discussed procedure, and the yielded AIE dots were further modified with a HIV-1 Tat (RKKRRQRRRC) though the click reaction between the surface maleimide and the thiol groups at the C-terminus of the peptide, affording the **382**-Tat dots (Figure 104A).<sup>645</sup> The obtained stable **382**-Tat dots are spherical in shape with a diameter of about 30 nm. Because of the AIE property of **382**, these dots emit intense green fluorescence peaked at 547 nm, with a large Stokes shift of 125 nm and high  $\Phi_F$  of  $63.0 \pm 2.0\%$ . As indicated by the wide-field fluorescence microscopy observation, these ultrabright AIE dots are highly photostable without photobleaching. It is noteworthy that the **382**-Tat dots are absent for the fluorescence intermittency (i.e., blinking), which is common to QDs such as QD655. The AIE-Tat dots can be readily internalized into live cells, such as human embryonic kidney 293T (HEK 293T) cells and homogeneously distributed inside the cellular cytoplasm with long retention and low cytotoxicity.

These AIE-Tat dots were further employed as a generic labeling agent and compared with green fluorescent protein

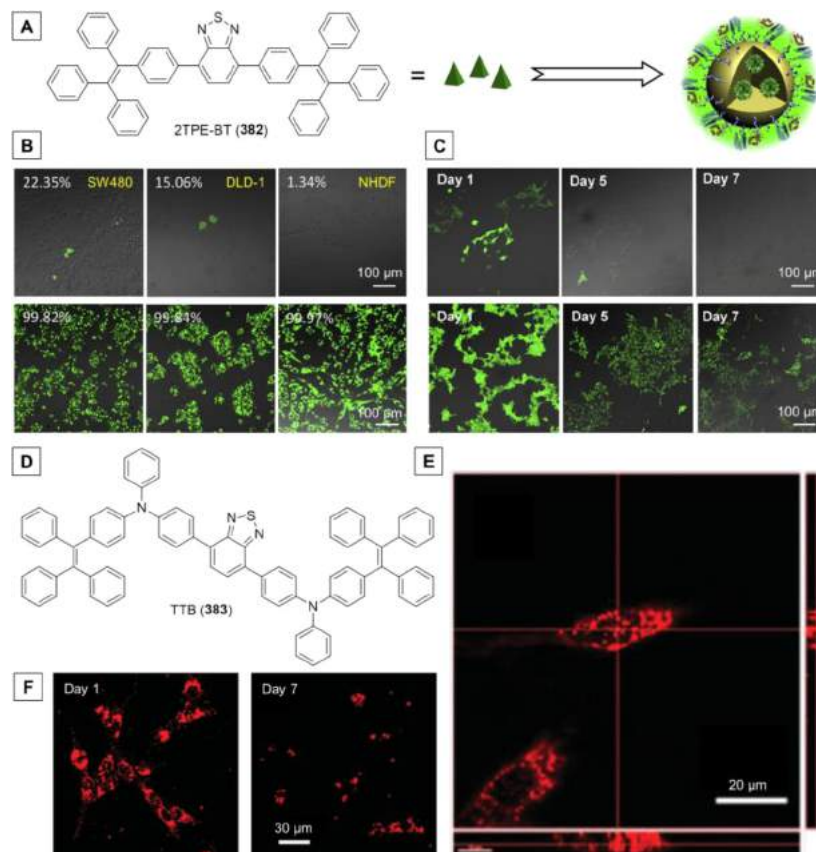


**Figure 104.** (A) Structure of 2TPE-BT (382) and the AIE-Tat dots constructed with 382. (B) The fluorescence/transmission overlay images of (upper) pMAX-GFP expressed cells and (lower) AIE-Tat dots labeled SW480 cells, DLD-1 cells, normal-human primary dermal fibroblast (NHDF) cell, respectively. Insets are labeling rates measured by flow cytometry. (C) CLSM images of HEK 293T cells labeled by (upper) pMAX-GFP or (lower) AIE-Tat dots at different days post-incubation. Adapted with permission from ref 645. Copyright 2014 Elsevier Ltd. (D) Molecular structure of TTB (383). (E) 3D sectional confocal images of MCF-7 breast cancer cells after incubation with 2 nM TTB-Tat dots for 6 h at 37 °C. (F) CLSM images of MCF-7 on designated days after the overnight incubation of Tat-TTB dots at a concentration of 2 nM. Adapted with permission from ref 647. Copyright 2014 Wiley-VCH Verlag GmbH & Co. KGaA.

(GFP), a dominated cell labeling agent for cell transplantation and tracking. The results clearly demonstrate the superior cell labeling as well as long-term cell tracking ability of AIE-Tat dots over GFP (Figure 104B,C). Specifically, among all the tested human cells of different tissue origins including human colon adenocarcinoma SW480 cells (SW480), human colon adenocarcinoma DLD-1 cells (DLD-1), and normal-human primary dermal fibroblast cells (NHDF cells), only HEK 293T cells display a relatively high GFP expression of 68.75%, while weak mean fluorescence and low GFP expression levels are observed for the other cells such as SW480 (22.35%), DLD-1 (15.06%), and NHDF cells (1.34%) (Figure 104B, upper panel). On the contrary, AIE-Tat dots show nearly 100% labeling efficiencies toward all the tested cell lines, with over 100-fold stronger mean fluorescence as compared with GFP-labelled cells (Figure 104B, lower panel). Furthermore, the comparative study on the in vitro cell tracing ability between AIE-Tat dots and GFP is performed with HEK 293T cells as the model cell line (Figure 104C). The HEK 293T cells labelled by 382-Tat dots show 99.98% label efficiency at the 1st day after incubation, which keeps above 90% on the 5th day and over 70% on the 7th day (Figure 104C, lower panel). In sharp contrast, from the 1st day on, the labeling rate of GFP is far below that of 382-Tat dots, and from the 7th day onwards, no GFP signal can be detected (Figure 104C, upper panel). The high brightness and long cell-tracing period suggested that 382-Tat dots could be efficiently internalized

into cell cytoplasm with high retention ability and efficiently transferred to daughter cells during cell proliferation.

Similar to 382, TTB (383) was constructed on the basis of TICT plus AIE strategy. Because of the extended electronic conjugation and strong D-A effect, efficient red emission and large Stokes shift have been achieved (Figure 104D). With the same fabrication protocol (Figure 103), AIE-Tat dots based on this large TPE derivative 383, DSPE-PEG<sub>2000</sub>/maleimide-DSPE-PEG<sub>2000</sub>, and an HIV-1 Tat (YGRKKRRQRRRC) have been fabricated and show outperforming photophysical properties as well as bioimaging ability over commercial QDs-based cell trackers.<sup>647</sup> The 383-Tat dots are spherical in shape with an average hydrodynamic diameter of ~36 nm and display intense red fluorescence with a  $\Phi_F$  of 55.0%. All these remarkable attributes ensure their possible superb performance as an imaging agent. No surprisingly, the 383-Tat dots can be efficiently internalized into living cells (e.g., MCF-7 cells) and mainly localize in the cytoplasm and perinuclear region. Intriguingly, with closer examination, it can be found that some orange-red emission is also observable in the nuclei region (Figure 104E), suggesting that some AIE dots are located in the nuclei. As indicated by the comparison between 383 dots and 383-Tat dots, the Tat peptide plays a vital role in enhancing the live cell internalization efficiency and facilitating the intranuclear translocation. Such an intranuclear localization property in a live cell will offer a promising platform for nucleus fluorescence imaging

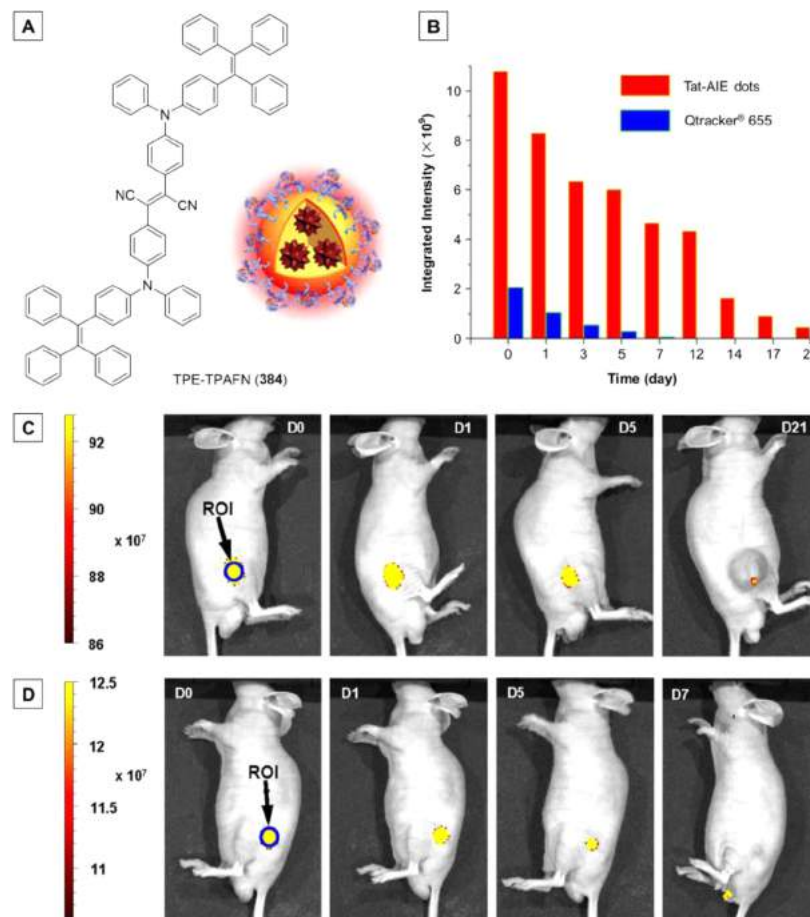


**Figure 105.** (A) Structure of TPE-TPAFN (384) and its corresponding AIE dots. (B) The integrated PL intensities of the regions of interest (ROI, blue circles) at the tumor sites from the images in panels C and D. In vivo fluorescence imaging of tumor cells by Tat-AIE dots. (C) Representative in vivo fluorescence images of the mouse subcutaneously injected with  $1 \times 10^6$  of C6 glioma cells after staining 2 nM Tat-AIE dots. (D) Data for Qtracker 655 obtained under similar conditions. The images were taken on designated days post cell injection. Adapted with permission from ref 126. Copyright 2013 Rights Managed by Nature Publishing Group.

and possible drug delivery. 383-Tat dots also exhibit low cytotoxicity and excellent photostability together with the ultrahigh brightness. These features enable these 383-Tat dots to trace MCF-7 breast cancer cells up to 7 days (Figure 104F). The 383-Tat dots indeed show superior cell tracking ability over their counterparts, e.g., Qtracker 585 dots, in terms of the brightness, labeling efficiency, and the time-dependent change in the labeling rate.

For in vivo cell tracing, it is particularly demanding to shift the excitation and emission to longer wavelengths, ideally to far-red/near-infrared (FR/NIR) region, which can avoid photodamage caused by the UV excitation, enable deep tissue penetration, and circumvent the spectral overlap with biosubstrate autofluorescence.<sup>649</sup> With smart design, the FR/NIR AIE emitters can be obtained. For example, by virtue of the AIE plus AIE principle, our research group synthesized an FR/NIR AIEgen through molecular fusion of two types of AIE units.<sup>126</sup> Conjugation of TPE units with AIE-active 2,3-bis[4-(diphenylamino)phenyl]fumaronitrile (i.e. TPafN) has afforded the adduct TPE-TPAFN (384; Figure 105A). Such a fusion not only preserves the AIE attributes of the building blocks but also brings about extra benefits such as long-wavelength absorption ( $\lambda_{\text{abs}} \sim 497$  nm), large molar absorptivity ( $3.68 \times 10^4 \text{ M}^{-1} \text{ cm}^{-1}$ ), and bright FR/NIR emission in the solid state ( $\Phi_F = 52.5\%$ ) to the new adduct. Following the route depicted in Figure 103, the

encapsulation of 384 with a mixture of DSPE-PEG<sub>2000</sub> and DSPE-PEG<sub>2000</sub>-NH<sub>2</sub> as polymer matrix generated bright AIE dots with abundant amine groups on the surface. Bioconjugation of the AIE dots with a cell penetrating peptide HIV-1 Tat (RKKRRQRRRC) through carbodiimide-mediated coupling further yielded 384-Tat dots which are in spherical shape with a uniform average size around 32 nm (Figure 105A). The dots give an intense absorption peaked at 511 nm and an emission maximum at 671 nm with a tail extending to 900 nm. These AIE-Tat dots also exhibit a higher  $\Phi_F$  (24.0%) in water than that of the commercial Qtracker 655 (15.0%). Moreover, 384-Tat dots are  $\sim 12\text{--}15$  times brighter than Qtracker 655 in single nanoparticle imaging analysis. Notably, the undesirable blinking behavior of QDs is absent in the 384-Tat dots. The high emission efficiency, large absorptivity, strong photobleaching resistance, excellent biocompatibility, and superb intracellular retention of 384-Tat dots collectively enable them to trace the in vitro live MCF-7 cells up to 12 generations. However, under the same protocol, the Qtracker 655 can only track 5–6 generations. Accordingly, all these advantages make the 384-Tat dots able to track the C6 glioma cells in vivo up to 21 days with high contrast (Figure 105B and 105C). Upon subcutaneous injection in live mice, the fluorescence signals from the cells treated with 384-Tat dots remained very high at day 12 post-injection ( $4.35 \times 10^9$ ), with the intensity twice that of the initial value obtained from the

Qtracker 655-labelled ones ( $2.05 \times 10^9$ ; Figure 105B). Moreover, the fluorescence signal from the cells treated with Qtracker 655 completely vanished at day 7 (Figure 105D). In sharp contrast, at 21 days post injection, the integrated fluorescence intensity at tumor site is still as high as  $4.5 \times 10^8$  (Figure 105B). Thanks to the large D- $\pi$ -A structure and AIE character of 384, the 384-Tat dots have also been reported to be an effective contrast agent for in vivo two-photon fluorescence tissue imaging.

With this superb FR/NIR-emissive AIEgen, namely, 384, AIE-Tat dots creatively utilized for noninvasive long-term tracking of stem cells and their regenerative capacity monitoring in living mice have been prepared through procedures shown in Figure 103.<sup>650</sup> Stem cells are undifferentiated biological cells that can differentiate into specialized cells. They are noted for the regenerative capacity and have been widely used in research areas especially the tissue engineering. Amongst various stem cell sources, adipose-derived stem cells (ADSCs) are promising cell-based regenerative medicine.<sup>651,652</sup> Monitoring and understanding long-term fate and regenerative therapy of the administered stem cells in vivo is of paramount importance to the development of efficient stem cell therapies. To this end, the 384-based AIE-Tat dots are intended as an exogenous contrast agent or imaging probe for stem cell tracking.<sup>650</sup> The polymer matrixes used here are DSPE-PEG<sub>2000</sub> and maleimide DSPE-PEG<sub>2000</sub>, and the Tat peptide is a HIV-1 Tat protein-derived cell penetrating peptide modified at C-terminus with cysteine. Although these AIE-Tat dots are slightly different from those discussed in Figure 105 in terms of nanoparticle synthesis, these two types of 384-based AIE-Tat dots generally share identical photophysical properties because of the same fluorescence source (384). These AIE-Tat dots are intensely fluorescent in the FR/NIR region with large Stokes shift (~160 nm), highly biocompatible (both in vitro and in vivo), very photostable and free of photoblinking, and can be efficiently internalized into live cells with excellent retention, rendering them eminently suitable for in vivo imaging with low disturbed absorption, minimum background signal, and deep tissue penetrability. Before in vivo investigation, the capability of these 384-Tat dots for in vitro ADSC tracing was examined first. As can be seen from Figure 106A, upon 1 day subculture, strong fluorescence signals are observed for all the 384-Tat dots-labelled ADSCs and the mean fluorescence intensity is ~6.2 and ~4.8-fold higher than that from the commercial long-term cell trackers Qtracker 655- (Figure 106B) and PKH26-labelled ones, respectively. After 5 days subculture, only low fluorescence signal is detectable from Qtracker 655-ADSCs with the labeling rate decreasing from 80.6% to 12.4% (Figure 106B). Similarly, the fluorescence of PKH26-labelled ADSCs becomes much weaker with the labeling rate reducing from 97.5% to 43.9%. On the contrary, the AIE-Tat dots-labelled ADSCs maintain the intense and homogeneous fluorescence signals with a labeling rate as high as 92.5% (initially 98.5%), indicative of their superior in vitro cell tracing ability over Qtracker 655 and PKH26.

The ADSC tracking studies in mice bearing ischemic hind limbs revealed that the AIE-Tat dots could precisely and quantitatively report the fate of ADSCs and their regenerative capacity in vivo for 6 weeks (Figure 106C), the longest in vivo cell tracing duration among the currently available exogenous fluorescent cell trackers. Since the ADSCs express GFP as well, the accuracy of AIE-Tat dots in tracking ADSCs in vivo at single-cell resolution has been evaluated by comparing the signals from AIE dots and GFP (Figure 106D). On day 30 after ADSC

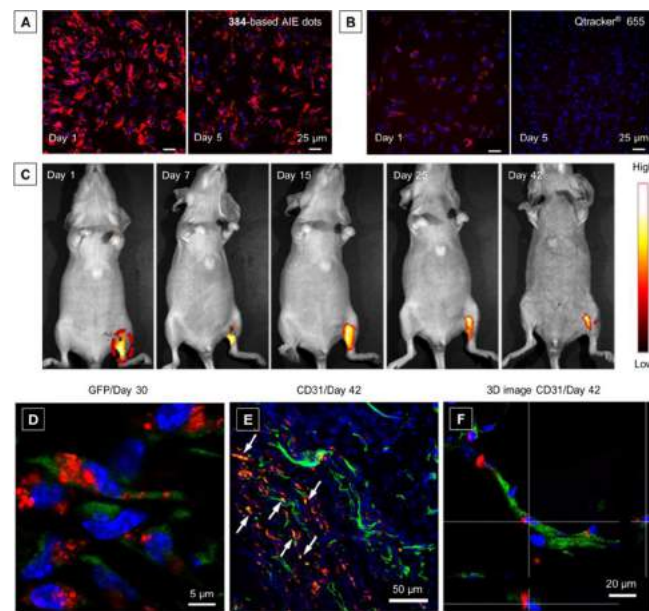


**Figure 106.** Precise and long-term tracking of adipose-derived stem cells (ADSCs) and their regenerative capacity via AIE-Tat dots constructed from TPE-TPAFN (384). CLSM images of ADSCs labeled with (A) AIE-Tat dots and (B) Qtracker 655 and then subcultured for 1 and 5 days, respectively. (C) Representative time-dependent in vivo fluorescence images of the ischemic hind limb-bearing mouse that was intramuscularly injected with AIE-Tat dot-labeled ADSC-containing Matrigel. (D) Tracking of ADSCs in vivo at single-cell resolution: enlarged CLSM image of ischemic hind limb slices from mice after administration of AIE-Tat dots-labeled ADSC-containing Matrigels for 30 days. (E and F) Long-term tracking of the regenerative capacity of ADSCs via AIE dots. (E) Representative CD31-staining CLSM image and (F) 3D sectional CLSM image of ischemic hind limb slices from mice treated with AIE dot-ADSC-Matrigels for 42 days. The green fluorescence indicates the CD31-positive blood vessels. The nuclei were stained by 4,6-diamidino-2-phenylindole (DAPI; blue). Adapted from ref 650. Copyright 2014 American Chemical Society.

administration, the red fluorescence signal from the 384-Tat dots and green fluorescence from GFP overlaps well in the cytoplasm of most transplanted ADSCs. Furthermore, the 384-Tat dots were also used to monitor the regenerative capacity of the ADSCs. Upon blood vessel staining against CD31 on day 42, it is found that most 384-Tat dot-labeled ADSCs (red fluorescence) are distributed near the CD31-positive blood vessels (green fluorescence; Figure 106E), implying the induction of therapeutic angiogenesis via the ADSCs. More importantly, as evidenced by the overlaid images, some AIE-Tat dots-labelled cells are located in the blood vessels, especially in the capillaries. The enlarged 3D sectional CLSM image shown in Figure 106F confirms that the AIE-Tat dots-labelled ADSCs can also engage in blood vessel formation through forming vascular structures. Therefore, by virtue of AIE-Tat dots labeling, it can be concluded that the ADSCs contribute to the angiogenesis in ischemic tissue via not only secreting angiogenic factors but also differentiating into necessary cells in vivo to participate in neovascularization. These results corroborate that the AIE-Tat dots are able to track and visualize the regenerative capacity of ADSCs in a long-term and high throughput manner. In a word, the AIE-Tat dots-labeling approach is simple, economic, safe, and effective and meanwhile the AIE-Tat dots are remarkably advantageous as a precise and long-term tracker (in vitro and in vivo) in terms of

their brightness, photobleaching resistance, safety, and stem cell tracing ability.

By virtue of the facile preparation strategy depicted in Figure 103, which enjoys general applicability, not only AIEgens with varying optical properties can be made into highly performed AIE dots but also diverse peptide sequences or other surface functional moieties, e.g., folic acid or folate, can be easily introduced into the AIE dots to add functions to them. Folate is a well-known tumor targeting motif that has been widely used in biological areas, because the folate receptor over-expressing is a hallmark of a spectrum of malignant tumors.<sup>653</sup> Simply modifying the PEG terminal of DSPE-PEG with folate moiety yields the DSPE-PEG<sub>5000</sub>-folate which is further used as an encapsulation matrix for AIE dots. As shown in Figure 107A,

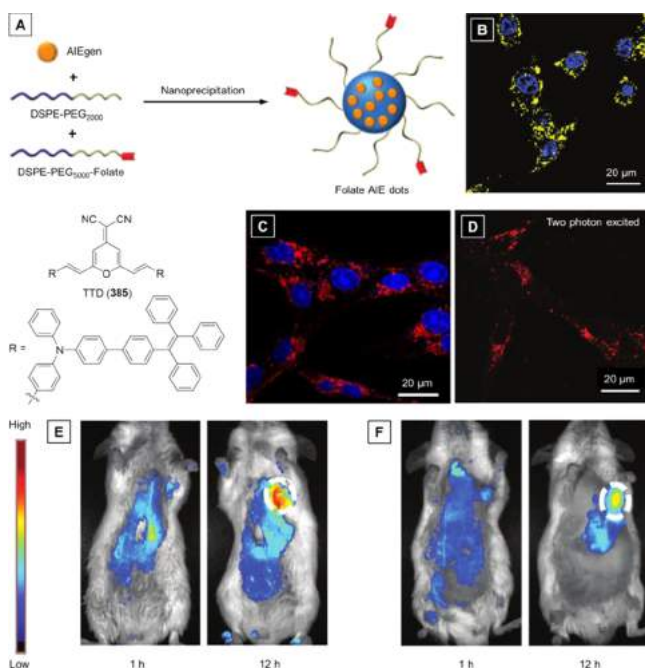


**Figure 107.** (A) Schematic illustration of the preparation of folate functionalized AIE dots with various AIEgens such as 112a and 385. (B) Confocal images of MCF-7 breast cancer cells after incubation with folate functionalized AIE dots constructed with 112a for 2 h at 37 °C, [112a] = 1  $\mu$ M. Adapted with permission from ref 654. Copyright 2011 Royal Society of Chemistry. (C) Confocal fluorescence image and (D) two-photon excited fluorescence image of MCF-7 breast cancer cells after 2 h incubation with the suspension of folate functionalized AIE dots based on TTD (385) at 0.1 nM NPs at 37 °C. The nuclei in part C were stained with DAPI. One-photon excited in vivo noninvasive fluorescence imaging of H22 tumor-bearing mice after intravenous injection of (E) folate functionalized AIE dots and (F) bare AIE dots of 385 at the same NP concentration of 1 nM. The white circles mark the tumor sites. Adapted with permission from ref 655. Copyright 2012 Wiley-VCH Verlag GmbH & Co. KGaA.

folate-functionalized AIE dots (folate AIE dots) can be facilely fabricated with an AIEgen, DSPE-PEG<sub>2000</sub>, and DSPE-PEG<sub>5000</sub>-folate via nanoprecipitation. For example, the folate AIE dots loading yellow emissive AIEgen 112a which was synthesized via an “ACQ-to-AIE” strategy have been constructed through this one-step synthesis procedure (Figure 107A).<sup>151,654</sup> The surface folate density can be fine-tuned by varying the feed ratio of DSPE-PEG<sub>5000</sub>-folate to DSPE-PEG<sub>2000</sub> in AIE dots fabrication. The obtained folate 112a-based AIE dots show small size (< 90 nm), large two-photon absorption (2PA) cross-section

( $\delta = 2015$  GM at 800 nm), and low cytotoxicity, making them promising for cell imaging (Figure 107B). The cellular uptake of these 112a-based AIE dots by MCF-7 cancer cells is raised with increased molar ratio of DSPE-PEG<sub>5000</sub>-folate in the nanoparticles preparation. Notably, these folate-functionalized AIE dots display good selectivity between cancerous (MCF-7) and normal cells (NIH/3T3 fibroblast cells) owing to the specific folate receptor-mediated endocytosis for MCF-7 cells and the presence of long PEG chains which inhibited nonspecific cellular internalization of the AIE dots.

Hereafter, Liu et al. further explored more folate-functionalized AIE dots and applied them for the *in vivo* fluorescence imaging.<sup>97,655</sup> To ensure their *in vivo* workability, FR/NIR emissive AIEgens such as 44 and TTD (385) have been selected as the fluorescence units of the NPs. Taking 385, for example, this fluorogen was synthesized using the TICT plus AIE principle and hence show TICT and AIE behaviors in the THF/water mixtures with different water fractions.<sup>656</sup> With long-wavelength absorption (> 480 nm) and emission (> 650 nm) as well as high emission efficiency, it is a good choice for AIE dots used for *in vivo* imaging.<sup>655</sup> The 385-based folate AIE dots retain the advantages of 385 such as bright FR/NIR fluorescence (684 nm); moreover, they are small in size (~50 nm) and biocompatible both *in vitro* and *in vivo*. These 385-based folate AIE dots can be sufficiently internalized into living MCF-7 cells, mainly located in the cytoplasm and visualize the cells (Figure 107C) with a high contrast. Uptake mechanism study manifests that the folate AIE dots are primarily internalized into MCF-7 breast cancer cells via folate receptor (caveolae)-mediated endocytosis. Additionally, these 385-based folate AIE dots also hold high 2PA cross-section ( $2.3 \times 10^6$  GM) due to the large D- $\pi$ -A structure and AIE effect, making them able to be used for two-photon excited fluorescence imaging (Figure 107D). The two-photon excited fluorescence signals are chiefly from cytoplasm and clearly distinguish the cell profile, which is similar to that obtained from the one-photon excited fluorescence imaging. *In vivo* fluorescence imaging of mice bearing murine hepatoma H<sub>22</sub> tumors with overexpressed folate receptors were conducted with 385-based folate AIE dots and AIE dots as probes. At 1 h post-injection, the fluorescence is observed from the tumor site in mice administrated with 385-based folate AIE dots and steadily increased in the following 6 and 12 h (Figure 107E). By contrast, the fluorescence signals from the tumor labelled by 385-based AIE dots are much weaker at each time point (Figure 107F). These results further verify that the 385-based folate AIE dots can efficiently accumulate in tumor tissues through both passive targeting by enhanced permeability and retention (EPR) effect and folate receptor-mediated active targeting effect. It has also been reported that deep tissue two-photon excited *ex vivo* fluorescence imaging with the penetration depth of at least 400  $\mu$ m can be realized with the aid of 385-based folate AIE dots.

In addition to cell imaging and tracking, the ultrabright AIE dots have also been utilized for *in vivo* two-photon fluorescence imaging of intravital tissues such as blood vessels.<sup>35,657</sup> Two-photon fluorescence imaging is emerging as a fairly attractive research subject for it allows noninvasive studies of cellular events at the single-cell level *in vivo*. By comparison with one-photon fluorescence imaging, two-photon fluorescence imaging is able to generate high-energy visible fluorescence from low-energy excitation in the NIR region (700–1000 nm).<sup>658,659</sup> Since there is minimal absorbance of biosubstrate in the NIR region, two-photon fluorescence imaging offers a unique and clear optical window for *in vivo* imaging due to its deep tissue penetration, high spatial resolution, low interference from autofluorescence,

as well as minimal phototoxicity or photo/thermal-damage to living biosubstrates.<sup>660–662</sup> The large 2PA cross-section ( $\delta$ ) and large two-photon action cross-section ( $\delta\Phi_F$ ) are two key parameters for a good two-photon imaging agent. Thus, it is believed that AIEgens possess great promise as efficient two-photon fluorescence imaging probes for their high emission efficiencies in the aggregate state. In the light of the high  $\Phi_F$  ( $63.0 \pm 2.0\%$ ) reported for the 382-Tat dots discussed in Figure 104A–C, 382 was chosen to fabricate a new kind of AIE dots for two-photon intravital vasculature imaging.<sup>35</sup> These 382-based dots were prepared with a single polymer matrix (i.e., DSPE-PEG<sub>2000</sub>) via the synthetic route shown in Figure 108A.

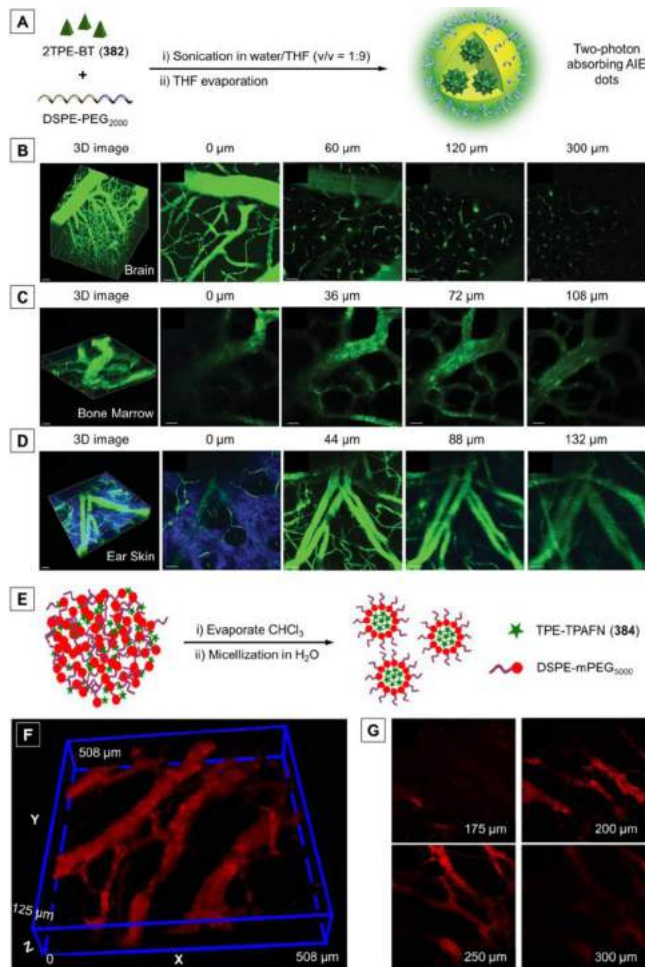


**Figure 108.** Schematic illustration the fabrication of two-photon absorbing AIE dot based on (A) 382 and (E) 384, respectively. (B–D) Intravital two-photon excited fluorescence of AIE-dot-stained blood vessels in different organs. 3D reconstructed images showing blood vessels in (B) brain, (C) bone marrow, and (D) mouse ear skin, and images at various vertical depths. Scale bar: 50  $\mu\text{m}$ . Adapted with permission from ref 35. Copyright 2013 Wiley-VCH Verlag GmbH & Co. KGaA. (F) A reconstructed 3D image showing the distribution of the 384-based AIE dots in the blood vessels at a depth range of 175–300  $\mu\text{m}$  of the brain of a mouse. (G) Individual images taken at the depths of 175  $\mu\text{m}$ , 200  $\mu\text{m}$ , 250  $\mu\text{m}$ , and 300  $\mu\text{m}$ . These data were recorded 30 min post-injection by a two-photon scanning microscope. Adapted with permission from ref 657. Copyright 2014 Rights Managed by Nature Publishing Group.

They show almost identical properties to the 382-Tat dots, such as small size (~33 nm) and intense green emission (547 nm,

$\Phi_F = 62.0 \pm 1.0\%$ ). More importantly, these AIE dots hold a high  $\delta\Phi_F$  of  $6.3 \times 10^4$  GM (810 nm), and low in vivo toxicity. Real-time two-photon blood vasculature imaging in live mice with 382-based dots verified that they are capable of working as an effective two-photon fluorescence imaging agent with deep-tissue penetration and high contrast (Figure 108B–D). Specifically, the major blood vessels, the smaller capillaries, and even the microvasculature deep in the brain lying beyond the pia matter (> 400  $\mu\text{m}$ ) are clearly visualized by AIE dots (Figure 108B). The high-contrasted imaging of vasculature system in skull bone marrow and skin are also realized (Figure 108C,D).

In the meantime, the AIE-active FR/NIR emitter 384 was also selected as a fluorescence source of new DSPE-PEG-based AIE dots which were also intended for in vivo two-photon bioimaging.<sup>657</sup> The preparation procedure for these 384-based AIE dots is illustrated in Figure 108E. The chloroform solutions of 384 and DSPE-mPEG<sub>5000</sub> were mixed first and the mixture then was subjected to sonication for several minutes to give a homogeneous red solution and dried by vacuum rotary evaporation. After the removal of chloroform, deionized water was added to the mixture and the solution was sonicated for a few minutes to afford the clear suspension of AIE dots. During the mixing of lipidic mass and water under continuous sonication, the DSPE domains intertwined with the hydrophobic 384 to form the core, while the PEG segments extended into the aqueous solution to ensure the high water dispersibility and good biocompatibility of the resulted nanodots. The particle sizes of these AIE dots fall in the range of 20–180 nm, depending on the feeding ratio of 384. The AIE dots were injected intravenously into the animal body for blood circulation in a facile and controllable fashion. The performances (e.g., flow and penetration) of the AIE dots in the blood vasculature can be readily manifested by the two-photon excited fluorescence signals. The 3D imaged region ( $508 \mu\text{m} \times 508 \mu\text{m} \times 125 \mu\text{m}$ ) at a depth range of 175–300  $\mu\text{m}$  in the mouse brain (Figure 108F,G) clearly show the deep tissue penetration and high resolution as well as high contrast of the AIE dots-based two-photon fluorescence imaging. The flow process of the AIE dots in the blood vessel of the brain can be dynamically and vividly demonstrated by the results obtained from the two-photon fluorescence imaging. These two examples indicate that AIE dots with good photostability, high brightness, and large two-photon action cross section can provide a novel platform to visualize blood vessels *in vivo* for addressing of complex biological processes, such as angiogenesis and vascular leakage. These studies also offer fundamental guidelines for future design and development of novel AIE probes with two-photon excited fluorescence imaging capability for potential clinical translation.

Besides the versatile DSPE-PEG matrix, BSA, a protein with broad biological and clinical applications for its biocompatibility and non-antigenicity, has also been demonstrated effective as the polymer matrix for AIE dots fabrication.<sup>656,663</sup> The preparation procedure of the fluorogen-loaded BSA NPs is schematically illustrated in Figure 109A.<sup>656</sup> Upon addition of the THF solution of AIEgen into the BSA aqueous solution, the AIE molecules aggregate and entangle with the hydrophobic segments of the BSA chains. Accompanying the hybridization with the hydrophobic AIEgen, the phase separation of BSA occurs. The fluorogen-loaded BSA NPs come into being instantly upon sonication. The BSA matrix is knitted together by an amine-reactive cross-linker, e.g., glutaraldehyde. After THF removal, the cross-linked NPs are further purified by filtration through a microfilter and subsequent washing with Milli-Q water. The

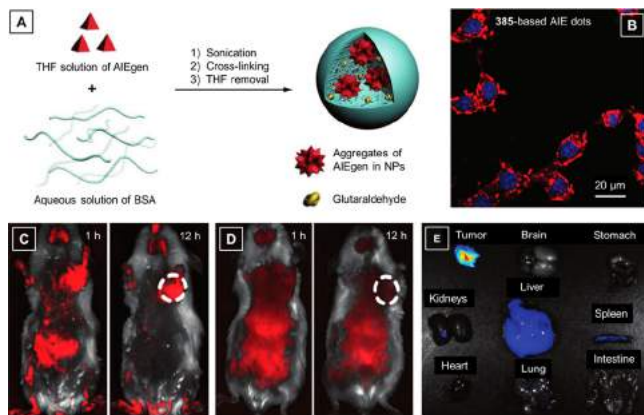


**Figure 109.** (A) Schematic illustration of the fabrication of BSA NPs loaded with AIEgens. (B) CLSM images of MCF-7 breast cancer cells after incubation with 385-loaded BSA NPs (with a fluorogen loading of 0.86%). (C,D) In vivo noninvasive fluorescence imaging of H<sub>22</sub>-tumor-bearing mice after intravenous injection of (C) 385-loaded BSA NPs with 0.86 wt % 385, and (D) bare 385 NPs at the same concentration of 385. (E) Ex vivo fluorescence imaging on tumor tissue and major organs of mice treated with 385-loaded BSA NPs, which were sacrificed at 24 h post-injection. Adapted with permission from ref 656. Copyright 2012 Wiley-VCH Verlag GmbH & Co. KGaA.

one-pot simple fabrication method is also highly applicable to various AIEgens. Using 385 as an example for demonstration, the encapsulation efficiencies and average size can be adjusted by the feeding ratio of 385. These BSA-based AIE dots are uniform with a spherical morphology and an average size in the range of ~100–150 nm. Similar to the DSPE-PEG-based AIE dots of 385, these BSA-based ones also possess high brightness and low cytotoxicity, ensuring their utility in biological imaging.

After incubation with the 385-loaded BSA dots for 2 h, the cytoplasm of the MCF-7 breast-cancer cells show intensive fluorescence signals that can be collected at or above 650 nm (Figure 109B), and the homogeneous distribution of 385-loaded BSA dots can also be easily observed. Time-dependent in vivo distribution profile and tumor accumulation of 385-loaded BSA dots in the H<sub>22</sub>-tumor-bearing mice is depicted in Figure 109C. A preferential accumulation in tumor site has been clearly shown. The capability of the 385-loaded BSA dots to favorably light up the tumor with a high contrast may be ascribed to the EPR effect of NPs with a uniform size of ~100 nm. The ex vivo fluorescence imaging gives a solid proof to the prominent EPR effect of these AIE dots, with the tumor showing the strongest fluorescence (Figure 109E). As compared with the 385-loaded BSA dots, bare 385 NPs (particle size ~300 nm) show much smaller cancer-cellular uptake and no obvious EPR effect (Figure 109D), clearly demonstrating the BSA formulation benefits the enhanced accumulation of AIEgen-loaded NPs in the tumor site.<sup>656</sup> The fluorescence signal of 385-loaded BSA dots can be further amplified for more than 5-fold via fluorescence resonance energy transfer (FRET) from the co-encapsulated poly(9,9-bis{2-[2-(2-methoxyethoxy)ethoxy]ethyl}fluorenylvinylene) (PFV) in BSA.<sup>663</sup> The negatively charged BSA matrix of such a FRET system allows self-assembly between the dots and RGD, yielding PFV/385-coloaded BSA-RGD dots with specific recognition ability of integrin receptor-overexpressed cancer cells both in vitro and in vivo.

Apart from DSPE-PEG and BSA, many other amphiphilic polymers can also be used as encapsulating matrixes with different preparation methods. Liu et al. have developed another

simple fabrication strategy for NPs loading AIEgens using poly(<sub>D,L</sub>-lactide-*co*-glycolide) (PLGA) and PLGA-PEG-folate as the encapsulation matrixes with different amounts of poly(vinyl alcohol) (PVA) as the emulsifier.<sup>664</sup> AIEgen 384 was selected as a model fluorogen to verify the feasibility of this strategy. Such an oil-in-water single emulsion and solvent evaporation approach could realize eccentric or homogeneous loading of AIEgens through adjusting the amount of the emulsifier. When the PVA amount is 0.25%, an eccentric location of 384 fluorogens inside the NPs was observed and rationalized to result from the evaporation-induced phase separation between the hydrophobic 384 and amphiphilic PLGA. With 2.5% PVA, molecules of 384 were almost homogeneously distributed in the PLGA matrix, suggesting that the high PVA concentration helped to stabilize the NPs and homogenize 384 molecules within the polymer matrix. The quantum yields of these two types of AIE dots are affected by the loading mode. The  $\Phi_F$  of the eccentrically loaded NPs (34.0%) is higher than that of the homogeneously loaded ones (23.0%). This might be due to the fact that the eccentric pattern yielded a more compact aggregation of the AIEgens that imposes a larger restriction on the intramolecular motions and promotes the radiative decay pathways. In the light of the targeting capacity, low toxicity, high photostability, these PLGA encapsulated AIE dots show good cell imaging performance. This work provides new insights into the development of brilliant AIE dots by regulating internal architectures of the loaded fluorogens.

Other amphiphilic copolymers, such as poly(maleic anhydride-*alt*-1-octadecene)-polyethylene glycol (C18PMH-PEG) and PEG copolymers, have also been employed as polymeric matrixes of AIE dots.<sup>665,666</sup> Zhang's group have made full use of the spontaneous-aggregation of hydrophobic AIEgens in aqueous media to prepare a bis[4-(N-(2-naphthyl) phenylamino) phenyl]-fumaronitrile (NPAN or 386)-loaded polymeric NPs through a two-step approach and solvent exchange method for targeted cell imaging.<sup>666</sup> The THF solution of NPAN was dropped into the aqueous solution under vigorous stirring to generate bare NPAN NPs suspension, followed by the addition of an aqueous solution of amphiphilic C18PMH-PEG under ultrasonification to afford NPAN polymeric NPs with surface coating. The AIE dots are brightly fluorescent in NIR region with a  $\Phi_F$  of 14.9%. They exhibit an average size of ~70 nm in water, low cytotoxicity, and good photostability. The C18PMH-PEG-folate was used to further modify the NPAN-based AIE dots and endow them with tumor-targeting ability. The folate-functionalized NPAN-based AIE dots can visualize the tumor in a distinct, sensitive, and selective manner with high spatial resolution.

Furthermore, in pursuit of NPAN-loaded AIE dots with enhanced fluorescence, Jen et al. developed an elegant FRET strategy and investigated how the selection of amphiphilic polymer matrixes could affect the quantum yields of the AIE dots (Figure 110).<sup>667</sup> Three amphiphilic block copolymers, including poly(ethylene glycol)-*b*-poly(*ɛ*-caprolactone) (PEG-*b*-PCL), poly(ethylene glycol)-*b*-polystyrene (PEG-*b*-PS), and poly(methacrylic acid)-*b*-polystyrene (PMAA-*b*-PS), have been individually employed as a nanocarrier to load two AIEgens: the green emissive HPS and red light-emitting NPAN (386; Figure 110A). Both the HPS and NPAN dots encapsulated by PMAA-*b*-PS showed the highest  $\Phi_F$  values in aqueous media (HPS dots with 20% loading ratio, 62.1%; NPAN dots with 5% loading ratio, 22.3%). This is probably attributed to the smallest size of PMAA-*b*-PS micelles among these three systems that exerts stronger spatial confinement on the fluorophores and also

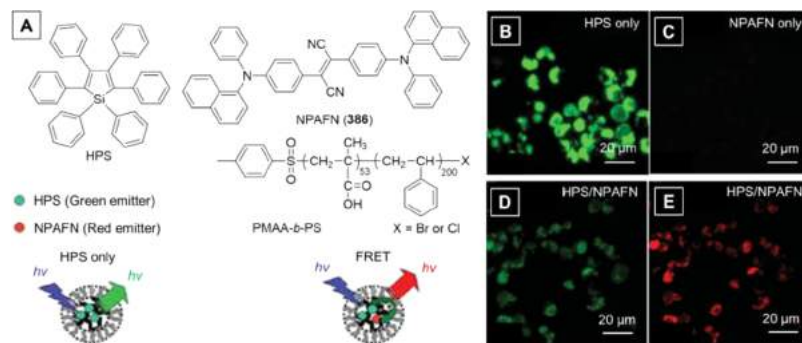


**Figure 110.** (A) Chemical structures of AIE molecules (HPS and 386) and amphiphilic block copolymers, and the schematic illustration of the resulted AIE dots. The confocal images of RAW cells incubated with PMAA-*b*-PS encapsulated HPS NPs using (B) donor channel, (C) PMAA-*b*-PS encapsulated NPAFN nanoparticles using FRET channel, and PMAA-*b*-PS encapsulated HPS/NPAFN NPs using (D) donor channel and (E) FRET channel, respectively. The identical HPS and NPAFN concentration are 64 and 8  $\mu\text{M}$ , respectively. The incubation time is 16 h. Adapted with permission from ref 667. Copyright 2010 Wiley-VCH Verlag GmbH & Co. KGaA.

the rigid PS core that stiffens the conformation of the fluorogens. The average size of PMAA-*b*-PS encapsulated AIE dots are found to increase from  $\sim$ 61 to  $\sim$ 68 nm with the increase in HPS loading ratio from 0% to 20%, while the sizes of PEG-*b*-PCL- and PEG-*b*-PS-based AIE dots were in the range of 67–91 nm and 72–90 nm, respectively. Further co-encapsulating HPS and NPAFN into these block copolymers produced FRET NPs, where the HPS served as the energy donor and NPAFN acted as the energy acceptor. Efficient energy transfer ( $>$  99%) and amplification of NPAFN emission ( $\sim$ 8 times) were achieved. Note that the amplification of emission from the NPAFN was estimated by comparing the fluorescence of NPAFN aggregates excited at 405 nm with and without HPS aggregates. As the PMAA-*b*-PS encapsulated HPS dots showed a more efficient cellular uptake as compared to the other two systems, the PMAA-*b*-PS encapsulated HPS/NPAFN dots were used for further study. After incubation with the mouse macrophage RAW cells, the PMAA-*b*-PS encapsulated HPS/NPAFN dots have been successfully internalized into cells as indicated by the CLSM images exhibited in Figure 110D,E. When excited at 405 nm and collected with a donor channel, intense green fluorescence signals could be observed from the cytoplasmic regions of cells co-incubated with PMAA-*b*-PS encapsulated HPS dots (Figure 110B). However, the green fluorescence could be efficiently suppressed in the cells stained with PMAA-*b*-PS encapsulated HPS/NPAFN dots as shown in Figure 110D. In contrast to the NPAFN-encapsulating polymeric NPs that show almost no fluorescence in the FRET channel (Figure 110C), a strong red fluorescence has been detected from the cells labelled with PMAA-*b*-PS encapsulated HPS/NPAFN dots (Figure 110E). The efficient suppression of green fluorescence and strong amplification of red fluorescence by the indirect excitation with 405 nm light (FRET channel) suggests efficient FRET from the HPS donor to the NPAFN acceptor after the internalization of PMAA-*b*-PS encapsulated HPS/NPAFN dots into cells. This work together with the BSA encapsulated PVF/385 dots (*vide supra*) has clearly demonstrated that coencapsulating two fluorogens which can undergo FRET process in the polymer matrix is an effective pathway to further increase the brightness of AIE dots.

In the systems discussed above, photonic energy, one-photon or two-photon, is used to excite the AIEgens or AIE dots. Other energy sources such as chemical energy can also be utilized to activate the luminescence processes of chromophores. Chemiluminescence is the light emission generated by a chemical reaction instead of photo-excitation. Chemiluminescence offers

ultrahigh sensitivity owing to the elimination of the noise associated with photo-excited autofluorescence from the background.<sup>668,669</sup> With elaborate design, systems that emit chemiluminescence can be achieved with AIEgens. Kim et al., for instance, have designed and fabricated AIEgen/peroxalate NPs with enhanced and tunable chemiluminescence for imaging of biogenic  $\text{H}_2\text{O}_2$  produced in cells and *in vivo*.<sup>670</sup> Sensitive detection and visualization of low-level  $\text{H}_2\text{O}_2$  in cells and tissues is very important for fundamental studies to understand its role in cellular processes as well as early diagnosis of inflammation diseases. Chemiluminescence has been widely exploited as a contrast signal for highly sensitive imaging of  $\text{H}_2\text{O}_2$ . The detection was realized via nonenzymatic peroxalate-based chemiluminescence reaction in the water-dispersed 387/peroxalate aggregated Pluronic NPs. AIEgen 387 was chosen as the signaling component for its efficient fluorescence in the aggregate state (Figure 111A). The 387/peroxalate NPs were formulated through a simple two-step procedure: homogenous mixing of Pluronic F-127,  $\text{H}_2\text{O}_2$ -responsive bis[3,4,6-trichloro-2-(pentyloxy carbonyl)phenyl] oxalate (CPPO) and 387 in a dichloromethane solution and subsequently adding water to the dried ternary mixture. During the latter step, uniform and well dispersed colloids with an average size of  $\sim$ 20 nm were spontaneously formed in water by self-assembly of the polymeric amphiphile Pluronic F-127. Thanks to the AIE feature of 387, these reactant-integrated nanoreactors have robust green chemiluminescence emission, whose intensity can be cumulatively enhanced by increasing the loading degree of 387. At 10 s after the addition of  $\text{H}_2\text{O}_2$ , 387/peroxalate NPs in water showed intense chemiluminescence emission that is 6.3-fold higher than that of the reactants in THF solution (insets in Figure 111B). The addition of  $\text{H}_2\text{O}_2$  triggered the reaction of CPPO and the released chemical energy activated the fluorescence of 387. Apart from the signal enhancement effect by AIE, it was found that the dense nanointegration approach also enabled the intraparticle energy transfer from  $\text{H}_2\text{O}_2$ -reactive peroxalates to dye aggregates and further to a low-energy dopant like Nile Red to facilely shift the emission towards the biologically more transparent window (red luminescent image in Figure 111B). The enhanced and tunable chemiluminescence of the AIE NPs allowed for the high-sensitivity imaging of endogenous  $\text{H}_2\text{O}_2$  overproduced during immune response and inflammation in cells and *in vivo* (Figure 111C). Such a work has definitely broadened the scope of AIE and meanwhile provided a design principle for the

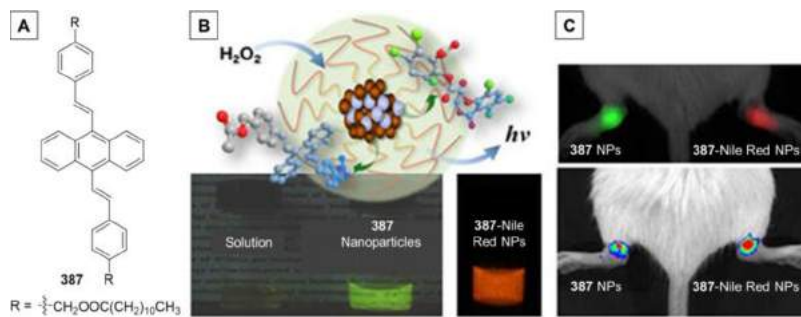


**Figure 111.** (A) Chemical structure of AIEgen 387 which was used as a chemiluminescent emitter in reactant-integrated nanoreactor. (B) Schematic representation the chemiluminescence of 387 generated by nonenzymatic peroxalate-based chemiluminescence reaction occurring in the reactant-integrated nanoreactor or nanoparticles. The input of H<sub>2</sub>O<sub>2</sub> oxidizes peroxalates to produce an electronically excited 1,2-dioxetanedione intermediate that subsequently transfers its energy to the coloaded emitting dyes 387 to generate fluorescence by purely chemical excitation. Insets: Fluorescent photograph of 387 in solution, and chemiluminescence emission from the 387/peroxalate nanoparticles with and without doping of Nile Red, generated by the input of H<sub>2</sub>O<sub>2</sub> in the dark. (C) In vivo chemiluminescence imaging of the lipopolysaccharide (LPS)-induced arthritis model with undoped (green luminescent) or Nile Red-doped (red luminescent) 387/peroxalate NPs, using an IVIS Spectrum imaging system. Green and red NPs were injected into each inflamed ankle just before imaging. Adapted from ref 670. Copyright 2012 American Chemical Society.

development of chemiluminescence AIE systems and nano-probes for biomedical imaging.

It can be easily seen from the above discussion that the AIE dots are unique and practically useful. Firstly, they are simple and convenient to prepare, usually obtained via only one- or two-step procedures. Moreover, the physical encapsulation allows facile tuning of their dye-loading rate, stability, size, and brightness. They require no pre-modification or special design of the AIEgens. Secondly, their encapsulation matrixes are remarkably diversified and the AIEgens are highly varied, rendering them rich in variety and functions. More importantly, they are small in size, uniform in morphology, ultra-bright, biocompatible, photostable, free of random blinking, and easy to be internalized into living cells with excellent retention. The AIE dots therefore can be applied for cell, tissue, or biospecies imaging and tracking with one-photon, two-photon excitation, or chemical energy activation, in a sensitive, noninvasive, high contrast, and superb resolution mode. The enormous efforts made on the AIE dots have undoubtedly expanded the scope of biological applications of AIEgens and offered new ideas to fluorescent bioprobe design. It can be envisioned that the integration of their imaging ability with other functions or modalities would definitely give birth to exhilarating new researches and applications. To our excitement, there are indeed some such works which will be discussed later.

**5.1.2.4. Silica NPs.** In addition to the pure organic AIE NPs expounded in the first three subparts, AIE-based inorganic–organic NPs have also been fabricated and utilized for biological imaging.<sup>142,671–677</sup> Silica nanoparticles (SNPs) have found wide use in areas varying from information technology to biological engineering. They are biocompatible, cytophilic, hydrophilic, transparent, but non-luminescent, making them ideal host materials for the preparation of fluorescent silica nanoparticles (FSNPs) for imaging purposes. FSNPs can be produced by introducing fluorophores into silica networks via chemical reactions or physical processes. The silica matrix serves as a protective shield, suppressing the possible penetrations of oxygen and other destructive species that may lead to photobleaching of the embedded fluorophores. Hybridization of the silica gel with AIEgens thus can endow the AIE NPs with high resistance to photobleaching and superior colloidal stability.

There already exist several synthesis methods for the covalent binding of luminogens to SNPs at the molecular level, amongst which the surfactant-free sol-gel reaction is the most frequently

used for the fabrication of AIEgen-based FSNPs.<sup>671–673,675</sup> For example, by virtue of this approach, our research team has performed a systematic work: we firstly incorporated the AIEgens into the SNPs and explored the bioapplications of these FSNPs. Then the universality of this method was validated by the subsequently developed dual-functional SNPs with fluorescence and magnetization as well as the recently explored biotin-decorated FSNPs for targeting cell imaging. Specifically, the FSNP hybridized with AIEgens can be fabricated through the sol–gel process in a one-pot reaction (Figure 112A).<sup>671</sup> Dibromo-terminated AIEgens 388, such as TPE (388a) and tetraphenylsilole derivative (388b), were first prepared and then coupled with (3-aminopropyl)triethoxysilane to generate 389. The resultant 389 underwent an ammonium hydroxide-catalyzed sol–gel reaction to afford the AIEgen-silica nanocores, which were further subjected to another sol–gel reaction with tetraethylorthosilicate (TEOS), ultimately yielding the FSNPs with the AIE-active luminogen core coated with a silica shell (FSNP-389). The FSNPs hold uniform size, high surface charge, and excellent colloidal stability. The diameter of these core-shell structured FSNPs can be fine-tuned in the range of 45–295 nm by altering the reaction conditions. These SNPs intensely fluoresce with blue (FSNP-389a) or green (FSNP-389b) emission. With low cytotoxicity, FSNP-389a and FSNP-389b have been efficiently internalized into living HeLa cells and selectively stain the cytoplasm regions with a high signal-to-noise ratio (Figure 112B).

NPs possessing efficient fluorescence and strong magnetization are highly attractive for their great potential in various high-tech applications, including ultrasensitive assays, living cell labeling, biological separation, specific drug delivery, magnetic resonance imaging, etc.<sup>678</sup> With 389b as a precursor, our laboratory prepared such dual-functional NPs with both intense fluorescence and strong magnetization via the one-pot sol–gel reaction depicted in Figure 112C.<sup>672</sup> Magnetite (Fe<sub>3</sub>O<sub>4</sub>) nanoparticles (MNP) were first prepared and then coated by stabilizer molecules, i.e., trisodium citrate to enhance their dispersion and stability in the solutions. The resulted citrate-modified MNPs (MNP-C) were purified and dried before being used as seeds for the formation of magnetic FSNPs (MFSNPs). Silole-functionalized siloxane (389b) was then subjected to the ammonium hydroxide-catalyzed sol–gel reaction with TEOS in the presence of MNP-C, furnishing MFSNPs with magnetic cores (mean diameter ~19 nm) coated with silole-containing

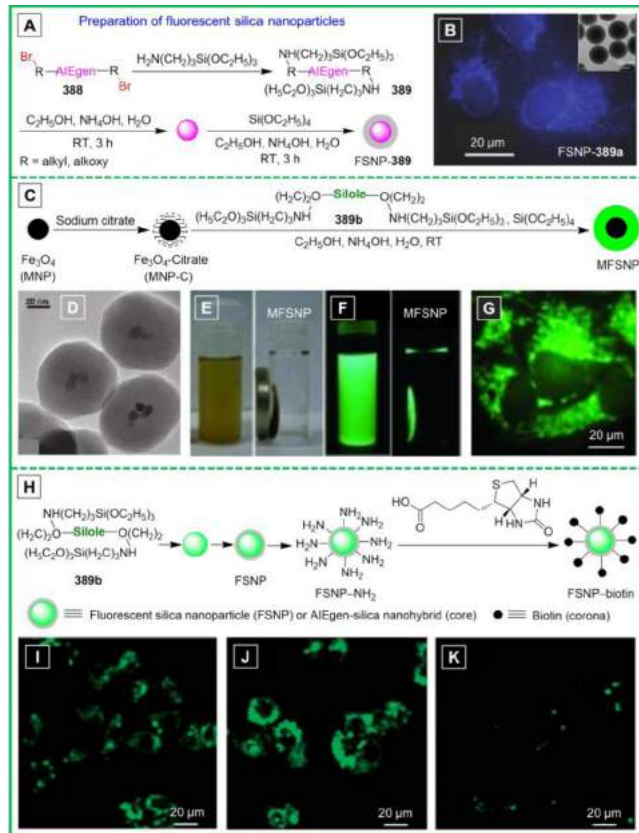


**Figure 112.** (A) General fabrication route towards AIegen-containing fluorescent silica nanoparticles (FSNPs) with a bromide AIe molecule (e.g., 388) as a precursor. (B) Fluorescence images of HeLa cells stained with FSNP-389a whose AIe core is TPE. Inset: TEM image of monodispersed FSNP-389a with an average particle size of 175 nm. Adapted with permission from ref 671. Copyright 2010 Wiley-VCH Verlag GmbH & Co. KGaA. (C) Synthetic route to magnetic fluorescent silica nanoparticles (MFSNPs) based on a silole derivative 389b. (D) TEM images of MFSNPs. Photographs of ethanol solutions of MFSNPs taken under (E) normal room lighting and (F) UV illumination in the (left) absence and (right) presence of external magnetic field from a bar magnet. (G) Fluorescence images of HeLa cells after labelling with MFSNPs. Reprinted with permission from ref 672. Copyright 2011 Wiley-VCH Verlag GmbH & Co. KGaA. (H) Fabrication of biotin-decorated FSNPs based on 389b. Fluorescence images of (I) HeLa, (J) BEL-7402, and (K) LO2 cells stained with FSNP-biotin for 3 h. Adapted with permission from ref 673. Copyright 2012 Royal Society of Chemistry.

silica shell (thickness ~28 nm; Figure 112D). The obtained MFSNPs are uniformly sized with smooth surface and positively charged at neutral pH and, hence, possess good colloidal stability. They are well dispersed in solutions and magnetically susceptible with zero remanence and coercivity, indicating that they are excellent superparamagnets with high magnetization (Figure 112E). Upon photoexcitation, brilliant green fluorescence with a  $\Phi_F$  of 7.1% is emitted from the MFSNPs due to the AIe characteristics of 389b (Figure 112F). The MFSNPs can function as a superb fluorescent visualizer which can selectively stain the cytoplasm of living cells (Figure 112G). Additionally, their surface can be readily modulated by varying the reactants, which offers more opportunities for further use.

By making use of the versatile sol–gel reaction, biotin-decorated FSNPs were successfully obtained by our group, in pursuit of widening the applicability of AIegen-loaded FSNPs.<sup>673</sup>

Biotin is one of the most well-known tumor recognition moieties and hence was introduced into the FSNPs with the aim of specific living tumor cell imaging. The sol–gel reaction of 389b and TEOS generated the FSNP-389b with a core-shell structure. Adding (3-aminopropyl)triethoxysilane into the reaction mixture yielded FSNP-NH<sub>2</sub> with abundant amino groups on the surface, which further underwent amidation reaction with biotin to afford FSNP-biotin (Figure 112H). The furnished FSNP-biotin is uniform in size (~51 nm), spherical in shape, and monodispersed with intense fluorescence. FSNP-biotin is nontoxic to living cells and can exclusively image the cytoplasm of living tumor cells (e.g., HeLa and BEL-7402) with overexpressed biotin receptors (Figure 112I,J). The low cellular uptake of FSNP-biotin by normal LO2 cells is attributed to the absence of biotin receptors on their cell membrane (Figure 112K). The FSNP-biotin can be retained inside the living cells for a long period of time, thereby enabling long-term tumor cell tracking over multiple passages and quantitative analysis of tumor cell migration.

Besides the sol–gel approach, other chemical reactions have also been employed to covalently link the AIegen to the silica networks. For example, our research team has taken advantage of the Cu(I)-catalyzed 1,3-dipolar cycloaddition (i.e. “click” reaction) to hybridize the SNPs with AIegen (Figure 113).<sup>674</sup>



**Figure 113.** Fabrication of AIegen-containing fluorescent silica nanoparticles FSNP-L and FSNP-S through “click” reaction. TEM images of (A) FSNP-L-391a (TPE-cored) and (C) FSNP-L-391b (dimethyltetraphenylsilole-cored) with particle sizes of about 150 and 240 nm, respectively. Fluorescence images of HeLa cells labeled with (B) FSNP-L-391a and (D) FSNP-S-391b. Adapted with permission from ref 674. Copyright 2011 Wiley-VCH Verlag GmbH & Co. KGaA.

The diyne-functionalized AIegen, e.g., TPE (390a) or silole (390b), and azide-decorated siloxane (PTEOS-azide) were synthesized first and then subjected to the click reaction, generating 391. FSNPs with core-shell architecture can be made from 391 by means of Stöber and reverse microemulsion methods. In the former approach, the molecules of 391 were hydrolyzed and condensed in an ethanol/water mixture containing ammonium hydroxide to form the AIegen-silica nanocores, which were then subjected to another sol–gel reaction with TEOS to afford FSNP-L. Microemulsion is noted for its capability to produce nanometer-sized particles with narrow distribution. Amphiphilic surfactant Triton-X was used to facilitate the formation of thermodynamically stable nanoreactor. The nanodroplets of water in the bulk oil phase work as nanoreactors for discrete particle formation. The 391 was then added into the mixture and stirred for 30 min to yield the AIegen-silica cores, which further undergo the sol–gel reaction, furnishing small-sized FSNP-S with core-shell structure. These FSNPs are all uniformly sized with smooth surfaces and highly charged with good colloidal stability. The sizes of FSNPs can be tuned by altering the preparation method or varying the reaction parameters. The FSNP-L-391a (TPE-cored) and FSNP-L-391b (silole-cored) fabricated by the Stöber method have larger

particle sizes of  $\sim 150$  and  $\sim 240$  nm, respectively (Figure 113A,C), as compared to the FSNP-S-391a ( $\sim 40$  nm) and FSNP-S-391b ( $\sim 64$  nm) obtained via microemulsion method. As they are benign to living cells and strongly emissive, these FSNPs enjoy the capability to visualize living HeLa cells as fluorescent probes (Figure 113B,D). The appropriate sizes of FSNP-L-391a and FSNP-S-391a allow both of them show very similar cell imaging ability (Figure 113B), whereas the large size of FSNP-L-391b makes it less good in comparison with the FSNP-S-391b (Figure 113D), indicating the size-dependency of the cellular uptake.

In addition to the covalent hybridization between the AIEgens and SNPs, physical encapsulation which has no requirement for the reactivity of AIEgen has also been developed for the fabrication of FSNPs.<sup>142,675,676</sup> Belfield and coworker, for example, has constructed an aggregation-enhanced NIR emitting silica nanoprobe for bioimaging through encapsulating an AIE-active NIR emitter (i.e. **103**) in SNPs.<sup>142</sup> **103** was synthesized via the ACQ-to-AIE strategy as discussed in section 3.3. With a large D- $\pi$ -A- $\pi$ -D structure, **103** features not only the AIE characteristics but also a TICT effect and two-photon absorption (2PA) properties. To apply this hydrophobic AIEgen for two-photon fluorescence imaging, **103**-doped SNPs have been prepared following the synthetic route depicted in Figure 114A.

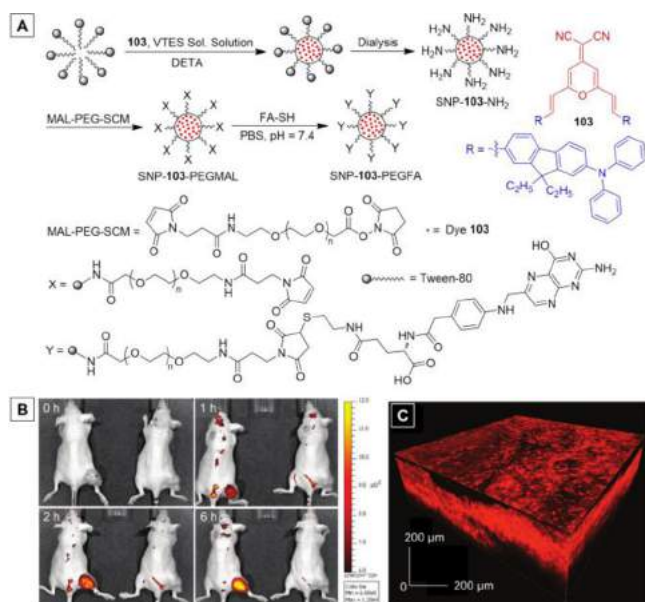


**Figure 114.** (A) Synthesis and surface modification of **103**-doped fluorescent SNPs with folate surface modification. (B) Representative in vivo fluorescence images of mice bearing HeLa tumors. The mice were intravenously administered with (left) **103**-containing folate SNP conjugate (SNP-**103**-PEGFA) or (right) **103**-containing SNP without folic acid modification (SNP-**103**-PEGMAL) at 3 nmol g<sup>-1</sup> body weight, and the fluorescence signal was monitored at different time points post-probe administration. (C) Representative 3D two-photon excited fluorescence images of the HeLa tumor from a mouse that was injected with SNP-**103**-PEGFA (3 nmol g<sup>-1</sup>) in the tail vein. Adapted from ref 142. Copyright 2011 American Chemical Society.

A prepolymerized triethoxyvinylsilane (VTES) sol solution was prepared prior to the synthesis of **103**-doped SNPs. The VTES sol solution was mixed with the solution of **103** and then coprecipitated within the nonpolar interior of aqueous Tween-80 micelles through a solvent exchange process. *N'*-[3-(Trimethylsilyl)propyl]diethylenetriamine (DETA) was afterwards added to the reaction mixture to introduce amino groups onto

the SNP surface for sequential bioconjugation, affording SNP-**103**-NH<sub>2</sub>. The resultant SNP-**103**-NH<sub>2</sub> are uniform in size with an average diameter of  $\sim 25$  nm (20 wt % **103**), which is small enough to suppress the clearance of the host's immune system, prolong the circulation time of the FSNPs in live animals and thus augment FSNPs accumulation in the targeted tumors. The SNP-**103**-NH<sub>2</sub> dispersed in water exhibited an intense red emission peaked at  $\sim 650$  nm with a high  $\Phi_F$  of  $18.0 \pm 4.0\%$ , and a maximum 2PA cross-section ( $\delta$ ) of  $\sim 2100$  GM at 980 nm, which was  $\sim 3$  times higher than the free **103** in THF. The high aggregate-state  $\Phi_F$  and  $\delta$  are attributed to the AIE activity of **103**, whose intramolecular motions are significantly hindered by the physical confinement in the SNPs.

To screen the silica nanoprobe from the host's immune system and target folate receptor-overexpressed tumors, the surface of the SNPs was further embellished with maleimide-terminated PEG and then folate (FA; Figure 114A). The maleimide-poly(ethylene glycol)-succinimidyl carboxymethyl (MAL-PEG-SCM,  $M_w = 3400$ ) was first utilized to react with the SNPs, generating a maleimide functional group on the surface (SNP-**103**-PEGMAL) to react with the thiol-modified folate to yield the folate-conjugated SNPs (SNP-**103**-PEGFA). The photo-stability of the fluorescent SNP-**103**-PEGFA (photodecomposition quantum yield  $\Phi_d = 3.7 \times 10^{-7}$ ) was  $\sim 4$ -fold higher than the free **103**, giving rise to an impressively high figure of merit ( $F_M = \delta\Phi_F/\Phi_d$ ) value of  $\sim 1.1 \times 10^9$  GM. SNP-**103**-PEGFA showed low cytotoxicity and can be selectively taken up by the folate receptor overexpressed HeLa cells as verified by the in vitro one-photon and two-photon fluorescent imaging. Comparative in vivo tumor imaging with SNP-**103**-PEGFA and SNP-**103**-PEGMAL nanoparticles demonstrated the capability of SNP-**103**-PEGFA as an efficient nanoprobe for in vivo fluorescence bioimaging upon intravenous administration into mice bearing HeLa tumors (Figure 114B). At 0.5 h post-injection with SNP-**103**-PEGFA, an obvious fluorescence signal was detected in the tumor of mice, and a steady increase in the fluorescence intensity from the tumor site was observed during the next few hours with a maximum reached at 6 h. Whereas the mice injected with SNP-**103**-PEGMAL maintained no fluorescence in the tumor region in the observation period. These results manifest that the SNP-**103**-PEGFA can be delivered to tumor sites effectively and accumulated there. Furthermore, the two-photon fluorescence imaging of the tumor excised from the nanoprobe-administered mice revealed that the SNP-**103**-PEGFA nanoprobes appeared to be chiefly distributed in the cytoplasm of cancer cells. Deep tissue ex vivo two-photon fluorescence imaging ( $\sim 350$   $\mu$ m) has been achieved with 3D cellular-level resolution of a solid tumor. The tumor from the mouse injected with SNP-**103**-PEGFA clearly exhibited strong fluorescence (Figure 114C), whilst there is no significant signal collected for nonfolate-conjugated SNP-**103**-PEGMAL, providing a further proof to the fact that the folate-mediated active targeting strategy is more effective than the passive pathways via EPR in terms of the selectivity and cellular uptake. Such a comprehensive work has provided guidance for the development of silica nanoprobes loading AIEgens.

There are some other studies where the AIEgens have been non-covalently encapsulated into the SNPs and used for bioapplications.<sup>675–677</sup> For example, by virtue of the one-pot surfactant template method, DSA derivative **392** has been facilely incorporated into the mesoporous silica nanoparticles (MSNPs) for intracellular imaging and cancer therapy (Figure 115).<sup>676</sup> The THF solution of AIEgen **392** and the aqueous solution of cetyltrimethylammonium bromide (CTAB), a common cationic

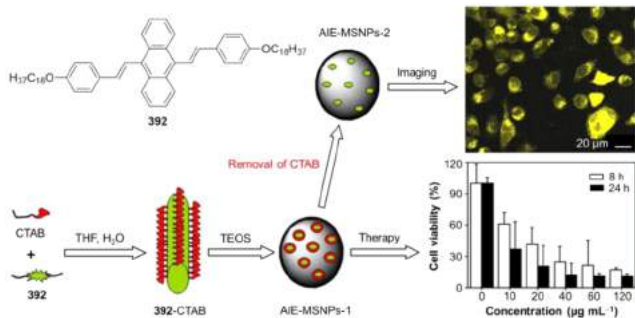


**Figure 115.** Schematic showing the preparation of 392-based AIE-MSNPs and their application for cell imaging and cancer therapy applications. Insets: (upper panel) CLSM images of A549 cells incubated with 50  $\mu\text{g mL}^{-1}$  of AIE-MSNPs-2 for 3 h and (lower panel) cell viability of AIE-MSNPs-1. A549 cells were incubated with different concentrations of AIE-MSNPs-1 for 8 and 24 h. Adapted from ref 676. Copyright 2013 American Chemical Society.

surfactant, were first mixed. The amphiphilic complexes 392-CTAB could be easily generated in the THF/water mixture with high water content. The 392-CTAB further function as the structure-directing template for the preparation of MSNPs. TEOS was then added dropwise into the aforesaid solution to undergo a sol–gel reaction to form the mesoporous silica shell. Removing THF from the reaction system afforded the fluorescent AIE-MSNPs-1 with 392 encapsulated in the MSNPs. AIE-MSNPs-1 holds a spherical shape and uniform particle size  $\sim$ 200 nm. The surfactants CTAB can be removed by washing the as-synthesized AIE-MSNPs-1 with methanol and diluted hydrochloric acid to furnish AIE-MSNPs-2. Both the BET surface areas and pore diameter of AIE-MSNPs-2 are larger than AIE-MSNPs-1. AIE-MSNPs-2 is biocompatible and hence can be used for cell imaging. After incubation with A549 cells, the AIE-MSNPs-2 was internalized by the cells, located mainly in the cytoplasm and lighted up the cytoplasm with strong green-yellow fluorescence (CLSM image in Figure 115). On the other hand, CTAB has been acknowledged as a broad-spectrum antiseptic reagent and cheap tumoricidal agent, and the possible anticancer mechanism is ascribed to its promoting effect on the cell apoptosis. The anticancer effectiveness of AIE-MSNPs-1 was hence evaluated. The results shown in Figure 115 have manifested the anticancer ability of AIE-MSNPs-1 as an efficient cell killing agent, with the half maximal effective concentration ( $\text{EC}_{50}$ ) values as low as 14.4 and 3.5  $\mu\text{g mL}^{-1}$  for 8 and 24 h incubation, respectively. Given the facile preparation and combination properties of AIEgen 392, CTAB, and MSNPs, these AIEgen-encapsulated nanohybrids are promising for cell imaging, cancer therapy, and other bioapplications.

The AIEgen-loaded SNPs always enjoy uniform size and morphology, excellent colloidal stability, good biocompatibility, and superb surface modifiability and can be customized for cell imaging and tracking, two-photon fluorescence imaging, tumor targeting imaging, or even cancer therapy, by varying the AIEgens, surface functional groups or coreagents. Given the good performance yet not much work published, there is still large development space for this class of fluorescent NPs.

**5.1.2.5. Dual Modalities.** The examples shown in the above subsections are mainly reflecting the single-function applications of AIEgens in biological areas. Along with the development of AIE research and the progress in biomedical areas, recently, there has emerged a string of fabulous AIE systems that enjoy dual functions and can be applied for clinical diagnostics or

theranostics. In this part, we sort out the most representative works and discuss them in detail, in hope of presenting the charm, powerfulness, adaptability, as well as the flexibility of AIE and stimulating more and better work in this area.

Understanding the cancer metastasis mechanism and process becomes a major concern in modern biomedical research for its great significance lying in cancer diagnosis and treatment.<sup>679</sup> Although several medical imaging techniques including optical, magnetic, and radionuclide imaging have been developed in this regard, each imaging modality has its own superiorities and limitations. For instance, fluorescence imaging holds high sensitivity but is hardly able to provide quantitative evaluation of cell distribution, whilst MRI and radionuclide imaging offer desired tissue penetration depth but suffer from low sensitivity and resolution under the single cellular level.<sup>680</sup> In comparison with single-modal imaging probing systems, integration of two or more imaging modalities into a single probing system will generate multimodal imaging probe with complementary and synergistic benefits, which is highly demanded in modern biological imaging.<sup>681–683</sup> As discussed in section 5.1.2.3, the versatile matrixes for AIEgen encapsulation, e.g., DSPE-PEG, can decorate the surface of AIE dots with different active functional groups, such as maleimide, amino, and carboxyl groups, which enable further functionalization to accomplish the goal of multimodal imaging. In the light of this, Liu and coworkers inventively fabricated AIE dots with fluorescent-magnetic dual-modality and utilized them to study the *in vivo* tumor cell metastasis (Figure 116A–D).<sup>684</sup> A mixture of DSPE-PEG<sub>2000</sub>-NH<sub>2</sub> and DSPE-PEG<sub>2000</sub>-Mal was used as the encapsulation matrix for FR/NIR AIEgen 384 to afford biocompatible AIE dots with surface amine and maleimide groups for subsequent conjugation. The resultant AIE dots are spherical in shape with an average particle size  $\sim$ 32 nm. These AIE dots exhibits almost identical properties to those constructed from 384 and DSPE-PEG, in terms of their absorption ( $\lambda_{\text{ab}} = 512 \text{ nm}$ ), emission ( $\lambda_{\text{em}} = 670 \text{ nm}$ ), and  $\Phi_{\text{F}}$  (25%). To integrate the MR contrast with the fluorescent AIE dots, diethylenetriaminepentaacetic (DTPA) dianhydride was used to conjugate with amine groups on the dot surface for further chelation of gadolinium(III). The resultant Gd(III)-chelated dots were then conjugated with HIV-1 Tat peptide (RKKRRQRRRC) through reaction between maleimide groups on dot surface and thiol groups at C-terminus of Tat peptide, furnishing the Tat-Gd-AIE dots.

As implied by the *in vitro* cell imaging results, the Tat conjugation indeed greatly enhanced the cellular uptake of the obtained Tat-Gd-AIE dots. The high brightness of Tat-Gd-AIE dots allows sensitive imaging of the transplanted cells (Figure 116C) as well as direct indicating of their biodistribution, which has been clearly verified by the *in vivo* and *ex vivo* living C6 glioma cell tracing experiments in the mouse. At each time point post injection, the lung (Figure 116B) and liver of mouse show intense fluorescence; on the contrary, negligible fluorescence signal is observed from the kidney and heart. The incorporation of Gd(III) on the AIE dots enables quantification of the biodistribution of injected cancer cells in an accurate manner, showing that  $\sim$ 35% and 48% of the cells are engrafted in the lung and liver at 1 h post injection, while only  $\sim$ 17% of cells are in heart, spleen, and kidney. By virtue of the high emission efficiency of Tat-Gd-AIE dots, the localization of injected cells in organs and their engraftment after transplantation can be monitored with high resolution and sensitivity at the single cell level (Figure 116C), which is highly important to cancer metastasis and therapy studies. The Tat-Gd-AIE dots have been

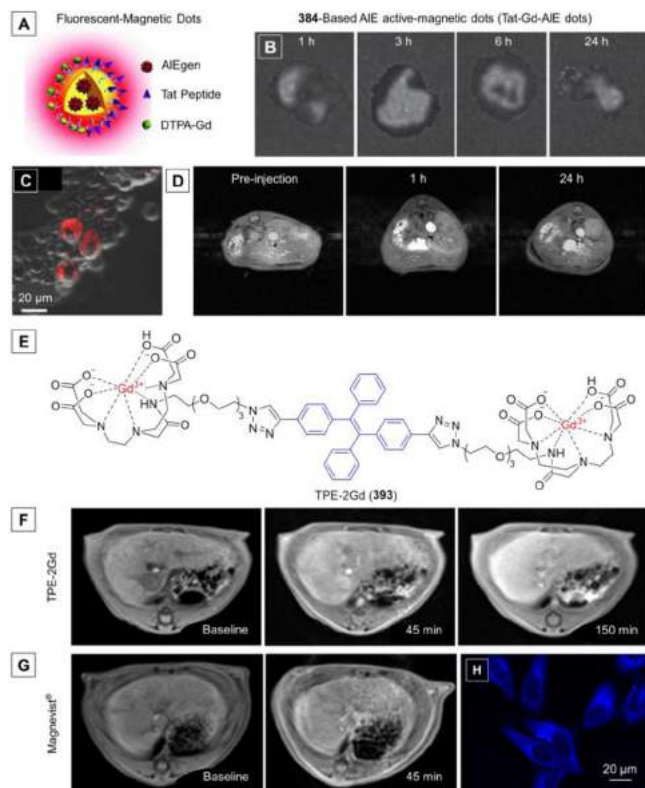


**Figure 116.** (A) Schematic illustration of structure of the fluorescent magnetic dots loaded with AIEgens, e.g., 384 and gadolinium(III) complex. (B) Representative ex vivo fluorescence images of lung collected from the mice injected with C6 glioma cells labeled by 384-based magnetic AIE dots at 1, 3, 6, and 24 h post injection. (C) Enlarged confocal images of the tissue sections of lung collected from the mouse injected with C6 cells labeled by 384-based magnetic AIE dots. (D)  $T_1$ -weighted magnetic resonance (MR) images of mice injected with Tat-Gd-AIE dot-labeled C6 cells ( $3 \times 10^6$ ) at 0, 1, and 24 h post-injection. Adapted with permission from ref 684. Copyright 2013 Wiley-VCH Verlag GmbH & Co. KGaA. (E) Molecular structure of dual-modal MRI contrast agent TPE-2Gd (393). Axial  $T_1$ -weighted MR images through the liver of rat after intravenous injection of (F) TPE-2Gd and (G) Magnevist with concentration of  $0.1 \text{ mmol kg}^{-1} \text{ Gd}^{3+}$ . Adapted from ref 685. Copyright 2014 American Chemical Society.

proven to be an efficient  $T_1$  contrast agent with desired longitudinal relaxation time ( $7.91 \text{ mM}^{-1} \text{ s}^{-1}$ ), but the stained cells cannot be detected by MRI upon intravenous injection into the mice (Figure 116D), which is ascribed to the relatively low sensitivity of MRI and the inadequate amount of Gd(III) in the injected cells. Further optimization of the formulation of AIE dots may provide solutions to improve the MR imaging ability. Such a pioneering work definitely has opened up new avenues for more dual-modal or even multimodal imaging systems constructed on the basis of AIEgens.

Delightfully, by means of incorporating Gd(III) into TPE derivative, a dual-modal MRI contrast reagent with AIE characteristics, namely, TPE-2Gd (393), has been designed and synthesized by Tang and Zheng et al.<sup>685</sup> TPE-2Gd (393) holds the capability of both MR and fluorescence imaging. Comprised of a hydrophobic TPE fluorophore and two hydrophilic Gd diethylenetriaminepentaacetic acid moieties (Figure 116E), TPE-2Gd (393) is an amphiphilic molecule, which can spontaneously aggregate into nanomicelles with strong fluorescence at a high concentration in aqueous media. 393 can be used as a fluorescent probe for cell imaging, and it shows negligible

cytotoxicity and excellent photostability ascribable to its AIE property. 393 can be readily taken up by the living HeLa cells and selectively light up their cytoplasm regions with intense blue fluorescence (Figure 116H). Notably, 393 is able to be employed as a MRI contrast agent, demonstrating longitudinal relaxivity in water ( $R_{1,\text{TPE-2Gd}} = 3.36 \pm 0.10 \text{ s}^{-1}$  per mM of  $\text{Gd}^{3+}$ ) comparable to those commercial Gd-based MRI contrast agents (e.g., Magnevist,  $R_{1,\text{TPE-2Gd}} = 3.70 \pm 0.02 \text{ s}^{-1}$  per mM of  $\text{Gd}^{3+}$ ). As compared with Magnevist, the circulation lifetime of 393 nanoaggregates in living rats is prolonged from 10 min to 1 h. The longer circulation time and higher contrast of MRI achieved by 393 can be attributed to its ability to form nanoaggregates and enter the intracellular regions. With relatively high specificity to the liver, the MR imaging could maintain hyperintense in liver even after 150 min post administration (Figure 116F), outperforming the Magnevist (45 min; Figure 116G). Thus, 393 could be utilized to discriminate lesion and normal tissues. These nanoaggregates can be eliminated from body gradually through renal filtration owing to the disintegration of the nanoaggregates into small particles or molecules during circulation. 393 thereby possess great potential to be applied as a liver-specific MRI contrast agent for clinical diagnosis. Such a study represents a new generation of materials which fuse the AIE activity and magnetic relaxivity to afford a dual-modal MRI-fluorescent reagent and undoubtedly offers new insights to the exploration of other multimodal imaging systems.

The sole role of conventional drug delivery systems (DDSs) is to deliver drugs into cancer cells. These DDSs are invisible and difficult to trace after they enter the cells and release the drugs. Unveiling the endocytosis or phagocytosis behaviors of the DDS is vital to the design of sophisticated drug therapies. It is thus of great importance to uncover the cell uptake mechanisms of DDS. At present, the most commonly used method is fluorescent tagging. However, the fluorescent tagging methods may suffer from some problems: (i) the fluorescent tag may interfere with the work of DDS, and (ii) the fluorescent tag may be hydrolyzed or detached from the DDS during the delivery process and hence gives false information or loses its indicating function. Therefore, it is highly desirable to develop self-luminescent drug delivery systems which have low or no cytotoxicity but can provide real-time and true information about their locations and distributions inside cells. Enlightened by the excellent performance of AIE materials in the biological areas, some research groups have recently taken advantage of AIEgens to make an attempt to construct such self-luminescent DDSs and have achieved some good results.

For example, Liang et al. have originally developed a self-indicating drug delivery system (SIDDS) with tunable aggregation emission, which holds the capability of revealing spatiotemporal drug release (Figure 117A–C).<sup>686</sup> The carboxylate TPE derivative (i.e., 394) spontaneously assembled into spherical NPs in aqueous media with an average size of 70 nm, which were strongly luminescent due to its AIE attribute and self-tracked their actual position within cells. 394 NPs showed no cytotoxicity and distributed in the cytoplasm rather than entered the nuclei of cells, which are the function implementation sites of the drugs (doxorubicin or DOX). The 394 NPs system outshined conventional DDSs and quantum dots for they are cytocompatible, easy to fabricate, ACQ-free, and do not interfere with the drug functions. Moreover, antitumor drug DOX bonded to 394 NPs and formed a new drug delivery nanoparticle system (394-DOX NPs) with an average size of 8 nm. The dissociation of DOX from 394-DOX NPs was regulated by the pH, rendering

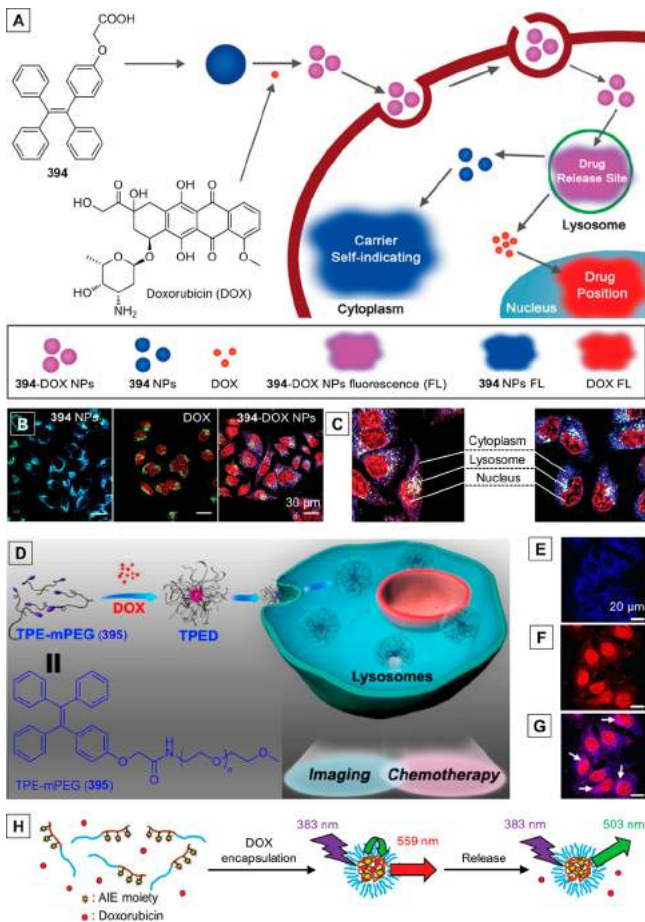


**Figure 117.** (A) Schematic illustration showing the formation of 394-DOX NPs, the drug releasing site, and real sub-cellular positions of 394 NPs and DOX by the “emission colors” transitions of this DDS. (B) Spatial distributions of 394 NPs, DOX, and 394-DOX NPs in MCF-7s cells. CLSM images of 394 NPs, DOX and 394-DOX NPs distribution, and lysosomes, indicated by Lysotracker Green. The breast cancer MCF-7s cells were incubating with 394 NPs ( $40 \mu\text{M}$ ), DOX ( $4 \mu\text{M}$ ), and 394-DOX NPs ( $40 \mu\text{M}$ ) for 2 h. (C) Detailed 394-DOX NPs spatiotemporal distributions in MCF-7s cells. Adapted with permission from ref 686. Copyright 2013 Wiley-VCH Verlag GmbH & Co. KGaA. (D) Schematic illustration of DOX-loaded self-assemble micelle (TPED) with AIE as a novel multifunctional theranostic platform for intracellular imaging and cancer treatment. Spatial distributions of TPED in MCF-7 cells using (E) donor channel, (F) acceptor channel, and (G) their overlay image. Adapted from ref 687. Copyright 2014 American Chemical Society. (H) Schematic illustration of using AIEgen labeled amphiphilic block copolymers to encapsulate DOX and monitoring the encapsulation and release. Adapted with permission from ref 688. Copyright 2013 Wiley-VCH Verlag GmbH & Co. KGaA.

the DOX to be released in lysosomes (pH 5.0; Figure 117A). As can be seen from the CLSM images, 394 NPs, 394-DOX NPs, and free DOX displayed three distinct “colors” (Figure 117A–C). Through observing the transition of these “colors”, the subcellular location of 394 NPs and free DOX can be identified, and the drug releasing site of 394-DOX NPs was indicated as well (Figure 117B,C). Specifically, 394-DOX NPs were first internalized into cells and transported into lysosomes, where the DOX detached from 394-DOX NPs. Then, the released DOX escaped from the lysosome, entered, and lighted up the cell nucleus with red fluorescence, while the 394-NPs stayed in the cytoplasm and emitted a blue light (Figure 117A). Additionally, the SIDDS exerted a stronger inhibition effect on the

proliferation of cancer cells owing to the higher DOX delivery efficiency. In short, this innovative dual-modal SIDDS not only determined the subcellular location of the delivery system but also improved the therapeutic effect.

Soon afterwards, the same group further developed another dual-modal DDS on the basis of a TPE derivative to visualize the intracellular anticancer drug delivery by the self-assembled micelles with the AIE effect.<sup>687</sup> In this work, they introduced the biocompatible polymer PEG into the molecular design to further improve the above discussed dual-functional DDS. Amino-methoxypolyethylene glycol (mPEG<sub>2000</sub>-NH<sub>2</sub>) was grafted to 394 and the afforded conjugate (TPE-mPEG, 395) was used to generate stable amphiphilic polymeric AIE micelles via self-assembly (Figure 117D). The PEG acted as the hydrophilic arm, while the TPE moiety serves both as an imaging agent and the hydrophobic motif of the DDS for the encapsulation of hydrophobic anticancer drugs. TPE-mPEG (395) micelles loading DOX (TPED) were prepared via the film dispersion approach, with a spherical shape and a diameter of  $\sim 30 \text{ nm}$ . The drug loading efficiency of TPED is up to 15.3% by weight, which ensures a higher anticancer efficiency than that of the free DOX. With this traceable nanoformulation, the drug delivery process can be closely monitored. The AIE renders the nanocarriers visible for high-quality imaging and the emission on-off switching is intrinsically modulated by the assembly and disassembly of the nanomicelles. Thanks to the AIE feature, the micelles can be used as a fluorescent probe for intracellular imaging and self-localization at a subcellular level (Figure 117E–G). In like manner, this TPED nanomicelle system can be taken as a multifunctional theranostic platform for intracellular imaging and cancer treatment.

In addition to TPE derivatives, siloles can also be utilized to do similar work. Wu and coworkers developed a type of fluorescent polymeric micelles with AIE properties to monitor the encapsulation and release of DOX (Figure 117H).<sup>688</sup> A series of silole-labeled amphiphilic block copolymers which consist of a hydrophilic PEG block and a hydrophobic domain obtained by copolymerizing a vinyl-modified silole derivative with styrene, self-assembled to form fluorescent micelles. When loaded with the fluorescent anticancer drug DOX, the encapsulation and release of the drug can be monitored by the fluorescence change of the complex system. Owing to the spectral overlap, FRET from the copolymer to DOX takes place upon the encapsulation. The occurrence and subsequent decrement of FRET from the DOX-loaded micelles hence can work as an indicator for the encapsulation and sequential release of the drug, respectively (Figure 117H). Moreover, these fluorescent polymeric micelles are not only fluorescent probes but also anticancer drug carriers simultaneously.

Thus, it can be easily seen from the above discussion that new-generation DDSs with the capacity for simultaneous imaging and therapeutic treatment have received more and more attention. To make the vehicle visible, luminogens can be linked to or physically encapsulated in DDSs. In the examples displayed in Figure 117, the DOX was loaded into AIE NPs or nanomicelles through physical processes. Liu and Tang et al. also took advantage of the unique fluorescence property of AIEgens. They designed a series of prodrugs composed of cisplatin (Pt(II)) or cisplatin/DOX covalently conjugated to AIEgens together with hydrophilic or enzyme-cleavable peptide sequence, which released cisplatin and simultaneously reported the event upon the reduction of prodrug(s) or being cleaved by intracellular protease.<sup>689–691</sup> Although cisplatin has been extensively used in

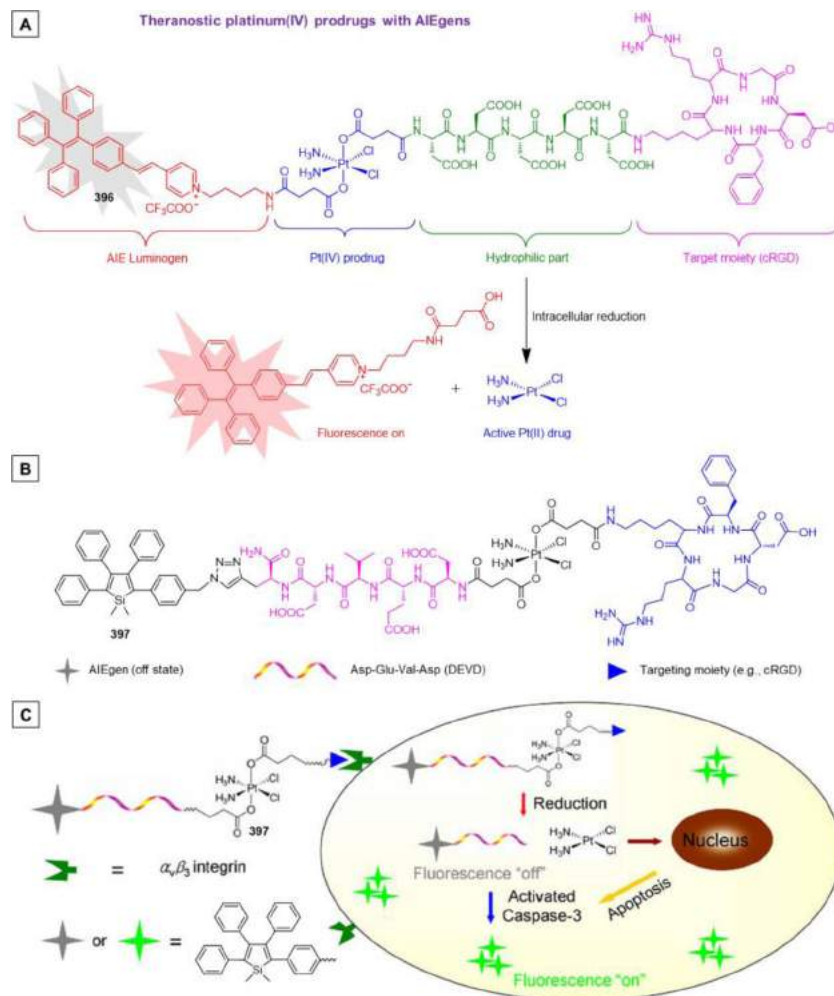


**Figure 118.** (A) Schematic illustration of TPE-based prodrug 396 design strategy and the fluorescence turn-on monitoring of drug activation. Reprinted with permission from ref 689. Copyright 2014 Royal Society of Chemistry. (B) The molecular structure of the targeted theranostic platinum(IV) prodrug 397. (C) Schematic illustration of the targeted theranostic platinum(IV) prodrug 397 with a built-in AIE light-up apoptosis sensor for noninvasive *in situ* early evaluation of its therapeutic responses. Reprinted from ref 690. Copyright 2014 American Chemical Society.

clinics to treat a broad spectrum of human malignancies, like most other cytotoxic anticancer drugs, it suffers from severe side effects which limit its direct clinical use.<sup>692</sup> To overcome these restrictions, an alternative approach has been established by making use of the nontoxic Pt(IV) prodrugs which can be intracellularly reduced to active Pt(II) complex and further restore their latent cytotoxic activity.<sup>693,694</sup> The use of Pt(IV) prodrugs have been proven successful in improving the efficacy of platinum-based drugs; however, the elucidation of how and when the Pt(IV) prodrugs are reduced after being taken up by cells is hard and rare. Thus, the theranostic system that can specifically deliver the Pt(IV) prodrugs to tumor cells with minimized side effects and simultaneously monitor the drug activation and efficacy *in situ* and in real time in living cells is highly demanded. To this end, Liu and Tang et al. first synthesized and biologically evaluated a targeted theranostic platinum(IV) prodrug delivery system 396 on the basis of an AIEgen for *in situ* monitoring of the platinum(IV) prodrug activation.<sup>689</sup> The theranostic system 396 is primarily comprised of four components: (i) the chemotherapeutic prodrug platinum(IV), which can be reduced to active nontoxic Pt(II) form inside the cells, (ii) a tetraphenylethene pyridium unit with AIE property, (iii) a short hydrophilic peptide with five aspartic

acid (D5) units to endow the water solubility, and (iv) a cRGD tripeptide as a targeting ligand (Figure 118A). The resultant prodrug system 396 enjoys high water solubility and preferential accumulation in cancer cells overexpressing integrin  $\alpha_v\beta_3$ . Owing to the unique nature of the AIEgen, the highly hydrophilic prodrug 396 is practically non-emissive in aqueous media but becomes highly fluorescent when reduced inside cancer cells. The fluorescence turn-on is ascribed to the activation of RIM process of the less hydrophilic cleaved residues, which promotes the radiative relaxation pathways. This prodrug design provides a platform for efficient platinum drug delivery and real-time monitoring of the drug activation with a high signal-to-noise ratio.

In the meantime, Liu and Tang et al. have reported another targeted theranostic platinum(IV) prodrug system, considering the high importance of such work in the personalized medicine.<sup>690</sup> Different from 396, this silole-based prodrug system (397) contains a built-in AIE light-up apoptosis sensor and can be used for noninvasive *in situ* early evaluation of its therapeutic responses. Therapeutic drugs generally kill the cancer cells by activating apoptosis within a short time, thus the incorporation of apoptosis-specific moiety in the probe could enable the assessment of the therapy efficacy at a very early

stage.<sup>695</sup> On the basis of their research conducted on the caspase and apoptosis detection, Liu and Tang et al. selected the specific caspase-cleavable DEVD peptide sequence as an apoptosis-responsive motif to establish the aimed prodrug system. In this way, at its two axial positions, the Pt(IV) prodrug was embellished with a tumor-targeting cRGD peptide and an apoptosis “reporter” which is composed of an AIE-active TPS fluorogen and a caspase-3 enzyme-specific DEVD peptide (Figure 118B). The obtained targeted Pt(IV) prodrug is able to selectively bind to integrin  $\alpha_5\beta_3$ -overexpressed cancer cells and facilitate the cellular uptake. Furthermore, the Pt(IV) prodrug is intracellularly reduced to active Pt(II), releasing the apoptosis sensor TPS-DEVD simultaneously. The Pt(II) drug can induce the cell apoptosis and trigger the caspase-3 enzyme to specifically cleave DEVD peptide sequence on TPS-DEVD and generate a hydrophobic TPS residue. The original TPS-DEVD is soluble and thus non-fluorescent in aqueous media due to the dynamic intramolecular rotations, whereas the resultant TPS residue is hydrophobic and tends to aggregate, rendering the RIR process coming into play and turning on the fluorescence (Figure 118C). Such a fluorescence light-up response enables the early assessment of the drug therapeutic efficacy in cells with high signal-to-noise ratios. The apoptosis-induced fluorescence enhancement in the U87-MG cells exhibits a good correlation with the prodrug concentration and the cell viability, indicating that this prodrug delivery system allows for efficient tumor-targeting drug delivery and instant drug therapeutic response evaluation, which is essential to guide the therapeutic decisions.

As cisplatin (Pt(II)) and DOX are two most effective antitumor drugs utilized in clinics and it has been reported that the co-administration of these two drugs could show a synergistic anticancer effect,<sup>696</sup> Liu and Tang et al. further designed and constructed a traceable targeted theranostic delivery system (398) containing cisplatin prodrug and DOX.<sup>691</sup> Such a system can be employed to track the location and distribution of prodrugs, monitor the dual-drug activation with minimized side effects, and enhance the therapeutic efficiency. This prodrug consists of a tumor-targeting cRGD motif, a TPE moiety with AIE activity, a red fluorescent drug DOX, and a Pt(IV) prodrug as a linker (Figure 119). In this prodrug system, the TPE and DOX are intended for two roles: serving as an energy transfer pair and acting as drug tracking agents. With the aid of cRGD, the prodrug can accumulate preferentially in cells overexpressing integrin  $\alpha_5\beta_3$  via receptor-mediated endocytosis. Upon cellular internalization and intracellular reduction, the prodrug releases the active Pt(II) as well as DOX anticancer drugs synchronously. Before the drug activation or intracellular reduction, the fluorescence of TPE is quenched as a result of the FRET to DOX, while the red fluorescence of DOX can be used for prodrug tracing. Accompanying with the drug activation, the TPE and DOX moieties are separated, resulting in the fluorescence recovery of TPE which can be utilized to monitor the activation of both drugs in real time (Figure 119). Moreover, the concomitant activation of cisplatin and DOX can give rise to synergistic anticancer effects. Such a theranostic dual-acting prodrug delivery system with drug tracking and real-time activation monitoring capabilities developed for visualizing cancer cell ablation with dramatically enhanced anticancer effects will definitely benefit the cancer therapy.

The studies highlighted in Figures 117–119 are all superb drug delivery systems for they show enhanced therapeutic effects and integrated extra imaging function which makes the drug delivery process visible. Notably, they are generally progressive in terms

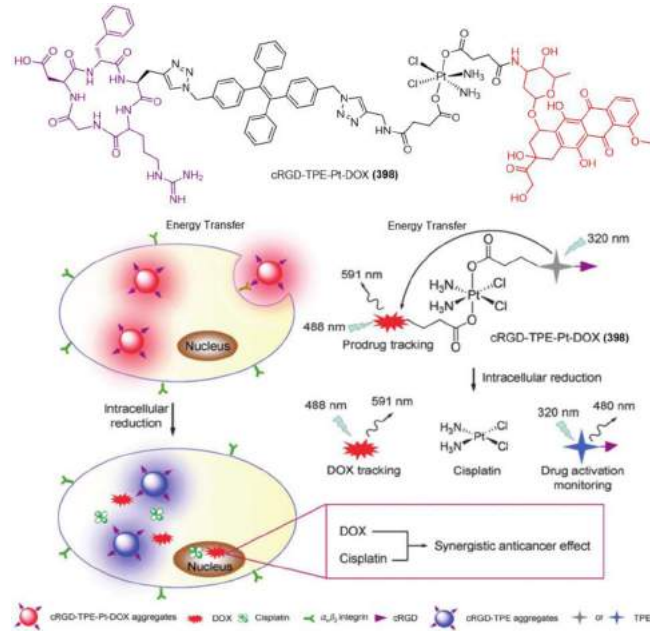


**Figure 119.** Schematic illustration of the targeted theranostic dual-acting prodrug 398 for real-time drug tracking and activation monitoring. Reprinted with permission from ref 691. Copyright 2014 Royal Society of Chemistry.

of their characteristic performance: the work shown in Figure 117 can be used for the subcellular location tracking of the drugs but without tumor targeting ability; whereas the ones depicted in Figure 118 possess the capability of directing the prodrug to targeted cancer cells and monitoring the prodrug activation in real time or its therapeutic response in early stage, but the actual drug location cannot be traced. The work exhibited in Figure 119 is highly integrated and multifunctional for it can simultaneously realize targeted drug delivery, drug tracking, as well as drug activation monitoring. It can be envisaged that smart combination of 397 and 398 might afford an even more powerful theranostic DDS which can achieve all the functions of 397 and 398. In this case, more general theranostic systems based on AIEgens for simultaneous targeted drug delivery, drug tracing, activation monitoring, and therapeutic effect evaluation can be developed.

It is thus clear that image-guided delivery systems combining both medical diagnostics and therapeutics have received great attention for personalized medication and therapy. Besides the above mentioned new-generation DDSs, photodynamic therapy (PDT) has been proven to be one of the most elegant strategies for cancer therapy as the treatment can be readily regulated by a beam of light in a noninvasive, precisely controllable, and spatiotemporally precise manner. PDT has thus been recognized as a treatment modality which is both minimally invasive and minimally toxic. There are three key components involved in most of the modern PDT systems: a photosensitizer, a light source, and tissue oxygen. A photosensitizer is a chemical compound that can be promoted to its excited state by a light source (absorption light) and undergo intersystem crossing with oxygen to generate singlet oxygen ( $^1\text{O}_2$ ; ROS). A wide variety of photosensitizers for PDT exist and fall into three categories: porphyrins, chlorophylls, and other organic dyes.<sup>697</sup> Although there are many different PDT systems used for different treatments, they all aim to achieve certain characteristics: high absorption at long wavelengths to allow deep tissue penetration,

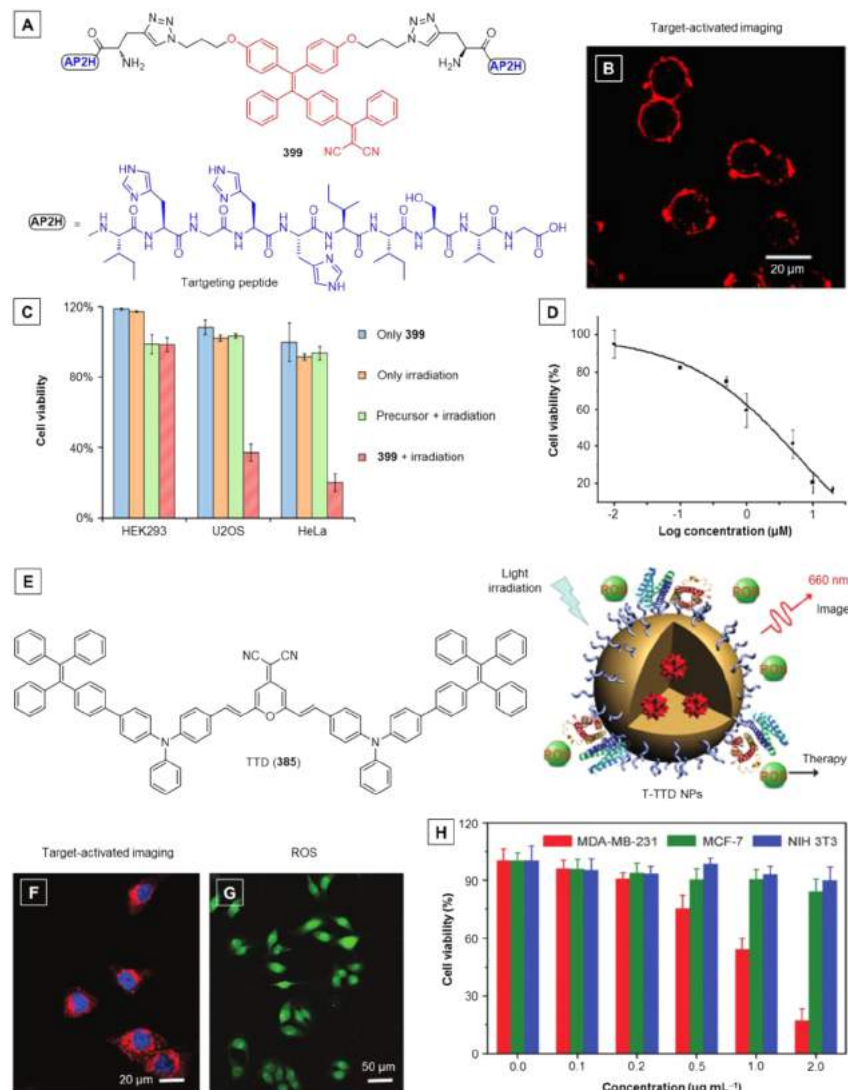


**Figure 120.** (A) Molecular structure of a red emissive AIE probe 399 for targeted bioimaging and photodynamic therapy of cancer cells. (B) CLSM images of HeLa cells after incubation with 399 ( $10 \mu\text{M}$ ) in acidic ( $\text{pH } 5.5$ ) environment. 399 was excited with a  $488 \text{ nm}$  laser, and the emission was collected with the  $580\text{--}680 \text{ nm}$  filter. (C) Comparison of cell viability for HeLa cells, U2OS cells, and HEK293 cells under different conditions. (D) Variation of cell viability for HeLa cells versus the concentration of 399 in the incubation solution. Adapted from ref 701. Copyright 2014 American Chemical Society. (E) Schematic illustration of T-TTD NPs structure and its dual functions. (F) Confocal images of MDA-MB-231 cells after incubation with T-TTD NPs ( $1 \text{ mg mL}^{-1}$ ) for 1 h. The blue fluorescence is from the nuclei of cells stained by Hoechst 33342, and the red fluorescence is from T-TTD NPs. (G) Detection of intracellular ROS production by dichlorofluorescein diacetate (DCF-DA) in MDA-MB-231 cells after incubation with T-TTD NPs ( $1 \text{ mg mL}^{-1}$ ) followed by light irradiation. (H) Inhibition of growth of MDA-MB-231, MCF-7, and NIH 3T3 cells in the presence of different concentrations of T-TTD NPs with light irradiation ( $0.25 \text{ W cm}^{-2}$ , 2 min) followed by further incubation of the cells for 24 h. Adapted with permission from ref 36. Copyright 2014 Royal Society of Chemistry.

high singlet oxygen quantum yield, low photobleaching, natural fluorescence, high chemical stability, low dark toxicity, and preferential uptake in targeted tissue.<sup>698</sup> As most photosensitizers are potential fluorophores, fluorescence imaging-guided PDT is appealing for improving the therapeutic accuracy.<sup>699,700</sup> In addition, most photosensitizers are hydrophobic and severely aggregated in aqueous media, leading to the dramatic reduction in the fluorescence and photosensitizing efficacy. In view of this, developing efficient photosensitizers based on AIogens whose aggregation is always beneficial to their properties is promising, for that the intrinsic and natural aggregate-state emission will realize both imaging and PDT in a single system. To this end, several research groups have carried out correlative studies and accomplished some exciting results.<sup>36,701</sup>

Zhang and Yang et al., for example, have reported an activatable red fluorescent AIogen (i.e. 399) for targeted bioimaging and PDT therapy of cancer cells (Figure 120A–D).<sup>701</sup> As displayed in Figure 120A, this dual-functional system has been designed according to the requirements for both a targeted bioimaging probe and a photosensitizer (vide supra). The TPE core is a typical AIE motif, which ensures the good photobleaching resistance and high brightness of the probe. The D-A structure is adopted to red shift the absorption and emission. The presence of  $-\text{[PhC=C(CN)<sub>2</sub>]}$  moiety is expected to endow the probe with strong photosensitizing ability to induce the formation of  ${}^1\text{O}_2$  after light irradiation. The introduction of the AP2H (IHGHIIISVG) peptide is aimed to confer the cancer cell-specific targeting on the probe. As previously mentioned in section 5.1.2.1, the AP2H peptide can selectively binds to

LAPTM4B, a tumor-related protein which is overexpressed in most solid tumors. By virtue of its AIE behavior and distinct red fluorescence,<sup>399</sup> was successfully applied for high-contrast activated fluorescence imaging of living cancer cells, with high signal-to-noise ratio and without involving multiple washing steps (Figure 120B). Apart from targeting the membrane-anchored LAPTM4B protein, the tracing of the intracellular movement of LAPTM4B protein and responding to the tumor acidosis was also successfully achieved with <sup>399</sup>. The generation of <sup>1</sup>O<sub>2</sub> by <sup>399</sup> under visible light irradiation was also realized in the cytoplasm of cancer cells which was facilitated by its excellent cell permeability via LAPTM4B transportation. The high phototoxicity of <sup>399</sup> to cancer cells and low toxicity to normal cells has clearly demonstrated its targetable PDT capability (Figure 120C). Additionally, the PDT effect showed dependency on the concentration of <sup>399</sup> used for incubation with cancer cells (Figure 120D). Therefore, such PDT effect of <sup>399</sup> can be modulated in accordance with the expression level of the target LAPTM4B protein and the progression status of tumors. This fantastic work has provided new insights and guidance to the development of dual-functional AIEgens for the targeted bioimaging and PDT.

Even a bit earlier than the above work, a targeted and image-guided PDT system had been reported by Liu and coworkers.<sup>36</sup> This dual-functional PDT system is constructed from the 385-based AIE dots (Figure 120E) in which the AIEgen 385 serves simultaneously as a photosensitizer and a fluorescent imaging probe. Such AIE dots (i.e. T-TTD NPs) were fabricated according to the nanoprecipitation procedure discussed in section 5.1.2.3, using DSPE-PEG-Mal to encapsulate the 385 molecules and the cRGD tripeptide to functionalize the dot surface (Figure 120E). The obtained T-TTD NPs hold an average size of ~32 nm with a low polydispersity of ~0.12. The T-TTD NPs can efficiently generate ROS to selectively image and kill the MDA-MB-231 cells upon light irradiation (Figure 120F–H). Specifically, T-TTD NPs can be exclusively taken up by MDA-MB-231 cells via integrin  $\alpha_3\beta_3$  receptor-mediated endocytosis and, hence, specifically labelled the cellular cytoplasm with intense red fluorescence (Figure 120F). As exhibited in Figure 120G, the efficient ROS generation from the internalized T-TTD NPs has been verified by the strong green fluorescence of the ROS generation indicator dichlorofluorescein (DCF). Upon incubation with MDA-MB-231, MCF-7, and NIH 3T3 cells, the T-TTD NPs only displayed obvious cytotoxicity to MDA-MB-231 cells with a half-maximal inhibitory concentration ( $IC_{50}$ ) of 1.1  $\mu$ g mL<sup>-1</sup> (Figure 120H). It is noteworthy that T-TTD NPs were nontoxic in the dark. These AIE NPs showed aggregation-enhanced ROS generation for image-guided PDT. Compared with <sup>399</sup>, this PDT platform is simpler and more flexible in terms of the design and preparation, and it thereby offers new opportunities for image-guided PDT.

In this part, we have demonstrated the dual-functional utilities of AIE systems in biological and medical areas. The dual-modal MRI contrast reagents with fluorescent and magnetic imaging capability have been developed by incorporating Gd(III) on the surface of AIE dots (e.g., Tat-Gd-AIE dots) or into the molecular structure of AIEgens (TPE-2Gd). The fluorescence imaging and MRI in these dual-modal AIE systems are synergic and complementary, demonstrating a win-win effect. As for personalized medicine, self-luminescent drug delivery systems constructed by physically encapsulating or chemically binding the anticancer drugs/prodrugs with AIEgens can achieve enhanced therapeutic effects and intracellular imaging of the drug delivery process.

With judicious design, targeted drug delivery, real-time drug tracking, and activation monitoring can be realized simultaneously. As to image-guided therapy, targeted and image-guided PDT systems based on AIEgens or AIE dots have been developed by utilizing AIEgens as efficient photosensitizers with aggregation-enhanced photosensitizing efficacy, which are distinct from and outshine conventional photosensitizers. All such studies have provided direct and strong proofs to the superiorities of AIE. Taking advantage of this jigsaw puzzle, unlimited dual-functional utilities or even multifunctional systems can be realized, which can undoubtedly broaden the scope of AIE research and meanwhile benefit the biological research as well as clinical applications.

## 5.2. Chemical Sensing

Sensing refers to the detection of a particular entity, such as matter and energy, by a specialized system, namely, sensor or probe. Sensors are tied to and used in daily life and have been utilized in various areas including medicine, industry, and environmental protection and control, etc. Hence, the development of sensors is of great significance, and many endeavors have been made in this area. Generally speaking, according to the origin of analytes or applied area, sensing can be divided into biosensing and chemosensing. Because of the fact that luminescence is a highly versatile spectroscopic approach that can be employed in real time and *in situ*, using low concentration of the sensors or probes with emission that can be detected using cheap instruments, and it also offers high sensitivity, the luminescent sensing or probing is now becoming a predominant detection modality. As discussed in section 5.1, the AIE strategy and AIEgens have shown incredibly splendid performance in biological applications including biosensing, bioimaging, and dual-functional utilities. It can be anticipated that AIEgens together with the AIE strategy should also play brilliantly in chemosensing areas. Since there have existed a wealth of AIE probes for chemosensing, we strive to touch upon each of the elements and select examples for in-depth discussions. We have assorted the AIE-based chemosensors and put them into 12 groups according to the detection objects. The AIE systems utilized for ion detection, pH sensing, gas detection, explosive detection, peroxide sensing, hazardous species detection, fingerprint visualization, chiral recognition, viscosity evaluation, conformation probing, self-assembly monitoring, and morphology visualization will be sequentially introduced in this section.

**5.2.1. Ions.** Ion detection has occupied a large portion of chemosensing, and it can be further classified into cation and anion detection. In this part, AIE systems for cation sensing will be discussed first in the order of valency and atomic number, following that is the illustration of AIE-based probes for anion detection. Note that there are not too many examples for anion sensing, and thus only the detection on cyanide ion will be highlighted in this review.

As a monovalent metal ion, K<sup>+</sup> has attracted tremendous research interest for its extremely important roles in diverse physiological activities and biological functions.<sup>702–705</sup> The sensitive detection of K<sup>+</sup> is of great significance. Considering the advantages of AIE probes such as high sensitivity and selectivity, high signal-to-background ratio, and high contrast, Liu and Zhang et al. integrated the AIE concept with the specific recognition between K<sup>+</sup> ions and crown ether moieties, with the aim of facilely developing a more effective fluorometric K<sup>+</sup> probe.<sup>706</sup> For this purpose, TPE core was functionalized with four crown ether moieties via thiol–ene click reaction between

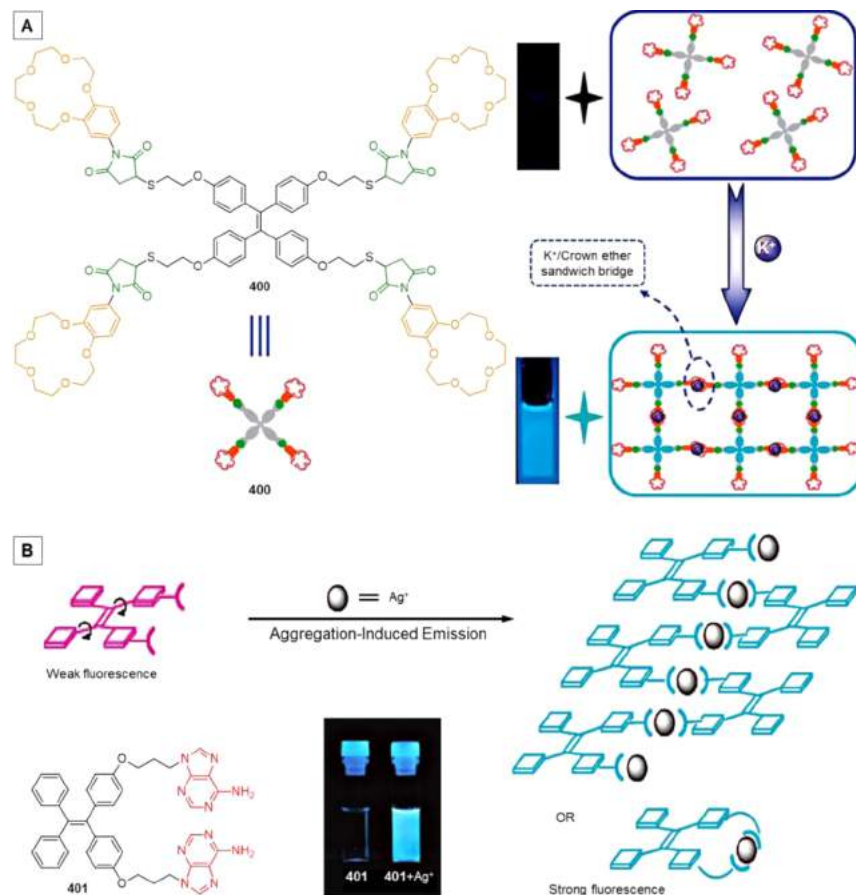


**Figure 121.** Representative examples of detecting monovalent cations, e.g.,  $\text{K}^+$  and  $\text{Ag}^+$  based on AIE. (A) Schematic illustration of the construction of a “light-up” fluorometric  $\text{K}^+$  probe based on AIE of crown ether-functionalized TPE **400**, induced by supramolecular recognition between  $\text{K}^+$  ions and crown ether. Reprinted with permission from ref 706. Copyright 2012 Royal Society of Chemistry. (B) Schematic illustration of a specific chemosensor for  $\text{Ag}^+$  based on the coordination interaction between  $\text{Ag}^+$  and the adenine-decorated TPE **401**. Reprinted from ref 710. Copyright 2008 American Chemical Society.

the thiol-modified TPE and maleimide-decorated benzo-15-crown-5, affording the targeted probe **400**, where the AIE motif (i.e. TPE core) and the peripheral crown ether segments serve as signaling moiety and supramolecular  $\text{K}^+$ -recognition functionalities, respectively (Figure 121A). When **400** was molecularly dissolved in THF, no discernible fluorescence was observed, whereas upon the addition of  $\text{K}^+$ , intense fluorescent signal was detected. The turn-on response originated from the aggregation of **400** induced by the  $\text{K}^+$ -mediated cross-linking through the formation of  $\text{K}^+$ /crown ether (1/2 molar ratio) molecular recognition complex in a sandwiched fashion. In this way, the TPE moieties were trapped in the supramolecular networks, which make their intramolecular motions greatly restricted and the light emission hence triggered. This AIE-based probe for  $\text{K}^+$  achieved a detection limit of  $\sim 1.0 \mu\text{M}$  and showed excellent selectivity over other common metal ions including  $\text{Li}^+$ ,  $\text{Na}^+$ ,  $\text{NH}_4^+$ ,  $\text{Ca}^{2+}$ ,  $\text{Mg}^{2+}$ , and  $\text{Pb}^{2+}$ .

Another monovalent metal ion, i.e.,  $\text{Ag}^+$ , has been reported to have some adverse biological effects, bioaccumulation, and toxicity, such as the  $\text{Ag}^+$ -caused inactivation of sulfhydryl enzymes and the combination of  $\text{Ag}^+$  with amine, imidazole, and carboxyl groups of various metabolites.<sup>707–709</sup> Hence, the development of sensitive and selective chemosensing probes for  $\text{Ag}^+$  is considerably important to environmental protection as well as human health. Traditional fluorescent probes for  $\text{Ag}^+$  typically work in a fluorescence turn-off manner due to the

“heavy metal” effect of  $\text{Ag}^+$ . However, by making use of the unique AIE feature of TPE motif and the specific binding ability of adenine to  $\text{Ag}^+$ , Zhang’s group developed a fluorescence turn-on sensor for  $\text{Ag}^+$ .<sup>710</sup> The TPE core was embellished with two adenine moieties with the propoxy groups as spacers, yielding the probe **401** (Figure 121B). The detection of  $\text{Ag}^+$  was carried out in the water/THF mixture (5/1, v/v), where the probe showed rather weak emission with a low background signal. The fluorescence emission of TPE units was switched on by the addition of  $\text{AgClO}_4$ . Such a fluorescence turn-on response can be observed by naked eyes under UV illumination owing to the high signal-to-background ratio. The fluorescence enhancement was ascribed to the coordination of adenine motifs of **401** with  $\text{Ag}^+$ , resulting in the formation of coordination complexes which were prone to aggregate due to the lower solubility. As a consequence, the RIR process was activated to induce strong fluorescence (Figure 121B). **401** exhibited good selectivity and sensitivity to  $\text{Ag}^+$ , with a detection limit of  $0.34 \mu\text{M}$  and a linear response range of  $0$ – $75 \mu\text{M}$ .

Copper is a basic trace element for all living systems. However, an excess of unbound copper ion is quite harmful.<sup>711,712</sup> As  $\text{Cu}^{2+}$  is the natural form of free copper in biological media, an elevated level of  $\text{Cu}^{2+}$  in body is associated with severe neurodegenerative diseases, including Wilson’s and Alzheimer’s diseases. Meanwhile,  $\text{Cu}^{2+}$  can be an environmental pollutant, thus the  $\text{Cu}^{2+}$  detection is not only of great biological value but also have

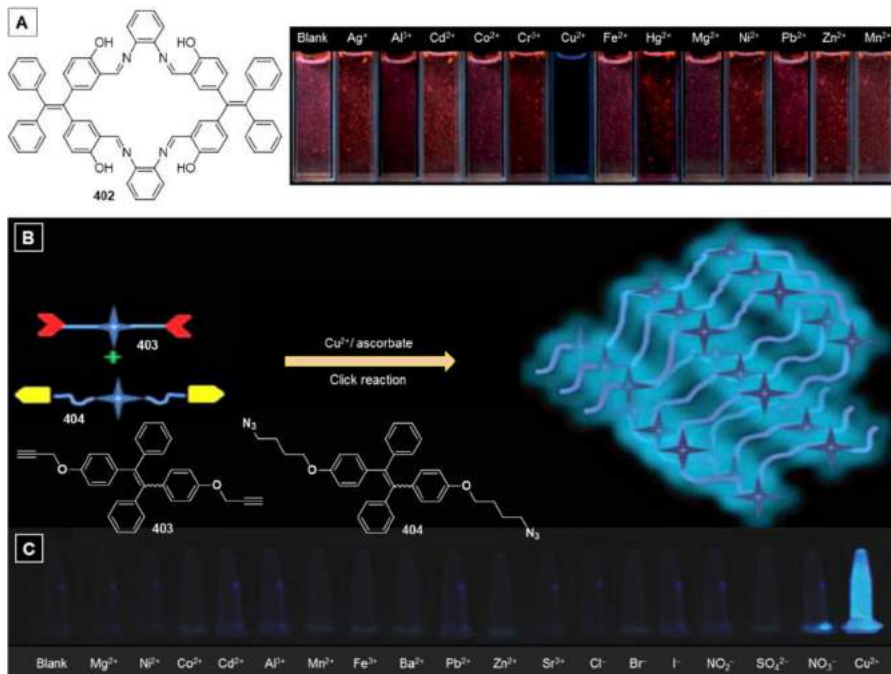


**Figure 122.** Representative examples of utilizing AIEgens to detect  $\text{Cu}^{2+}$  ions. (A) Chemical structure of the TPE Schiff base macrocyclic compound 402, and the fluorescent photos of 402 in the mixture of water/THF (9/1 in volume) with different metal ions. Reprinted with permission from ref 713. Copyright 2013 Royal Society of Chemistry. (B) AIE-based “turn-on” fluorescent chemodosimeter for the selective detection of  $\text{Cu}^{2+}$ /ascorbate ions developed by the azide–alkyne “click” polymerization between two TPE derivatives (403 and 404). (C) Fluorescent photos of the mixture of 403 and 404 in different ions in the presence of ascorbate. Adapted with permission from ref 716. Copyright 2013 Royal Society of Chemistry.

implications in environmental protection and monitoring. To this end, an array of AIE-based probes for  $\text{Cu}^{2+}$  ions have been developed by different research groups via diverse sensing mechanisms.<sup>713–718</sup> Zheng et al., for instance, have constructed a fluorometric probe for the visual detection of  $\text{Cu}^{2+}$  in water by taking advantage of AIE as well as the coordination between an AIEgen and  $\text{Cu}^{2+}$  ions.<sup>713</sup> The condensation reaction of the dialdehyde-modified TPE derivative and 1,2-benzenediamine generated a TPE Schiff base macrocycle 402, which could aggregate into nanofibers in aqueous solution giving a stable and fluorescent suspension. Owing to the AIE and ESIPT effects, the emission of nanofibers was located in the red region with a maximum at 595 nm, showing a dramatic Stokes shift up to 260 nm. Such intensively red fluorescent nanofibers exhibited a highly selective response to  $\text{Cu}^{2+}$  ions in an aqueous media (Figure 122A), with a detection limit as low as 1.1 nM and a linear response range spanning from 5.0 nM to 20  $\mu\text{M}$  (logarithm of copper concentration versus fluorescence intensity). Comitantly with the fluorescence change, there was a color transition from colorless to yellow brown at a concentration of  $\sim 10 \mu\text{M}$ , which allows a direct judgement of the  $\text{Cu}^{2+}$  level. Note that the maximum allowable  $\text{Cu}^{2+}$  level in drinking water set by the U.S. Environmental Protection Agency (EPA) is  $\sim 20 \mu\text{M}$ . Moreover, the  $\text{Cu}^{2+}$  ions in pork juice-containing water could also be detected by 402 via visual fluorescence decrease and color change, indicating the potential of 402 for practical use such as real-sample detection. It is worth mentioning that the selectivity of 402 for  $\text{Cu}^{2+}$  should originate from the macrocyclic framework, which makes the room between the two neighboring imine groups just perfect for the accommodation of  $\text{Cu}^{2+}$  ion. The sensitivity is attributed to the AIE effect and the highly emissive nanofibers, which are conducive to a fluorescence turn-off response.

In addition to fluorescence turn-off  $\text{Cu}^{2+}$  probes,<sup>713–715</sup> fluorescence light-up probes for  $\text{Cu}^{2+}$  detection have also been established by virtue of AIE effect and click reactions catalyzed by copper species.<sup>716–718</sup> Sanji and Tanaka et al. developed a fluorometric  $\text{Cu}^{2+}$  sensor with an azide-functionalized TPE derivative on the basis of the click reaction in aqueous solution.<sup>717</sup> Upon addition of  $\text{Cu}^{2+}$ , the TPE derivative decorated with four azide groups reacted with a diethylene glycol dipropionate in the presence of sodium ascorbate to afford covalently cross-linked networks, giving rise to a remarkable fluorescence enhancement. Thus, the level of  $\text{Cu}^{2+}$  can be detected in a fluorescence turn-on and visual manner with high selectivity and a detection limit ( $\sim 1 \mu\text{M}$ ) substantially lower than the action level of  $\text{Cu}^{2+}$  in drinking water. Similarly, by making use of the azide–alkyne click reaction, Chatterjee and Banerjee et al. designed another turn-on fluorescent chemodosimeter for the selective detection of  $\text{Cu}^{2+}$  and ascorbate ions (Figure 122B,C).<sup>716</sup> In the presence of ascorbate, the addition of  $\text{Cu}^{2+}$  readily triggered the linear polymerization of the diyne-TPE (403) and diazide-TPE (404) monomers, yielding an insoluble TPE-based polytriazole with intense fluorescence due to the activation of the RIM process (Figure 122B). Certainly, such a simple and rapid probing system also showed excellent selectivity to  $\text{Cu}^{2+}$  (Figure 122C).

Zinc is an essential trace element that is necessary to plants, animals, and microorganisms.<sup>719</sup> It is the second most abundant transition metal in the human body after iron.  $\text{Zn}^{2+}$  is one of the most important cations as the catalytic center and structural cofactor of many enzymes and metalloproteins.<sup>720–722</sup> It is also an essential factor in numerous biological processes as well as the pathological processes in many diseases, including Alzheimer’s disease, epilepsy, and ischemic stroke.<sup>723</sup> Unlike other transition metal ions such as  $\text{Fe}^{2+}$  and  $\text{Cu}^{2+}$ ,  $\text{Zn}^{2+}$  is spectroscopically and

magnetically silent due to its  $d^{10}$  electron configuration. In view of this, sensitive and noninvasive fluorescence-based techniques stand out as a good choice for zinc analysis and sensing.<sup>723,724</sup> AIE has emerged as a powerful fluorescence methodology for the assay of  $Zn^{2+}$ .<sup>725–728</sup> For example, our research group constructed some fluorogenic  $Zn^{2+}$  sensors by embellishing AIEgens such as TPE or silole with  $Zn^{2+}$  chelating moieties, e.g., terpyridine groups (Figure 123A).<sup>725,726</sup> These AIEgens were

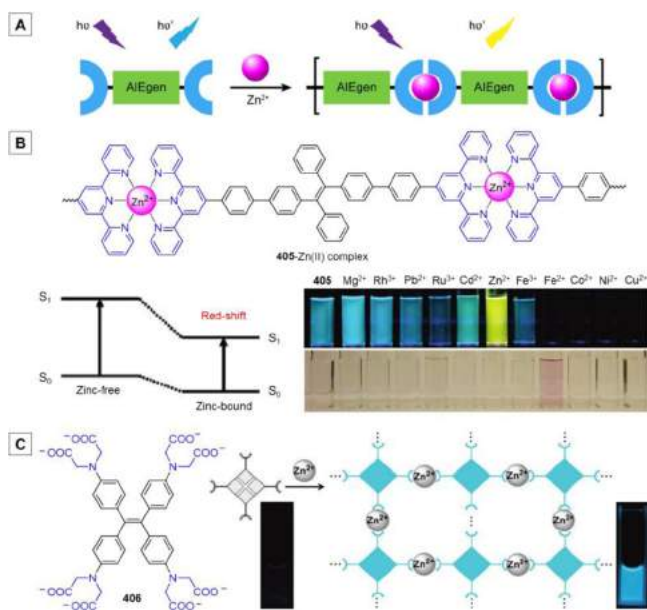


**Figure 123.** Representative examples of fluorescent chemosensors for  $Zn^{2+}$  on the basis of AIEgens. (A) Possible stoichiometry of **405**–Zn(II) complex. (B) Structure of zinc-bound **405**, and proposed mechanism for the spectral red-shift of **405** upon binding to  $Zn^{2+}$ . Insets: Photographs of the aqueous solutions of **405**/cation mixtures taken under (upper) UV illumination and (lower) daylight. Adapted from ref 725. Copyright 2011 American Chemical Society. (C) Schematic illustration of the “turn-on” detection of  $Zn^{2+}$  via the coordination between the AIEgen **406** and  $Zn^{2+}$ . Adapted from ref 727. Copyright 2011 American Chemical Society.

envisioned to chelate  $Zn^{2+}$  to form coordination complexes or even polymers, which would lead to the rigidification of their molecular structures as well as an emission enhancement/turn-on and red-shift in their fluorescence. Taking the TPE-terpyridine derivative (**405**) as an example, **405** was virtually non-luminescent in THF solution, while addition of  $Zn^{2+}$  into the THF solution switched on the fluorescence with a pronounced emission peak at around 550 nm, which was greatly red-shifted as compared with the nanoaggregates of **405** (490 nm). Upon coordination with  $Zn^{2+}$ , the formation of **405**-Zn(II) oligomeric or polymeric complex enlarged the electronic conjugation and might also strengthened the push-pull effect, which decreased the energy level of the lowest unoccupied molecular orbital (LUMO) and narrowed the energy gap, thus resulting in the red shift of fluorescence (Figure 123B). It is notable that the recognition of  $Zn^{2+}$  can also be carried out in the aggregate state (THF/water with  $f_w = 99$  vol %) or even solid state (e.g., on filter paper or TLC plate), with the aid of the characteristic red-shift (Figure 123B). Additionally, because of the ligand-to-metal charge transfer (LMCT) process, the solution of **405** showed an obvious magenta color upon binding with  $Fe^{2+}$ , permitting a rapid identification of  $Fe^{2+}$  by naked eyes.

Apart from the terpyridine moieties, other  $Zn^{2+}$  chelating motifs, such as  $-N(CH_2COO^-)_2$ , can also be employed to endow the AIEgens with  $Zn^{2+}$  sensing ability. For example, Zhang’s group designed and synthesized a fluorescence turn-on sensor for  $Zn^{2+}$  in aqueous media (**406**; Figure 123C).<sup>727</sup> By decorating with four  $-N(CH_2COO^-)_2$  groups on a TPE core, the resulting TPE derivative **406** can be well dissolved in aqueous solution, showing almost no fluorescence. After addition of  $Zn^{2+}$ , the fluorescence of the **406** solution was gradually intensified with an emission maximum at 485 nm. Thus, **406** can be taken as a light-up fluorescent probe for  $Zn^{2+}$ . The turn-on response should be ascribed to the selective coordination between  $Zn^{2+}$  and  $-N(CH_2COO^-)_2$  groups on **406**, which generated coordination oligomers or polymers that restricted the intramolecular motions of the TPE moieties (Figure 123C).

$Hg^{2+}$  has been recognized to be a severe environmental pollutant and a toxicant to the human body which can cause nausea, vomiting, stomach ache, Minamata disease, and damages of liver, kidney, as well as brain. After the absorption of  $Hg^{2+}$  by aquatic microorganisms, it can be turned into methyl mercury and thus enters the food chain.<sup>729</sup> The assay of  $Hg^{2+}$  has thereby attracted growing attention. AIE as a novel detection strategy has performed well in the fluorometric sensing of  $Hg^{2+}$ , and to date, a large variety of AIE-based  $Hg^{2+}$  probes have been reported.<sup>37,730–737</sup> For example, our group constructed a turn-on fluorescent sensor for  $Hg^{2+}$  in aqueous solution by taking advantage of the TPE-functionalized benzothiazolium salt (**407**) with iodide as the counterion (**407**–I).<sup>37</sup> **407**–I showed relatively intense fluorescence in the solution state, where the **407**–I molecules existed in the form of solvent-separated ion pairs. Such a structure experienced a low rate of colliding and hence hindered the heavy-atom effect of  $I^-$ . However, the **407**–I was non-luminescent in the aggregate or solid state due to the fact that in the condensed phase, the excitons were annihilated by the drastic collision between the iodide ion and the cationic unit in the state of closely contacting ion pairs (Figure 124A). Such a quenching effect provides a very low background for the further light-up detection of  $Hg^{2+}$ .  $Hg^{2+}$  has been known to show a high affinity towards the iodide and can thus be envisioned to displace the cationic unit of **407**–I (Figure 124A). The response of **407**–I to  $Hg^{2+}$  was conducted in the aqueous buffer solution (pH 7.4, HEPES buffer with 1% DMSO) to ensure an emission-off initial state. Upon addition of  $Hg^{2+}$ , bright red fluorescence emerged and was boosted by the increasing amount of  $Hg^{2+}$ . It is clear that **407**–I can function as a fluorescence light-up probe for  $Hg^{2+}$  with superb specificity and selectivity (Figure 124A). The working mechanism of this fluorescent sensor has been rationalized to be the elimination of the quenching effect of the iodide via the formation of  $HgI_2$  as well as the aggregate formation induced by the complexation of  $Hg^{2+}$  with the sulfur atom on the benzothiazolium unit on **407**–I. A handy solid film of **407**–I was fabricated and used to monitor the level of  $Hg^{2+}$  in aqueous solution. A detection limit of 1  $\mu M$  has been achieved by this simple and economic displacement approach.

Coordination is one of the most common and useful strategies for metal ion detection. Similar to  $Cu^{2+}$  and  $Zn^{2+}$ ,  $Hg^{2+}$  also possesses strong coordination ability. In the light of this, coordination between the AIEgens and  $Hg^{2+}$  has been utilized as a pathway to trigger the aggregation or conformational rigidification of the AIEgens and subsequently induce their fluorescence response.<sup>730–733,738</sup> AIEgen **408**, for example, is a fluorometric probe of  $Hg^{2+}$ , which has been designed on the basis of aforesaid principle.<sup>730</sup> **408** is composed of a triphenylamine-triazine

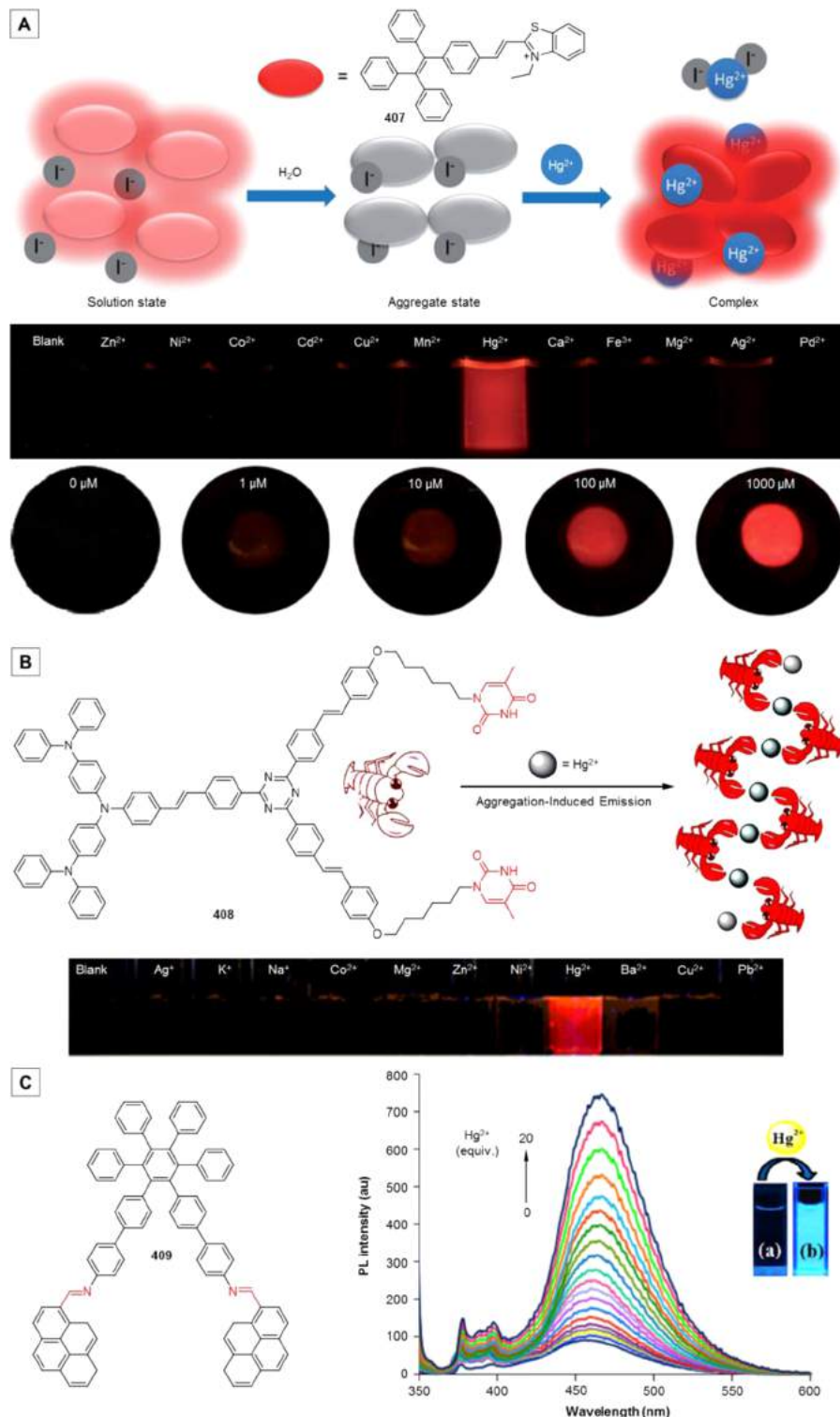


**Figure 124.** Representative examples of AIEgens applied for the specific sensing of mercury(II). (A) The proposed ion replacement or exchange mechanism of **407** for the “turn-on” detection of  $\text{Hg}^{2+}$ . Insets: Fluorescent photographs of (upper) **407**-I in aqueous buffer solutions ( $20 \mu\text{M}$ ) with various metal ions and (lower) thin films of **407**-I in the presence of different concentrations of  $\text{Hg}^{2+}$  in aqueous solution. Adapted with permission from ref 37. Copyright 2014 Wiley-VCH Verlag GmbH & KGaA. (B) Schematic illustration of the coordination mode between thymine-functionalized AIEgen **408** and  $\text{Hg}^{2+}$ . Inset: Fluorescent images of **408** in the mixture of DMSO/water (9/1 in volume) after addition of different metal ions. Reprinted with permission from ref 730. Copyright 2012 Elsevier Ltd. (C) Molecular structure of an AEE-active probe **409** for  $\text{Hg}^{2+}$  sensing and its response to different amounts  $\text{Hg}^{2+}$  in HEPES buffer/EtOH (1/1, v/v) with pH = 7.05. Inset: Corresponding fluorescent photographs taken (a) before and (b) after the addition of  $\text{Hg}^{2+}$ . Reprinted with permission from ref 733. Copyright 2013 Elsevier B.V.

motif which is AIE-active and red emissive in the aggregate state and two thymine groups that can selectively bind with  $\text{Hg}^{2+}$ . **408**

exhibited very weak emission at a concentration of  $50 \mu\text{M}$  in the DMSO/water mixture (9/1, v/v), with a  $\Phi_F$  of 1.2%. After the

addition of  $\text{Hg}(\text{CH}_3\text{COO})_2$ , the emission band peaked at 610 nm emerged and started to increase. The increase in the fluorescence intensity nearly followed a linear trend in the  $\text{Hg}(\text{CH}_3\text{COO})_2$  concentration range of 0–50  $\mu\text{M}$  with a detection limit as low as ~66 nM. As compared to the original state, the  $\Phi_F$  (24.0%) showed an approximately 20-fold increment after addition of 50  $\mu\text{M}$  of  $\text{Hg}^{2+}$ . Such a light-up fluorescence response is ascribed to the coordination of thymine moieties of **408** with  $\text{Hg}^{2+}$ , which leads to the activation of the RIM process as well as the AIE effect (Figure 124B). Moreover, the specific binding between thymine moieties of **408** and  $\text{Hg}^{2+}$  also endowed the high selectivity of **408** to  $\text{Hg}^{2+}$  (Figure 124B). Apart from triphenylamine-triazines, other AIEgens such as DSA or even TPE polymers have been decorated with thymine groups to realize the turn-on detection of  $\text{Hg}^{2+}$  in a specific and sensitive manner, demonstrating the universality of the coordination-coupled AIE strategy.<sup>731,732</sup>

Besides the thymine group, imine can also coordinate with  $\text{Hg}^{2+}$  and hence was utilized to embellish AIE motifs to yield  $\text{Hg}^{2+}$  probes. **409** is such an example.<sup>733</sup> The imine-bridged HPB-pyrene adduct **409** features the AEE characteristics. The **409** in HEPES buffer/EtOH mixture (1/1, v/v) exhibited a moderate fluorescence with a  $\Phi_F$  of 7.6% owing to the slight aggregation. The addition of  $\text{Hg}^{2+}$  in the mixture gradually enhanced the fluorescence (Figure 124C). An approximately 10-fold increase in fluorescence intensity ( $\Phi_F = 74.0\%$ ) was observed upon addition of 100  $\mu\text{M}$  of  $\text{Hg}^{2+}$ . It is believed that the binding of  $\text{Hg}^{2+}$  ions with imine linkages rigidified the AIE molecules and resulted in the formation of aggregates or self-assembled structures, which promoted the RIM process and subsequently intensified the fluorescence. Notably, **409** showed an excellent selectivity to  $\text{Hg}^{2+}$  with a very low detection limit of 4.5 nM. Additionally, the highly fluorescent supramolecular ensemble of **409**- $\text{Hg}^{2+}$  could be employed as a simple, portable, and economic probe to explosives such as PA. By giving these examples, it can be seen that the coordination coupled with AIE strategy is highly adaptable and flexible, for both the signaling motif (AIEgen) and the recognition moiety (coordinating group) are variable and moreover the detection performance is tunable as well.

In addition to the quencher displacement and coordination methods, other detection strategies can also be utilized for the construction of AIE-based sensors for  $\text{Hg}^{2+}$ . For example, the solubility change strategy depicted in Figure 125A has been

verified to be effective for  $\text{Hg}^{2+}$  sensing by Atilgan et al.<sup>734</sup> In this approach, two carboxylic groups were attached to the TPE moiety via Lewis acid-mediated dithioacetal formation and subsequent hydrolysis of ester groups, affording the hydrophilic AIEgen **410**. This AIEgen was practically non-luminescent in aqueous solution owing to the active intramolecular motions. **410** can be selectively transformed into a hydrophobic AIEgen **338b** by  $\text{Hg}^{2+}$ , which would be induced to form emissive aggregates due to the activated RIM process. **410** can thereby work as a fluorescence light-up probe for  $\text{Hg}^{2+}$ . As anticipated, the fluorescence from the DMSO/water mixture ( $f_w = 99$  vol %) containing probe **410** was readily switched on by the addition of  $\text{Hg}^{2+}$ , indicating the elimination of the hydrophilic groups. Fluorescence of the detection system was boosted swiftly with the increase in the concentration of  $\text{Hg}^{2+}$ . When one equivalent of  $\text{Hg}^{2+}$  (2  $\mu\text{M}$ ) was added, the fluorescence reached its maximum with a 410-fold enhancement. A detection limit of 0.1  $\mu\text{M}$  of  $\text{Hg}^{2+}$  and a good selectivity have been achieved with this AIE probe. Furthermore, the sensing of  $\text{Hg}^{2+}$  can also be realized in live cells with light-up fluorescence.

There had been a work published on the sequential recognition of iron(III) (i.e.,  $\text{Fe}^{3+}$ ) and  $\text{Hg}^{2+}$ , where the  $\text{Hg}^{2+}$  induced the specific cleavage of the dithioacetals (Figure 125B).<sup>735</sup> The dithioacetals with carboxylic groups (highlighted in red in Figure 125) were also used to functionalize the TPE motif to create the probe **411**. The dithioacetals with carboxylic groups played multiple roles: binding to metal ions, improving hydrophilicity, and recognizing  $\text{Hg}^{2+}$  ions. Although bearing four carboxylic groups, **411** cannot be completely dissolved in water owing to its large hydrophobic fragment, rendering a strong emission. Once  $\text{Fe}^{3+}$  was added to the suspension of **411** in water, the emission was turned off. With this “off”-state **411**- $\text{Fe}^{3+}$  complex,  $\text{Hg}^{2+}$  can be sequentially detected in a fluorescence turn-on mode. Upon  $\text{Hg}^{2+}$  addition, the highly hydrophobic **412** was readily generated and formed aggregates, which restricted the intramolecular motions of TPE units and led to the fluorescence enhancement. The **411**- $\text{Fe}^{3+}$  complex can detect  $\text{Hg}^{2+}$  in a wide-range pH with excellent selectivity and appreciable sensitivity in water (detection limit, 2 ppb). The peculiarity of this work lies in the fluorescence “on–off–on” sequential detection of two types of heavy transition metal ions in water with a single AIEgen. The two studies shown in Figure 125 give a direct proof to the flexibility of AIE strategy: even with the same recognition moiety and signaling motif, by altering the

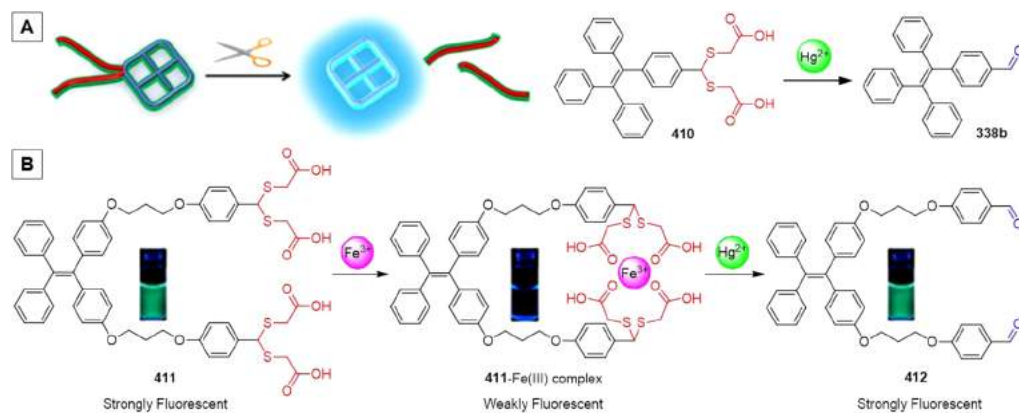


**Figure 125.** (A) Schematic illustration of the fluorescence “turn-on” chemosensor (**410**) for  $\text{Hg}^{2+}$  detection based on the polarity and solubility change. Adapted with permission from ref 734. Copyright 2013 Published by Elsevier Ltd. (B) Fluorescence “on–off–on” chemosensor (**411**) for sequential recognition of  $\text{Fe}^{3+}$  and  $\text{Hg}^{2+}$  in water. Adapted with permission from ref 735. Copyright 2012 Elsevier Ltd.

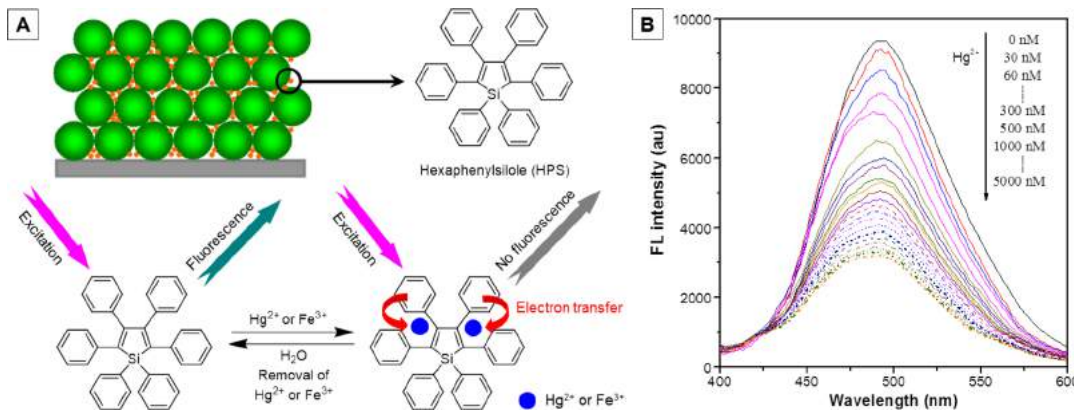


**Figure 126.** (A) Schematic illustration of the sensing of  $\text{Hg}^{2+}$  or  $\text{Fe}^{3+}$  by HPS-infiltrated photonic crystal (HPS-PC) films. (B) The FL spectra of the HPS-PC film with different concentrations of  $\text{Hg}^{2+}$ . Adapted with permission from ref 736. Copyright 2014 Wiley-VCH Verlag GmbH & Co. KGaA.

molecular design or experimental conditions, the sensing behaviors of the AIE probes can be easily modulated.

As previously mentioned, the AIE effect not only favors turn-on detection but also benefits turn-off sensing, because it provides a highly emissive aggregate state. For example, Heng et al. have made full use of the AIE attribute of HPS to develop a strongly emissive silole-infiltrated photonic crystal (PC) film, which was used as a highly effective fluorescence turn-off sensor with high sensitivity, good selectivity, and excellent reproducibility for  $\text{Hg}^{2+}$  and  $\text{Fe}^{3+}$  ions (Figure 126).<sup>736</sup> The HPS-infiltrated PCs (HPS-PC) exhibited amplified fluorescence owing to the slow photon effect of PC. This is because the emission wavelength of HPS is at the blue band edge of the selected PC's stopband. The fluorescence of HPS-PC can be effectively quenched by  $\text{Hg}^{2+}/\text{Fe}^{3+}$  with high electrode potential and small size, due to the electron transfer from HPS to metal ions (Figure 126A). The amplified fluorescence came from the AIE and slow photon effects of PC enhanced the sensitivity, with the detection limit as low as 5 nM for  $\text{Hg}^{2+}/\text{Fe}^{3+}$ . Moreover, this HPS-PC film show negligible response to other metal ions and can be facilely reproduced and reused by removing the  $\text{Hg}^{2+}/\text{Fe}^{3+}$  ions with pure water as a result of the special surface wettability of PC. Specifically, when the film was immersed into the aqueous solutions containing different amounts of  $\text{Hg}^{2+}$ , its emission decreased with the increase in  $\text{Hg}^{2+}$  concentration (Figure 126B). A linear response of the quenching efficiency ( $1 - I/I_0$ ) against the concentration of  $\text{Hg}^{2+}$  was obtained over the range of 5–210 nM. It is noteworthy that the HPS-PC film should be sensitive enough for evaluating the level of  $\text{Hg}^{2+}/\text{Fe}^{3+}$  in foodstuffs and environmental samples, for its detection limit (5 nM) is lower than the U.S. EPA's allowable level of  $\text{Hg}^{2+}$  (10 nM) and  $\text{Fe}^{3+}$  (5.4  $\mu\text{M}$ ) ions in drinking water.

Lead has extensive applications in various industrial products and fields, including storage batteries, alloys, lead wires, paints, high quality glasses, soldering of electronic devices, and foundries.<sup>739</sup> However, it has been recognized as one of the most hazardous and poisonous metals to humans, damaging the nervous system and resulting in brain disorders. It is a neurotoxin that accumulates in both soft tissues and bones. Exposing to high concentration of lead for a long period of time may cause a number of diseases such as hemotoxic effects, reproductive dysfunction, and nephropathies, etc.<sup>740</sup>  $\text{Pb}^{2+}$  is therefore a typical heavy metal ion that poses a huge threat to public health and the environment. In particular, it is dangerous for children for it can cause mental retardation.<sup>741–743</sup> In view of its significant adverse

health effects, the safe threshold level for  $\text{Pb}^{2+}$  in drinking water has been set as 15 and 10 ppb, respectively, by the U.S. EPA and the International Agency for Research on Cancer (IARC).<sup>744</sup> It is thus of crucial importance to develop lead sensors with high selectivity and sensitivity that are workable at concentrations lower than these action levels. For this purpose, AIE has been singled out from a large group of sensing approaches by Chatterjee and Banerjee et al. and has been exploited as a working principle for the sensitive and selective detection of  $\text{Pb}^{2+}$ .<sup>745</sup> The TPE monoester of phosphoric acid (**413**) was developed as an AIE-based fluorescence chemodosimeter for  $\text{Pb}^{2+}$  detection, bearing the idea in mind that alkyl phosphates have a very strong affinity towards  $\text{Pb}^{2+}$  ions and the resulting lead-phosphate complex is insoluble in the detection system (Figure 127A). The lead-phosphate complexation will lead to the

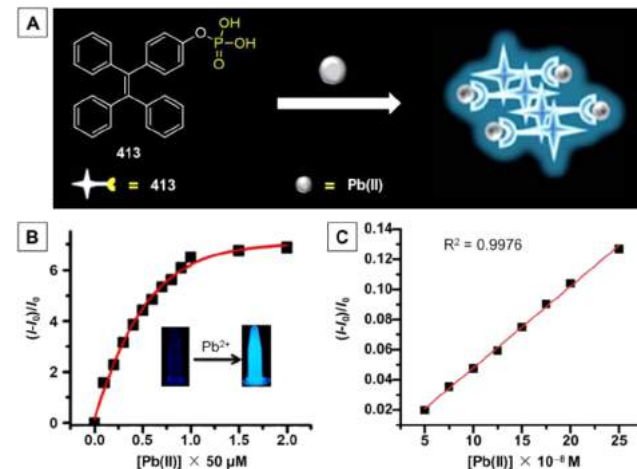


**Figure 127.** (A) Schematic illustration of the sensing process of probe **413** based on AIE mechanism. (B) Plot of the increment in fluorescence intensity against the concentration of  $\text{Pb}(\text{II})$ . (C) Relative fluorescence response of **413** at the lower concentration range of  $\text{Pb}(\text{II})$  (concentration range, 50–250 nM). Adapted with permission from ref 745. Copyright 2014 Royal Society of Chemistry.

aggregate formation, restricting the intramolecular motions of the TPE segments and triggering the fluorescence. As shown in Figure 127B, the fluorescence of **413** in THF/water mixture with  $f_w = 95$  vol % was very faint (inset in Figure 127B). Upon gradual addition of  $\text{Pb}^{2+}$  ions, the fluorescence response from the detection system emerged and was slowly intensified, with a linear

relationship between the corresponding output and the concentration of  $\text{Pb}^{2+}$  ( $< 50 \mu\text{M}$ ). By plotting relative fluorescence intensity ( $I - I_0$ )/ $I_0$  against concentration of  $\text{Pb}^{2+}$  ions, a good linear correlation ( $R^2 = 0.9967$ ) was obtained even at nanomolar level in the range of 50–250 nM, from which a detection limit has been estimated to be as low as 10 ppb (Figure 127C). Such a simple, efficient, and economic detection system has also displayed high selectivity to  $\text{Pb}^{2+}$  over various metal ions.

Like the toxic divalent metal ions, such as  $\text{Cu}^{2+}$ ,  $\text{Hg}^{2+}$ , and  $\text{Pb}^{2+}$ , the design and synthesis of chemosensors for trivalent metal ions with toxic effects, e.g., aluminum ( $\text{Al}^{3+}$ ), has also attracted considerable research interest.  $\text{Al}^{3+}$  is widely used in food additives, kitchen utensils, packing materials, and some drugs, which increases the risk of  $\text{Al}^{3+}$  entering into human bodies through digestive system.  $\text{Al}^{3+}$  ions can exert some neurotoxic effects in organisms and also have close association with Alzheimer's and Parkinson's disease, bone softening, chronic renal failure, and smoking-related diseases, etc.<sup>746–751</sup> In 1989, the World Health Organization (WHO) listed  $\text{Al}^{3+}$  to be one of the food pollution sources and limited  $\text{Al}^{3+}$  concentration to  $200 \mu\text{g L}^{-1}$  ( $7.41 \mu\text{M}$ ) in drinking water. AIE-based fluorescence approaches have been proven efficient in the detection of  $\text{Al}^{3+}$  ions.<sup>222,752–755</sup> For example, Tong and Dong et al. designed a new aryl-substituted pyrrole derivative, namely, 4-(2,5-diphenyl-1*H*-pyrrol-1-yl) benzoate (414), which is highly hydrophilic and AIE-active.<sup>752</sup> The introduction of carboxylic salt into the AIE core not only enhanced the water solubility but also endowed the whole molecule with metal ion recognizing ability due to its negative charge in aqueous media. The fluorescence of  $100 \mu\text{M}$  414 in THF/water mixture (25/75, v/v) was obviously intensified with the increase in  $\text{Al}^{3+}$  concentration from 0 to  $20 \mu\text{M}$ . The increase rate of fluorescence intensity became slower when  $\text{Al}^{3+}$  concentration was over  $20 \mu\text{M}$  and nearly zero after  $28 \mu\text{M}$ . It is implied that each  $\text{Al}^{3+}$  cations can couple with three 414 anions. As illustrated in Figure 128A, the fluorescence turn-on response of 414 to  $\text{Al}^{3+}$  was ascribed to the aggregation of the 414/ $\text{Al}^{3+}$  complex induced by the electrostatic attraction, which triggered the RIM process and suppressed the non-radiative decay. The fast formation of nanoscaled aggregates resulted in a rapid fluorescence response, providing a potential "zero-wait" detection method for  $\text{Al}^{3+}$ . It was found that the fluorescence was increased linearly with the concentration of  $\text{Al}^{3+}$  in the range of 1–11  $\mu\text{M}$ , which covering the allowable level set by the WHO. 414 exhibited high sensitivity to  $\text{Al}^{3+}$  (Figure 128B), which was probably due to the lower electrostatic binding affinity between 414 and other metal ions as well as the poorer solubility of the resulted 414/ $\text{Al}^{3+}$  complex. To further improve the sensing performance of such AIEgens and verify the detection mechanism, 4,4',4''-(1*H*-pyrrole-1,2,5-triyl)tribenzoate, an analogue of 414 with two extra carboxylic groups, has been developed by the same group.<sup>753</sup> With better water solubility, the  $\text{Al}^{3+}$  assay can be carried out in the THF/water mixture with a much higher  $f_w$  (96 vol %). Such a probe responded to  $\text{Al}^{3+}$  in less than 10 s upon addition of  $\text{Al}^{3+}$ . The probe is specific to  $\text{Al}^{3+}$  among various metal ions with a detection limit of  $5.3 \mu\text{M}$  and a linear increase within the range of 5–120  $\mu\text{M}$ . Therefore, such a strategy should be universal because both the AIE core and the negatively charged functional groups are replaceable, and the detection output (e.g., sensitivity, response time, selectivity, etc.) could be adjustable.

Ratiometric analysis based on the ratio of emission intensities at two or more wavelengths can minimize the errors arising from the physical or chemical variations in the samples to be tested, and the shift in the emission wavelength can also enable rapid visual observation through color changes.<sup>756</sup> The integration of

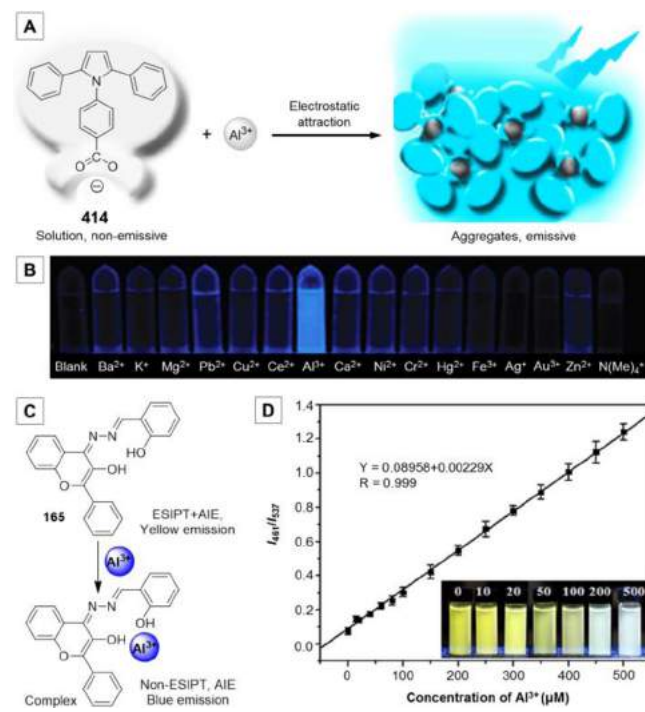


**Figure 128.** Representative examples of  $\text{Al}^{3+}$  sensing utilizing AIEgens. (A) Schematic illustration of fluorescence "turn-on" detection of  $\text{Al}^{3+}$  based on 414. (B) Fluorescent photographs of 414 solutions with different cations. Adapted with permission from ref 752. Copyright 2011 Royal Society of Chemistry. (C) Schematic presentation for the ratiometric fluorescence change of 165 upon binding with  $\text{Al}^{3+}$ . (D) Calibration curve based on the ratio of fluorescence intensities ( $I_{461}/I_{537}$ ) as a function of  $\text{Al}^{3+}$  concentrations. Inset: Photographs of 165 ( $20 \mu\text{M}$ ) upon the addition of different amounts of  $\text{Al}^{3+}$  (0–500  $\mu\text{M}$ ) under a UV lamp (365 nm). Adapted with permission from ref 222. Copyright 2014 Elsevier B.V.

ratiometric analysis with AIE was envisioned to be interesting and meaningful, for it might bring about novel and highly-performed ratiometric fluorescent sensors. ESIPT fluorophores are potential ratiometric probes for their emissions are largely dependent on the intramolecular hydrogen bonding and can be switched between the enol-form and keto-/IPT-form. In the light of this, AIE-active ESIPT luminogens should be ideal for the development of AIE-based ratiometric fluorescent chemosensors. Such an assumption has been fully vindicated by the detection of  $\text{Al}^{3+}$  reported by Tong and coworkers.<sup>222</sup> The ESIPT and AIE properties of compound 165 have been discussed in section 4.2.3. The AIE and ESIPT effects are, respectively, responsible for the intense fluorescence and large Stokes shift (167 nm) of 165 in the aggregate or solid state. In the 10 mM HEPES buffer solution containing 0.2% DMSO, 165 emitted strong fluorescence at 537 nm. Whereas upon the addition of  $\text{Al}^{3+}$ , the emission band at 537 nm decreased while that at 461 nm increased accordingly, resulting in fluorescence color change from yellow to white (Figure 128D). The intensity ratio  $I_{461}/I_{537}$  showed an almost linear dependency on the concentration of  $\text{Al}^{3+}$ , exhibiting a dynamic range at least from 0 to 500  $\mu\text{M}$  with a detection limit of  $0.29 \mu\text{M}$ . The detection principle was attributed to the chelation between  $\text{Al}^{3+}$  and the two hydroxyl groups from 165, which gave rise to the formation of 165- $\text{Al}^{3+}$  complex and disrupted the intramolecular hydrogen-bonding as well as the ESIPT process (Figure 128C). Consequently, the emission was blue-shifted, but the AIE effect was retained because the luminogenic molecules were still aggregated

or the molecular conformation was still stiffened. **165** was also highly selective to  $\text{Al}^{3+}$  over various physiologically associated metal ions. By virtue of its AIE characteristics, simple and rapid detection of  $\text{Al}^{3+}$  can also be realized on test papers. Additionally, this AIE-based chemosensor could be used for the ratiometric fluorescence imaging of  $\text{Al}^{3+}$  in living cells. Some other AIE-active ESIPT compounds have also been reported as fluorescence turn-on probes for  $\text{Al}^{3+}$  sensing, demonstrating the high applicability and flexibility of AIE approach.<sup>755</sup>

Among biologically important metal ions, iron in trivalent state is critical to oxygen-uptake by heme, oxygen metabolism, and electron transfer in the body.<sup>757</sup> Both its deficiency and excess in human body will lead to many diseases, such as anemia, breathing problems, hepatic cirrhosis, Alzheimer's, Huntington's, and Parkinson's disease.<sup>758</sup> In view of the importance of  $\text{Fe}^{3+}$ , Bhalla and Kumar et al. have taken advantage of AIE to construct a sensor for  $\text{Fe}^{3+}$ .<sup>136</sup> The pentacenequinone-based AIEgen **95** formed nanoaggregates in the THF/water mixture with a  $f_w = 90$  vol % and exhibited a strong emission peaked at 560 nm. Considering that sulfur-containing molecules usually have a capability of binding transition metal ions to form stable complexes, the nanoaggregates of **95** were used to assess its sensing ability toward different metal ions and showed a specific response to  $\text{Fe}^{3+}$  with visible decrease in fluorescence. The fluorescence turn-off response of nanoaggregates of **95** to  $\text{Fe}^{3+}$  was ascribed to the complexation of the molecules of **95** with  $\text{Fe}^{3+}$  ions via coordination, leading to the electron transfer and the subsequent non-radiative process (Figure 129A). The

Stern–Volmer plots displayed a linear dependence of  $I/I_0$  on the concentration of  $\text{Fe}^{3+}$  ranging from 0 to 1000  $\mu\text{M}$ , with a quenching constant of  $1.5 \times 10^4 \text{ M}^{-1}$  and a detection limit of 100 nM. Moreover, the paper strips coated with a solution of nanoaggregates of **95** were also able to detect  $\text{Fe}^{3+}$  at the picogram level with a detection limit of 11.16 pg, indicative of the sensitivity, simplicity, portability as well as low cost of this AIE-based  $\text{Fe}^{3+}$  sensor. Similarly, a pyridine and thiophene groups-substituted TPE derivative in its aggregate state has also been reported to show sensitive and selective fluorescence turn-off response to  $\text{Fe}^{3+}$ , with a detection limit of 0.7  $\mu\text{M}$ .<sup>759</sup> Additionally, imidazole-bearing TPE derivative can also work as a fluorescent probe for  $\text{Fe}^{3+}$  via fluorescence turn-off due to coordination-induced electron transfer.<sup>760</sup> Such works have further verified that AIE is also conducive to the detection systems in a turn-off mode.

Owing to their biological significance and environmental effects, development of chemosensors for trivalent metal ions ( $\text{M}^{3+}$ ) is very important. An AIE-based chemosensor specific to  $\text{Al}^{3+}$  and  $\text{Cr}^{3+}$  ions based on chelation-enhanced fluorescence has been reported by Zhou and Yang et al.<sup>203</sup> It is noteworthy that our group also have recently developed an AIE-based strategy for the selective and ratiometric recognition of  $\text{M}^{3+}$  ions in a distinct working mechanism (Figure 129B).<sup>761</sup> Pyridinyl was used to decorate the TPE moiety to gain the metal-recognition ability, yielding the new AIEgen **415**, which displayed very weak fluorescence in ethanol solution but intense emission in the aggregate state. In the ethanol/water mixture with  $f_w = 0.5$  vol %, **415** weakly fluoresces with a blue light at 488 nm. When various mono-, di-, and trivalent metal ions were separately added into the solution of **415**, only  $\text{Cr}^{3+}$ ,  $\text{Fe}^{3+}$ , and  $\text{Al}^{3+}$  could change the emission from weak blue to strong red with a new peak emerging at 630 nm (fluorescent photographs in Figure 129B). Concomitantly with the ratiometric fluorescence change, there was also a color transition from colorless to yellow observed for the mixtures containing trivalent metal cations (room-light photographs in Figure 129B), suggestive of colorimetric responses. By thorough analyses, the ratiometric fluorescent and colorimetric responses were ascribed to the protonation of **415**. The protonated **415** became poorly soluble and formed aggregates in the detection medium, resulting in the emission enhancement. In the meantime, the enlarged electronic conjugation together with the strong D-A effect of the protonated **415** give rise to the red-shift in the emission. The selectivity of **415** to  $\text{M}^{3+}$  over  $\text{M}^{2+}$  and  $\text{M}^+$  should be attributed to the higher hydrolyzing ability of  $\text{M}^{3+}$ , which release more protons in the polar media (Figure 129B).

Ruthenium(III) complexes are used extensively as catalysts in oxidation and metathesis reactions; however, they are corrosive and detrimental to respiratory and digestive tracts, eyes, and skin. They have been recognized as a risk to aquatic organisms and might induce long-term adverse effects on the aquatic environment. Although the sensing of  $\text{Ru}^{3+}$  is important, fluorescent probes for  $\text{Ru}^{3+}$  are currently rare. Our research team therefore made some efforts on this issue.<sup>762,763</sup> We first investigated the possibility of using small AIEgens as fluorescent sensors for  $\text{Ru}^{3+}$  detection. It was found that the emission of nanoaggregates of the benzene-cored AIEgens can be selectively quenched by  $\text{Ru}^{3+}$ . For example, **416** displayed a static quenching constant up to  $\sim 6.0 \times 10^5 \text{ M}^{-1}$  at the initial stage of the Stern–Volmer plot (Figure 130A).<sup>762</sup> A low  $\text{Ru}^{3+}$  concentration of 1  $\mu\text{g mL}^{-1}$  (1 ppm) can be recognized by the PL quenching of **416** nanoaggregates. Our group further extended the scope of

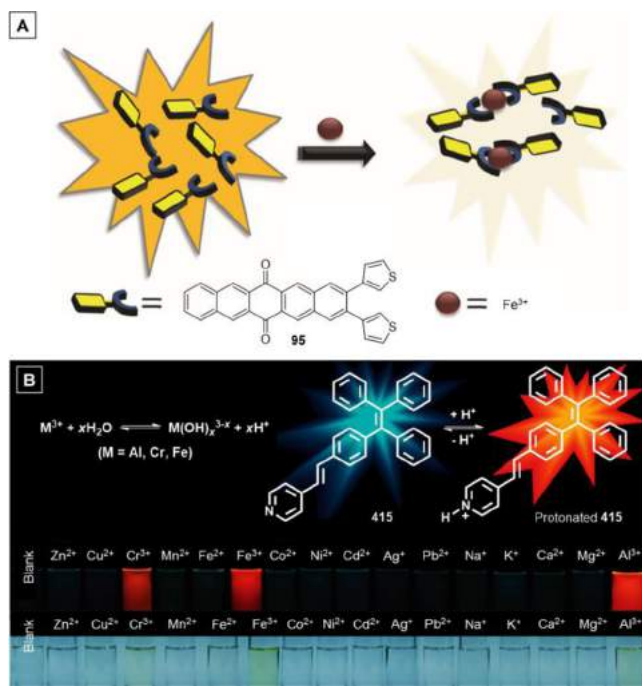


**Figure 129.** (A) Schematic representation of the  $\text{Fe}^{3+}$  sensor based on the fluorescence quenching of nanoaggregates of AIEgen **95**. Reprinted with permission from ref 136. Copyright 2013 Royal Society of Chemistry. (B) Schematic illustration of the mechanism for the detection of trivalent cations with an AIE-active pyridinyl-functionalized TPE (**415**). Insets: Photographs of **415** in ethanol/water mixtures in the presence of 10 equiv of different metal cations taken under UV light ( $\lambda_{\text{ex}} = 365 \text{ nm}$ ) and daylight, respectively. [**415**] = 10  $\mu\text{M}$ . Reprinted with permission from ref 761. Copyright 2013 Royal Society of Chemistry.

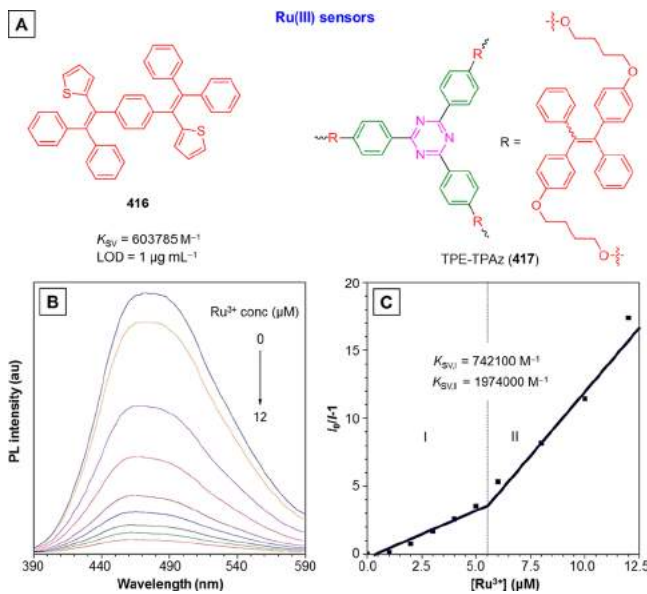


**Figure 130.** (A) Representative AIEgens (**416** and **417**) for Ru(III) sensing. (B) PL spectra of AIE-active hyperbranched polymer **417** in THF/H<sub>2</sub>O mixtures (1/9 in volume; 10  $\mu\text{M}$ ) with various Ru<sup>3+</sup> concentrations. (C) Stern–Volmer plot of ( $I_0/I - 1$ ) values versus Ru<sup>3+</sup> concentrations in THF/H<sub>2</sub>O mixtures (1/9 in volume) of **417**.  $I_0$  = intensity in the absence of metal ions. Adapted from ref 763. Copyright 2013 American Chemical Society.

AIE-based Ru<sup>3+</sup> sensors to AIE polymers.<sup>763</sup> For examples, the hyperbranched nitrogen-rich polytriazine bearing TPE motifs (Figure 130A), namely, **417**, has been prepared via the polycyclotrimerization of corresponding dinitriles. **417** inherited the AIE feature from the TPE moiety, showing intensive fluorescence in the THF/water mixture (1/9, v/v) in the form of nanoaggregates. The emission was progressively decreased by the gradual addition of Ru<sup>3+</sup> to the aforesaid nanoparticle suspension of **417** (Figure 130B).<sup>763</sup> The quenching effect can still be clearly seen even at a Ru<sup>3+</sup> concentration of 1  $\mu\text{g mL}^{-1}$ , and the fluorescence was almost completely quenched at a Ru<sup>3+</sup> concentration of 12  $\mu\text{M}$ . As shown in Figure 130C, the Stern–Volmer plot of  $I_0/I - 1$  against Ru<sup>3+</sup> concentrations is bending upward with two stages. In stage I or the low concentration range of Ru<sup>3+</sup> ( $\leq 5.0 \mu\text{M}$ ), the plot is linear with a  $K_{SV,I}$  value of 742 100  $\text{M}^{-1}$ . Whilst in stage II, where higher concentration of Ru<sup>3+</sup> ( $> 5.0 \mu\text{M}$ ) was added, the plot follows another linear relationship with a much higher  $K_{SV,II}$  value up to 1 974 000  $\text{M}^{-1}$ , implying a superamplification effect in the emission quenching process. It is because the nanoaggregates of the hyperbranched polymer **417** have a lot of cavities for quencher molecules to interact with and a large number of interchain diffusion pathways for excitons to migrate, thereby rendering the quenching highly efficient. Such a fluorescence quenching effect of the nanoaggregates of **417** is specific to Ru<sup>3+</sup> over a variety of metal ions. The reason for such a high selectivity has not been figured out so far; however, it is probably ascribable to the strong electron-deficiency of Ru<sup>3+</sup> which favors electron transfer from the electron-rich luminophores like TPE to Ru<sup>3+</sup> and leads to the fluorescence annihilation. Therefore, further comparative study should be carried out to testify this hypothesis.

Uranium is an important nuclear material and also a toxic and radioactive metal.<sup>764</sup> The analysis of uranium is vital in every step of nuclear industry. Uranium naturally possesses several oxidation states, i.e. 2+, 3+, 4+, 5+, and 6+, but it appears

mostly in hexavalent form. Usually, uranium is associated with oxygen, giving the uranyl ion ( $\text{UO}_2^{2+}$ ). To this end, Chen and coworkers developed a detection system for  $\text{UO}_2^{2+}$  by making use of AIE strategy in pursuit of detecting trace amounts of  $\text{UO}_2^{2+}$  with high sensitivity.<sup>765</sup> An ESIPT compound, namely, 4-pethoxycarboxyl salicylaldehyde azine (**418**), was designed as the  $\text{UO}_2^{2+}$  probe in view of its facile synthesis and marked AIE property (Figure 131A). By adjusting the pH to 10.3, the two

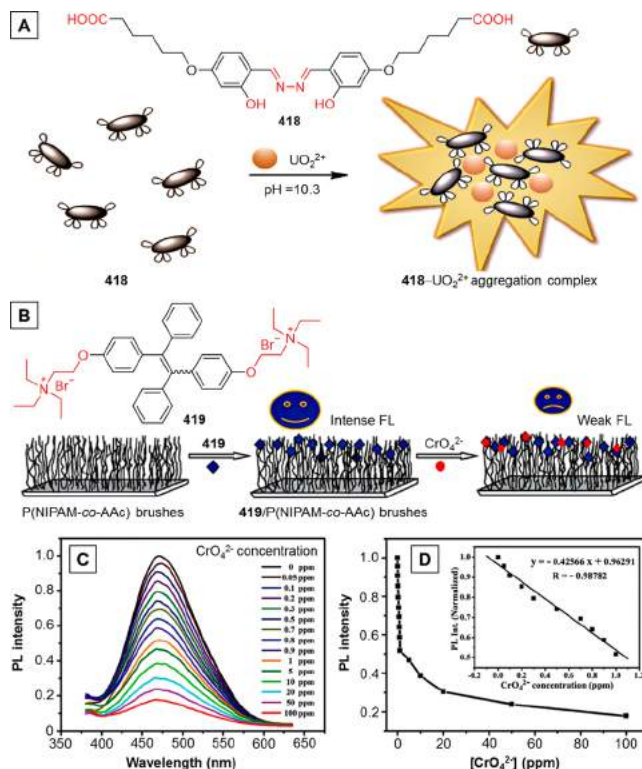


**Figure 131.** Representative examples of using AIEgens to detect metallic oxides. (A) The design rationale of the fluorescence “turn-on” detection of  $\text{UO}_2^{2+}$  based on AIEgen **418**. Adapted with permission from ref 765. Copyright 2014 Elsevier B.V. (B) Schematic illustration of the synthesis of **419**/P(NIPAM-co-AAc) brushes which were used for the “turn-off” detection of  $\text{CrO}_4^{2-}$ . (C) The normalized PL spectra of the **419**/P(NIPAM-co-AAc) brushes in the presence of various concentrations of  $\text{CrO}_4^{2-}$  (0–100 ppm). (D) The corresponding plot of PL intensities versus various concentrations of  $\text{CrO}_4^{2-}$ . Inset: A linear relationship ( $R = -0.98782$ ) between the PL intensities and low concentration (0–1 ppm). Adapted with permission from ref 767. Copyright 2013 Royal Society of Chemistry.

carboxyl groups on **418** were deprotonated, affording **418**<sup>2-</sup> which was non-luminescent in aqueous media owing to the good solubility. After the addition of  $\text{UO}_2^{2+}$ , the fluorescence at 540 nm was dramatically boosted with the increase in  $\text{UO}_2^{2+}$  concentration. An over 100-fold enhancement in the fluorescence intensity was observed at 30 ppb of  $\text{UO}_2^{2+}$ . The mechanism of such a fluorescence turn-on sensing of  $\text{UO}_2^{2+}$  was attributed to the aggregation of **418** molecules induced by the coordination of carboxylate and Schiff-base groups with  $\text{UO}_2^{2+}$ , which suppressed the intramolecular motions of the AIE moieties and hindered the non-radiative deactivation of their excited states, thus resulting in efficient fluorescence (Figure 131A). A linear range of 1–25 ppb  $\text{UO}_2^{2+}$  with a detection limit of 0.2 ppb has been achieved. Thanks to its simple operation, high sensitivity, good selectivity, as well as fluorescence turn-on response,

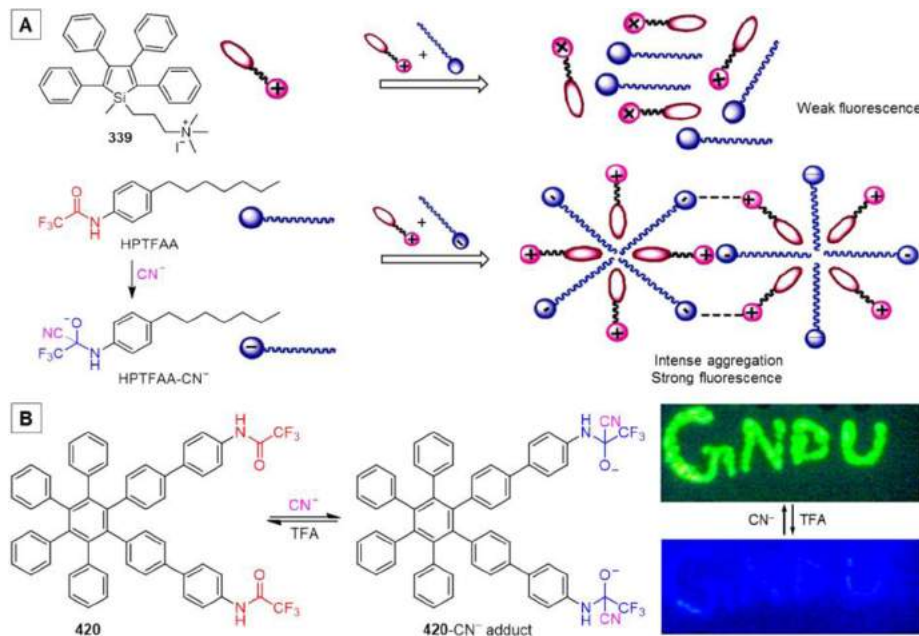


**Figure 132.** Representative examples of AIEgens used for CN<sup>-</sup> detection based on the nucleophilic reaction between CN<sup>-</sup> and trifluoroacetylamo (TFAA) group and the AIE features of 339 and 420. Insets: images showing the fluorescence change of paper strips coated with chemosensor 420 in response to CN<sup>-</sup> ions ( $10^{-3}$  M) and TFA ( $10^{-3}$  M). Panel A is adapted from ref 768. Copyright 2009 American Chemical Society. Panel B is adapted from ref 770. Copyright 2014 American Chemical Society.

this AIE-based probe has been successfully applied to the quantification of UO<sub>2</sub><sup>2+</sup> in diluted fuel processing wastewater.

Chromate ions, i.e., Cr(VI), existing in the form of CrO<sub>4</sub><sup>2-</sup> in water, which are isostructural with SO<sub>4</sub><sup>2-</sup>, are rather harmful to human beings. They can be taken into mammalian cells by sulfate transporters and oxidatively damage DNA.<sup>766</sup> Posing serious health risks, Cr(VI) species have been regulated by the U.S. EPA with a maximum allowable level of total chromium concentrations in drinking water as 100 ppb.<sup>766</sup> It is thus of great importance to distinguish destructive Cr(VI) from benign Cr(III) in water. By taking advantage of AIE as well as polymer brushes, selective and sensitive detection of Cr(VI) over Cr(III) has been achieved by Lin and coworkers (Figure 131B–D).<sup>767</sup> A hybrid thermoresponsive fluorescent copolymer brushes device, i.e., 419/P(NIPAM-*co*-AAc), was first built up as a detection platform by doping cationic TPE derivative 419 into the poly[(*N*-isopropylacrylamide)-*co*-acrylic acid] brushes via Coulombic force (Figure 131B). The resultant 419/P(NIPAM-*co*-AAc) brushes showed a linear and reversible fluorescence response to temperature in a broad range from 4 to 60 °C. 419 served as a fluorescence source in the thermoresponsive 419/P(NIPAM-*co*-AAc) brushes. Upon interaction with CrO<sub>4</sub><sup>2-</sup>, the fluorescence of 419/P(NIPAM-*co*-AAc) brushes film was significantly quenched (Figure 131C,D). The decrease in the fluorescence intensity exhibited a linear relationship with the concentration of CrO<sub>4</sub><sup>2-</sup> in the range of 0–1 ppm (inset in Figure 131D), which was beneficial to the quantitative analysis of CrO<sub>4</sub><sup>2-</sup>. Moreover, the detection limit was determined as 0.05 ppm, which was lower than the U.S. EPA level (0.1 ppm). The electron transfer from the electron donor 419 to the strong electron acceptor CrO<sub>4</sub><sup>2-</sup> was regarded as the mechanism of this fluorescence turn-off detection.

In comparison with the research efforts put into cations sensing, the attention paid on the detection and recognition of anions is much less. Besides the sensing significance and necessity, one of the reasons for this difference might lie in the

difficulty to attain simple and effective detection approaches for anions. AIE recently has been found to be a good methodology for the sensing of anions and there have been quite a few such examples.<sup>131,144,146,768–775</sup> Take the detection of cyanide (CN<sup>-</sup>) for example. A variety of AIE-based sensing systems have been established for this unique anion,<sup>146,768–772</sup> among which we have screened out some representative ones and highlighted them in Figure 132 and Figure 133. Cyanide anion is highly toxic and harmful to human health and the environment, for it is an inhibitor of the enzyme cytochrome *c* oxidase and can disrupt the mitochondrial electron-transport chain.<sup>776</sup> A high level of cyanide in blood (~20 μM) is very poisonous or even fatal.<sup>777,778</sup> Moreover, the safe level of cyanide in drinking water has been required to be lower than 1.9 μM, according to the World Health Organization (WHO).<sup>779</sup> Considering the utility of cyanide ions in daily life, it is vitally important to explore sensitive and selective chemosensors for cyanide. On the basis of the AIE feature of a silole derivative 339, Zhang's group has reported a fluorescence turn-on sensing ensemble for cyanide in aqueous solution.<sup>768</sup> Such an ensemble for cyanide sensing was constructed of 339 and the heptylphenyltrifluoroacetamide (HPTFAA). As schematically illustrated in Figure 132A, silole 339 carrying a positively charged ammonium group was only faintly fluorescent in aqueous solution. Even coexisting with the HPTFAA, the solution of 339 still exhibited very weak fluorescence. When the cyanide was added and reacted with the trifluoroacetylamino (TFAA) group through nucleophilic addition, the hydrophobic and neutral HPTFAA was readily converted into an amphiphilic compound with a negative head group (HPTFAA-CN<sup>-</sup>), which further formed heteroaggregates with silole 339 via intermolecular electrostatic attraction and hydrophobic interaction. The occurrence of strong coaggregation results in the activation of RIR process of silole and subsequent switch-on of the fluorescence. In this way, the CN<sup>-</sup> can be detected in a selective and fluorescence light-up manner.

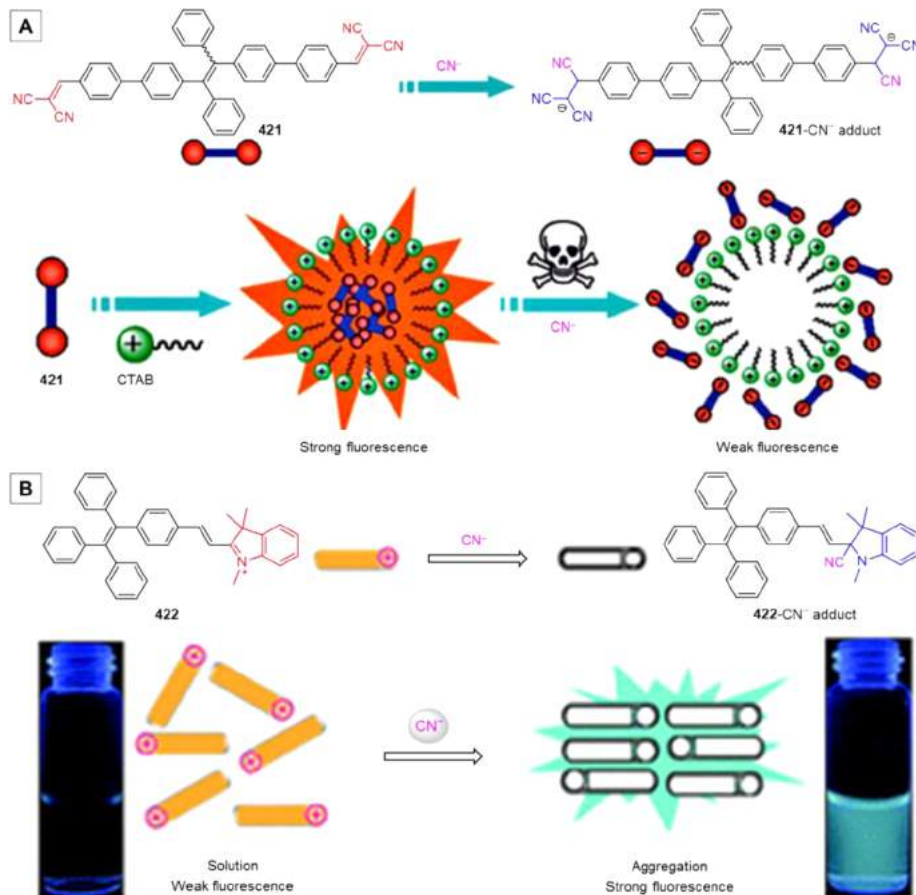


**Figure 133.** Representative examples of AIEgens used for  $\text{CN}^-$  detection based on the nucleophilic addition reactions. (A) Schematic illustration of the formation of aggregates of 421 in CTAB solution and the disassembly of the aggregates in the presence of cyanide anions. Adapted with permission from ref 771. Copyright 2014 Royal Society of Chemistry. (B) Fluorescence turn-on detection of  $\text{CN}^-$  developed by taking advantage of AIE behavior of TPE units and the nucleophilic addition of  $\text{CN}^-$  on the indolium group in compound 422. Adapted with permission from ref 772. Copyright 2012 Royal Society of Chemistry.

with a wide linear response range from 0 to  $120\ \mu\text{M}$  and a detection limit of  $\sim 7.7\ \mu\text{M}$ .

It is apparent that the TFAA group is really a good recognition moiety to  $\text{CN}^-$ . Enlightened by this fact, it is predictable that AIEgens directly functionalized with the TFAA group(s) can be utilized as high-performance  $\text{CN}^-$  sensors, and there indeed have existed some nice examples.<sup>769,770</sup> For instance, an HPB derivative bearing two TFAA groups (420) has been synthesized and its fluorescent spherical aggregates formed in the aqueous media have been applied for the detection of  $\text{CN}^-$  (Figure 132B).<sup>770</sup> The strong fluorescence of these aggregates in the EtOH/water mixture (2/8, v/v) arose from the AIE attribute of 420, with an emission maximum at 380 nm. Adding cyanide ions to the aforesaid mixture, the fluorescence at 380 nm gradually decreased and meanwhile a new band emerged at 485 nm and progressively increased. Simultaneously, the emission color shifted from blue to green and the solution color changed from colorless to yellow, indicative of a unique colorimetric and ratiometric fluorescent response to cyanide. Such a response was ascribed to the nucleophilic addition of  $\text{CN}^-$  ions to the TFAA groups, which altered the packing mode of the aggregates. The resultant 420- $\text{CN}^-$  adduct can be converted back into 420 by the addition of trifluoroacetic acid (TFA), accompanying with the restoration of the original blue fluorescence (Figure 132B). The detection limit of this fluorescent  $\text{CN}^-$  sensor in the aqueous media was estimated to be 11 nM. A sensitive detection of  $\text{CN}^-$  ions at the level

of  $\sim 2.6\ \text{ng cm}^{-2}$  can be realized by using disposable filter paper-based test strips (insets in Figure 132B), and a simple and low-cost approach for the on-site and instant detection of  $\text{CN}^-$  ions in aqueous media has thus been provided. Moreover, 420 can also function as a set-reset memorized sequential logic circuit with chemical inputs of  $\text{CN}^-$  ions and  $\text{TFA}/\text{H}^+$  ( $\text{pH} \leq 3$ ).

In addition to the TFAA group, dicyanovinyl group as a reactive unit has also been widely utilized for the construction of reaction-based cyanide sensors.<sup>146,771</sup> Using 421 as an example, this dicyanovinyl-containing TPE derivative possessing both solvatochromism and AIE properties has been developed as a highly efficient cyanide chemosensor by Yu's group (Figure 133A).<sup>771</sup> As 421 is highly hydrophobic, with the aim of detecting cyanide in water, strongly emissive micelles encapsulating 421 were fabricated with the aid of CTAB to make 421 well-dispersed in water (containing 1 vol % DMSO). The cationic surfactant CTAB offered a hydrophobic environment for 421 as well as electrostatic attractions to promote the nucleophilic addition of  $\text{CN}^-$  ions to the dicyanovinyl groups. As a consequence of the nucleophilic addition reaction, a water-soluble adduct (421- $\text{CN}^-$ ) was generated and the nanomicelles were disassembled, resulting in the fluorescence decrease. Meanwhile, the conjugation between the dicyanovinyl groups and TPE moiety was disrupted and the strong D-A effect was also eliminated, further causing blue-shift in absorption and emission wavelength. Specifically, with the addition of  $\text{CN}^-$  ions, the absorption band

at 398 nm vanished and a new peak at 266 nm appeared, with the appearance color changing from yellow to colorless. Correspondingly, the emission changed from intense orange (573 nm) to weak blue. A low detection limit of 0.2  $\mu\text{M}$  and a short response time of merely 100 s towards  $\text{CN}^-$  ions have been achieved. Meanwhile, a rapid and convenient sensing of  $\text{CN}^-$  ions without resorting to instrumental analysis can be performed on test papers loading 421.

Through combining the AIE feature of TPE derivatives and the reaction of  $\text{CN}^-$  with the indolium group, a selective and sensitive fluorescence turn-on detection of  $\text{CN}^-$  was established with a simple AIEgen (i.e. 422) by Zhang et al. (Figure 133B).<sup>772</sup> Carrying a positively charged indolium moiety, AIEgen 422 was well dissolved in aqueous solution and showed very weak fluorescence. The indolium moiety not only conferred the water-solubility on 422 but also endowed 422 with selective recognition ability to  $\text{CN}^-$  via the specific reaction to afford 422-CN<sup>-</sup> adduct, which was highly hydrophobic and hence formed aggregates in the aqueous media, ultimately switching on the fluorescence as a result of RIR (Figure 133B). Therefore, the detection of  $\text{CN}^-$  ions can be realized in aqueous solution in a turn-on manner with good selectivity and high sensitivity.  $\text{CN}^-$  with a concentration as low as 91 nM can be detected using this AIE-based fluorescent probe. A simple paper test strip system has been fabricated as well for rapid sensing of  $\text{CN}^-$ .

Besides the above discussed examples for  $\text{CN}^-$  detection, there have been some other AIEgens designed for the detection of other anionic species, such as fluoride,<sup>774,775</sup> bisulfite anion,<sup>131</sup> pyrophosphate,<sup>773</sup>  $\text{H}_2\text{PO}_4^-$ , and  $\text{ClO}_4^-$ .<sup>144</sup> To sum up this ion detection part, AIE can definitely be taken as a powerful approach to achieve high-performance chemosensors for ion detection in terms of its simplicity, low-cost, high sensitivity, excellent efficiency, flexibility, and adaptability. AIE-based ion probes can work in turn-on or turn-off and/or ratiometric modes, depending on the molecular and experimental designs. No matter which mode is adopted, AIE benefits the outcomes. Note that the AIE strategy is highly flexible, for even the same AIEgen can be tailored for different purposes, and in turn diverse AIEgens can be designed for the same aim. Thanks to this distinctive and powerful strategy, a large number of chemosensing systems have shown great promise for real-sample assays in view of their superb sensitivity, high selectivity, and workability in aqueous phase or even solid state.

**5.2.2. pH.** As previously pointed out, pH is very important to cellular functions. Actually, pH is crucial to all life forms. A subtle variation in environmental pH can even devastate quite a few plant and animal lives. Acidification of soils, streams, lakes, and seawater caused by acid rain, excessive human activities, and untreated sewage can induce ecological disasters, which might further lead to the extinction of individual species, reduction of biodiversity, the elimination of specific strains, etc. Additionally, pH value is also a critical factor for medicines, foods, and drinking water, etc. Monitoring the pH level is thus vital to the preservation of our living environment as well as life quality. Amongst various analytical methods, fluorescence-based techniques have caught special attention for its superior sensitivity, rapidity, portability, etc. Since the pH detection should be carried out preferably in aqueous solution, thus for the sake of higher sensing efficiency, AIEgens would be better choices for their unique solution- and aggregate-state behaviors. Indeed, a number of AIE-based pH sensors have been developed with good performance.<sup>332,441,603,780–782</sup>

Our research group has made use of various AIEgens to develop fluorescent pH detection systems that sensitively respond to small pH changes. For instance, diethylaminomethyl-functionalized HPS derivative A<sub>2</sub>HPS (350) can be readily dissolved in acidic aqueous media owing to the transformation of its tertiary amino groups to ammonium salts, making it non-luminescent under this situation.<sup>460</sup> As can be seen from the inset in Figure 134B, when the pH value of the solution was

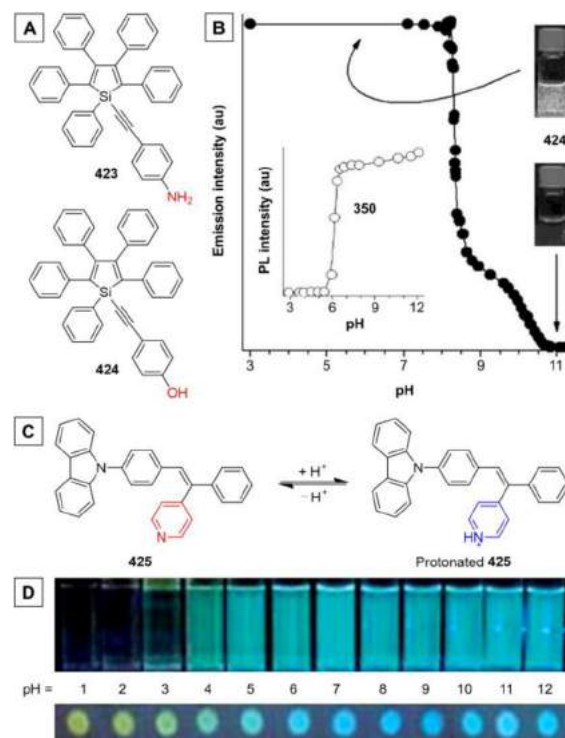


**Figure 134.** Representative examples of AIEgens with different pH sensing behaviors: (A) molecular structures of silole derivatives which exhibit fluorescence turn-on effect under basic and acidic conditions, respectively. (B) Changes in emission intensity of 424 and 350 with pH value of the aqueous medium. Reprinted with permission from ref 780. Copyright 2009 Wiley-VCH Verlag GmbH & Co. KGaA. (C) Reversible transformation between 425 and protonated 425 by repeated protonation and deprotonation. (D) Fluorescent photos of 425 (upper panel) in the THF/buffer mixture (1/9 in volume) and (lower panel) deposited on filter paper at (left) pH 1 to (right) 12 taken under 365 nm UV irradiation. Adapted with permission from ref 781. Copyright 2013 Royal Society of Chemistry.

gradually adjusted from 2 to 5.4, the emission remained in an “off” state but afterwards swiftly increased with an increment over 150-fold at a pH of 6.35 as compared to that at pH = 2. It is because when the pH value exceeded 5.4, the ammonium salts were converted back to their amine form, which decreased the hydrophilicity and induced the aggregation of chromophores as well as the turn-on of fluorescence. At pH > 6.35, the fluorescence maintained a hyperintense but did not change much anymore. The working mechanism involved in this pH sensing process is the dissolution/deaggregation and aggregation of the AIEgens at the appropriate pH value. Therefore, the amino-decorated silole derivative (423; Figure 134A) should work in the same way. However, because of its poor water-miscibility, its pH sensing behavior was not closely studied.<sup>780</sup> Nevertheless, a DSA derivative which was modified with two diethylaminoethoxy groups, namely, 9,10-bis{4-[2-(diethylamino)ethoxy]styryl}-anthracene, has been

found to show similar pH response as 350.<sup>441</sup> The fluorescence emission of this DSA derivative was switched off at low pH (< 4.0) and was turned on at high pH, as a result of ionization and deionization under strongly acidic and basic conditions, respectively. Following this principle, the fluorescent pH probe with the opposite response can be easily designed. For example, by embellishing the AIE cores with phenolic hydroxyl group(s), strong fluorescence would be observed from aqueous media with low pH value whereas non-fluorescent state would be afforded under basic condition with high pH value.<sup>441,780</sup> For example, 424, a silole derivative bearing one phenol group (Figure 134A), displayed no fluorescence signal in the alkalinized aqueous medium with a high pH value due to the ionization.<sup>780</sup> The non-luminescent state remained unchanged when the pH was decreased from 12.0 to 10.8 by adding hydrochloric acid, but afterwards, the fluorescence started to increase rapidly (Figure 134B). At a pH of 8.14, the emission was more than 100 times higher than that at pH = 12.0. Further acidification caused no obvious change in the fluorescence. At pH lower than 8.1, the mixture was emissive and turbid, indicating the formation of aggregates (cf., inset in Figure 134B). In this way, pH sensing systems that work in two opposite directions can be developed with ease by molecular engineering or altering the ionizable substituents of AIEgens (Figure 134B).

It can be easily seen that protonation of some heteroatom-containing groups, such as amino, phenol, and pyridinyl, will greatly alter their electron-withdrawing properties and subsequently exert some effects on the emission properties (e.g., intensity, color, etc.) of the luminogens with these pH-sensitive moieties. In view of this, new heteroatom-containing fluorophore has been constructed from diphenylethene, carbazole, and pyridine building units and further employed for pH sensing (Figure 134C,D).<sup>781</sup> The resultant 425 is AIE-active and features the TICT property because of the D-A interaction between the carbazolyl and pyridinyl blocks. 425 showed an intense blue emission in the aggregate state owing to its AIE character, whilst its protonated state exhibited dim yellow fluorescence due to a much stronger ICT effect. The light emission of 425 can be reversibly switched between dark and blue states by repeated protonation and deprotonation (Figure 134C), thus enabling 425 to function as a fluorescent probe for pH sensing in both the solution and solid states as well as a sensor for detecting organic vapors with high acidity or basicity (Figure 134D). The change in electron affinity of the pyridinyl unit and molecular conformation of 425 upon protonation was believed to account for such sensing process, as proved by the analyses of the results obtained from NMR, single-crystal X-ray diffraction, and theoretical calculation.

As briefly mentioned in section 5.1.2.1, the zwitterionic hemicyanine fluorophore, 336a (i.e., TPE-Cy), is a pH sensor which showed fluorescence response to the pH change in the whole range (0–14) and has hence been used for intracellular pH imaging and monitoring.<sup>604</sup> Here in this subsection, its working mechanism for pH sensing as well as the corresponding main results will be discussed in detail (Figure 135).<sup>603</sup> Specifically, containing a TPE unit and a N-alkylated indolium moiety, 336a enjoys an AIE feature and a large Stokes shift (>185 nm).<sup>603</sup> Its AIE activity and chemical reactivity towards OH<sup>-</sup>/H<sup>+</sup> enabled it to sense pH in a broad range (the broadest thus far) by displaying colorimetric and ratiometric fluorescent responses. The mechanistic picture illustrating how 336a works as a pH-sensitive fluorescent probe is exhibited in Figure 135A. In buffer solutions with neutral pH, although 336a is zwitterionic, it can hardly be molecularly dissolved due to the large hydrophobic part. A few

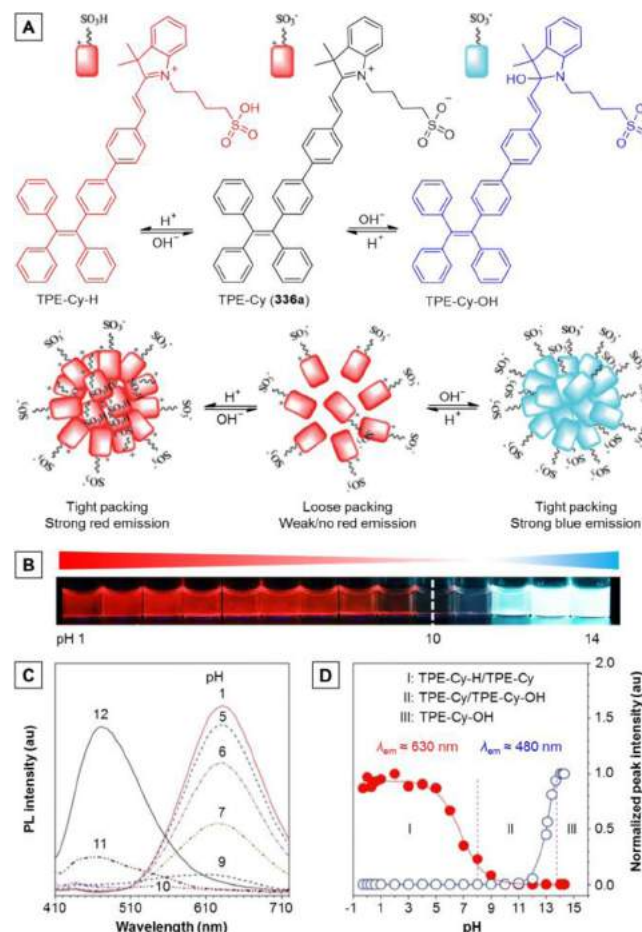


**Figure 135.** Full-range pH sensing based on the AIE-active hemicyanine fluorogen TPE-Cy (336a). (A) Proposed mechanism for colorimetric and fluorometric switching of 336a in response to acid and base. (B) The fluorescent photographs of 336a in buffer solutions (pH = 1–13, from left to right with an interval of 1). (C) PL spectra of 336a in aqueous solutions with different pH values. (D) Their corresponding plots of emission peak intensities at indicated wavelengths versus pH value. Adapted with permission from ref 603. Copyright 2012 Royal Society of Chemistry.

molecules of 336a may cluster into loosely packing aggregates, which hold a large internal free volume that cannot sufficiently suppress the intramolecular motions, thus making it only weakly emissive. Upon acidification, the dangling sulfonate group of 336a is protonated to yield TPE-Cy-H, increasing the hydrophobicity of the whole molecule. As a consequence, compact aggregates of TPE-Cy-H are formed, activating the RIM process and thus switching on the red emission. On the other hand, in the basic environment, the OH<sup>-</sup> attacks the double bond on the indolium moiety of 336a, breaking the electronic conjugation and D-A system between the bulky aromatic core and indolium moiety. As a result, the blue emissive TPE-Cy-OH is generated which is more hydrophobic than 336a owing to the loss of a positive charge. In the aqueous media, the molecules of TPE-Cy-OH tend to aggregate and trigger the AIE process. In this way, as displayed in Figure 135B–D, the 336a showed a “switch + knob” effect: strong red fluorescence ( $\lambda_{\text{em}} = 630 \text{ nm}$ ) at pH < 5, strong to moderate red emission at pH = 5–7, weak to almost no fluorescence in the pH region of 7–10, nearly no to intense blue fluorescence at pH = 10–14, and intensive blue emission ( $\lambda_{\text{em}} = 480 \text{ nm}$ ) at pH > 14. In the whole process, the chemical reaction

with  $\text{OH}^-/\text{H}^+$  served the role of “switch”, while the photo-physical AIE attribute acted as a “knob”. Meanwhile, with the pH changing from 1 to 13, the absorption peak at 440 nm decreased and disappeared while the new peak at 330 nm increased, thus the solution color changed from yellow to colorless. It is noteworthy that there is a good linear correlation between the emission intensity and the pH in the physiological range of pH 5–7, indicative of its capability as a pH sensitive bioprobe.

**5.2.3. Gases.** In this subsection, a few cases where AIE-based systems have been smartly designed or engineered to satisfy the applications for the sensing of some special gases, such as carbon dioxide ( $\text{CO}_2$ ), primary amine gas, and hydrogen sulfide ( $\text{H}_2\text{S}$ ), will be presented and expounded.  $\text{CO}_2$  sensing has great societal implications, because  $\text{CO}_2$  is a component of gas mixtures that are released from many natural processes (e.g., volcanic explosion, earthquake, and tsunami) and anthropogenic activities (e.g., blackdamp, natural gas production, and industrial exhaust gas emission) and it has huge impacts on globe climate and human well-being. Especially, it has been widely accepted that  $\text{CO}_2$  is closely associated with the global greenhouse effect. Currently, electrochemical (EC) and IR methods are the main analytical tools for  $\text{CO}_2$  sensing. Both of these two techniques have their own limitations. The EC sensors require large amount of powers while the IR sensors are bulky and costly and susceptible to the interference of CO. Besides that, both these chemosensors are cross-sensitive to water. Other analytical tools including GC-MS and field-effect transistors are time-consuming, expensive, and complicated. By virtue of AIE, alternative schemes for selective detection and quantitative assays of  $\text{CO}_2$  gas in a simple, rapid, and visual manner have been developed.<sup>783,784</sup>

Enlightened by the fact that bubbling  $\text{CO}_2$  through an amine solution can furnish a carbamate ionic liquid (CIL) resulting in the increases in polarity and viscosity, the  $\text{CO}_2$ -induced *in-situ* generation of CIL has been made full use of to arouse the fluorescence response from the AIEgen. As the scheme depicted in Figure 136,<sup>783</sup> HPS was dissolved in dipropylamine (DPA), affording a non-luminescent solution. Purging the DPA solution of HPS with a stream of  $\text{CO}_2$ , a CIL was readily yielded via the reaction between  $\text{CO}_2$  and DPA (Figure 136A), and the green fluorescence from the mixture was observed (insets in Figure 136A). With the increasing amount of  $\text{CO}_2$ , the fluorescence was intensified (Figure 136B). The potential of this scheme for practical use has been assessed by utilizing  $\text{CO}_2/\text{N}_2$  mixtures as a model system. The presence of  $\text{CO}_2$  was visualized and the plot of  $\log I$  versus fraction of  $\text{CO}_2$  gave a linear line over the whole concentration range from 0 to 100 vol % (Figure 136C), enabling quantification of  $\text{CO}_2$  under various conditions, especially for the gas mixtures with very high  $\text{CO}_2$  contents. Moreover, the addition of water droplets, CO, and other amines such as diethylamine, butylamine, piperidine, and pyridine (far left of the inset in Figure 136A) exerted little effect on the detection of  $\text{CO}_2$ . The operating mechanism of this  $\text{CO}_2$  sensing process was attributed to the formation of viscous and polar CIL with poor solvating power to HPS, which set off the RIR process of HPS, thus blocking the non-radiative relaxation pathways and triggering the light emission of HPS in the CIL mixture. This assay kit is efficient, visual, portable, and energy- and cost-effective and, hence, promising for predicting disasters and signaling dangers in the environment. A similar work has been done by Wang and Guo et al. with TPE and other amine-based ionic liquid,<sup>784</sup> which provides a further validation to the universality of the above-discussed scheme.

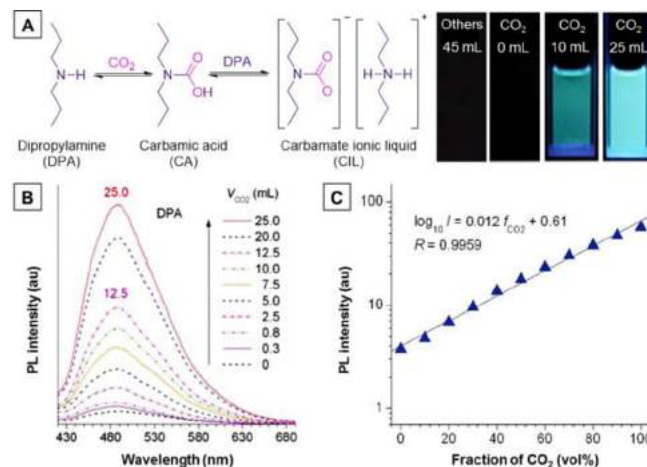


**Figure 136.** Example of AIEgens using as fluorescent chemosensors for detection and quantitation of carbon dioxide. (A) Formation of carbamate ionic liquid (CIL) by bubbling  $\text{CO}_2$  through dipropylamine (DPA) liquid. Insets: Fluorescent photographs of HPS in other amines bubbled with 45 mL of  $\text{CO}_2$ , and HPS in DPA before and after bubbling with different volumes of  $\text{CO}_2$  ( $V_{\text{CO}_2}$ ). (B) PL spectra of HPS in DPA before and after bubbling with different volumes of  $\text{CO}_2$ . (C) The plot of PL intensities of HPS versus fractions of  $\text{CO}_2$  in  $\text{CO}_2/\text{N}_2$  mixtures. Adapted from ref 783. Copyright 2010 American Chemical Society.

Amines are extensively utilized in dyeing and food industries,<sup>785–787</sup> gas treatment plants, and clinical diagnosis.<sup>788</sup> However, low molecular-weighted amines are toxic and easily absorbable through the skin. On the other hand, many amines with high molecular weight are biologically active. The sensing of amines is thereby of academic value and has technological implications. Most of the amine sensors have been developed for solution detection, but it is more favorable for practical application to realize detection on a solid support, because it is simple, quick, convenient, and green. However, such sensing systems are rather rare. To this end, our group and Dong’s team have developed a fluorescence-switchable luminogen which can sensitively and selectively detect primary amine gas in the solid state.<sup>788</sup> 414-H is practically non-emissive in both the solution and aggregate/solid states, which behaves quite differently from its salt form (414) and ester derivative. It has been found that the dimer formation primarily accounts for the emission quenching of 414-H in the aggregate state. Whereas fuming the 414-H-loaded filter paper strip with primary amines readily turned on the emission. The generation of 414-H-amine complex through hydrogen bonding between the carboxylic acid group and amine disrupts the dimer structure and restores the fluorescence of 414-H arising from its AIE attribute (Figure 137A). Thus, 414-H can work as a fluorescence turn-on chemosensor for specific primary amine gas detection in the aggregate state (Figure 137B). Moreover, this light-up sensing of primary amines is fairly rapid and the fluorescence output is strong, rendering it observable by the naked eye. In addition, such a detection method also enjoys good reversibility and reproducibility (Figure 137B). The fluorescence of the amine-fumed 414-H film can be switched off by heating at 100 °C for 60 s. The dark and bright states can be interconverted to each other for many times without obvious fatigue and loss in the emission intensity, demonstrating its possibility for real-world application.

$\text{H}_2\text{S}$  has long been deemed as a toxic gas with rotten egg smell, however, it has recently been suggested as an important endogenous gasotransmitter existing in the biological systems

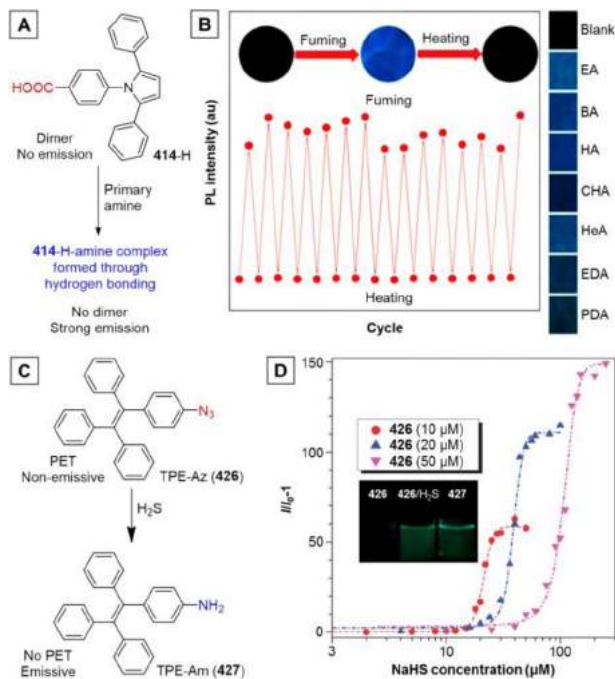


**Figure 137.** (A) Proposed mechanism for the detection of primary amine gases based on 414-H, whose emission can be turned on by means of disruption of dimer formation. (B) Reversible switching of the light emission of 414-H film between dark and bright states by repeated fuming and heating processes. Adapted with permission from ref 788. Copyright 2013 Royal Society of Chemistry. (C) Schematic illustration of detection of hydrogen sulfide by the azido-containing fluorophores 426. (D) Relative PL intensity of 426 versus the concentration of H<sub>2</sub>S in DMSO/HEPES buffer mixtures with the buffer fraction of 80 vol %. Insets: Fluorescent photographs of 426, 426 + H<sub>2</sub>S, and 427 in DMSO/HEPES buffer mixtures with the buffer fraction of 80 vol %. Reprinted with permission from ref 798. Copyright 2014 Royal Society of Chemistry.

including human body.<sup>789,790</sup> It is important in various physiological processes, including the regulation of cell growth,<sup>791</sup> the stimulation of angiogenesis,<sup>792</sup> cardiovascular protection,<sup>793</sup> the modulation of neuronal transmission,<sup>794</sup> the antioxidative and the anti-inflammation effect,<sup>795</sup> etc. The deregulation of H<sub>2</sub>S is relevant to the symptoms of Alzheimer's disease, diabetes, etc.<sup>796,797</sup> In view of the significance of H<sub>2</sub>S, our group has developed an accurate and reliable approach for H<sub>2</sub>S sensing and direct indication of its concentration, by taking advantage of AIE and the chemical reactivity of azido group to H<sub>2</sub>S.<sup>798</sup> An azido-functionalized TPE derivative TPE-Az (426) was nonluminescent in both solution and aggregate states, indicative of the quenching effect (PET) caused by the azido group (Figure 137C). Upon incubation with NaHS, a commonly-used source of H<sub>2</sub>S, remarkably increased fluorescence has been observed from the DMSO/HEPES buffer mixture (2/8, v/v) containing 426 nanoaggregates. The turn-on fluorescence arose from the reduction of 426, which yielded the amino-substituted TPE derivative 427, thereby eliminating the PET effect and restoring the AIE of the TPE moiety (Figure 137C and insets in Figure 137D). The fluorescence intensity hence mirrored the concentration level of H<sub>2</sub>S. In addition to its short response time (2 min), 426 holds a detection threshold due to the AIE effect and hence can be able to indicate the concentration of H<sub>2</sub>S simply by light-up fluorescence when 427 formed aggregates. More importantly, the detection threshold can be fine-tuned in a broad range via

varying the 426 concentration (Figure 137D), making it possible to directly indicate the concentration of H<sub>2</sub>S in blood and unknown samples.

**5.2.4. Explosives.** There is a recent rise in concerns on global terror threats and anti-terrorism activities, making the sensitive detection of trace explosive materials and their precursors in security screening processes highly and urgently demanded. The development of reliable methods and processes for this purpose thus has antiterrorism and homeland-security implications. Among the large variety of analytical techniques, fluorescence-based sensing has drawn much attention from academic to industry, due to its high sensitivity, convenience, and low cost as well as on-site workability. In general, most of the conventional fluorescent chemosensors suffer from the unsatisfactory sensing performance owing to the ACQ effect. However, aggregation, no matter intrinsic autoaggregation or analyte-induced aggregation, is beneficial to the emission of AIEgens and the subsequent sensing behaviors. Regarding this, an enormous number of AIEgens or AIE systems varying from small AIEgens including organic luminogens and metal complexes, to AIE linear polymers and AIE/AEE-active hyperbranched polymers, then to organic/inorganic hybrids and MOFs with AIE elements have been exploited to develop highly-performed fluorescent chemosensors for explosives.<sup>38,278,279,286,288,306,308,309,314,343,351,733,762,780,799–822</sup> This subsection will be a showcase for the representative ones which we selected out in terms of their performance and/or special design.

With regard to explosive detection, there exist a large array of small AIEgens ranging from the derivatives of some archetypal AIEgens such as TPE and silole to newly developed AIEgens and even AIE-active metal complexes.<sup>343,351,733,762,780,799–804</sup> Though with the aid of the AIE effect, all of them work well as efficient explosive sensors with low detection limits and high quenching constants, rational and elaborate design is still necessary to the further improvement of their detection performance. For example, most of them show emission quenching response to almost all the explosive species without obvious selectivity; however, the determination of the chemical compositions of explosives is crucial to the tracking of their source and terrorist provenance. In view of this, Zheng's group has recently developed some TPE macrocycles which preserved the AIE attribute and have been found to show highly sensitive and selective detection ability to some specific explosive(s).<sup>800,801</sup> For example, the TPE Schiff-base macrocycle 428 (Figure 138A), which was synthesized through the formylation and subsequent condensation reaction of the 4,4'-(2,2-diphenylethene-1,1-diy)diphenol (TPE-2OH), self-aggregated into nanospheres and emitted intense yellow fluorescence in aqueous media.<sup>800</sup> Thanks to its AIE activity, 428 could selectively and sensitively respond to 2,4,6-trinitrophenol (TNP or PA) and 2,4-dinitrophenol (DNP) in a fluorescence turn-off fashion, among other nitroaromatic compounds. Even only in the presence of 1 nM (0.2  $\mu$ g L<sup>-1</sup>) DNP and 5 nM (1.1  $\mu$ g L<sup>-1</sup>) PA, the fluorescence of the nanoaggregates of 428 could display a dramatic decrease, suggestive of its high sensitivity. Furthermore, this sensing system showed a superamplified quenching effect with DNP but not with PA, offering a possible pathway to differentiate these two explosives. It has been found that the cavity of the macrocycle is critical for the selectivity of 428 to DNP over PA. Such a macrocyclic AIEgen-based detection system is also workable in its solid state and can be applied for real water samples.

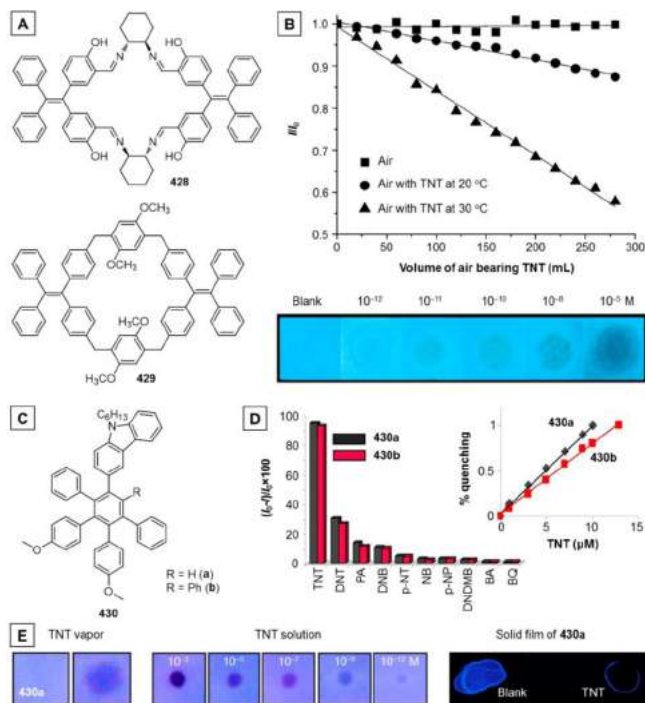


**Figure 138.** Representative AIE-active small molecules used for explosive detection. (A and C) Molecular structures of **428**, **429**, and **430**. (B) Change in  $I/I_0$  ratio of **429** in  $\text{H}_2\text{O}/\text{THF}$  mixture (95/5 in volume) with different volumes of air containing TNT vapor. [**429**] = 1  $\mu\text{M}$ . Inset: Fluorescent photos of the TNT test paper containing **429** before and after being spotted at different concentrations of TNT. Adapted with permission from ref 801. Copyright 2014 Royal Society of Chemistry. (D) Selectivity test of **430a** and **430b** toward TNT for 10 and 13  $\mu\text{M}$  analyte, respectively. The inset shows the Stern–Volmer plot of % quenching versus TNT concentration. (E) Paper strip test. (left) Vapor-mode detection of TNT before and after placing the test strips of **430a** over the glass vial containing TNT for 5 min. (middle) Application of small spots of different concentrations of TNT on test strips of **430a**. (right) Change in the fluorescence of **430a** in the solid state in the presence of TNT. Adapted from ref 802. Copyright 2012 American Chemical Society.

Afterwards, Zheng's group further designed a new macrocyclic AIEgen for the selective sensing of 2,4,6-trinitrotoluene (TNT).<sup>801</sup> TNT is one of the most widely used explosives in military activities, terrorist attacks, blasting engineering. To identify a single explosive is of vital importance but very challenging. For example, TNT and PA are very difficult to discriminate at diluted concentrations as they both bear three nitro groups. Pillararenes, a new class of macrocycles, have exhibited a highly selective recognition for electron-deficient guest molecules such as herbicide paraquat, because they are comprised of multiple electron-rich 1,4-benzenedioxy units. The aggregates of pillar[5]arenes can even absorb the strongly electron-deficient TNT but cannot detect TNT for the lack of signaling moiety. For this reason, Zheng et al. have established an elegant strategy to integrate the TPE with pillararene by conjugating the TPE cores with 1,4-benzenedioxy units. The afforded TPE pillar[6]arene **429** (Figure 138A) inherits the AIE feature from its TPE parent and meanwhile possesses the capability of exclusively recognizing TNT over a large number of nitroaromatic compounds due to its characteristics as pillararene. The suspension of **429** in THF/water mixture with a  $f_w$  of 95 vol % showed much higher quenching efficiency and by far faster quenching to TNT as compared to other nitroaromatics

including PA. Besides the fluorescence turn-off detection of TNT in aqueous media, the TNT vapor or TNT in air can also be detected both qualitatively and quantitatively owing to the linear correlation between fluorescence intensity and the volume of air containing TNT vapor (Figure 138B). Such a TNT-selective detection system also held a high sensitivity with the minimum concentration of TNT that could be detected by naked eye as low as  $1.0 \times 10^{-12} \text{ M}$  and a detection limit of about  $4.5 \text{ pg cm}^{-2}$ . The outstanding selectivity, sensitivity, as well as fast response should be ascribed to the synergistic effect contributed by the AIE character, electron-rich pillararene structure, and the cavity of macrocycle, which provided strong aggregate-state fluorescence, strong electron-donating ability for charge transfer and fluorescence quenching, as well as suitable accommodation and sufficient fluorophore–analyte interaction. Such kind of work is hence of instructive significance to more sophisticated design of fluorescent chemosensors for the selective and sensitive detection of explosives.

In addition to **429**, some other AIEgens bearing electron-rich groups can also show highly selective fluorescence quenching to TNT, as reported by Kumar and Bhalla et al.<sup>802</sup> The hetero-oligophenylen carbazole derivative **430a** and **430b** (Figure 138C) exhibited typical AEE behaviors and were used as fluorescent probes for explosive detection with excellent selectivity to TNT among other nitroaromatics such as 2,4-dinitrotoluene (DNT), 1,3-dinitrobenzene (DNB), and PA (Figure 138D). The aggregates of **430a** and **430b** in the mixture of THF/water (2/8, v/v) displayed detection limits of 30 nM and 40 nM, respectively, as well as linear Stern–Volmer plots giving quenching constants ( $K_{SV}$ ) of  $13.3 \times 10^5$  and  $10.0 \times 10^5 \text{ M}^{-1}$ , respectively (inset of Figure 138D). As revealed by the electrochemical analysis, the charge-transfer mechanism is mainly responsible for the selective fluorescence response of the **430a** and **430b** aggregates to TNT, and the electron-rich and donating carbazole unit also plays an important role in this regard. Disposable paper strips coated with aggregates of **430a** and **430b** could sense TNT at the picogram level ( $10^{-12} \text{ M}$ ; Figure 138E). Meanwhile, these AIEgens can detect TNT in the vapor, aqueous, and solid phases with a superb selectivity and high sensitivity, providing a superior chemosensor for TNT sensing (Figure 138E).

Apart from small AIEgens, there are a large quantity of polymeric AIEgens that have been reported to show good explosive detection ability.<sup>278,279,286,288,306,308,309,314,805–819</sup> We can hardly cover all of them in this review. To make the discussion as comprehensive as we can, we have carefully examined their performance and compared their molecular structures and finally sorted out some examples which may help us gain deeper insights into the molecular design of efficient explosive sensing systems based on AIEgens. The discussion will be initiated with linear AIE-active polymers (Figure 139).

Since TPE is an iconic AIEgen, it has become the most frequently used building block for the construction of functional AIE systems and polymers with AIE characteristics. For example, directly conjugating the TPE moieties together via Suzuki coupling afforded the fully-conjugated AIE polymer **221** (cf., section 4.3.1), which can sensitively detect explosive like PA with discernable fluorescence quenching even at a PA concentration of 1.0 ppm.<sup>278</sup> The fluorescence quenching is possibly attributed to the Lewis acid–base interaction (charge transfer) and the energy transfer between the TPE units and the nitroaromatics. Even **221** is already a good sensor for explosives, but there is still room for improvement. With extra spacers to separate the TPE units, the nonconjugated polytriazoles

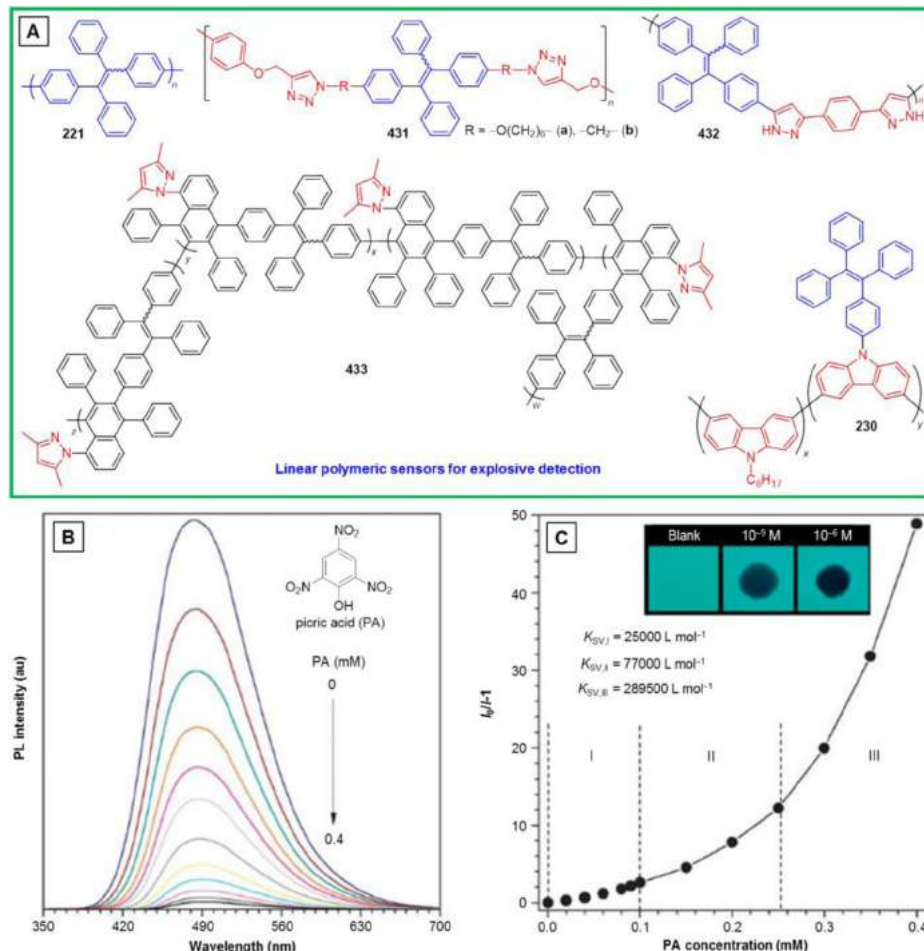


**Figure 139.** (A) Representative AIE-active linear polymers for explosive sensing. (B) PL spectra of 433 in THF/water mixtures with  $f_w = 99$  vol % containing different amounts of PA. (C) Stern–Volmer plot of  $(I_0/I - 1)$  values versus PA concentrations in 99 vol % aqueous mixtures of 433.  $I_0$  = peak intensity at  $[PA] = 0$  M. Insets: Chemical structure of PA and fluorescent photographs of 433 coated on TLC plates before and after spotting with aqueous PA solutions with different concentrations. Reprinted with permission from ref 807. Copyright 2013 Royal Society of Chemistry.

(431a and 431b; Figure 139A) could show observable fluorescence quenching to PA with a concentration of 0.1 ppm or  $0.1 \mu\text{g mL}^{-1}$ .<sup>805</sup> When the concentrations of PA were below 10 and 30 ppm, the aggregates of 431a and 431b exhibited linear Stern–Volmer plots with quenching constants of  $\sim 0.99 \times 10^5$  and  $1.10 \times 10^5 \text{ M}^{-1}$ , respectively. Both the 431a and 431b displayed higher sensitivity/quenching-efficiency than 221, implying that the conjugation degree might have some impact on the photophysical properties of the AIE polymers and the subsequent detection behavior. As they share the same fluorophore, namely, TPE, their charge-transfer ability from fluorophore to analyte should be almost equal. However, why do they show different detection performances? Through comparative study on the emission spectra of 221 and 431 in the aggregate state, it has been found that due to the more extended electronic conjugation, the emission of 221 (506 nm) is redder than those of 431 (480.5 nm), which results in a smaller overlap with the absorption of PA, indicating less efficient energy transfer between 221 and PA. In other words, the reinforced energy transfer helps the fluorescence quenching, which has been further proved by the research conducted with 432 and 433. The polymer 432 consisting of TPE and pyrazole units showed intense green fluorescence in the aggregate state and can work as a fluorescent explosive sensor with a superamplification effect.<sup>806</sup> It is worth mentioning that the sensitivity of this polymer ( $K_{SV}$  up

to  $1.09 \times 10^6 \text{ M}^{-1}$ ) was higher than that of its polymeric precursor (maximum  $K_{SV} = 2.33 \times 10^5 \text{ M}^{-1}$ ) which had no pyrazole moiety and exhibited weak yellow emission. The stronger light emission and larger overlapping between the emission spectrum of 432 and the absorption spectrum of PA might be responsible for its superior performance to PA than its precursor. The poly(pyrazolylnaphthalene) 433 was synthesized via a novel polymerization route, namely, rhodium-catalyzed oxidative polycoupling of phenylpyrazole and internal diynes. It has been utilized for explosive detection in view of its AIE feature (Figure 139B,C).<sup>807</sup> The fluorescence quenching of the nanoaggregates of 433 was clearly observable even at a low PA concentration of  $10 \mu\text{M}$ . With the addition of PA, the fluorescence kept decreasing until being completely quenched at a PA concentration of  $0.4 \text{ mM}$  (Figure 139B). Its Stern–Volmer plot of  $I_0/I - 1$  versus the PA concentration displayed an upward-bending curve with a  $K_{SV,III}$  of  $2.89 \times 10^5 \text{ M}^{-1}$ , suggestive of a superamplification effect (Figure 139C). Detecting PA on the TLC plates loading 433 lowered the detection limit to  $10^{-9} \text{ M}$  (inset of Figure 139C), indicating that strong emission and the AIE feature of 433 definitely benefited the turn-off detection processes. The broad emission band peaked at 490 nm rendered an appreciable overlap with the absorption of PA, which aided the energy transfer process. The energy transfer and the charge

transfer are supposed to work collaboratively to result in the fluorescence quenching.

Unlike the cases in the above discussed four polymers, the TPE units in polymer **230** are at the pendants instead of in the polymer backbone (Figure 139A). However, such a TPE-substituted polycarbazole still possessed AIE property, rendering them highly fluorescent with bluish-green emission peaked at  $\sim 495$  nm in the aggregate state.<sup>288</sup> 1,3,5-Trinitrobenzene (TNB) was chosen as a model nitroaromatic analyte to test the explosive detection ability of **230**. The onset of fluorescence quenching was found at 50 nM of TNB and the fluorescence of the nanoaggregates of **230** was fully quenched by TNB with a concentration of 58  $\mu$ M. For TNB below 21  $\mu$ M, a linear Stern–Volmer plot was shown with a  $K_{SV}$  of  $2.14 \times 10^5$  M $^{-1}$ , while the  $K_{SV}$  reached  $\sim 1.26 \times 10^6$  M $^{-1}$  in the TNB concentration range of 43–58  $\mu$ M with a Stern–Volmer curve bending upward, exhibiting an amplified quenching. Such an amplified quenching effect was ascribed to the twisted 3D topology of the polymer chains in the nanoaggregates, which resulted in the formation of an increased number of quenching sites for the interaction with TNB molecules and/or promoted excitation diffusions to quenching sites. As there is no spectral overlap between the emission spectrum of **230** and the absorption spectrum of TNB, the main quenching mechanism for TNB detection should be ascribed to the excited-state charge-transfer from the electron-rich TPE-substituted polycarbazole to the electron-deficient TNB, which has been confirmed by the cyclic voltammetry. Additionally, the vapor-mode detection of TNB can also be achieved by this polymeric AIEgen.

In addition to the AIE-active linear polymers with TPE units in the backbones or as pendants on the side chains, linear polymers capped with TPE moieties can also be employed as explosive sensors. With judicious design, crystalline polymer terminated with TPE units was customized to sensitively detect explosives by our group (Figure 140).<sup>809</sup> Poly( $\epsilon$ -caprolactone) capped with TPE, i.e., TPE-PCL (**434**; Figure 140A) was produced by

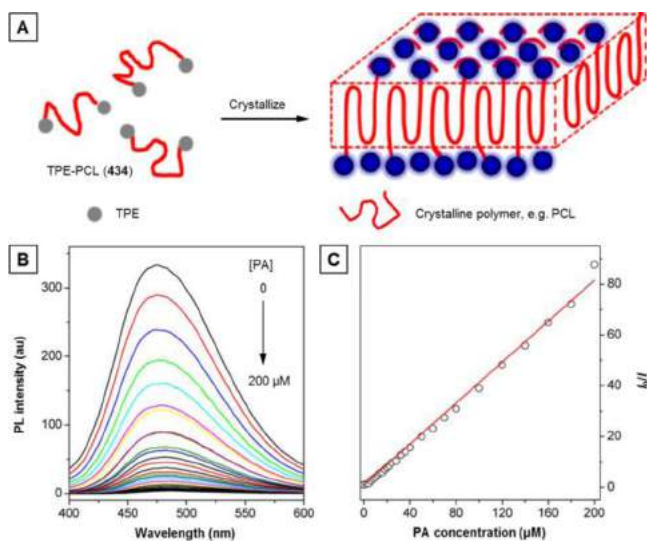


**Figure 140.** (A) Schematic illustration of crystallization-induced nanosheets of AIEgen-labeled polymer, TPE-PCL (**434**). (B) PL spectra of TPE-PCL nanosheets suspension containing various amount of PA and (C) plots of  $I_0/I$  values versus PA concentrations in TPE-PCL suspension. The static quenching constant ( $K$ ) was  $380\,000$  L mol $^{-1}$  for TPE-PCL nanosheets. Adapted from ref 809. Copyright 2014 American Chemical Society.

condensation reactions between monocarboxylic acid-substituted TPE and PCL. **434** exhibited the typical AIE behavior with an intensive aggregate-state emission. Fluorescent organic hybrid nanosheets of **434** were generated by the crystallization of PCL. The TPE moieties were found to be expelled out of the lamellar crystals of **434** and finally located on the surface of the TPE-PCL nanosheets (Figure 140A). In the light of this, the strong fluorescence of nanosheets suspended in aqueous media was used to sense explosives, which was gradually quenched by the addition of PA (Figure 140B). The value of  $I_0/I$  displayed a linear dependency on the PA concentration in the range of 0–200  $\mu$ M (Figure 140C), giving a static quenching constant up to  $3.80 \times 10^5$  M $^{-1}$ , which was much larger than that of the bare TPE ( $4.87 \times 10^4$  M $^{-1}$ ). The large quenching constant is presumably associated with the novel structure of nanosheets where the fluorescent TPE units are resided on the surface. Interestingly, the nanosheets in the presence of PA gave the largest  $I_0/I$  value among the ones with PA analogues, indicative of the selectivity of these TPE-modified nanosheets towards PA. Such a detection system is simple, cost-effective, sensitive, and selective, hence providing a new avenue to more AIEgen-based nanosensors with potential applications in the areas including explosive detection.

Hyperbranched polymers possess 3D topological structures with abundant internal voids or cavities for the capturing of analyte species. They also have multidimensional pathways for excitation migration, which may give rise to superior signal-amplifying effect and binding ability to analytes through energy transfer and/or charge transfer. In view of these superiorities, a large group of hyperbranched polymers with AIE/AEE characteristics have been employed for explosive detection.<sup>306,308,309,314,815–819</sup> For example, hyperbranched polyTPE (**435**; Figure 141A) was created by homopolycyclotrimerization of an  $A_4$ -type tetrayne.<sup>815</sup> This fully-conjugated hyperbranched polymer is AEE-active showing an intense green fluorescence with an emission maximum at  $\sim 510$  nm in the aggregate state. The nanoaggregates of **435** in THF/water mixtures with 70 vol % and 90 vol % water fractions were used as probing systems for the PA assay, and the detection of PA with **435** molecules dispersed in pure THF solution was also performed for comparison. As illustrated in Figure 141B, the nanoaggregates displayed much higher sensitivity to PA than their isolated species in THF solution, with a large  $K_{SV,III}$  up to  $7.58 \times 10^5$  M $^{-1}$  which is much higher than that of **435** solution ( $K_{SV,III} = 1.86 \times 10^5$  M $^{-1}$ ). This is due to the existence of numerous intermolecular voids afforded by the loose packing of the globular sphere of **435** containing bulky and twisted TPE moieties, which makes the nanoaggregates able to interact with more PA molecules and leads to more efficient quenching. Furthermore, superamplification effect can be clearly seen from the upward-bending Stern–Volmer plot of  $I_0/I$  versus PA concentration (Figure 141B). Such amplification effect is related to the AEE feature and hyperbranched structure of the polymer. In addition, when more PA molecules are diffused into the internal voids, the polymer swells, imparting larger surface area which can potentially interact with more PA molecules. On the other hand, the interior phenyl rings have relatively larger freedom to rotate, which helps to quench the light emission. These two effects give rise to higher sensitivity at a high quencher concentration.

The hyperbranched polytriazoles with spring-like architectures **244a** and **244b** (Figure 141C) are AIE-active and have been exploited as chemosensors for explosive detection by our group (Figure 141D).<sup>309</sup> Using **244a** as an example for demonstration, its aggregates suspended in the solvents mixture with 90 vol %

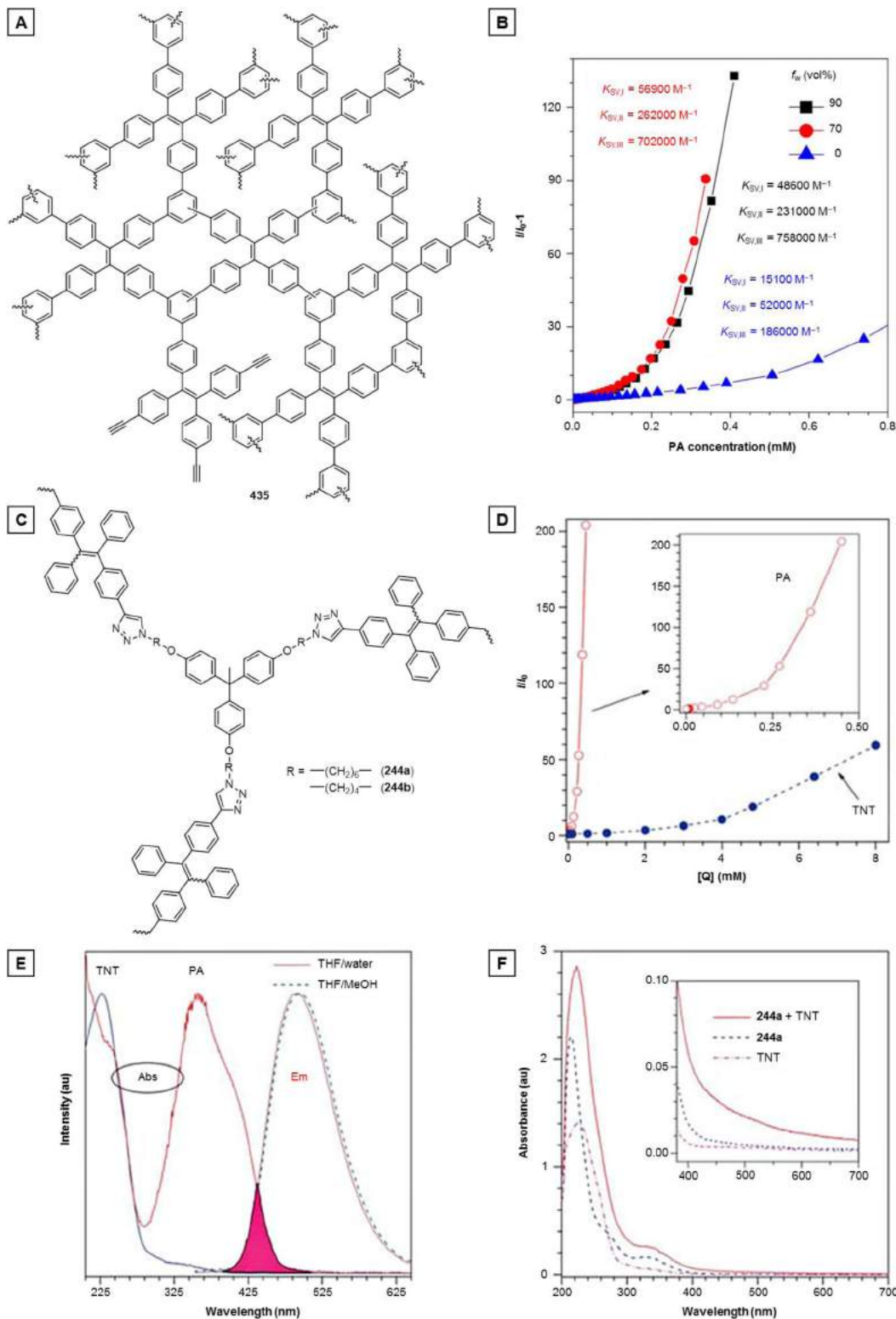


**Figure 141.** Representative hyperbranched polymers with AIE feature used for superamplified explosive detection. (A and C) Molecular structures of 435 and 244. (B) Stern–Volmer plots of  $(I_0/I) - 1$  values versus the PA concentrations in THF solution and THF/water mixtures with 70 and 90 vol % water contents of 435. Reprinted with permission from ref 815. Copyright 2013 Wiley Periodicals, Inc. (D) Stern–Volmer plots of  $I_0/I$  versus [PA] in THF/water with  $f_w = 90$  vol % and [TNT] in THF/methanol with  $f_m = 90$  vol %. Inset: Enlarged plot of  $I_0/I$  versus [PA]. [Q] represents the concentration of PA and TNT. (E) Normalized absorption spectra of TNT and PA, as well as the PL spectrum of 244a in THF/methanol ( $f_m = 90$  vol %) and THF/water ( $f_w = 90$  vol %). (F) Absorption spectra of TNT, 244a, and their mixture in THF/methanol ( $f_m = 90$  vol %). Inset: enlarged UV spectra of TNT, 244a, and their mixture in the range of 380–700 nm. Adapted with permission from ref 309. Copyright 2011 Royal Society of Chemistry.

water contents were used as probes for the detection of PA and TNT. The fluorescence was progressively attenuated with the sequential addition of the explosives (Figure 141D). When the concentration of PA and TNT were, respectively, below 0.09 and 1.0 mM, the Stern–Volmer plots of **244a** were exhibited as linear lines with quenching constants of  $56\ 848\ M^{-1}$  and  $704\ M^{-1}$ , respectively. The superamplified quenching effect of **244a** aggregates to PA and TNT has also been revealed by the Stern–Volmer plots which bent upward at high quencher concentrations. It was noticed that the fluorescence quenching of **244a** aggregates was more sensitive to PA than TNT. By studying the UV spectra of TNT and PA as well as the emission spectrum of **244a** (Figure 141E), obvious spectral overlap between the absorption of PA and the emission of **244a** in the range of 390 to 500 nm suggests that efficient energy transfer from the excited state of **244a** to the ground state of PA is involved in the quenching process of PA detection. In contrast, there is no discernible spectral overlap between the absorption of TNT and the emission of **244a**, indicating that the energy transfer plays a negligible role in the fluorescence quenching. Further examining the UV spectra of TNT, **244a**, and the mixture of TNT and **244a**, a tail in the absorption of the mixture of TNT and **244a** was observed (Figure 141F). It implied the existence of their interactions that may facilitate the charge transfer between **244a** and TNT. Results obtained from cyclic voltammetry measurement has further substantiated that such charge transfer indeed can take place during the detection process due to the matched energy levels between the LUMO of **244a** and the HOMO of TNT. Therefore, in this case, charge transfer mainly accounted for the quenching mechanism for TNT; while for PA, maybe both the energy transfer and charge transfer contributed. Moreover, the energy transfer is a long-range process whereas the charge transfer is a short-range one. In the polymer aggregates, TNT molecules can only quench the fluorescence of the luminophores that have close contacts with them via charge transfer; in contrast, PA molecules can interact with the fluorophores surrounding them. That's why the **244a** aggregates showed more sensitive response to PA than TNT. Such a comparative study undoubtedly provides an in-depth understanding on the detection mechanism of AIEgens to different kinds of explosives. On the basis of this work, more elaborate designs on the efficient chemosensors for explosive detection can be derived. More importantly, AIE-based selective chemosensors for a specific explosive can also be developed. Moreover, fluorescent inorganic–organic hybrid polymer, namely, the cross-linked poly(tetraphenylethylene-*co*-cyclotriphosphazene) (TPE-CP or **248**) has also been reported to show more sensitive fluorescence quenching to PA over TNT for the same reason discussed above, providing a solid proof to the conclusion drawn from the work done with **244a**.<sup>314</sup>

Besides suspending AIE aggregates in mixed solvents and coating the AIEgens on the filter paper or TLC plates, doping or hybridizing the AIEgens into some special solid substrates can also generate highly fluorescent sensing systems for explosive detection (Figure 142).<sup>820–822</sup> For example, Fang et al. have fabricated a composite film by doping the aggregates of HPS into a chitosan film via physical process, which is very stable and highly emissive due to the AIE feature of HPS.<sup>820</sup> The fluorescence of such composite film can be sensitively and selectively quenched by PA with a detection limit as low as  $\sim 2.1 \times 10^{-8}\ M$ . This high sensitivity was owing to the combination of the surface enrichment effect of chitosan films to the quencher and the AIE effect of HPS. Other nitroaromatics such as TNT, DNT, and

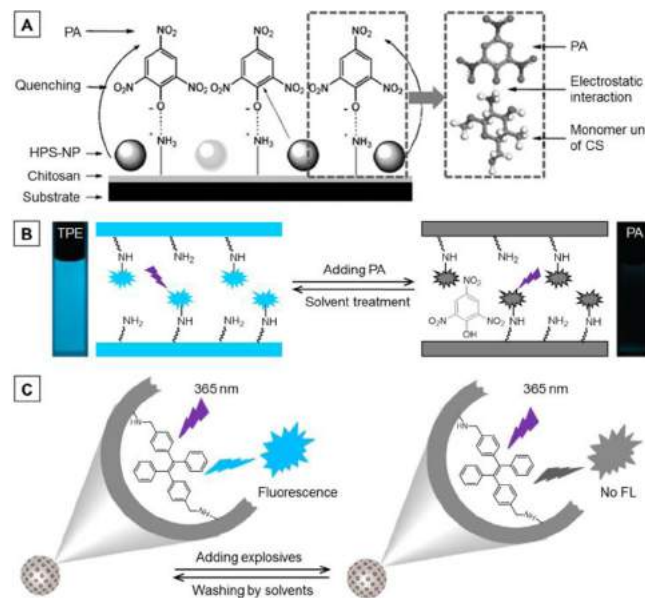


**Figure 142.** (A) Schematic representation of the selective sensing of PA by a HPS-chitosan composite film via combination of the surface enrichment effect of chitosan films and the AIE effect of HPS, and the simulation result of the electrostatic interaction between PA and the monomer unit of CS. Adapted with permission from ref 820. Copyright 2009 Royal Society of Chemistry. (B and C) Reversible fluorescence quenching mechanism of AIEgen-functionalized mesoporous materials (e.g., silica rods or silica nanoparticles) with PA based on photoinduced electron (charge) transfer and/or energy transfer. Panel B is reprinted with permission from ref 821. Copyright 2012 Royal Society of Chemistry. Panel C is reprinted with permission from ref 822. Copyright 2014 Elsevier Inc.

nitrobenzene (NB), organic solvents such as phenol, benzene, toluene, methanol, and ethanol, or nitrates like zinc nitrate, exerted little effect on the fluorescence of the film. The selectivity of the film to PA was ascribed to the specific electrostatic attraction effect of the protonated chitosan film to picrate anion and the screening effect of the film to the interferents (Figure 142A). The fluorescence quenching of this composite film caused by PA is static in nature as revealed by the fluorescence lifetime measurements. Moreover, this simple fluorescent chemosensor based on composite film is fully reusable, which improves the applicability of AIE-based explosive sensors.

The high pore volume and large surface area bestow the unique capability of rapidly associating analytes inside the pores via physical diffusion and/or chemical interactions on the ordered mesoporous materials. In this regard, it can be envisaged that the AIEgen-functionalized mesoporous materials can serve as fluorescent chemo/biosensors with remarkable performance. From the structural point of view, the pore sizes of mesoporous materials typically lie in the working distances of the photo-induced electron (charge) transfer and/or energy transfer, allowing the analytes in the pores to efficiently interact with the AIEgens in/on the pore wall, resulting in a significantly enhanced sensing performance. Regarding this, there have been two explosive sensors based on mesoporous AIE systems developed by Yu and Tang et al. (Figure 142B,C).<sup>821,822</sup> Amine-decorated mesoporous silica SBA-15 was reacted with different amounts of 1,2-bis[4-(bromomethyl)phenyl]-1,2-diphenylethane, which yielded the TPE-functionalized mesoporous SBA-15 which combined the advantages of the unique properties of AIEgen and mesoporous materials. PA was used as

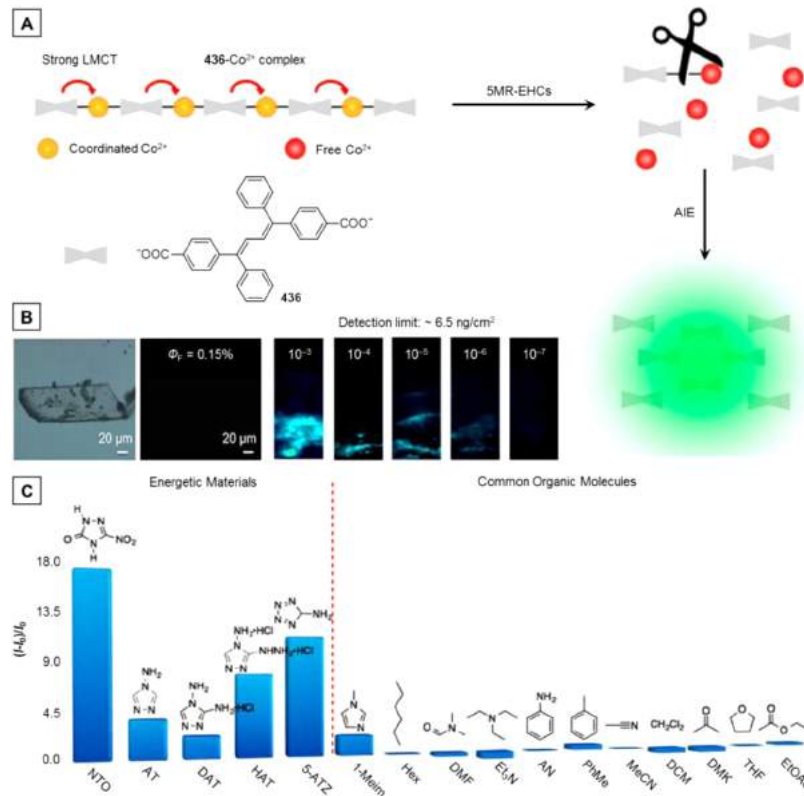


**Figure 143.** (A) Schematic representation of the mechanism of the detection of energetic heterocyclic compounds by the 436-Co<sup>2+</sup>-MOF. LMCT: ligand-to-metal charge transfer. (B) Bright-field and fluorescent images of 436-Co<sup>2+</sup>-MOF, and fluorescent photographs of 436-Co<sup>2+</sup>-MOF-deposited paper strips upon addition of THF solution of 5-nitro-2,4-dihydro-3H-1,2,4-triazole-3-one (NTO) at different concentrations. (C) Fluorescence enhancement efficiencies  $[(I - I_0)/I_0]$  obtained from different analytes by 436-Co<sup>2+</sup>-MOF. Adapted from ref 38. Copyright 2014 American Chemical Society.

a model to conduct the explosive detection with the chemically bonded TPE-SBA-15 hybrid as a probe (Figure 142B). The fluorescence quenching can be clearly distinguished at a low PA concentration of  $1.7 \mu\text{M}$  or 0.4 ppm. A quenching constant up to  $2.5 \times 10^5 \text{ M}^{-1}$  in the low concentration range of PA has been achieved, which was much higher than that of TPE itself in the THF/water mixture (1/9, v/v) of  $3.4 \times 10^4 \text{ M}^{-1}$ . The quenching mechanism can be ascribed to the energy transfer and/or charge transfer. When PA was added into the solution of the TPE-functionalized mesoporous SBA-15, the PA molecules can quickly diffuse into the pores and be adsorbed around the TPE units by the formation of PA-amine complexes through acid–base interaction, which facilitates the charge transfer process and thus promote the sensing efficiency. Meanwhile, there is an evident spectral overlap between the emission of the hybrid mesoporous SBA-15 and the absorption of PA in the range of 380–487 nm, permitting the energy transfer and thus further boosting the quenching efficiency. It hence can be seen that the high pore volume and large surface area of the mesoporous materials can ensure the efficient mass transport and strong interactions with the absorbed explosive molecules. Furthermore, such a fluorescent mesoporous sensing system can be facilely recycled and reused. To further improve the dispersibility of the AIEgen-functionalized mesoporous systems, MSNPs were used to serve as the matrix for the TPE units (Figure 142C).<sup>822</sup> The same TPE derivative was employed to modify the MSNPs, generating AIEgen-MSNPs which were further used as explosive sensors with high sensitivity. Similarly, this AIEgen-MSNPs system is also recyclable and environmentally friendly. These two

pieces of work represent a general strategy of constructing efficient and simple sensing systems for explosive with cost-effective and environment-friendly mesoporous materials and highly fluorescent AIEgens.

The above discussed sensors for explosives all work in a fluorescence turn-off manner; however, through smart design, fluorescence turn-on/light-up probes can be built up for some explosives. In particular, Wang and Feng et al. have taken full advantage of the AIE effect and the MOF structure to construct an AIEgen-linked MOF probe for turn-on detection of five-membered-ring energetic heterocyclic compounds (5MR-EHCs).<sup>38</sup> The design rationale and working principle of this novel AIEgen-based MOF sensor are schematically presented in Figure 143A. The AIEgen 436 was employed as an organic ligand which coordinated with the metal nodes, i.e. Co<sup>2+</sup>, to form the one-dimensional (1D) 436-Co<sup>2+</sup>-MOF. No emission was discerned from this MOF due to the strong ligand-to-metal charge transfer (LMCT) transitions which govern the intrinsic optical properties of the MOF and thus quench its fluorescence. 5MR-EHCs, i.e., triazoles, tetrazoles, azoxyfurazans, and their derivatives, salts and hybrid systems possess distinct molecular structures, substituents, and orbital energies, but they share one common feature that there are C=N and/or N=N bonds in the heterocyclic rings. Such a character allows the dissociation of coordination bonds between carboxylate groups and metal ions in MOFs via competitive coordination substitution. Thereby, once the 5MR-EHC is introduced to the detection system built with 436-Co<sup>2+</sup>-MOF where the MOF skeleton is constructed using AIE linkers with carboxylate groups, the AIE molecules will

be released and subsequently assemble into fluorescent aggregates as a result of RIM process. In this way, the SMR-EHC can be detected in a turn-on fashion. The **436**-Co<sup>2+</sup>-MOF exhibited a  $\Phi_F$  as low as 0.15%, providing a low background to afford a high signal-to-background ratio. As a heterocyclic high-energy-density material, 5-nitro-2,4-dihydro-3H-1,2,4-triazole-3-one (NTO) was first chosen as a target to evaluate the sensing ability of **436**-Co<sup>2+</sup>-MOF. The visual response of **436**-Co<sup>2+</sup>-MOF to NTO at different concentrations in spot testing is displayed in Figure 143B. The minimum naked-eye-readable detection amount of NTO was as low as 10  $\mu\text{L}$  of a  $1.0 \times 10^{-6}$  M THF solution of NTO, corresponding to a visible detection limit of about 6.5 ng cm<sup>-2</sup>. A rapid and quantitative detection of NTO in THF/hexane could be achieved by **436**-Co<sup>2+</sup>-MOF in the concentration range of  $4.0 \times 10^{-8}$  M to  $1.0 \times 10^{-3}$  M. In addition to its excellent sensitivity and response rapidity, the **436**-Co<sup>2+</sup>-MOF holds high applicability and selectivity to highly dangerous SMR-EHCs and their sources (Figure 143C). As revealed by the spot tests on paper strips and solution measurements with fluorescence spectroscopy, no obvious fluorescence changes were detected for common organic molecules and nitroaromatics, such as hexane (Hex), DMF, triethylamine (Et<sub>3</sub>N), aniline (AN), toluene (PhMe), acetonitrile (MeCN), DCM, acetone (DMK), THF, ethyl acetate (EtOAc), and TNT, etc. It suggested that the sensing results will not be affected by the amino, carbonyl, nitro, and hydroxyl groups, aromatic rings, aliphatic chains, as well as alkalescent conditions. Such an AIE-MOF approach enjoys advantages of high sensitivity, easy visualization, and universality, which may shed light on the design of new AIE-based turn-on probes.

In the present subsection, various AIE systems serving the purpose of explosive sensing have been expounded with special attention on their design, working principle, and detection performance. By virtue of the AIE effect, no matter the AIE system is small molecules, linear polymers, hyperbranched polymers, hybrids, or even MOFs, highly-efficient explosive detection can be realized. With elaborate design, some AIE-based sensing systems can selectively respond to a single explosive or a small group of explosives. Much work has been done to make the existing systems more suitable for practical use, such as, great effort has directed to the explosive sensing on paper strips or other solid substrates (e.g., chitosan film, mesoporous materials). However, what we have achieved has not played the AIE to its extremes. There is still large room for development and undoubtedly the objective of real-world application will be accomplished with continuous effort.

**5.2.5. Peroxides.** Hydrogen peroxide (H<sub>2</sub>O<sub>2</sub>) is the simplest peroxide and finds wide use as a strong oxidizer, bleaching agent, and disinfectant. It is also an important member of the ROS family. Despite its hazardness to organisms, H<sub>2</sub>O<sub>2</sub> is ubiquitous because it is a by-product of many metabolic reactions. It is thus linked to many physiological processes, such as oxidative damage, defense response, and cellular signal transduction. The homeostasis of H<sub>2</sub>O<sub>2</sub> and other ROS is associated with the aging of organisms and age-related diseases. Therefore, it is highly desirable to develop efficient and simple sensing systems to monitor H<sub>2</sub>O<sub>2</sub> concentration level in not only environment and industries but also biological systems. On the basis of AIE, an array of good fluorescent chemosensors for H<sub>2</sub>O<sub>2</sub> has been established.<sup>387,823,824</sup>

Li and Yu et al. have recently developed a selenium-containing fluorescent probe for turn-on detection of H<sub>2</sub>O<sub>2</sub> by making use of the reaction between selenium and H<sub>2</sub>O<sub>2</sub> and the AIE attribute of

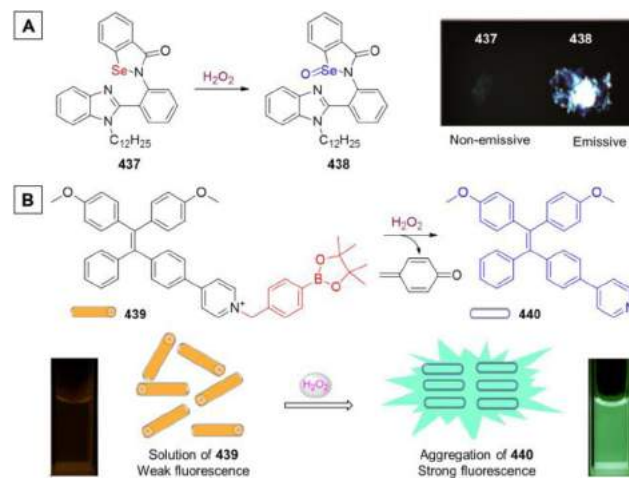


**Figure 144.** Representative examples of H<sub>2</sub>O<sub>2</sub> detection based on the AIE effect. (A) The reaction of the compound **437** and H<sub>2</sub>O<sub>2</sub>. Inset: Fluorescent images of solid state emission of compounds **437** and **438**. Reprinted with permission from ref 823. Copyright 2014 Royal Society of Chemistry. (B) The chemical structure of **439** and **440**, and the detection mechanism for the fluorescence turn-on detection of H<sub>2</sub>O<sub>2</sub>. Inset: Fluorescent photos of the solution of **439** (5.0  $\mu\text{M}$ ) (left) before and (right) after incubation with 150.0  $\mu\text{M}$  of H<sub>2</sub>O<sub>2</sub>. Reprinted with permission from ref 387. Copyright 2014 Elsevier Ltd.

the resultant (Figure 144A).<sup>823</sup> The aggregates of probe **437** exhibited very weak fluorescence with a  $\Phi_F$  of 0.3% in the mixture of DMSO/HEPES buffer (1/99, v/v) due to the PET process. After being treated with 20 equiv of H<sub>2</sub>O<sub>2</sub>, strong fluorescence was observed from the mixture, with a  $\Phi_F$  of 9.6% which was over 30-fold higher than that of **437**. The fluorescence turn-on was attributed to the inhibition of PET process via the selenium oxidation and the AIE effect of the oxidized product **438**. The undetectable solid-state emission of **437** and strong fluorescence of pure **438** in solid state with a  $\Phi_F$  of ~11.4% as shown in Figure 144A have provided a direct evidence to the detection mechanism. The probe showed a high selectivity toward H<sub>2</sub>O<sub>2</sub> over other ROS.

Beside the selenium oxidation, other reactions such as the cleavage of boronate group were also utilized for the specific detection of H<sub>2</sub>O<sub>2</sub>. For example, Zhang et al. have reported a TPE-based fluorescence light-up probe for H<sub>2</sub>O<sub>2</sub> (Figure 144B).<sup>387</sup> The probe **439** is composed of a TPE moiety and a *N*-4-(benzyl boronic pinacol ester) pyridinium bromide moiety. As illustrated in Figure 144B, the pyridinium unit conferred the water-solubility on the probe and rendered it weakly emissive in aqueous solution. After being incubated with H<sub>2</sub>O<sub>2</sub>, the aqueous mixture containing **439** became brightly emissive, indicating the turn-on detection of H<sub>2</sub>O<sub>2</sub>. The addition of H<sub>2</sub>O<sub>2</sub> induced the oxidation of the phenylboronic pinacol ester, which was followed by the hydrolysis and 1,6-elimination of *p*-quinone-methide, yielding the *p*-pyridine-substituted TPE (**440**). The resultant **440** was electroneutral and hydrophobic and thereby prone to aggregate in the aqueous media to switch on the emission as a result of the activated RIM process. The fluorescence enhancement ( $I/I_0 - 1$ ) at 510 nm displayed a linear relationship with the concentration of H<sub>2</sub>O<sub>2</sub> in the range of 10.0–110.0  $\mu\text{M}$ . A detection limit of H<sub>2</sub>O<sub>2</sub> estimated to be 180 nM and a high selectivity toward H<sub>2</sub>O<sub>2</sub> were achieved. In the light of the fact that D-glucose can be oxidized with the aid of glucose oxidase generating H<sub>2</sub>O<sub>2</sub>, the H<sub>2</sub>O<sub>2</sub>-specific probe **439** was also used for the detection of D-glucose with a detection limit of 3.0  $\mu\text{M}$  and good selectivity. Apart from the turn-on sensors, ratiometric

fluorescent sensing systems have been constructed as well.<sup>824</sup> By protecting the hydroxyl group of an AIE-active ESIPT compound with a H<sub>2</sub>O<sub>2</sub>-cleavable boronate-based benzyl group, the ESIPT process was blocked and only weak emission was observed owing to the active intramolecular motions. The H<sub>2</sub>O<sub>2</sub>-triggered boronate cleavage would liberate the ESIPT process. Meanwhile, the AIE was aroused by the restored intramolecular hydrogen-bonding which restricted the intramolecular motions of the fluorophore. In this way, a ratiometric response of the detection system was shown to H<sub>2</sub>O<sub>2</sub>. Although the H<sub>2</sub>O<sub>2</sub> sensing is of great importance, little work has been done in this field with AIEgens. In view of the successful works demonstrated here, there are numerous opportunities to achieve more exciting results, and what they call for is interest and enthusiasm.

**5.2.6. Hazardous Species.** Apart from heavy metal ions, toxic anions, as well as explosives, there are quite a few other threats or hazardous species existing in our daily life, such as melamine, gamma-ray radiation, etc. AIE as a powerful tool has been utilized for the detection of such species.<sup>825,826</sup> For instance, Sanji and Tanaka et al. have designed a melamine-specific fluorescence turn-on probe by decorating the AIE-active TPE moiety with cyanuric acid groups (**441**; Figure 145).<sup>825</sup>

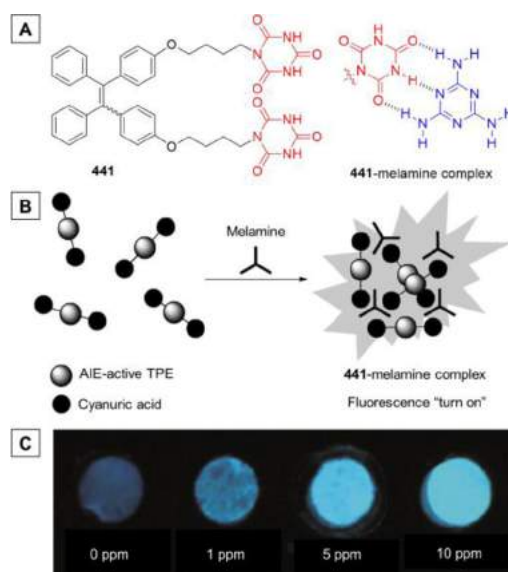


**Figure 145.** (A) Chemical structure of cyanuric acid decorated **441** and melamine–cyanuric acid adduct formed through multivalent hydrogen bonds. (B) Schematic representation of a “turn-on” fluorescent sensing of melamine by using cyanuric acid modified TPE based on the AIE effect. (C) Fluorescent images of test papers for the detection of melamine in infant powdered milk. Adapted with permission from ref 825. Copyright 2012 Wiley-VCH Verlag GmbH & Co. KGaA.

Melamine has many industrial utilities but was found as a contaminant in pet food, milk products, as well as infant formula. In these incidents, melamine was illegally added into the foods in order to increase the apparent protein content for its high percent mass of nitrogen (66.6%), which would result in renal failure in infants and children as well as pets. The safe concentration level of melamine for foods and for powdered infant formula has been, respectively, set as 2.5 and 1.0 ppm, by the U.S. Food and Drug Administration (FDA). As there is a growing public concern on food safety, methods for melamine-selective detection in these products are in great demand. The currently available analytical approaches for melamine screening

and quantification require expensive and complicated equipment that are not easy to operate. The fluorescence-based assay for melamine developed by Sanji and Tanaka et al. is much simpler and suited to routine and on-site use dispensing with complicated instruments. The melamine holds a capability of forming a stable and tight adduct with cyanuric acid via multiplex hydrogen-bonding interactions (Figure 145A). As a consequence, after the addition of melamine to the non-luminescent solution of **441**, intense emission was detected both by fluorescence spectroscopy and the naked eye. At a concentration of melamine above 5.0 μM (0.6 ppm), the fluorescence began to appear and increased with the gradual addition of melamine. A linear increase of the fluorescence intensity has been recorded with the melamine concentration in the range of 5.0–20.0 μM, which facilitated the quantification of melamine in real samples. The working principle of this probe for melamine is lying in the aggregation triggered by the multiple hydrogen-bonding formed between melamine and cyanuric-functionalized **441**, which induced the emission of TPE units due to the activated RIR process (Figure 145B). **441** is highly specific to melamine without showing any fluorescence response to relevant analytes such as ammeline, ammelide, uracil, cytosine, and thymine. More importantly, **441** is also workable in powdered infant formula spiked with melamine, showing a turn-on response at melamine concentration above 1 ppm with naked-eye observable fluorescence (Figure 145C), indicating its potential for practical applications.

Gamma (γ)-ray radiation is one type of ionizing radiation existing in many areas including astrophysics research, nuclear power industry, as well as biological, medical, and sterilization applications. In the meantime, it has also been known as a very hazardous species to human health. For the sake of security, facile and convenient detection approaches for gamma-ray radiation is of importance and highly demanded. Zhang et al. smartly took advantage of the AIE characteristics of silole and the degradation of polymers with sulfone (−SO<sub>2</sub>−) groups in the main chain caused by gamma-ray radiation to fabricate a handy and efficient sensing system for gamma-ray radiation (Figure 146).<sup>826</sup> Cationic silole derivative **339** is water-miscible and almost non-luminescent in aqueous solution due to the dynamic intramolecular motions which non-radiatively exhaust the excited-state energy. Upon addition of the negatively charged polyelectrolyte containing −SO<sub>2</sub>− groups in the main chain and −COONa groups in the side chain, brilliant fluorescence was emitted from the mixture. Such a fluorescence enhancement was attributed to the aggregates formation resulting from the electrostatic and hydrophobic interactions (Figure 146A). This intensively fluorescent ensemble of **339** and the polyelectrolyte was supposed to be used as a probe for the detection of gamma-ray radiation. However, technically, since silole can also be degraded by the gamma-ray radiation, the aforesaid mixture was not directly exposed to gamma-ray radiation. Instead, the aqueous solution of polyelectrolyte was subjected to the irradiation of different doses of gamma-ray radiation prior to the mixing with silole **339**. The fluorescence from the ensemble of **339** and the irradiated polyelectrolyte gradually decreased with the increase in the dose of gamma-ray (Figure 146B). Such a fluorescence decrease can be observed with naked eyes as depicted in the inset of Figure 146B. The detection mechanism can be interpreted as follows: the gamma-ray radiation degraded the polyelectrolyte into small fragments by cleaving the C–S bonds, and as a consequence, the interaction between the polymer residues and silole **339** became weak and the coaggregation

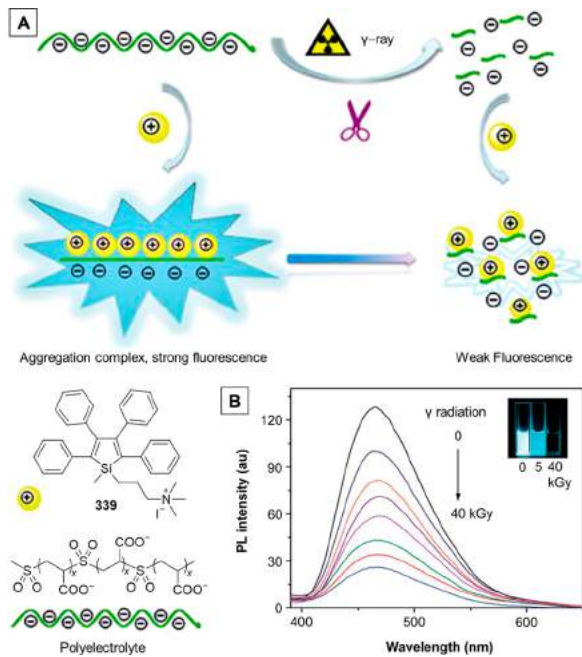


**Figure 146.** (A) Illustration of the working principle of 339 for the fluorescence detection of gamma-ray radiation. (B) Fluorescence response of the aqueous solution of 339 ( $10 \mu\text{M}$ ) and the polyelectrolyte ( $15 \text{ mg L}^{-1}$ ) before and after exposure to different doses of gamma-ray radiation. Insets: the corresponding fluorescent images. Adapted with permission from ref 826. Copyright 2011 Royal Society of Chemistry.

tendency was also reduced, resulting in the decrease in fluorescence as compared to the complex of 339 and intact polymer. The present work can be performed under ambient conditions and has a good sensitivity with a detection limit of  $0.13 \text{ kGy}$  dose of gamma-ray radiation. Further studies, however, are needed to optimize the chemical structures of AIE-based probe and the polymer with sulfone groups as well as the detection conditions which could enable the fluorescence detection of gamma-ray radiation to be performed *in situ* with higher sensitivity. In this small part, only two examples of hazardous species detection have been showcased. However, in principle, countless species can be sensed by virtue of AIE with appropriate designs.

**5.2.7. Fingerprints.** Latent fingerprints (LFPs) at the crime scene are very crucial clues in forensic investigations due to their uniqueness and stabilities. The uniqueness is identified by careful study of their ridge and groove characteristics, such as enclosure, island, bifurcation, and ridge ending.<sup>827</sup> However, LFPs are seldom clear enough to detect, and hence a combination or succession of different “development” treatments are often required to enable the visual contrast between the prints and their backgrounds in a forensic practice. At present, the widely used methods and techniques such as powder dusting have some drawbacks, including potential health hazard to the examiners and inevitable destruction of the fingerprints details.<sup>828</sup> Developing new methods to enhance the visualization of LFPs in a facile, rapid, efficient, and user-friendly manner is of considerable significance.

To this end, Su’s group has recently carried out a systematic work to explore the possibility of identifying and visualizing LFPs on the basis of AIEgens (Figure 147).<sup>39,829</sup> As shown in Figure 147A, AIEgens TPE, HPS, and 442 have been individually

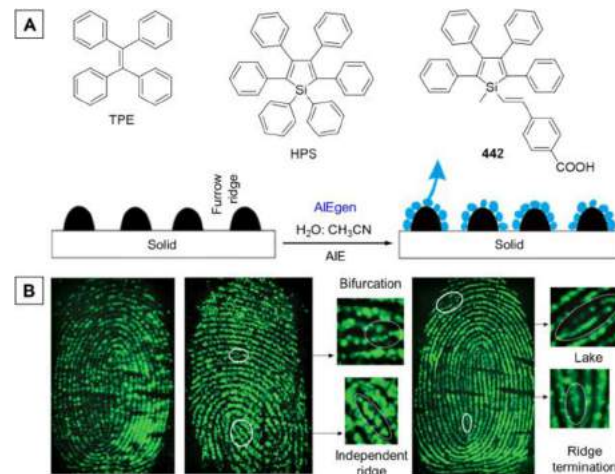


**Figure 147.** (A) Representative AIEgens which have been used for the recognition and visualization of latent fingerprints and the illustration of working principle. (B) False color fluorescence images of sebaceous fingerprints on microscopic glass, stainless steel sheet, and aluminum foil (from left to right) developed by the AIE of TPE aggregates. Reprinted with permission from ref 39. Copyright 2012 Royal Society of Chemistry.

employed as a fluorescent visualizing agent. A versatile procedure has been established for the AIEgen-based fingerprints developing processes. Sebaceous (sebum-rich) fingerprints were obtained by gently rubbing the fingertips of the volunteers over the forehead and nose and then stamping them directly onto different substrates with a minimal pressure. The substrates bearing the sebaceous prints were immersed into the acetonitrile (or ethanol)/water mixtures of AIEgens (i.e. TPE, HPS, or 442) with different water fractions and incubated under stirring for 5 min; rinsed with a copious amount of ultrapure water and dried under argon stream; then these substrates were positioned in the dark box of a ChemiScope 2850 fluorescence imaging system for observation. As these AIEgens are lipophilic, thereby their aggregates preferentially adhere to the fingerprint ridges via hydrophobic interactions (Figure 147A). Such a visualizing mechanism has been validated by the comparative study between HPS and 442.<sup>829</sup> The fingerprint ridges hence strongly fluoresced under UV illumination and the visual contrast was significantly enhanced by the AIE effect of TPE, HPS, or 442.

Take the fingerprints developed by TPE aggregates, for example. As displayed in Figure 147B, the fingerprint patterns in different substrates including glass slides, stainless steel sheets, and aluminum foils are clearly resolved with high contrast.<sup>39</sup> The papillary ridges were lighted up with intense fluorescence which was designated by false green color in Su’s work. The intervening region between the ridges, namely, furrow areas, remained dark, thus providing a sufficiently strong visual contrast for identifying the class of fingerprints. The characteristic details and the second level of information, such as bifurcation, short independent ridge, lake, and ridge termination are apparently discernable by the naked eye in the fluorescence images of fingerprints, which are useful in the identification of individuals. Similar results have also been obtained for the fingerprints developed by HPS and 442.

Such an AIE development process on wet nonporous surfaces possesses several superiorities. First of all, the overall procedure is fairly simple and time-efficient, which can be accomplished in a few minutes with a single-step incubation treatment. Secondly, it is user-friendly, as it is performed in solutions and no powder or

fume treatment is involved. Thirdly, this approach takes advantage of the efficient emission of AIEgens' aggregates, rendering it free from the self-quenching effect which is usually encountered by conventional luminophores. Last but not least, this method is highly applicable and universal, and various other AIEgens can serve the same purpose with this strategy. This advantageous AIE strategy can be further improved by utilizing other functional AIEgens and its application scope can also be further expanded. For example, this approach can be used for the detection of human secretions and metabolites in fingerprint residues for diagnostic purposes as well as tracing explosives with security implications.

**5.2.8. Chirality.** Chiral recognition, serving as the mechanistic basis for HPLC enantioseparation, drug development, asymmetric catalysis, and so on, is of high importance. Chiral recognition through changes in fluorescence has attracted enormous and extensive interest as it can offer sensitive and time-efficient enantiomer determination of chiral agents, natural products, catalysts, and drugs.<sup>830–832</sup> However, the design and synthesis of fluorescent chiral receptors remains challenging. Nevertheless, AIE has brought cheerful prospect in this respect. Zheng's group has conducted a series of studies on highly selective chiral recognition systems based on diverse AIEgens.<sup>833–838</sup> As summarized in Figure 148 and Figure 149, these novel fluorescent

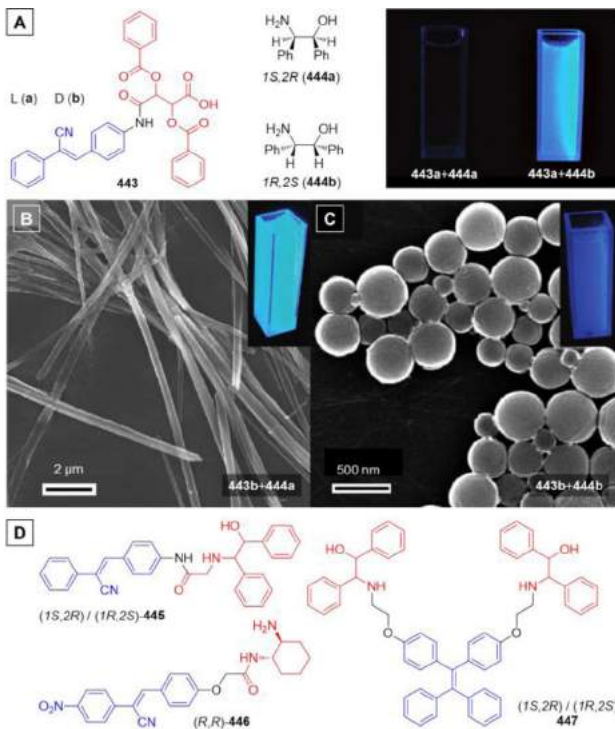


**Figure 148.** Representative AIEgens for the chiral recognition. (A) Molecular structure of chiral AIE compound 443 and chiral amines 444, and the fluorescent images of 443a interacted with different enantiomers of 444. Reprinted from ref 833. Copyright 2009 American Chemical Society. FM-SEM images and fluorescent photographs of (B) 443b + 444a and (C) 443b + 444b, respectively. Adapted from ref 834. Copyright 2011 American Chemical Society. (D) Molecular structures of chiral AIE compounds 445–447 which show similar chiral recognition abilities as 443.

chiral discrimination systems vary in AIE moieties and chiral recognizing groups as well as their combination modes (e.g., chemical bonding and physical admixing).

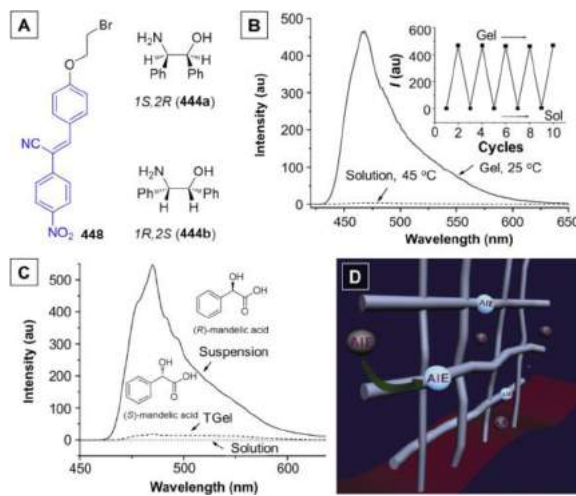


**Figure 149.** (A) Structure of AIE compound 448 and chiral amine 444a and 444b. (B) The fluorescence spectra of 448 added in gel and solution of a mixture of 444a and benzoic acid in 1,2-dichloroethane ( $[444a] = [acid] = 5[448] = 10 \mu\text{M}$ ). Inset: Fluorescence intensity of 448 with interconversion of gel at 25 °C and solution at 45 °C. (C) The fluorescence spectra of 448 in a mixture of enantiomers of mandelic acid and 444a. (D) Schematic illustration of the chiral recognition working principle. Reprinted with permission from ref 838. Copyright 2011 Royal Society of Chemistry.

Zheng and coworkers first prepared a pair of chiral compounds, namely, 443a (L) and 443b (D).<sup>833</sup> Each of them bears an AIE-active (*Z*)-2,3-diphenylacrylonitrile moiety and a chiral tartaric acid group (Figure 148A). 443a (L) and 443b (D) were found to exhibit typical AIE behaviors and luminesce only when they are aggregated, allowing them to discriminate different enantiomers of amines via fluorescence change. They exclusively aggregate with one enantiomer of various chiral amines so that one enantiomer resulted in strong fluorescence while the other one displayed no or weak emission. Use the differentiation of (1*S*,2*R*)-2-amino-1,2-diphenylethanol (444a) and its (1*R*,2*S*) enantiomer 444b as an example for illustration. The L-configuration of 443 (i.e., 443a) enantioselectively formed aggregates with 444b instead of its enantiomer 444a. Owing to the AIE feature, the aggregates of the 443a/444b complex were pretty emissive, whereas the non-aggregative solution of the 443a + 444a mixture was non-luminescent (Figure 148A). It is noteworthy that the fluorescence of the 443a/444b complex was boosted with increasing concentration of 443a and 444b (molar ratio 1:1). More valuably, when the concentration was below  $5.5 \times 10^{-4} \text{ M}$ , the fluorescence intensity showed a linear relationship with the concentration. Such a character enables the determination of the enantiomer concentration or chiral excess, which counts a great deal to the high-throughput analysis of enantiomer purity of chiral drugs and reagents.

Accordingly, the D-form of 443, i.e., 443b, also holds a capability of discerning 444a and 444b.<sup>833,834</sup> 443b enantioselectively self-assembled with an enantiomer of 444 to form either nanofibers (443b/444a; Figure 148B) or nanospheres (443b/444b; Figure 148C). The nanofibers possessed higher efficiency in fluorescence and longer wavelengths in both the absorption and emission in comparison with the nanospheres. This is probably due to the fact that nanofibers have stronger  $\pi$ - $\pi$  interactions which increased the conjugation and rigidified the molecular conformation to a larger extent resulting in stronger RIM and subsequent more intense and redder fluorescence.

Interestingly, adjusting the solvent composition from water/ethanol to water/THF would give rise to nanospheres with holes as a result of the dissolution of defects and a decreased bending energy.

Following the chiral recognition of amines with the chiral (*Z*)-2,3-diphenylacrylonitrile-tartaric acids (**443a** and **443b**), Zheng's group have further developed an AIE system for the enantiomer analysis of chiral carboxylic acids.<sup>835</sup> By decorating the AIE-active (*Z*)-2,3-diphenylacrylonitrile with an optically pure aminol group, a pair of chiral AIEgens, i.e., (1*S*,2*R*)/(1*R*,2*S*)-**445** were generated (Figure 148D).<sup>835</sup> The analysis of pure enantiomers of chiral carboxylic acids, which are a class of important biomolecules, chiral drugs, chiral reagents, etc., usually requires complicated chiral receptors or expensive instruments. Zheng et al. made use of the AIE-active (1*S*,2*R*)/(1*R*,2*S*)-**445** as receptors to realize the chiral recognition of 2,3-dibenzoyltartaric acid and mandelic acid in a simple and reliable manner. Likewise, the (1*S*,2*R*)- or (1*R*,2*S*)-form of **445** aggregated enantioselectively with one enantiomer of the acids and exhibited large difference in the fluorescence intensities of the two enantiomers. Moreover, such a chiral discriminative system could also be employed to the quantitative analysis of enantiomer content of chiral acids. Afterwards, the same research group further designed a chiral  $\alpha$ -aromatic cinnamyl nitrile derivative, namely, (*R*,*R*)-**446** (Figure 148D), exploiting AIEgen and chiral amine.<sup>836</sup> Such a chiral AIE system was found to show not only an exceptionally high enantioselectivity but also a wide applicability to a broad range of chiral carboxylic acids. With a fluorescence intensity ratio of two enantiomers ranging from 10 to  $1.6 \times 10^4$ , it can be utilized to determine the purity of the enantiomers. Definitely, apart from (*Z*)-2,3-diphenylacrylonitrile, other AIEgens such as TPE can also be used for the same purpose, as manifested by Zheng's group.<sup>837</sup> The TPE unit was embellished with two chiral aminol moieties, affording chiral TPE derivatives (1*S*,2*R*)/(1*R*,2*S*)-**447** (Figure 148D) which were further applied for the qualitative discrimination as well as quantitative determination of enantiomeric composition of chiral acids. Thanks to the AIE effect, (1*S*,2*R*)-**447** and (1*R*,2*S*)-**447** were able to display high enantioselectivity for a large number of chiral acids as well as a high sensitivity with a level of  $3.0 \times 10^{-6}$  M. Unsurprisingly, these chiral sensors could quantitatively determine the enantiomeric purity of chiral acids.

The chiral AIE systems discussed above were constructed by covalently bonding an AIE unit with one or two chiral groups. In other words, for each of these chiral recognition systems, a chiral receptor needs to be synthesized. To further simplify the chiral recognition on the basis of AIE strategy, a group of simple and easy-to-prepare achiral AIEgens with varying fluorescence intensities in gel, suspension, and precipitates were applied by Zheng and coworkers for the fluorescence switches and quantitative determination of enantiomer composition (Figure 149).<sup>838</sup> AIEgen **448** (Figure 149A), for example, was practically non-fluorescent in 1,2-dichloroethane. The commercially available chiral amines **444a** and **444b** can form organogels with a large variety of carboxylic acids in a wide range of organic liquids. For instance, heating the mixture of **444a** and benzoic acid to dissolve them (molar ratio 1:1) in 1,2-dichloroethane gave rise to a transparent gel after cooling. When 20 mol % of **448** was added, strong fluorescence was observed for the gel of **444a**/benzoic acid while no emission was detected for the corresponding solution. Since the gel and solution could be interconverted by repeatedly heating over 44 °C and cooling to room temperature, the fluorescence can be switched on and off for more than five cycles without any loss in the emission intensity (Figure 149B).

In the case of chiral carboxylic acids, **444a** and **444b** not only readily formed gels but also showed enantioselectivity towards enantiomers of the acids and thereby can be used as chiral recognition bases in this analytical protocol. Also take **444a** for example. When **444a** was mixed with (*S*)-mandelic acid in a 1:1 molar ratio, an optically transparent gel (TGel) was afforded, whereas the admixing of **444a** with (*R*)-mandelic acid only resulted in a suspension. The results obtained with **444b** as a base were opposite. After being added into the admixture of **444a** and enantiomer of the acid, **448** in the gel, suspension, and precipitates exhibited different emission intensities. As depicted in Figure 149C, **448** was emissive both in the TGel which was formed by the mixture of **444a**/*(S)*-mandelic acid and in the suspension of **444a**/*(R)*-mandelic acid, but the fluorescence intensity in the suspension was much higher than that in the TGel. The fluorescence ratio ( $I_R/I_S$ ) of **448** in the suspension ( $I_R$ ) and TGel ( $I_S$ ) arising from the two enantiomers of mandelic acids was up to 32. **448** in the solution produced by heating the TGel was nearly non-luminescent. Similar results were obtained for other carboxylic acids. The difference in the fluorescence intensity was ascribed to the different degrees of aggregation of **448** in the mixtures due to the involvement of specific steric effects (physical constraints) and chiral interactions (Figure 149D). By virtue of the **444a** and **444b**, enantiomeric compositions of various carboxylic acids were quantitatively determined. Other AIEgens such as TPE derivatives behaved in a similar manner to **448** for the chiral recognition with the help of a chiral species.<sup>838</sup>

In the present subsection, highly enantioselective chiral recognitions have been achieved with the combination of AIE and chirality through chemical bonding or physical interactions. These studies not only provided a simple and versatile strategy for the construction of chiral receptors but also offered a new methodology for the quantitative determination of enantiomer composition via monitoring the fluorescence change of AIEgens. Since the AIEgens themselves have so many varieties and so do the chiral species, infinite AIE-based chiral recognition systems can be built up.

**5.2.9. Viscosity.** Viscosity is a very important physical characteristic for fluids and fluidic materials or systems, and its level is closely associated with the chemical compositions of the fluids or fluidic media. The measurement of viscosity is not only of significance to scientific research but also has great implications for various industrial productions. Generally, viscosity is measured with various types of viscometers and rheometers. Although the techniques based on viscometers and rheometers are useful and reliable, the instruments are either expensive or difficult to operate, making the viscosity determination time-consuming or laborious. Fluorescence-based techniques for viscosity evaluation are attractive for their convenience, simplicity, sensitivity as well as on-site and real-time applicability. Fluorescent systems employed for viscosity evaluation are primarily built on fluorescent molecular rotors which are molecules containing at least two moieties that can rotate relative to one another and whose excited-state processes are dependent on the intramolecular torsional and/or rotational motions. As their intramolecular motions are impaired in viscous media, these species have been utilized as molecular-sized probes to report the viscosity level in a diversity of media, such as solvents, cyclodextrins, polymers, and biological media including plasma, phospholipid bilayers, as well as intracellular fluid. Despite that AIEgens have not yet been widely used as molecular rotor probes, they do meet the criteria. As described in the mechanism part (section 2.1), their fluorescence quantum efficiencies are highly dependent on the viscosity of the medium where they are placed.

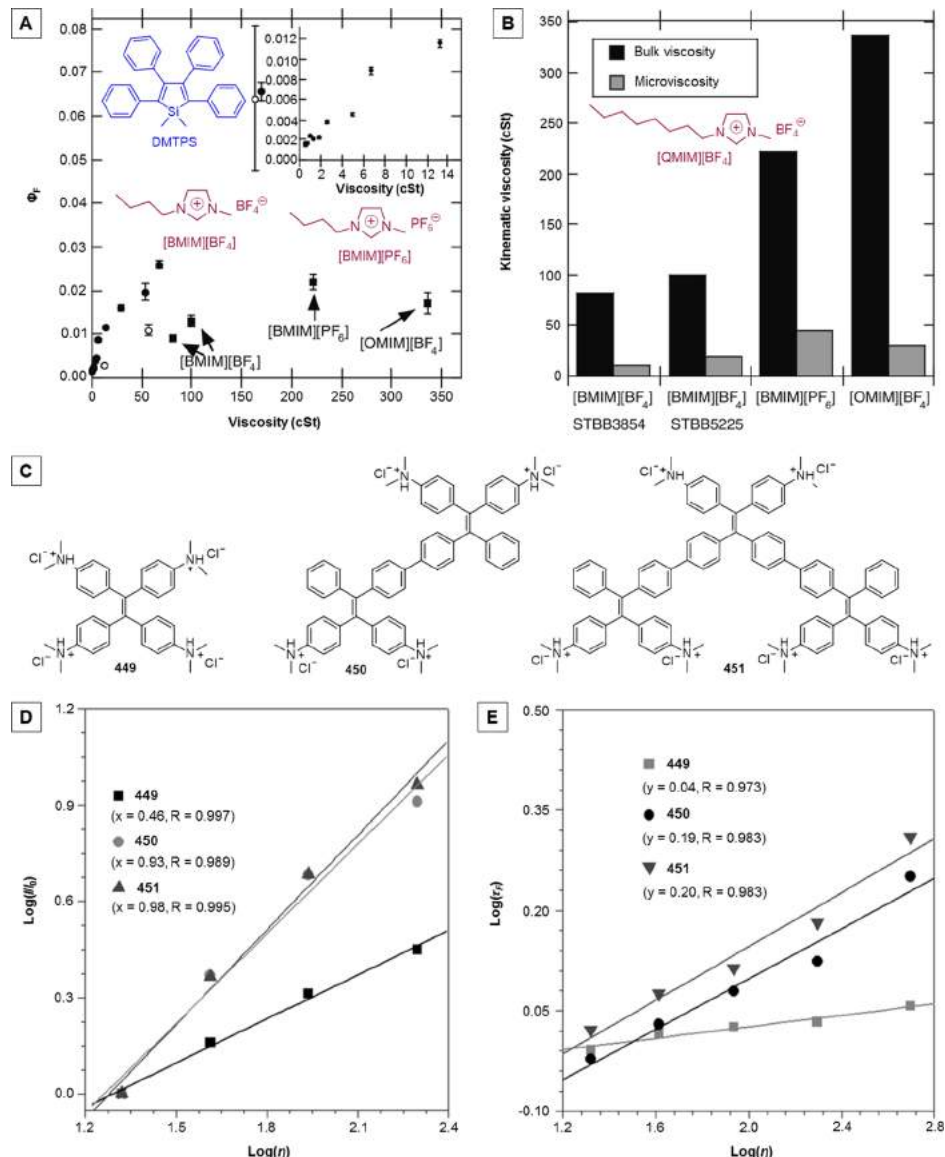


**Figure 150.** Representative examples of using AIEgens as viscosity probes. (A) Fluorescence quantum yield of DMTPS as a function of viscosity for the range of systems studied: nonpolar viscous media (hydrocarbons, filled circles), polar viscous media (glycerol/ethanol mixtures, open circles) and ionic liquids (IL, squares). Inset: Expansion of the data obtained for the nonpolar viscous media (100 vol % hexane to 10 vol % hexane/90 vol % light mineral oil) for clarity. (B) Bar chart illustrating the difference between the measured bulk kinematic viscosities of the four ILs studied and their corresponding microviscosities. Adapted with permission from ref 839. Copyright 2013 Springer Science+Business Media New York. (C) Molecular design for the TPE-based viscosity sensors. (D) Plots of  $\log I/I_0$  versus  $\log \eta$  of 449, 450, and 451. (E) Plots of  $\log \tau_f$  versus  $\log \eta$  of 449, 450, and 451. Reprinted with permission from ref 840. Copyright 2015 Wiley-VCH Verlag GmbH & Co. KGaA.

In this sense, AIEgens are intrinsically ideal probes for viscosity. Delightfully, such a potential of AIEgens has been primely corroborated by the examples highlighted in Figure 150.

Room temperature ionic liquids (ILs) have caught much attention for a broad range of applications. However, many details regarding their physicochemical properties including how their bulk properties differ from those on the microscopic scale remain unclear. The ultrahigh sensitivity to the polarity and viscosity of the systems in which they are dispersed as well as the marked AIE effect make AIEgens promising probes for the microenvironments present in ILs. 1,1-Dimethyl-2,3,4,5-tetraphenylsilole (DMTPS), for example, was employed as a molecular probe for the investigation on the microviscosities of three imidazolium ILs: butylmethylimidazolium tetrafluoroborate ([BMIM][BF<sub>4</sub>]), butylmethylimidazolium hexafluorophosphate ([BMIM][PF<sub>6</sub>]), and octylmethylimidazolium tetrafluoroborate ([QMIM][BF<sub>4</sub>]).<sup>839</sup> Since ILs are viscous and composed of ions, the  $\Phi_F$  values for DMTPS in these ILs were measured and compared with those recorded for the same probe in nonpolar (hexane/mineral oil) and polar viscous (glycerol/ethanol) solvent systems (Figure 150A). The microviscosities were calculated using the Förster–Hoffmann equation. In the viscous nonpolar media, the  $\Phi_F$  of DMTPS monotonically increased with the viscosity as revealed by the inset of Figure 150A. DMTPS in the viscous polar glycerol/ethanol mixtures exhibited overall lower  $\Phi_F$  values in comparison with the aforesaid hydrocarbon solvents with similar viscosity. Meanwhile, there was a greater propensity for DMTPS aggregation with increasing glycerol content. Collectively these results indicate that DMTPS is not homogeneously dissolved in these

phate ([BMIM][PF<sub>6</sub>]), and octylmethylimidazolium tetrafluoroborate ([QMIM][BF<sub>4</sub>] ).<sup>839</sup> Since ILs are viscous and composed of ions, the  $\Phi_F$  values for DMTPS in these ILs were measured and compared with those recorded for the same probe in nonpolar (hexane/mineral oil) and polar viscous (glycerol/ethanol) solvent systems (Figure 150A). The microviscosities were calculated using the Förster–Hoffmann equation. In the viscous nonpolar media, the  $\Phi_F$  of DMTPS monotonically increased with the viscosity as revealed by the inset of Figure 150A. DMTPS in the viscous polar glycerol/ethanol mixtures exhibited overall lower  $\Phi_F$  values in comparison with the aforesaid hydrocarbon solvents with similar viscosity. Meanwhile, there was a greater propensity for DMTPS aggregation with increasing glycerol content. Collectively these results indicate that DMTPS is not homogeneously dissolved in these

polar viscous systems and likely take up “domains” that are ethanol-rich. As a consequence, the measured (bulk) kinematic viscosity of these glycerol/ethanol mixtures did not represent the local viscosity experienced by the silole molecules. The bulk (measured) viscosity was higher than the local viscosity in the ethanol-rich regions where the silole is preferentially distributed. In ILs, the  $\Phi_F$  values of the DMTPS probe were higher than those in molecular solvents with low viscosities, e.g., dioxane, hexane, THF, ethanol, etc., but were apparently lower than those measured in nonpolar solvents having similar bulk viscosity (Figure 150A). Such an observation has revealed that the microviscosities experienced by the silole molecular rotor probe in the ILs were significantly smaller than the measured bulk viscosity of the ILs (Figure 150B). Furthermore, it seems that the AIE effect of DMTPS did not come into play in the ILs, suggesting that silole species may occupy some relatively nonpolar regions or “domains” within the IL matrixes where the silole molecules are well dispersed with sufficient free volume to rotate and non-radiatively dissipate the excited-state energy to a larger extent. In this way, by taking advantage of the correlation between the RIR and  $\Phi_F$  of silole, the potential application of AIEgens as molecular rotor-type probes has been demonstrated.

Recently, our group has carried out a systematic investigation on the molecular design of efficient probes for viscosity sensing.<sup>840</sup> Taking such factors as the number of rotors, motional freedom of rotors, electronic conjugation, molecular size, conformational crowdedness and so forth into consideration, a series of molecules with varying numbers of TPE units were covalently linked together to afford AIE rotors (449–451; Figure 150C). These TPE derivatives with multiple rotors have been employed as sensors for viscosity evaluation. In the glycol/glycerol mixtures with different glycerol fractions, the fluorescence of 449–451 was gradually intensified with the increasing glycerol fraction. The more viscous the medium is, the smaller the free volume and the more intense the friction between solvent and AIE molecules would be. This viscous medium activates the RIR process of the AIE molecules and hinders the non-radiative decay and hence enhances the fluorescence. As can be seen from Figure 150D, the plots of  $\log I/I_0$  versus  $\log \eta$  for 449, 450, and 451 all exhibit linear characteristics with the corresponding viscosity factors ( $x$ ) determined to be 0.46, 0.93, and 0.98, respectively. These results indicated that these AIE rotors are promising candidate probes for the assessment of bulk viscosity in solution. 450 and 451 are more viscosensitive as compared to the previously reported molecular rotors (0.4–0.6) and TPA-based rotors (0.57–0.88). The extraordinary viscosity factor displayed by 451 (0.98) is the highest one reported thus far. Moreover, the viscosity sensitivity showed an order of 451 > 450 > 449, manifesting that the addition of more peripheral rotatable phenyl rings gives rise to more sensitive viscosity responses. The increased number of rotors, enhanced quantum yield and enlarged molecular size have synergistically made the light emission of 450 and 451 highly sensitive to viscosity changes in the microenvironment and such results offer an effective strategy for the design of highly viscosensitive AIEgens. Further expanding the molecular size from 450 to 451 only resulted in a limited increase in effective rotors and a slight enhancement in sensitivity of the viscosity probes. This is owing to the accordingly increased rotation barriers. As suggested by the plots shown in Figure 150E, the  $\log \tau_f$  of each AIEgen showed a linear dependency on the  $\log \eta$  of the solvent systems with calculated viscosity factors ( $y$ ) of 0.04, 0.19, and 0.20, respectively. The  $y$  values became larger with the increase in the number of rotatable phenyl rings as well as molecular size,

showing a similar trend as the  $x$  values derived from fluorescence intensity. The much smaller  $y$  values compared to  $x$  values reveal that the fluorescence is more viscosensitive than the fluorescence lifetime for the AIE sensors. Nevertheless, lifetime measurements are more reliable and more unjammable, providing another alternative for viscosity determination using AIE probes. Such a molecular design and engineering strategy not only provides a feasible route to tune the viscosensitivity of AIE rotors but also offers a more detailed in-depth understanding of the AIE mechanism for rotatory AIEgens, namely, the RIR principle.

**5.2.10. Conformation.** The conformational change refers to the change in the shape of a macromolecule induced by environmental factors. A macromolecule is usually flexible and dynamic, and as a result its shape could be changed in response to the variations in many factors, such as temperature, pH, voltage, ion concentration, the binding of a ligand, and so on. Each possible shape is called as a conformation and the transition between them is referred to as a conformation change. Probing and visualizing conformation change is a highly important issue to the biological study and macromolecular research. However, it is hard to monitor or detect the subtle details of the conformation change processes. AIEgens, as previously pointed out and discussed, are very sensitive to the changes in the microenvironments where they are placed. As they have shown good performances in monitoring conformation change/transition of proteins (cf. section 5.1.1.2) which are one class of biomacromolecules, AIEgens were anticipated to be promising sensors to probe the conformation change of other macromolecules. To our delight, such an expectation has been realized,<sup>841–847</sup> as evidenced by the examples showcased in Figures 151–153.

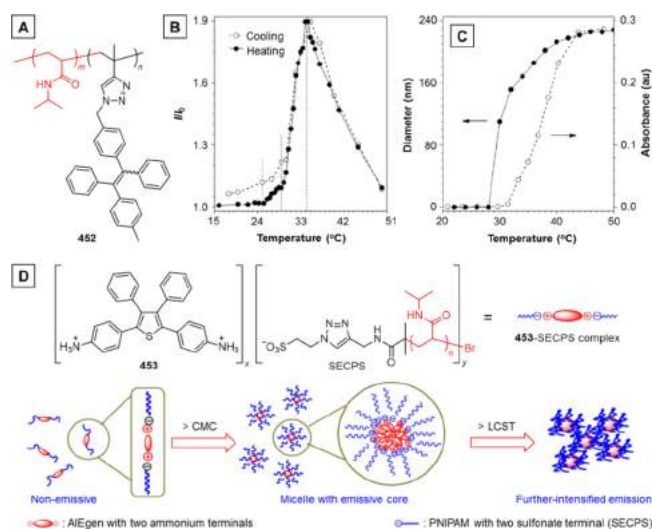


**Figure 151.** Representative examples of conformation probes constructed with AIEgens. (A) Molecular structure of TPE-labeled PNIPAM (452) which was used as an *in-situ* fluorescent probe for the thermal-induced conformation change of the polymer chain. Effects of temperature on (B) FL intensity ( $I$ ) at 468 nm and (C) particle size and solution turbidity of 452 (1 mg mL<sup>-1</sup>).  $\lambda_{ex} = 322$  nm;  $I_0$  = intensity at 468 nm at 14 °C. Turbidity data measured as a function of absorbance at 650 nm. Reprinted with permission from ref 841. Copyright 2009 Royal Society of Chemistry. (D) Schematic illustrations for self-assembled micelles structure of 453-SECPS above critical micelle concentration (CMC) and the subsequent global micelle aggregation at temperatures above the lower critical solution temperature (LCST). Reprinted from ref 844. Copyright 2012 American Chemical Society.

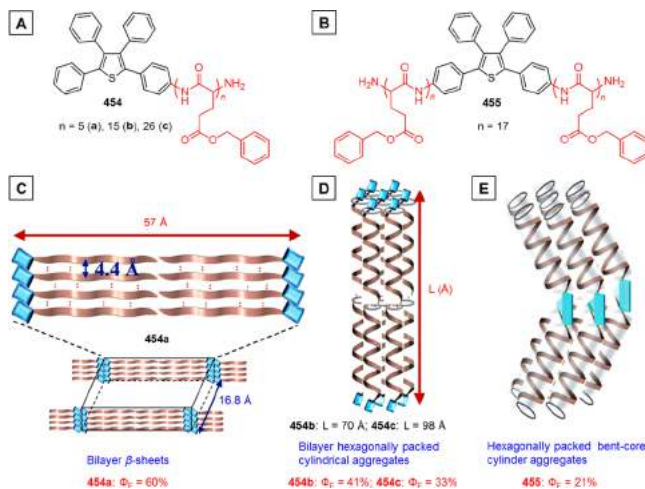


**Figure 152.** Representative examples of probing the secondary structure of polyptides by monitoring the fluorescence response of AIEgen-labelled conjugates. (A and B) Molecular structures of the AIEgen-labelled conjugates (**454** and **455**) varying in substitution numbers and chain lengths. The proposed model of (C) the bilayer  $\beta$ -sheet structure of **454a** and (D) the bilayer hexagonally packed cylindrical aggregates ( $\alpha$ -helix) of **454b** and **454c** as well as (E) the hexagonally packed bent-core cylinder aggregates ( $\alpha$ -helix) of **455**. Their corresponding film-state  $\Phi_F$  was highlighted in red. Reprinted with permission from ref 845. Copyright 2012 Royal Society of Chemistry.

Poly(*N*-isopropylacrylamide) (PNIPAM) is a well-known thermoresponsive synthetic polymer which undergoes the conformational transition from hydrated coil to dehydrated globule in water at a temperature around the body temperature. Such a polymer is thus a nice model for the investigation of thermal transitions occurring in natural macromolecules. A reversible liquid-solid phase transition takes place in an aqueous solution of PNIPAM at approximate 32 °C, which has been defined as its lower critical solution temperature (LCST). The good biocompatibility and near-body-temperature LCST of PNIPAM have inspired much work on its utilization exploration in biotechnology. The study of the thermal transition of PNIPAM thereby has great technological implications in its own right.

In view of this, our group has made some efforts in this regard.<sup>841</sup> Vinylidene-functionalized TPE derivative was introduced into the PNIPAM architecture by simple radical polymerization of the NIPAM monomer in the presence of small amounts of TPE monomer. The resultant TPE-labelled PNIPAM (**452**; Figure 151A) is AIE-active, and the molecular weight and polydispersity of the polymer have hardly been altered by the labeling, suggesting that the built-in fluorescent probe would not interfere with the bulk behaviors of the polymer chain. When its aqueous solution was heated from 14 to 25 °C, little change in the fluorescence intensity of **452** was recorded, whereas a small bump was observed in the range of 25–29 °C (Figure 151B). Above 29 °C, the fluorescence of **452** was swiftly boosted with the increase in temperature and reached a maximum at 34.2 °C. Further heating resulted in a continuous decline in the fluorescence intensity. Cooling the aqueous mixture of **452** from 50 to 18 °C furnish a largely reversed  $I/I_0$ –temperature curve with the big peak and small bump being detected in the similar temperature regions. When the solution of **452** was heated to 25 °C, the PNIPAM chains began to dehydrate probably from the isopropyl pendants, which partially broke the water cages surrounding the polymer coils and

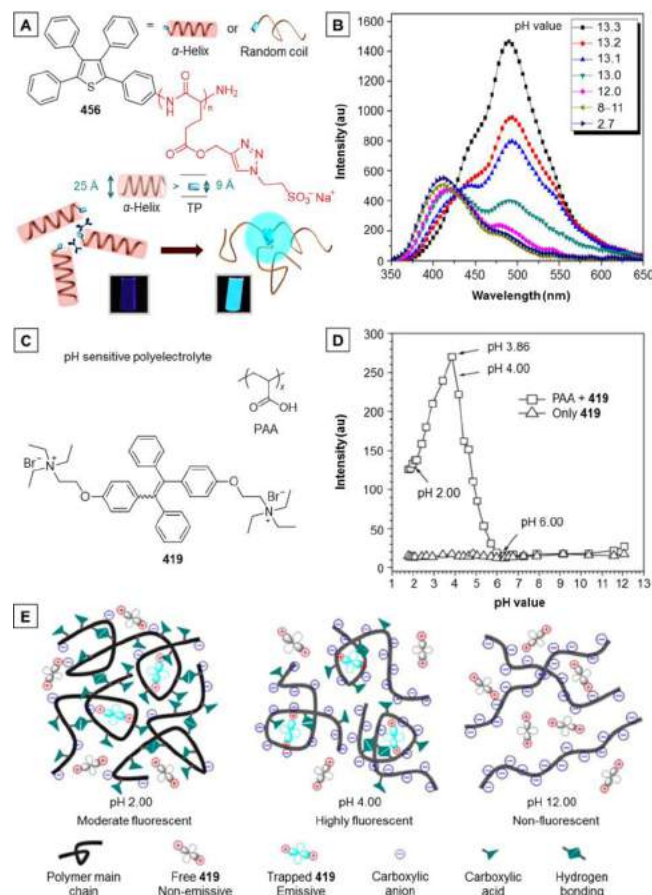


**Figure 153.** Representative examples of probing the conformation change of pH-sensitive polymers by taking advantage of the environmental sensitivity of AIEgens. (A) Chemical structure of TP-labelled poly( $\gamma$ -propargyl-L-glutamate) (**456**) and the feasibility of intermolecular aggregation among TP terminals connected by different secondary structures. (B) PL emission spectra of the aqueous **456** solutions with different pH values. Reprinted from ref 846. Copyright 2014 American Chemical Society. (C) Chemical structure of a pH sensitive polyelectrolyte PAA and a water-soluble AIEgen **419**. (D) Peak intensity of **419** (10  $\mu$ M) to pH variation in a Britton-Robinson buffer solution (40 mM) in the presence of PAA (1 g L<sup>-1</sup>) (□) and the absence of PAA (Δ). pH range: 1.78–12.06. (E) An illustration of the dynamic conformation changes of PAA chains at different pH values. PAA concentration: 1 g L<sup>-1</sup>. Reprinted with permission from ref 847. Copyright 2013 Science China Press and Springer-Verlag Berlin Heidelberg.

promoted the dehydrated chain segments to undergo an initial stage of coil–globule transition. The volume shrinkage accompanying the transition impeded the intramolecular rotations of TPE and hence made it more emissive. In the range from 29 to 34 °C, coil–globule transition further proceeded with the pendants, segments, as well as the whole polymer chains dehydrating, resulting in the formation of compact aggregates which dramatically activates the RIR process of the TPE moieties. Further heating of the polymer mixture to above 34 °C might hardly cause big change in the compactness of the polymer aggregates as the phase transition had already finished at the LCST. The aggregates continued to grow in size, making the TPE moieties buried in the big aggregates hardly able to be excited by the UV beam. In the meantime, heating accelerated the intramolecular motions. These two effects work collaboratively to make the polymer mixture less emissive, as can

be seen from the continuing decrease in the fluorescence at the high temperature region. It is clear that **452** functioned as a nonmonotonic probe that unveiled the fine details and provided more information about the thermal transition, which was inaccessible by other analytical methods. For example, the commonly-used DLS and solution turbidity measurements afforded curves which started to monotonously increase from 28 and 31 °C, respectively (Figure 151C). Such monotonic-pattern data implied that the PNIPAM chains started to aggregate from a specific temperature but failed to offer detailed information on the transition processes due to their lower sensitivity compared to that of the fluorescence-based technique. The working mode of **452** can be fine-tuned between non-monotonic and monotonic by varying the labelling degree of the polymer.

Besides TPE, other AIEgens such as tetraphenylthiophene (TP) derivatives can also be exploited to serve as conformation probes. Hong's group carried out a work on probing the LCST of PNIPAM by decorating both sides of the TP core with PNIPAM chains via click reaction.<sup>843</sup> Afterwards, they prepared a cationic TP derivative (**453**) to complex with the anionic sulfonate-terminated PNIPAM (SECPS) in different molar ratios via ionic bonds to generate three amphiphilic **453**-SECPS complexes, which were AIE-active owing to the built-in TP cores (Figure 151D).<sup>844</sup> These complexes were further utilized to explore the AIE-operative fluorescence responses toward LCST and critical micelle concentration (CMC). Dilute water solutions of **453**-SECPS complexes were non-luminescent but became highly emissive when their concentrations were above CMC. At CMC, the **453**-SECPS chains self-assembled into micelles, which greatly hampered the intramolecular motions of the TP cores and hence switched on the emission. Heating the micelle solution to temperature above LCST resulted in further increase in the fluorescence intensity. Such fluorescence responses were rationalized to be caused by the shrinkage of **453** aggregates, which further reinforced the constraints on the intramolecular motions of TP units. In this way, the conformation transition of an ionic thermal-responsive polymer was probed with the aid of AIE.

There have been considerable efforts dedicated to the investigation of polypeptides in view of their potential applications in diverse scientific fields and their close association with proteins and molecular recognition. The secondary structures of peptide chains play critical roles in the formation of well-defined tertiary structures of proteins. The study on the synthetic poly( $\gamma$ -benzyl-L-glutamate) (PBLG) and its chain conformation in organic solvents demonstrates one of the major efforts directed for the understanding of the complicated protein–protein interactions. PBLG exhibits diverse conformational possibilities and aggregation structures in various organic solvents. Labelling PBLG with fluorophores has been verified to be a useful methodology to probe the aggregation behavior of the PBLG chain. Undoubtedly, AIEgens stand out as nice labelling agents for their aggregation-beneficial emissions. Hong and coworkers incorporated the AIE-active TP fluorogen into PBLG to study the relationship between the fluorescence response and the secondary structures of peptide.<sup>845</sup> With this aspect, three TP-terminated (**454a**–**454c**; Figure 152A) and one TP-centered (**455**; Figure 152B) TP-PBLG conjugates have been prepared by ring opening polymerization, in anticipation of reflecting their secondary structures (e.g.,  $\alpha$ -helix,  $\beta$ -sheet, and random coil) in solution and solid state by means of their fluorescence behaviors.

The resultant **454a**–**454c** exhibited AEE features with the emission intensified by the increased water content in their THF/water mixtures. In contrast, aggregation of **455** in such solvent mixtures only brought about a little emission increment. It was because the intermolecular mutual approaches of the central TP moieties in **455** molecules were sterically impeded by the neighboring PBLG chains in the large  $\alpha$ -helical conformation. The TFA-induced helix–coil transition of **455** gave rise to the enhancement with the ready aggregation of TP units bisected by coil-like PBLG chains. The emissions of these TP-PBLG conjugates in the solid films were also shown to be associated with the varied fractions of the large  $\alpha$ -helical secondary structure (Figure 152C–E). TP cores in **455** were severely isolated by the vicinal  $\alpha$ -helix PBLG rods, resulting in the less efficient AEE-oriented emission in comparison to **454a**–**454c**. As can be seen from Figure 152C,D, lengthening the chains of PBLG moieties resulted in the increasing proportion of the  $\alpha$ -helical rods, which was responsible for the reduced fluorescence intensity in the order of **454a** (5) > **454b** (15) > **454c** (26). The high content of  $\alpha$ -helix rods accounted for the low emission efficiency of the **455** film (Figure 152E). The wide-angle X-ray diffraction and small-angle X-ray scattering techniques were used to confirm the results obtained by the fluorescence technique. The self-assembled  $\beta$ -sheet with bilayer structure and the  $\alpha$ -helix rod in the packing of bilayer hexagonal cylinder were both found in **454a**–**454c**. And the major  $\beta$ -sheet conformation of **454a** was gradually transformed into the predominant  $\alpha$ -helix conformation by increasing the chain length from 5 to 26 (Figure 152C,D). As for **455**, the bent core linked by two cylindrical rods was found to self-assemble in a dense hexagonal packing, resulting in its low emission efficiency owing to the sterical isolation effect exerted by the two large  $\alpha$ -helical rods. Such an elaborate work has not only provided valuable information to the polypeptide research but also offered a feasible methodology for the conformation probing of dynamic macromolecules.

Recently, following their work on TP-PBLG conjugates, Hong and coworkers further developed a different series of water-soluble polypeptides, each of which is comprised of an AEE-active TP terminal and a poly( $\gamma$ -propargyl-L-glutamate) (PPLG) chain with an ionic sulfonate pendant group.<sup>846</sup> The introduction of ionic sodium sulfonate groups via the click reaction was to facilely endow the resultant peptide polymers (**456**; Figure 153A) with water solubility. Such ionic TP-PPLG conjugates offered access to study the impact of the sulfonate side group on the secondary structure of the peptide chain as well as the relationship between the AEE-operative emission behaviors and the secondary structures (Figure 153A,B). Both the ionic side group and the molecular weight of the polypeptides were found to influence the secondary structure of the peptide chain. The ionic sulfonate pendant group in **456** raised the proportion of  $\alpha$ -helical structure compared to the neutral precursors without this ionic group. With the higher molecular weight, **456** in the solid state exhibited higher fraction of  $\alpha$ -helix structures when compared to those with low molecular weight. As  $\alpha$ -helical conformation is efficient in sterically hindering the intermolecular aggregation of the TP blocks, the fluorescence spectrum of high-molecular-weight **456** contained smaller aggregate-to-monomer emission ratio in comparison to the ones with lower  $\alpha$ -helical contents.

The geometrical factor affecting the intermolecular aggregation extent of TP units in **456** is schematically illustrated in Figure 153A. In the solution state, the TP units with a molecular width of 9 Å can be more effectively isolated and accordingly less

emissive when they possessed a large  $\alpha$ -helix chain with a diameter of 25 Å, as compared to those exist in the flexible random coils or  $\beta$ -sheets. In this context, the conformational transition in solution induced by pH change can therefore be correlated with the AEE-based emission behavior, which is closely relevant to the extent of molecular aggregation of the TP moieties in 456 (Figure 153B). A progressive transformation on the fluorescence spectra of 456 with low molecular weight upon increasing pH from 7 to 13.3 was clearly shown. Emission profiles of the aqueous solution containing 456 at pH 2 and 7 were virtually identical. The ionic sulfonate lateral groups in 456 molecules served as electrostatic shields to prevent the peptide main chain from the attacks of the acidic species and thus made the polymers rather stable in acidic media. However, with the gradual addition of NaOH, the initial monomer emission of this solution was continuously transformed into an aggregate-predominant emission. The emission transition occurred at a pH value between 11 and 13.3, which mirrored the helix-to-coil conformational transformation of the polymer chain.

Apart from the study on the pH-induced conformation change using TP built-in probes, there is another interesting work conducted with an AIEgen for the probing of conformation transition of a polyelectrolyte caused by the pH variation.<sup>847</sup> Different from the above discussed work, the probe used in this study was a dicationic TPE derivative 419, which was not chemically bonded to the polymer chain. Investigation of the chain dynamics of polyelectrolytes in aqueous solution is very important and meaningful for both academic research and practical applications. The dynamics of DNAs which are a class of natural polyelectrolytes, for example, remain mysterious and to be understood. Tremendous research efforts have been devoted to studying the polyelectrolyte chain dynamics. Most of the studies were restricted to only dilute solutions and/or incapable of investigating short-range chain dynamics due to the ACQ effect of the fluorescent probes. The unparallel strategy reported by our group was intended for the study of the polymer chain dynamics in relatively concentrated polymer solution (1 g L<sup>-1</sup>) by utilizing the cationic AIEgen as an external fluorescent probe (Figure 153C). Poly(acrylate acid) (PAA) was employed as the representative polyelectrolyte in consideration of the fact that the conformation of PAA chains varies with the change in pH values in aqueous solution.

The AIE effect of 419 and its RIR mechanism allowed us to exhibit the whole range dynamic scenario of PAA chains in a wide pH range from 1.78 to 12.06 (Figure 153D,E). 419 was almost non-emissive in water and neutral buffer solution. The fluorescence turn-on point of 419 in the buffer solution containing 1 g L<sup>-1</sup> PAA was located at pH 6.0 and the maximum emerged at pH 3.86 (Figure 153D). There was a monotonous descending in the fluorescence intensity as the pH was decreased from 3.86 to 1.78. Such fluorescence behaviors of 419 in the PAA solution with pH varying in the region of 1.78–12.06 reflected the dynamic process of the PAA chain (Figure 153E). Specifically, at pH > 6.0, the anionic carboxylic pendant groups played a dominant role and the polymer chains adopted an extended and nonfolding conformation. The molecules of 419 were well isolated and thus non-luminescent. In the lower pH region from 6.0 to 3.86, a portion of carboxylic anions were protonated. This reduced the density of negative charge on the polymer chains, leading to the formation of intra-/intermolecular hydrogen bonding and ultimately inducing the PAA chains to take a coil-like conformation. Some of the 419 molecules were attracted to the PAA chains by electrostatic interaction, with part

of them even being embedded into the coils due to the hydrophobic effect. As a result, the intramolecular motions of the 419 molecules were confined to some extent and the fluorescence was hence switched on. Further decreasing the pH from 3.86 to 1.78, the protonated carboxylic groups became dominant, resulting in a reduction in electrostatic interaction between the PAA chains and the 419 molecules. The reinforced intra- and interchain hydrogen-bonding gave rise to more compact polymer conformation, impeding the probe molecules from entering the PAA coils and thereby causing a decreased fluorescence. Distinct from the previous studies, our work was performed in more concentrated solutions and uncovered more details in the processes of conformational transitions.

In the examples shown in this part, AIEgens were used as built-in or external fluorescent probes to study the conformation changes induced by varying temperature, chain length/molecular weight of the polymer, or pH value of the polymer solutions. The AIE-based probes can be TPE, TP, or other AIEgens, with or without charge(s). With the aid of AIE effect and RIM process, the subtle details in conformational transitions can be caught by the AIE-based probes. As a matter of fact, these works are the tip of the iceberg, and there should be much more work remaining to be done.

**5.2.11. Self-Assembly.** Self-assembly is a process that disordered components form an ordered structure or pattern as a result of specific interactions like van der Waals, capillary,  $\pi-\pi$ , and hydrogen-bonding interactions among the components themselves, without external direction. There are various types of self-assemblies as well as the resultant structures. Monitoring and visualizing the processes of self-assembly is of great value to both scientific research and real-world applications. Self-assembly in essence is a special fashion of aggregation, rendering the fluorophores exhibiting AIE features suitable for the monitoring and visualization of such aggregation processes. Indeed, to date, AIEgens have been widely utilized in diverse self-assembly systems serving as fluorescent probes.<sup>848–856</sup>

For example, micelles are aggregates of surfactant molecules dispersed in a liquid colloid. The micelles generation process is called micellization, which is a form of self-assembly. Micelles form only when the concentration of surfactant is above the CMC. Considering that micelles are ubiquitous and interesting entities which have found wide applications in many important fields such as emulsion polymerization, template of nanosized materials synthesis, controllable drug delivery, and macromolecular self-assembling, the determination of CMC and the monitoring of micellization become an essential task. The routinely-used methods, such as osmotic pressure, equivalent conductivity, and surface and interfacial tension, strongly rely on the uses of professional instruments and thus are time-consuming and costly. Facile and efficient fluorescent approaches for CMC measurement and micellization process visualization have been established by taking advantage of AIE properties.<sup>848–850</sup>

On the basis of the related works, we have summarized two basic principles for the AIE-based CMC detection, which have been schematically illustrated in Figure 154. In the case shown in Figure 154A,B, when the molecules of a water-soluble AIEgen are dissolved in a dilute aqueous solution of surfactant molecules (I in Figure 154B), very faint or even no luminescence was recorded due to active intramolecular motions. The lipophilic core of the AIEgen renders it to be encapsulated into the hydrophobic cores of the micelles and form aggregates there (II in Figure 154B). Upon UV illumination, intense emission from the aggregates was

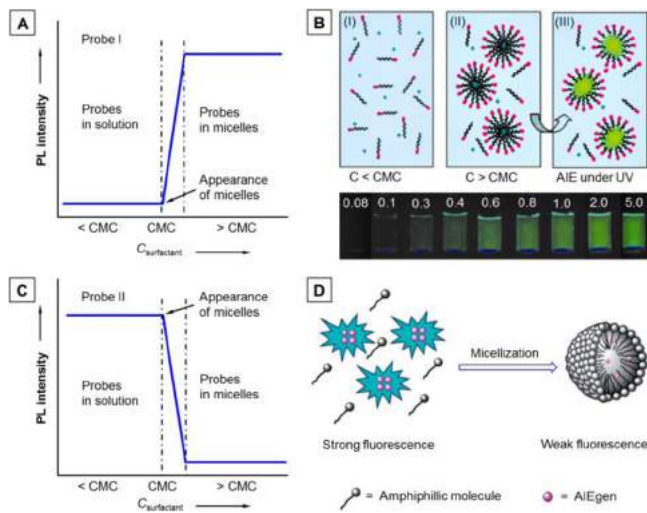


**Figure 154.** General probing modes of the CMC detection with AIEgens. Schematic illustration of the PL response to the surfactant concentration with (A) a water-soluble and (C) water insoluble AIEgen. Adapted with permission from ref 850. Copyright 2013 Royal Society of Chemistry. (B) Schematic illustration of the detection of CMC based on a water-soluble AIEgen such as protonated 350. The pink spindle and black ripple line stand for the hydrophilic head and hydrophobic tail of a surfactant molecule, and the blue diamonds and green burst-stars for the AIE aggregates and light emission, respectively. Inset: Fluorescent photographs of protonated 350 in aqueous solution with different  $[CTAB]$  taken under UV irradiation.  $[350] = 10^{-4}$  mol L<sup>-1</sup>, pH 4. Reprinted with permission from ref 848. Copyright 2009 Science in China Press and Springer-Verlag GmbH. (D) Schematic illustration of the detection of the CMC based on water insoluble AIEgens, such as 1,2-diphenyl-1,2-di(*p*-tolyl)ethene. Adapted with permission from ref 849. Copyright 2011 Royal Society of Chemistry.

observed (III in Figure 154B). Such a process can be abstractly represented with the plot depicted in Figure 154A.<sup>850</sup> The fluorescence turn-on point or the inflection in the plot of fluorescence intensity against the surfactant concentration can be assigned as the CMC of the surfactant. Taking 350 as an example, 350 in buffer solution with pH = 4.0 was protonated and became water dissolvable with very weak fluorescence.<sup>848</sup> When the concentration of the coexisting cationic surfactant CTAB was lower than 0.1 mg mL<sup>-1</sup>, no obvious change in the fluorescence intensity was detected. At a concentration of 0.3 mg mL<sup>-1</sup>, the emission intensity abruptly rose. Further increasing the surfactant concentration to 5.0 mg mL<sup>-1</sup>, the fluorescence was significantly intensified. From the photographs exhibited in the inset of Figure 154B, an apparent critical fluorescence change can be seen at  $\sim$ 0.3 mg mL<sup>-1</sup>, which is well consistent with the accredited data. Such a method is widely applicable and can be used for the CMC detection of cationic and anionic surfactants, amphiphilic biomolecules, and block copolymers. Moreover, the micelle formation via self-assembly process can be directly observed under UV light.

In the second case displayed in Figure 154C,D, a hydrophobic and water-insoluble AIEgen was used as a fluorescent probe for determining the CMC and probing the assembling/disassembling of amphiphilic molecules (e.g., surfactants).<sup>849,850</sup> At low concentration of surfactants, a large number of AIE molecules aggregated in the aqueous phase, furnishing a strong fluorescence emission due to the RIM process. However, as the surfactant concentration was increased and the surfactant molecules gradually self-assembled into micelles, the AIE molecules were

trapped into and dispersed well in the hydrophobic interior of the micelles as driven by hydrophobic interactions. The fluorescence intensity of the AIEgen was decreased owing to the weakened RIM. The plot of fluorescence intensity versus surfactant concentration in this case was opposite to the former one, with the determination of CMC in a fluorescence turn-off manner (Figure 154C).<sup>850</sup> Likewise, from the fluorescence turn-off point or the transition of the curve, the CMC can be easily determined. The TPE derivative, namely 1,2-diphenyl-1,2-di(*p*-tolyl)ethene, was used as an example to demonstrate the workability of this strategy. Ji and Tang et al. have found that it held the capability of monitoring the formation process of micelles and determining the CMC of surfactants (Figure 154D).<sup>849</sup> The temperature-dependent micellization of Pluronic F127, a pharmaceutically important PEO-PPO-PEO copolymer, was studied with this TPE derivative. The results obtained via this fluorescent method showed good agreement with the previously reported ones, suggestive of the reliability of the AIE-based methodology. More importantly, when compared to the ACQ-based approaches, the present method is more advantageous in the monitoring and visualization of the assembling/disassembling process of the colored amphiphilic compound 1-[4-(3-phenylazophenoxy)-butyl]triethylamine bromide (AzoC4), whose CMC value had not been reported before then. The TPE fluorescence primarily came from the aqueous phase in this case instead of being from the inside of the hydrophobic core of the micelles, making the fluorescence free from the interference of the colored surfactant. On the basis of these two design rationales elucidated here, numerous AIEgens could be made use of to serve the purpose of CMC determination and micellization monitoring for diverse amphiphilic species.

Layer-by-layer (LbL) deposition of polyelectrolytes (i.e. polycations and polyanions) has been regarded as a versatile assembling process which has been widely applied in the construction of functional thin films, patterned surfaces, wall of capsules, and so forth. It is necessary to monitor the growth of the deposit films *in situ* and in real time to confirm that the assembling process is under control. The UV-vis absorption is often used to monitor the assembling process; however, this method requires that the polyelectrolytes should have chromophores or strong absorptivity and that the substrate (i.e., quartz plate) should be transparent, hence preventing this technique from being widely used. LbL assembly is fundamentally a polymer aggregation process, which thereby provides a stage for AIEgens to perform as probes for *in-situ* and real-time monitoring.<sup>851-853</sup>

When an admixture of protonated salt of 350 and poly(diallyldimethylammonium chloride) (PDDAC) was used as a co-cation to assemble with poly(styrene-sulfonate) (PSS) anion by the LbL deposition process on a quartz plate (Figure 155A), the fluorescence intensity of the protonated 350 was linearly boosted with the increasing number of the bilayers (Figure 155B).<sup>851</sup> An identical linear calibration curve was also obtained when the inexpensive glass plate served as a substrate. The utilization of AIEgens is not confined to the example given in Figure 155A. In principle, they can be employed as probes to directly monitoring the assemblies of chromophore-free polyelectrolytes on any substrates, including the technologically useful but opaque substrates such as silicon wafer and mica.

AIEgens that were incorporated into the chains of polyelectrolytes can work as built-in fluorescent monitors. Wang, Hu, and Tang et al. have recently reported such a work in which the chitosan-based fluorescent bioconjugate 231 was

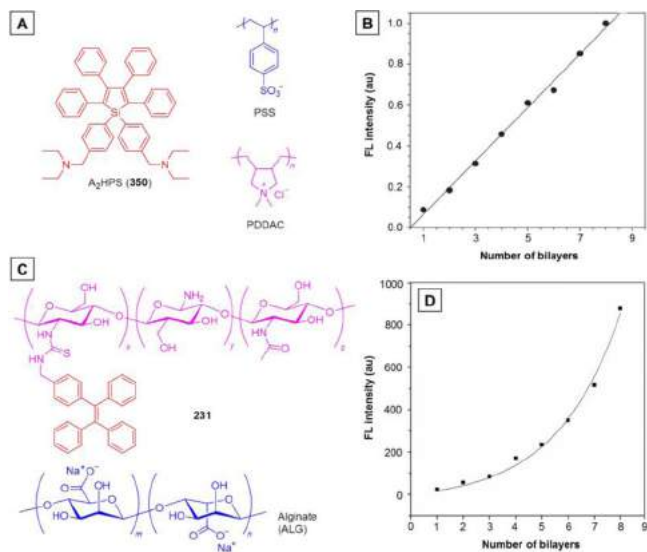


**Figure 155.** Representative examples of using AIEgens to monitor layer-by-layer self-assembling processes of ionic polymers. Chemical structure of (A) probe 350, anionic polyelectrolyte PSS and cationic polyelectrolyte PDDAC, and (C) TPE-chitosan bioconjugate 231 and anionic natural polyelectrolyte alginate. Panels B and D show the variation of FL intensity with bilayer numbers for systems depicted in panels A and C, respectively. Panel B is reprinted with permission from ref 851. Copyright 2008 Elsevier B.V. Panel D is reprinted with permission from ref 852. Copyright 2014 Royal Society of Chemistry.

exploited as a fluorescent probe for the monitoring of LbL self-assembly process of natural polyelectrolytes (Figure 155C,D).<sup>852</sup> Owing to the protonation of amine groups in the polymer chains, 231 can be transformed into polycations under low pH conditions such as pH = 4.5. In this way, this cationic bioconjugate can assemble with the anionic alginate (ALG) through LbL deposition via electrostatic interactions, which has been evidenced by the quartz crystal microbalance results and contact angle measurement. More importantly, such a self-assembly process has also been witnessed by the ellipsometry and fluorescence spectroscopy, which exhibited an exponential growth of the 231/ALG multilayer films. Furthermore, the exponential correlation between the fluorescence intensity and the number of bilayers (Figure 155D), which was in good accord with the thickness change of multilayer films, offered solid proof for the capacity of 231 as a fluorescent probe to monitor the LbL self-assembly process.

Besides pure organic self-assembly systems, AIEgens can also be incorporated into inorganic–organic hybrid systems and can even serve dual/multiple roles. Such work has recently been reported by Lu's group.<sup>853</sup> As schematically illustrated in Figure 156, they demonstrated a strategy to fabricate functional patterning of two-color optically active ultrathin films (UTFs) via LbL assembly of layered double hydroxide (LDH) nanosheets with a small AIEgen (354) in the absence/presence of poly(styrene 4-sulfonate) (PSS). The (354–LDH)<sub>n</sub> UTFs and (354/PSS–LDH)<sub>n</sub> UTFs enjoyed the combined advantages of LDH host matrixes and AIEgen 354. LDHs, as a class of inorganic layered solid host matrixes with positively charged layers and interlayer balancing anionic species and water molecules, possess a tunable layer charge density, variable elemental composition, as well as high chemical stability. Positively charged LDH monolayers are good building blocks for the fabrication of UTFs through LbL electrostatic assembly. The anionic AIEgen 354 in this work is

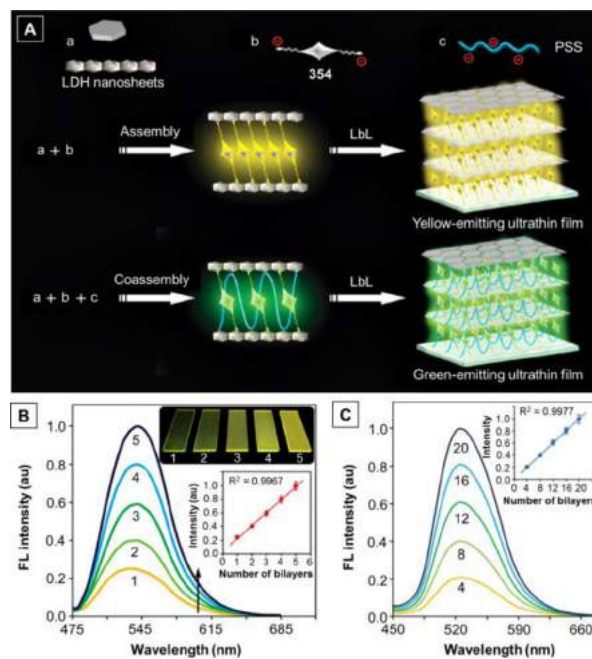


**Figure 156.** (A) Tunable luminescence ultrathin films (UTFs) fabricated by controllable and ordered assembly of (a) layered double hydroxide (LDH) nanosheets with (b) 354 and (c) PSS. (B) Normalized fluorescence spectra of yellow (354–LDH)<sub>n</sub> UTFs ( $n = 1\text{--}5$ ); the inset shows the linear correlation between FL intensity at 545 nm and the bilayer number and the fluorescent photographs of these UTFs. (C) Normalized fluorescence spectra of (354/PSS–LDH)<sub>n</sub> UTFs ( $n = 4\text{--}20$ ). Adapted with permission from ref 853. Copyright 2014 Royal Society of Chemistry.

not only a guest component for LbL self-assembly but also a built-in fluorescent probe in its own right for the self-assembly monitoring.

For the yellow-emitting (354–LDH)<sub>n</sub> UTFs, the average distance between the centers of neighboring 354 molecules was about 5 Å, which could sufficiently avoid the intermolecular  $\pi$ – $\pi$  interaction, rendering the immobilized 354 to emit at the same wavelength as that in aqueous solution. (354–LDH)<sub>5</sub> UTFs showed an absolute  $\Phi_F$  of 46.2%, which was much higher than those in water (0.1%) and the water/THF mixture (2/98, v/v;  $\Phi_F$  = 18.4%). These observations suggested that the ordered assembly and tight arrangement of 354 between the rigid frameworks of LDH monolayers can efficiently inhibit the intramolecular motions and block the non-radiative decay pathways. The self-assembly process of 354 and LDH can be monitored *in situ* and in real time as well as be clearly visualized by both fluorescence spectroscopy (Figure 156B) and naked eyes (inset photographs in Figure 156B). The intensity of fluorescence peaked at  $\sim$ 545 nm was progressively boosted with the self-assembly deposition progress. A linear relationship ( $R^2 = 0.9967$ ) between the fluorescence intensity and number of bilayers was obtained (inset plot in Figure 156B), demonstrating the monitoring ability of 354 as a fluorescent probe.

The profiles of the emission spectra of the (354/PSS–LDH)<sub>n</sub> UTFs were similar to those of (354–LDH)<sub>n</sub> UTFs but with emission maximum located at a different wavelength of  $\sim$ 525 nm (Figure 156C). Their emission peaks were also very similar to that of 354/PSS solution but showing an obvious blue-shift compared to the 354 solution. This suggested that some supramolecular structure might form through the intermolecular interactions between 354 and PSS, which resulted in more

twisted conformations of **354** to experience a lower degree of electronic conjugation. On the other hand, the intermolecular interactions between **354** and PPS, and the confinement from the PSS–LDH frameworks collectively restricted the intramolecular motions of **354**, leading to the green emission with high brightness. Likewise, the LbL deposition process of (**354**/PSS–LDH)<sub>n</sub> UTGs ( $n = 4–20$ ) was also monitored by the fluorescence spectrometer (Figure 156C). The linear plot of fluorescence intensity versus bilayers number (inset in Figure 156C) further demonstrated the role of **354** in the monitoring of the LbL self-assembly process. It is also clear that the coassembly strategy of **354** and PSS can function as a facile approach for the modulation of UTGs luminescence.

In addition to the micellization and LbL deposition, self-assembly can also be involved in some gelation process. Self-assembled molecular hydrogels are a newly emerging class of soft materials, which have shown great potential for drug delivery, tissue engineering, and biosensors, etc. Among them, the self-assembled luminescent hydrogels have received considerable attention due to their advanced utilizations for luminescent probes and biosensors. However, the fabrication of luminescent hydrogels with traditional luminophores is a difficult task and usually a dilemma as a result of the ACQ effect suffered by the self-assembled structures. The AIEgens are beyond doubt good building blocks for luminescent hydrogels. Moreover, the brightness change of AIEgens in the hydrogelation process is significantly associated with and reflects the gelation progress, owing to the RIM mechanism. In other words, the incorporation of AIEgens into gelatable systems will not only afford excellent luminescent hydrogels but also bring about built-in probes for the gelation monitoring.

Liang and coworkers have reported a work on the AIE-based hydrogel that can be used as a proof of this concept (Figure 157).<sup>854</sup> The TPE unit was grafted to the salt-responsive peptide Q19 via amidation reaction, generating a luminescent hydrogelator **457** (Figure 157A). The peptide Q19 (KRKRSG-SGQQEFQFQFKQQ) was derived from peptide Q11 (Am-QQEFQFQFKQQ-Ac) which has been reported to be able to self-assemble into a  $\beta$ -sheet fibrillar structure in salt-containing aqueous environments and then entangle to form a gel network. It was thus found that hydrogelator **457** self-assembled into a hydrogel network with bright fluorescence switched on only in the presence of salt (Figure 157A). The gelation process can be clearly visualized and self-monitored via the emission change of the system (Figure 158B). Under UV illumination, the originally faintly emissive solution of **457** gradually developed into brightly fluorescent gel when the NaCl concentration was increased from 0 to 1.5 M. As a consequence, the fluorescence intensity at 466 nm corresponding to TPE was almost linearly enhanced with the increasing concentration of NaCl. These data demonstrated that the dynamic change in luminescence caused by the salt-induced aggregation enabled the real-time and *in-situ* monitoring of the hydrogel formation process. Conjugating AIEgens to stimuli-responsive peptides is a thus promising strategy to develop self-revealing soft materials for biological applications.

Study on spontaneous interfacial self-assembly processes has been and continues to be a captivating research aspect due to the basic roles in nature, ubiquity, as well as aesthetic appeal of the interfacial self-assembly. Gaining in-depth understandings of dynamic interfacial self-assembly processes is vitally important for a broad spectrum of topics in theoretical physics, materials design, and biomedical research, but it is also a challenging task. Direct monitoring of such processes was obstructed due to the



**Figure 157.** (A) Chemical structures of peptides used for molecular hydrogelations and schematic illustration of the formulation of luminescent hydrogel by TPE-grafted stimuli-responsive peptide **457**. (B) Fluorescence images of the progressive gelation of **457** (0.5 wt %) incubated with different concentrations of NaCl under a 365 nm UV lamp. Adapted from ref 854. Copyright 2014 American Chemical Society.

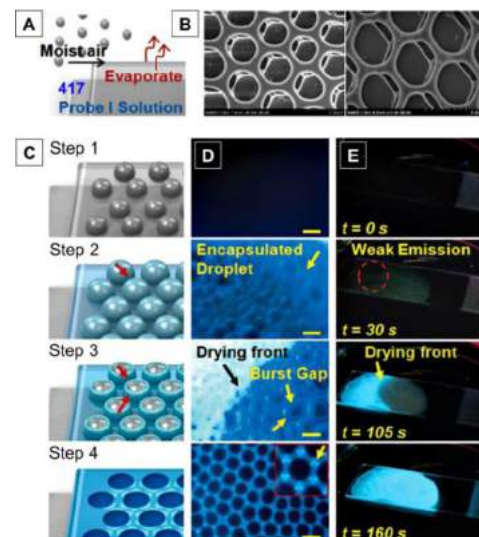


**Figure 158.** AIE platform for direct visualization of interfacial dynamic self-assembly. (A) Schematic of breath-figure formation. (B) Representative SEM images of the ordered porous **417** film formed by breath figures. (C) Schematic of the four main steps of breath figures observed with *in-situ* AIE imaging. (D) Fluorescence microscopy images taken during the breath-figure formation corresponding to steps 1–4. The inset in step 4 shows an enlarged ordered cloverlike fluorescent pattern (yellow arrow). Scale bar, 3  $\mu$ m. (E) Representative progressing frames showing macroscopic evolution of emission signal during steps 1–4 of the breath-figure formation process. Adapted with permission from ref 855. Copyright 2014 Wiley-VCH Verlag GmbH & Co. KGaA.

unsatisfactory imaging contrast of thin interfacial layer. Recently, our group has innovatively established an *in-situ* and real-time fluorescence imaging/monitoring platform which exploited the unique AIE effect to directly visualize the dynamic interfacial evolution.<sup>855</sup> Since the AIE mechanism of RIM can take place at the level of individual AIE-active units, the transitions from non-emissive to luminescent state are solely defined by the characteristics of AIEgens irrespective of the size of aggregates or proximity of AIE-active moieties, thereby enabling high-contrast imaging of the thin phase-boundary layer with commonly-used fluorescence microscopy and offering a useful tool for selectively monitoring the interfacial dynamic self-assembly in real time.

Such a platform was first applied to decipher one of the most interesting interfacial self-assembly puzzles, namely, breath-figure formation, an extremely useful yet poorly understood process (Figure 158). The AIE-active hyperbranched polymer 417 carrying TPE moieties was chosen for this study. 417 can simultaneously function as the structural material for breath figure pattern fabrication and as a fluorescent probe for high-contrast monitoring of the dynamic self-assembly process. Characteristic honeycomb-like porous structures can be yielded by casting the chloroform solution of 417 onto a glass slide under humid airflow (Figure 158A). Such ordered porous arrays were confirmed by the SEM (Figure 158B) and the fluorescence microscopy, proving the ability of 417 to form highly fluorescent and ordered breath figures.

The four major steps in breath-figure formation (Figure 158C) were demonstrated through monitoring AIE signal development with fluorescence microscopy (Figure 158D) and macroscopical observation under a UV lamp (Figure 158E). In step 1, tiny water droplets nucleated on the surface of 417/chloroform solution and no fluorescence was observed, indicating the well-dissolved state of 417 and the absence of 417 aggregates at the water/oil interface during this period. In step 2, water droplets emitting weak fluorescence started emerging when they stopped growing and completed assembling into order arrays, suggesting the fast chloroform evaporation, enrichment, and aggregation of 417 at the interface. In step 3, upon further evaporation of the chloroform, the film encapsulating water droplets began bursting in different directions. In the meantime, the fluorescent material was enriched around the edges of bursting gaps. In step 4, with the complete evaporation of the water, highly fluorescent and ordered porous arrays were formed, exhibiting “clover-like” patterns. The AIE imaging highlighted the crucial role of the water droplet encapsulation by a thin polymer layer which was followed by its rupture and expansion in breath figure self-assembly. Such a mechanistic model has been further supported by the simulation and theoretical analysis. This simple and versatile imaging platform based on AIE can also be used for the direct visualization of other complex interfacial processes such as microemulsion and coffee-ring. It can thus be expected that such a platform would offer insights into the dynamic phase-transition phenomena, deepen the understanding of interfacial biological processes, and guide the development of novel self-assembly technologies.

This subsection has provided a clear view into the capability of AIE as a powerful fluorescent tool for the real-time and *in-situ* monitoring of various self-assembly processes spanning from micellization, LbL deposition, hydrogelation to interfacial dynamic self-assembly such as breath-figure formation. In most cases, the AIEgens played a dual role, as they were often both a fluorescent monitor and a component of the self-assembly structures. The AIEgens that can be employed for this purpose definitely are not limited to the ones exhibited here, and accordingly the self-assembly processes that can be monitored and visualized are not restricted to those demonstrated in this review.

**5.2.12. Morphology.** Besides probing conformational change and monitoring self-assembly, the investigations on the morphologies of polymers, including their shape, size, composition, texture, architecture, as well as phase distribution are also of great significance. The microphase separations, for example, in block copolymers and polymer blends greatly impact their self-assembled structures and mechanical properties. However, to date, utilizing aggregatochromic luminogens inside

polymer matrixes for the preparation of “built-in” temperature and deformation probes/indicators/visualizers have been seldom realized, due to the lack of effective and versatile aggregatochromic luminogens. AIEgens, on the other hand, are promising candidates for such kind of utilities, because of their distinct light emission behaviors between molecularly-dispersed and aggregate states. Most recently, there have emerged a few AIE-based systems that were exploited for the morphology visualization.<sup>857–861</sup> In this subsection, these examples will be showcased with their main results highlighted in Figure 159 and Figure 160.

Pucci and coworkers have ingeniously applied TPE as an aggregatochromic morphological probe for a group of thermoplastic styrene-based polymers and explored its ability to distinguish the host polymer matrixes according to their different compositions, architectures, and inherent viscosities as well as the intrinsic stiffness.<sup>857,858</sup> The TPE was doped into the thermoplastic polymers, namely, poly(styrene) (PS), poly(styrene-block-butadiene-block-styrene) (SBS), and poly(styrene-co-butadiene) (SBR) at diverse weight percentages (0.005–0.1 wt %), producing TPE/polymer films with thickness of 150–200 μm by compression molding of the mixture obtained after drying TPE/polymer chloroform solutions.<sup>858</sup> SBS is a thermoplastic elastomer whose triblock-structure combines the properties of the hard-segment polystyrene blocks (glass transition temperature ( $T_g$ ) = 70 °C) and the soft-segment polybutadiene blocks ( $T_g$  = –87 °C). SBR, on the other hand, is a random styrene/butadiene copolymer with a single  $T_g$  of –21 °C. As displayed in Figure 159A, progressively intensified emission peaked in the range of 455–475 nm was observed on passing from SBR to SBS and to PS at a TPE doping concentration of 0.01 wt %. The  $\Phi_F$  values of TPE in these polymers were ~0.5%, 2.2–3.2%, and 8.5–11.1%, respectively. It can be interpreted as follows: when TPE was blended with a polymer featuring a  $T_g$  above ambient temperature, stronger fluorescence was exhibited, due to the restricted motions of phenyl rotors; by contrast, in the random matrix like SBR, the TPE had sufficient freedom of intramolecular motions and hence merely showed weak luminescence. Thus, the morphological properties of these host polymers can be indicated. Moreover, both in SBS and SBR, there were notable positive correlations between the fluorescence intensity and the TPE doping concentration (Figure 159B).<sup>858</sup> In addition to the higher brightness, as compared to that of TPE/SBR, the fluorescence of TPE/SBS also had a ~15 nm blue-shift, further implying that the TPE molecules experienced a more rigid and confined microenvironment in the block polymer SBS, which made them take more twisted conformations with smaller conjugation.

A closer scrutiny and deeper analysis of SBS and SBR samples containing 0.05 wt % TPE have been carried out with the scanning near-field optical microscopy (SNOM) to study the emission profile that refers to the spatial distribution of the fluorescence intensity at the sample surface. In accordance with the macroscopic analysis, the average fluorescence intensity of the maps was higher in TPE/SBS than in TPE/SBR blends (Figure 159D), owing to the distinct morphologies of the supporting matrixes. The SNOM correlated the fluorescence behaviors of TPE in the AIEgen/polymer blends with different matrix morphologies. Fluorescence domains were practically randomly distributed and less contrasted in TPE/SBR. In comparison, they appeared to coalesce with each other in TPE/SBS with a broader and island-like topology as well as a more emissive fluorescence feature because of the block morphology

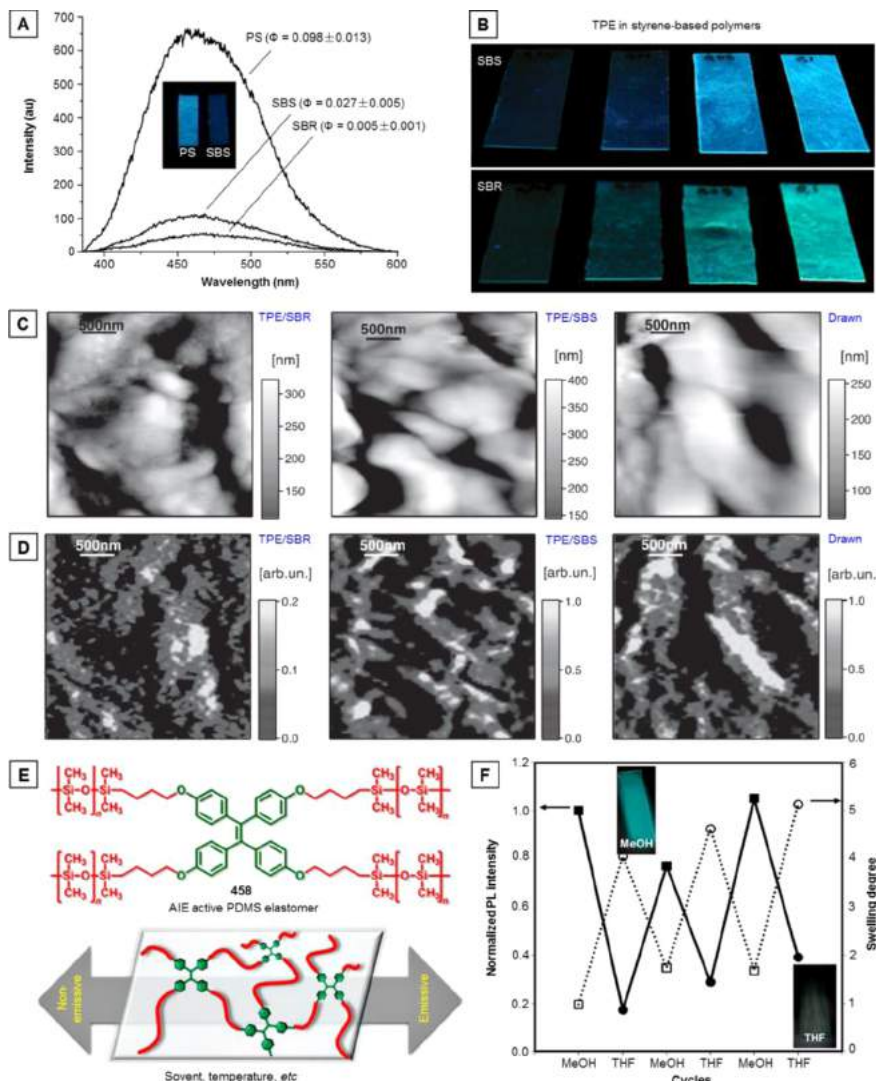


**Figure 159.** Representative examples of AIE-active systems designed for morphology visualization. (A) Emission spectra of 0.01 wt % TPE/styrene-based polymer films with the indication of the corresponding  $\Phi$  (brackets). (B) Fluorescent photographs of the SBS and SBR films doped with different weight percentages of TPE. (C) Topography and (D) fluorescence maps at  $\lambda > 450$  nm. Samples: TPE/SBR (left panel in C and D); TPE/SBS (middle panel); TPE/SBS upon uniaxial drawing (drawing ratio roughly 3) along a direction approximately lying on the diagonal of the map (right panel). Note the different scales, in arbitrary units, reflects the lower fluorescence intensity found in TPE/SBR with respect to TPE/SBS. Adapted with permission from ref 858. Copyright 2014 Wiley-VCH Verlag GmbH & Co. KGaA. (E) Schematic illustration of the fluorescence change of AIE-active PDMS (polysiloxanes) elastomer 458 upon stimuli-induced morphology or shape change. (F) Fluorescence switching of 458 in between THF (circle) and methanol (square). Insets: Corresponding fluorescent photographs of 458. Adapted from ref 859. Copyright 2014 American Chemical Society.

(Figure 159C,D). The SNOM analysis results provided a spatial resolution high enough to visualize the aggregates of blocks/segments, i.e., regions at the surface where either S or B blocks were clustered, characterized by either higher or lower fluorescent quantum yield. Further studies can be extended to other polymeric materials and different AIEgens in order to validate the polymer tracing method illustrated here. Among all the AIEgens, those with mechanochromic characteristics hold especially great potentials to be developed into visualizers for examining polymer morphologies.

Besides physical blending, AIEgens can be covalently incorporated into polymeric systems and play an essential role in the visualizing of morphology. For example, TPE unit was integrated with poly(dimethylsiloxane) (PDMS) system through the hydrosilylation reaction of tetravinyl-modified TPE derivative and H-terminated PDMS and served as a built-in fluorescent visualizer for monitoring the morphology/shape changes of the

PDMS elastomer induced by solvents, temperature, and so on (Figure 159E).<sup>859</sup> The resultant AIE elastomer 458 exhibited in Figure 159E was swelled when it was immersed in such organic solvents as THF, chloroform, and hexane, with the fluorescence remarkably decreased as compared to its dry state. On the other hand, when immersed in organic solvents like methanol, the elastomer did not get swelled and its fluorescence remained unchanged. Such a solvent-selective fluorescence response of 458 exhibited a dependency on its swelling behavior: the larger the swelling degree, the weaker the fluorescence would be and vice versa (Figure 159F). The fluorescence can hence reflect the swelling degree or the deformation of the polymer. In the swollen state, the AIE-crosslinker, namely, TPE moiety, experienced smaller confinement from the PDMS chains, rendering active intramolecular motions and hence quenching the fluorescence. Cooling the elastomer gave rise to an obvious hypsochromic shift and dramatic enhancement in its fluorescence in comparison to

that measured at room temperature. This was because that under low temperature, the PDMS matrix significantly hampered the intramolecular motions of TPE and twisted its conformation.

Similarly, other AIEgens such as *o*-carborane derivatives were also used as crosslinkers in polymers to afford systems that can self-indicate the polymer morphology especially the size/shape change upon external stimuli.<sup>860</sup> A diglycidyl *o*-carborane derivative **459** (Figure 160A) showing AIE properties was employed as a cross-linking reagent, producing translucent

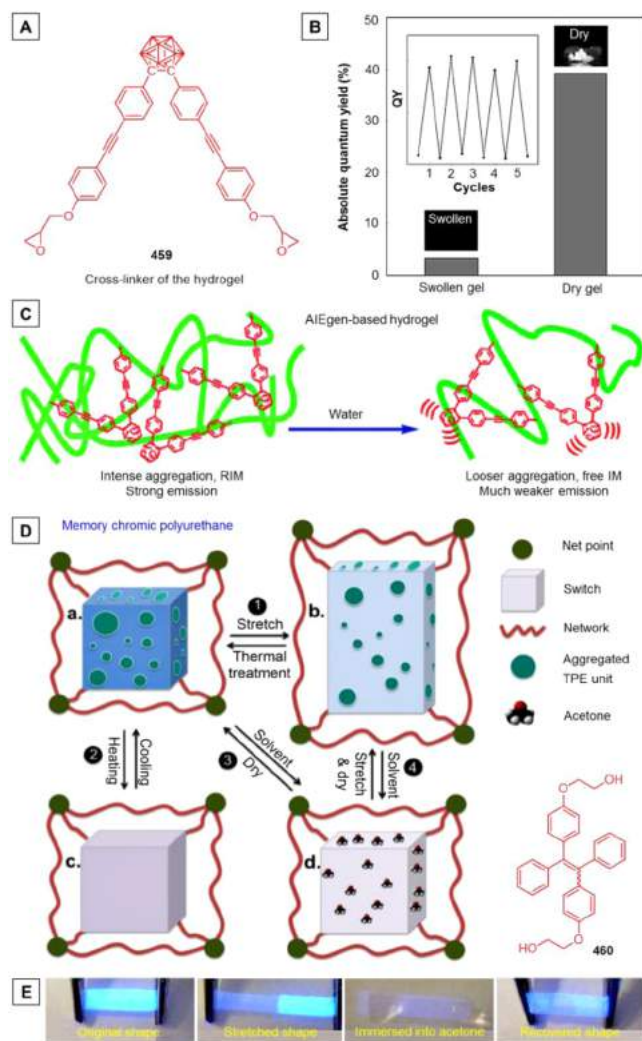


**Figure 160.** AIEgen-based morphology visualizers for hydrogels and shape-memory polymers. (A) Molecular structure of the diglycidylxyl cross-linker **459** derived from AIE-active *o*-carborane. (B) Absolute fluorescence quantum yields of **459**-crosslinked hydrogel in swollen and dry states. Insets: The fluorescence switching of **459**-crosslinked hydrogel between swollen and dry states, and the corresponding fluorescent photographs of **459**-crosslinked hydrogel in these states. (C) Schematic illustration of the fluorescence response of AIEgen-based hydrogel to the water-induced shape change. Adapted from ref 860. Copyright 2010 American Chemical Society. (D) Model to illustrate the molecular mechanism during (1) stretch-recovery process, (2) heating-cooling process, (3) solvent-dry process, and (4) solvent-induced shape recovery process of the **460**-polyurethane copolymers. (E) The fluorescent images of the polymer film which was first stretched and then immersed into acetone and then taken out from solvent and dried at room temperature. Adapted with permission from ref 861. Copyright 2013 Wiley Periodicals, Inc.

hydrogels composed of poly( $\gamma$ -glutamic acid), a bioproduct secreted by a *Bacillus subtilis* strain. The fluorescence was correlated to the swelling ratio of the resultant hydrogels, which was dependent on the cross-linking degree or ionic strength. Moreover, the hydrogels displayed a fluorescence decrease/increase switching between the swollen and dry states (Figure 160B), which can be observed by the naked eye and fluorescence spectroscopy. Such a fluorescence switching behavior reflected the compactness of the hydrogel networks (Figure 160C). In the dry state, the polymers chains severely twined each other furnishing a highly compact network. In such a confined environment, the AIE-crosslinkers were aggregated with the polymeric matrix, the conformation was rigidified, the intramolecular motions were strongly restricted, and hence strong fluorescence was exhibited. When the polymer was swollen, the network was expanded, making the microenvironment less crowded. As a result, looser aggregation and less restriction on the intramolecular motions gave rise to the reduction in fluorescence efficiency.

Hu's group has exploited TPE as a built-in aggregatochromic probe to investigate the morphological changes such as deformation of shape memory polymers (SMPs), which were induced by mechanic forces, solvents, and thermal treatment.<sup>861</sup> The model SMP was made of shape memory polyurethane with TPE units (0.1 wt %) derived from **460** covalently connected to the soft-segments (PCL). The fluorescence intensity showed negative correlation with volume increase, temperature rise, as well as the existence of solvent (Figure 160D). When stretched (process 1), the emission of the TPE-based SMPs was decreased as a result of the deaggregation of TPE units and the reduction in the local luminogen concentration. On the other hand, the shape recovery of the film upon heating enabled the restoration of fluorescence. When the **460**-polyurethane copolymer was exposed to heat (process 2) or solvent (process 3), the TPE units were dissolved in molten PCL region or in the solvent, leading to the decrease in the light emission due to active intramolecular motions. Moreover, the shape recovery of the pre-stretched sample induced by solvent such as acetone (process 4) displayed further decreased fluorescence owing to the dissolving of the crystal region and transformation of PCL into elastomer, which liberated the TPE units from the strong confinement exerted by the polymer network. The photographs taken under UV illumination which are shown in Figure 160E have given a clear expression to the model depicted in Figure 160D. As the intramolecular motions of the TPE clusters were governed indirectly by the shape memory properties such as shape deformation, shape recovery, and stimuli-induced shape change, the fluorescence of the TPE-based SMPs can hence visualize their morphology changes occurring at both macroscopic and microscopic levels.

As can be seen from the examples demonstrated in this small part, the morphology visualization can truly be realized by taking advantage of the AIE effect. However, in comparison to other chemosensing areas, the visualizing of morphology using AIEgens is still in its infancy with much less work done in this regard. In view of this, this new application territory of AIE calls for more attention and efforts, which in turn will be repaid with exciting results that benefit both the fundamental research and practical applications.

### 5.3. Optoelectronic Systems

Optoelectronic devices refer to electrical-to-optical or optical-to-electrical transducers or instruments that use such devices in

their operation. Optoelectronic devices are the key and core component of optoelectronic technology, a cutting-edge research field in modern photoelectric and microelectronics technologies and also an important constituent part of information technology. In photoelectronic areas, the light-emitting materials can be used to serve various purposes and in most cases, the luminogens are utilized in the solid state. Thus, AIEgens are ideal candidates for optoelectronic applications and a wealth of examples indeed have been documented to support this proposition. The utilities of AIEgens in OLEDs, self-assembly systems, OFETs, optical waveguides, CPL, LCs, and photovoltaics will be introduced one by one in this section.

**5.3.1. Organic Light-Emitting Diodes (OLEDs).** OLEDs have attracted tremendous attention because of their huge potentials in such applications as new display devices and solid-state lighting.<sup>6,862</sup> With the aim of attaining efficient full-color display and white light illumination, AIEgens with emission colors covering the whole range of visible lights have been designed and synthesized.<sup>12–14,17,18</sup> Herein, AIEgens utilized mainly as emitting layers for blue, cyan, green, yellow, red/infrared, and white OLEDs will be discussed first, followed by AIEgens with hole-transporting or electron-transporting properties or bipolar carrier mobility in addition to their light-emitting properties. OLEDs based on polymeric AIEgens, namely, PLEDs, will also be touched upon.

Although blue OLEDs are crucial components for full-color display, their poor performance has become a barricade to the achievement of full-color displays. The intrinsically wide band gaps of blue light emitters make it very difficult to inject charges into the active layers of the devices, resulting in unsatisfactory device performances.<sup>863,864</sup> A large quantity of blue light-emitting materials built from anthracene, styrylarylene, and fluorene derivatives have been reported.<sup>865–867</sup> However, when fabricated into thin solid films in OLEDs, most of them inevitably suffer from the notorious ACQ effect, which deteriorates the device performances to varying extents. AIEgens are anticipated to offer a solution to such a problem.<sup>12,762,868–877</sup>

Utilizing TPE as a building block, a large number of blue-emitting AIEgens have been created through smart designs and facile syntheses. Representative examples of them are exhibited in Figures 161–163 and those with outstanding performances are highlighted in Table 1. Directly hooking up the two TPE units through a *para* linkage gave rise to a bisadduct *p*TPE-*p*TPE (**461**; Figure 161), which was found to show a sky blue EL with a maximum ( $\lambda_{\text{EL}}$ ) at 488 nm.<sup>869</sup> Multilayer OLED with a configuration of ITO/NPB (60 nm)/**461** (20 nm)/TPBi (10 nm)/Alq<sub>3</sub> (30 nm)/LiF (1 nm)/Al (100 nm) showed fairly good EL performance with a low turn-on bias ( $V_{\text{on}}$ ) down to ~4 V, brilliant luminance up to 11 180 cd m<sup>-2</sup> at 15 V, and current efficiency ( $\eta_{\text{C,max}}$ ) and external quantum efficiency ( $\eta_{\text{ext,max}}$ ) reaching to 7.26 cd A<sup>-1</sup> and 3.17%, respectively, at a bias of 6 V (Table 1). Although the device configuration was yet to be optimized, the EL data was much better than that of its parent form (TPE). This has already well exemplified the proverb that “two is better than one”. In an effort to control the extent of  $\pi$ -conjugation and to obtain desired deep-blue emission, an array of new bis-TPE adducts, namely, *m*TPE-*p*TPE (**462**), *o*TPE-*p*TPE (**463**), *m*TPE-*m*TPE (**464**), and *o*TPE-*m*TPE (**465**), have been prepared by Li’s group through combinations of *ortho*-, *meta*-, and *para*-linkages (Figure 161).<sup>870</sup> When used as emitters in OLEDs, all these four AIEgens (**462**–**465**) exhibited deep-blue EL in the range of 459–435 nm with Commission International de l’Eclairage (CIE) chromaticity coordinates of

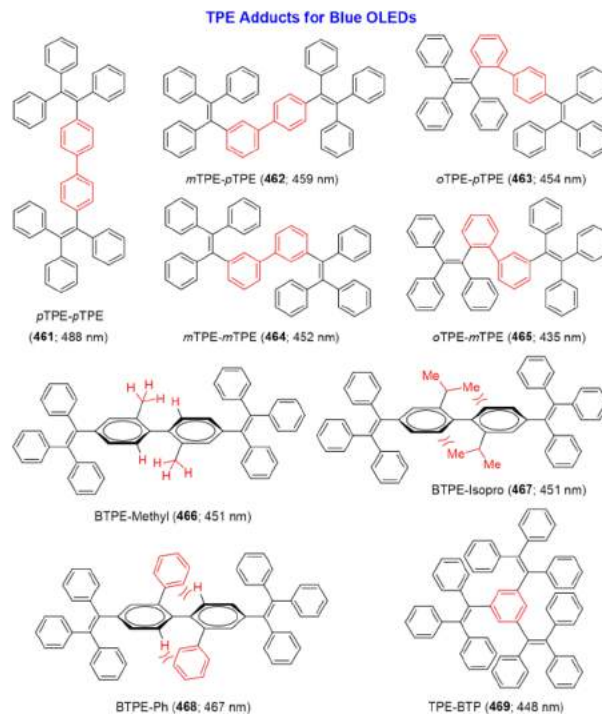


**Figure 161.** Examples of AIEgens constructed as TPE adducts showing excellent OLED performances with blue light emissions. Their EL maxima are given in parentheses.

**Table 1. EL Performance for Some Representative TPE-Ar Adducts**

AIEgen	device	$\lambda_{\text{EL}}$ (nm)	$L_{\text{max}}$ (cd m <sup>-2</sup> )	$V_{\text{on}}$ (V)	$\eta_{\text{C,max}}$ (cd A <sup>-1</sup> )	$\eta_{\text{P,max}}$ (lm W <sup>-1</sup> )	$\eta_{\text{ext,max}}$ (%)
461	A <sup>a</sup>	488	11 180	4.0	7.26		3.17
472	B <sup>b</sup>	448	26 697	3.0	3.37	2.40	
473	B <sup>b</sup>	451	14 854	3.3	2.76	1.80	
478	C <sup>c</sup>	470	19 023	2.9	7.05	6.17	3.70
479	C <sup>c</sup>	480	13 639	3.1	8.03	7.04	3.99
480	C <sup>c</sup>	469	10 709	3.1	5.46	5.03	3.06

<sup>a</sup>Device configuration A: ITO/NPB (60 nm)/AIEgen (20 nm)/TPBi (10 nm)/Alq<sub>3</sub> (30 nm)/LiF (1 nm)/Al (100 nm). <sup>b</sup>Device configuration B: ITO/PEDOT:PSS (30 nm)/NPB (30 nm)/AIEgen (15 nm)/TPBi (10 nm)/Alq<sub>3</sub> (30 nm)/LiF (1 nm)/Ca:Ag (100 nm). <sup>c</sup>Device configuration C: ITO/MoO<sub>3</sub> (10 nm)/NPB (60 nm)/AIEgen (15 nm)/TPBi (35 nm)/LiF (1 nm)/Al. Abbreviations:  $L_{\text{max}}$  = maximum luminance,  $V_{\text{on}}$  = turn-on voltage,  $\eta_{\text{C,max}}$  = maximum current efficiency,  $\eta_{\text{P,max}}$  = maximum power efficiency, and  $\eta_{\text{ext,max}}$  = maximum external quantum efficiency.

(0.16, 0.14), (0.15, 0.11), (0.16, 0.14), (0.16, 0.16). The well-controlled  $\pi$ -conjugations in these AIEgens have enabled them to emit in higher efficiencies (1.8–2.8 cd A<sup>-1</sup>) than TPE (0.45 cd A<sup>-1</sup>). Apart from controlling the conjugation by modulating the linkage mode of the TPE-bisadducts, Li and Ma et al. reported that the attainment of deep-blue emitters could also be realized through ingeniously modifying the dihedral angle to tune the conjugation degree of two TPE or aromatic blocks.<sup>871</sup> Simply attaching additional groups with different size and conjugation extent, i.e., methyl, isopropyl, and phenyl groups, to the 2,2'-positions of **461** yielded three TPE adducts **466**, **467**, and **468** (Figure 161), which emitted blue/deep-blue EL with the emission maximum located at 451, 451, and 467 nm, respectively, as a result of the large dihedral angles of the biphenyl cores

(up to  $\sim 89^\circ$ ). In a similar manner, by taking advantage of conformation twisting strategy as well as conjugation control, other TPE adducts could also be carved into deep-blue emitters. **469**, for example, was obtained by welding three TPE units into one molecule (Figure 161). Owing to its highly twisted conformation which resulted from the severe steric crowdedness, the effective  $\pi$ -conjugation of **469** was close to that of TPE. Thus, the compound emitted a deep-blue EL of 448 nm with appreciable  $\eta_{C,\max}$  and  $\eta_{ext,\max}$  of  $2.8 \text{ cd A}^{-1}$  and 1.6%, respectively.

The conjugation control and conformation twisting strategy also work efficiently in hetero-TPE adducts for the construction of deep-blue luminogens. In pursuit of deep-blue emitters with better performances, fluorene, a well-known deep-blue-emitting building block, was integrated with the TPE unit at the unconjugated 9-position through *para*- or *meta*-linkage to partially tune the conjugation of the resulting TPE-fluorene adducts TPE-*p*tol (**470**) and TPE-*m*tol (**471**; Figure 162).<sup>877</sup> Replacing the

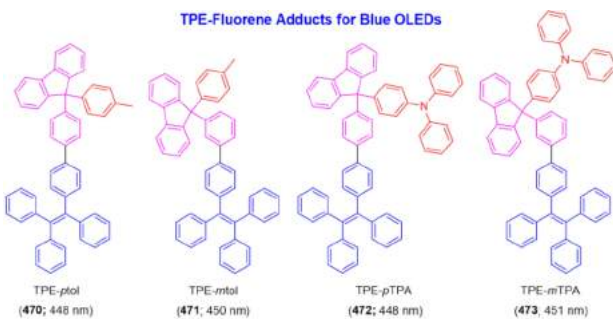


**Figure 162.** Examples of AIEgens constructed as TPE-fluorene adducts showing excellent OLED performances with blue light emissions. Their EL maxima are given in parentheses.

toluene groups of **470** and **471** with hole-dominated TPA moieties generated TPE-*p*TPA (**472**) and TPE-*m*TPA (**473**; Figure 162), respectively. All these TPE-fluorene adducts featured remarkable AIE characteristics and exhibited good thermal and morphological stability, thanks to the bulky aromatic moieties. The introduction of fluorene and TPA through unconjugated linkage allowed the intrinsic inconsistency between high efficiencies and deep-blue EL in the construction of AIE-active blue luminogens to be partially overcome. When fabricated as emitting layers in non-doped OLEDs, the EL maxima of **470–473** were in the region of 448–451 nm. As can be seen from the CIE coordinates, the EL devices constructed from TPE-*m*tol (0.16, 0.14) and TPE-*m*TPA (0.15, 0.15) were bluer than those made from TPE-*p*tol (0.16, 0.19) and TPE-*p*TPA (0.16, 0.16). This was ascribed to the fact that the *meta*-linkage contributed less to the elongation of the conjugation in comparison to the *para*-linkage. With additional TPA units, **472** and **473** performed better than **470** and **471** in OLEDs, due to the more efficient carrier transport and excitation combination. As displayed in Table 1, low  $V_{on}$  (down to 3.0 V) and high EL efficiencies with maximum luminance ( $L_{\max}$ ),  $\eta_{C,\max}$  and maximum power efficiency ( $\eta_{P,\max}$ ) up to  $26\,697 \text{ cd m}^{-2}$ ,  $3.37 \text{ cd A}^{-1}$ , and  $2.40 \text{ lm W}^{-1}$  have been recorded for the device of **472**, while the EL performance of **473** was a bit worse than that of **472** but was still appreciable. Obviously, the EL properties of TPE could be greatly improved without sacrificing the deep-blue emission through rational molecular design. It is believed that making full use of such a design idea will give rise to more efficient blue or deep-blue TPE-based emitters.

The important role of TPA in the construction of efficient blue emitters has been implied by the work discussed above. In the light of this, Li's group directly merged the TPA and TPE moieties together with different linkage modes (i.e., **474–477**) in an attempt to generate blue or even deep-blue AIEgens.<sup>875</sup> As displayed in Figure 163, all these four TPE-TPA adducts have

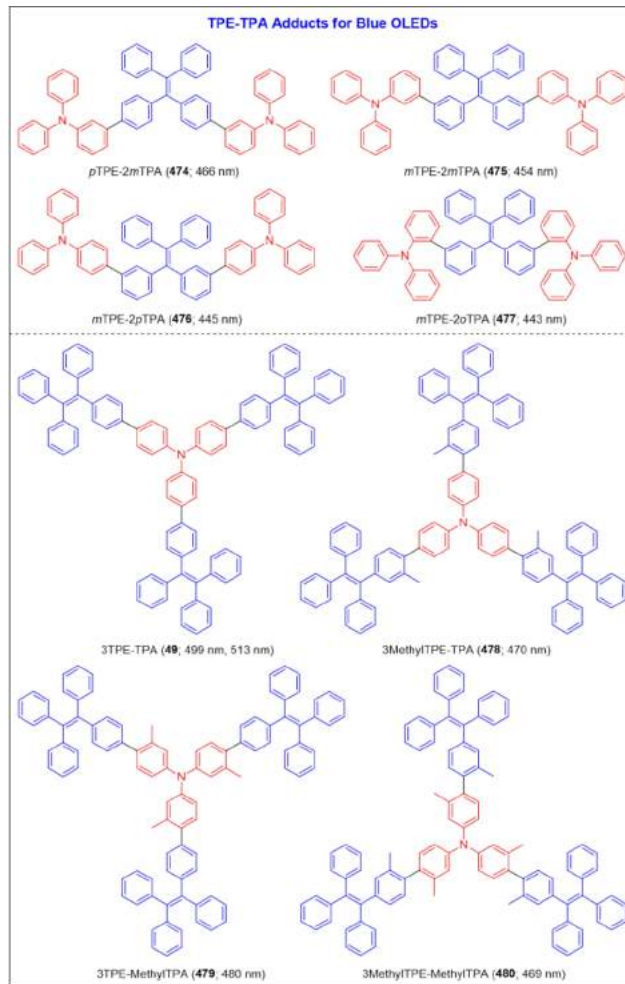


**Figure 163.** Examples of AIEgens constructed as TPE-TPA adducts showing excellent OLED performances with blue light emissions. Their EL maxima are given in parentheses.

defined chemical structures without any isomers. *p*TPE-*2m*TPA (**474**) was facilely synthesized first and emitted a blue EL of 466 nm, which was significantly blue-shifted as compared to its isomers constructed through *para*-only linkage (514 nm). Three other TPE-TPA adducts, which are the isomers of **474** (i.e., **475–477**), have also been synthesized by attaching TPA units to the TPE core at the *meta*-position of TPE. The large band gaps resulted from the less conjugated linking fashion were retained to ensure their emissions lying in the blue region. When applied as emitting layers in non-doped OLEDs, all the luminogens **475–477** showed deep-blue EL with maxima ranging from 454–443 nm with CIE coordinates of (0.16, 0.16), (0.16, 0.15), and (0.16, 0.13), respectively. Despite their device configurations not being optimized, the  $L_{\max}$ ,  $\eta_{C,\max}$  and  $\eta_{P,\max}$  attained ( $8160 \text{ cd m}^{-2}$ ,  $3.79 \text{ cd A}^{-1}$ , and  $2.94 \text{ lm W}^{-1}$ , respectively) are much higher than that of TPE, indicating the effectiveness of smart alliance.

In addition to the TPE-cored adducts of TPE and TPA, AIEgen-based blue OLEDs have also been constructed from TPE-TPA adducts with the TPA unit as a core.<sup>876</sup> To fine-tune the conjugation and blue-shift the emission, additional methyl groups are employed to enlarge the dihedral angles of the biphenyl moieties and consequently increase the twisting degree of the whole luminogens (Figure 163). Decorating the TPA core with three TPE units through *para*-linkage yielded the AIEgen **49** with bluish green EL (499 and 513 nm) due to the good conjugation between the central TPA and peripheral TPE moieties. When each of the TPE units of **49** was modified with a methyl group at the *meta*-position of the phenyl ring connected to the TPA unit, the AIEgen 3MethylTPE-TPA (**478**) was afforded with a largely blue-shifted EL of 470 nm. The additional methyl groups have dramatically boosted the steric crowdedness, which imparts a more twisted conformation. This resulted in a shortened conjugation of the overall molecule and hence blue-shifted the emission. When the central TPA unit of **49** was embellished with one methyl group at the *meta*-position of each phenyl ring, another blue-emissive AIEgen 3TPE-MethylTPA (**479**) with EL of 480 nm was obtained. Ultimately, 3MethylTPE-MethylTPA (**480**) was constructed by decorating each of the phenyl rings connecting the TPA and TPE units with a methyl group at the *meta*-position. When used as an emitting layer in the multilayered OLED, **480** emitted at 469 nm with a low  $V_{on}$  of 3.1 V, fairly high efficiencies with  $L_{max}$ ,  $\eta_{C,max}$ ,  $\eta_{P,max}$  and  $\eta_{ext,max}$  of 10 709 cd m<sup>-2</sup>, 5.46 cd A<sup>-1</sup>, 5.03 lm W<sup>-1</sup>, and 3.06%, respectively. As shown in Table 1, the EL results obtained from the blue OLEDs of **478** and **479** are even better as compared to those of the device constructed from **480**. The OLED based on **479** displayed superb EL efficiencies with  $L_{max}$ ,  $\eta_{C,max}$ ,  $\eta_{P,max}$  and  $\eta_{ext,max}$  up to 13 639 cd m<sup>-2</sup>, 8.03 cd A<sup>-1</sup>, 7.04 lm W<sup>-1</sup>, and 3.99%, respectively, making them among the best EL performances for blue AIEgens. All the above introduced blue/deep-blue emitters were developed through tuning the balance between the molecular rotation and conjugation either by utilizing different linkage modes or increasing the intramolecular torsion with additional groups. These facile strategies can hence be taken as general approaches for the construction of efficient blue AIEgens for the applications in OLEDs.

Decorating ACQphores with AIE motifs has been verified to be an effective pathway to facilely transform the ACQ systems into AIEgens (cf., section 3.1). Some “win-win” situations achieved by this strategy are shown in Figure 164 and Table 2. For instance, linking TPE unit(s) to pyrene group(s) in different number ratios has not only overcome the ACQ effect of pyrene with the generation of new AIEgens TPE-2Py (**42**), TPE-Py (**41**), and 4TPE-Py (**40**) but has also enhanced the emission efficiency of TPE systems making them excellent emitters for OLEDs.<sup>92,94</sup> The turning “stone” into “gold” strategy was operated based on the RIR principle as well as the twisted conformation of TPE which hampered the intermolecular  $\pi$ - $\pi$  stacking between the planar pyrene segments. By varying the TPE-to-pyrene ratio from 1:2, 1:1, to 4:1, the EL performance of the resulting adducts became better (Table 2). The multilayered OLED fabricated using **42** as the emitting layer was turned on at 4.8 V and emitted a cyan light of 516 nm, with  $L_{max}$ ,  $\eta_{C,max}$ ,  $\eta_{P,max}$  and  $\eta_{ext,max}$  of 13 370 cd m<sup>-2</sup>, 5.8 cd A<sup>-1</sup>, 2.0 lm W<sup>-1</sup>, and 2.00%, respectively. With a smaller conjugation, the EL of **41** was blue-shifted to 484 nm and turned on at a lower bias of 3.6 V, with the  $L_{max}$ ,  $\eta_{C,max}$ ,  $\eta_{P,max}$  and  $\eta_{ext,max}$  increased to 13 400 cd m<sup>-2</sup>, 7.3 cd A<sup>-1</sup>, 5.6 lm W<sup>-1</sup>, and 3.00%, respectively. **40** showed extraordinary performances in OLEDs with different device

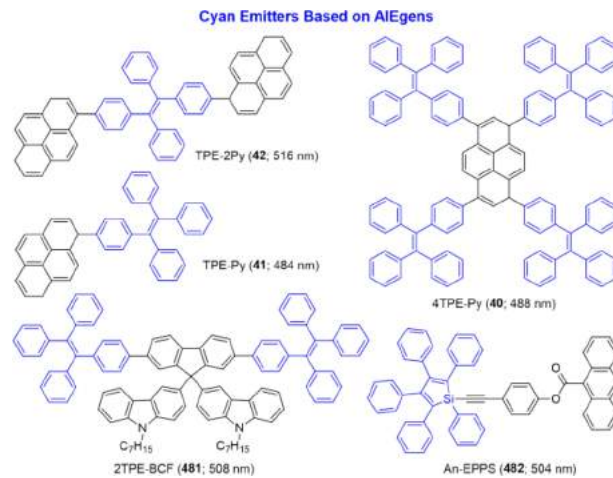


**Figure 164.** Representative examples of AIEgens showing excellent OLED performances with cyan light emissions. Their EL maxima are given in parentheses.

**Table 2. EL Performances of Representative Cyan AIE Emitters and Alq<sub>3</sub>**

AIEgen	device	$\lambda_{EL}$ (nm) <sup>a</sup>	$L_{max}$ (cd/m <sup>2</sup> )	$V_{on}$ (V)	$\eta_C$ (cd/A)	$\eta_P$ (lm/W)	$\eta_{ext,max}$ (%)
TPE-2Py (42)	A <sup>a</sup>	516	13 370	4.8	5.8	2.0	2.00
TPE-Py (41)	A <sup>a</sup>	484	13 400	3.6	7.3	5.6	3.00
4TPE-Py (40)	B <sup>b</sup>	492	18 000	4.7	10.6 <sup>g</sup>	5.0 <sup>h</sup>	4.04
4TPE-Py (40)	C <sup>c</sup>	488	36 300	3.6	12.3 <sup>g</sup>	7.0 <sup>h</sup>	4.95
481	D <sup>d</sup>	508	13 760	5.5	7.2	2.8	2.60
482	E <sup>e</sup>	504	16 826	3.9			3.00
Control (Alq <sub>3</sub> )	F <sup>f</sup>	520	27 600	3.5	5.3 <sup>g</sup>	2.7 <sup>h</sup>	1.60

<sup>a</sup>Device configuration A: ITO/NPB (60 nm)/AIEgen (20 nm)/TPBi (10 nm)/Alq<sub>3</sub> (40 nm)/LiF (1 nm)/Al (100 nm). <sup>b</sup>Device configuration B: ITO/NPB (60 nm)/AIEgen (40 nm)/TPBi (20 nm)/LiF (1 nm)/Al (100 nm). <sup>c</sup>Device configuration C: ITO/NPB (60 nm)/AIEgen (26 nm)/TPBi (20 nm)/LiF (1 nm)/Al (100 nm).

<sup>d</sup>Device configuration D: ITO/NPB (60 nm)/AIEgen (20 nm)/TPBi (40 nm)/LiF (1 nm)/Al (100 nm). <sup>e</sup>Device configuration E: ITO/NPB (50 nm)/AIEgen (40 nm)/Alq<sub>3</sub> (10 nm)/LiF (1 nm)/Al (150 nm). <sup>f</sup>Device configuration F: ITO/NPB (60 nm)/Alq<sub>3</sub> (40 nm)/TPBi (20 nm)/LiF (1 nm)/Al (100 nm). Abbreviations:

$L_{max}$  = maximum luminance,  $V_{on}$  = turn-on voltage,  $\eta_C$  = maximum current efficiency,  $\eta_P$  = maximum power efficiency. <sup>g</sup> $\eta_C$  = current efficiency (at 100 cd m<sup>-2</sup>). <sup>h</sup> $\eta_P$  = power efficiency (at 100 cd m<sup>-2</sup>), and  $\eta_{ext,max}$  = maximum external quantum efficiency.

configurations. The OLED with configuration of ITO/NPB (60 nm)/**40** (26 nm)/TPBi (20 nm)/LiF (1 nm)/Al (100 nm) was turned on at 3.6 V, exhibiting a cyan EL at 488 nm with  $L_{max}$ ,  $\eta_C$  (at 100 cd m<sup>-2</sup>),  $\eta_P$  (at 100 cd m<sup>-2</sup>), and  $\eta_{ext,max}$  up to 36 300 cd m<sup>-2</sup>, 12.3 cd A<sup>-1</sup>, 7.0 lm W<sup>-1</sup>, and 4.95%, respectively. Such results are far better than those of Alq<sub>3</sub>, which is demonstrative of the superiority of AIEgens.

Besides pyrene, carbazole and fluorene are also ACQphores. Using the same decoration strategy, the ACQ-active moiety (BCF) constructed by attaching two carbazole units to the fluorene ring at the 9,9'-positions was converted into a luminogen with marked AEE effect (**481**; Figure 164) by introducing TPE units at its 2,7-positions.<sup>878</sup> The multiple aromatic rings endowed **481** with high thermal stability, while the 3D conformation helped hinder the close packing between neighboring molecules, preventing the formation of detrimental species. Good EL results with  $\lambda_{EL}$ ,  $L_{max}$ ,  $\eta_{C,max}$ ,  $\eta_{P,max}$  and  $\eta_{ext,max}$  of 508 nm, 13 760 cd m<sup>-2</sup>, 7.2 cd A<sup>-1</sup>, 2.8 lm W<sup>-1</sup>, and

2.60%, respectively, have been obtained from the OLED built with **481** as an emitting layer. Besides TPE, embellishing ACQphores with other AIEgens such as silole derivatives can also transform them into AIE/AEE-active systems. For example, fusing silole with an anthracene moiety created a new luminogen **482** (Figure 164) with good thermal stability due to the bulky, robust and aromatic nature of the ACQphore and high emission efficiency in the aggregate state, making it a good cyan emitter for OLEDs.<sup>780</sup> The device started to emit at a low bias of  $\sim 3.9$  V with the luminance and  $\eta_{\text{ext,max}}$  reaching  $16\,826 \text{ cd m}^{-2}$  and 3.00%, respectively. All these results further verify that the strategy of tethering AIEgens to ACQphores is versatile to solve the ACQ problem and, at the same time, to create highly performed solid-state emitters for OLEDs.

Through the utilization of the RIM principle, AIEgens with green emission can be readily designed and prepared.<sup>128,163,762,879,880</sup> A greenish emitter **416** was simply generated by incorporating electron-withdrawing thiophene groups into a benzene-cored luminogen carrying multiple triarylviny units (Figure 165).<sup>762</sup>

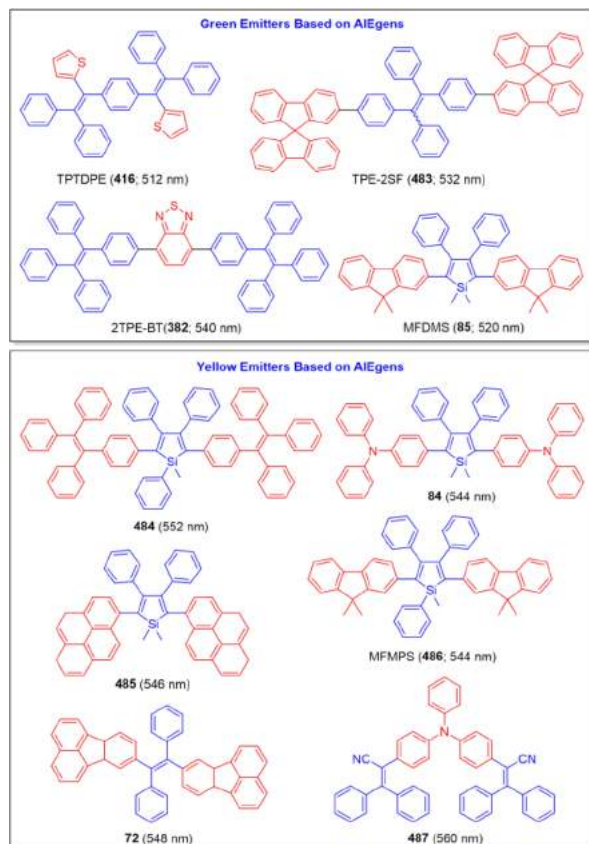


**Figure 165.** Examples of AIE-active green and yellow emitters for excellent OLED devices. Their EL maxima are given in parentheses.

Thanks to the multiple aromatic rotors as well as the highly twisted conformation, **416** exhibited AEE activity and was employed as a green emitting layer ( $\lambda_{\text{EL}} = 512 \text{ nm}$ ) in an EL device with the  $V_{\text{on}}$ ,  $L_{\text{max}}$ ,  $\eta_{\text{C,max}}$ ,  $\eta_{\text{P,max}}$  and  $\eta_{\text{ext,max}}$  recorded as 4.2 V,  $7\,620 \text{ cd m}^{-2}$ ,  $3.0 \text{ cd A}^{-1}$ ,  $2.2 \text{ lm W}^{-1}$ , and 1.10%, respectively. The TPE-fluorene adduct **483** consisting of a TPE core and two terminal ACQ-active spirobifluorene groups exhibited typical AIE behaviors with a film-state  $\Phi_F$  up to 99.0% (Figure 165).<sup>879</sup> The OLED based on **483** was turned on at 5.6 V and emitted a green EL peaked at 532 nm with a  $L_{\text{max}}$  of  $11\,100 \text{ cd m}^{-2}$ . Its  $\eta_{\text{C,max}}$ ,  $\eta_{\text{P,max}}$  and  $\eta_{\text{ext,max}}$  were measured to be  $6.0 \text{ cd A}^{-1}$ ,  $2.6 \text{ lm W}^{-1}$ , and 1.90%, respectively.

To red-shift the emission, benzo-2,1,3-thiadiazole, a widely used building block for constructing green to red luminogens, was incorporated into **461** as a core, furnishing a yellowish-green emitter **382** (Figure 165) with a film-state  $\Phi_F$  of 89.0%.<sup>880</sup> The OLED with **382** as an emitting layer displayed a good EL performance with  $V_{\text{on}}$ ,  $L_{\text{max}}$ ,  $\eta_{\text{C,max}}$ ,  $\eta_{\text{P,max}}$  and  $\eta_{\text{ext,max}}$  of  $3.9 \text{ V}$ ,  $13\,540 \text{ cd m}^{-2}$ ,  $5.2 \text{ cd A}^{-1}$ ,  $3.0 \text{ lm W}^{-1}$ , and 1.50%, respectively. Different from the blue-emissive TPE, silole derivatives are always apt to show redder emissions. Bulky 9,9'-dimethylfluorenyl substituents were introduced into the 2,5-positions of a silole ring.<sup>128</sup> The resulting 2,5-difluorenyl-substituted silole derivative **85** is thermally stable and possesses a low-lying LUMO energy level (Figure 165). The OLED fabricated from **85** with a configuration of ITO/NPB (60 nm)/**85** (20 nm)/TPBi (40 nm)/LiF (1 nm)/Al (100 nm) was turned on at a low voltage of 3.2 V and exhibited a green EL at 520 nm with a CIE coordinate of (0.31, 0.57). As shown in Table 3,

**Table 3.** EL Performances of Representative Green to Infrared AIEgens

AIEgen	device	$\lambda_{\text{EL}}$ (nm)	$L_{\text{max}}$ (cd/m <sup>2</sup> )	$V_{\text{on}}$ (V)	$\eta_{\text{C,max}}$ (cd/A)	$\eta_{\text{P,max}}$ (lm/W)	$\eta_{\text{ext,max}}$ (%)
<b>85</b>	A <sup>a</sup>	520	27 600	3.2	12.9	11.6	4.00
<b>486</b>	A <sup>a</sup>	544	31 900	3.2	16.0	13.5	4.80
<b>489a</b>	A <sup>a</sup>	590	13 535	4.3	6.81	4.96	2.88
<b>489b</b>	A <sup>a</sup>	616	10 573	3.3	4.24	4.06	2.53
<b>490</b>	B <sup>b</sup>	692	780	4.4			1.54

<sup>a</sup>Device configuration A: ITO/NPB (60 nm)/AIEgen (20 nm)/TPBi (40 nm)/LiF (1 nm)/Al (100 nm).

<sup>b</sup>Device configuration B: ITO/PEDOT:PSS (40 nm)/NPB (80 nm)/TCTA (5 nm)/AIEgen (30 nm)/TPBi (30 nm)/LiF (0.5 nm)/Al (120 nm). Abbreviations:  $L_{\text{max}}$  = maximum luminance,  $V_{\text{on}}$  = turn-on voltage,  $\eta_{\text{C,max}}$  = maximum current efficiency,  $\eta_{\text{P,max}}$  = maximum power efficiency, and  $\eta_{\text{ext,max}}$  = maximum external quantum efficiency.

this OLED displayed a splendid performance with  $L_{\text{max}}$ ,  $\eta_{\text{C,max}}$ ,  $\eta_{\text{P,max}}$  and  $\eta_{\text{ext,max}}$  of  $27\,600 \text{ cd m}^{-2}$ ,  $12.9 \text{ cd A}^{-1}$ ,  $11.6 \text{ lm W}^{-1}$ , and 4.0%, respectively.

Attaching TPE moieties to the methylpentaphenylsilole core as peripheries at 2,5-positions generated a yellow-emissive AIEgen **484** (Figure 165).<sup>881</sup> This TPE-silole adduct exhibited pretty good thermal stability and high film-state  $\Phi_F$  (51.2%). OLED constructed with **484** as an emitting layer displayed a yellow EL at 552 nm with a turn-on voltage of 5.2 V and an  $L_{\text{max}}$  as high as  $12\,560 \text{ cd m}^{-2}$ . Its  $\eta_{\text{C,max}}$ ,  $\eta_{\text{P,max}}$  and  $\eta_{\text{ext,max}}$  were  $6.4 \text{ cd A}^{-1}$ ,  $\sim 2.5 \text{ lm W}^{-1}$ , and 1.98%, respectively. The fusion of TPA units and silole at the 2,5-positions of the silole ring not only turned the ACQphore into AIEgen but also created an efficient yellow emitter **84** (Figure 165). A multilayered OLED utilizing **84** as an emitting layer showed a very good EL performance with  $\lambda_{\text{EL}}$ ,  $V_{\text{on}}$ ,  $L_{\text{max}}$ ,  $\eta_{\text{C,max}}$ ,  $\eta_{\text{P,max}}$  and  $\eta_{\text{ext,max}}$  of 544 nm, 3.1 V,  $13\,405 \text{ cd m}^{-2}$ ,  $8.28 \text{ cd A}^{-1}$ ,  $7.88 \text{ lm W}^{-1}$ , and 2.42%, respectively. Moreover, thanks to the hole-transporting TPA groups, **84** can simultaneously serve as emitting layer and hole-transporting layer. The device constructed without an additional hole-transporting layer exhibited performance comparable to that of the aforesaid one. When planar ACQ-active pyrene units were incorporated into the silole ring at the 2,5-positions, a new silole compound **485** with AEE effect was generated (Figure 165).<sup>882</sup> The OLED built from **485** was turned on at 3.5 V, emitting a yellow EL of 546 nm (CIE = 0.36, 0.53) with a superb performance. The  $L_{\text{max}}$ ,  $\eta_{\text{C,max}}$ ,  $\eta_{\text{P,max}}$  and  $\eta_{\text{ext,max}}$  attained by this device were  $49\,000 \text{ cd m}^{-2}$ ,  $9.1 \text{ cd A}^{-1}$ ,  $7.1 \text{ lm W}^{-1}$ , and 3.0%, respectively. This is another example of win-win situation

achieved by ACQ-to-AIE transformation. Replacing the TPE units in **484** with ACQ-active 9,9'-dimethylfluorenyl moieties readily created another silole derivative **486** (Figure 165) with a yellow EL of 544 nm (CIE = 0.37, 0.57).<sup>128</sup> The OLED of **486** with a simple and unoptimized configuration already showed an extraordinarily good performance as indicated by the data shown in Table 3. Further optimization of the configuration to ITO/MoO<sub>3</sub> (5 nm)/NPB (60 nm)/**486** (20 nm)/TPBi (60 nm)/LiF (1 nm)/Al (100 nm) gave rise to a OLED which was turned on at 3.3 V and radiated intense yellow light with an  $L_{\max}$  of 37 800 cd m<sup>-2</sup>, extremely high  $\eta_{C,\max}$  of 18.3 cd A<sup>-1</sup> and  $\eta_{P,\max}$  of 15.7 lm W<sup>-1</sup>. Notably, an impressive  $\eta_{ext,\max}$  as high as 5.5% was obtained, which was a breakthrough in AIEgen-based yellow OLEDs achieved by judicious molecular engineering as well as device optimization.

Merging TPE with fluoranthene, a planar ACQphore, has generated a nonplanar fluoranthene-substituted ethene **72** (Figure 165).<sup>119</sup> **72** suffers no ACQ effect and instead it is AIE-active. Because of its good thermal stability and up to unity solid-state  $\Phi_F$ , **72** is a promising emitter for OLED application. The device based on **72** emitted a yellow EL peaked at 548 nm, exhibiting a quite good performance with  $L_{\max}$ ,  $\eta_{C,\max}$ ,  $\eta_{P,\max}$  and  $\eta_{ext,\max}$  measured to be 20 520 cd m<sup>-2</sup>, 10.0 cd A<sup>-1</sup>, 5.7 lm W<sup>-1</sup>, and 3.1%, respectively. Compound **487** with D-A structure and a sterically crowded and twisted conformation has been designed and synthesized from arylamine and propeller-like triphenylacrylonitrile units by Yuan and Zhang et al.<sup>883</sup> **487** was found to show typical TICT and AIE characteristics with a high crystal-state  $\Phi_F$  of 99.0%. Excellent performance was recorded for the OLED constructed from **487**: the device displayed a  $V_{on}$  of 4.8 V, with  $L_{\max}$ ,  $\eta_{C,\max}$ ,  $\eta_{P,\max}$  and  $\eta_{ext,\max}$  of 11 430 cd m<sup>-2</sup>, 10.7 cd A<sup>-1</sup>, 4.9 lm W<sup>-1</sup>, and 3.3%, respectively. It is worth mentioning that the OLED of AIEgen **101** fabricated by solution processing displays a bright yellow EL with CIE coordinates of (0.46, 0.52) and a low  $V_{on}$  of 3.5 V. The  $L_{\max}$ ,  $\eta_{C,\max}$  and  $\eta_{P,\max}$  were found to be 26 551 cd m<sup>-2</sup>, 12.3 cd A<sup>-1</sup>, and 7.8 lm W<sup>-1</sup>, respectively.

As red is one of the three primary colours, luminogens with efficient red emissions are always unremitting pursuits for scientists and technologists working in the field of OLEDs. Although they are indispensable components for full-color display systems, red organic emitters with high EL efficiency and good thermal stability are much scarcer than the blue and green ones. Red luminophores are usually large molecules with extended  $\pi$ -conjugation and planar conformation or D- $\pi$ -A molecules with strong charge transfer characters. They often suffer from the ACQ effect. In an effort to enlarge the family of red luminogens, **488** was prepared by the attachment of three TPE units to the 4,7-di(thiophen-2-yl)benzo-2,1,3-thiadiazole core (Figure 166).<sup>884</sup> Despite its strong emission in solution, **488** was also fluorescent in the film state due to its highly twisted 3D conformation, which prevented close molecular packing and enabled its utility in OLEDs. The non-doped EL device with **488** as an emitting layer exhibited a relatively low  $V_{on}$  of 4.2 V and radiated intense red light at 650 nm (inset in Figure 166) with CIE coordinates of (0.67, 0.32). The  $L_{\max}$ ,  $\eta_{C,\max}$  and  $\eta_{ext,\max}$  of this device were 3750 cd m<sup>-2</sup>, 2.4 cd A<sup>-1</sup>, and 3.7%, respectively. Thermally stable red luminogens (**489a** and **489b**; Figure 166) with AIE attributes have been constructed through embellishing D- $\pi$ -A cores (e.g., D = TPA and A = benzo-2,1,3-thiadiazole) with AIE units (e.g., TPE and triphenylethene).<sup>885</sup> Multilayered OLEDs built from **489a** and **489b** emitted EL of ~590 and 616 nm, with turn-on voltages of 4.3 and 3.3 V, respectively. The  $L_{\max}$  of the devices was 13 535 cd m<sup>-2</sup> for **489a** and 10 573 cd m<sup>-2</sup> for

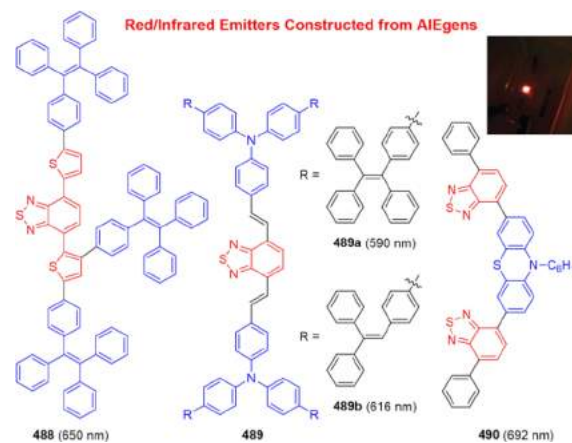


**Figure 166.** Examples of red/infrared emitters constructed from AIEgens. Their EL maxima are given in parentheses. Inset: Photograph of red emissive OLED constructed from **488**. Reprinted with permission from ref 884. Copyright 2012 Royal Society of Chemistry.

**489b**. The  $\eta_{C,\max}$ ,  $\eta_{P,\max}$  and  $\eta_{ext,\max}$  achieved by the device of **489a** were 6.81 cd A<sup>-1</sup>, 4.96 lm W<sup>-1</sup>, and 2.88%, while those were 4.24 cd A<sup>-1</sup>, 4.06 lm W<sup>-1</sup>, and 2.53% for **489b**-based device (Table 3). Moreover, the EL device of **489a** was reported to be the brightest non-doped red OLED developed so far.

Further strengthening the D-A effect can further red-shift the emission wavelength. For example, a butterfly-shaped D-A compound **490** (Figure 166) composed of the electron-donating phenothiazine and electron-accepting benzothiadiazole groups emitted a NIR light with a peak at 700 nm.<sup>73</sup> Owing to its AIE feature, the film of **490** showed a  $\Phi_F$  of 16.0%. Remarkably, non-doped OLED based on **490** was fabricated, which gave a NIR EL of 692 nm with  $\eta_{ext,\max}$  of 1.54% and  $L_{\max}$  of 780 cd m<sup>-2</sup> (Table 3). A low efficiency roll-off and a high radiative exciton ratio of 48% which exceeded the limit of 25% in conventional fluorescent OLEDs were also measured due to the AIE property of **490**. In addition, an array of NIR AIEgens were synthesized by introducing TPE moieties into [1,2,5]thiadiazolo[3,4-g]quinoxaline and benzo[1,2-c;4,5-c']bis[1,2,5]-thiadiazole structures.<sup>886</sup> Non-doped OLEDs with these AIEgens as emitting layers exhibited NIR light with peak wavelength extending to 864 nm and  $\eta_{ext,\max}$  as high as 0.89%.

White LEDs have attracted considerable interest in recent years owing to their potential applications in lighting and display. As a large number of AIEgens with emission colors covering the whole visible spectral region have been found to exhibit outstanding EL performance, this not only allows the fabrication of full-color display but also the realization of efficient white LEDs.<sup>887,888,890</sup> Some nice examples are given in Figure 167, which demonstrate the applications of AIEgens in white LEDs. Wong and coworkers demonstrated hybrid white light emitters by exploiting gallium nitride (GaN)-based LEDs as blue emitters and AIE-active **382** as a down-converted yellow emitter.<sup>887</sup> White LEDs (WLEDs) with good performance can be fabricated in a relatively simple manner by facilely coating the efficient yellow-emitting organic AIEgen onto the commercial blue GaN LEDs (Figure 167). At a driving current of 30 mA, the obtained hybrid GaN/382 WLED displayed a high maximum luminous efficacy of 123.8 lm W<sup>-1</sup> and a luminance of 140 000 cd m<sup>-2</sup>. The CIE coordinate was (0.32, 0.33), approaching the ideal white color. An optical extraction efficiency of 45.4% from **382** layer with a pump leakage of 17.3% was measured for this hybrid WLED. This work suggests that the aggregate formation in AIE materials such as **382** was capable of greatly enhancing the device

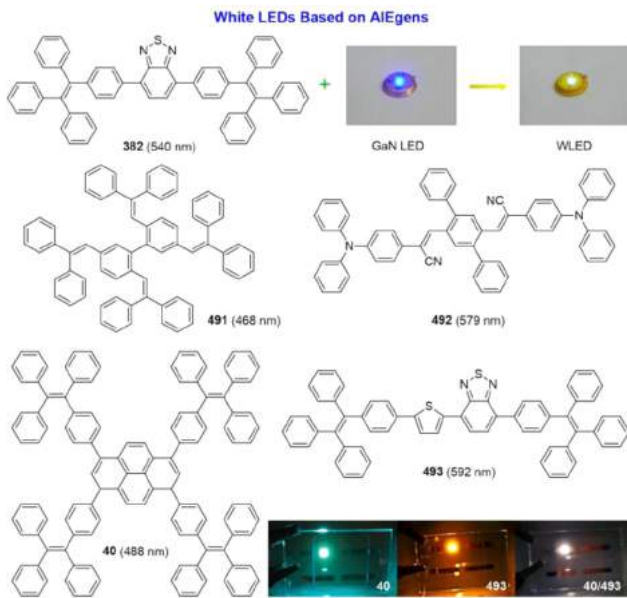


**Figure 167.** Representative examples of AIEgens used for white OLEDs. The EL maxima are given in parentheses. Insets: (upper) Photographs of blue emissive GaN LED and its resulting white device with AIEgen 382 (Adapted with permission from ref 887. Copyright 2013 The Optical Society.) and (lower) cyan, orange and white light-emitting EL devices using pure 40 and 493 and a mixture of them (40/493) as emitting layers, respectively. Reprinted from ref 890. Copyright 2010 IOP Publishing Ltd. Ref 890 is licensed under a Creative Commons Attribution 3.0 Unported Licence via <http://creativecommons.org/licenses/by/3.0/>.

extraction efficiency as well as improving the hybrid WLED performance.

Among the WLEDs, white OLEDs (WOLEDs) have drawn particular attention due to their merits such as low-cost fabrication process, high efficiency, light weight, ultrathin thickness, planar light emitting, and so forth. WOLEDs are generally required to hold long-term stability when working at high brightness and current density. Owing to their unique photochemical properties (e.g., high quantum yield, photostability and thermal stability) in the aggregate state, the AIE materials may be propitious to the attainment of long-term and color stable WOLEDs. In the light of such possibility, Ma's group has taken advantage of AIE materials to obtain such kind of WOLEDs.<sup>88</sup> Blue and orange light-emitting AIEgens, namely, 2,5,2',5'-tetrakis(2,2-diphenylvinyl)biphenyl (i.e., 491) and 1,4-bis(acyano-4-diphenylaminostyryl)-2,5-diphenyl-benzene (i.e., 492) were chosen as two complementary components for the WOLED construction (Figure 167). The non-doped blue OLED based on 491 showed an EL of 468 nm with a CIE coordinate of (0.16, 0.21),  $L_{\max}$  over 31 170 cd m<sup>-2</sup>, and  $\eta_{C,\max}$  of 6.2 cd A<sup>-1</sup>. The remarkably improved film quality and thermal stability have resulted from the cruciform structure of 491. The non-doped device constructed from 492 exhibited an orange EL peaked at 579 nm corresponding to a CIE coordinate of (0.50, 0.50). Compound 492 exhibited a better EL performance than that of the classical orange organic emitters such as rubrene, with  $V_{on}$ ,  $L_{\max}$ , and  $\eta_{C,\max}$  of 5 V, 14 667 cd m<sup>-2</sup>, and 4.0 cd A<sup>-1</sup>, respectively. On the basis of these two AIEgens, an efficient WOLED with a configuration of ITO/NPB (50 nm)/491 (20 nm)/492 (0.5 nm)/TPBi (60 nm)/LiF (0.5 nm)/Al (100 nm) has been constructed, which showed  $V_{on}$ ,  $L_{\max}$ ,  $\eta_{C,\max}$ , and  $\eta_{P,\max}$  recorded as 3.5 V, 25 350 cd m<sup>-2</sup>, 7.9 cd A<sup>-1</sup>, and 6.2 lm W<sup>-1</sup>, respectively. Such a device exhibited different CIE coordinates

located in the white light zone at various voltages, shifting from (0.36, 0.38) at low voltage (4 V) to (0.24, 0.29) at high voltage (10 V). Besides the high performance, this AIE-based WOLED showed advantages of simple device fabrication and excellent color stability, rendering it on the list of the best fluorescent WOLED.

There is another example to demonstrate the benefits that AIE materials have brought about to the area of WOLEDs. By employing AIE-active cyan and orange-red luminogens, Kwok and coworkers established non-doped WOLEDs with good performance. The cyan AIEgen 40 has been previously discussed as a superb light-emitting material for OLEDs (cf., Figure 164 and the inset of Figure 167). The AIEgen 493 possessed a  $\Phi_F$  of 55.4% in the film state. Its non-doped monochromatic OLED was turned on at 5.4 V and emitted an orange-red EL with  $L_{\max}$ ,  $\eta_{C,\max}$ , and  $\eta_{P,\max}$  of 8333 cd m<sup>-2</sup>, 6.3 cd A<sup>-1</sup>, and 2.9 lm W<sup>-1</sup>, respectively (inset in Figure 167).<sup>889</sup> Through utilization of these two complementary AIEgens as emitting layers, non-doped WOLEDs (inset in Figure 167) were fabricated, showing reduced efficiency roll-off.<sup>890</sup> The efficiency, white color purity, color rendering index (CRI), and color stability can be readily tuned by altering the thickness of the electron-blocking layer, i.e. *N,N'*-di(1-naphthyl)-*N,N'*-diphenyl-(1,1'-biphenyl)-4,4'-diamine (NPB). The WOLED with a 3 nm-thick NPB electron-blocking layer showed bright luminance ( $L_{\max}$ ) of 18 000 cd m<sup>-2</sup>, and good efficiencies of 7.4 cd A<sup>-1</sup> ( $\eta_{C,\max}$ ) and 4.0 lm W<sup>-1</sup> ( $\eta_{P,\max}$ ) with a high CRI of 90, while an impressive color stability with CIE coordinates changing from (0.34, 0.42) to (0.34, 0.40) was observed in the WOLED with a 4 nm thick NPB layer over a wide range of driving voltages. Performances of conventional doped-WOLEDs or other non-doped WOLEDs are usually sensitive to the doping concentration/dopant distribution or layer thickness, thus requiring stringent fabrication conditions. In comparison, the non-doped AIE-based WOLEDs are free of such problem and are hence more suitable for mass production due to their simple manufacture.

Besides their use as emitting layers by taking advantage of their highly efficient solid-state emission in OLEDs, the incorporation of some particular groups into the molecular structures would make the AIEgens capable of serving dual-/multifunctions. A series of AIEgens with good hole-transporting and electron-transporting properties and bipolar carrier mobility have been prepared and shown in Figure 168.<sup>104–106,111,112,117,121,123,124,891–897</sup> Their EL performances are summarized in Table 4. Carbazole is a nitrogen-bridged biphenyl isoelectronic to fluorene. Its HOMO energy level is higher than fluorene and it thus shows a good hole-transporting capability.<sup>111,117,121</sup> A carbazole-containing tetrasubstituted ethene 74 (Figure 168), which can be regarded to be made from TPE by replacing its two phenyl rings with carbazolyl groups, has been found to show good hole-transporting ability.<sup>121</sup> The OLED employing this AIEgen as both light-emitting and hole-transporting material showed a superior performance than the one using it solely as an emitter. As TPA is a famous hole-transporting moiety, it has been extensively used as a building block for the construction of AIE-active luminogens with hole-transporting properties.<sup>104–106,117,123,124</sup> Because of its multiple aromatic rotors and 3D conformation, the TPA-substituted TPE derivative 66 (Figure 168) is AIE-active and in the meantime it inherits the hole-transporting ability from the TPA unit. The OLED with a configuration of ITO/66/TPBi (40 nm)/LiF (1 nm)/Al (100 nm) emitted at 488 nm, exhibiting an  $L_{\max}$ ,  $\eta_{C,\max}$ ,  $\eta_{P,\max}$ , and  $\eta_{ext,max}$  of 11 700 cd m<sup>-2</sup>, 2.4 cd A<sup>-1</sup>, 1.0 lm W<sup>-1</sup>, and 1.1%, respectively. Though these data are much inferior to the one with an extra hole-transporting layer (HTL), they have demonstrated the great

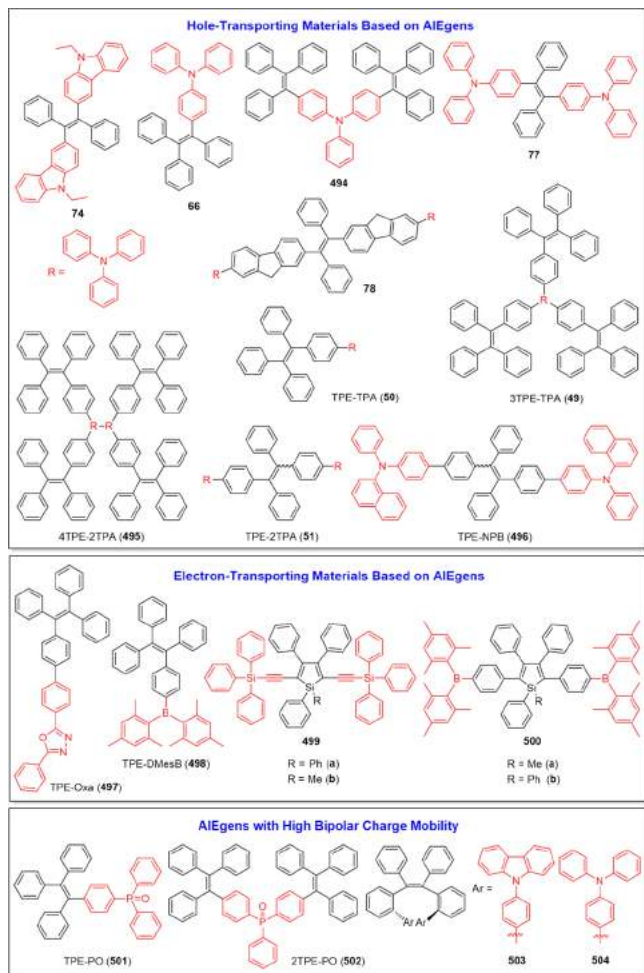


**Figure 168.** Examples of AIEgens showing excellent hole-transporting, electron-transporting properties, or bipolar carrier mobility in addition to their light-emitting properties.

potential of **66** as both an emitter and a hole-transporting material. When bridging the TPE moieties with a TPA unit, a cyan emissive AIEgen **494** was afforded. A win-win situation has been observed in **494** in terms of optical and electrical properties.<sup>123</sup> Luminogen **494** can act as an emitting layer and also a hole-transporting layer for fabricating OLEDs. The OLEDs based on **494** with and without an additional hole-transporting layer performed similarly. When substituting two of the phenyl rings of TPE with TPA units, the resulting AIEgen **77** performed better both in light emission and hole-transporting ability than **494**.<sup>123</sup> The  $L_{\max}$  and  $\eta_{C,\max}$  were  $15\,487\text{ cd m}^{-2}$ ,  $7.04\text{ cd A}^{-1}$  for the EL device of **77** without an extra hole-transporting layer, which are even higher than those recorded for the device using **77** only as a light-emitting material.

In addition to the replacement or substitution strategy, decorating the TPA moiety to AIE systems is also an effective approach to bestow the hole-transporting properties on these molecules. When an enlarged tetrasubstituted alkene was decorated with TPA units at its termini, the generated AIEgen **78** (Figure 168) showed improved performance than its shorter analogues.<sup>124</sup> The **78**-based devices with and without a dedicated HTL were both turned on at a low bias of 3.4 V. Although the  $L_{\max}$  of the device without a dedicated HTL ( $19\,100\text{ cd m}^{-2}$ ) was lower than that of the one with an NPB layer ( $25\,550\text{ cd m}^{-2}$ ), their brightness was almost identical at the same current density. Because of a lower current density under the same bias, the

device without HTL showed superior efficiencies in both  $\eta_{C,\max}$  and  $\eta_{P,\max}$  ( $13.7$  versus  $13.2\text{ cd A}^{-1}$  and  $11.3$  versus  $11.0\text{ lm W}^{-1}$ , respectively). Such results indicate that **78** works well as both a light emitter and a hole-transporting material, which is conducive to the simplification of device fabrication process and the reduction of production cost.

The TPE-TPA adducts with TPE-to-TPA number ratio varying from 3:1 (**49**),<sup>104</sup> 4:2 (**495**),<sup>104</sup> 1:1 (**50**)<sup>105</sup> to 1:2 (**51**)<sup>105</sup> have been designed and synthesized. All the adducts showed remarkable AIE properties and retained excellent hole-transporting capability of their TPA unit(s). Compared to the one with HTL, the EL device of **49** without the NPB layer exhibited a lower  $V_{on}$  (4.5 V), higher brightness ( $L_{\max} = 6\,935\text{ cd m}^{-2}$ ) and efficiencies ( $\eta_{C,\max} = 4.0\text{ cd A}^{-1}$ ,  $\eta_{P,\max} = 1.9\text{ lm W}^{-1}$ , and  $\eta_{ext,max} = 1.5\%$ ). The use of additional HTL sometimes is not necessarily good as it may break the charge balance in the EL devices. The OLED fabricated from **495** without a NPB layer showed fairly good performance. It started to emit at a low voltage of 4.1 V and its  $L_{\max}$ ,  $\eta_{C,\max}$ ,  $\eta_{P,\max}$  and  $\eta_{ext,max}$  reached  $10\,723\text{ cd m}^{-2}$ ,  $8.0\text{ cd A}^{-1}$ ,  $5.2\text{ lm W}^{-1}$ , and 3.7%, respectively. The devices based on **50** or **51** without HTL show performances comparable to or better than those with HTL, presumably due to the high hole-mobility of **50** and **51** coupled with the matching of their energy levels with the anode.<sup>105</sup> It is noteworthy that the non-doped OLED constructed with **51** simultaneously both as a light-emitting layer and a HTL shows superb EL performances. As displayed in Table 4, this device was turned on at a low voltage of 3.2 V and emitted a cyan light with the maximum brightness  $L_{\max}$  as high as  $33\,770\text{ cd m}^{-2}$ , and the  $\eta_{C,\max}$ ,  $\eta_{P,\max}$  and  $\eta_{ext,max}$  up to  $13.0\text{ cd A}^{-1}$ ,  $11.0\text{ lm W}^{-1}$ , and 4.4%, respectively.

NPB is among the most well-known hole-transporting materials for the OLEDs, and it also possesses high thermal and morphological stability. However, it is not a good luminoaphore in the solid state because of the severe intermolecular  $\pi-\pi$  stacking interactions. Introducing a TPE unit as a spacer into the NPB structure has generated an efficient solid emitter, which overcame the shortcoming of NPB.<sup>112</sup> The twisted and nonplanar TPE-NPB adduct **496** enjoys the properties of both components, namely, the AIE feature and hole-transporting nature as well as high thermal and morphological stability, which is suggestive of a win-win situation. Non-doped device utilizing **496** as an emitting layer emitted a green light with  $L_{\max}$  and  $\eta_{C,\max}$  of  $11\,981\text{ cd m}^{-2}$  and  $11.9\text{ cd A}^{-1}$ , respectively. Its  $\eta_{P,\max}$  and  $\eta_{ext,max}$  are  $8.9\text{ lm W}^{-1}$  and 4.0%, respectively. Even better EL performances were observed from the device with a configuration of ITO/**496** (60 nm)/TPBi (40 nm)/LiF (1 nm)/Al (100 nm), with the  $L_{\max}$ ,  $\eta_{C,\max}$ ,  $\eta_{P,\max}$  and  $\eta_{ext,max}$  as high as  $12\,607\text{ cd m}^{-2}$ ,  $13.1\text{ cd A}^{-1}$ ,  $7.8\text{ lm W}^{-1}$ , and 4.2%, respectively. These results manifest that **496** is a bifunctional AIEgen which can be used simultaneously as a light-emitting layer and HTL.

It is clear that EL materials with dual functions are more useful for technological applications and in great demand as they can largely simplify the device structure, shorten the processing, and lower the fabrication cost. Regarding this, AIEgens with electron-transporting properties should also be favorable to the OLED applications. Materials with efficient electron-transporting capabilities are essential to EL devices. Integration of electron-transporting and emitting layers into one can simplify the transport process, lower the barrier for charge injection, and hence enhance the device efficiency. 2,5-Diaryl-1,3,4-oxadiazole (Oxa) is an attractive building block for electron-transporting materials because of its electron-deficient aromatic units necessary for electron-transport along with its good stability and little negative

Table 4. EL Performances of Some Representative AIEgens with HT and/or ET Properties

AIEgen	device	TL	$\lambda_{\text{EL}}$ (nm)	$L_{\text{max}}^{\text{h}}$ (cd/m <sup>2</sup> )	$V_{\text{on}}^{\text{h}}$ (V)	$\eta_{\text{C,max}}^{\text{h}}$ (cd/A)	$\eta_{\text{P,max}}^{\text{h}}$ (lm/W)	$\eta_{\text{ext,max}}^{\text{h}}$ (%)
TPE-2TPA ( <b>51</b> )	A <sup>a</sup>	HTL: ✓	514	32 230	3.4	12.3	10.1	4.00
	B <sup>b</sup>	HTL: ×	512	33 770	3.2	13.0	11.0	4.40
<b>500a</b>	C <sup>c</sup>	ETL: ✓	552	9 610	7.5	6.6	2.4	2.13
	D <sup>d</sup>	ETL: ×	520	13 900	3.9	13.0	10.5	4.12
<b>500b</b>	C <sup>c</sup>	ETL: ✓	548	15 200	5.4	8.4	4.1	2.62
	D <sup>d</sup>	ETL: ×	524	12 200	4.3	13.9	11.6	4.35
<b>503</b>	E <sup>e</sup>	HTL: ×	489	6 250	6.8	4.8		2.10
	F <sup>f</sup>	ETL: ×	492	8 010	4.5	7.9		3.10
	G <sup>g</sup>	HTL, ETL: ✓	488	5 890	6.8	5.8		2.60
<b>504</b>	E <sup>e</sup>	HTL: ×	488	7 070	3.4	5.1		2.40
	F <sup>f</sup>	ETL: ×	492	9 060	8.0	3.3		1.30
	G <sup>g</sup>	HTL, ETL: ✓	492	6 420	4.3	4.7		2.00

<sup>a</sup>Device configuration A: ITO/NPB (40 nm)/AIEgen (20 nm)/TPBi (10 nm)/Alq<sub>3</sub> (30 nm)/LIF/Al (200 nm). <sup>b</sup>Device configuration B; ITO/AIEgen (20 nm)/TPBi (10 nm)/Alq<sub>3</sub> (30 nm)/LiF/Al (200 nm). <sup>c</sup>Device configuration C: ITO/NPB (60 nm)/AIEgen (20 nm)/TPBi (40 nm)/LiF (1 nm)/Al (100 nm). <sup>d</sup>Device configuration D: ITO/NPB (60 nm)/AIEgen (60 nm)/LiF (1 nm)/Al (100 nm). <sup>e</sup>Device configuration E: ITO/AIEgen (80 nm)/TPBi (10 nm)/Alq<sub>3</sub> (30 nm)/LIF (1 nm)/Al (100 nm). <sup>f</sup>Device configuration F: ITO/NPB (60 nm)/AIEgen (60 nm)/LiF (1 nm)/Al (100 nm). <sup>g</sup>Device configuration G: ITO/NPB (60 nm)/AIEgen (20 nm)/TPBi (10 nm)/Alq<sub>3</sub> (30 nm)/LiF (1 nm)/Al (100 nm).

<sup>h</sup>Abbreviations:  $L_{\text{max}}$  = maximum luminance,  $V_{\text{on}}$  = turn-on voltage,  $\eta_{\text{C,max}}$  = maximum current efficiency,  $\eta_{\text{P,max}}$  = maximum power efficiency, and  $\eta_{\text{ext,max}}$  = maximum external quantum efficiency.

effect on the luminescence process. Considering this, the Oxa moiety was covalently linked to the TPE unit, affording a new luminescent (**497**; Figure 168) featured with both AIE characteristic and electron-transporting property.<sup>891</sup> **497** possesses low-lying electronic band energies inherited from the Oxa part. Benefiting from its AIE activity, good electron-transporting, and hole-blocking properties, the two-layered device employing **497** as both a light-emitting material and an electron-transporting layer (ETL) exhibited superior performance to the device with a dedicated ETL. Three-coordinated organoboron compounds are particularly appealing and promising electron-transporting materials owing to their unique properties originating from the p<sub>π</sub>–π\* conjugation between the vacant p orbital on the boron atom and the π\* orbital of the π-conjugated skeleton.<sup>898–900</sup> A dimesitylboron moiety was incorporated into the TPE group, which generated a new three-coordinated boron compound **498** (Figure 168).<sup>892</sup> Synergistic effect has been observed for **498**: it showed typical AIE behaviors with a solid-state Φ<sub>F</sub> up to unity. Coupled with its good electron-transport capability, it showed excellent EL performance. Without an additional ETL, the two-layered OLED constructed from **498** performed even better than the one with ETL. The  $L_{\text{max}}$ ,  $\eta_{\text{C,max}}$ ,  $\eta_{\text{P,max}}$ , and  $\eta_{\text{ext,max}}$  were 5 170 cd m<sup>-2</sup>, 7.1 cd A<sup>-1</sup>, 3.2 lm W<sup>-1</sup>, and 2.7%, respectively, for the EL device where **498** functioned both as an emitter and an ETL.

Compared to TPE, siloles are better electron-transporting building blocks because they enjoy low-lying LUMO energy levels. As a consequence, siloles always show high electron affinity and fast electron mobility.<sup>901,902</sup> 2,5-Bis(triphenylsilyl)ethynyl-3,4-diphenylsiloles with different 1,1-substituents (**499a** and **499b**; Figure 168) have been reported to be remarkable AIEgens and excellent electron-transporting materials.<sup>893</sup> The attachment of electron-withdrawing triphenylsilyl ethynyl groups further allowed them to possess low HOMO and LUMO energy levels. The electron mobility of **499b** was in the range of  $5.0 \times 10^{-6}$ – $1.2 \times 10^{-5}$  cm<sup>2</sup> V<sup>-1</sup> s<sup>-1</sup>, and that for **499a** was  $3.1 \times 10^{-6}$ – $6.3 \times 10^{-6}$  cm<sup>2</sup> V<sup>-1</sup> s<sup>-1</sup>. Both values were higher than those of HPS, MPPS,<sup>903</sup> and tris(8-hydroxyquinolinato)aluminum (Alq<sub>3</sub>), a widely used electron-transport material with an electron mobility of  $2.3 \times 10^{-6}$  cm<sup>2</sup> V<sup>-1</sup> s<sup>-1</sup> under the same conditions.<sup>904</sup> Superb electron-transporting properties were

also found in other siloles,<sup>894,895</sup> such as **500a** and **500b** (Figure 168).<sup>895</sup> The integration of two potential electron-transporting elements, i.e., silole and dimesitylboron moiety, gave rise to tailored n-type emitters (**500a** and **500b**). These siloles possess AIE attributes with high Φ<sub>F</sub>s in the solid film state and enjoy lower LUMO energy levels than the corresponding parents 2,3,4,5-tetraphenylsiloles. Therefore, they are outstanding bifunctional EL materials with both excellent light-emitting and electron-transporting properties as indicated by the data shown in Table 4. Generally, their EL devices without dedicated ETLs showed much superior performances to the ones with additional ETLs. For example, the double-layer device based on **500b** exhibited greatly improved performances relative to its triple-layer device using **500b** as a light emitter and TPBi as an electron-transporting layer. The  $L_{\text{max}}$ ,  $V_{\text{on}}$ ,  $\eta_{\text{C,max}}$ ,  $\eta_{\text{P,max}}$ , and  $\eta_{\text{ext,max}}$  for the two-layer device of **500b** were 12 200 cd m<sup>-2</sup>, 4.3 V, 13.9 cd A<sup>-1</sup>, 11.6 lm W<sup>-1</sup>, and 4.35%, respectively. As far as we know, **500a** and **500b** are among the best n-type luminescent materials for the non-doped OLEDs.

Apart from those p-type (hole-dominated) and n-type (electron-dominated) AIE systems, through elaborate design, ambipolar (both hole- and electron-transporting) AIEgens can be achieved.<sup>896,897</sup> Since TPE itself is a hole-dominated unit with a hole mobility one order of magnitude higher than its electron mobility, TPE and its derivative are mainly used as hole-transporting and p-type host materials. Wang and Zhu et al. performed interesting work on the exploration of ambipolar AIEgens constructed from TPE systems.<sup>896</sup> To achieve this goal, the versatile phosphine oxide (PO) moiety which holds good electron-injection and electron-transporting properties was selected as an electron-transporting unit to fuse with the TPE unit(s). By gradually tuning the proportion of TPE and PO units, an array of n-type, ambipolar and p-type AIEgens were afforded. At a TPE/PO ratio of 1:1, almost identical electron and hole mobilities ( $\sim 2.3 \times 10^{-4}$  cm<sup>2</sup> V<sup>-1</sup> s<sup>-1</sup>) were achieved in AIEgen **501** (Figure 168). This suggests that **501** is a perfect ambipolar luminogen. At a TPE/PO ratio of 2:1, the resulting luminogen **502** showed a hole mobility higher than electron mobility. However, the difference is not very large and hence this luminogen could be considered to be bipolar.

Intriguingly, with ingenious molecular engineering, AEE-active luminogens based solely on hole-dominated building blocks can even be carved into luminescent materials with high bipolar charge mobility.<sup>897</sup> The cross-shaped (chiasmatic) luminogens (*Z*-1,2-bis[4'-(9-carbazolyl) biphenyl-2-yl]-1,2-diphenylethane (**503**) and (*Z*-1,2-bis[4'-(diphenylamino)-biphenyl-2-yl]-1,2-diphenylethane (**504**) were intensively emissive in the solution state due to their highly crowded structure, which greatly impaired the intramolecular motions (Figure 168). Nevertheless, they emitted more efficiently in the solid state with  $\Phi_{fs}$ s up to 100.0% and 85.0%, respectively. Fascinating properties were given by the rigid chiasmatic conformation coupled with intramolecular  $\pi$ - $\pi$  interactions. Although their corresponding linear isomers only displayed the hole-transporting property, **503** and **504** exhibited bipolar charge mobility. This is quite different from many organic luminophores, where the charge transport is dominated either by holes or electrons. Hole and electron mobilities as high as  $4.9 \times 10^{-4} \text{ cm}^2 \text{ V}^{-1} \text{ s}^{-1}$  and  $4.3 \times 10^{-4} \text{ cm}^2 \text{ V}^{-1} \text{ s}^{-1}$ , respectively, have been determined for **503**. **504** showed a similar bipolar charge-transporting capability with hole and electron mobilities of  $3.7 \times 10^{-4} \text{ cm}^2 \text{ V}^{-1} \text{ s}^{-1}$  and  $3.3 \times 10^{-4} \text{ cm}^2 \text{ V}^{-1} \text{ s}^{-1}$ , respectively. Thanks to the high bipolar charge mobility, OLEDs fabricated from the chiasmatic luminogens **503** and **504** without NPB (HTL) or TPBi/Alq<sub>3</sub> (ETL) layers performed well and exhibited good EL efficiencies (Table 4), demonstrating their multifunctionality. Notably, with  $L_{max}$ ,  $\eta_{C,max}$  and  $\eta_{ext,max}$  of  $8\,010 \text{ cd m}^{-2}$ ,  $7.9 \text{ cd A}^{-1}$ , and 3.10%, respectively, the device of **503** without the TPBi/Alq<sub>3</sub> layers performed much better than the one with both NPB and TPBi/Alq<sub>3</sub> layers and that without NPB layer.

Besides the OLEDs based on small molecules, there are another family of OLEDs which are built on light-emitting polymers and hence are referred to as PLEDs. Vacuum deposition which is a commonly-used fabrication method for small molecule-based OLEDs is not suitable for the fabrication of thin films of polymers. Nevertheless, solution processing such as simple spin coating makes the PLEDs more attractive, because this method is more suited to forming large-area films as compared to thermal evaporation. In comparison to a vast number of low molecular weight AIEgens used in OLEDs, a few polymeric counterparts with linear and hyperbranched structures are used in fabricating PLEDs.<sup>279,281,292,819,905</sup> For example, TPE-containing conjugated polymers **505** and **506** (Figure 169) featured with AIE characteristics have been utilized as light-emitting layers in the corresponding PLEDs.<sup>279</sup> Since achieving efficient charge injection as well as balanced mobility of both charge carriers inside the electroluminescent polymers is critical to the improvement of EL efficiency, hole-transporting carbazole group and electron-transporting Oxa moiety are introduced into the backbones of polyTPE, furnishing **505** and **506**, respectively. The PLEDs with unoptimized configurations of ITO/PEDOT:PSS (25 nm)/Poly-TPD (25 nm)/**505** or **506** (32 nm)/TPBi (35 nm)/Cs<sub>2</sub>CO<sub>3</sub> (8 nm):Ag (100 nm) were fabricated. Results showed that the EL performances of **505** and **506** were much better than those without carbazole and Oxa groups, with  $V_{on}$ ,  $L_{max}$  and  $\eta_{C,max}$  of 5.7 and 4.8 V, 3 609 and 3 109 cd m<sup>-2</sup>, and 1.17 and 1.14 cd A<sup>-1</sup>, respectively. These preliminary results demonstrate the application potential of AIE polymers in the area of PLEDs.

Polyfluorene is one of the typical polymers used in PLED displays. However, it is ACQ-active. Like the small molecular systems, the incorporation of TPE units into the fluorene-based polymeric systems through appropriate covalent bonding can

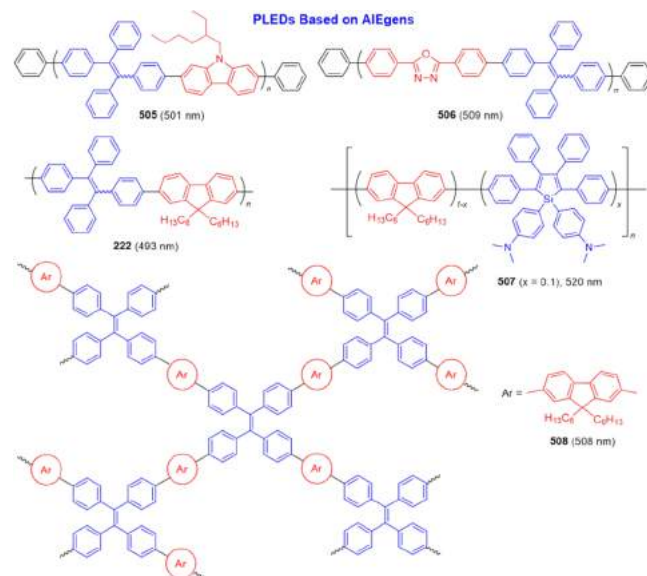


Figure 169. Examples of AIE-active polymers applied for polymer light-emitting diodes (PLEDs). Their EL maxima are given in parentheses.

also turn around the ACQ effect. The TPE-containing conjugated polyfluorene **222** is such an example (Figure 169).<sup>281</sup> Thanks to its AEE property, it was adopted as an emitter in the EL devices with configurations of ITO/PEDOT:PSS (45 nm)/PVK:**222** (1:1 wt %, 55 nm)/TPBi (38 nm)/Ca:Ag (device I) and ITO/PEDOT:PSS (45 nm)/PVK:OXD-7:**222** (3:1:3 wt %, 55 nm)/TPBi (38 nm)/Ca:Ag (device II). In these devices, PVK was blended with **222** to enhance the film quality and hole-transporting capability. The OXD-7 in device II was employed as an electron-transporting dopant to balance the holes and electrons. The  $V_{on}$ ,  $L_{max}$  and  $\eta_{C,max}$  were 4.6 V, 1 527 cd m<sup>-2</sup>, and 0.95 cd A<sup>-1</sup>, respectively, for device I, and 5.0 V, 2 300 cd m<sup>-2</sup> and 1.49 cd A<sup>-1</sup>, respectively, for device II, indicating the importance of charge-carrier balance for the EL efficiency. In like manner, the silole derivatives can work as ACQ-to-AIE converters. The HPS derivative with dimethylamino groups on the 1,1-positioned phenyl rings of the silole core was copolymerized with fluorene monomers in different ratios to afford the HPS-containing conjugated polymers which emit efficiently in the aggregate state.<sup>905</sup> These polymers were utilized as light-emitting materials in PLEDs, among which, the EL device built on **507** (Figure 169) performed best with a configuration of ITO/PEDOT (50 nm)/**507** (80 nm)/TPBi (30 nm)/Ba/Al. Such a device was turned on at 6.4 V, emitting a green light at 520 nm with  $L_{max}$ ,  $\eta_{C,max}$  and  $\eta_{ext,max}$  of  $4\,880 \text{ cd m}^{-2}$ ,  $7.96 \text{ cd A}^{-1}$ , and 3.18%, respectively. The results obtained from **222** and **507** have clearly demonstrated the feasibility of using AIEgens to improve the performance of ACQ-active polymers in PLEDs.

Hyperbranched TPE-fluorene polymer **508** (Figure 169) was found to exhibit marked AIE feature and high thermal stabilities.<sup>819</sup> The device with a configuration of ITO/PEDOT:PSS (25 nm)/Poly-TPD (25 nm)/**508** (32 nm)/TPBi (35 nm)/Cs<sub>2</sub>CO<sub>3</sub> (8 nm):Ag (100 nm) was fabricated to investigate the EL properties of **508**. The AIE-active hyperbranched conjugated polymer **508** showed relatively better EL performance in comparison with most of the conjugated hyperbranched polymers, with a low turn-on voltage of 7.5 V and maximum current density up to  $164 \text{ mA cm}^{-2}$  and an  $L_{max}$  of  $948 \text{ cd m}^{-2}$ . The  $\eta_{C,max}$  was up to  $1.15 \text{ cd A}^{-1}$ , which was higher than most of the conjugated hyperbranched polymers

reported so far. These good results should be ascribed to the AIE activity of **508**.

In general, AIEgens possess very high luminescence quantum efficiencies in the aggregate state with many of their values close to 100.0%. They are usually quite stable in air and show excellent thermal and morphological stabilities. Furthermore, their molecular structures are easy to modify by molecular engineering endeavors to give new luminophors with different emission colors. Thus, AIEgens are a class of promising materials for OLED applications. More specifically, as we discussed in this subsection, the full-color display and white OLEDs can be realized with AIEgens as their emission colors cover the whole visible spectrum. Fusion of ACQphores and AIEgens always results in win-win situations with improved EL performances and/or bi-/multi-functionalities. Considering these satisfactory results and works, the commercialization of AIE-based EL materials may be one of their development trends. Moreover, the research on red emitters and light-emitting polymers used for EL devices leaves relatively large room for development.

**5.3.2. Self-Assembly Systems.** Self-assembly itself is an interesting process that has attracted tremendous research interest. When such a process is related to fluorescent molecules, it is particularly intriguing owing to the potential fabrication of nano/microstructured materials, which provide opportunities for the manufacture of miniaturized high-performance photonic and electronic devices. For instance, fluorescent nanowires prepared from  $\pi$ -conjugated organic molecules via an *in-situ* and low-cost self-assembly approach usually possess high flexibility and diversity, high volume production, and easy modulation of photoelectric properties. Thus, they are promising materials for innovative nanodevices and applications, especially in nanoscale photonics and optoelectronics, such as OLEDs, field-effect transistors (FETs), organic light emitting transistors (OLETs), and solar cells. Recent studies show that the self-assembled nano/micro-scaled ordered structures are closely associated with the photoelectric properties of fluorescent molecules, such as waveguiding, polarized emission, high carrier mobility, and so on. AIE molecules are a family of unique luminescent materials and thereby their self-assembly and the resulting assembled structures deserve special attention and penetrating research. There are quite a few interesting works exemplifying the peculiarities of self-assembling AIE systems.<sup>98,138,139,256,893,906–912</sup>

For example, the TPE derivative decorated with (*S*)-(+)-2-(6-methoxynaphthalen-2-yl)propanoate moieties (**509**; Figure 170A) showed a typical AIE activity.<sup>906</sup> Fluorescent nanowires can be facilely fabricated with this AIEgen (**509**) through a simple self-assembly process. Since 1D nanowires have attracted particular interest due to their small size, high aspect ratio, and possible quantum confinement effects,<sup>913,914</sup> the attainment of fluorescent nanowires is of great value (Figure 170B). Furthermore, in the solution, the fluorescent nanowires of **509** could further self-assemble to form macroscopic fluorescent thin films (Figure 170C,D). With the aid of SEM analysis, the detailed self-assembly process from nanospheres to nanowires and further to fluorescent thin films has been clearly elucidated (Figure 170A). The nanospheres self-assembled to form well-aligned lines which resembled strings of pearls. Following such a “polymerization” process, the aligned nanoparticles further merged to afford nanowires which then intertwined and overlaid to generate a macroscopic thin film. As the  $\pi-\pi$  interaction between the naphthalene units in the molecules of **509** was supposed to be the most possible driving force for the self-assembly, the naphthalene

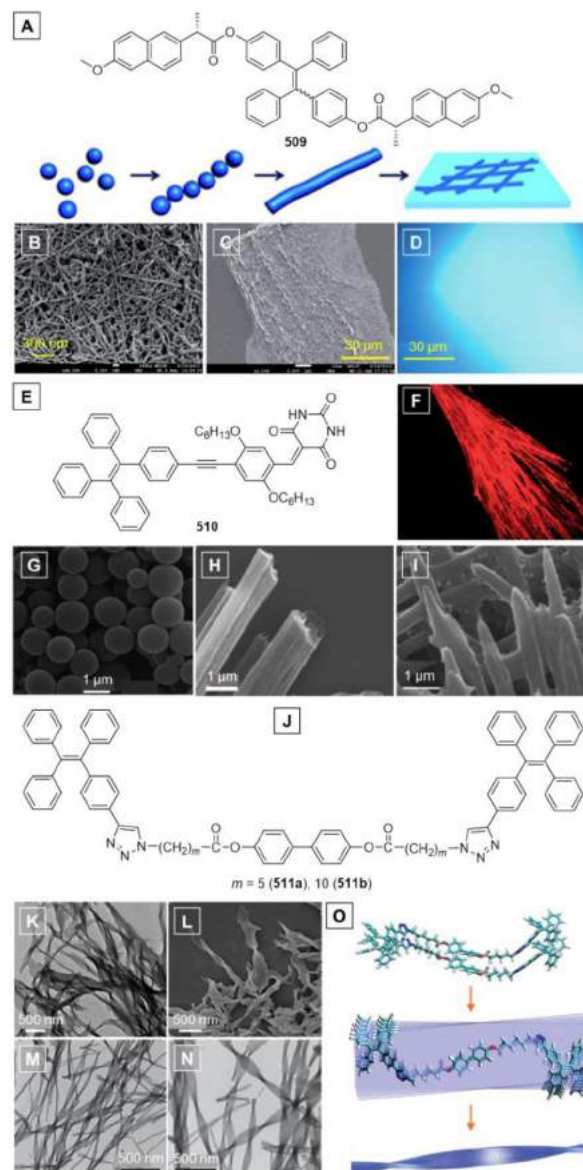


**Figure 170.** Representative examples of AIEgens decorated with self-assembly directing moieties and showing various assembled micro/nanostructures. (A) Molecular structure of **509** and schematic illustration of the formation of self-assembled nanowires and films of **509**. SEM images of (B) self-assembled nanowires and (C) thin films of **509**. (D) Fluorescence microscopy of the thin-film shown in panel C. Adapted with permission from ref 906. Copyright 2014 Royal Society of Chemistry. (E) Molecular structure and (F) fluorescent photograph of microrods formed by **510**. (G) SEM images of micro/nano-spheres of **510**. (H) SEM images of (I) nanotubes formed by the coassembly of **510** and melamine. Adapted with permission from ref 907. Copyright 2013 Royal Society of Chemistry. (J) Molecular structure of **511**. (K) TEM and (L) SEM morphologies for the gel of **511b**. (M and N) TEM images for the precipitates of **511a** formed in THF/water mixture (4/6 in volume) formed upon standing for 6 h. (O) A possible packing motif of **511a** and the mechanism for the formation of helical nanofibers. Adapted with permission from ref 908. Copyright 2012 Royal Society of Chemistry.

groups were hence considered to be the self-assembly directing moieties.

Hydrogen-bonding is another well-known non-covalent force driving the molecular self-assembly. Barbituric acid is a widely used building block for hydrogen-bonding-dominated self-assem-

systems. Regarding this, the TPE unit was functionalized with barbituric acid through a 1,4-bis(hexyloxy)-2-(prop-1-yn-1-yl)-benzene bridge in an effort to create an AIE-active self-assembly system.<sup>907</sup> The resulting TPE derivative **510** displayed the characteristics of TICT plus AIE and emitted a red light due to the strong D-A effect and extended  $\pi$ -conjugation (Figure 170E,F). Luminogen **510** possessed the ability to self-assemble into nanospheres upon natural evaporation of its solutions, such as pure acetonitrile, acetonitrile/ethanol mixture and acetonitrile/water mixture (Figure 170G). More importantly, **510** could facilely self-assemble into highly fluorescent crystalline microrods from its diethyl ether/hexane mixtures (Figure 170F), which exhibited good optical wave-guiding behaviours that would be discussed later. Moreover, this barbituric acid-decorated AIEgen could co-assemble with melamine through the hydrogen-bonding interactions. In the presence of 10 equiv of melamine, nanotubes/nanorods were formed, with most of their ends unsealed (Figure 170H). Increasing the melamine amount sealed the tubes' ends (Figure 170I). The cooperative effect of non-covalent forces, such as hydrogen bonding,  $\pi$ - $\pi$  interaction, and van der Waals forces might be the main driving forces for the self-assembly of **510**.

AIEgens **511a** and **511b** with solid-state  $\Phi_F$ s up to unity were generated by melding alkyne-modified TPE with diazide-carrying biphenyl via "click chemistry" (Figure 170J).<sup>908</sup> Luminogens **511a** and **511b** could form gels upon cooling their condensed hot solutions to room temperature or 4 °C. Self-assembled white wooly solids were generated through slow addition of dilute THF solutions of **511a** and **511b** into non-solvents such as *n*-hexane and water. As revealed by the TEM and SEM analyses, both gels and precipitates of **511a** and **511b** exhibit structures similar to those of the aggregates formed in non-solvents (Figure 170K–N). These results indicate that these AIEgens can facilely self-assemble into brightly emissive (twisted/helical) nanofibers. Visual molecular dynamics simulation of **511a** was performed with the aim to gain further insights into the self-assembly processes and their mechanism. As depicted in Figure 170O, adjoining molecules were packed together with the help of effective intermolecular interactions. Whilst the biphenyl and TPE units were stacked face to face, which favored the formation of assemblies with tiny twisted angles as a result of their nonplanar conformations with flexible alkyl chains. In this sense, the central alkyl-substituted biphenyl groups can be taken as directing moieties for the self-assembly. Such twistingly packed molecules finally gave rise to mesoscopic helical fibrous aggregates. The high emission efficiency and inherent self-assembling capacity make **511a** and **511b** attractive materials for optoelectronic nanodevices.

Perylene bisimides (PBIs) possess electron-transporting capability and ready-to-form well-tailored supramolecular structures. However, they suffer from the ACQ effect, which restricts their potential applications. Such a problem has been successfully tackled by chemically modifying the PBI core with two TPE units at the bay positions (e.g., 1- and 7-positions) but without sacrificing the self-assembly nature of PBI.<sup>908</sup> Luminogen **43** exhibited an evident AIE behavior and emitted brilliant red fluorescence in the solid state (Figure 171A). As shown in Figures 171B–I, the attachment of bulky and twisted TPE motifs did not interrupt the formation of ordered assemblies. Well-defined fluorescent 1D microstructures, such as fibers (Figures 171B–E), wires (Figure 171F,G) and rods (Figure 171H,I) were formed in different non-solvent/solvent mixtures, such as water/THF, methanol/DCM, hexane/DCM, methanol/dioxane, etc. The crystalline fibrils and prism-like microstructures implied their potential wave-guiding ability.

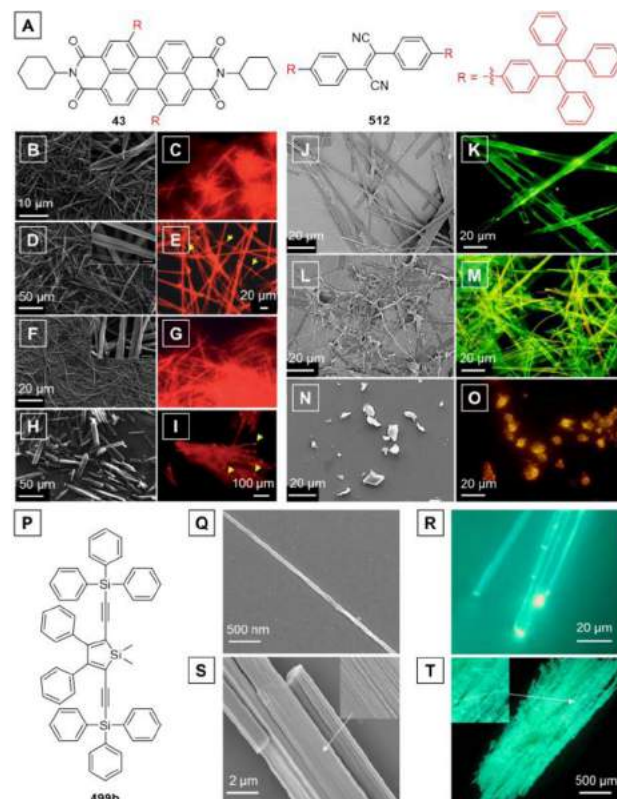


**Figure 171.** Representative examples of AIEgens showing self-assembly properties carrying no directing moieties. Chemical structures of (A) **43** and **512**, and (P) **499b**. (B, D, F, H) SEM images of the morphologies and (C, E, G, I) corresponding confocal fluorescence images of the aggregates formed by **43** molecules in different conditions. (J, L, N) SEM and (K, M, O) fluorescence microscopic images of **512** formed from THF/water mixtures with different  $f_w$ : (J, K)  $f_w = 50$  vol %, (L, M)  $f_w = 60$  vol %, and (N, O)  $f_w = 70$  vol %. (Q, S) SEM micrographs of fibrils of **499b** obtained from methanol/dichloromethane mixtures and (R, T) fluorescent micrographs of microrods of **499b**. Panels B–I are reprinted with permission from ref 98. Copyright 2012 Royal Society of Chemistry. Panels J–O are reprinted from ref 909. Copyright 2013 American Chemical Society. Panels Q–T are reprinted with permission from ref 893. Copyright 2013 Wiley-VCH Verlag GmbH & Co. KGaA.

Since there was no additional directing moiety, the self-assembly of **43** was rationalized to be driven by the robust  $\pi$ - $\pi$  interactions between the large planar PBI cores. Different from **43**, no large planar moiety was present in the molecular structure of **512** (Figure 171A). Instead, the twisted TPE substituents hampered close  $\pi$ - $\pi$  interactions, making the self-assembly process a daunting task. The dipole–dipole interactions between the cyano groups were hence regarded to be the primary driving force for the self-assembly of **512**.<sup>909</sup> Distinct microstructures were obtained under different conditions (Figure 171J–O). The ordered microribbons formed in the THF/water mixture with  $f_w = 50$  vol % emitted intense yellowish-green light (Figure 171J,K). The self-assemblies under this situation are microcrystals. When the  $f_w$  was increased to 60 vol %, the sizes of the microscaled ribbons became smaller and simultaneously the morphology regularity was also lowered. Instead, thinner and irregular microfibers with yellow emissions were obtained under such conditions (Figure 171L,M). No ordered microstructures were obtained when  $f_w$  rose to 70 vol % (Figure 171N) and featureless aggregates with orange luminescence were generated, which was indicative of their amorphous nature (Figure 171O).

Apart from TPE-based AIEgens, quite a few other AIE-active luminogens have also been found to undergo self-assembly under proper conditions. The previously discussed silole derivative **499b** (Figure 171P), for example, could easily generate ordered microstructures through a simple natural admixing and the subsequent evaporation of its DCM/methanol (Figures 171Q–T).<sup>893</sup> To be specific, the addition of poor solvent like methanol into the DCM solution of **499b** with a concentration of  $1 \text{ mg mL}^{-1}$  afforded thin 1D nanorods at the solvent interface. The fibrils were nano-scaled in diameter and tens of micrometers in length (Figure 171Q). As the solvents evaporated, more and more nanocables were formed and their association resulted in fibrils with micrometer sizes (Figure 171S). Further gathering of the microrods resulted in the formation of bundles of **499b**. It is noteworthy that the majority of the rods are uniformly arranged in a parallel fashion, indicating that the microfibrils are constructed through side-by-side self-assembly of the nanorods. The well-organized cables exhibited strong green light (Figure 171T), especially at the cross sections (Figure 171R). The self-assembly process driven by  $\pi$ – $\pi$  interactions together with the intense light emission of **499b** makes the luminogen a promising candidate in the fabrication of miniature optoelectronic devices.

Actually, besides the prototypical AIEgens such as TPE derivatives and siloles, a number of newly developed AIEgens have shown the self-assembling behaviors, most of which are red emitters.<sup>138,139,256,912</sup> Take **195** for example.<sup>256</sup> Fluorophore **195** (Figure 172) features an AIE effect and possesses a D-A electronic structure, resulting in bright red fluorescence in the aggregate state. Large-scale nanoballs (i.e., nanospheres) with open holes on their surfaces were readily formed, when the sample was collected on the silicon grid immediately after the injection of its THF solution into hexane under vigorous stirring (Figure 172B). As confirmed by the TEM analyses, all the spherical nanostructures were hollow in nature with an average diameter of 150 nm and most of them started to form open holes (Figure 172C). It is notable that the vesicles were not well isolated. Instead, their edges were cohered and their membranes were shared. The adjoining nanovesicles fused with one another, which eroded some of their membranes, representing a growing tendency of the vesicles. Samples obtained after aging in the THF/hexane mixture for 3 min were the intermediate states of the morphology transition. As revealed by both the SEM (Figure 172E) and TEM (Figure 172F) images, the growing of the vesicles was 1-D. They were aligned one-by-one in a linear way, leading to a “pearl-necklace”-like morphology. The membranes of the vesicles were got through to afford a tubular structure (inset in Figure 172F). The coexistence of 0-D nanovesicles and 1-D nanostructures was also witnessed by the SEM examination (Figure 172G). The sample prepared after mixing the THF solution with hexane for 30 min presented the view of large-scale 1-D nanotubes (Figure 172H). Such a morphology transition in the self-assembled structure can also be observed under CLSM (Figure 172D,I). To fully understand the fusion–erosion–reconstruction morphology transition process, a scheme was drawn and shown in Figure 172J. The dipole–dipole interactions with varying strengths and directions drove the molecules of **195** to assemble into 0-D nanostructures and finally developed into 1-D nanotubes. The dipole–dipole interactions, van der Waals forces (e.g., amphiphilic effect), and  $\pi$ – $\pi$  interactions collectively functioned as driving forces for the self-assembling into hollow nanospheres. The vesicles were fused one by one in a 1-D fashion and were eroded into thermodynamically more stable tubular structures. The nanostructures were further

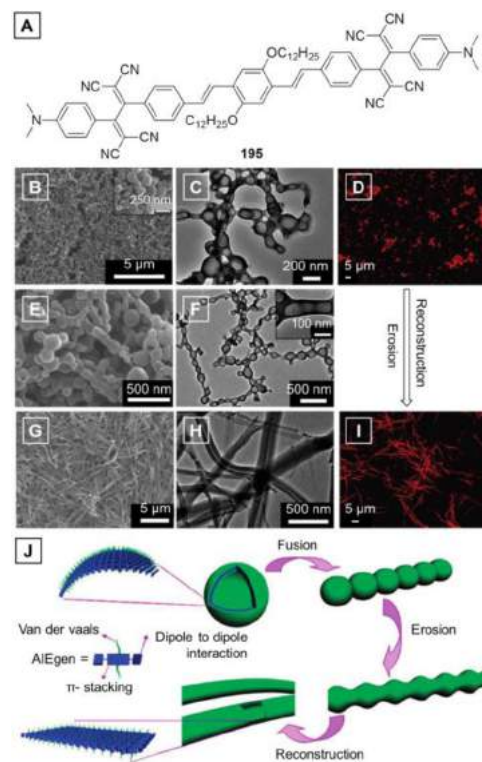


**Figure 172.** Representative example of AIEgen showing self-assembly property as a result of multiple intermolecular interactions. (A) Chemical structure of **195**. (B, C, E–H) Typical morphologies and (D, I) the corresponding CLSM images of the nanostructures formed by **195**. (B, C) SEM and TEM images of large-scale vesicles collected immediately after injecting the solution in THF into well-stirred hexane. The inset in panel B shows the magnified SEM image. (E, F) SEM and TEM images of intermediates of morphology transition. (G, H) SEM and TEM images of the final formed 1-D nanostructures. (J) Schematic representation of the nanostructure formation of **195** and the morphology transition process. Adapted from ref 256. Copyright 2008 American Chemical Society.

reconstructed, releasing the curvature energy (i.e., strain) and aiding the ultimate formation of 1-D nanotubes.

**5.3.3. Organic Field-Effect Transistors (OFETs).** The research field of OFETs is very active, with newly synthesized and tested organic compounds reported weekly in prominent research journals. Many review articles exist documenting the development of this area.<sup>915–917</sup> Since an electric current flows through such a transistor, it can be utilized as a light-emitting device, thus integrating current modulation with light emission. In this regard, AIEgens are expected to be advantageous to the conventional OFET materials in terms of its efficient solid-state light emission. Although the OFET-related AIE research is in its infancy stage, to our delight, there have been some examples demonstrating the application prospect of AIE systems in OFETs, as shown in Figure 173.<sup>255,918,919</sup> The emission colors of these luminogens vary from cyan to red and then to NIR.

Inspired by the good results achieved in the OLED using **51** as both light-emitting and hole-transporting material (*vide supra*, cf., Table 4), Tang and Miao et al. further investigated its OFET application.<sup>918</sup> Before its utility in OFETs, the good hole-transporting property of AIEgen **51** was further confirmed by cyclic voltammetry analysis and time-of-flight (TOF) transient photocurrent technique. A high HOMO energy level ( $-5.15 \text{ eV}$ ), which was close to the work function of metallic gold

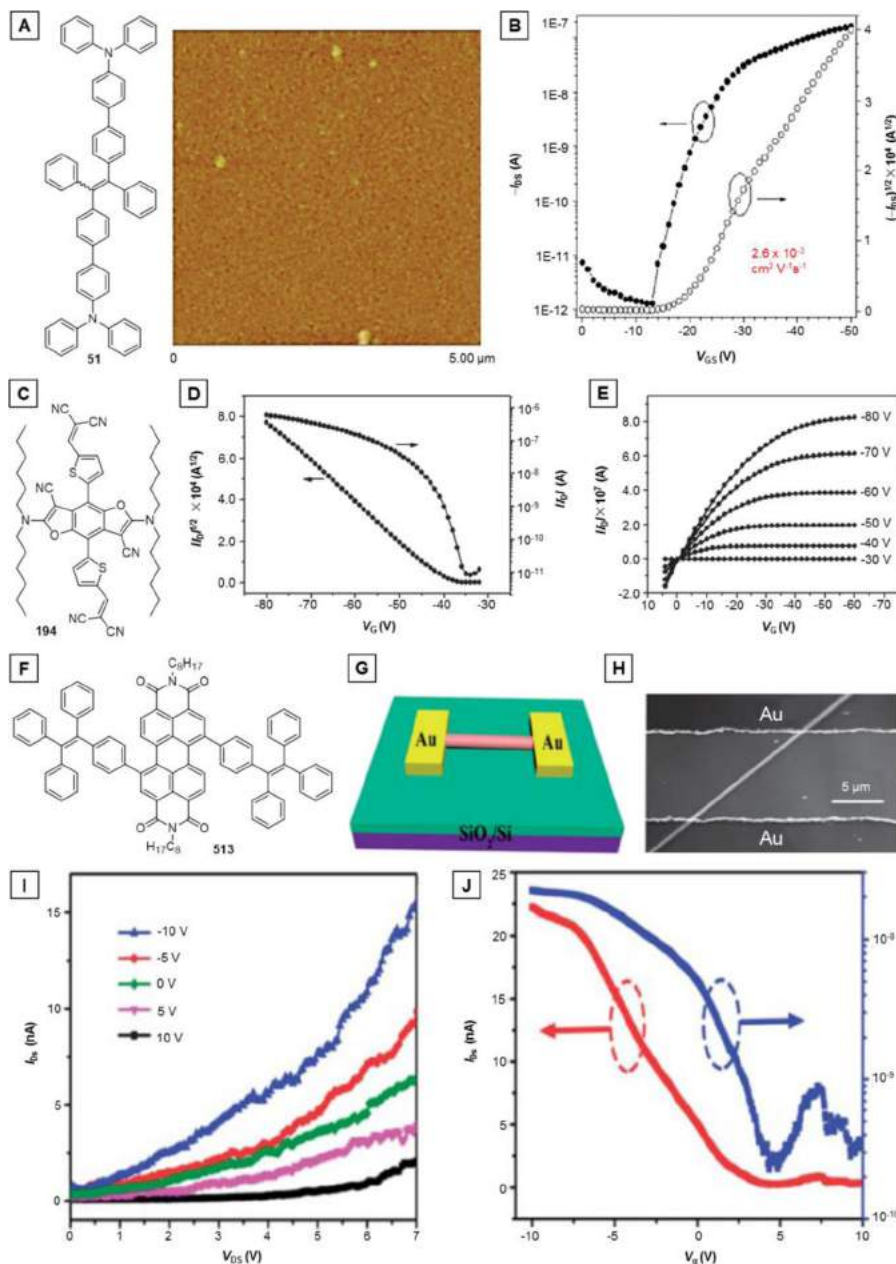


**Figure 173.** Representative examples of AIEgens used for organic field effect transistors (OFETs). Chemical structures of (A) **51**, (C) **194**, and (F) **513**. (A) AFM image of thin film of **51** deposited on the OTS-treated silicon substrate. (B) Drain current ( $-I_{DS}$ ) and ( $-I_{DS}$ ) $^{1/2}$  versus gate voltage ( $V_{GS}$ ) at a drain voltage ( $V_{DS}$ ) of  $-50$  V in a FET device of **51** with a channel length ( $L$ ) of  $100$  nm and a channel width ( $W$ ) of  $1$  mm. Reprinted with permission from ref 918. Copyright 2011 Royal Society of Chemistry. (D) Transfer and (E) output characteristics for OFET based on thin-film of **194** deposited on OTS-modified  $\text{SiO}_2/\text{Si}$  substrate at  $70$  °C. Reprinted with permission from ref 255. Copyright 2014 Wiley-VCH Verlag GmbH & Co. KGaA. (G) Schematic illustration and (H) SEM image of a FET based on an individual organic nanowire of **513**. (I)  $I_{DS}$  versus  $V_{DS}$  curves measured at room temperature under gate voltage ranging from  $-10$  V to  $10$  V with a step of  $5$  V. (J) Corresponding  $I_{DS}$  versus  $V_g$  curves of the device at  $V_{DS} = 10$  V. Reprinted with permission from ref 919. Copyright 2013 Royal Society of Chemistry.

( $-5.10$  eV) and favorable for the fabrication of OLEDs and OFETs, was determined. The hole mobility was estimated to be  $5.2 \times 10^{-4} \text{ cm}^2 \text{ V}^{-1} \text{ s}^{-1}$ , which was higher than that of *N,N'*-diphenyl-*N,N'*-bis(3-methylphenyl)-1,1'-biphenyl-4,4'-diamine, a well-known hole-transporting material, under the same test conditions. The FETs were fabricated by depositing  $60$  nm-thick **51** films onto silicon wafers which had been pretreated with self-assembled monolayer of octadecyltrichlorosilane (OTS) through thermal evaporation under high vacuum. The amorphism of the obtained **51** film was indicated by the absence of sharp peaks from X-ray diffractogram and the smooth

morphology as observed under the atomic force microscope (AFM; Figure 173A).<sup>918</sup> FETs of **51** with different channel lengths and widths were tested in air under ambient conditions, with the results showing that **51** worked as a p-type semiconductor. The transfer  $I$ - $V$  curve of **51** recorded under optimized conditions is exhibited in Figure 173B, from which a field-effect mobility up to  $2.6 \times 10^{-3} \text{ cm}^2 \text{ V}^{-1} \text{ s}^{-1}$  was calculated in the saturation regime using a specific equation. Such a value was quite high for amorphous organic semiconductor films. Moreover, the on/off ratio of the drain current acquired between  $0$  and  $-50$  V gate bias from the transfer  $I$ - $V$  curve was larger than

$2 \times 10^4$ . Combining its OFET performance with its efficient photoluminescence and EL, the dual-/multifunctional **51** is anticipated to find an array of applications in organic electronics and optics.

The new cruciform D-A molecule **194** was reported to be AIE-active (Figure 173C).<sup>255</sup> It is another dual-functional luminogen with both remarkable solid-state red emission and p-type semiconducting capability. Its dual functions are ascribable to its unique crystal structure with massive intermolecular CN $\cdots\pi$  and hydrogen bonding interactions rather than intermolecular face-to-face  $\pi\cdots\pi$  stacking interactions. The molecules of **194** were vacuum deposited at different temperatures to form thin films on the OTS-modified substrates. The typical transfer and output characteristics of an OFET constructed with a thin film of **194** are displayed in Figure 173D,E, manifesting its p-type semiconducting behavior as the drain current ( $I_{DS}$ ) was increased by applying the negative  $V_{GS}$ . Such a result was in good accordance with the HOMO energy level ( $-5.26$  eV) of **194**. The as-prepared OFET exhibited a low hole mobility ( $3.0 \times 10^{-4}$  cm $^2$  V $^{-1}$  s $^{-1}$ ), which can be further improved by the temperature elevation. When the OTS-treated substrate was heated to 70 °C, the hole mobility became higher and reached  $1.5 \times 10^{-3}$  cm $^2$  V $^{-1}$  s $^{-1}$ , with an on/off ratio and threshold voltage of  $10^5$  and 40–41 V, respectively. Such a dependence of the **194**-based FETs on the substrate temperature was attributed to the variation of the thin film morphology and intermolecular packing order caused by the temperature change. Notably, its p-type semiconducting properties such as mobility, on/off ratio, and threshold voltage are air stable and reproducible.

From the structure point of view, the TPE-PBI adduct **513** shown in Figure 173F is quite analogous to **43**, which is a red/NIR-emissive AIEgen with self-assembly ability. Naturally, as determined by the structure, similar properties were possessed by **513**.<sup>919</sup> For example, it could undergo interfacial self-assembly in a DCM/methanol (1/2, v/v) biphasic system, affording highly ordered and uniform microwires with intense red emission, due to the AIE attribute. A microwire field-effect transistor (MFET) device was constructed using the self-assembled microwire of **513**. With the aim of studying the electrical properties of the organic microwire, individual MFET was fabricated by dispersing the as-prepared microwire of **513** on the SiO<sub>2</sub>-coated silicon substrate (Figure 173G,H). The  $I_{DS}$  versus source-drain voltage ( $V_{DS}$ ) of a single MFET was measured at ambient conditions under varied gate voltage ( $V_g$ ) in the range of -10 V to 10 V with a step of 5 V (Figure 173I). As can be seen from Figure 173J, at an identical  $V_{DS}$ , the  $I_{DS}$  decreased with an increase in the  $V_g$ , which was suggestive of typical p-type semiconducting characteristics of the microwire of **513**. The  $I_{DS}$ – $V_g$  curve of the device was also plotted in linear and log scale. The on/off ratio and threshold voltage were recorded to be  $\sim 10^2$  and 3.5 V, respectively. The effective hole mobility and capacitance were estimated to be  $\sim 3.1 \times 10^{-5}$  cm $^2$  V $^{-1}$  s $^{-1}$  and  $\sim 1.5 \times 10^{-15}$  F, respectively.

**5.3.4. Optical Waveguides.** Luminescent materials with optical waveguiding properties are a class of attractive functional materials.<sup>920</sup> A large variety of AIEgens possessing optical waveguide effects with their emission color spanning the whole visible spectral region have been developed.<sup>32,163,255,907,912,921–923</sup> Di(*p*-methoxyphenyl)dibenzofulvene (**514**; Figure 174A), for example, has been reported to be a member of this family.<sup>921</sup> The RIR-dominated AIE attribute renders it highly fluorescent in the solid state and the variation in the molecular conformation accounts for its polymorphism-dependent emission (Figure 174A). Polymorph **514a** emitted a blue light peaked at 466 nm, while

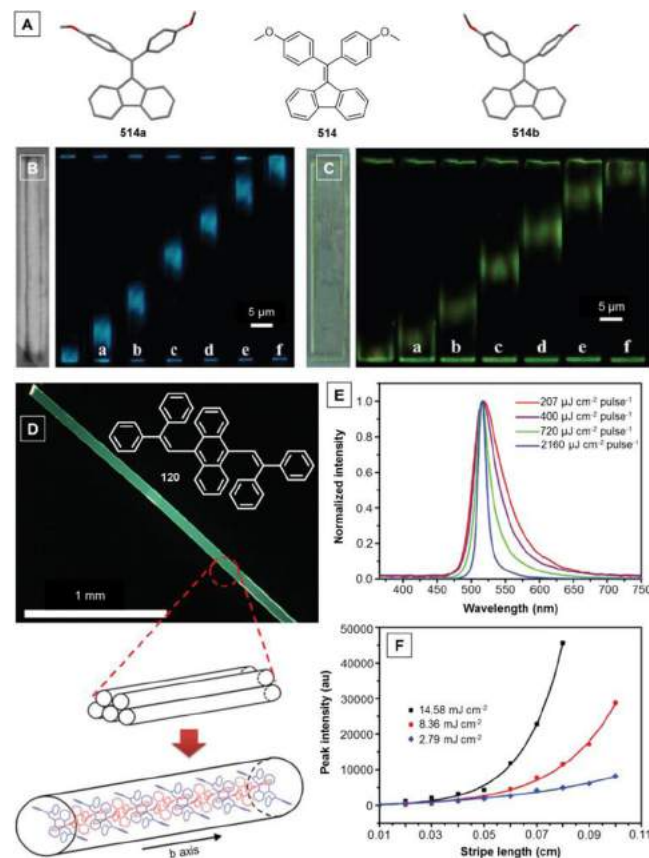


**Figure 174.** Representative examples of blue and green light-emitting AIEgens with waveguiding properties. (A) Chemical structure and crystal structures of the two polymorphs of **514**. Bright-field images (on the left side of each PL image) and microarea PL images by exciting identical microcrystals of (B) **514a** and (C) **514b** at six different positions, respectively. Both samples were excited with a focused UV laser (351 nm). Reprinted with permission from ref 921. Copyright 2012 Wiley-VCH Verlag GmbH & Co. KGaA. The crystal structures of **514a** and **514b** are retrieved free of charge from CCDC (833259 and 833260) via [www.ccdc.cam.ac.uk](http://www.ccdc.cam.ac.uk). (D) Fluorescent image of the single crystal of **120** and the stacking of molecular columns in the crystal structure. (E) PL spectra of a **120** crystal as the function of the pump laser energy. (F) Peak intensity at the emission maximum as a function of pump stripe length under different pump energies. Reprinted with permission from ref 163. Copyright 2013 Wiley-VCH Verlag GmbH & Co. KGaA.

**514b** showed a green fluorescence with the emission maximum located at 518 nm. The microrods of both **514a** and **514b** displayed remarkable optical waveguiding behaviors, with brighter luminescence at the rod-ends than the rod-bodies (Figure 174B,C). When the microrods were excited with a focused laser at different local positions along the length of the microrods, characteristics of active waveguides were clearly observed for **514a** and **514b**. The optical loss coefficient values for microrods of **514a** and **514b** were estimated to be 76.5 and 56.7 dB mm $^{-1}$ , respectively. Thanks to their outstanding optical waveguiding properties, amplified spontaneous emission (ASE) of **514b** and multimode-lasing behavior of **514a** were detected by increasing the pump laser energy.

Waveguided propagation of luminescence emission is generally considered to be one prerequisite for ASE and laser, which has been verified by the aforesaid cases. Here, there is another luminogen that can serve as an example for further

demonstration. The butterfly-shaped DSA derivative **120** (inset in Figure 174D) is AEE-active with a crystal-state  $\Phi_F$  of 60.0%.<sup>163</sup> The large single crystals of **120** were grown by physical vapor deposition, exhibiting brilliant green emission. The crystal structure of **120** features a cross dipole stacking of molecules in the formed 1D molecular column along the *b* axis (Figure 174D). Intense fluorescence observed at the tip of the ribbonlike **120** crystals suggested the property of optical waveguiding. The high radiative deactivation rate and high  $\Phi_F$  stemming from the AEE effect, 1D cross dipole stacking and the ordered 2D layer-by-layer structure, and self-waveguided property synergistically endowed the crystals of **120** with ASE. With an increase in the pump laser energy, the spontaneously emitted light was stimulated as a result of a single transit through the waveguiding geometry of the crystals, the full width at half maximum (FWHM) was reduced from 65 to 12 nm, and the fluorescence intensity collected at the terminal of the crystal was enhanced drastically (Figure 174E). The light emission was approximately proportional to the energy to  $207 \mu\text{J cm}^{-2}$  per pulse, and afterwards, the characteristic hyper-linear dependence was observed. The onset of spectral narrowing, i.e., phenomenological threshold, was determined to be  $207 \mu\text{J cm}^{-2}$ , which was one of the lowest values in crystals. The relationship between the ASE intensity and the stripe length is shown in Figure 174F. The net gain coefficient at 516 nm was determined to be as high as  $69 \text{ cm}^{-1}$  under  $14.58 \mu\text{J cm}^{-2}$ , which was comparable to those of polymeric materials.<sup>924</sup> Moreover, the loss coefficient was calculated to be  $7.3 \text{ cm}^{-1}$ , which contributed to the high net gain.

The AIEgen **515** prepared by decorating the TPE groups with dicyanovinyl units is a strong emitter with green fluorescence (Figure 175A).<sup>922</sup> The microcrystals of **515** can be facilely obtained by slow evaporation of its DCM/ethanol mixture. The resulting two kinds of microcrystals, namely, microrods and microslices were found to be optical waveguides (Figure 175B). As revealed by the distance-dependent microarea fluorescent images of a chosen microrod, green light emission appeared at one tip of the microrod near to the excited site when excited with a uniform focused laser at seven different positions. The peak intensities at the fixed end and the excited position of the microrod were collected, and the value of optical loss coefficient was calculated to be  $32.0 \text{ dB mm}^{-1}$  by a single exponential fitting. It is noteworthy that the length of as-prepared microrods is quite long, enabling them to be promising optical waveguiding materials for practical use. The optical loss coefficient value of the microslice was  $79.0 \text{ dB mm}^{-1}$ . Such excellent optical waveguiding properties are attributed to the negligible reabsorption, well-ordered arrangement in crystal structure, and a smooth crystal surface.

The luminophore **370** (Figure 175A) was designed and synthesized by linking a pyridium unit to TPE skeleton with the vinyl bridge.<sup>32</sup> The crystalline microrods of **370** were formed by its self-organization in DCM/hexane mixture and emitted an intense green light, thanks to its AIE feature (Figure 175C). Owing to the large Stokes shift which suppressed the reabsorption and the highly ordered molecular arrangement, these crystalline microrods showed marked optical waveguide effect, as confirmed by the distance-dependent fluorescent images of an individual microrod. As displayed in Figure 175D, bright fluorescence was also observed at both ends of a microrod besides the excited local sites. Because the length of microrod is long, only the ends labelled with numbers 1–5 are exhibited. This phenomenon might occur in the following way: **370** molecules absorb the excitation light and propagate the light

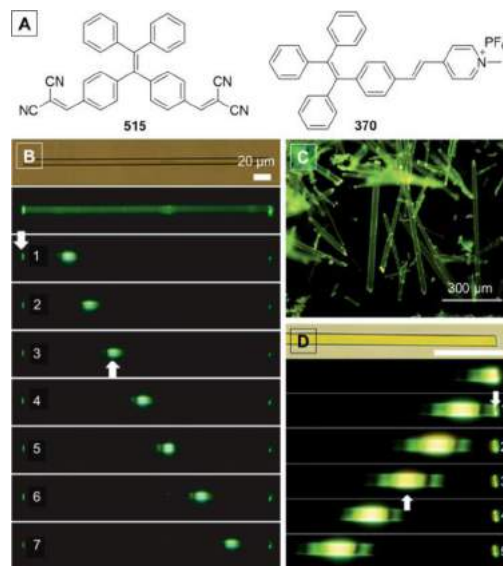


**Figure 175.** Representative examples of green emissive AIEgens which show waveguiding properties. (A) Chemical structures of TPE derivatives **515** and **370**. Microarea fluorescent images of (B) **515** and (D) **370** obtained by exciting an identical microrod at different positions: up arrow (excited site) and down arrow (emission tip). (C) Fluorescent image of crystalline microrods of **370** taken under UV irradiation on a fluorescent microscope. Panel B is reprinted with permission from ref 922. Copyright 2014 Wiley-VCH Verlag GmbH & Co. KGaA. Panels C and D are reprinted with permission from ref 32. Copyright 2013 Royal Society of Chemistry.

emission to the rod ends. This is a hallmark of optical waveguide. Since the light arise from the light emission process, **370** thus falls in the category of active waveguide materials. The optical loss coefficient was determined to be  $\sim 32.0 \text{ dB mm}^{-1}$ .

In addition to those with blue or green emission colors, red emissive AIEgen-based optical waveguiding systems have also been developed.<sup>255,907,912,923</sup> The previously mentioned crystalline microrods obtained from the self-assembly of **510** (Figure 176A) in diethyl ether/hexane mixture possessed appropriate length and regular shape and hence its waveguiding properties was studied.<sup>907</sup> As shown in Figure 176B, when the defect-free microrod was excited with a 400 nm UV light generated by an 800 nm laser device at different positions, the emission detected at the rod end became weaker as the excited spot moved gradually to the opposite end of the rod. The large Stokes shift ( $\sim 100 \text{ nm}$ ) and the smooth and flat end facets of the microrods helped minimize the optical loss, rendering an optical loss coefficient of  $\sim 137.0 \text{ dB mm}^{-1}$ , which was pretty low among the AIEgens with red luminescence.

The AIEgen **194** holds a cruciform molecular shape with multiple cyano groups and four alkyl tails, making it prone to self-assemble or self-organize into ordered nano-/microstructures presumably through dipole to dipole interactions and van der Waals force.<sup>255</sup> For example, 1D microrods with strong emission at around 676 nm and 2D microplates emitting red-shifted fluorescence with a shoulder at around 709 nm can be readily afforded. In a surface-smooth 1D microrod, bright luminescence was detected at both ends, whereas the remaining areas showed only a relatively weak red emission (Figure 176C). Clearly, **194** can function as active optical waveguides. The intensity of the outcoupled light at the microrod tips decreased exponentially with the increase in the propagation distance. The optical loss coefficient was estimated to be as low as  $60.0 \text{ dB mm}^{-1}$ . The well-defined 2D

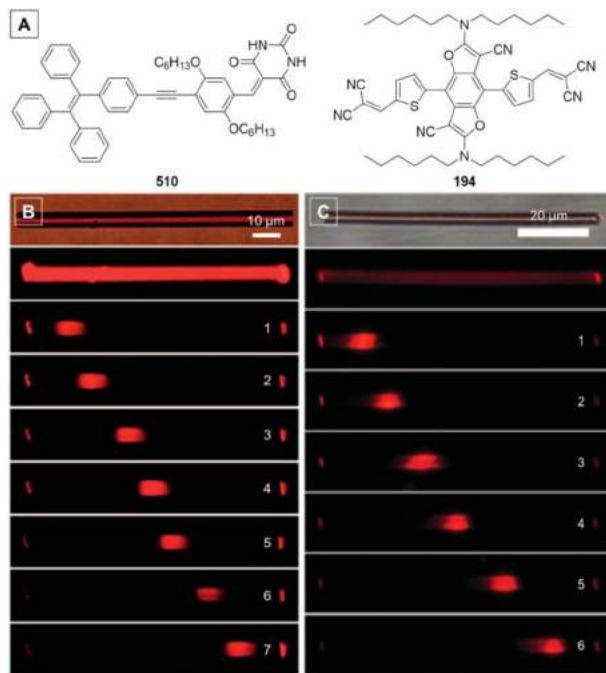


**Figure 176.** Representative examples of waveguiding AIEgens with red fluorescence. (A) Molecular structures of **510** and **194**. Microarea fluorescent images of the microrods of (B) **510** and (C) **194** obtained by exciting at seven different positions with a focused UV laser. Panel B is reprinted with permission from ref 907. Copyright 2013 Royal Society of Chemistry. Panel C is reprinted with permission from ref 255. Copyright 2014 Wiley-VCH Verlag GmbH & Co. KGaA.

microplate exhibited a similar property, with their edges emitting brighter red fluorescence than the other regions, suggesting the occurrence of efficient light guiding within the 2D microplates of **194**. Close inspection revealed that the bright outcoupled red lights emitted from the four edges of the 2D microplates were marginally different. Such slight anisotropic light propagation efficiencies may be associated with the direction of intermolecular arrangement, because the dielectric properties and photon transport capabilities depend on the molecular packing and the orientation of the optical transition dipole moment.

As demonstrated in this small section, AIEgens that can form defectless, smooth, and well-ordered microstructures through self-assembly or self-organization usually possess the capability of waveguiding. The large Stokes shifts and ordered alignments of the luminogenic molecules benefit the waveguide efficiency. Moreover, because of their luminescence nature, these AIEgens can be considered as active waveguiding materials. Further research in this area can be focused on the enrichment of their type and the improvement of their performance. Additionally, in view of their efficient luminescence in the solid state and superb waveguiding properties, AIEgen-based waveguides are promising for the realization of ASE and organic lasers.

**5.3.5. Circularly Polarized Luminescence (CPL).** CPL is a property that reflects the chirality of a material in the excited state. Through studying their spectroscopic CPL signatures, the stereochemical, conformational, and 3D structural information on the chiral materials can be obtained.<sup>925–927</sup> Materials with CPL can be used in various areas such as optoelectronics (e.g., stereoscopic optical processing, display, and storage), pharmaceutical industries, and biological systems (e.g., chiral recognition). All these technological applications require materials with high CPL performance. Two essential parameters have been used to assess

the performance of CPL-active materials: one is the emission dissymmetry factor [ $g_{\text{em}} = 2(I_L - I_R)/(I_L + I_R)$ ], whose value generally falls in the range from  $-2$  to  $2$ . The other is the luminescence efficiency, especially the value in the condensed phase when taking the real-world applications into consideration. Most of the existing CPL systems were investigated in the solution state and showed small  $g_{\text{em}}$  values. Their performance in the condensed phase became even worse because of the ACQ effect. In this context, it is challenging to develop new chiral luminescent systems with both large  $g_{\text{em}}$  value and high emission efficiency.

Organic chiral  $\pi$ -conjugated molecules are among the most promising candidate materials for utilities in advanced electronic CPL devices owing to their high flexibility and processability, low cost, and tailored synthetic feasibility. Theoretically, luminogens with helical organization can generate CPL signals upon photo- or electroexcitation. As schematically shown in Figure 177A, a

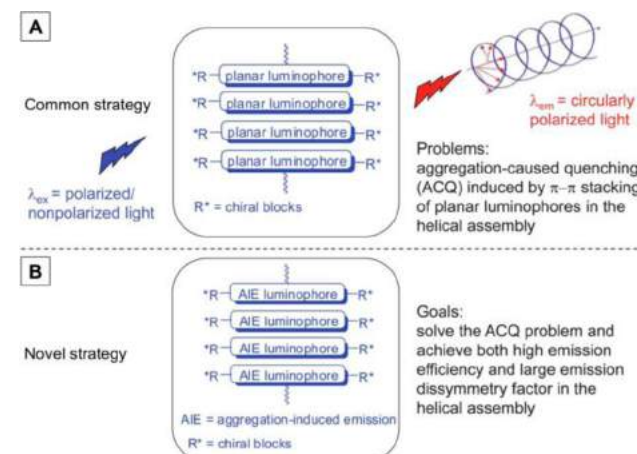


**Figure 177.** Comparison of molecular design strategies for making CPL-active materials. CPL (output  $\lambda_{\text{em}}$ ) is generated from helical assemblies of luminescent chiral molecules bearing (A) conventional planar and (B) AIEgens under the excitation of polarised/nonpolarised light (input  $\lambda_{\text{ex}}$ ). Reprinted with permission from ref 40. Copyright 2012 Royal Society of Chemistry.

common strategy for the construction of CPL-active luminophores is to synthesize molecules with chiral motifs at the peripheries and planar  $\pi$ -conjugated chromophores in the core, which can form helical self-assembly structures driven by  $\pi-\pi$  stacking interactions. On the other hand, the formation of detrimental species resulted from  $\pi-\pi$  stacking interactions in the aggregate state makes the CPL of the assembly suffer the intrinsic ACQ effect, giving rise to poor emission efficiency and spectral instability. To surmount the severe limitation of ACQ, efficient solid emitters and judicious construction strategy are in high demand. Syntheses of the AIE-based CPL luminogens are expected to be a possible solution. Bearing this idea in mind, our group has opened up a new avenue to the creation of high-performance CPL-active organic materials by appropriately welding AIEgens with chiral moieties (Figure 177B).<sup>40</sup> On the basis of this versatile molecular design rationale, an array of CPL-active AIE systems has been established.<sup>40,928–931</sup>

As a proof of concept, a molecule containing an AIE-active silole core and two chiral sugar pendants has been prepared and fully characterized (**516**; Figure 178A).<sup>40</sup> In solution, **516** showed no circular dichroism (CD) signal and fluorescence, whereas upon aggregation, both the CD absorption and light emission were simultaneously switched on, exhibiting aggregation-induced CD

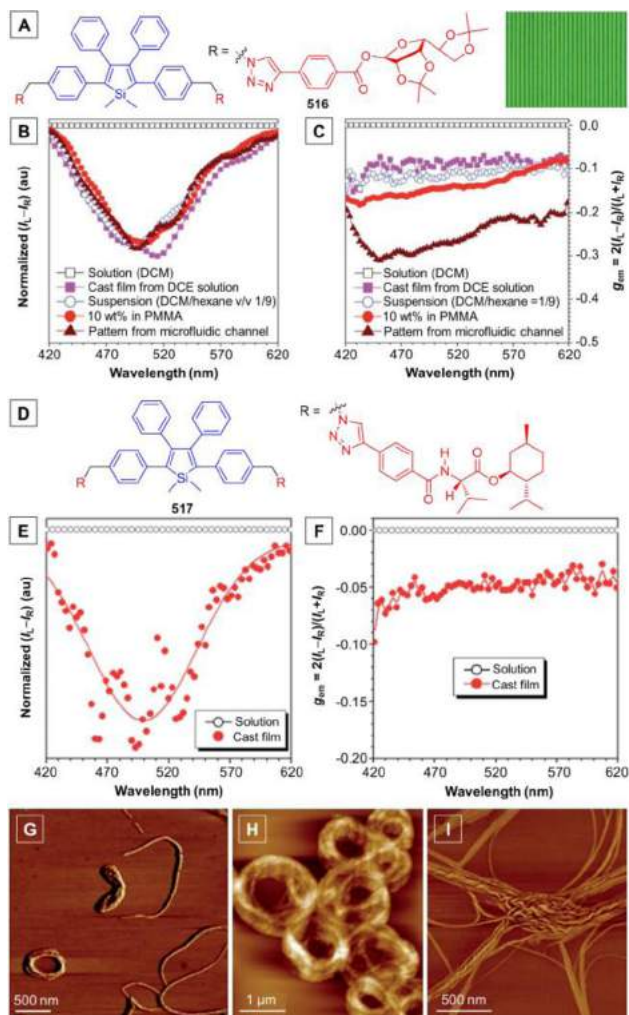


**Figure 178.** Silole-based AIEgens functionalized with chiral moieties with circularly polarized luminescence (CPL). Molecular structures of (A) **516** and (D) **517**. Inset in panel A: fluorescent images of the solid sample prepared by evaporation of the DCM/toluene solution in microfluidic channels on quartz substrates. (B, E) Plots of  $(I_L - I_R)$  and (C, F) CPL dissymmetry factor  $g_{em}$  versus wavelength for **516** and **517** in different forms, respectively. AFM images of helical assemblies of **517** obtained by evaporation of its THF/water mixtures. The water content are (G) 5 vol %, (H) 20 vol %, and (I) 90 vol %. Panels A–C are reprinted with permission from ref 40. Copyright 2012 Royal Society of Chemistry. Panels E–I are reprinted with permission from ref 928. Copyright 2014 Royal Society of Chemistry.

(AICD) and AIE effects. The AICD effect was further proved by the fact that the molecules of **516** self-assembled into right-handed helical nanoribbons and superhelical ropes when aggregated. The  $\Phi_F$  was boosted from ~0.6% in solution to 81.3% in the solid state due to the AIE effect. The helical assemblies of **516** preferentially emitted right-handed CPL (Figure 178B) and exhibited large  $g_{ems}$ , whose absolute values fall in the range of 0.08–0.32 (Figure 178C). Such values are two orders of magnitude higher than those of previously reported organic materials. A Telfon-based microfluidic technique was demonstrated for the fabrication of fluorescent pattern (inset in Figure 178A). Such fluorescent pattern showed the highest  $g_{em}$  of –0.32 probably owing to the augmented assembling order in the confined environment provided by the microchannels. The CPL performance was retained even after being stored under ambient conditions for more than half a year, confirming its excellent

spectral stability. Computational simulation was conducted to uncover how the molecules were organized at the molecular level in the helical assemblies.

To further validate the feasibility of the above design strategy, the luminogenic compound **517** with a silole core bearing two chiral valine pendants was designed and synthesized (Figure 178D).<sup>928</sup> The attachment of chiral valine to the silole unit was intended to endow the luminogen with chirality and exert an asymmetric force on the silole moiety to induce a helical conformation. As anticipated, **517** not only showed typical AIE, CD, and CPL properties (Figure 178E,F), but also possessed the capability of self-assembly (Figure 178G–I).<sup>928</sup> More specifically, owing to the AIE effect, the  $\Phi_F$  increased from ~0.3% in pure THF solution to a maximum value of 18.9% in the THF/water mixture with  $f_w = 90$  vol %, exhibiting an approximately 57-fold enhancement. The  $\Phi_F$  value of its film state determined by a calibrated integrating sphere was up to 80.3%. Similar to **516**, **517** displayed almost no CD signal in solution but exhibited strong CD signals in the aggregate state (e.g., film state), demonstrating the AICD effect. No CPL signal was observed when **517** was molecularly dissolved in solution, due to the absence of luminescence and the randomization of molecular conformation caused by active intramolecular rotations (Figure 178E). Once the molecules of **517** aggregated or when the luminogen was casted into solid film, all the  $\Delta I = I_L - I_R$  signals became negative, suggesting that the molecular packing in the aggregates preferred to adopt a one-handed helical structures. The  $g_{em}$  was measured to be –0.05 on average in the monitored spectral region (Figure 178F), which was much higher than those reported for conventional pure organic molecules (~ $10^{-5}$  to  $10^{-2}$ ). The amphiphilic valine decoration enabled the molecules of **517** to aggregate into complex architectures through a self-assembling process as revealed by the AFM images (Figure 178G–I). The luminophore **517** self-assembled into helical fibers with the evaporation of its THF solution, which was consistent with its CD and CPL properties. Addition of a poor solvent such as water or hexane to the THF solution also resulted in the formation of chiral aggregates. Further increase of the water content led to dramatic morphological transitions from extended helical fibers to loops (Figure 178H) and finally to thicker fibers (Figure 178I), which was accompanied by the helical enhancement as well as inversion in handedness to different extents.

Attaching chiral amino acids or their variants to AIE-active cores besides silole has further proved the universality of the strategy discussed above, as demonstrated by L-valine methyl ester-containing TPE derivative **518**. This compound was synthesized through the “click” reaction between an azide-functionalized TPE unit and an alkynyl-substituted L-valine methyl ester (Figure 179A).<sup>929</sup> Luminogen **518** preserved the AIE attribute of TPE and showed bright solid-state emission. In sharp contrast to the very weak CD signal in solutions, strong absorption peaks were observed in the CD spectra of **518** in the aggregate and the film states, which was indicative of an AICD effect and the successful chirality transfer from the valine-containing moiety to the TPE unit in the aggregate state. Good CPL performances of **518** have been observed in the solid state. The fluorescent microfibers of **518** showed a positive signal in the CPL spectrum with an average  $g_{em}$  value of 0.03 (Figure 179B,C). The fine substructures of the aforesaid fibers of **518** were further investigated by SEM and TEM. The twisting between elementary fibers resulted in the formation of thick entangled fibers. The elementary fibers were in fact “nanofibers”, each of which clearly displayed a left-handed screw sense in accordance with the positive

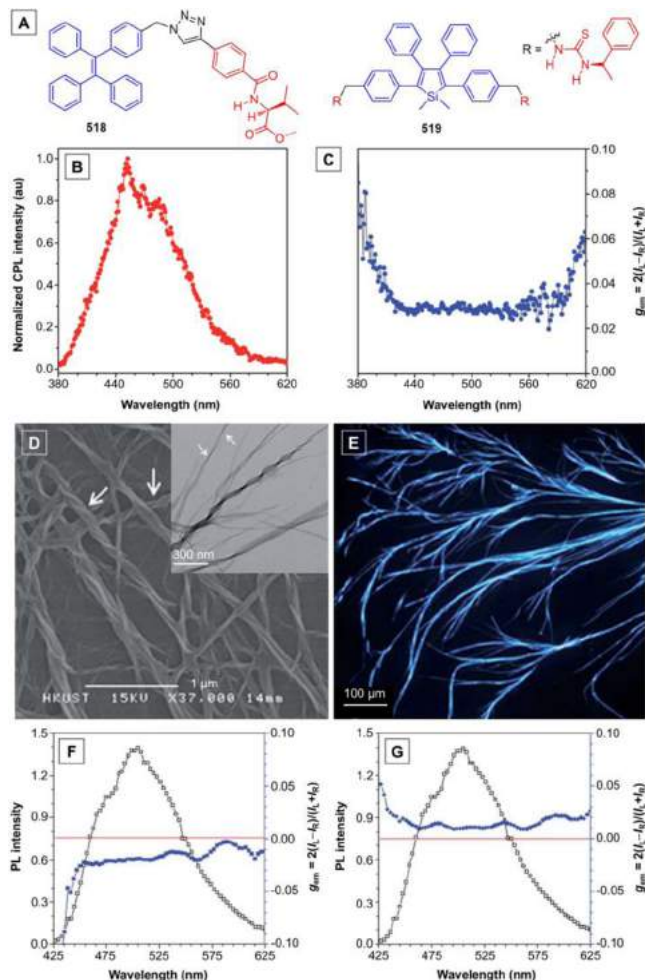


**Figure 179.** (A) Molecular structure of **518** and **519**. Plots of (B) CPL intensity and (C) CPL dissymmetry factor  $g_{\text{gem}}$  versus wavelength of fibers formed by **518**. (D) SEM and TEM (inset) of the aggregates of **518** formed upon the evaporation of its dichloroethane/hexane solution (1/9, v/v),  $[\mathbf{519}] = 10^{-4}$  M. (E) Fluorescent image of **518** after the evaporation of its DMF solution on quartz substrates in the micropatterned channel taken under UV excitation. Reprinted with permission from ref 929. Copyright 2014 Royal Society of Chemistry. Plots of PL intensity and  $g_{\text{gem}}$  versus wavelength for **519** in the presence of (F) R-(−) or (G) S-(+)-mandelic acid ( $[\mathbf{519}]/[\text{acid}] = 1/40$  by mole) in the solid film state, respectively. Reprinted with permission from ref 931. Copyright 2013 Royal Society of Chemistry.

CPL signal (Figure 179D). The fluorescence image exhibited in Figure 179E revealed that the nano/microfibers were highly emissive with length more than 1 mm, manifesting the capability of **518** to undergo self-assembly processes due to its amphiphathy and chirality. The helical conformation and the supramolecular assemblies can be further stabilized by hydrogen bonds between the amino acid pendants and possible  $\pi-\pi$  interactions of the TPE scaffold. Besides small molecules, a TPE-based chiral polymer synthesized through the polymerization of 1,2-bis(4-ethynylphenyl)-1,2-diphenylethene and 3',5'-diiodo-N-*tert*-butoxycarbonyl-O-octyl-L-tyrosine methyl ester via Sonogashira cross-coupling has been reported to be CPL-active in both solution and aggregate states.<sup>930</sup> This AIE-active conjugated polymer exhibited a high  $g_{\text{em}}$  value which was tunable in the range of 0.44–0.08 by altering the  $f_w$  in its THF/water mixtures.

The CPL signals obtained from the above AIEgens with screw-shaped molecular structures can hardly be changed or modified.

Our group hence further devoted some efforts to create CPL-active materials with controllable signals. The AIEgen **519** with a silole core, thiourea linkages, and chiral phenylethanamine groups was synthesized to this end (Figure 179A).<sup>931</sup> When it was molecularly dissolved, neither CD nor fluorescence signal was observed for **519**. Aggregation of its molecules in a poor solvent or in a thin solid film induced intense green fluorescence with a solid-state  $\Phi_F$  as high as 95.0%. No CD signal, however, was detected yet in this situation. Owing to the hydrogen-bonding interaction between the thiourea and carboxyl groups, the complexation of **519** with specific chiral acids in the solid state can generate CD and CPL signals in the condensed phase, exhibiting a unique complexation-induced CD (CICD) characteristic. Such a CICD behavior was found to be the most effective in the complexation of **519** with mandelic acid. On the basis of the AIE and CICD effects, the CPL performance of **519**/mandelic acid complex was evaluated in the condensed phase. The  $g_{\text{em}}$  values of **519** with R-(−)-mandelic acid and S-(+)-mandelic acid were about −0.01 (Figure 179F) and +0.01 (Figure 179G) on average, respectively. It means that the predominant CPL can be tuned to be right- or left-handed circularly polarized light by the type of enantiomers of mandelic acid used.

**5.3.6. Liquid Crystals (LCs).** The creation of liquid crystals with intrinsic light-emitting properties is of great interest because such light-emitting liquid crystals (LELCs) may find a large variety of technological applications in diverse areas, such as polarized organic lasers,<sup>932</sup> anisotropic OLEDs,<sup>933</sup> one-dimensional semiconductors,<sup>934</sup> chemosensors, optical information storage, and liquid-crystal displays (LCDs).<sup>935,936</sup> The optoelectronic devices constructed from LELCs may enjoy quite a few advantageous features. For example, an LCD built on LELC materials will show simple device configuration, low fabrication cost, and remarkably enhanced brightness, efficiency, contrast, and viewing angle.<sup>937</sup> More importantly, the power-consuming extra backlight will be eliminated. Despite these thrilling prospects, developing high-performance LELCs remains a challenging task. Aggregation or self-organization is a natural process accompanying the formation of a mesophase, which accounts for the difficulty in incorporating conventional luminophores into mesogens with preservation of their mesomorphic and luminescent properties.<sup>938</sup> As aggregation is needed to activate the RIM processes and realize their light emission, the AIEgens, being non-conventional luminogenic systems, are promising candidates for developing LELCs. During the past few years, there have emerged a number of AIE-based LELCs,<sup>41,233,327,365,939–949</sup> and some of them are presented in Figures 180–184.<sup>41,327,943,946–949</sup>

The attachment of flexible alkoxy group(s) to the rigid AIE-active core has been found to be an effective construction strategy for AIE-active mesogens. A group of such systems have been built with diverse AIE cores decorated with varying numbers of alkyl/alkoxy tails.<sup>233,327,365,939–947</sup> For example, Cho et al. have prepared two TPE-based propeller-shaped molecules **520a** and **520b**, each of which possesses multiple long alkyl chains and a TPE core (Figure 180A).<sup>943</sup> The 1,2,3-triazolyl groups were introduced as linkages between the TPE unit and substituted phenyl rings through click chemistry, whose polar character was expected to reinforce the microphase separation and hence produce stable LC phases. Since the space-filling of alkyl chains could affect the packing of propeller-shaped mesogens, in order to manipulate the stacking mode of these propeller-like molecules, the number of peripheral dodecyl chains was altered from eight in **520a** to 12 in **520b**. Analysis of **520a** by differential scanning calorimetry (DSC), two first-order

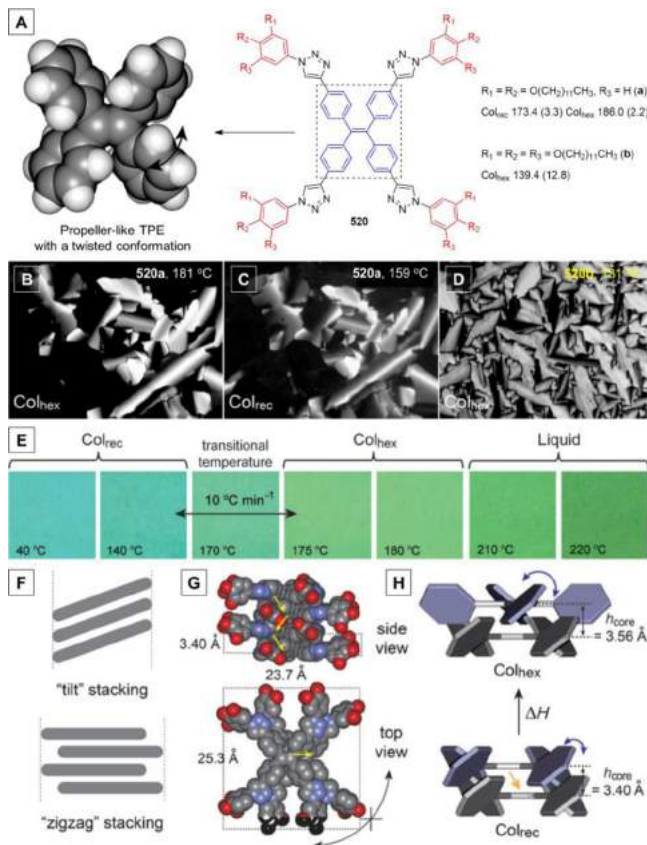


**Figure 180.** (A) Molecular structures of **520** with the propeller-like TPE unit. The double-ended arrow indicates the torsional variation by the rotation of the phenyl rotor. Temperatures are given in °C. The values in parentheses are the enthalpy change ( $\text{kJ mol}^{-1}$ ) of each transition. Optical textures of (B) **520a** at 181 °C, (C) **520a** at 159 °C, and (D) **520b** at 131 °C. Abbreviations: Col<sub>hex</sub> hexagonal columnar; Col<sub>rec</sub> rectangular columnar. (E) Emission color change of **520a** as a function of temperature under 365 nm UV light at a heating rate of 10 °C min<sup>-1</sup>. (F) Models of “tilt” and “zigzag” stackings. (G) The molecular organization in the zigzag stacking of the Col<sub>rec</sub> phase of **520a** and (H) schematics for the variation in the degree of interdigitation between propeller-like mesogens at the intercolumnar transition. Reprinted with permission from ref 943. Copyright 2014 Wiley-VCH Verlag GmbH & Co. KGaA.

transitions were detected at 173.4 °C and 186.0 °C during the heating scan, which were reversible as two corresponding peaks were also recorded in the cooling scan. Such a thermal behavior was also investigated by polarized optical microscopy (POM). On cooling from the isotropic liquid state, a typical fan-like texture associated with the formation of a columnar LC phase was observed at 181 °C (Figure 180B). Further cooling to 159 °C, the second LC phase was attained and the fanlike texture remained unchanged even when cooled to room temperature (Figure 180C). Only the texture color altered due to the variation in the sample thickness with temperature. This implies a significant structural change with the LC-to-LC (smectic-to-smectic phase) transition of **520a**. Compared with **520a**, **520b** showed only one transition peak at 139.4 °C in the DSC thermogram and a fanlike texture at 131 °C under the POM observation (Figure 180D).

Thanks to their intrinsic AIE attributes, **520a** and **520b** possess obvious thermochromics properties, or in other words, their emission color and intensity varied with temperature. For

**520a**, the fluorescence color was sky blue for the rectangular columnar (Col<sub>rec</sub>) phase, which changed to emerald at the transition temperature of 170 °C and displayed a green color in the hexagonal columnar (Col<sub>hex</sub>) phase (Figure 180E). When the temperature was further increased, the emission became dimmer. The emission color of **520b** exhibited a continuous change from sky blue to green in the Col<sub>hex</sub> phase. The fluorescence intensity also decreased with the increasing temperature. Such an unusual stacking transformation in LC columnar assemblies, namely, the transition from Col<sub>rec</sub> to Col<sub>hex</sub> phase, has been rationalized to be a first-order transition involving an unprecedented zigzag stacking of aromatic propellers in the Col<sub>rec</sub> phase (Figure 180F,G). This was in contrast to the second-order intercolumnar transitions based on a common tilt mechanism (Figure 180F). The closer packing of the molecules in Col<sub>rec</sub> phase as compared to that in Col<sub>hex</sub> phase makes the aromatic wings more interdigitated and twisted, which impedes the intramolecular rotations of the mesogens and hence results in bluer and brighter fluorescence in the Col<sub>rec</sub> phase (Figure 180 H).

As we mentioned above, by decorating the AIE cores with long alkyl/alkoxy chains, various AIE-active mesogens can be easily generated. Using this strategy, cyanostilbene, a specific AIEgen that readily undergoes the *E*-Z isomerization process under certain conditions, has been exploited as a building block to create new mesogenic AIEgens with modulated emission properties.<sup>946,947</sup> AIEgen **521a**, for example, namely, (Z)-2-(4-aminophenyl)-3-(4-(dodecyloxy)phenyl) acrylonitrile, is constructed from a cyanostilbene core and a dodecyloxy tail (Figure 181A). The electron-donating amino group was incorporated to enhance the luminogens’ compatibility with other LC molecules and made **521a** form gels in the liquid crystalline phase. The mesomorphic behaviors of **521a** were investigated by means of POM and DSC. At a heating rate of 10 °C min<sup>-1</sup>, **521a** entered the liquid crystalline phase at around 80 °C and converted to its isotropic melt state at ~112 °C. A smectic phase was observed in both heating and cooling cycles, revealing that **521a** was an enantiotropic LC. This was proved by the appearance of a focal conic fan-shaped texture at 75 °C in the POM image (Figure 181C). The thin film of **521a** sandwiched between two quartz plates emitted an intensive green luminescence with a  $\Phi_F$  of 19.5% (Figure 181B). After being irradiated by 365 nm UV light for 2 h in the LC phase at 90 °C, the fluorescence shifted to blue accompanied by a decrease in the  $\Phi_F$  to 9.2% (Figure 181B). Well-ordered microcrystalline and amorphous structures in the thin film of **521a** before and after irradiation, respectively, were revealed by the XRD analysis. Such fluorescence and morphology changes were ascribed to the photoinduced isomerization from **521a** (Z-form) to **521b** (E-form) in the LC phase (Figure 181A). Unlike **521a**, **521b** is bent rather than rodlike in shape. This prevents its molecules from packing well and thus reduces its effective  $\pi$ -conjugation length, resulting in the decreased and hypsochromically-shifted fluorescence and the loss of LC phase. Taking advantage of this photoisomerization of **521a**, fluorescent molecule-dispersed liquid crystals were prepared by blending **521a** with a commercially available LC compound. Through a photoisomerization-induced phase separation method, the photoluminescence could be repeatedly switched by an electric field.

Another cyanostilbene-based columnar LC compound, namely, (Z)-2,3-bis(3,4,5-tris(dodecyloxy)phenyl) acrylonitrile (**522a**; Figure 181D), was synthesized and showed both AIE effect and photoisomerization property.<sup>947</sup> The cyanostilbene moiety was designed to serve as the core of columnar LC through its strong dipole–dipole interactions and possible  $\pi$ – $\pi$

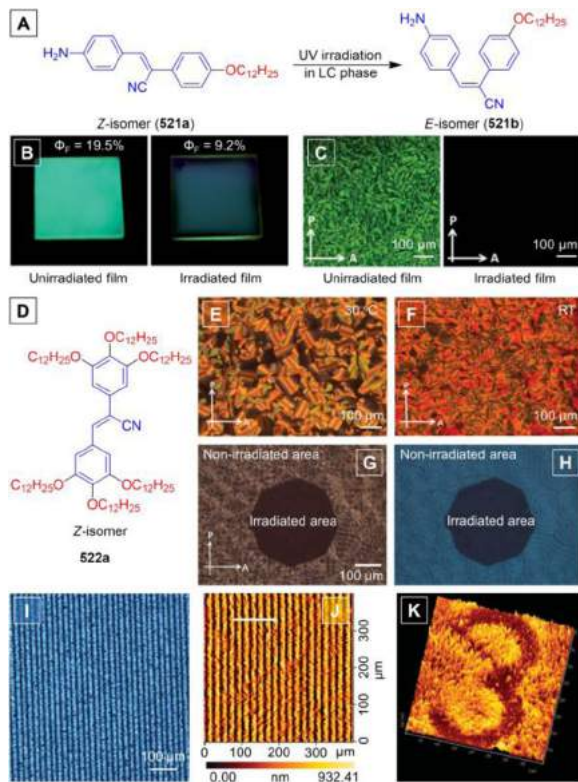


**Figure 181.** (A) Schematic illustration of Z–E isomerization of **521** upon UV irradiation in the liquid crystal phase. (B) Photoimages of (left) unirradiated and (right) irradiated films of **521a** on the quartz cells. (C) POM images of the (left) unirradiated film and (right) irradiated film of **521a**. Reprinted with permission from ref 946. Copyright 2013 Royal Society of Chemistry. (D) Molecular structure of **522a** (Z-isomer of **522**). (E) POM image of the hexagonal phase of **522a** obtained at 30 °C during cooling. (F) POM image of the crystal phase of **522a** obtained at room temperature during cooling. (G) POM image and (H) fluorescence optical microscopic image of the crystalline film. (I) Fluorescence optical microscopic image and (J) topographical AFM images of the photo-triggered surface relief structure of **522a** crystalline films. (K) 3D topological AFM images of surface relief formation with photomasks. Reprinted with permission from ref 947. Copyright 2013 Wiley-VCH Verlag GmbH & Co. KGaA.

interactions. The peripheral flexible side chains of the tris(dodecyloxy) groups were directly attached to the mesogenic core to facilitate mesomorphic organization. A typical focal-conic fan-shaped texture was observed at about 30 °C upon fast cooling its isotropic melt at around 10 °C min<sup>-1</sup>, indicating the formation of a columnar hexagonal phase (Figure 181E). It is worth mentioning that the judicious increase in the number of alkyl/alkoxy chain can lower the LC phase transition temperature, as indicated by the results obtained for **520a** and **520b**, and **521a** and **522a**. The isothermal crystallization of **522a** was observed at a temperature near room temperature. Thus, the liquid crystals were transformed to crystals under prolonged natural cooling with sufficient time (Figure 181F). The molecules of **522a** showed a strong tendency to form a crystalline phase with a tetragonal arrangement. Similarly, the Z–E photoisomerization took place accompanying with the collapses of crystalline phase (Figure 181G), resulting in the dramatic decrease in the fluorescence intensity (Figure 181H). The reduced structural order facilitated the photoisomerization, and in turn, the generation of bent-structured E-isomer of **522** would accelerate the phase transition, leading to the fluorescence quenching and disappearance

of crystalline phase when the crystalline film of **522a** was irradiated by UV light at 39 ± 1 °C for less than 90 s. The surface relief grating (SRG) structure was constructed on a thin film of **522a** by its exposure to the irradiation from a nonpolarized Hg lamp at 365 nm (1 mW cm<sup>-2</sup>) through a micropatterned-photomask (Figure 181I,J). Even at a photon dose as small as 150 mJ cm<sup>-2</sup>, **522a** molecules showed a high diffraction efficiency of ~30% and rapid SRG formation within 150 s with a high surface modulation close to 200%. Because of the AIE attribute of **522a**, strongly fluorescent micropattern with high contrast was generated (Figure 181I). The solid crystalline film of **522a** exhibited a strong fluorescence with a  $\Phi_F$  of 22.0%. A different photomasked pattern with character “3” could also be easily inscribed into the luminescent film (Figure 181K), manifesting the versatility of such an approach.

Besides organic AIE-active mesogens, some metal complexes with AIE characteristics, such as gold(I) complexes, have been reported to show LC properties (Figure 182). Each of these

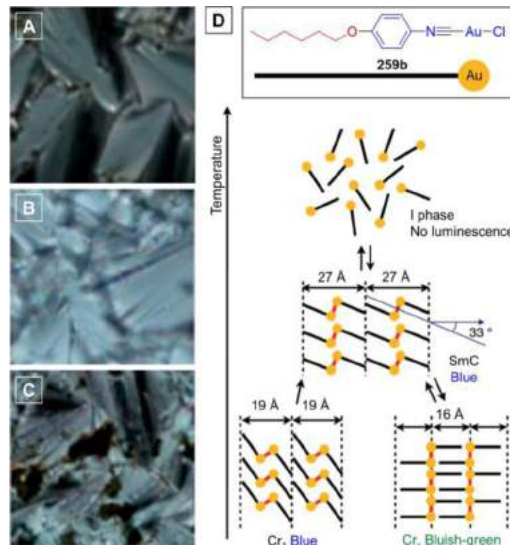


**Figure 182.** Optical texture of complexes observed by POM: (A) **259a** at 157 °C, (B) **259b** at 155 °C, and (C) **259c** at 147 °C. (D) Schematic illustration of the mesogenic unit and plausible molecular packing in crystalline and LC phases of complex **259b**. Reprinted with permission from ref 327. Copyright 2014 Royal Society of Chemistry.

AIE mesogens is comprised of a rigid body with a flexible alkoxy tail. Their symmetric rodlike structures allowed them to show typical LC properties. All the complexes **259a**–**259c** displayed enantiotropic smectic (Sm) phases, as revealed by the appearance of typical fan-shaped textures (Figure 182A–C). Moreover, all of them exhibited polymorphism in the crystalline phase. **259b** was used as a representative for the elucidation of their crystalline and LC phase structural analyses. As illustrated in Figure 182D, **259b** formed many unidentified and complicated crystalline phases (e.g., Cr<sub>1</sub> and Cr<sub>x</sub>) during the cooling process. The molecules of complex **259b** stacked in a dimeric manner in the Sm phase, and the dimer acted as a mesogenic unit. The tilted mesogens (i.e., dimers) were packed into a smectic C (SmC) phase. The tilt angle, which was defined as the angle between the vector normal to the Sm layer and the long axis of the mesogen, was equal to 33° (Figure 182D). Both the SmC and crystalline phase Cr<sub>1</sub> of **259b** showed a deep-blue fluorescence while the Cr<sub>x</sub> phase emitted a pale bluish-green light with 35 nm red-shift as compared to that of SmC and Cr<sub>1</sub>. The corresponding CIE

coordinates were (0.17, 0.10) in the Cr<sub>1</sub> phase at 40 °C on first heating, (0.18, 0.13) in the SmC phase at 130 °C, and (0.21, 0.29) in the Cr<sub>x</sub> phase at 40 °C. The luminescence color could be reversibly controlled by the phase transition between the LC (i.e., SmC) and crystalline (i.e., Cr<sub>x</sub>) phases. Moreover, owing to the AIE effect, reversible “on-off” switching of the luminescence can be modulated by the transition between the LC and isotropic phases.

Direct integration of AIEgens with mesogens is another pathway to achieve AIE-active LCs.<sup>41,948,949</sup> Such an amalgamation can generate LELCs that meld the best parts of each constituent. Our group has made some efforts in this regard and has successfully obtained some high-performance AIE-active mesogens ranging from small molecules to polymeric systems.<sup>41,948,949</sup> The efficient LELC 523 was created by rational combination of the AIE-active TPE core and four peripheral mesogens (Figure 183A).<sup>948</sup> The AIE feature was well preserved

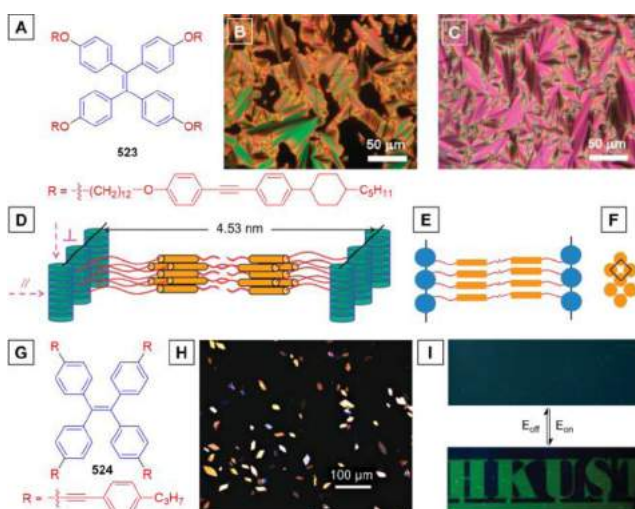


**Figure 183.** Molecular structures of mesogen-decorated AIEgens (**A**) **523** and (**G**) **524**. POM images recorded on cooling **523** to (**B**) 190 and (**C**) 100 °C from its isotropic state. Schematic illustration of the biaxially oriented packing model of **523** in the low temperature phase: (**D**) side view perpendicular to the side-chain mesogens, (**E**) top view, and (**F**) side view along the side-chain mesogens of the model. Reprinted with permission from ref 948. Copyright 2012 Royal Society of Chemistry. (**H**) POM photograph recorded on heating **524** to 222 °C. (**I**) Photograph of the LE-LCD device in the electric field-off and field-on states using the light-emitting LC mixture. The LC mixture = nematic LC PA0182 + 0.1 wt % **524**. Reprinted with permission from ref 41. Copyright 2014 Wiley-VCH Verlag GmbH & Co. KGaA.

in this LELC system, showing an absolute  $\Phi_F$  as high as  $67.4 \pm 5.0\%$ . **523** showed typical mesomorphic properties, which were studied by means of DSC and POM. When **523** was cooled from its isotropic phase to  $190^\circ\text{C}$ , fan-shaped anisotropic mesomorphic texture emerged from the homotropic dark background (**Figure 183B**). Further cooling to  $100^\circ\text{C}$  did not crystallize the molecules of **523** but transformed them into a more ordered mesophase (**Figure 183C**). Two respective first-order phase transitions were traced by the DSC measurements during the cooling and heating scans, which was consistent with the POM observations. The transition at high temperatures was assigned to the isotropic-to-LC mutual transition while that at low temperature corresponded to the LC-to-LC transition. As suggested by the WAXD analysis, the molecules of **523** exhibited a unique biaxially oriented mesomorphic arrangement, which was

schematically illustrated in Figure 183D–F. Although the conformations of the TPE units were strikingly twisted, they were still able to pack together to afford face-on aligned columns in the LC state. In the meantime, the mesogenic pendants decoupled from the TPE cores by dodecyl spacers preferentially self-assembled into tetragonal smectic building blocks which were orthogonal to the TPE columns.

Conjugating four mesogenic units to the TPE core through the Sonogashira coupling reaction between a brominated TPE and 4-ethynylpropylbenzene afforded an AIEgen-mesogen conjugate (i.e., **524**) with both luminogenic and mesogenic properties (**Figure 183G**).<sup>41</sup> When **524** was heated above 218 °C, an anisotropic mesomorphic texture was clearly exhibited (**Figure 183H**). No mesomorphic texture was observed during the cooling process, suggesting that **524** was a monotropic liquid crystal. The results recorded from the DSC thermograms agreed very well with those obtained from the POM observation. The LC phase, namely, thermotropic disc SmC phase, appeared within the range from 218 to 228 °C during the heating scan. Making use of the AIE effect and the mesomorphic property, a LC mixture containing nematic LC PA0182 and **524** (0.1 wt %) was prepared to attain polarized fluorescence. Such a LC mixture was successfully utilized to fabricate two types of light-emitting LC (LE-LC) devices by simplified process with low energy consumption. The performance of these LE-LC devices could be easily controlled by an electric field (**Figure 183I**). Such a work has paved the way to both the development and fabrication of high efficiency LE-LC devices based on the AIE-LC materials.

In addition to small molecular weight AIE-LC systems, AIE-active liquid crystalline polymers (AIE-LCPs) can also be obtained by smart integration of mesogens with AIEgens.<sup>949</sup> The polymers shown in Figure 184A were produced by click

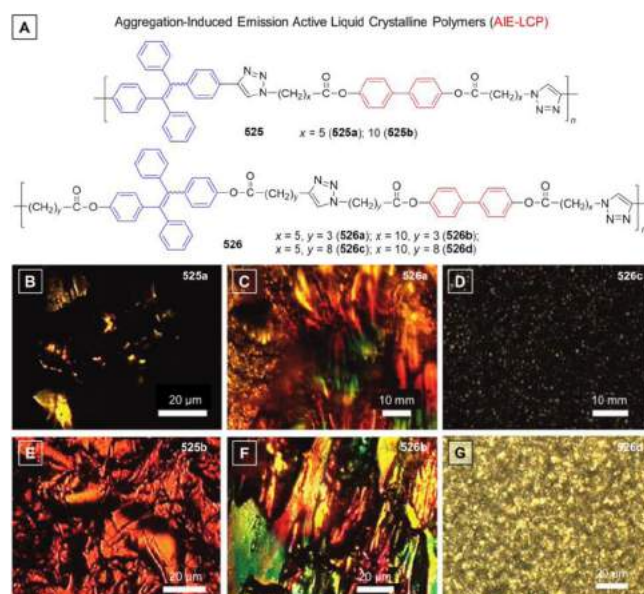


**Figure 184.** (A) Molecular structures of AIE-active liquid crystalline polymers **525** and **526**. Mesomorphic textures observed on cooling (B) **525a** to 159.9 °C, (C) **526a** to 89.9 °C, (D) **526c** to 94.9 °C, (E) **525b** to 250.6 °C, (F) **526b** to 69.8 °C, and (G) **526d** to 114.9 °C from their melting states at a cooling rate of 1 °C/min. Photos in parts B, C, E, and F were taken after application of a shearing force. Reprinted from ref 949. Copyright 2011 American Chemical Society.

polymerization of TPE-carrying diynes and biphenyl-containing diazides with different aliphatic spacer lengths. These polytriazoles,

i.e., **525a**, **525b**, and **526a–526d**, exhibited good solubility, high regioregularity, and more importantly, LC properties as well as AIE features with high solid-state emission efficiencies up to 63.7%. The photophysical properties of these main chain LC polytriazoles were dependent on their molecular structures, with those having longer spacer length showing lower solid-state  $\Phi_F$ . Moreover, the spacer length also exerted an obvious impact on the mesomorphic properties. Whereas polytriazoles with rigid main chains (**525a** and **525b**; Figure 184B,E) showed nematicity, those with longer spacer lengths displayed better mesogenic packing (**526a** and **526b**; Figure 184C,F) and formed smectic phases (**526c** and **526d**; Figure 184D,G). The reason for such difference is that the high rigidity of the main chain hinders the packing arrangements of the mesogenic units, while the longer flexible spacers provide the mesogenic units with larger freedom to pack.

The research on AIE-active LCs is truly an area with tantalising prospect. Two general strategies have been established for the construction of AIE-LCs: one is attaching long alkyl/alkoxy groups to the AIE cores and the other one is amalgamating AIEgens with mesogens. Besides the enrichment in the variety of AIE-LCs, further efforts in this area can be made on the exploration of the real-world applications of these superior LC materials, especially in the fabrication of LE-LC devices.

**5.3.7. Photovoltaics.** Photovoltaics are also known as solar cells, which generate electric power by converting energy from the sun into a flow of electrons. Owing to its great impacts on environments and economics, photovoltaics are now, after hydroenergy and wind power, the third most important renewable energy sources in terms of globally installed capacity. Amongst various photovoltaics, organic photovoltaic cells (OPVs) are viable alternatives that relieve energy pressure and environmental problems from increasing combustion of fossil fuels. Although the research area on photovoltaics is really attractive and dynamic, the application of AIE systems in this field is rare. As far back as 2005, our group reported a photovoltaic-active AIEgen constructed by appending carbazolyl groups to a HPS core.<sup>950</sup> The resultant HPS-carbazole adduct was thermally and morphologically stable. Owing to its D-A structure, photovoltaic cells built from this AIE compound performed well and offered an external quantum efficiency as high as 2.19%, demonstrating the great potential of AIEgens in the applications of photovoltaic cells.

Besides the utilization as photovoltaically active materials, direct uses of AIEgens as luminogenic materials in photovoltaic cells have been recently reported.<sup>951</sup> An example of such work is shown in Figure 185. Prior to the discussion of this work, there are some fundamental issues that should be noted first. The

solar cells based on cadmium telluride (CdTe) are one class of currently widely used solar cells. Although these devices enjoy the advantages of low-cost and easy-fabrication, their relatively low efficiency with an average value of 12.6% at the module level limits its broader applications as compared to the conventional crystalline silicon solar cells.<sup>952,953</sup> One chief reason for their low efficiency lies in the spectral mismatch with the solar spectrum. Its spectral response shows a cut-off in the short-wavelength region (<500 nm). The most effective way to address this issue is not through the optimization of the cell structure but to employ a layer of light-emitting down-shifting (LDS) material. The LDS material is supposed to convert the unfavorable photons (<500 nm) into favorable ones (>550 nm) before the incident light reaches the cell surface. Three criteria are required for effective LDS materials: strong absorption in the region where the spectral response of the CdTe solar cells is weak, a close to unity  $\Phi_F$  in a region where the CdTe solar cells show strong spectral response, and a large Stokes shift to minimize the photo self-absorption. The commercially available fluorophores such as the BASF Lumogen F dye Yellow 083 (Y083) can hardly meet the above requirements. The absorption of Y083 in the UV light region of 300–400 nm is not strong, and its emission spectrum mismatches the spectral response of the CdTe solar cells.<sup>954</sup> More importantly, it suffers from the ACQ effect which has been considered to be a common problem for many luminogens and prevents them from serving as LDS materials for solar cells.<sup>955</sup> Luminogens with AIE effects that are opposite to the ACQ features are hence promising candidates for LDS materials.

To make full use of the AIE effect and explore the potential application of AIEgens in CdTe solar cells, an array of TPE-based AIEgens where the TPE units serve as electron donors with strong electron-withdrawing moieties have been designed and synthesized.<sup>951</sup> The molecular structures and photophysical properties of these AIEgens are exhibited in Figure 185A. The D-A conjugated fluorophores **527a–527c** consist of TPE and malononitrile components with different aromatic rings as conjugating bridges. The ICT and AIE effects of these fluorophores resulted in large Stokes shifts and high  $\Phi_F$ s in solid medium (e.g., PMMA matrix). With desirable photophysical properties that satisfy the criteria mentioned above (*vide supra*), **527a–527c** had significantly improved the spectral response of the CdTe solar cells to photons in short-wavelength region (<500 nm) when these fluorophores were doped in PMMA films as LDS materials. Ultimately, when these AIEgen-doped PMMA films were applied to the surfaces of the solar cells, the measured short circuit current density ( $J_{sc}$ ) was dramatically enhanced by a magnitude of 6–10% (Figure 185B). Especially, the maximum increase in  $J_{sc}$

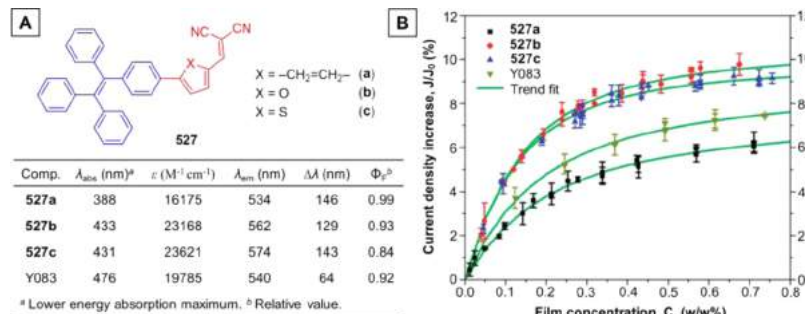


**Figure 185.** Representative examples of AIEgens used in the field of solar cells. (A) (upper panel) Molecular structures of AIEgens **527a–527c** and (table in the lower panel) a summary of their photophysical parameters. Note that the  $\Phi_F$  values were relative to the  $\Phi_F$  of Y083. (B) The increase in short circuit current density ( $J_{sc}$ ) versus the concentration of fluorophores **527a–527c** and Y083 in the LDS film placed on the CdTe solar cell surfaces. Adapted with permission from ref 951. Copyright 2013 Royal Society of Chemistry.

was 10% and 9% for **527b** and **527c**, respectively, whose values were higher than that of Y083. Such work might blaze a new path for the development of effective LDS materials in the future and suggested that the applications of AIEgens in the photovoltaic area are not restricted to the use as photovoltaic-active materials.

#### 5.4. Stimuli Responses

Molecular systems that change their properties in response to a single stimulus or multiple stimuli are called “smart” or stimuli-responsive materials. There exist multifarious and numerous such systems. Interestingly, a large variety of AIEgens have been reported to be “smart” or “intelligent” materials. Their luminescence properties alter in response to the external stimuli or environmental variations, such as mechanical force, temperature (thermal treatment such as heating/cooling), pH, fuming (vapor), photonic irradiation (light), solvent polarity, and electric field and so on. We have summarized the newly emerged stimuli-responsive AIE systems, picked up some examples, and put them into figures. In terms of the stimulus/stimuli which they respond to, the discussion in this subsection will be divided into six small parts: force, heat, pH, vapor, photon, and multiplex.

**5.4.1. Force.** Mechanochromism refers to a phenomenon that the luminescence of a luminophore changes with mechanical force. Materials exhibiting mechanochromism are widely utilized in sensors, memory chips, optical storage, and security inks, optoelectronic devices, and so forth. Such a chromic effect has been commonly observed in a great quantity of AIEgens. A propeller-like shape with a highly twisted 3D conformation is one of the most distinct structural features of a RIR-dominated AIEgen. The loose packing of such propeller-shaped AIEgens is sensitive to external perturbation, thus leading to a chromic response. Quite a few AIE-based mechanochromic systems have been covered in the review article published by Chi and Xu et al.<sup>20</sup> Herein, we will just select some examples of newly developed mechanochromic systems for discussion. It is noted that the mechanochromic process often coexists with other chromic processes (e.g., thermochromism and vapochromism) in a reversible system.<sup>32,42,133,189,190,204,246,260,328,330,361, 418,879,883,909,912, 919, 945,956–984</sup>

As mentioned above, the 3D structural feature of RIR-dominated AIEgens plays an essential role in their mechanochromic effects. Zou’s group performed the high-pressure studies on TPE by means of diamond anvil cell technique and associated spectroscopic measurements.<sup>956</sup> The results obtained in this work have shed light on the role of intermolecular interactions for the mechanochromic processes and also provide a deeper insight into the role of the highly twisted 3D conformation in modulating the luminescence properties of AIEgens. Under ambient conditions, TPE showed a deep-blue fluorescence with a maximum at 448 nm in the crystalline state. Upon compression, the emission maximum and color gradually red-shifted to 467 nm and sky blue at 5.3 GPa and eventually to 488 nm and spring green at 10 GPa (Figure 186A,B). Generally speaking, the conformational planarization induced by the high pressure accounts for the red-shift in the PL spectra of luminogens. It is notable that there is a larger red-shift in the emission of TPE crystals when the pressure is beyond ~4 GPa, which is suggestive of the augmentation of conformational planarization (Figure 186A). Such a large red-shift arises from the deformation of the C–H···π and C–H···C network associated with the amorphization process, which has impact on the fluorescence efficiency upon compression. Since previous report shows that TPE is irresponsive to the mechanical grinding, the distinct luminescence response to stresses imply that the aromatic C–H···π and C–H···C contacts are strong enough for the stabilization of molecular

packing patterns under mechanical grinding but mutable to extreme pressure. A remarkable enhancement in emission efficiency was recorded in the pressure range of 1.5–5.3 GPa, in contrast to the fluorescence decrease in the ranges of 0.1–1.5 GPa and 5.3–10 GPa. The maximum fluorescence intensity ( $\lambda_{\text{em}} = 467 \text{ nm}$ ) at 5.3 GPa was around three times higher than that ( $\lambda_{\text{em}} = 455.8 \text{ nm}$ ) at 1.5 GPa (Figure 186A). Such a pressure-dependent color and intensity change could be readily observed by the naked eye as well (Figure 186B). When the pressure was gradually released to ambient conditions, the original PL spectrum was restored.

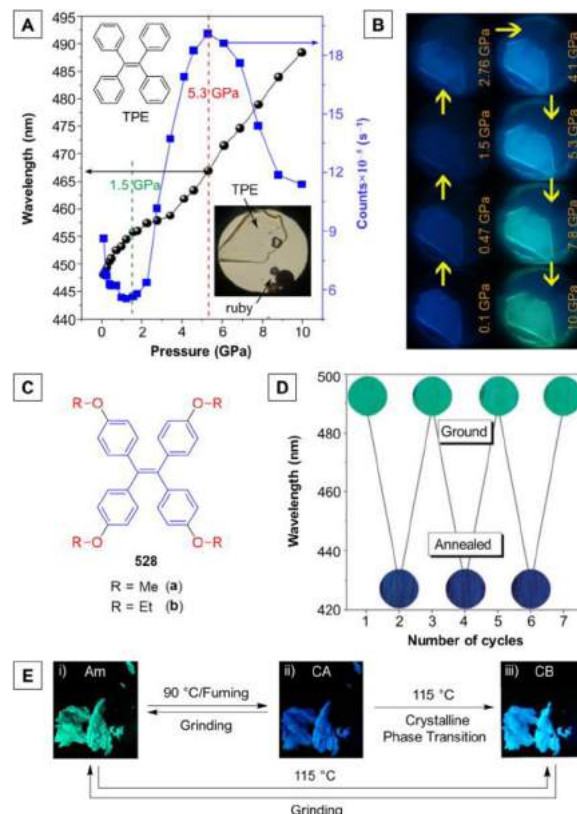


**Figure 186.** (A) Pressure-dependent PL maximum and intensity of TPE crystals. The insets show the molecular structure of TPE and the optical photograph of TPE crystals in the diamond anvil cell. (B) Corresponding typical photographs under UV irradiation ( $\lambda_{\text{ex}} = 375 \text{ nm}$ ). Adapted from ref 956. Copyright 2014 American Chemical Society. (C) Molecular structures of alkoxy-substituted TPE derivatives **528a** and **528b**. (D) Switching the fluorescence of luminogen **528a** by repeated shearing on the inner wall of a quartz cell and heating. Reprinted with permission from ref 957. Copyright 2013 Royal Society of Chemistry. (E) Photos of ground solid form of **528b**, i.e., CA, (i) before and after annealing at (ii) 90 and (iii) 115 °C. Adapted from ref 958. Copyright 2012 American Chemical Society.

This reversible pressure-dependent fluorescence change demonstrated the role of aromatic C–H···π and C–H···C interactions in the structure recovery. In the pressure range of 1.5–5.3 GPa, the formation and further strengthening of such interactions could restrict and dampen the intramolecular motions of the aromatic moieties in a more significant manner, thus boosting the emission. Further compression led to the deformation of the C–H···π and C–H···C network related to the amorphization. Accordingly, at pressure higher than 5.3 GPa, the RIR effect was weakened and the formation of detrimental excimeric species became favorable, which resulted in emission

quenching. In this way, the respective role of twisted 3D conformation, intermolecular contacts, and RIR effect in the luminescence response of TPE to high-pressure was clearly illustrated. This kind of study offers instructive information to the design of mechanochromic AIEgens for a particular purpose and the understanding of their work mechanisms.

Introducing weak interactions into AIE-active molecules may produce polymorphic compounds owing to the varied balance of the weak interactions between luminogens in the solid state. The twisted 3D conformations of AIEgens afford loose packing fashions in the solid state, which facilitate the transformation between different aggregate states. In the light of these facts, extra weak interactions, such as C–H···O and C–H··· $\pi$  contacts were introduced to TPE by simple modification of TPE with alkoxy groups.<sup>957,958</sup> As a consequence, a series of mechanochromic TPE derivatives were yielded, among which **528a** and **528b** would be discussed as representative examples (Figure 186C).<sup>957,958</sup> The solid-state fluorescence emission of tetrakis(4-methoxyphenyl)ethylene **528a** would be repeatedly switched between deep blue (~421 nm) and bluish green (~491 nm) by grinding/heating (annealing)/fuming cycles (Figure 186D).<sup>957</sup> The grinding of as-prepared **528a** solids destroyed the crystalline structure and even converted the crystals to amorphous powders, whereas both heating and fuming recrystallized the molecules and led to the subsequent fluorescence recovery. Depending on the packing patterns, **528b** behaved in a similar way as **528a** during the grinding, heating, and fuming processes.<sup>958</sup> As depicted in Figure 186E, the deep-blue emissive CA (crystalline) form of **528b** was turned to the green Am (amorphous) state upon grinding. Such a process was reversible aided by the heating/annealing at 90 °C or fuming with solvent vapor. Annealing the Am phase or CA state of **528b** at 115 °C both afforded another crystalline state (CB) with sky-blue emission. Grinding the CB form of **528b** also resulted in the green-emissive Am powders.

Attaching moieties larger than alkoxy groups to the TPE units could also generate mechanochromic AIEgens.<sup>879,959,960</sup> For example, incorporation of two (6-phenoxyhexyl)-1*H*-1,2,3-triazole moieties into a TPE system by click reaction generated luminogen **529** (Figure 187A).<sup>959</sup> The as-prepared solid of **529** emitted a pure blue light at 447 nm with a CIE coordinate of (0.15, 0.12). Upon grinding, the emission maximum was red-shifted to 477 nm, due to the morphological transition from the crystalline to the amorphous phase. The thermal annealing or vapor fuming with a polar solvent readily recovered the fluorescence. The writing-erasing process clearly demonstrated its potential for practical applications such as being utilized as a security ink for rewritable information storage system. Likewise, connecting two phenyl rings to the TPE core through single bonds could enlarge the molecular structure and lead to a looser molecular packing compared to that in TPE crystal, which left more room for structural adjustment upon external stimuli (Figure 187B).<sup>960</sup> Moreover, the periphery aromatic rings were flexible and prone to undergo conformational change, as reflected by the fluorescence variation. Collectively, these effects rendered **530** mechanochromic: the blue fluorescence (444 nm) of its as-obtained crystals turned to green light (505 nm) upon grinding, and the green emission was reverted back to the original state by solvent-fuming or thermal annealing (Figure 187B).<sup>960</sup> The mechanochromism of **530** was also attributed to the grinding-induced amorphization and the annealing/fuming-caused recrystallization of the ground samples. Similarly, the fluorescence emission of the hydrocarbonic AIEgen **531** could be

easily interconverted between blue (445 nm) and green (503 nm) color by the grinding-heating/fuming processes (Figure 187C).<sup>879</sup>

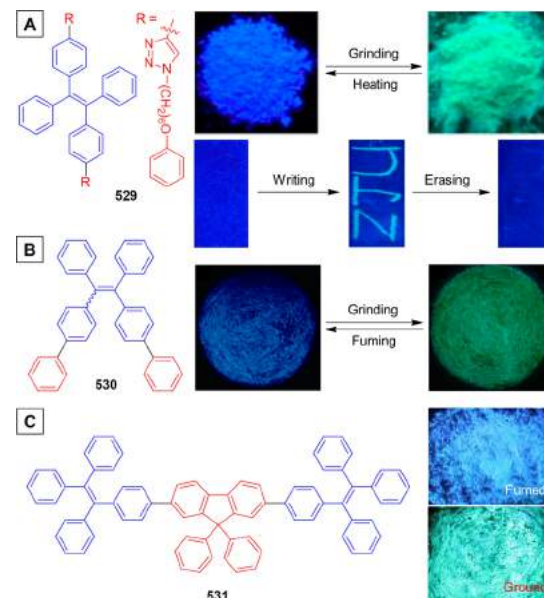


**Figure 187.** Representative examples of mechanochromic TPE derivatives with larger substituents. Molecular structures of (A) **529**, (B) **530**, and (C) **531** and their fluorescent images demonstrating their mechanochromic properties. Panel A is adapted from ref 959. Copyright 2012 American Chemical Society. Panel B is adapted with permission from ref 960 which was published by Springer and distributed under the terms of the Creative Commons Attribution License. Copyright 2013 The Author(s). Panel C is adapted with permission from ref 879. Copyright 2014 Elsevier Ltd.

In the above discussed writing-erasing cycles, the fluorescence colors were hopping back and forth between blue and green. Indeed, the luminescence switching can be shifted to the longer-wavelength region through smart molecular design. Establishing D–A structures in the AIEgens is an effective pathway to red shift the emission. Moreover, as mentioned above, mechanochromism normally results from the perturbation of molecular packing and intermolecular interactions. Therefore, it is crucial to introduce multiple adjustable interactions for the design of ideal mechanochromic materials. These interactions should be strong enough to maintain the orientation and arrangement of the fluorophores but mutable to external mechanical forces. In view of this, a group of triphenylacrylonitrile derivatives (**532**, **533**, and **54**) were rationally designed and synthesized (Figure 188A).<sup>42</sup> Synergistic interplay between the twisted 3D molecular conformation, multiple intra- and intermolecular interactions, including C–H··· $\pi$ , C–H···H–C, C–H···N contacts, van der Waals forces, and dipole–dipole interaction, etc., endowed these compounds with remarkable AIE effects, high solid-state  $\Phi_F$  values, and marked mechanochromism with dramatic changes in the emission color and efficiency (Figure 188B–G).<sup>42</sup> Because of the stronger D–A interaction in AIEgen **54**, it displayed a stronger mechanochromic activity: it showed a higher contrast in the fluorescence color ( $\Delta\lambda = 78$  nm; Figure 188F,G) and a larger variation in the  $\Phi_F$  ( $\Delta\Phi = 24.0\%$ ), in comparison to those of **532** ( $\Delta\lambda = 72$  nm and  $\Delta\Phi = 11.0\%$ ; Figure 188B,C) and **533** ( $\Delta\lambda = 61$  nm and  $\Delta\Phi = 13.0\%$ ; Figure 188D,E). The planarization of the twisted conformation and disruption of the multiple intermolecular interactions in the crystalline state by applying a mechanical stimulation led to the crystal-to-amorphous phase transition and hence were responsible

for the observed high-contrast mechanochromic effect. The TPE trimer **534** (Figure 188H) showed a strong AIE effect but exhibited a merely unobtrusive mechanochromic effect with a  $\Delta\lambda$  as small as 8 nm, when its pristine powder of **534** was ground (Figure 188I).<sup>909</sup> In contrast, the introduction of cyano groups into the trimeric TPE system had greatly altered the properties of the luminogen. The cyano groups endowed the luminophore **512** with the D-A effect, dipole to dipole interaction, and C-H···N contact, which resulted in better crystallinity and greater mechanochromic activity (Figure 188H). The as-prepared solid of **512** emitted a yellow light peaked at 541 nm, while its ground powder showed an orange fluorescence at 563 nm, giving a  $\Delta\lambda$  value of 22 nm (Figure 188J). Such a mechanochromic behavior was reversible and could be repeated for many times by simple grinding-annealing or grinding-fuming processes.

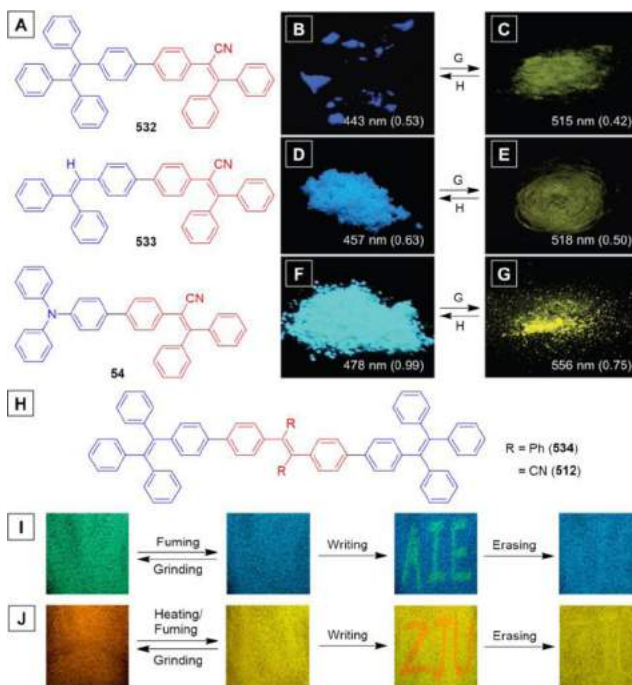


**Figure 188.** Representative examples of AIEgens with moderate D-A effects and showing higher contrasts in the mechanochromic processes. (A, H) Molecular structures of **532**, **533**, **54**, **534**, and **512** and (B–G, I, J) their fluorescent images demonstrating the mechanochromic properties. Panels B–G are reprinted with permission from ref 42. Copyright 2013 Wiley-VCH Verlag GmbH & Co. KGaA. Panels I and J are reprinted from ref 909. Copyright 2013 American Chemical Society.

The D-A interactions in the examples depicted in Figure 188 are moderate. Further strengthening the D-A effect can shift the luminescence switching to an even longer wavelength region. For example, decoration of electron-donating TPE with an electron-accepting pyridinium unit through vinyl functionality yielded luminogen **370** (Figure 189A), which showed typical TICT and AIE effects due to the strong D-A interaction and multiple rotatable moieties.<sup>32</sup> The crystals of **370** showed an intensive green light at 515 nm with a  $\Phi_F$  of 31.8%. Gently grinding the crystals afforded powders emitting orange-red fluorescence at 600 nm, with the  $\Phi_F$  dropping to 20.4% (Figure 189B). The mechanochromism is high-contrasted with a  $\Delta\lambda$  up to  $\sim$ 85 nm. Such a luminescence transformation could be reversed by fuming the ground sample with acetone vapor or heating it at 150 °C (Figure 189B). Thus, **370** has a potential to be applied as a recyclable optical storage medium, which

was demonstrated by the facile writing-erasing-rewriting cycles (Figure 189C). In a like manner, other electron-withdrawing groups such as 1,3-indandione group and benzothiazolium unit can also be separately attached to the TPE motif through a vinyl bridge. The resultant AIEgens **338a** (Figure 189D) and **535** (Figure 189G) possess strong D-A effects and mechanochromic properties.<sup>418,966</sup> The large red-shift from green fluorescence peaked at 510 nm to orange emission at 562 nm was induced by grinding of the as-obtained powder sample of **338a** (Figure 189E).<sup>418</sup> Thermal annealing or solvent-fuming could recover the green emission. The mechanochromic process could be repeatedly produced by grinding-solvent-fuming or grinding-thermal annealing cycles (Figure 189F). Owing to the enhanced D-A interaction in **535** than in **370**, the pristine crystals of **535** exhibited a bright yellow emission at 565 nm.<sup>966</sup> Grinding this sample formed powders with red fluorescence peaked at 650 nm. The yellow and red emission colors could be interconverted by the grinding-fuming process for many times without fatigue (Figure 189H), because these stimuli were nondestructive in nature. Heating the ground sample at

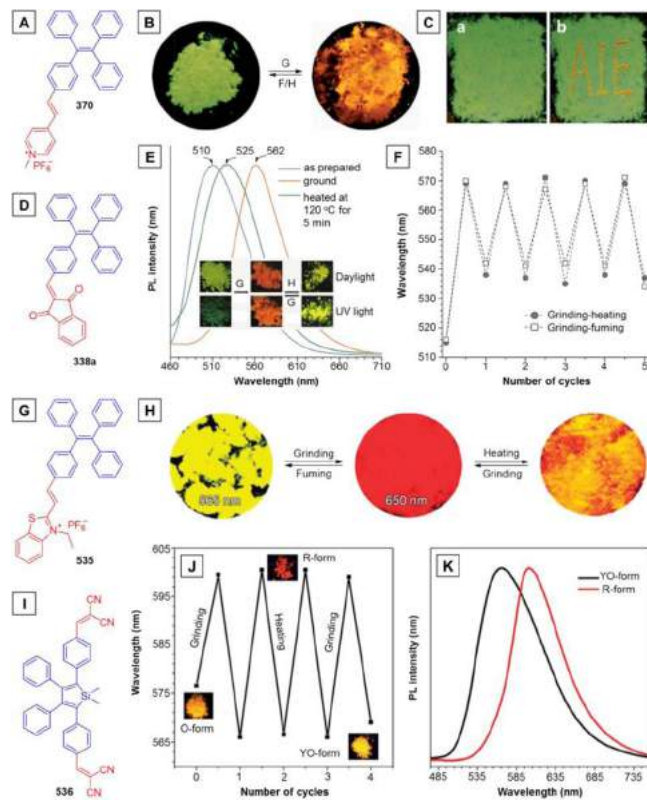


**Figure 189.** Representative examples of AIEgens with strong D-A effects and relatively large conjugation and showing high contrasts and long-wavelength emission inter-conversion in their mechanochromic processes. (A, D, G, I) Molecular structures of **370**, **338a**, **535**, and **536** and (B, C, H) their fluorescent images as well as (E, F, J, K) the PL spectra depicting the mechanochromic properties. Panels B and C are reprinted with permission from ref 32. Copyright 2013 Royal Society of Chemistry. Panels E and F are reprinted with permission from ref 418. Copyright 2014 Wiley-VCH Verlag GmbH & Co. KGaA. Panel H is reprinted with permission from ref 966. Copyright 2012 Royal Society of Chemistry. Panels J and K are reprinted with permission from ref 967. Copyright 2011 Royal Society of Chemistry.

150 °C for 10 min only shifted the emission color from red to orange, and such a process was also reversible.

Not just TPE systems can be tailored into materials with high-contrasted mechanochromic properties in the long-wavelength region through the incorporation of D-A effects into their structures, other AIE-active systems can also be designed into desirable mechanical-force responsive materials in a similar manner.<sup>883,912,967,974,976,977,983</sup> For example, the dicyanovinyl-containing DMTPS derivative **536** possessed strong D-A effect and AEE activity, which gave efficient emission located in long wavelength spectral region (Figure 189I).<sup>967</sup> Its twisted 3D molecular conformation and multiple intermolecular interactions such as dipole-to-dipole, C-H···N, and C-H···π interactions endowed it with porous crystal structures, multiple structural transformability, and mechanochromism ability. The as-prepared crystals of **536** exhibited an orange (O-form) emission with a maximum at 576.5 nm. Whereas after grinding, the emission was converted to red fluorescence (R-form) peaked at 600.5 nm (Figure 189J,K). Thermal annealing of the ground sample at 150 °C could readily restore intense yellow-orange fluorescence at 566 nm (YO-form). The interconversion between the YO-form and R-form was reversible and repeatable by grinding and heating cycles (Figure 189J). The mechanochromism of all the AIEgens shown in Figure 189 was attributed to the morphological change from the thermodynamically stable crystalline phase to the metastable amorphous state.

In the AIEgen-based mechanochromic systems discussed above, the response in luminescence upon the application of mechanical force mainly lies in the emission color change. In the meantime, the emission efficiency is decreased to some extents in most cases. In some systems, the fluorescence could be completely quenched upon mechanical force stimulation.<sup>968,969</sup> For example, a group of diphenyldibenzofulvene derivatives were reported to show a phenomenon of CIE/CEE. These luminogens emitted faintly in the solution and amorphous phases but showed strong light emission in the crystalline state. AIEgens **537a**, **537b**, and **538** were members of such a family (Figure 190A), which showed thermochromic and mechanochromic fluorescence due to their striking CEE/CIE effects. The amorphous state of **537a** exhibited a weak emission, while its crystals showed intense fluorescence.<sup>968</sup> As shown in Figure 190B, the fluorescence of **537a** could be switched between “bright” and “nearly dark” states by grinding-thermal annealing or writing-erasing processes.<sup>968</sup> Compared with **537a**, the amorphous-state emission of **537b** and **538** was even weaker ( $\Phi_F < 1.0\%$ ), rendering the fluorescence of their ground samples in the “dark” state. Single crystals of **537b** with bright green emission ( $\Phi_F = 82.1\%$ ) were easily obtained by slowly evaporating its chloroform/ethanol solution, while the evaporation of its chloroform/isopropyl alcohol mixture afforded needlelike single crystal with yellow fluorescence ( $\Phi_F = 56.2\%$ ). This demonstrated the polymorphism of **537b**. The emission difference between these two polymorphs originated from the different extents of C-H···O and C-H···π interactions. Interestingly, the yellow-emissive crystals could be transformed to the ones with green emission by thermal annealing at 120 °C for 1 min, as a result of the crystal-to-crystal phase transition (Figure 190C). The CIE features of **537b** and **538** endowed them with the capability to interconvert between the “dark (off)” and “bright (on)” states by grinding-annealing cyclic operations (Figure 190D,E). The mechanochromic effects of these three diphenyldibenzofulvene compounds are

attributed to the amorphization and crystallization induced by grinding and heating, respectively.

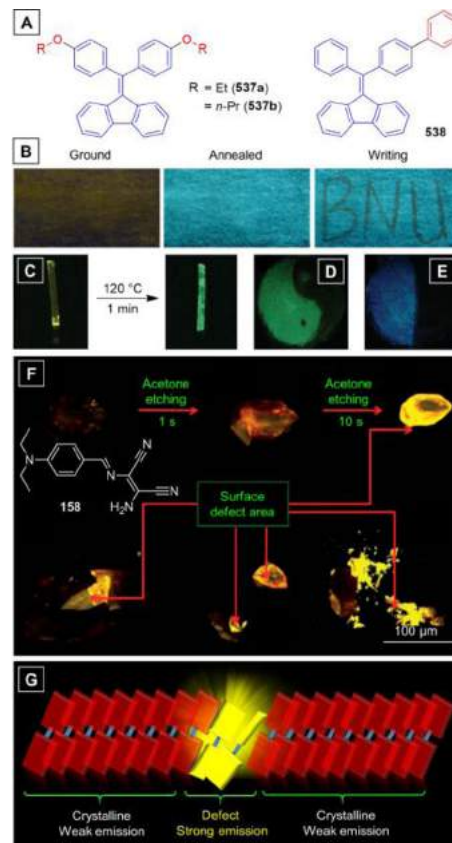


**Figure 190.** Representative examples of AIEgens exhibiting solid-state emission switches between dark and bright states. (A) Molecular structures of CIE/CEE-active **537** and **538**. (B) Switching of solid-state emission of **537a** by repeated grinding-annealing processes. Reprinted with permission from ref 968. Copyright 2013 Science China Press and Springer-Verlag Berlin Heidelberg. (C) Fluorescent photographs showing the conversion from weakly yellow emissive state to highly green emissive state of **537b**. Fluorescent photographs showing the emission-off/on switch of (D) **537b** and (E) **538** upon grinding and annealing treatments. Adapted with permission from ref 969. Copyright 2011 Wiley-VCH Verlag GmbH & Co. KGaA. (F) Micrographs of single crystals of **158** taken under UV irradiation: pristine single crystals, crystals before and after acetone etching for 1 and 10 s, and crystals with surface defects. (G) Schematic illustration of the defect-sensitive behavior of **158** and its working mechanism. Reprinted with permission from ref 204. Copyright 2013 Royal Society of Chemistry.

The luminescence efficiency of the above discussed AIEgens was all decreased after being mechanically ground. Mechanical force-induced light emission, however, has been observed in some AIE-active systems.<sup>204,328,984</sup> The diaminomaleonitrile-functionalized Schiff base **158** was a representative among these special AIEgens.<sup>204</sup> The intact crystals of **158** were virtually non-luminescent (Figure 190F). After being etched by acetone for 1 s, the light emission peaked at 563 nm was turned on. The elongation of the etching time could further boost the luminescence. Applying mechanical forces such as rubbing, pressing, crushing, shearing, and ultrasonic vibration, etc., which can generate defects on the crystals, could also induce the light emission. Thus, **158** showed remarkable defect-sensitive property and turn-on type mechanochromism. After being ground

or hit by a glass rod, powders with brilliant yellow emission were furnished with  $\Phi_F$  as high as 48.8% and decay lifetime of 5.99 ns. The fluorescence intensity was proportional to the force applied to generate the defects, with the detection limit reaching 0.1 N due to its light-up nature. Such a defect-induced emission resulted from the rearrangement of molecular packing. Molecules of **158** were organized in an antiparallel face-to-face packing fashion with strong intermolecular  $\pi$ - $\pi$  stacking interaction in the crystal lattice, which favored the formation of detrimental excimer species. Once an exogenic force was exerted onto the crystals, the regular face-to-face organization was destroyed and consequently the  $\pi$ - $\pi$  stacking interaction was weakened. Free from such restraints, the molecules of **158** could adopt a twisted conformation and undergo radiative relaxation, leading to the activation of the luminescence process (Figure 190G).

To sum up this section, mechanochromic materials with the AIE/AEE characteristic have been intensively expanded in the past few years. The highly twisted 3D conformation of AIEgens was one of the critical factors for their mechanochromic activity. Introduction of adjustable intermolecular interactions in the molecular packing could benefit the mechanochromism for it can enhance the contrast. Incorporating D-A interaction could red-shift the luminescence switching and usually also bring about higher contrasts. The emission color and efficiency of most AIEgens were red-shifted and decreased upon the application of mechanical force. Occasionally, the light emission of some CIE-/CEE-active luminogens could be totally quenched by mechanical stimulation, and hence they exhibited an off-on luminescence switching. In some special AIE systems, their luminescence was turned on in the presence of mechanical stimulus.

**5.4.2. Heat.** Thermal/heat-driven fluorescence switches can be easily realized in AIE-active systems.<sup>43,270,326,853,985–990</sup> Fabricating AIEgen-based organic gelators is an effective and frequently-used approach to achieve thermoresponsive AIE systems.<sup>43,987–989</sup> Various archetypal AIEgens have been functionalized with different moieties to yield diverse AIE-active gelators. For example, organic gelators **539** and **540** were built from the silole framework and preserved the AIE attributes (Figure 191A).<sup>43</sup> They were almost non-luminescent in the solution state but became much more emissive in the aggregate state. Gelation of **539** and **540** could readily occur in hexane, methylcyclohexane, and heptane, which gave gels with bright blue and green fluorescent, respectively. As depicted in Figure 191B,C, thermal-switchable fluorescence organogels were developed by taking advantage of their AIE activity. The fluorescence could be reversibly switched between on and off states by the gel-solution transition via alternating cooling and heating processes. Such thermoresponsive AIEgen-based organogels thus possess potentials to be utilized in information storage, optical devices, and biological applications.

Supramolecular self-assembly is another useful methodology for the construction of thermoresponsive systems. Yang's group recently developed a thermoresponsive supramolecular system based on a pillar[5]arene tetramer derivative **541** with a TPE core and four pillararene cavities (Figure 191D).<sup>985</sup> This TPE-bridged pillararene tetramer featured with AIE characteristic and could act as a host that could bind strongly to a linear neutral guest linker **542** with cyano and triazole sites to form an A<sub>4</sub>/B<sub>2</sub>-type supramolecular polymer (i.e., host-guest inclusion complex) in chloroform through non-covalent interactions. The host-guest inclusion complexes could further undergo supermolecular self-assembly, leading to a significant enhancement in the blue fluorescence due to the further activation of the RIR process. These 3D

assemblies were thermally responsive (Figure 191E,F). Gradually increasing the temperature of the assemblies (i.e., mixture of **541**

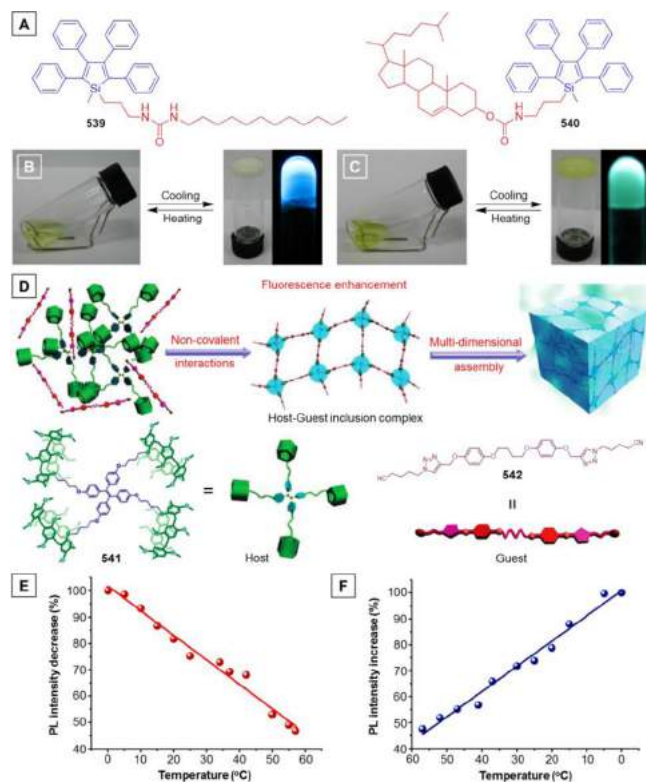


**Figure 191.** Representative examples of thermal responsive AIE gelation systems. (A) Chemical structures of silole-based organic gelators **539** and **540**. Illustration of the gel formation for compounds (B) **539** (23 mg/mL in hexane) and (C) **540** (150 mg/mL in *n*-heptane) and photos of the formed gels taken under the 365 nm UV light illumination. Adapted with permission from ref 43. Copyright 2009 Elsevier B.V. (D) Schematic illustration of the construction of fluorescent supramolecular polymers from TPE-bridged pillararene tetramer **541** and triazole-based neutral linker **542**. (E) Relative change in emission intensity at 488 nm with elevating the temperature from 0 °C to 57 °C (PL intensity decrease (%) =  $I/I_0 \times 100\%$ ). (F) Relative change in emission intensity at 488 nm with lowering the temperature. Adapted with permission from ref 985. Copyright 2014 Royal Society of Chemistry.

and **542**) in chloroform from 0 to 57 °C decreased the fluorescence by 53.3% (Figure 191E). Conversely, the emission intensity of this host-guest mixture was boosted by 110.7% upon lowering the temperature from 57 to 0 °C (Figure 191F). Such a temperature-dependent fluorescence change was reversible and could be repeated for many cycles. Temperature elevation always reduces the stability of the host-guest systems owing to the more favorable entropy term ( $T\Delta S^\circ$ ) governing their complexation free energy. The stability change of the formed supramolecular assemblies induced by temperature variation modulates the fluorescence intensity by affecting the RIR process of the AIE-active host **541**.

The solid-state thermoresponsive behavior of an interesting aryl-substituted pyrrole derivative, namely, 4-(2,5-diphenyl-1H-pyrrol-1-yl)benzoic acid (**414-H**; Figure 192A) was investigated by Dong, Shi, and Tang et al.<sup>990</sup> Attaching a carboxylic acid group to the triphenylpyrrole unit generated a luminogen which only fluoresced strongly in a certain aggregation form, e.g., the crystals grown from its DMF solution. By exploiting such a fascinating property, a solid material responsive to heat stimulation was

developed. Upon heating, the fluorescence of this crystalline solid kept almost unchanged at relatively low temperature range ( $<70$  °C) but was greatly decreased when the temperature reached  $\sim 85$  °C (Figure 192A). Such a distinct quenching effect was rationalized to be ascribed to the thermal volatilization of DMF molecules. Inevitably, the molecular packing was loosened by the loss of DMF molecules in the crystal lattice, thereby switching on the non-radiative relaxation channels owing to the deactivation of RIM process. The fluorescence response of **414-H** to the temperature change enjoyed good reversibility and reproducibility. Thus, light emission of the DMF-induced crystal film of **414-H** was rapidly quenched by heating at 100 °C for 40 s, while the luminescence of the quenched film could be reinstalled by recrystallization in DMF vapor at 60 °C (Figure 192B). As the fuming and thermal treatment were non-destructive in nature, the fluorescence of the film could hop back and forth between the “on” and “off” states for many times without fatigue and loss. The fast response (<30 s), high selectivity (>85 °C), good reversibility, and solvent-free procedure make **414-H** promising for fascinating temperature-monitoring devices.

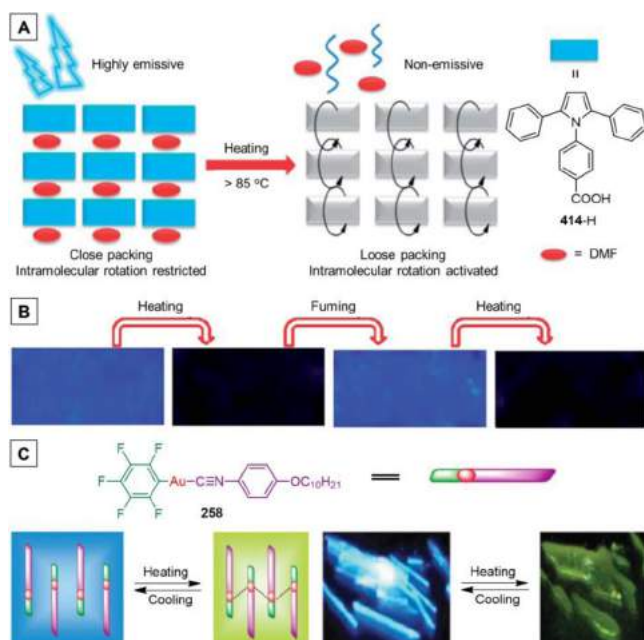


**Figure 192.** Representative examples of solid-state thermal-responsive systems based on AIEgens. (A) Schematic illustration of the thermoresponsive behaviors of **414-H** and the corresponding mechanism. (B) Reversible switching of the light emission of the **414-H** film between dark and bright states by repeated fuming with DMF vapour at 60 °C for 2 min and heating at 100 °C for 40 s. Reprinted with permission from ref 990. Copyright 2013 Royal Society of Chemistry. (C) An illustration of the luminescence change of **258** before heating and after heating, and its corresponding fluorescent images under 365 nm UV illumination. Adapted with permission from ref 326. Copyright 2013 Royal Society of Chemistry.

The above discussed thermoresponsive AIE materials all change their fluorescence intensity in response to the temperature variation. There are some other AIE-active systems whose emission color is sensitive to temperature change. The AIE-active gold(I) complex **258** is such an example.<sup>326</sup> The photoluminescence spectra of the crystals of **258** displayed two emission bands at 407 and 428 nm, respectively, which were assigned to

the fluorescence from the intra-ligand localized  $\pi-\pi^*$  excited state. Gentle heating (>55 °C) of the sample on a slender piece of glass resulted in a broad emission band peaked at 530 nm (Figure 192C). The aurophilic interactions might be the cause for the generation of new ligand-to-metal–metal charge transfer excited state. Thanks to its AIE attribute, complex **258** exhibited the thermochromic property in the solid state, as indicated by the temperature-induced luminescence switches. When the temperature dropped to 25 °C, the solid showed an emission band similar to that of the original sample. The blue-to-yellow-green fluorescence switching was repeatable and could be implemented by consecutive heating and cooling cycles in the temperature range of 25–59 °C.

**5.4.3. pH.** pH-Driven luminescence switches can be facilely obtained by taking advantage of AIEgens capable of undergoing repeatable protonation and deprotonation. Supramolecular polymers formed by non-covalent interactions (e.g., host-guest inclusion, metal-ligand interaction, donor-acceptor interaction, hydrogen bonding, and van der Waals forces) are versatile stimuli-responsive systems. This is due to the reversibility of non-covalent interactions which endows the supramolecular polymers with reversible responsiveness to external stimuli. Apart from the thermoresponsive AIE system built upon a supramolecular polymer with TPE derivative **541** as a host, an AIE encoded supramolecular polymer with pH-responsive property has also been reported (Figure 193).<sup>991</sup> This pH-responsive supramolecular polymer was constructed with AIE-active 1,1,2,2-tetrakis(4-(pyridine-4-yl)phenyl)ethene (**15**) as the guest building block and homoditopic bis-*p*-sulfonatocalix[4]arene serving as the host building block in aqueous media. The RIR process of **15** was activated by the formation of host-guest supramolecular polymer under acidic conditions, giving bright yellow fluorescence peaked at  $\sim 550$  nm. Intriguingly, the pH response of this supramolecular polymer could be presented in two modes. When adding the NaOH into the solution, the protonated **15** was returned to the original state (i.e., **15**). This disrupted the supramolecular interactions and resulted in the disassembly of the supramolecular polymer. When the experiments were carried out in water, the poor water-solubility of **15** had forced its molecules to form aggregates with strong green emission at  $\sim 505$  nm. However, different results were obtained when the supramolecular polymer was formed in THF/water mixture (1/1, v/v). The released AIEgens were soluble in this solvent mixture and thus exhibited almost no fluorescence owing to the active intramolecular motions. In this case, the emission could be modulated by pH between on ( $\Phi_F \sim 26.4\%$ ) and off ( $\Phi_F \sim 0.4\%$ ) states. Both the yellow-green and on-off fluorescence switching processes were reversible and repeatable.

In addition to the pyridyl motif, dimethylamino group can also be protonated and deprotonated in the presence of acid and base, respectively. In the light of this, a number of pH-responsive AIE systems have been developed based on such a mechanism.<sup>190,992–994</sup> Some examples are shown in Figure 194. The evaluation of their pH responsiveness could be conducted in the solid state. HCl or TFA gas and NH<sub>3</sub> or triethylamine (TEA) vapor were employed as pH stimuli. The AIE-active boron compound **543** deposited on a TLC plate appeared red under ambient light and emitted a red light under UV illumination (Figure 194A).<sup>992</sup> Its red color faded when exposed to HCl gas accompanied by emission shift to the blue region. After being fumed with NH<sub>3</sub> vapor, its original state was recovered. As illustrated in Figure 194A, such a pH-responsive behavior was

ascribable to the protonation-caused destruction of the intramolecular charge transfer (ICT).

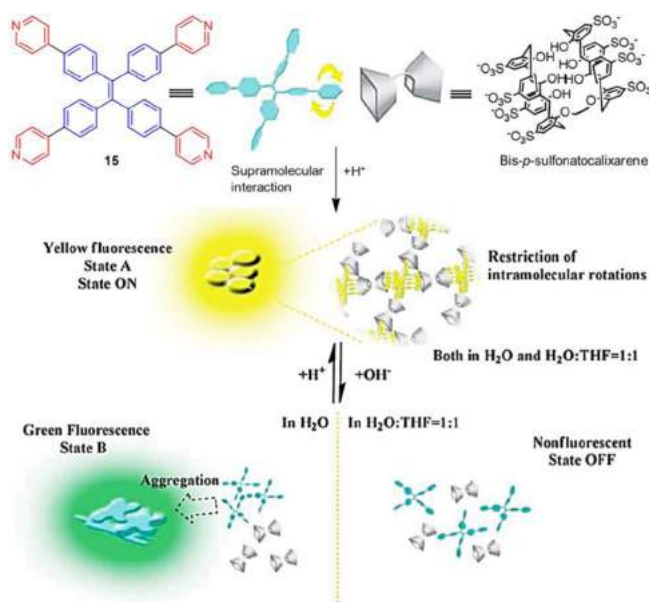


**Figure 193.** Schematic representation for the preparation of supramolecular polymer from tetrapyridine-TPE (**15**) and sulfonato-calixarene and switching between states A (yellow fluorescence) and B (green fluorescence) in  $\text{H}_2\text{O}$  and state ON (yellow fluorescence) and state OFF (non-fluorescent) in  $\text{H}_2\text{O}/\text{THF}=1:1$  in volume. Reprinted with permission from ref 991. Copyright 2014 Royal Society of Chemistry.

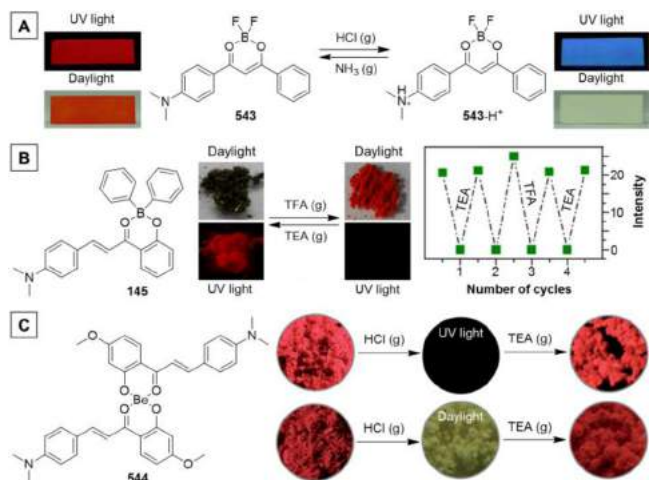


**Figure 194.** Representative examples of pH-responsive systems based on AIEgens carrying dimethylamino groups (**543**, **145**, and **544**). Panel A is adapted with permission from ref 992. Copyright 2013 Elsevier Ltd. Panel B is adapted from ref 190. Copyright 2014 American Chemical Society. Panel C is reprinted with permission from ref 993. Copyright 2014 Royal Society of Chemistry.

Similarly, another AEE-active boron compound **145**, which also has a dimethylamino group in its molecular structure, showed a prominent polar nature and a Lewis base character (Figure 194B).<sup>190</sup> The dark green crystalline samples with bright NIR fluorescence could be turned into completely non-luminescent red ones upon treatment with TFA vapor in an enclosed container. The on/off fluorescence conversion might

result from the protonation of the dimethylamino group, which eliminated the intrinsic ICT effect of the D-A molecule. Moreover, the variation in the molecular conformation and/or alteration in the molecular packing induced by protonation might also be responsible for the acid-induced emission quenching. The fluorescence “on” state could be readily recovered by fuming the sample with TEA vapor. Such solid-state fluorescence on-off switching process was reversible and could be reproduced by simple acid–base fuming processes for many times (Figure 194B). Actually, in addition to its pH-responsive ability, **145** also possessed a mechanochromic activity: its fluorescence could be turned off by mechanically grinding its crystals and restored by fuming the ground sample with solvent vapor.

Besides boron-based AIE systems, a class of beryllium complexes had also been reported to show a similar behavior upon pH variation.<sup>993</sup> These complexes featured the CEE characteristics and showed morphology-dependent dark and bright red/NIR light emission. They exhibited faint fluorescence in the amorphous state but strong red/NIR emission in the crystalline form. Their luminescence could be switched off and on by simple acid/base vapor fuming. Take **544** as an example (Figure 194C). Upon exposure to  $\text{HCl}$  vapor, the color of the solid sample of **544** gradually faded from red to yellow through an orange intermediate state, accompanied by emission color change from deep red (658 nm) to orange red (630 nm) and ultimately to yellow (574 nm) and drastic fluorescence quenching. Such a process was completely reversible. The yellow sample gradually reverted to the original state after being treated with TEA vapor for several minutes. The switching between fluorescence off and on states induced by acid (low pH)/base (high pH) vapor could be performed repeatedly without obvious intensity loss. Analogous to **543** and **145**, the pH responsiveness of **544** was also attributed to the protonation/deprotonation of the dimethylamino groups, which shut off/turned on the ICT effect and also altered the molecular conformation and packing fashion.

**5.4.4. Vapor.** Some AIE-involved systems have been found to exhibit vaporchromism.<sup>44,995</sup> In other words, the variation in their luminescence properties (emission intensity and/or wavelength) would be triggered by treatment with different solvent vapors and hence they are also referred to as vapor-responsive materials. For example, *o*-carborane-containing poly(fluorene) **545** was reported to show response to solvent vapors (Figure 195).<sup>995</sup> Conjugated polymers built from *o*-carborane are of particular interest for applications in sensing and stimuli-responsive materials due to the  $\text{C}_2\text{B}_{10}$  cage’s unique bonding scheme as well as its bent geometry. In particular, it has generally been accepted that *o*-carborane can promote the AIE effect in conjugated polymer systems, which makes the combination of *o*-carborane and conjugated polymeric skeleton even more attractive. The introduction of *o*-carborane into the poly(fluorene) framework via direct bonding in the aromatic backbone repeat structure indeed imparted some new properties (Figure 195A). Such a hybrid conjugated polymer exhibited a complicated photoluminescence spectrum in dilute chloroform solution: typical blue fluorescence was observed for the fluorene segments near 420 nm, a green fluorescence ascribed to the aggregation-induced emission phenomenon was located at around 525 nm, and a lower energy orange/red emission band was peaked at  $\sim 570$  nm which likely arose from the energy transfer from the excited fluorene moieties to the electron-deficient *o*-carborane units. This *o*-carborane-bearing poly(fluorene) was found to feature the AIE property, showing bright green light emission in the solid state, which was rationalized to

result from the fluorene segments adjoining the *o*-carborane cages. The luminescence behaviors were greatly dependent on the proximity and packing of the fluorene segments in the polymer.

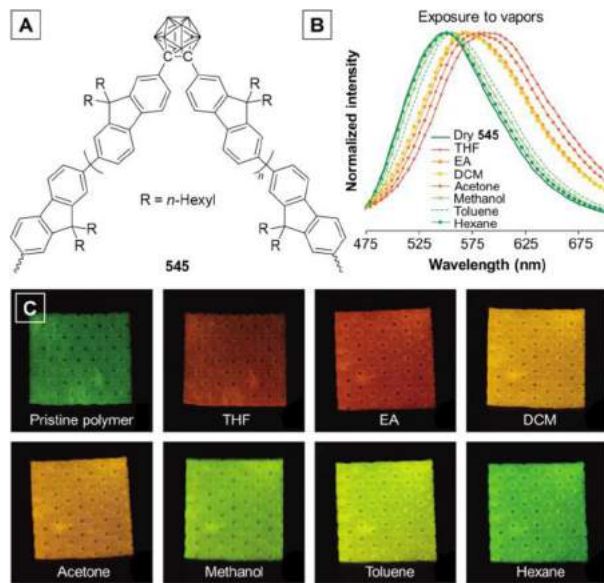


**Figure 195.** (A) Chemical structure of carborane-containing poly-fluorene 545. (B, C) Its response to solvent vapors (spectra and fluorescent images). Adapted from ref 995. Copyright 2011 American Chemical Society.

The emission modulation of 545 in the solid state was realized through interactions with small molecules such as solvent vapors (Figure 195B,C). This polymer in the solid state underwent a change in its emission wavelength when exposed to organic solvents or their vapors, shifting from bright green to shade of yellow, orange, or red depending on the solvent used. As shown in Figure 195B, the shift correlated most closely to the polarity of the solvent vapor, and the higher the solvent polarity, the larger the red-shift in the emission would be. Such phenomenon is similar to the solvatochromism observed for some luminescent molecules in the solution phase. When exposed to solvent vapors, the emission intensity also became lower, which was likely associated with the activation of the intramolecular motions of the *o*-carborane systems. For simpler and better demonstration of such a vapor-responsive phenomenon, the polymer was coated onto small squares of laboratory wipes via dip coating. The obtained polymer-coated substrate luminesced at 550 nm under UV illumination. These solid samples of polymer 545 displayed distinct fluorescent emissions after being exposed to different solvent vapors, which could be observable with the naked eye (Figure 195C). The vapor-fumed samples could easily and quickly regain their original green-emissive state upon exposure to ambient air, as the vapors volatilized. Such vapor-induced fluorescence switching could be reproduced using different solvents without evident fatigue.

The change in luminescence property caused by solvent vapors could give rise to variations in metallophilic interactions,<sup>996</sup> solvent–metal bonds,<sup>997</sup> hydrogen bonding,<sup>998,999</sup> and aromatic  $\pi$ – $\pi$  interactions.<sup>1000,1001</sup> A large number of organometallics and coordination complexes have been utilized as vapor-responsive luminescent materials.<sup>1002–1008</sup> Metallophilic interactions between metal centers were either disrupted or enhanced upon vapor fuming, thereby altering the energy gaps

between HOMO and LUMO levels and thus resulting in distinct change in the photoluminescence spectra. In this context, two iridium(III) diimine complexes, namely, 546 and 275, have been synthesized via a single two-step reaction (Figure 196A).<sup>44</sup> 546 and 275 exhibited typical AIE behaviors: they emitted faintly in solution but brightly in the solid state. The RIR principle and their distorted octahedral geometries accounted for their AIE activities. The emission of solid thin films of 546 and 275 was sensitive to the polarity of solvent vapors. More specifically, using 546 as an example for illustration, the sample of 546 obtained by recrystallization from its DCM solution luminesced a greenish yellow light. Upon exposure to 1,4-dioxane, the emission color changed to bluish green. The original greenish-yellow luminescence was restored after being exposed to the DCM vapor. The emission could hence be repeatedly interconverted between greenish yellow and bluish green when the thin film was alternatively fumed with 1,4-dioxane and DCM vapors (Figure 196B). Moreover, the luminescence color was greatly dependent on the polarity of the solvent vapor. 546 exhibited luminescence at the longer wavelength upon exposure to solvent vapor with a higher polarity (Figure 196C). For example, the emission peak shifted from 500 nm in 1,4-dioxane vapor to 540 nm in acetonitrile vapor. The mechanism for such vapor-responsive behavior was ascribed to the fact that space exists in the crystal lattice for the accommodation of small organic solvent molecules. The nature of the lowest excited states of 546 in the film state was predominately comprised of ligand-centered states on exposure to nonpolar solvent vapor, whereas that changed to a metal-to-ligand charge transfer (MLCT) character when exposed to polar solvents.

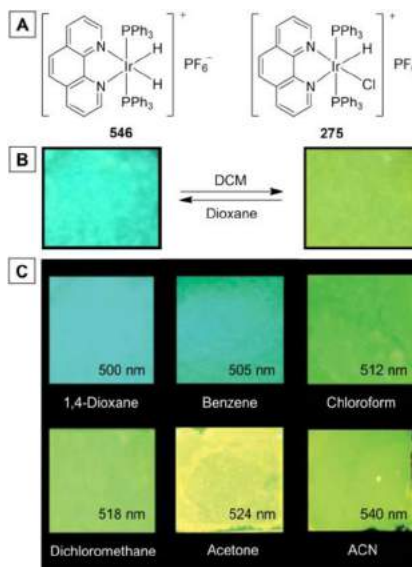


**Figure 196.** (A) Chemical structures of the vaporchromic AIE-active organometallic complexes 546 and 275. (B) A solid-state reversal of emission color of 546 between bluish green and yellowish green via exposure to DCM and dioxane. (C) Change in thin-film emission color of 546 (bluish-green to yellow) with systematic increase in solvent polarity (polarity increased in the order of 1,4-dioxane < benzene < chloroform < dichloromethane < acetone < acetonitrile). The photos were taken under UV irradiation. Adapted with permission from ref 44. Copyright 2014 Wiley-VCH Verlag GmbH & Co. KGaA.

**5.4.5. Photon.** Photoactivatable or photo-responsive materials have been widely applied in many technological fields especially those related to biological applications such as

super-resolution imaging and macromolecular movement tracking. Our group recently developed a photoactivatable system which is presented in Figure 197.<sup>45</sup> This caged AIEgen (**547**; Figure 197A) was constructed by capping a TPE derivative (**548**) with a 2-nitrobenzene group (**549**), a frequently used quencher for constructing caged fluorophores. **547** was practically non-luminescent both in solution and aggregate states as a result of photoinduced electron transfer. In the presence of UV irradiation, the quenching (i.e., 2-nitrobenzene) moiety was removed from **547**, thus allowing the TPE motif in the resulting product to emit intensively in the aggregate state (Figure 197A).

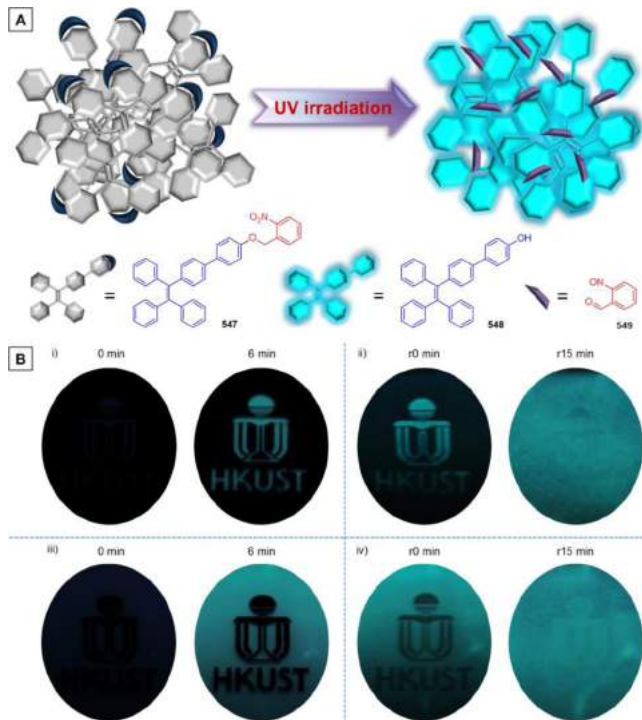


**Figure 197.** (A) Schematic illustration of the uncaging process of **547** upon UV irradiation. (B) Photographs of (i and iii) the process of photo-patterning of **547** using a mask with the HKUST logo under UV irradiation and (ii and iv) pattern-erasing process after removing the mask and subsequent irradiation with UV light. Adapted with permission from ref 45. Copyright 2014 Royal Society of Chemistry.

The photoresponsive capability of **547** makes it useful for practical applications in such as photopatterning and anticounterefeiting. For example, the photopatterns exhibited in Figure 197B have clearly demonstrated such a possibility. Filter papers loaded with **547** were prepared by simply soaking them in the THF solution of **547** followed by drying using compressed air. Two kinds of patterns could be obtained by applying two different projector films with HKUST logo as patterned masks to cover onto the aforesaid filter papers. The logo image in one mask was transparent [group (i) in Figure 197B] while in the other one was dark [group (iii) in Figure 197B]. Upon UV irradiation, the HKUST logo in each case became visible. For the one masked with a transparent logo, the frame structure was much brighter than the background. On the contrary, when a dark mask was used, the logo observed displayed a much dimmer fluorescence than the surroundings. The patterns could be erased by further photo-irradiation after the removal of the masks which enables the photocleavage of the quenching groups in the caged molecules all

over the filter paper [group (ii) and (iv) in Figure 197B]. This work has set up a new and effective approach for the development of AIEgen-based photoactivatable materials.

**5.4.6. Multiplex.** Judicial combinations of different chromic effects will enable the AIEgens to find a large array of high-tech applications. AIE systems which can respond to multistimuli have been developed and reported.<sup>190,993,1009,1010</sup> The pH-responsive AIEgen **544** discussed above actually could be considered as a multiresponsive system as it showed reversible triple-channel solid-state fluorescence on-off switching by grinding-fuming, acid-base vapor fuming, and heating-fuming treatments. Another example of multiresponsive AIEgens was exhibited in Figure 198. AIE-active luminogen **550** was made by employing TPE as a building block and introducing 6-hydroxybenzothiazole as an acid-specific reaction site.<sup>1009</sup> Benefiting from its AIE characteristic, the as-obtained solid powder of **550** emitted a bright blue light peaked at 454 nm with a  $\Phi_F$  of 25.0% ( $B_1$  form). Fuming the sample with HCl vapor dramatically changed the emission from blue to yellow at 550 nm with a  $\Phi_F$  of 19.0% ( $Y_1$  form), indicative of its pH-responsive capability. When subsequently exposed to NH<sub>3</sub> vapor, the initial blue-emissive  $B_1$  state was fully restored. This reversible fluorescence switching manipulated by HCl and NH<sub>3</sub> vapor fuming was associated with the corresponding protonation and deprotonation of **550** (Figure 198).

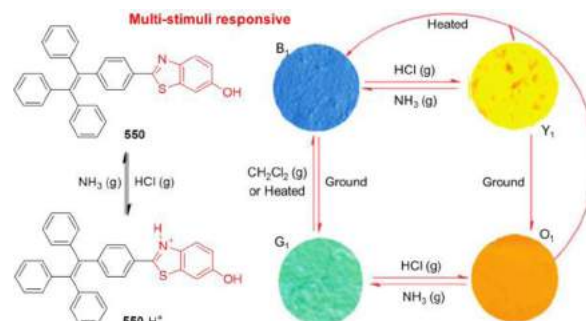


**Figure 198.** Representative example of AIEgen-based smart material showing multistimuli responsiveness. Adapted with permission from ref 1009. Copyright 2014 Royal Society of Chemistry.

In the meantime, mechanical stimuli such as grinding and shearing could facilely shift the blue fluorescence of the pristine solid powder of **550** to emerald with a maximum at 492 nm and a  $\Phi_F$  of 15.0% ( $G_1$  form). Thermal annealing or solvent fuming enabled the full recovery of the original  $B_1$  state, suggesting that the mechanochromic effect was reversible. Interestingly, as the mechanochromic process merely altered the mode of molecular packing rather than changed the chemical structure, the ground sample ( $G_1$  form) preserved the property of protonation-deprotonation and hence was also pH-responsive. Upon fumigation of HCl vapor, the emerald luminescence was turned into orange light ( $O_1$  form) at around 565 nm with a  $\Phi_F$  of 27.0%. The deprotonation of **550** induced by NH<sub>3</sub> vapor also led to the restoration of the original bluish-green state. Moreover, when the  $Y_1$  powder was ground, its fluorescence was converted to orange similar to that of the  $O_1$  form. Both the protonated powders  $Y_1$  and  $O_1$  could be easily reverted to the initial  $B_1$  state by heating, suggestive of a lossless fluorescence switching. In this way, a reversible four-color luminescence switching built upon a single AIEgen in the solid state has been achieved.

## 6. CONCLUSIONS AND PERSPECTIVES

AIE, just as its name implies, refers to a photophysical effect that light emission of a luminogen is activated by aggregate formation. The luminogens with AIE effects are called AIEgens. They luminesce more efficiently in the practically useful aggregate state than the solution state and follow the general collective quantity–effect rule. In contrast to ACQphores, AIEgens perfectly embody the philosophical belief that “*United we stand, divided we fall.*” Since the concept was coined in 2001, AIE has changed people’s way of thinking about chromophore aggregation and brought forth a revolution both conceptually and technically. AIE-related research is booming now, which has permeated a large number of research disciplines with a widespread influence. As mentioned in the [Introduction](#) section, AIE is ranked no. 3 among the top 100 research frontiers in the field of Chemistry and Materials Science in 2013 (cf., Thomson Reuters Essential Science Indicators). In response to the worldwide research enthusiasm, we have meticulously written this comprehensive review article. We have set forth the mechanistic understanding of AIE systems gained so far from both experimental and theoretical viewpoints, introduced the design strategies derived from RIM principle for transforming conventional ACQphores into AIEgens, showcased typical examples of various types of AIEgens, and illustrated their technological applications in bioimaging, chemosensing, optoelectronics, and stimuli-responsive systems.

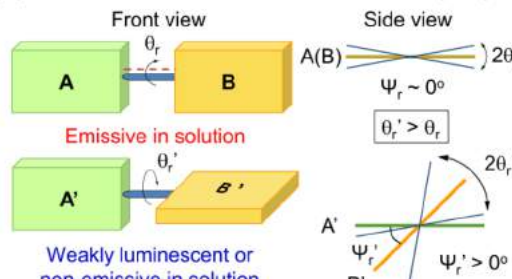
AIEgens are typically nonplanar molecules that are nonluminescent as isolated species. They thus likely meet with premature elimination in the early materials screening process, because the assessments of photophysical properties have usually been conducted in dilute solutions. It has commonly believed that a poor light emitter in the solution state will not emit efficiently in the solid state. The AIE effect, however, teaches us that such cognition is not necessarily correct. Instead of being a “useless stone”, a poor light emitter in a dilute solution could be a solid “shining gold”. This widens the avenues of search for efficient light-emitting materials in the solid state, which can be used to fabricate useful optoelectronic devices such as OLEDs.

The AIE study is of great academic value. AIE has provided a new platform to decipher the non-radiative processes that lead to emission quenching of luminogens in the solution state and to understand the underlying mechanisms that bring about radiative decay in the aggregate state. These fundamental photophysics issues had rarely been touched upon before the advent of the AIE concept. Whilst there are rather matured theories to explicate the ACQ effect, new models need to be built to interpret the AIE process. We proposed the RIM model as a unified working mechanism for AIE.<sup>12</sup> In this review article, we have further examined its validity on the basis of experimental and computational results. The mechanistic picture of the AIE process has become clear now: the dynamic intramolecular motions, also known as low-frequency modes of reorganization energy, dissipate the excited-state energy of AIEgens via non-radiative channels, whereas the activated RIM process boosts their light emissions. Conformational stiffening or structural rigidification has been found to be the essence of the RIM process.

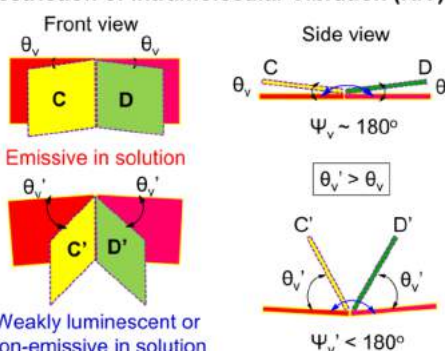
We have correlated conformational planarity and structural flexibility of an AIEgen with its light emission behavior in a recent review article.<sup>12</sup> Whereas every molecule can in principle undergo intramolecular motions including rotation (*r*) and vibration (*v*), not all molecules exhibit AIE activity. As can be seen from the models illustrated in panels A and B of [Figure 199](#), whether a

luminogen shows AIE effect is largely dependent on its conformational flexibility (defined by  $\psi_r$  or  $\psi_v$ ) and motional amplitude (defined by  $\theta_r$  or  $\theta_v$ ).<sup>12</sup> The quenching of solution emission is a key step in the AIE process of a structurally flexible luminogen (with a large  $\psi$ ) and it is resulted from the energy consumption caused by the vigorous intramolecular motion (with a large  $\theta$ ). The dissipation of the excited-state energy ( $\Delta E$ ) via the intramolecular motions is associated with multiple factors: the amplitude (*A*) and the frequency (*v*) of the rotational/vibrational motion, the number (*N*) of the rotors/vibrators in a single molecule, the volume (*V*) of each rotor/vibrator (determined by its size, shape, etc.), the position (*P*) of the rotor/vibrator, the linking mode (*L*) between the rotor/vibrator and the stator, and so on ([Figure 199C](#)). These factors work together synergistically to determine the efficiency of the solution-state luminescence, whose quantitative relationship, however, remains to be established.

### (A) Restriction of Intramolecular Rotation (RIR)



### (B) Restriction of Intramolecular Vibration (RIV)



### (C) Factors Affecting Exciton Energy Dissipation

$$\Delta E = f(A, v, N, V, P, L \dots)$$

Where,

$\Delta E$  = energy dissipated via intramolecular motion

$A$  = amplitude of intramolecular motion

$v$  = frequency of intramolecular motion

$N$  = number of moving units (rotors/vibrators)

$V$  = volume of each moving unit

$P$  = position of moving unit

$L$  = linkage between moving unit and stator

**Figure 199.** Factors affecting (A) RIR and (B) RIV processes and (C) non-radiative relaxations of excitons of AIEgens. Panels A and B are reprinted with permission from refs<sup>14</sup> (Copyright 2011 Royal Society of Chemistry) and <sup>12</sup> (Copyright 2014 Wiley-VCH Verlag GmbH & Co. KGaA), respectively.

Before the debut of the AIE concept, various chemical, physical, and engineering methods had been employed to tackle the ACQ problem. Most of them aim at impeding aggregate formation. Unfortunately, however, these conventional approaches had met with only limited success, as they were wrestling with a natural process, that is, chromophore aggregation in solid state.

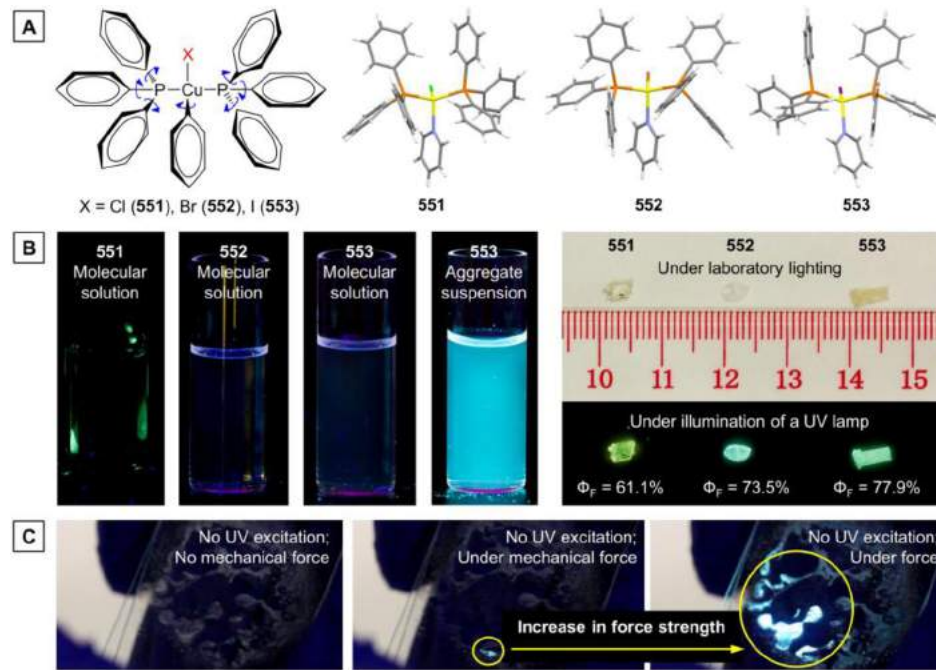


**Figure 200.** Examples of AIE-active mechanoluminescence (ML) systems. (A) Chemical and crystal structures of Cu(I) complexes **551**–**553**. (B) (Left) Fluorescent photographs of **551**–**553** in solutions and **553** in a pyridine/water mixture with  $f_w = 90$  vol % taken under UV excitation; (right) photographs of their crystals taken under (upper) room lighting and (lower) UV illumination. (C) Complex **553** showing intensified ML with application of increased strength of mechanical force without UV excitation; photographs taken under laboratory lighting. Courtesy of Dr. N. Xie, the author of ref 1011

The ACQ effect has often been partially and/or temporarily alleviated at the expense of generating new problems or troubles. Our strategies are based on the utilization of aggregation process and can eradicate the ACQ problem without causing negative effects. The ingenious integration of AIEgens with ACQphores creates new AIE materials that are completely free of ACQ problem and meanwhile retain the excellent functionalities of their components, leading to the desired win-win situations.

The AIEgens enjoy great diversity in molecular structure: they can be pure hydrocarbons, heteroatom-containing compounds, organometallic complexes, synthetic or natural polymers, or even unorthodox (macro)molecules without conventional chromophores. Evidently, AIE is not an isolated odd case but a ubiquitously observable photophysical phenomenon. Although the earlier AIEgens were hunted by serendipity, the later AIE systems have been developed largely by design, mostly under the guidance of the RIM working principle. Many of the AIEgens (e.g., TPE, DSA, and silole) can be easily modified further or structurally tailored by simple reactions and procedures to cater for the requirements of various high-tech applications.

Amongst the AIE systems developed thus far, the luminogens without chromophores in classic sense are of particular interest. Their unorthodox luminescence processes are rationalized to be associated with RIE and their emitting species are attributed to the nanoaggregates or clusters of electron-rich atoms or groups. In the clusters, the electron-rich atoms overlap with each other to share their lone-pair electrons and serve as clustoluminogens with narrowed energy gaps. We have demonstrated that three kinds of electronic interactions, i.e., *through-bond*, *through-space*, and *through-bond and -space* conjugations, are involved in these AIE systems. The non-covalent *through-space* conjugation plays a critical role in the unorthodox emission processes of the non-conventional luminogens. Further studies in this area are to

be directed to the acquisition of in-depth insights into the detailed mechanisms for the emission processes of this group of unique AIEgens. The elaborate utilization of the RIM principle has made impossible possible. RTP has been achieved in pure organic, and even non-conventional, AIEgen systems. The conformational rigidification enables the triplet excitons to undergo radiative decays under ambient conditions. It can be envisioned that the AIEgens with highly efficient RTP and long lifetimes will be attained by judiciously taking advantage of the RIM process and the RIE effect.

The study of AIE effect has far-reaching practical implications. In the AIE systems, one can buoyantly make use of the aggregate process, instead of fighting against it. The turn-on nature of the AIE probes makes them promising for field trial, on-site screening, household testing, real-time monitoring, etc. The high emission efficiencies of their aggregates or solids also benefit turn-off detections in terms of amplified quenching and superb sensitivity. The most thrilling applications of AIEgens are in the fields of life science and biomedical engineering. The AIE nanoparticles can be used for *in vitro* and *in vivo* imaging of biological structures (organelles, cells, tissues, etc.) and monitoring of cellular processes (apoptosis, metastasis, etc.). The excellent brightness, extraordinary photostability, nonblinking feature, high biocompatibility, efficient cellular uptake and retention, and large optical nonlinearity of the AIE nanoparticles enable them to be used for *in-depth* and *long-term* tracing. The development of multimodality imaging systems (e.g., AIE + MRI) and the combination with other medication processes (e.g., targeted drug delivery systems) as well as imaging-guided PDT have further broadened the scope of biomedical applications of AIE systems to such areas as clinical diagnosis and therapeutic treatment. Their up to unity solid-state luminescence efficiencies make them the choice of materials for optoelectronic applications. Their highly

twisted 3D conformations and readily adjustable intermolecular interactions endow them with inherent mechanochromism.

Further investigation of AIE is expected to bring forth more surprising results: novel AIEgens, innovative applications, etc. An example supporting this prospect is the discovery of luminogens with AIE and mechanoluminescence (ML).<sup>1011</sup> ML refers to the luminescence resulting from any mechanical action applied on a substrate. The Cu(I) complexes 551–553 shown in Figure 200A are facilely prepared and show fascinating photophysical behaviors. They are non-emissive when dissolved in solutions but emit strongly when aggregated in poor solvents or the solid state (Figure 200B). This is indicative of their remarkable AIE characteristics. Their emission colors vary with the halogen ligands. The complexes readily crystallize and their crystals emit brilliantly in high quantum yields (61.1–77.9%). As can be comprehended from their molecular structures, the RIR processes and distorted 3D conformations are responsible for their AIE activity. Intense ML is readily induced upon application of mechanical forces, e.g., crashing, crushing, pressing, rubbing, ripping, and scratching (Figure 200C). Thanks to the AIE effect, the ML of the Cu(I) complexes is brighter than that of their non-AIE counterparts. The incredible AIE-ML effect may enable the Cu(I) complexes to find technological applications in stimuli-responsive systems, such as smart sensor networks, real-time pressure mapping, wind-tunnel aerodynamic testing, human-machine interfaces, and high-level security devices.

During the preparation of this review article, many excellent papers have appeared in various journals, indicative of the fast development in the area of AIE research. Whilst we have tried our best to prepare a comprehensive review article, it is technically impossible for us to cover every piece of published papers, as the “old” papers are too numerous to enumerate and the “new” ones are published in a speed too fast to catch. In an effort to compensate this loss, we herein provide a list of representative papers published recently by different research laboratories in the world in the reference section.<sup>1012–1115</sup> AIE offers a large platform and colorful palette for researchers to explore and paint. There exist many opportunities as well as challenges in the area of research. It is envisioned that grasping the opportunities through overcoming the challenges will deepen our understanding in photophysics and engender innovative light-based technologies.

## ASSOCIATED CONTENT

### Special Issue Paper

This paper is an additional review for *Chem. Rev.* 2015, 115, 15, “Supramolecular Chemistry”.

## AUTHOR INFORMATION

### Corresponding Author

\*E-mail: [tangbenz@ust.hk](mailto:tangbenz@ust.hk). Telephone: +852-2358-7375. Fax: +852-2358-1594.

### Author Contributions

<sup>†</sup>J.M. and N.L.C.L. contributed equally.

### Notes

The authors declare no competing financial interest.

## Biographies



Ju Mei received her B.S. degree in Materials Chemistry from China University of Geosciences in 2008. She conducted her graduate study under the supervision of Prof. Ben Zhong Tang and obtained her Ph.D. degree in Polymer Chemistry and Physics from Zhejiang University in 2013. She is now carrying out her postdoctoral research in Prof. Tang's laboratories at HKUST. Her research is mainly on the development of new functional AIE materials.



Nelson L. C. Leung received his B.S. degree from HKUST in 2013 and is currently a Ph.D. student under the supervision of Prof. Tang. He is conducting research on new luminescent materials with AIE characteristics.



Ryan T. K. Kwok received his Ph.D. degree from HKUST in 2013 under the supervision of Prof. Tang. He is now conducting his postdoctoral work on the development of functional luminescent materials with AIE characteristics and exploration of their biological applications in Prof. Tang's laboratories.



Jacky W. Y. Lam received his Ph.D. degree from HKUST in 2003 under the supervision of Prof. Tang. He carried out his postdoctoral work on novel macromolecules with linear and hyperbranched structures and advanced functional properties in Tang's group in 2003–2007. He is currently a Research Assistant Professor of Chemistry at HKUST.



Ben Zhong Tang received his B.S. and Ph.D. degrees from South China University of Technology and Kyoto University, respectively. He conducted his postdoctoral research at University of Toronto. He joined HKUST in 1994 and was promoted to Chair Professor in 2008. He received a Natural Science Award from the Chinese Government in 2007 and was elected to the Chinese Academy of Sciences in 2009. He is now serving as Editor-in-Chief of *Polymer Chemistry Series* and Associate Editor of *Polymer Chemistry* (RSC).

## ACKNOWLEDGMENTS

This work was partially supported by the National Basic Research Program of China, i.e., 973 Program (Grant 2013CB834701), the National Natural Science Foundation of China (Grants 21490570 and 21490574), the Research Grants Council of Hong Kong (Grants 604913, 6301614, 16305014, 16305015, and N\_HKUST604/14), the University Grants Committee of Hong Kong (Grant AoE/P-03/08), and the Innovation and Technology Commission (Grant ITCPD/17-9). B.Z.T. thanks the financial support from the Guangdong Innovative Research Team Program (Grant 201101C0105067115).

## REFERENCES

- (1) Förster, T.; Kasper, K. Ein Konzentrationsumschlag der Fluoreszenz. *Z. Phys. Chem. (Muenchen, Ger.)* **1954**, *1*, 275–277.
- (2) *Photophysics of Aromatic Molecules*; Birks, J. B., Ed.; Wiley: London, 1970.
- (3) Zhelev, Z.; Ohba, H.; Bakalova, R. Single Quantum Dot-Micelles Coated with Silica Shell as Potentially Non-Cytotoxic Fluorescent Cell Tracers. *J. Am. Chem. Soc.* **2006**, *128*, 6324–6325.
- (4) Bakalova, R.; Zhelev, Z.; Aoki, I.; Ohba, H.; Imai, Y.; Kanno, I. Silica-Shelled Single Quantum Dot Micelles as Imaging Probes with Dual or Multimodality. *Anal. Chem.* **2006**, *78*, 5925–5932.
- (5) *Fluorescence Sensors and Biosensors*; Thompson, R. B., Ed.; CRC: Boca Raton, FL, 2006.
- (6) Tang, C. W.; VanSlyke, S. A. Organic Electroluminescent Diodes. *Appl. Phys. Lett.* **1987**, *51*, 913–915.
- (7) *Advanced Concepts in Fluorescence Sensing*; Geddes, C. D., Lakowicz, J. R., Eds.; Springer: Norwell, 2005.
- (8) Jares-Erijman, E. A.; Jovin, T. M. FRET Imaging. *Nat. Biotechnol.* **2003**, *21*, 1387–1395.
- (9) Saigusa, H.; Lim, E. C. Excited-State Dynamics of Aromatic Clusters: Correlation between Exciton Interactions and Excimer Formation Dynamics. *J. Phys. Chem.* **1995**, *99*, 15738–15747.
- (10) Luo, J.; Xie, Z.; Lam, J. W. Y.; Cheng, L.; Tang, B. Z.; Chen, H.; Qiu, C.; Kwok, H. S.; Zhan, X.; Liu, Y.; et al. Aggregation-Induced Emission of 1-Methyl-1,2,3,4,5-pentaphenylsilole. *Chem. Commun.* **2001**, 1740–1741.
- (11) Tang, B. Z.; Zhan, X.; Yu, G.; Sze Lee, P. P.; Liu, Y.; Zhu, D. Efficient Blue Emission from Siloles. *J. Mater. Chem.* **2001**, *11*, 2974–2978.
- (12) Mei, J.; Hong, Y.; Lam, J. W. Y.; Qin, A.; Tang, Y.; Tang, B. Z. Aggregation-Induced Emission: The Whole Is More Brilliant than the Parts. *Adv. Mater.* **2014**, *26*, 5429–5479.
- (13) Hong, Y.; Lam, J. W. Y.; Tang, B. Z. Aggregation-Induced Emission: Phenomenon, Mechanism and Applications. *Chem. Commun.* **2009**, 4332–4353.
- (14) Hong, Y.; Lam, J. W. Y.; Tang, B. Z. Aggregation-Induced Emission. *Chem. Soc. Rev.* **2011**, *40*, 5361–5388.
- (15) Hu, R.; Leung, N. L.; Tang, B. Z. AIE Macromolecules: Syntheses, Structures and Functionalities. *Chem. Soc. Rev.* **2014**, *43*, 4494–4562.
- (16) Wang, M.; Zhang, G.; Zhang, D.; Zhu, D.; Tang, B. Z. Fluorescent Bio/chemosensors Based on Silole and Tetraphenylethene Luminogens with Aggregation-Induced Emission Feature. *J. Mater. Chem.* **2010**, *20*, 1858–1867.
- (17) Liu, J.; Lam, J. W. Y.; Tang, B. Z. Aggregation-Induced Emission of Silole Molecules and Polymers: Fundamental and Applications. *J. Inorg. Organomet. Polym. Mater.* **2009**, *19*, 249–258.
- (18) Zhao, Z.; Lam, J. W. Y.; Tang, B. Z. Tetraphenylethene: A Versatile AIE Building Block for the Construction of Efficient Luminescent Materials for Organic Light-Emitting Diodes. *J. Mater. Chem.* **2012**, *22*, 23726–23740.
- (19) (a) Ding, D.; Li, K.; Liu, B.; Tang, B. Z. Bioprosbes Based on AIE Fluorogens. *Acc. Chem. Res.* **2013**, *46*, 2441–2453. (b) Kwok, R. T. K.; Leung, C. W. T.; Lam, J. W. Y.; Tang, B. Z. Biosensing by Luminogens with Aggregation-Induced Emission Characteristics. *Chem. Soc. Rev.* **2015**, *44*, 4228–4238.
- (20) (a) Chi, Z.; Zhang, X.; Xu, B.; Zhou, X.; Ma, C.; Zhang, Y.; Liu, S.; Xu, J. Recent Advances in Organic Mechanofluorochromic Materials. *Chem. Soc. Rev.* **2012**, *41*, 3878–3896. (b) *Mechanochromic Fluorescent Materials: Phenomena, Materials and Applications*; Xu, J., Chi, Z., Eds.; Royal Society of Chemistry: London, U.K., 2014.
- (21) Luo, J.; Song, K.; Gu, F. L.; Miao, Q. Switching of Non-Helical Overcrowded Tetrabenzohexafulvalene Derivatives. *Chem. Sci.* **2011**, *2*, 2029–2034.
- (22) Leung, N. L.; Xie, N.; Yuan, W.; Liu, Y.; Wu, Q.; Peng, Q.; Miao, Q.; Lam, J. W. Y.; Tang, B. Z. Restriction of Intramolecular Motions: The General Mechanism behind Aggregation-Induced Emission. *Chem. - Eur. J.* **2014**, *20*, 15349–15353.
- (23) Thomas, S. W., III; Joly, G. D.; Swager, T. M. Chemical Sensors Based on Amplifying Fluorescent Conjugated Polymers. *Chem. Rev.* **2007**, *107*, 1339–1386.
- (24) *Molecular Fluorescence: Principle and Applications*; Valeur, B., Ed.; Wiley: Weinheim, Germany, 2005.
- (25) Bunz, U. H. F. Poly(aryleneethynylene)s: Syntheses, Properties, Structures, and Applications. *Chem. Rev.* **2000**, *100*, 1605–1644.
- (26) Hide, F.; Diaz-Garcia, M. A.; Schwartz, B. J.; Heeger, A. J. New Developments in the Photonic Applications of Conjugated Polymers. *Acc. Chem. Res.* **1997**, *30*, 430–436.

- (27) Borisov, S. M.; Wolfbeis, O. S. Optical Biosensors. *Chem. Rev.* **2008**, *108*, 423–461.
- (28) Liu, Y.; Deng, C.; Tang, L.; Qin, A.; Hu, R.; Sun, J. Z.; Tang, B. Z. Specific Detection of D-Glucose by a Tetraphenylethene-Based Fluorescent Sensor. *J. Am. Chem. Soc.* **2011**, *133*, 660–663.
- (29) Hong, Y. N.; Chen, S. J.; Leung, C. W. T.; Lam, J. W. Y.; Tang, B. Z. Water-Soluble Tetraphenylethene Derivatives as Fluorescent “Light-Up” Probes for Nucleic Acid Detection and Their Applications in Cell Imaging. *Chem. - Asian J.* **2013**, *8*, 1806–1812.
- (30) Hong, Y.; Meng, L.; Chen, S.; Leung, C. W. T.; Da, L.-T.; Faisal, M.; Silva, D.-A.; Liu, J.; Lam, J. W. Y.; Huang, X.; et al. Monitoring and Inhibition of Insulin Fibrillation by a Small Organic Fluorogen with Aggregation-Induced Emission Characteristics. *J. Am. Chem. Soc.* **2012**, *134*, 1680–1689.
- (31) Zhang, C.; Jin, S.; Yang, K.; Xue, X.; Li, Z.; Jiang, Y.; Chen, W.-Q.; Dai, L.; Zou, G.; Liang, X.-J. Cell Membrane Tracker Based on Restriction of Intramolecular Rotation. *ACS Appl. Mater. Interfaces* **2014**, *6*, 8971–8975.
- (32) Zhao, N.; Li, M.; Lam, J. W. Y.; Zhang, Y. L.; Zhao, Y. S.; Wong, K. S.; Tang, B. Z. A Tetraphenylethene-Substituted Pyridinium Salt with Multiple Functionalities: Synthesis, Stimuli-Responsive Emission, Optical Waveguide and Specific Mitochondrion Imaging. *J. Mater. Chem. C* **2013**, *1*, 4640–4646.
- (33) *Aggregation-Induced Emission: Applications*; Qin, A., Tang, B. Z., Eds.; Wiley: Singapore, 2013.
- (34) Zhao, E.; Hong, Y.; Chen, S.; Leung, C. W. T.; Chan, C. Y. K.; Kwok, R. T. K.; Lam, J. W. Y.; Tang, B. Z. Highly Fluorescent and Photostable Probe for Long-Term Bacterial Viability Assay Based on Aggregation-Induced Emission. *Adv. Healthcare Mater.* **2014**, *3*, 88–96.
- (35) Ding, D.; Goh, C. C.; Feng, G.; Zhao, Z.; Liu, J.; Liu, R.; Tomczak, N.; Geng, J.; Tang, B. Z.; Ng, L. G.; et al. Ultrabright Organic Dots with Aggregation-Induced Emission Characteristics for Real-Time Two-Photon Intravital Vasculature Imaging. *Adv. Mater.* **2013**, *25*, 6083–6088.
- (36) Yuan, Y.; Feng, G.; Qin, W.; Tang, B. Z.; Liu, B. Targeted and Image-Guided Photodynamic Cancer Therapy Based on Organic Nanoparticles with Aggregation-Induced Emission Characteristics. *Chem. Commun.* **2014**, *50*, 8757–8760.
- (37) Zhao, N.; Lam, J. W. Y.; Sung, H. H. Y.; Su, H. M.; Williams, I. D.; Wong, K. S.; Tang, B. Z. Effect of the Counterion on Light Emission: A Displacement Strategy to Change the Emission Behaviour from Aggregation-Caused Quenching to Aggregation-Induced Emission and to Construct Sensitive Fluorescent Sensors for Hg<sup>2+</sup> Detection. *Chem. - Eur. J.* **2014**, *20*, 133–138.
- (38) Guo, Y.; Feng, X.; Han, T.; Wang, S.; Lin, Z.; Dong, Y.; Wang, B. Tuning the Luminescence of Metal–Organic Frameworks for Detection of Energetic Heterocyclic Compounds. *J. Am. Chem. Soc.* **2014**, *136*, 15485–15488.
- (39) Li, Y.; Xu, L.; Su, B. Aggregation Induced Emission for the Recognition of Latent Fingerprints. *Chem. Commun.* **2012**, *48*, 4109–4111.
- (40) Liu, J.; Su, H.; Meng, L.; Zhao, Y.; Deng, C.; Ng, J. C. Y.; Lu, P.; Faisal, M.; Lam, J. W. Y.; Huang, X.; et al. What Makes Efficient Circularly Polarised Luminescence in the Condensed Phase: Aggregation-Induced Circular Dichroism and Light Emission. *Chem. Sci.* **2012**, *3*, 2737–2747.
- (41) Zhao, D.; Fan, F.; Cheng, J.; Zhang, Y.; Wong, K. S.; Chigrinov, V. G.; Kwok, H. S.; Guo, L.; Tang, B. Z. Light-Emitting Liquid Crystal Displays Based on an Aggregation-Induced Emission Luminogen. *Adv. Opt. Mater.* **2015**, *3*, 199–202.
- (42) Yuan, W. Z.; Tan, Y.; Gong, Y.; Lu, P.; Lam, J. W. Y.; Shen, X. Y.; Feng, C.; Sung, H. H. Y.; Lu, Y.; Williams, I. D.; et al. Synergy between Twisted Conformation and Effective Intermolecular Interactions: Strategy for Efficient Mechanochromic Luminogens with High Contrast. *Adv. Mater.* **2013**, *25*, 2837–2843.
- (43) Wang, M.; Zhang, D. Q.; Zhang, G. X.; Zhu, D. B. Fluorescence Enhancement upon Gelation and Thermally-Driven Fluorescence Switches Based on Tetraphenylsilole-Based Organic Gelators. *Chem. Phys. Lett.* **2009**, *475*, 64–67.
- (44) Alam, P.; Karanam, M.; Bandyopadhyay, D.; Choudhury, A. R.; Laskar, I. R. Aggregation-Induced Emission Activity in Iridium(III) Diimine Complexes: Investigations of Their Vapochromic Properties. *Eur. J. Inorg. Chem.* **2014**, *2014*, 3710–3719.
- (45) Yu, C. Y. Y.; Kwok, R. T. K.; Mei, J.; Hong, Y.; Chen, S.; Lam, J. W. Y.; Tang, B. Z. A Tetraphenylethene-Based Caged Compound: Synthesis, Properties and Applications. *Chem. Commun.* **2014**, *50*, 8134–8136.
- (46) Chen, J.; Law, C. C. W.; Lam, J. W. Y.; Dong, Y.; Lo, S. M. F.; Williams, I. D.; Zhu, D.; Tang, B. Z. Synthesis, Light Emission, Nanoaggregation, and Restricted Intramolecular Rotation of 1,1-Substituted 2,3,4,5-Tetraphenylsiloles. *Chem. Mater.* **2003**, *15*, 1535–1546.
- (47) Fan, X.; Sun, J.; Wang, F.; Chu, Z.; Wang, P.; Dong, Y.; Hu, R.; Tang, B. Z.; Zou, D. Photoluminescence and Electroluminescence of Hexaphenylsilole are Enhanced by Pressurization in the Solid State. *Chem. Commun.* **2008**, 2989–2991.
- (48) Ren, Y.; Lam, J. W. Y.; Dong, Y.; Tang, B. Z.; Wong, K. S. Enhanced Emission Efficiency and Excited State Lifetime Due to Restricted Intramolecular Motion in Silole Aggregates. *J. Phys. Chem. B* **2005**, *109*, 1135–1140.
- (49) Li, Z.; Dong, Y.; Mi, B.; Tang, Y.; Häussler, M.; Tong, H.; Dong, Y.; Lam, J. W. Y.; Ren, Y.; Sung, H. H. Y.; et al. Structural Control of the Photoluminescence of Silole Regioisomers and Their Utility as Sensitive Regiodiscriminating Chemosensors and Efficient Electroluminescent Materials. *J. Phys. Chem. B* **2005**, *109*, 10061–10066.
- (50) Zhao, E.; Lam, J. W. Y.; Hong, Y.; Liu, J.; Peng, Q.; Hao, J.; Sung, H. H. Y.; Williams, I. D.; Tang, B. Z. How Do Substituents Affect Silole Emission? *J. Mater. Chem. C* **2013**, *1*, 5661–5668.
- (51) Chen, B.; Nie, H.; Lu, P.; Zhou, J.; Qin, A.; Qiu, H.; Zhao, Z.; Tang, B. Z. Conjugation versus Rotation: Good Conjugation Weakens the Aggregation-Induced Emission Effect of Siloles. *Chem. Commun.* **2014**, *50*, 4500–4503.
- (52) Liang, G. D.; Lam, J. W. Y.; Qin, W.; Li, J.; Xie, N.; Tang, B. Z. Molecular Luminogens Based on Restriction of Intramolecular Motions Through Host–Guest Inclusion for Cell Imaging. *Chem. Commun.* **2014**, *50*, 1725–1727.
- (53) Li, S.; Langenegger, S. M.; Häner, R. Control of Aggregation-Induced Emission by DNA Hybridization. *Chem. Commun.* **2013**, *49*, 5835–5837.
- (54) Zhang, G.-F.; Chen, Z.-Q.; Aldred, M. P.; Hu, Z.; Chen, T.; Huang, Z.; Meng, X.; Zhu, M.-Q. Direct Validation of the Restriction of Intramolecular Rotation Hypothesis via the Synthesis of Novel ortho-Methyl Substituted Tetraphenylethenes and Their Application in Cell Imaging. *Chem. Commun.* **2014**, *50*, 12058–12060.
- (55) Zhao, Z.; He, B.; Nie, H.; Chen, B.; Lu, P.; Qin, A.; Tang, B. Z. Stereoselective Synthesis of Folded Luminogens with Arene–Arene Stacking Interactions and Aggregation-Enhanced Emission. *Chem. Commun.* **2014**, *50*, 1131–1133.
- (56) Zhao, J.; Yang, D.; Zhao, Y.; Yang, X.-J.; Wang, Y.-Y.; Wu, B. Anion-Coordination-Induced Turn-On Fluorescence of an Oligourethane-Functionalized Tetraphenylethene in a Wide Concentration Range. *Angew. Chem., Int. Ed.* **2014**, *53*, 6632–6636.
- (57) Huang, G.; Zhang, G.; Zhang, D. Turn-On of the Fluorescence of Tetra(4-pyridylphenyl)ethylene by the Synergistic Interactions of Mercury(II) Cation and Hydrogen Sulfate Anion. *Chem. Commun.* **2012**, *48*, 7504–7506.
- (58) Shi, J.; Chang, N.; Li, C.; Mei, J.; Deng, C.; Luo, X.; Liu, Z.; Bo, Z.; Dong, Y. Q.; Tang, B. Z. Locking the Phenyl Rings of Tetraphenylethene Step by Step: Understanding the Mechanism of Aggregation-Induced Emission. *Chem. Commun.* **2012**, *48*, 10675–10677.
- (59) Jiang, B.-P.; Guo, D.-S.; Liu, Y.-C.; Wang, K.-P.; Liu, Y. Photomodulated Fluorescence of Supramolecular Assemblies of Sulfonatocalixarenes and Tetraphenylethene. *ACS Nano* **2014**, *8*, 1609–1618.
- (60) Tong, H.; Dong, Y.; Hong, Y.; Häussler, M.; Lam, J. W. Y.; Sung, H. H. Y.; Yu, X.; Sun, J.; Williams, I. D.; Kwok, H. S.; et al. Aggregation-Induced Emission: Effects of Molecular Structure, Solid-State Conformation, and Morphological Packing Arrangement on

- Light-Emitting Behaviors of Diphenyldibenzofulvene Derivatives. *J. Phys. Chem. C* **2007**, *111*, 2287–2294.
- (61) Parrott, E. P. J.; Tan, N. Y.; Hu, R.; Zeitler, J. A.; Tang, B. Z.; Pickwell-MacPherson, E. Direct Evidence to Support the Restriction of Intramolecular Rotation Hypothesis for the Mechanism of Aggregation-Induced Emission: Temperature Resolved Terahertz Spectra of Tetraphenylethene. *Mater. Horiz.* **2014**, *1*, 251–258.
- (62) Li, Q.; Blancfort, L. A Conical Intersection Model to Explain Aggregation Induced Emission in Diphenyl Dibenzofulvene. *Chem. Commun.* **2013**, *49*, 5966–5968.
- (63) Shuai, Z.; Peng, Q. Excited States Structure and Processes: Understanding Organic Light-Emitting Diodes at the Molecular Level. *Phys. Rep.* **2014**, *537*, 123–156.
- (64) Wu, Q.; Zhang, T.; Peng, Q.; Wang, D.; Shuai, Z. Aggregation Induced Blue-Shifted Emission—the Molecular Picture from a QM/MM Study. *Phys. Chem. Chem. Phys.* **2014**, *16*, 5545–5552.
- (65) Deng, C.; Niu, Y.; Peng, Q.; Qin, A.; Shuai, Z.; Tang, B. Z. Theoretical Study of Radiative and Non-Radiative Decay Processes in Pyrazine Derivatives. *J. Chem. Phys.* **2011**, *135*, 014304.
- (66) Wu, Q.; Deng, C.; Peng, Q.; Niu, Y.; Shuai, Z. Quantum Chemical Insights into the Aggregation Induced Emission Phenomena: A QM/MM Study for Pyrazine Derivatives. *J. Comput. Chem.* **2012**, *33*, 1862–1869.
- (67) Yin, S. W.; Peng, Q.; Shuai, Z.; Fang, W. H. Y.; Wang, Y. H.; Luo, Y. Aggregation-Enhanced Luminescence and Vibronic Coupling of Silole Molecules from First Principles. *Phys. Rev. B: Condens. Matter Mater. Phys.* **2006**, *73*, 205409.
- (68) Qin, A.; Lam, J. W. Y.; Mahtab, F.; Jim, C. K. W.; Tang, L.; Sun, J.; Sung, H. H. Y.; Williams, I. D.; Tang, B. Z. Pyrazine Luminogens with “Free” and “Locked” Phenyl Rings: Understanding of Restriction of Intramolecular Rotation as a Cause for Aggregation-Induced Emission. *Appl. Phys. Lett.* **2009**, *94*, 253308.
- (69) Kumar, S.; Singh, P.; Mahajan, A.; Kumar, S. Aggregation Induced Emission Enhancement in Ionic Self-Assembled Aggregates of Benzimidazolium Based Cyclophane and Sodium Dodecylbenzenesulfonate. *Org. Lett.* **2013**, *15*, 3400–3403.
- (70) Nishiuchi, T.; Tanaka, K.; Kuwatani, Y.; Sung, J.; Nishinaga, T.; Kim, D.; Iyoda, M. Solvent-Induced Crystalline-State Emission and Multichromism of a Bent  $\pi$ -Surface System Composed of Dibenzocyclooctatetraene Units. *Chem. - Eur. J.* **2013**, *19*, 4110–4116.
- (71) Yuan, C.; Saito, S.; Camacho, C.; Kowalczyk, T.; Irle, S.; Yamaguchi, S. Hybridization of a Flexible Cyclooctatetraene Core and Rigid Aceneimide Wings for Multiluminescent Flapping  $\pi$  Systems. *Chem. - Eur. J.* **2014**, *20*, 2193–2200.
- (72) Yuan, C.-X.; Tao, X.-T.; Ren, Y.; Li, Y.; Yang, J.-X.; Yu, W.-T.; Wang, L.; Jiang, M.-H. Synthesis, Structure, and Aggregation-Induced Emission of a Novel Lambda ( $\Lambda$ )-Shaped Pyridinium Salt Based on Tröger’s Base. *J. Phys. Chem. C* **2007**, *111*, 12811–12816.
- (73) Yao, L.; Zhang, S.; Wang, R.; Li, W.; Shen, F.; Yang, B.; Ma, Y. Highly Efficient Near-Infrared Organic Light-Emitting Diode Based on a Butterfly-Shaped Donor–Acceptor Chromophore with Strong Solid-State Fluorescence and a Large Proportion of Radiative Excitons. *Angew. Chem., Int. Ed.* **2014**, *53*, 2119–2123.
- (74) Liu, J.; Meng, Q.; Zhang, X.; Lu, X.; He, P.; Jiang, L.; Dong, H.; Hu, W. Aggregation-Induced Emission Enhancement Based on 11,11,12,12-Tetracyano-9,10-anthraquinodimethane. *Chem. Commun.* **2013**, *49*, 1199–1201.
- (75) Sharma nee Kamaldeep, K.; Kaur, S.; Bhalla, V.; Kumar, M.; Gupta, A. Pentacenequinone Derivatives for Preparation of Gold Nanoparticles: Facile Synthesis and Catalytic Application. *J. Mater. Chem. A* **2014**, *2*, 8369–8375.
- (76) Banal, J. L.; White, J. M.; Ghiggino, K. P.; Wong, W. W. H. Concentrating Aggregation-Induced Fluorescence in Planar Waveguides: A Proof-of-Principle. *Sci. Rep.* **2014**, *4*, 4635.
- (77) Zhang, C.; Wang, Z.; Song, S.; Meng, X.; Zheng, Y.-S.; Yang, X.-L.; Xu, H.-B. Tetraphenylethylene-Based Expanded Oxacalixarene: Synthesis, Structure, and Its Supramolecular Grid Assemblies Directed by Guests in the Solid State. *J. Org. Chem.* **2014**, *79*, 2729–2732.
- (78) Wang, J.-H.; Feng, H.-T.; Luo, J.; Zheng, Y.-S. Monomer Emission and Aggregate Emission of an Imidazolium Macrocycle Based on Bridged Tetraphenylethylene and Their Quenching by C<sub>60</sub>. *J. Org. Chem.* **2014**, *79*, 5746–5751.
- (79) Karthik, G.; Krushna, P. V.; Srinivasan, A.; Chandrashekar, T. K. Calix[2]thia[4]phyrin: An Expanded Calixphyrin with Aggregation-Induced Enhanced Emission and Anion Receptor Properties. *J. Org. Chem.* **2013**, *78*, 8496–8501.
- (80) Salini, P. S.; Thomas, A. P.; Sabarinathan, R.; Ramakrishnan, S.; Sreedevi, K. C.; Reddy, M. L.; Srinivasan, A. Calix[2]-m-benzo[4]phyrin with Aggregation-Induced Enhanced-Emission Characteristics: Application as a Hg<sup>II</sup> Chemosensor. *Chem. - Eur. J.* **2011**, *17*, 6598–6601.
- (81) Wang, J.; Zhao, Y.; Dou, Y. C.; Sun, H.; Xu, P.; Ye, K.; Zhang, J.; Jiang, S.; Li, F.; Wang, Y. Alkyl and Dendron Substituted Quinacridones: Synthesis, Structures, and Luminescent Properties. *J. Phys. Chem. B* **2007**, *111*, 5082–5089.
- (82) Hecht, S.; Fréchet, J. M. J. Dendritic Encapsulation of Function: Applying Nature’s Site Isolation Principle from Biomimetics to Materials Science. *Angew. Chem., Int. Ed.* **2001**, *40*, 74–91.
- (83) Nguyen, B. T.; Gautrot, J. E.; Ji, C.; Brunner, P.-L.; Nguyen, M. T.; Zhu, X. X. Enhancing the Photoluminescence Intensity of Conjugated Polycationic Polymers by Using Quantum Dots as Antiaggregation Reagents. *Langmuir* **2006**, *22*, 4799–4803.
- (84) Chen, L.; Xu, S.; McBranch, D.; Whitten, D. Tuning the Properties of Conjugated Polyelectrolytes through Surfactant Complexation. *J. Am. Chem. Soc.* **2000**, *122*, 9302–9303.
- (85) Taylor, P. N.; O’Connell, M. J.; McNeill, L. A.; Hall, M. J.; Aplin, R. T.; Anderson, H. L. Insulated Molecular Wires: Synthesis of Conjugated Polyrotaxanes by Suzuki Coupling in Water. *Angew. Chem., Int. Ed.* **2000**, *39*, 3456–3460.
- (86) Shen, X. Y.; Wang, Y. J.; Zhang, H.; Qin, A.; Sun, J. Z.; Tang, B. Z. Conjugates of Tetraphenylethene and Diketopyrrolopyrrole: Tuning the Emission Properties with Phenyl Bridges. *Chem. Commun.* **2014**, *50*, 8747–8750.
- (87) Jin, Y.; Xu, Y.; Liu, Y.; Wang, L.; Jiang, H.; Li, X.; Cao, D. Synthesis of Novel Diketopyrrolopyrrole-Based Luminophores Showing Crystallization-Induced Emission Enhancement Properties. *Dyes Pigm.* **2011**, *90*, 311–318.
- (88) Shih, P. I.; Chuang, C. Y.; Chien, C. H.; Diau, E. W. G.; Shu, C. F. Highly Efficient Non-Doped Blue-Light-Emitting Diodes Based on an Anthracene Derivative End-Capped with Tetraphenylethylene Groups. *Adv. Funct. Mater.* **2007**, *17*, 3141–3146.
- (89) Huang, J.; Su, J.-H.; Tian, H. The Development of Anthracene Derivatives for Organic Light-Emitting Diodes. *J. Mater. Chem.* **2012**, *22*, 10977–10989.
- (90) *Handbook of Fluorescence Spectra of Aromatic Molecules*; Berlman, I. B., Ed.; Academic Press: London, 1971.
- (91) Zhao, Z.; Lu, P.; Lam, J. W. Y.; Wang, Z.; Chan, C. Y. K.; Sung, H. H. Y.; Williams, I. D.; Ma, Y.; Tang, B. Z. Molecular Anchors in the Solid State: Restriction of Intramolecular Rotation Boosts Emission Efficiency of Luminogen Aggregates to Unity. *Chem. Sci.* **2011**, *2*, 672–675.
- (92) Zhao, Z.; Chen, S.; Chan, C. Y. K.; Lam, J. W. Y.; Jim, C. K. W.; Lu, P.; Chang, Z.; Kwok, H. S.; Qiu, H.; Tang, B. Z. A Facile and Versatile Approach to Efficient Luminescent Materials for Applications in Organic Light-Emitting Diodes. *Chem. - Asian J.* **2012**, *7*, 484–488.
- (93) Winnik, F. M. Photophysics of Preassociated Pyrenes in Aqueous Polymer Solutions and in Other Organized Media. *Chem. Rev.* **1993**, *93*, 587–614.
- (94) Zhao, Z.; Chen, S.; Lam, J. W. Y.; Lu, P.; Zhong, Y.; Wong, K. S.; Kwok, H. S.; Tang, B. Z. Creation of Highly Efficient Solid Emitter by Decorating Pyrene Core with AIE-Active Tetraphenylethene Peripheries. *Chem. Commun.* **2010**, *46*, 2221–2223.
- (95) Hoeben, F. J.; Jonkheijm, M. P.; Meijer, E. W.; Schenning, A. P. H. J. About Supramolecular Assemblies of  $\pi$ -Conjugated Systems. *Chem. Rev.* **2005**, *105*, 1491–1546.
- (96) Ning, Z. J.; Chen, Z.; Zhang, Q.; Yan, Y. L.; Qian, S. X.; Cao, Y.; Tian, H. Aggregation-induced Emission (AIE)-active Starburst Triarylamine Fluorophores as Potential Non-doped Red Emitters for Organic

- Light-emitting Diodes and Cl<sub>2</sub> Gas Chemodosimeter. *Adv. Funct. Mater.* **2007**, *17*, 3799–3807.
- (97) Zhao, Q.; Li, K.; Chen, S.; Qin, A.; Ding, D.; Zhang, S.; Liu, Y.; Liu, B.; Sun, J. Z.; Tang, B. Z. Aggregation-Induced Red-NIR Emission Organic Nanoparticles as Effective and Photostable Fluorescent Probes for Bioimaging. *J. Mater. Chem.* **2012**, *22*, 15128–15135.
- (98) Zhao, Q.; Zhang, S.; Liu, Y.; Mei, J.; Chen, S.; Lu, P.; Qin, A.; Ma, Y.; Sun, J. Z.; Tang, B. Z. Tetraphenylethenyl-Modified Perylene Bisimide: Aggregation-Induced Red Emission, Electrochemical Properties and Ordered Microstructures. *J. Mater. Chem.* **2012**, *22*, 7387–7394.
- (99) Zhao, Q.; Zhang, X. A.; Wei, Q.; Wang, J.; Shen, X. Y.; Qin, A.; Sun, J. Z.; Tang, B. Z. Tetraphenylethene Modified Perylene Bisimide: Effect of the Number of Substituents on AIE Performance. *Chem. Commun.* **2012**, *48*, 11671–11673.
- (100) Hu, R.; Gómez-Durán, C. F. A.; Lam, J. W. Y.; Belmonte-Vázquez, J. L.; Deng, C.; Chen, S.; Ye, R.; Peña-Cabrera, E.; Zhong, Y.; Wong, K. S.; et al. Synthesis, Solvatochromism, Aggregation-Induced Emission and Cell Imaging of Tetraphenylethene-Containing BODIPY Derivatives with Large Stokes Shifts. *Chem. Commun.* **2012**, *48*, 10099–10101.
- (101) Grabowski, Z. R.; Rotkiewicz, K.; Rettig, W. Structural Changes Accompanying Intramolecular Electron Transfer: Focus on Twisted Intramolecular Charge-Transfer States and Structures. *Chem. Rev.* **2003**, *103*, 3899–4032.
- (102) Reed, A. E.; Curtiss, L. A.; Weinhold, F. Intermolecular Interactions from a Natural Bond Orbital, Donor-Acceptor Viewpoint. *Chem. Rev.* **1988**, *88*, 899–926.
- (103) Albota, M.; Beljonne, D.; Bredas, J. L.; Ehrlich, J. E.; Fu, J. Y.; Heikal, A. A.; Hess, S. E.; Kogej, T.; Levin, M. D.; Marder, S. R.; et al. Design of Organic Molecules with Large Two-Photon Absorption Cross Sections. *Science* **1998**, *281*, 1653–1656.
- (104) Yuan, W. Z.; Lu, P.; Chen, S. M.; Lam, J. W. Y.; Wang, Z. M.; Liu, Y.; Kwok, H. S.; Ma, Y. G.; Tang, B. Z. Changing the Behavior of Chromophores from Aggregation-Caused Quenching to Aggregation-Induced Emission: Development of Highly Efficient Light Emitters in the Solid State. *Adv. Mater.* **2010**, *22*, 2159–2163.
- (105) Liu, Y.; Chen, S.; Lam, J. W. Y.; Lu, P.; Kwok, R. T. K.; Mahtab, F.; Kwok, H. S.; Tang, B. Z. Tuning the Electronic Nature of Aggregation-Induced Emission Luminogens with Enhanced Hole-Transporting Property. *Chem. Mater.* **2011**, *23*, 2536–2544.
- (106) Yuan, W. Z.; Gong, Y.; Chen, S.; Shen, X. Y.; Lam, J. W. Y.; Lu, P.; Lu, Y.; Wang, Z.; Hu, R.; Xie, N.; et al. Efficient Solid Emitters with Aggregation-Induced Emission and Intramolecular Charge Transfer Characteristics: Molecular Design, Synthesis, Photophysical Behaviors, and OLED Application. *Chem. Mater.* **2012**, *24*, 1518–1528.
- (107) Gong, W.-L.; Wang, B.; Aldred, M. P.; Li, C.; Zhang, G.-F.; Chen, T.; Wang, L.; Zhu, M.-Q. Tetraphenylethene-Decorated Carbazoles: Synthesis, Aggregation-Induced Emission, Photo-Oxidation and Electroluminescence. *J. Mater. Chem. C* **2014**, *2*, 7001–7012.
- (108) Huang, J.; Yang, X.; Wang, J.; Zhong, C.; Wang, L.; Qin, J.; Li, Z. New Tetraphenylethene-Based Efficient Blue Luminophors: Aggregation Induced Emission and Partially Controllable Emitting Color. *J. Mater. Chem.* **2012**, *22*, 2478–2484.
- (109) Xu, B. J.; Chi, Z. G.; Yang, Z. Y.; Chen, J. B.; Deng, S. Z.; Li, H. Y.; Li, X. F.; Zhang, Y.; Xu, N. S.; Xu, J. R. Facile Synthesis of a New Class of Aggregation-Induced Emission Materials Derived from Triphenylethylene. *J. Mater. Chem.* **2010**, *20*, 4135–4141.
- (110) Zhao, Z.; Chen, B.; Geng, J.; Chang, Z.; Aparicio-Ixta, L.; Nie, H.; Goh, C. C.; Ng, L. G.; Qin, A.; Ramos-Ortiz, G.; et al. Red Emissive Biocompatible Nanoparticles from Tetraphenylethene-Decorated BODIPY Luminogens for Two-Photon Excited Fluorescence Cellular Imaging and Mouse Brain Blood Vascular Visualization. *Part. Part. Syst. Charact.* **2014**, *31*, 481–491.
- (111) Zhao, Z.; Chan, C. Y. K.; Chen, S.; Deng, C.; Lam, J. W. Y.; Jim, C. K. W.; Hong, Y.; Lu, P.; Chang, Z.; Chen, X.; et al. Using Tetraphenylethene and Carbazole to Create Efficient Luminophores with Aggregation-Induced Emission, High Thermal Stability, and Good Hole-Transporting Property. *J. Mater. Chem.* **2012**, *22*, 4527–4534.
- (112) Qin, W.; Liu, J.; Chen, S.; Lam, J. W. Y.; Arseneault, M.; Yang, Z.; Zhao, Q.; Kwok, H. S.; Tang, B. Z. Crafting NPB with Tetraphenylethene: A Win–Win Strategy to Create Stable and Efficient Solid-State Emitters with Aggregation-Induced Emission Feature, High Hole-Transporting Property and Efficient Electroluminescence. *J. Mater. Chem. C* **2014**, *2*, 3756–3761.
- (113) Zhang, X.; Chi, Z.; Xu, B.; Li, H.; Yang, Z.; Li, X.; Liu, S.; Zhang, Y.; Xu, J. Synthesis of Blue Light Emitting Bis(triphenylethylene) Derivatives: A Case of Aggregation-Induced Emission Enhancement. *Dyes Pigm.* **2011**, *89*, 56–62.
- (114) Xu, B. J.; Chi, Z. G.; Li, X. F.; Li, H. Y.; Zhou, W.; Zhang, X. Q.; Wang, C. C.; Zhang, Y.; Liu, S. W.; Xu, J. R. Synthesis and Properties of Diphenylcarbazole Triphenylethylene Derivatives with Aggregation-Induced Emission, Blue Light Emission and High Thermal Stability. *J. Fluoresc.* **2011**, *21*, 433–441.
- (115) Lu, Y. W.; Tan, Y. Q.; Gong, Y. Y.; Li, H.; Yuan, W. Z.; Zhang, Y. M.; Tang, B. Z. High Efficiency D-A Structured Luminogen with Aggregation-Induced Emission and Mechanochromic Characteristics. *Chin. Sci. Bull.* **2013**, *58*, 2719–2722.
- (116) Liang, Z.-Q.; Li, Y.-X.; Yang, J.-X.; Ren, Y.; Tao, X.-T. Suppression of Aggregation-Induced Fluorescence Quenching in Pyrene Derivatives: Photophysical Properties and Crystal Structures. *Tetrahedron Lett.* **2011**, *52*, 1329–1333.
- (117) Chan, C. Y. K.; Lam, J. W. Y.; Zhao, Z. J.; Chen, S. M.; Lu, P.; Sung, H. H. Y.; Kwok, H. S.; Ma, Y. G.; Williams, I. D.; Tang, B. Z. Aggregation-Induced Emission, Mechanochromism and Blue Electroluminescence of Carbazole and Triphenylamine-Substituted Ethenes. *J. Mater. Chem. C* **2014**, *2*, 4320–4327.
- (118) Zhao, Z.; Chang, Z.; He, B.; Chen, B.; Deng, C.; Lu, P.; Qiu, H.; Tang, B. Z. Aggregation-Induced Emission and Efficient Solid-State Fluorescence from Tetraphenylethene-Based N,C-Chelate Four-Coordinate Organoborons. *Chem. - Eur. J.* **2013**, *19*, 11512–11517.
- (119) Liu, Y.; Lv, Y.; Zhang, X.; Chen, S.; Lam, J. W. Y.; Lu, P.; Kwok, R. T. K.; Kwok, H. S.; Tao, X.; Tang, B. Z. From a Fluorescent Chromophore in Solution to an Efficient Emitter in the Solid State. *Chem. - Asian J.* **2012**, *7*, 2424–2428.
- (120) Kwok, R. T. K.; Geng, J.; Lam, J. W. Y.; Zhao, E.; Wang, G.; Zhan, R.; Liu, B.; Tang, B. Z. Water-Soluble Bioprobes with Aggregation-Induced Emission Characteristics for Light-Up Sensing of Heparin. *J. Mater. Chem. B* **2014**, *2*, 4134–4141.
- (121) Liu, Y.; Ye, X.; Liu, G.; Lv, Y.; Zhang, X.; Chen, S.; Lam, J. W. Y.; Kwok, H. S.; Tao, X.; Tang, B. Z. Structural Features and Optical Properties of a Carbazole-Containing Ethene as a Highly Emissive Organic Solid. *J. Mater. Chem. C* **2014**, *2*, 1004–1009.
- (122) Xie, N.; Liu, Y.; Hu, R.; Leung, N. L. C.; Arseneault, M.; Tang, B. Z. Synthesis, Aggregation-Induced Emission, and Electroluminescence of Dibenzothiophene- and Dibenzofuran-Containing Tetraarylethenes. *Isr. J. Chem.* **2014**, *54*, 958–966.
- (123) Liu, Y.; Chen, X.; Lv, Y.; Chen, S.; Lam, J. W. L.; Mahtab, F.; Kwok, H. S.; Tao, X.; Tang, B. Z. Systemic Studies of Tetraphenylethene-Triphenylamine Oligomers and a Polymer: Achieving Both Efficient Solid-State Emissions and Hole-Transporting Capability. *Chem.—Eur. J.* **2012**, *18*, 9929–9938.
- (124) Liu, Y.; Lv, Y.; Xi, H.; Zhang, X.; Chen, S.; Lam, J. W. Y.; Kwok, R. T. K.; Mahtab, F.; Kwok, H. S.; Tao, X.; Tang, B. Z. Enlarged Tetrasubstituted Alkenes with Enhanced Thermal and Optoelectronic Properties. *Chem. Commun.* **2013**, *49*, 7216–7218.
- (125) Zhou, J.; Chang, Z.; Jiang, Y.; He, B.; Du, M.; Lu, P.; Hong, Y.; Kwok, H. S.; Qin, A.; Qiu, H.; et al. From Tetraphenylethene to Tetraphenylethene: Structural Evolution in AIE Luminogen Continues. *Chem. Commun.* **2013**, *49*, 2491–2493.
- (126) Li, K.; Qin, W.; Ding, D.; Tomczak, N.; Geng, J.; Liu, R.; Liu, J.; Zhang, X.; Liu, H.; Liu, B.; et al. Photostable Fluorescent Organic Dots with Aggregation-Induced Emission (AIE dots) for Noninvasive Long-Term Cell Tracing. *Sci. Rep.* **2013**, *3*, 1150.
- (127) Mei, J.; Wang, J.; Sun, J. Z.; Zhao, H.; Yuan, W.; Deng, C.; Chen, S.; Sung, H. H. Y.; Lu, P.; Qin, A.; et al. Siloles Symmetrically Substituted on Their 2,5-Positions with Electron-Accepting and

- Donating Moieties: Facile Synthesis, Aggregation-Enhanced Emission, Solvatochromism, and Device Application. *Chem. Sci.* **2012**, *3*, 549–558.
- (128) Chen, B.; Jiang, Y.; Chen, L.; Nie, H.; He, B.; Lu, P.; Sung, H. H. Y.; Williams, I. D.; Kwok, H. S.; Qin, A.; et al. 2,5-Difluorenyl-Substituted Siloles for the Fabrication of High-Performance Yellow Organic Light-Emitting Diodes. *Chem. - Eur. J.* **2014**, *20*, 1931–1939.
- (129) Du, X.; Wang, Z. Y. Donor–Acceptor Type Silole Compounds with Aggregation-Induced Deep-Red Emission Enhancement: Synthesis and Application for Significant Intensification of Near-Infrared Photoluminescence. *Chem. Commun.* **2011**, *47*, 4276–4278.
- (130) Xu, B.; He, J.; Dong, Y.; Chen, F.; Yu, W.; Tian, W. Aggregation Emission Properties and Self-Assembly of Conjugated Oligocarbazoles. *Chem. Commun.* **2011**, *47*, 6602–6604.
- (131) Yang, B.; Niu, X.; Huang, Z.; Zhao, C.; Liu, Y.; Ma, C. A Novel Kind of Dimmer (Excimer)-Induced-AIE Compound 2-Phenylisothiazolo[5,4-*b*]pyridin-3(2H)-one as High Selective Bisulfite Anion Probe. *Tetrahedron* **2013**, *69*, 8250–8254.
- (132) Chou, C. A.; Chien, R. H.; Lai, C. T.; Hong, J. L. Complexation of Bulky Camphorsulfonic Acid to Enhance Emission of Organic and Polymeric Fluorophores with Inherent Quinoline Moiety. *Chem. Phys. Lett.* **2010**, *501*, 80–86.
- (133) Yuan, M.-S.; Wang, D.-E.; Xue, P.; Wang, W.; Wang, J.-C.; Tu, Q.; Liu, Z.; Liu, Y.; Zhang, Y.; Wang, J. Fluorenone Organic Crystals: Two-Color Luminescence Switching and Reversible Phase Transformations between  $\pi$ – $\pi$  Stacking-Directed Packing and Hydrogen Bond-Directed Packing. *Chem. Mater.* **2014**, *26*, 2467–2477.
- (134) Liu, Y.; Zhang, Y.; Wu, X.; Lan, Q.; Chen, C.; Liu, S.; Chi, Z.; Jiang, L.; Chen, X.; Xu, J. Deep-Blue Luminescent Compound that Emits Efficiently Both in Solution and Solid State with Considerable Blue-Shift upon Aggregation. *J. Mater. Chem. C* **2014**, *2*, 1068–1075.
- (135) Mazumdar, P.; Das, D.; Sahoo, G. P.; Salgado-Morán, G.; Misra, A. Aggregation Induced Emission Enhancement from Bathophenanthroline Microstructures and Its Potential Use as Sensor of Mercury Ions in Water. *Phys. Chem. Chem. Phys.* **2014**, *16*, 6283–6293.
- (136) Bhalla, V.; Gupta, A.; Kumar, M. A Pentacenequinone Derivative with Aggregation-Induced Emission Enhancement Characteristics for the Picogram Detection of Fe<sup>3+</sup> Ions in Mixed Aqueous Media. *Dalton Trans.* **2013**, *42*, 4464–4469.
- (137) Li, J.; Li, P.; Wu, J.; Gao, J.; Xiong, W.-W.; Zhang, G.; Zhao, Y.; Zhang, Q. [4 + 2] Cycloaddition Reaction To Approach Diazatwist-pentacenes: Synthesis, Structures, Physical Properties, and Self-assembly. *J. Org. Chem.* **2014**, *79*, 4438–4445.
- (138) Chen, S.; Qin, Z.; Liu, T.; Wu, X.; Li, Y.; Liu, H.; Song, Y.; Li, Y. Aggregation-Induced Emission on Benzothiadiazole Dyads with Large Third-Order Optical Nonlinearity. *Phys. Chem. Chem. Phys.* **2013**, *15*, 12660–12666.
- (139) Chen, S.; Chen, N.; Yan, Y. L.; Liu, T.; Yu, Y.; Li, Y.; Liu, H.; Zhao, Y. S.; Li, Y. Controlling Growth of Molecular Crystal Aggregates for Efficient Optical Waveguides. *Chem. Commun.* **2012**, *48*, 9011–9013.
- (140) Ananthakrishnan, S. J.; Varathan, E.; Ravindran, E.; Somanathan, N.; Subramanian, V.; Mandal, A. B.; Sudha, J. D.; Ramakrishnan, R. A. Solution Processable Fluorene–Fluorenone Oligomer with Aggregation Induced Emission Enhancement. *Chem. Commun.* **2013**, *49*, 10742–10744.
- (141) Li, Y.; Wu, Y.; Chang, J.; Chen, M.; Liu, R.; Li, F. A Bioprobe Based on Aggregation Induced Emission (AIE) for Cell Membrane Tracking. *Chem. Commun.* **2013**, *49*, 11335–11337.
- (142) Wang, X.; Morales, A. R.; Urakami, T.; Zhang, L.; Bondar, M. V.; Komatsu, M.; Belfield, K. D. Folate Receptor-Targeted Aggregation-Enhanced Near-IR Emitting Silica Nanoprobe for One-Photon *in vivo* and Two-Photon *ex vivo* Fluorescence Bioimaging. *Bioconjugate Chem.* **2011**, *22*, 1438–1450.
- (143) Li, Q. Q.; Yu, S. S.; Li, Z.; Qin, J. G. New Indole-Containing Luminophores: Convenient Synthesis and Aggregation-Induced Emission Enhancement. *J. Phys. Org. Chem.* **2009**, *22*, 241–246.
- (144) Gao, C.; Gao, G.; Lan, J.; You, J. An AIE Active Monoimidazolium Skeleton: High Selectivity and Fluorescence Turn-on for H<sub>2</sub>PO<sub>4</sub><sup>-</sup> in Acetonitrile and ClO<sub>4</sub><sup>-</sup> in Water. *Chem. Commun.* **2014**, *50*, 5623–5625.
- (145) Skardžiūtė, L.; Kazlauskas, K.; Dodonova, J.; Bucevičius, J.; Tumkevičius, S.; Juršėnas, S. Optical Study of the Formation of Pyrrolo[2,3-d]pyrimidine-Based Fluorescent Nanoaggregates. *Tetrahedron* **2013**, *69*, 9566–9572.
- (146) Fu, G.-L.; Zhao, C.-H. An Aggregation-Induced Emissive Chromophore as a Ratiometric Fluorescent Sensor for Cyanide in Aqueous Media. *Tetrahedron* **2013**, *69*, 1700–1704.
- (147) Hu, R. R.; Lager, E.; Aguilar-Aguilar, A.; Liu, J. Z.; Lam, J. W. Y.; Sung, H. H. Y.; Williams, I. D.; Zhong, Y. C.; Wong, K. S.; Pena-Cabrera, E.; et al. Twisted Intramolecular Charge Transfer and Aggregation-Induced Emission of BODIPY Derivatives. *J. Phys. Chem. C* **2009**, *113*, 15845–15853.
- (148) Wang, B.; He, N.; Li, B.; Jiang, S.; Qu, Y.; Qu, S.; Hua, J. Aggregation-Induced Emission and Large Two-Photon Absorption Cross-Sections of Diketopyrrolopyrrole (DPP) Derivatives. *Aust. J. Chem.* **2012**, *65*, 387–394.
- (149) Ishi-i, T.; Ikeda, K.; Kichise, Y.; Ogawa, M. Red-Light-Emitting System Based on Aggregation of Donor–Acceptor Derivatives in Polar Aqueous Media. *Chem. - Asian J.* **2012**, *7*, 1553–1557.
- (150) Wang, B.; Wang, Y.; Hua, J.; Jiang, Y.; Huang, J.; Qian, S.; Tian, H. Starburst Triarylamine Donor–Acceptor–Donor Quadrupolar Derivatives Based on Cyano-Substituted Diphenylaminostyrylbenzene: Tunable Aggregation-Induced Emission Colors and Large Two-Photon Absorption Cross Sections. *Chem. - Eur. J.* **2011**, *17*, 2647–2655.
- (151) Jiang, Y. H.; Wang, Y. C.; Hua, J. L.; Tang, J.; Li, B.; Qian, S. X.; Tian, H. Multibranched Triarylamine End-capped Triazines with Aggregation-Induced Emission and Large Two-Photon Absorption Cross-Sections. *Chem. Commun.* **2010**, *46*, 4689–4691.
- (152) Gao, Y.; Zhang, H.; Jiang, T.; Yang, J.; Li, B.; Li, Z.; Hua, J. Synthesis, Two-photon Absorption and AIE Properties of Multi-branched Thiophene-Based Triphenylamine Derivatives with Triazine Core. *Sci. China: Chem.* **2013**, *56*, 1204–1212.
- (153) Huang, W.; Wang, H.; Sun, L.; Li, B.; Su, J. H.; Tian, H. Propeller-Like D– $\pi$ –A Architectures: Bright Solid Emitters with AIEE Activity and Large Two-photon Absorption. *J. Mater. Chem. C* **2014**, *2*, 6843–6849.
- (154) Huang, W.; Tang, F.; Li, B.; Su, J.; Tian, H. Large Cyano- and Triazine-substituted D– $\pi$ –A– $\pi$ –D Structures as Efficient AIEE Solid Emitters with Large Two-photon Absorption Cross Sections. *J. Mater. Chem. C* **2014**, *2*, 1141–1148.
- (155) Shimizu, M.; Tatsumi, H.; Mochida, K.; Shimono, K.; Hiyama, T. Synthesis, Crystal Structure, and Photophysical Properties of (1E,3E,5E)-1,3,4,6-Tetraarylhexa-1,3,5-trienes: A New Class of Fluorophores Exhibiting Aggregation-Induced Emission. *Chem. - Asian J.* **2009**, *4*, 1289–1297.
- (156) Yang, L.; Ye, J.; Xu, L.; Yang, X.; Gong, W.; Lin, Y.; Ning, G. Synthesis and Properties of Aggregation-Induced Emission Enhancement Compounds Derived from Triarylcyclopentadiene. *RSC Adv.* **2012**, *2*, 11529–11535.
- (157) Ye, J.; Deng, D.; Gao, Y.; Wang, X.; Yang, L.; Lin, Y.; Ning, G. Synthesis, Molecular Structure and Photoluminescence Properties of 1,2-Diphenyl-4-(3-methoxyphenyl)-1,3-cyclopentadiene. *Spectrochim. Acta, Part A* **2015**, *134*, 22–27.
- (158) Zhang, X.; Ye, J.; Xu, L.; Yang, L.; Deng, D.; Ning, G. Synthesis, Crystal Structures and Aggregation-Induced Emission Enhancement of Aryl-Substituted Cyclopentadiene Derivatives. *J. Lumin.* **2013**, *139*, 28–34.
- (159) Zhang, Z.; Xu, B.; Su, J.; Shen, L.; Xie, Y.; Tian, H. Color-Tunable Solid-State Emission of 2,2'-Biindenyl-Based Fluorophores. *Angew. Chem., Int. Ed.* **2011**, *50*, 11654–11657.
- (160) Hu, R.; Lam, J. W. Y.; Liu, Y.; Zhang, X.; Tang, B. Z. Aggregation-Induced Emission of Tetraphenylethene–Hexaphenylbenzene Adducts: Effects of Twisting Amplitude and Steric Hindrance on Light Emission of Nonplanar Fluorogens. *Chem. - Eur. J.* **2013**, *19*, 5617–5624.

- (161) Feng, J.; Chen, X.; Han, Q.; Wang, H.; Lu, P.; Wang, Y. Naphthalene-Based Fluorophores: Synthesis Characterization, and Photophysical Properties. *J. Lumin.* **2011**, *131*, 2775–2783.
- (162) He, J. T.; Xu, B.; Chen, F. P.; Xia, H. J.; Li, K. P.; Ye, L.; Tian, W. J. Aggregation-Induced Emission in the Crystals of 9,10-Distyrylanthracene Derivatives: The Essential Role of Restricted Intramolecular Torsion. *J. Phys. Chem. C* **2009**, *113*, 9892–9899.
- (163) Zhang, J.; Xu, B.; Chen, J.; Ma, S.; Dong, Y.; Wang, L.; Li, B.; Ye, L.; Tian, W. An Organic Luminescent Molecule: What Will Happen When the “Butterflies” Come Together? *Adv. Mater.* **2014**, *26*, 739–745.
- (164) Li, Y.-X.; Chen, Z.; Cui, Y.; Xia, G.-M.; Yang, X.-F. Substitution Position Directing the Molecular Packing, Electronic Structure, and Aggregate Emission Property of Bis[2-(9-anthracenyl)vinyl]benzene System. *J. Phys. Chem. C* **2012**, *116*, 6401–6408.
- (165) Li, Y.-X.; Jia, J.; Tao, X.-T. Intramolecular H···H Steric Hindrance Modulated Aggregate Packing and Optoelectronic Properties in 1-Naphthyl, 9-Anthryl End-Capped Styrylarylene Derivatives. *CrystEngComm* **2012**, *14*, 2843–2848.
- (166) Li, Y.-X.; Sun, G.-X.; Miao, J.-L.; Nie, Y.; Zhang, Z.-W.; Tao, X.-T. Effect of Vinylene Bond Geometry on the Molecule Packing and Aggregation-Enhanced Emission Property of a Pair of 1-[ (9-Anthracenyl)vinyl]pyrene Isomers. *Tetrahedron Lett.* **2013**, *54*, 3263–3267.
- (167) Levell, J. W.; Ruseckas, A.; Henry, J. B.; Wang, Y.; Stretton, A. D.; Mount, A. R.; Galow, T. H.; Samuel, I. D. W. Fluorescence Enhancement by Symmetry Breaking in a Twisted Triphenylene Derivative. *J. Phys. Chem. A* **2010**, *114*, 13291–13295.
- (168) Di Donato, E.; Vanzo, D.; Semeraro, M.; Credi, A.; Negri, F. Tuning Fluorescence Lifetimes through Changes in Herzberg–Teller Activities: The Case of Triphenylene and Its Hexamethoxy-Substituted Derivative. *J. Phys. Chem. A* **2009**, *113*, 6504–6510.
- (169) He, Z.; Shan, L.; Mei, J.; Wang, H.; Lam, J. W. Y.; Sung, H. H. Y.; Williams, I. D.; Gu, X.; Miao, Q.; Tang, B. Z. Aggregation-Induced Emission and Aggregation-Promoted Photochromism of Bis(diphenylmethylene)dihydroacenes. *Chem. Sci.* **2015**, *6*, 3538–3543.
- (170) Mullin, J. L.; Tracy, H. J.; Ford, J. R.; Keenan, S. R.; Fridman, F. Characteristics of Aggregation Induced Emission in 1,1-Dimethyl-2,3,4,5-tetraphenyl and 1,1,2,3,4,5-Hexaphenyl Siloles and Germoles. *J. Inorg. Organomet. Polym. Mater.* **2007**, *17*, 201–213.
- (171) Tracy, H. J.; Mullin, J. L.; Klooster, W. T.; Martin, J. A.; Haug, J.; Wallace, S.; Rudloe, I.; Watts, K. Enhanced Photoluminescence from Group 14 Metalloles in Aggregated and Solid Solutions. *Inorg. Chem.* **2005**, *44*, 2003–2011.
- (172) Bandrowsky, T. L.; Carroll, J. B.; Braddock-Wilking, J. Synthesis, Characterization, and Crystal Structures of 1,1-Disubstituted-2,3,4,5-tetraphenylgermoles That Exhibit Aggregation-Induced Emission. *Organometallics* **2011**, *30*, 3559–3569.
- (173) Feng, X. A.; Tong, B.; Shen, J. B.; Shi, J. B.; Han, T. Y.; Chen, L.; Zhi, J. G.; Lu, P.; Ma, Y. G.; Dong, Y. P. Aggregation-Induced Emission Enhancement of Aryl-Substituted Pyrrole Derivatives. *J. Phys. Chem. B* **2010**, *114*, 16731–16736.
- (174) Fukazawa, A.; Ichihashi, Y.; Yamaguchi, S. Intense Fluorescence of 1-Aryl-2,3,4,5-Tetraphenylphosphole Oxides in the Crystalline State. *New J. Chem.* **2010**, *34*, 1537–1540.
- (175) Shiraishi, K.; Kashiwabara, T.; Sanji, T.; Tanaka, M. Aggregation-Induced Emission of Dendritic Phosphole Oxides. *New J. Chem.* **2009**, *33*, 1680–1684.
- (176) Sanji, T.; Shiraishi, K.; Tanaka, M. Sugar–Phosphole Oxide Conjugates as “Turn-on” Luminescent Sensors for Lectins. *ACS Appl. Mater. Interfaces* **2009**, *1*, 270–273.
- (177) Ren, Y.; Baumgartner, T. Structure–Property Studies toward the Stimuli-Responsive Behavior of Benzyl–Phospholium Acenes. *Inorg. Chem.* **2012**, *51*, 2669–2678.
- (178) Lai, C. T.; Hong, J. L. Aggregation-Induced Emission in Tetraphenylthiophene-Derived Organic Molecules and Vinyl Polymer. *J. Phys. Chem. B* **2010**, *114*, 10302–10310.
- (179) Jahnke, A. A.; Seferos, D. S. Polytellurophenes. *Macromol. Rapid Commun.* **2011**, *32*, 943–951.
- (180) He, G.; Torres Delgado, W.; Schatz, D. J.; Merten, C.; Mohammadpour, A.; Mayr, L.; Ferguson, M. J.; McDonald, R.; Brown, A.; Shankar, K.; et al. Coaxing Solid-State Phosphorescence from Tellurophenes. *Angew. Chem., Int. Ed.* **2014**, *53*, 4587–4591.
- (181) Kokado, K.; Chujo, Y. Emission via Aggregation of Alternating Polymers with *o*-Carborane and *p*-Phenyleno–Ethyne Sequences. *Macromolecules* **2009**, *42*, 1418–1420.
- (182) Kokado, K.; Chujo, Y. Multicolor Tuning of Aggregation-Induced Emission through Substituent Variation of Diphenyl-*o*-carborane. *J. Org. Chem.* **2011**, *76*, 316–319.
- (183) Kokado, K.; Chujo, Y. A Luminescent Coordination Polymer Based on Bisterpyridyl Ligand Containing *o*-Carborane: Two Tunable Emission Modes. *Dalton Trans.* **2011**, *40*, 1919–1923.
- (184) Inagi, S.; Hosoi, K.; Kubo, T.; Shida, N.; Fuchigami, T. *o*-Carborane-Triphenylamine Dyad: Studies on Its Acceptor-Donor Behavior toward Dual Redox Mediator. *Electrochemistry* **2013**, *81*, 368–370.
- (185) Kokado, K.; Nagai, A.; Chujo, Y. Energy Transfer from Aggregation-Induced Emissive *o*-Carborane. *Tetrahedron Lett.* **2011**, *52*, 293–296.
- (186) Bae, H. J.; Kim, H.; Lee, K. M.; Kim, T.; Lee, Y. S.; Do, Y.; Lee, M. H. Through-Space Charge Transfer and Emission Color Tuning of *Di-o*-carborane Substituted Benzene. *Dalton Trans.* **2014**, *43*, 4978–4985.
- (187) Pan, H.; Fu, G. L.; Zhao, Y. H.; Zhao, C. H. Through-Space Charge-Transfer Emitting Biphenyls Containing a Boryl and an Amino Group at the *o,o'*-Positions. *Org. Lett.* **2011**, *13*, 4830–4833.
- (188) Zhao, C. H.; Sakuda, E.; Wakamiya, A.; Yamaguchi, S. Highly Emissive Diborylphenylene-Containing Bis(phenylethynyl)benzenes: Structure–Photophysical Property Correlations and Fluoride Ion Sensing. *Chem. - Eur. J.* **2009**, *15*, 10603–10612.
- (189) Galer, P.; Korošec, R. C.; Vidmar, M.; Šket, B. Crystal Structures and Emission Properties of the  $\text{BF}_2$  Complex 1-Phenyl-3-(3,5-dimethoxyphenyl)-propane-1,3-dione: Multiple Chromisms, Aggregation- or Crystallization-Induced Emission, and the Self-Assembly Effect. *J. Am. Chem. Soc.* **2014**, *136*, 7383–7394.
- (190) Cheng, X.; Li, D.; Zhang, Z.; Zhang, H.; Wang, Y. Organoboron Compounds with Morphology-Dependent NIR Emissions and Dual-Channel Fluorescent ON/OFF Switching. *Org. Lett.* **2014**, *16*, 880–883.
- (191) Dong, Y.; Lam, J. W. Y.; Qin, A.; Li, Z.; Sun, J.; Sung, H. H. Y.; Williams, I. D.; Tang, B. Z. Switching the Light Emission of (4-Biphenyl)phenyldibenzofulvene by Morphological Modulation: Crystallization-Induced Emission Enhancement. *Chem. Commun.* **2007**, 40–42.
- (192) Yoshii, R.; Nagai, A.; Tanaka, K.; Chujo, Y. Highly Emissive Boron Ketoiminate Derivatives as a New Class of Aggregation-Induced Emission Fluorophores. *Chem. - Eur. J.* **2013**, *19*, 4506–4512.
- (193) Yoshii, R.; Tanaka, K.; Chujo, Y. Conjugated Polymers Based on Tautomeric Units: Regulation of Main-Chain Conjugation and Expression of Aggregation Induced Emission Property via Boron-Complexation. *Macromolecules* **2014**, *47*, 2268–2278.
- (194) Kubota, Y.; Ozaki, Y.; Funabiki, K.; Matsui, M. Synthesis and Fluorescence Properties of Pyrimidine Mono- and Bisboron Complexes. *J. Org. Chem.* **2013**, *78*, 7058–7067.
- (195) Kubota, Y.; Tanaka, S.; Funabiki, K.; Matsui, M. Synthesis and Fluorescence Properties of Thiazole–Boron Complexes Bearing a  $\beta$ -Ketoiminate Ligand. *Org. Lett.* **2012**, *14*, 4682–4685.
- (196) Yan, W. B.; Wan, X. J.; Chen, Y. S. Phenalenyl-based Boron–Fluorine Complexes: Synthesis, Crystal Structures and Solid-state Fluorescence Properties. *J. Mol. Struct.* **2010**, *968*, 85–88.
- (197) Yan, W.; Hong, C.; Long, G.; Yang, Y.; Liu, Z.; Bian, Z.; Chen, Y.; Huang, C. Synthesis, Crystal Structures and Photophysical Properties of Novel Boron-Containing Derivatives of Phenalene with Bright Solid-State Luminescence. *Dyes Pigm.* **2014**, *106*, 197–204.
- (198) Yoshii, R.; Hirose, A.; Tanaka, K.; Chujo, Y. Boron Diiminate with Aggregation-Induced Emission and Crystallization-Induced Emission-Enhancement Characteristics. *Chem. - Eur. J.* **2014**, *20*, 8320–8324.

- (199) Yang, Y.; Su, X.; Carroll, C. N.; Aprahamian, I. Aggregation-Induced Emission in  $\text{BF}_3$ -Hydrazone (BODIHY) Complexes. *Chem. Sci.* **2012**, *3*, 610–613.
- (200) Zhao, D.; Li, G.; Wu, D.; Qin, X.; Neuhaus, P.; Cheng, Y.; Yang, S.; Lu, Z.; Pu, X.; Long, C.; et al. Regiospecific *N*-Heteroarylation of Amidines for Full-Color-Tunable Boron Difluoride Dyes with Mechanochromic Luminescence. *Angew. Chem., Int. Ed.* **2013**, *52*, 13676–13680.
- (201) Gozem, S.; Mirzakulova, E.; Schapiro, I.; Melaccio, F.; Glusac, K. D.; Olivucci, M. A Conical Intersection Controls the Deactivation of the Bacterial Luciferase Fluorophore. *Angew. Chem., Int. Ed.* **2014**, *53*, 9870–9875.
- (202) Yu, Z.; Duan, Y.; Cheng, L.; Han, Z.; Zheng, Z.; Zhou, H.; Wu, J.; Tian, Y. Aggregation Induced Emission in the Rotatable Molecules: The Essential Role of Molecular Interaction. *J. Mater. Chem.* **2012**, *22*, 16927–16932.
- (203) Liu, G.; Yang, M.; Wang, L.; Zheng, J.; Zhou, H.; Wu, J.; Tian, Y. Schiff Base Derivatives Containing Heterocycles with Aggregation-Induced Emission and Recognition Ability. *J. Mater. Chem. C* **2014**, *2*, 2684–2691.
- (204) Han, T.; Hong, Y.; Xie, N.; Chen, S.; Zhao, N.; Zhao, E.; Lam, J. W. Y.; Sung, H. H. Y.; Dong, Y.; Tong, B.; et al. Defect-Sensitive Crystals Based on Diaminomaleonitrile-Functionalized Schiff Base with Aggregation-Enhanced Emission. *J. Mater. Chem. C* **2013**, *1*, 7314–7320.
- (205) Douhal, A.; Lahmani, F.; Zewail, A. H. Proton-Transfer Reaction Dynamics. *Chem. Phys.* **1996**, *207*, 477–498.
- (206) Lochbrunner, S.; Schultz, T.; Schmitt, M.; Shaffer, J. P.; Zgierski, M. Z.; Stolow, A. Dynamics of Excited-State Proton Transfer Systems via Time-Resolved Photoelectron Spectroscopy. *J. Chem. Phys.* **2001**, *114*, 2519–2522.
- (207) Goodman, J.; Brus, L. E. Proton Transfer and Tautomerism in an Excited State of Methyl Salicylate. *J. Am. Chem. Soc.* **1978**, *100*, 7472–7474.
- (208) Ormson, S. M.; Brown, R. G. Excited-State Intramolecular Proton Transfer. Part 1: ESIPT to Nitrogen. *Prog. React. Kinet.* **1994**, *19*, 45–91.
- (209) Kuila, D.; Kvakovszky, G.; Murphy, M. A.; Vicari, R.; Rood, M. H.; Fritch, K. A.; Fritch, J. R. Tris(hydroxyphenyl)ethane Benzotriazole: A Copolymerizable UV Light Stabilizer. *Chem. Mater.* **1999**, *11*, 109–116.
- (210) Chou, P.; McMorrow, D.; Aartsma, T. J.; Kasha, M. The Proton-Transfer Laser. Gain Spectrum and Amplification of Spontaneous Emission of 3-Hydroxyflavone. *J. Phys. Chem.* **1984**, *88*, 4596–4599.
- (211) Kwon, J. E.; Park, S. Y. Advanced Organic Optoelectronic Materials: Harnessing Excited-State Intramolecular Proton Transfer (ESIPT) Process. *Adv. Mater.* **2011**, *23*, 3615–3642.
- (212) Zhao, J.; Ji, S.; Chen, Y.; Guo, H.; Yang, P. Excited State Intramolecular Proton Transfer (ESIPT): From Principal Photophysics to the Development of New Chromophores and Applications in Fluorescent Molecular Probes and Luminescent Materials. *Phys. Chem. Chem. Phys.* **2012**, *14*, 8803–8817.
- (213) Wu, J.; Liu, W.; Ge, J.; Zhang, H.; Wang, P. New Sensing Mechanisms for Design of Fluorescent Chemosensors Emerging in Recent Years. *Chem. Soc. Rev.* **2011**, *40*, 3483–3495.
- (214) Dick, B.; Ernsting, N. P. Excited-State Intramolecular Proton Transfer in 3-Hydroxyflavone Isolated in Solid Argon: Fluorescence and Fluorescence-Excitation Spectra and Tautomer Fluorescence Rise Time. *J. Phys. Chem.* **1987**, *91*, 4261–4265.
- (215) Kim, T.-I.; Kang, H. J.; Han, G.; Chung, S. J.; Kim, Y. A Highly Selective Fluorescent ESIPT Probe for the Dual Specificity Phosphatase MKP-6. *Chem. Commun.* **2009**, 5895–5897.
- (216) Rodembusch, F. S.; Campo, L. F.; Stefani, V.; Rigacci, A. The First Silica Aerogels Fluorescent by Excited State Intramolecular Proton Transfer Mechanism (ESIPT). *J. Mater. Chem.* **2005**, *15*, 1537–1541.
- (217) Mutai, T.; Tomoda, H.; Ohkawa, T.; Yabe, Y.; Araki, K. Switching of Polymorph-Dependent ESIPT Luminescence of an Imidazo[1,2-*a*]pyridine Derivative. *Angew. Chem., Int. Ed.* **2008**, *47*, 9522–9524.
- (218) Mutai, T.; Sawatani, H.; Shida, T.; Shono, H.; Araki, K. Tuning of Excited-State Intramolecular Proton Transfer (ESIPT) Fluorescence of Imidazo[1,2-*a*]pyridine in Rigid Matrices by Substitution Effect. *J. Org. Chem.* **2013**, *78*, 2482–2489.
- (219) Furukawa, S.; Shono, H.; Mutai, T.; Araki, K. Colorless, Transparent, Dye-Doped Polymer Films Exhibiting Tunable Luminescence Color: Controlling the Dual-Color Luminescence of 2-(2'-Hydroxyphenyl)imidazo[1,2-*a*]pyridine Derivatives with the Surrounding Matrix. *ACS Appl. Mater. Interfaces* **2014**, *6*, 16065–16070.
- (220) Tang, W. X.; Xiang, Y.; Tong, A. J. Salicylaldehyde Azines as Fluorophores of Aggregation-Induced Emission Enhancement Characteristics. *J. Org. Chem.* **2009**, *74*, 2163–2166.
- (221) Wei, R.; Song, P.; Tong, A. Reversible Thermochromism of Aggregation-Induced Emission-Active Benzophenone Azine Based on Polymorph-Dependent Excited-State Intramolecular Proton Transfer Fluorescence. *J. Phys. Chem. C* **2013**, *117*, 3467–3474.
- (222) Peng, L.; Zhou, Z.; Wang, X.; Wei, R.; Li, K.; Xiang, Y.; Tong, A. A Ratiometric Fluorescent Chemosensor for  $\text{Al}^{3+}$  in Aqueous Solution Based on Aggregation-Induced Emission and Its Application in Live-Cell Imaging. *Anal. Chim. Acta* **2014**, *829*, 54–59.
- (223) Cao, X.; Zeng, X.; Mu, L.; Chen, Y.; Wang, R.-x.; Zhang, Y.-q.; Zhang, J.-x.; Wei, G. Characterization of the Aggregation-Induced Enhanced Emission, Sensing, and Logic Gate Behavior of 2-(1-Hydroxy-2-naphthyl)methylene Hydrazine. *Sens. Actuators, B* **2013**, *177*, 493–499.
- (224) Xiao, H.; Chen, K.; Cui, D.; Jiang, N.; Yin, G.; Wang, J.; Wang, R. Two Novel Aggregation-Induced Emission Active Coumarin-Based Schiff Bases and Their Applications in Cell Imaging. *New J. Chem.* **2014**, *38*, 2386–2393.
- (225) Chen, P.; Lu, R.; Xue, P. C.; Xu, T. H.; Chen, G. J.; Zhao, Y. Y. Emission Enhancement and Chromism in a Salen-Based Gel System. *Langmuir* **2009**, *25*, 8395–8399.
- (226) Niu, C.; Zhao, L.; Fang, T.; Deng, X.; Ma, H.; Zhang, J.; Na, N.; Han, J.; Ouyang, J. Color- and Morphology-Controlled Self-Assembly of New Electron-Donor-Substituted Aggregation-Induced Emission Compounds. *Langmuir* **2014**, *30*, 2351–2359.
- (227) Li, S.; He, L.; Xiong, F.; Li, Y.; Yang, G. Enhanced Fluorescent Emission of Organic Nanoparticles of an Intramolecular Proton Transfer Compound and Spontaneous Formation of One-Dimensional Nanostructures. *J. Phys. Chem. B* **2004**, *108*, 10887–10892.
- (228) Chen, X.-t.; Xiang, Y.; Song, P.-S.; Wei, R.-r.; Zhou, Z.-j.; Li, K.; Tong, A.-j. *p*-Carboxyl-N-salicylideneanilines: Simple But Efficient Chromophores for One-dimensional Microrods with Aggregation-Induced Emission Enhancement (AIEE) Characteristics. *J. Lumin.* **2011**, *131*, 1453–1459.
- (229) Yang, M.; Xu, D.; Xi, W.; Wang, L.; Zheng, J.; Huang, J.; Zhang, J.; Zhou, H.; Wu, J.; Tian, Y. Aggregation-Induced Fluorescence Behavior of Triphenylamine-Based Schiff Bases: The Combined Effect of Multiple Forces. *J. Org. Chem.* **2013**, *78*, 10344–10359.
- (230) Ning, T.; Liu, L.; Jia, D.; Xie, X.; Wu, D. Aggregation-Induced Emission, Photochromism and Self-Assembly of Pyrazolone Phenyleimcarbazones. *J. Photochem. Photobiol., A* **2014**, *291*, 48–53.
- (231) Qian, Y.; Cai, M.; Zhou, X.; Gao, Z.; Wang, X.; Zhao, Y.; Yan, X.; Wei, W.; Xie, L.; Huang, W. More than Restriction of Twisted Intramolecular Charge Transfer: Three-Dimensional Expanded #-Shaped Cross-Molecular Packing for Emission Enhancement in Aggregates. *J. Phys. Chem. C* **2012**, *116*, 12187–12195.
- (232) Chen, Y.; Lv, Y.; Han, Y.; Zhu, B.; Zhang, F.; Bo, Z.; Liu, C.-Y. Dendritic Effect on Supramolecular Self-Assembly: Organogels with Strong Fluorescence Emission Induced by Aggregation. *Langmuir* **2009**, *25*, 8548–8555.
- (233) Shen, Y. T.; Li, C. H.; Chang, K. C.; Chin, S. Y.; Lin, H. A.; Liu, Y. M.; Hung, C. Y.; Hsu, H. F.; Sun, S. S. Synthesis, Optical, and Mesomorphic Properties of Self-Assembled Organogels Featuring Phenylethynyl Framework with Elaborated Long-Chain Pyridine-2,6-Dicarboxamides. *Langmuir* **2009**, *25*, 8714–8722.
- (234) Xu, D.; Liu, X.; Lu, R.; Xue, P.; Zhang, X.; Zhou, H.; Jia, J. New Dendritic Gelator Bearing Carbazole in Each Branching Unit: Selected

- Response to Fluoride Ion in Gel Phase. *Org. Biomol. Chem.* **2011**, *9*, 1523–1528.
- (235) Zhao, Y.; Lin, H.; Chen, M.; Yan, D. Niflumic Anion Intercalated Layered Double Hydroxides with Mechano-Induced and Solvent-Responsive Luminescence. *Ind. Eng. Chem. Res.* **2014**, *53*, 3140–3147.
- (236) Krishna Murthy, H. M.; Vijayan, M. Structural Crystallography and Crystal Chemistry. *Acta Crystallogr., Sect. B: Struct. Crystallogr. Cryst. Chem.* **1979**, *35*, 262–263.
- (237) Bernet, A.; Albuquerque, R. Q.; Behr, M.; Hoffmann, S. T.; Schmidt, H.-W. Formation of a Supramolecular Chromophore: A Spectroscopic and Theoretical Study. *Soft Matter* **2012**, *8*, 66–69.
- (238) Beppu, T.; Kawata, S.; Aizawa, N.; Pu, Y.-J.; Abe, Y.; Ohba, Y.; Katagiri, H. 2,6-Bis(arylsulfonyl)anilines as Fluorescent Scaffolds through Intramolecular Hydrogen Bonds: Solid-State Fluorescence Materials and Turn-On-Type Probes Based on Aggregation-Induced Emission. *ChemPlusChem* **2014**, *79*, 536–545.
- (239) Yeh, H.-C.; Wu, W.-C.; Wen, Y.-S.; Dai, D.-C.; Wang, J.-K.; Chen, C.-T. Derivative of  $\alpha,\beta$ -Dicyanostilbene: Convenient Precursor for the Synthesis of Diphenylmaleimide Compounds, *E-Z* Isomerization, Crystal Structure, and Solid-State Fluorescence. *J. Org. Chem.* **2004**, *69*, 6455–6462.
- (240) Upamali, K. A.; Estrada, L. A.; De, P. K.; Cai, X.; Krause, J. A.; Neckers, D. C. Carbazole-Based Cyano-Stilbene Highly Fluorescent Microcrystals. *Langmuir* **2011**, *27*, 1573–1580.
- (241) An, B.-K.; Gierschner, J.; Park, S. Y.  $\pi$ -Conjugated Cyanostilbene Derivatives: A Unique Self-Assembly Motif for Molecular Nanostructures with Enhanced Emission and Transport. *Acc. Chem. Res.* **2012**, *45*, 544–554.
- (242) Zhu, L.; Zhao, Y. Cyanostilbene-Based Intelligent Organic Optoelectronic Materials. *J. Mater. Chem. C* **2013**, *1*, 1059–1065.
- (243) Kurita, M.; Momma, M.; Mizuguchi, K.; Nakano, H. Fluorescence Color Change of Aggregation-Induced Emission of 4-[Bis(4-methylphenyl)amino]benzaldehyde. *ChemPhysChem* **2013**, *14*, 3898–3901.
- (244) Koenig, M.; Torres, T.; Barone, V.; Brancato, G.; Guldi, D. M.; Bottari, G. Ultrasound-Induced Transformation of Fluorescent Organic Nanoparticles from a Molecular Rotor into Rhomboidal Nanocrystals with Enhanced Emission. *Chem. Commun.* **2014**, *50*, 12955–12958.
- (245) Zhao, X.; Xue, P.; Wang, K.; Chen, P.; Zhang, P.; Lu, R. Aggregation-Induced Emission of Triphenylamine Substituted Cyanostyrene Derivatives. *New J. Chem.* **2014**, *38*, 1045–1051.
- (246) Song, Q.; Chen, K.; Sun, J.; Wang, Y.; Ouyang, M.; Zhang, C. Mechanical Force Induced Reversible Fluorescence Switching of Two 3-Aryl-2-cyano acrylamide Derivatives. *Tetrahedron Lett.* **2014**, *55*, 3200–3205.
- (247) Cao, Y.; Xi, W.; Wang, L.; Wang, H.; Kong, L.; Zhou, H.; Wu, J.; Tian, Y. Reversible Piezofluorochromic Nature and Mechanism of Aggregation-Induced Emission-Active Compounds Based on Simple Modification. *RSC Adv.* **2014**, *4*, 24649–24652.
- (248) Tian, G.; Huang, W.; Cai, S.; Zhou, H.; Li, B.; Wang, Q.; Su, J. Small Molecules Based on Diphenylamine and Carbazole with Large Two-Photon Absorption Cross Sections and Extraordinary AIEE Properties. *RSC Adv.* **2014**, *4*, 38939–38942.
- (249) Singh, A.; Lim, C.-K.; Lee, Y.-D.; Maeng, J.-h.; Lee, S.; Koh, J.; Kim, S. Tuning Solid-State Fluorescence to the Near-Infrared: A Combinatorial Approach to Discovering Molecular Nanoprobes for Biomedical Imaging. *ACS Appl. Mater. Interfaces* **2013**, *5*, 8881–8888.
- (250) Dai, Q.; Liu, W.; Zeng, L.; Lee, C.-S.; Wu, J.; Wang, P. Aggregation-Induced Emission Enhancement Materials with Large Red Shifts and Their Self-assembled Crystal Microstructures. *CrystEngComm* **2011**, *13*, 4617–4624.
- (251) Shao, A.; Guo, Z.; Zhu, S.; Zhu, S.; Shi, P.; Tian, H.; Zhu, W. Insight into Aggregation-Induced Emission Characteristics of Red-emissive Quinoline-malononitrile by Cell Tracking and Real-time Trypsin Detection. *Chem. Sci.* **2014**, *5*, 1383–1389.
- (252) Zheng, Z.; Yu, Z.; Yang, M.; Jin, F.; Zhang, Q.; Zhou, H.; Wu, J.; Tian, Y. Substituent Group Variations Directing the Molecular Packing, Electronic Structure, and Aggregation-Induced Emission Property of Isophorone Derivatives. *J. Org. Chem.* **2013**, *78*, 3222–3234.
- (253) Wang, L.; Shen, Y.; Zhu, Q.; Xu, W.; Yang, M.; Zhou, H.; Wu, J.; Tian, Y. Systematic Study and Imaging Application of Aggregation-Induced Emission of Ester-Isophorone Derivatives. *J. Phys. Chem. C* **2014**, *118*, 8531–8540.
- (254) Massin, J.; Dayoub, W.; Mлатиер, J.-C.; Aronica, C.; Bretonnière, Y.; Andraud, C. Near-Infrared Solid-State Emitters Based on Isophorone: Synthesis, Crystal Structure and Spectroscopic Properties. *Chem. Mater.* **2011**, *23*, 862–873.
- (255) Luo, H.; Chen, S.; Liu, Z.; Zhang, C.; Cai, Z.; Chen, X.; Zhang, G.; Zhao, Y.; Decurtins, S.; Liu, S.-X.; et al. A Cruciform Electron Donor–Acceptor Semiconductor with Solid-State Red Emission: 1D/2D Optical Waveguides and Highly Sensitive/Selective Detection of  $\text{H}_2\text{S}$  Gas. *Adv. Funct. Mater.* **2014**, *24*, 4250–4258.
- (256) Xu, J.; Liu, X.; Lv, J.; Zhu, M.; Huang, C.; Zhou, W.; Yin, X.; Liu, H.; Li, Y.; Ye, J. Morphology Transition and Aggregation-Induced Emission of an Intramolecular Charge-Transfer Compound. *Langmuir* **2008**, *24*, 4231–4237.
- (257) Javed, I.; Zhou, T.; Muhammad, F.; Guo, J.; Zhang, H.; Wang, Y. Quinoacridine Derivatives with One-Dimensional Aggregation-Induced Red Emission Property. *Langmuir* **2012**, *28*, 1439–1446.
- (258) Natarajan, P. Luminescence of Triarylphosphines and Their Application to Detection of Elemental Chlorine in Aqueous Solution. *Anal. Methods* **2014**, *6*, 2432–2435.
- (259) Bolzon, A.; Viglianti, L.; Bossi, A.; Mussini, P. R.; Cauteruccio, S.; Baldoli, C.; Licandro, E. Synthesis, Photophysics, and Electrochemistry of Tetra(2-thienyl)ethylene (TTE) Derivatives. *Eur. J. Org. Chem.* **2013**, *2013*, 7489–7499.
- (260) Han, T.; Zhang, Y.; Feng, X.; Lin, Z.; Tong, B.; Shi, J.; Zhi, J.; Dong, Y. Reversible and Hydrogen Bonding-Assisted Piezochromic Luminescence for Solid-state Tetraaryl-buta-1,3-diene. *Chem. Commun.* **2013**, *49*, 7049–7051.
- (261) Zhang, X.; Lu, X.; Zhen, Y.; Liu, J.; Dong, H.; Zhao, G.; He, P.; Wang, Z.; Jiang, L.; Hu, W. Synthesis and Aggregation-Induced Emissions of Thienyl Substituted Cyclobutene Derivatives. *J. Mater. Chem. C* **2014**, *2*, 5083–5086.
- (262) Namitharan, K.; Pitchumani, K. Cascade Synthesis of Bis-*N*-sulfonylcyclobutenes via Cu(I)/Lewis Acid-Catalyzed (3 + 2)/(2 + 2) Cycloadditions: Observation of Aggregation-Induced Emission Enhancement from Restricted C=N Photoisomerization. *Org. Biomol. Chem.* **2012**, *10*, 2937–2941.
- (263) Shimizu, M.; Asai, Y.; Takeda, Y.; Yamatani, A.; Hiyama, T. Twisting Strategy Applied to *N,N*-Diorganoquinacridones Leads to Organic Chromophores Exhibiting Efficient Solid-State Fluorescence. *Tetrahedron Lett.* **2011**, *52*, 4084–4089.
- (264) Shimizu, M.; Takeda, Y.; Higashi, M.; Hiyama, T. 1,4-Bis(alkenyl)-2,5-dipiperidinobenzenes: Minimal Fluorophores Exhibiting Highly Efficient Emission in the Solid State. *Angew. Chem., Int. Ed.* **2009**, *48*, 3653–3656.
- (265) Tanabe, K.; Kodama, D.; Hasegawa, M.; Kato, T. Aggregation-Induced Emission of a Liquid-Crystalline Quinolinium Salt Molecule in Aqueous Solution. *Chem. Lett.* **2014**, *43*, 184–186.
- (266) Wang, Z.; Zhou, H. J.; Hu, J. Y.; You, J. S.; Gao, G. Bisimidazole and Bisimidazolium Cruciforms: Synthesis and Discrimination of Organic Acids. *Acta Chim. Sin.* **2013**, *71*, 1257–1264.
- (267) Zhao, C. H.; Zhao, Y. H.; Pan, H.; Fu, G. L. Highly Solid-state Emissive *para*-Terphenyls Laterally Substituted with a Diphenylamino Group. *Chem. Commun.* **2011**, *47*, 5518–5520.
- (268) Wang, Z.; Fang, Y.; Sun, J.; Qin, A.; Tang, B. New Tetraphenylpyridinium-Based Luminogens with Aggregation-Induced Emission Characteristics. *Sci. China: Chem.* **2013**, *S6*, 1187–1190.
- (269) Tang, H. Y.; Zeng, Y.; Li, Y. Y.; Chen, J. P.; Li, Y. Synthesis and Aggregation-induced Emission of a Novel alpha-Pyrone Derivative. *Acta Chim. Sin.* **2011**, *69*, 2241–2247.
- (270) Rao, M. R.; Liao, C.-W.; Su, W.-L.; Sun, S.-S. Quinoxaline Based D–A–D Molecules: High Contrast Reversible Solid-state Mechano- and Thermo-responsive Fluorescent Materials. *J. Mater. Chem. C* **2013**, *1*, 5491–5501.
- (271) Kokil, A.; Chudomel, J. M.; Yang, B.; Barnes, M. D.; Lahti, P. M.; Kumar, J. Determining the Critical Particle Size to Induce Enhanced

- Emission in Aggregates of a Highly Twisted Triarylamine. *Chem-PhysChem* **2013**, *14*, 3682–3686.
- (272) Zhang, X.; Sorensen, J. K.; Fu, X.; Zhen, Y.; Zhao, G.; Jiang, L.; Dong, H.; Liu, J.; Shuai, Z.; Geng, H.; et al. Rubrene Analogues with the Aggregation-Induced Emission Enhancement Behavior. *J. Mater. Chem. C* **2014**, *2*, 884–890.
- (273) Matsui, M.; Shibata, T.; Fukushima, M.; Kubota, Y.; Funabiki, K. Fluorescence Properties of Indolenine Semi-squarylium Dyes. *Tetrahedron* **2012**, *68*, 9936–9941.
- (274) Nandakumar, A.; Perumal, P. T. Tetrasubstituted Olefinic Xanthene Dyes: Synthesis via Pd-Catalyzed 6-*exo-dig* Cyclization/C–H Activation of 2-Bromobenzyl-N-propargylamines and Solid State Fluorescence Properties. *Org. Lett.* **2013**, *15*, 382–385.
- (275) Kamino, S.; Horio, Y.; Komeda, S.; Minoura, K.; Ichikawa, H.; Horigome, J.; Tatsumi, A.; Kaji, S.; Yamaguchi, T.; Usami, Y.; et al. A New Class of Rhodamine Luminophores: Design, Syntheses and Aggregation-Induced Emission Enhancement. *Chem. Commun.* **2010**, *46*, 9013–9015.
- (276) Kamino, S.; Muranaka, A.; Murakami, M.; Tatsumi, A.; Nagaoka, N.; Shirasaki, Y.; Watanabe, K.; Yoshida, K.; Horigome, J.; Komeda, S.; et al. A Red-Emissive Aminobenzopyran-Xanthene Dye: Elucidation of Fluorescence Emission Mechanisms in Solution and in the Aggregate State. *Phys. Chem. Chem. Phys.* **2013**, *15*, 2131–2140.
- (277) Yao, Q.-C.; Lu, X.-L.; Xia, M. (Z)-3-(Quinolin-2-ylmethylene)-3,4-dihydroquinoxalin-2(1*H*)-one Derivatives: AIE-Active Compounds with Pronounced Effects of ESIPT and TICT. *New J. Chem.* **2014**, *38*, 2693–2700.
- (278) Hu, R.; Maldonado, J. L.; Rodriguez, M.; Deng, C.; Jim, C. K. W.; Lam, J. W. Y.; Yuen, M. M. F.; Ramos-Ortiz, G.; Tang, B. Z. Luminogenic Materials Constructed from Tetraphenylethylene Building Blocks: Synthesis, Aggregation-Induced Emission, Two-Photon Absorption, Light Refraction, and Explosive Detection. *J. Mater. Chem.* **2012**, *22*, 232–240.
- (279) Wu, W.; Ye, S.; Tang, R.; Huang, L.; Li, Q.; Yu, G.; Liu, Y.; Qin, J.; Li, Z. New Tetraphenylethylene-Containing Conjugated Polymers: Facile Synthesis, Aggregation-Induced Emission Enhanced Characteristics and Application as Explosive Chemsensors and PLEDs. *Polymer* **2012**, *53*, 3163–3171.
- (280) Shi, J.; Wu, Y.; Sun, S.; Tong, B.; Zhi, J.; Dong, Y. Tunable Fluorescence Conjugated Copolymers Consisting of Tetraphenylethylene and Fluorene Units: From Aggregation-Induced Emission Enhancement to Dual-Channel Fluorescence Response. *J. Polym. Sci., Part A: Polym. Chem.* **2013**, *51*, 229–240.
- (281) He, B.; Ye, S.; Guo, Y.; Chen, B.; Xu, X.; Qiu, H.; Zhao, Z. Aggregation-Enhanced Emission and Efficient Electroluminescence of Conjugated Polymers Containing Tetraphenylethene Units. *Sci. China: Chem.* **2013**, *S6*, 1221–1227.
- (282) Yao, B. C.; Mei, J.; Li, J.; Wang, J.; Wu, H. Q.; Sun, J. Z.; Qin, A. J.; Tang, B. Z. Catalyst-Free Thiol–Yne Click Polymerization: A Powerful and Facile Tool for Preparation of Functional Poly(vinylenesulfide)s. *Macromolecules* **2014**, *47*, 1325–1333.
- (283) Chan, C. Y. K.; Tseng, N.-W.; Lam, J. W. Y.; Liu, J.; Kwok, R. T. K.; Tang, B. Z. Construction of Functional Macromolecules with Well-Defined Structures by Indium-Catalyzed Three-Component Polycoupling of Alkynes, Aldehydes, and Amines. *Macromolecules* **2013**, *46*, 3246–3256.
- (284) Ma, C.; Ling, Q.; Xu, S.; Zhu, H.; Zhang, G.; Zhou, X.; Chi, Z.; Liu, S.; Zhang, Y.; Xu, J. Preparation of Biocompatible Aggregation-Induced Emission Homopolymeric Nanoparticles for Cell Imaging. *Macromol. Biosci.* **2014**, *14*, 235–243.
- (285) Chien, R.-H.; Lai, C.-T.; Hong, J.-L. Enhanced Aggregation Emission of Vinyl Polymer Containing Tetraphenylthiophene Pendant Group. *J. Phys. Chem. C* **2011**, *115*, 5958–5965.
- (286) Yuan, W. Z.; Zhao, H.; Shen, X. Y.; Mahtab, F.; Lam, J. W. Y.; Sun, J. Z.; Tang, B. Z. Luminogenic Polyacetylenes and Conjugated Polyelectrolytes: Synthesis, Hybridization with Carbon Nanotubes, Aggregation-Induced Emission, Superamplification in Emission Quenching by Explosives, and Fluorescent Assay for Protein Quantitation. *Macromolecules* **2009**, *42*, 9400–9411.
- (287) Wang, T.; Cai, Y.; Wang, Z.; Guan, E.; Yu, D.; Qin, A.; Sun, J.; Tang, B. Z.; Gao, C. Decomposition-Assembly of Tetraphenylethylene Nanoparticles with Uniform Size and Aggregation-Induced Emission property. *Macromol. Rapid Commun.* **2012**, *33*, 1584–1589.
- (288) Dong, W.; Fei, T.; Palma-Cando, A.; Scherf, U. Aggregation Induced Emission and Amplified Explosive Detection of Tetraphenylethylene-Substituted Polycarbazoles. *Polym. Chem.* **2014**, *5*, 4048–4053.
- (289) Wang, Z.; Chen, S.; Lam, J. W. Y.; Qin, W.; Kwok, R. T. K.; Xie, N.; Hu, Q.; Tang, B. Z. Long-Term Fluorescent Cellular Tracing by the Aggregates of AIE Bioconjugates. *J. Am. Chem. Soc.* **2013**, *135*, 8238–8245.
- (290) Li, M.; Hong, Y.; Wang, Z.; Chen, S.; Gao, M.; Kwok, R. T. K.; Qin, W.; Lam, J. W. Y.; Zheng, Q.; Tang, B. Z. Fabrication of Chitosan Nanoparticles with Aggregation-Induced Emission Characteristics and Their Applications in Long-Term Live Cell Imaging. *Macromol. Rapid Commun.* **2013**, *34*, 767–771.
- (291) Li, H.; Zhang, X.; Zhang, X.; Yang, B.; Yang, Y.; Wei, Y. Ultra-Stable Biocompatible Cross-Linked Fluorescent Polymeric Nanoparticles Using AIE Chain Transfer Agent. *Polym. Chem.* **2014**, *5*, 3758–3762.
- (292) Jia, W.; Yang, P.; Li, J.; Yin, Z.; Kong, L.; Lu, H.; Ge, Z.; Wu, Y.; Hao, X.; Yang, J. Synthesis and Characterization of a Novel Cyanostilbene Derivative and Its Initiated Polymers: Aggregation-Induced Emission Enhancement Behaviors and Light-Emitting Diode Applications. *Polym. Chem.* **2014**, *5*, 2282–2292.
- (293) Zhao, W.; Li, C.; Liu, B.; Wang, X.; Li, P.; Wang, Y.; Wu, C.; Yao, C.; Tang, T.; Liu, X.; et al. A New Strategy to Access Polymers with Aggregation-Induced Emission Characteristics. *Macromolecules* **2014**, *47*, 5586–5594.
- (294) Bosman, A. W.; Janssen, H. M.; Meijer, E. W. About Dendrimers: Structure, Physical Properties, and Applications. *Chem. Rev.* **1999**, *99*, 1665–1688.
- (295) Grayson, S. M.; Frechet, J. M. J. Convergent Dendrons and Dendrimers: From Synthesis to Applications. *Chem. Rev.* **2001**, *101*, 3819–3868.
- (296) Li, W. S.; Aida, T. Dendrimer Porphyrins and Phthalocyanines. *Chem. Rev.* **2009**, *109*, 6047–6076.
- (297) Astruc, D.; Boisselier, E.; Ornelas, C. Dendrimers Designed for Functions: From Physical, Photophysical, and Supramolecular Properties to Applications in Sensing, Catalysis, Molecular Electronics, Photonics, and Nanomedicine. *Chem. Rev.* **2010**, *110*, 1857–1959.
- (298) Huang, G.; Ma, B.; Chen, J.; Peng, Q.; Zhang, G.; Fan, Q.; Zhang, D. Dendron-Containing Tetraphenylethylene Compounds: Dependence of Fluorescence and Photocyclization Reactivity on the Dendron Generation. *Chem. - Eur. J.* **2012**, *18*, 3886–3892.
- (299) Arseneault, M.; Leung, N. L. C.; Fung, L. T.; Hu, R.; Morin, J.-F.; Tang, B. Z. Probing the Dendritic Architecture Through AIE: Challenges and Successes. *Polym. Chem.* **2014**, *5*, 6087–6096.
- (300) Zeng, Y.; Li, P.; Liu, X.; Yu, T.; Chen, J.; Yang, G.; Li, Y. A “Breathing” Dendritic Molecule—Conformational Fluctuation Induced by External Stimuli. *Polym. Chem.* **2014**, *5*, 5978–5984.
- (301) Leung, M.-k.; Lin, Y.-S.; Lee, C.-C.; Chang, C.-C.; Wang, Y.-X.; Kuo, C.-P.; Singh, N.; Lin, K.-R.; Hu, C.-W.; Tseng, C.-Y.; et al. Benzenetricarboxamide-Cored Triphenylamine Dendrimer: Nanoparticle Film Formation by an Electrochemical Method. *RSC Adv.* **2013**, *3*, 22219–22228.
- (302) Xu, B.; Zhang, J.; Fang, H.; Ma, S.; Chen, Q.; Sun, H.; Im, C.; Tian, W. Aggregation Induced Enhanced Emission of Conjugated Dendrimers with a Large Intrinsic Two-Photon Absorption Cross-Section. *Polym. Chem.* **2014**, *5*, 479–488.
- (303) Arseneault, M.; Levesque, I.; Morin, J. F. Efficient and Rapid Divergent Synthesis of Ethylene Oxide-Containing Dendrimers through Catalyst-Free Click Chemistry. *Macromolecules* **2012**, *45*, 3687–3694.
- (304) Voit, B.; Lederer, A. Hyperbranched and Highly Branched Polymer Architectures—Synthetic Strategies and Major Characterization Aspects. *Chem. Rev.* **2009**, *109*, 5924–5973.
- (305) Häufler, M.; Qin, A.; Tang, B. Z. Acetylenes with Multiple Triple Bonds: A Group of Versatile  $A_n$ -Type Building Blocks for the

- Construction of Functional Hyperbranched Polymers. *Polymer* **2007**, *48*, 6181–6204.
- (306) Liu, J.; Zhong, Y.; Lam, J. W. Y.; Lu, P.; Hong, Y.; Yu, Y.; Yue, Y.; Faisal, M.; Sung, H. H. Y.; Williams, I. D.; et al. Hyperbranched Conjugated Polysiloles: Synthesis, Structure, Aggregation-Enhanced Emission, Multicolor Fluorescent Photopatterning, and Superamplified Detection of Explosives. *Macromolecules* **2010**, *43*, 4921–4936.
- (307) Liu, J.; Zhong, Y.; Hong, Y.; Lam, J. W. Y.; Faisal, M.; Yu, Y.; Wong, K. S.; Tang, B. Z. A Superamplification Effect in the Detection of Explosives by a Fluorescent Hyperbranched Poly(silylenephylene) with Aggregation-Enhanced Emission Characteristics. *Polym. Chem.* **2010**, *1*, 426–429.
- (308) Lu, P.; Lam, J. W. Y.; Liu, J.; Jim, C. K. W.; Yuan, W.; Xie, N.; Zhong, Y.; Hu, Q.; Wong, K. S.; Cheuk, K. K. L.; et al. Aggregation-Induced Emission in a Hyperbranched Poly(silylenevinylene) and Superamplification in Its Emission Quenching by Explosives. *Macromol. Rapid Commun.* **2010**, *31*, 834–839.
- (309) Wang, J.; Mei, J.; Yuan, W.; Lu, P.; Qin, A.; Sun, J.; Ma, Y.; Tang, B. Z. Hyperbranched Polytriazoles with High Molecular Compressibility: Aggregation-Induced Emission and Superamplified Explosive Detection. *J. Mater. Chem.* **2011**, *21*, 4056–4059.
- (310) Hu, R.; Lam, J. W. Y.; Liu, J.; Sung, H. H. Y.; Williams, I. D.; Yue, Z.; Wong, K. S.; Yuen, M. M. F.; Tang, B. Z. Hyperbranched Conjugated Poly(tetraphenylethene): Synthesis, Aggregation-Induced Emission, Fluorescent Photopatterning, Optical Limiting and Explosive Detection. *Polym. Chem.* **2012**, *3*, 1481–1489.
- (311) Xu, Y.; Chen, L.; Guo, Z.; Nagai, A.; Jiang, D. Light-Emitting Conjugated Polymers with Microporous Network Architecture: Interweaving Scaffold Promotes Electronic Conjugation, Facilitates Exciton Migration, and Improves Luminescence. *J. Am. Chem. Soc.* **2011**, *133*, 17622–17625.
- (312) Chen, Q.; Wang, J.-X.; Yang, F.; Zhou, D.; Bian, N.; Zhang, X.-J.; Yan, C.-G.; Han, B.-H. Tetraphenylethylene-Based Fluorescent Porous Organic Polymers: Preparation, Gas Sorption Properties and Photoluminescence Properties. *J. Mater. Chem.* **2011**, *21*, 13554–13560.
- (313) Aggregation-Induced Emission: Fundamentals; Qin, A., Tang, B. Z., Eds.; Wiley: Singapore, 2014.
- (314) Hu, X.-M.; Chen, Q.; Zhou, D.; Cao, J.; He, Y.-J.; Han, B.-H. One-Step Preparation of Fluorescent Inorganic–Organic Hybrid Material Used for Explosive Sensing. *Polym. Chem.* **2011**, *2*, 1124–1128.
- (315) Cui, Y.; Yue, Y.; Qian, G.; Chen, B. Luminescent Functional Metal–Organic Frameworks. *Chem. Rev.* **2012**, *112*, 1126–1162.
- (316) Sumida, K.; Rogow, D. L.; Mason, J. A.; McDonald, T. M.; Bloch, E. D.; Herm, Z. R.; Bae, T.-H.; Long, J. R. Carbon Dioxide Capture in Metal–Organic Frameworks. *Chem. Rev.* **2012**, *112*, 724–781.
- (317) Shustova, N. B.; McCarthy, B. D.; Dinca, M. Turn-On Fluorescence in Tetraphenylethylene-Based Metal–Organic Frameworks: An Alternative to Aggregation-Induced Emission. *J. Am. Chem. Soc.* **2011**, *133*, 20126–20129.
- (318) Sun, H.-L.; Jiang, R.; Li, Z.; Dong, Y. Q.; Du, M. Novel (4,8)-Connected *scu* Coordination Framework Constructed by Tetrakis(4-benzoic acid)ethylene. *CrystEngComm* **2013**, *15*, 1669–1672.
- (319) Wei, Z.; Gu, Z.-Y.; Arvapally, R. K.; Chen, Y.-P.; McDougald, R. N.; Ivy, J. F.; Yakovenko, A. A.; Feng, D.; Omary, M. A.; Zhou, H.-C. Rigidifying Fluorescent Linkers by Metal–Organic Framework Formation for Fluorescence Blue Shift and Quantum Yield Enhancement. *J. Am. Chem. Soc.* **2014**, *136*, 8269–8276.
- (320) Zhang, M.; Feng, G.; Song, Z.; Zhou, Y.-P.; Chao, H.-Y.; Yuan, D.; Tan, T. T. Y.; Guo, Z.; Hu, Z.; Tang, B. Z.; et al. Two-Dimensional Metal–Organic Framework with Wide Channels and Responsive Turn-On Fluorescence for the Chemical Sensing of Volatile Organic Compounds. *J. Am. Chem. Soc.* **2014**, *136*, 7241–7244.
- (321) Zhang, H.-L.; Zhao, B.; Yuan, W.-G.; Tang, W.; Xiong, F.; Jing, L.-H.; Qin, D.-B. Syntheses and Characterizations of Two-Dimensional Polymers Based on Tetraimidazole Tetraphenylethylene Ligand with Aggregation-Induced Emission Property. *Inorg. Chem. Commun.* **2013**, *35*, 208–212.
- (322) Kapadia, P. P.; Widen, J. C.; Magnus, M. A.; Swenson, D. C.; Pigge, F. C. Tetrapyridyl Tetraphenylethylenes: Supramolecular Building Blocks with Aggregation-Induced Emission Properties. *Tetrahedron Lett.* **2011**, *S2*, 2519–2522.
- (323) Yu, Y.; Luo, Z.; Chevrier, D. M.; Leong, D. T.; Zhang, P.; Jiang, D.-e.; Xie, J. Identification of a Highly Luminescent  $\text{Au}_{22}(\text{SG})_{18}$  Nanocluster. *J. Am. Chem. Soc.* **2014**, *136*, 1246–1249.
- (324) Luo, Z.; Yuan, X.; Yu, Y.; Zhang, Q.; Leong, D. T.; Lee, J. Y.; Xie, J. From Aggregation-Induced Emission of  $\text{Au}(1)$ –Thiolate Complexes to Ultrabright  $\text{Au}(0)@\text{Au}(1)$ –Thiolate Core–Shell Nanoclusters. *J. Am. Chem. Soc.* **2012**, *134*, 16662–16670.
- (325) Pirie, N. W.; Pinhey, K. G. The Titration Curve of Glutathione. *J. Biol. Chem.* **1929**, *84*, 321–333.
- (326) Liang, J.; Chen, Z.; Yin, J.; Yu, G.-A.; Liu, S. H. Aggregation-Induced Emission (AIE) Behavior and Thermochromic Luminescence Properties of a New Gold(I) Complex. *Chem. Commun.* **2013**, *49*, 3567–3569.
- (327) Fujisawa, K.; Okuda, Y.; Izumi, Y.; Nagamatsu, A.; Rokusha, Y.; Sadaike, Y.; Tsutsumi, O. Reversible Thermal-Mode Control of Luminescence from Liquid-Crystalline Gold(I) Complexes. *J. Mater. Chem. C* **2014**, *2*, 3549–3555.
- (328) Liang, J.; Chen, Z.; Xu, L.; Wang, J.; Yin, J.; Yu, G.-A.; Chen, Z.-N.; Liu, S. H. Aggregation-Induced Emission-Active Gold(I) Complexes with Multi-Stimuli Luminescence Switching. *J. Mater. Chem. C* **2014**, *2*, 2243–2250.
- (329) Ito, H.; Saito, T.; Oshima, N.; Kitamura, N.; Ishizaka, S.; Hinatsu, Y.; Wakeshima, M.; Kato, M.; Tsuge, K.; Sawamura, M. Reversible Mechanochromic Luminescence of  $[(\text{C}_6\text{F}_5\text{Au})_2(\mu\text{-1,4-Diisocyanobenzene})]$ . *J. Am. Chem. Soc.* **2008**, *130*, 10044–10045.
- (330) Jobbág, C.; Molnár, M.; Baranyai, P.; Hamza, A.; Pálkás, G.; Deák, A. A Stimuli-Responsive Double-Stranded Digold(I) Helicate. *CrystEngComm* **2014**, *16*, 3192–3202.
- (331) Jia, X.; Li, J.; Wang, E. Supramolecular Self-Assembly of Morphology-Dependent Luminescent Ag Nanoclusters. *Chem. Commun.* **2014**, *50*, 9565–9568.
- (332) Jia, X.; Yang, X.; Li, J.; Li, D.; Wang, E. Stable Cu Nanoclusters: From an Aggregation-Induced Emission Mechanism to Biosensing and Catalytic Applications. *Chem. Commun.* **2014**, *50*, 237–239.
- (333) Xin, X.-L.; Chen, M.; Ai, Y.-b.; Yang, F.-l.; Li, X.-L.; Li, F. Aggregation-Induced Emissive Copper(I) Complexes for Living Cell Imaging. *Inorg. Chem.* **2014**, *53*, 2922–2931.
- (334) Xie, Y.-Z.; Shan, G.-G.; Li, P.; Zhou, Z.-Y.; Su, Z.-M. A Novel Class of Zn(II) Schiff Base Complexes with Aggregation-Induced Emission Enhancement (AIEE) Properties: Synthesis, Characterization and Photophysical/Electrochemical Properties. *Dyes Pigm.* **2013**, *96*, 467–474.
- (335) Kuwabara, J.; Ogawa, Y.; Taketoshi, A.; Kanbara, T. Enhancement of the Photoluminescence of a Thioamide-Based Pincer Palladium Complex in the Crystalline State. *J. Organomet. Chem.* **2011**, *696*, 1289–1293.
- (336) Honda, H.; Ogawa, Y.; Kuwabara, J.; Kanbara, T. Emission Behavior of Secondary Thioamide-Based Cationic Pincer Platinum(II) Complexes in the Aggregate State. *Eur. J. Inorg. Chem.* **2014**, *2014*, 1865–1869.
- (337) Li, Y.; Tsang, D. P.-K.; Chan, C. K.-M.; Wong, K. M.-C.; Chan, M.-Y.; Yam, V. W.-W. Synthesis of Unsymmetric Bipyridine–Pt<sup>II</sup>–Alkynyl Complexes through Post-Click Reaction with Emission Enhancement Characteristics and Their Applications as Phosphorescent Organic Light-Emitting Diodes. *Chem. - Eur. J.* **2014**, *20*, 13710–13715.
- (338) Chen, Z.; Wong, K. M.; Kwok, E. C.; Zhu, N.; Zu, Y.; Yam, V. W. Electrogenerated Chemiluminescence of Platinum(II) Alkynyl Terpyridine Complex with Peroxydisulfate as Coreactant. *Inorg. Chem.* **2011**, *50*, 2125–2132.
- (339) Komiya, N.; Muraoka, T.; Iida, M.; Miyanaga, M.; Takahashi, K.; Naota, T. Ultrasound-Induced Emission Enhancement Based on Structure-Dependent Homo- and Heterochiral Aggregations of Chiral Binuclear Platinum Complexes. *J. Am. Chem. Soc.* **2011**, *133*, 16054–16061.
- (340) Kalyanasundaram, K.; Grätzel, M. Applications of Functionalized Transition Metal Complexes in Photonic and Optoelectronic Devices. *Coord. Chem. Rev.* **1998**, *177*, 347–414.

- (341) Chen, Y.; Xu, W. C.; Kou, J. F.; Yu, B. L.; Wei, X. H.; Chao, H.; Ji, L. N. Aggregation-Induced Emission of Ruthenium(II) Polypyridyl Complex  $[\text{Ru}(\text{bpy})_2(\text{pzta})]^{2+}$ . *Inorg. Chem. Commun.* **2010**, *13*, 1140–1143.
- (342) Procopio, E. Q.; Mauro, M.; Panigati, M.; Donghi, D.; Mercandelli, P.; Sironi, A.; D’Alfonso, G.; Cola, L. D. Highly Emitting Concomitant Polymorphic Crystals of a Dinuclear Rhenium Complex. *J. Am. Chem. Soc.* **2010**, *132*, 14397–14399.
- (343) Sathish, V.; Ramdass, A.; Lu, Z.-Z.; Velayudham, M.; Thanasekaran, P.; Lu, K.-L.; Rajagopal, S. Aggregation-Induced Emission Enhancement in Alkoxy-Bridged Binuclear Rhenium(I) Complexes: Application as Sensor for Explosives and Interaction with Microheterogeneous Media. *J. Phys. Chem. B* **2013**, *117*, 14358–14366.
- (344) Alam, P.; Das, P.; Climent, C.; Karanam, M.; Casanova, D.; Choudhury, A. R.; Alemany, P.; Jana, N. R.; Laskar, I. R. Facile Tuning of the Aggregation-Induced Emission Wavelength in a Common Framework of a Cyclometalated Iridium(III) Complex: Micellar Encapsulated Probe in Cellular Imaging. *J. Mater. Chem. C* **2014**, *2*, 5615–5628.
- (345) Huang, K.; Wu, H.; Shi, M.; Li, F.; Yi, T.; Huang, C. Reply to Comment on ‘Aggregation-Induced Phosphorescent Emission (AIPE) of Iridium(III) Complexes’: Origin of the Enhanced Phosphorescence. *Chem. Commun.* **2009**, 1243–1245.
- (346) Zhao, Q.; Li, L.; Li, F.; Yu, M.; Liu, Z.; Yi, T.; Huang, C. Aggregation-Induced Phosphorescent Emission (AIPE) of Iridium(III) Complexes. *Chem. Commun.* **2008**, 685–687.
- (347) Shin, C. H.; Huh, J. O.; Baek, S. J.; Kim, S. K.; Lee, M. H.; Do, Y. Dinuclear Iridium(III) Complexes Linked by a Bis( $\beta$ -diketonato) Bridging Ligand: Energy Convergence versus Aggregation-Induced Emission. *Eur. J. Inorg. Chem.* **2010**, *2010*, 3642–3651.
- (348) Shin, C. H.; Huh, J. O.; Lee, M. H.; Do, Y. Polymorphism-Induced Dual Phosphorescent Emission from Solid-State Iridium(III) Complex. *Dalton Trans.* **2009**, 6476–6479.
- (349) Howarth, A. J.; Patia, R.; Davies, D. L.; Lelj, F.; Wolf, M. O.; Singh, K. Elucidating the Origin of Enhanced Phosphorescence Emission in the Solid State (EPESS) in Cyclometallated Iridium Complexes. *Eur. J. Inorg. Chem.* **2014**, *2014*, 3657–3664.
- (350) Wu, Y.; Sun, H.-Z.; Cao, H.-T.; Li, H.-B.; Shan, G.-G.; Duan, Y.-A.; Geng, Y.; Su, Z.-M.; Liao, Y. Stepwise Modulation of the Electron-Donating Strength of Ancillary Ligands: Understanding the AIE Mechanism of Cationic Iridium(III) Complexes. *Chem. Commun.* **2014**, *50*, 10986–10989.
- (351) Hou, X.-G.; Wu, Y.; Cao, H.-T.; Sun, H.-Z.; Li, H.-B.; Shan, G.-G.; Su, Z.-M. A Cationic Iridium(III) Complex with Aggregation-Induced Emission (AIE) Properties for Highly Selective Detection of Explosives. *Chem. Commun.* **2014**, *50*, 6031–6034.
- (352) Zhu, C.; Li, S.; Luo, M.; Zhou, X.; Niu, Y.; Lin, M.; Zhu, J.; Cao, Z.; Lu, X.; Wen, T.; et al. Stabilization of Anti-aromatic and Strained Five-membered Rings with a Transition Metal. *Nat. Chem.* **2013**, *5*, 698–703.
- (353) Dou, X.; Yuan, X.; Yu, Y.; Luo, Z.; Yao, Q.; Leong, D. T.; Xie, J. Lighting Up Thiolated Au@Ag Nanoclusters via Aggregation-Induced Emission. *Nanoscale* **2014**, *6*, 157–161.
- (354) Koshevoy, I. O.; Chang, Y.-C.; Karttunen, A. J.; Shakirova, J. R.; Jänis, J.; Haukka, M.; Pakkanen, T.; Chou, P.-T. Solid-State Luminescence of Au–Cu–Alkynyl Complexes Induced by Metal-lphilicity-Driven Aggregation. *Chem. - Eur. J.* **2013**, *19*, 5104–5112.
- (355) Li, G.; Wu, Y.; Shan, G.; Che, W.; Zhu, D.; Song, B.; Yan, L.; Su, Z.; Bryce, M. R. New Ionic Dinuclear Ir(III) Schiff Base Complexes with Aggregation-Induced Phosphorescent Emission (AIPE). *Chem. Commun.* **2014**, *50*, 6977–6980.
- (356) Wang, H.; Zhao, E.; Lam, J. W. Y.; Tang, B. Z. AIE Luminogens: Emission Brightened by Aggregation. *Mater. Today* **2015**, *18*, 365–377.
- (357) Zhu, Q.; Huang, L.; Chen, Z.; Zheng, S.; Lv, L.; Zhu, Z.; Cao, D.; Jiang, H.; Liu, S. A New Series of C-6 Unsubstituted Tetrahydropyrimidines: Convenient One-Pot Chemoselective Synthesis, Aggregation-Induced and Size-Independent Emission Characteristics. *Chem. - Eur. J.* **2013**, *19*, 1268–1280.
- (358) Gong, Y. Y.; Tan, Y. Q.; Li, H.; Zhang, Y. R.; Yuan, W. Z.; Zhang, Y. M.; Sun, J. Z.; Tang, B. Z. Crystallization-Induced Phosphorescence of Benzils at Room Temperature. *Sci. China: Chem.* **2013**, *56*, 1183–1186.
- (359) Cariati, E.; Lanzeni, V.; Tordin, E.; Ugo, R.; Botta, C.; Giacometti Schieroni, A.; Sironi, A.; Pasini, D. Efficient Crystallization Induced Emissive Materials Based on a Simple Push-Pull Molecular Structure. *Phys. Chem. Chem. Phys.* **2011**, *13*, 18005–18014.
- (360) Guieu, S.; Rocha, J.; Silva, A. M. S. Crystallization-Induced Light-Emission Enhancement of Diphenylmethane Derivatives. *Tetrahedron* **2013**, *69*, 9329–9334.
- (361) Qian, L. J.; Tong, B.; Shen, J. B.; Shi, J. B.; Zhi, J. G.; Dong, Y. Q.; Yang, F.; Dong, Y. P.; Lam, J. W. Y.; Liu, Y.; et al. Crystallization-Induced Emission Enhancement in a Phosphorus-Containing Heterocyclic Luminogen. *J. Phys. Chem. B* **2009**, *113*, 9098–9103.
- (362) Kato, T.; Naka, K. Arylaminomaleimides as a New Class of Aggregation-induced Emission-active Molecules Obtained from Organoarsenic Compounds. *Chem. Lett.* **2012**, *41*, 1445–1447.
- (363) Boominathan, M.; Sathish, V.; Nagaraj, M.; Bhuvanesh, N.; Muthusubramanian, S.; Rajagopal, S. Aggregation Induced Emission Characteristics of Maleimide Derivatives. *RSC Adv.* **2013**, *3*, 22246–22252.
- (364) Zhou, T.; Li, F.; Fan, Y.; Song, W.; Mu, X.; Zhang, H.; Wang, Y. Hydrogen-Bonded Dimer Stacking Induced Emission of Aminobenzoic Acid Compounds. *Chem. Commun.* **2009**, 3199–3201.
- (365) Zhang, P.; Wang, H. T.; Liu, H. M.; Li, M. Fluorescence-Enhanced Organogels and Mesomorphic Superstructure Based on Hydrazine Derivatives. *Langmuir* **2010**, *26*, 10183–10190.
- (366) Fermi, A.; Bergamini, G.; Peresutti, R.; Marchi, E.; Roy, M.; Ceroni, P.; Gingras, M. Molecular Asterisks with a Persulfurated Benzene Core are Among the Strongest Organic Phosphorescent Emitters in the Solid State. *Dyes Pigm.* **2014**, *110*, 113–122.
- (367) Yuan, W. Z.; Shen, X. Y.; Zhao, H.; Lam, J. W. Y.; Tang, L.; Lu, P.; Wang, C.; Liu, Y.; Wang, Z.; Zheng, Q.; et al. Crystallization-Induced Phosphorescence of Pure Organic Luminogens at Room Temperature. *J. Phys. Chem. C* **2010**, *114*, 6090–6099.
- (368) Bolton, O.; Lee, K.; Kim, H.-J.; Lin, K. Y.; Kim, J. Activating Efficient Phosphorescence from Purely Organic Materials by Crystal Design. *Nat. Chem.* **2011**, *3*, 207–212.
- (369) Lee, D.; Bolton, O.; Kim, B. C.; Youk, J. H.; Takayama, S.; Kim, J. Room Temperature Phosphorescence of Metal-Free Organic Materials in Amorphous Polymer Matrices. *J. Am. Chem. Soc.* **2013**, *135*, 6325–6329.
- (370) Kwon, M. S.; Lee, D.; Seo, S.; Jung, J.; Kim, J. Tailoring Intermolecular Interactions for Efficient Room-Temperature Phosphorescence from Purely Organic Materials in Amorphous Polymer Matrices. *Angew. Chem., Int. Ed.* **2014**, *53*, 11177–11181.
- (371) Hirata, S.; Totani, K.; Zhang, J.; Yamashita, T.; Kaji, H.; Marder, S. R.; Watanabe, T.; Adachi, C. Efficient Persistent Room Temperature Phosphorescence in Organic Amorphous Materials under Ambient Conditions. *Adv. Funct. Mater.* **2013**, *23*, 3386–3397.
- (372) Gong, Y.; Tan, Y.; Mei, J.; Zhang, Y.; Yuan, W.; Zhang, Y.; Sun, J.; Tang, B. Z. Room Temperature Phosphorescence from Natural Products: Crystallization Matters. *Sci. China: Chem.* **2013**, *56*, 1178–1182.
- (373) Ruff, Y.; Buhler, E.; Candau, S. J.; Kesselman, E.; Talmon, Y.; Lehn, J. M. Glycodynamers: Dynamic Polymers Bearing Oligosaccharides Residues—Generation, Structure, Physicochemical, Component Exchange, and Lectin Binding Properties. *J. Am. Chem. Soc.* **2010**, *132*, 2573–2584.
- (374) (a) Zhao, E.; Lam, J. W. Y.; Meng, L.; Hong, Y.; Deng, H.; Bai, G.; Huang, X.; Hao, J.; Tang, B. Z. Poly[(maleic anhydride)-alt-(vinyl acetate)]: A Pure Oxygenic Nonconjugated Macromolecule with Strong Light Emission and Solvatochromic Effect. *Macromolecules* **2015**, *48*, 64–71. (b) Lu, H.; Feng, L.; Li, S.; Zhang, J.; Lu, H.; Feng, S. Unexpected Strong Blue Photoluminescence Produced from the Aggregation of Unconventional Chromophores in Novel Siloxane–Poly(amidoamine) Dendrimers. *Macromolecules* **2015**, *48*, 476–482. (c) Wang, R.-b.; Yuan, W.-z.; Zhu, X.-y. Aggregation-induced Emission of Non-conjugated Poly(amido amine)s: Discovering, Luminescent

- Mechanism Understanding and Bioapplication. *Chin. J. Polym. Sci.* **2015**, *33*, 680–687.
- (375) VanEngelenburg, S. B.; Palmer, A. E. Fluorescent Biosensors of Protein Function. *Curr. Opin. Chem. Biol.* **2008**, *12*, 60–65.
- (376) Domaille, D. W.; Que, E. L.; Chang, C. J. Synthetic Fluorescent Sensors for Studying the Cell Biology of Metals. *Nat. Chem. Biol.* **2008**, *4*, 168–175.
- (377) Giepmans, B. N. G.; Adams, S. R.; Ellisman, M. H.; Tsien, R. Y. The Fluorescent Toolbox for Assessing Protein Location and Function. *Science* **2006**, *312*, 217–224.
- (378) Michalet, X.; Pinaud, F. F.; Bentolila, L. A.; Tsay, J. M.; Doose, S.; Li, J. J.; Sundaresan, G.; Wu, A. M.; Gambhir, S. S.; Weiss, S. Quantum Dots for Live Cells, *in vivo* Imaging, and Diagnostics. *Science* **2005**, *307*, 538–544.
- (379) (a) Burns, A.; Ow, H.; Wiesner, U. Fluorescent Core–Shell Silica Nanoparticles: Towards “Lab on a Particle” Architectures for Nanobiotechnology. *Chem. Soc. Rev.* **2006**, *35*, 1028–1042. (b) Rosi, N. L.; Mirkin, C. A. Nanostructures in Biodiagnostics. *Chem. Rev.* **2005**, *105*, 1547–1562.
- (380) Medintz, I. L.; Uyeda, H. T.; Goldman, E. R.; Mattoussi, H. Quantum Dot Bioconjugates for Imaging, Labelling and Sensing. *Nat. Mater.* **2005**, *4*, 435–446.
- (381) Klostranec, J. M.; Chan, W. C. W. Quantum Dots in Biological and Biomedical Research: Recent Progress and Present Challenges. *Adv. Mater.* **2006**, *18*, 1953–1964.
- (382) Krebs, F. C.; Miller, S. R.; Catalone, B. J.; Fichorova, R.; Anderson, D.; Malamud, D.; Howett, M. K.; Wigdahl, B. Comparative in vitro Sensitivities of Human Immune Cell Lines, Vaginal and Cervical Epithelial Cell Lines, and Primary Cells to Candidate Microbicides Nonoxynol 9, C31G, and Sodium Dodecyl Sulfate. *Antimicrob. Agents Chemother.* **2002**, *46*, 2292–2298.
- (383) Li, H.; Zhou, Q.; Liu, W.; Yan, B.; Zhao, Y.; Jiang, G. Progress in the Toxicological Researches for Quantum Dots. *Sci. China, Ser. B: Chem.* **2008**, *51*, 393–400.
- (384) Chen, I.; Ting, A. Y. Site-Specific Labeling of Proteins with Small Molecules in Live Cells. *Curr. Opin. Biotechnol.* **2005**, *16*, 35–40.
- (385) Jovanovic, L. The Importance of Postprandial Glucose Concentration: Lessons Learned from Diabetes and Pregnancy. *Drug Dev. Res.* **2006**, *67*, 591–594.
- (386) Saltiel, A. R.; Kahn, C. R. Insulin Signalling and the Regulation of Glucose and Lipid Metabolism. *Nature* **2001**, *414*, 799–806.
- (387) Hu, F.; Huang, Y.; Zhang, G.; Zhao, R.; Zhang, D. A Highly Selective Fluorescence Turn-On Detection of Hydrogen Peroxide and  $\alpha$ -Glucose Based on the Aggregation/Deaggregation of a Modified Tetraphenylethylene. *Tetrahedron Lett.* **2014**, *55*, 1471–1474.
- (388) Shen, X.; Shi, Y.; Peng, B.; Li, K.; Xiang, J.; Zhang, G.; Liu, Z.; Chen, Y.; Zhang, D. Fluorescent Polymeric Micelles with Tetraphenylethylene Moieties and Their Application for the Selective Detection of Glucose. *Macromol. Biosci.* **2012**, *12*, 1583–1590.
- (389) Wang, X.; Hu, J.; Zhang, G.; Liu, S. Highly Selective Fluorogenic Multianalyte Biosensors Constructed via Enzyme-Catalyzed Coupling and Aggregation-Induced Emission. *J. Am. Chem. Soc.* **2014**, *136*, 9890–9893.
- (390) Zhang, L.; Zhang, Z.-Y.; Liang, R.-P.; Li, Y.-H.; Qiu, J.-D. Boron-Doped Graphene Quantum Dots for Selective Glucose Sensing Based on the “Abnormal” Aggregation-Induced Photoluminescence Enhancement. *Anal. Chem.* **2014**, *86*, 4423–4430.
- (391) Anslyn, E. V. Supramolecular and Chemical Cascade Approaches to Molecular Sensing. *J. Am. Chem. Soc.* **2010**, *132*, 15833–15835.
- (392) James, T. D.; Samankumara Sandanayake, K. R. A.; Shinkai, S. Saccharide Sensing with Molecular Receptors Based on Boronic Acid. *Angew. Chem., Int. Ed. Engl.* **1996**, *35*, 1910–1922.
- (393) Yan, J.; Fang, H.; Wang, B. Boronolectins and Fluorescent Boronolectins: An Examination of the Detailed Chemistry Issues Important for the Design. *Med. Res. Rev.* **2005**, *25*, 490–520.
- (394) Edwards, N. Y.; Sager, T. W.; McDevitt, J. T.; Anslyn, E. V. Boronic Acid Based Peptidic Receptors for Pattern-Based Saccharide Sensing in Neutral Aqueous Media, an Application in Real-Life Samples. *J. Am. Chem. Soc.* **2007**, *129*, 13575–13583.
- (395) Chen, X.; Zhou, Y.; Peng, X.; Yoon, J. Fluorescent and Colorimetric Probes for Detection of Thiols. *Chem. Soc. Rev.* **2010**, *39*, 2120–2135.
- (396) Riederer, B. M. Oxidation Proteomics: The Role of Thiol Modifications. *Curr. Proteomics* **2009**, *6*, 51–62.
- (397) Townsend, D. M.; Tew, K. D.; Tapiero, H. The Importance of Glutathione in Human Disease. *Biomed. Pharmacother.* **2003**, *57*, 145–155.
- (398) Zhou, Y.; Yoon, J. Recent Progress in Fluorescent and Colorimetric Chemosensors for Detection of Amino Acids. *Chem. Soc. Rev.* **2012**, *41*, 52–67.
- (399) Zhang, M.; Yu, M. X.; Li, F. Y.; Zhu, M. W.; Li, M. Y.; Gao, Y. H.; Li, L.; Liu, Z. Q.; Zhang, J. P.; Zhang, D. Q.; et al. A Highly Selective Fluorescence Turn-on Sensor for Cysteine/Homocysteine and Its Application in Bioimaging. *J. Am. Chem. Soc.* **2007**, *129*, 10322–10323.
- (400) Refsum, H.; Ueland, P. M.; Nygård, O.; Vollset, S. E. Homocysteine and Cardiovascular Disease. *Annu. Rev. Med.* **1998**, *49*, 31–62.
- (401) Jager, A.; Kostense, P. J.; Nijpels, G.; Dekker, J. M.; Heine, R. J.; Bouter, L. M.; Donker, A. J.; Stehouwer, C. D. Serum Homocysteine Levels Are Associated With the Development of (Micro)albuminuria. *The Hoorn Study. Arterioscler., Thromb., Vasc. Biol.* **2001**, *21*, 74–81.
- (402) Chen, W.; Zhao, Y.; Seefeldt, T.; Guan, X. M. Determination of Thiols and Disulfides via HPLC Quantification of 5-Thio-2-nitrobenzoic Acid. *J. Pharm. Biomed. Anal.* **2008**, *48*, 1375–1380.
- (403) Windelberg, A.; Arseth, O.; Kvalheim, G.; Ueland, P. M. Automated Assay for the Determination of Methylmalonic Acid, Total Homocysteine, and Related Amino Acids in Human Serum or Plasma by Means of Methylchloroformate Derivatization and Gas Chromatography–Mass Spectrometry. *Clin. Chem.* **2005**, *51*, 2103–2109.
- (404) Wang, W.; Li, L.; Liu, S.; Ma, C.; Zhang, S. Determination of Physiological Thiols by Electrochemical Detection with Piazselenole and Its Application in Rat Breast Cancer Cells 4T-1. *J. Am. Chem. Soc.* **2008**, *130*, 10846–10847.
- (405) Sudeep, P. K.; Joseph, S. T. S.; Thomas, K. G. Selective Detection of Cysteine and Glutathione Using Gold Nanorods. *J. Am. Chem. Soc.* **2005**, *127*, 6516–6517.
- (406) Gill, R.; Zayats, M.; Willner, I. Semiconductor Quantum Dots for Bioanalysis. *Angew. Chem., Int. Ed.* **2008**, *47*, 7602–7625.
- (407) Peng, L.; Zhou, Z.; Wei, R.; Li, K.; Song, P.; Tong, A. A Fluorescent Probe for Thiols Based on Aggregation-Induced Emission and Its Application in Live-Cell Imaging. *Dyes Pigm.* **2014**, *108*, 24–31.
- (408) Zhang, R.; Yuan, Y.; Liang, J.; Kwok, R. T. K.; Zhu, Q.; Feng, G.; Geng, J.; Tang, B. Z.; Liu, B. Fluorogen–Peptide Conjugates with Tunable Aggregation-Induced Emission Characteristics for Bioprobe Design. *ACS Appl. Mater. Interfaces* **2014**, *6*, 14302–14310.
- (409) Yuan, Y.; Kwok, R. T. K.; Feng, G.; Liang, J.; Geng, J.; Tang, B. Z.; Liu, B. Rational Design of Fluorescent Light-Up Probes Based on an AIE Luminogen for Targeted Intracellular Thiol Imaging. *Chem. Commun.* **2014**, *50*, 295–297.
- (410) Yu, Y.; Li, J.; Chen, S. J.; Hong, Y. N.; Ng, K. M.; Luo, K. Q.; Tang, B. Z. Thiol-Reactive Molecule with Dual-Emission-Enhancement Property for Specific Prestaining of Cysteine Containing Proteins in SDS-PAGE. *ACS Appl. Mater. Interfaces* **2013**, *5*, 4613–4616.
- (411) Liu, Y.; Yu, Y.; Lam, J. W. Y.; Hong, Y. N.; Faisal, M.; Yuan, W. Z.; Tang, B. Z. Simple Biosensor with High Selectivity and Sensitivity: Thiol-Specific Biomolecular Probing and Intracellular Imaging by AIE Fluorogen on a TLC Plate through a Thiol–Ene Click Mechanism. *Chem. - Eur. J.* **2010**, *16*, 8433–8438.
- (412) Cheng, W.; Wang, G.; Pan, X.; Zhang, Y.; Tang, B. Z.; Liu, Y. Redox-Responsive Nanoparticles with Aggregation-Induced Emission (AIE) Characteristic for Fluorescence Imaging. *Macromol. Biosci.* **2014**, *14*, 1059–1066.
- (413) Li, X.; Zhang, X.; Chi, Z.; Chao, X.; Zhou, X.; Zhang, Y.; Liu, S.; Xu, J. Simple Fluorescent Probe Derived from Tetraphenylethylene and Benzoquinone for Instantaneous Biothiol Detection. *Anal. Methods* **2012**, *4*, 3338–3343.

- (414) Lou, X. D.; Hong, Y. N.; Chen, S. J.; Leung, C. W. T.; Zhao, N.; Situ, B.; Lam, J. W. Y.; Tang, B. Z. A Selective Glutathione Probe Based on AIE Fluorogen and Its Application in Enzymatic Activity Assay. *Sci. Rep.* **2014**, *4*, 4272.
- (415) Chen, S.; Hong, Y.; Liu, J.; Tseng, N.-W.; Liu, Y.; Zhao, E.; Yip, Lam, J. W.; Tang, B. Z. Discrimination of Homocysteine, Cysteine and Glutathione Using an Aggregation-Induced-Emission-Active Hemicyanine Dye. *J. Mater. Chem. B* **2014**, *2*, 3919–3923.
- (416) Mei, J.; Wang, Y.; Tong, J.; Wang, J.; Qin, A.; Sun, J. Z.; Tang, B. Z. Discriminatory Detection of Cysteine and Homocysteine Based on Dialdehyde-Functionalized Aggregation-Induced Emission Fluorophores. *Chem. - Eur. J.* **2013**, *19*, 613–620.
- (417) Mei, J.; Tong, J.; Wang, J.; Qin, A.; Sun, J. Z.; Tang, B. Z. Discriminative Fluorescence Detection of Cysteine, Homocysteine and Glutathione via Reaction-Dependent Aggregation of Fluorophore-Analyte Adducts. *J. Mater. Chem.* **2012**, *22*, 17063–17070.
- (418) Tong, J.; Wang, Y.; Mei, J.; Wang, J.; Qin, A.; Sun, J. Z.; Tang, B. Z. A 1,3-Indandione-Functionalized Tetraphenylethene: Aggregation-Induced Emission, Solvatochromism, Mechanochromism, and Potential Application as a Multiresponsive Fluorescent Probe. *Chem. - Eur. J.* **2014**, *20*, 4661–4670.
- (419) Shen, X.; Zhang, G.; Zhang, D. A New Fluorometric Turn-On Detection of L-Lactic Acid Based on the Cascade Enzymatic and Chemical Reactions and the Abnormal Fluorescent Behavior of Silole. *Org. Lett.* **2012**, *14*, 1744–1747.
- (420) Zhao, M. C.; Wang, M.; Liu, H.; Liu, D. S.; Zhang, G. X.; Zhang, D. Q.; Zhu, D. B. Continuous On-Site Label-Free ATP Fluorometric Assay Based on Aggregation-Induced Emission of Silole. *Langmuir* **2009**, *25*, 676–678.
- (421) Noguchi, T.; Shiraki, T.; Dawn, A.; Tsuchiya, Y.; Lien le, T. N.; Yamamoto, T.; Shinkai, S. Nonlinear Fluorescence Response Driven by ATP-Induced Self-Assembly of Guanidinium-Tethered Tetraphenylethene. *Chem. Commun.* **2012**, *48*, 8090–8092.
- (422) Li, C.; Wu, T.; Hong, C.; Zhang, G.; Liu, S. A General Strategy to Construct Fluorogenic Probes from Charge-Generation Polymers (CGPs) and AIE-Active Fluorogens through Triggered Complexation. *Angew. Chem., Int. Ed.* **2012**, *51*, 455–459.
- (423) Nakamura, M.; Sanji, T.; Tanaka, M. Fluorometric Sensing of Biogenic Amines with Aggregation-Induced Emission-Active Tetraphenylethenes. *Chem. - Eur. J.* **2011**, *17*, 5344–5349.
- (424) Noguchi, T.; Roy, B.; Yoshihara, D.; Tsuchiya, Y.; Yamamoto, T.; Shinkai, S. Cyclization-Induced Turn-On Fluorescence System Applicable to Dicarboxylate Sensing. *Chem. - Eur. J.* **2014**, *20*, 381–384.
- (425) Noguchi, T.; Dawn, A.; Yoshihara, D.; Tsuchiya, Y.; Yamamoto, T.; Shinkai, S. Selective Detection of NADPH among Four Pyridine-Nucleotide Cofactors by a Fluorescent Probe Based on Aggregation-Induced Emission. *Macromol. Rapid Commun.* **2013**, *34*, 779–784.
- (426) Capila, I.; Linhardt, R. J. Heparin-Protein Interactions. *Angew. Chem. Int. Ed.* **2002**, *41*, 391–412.
- (427) Fareed, J.; Hoppensteadt, D. A.; Bick, R. L. An Update on Heparins at the Beginning of the New Millennium. *Semin. Thromb. Hemostasis* **2000**, *26*, 5–22.
- (428) Warkentin, T. E.; Levine, M. N.; Hirsh, J.; Horsewood, P.; Roberts, R. S.; Gent, M.; Kelton, J. G. Heparin-Induced Thrombocytopenia in Patients Treated with Low-Molecular-Weight Heparin or Unfractionated Heparin. *N. Engl. J. Med.* **1995**, *332*, 1330–1336.
- (429) Despotis, G. J.; Graylee, G.; Filos, K.; Levy, J. Anticoagulation Monitoring During Cardiac Surgery: A Review of Current and Emerging Techniques. *Anesthesiology* **1999**, *91*, 1122–1151.
- (430) Liu, H.; Song, P.; Wei, R.; Li, K.; Tong, A. A Facile, Sensitive and Selective Fluorescent Probe for Heparin Based on Aggregation-Induced Emission. *Talanta* **2014**, *118*, 348–352.
- (431) Dong, Y.; Wang, W.; Zhong, C.; Shi, J.; Tong, B.; Feng, X.; Zhi, J.; Dong, Y. Investigating the Effects of Side Chain Length on the AIE Properties of Water-Soluble TPE Derivatives. *Tetrahedron Lett.* **2014**, *55*, 1496–1500.
- (432) Gu, X.; Zhang, G.; Zhang, D. A New Ratiometric Fluorescence Detection of Heparin Based on the Combination of the Aggregation-Induced Fluorescence Quenching and Enhancement Phenomena. *Analyst* **2012**, *137*, 365–369.
- (433) Hu, R. R.; Ye, R. Q.; Lam, J. W. Y.; Li, M.; Leung, C. W. T.; Tang, B. Z. Conjugated Polyelectrolytes with Aggregation-Enhanced Emission Characteristics: Synthesis and Their Biological Applications. *Chem. - Asian J.* **2013**, *8*, 2436–2445.
- (434) Chen, D.; Shi, J.; Wu, Y.; Tong, B.; Zhi, J.; Dong, Y. An AIEE Polyelectrolyte as a Light-Up Fluorescent Probe for Heparin Sensing in Full Detection Range. *Sci. China: Chem.* **2013**, *S6*, 1239–1246.
- (435) Shi, J.; Wu, Y.; Tong, B.; Zhi, J.; Dong, Y. Tunable Fluorescence upon Aggregation: Photophysical Properties of Cationic Conjugated Polyelectrolytes Containing AIE and ACQ Units and Their Use in the Dual-channel Quantification of Heparin. *Sens. Actuators, B* **2014**, *197*, 334–341.
- (436) Xu, B.; Wu, X.; Li, H.; Tong, H.; Wang, L. Fluorescent Detection of Heparin by a Cationic Conjugated Polyfluorene Probe Containing Aggregation-Induced Emission Units. *Polymer* **2012**, *53*, 490–494.
- (437) Wang, L.; Li, Y.; Sun, J.; Lu, Y.; Sun, Y.; Cheng, D.; Li, C. Conjugated Poly(pyridinium salt)s as Fluorescence Light-Up Probes for Heparin Sensing. *J. Appl. Polym. Sci.* **2014**, *131*, 40933.
- (438) Rabenstein, D. L. Heparin and Heparan Sulfate: Structure and Function. *Nat. Prod. Rep.* **2002**, *19*, 312–331.
- (439) Xu, X.; Yan, S.; Zhou, Y.; Huang, R.; Chen, Y.; Wang, J.; Weng, X.; Zhou, X. A Novel Aggregation-Induced Emission Fluorescent Probe for Nucleic Acid Detection and Its Applications in Cell Imaging. *Bioorg. Med. Chem. Lett.* **2014**, *24*, 1654–1656.
- (440) Zhu, Z.; Xu, L.; Li, H.; Zhou, X.; Qin, J.; Yang, C. A Tetraphenylethene-Based Zinc Complex as a Sensitive DNA Probe by Coordination Interaction. *Chem. Commun.* **2014**, *50*, 7060–7062.
- (441) Lu, H. G.; Xu, B.; Dong, Y. J.; Chen, F. P.; Li, Y. W.; Li, Z. F.; He, J. T.; Li, H.; Tian, W. J. Novel Fluorescent pH Sensors and a Biological Probe Based on Anthracene Derivatives with Aggregation-Induced Emission Characteristics. *Langmuir* **2010**, *26*, 6838–6844.
- (442) Jin, J.; Chen, X.; Liu, Y.; Qin, A.; Sun, J.; Tang, B. Detection of ctDNA with Water Soluble Tetraphenylene-Based Fluorescence Probe. *Gaofenzi Xuebao* **2011**, *011*, 1079–1085.
- (443) Yu, Y.; Liu, J.; Zhao, Z.; Ng, K. M.; Luo, K. Q.; Tang, B. Z. Facile Preparation of Non-Self-quenching Fluorescent DNA Strands with the Degree of Labeling Up to the Theoretic Limit. *Chem. Commun.* **2012**, *48*, 6360–6362.
- (444) Sun, J.; Lu, Y.; Wang, L.; Cheng, D.; Sun, Y.; Zeng, X. Fluorescence Turn-On Detection of DNA Based on the Aggregation-Induced Emission of Conjugated Poly(pyridinium salt)s. *Polym. Chem.* **2013**, *4*, 4045–4051.
- (445) Hong, Y.; Häufler, M.; Lam, J. W. Y.; Li, Z.; Sin, K. K.; Dong, Y.; Tong, H.; Liu, J.; Qin, A.; Renneberg, R.; et al. Label-Free Fluorescent Probing of G-Quadruplex Formation and Real-Time Monitoring of DNA Folding by a Quaternized Tetraphenylethene Salt with Aggregation-Induced Emission Characteristics. *Chem. - Eur. J.* **2008**, *14*, 6428–6437.
- (446) Hong, Y. N.; Xiong, H.; Lam, J. W. Y.; Haussler, M.; Liu, J. Z.; Yu, Y.; Zhong, Y. C.; Sung, H. H. Y.; Williams, I. D.; Wong, K. S.; et al. Fluorescent Bioprobe: Structural Matching in the Docking Processes of Aggregation-Induced Emission Fluorogens on DNA Surfaces. *Chem. - Eur. J.* **2010**, *16*, 1232–1245.
- (447) Williamson, J. R.; Raghuraman, M. K.; Cech, T. R. Monovalent Cation-Induced Structure of Telomeric DNA: The G-quartet Model. *Cell* **1989**, *59*, 871–880.
- (448) Davis, J. T. G-Quartets 40 Years Later: From 5'-GMP to Molecular Biology and Supramolecular Chemistry. *Angew. Chem., Int. Ed.* **2004**, *43*, 668–698.
- (449) Collins, K. Mammalian Telomeres and Telomerase. *Curr. Opin. Cell Biol.* **2000**, *12*, 378–383.
- (450) Mergny, J.-L.; Riou, J.-F.; Milliet, P.; Teulade-Fichou, M.-P.; Gilson, E. Natural and Pharmacological Regulation of Telomerase. *Nucleic Acids Res.* **2002**, *30*, 839–865.
- (451) Cian, A. D.; DeLemos, E.; Mergny, J.-L.; Teulade-Fichou, M.-P.; Monchaud, D. Highly Efficient G-Quadruplex Recognition by Bisquinolinium Compounds. *J. Am. Chem. Soc.* **2007**, *129*, 1856–1857.

- (452) Pennarun, G.; Granotier, C.; Gauthier, L. R.; Gomez, D.; Hoffschir, F.; Mandine, E.; Riou, J. F.; Mergny, J. L.; Mailliet, P.; Boussin, F. D. Apoptosis Related to Telomere Instability and Cell Cycle Alterations in Human Glioma Cells Treated by New Highly Selective G-quadruplex Ligands. *Oncogene* **2005**, *24*, 2917–2928.
- (453) Paeschke, K.; Simonsson, T.; Postberg, J.; Rhodes, D.; Lipps, H. J. Telomere End-binding Proteins Control the Formation of G-quadruplex DNA Structures in vivo. *Nat. Struct. Mol. Biol.* **2005**, *12*, 847–854.
- (454) Fakhouri, J.; Nimmo, G. A. M.; Autexier, C. Harnessing Telomerase in Cancer Therapeutics. *Anti-Cancer Agents Med. Chem.* **2007**, *7*, 475–483.
- (455) Huang, J.; Wang, M.; Zhou, Y. Y.; Weng, X. C.; Shuai, L.; Zhou, X.; Zhang, D. Q. Visual Observation of G-Quadruplex DNA with the Label-Free Fluorescent Probe Silole with Aggregation-Induced Emission. *Bioorg. Med. Chem.* **2009**, *17*, 7743–7748.
- (456) Xu, L.; Zhu, Z.; Zhou, X.; Qin, J.; Yang, C. A Highly Sensitive Nucleic Acid Stain Based on Amino-Modified Tetraphenylethene: The Influence of Configuration. *Chem. Commun.* **2014**, *50*, 6494–6497.
- (457) Li, X.; Ma, K.; Lu, H.; Xu, B.; Wang, Z.; Zhang, Y.; Gao, Y.; Yan, L.; Tian, W. Highly Sensitive Determination of ssDNA and Real-Time Sensing of Nuclease Activity and Inhibition Based on the Controlled Self-Assembly of a 9,10-Distyrylanthracene Probe. *Anal. Bioanal. Chem.* **2014**, *406*, 851–858.
- (458) Li, X.; Ma, K.; Zhu, S.; Yao, S.; Liu, Z.; Xu, B.; Yang, B.; Tian, W. Fluorescent Aptasensor Based on Aggregation-Induced Emission Probe and Graphene Oxide. *Anal. Chem.* **2014**, *86*, 298–303.
- (459) Xu, X.; Li, J.; Li, Q.; Huang, J.; Dong, Y.; Hong, Y.; Yan, J.; Qin, J.; Li, Z.; Tang, B. Z. A Strategy for Dramatically Enhancing the Selectivity of Molecules Showing Aggregation-Induced Emission towards Biomacromolecules with the Aid of Graphene Oxide. *Chem. - Eur. J.* **2012**, *18*, 7278–7286.
- (460) Dong, Y.; Lam, J. W. Y.; Qin, A.; Li, Z.; Liu, J.; Sun, J.; Dong, Y.; Tang, B. Z. Endowing Hexaphenylsilole with Chemical Sensory and Biological Probing Properties by Attaching Amino Pendants to the Siloly Core. *Chem. Phys. Lett.* **2007**, *446*, 124–127.
- (461) Li, Y.; Kwok, R. T. K.; Tang, B. Z.; Liu, B. Specific Nucleic Acid Detection Based on Fluorescent Light-Up Probe from Fluorogens with Aggregation-Induced Emission Characteristics. *RSC Adv.* **2013**, *3*, 10135–10138.
- (462) Lou, X.; Leung, C. W. T.; Dong, C.; Hong, Y.; Chen, S.; Zhao, E.; Lam, J. W. Y.; Tang, B. Z. Detection of Adenine-Rich ssDNA Based on Thymine-Substituted Tetraphenylethene with Aggregation-Induced Emission Characteristics. *RSC Adv.* **2014**, *4*, 33307–33311.
- (463) Damerger, F. F.; Christen, B.; Perez, D. R.; Hornemann, S.; Wuethrich, K. Cellular Prion Protein Conformation and Function. *Proc. Natl. Acad. Sci. U. S. A.* **2011**, *108*, 17308–17313.
- (464) Pavelcik, F.; Václavík, J. Performance of Phased Rotation, Conformation and Translation Function: Accurate Protein Model Building with Tripeptidic and Tetrapeptidic Fragments. *Acta Crystallogr., Sect. D: Biol. Crystallogr.* **2010**, *66*, 1012–1023.
- (465) Vasil'ev, S.; Bruce, D. A Protein Dynamics Study of Photosystem II: The Effects of Protein Conformation on Reaction Center Function. *Biophys. J.* **2006**, *90*, 3062–3073.
- (466) Ahmed, M. A.; Bamm, V. V.; Harauz, G.; Ladizhansky, V. Solid-State NMR Spectroscopy of Membrane-Associated Myelin Basic Protein—Conformation and Dynamics of an Immunodominant Epitope. *Biophys. J.* **2010**, *99*, 1247–1255.
- (467) Roberts, G. C. K. Folding and Unfolding for Binding: Large-Scale Protein Dynamics in Protein–Protein Interactions. *Biochem. Soc. Trans.* **2006**, *34*, 971–974.
- (468) Hong, Y. N.; Feng, C.; Yu, Y.; Liu, J. Z.; Lam, J. W. Y.; Luo, K. Q.; Tang, B. Z. Quantitation, Visualization, and Monitoring of Conformational Transitions of Human Serum Albumin by a Tetraphenylethene Derivative with Aggregation-Induced Emission Characteristics. *Anal. Chem.* **2010**, *82*, 7035–7043.
- (469) Sun, B.; Yang, X.; Ma, L.; Niu, C.; Wang, F.; Na, N.; Wen, J.; Ouyang, J. Design and Application of Anthracene Derivative with Aggregation-Induced Emission Characteristics for Visualization and Monitoring of Erythropoietin Unfolding. *Langmuir* **2013**, *29*, 1956–1962.
- (470) Wang, Z.; Ma, K.; Xu, B.; Li, X.; Tian, W. A Highly Sensitive “Turn-on” Fluorescent Probe for Bovine Serum Albumin Protein Detection and Quantification Based on AIE-Active Distyrylanthracene Derivative. *Sci. China: Chem.* **2013**, *56*, 1234–1238.
- (471) Yu, D.; Deng, M.; He, C.; Fan, Y.; Wang, Y. Fluorescent Nanofibrils Constructed by Self-Assembly of a Peptide Amphiphile with an Anionic Dye. *Soft Matter* **2011**, *7*, 10773–10779.
- (472) Sathish, V.; Babu, E.; Ramdass, A.; Lu, Z.-Z.; Velayudham, M.; Thanasekaran, P.; Lu, K.-L.; Rajagopal, S. Alkoxy Bridged Binuclear Rhenium (I) Complexes as a Potential Sensor for  $\beta$ -Amyloid Aggregation. *Talanta* **2014**, *130*, 274–279.
- (473) Kelly, J. W. Alternative Conformation of Amyloidogenic Proteins and Their Multi-step Assembly Pathways. *Curr. Opin. Struct. Biol.* **1998**, *8*, 101–106.
- (474) Stefani, M.; Dobson, C. Protein Aggregation and Aggregate Toxicity: New Insights into Protein Folding, Misfolding Diseases and Biological Evolution. *J. Mol. Med.* **2003**, *81*, 678–699.
- (475) Sipe, J. D.; Cohen, A. S. Review: History of the Amyloid Fibril. *J. Struct. Biol.* **2000**, *130*, 88–98.
- (476) Morris, K.; Serpell, L. From Natural to Designer Self-assembling Biopolymers, the Structural Characterisation of Fibrous Proteins & Peptides Using Fibre Diffraction. *Chem. Soc. Rev.* **2010**, *39*, 3445–3453.
- (477) Greenwald, J.; Riek, R. Biology of Amyloid: Structure, Function, and Regulation. *Structure* **2010**, *18*, 1244–1260.
- (478) Dobson, C. M. Protein Folding and Misfolding. *Nature* **2003**, *426*, 884–890.
- (479) Hardy, J.; Selkoe, D. J. The Amyloid Hypothesis of Alzheimer's Disease: Progress and Problems on the Road to Therapeutics. *Science* **2002**, *297*, 353–356.
- (480) Bernstein, S. L.; Dupuis, N. F.; Lazo, N. D.; Wyttenbach, T.; Condron, M. M.; Bitan, G.; Teplow, D. B.; Shea, J.-E.; Ruotolo, B. T.; Robinson, C. V.; et al. Amyloid- $\beta$  Protein Oligomerization and the Importance of Tetramers and Dodecamers in the Aetiology of Alzheimer's Disease. *Nat. Chem.* **2009**, *1*, 326–331.
- (481) Kayed, R.; Head, E.; Thompson, J. L.; McIntire, T. M.; Milton, S. C.; Cotman, C. W.; Glabe, C. G. Common Structure of Soluble Amyloid Oligomers Implies Common Mechanism of Pathogenesis. *Science* **2003**, *300*, 486–489.
- (482) Ivanova, M. I.; Sievers, S. A.; Sawaya, M. R.; Wall, J. S.; Eisenberg, D. Molecular Basis for Insulin Fibril Assembly. *Proc. Natl. Acad. Sci. U. S. A.* **2009**, *106*, 18990–18995.
- (483) Karlsson, K. A. Bacterium-Host Protein-Carbohydrate Interactions and Pathogenicity. *Biochem. Soc. Trans.* **1999**, *27*, 471–474.
- (484) Geijtenbeek, T.; Torensma, R.; van Vliet, S.; van Duijnhoven, G.; Adema, G.; van Kooyk, Y.; Figdor, C. Identification of DC-SIGN, a Novel Dendritic Cell-Specific ICAM-3 Receptor That Supports Primary Immune Responses. *Cell* **2000**, *100*, 575–585.
- (485) Sacchettini, J. C.; Baum, L. G.; Brewer, C. F. Multivalent Protein–Carbohydrate Interactions: A New Paradigm for Supermolecular Assembly and Signal Transduction. *Biochemistry* **2001**, *40*, 3009–3015.
- (486) Kansas, G. S. Selectins and Their Ligands: Current Concepts and Controversies. *Blood* **1996**, *88*, 3259–3287.
- (487) Lee, Y. C.; Lee, R. T. Carbohydrate-Protein Interactions: Basis of Glycobiology. *Acc. Chem. Res.* **1995**, *28*, 321–327.
- (488) Lundquist, J. J.; Toone, E. J. The Cluster Glycoside Effect. *Chem. Rev.* **2002**, *102*, 555–578.
- (489) Holgersson, J.; Gustafsson, A.; Breimer, M. E. Special Feature: Glycobiology of Xenotransplantation and Cancer Part II. *Immunol. Cell Biol.* **2005**, *83*, 694–708.
- (490) de la Fuente, J. M.; Barrientos, A. G.; Rojas, T. C.; Rojo, J.; Cañada, J.; Fernández, A.; Penadés, S. Gold Glyconanoparticles as Water-Soluble Polyvalent Models To Study Carbohydrate Interactions. *Angew. Chem. Int. Ed.* **2001**, *113*, 2317–2321.
- (491) Otsuka, H.; Akiyama, Y.; Nagasaki, Y.; Kataoka, K. Quantitative and Reversible Lectin-Induced Association of Gold Nanoparticles

- Modified with  $\alpha$ -Lactosyl- $\omega$ -mercapto-poly(ethylene glycol). *J. Am. Chem. Soc.* **2001**, *123*, 8226–8230.
- (492) Thaxton, J.-M. C. S.; Mirkin, C. A. Nanoparticle-Based Bio-Bar Codes for the Ultrasensitive Detection of Proteins. *Science* **2003**, *301*, 1884–1886.
- (493) Charych, D. H.; Nagy, J. O.; Spevak, W.; Bednarski, M. D. Direct Colorimetric Detection of a Receptor-Ligand Interaction by a Polymerized Bilayer Assembly. *Science* **1993**, *261*, 585–588.
- (494) Dwight, S. J.; Gaylord, B. S.; Hong, J. W.; Bazan, J. G. C. Perturbation of Fluorescence by Nonspecific Interactions between Anionic Poly(phenylenevinylene)s and Proteins: Implications for Biosensors. *J. Am. Chem. Soc.* **2004**, *126*, 16850–16859.
- (495) Wang, J.-X.; Chen, Q.; Bian, N.; Yang, F.; Sun, J.; Qi, A.-D.; Yan, C.-G.; Han, B.-H. Sugar-Bearing Tetraphenylethylene: Novel Fluorescent Probe for Studies of Carbohydrate–Protein Interaction Based on Aggregation-Induced Emission. *Org. Biomol. Chem.* **2011**, *9*, 2219–2226.
- (496) Sanji, T.; Shiraishi, K.; Nakamura, M.; Tanaka, M. Fluorescence Turn-On Sensing of Lectins with Mannose-Substituted Tetraphenylethenes Based on Aggregation-Induced Emission. *Chem. - Asian J.* **2010**, *5*, 817–824.
- (497) Hatano, K.; Saeki, H.; Yokota, H.; Aizawa, H.; Koyama, T.; Matsuoka, K.; Terunuma, D. Fluorescence Quenching Detection of Peanut Agglutinin Based on Photoluminescent Silole-Core Carbosilane Dendrimer Peripherally Functionalized with Lactose. *Tetrahedron Lett.* **2009**, *50*, 5816–5819.
- (498) Hu, X.-M.; Chen, Q.; Wang, J.-X.; Cheng, Q.-Y.; Yan, C.-G.; Cao, J.; He, Y.-J.; Han, B.-H. Tetraphenylethylene-Based Glycoconjugate as a Fluorescence “Turn-On” Sensor for Cholera Toxin. *Chem. - Asian J.* **2011**, *6*, 2376–2381.
- (499) Kato, T.; Kawaguchi, A.; Nagata, K.; Hatanaka, K. Development of Tetraphenylethylene-Based Fluorescent Oligosaccharide Probes for Detection of Influenza Virus. *Biochem. Biophys. Res. Commun.* **2010**, *394*, 200–204.
- (500) Sack, D. A.; Sack, R. B.; Nair, G. B.; Siddique, A. K. Cholera. *Lancet* **2004**, *363*, 223–233.
- (501) Nisato, R. E.; Tille, J. C.; Jonczyk, A.; Goodman, S. L.; Pepper, M. S.  $\alpha_v\beta_3$  and  $\alpha_v\beta_5$  Integrin Antagonists Inhibit Angiogenesis in vitro. *Angiogenesis* **2003**, *6*, 105–119.
- (502) Hodivala-Dilke, K. M.; Reynolds, A. R.; Reynolds, L. E. Integrins in Angiogenesis: Multitalented Molecules in a Balancing Act. *Cell Tissue Res.* **2003**, *314*, 131–144.
- (503) Cairns, R. A.; Khokha, R.; Hill, R. P. Molecular Mechanisms of Tumor Invasion and Metastasis: An Integrated View. *Curr. Mol. Med.* **2003**, *3*, 659–671.
- (504) Felding-Habermann, B. Integrin Adhesion Receptors in Tumor Metastasis. *Clin. Exp. Metastasis* **2003**, *20*, 203–213.
- (505) Gasparini, G.; Brooks, P. C.; Biganzoli, E.; Vermeulen, P. B.; Bonoldi, E.; Dirix, L. Y.; Ranieri, G.; Miceli, R.; Cheres, D. A. Vascular Integrin  $\alpha_v\beta_3$ : A New Prognostic Indicator in Breast Cancer. *Clin. Cancer Res.* **1998**, *4*, 2625–2634.
- (506) Shi, H.; Liu, J.; Geng, J.; Tang, B. Z.; Liu, B. Specific Detection of Integrin  $\alpha_v\beta_3$  by Light-Up Bioprobe with Aggregation-Induced Emission Characteristics. *J. Am. Chem. Soc.* **2012**, *134*, 9569–9572.
- (507) Peng, L.; Wei, R.; Li, K.; Zhou, Z.; Song, P.; Tong, A. A Ratiometric Fluorescent Probe for Hydrophobic Proteins in Aqueous Solution Based on Aggregation-Induced Emission. *Analyst* **2013**, *138*, 2068–2072.
- (508) Wang, F.; Wen, J.; Huang, L.; Huang, J.; Ouyang, J. A Highly Sensitive “Switch-On” Fluorescent Probe for Protein Quantification and Visualization Based on Aggregation-Induced Emission. *Chem. Commun.* **2012**, *48*, 7395–7397.
- (509) Liu, Y.; Wang, Z.; Zhang, G.; Zhang, W.; Zhang, D.; Jiang, X. Rapid Casein Quantification in Milk Powder with Aggregation Induced Emission Character of Tetraphenylethene Derivative. *Analyst* **2012**, *137*, 4654–4657.
- (510) Xu, J.-P.; Fang, Y.; Song, Z.-G.; Mei, J.; Jia, L.; Qin, A. J.; Sun, J. Z.; Ji, J.; Tang, B. Z. BSA-Tetraphenylethene Derivative Conjugates with Aggregation-Induced Emission Properties: Fluorescent Probes for Label-Free and Homogeneous Detection of Protease and  $\alpha$ 1-Antitrypsin. *Analyst* **2011**, *136*, 2315–2321.
- (511) Xu, X.; Huang, J.; Li, J.; Yan, J.; Qin, J.; Li, Z. A Graphene Oxide-Based AIE Biosensor with High Selectivity toward Bovine Serum Albumin. *Chem. Commun.* **2011**, *47*, 12385–12387.
- (512) Tong, H.; Hong, Y.; Dong, Y.; Häußler, M.; Lam, J. W. Y.; Li, Z.; Guo, Z.; Guo, Z.; Tang, B. Z. Fluorescent “Light-Up” Bioprobes Based on Tetraphenylethylene Derivatives with Aggregation-Induced Emission Characteristics. *Chem. Commun.* **2006**, *3705*–3707.
- (513) Yu, Y.; Qin, A.; Feng, C.; Lu, P.; Ng, K. M.; Luo, K. Q.; Tang, B. Z. An Amine-Reactive Tetraphenylethylene Derivative for Protein Detection in SDS-PAGE. *Analyst* **2012**, *137*, 5592–5596.
- (514) Xue, W. X.; Zhang, G. X.; Zhang, D. Q.; Zhu, D. B. A New Label-Free Continuous Fluorometric Assay for Trypsin and Inhibitor Screening with Tetraphenylethene Compounds. *Org. Lett.* **2010**, *12*, 2274–2277.
- (515) Chen, X.-t.; Xiang, Y.; Li, N.; Song, P.-S.; Tong, A.-j. Fluorescence Turn-On Detection of Protamine Based on Aggregation-Induced Emission Enhancement Characteristics of 4-(6'-Carboxyl)hexyloxysalicylaldehyde Azine. *Analyst* **2010**, *135*, 1098–1105.
- (516) Hirota, M.; Ohmura, M.; Baba, H. The Role of Trypsin, Trypsin Inhibitor, and Trypsin Receptor in the Onset and Aggravation of Pancreatitis. *J. Gastroenterol.* **2006**, *41*, 832–836.
- (517) Yu, C.; Wu, Y.; Zeng, F.; Li, X.; Shi, J.; Wu, S. Hyperbranched Polyester-Based Fluorescent Probe for Histone Deacetylase via Aggregation-Induced Emission. *Biomacromolecules* **2013**, *14*, 4507–4514.
- (518) Peng, L. H.; Zhang, G. X.; Zhang, D. Q.; Wang, Y. L.; Zhu, D. B. A Direct Continuous Fluorometric Turn-On Assay for Monoamine Oxidase B and Its Inhibitor-Screening Based on the Abnormal Fluorescent Behavior of Silole. *Analyst* **2010**, *135*, 1779–1784.
- (519) Xie, H.; Zeng, F.; Wu, S. Ratiometric Fluorescent Biosensor for Hyaluronidase with Hyaluronan as both Nanoparticle Scaffold and Substrate for Enzymatic Reaction. *Biomacromolecules* **2014**, *15*, 3383–3389.
- (520) Selkoe, D. J. Alzheimer’s Disease: Genes, Proteins, and Therapy. *Physiol. Rev.* **2001**, *81*, 741–766.
- (521) Wang, M.; Gu, X. G.; Zhang, G. X.; Zhang, D. Q.; Zhu, D. B. Convenient and Continuous Fluorometric Assay Method for Acetylcholinesterase and Inhibitor Screening Based on the Aggregation-Induced Emission. *Anal. Chem.* **2009**, *81*, 4444–4449.
- (522) Shen, X.; Liang, F.; Zhang, G.; Zhang, D. A New Continuous Fluorometric Assay for Acetylcholinesterase Activity and Inhibitor Screening with Emissive Core–Shell Silica Particles Containing Tetraphenylethylene Fluorophore. *Analyst* **2012**, *137*, 2119–2123.
- (523) Peng, L. H.; Zhang, G. X.; Zhang, D. Q.; Xiang, J. F.; Zhao, R.; Wang, Y. L.; Zhu, D. B. A Fluorescence “Turn-On” Ensemble for Acetylcholinesterase Activity Assay and Inhibitor Screening. *Org. Lett.* **2009**, *11*, 4014–4017.
- (524) Chen, Q.; Bian, N.; Cao, C.; Qiu, X.-L.; Qi, A.-D.; Han, B.-H. Glucosamine Hydrochloride Functionalized Tetraphenylethylene: A Novel Fluorescent Probe for Alkaline Phosphatase Based on the Aggregation-Induced Emission. *Chem. Commun.* **2010**, *46*, 4067–4069.
- (525) Liu, H.; Lv, Z.; Ding, K.; Liu, X.; Yuan, L.; Chen, H.; Li, X. Incorporation of Tyrosine Phosphate into Tetraphenylethylene Affords an Amphiphilic Molecule for Alkaline Phosphatase Detection, Hydrogelation and Calcium Mineralization. *J. Mater. Chem. B* **2013**, *1*, 5550–5556.
- (526) Gu, X.; Zhang, G.; Wang, Z.; Liu, W.; Xiao, L.; Zhang, D. A New Fluorometric Turn-On Assay for Alkaline Phosphatase and Inhibitor Screening Based on Aggregation and Deaggregation of Tetraphenylethylene Molecules. *Analyst* **2013**, *138*, 2427–2431.
- (527) Liang, J.; Kwok, R. T. K.; Shi, H. B.; Tang, B. Z.; Liu, B. Fluorescent Light-Up Probe with Aggregation-Induced Emission Characteristics for Alkaline Phosphatase Sensing and Activity Study. *ACS Appl. Mater. Interfaces* **2013**, *5*, 8784–8789.
- (528) Song, Z.; Hong, Y.; Kwok, R. T. K.; Lam, J. W. Y.; Liu, B.; Tang, B. Z. A Dual-Mode Fluorescence “Turn-On” Biosensor Based on an

- Aggregation-Induced Emission Luminogen. *J. Mater. Chem. B* **2014**, *2*, 1717–1723.
- (529) Millán, J. L. Alkaline Phosphatases: Structure, Substrate Specificity and Functional Relatedness to other Members of a Large Superfamily of Enzymes. *Purinergic Signalling* **2006**, *2*, 335–341.
- (530) Ooi, K.; Shiraki, K.; Morishita, Y.; Nobori, T. High-Molecular Intestinal Alkaline Phosphatase in Chronic Liver Diseases. *J. Clin. Lab. Anal.* **2007**, *21*, 133–139.
- (531) Christenson, R. H. Biochemical Markers of Bone Metabolism: An Overview. *Clin. Biochem.* **1997**, *30*, 573–593.
- (532) McIlwain, D. R.; Berger, T.; Mak, T. W. Caspase Functions in Cell Death and Disease. *Cold Spring Harbor Perspect. Biol.* **2013**, *5*, a008656.
- (533) Riedl, S. J.; Shi, Y. Molecular Mechanisms of Caspase Regulation during Apoptosis. *Nat. Rev. Mol. Cell Biol.* **2004**, *5*, 897–907.
- (534) Shi, H.; Kwok, R. T. K.; Liu, J.; Xing, B.; Tang, B. Z.; Liu, B. Real-Time Monitoring of Cell Apoptosis and Drug Screening Using Fluorescent Light-Up Probe with Aggregation-Induced Emission Characteristics. *J. Am. Chem. Soc.* **2012**, *134*, 17972–17981.
- (535) Shi, H.; Zhao, N.; Ding, D.; Liang, J.; Tang, B. Z.; Liu, B. Fluorescent Light-Up Probe with Aggregation-Induced Emission Characteristics for *in vivo* Imaging of Cell Apoptosis. *Org. Biomol. Chem.* **2013**, *11*, 7289–7296.
- (536) Ding, D.; Liang, J.; Shi, H.; Kwok, R. T. K.; Gao, M.; Feng, G.; Yuan, Y.; Tang, B. Z.; Liu, B. Light-Up Bioprobe with Aggregation-Induced Emission Characteristics for Real-Time Apoptosis Imaging in Target Cancer Cells. *J. Mater. Chem. B* **2014**, *2*, 231–238.
- (537) Liang, J.; Shi, H.; Kwok, R. T. K.; Gao, M.; Yuan, Y.; Zhang, W.; Tang, B. Z.; Liu, B. Distinct Optical and Kinetic Responses from *E/Z* Isomers of Caspase Probes with Aggregation-Induced Emission Characteristics. *J. Mater. Chem. B* **2014**, *2*, 4363–4370.
- (538) Wang, X.; Liu, H.; Li, J.; Ding, K.; Lv, Z.; Yang, Y.; Chen, H.; Li, X. A Fluorogenic Probe with Aggregation-Induced Emission Characteristics for Carboxylesterase Assay through Formation of Supramolecular Microfibers. *Chem. - Asian J.* **2014**, *9*, 784–789.
- (539) Satoh, T.; Hosokawa, M. Carboxylesterases: Structure, Function and Polymorphism in Mammals. *J. Pestic. Sci.* **2010**, *35*, 218–228.
- (540) Satoh, T.; Hosokawa, M. The Mammalian Carboxylesterases: From Molecules to Functions. *Annu. Rev. Pharmacol. Toxicol.* **1998**, *38*, 257–288.
- (541) Imai, T. Human Carboxylesterase Isozymes: Catalytic Properties and Rational Drug Design. *Drug Metab. Pharmacokinet.* **2006**, *21*, 173–185.
- (542) Gutova, M.; Najbauer, J.; Chen, M. Y.; Potter, P. M.; Kim, S. U.; Aboody, K. S. Therapeutic Targeting of Melanoma Cells Using Neural Stem Cells Expressing Carboxylesterase, a CPT-11 Activating Enzyme. *Curr. Stem Cell Res. Ther.* **2010**, *5*, 273–276.
- (543) Vellodi, A. Lysosomal Storage Disorders. *Br. J. Haematol.* **2005**, *128*, 413–431.
- (544) Anderson, R. A.; Byrum, R. S.; Coates, P. M.; Sando, G. N. Mutations at the Lysosomal Acid Cholesteryl Ester Hydrolase Gene Locus in Wolman Disease. *Proc. Natl. Acad. Sci. U. S. A.* **1994**, *91*, 2718–2722.
- (545) Gao, M.; Hu, Q.; Feng, G.; Tang, B. Z.; Liu, B. A Fluorescent Light-Up Probe with “AIE + ESIPT” Characteristics for Specific Detection of Lysosomal Esterase. *J. Mater. Chem. B* **2014**, *2*, 3438–3442.
- (546) Liu, H.; Zhang, J. J.; Wang, S. J.; Zhang, X. E.; Zhou, N. Y. Plasmid-Borne Catabolism of Methyl Parathion and *p*-Nitrophenol in *Pseudomonas* sp. Strain WBC-3. *Biochem. Biophys. Res. Commun.* **2005**, *334*, 1107–1114.
- (547) Chen, S.; Huang, J.; Du, D.; Li, J.; Tu, H.; Liu, D.; Zhang, A. Methyl Parathion Hydrolase Based Nanocomposite Biosensors for Highly Sensitive and Selective Determination of Methyl Parathion. *Biosens. Bioelectron.* **2011**, *26*, 4320–4325.
- (548) Zhao, G. N.; Tang, B.; Dong, Y. Q.; Xie, W. H.; Tang, B. Z. A Unique Fluorescence Response of Hexaphenylsilole to Methyl Parathion Hydrolase: A New Signal Generating System for the Enzyme Label. *J. Mater. Chem. B* **2014**, *2*, 5093–5099.
- (549) van Meer, G.; Voelker, D. R.; Feigenson, G. W. Membrane Lipids: Where They Are and How They Behave. *Nat. Rev. Mol. Cell Biol.* **2008**, *9*, 112–124.
- (550) Stavru, F.; Palmer, A. E.; Wang, C.; Youle, R. J.; Cossart, P. Atypical Mitochondrial Fission upon Bacterial Infection. *Proc. Natl. Acad. Sci. U. S. A.* **2013**, *110*, 16003–16008.
- (551) McMillin, J. B.; Dowhan, W. Cardiolipin and Apoptosis. *Biochim. Biophys. Acta, Mol. Cell Biol. Lipids* **2002**, *1585*, 97–107.
- (552) *Functional Roles of Lipids in Membrane*. *Biochemistry of Lipids, Lipoproteins and Membranes*, 4th ed.; Dowhan, W., Bogdanov, M., Eds.; Elsevier Science B. V.: Amsterdam, The Netherlands, 2002; Chapter 1, p1.
- (553) Shidoji, Y.; Hayashi, K.; Komura, S.; Ohishi, N.; Yagi, K. Loss of Molecular Interaction between Cytochrome c and Cardiolipin Due to Lipid Peroxidation. *Biochem. Biophys. Res. Commun.* **1999**, *264*, 343–347.
- (554) Kagan, V. E.; Tyurin, V. A.; Jiang, J.; Tyurina, Y. Y.; Ritov, V. B.; Amoscato, A. A.; Osipov, A. N.; Belikova, N. A.; Kapralov, A. A.; Kini, V.; et al. Cytochrome c Acts as a Cardiolipin Oxygenase Required for Release of Proapoptotic Factors. *Nat. Chem. Biol.* **2005**, *1*, 223–232.
- (555) Bergstrom, C. L.; Beales, P. A.; Lv, Y.; Vanderlick, T. K.; Groves, J. T. Cytochrome c Causes Pore Formation in Cardiolipin-Containing Membranes. *Proc. Natl. Acad. Sci. U. S. A.* **2013**, *110*, 6269–6274.
- (556) Kagan, V. E.; Borisenko, G. G.; Tyurina, Y. Y.; Tyurin, V. A.; Jiang, J.; Potapovich, A. I.; Kini, V.; Amoscato, A. A.; Fujii, Y. Oxidative Lipidomics of Apoptosis: Redox Catalytic Interactions of Cytochrome c with Cardiolipin and Phosphatidylserine. *Free Radical Biol. Med.* **2005**, *37*, 1963–1985.
- (557) Valianpour, F.; Wanders, R. J.; Overmars, H.; Vaz, F. M.; Barth, P. G.; van Gennip, A. H. Linoleic Acid Supplementation of Barth Syndrome Fibroblasts Restores Cardiolipin Levels Implications for Treatment. *J. Lipid Res.* **2003**, *44*, 560–566.
- (558) Fobker, M.; Voss, R.; Reinecke, H.; Crone, C.; Assmann, G.; Watler, M. Accumulation of Cardiolipin and Lysocardiolipin in Fibroblasts from Tangier Disease Subjects. *FEBS Lett.* **2001**, *500*, 157–162.
- (559) Leung, C. W. T.; Hong, Y.; Hanske, J.; Zhao, E.; Chen, S.; Pletneva, E. V.; Tang, B. Z. Superior Fluorescent Probe for Detection of Cardiolipin. *Anal. Chem.* **2014**, *86*, 1263–1268.
- (560) Yu, Y.; Feng, C.; Hong, Y.; Liu, J.; Chen, S.; Ng, K. M.; Luo, K. Q.; Tang, B. Z. Cytophilic Fluorescent Bioprobes for Long-Term Cell Tracking. *Adv. Mater.* **2011**, *23*, 3298–3302.
- (561) *Guyton and Hall Textbook of Medical Physiology*, 12th ed.; Hall, J. E., Ed.; Saunders: Philadelphia, PA, 2010.
- (562) *Molecular Biology of the Cell*; Alberts, B., Johnson, A., Lewis, J., Raff, M., Roberts, K., Walter, P., Eds.; Garland Science: New York, 2002.
- (563) Yang, Y.; Zhao, Q.; Feng, W.; Li, F. Luminescent Chemosensors for Bioimaging. *Chem. Rev.* **2013**, *113*, 192–270.
- (564) Zhao, J.; Wu, W.; Sun, J.; Guo, S. Triplet Photosensitizers: From Molecular Design to Applications. *Chem. Soc. Rev.* **2013**, *42*, 5323–5351.
- (565) Ma, D.-L.; Ma, V. P.-Y.; Chan, D. S.-H.; Leung, K.-H.; He, H.-Z.; Leung, C.-H. Recent Advances in Luminescent Heavy Metal Complexes for Sensing. *Coord. Chem. Rev.* **2012**, *256*, 3087–3113.
- (566) Wu, X.; Chang, S.; Sun, X.; Guo, Z.; Li, Y.; Tang, J.; Shen, Y.; Shi, J.; Tian, H.; Zhu, W. Constructing NIR Silica–cyanine Hybrid Nanocomposite for Bioimaging *in vivo*: A Breakthrough in Photostability and Bright Fluorescence with Large Stokes Shift. *Chem. Sci.* **2013**, *4*, 1221–1228.
- (567) Liu, M.; Li, Z. H.; Xu, F. J.; Lai, L. H.; Wang, Q. Q.; Tang, G. P.; Yang, W. T. An Oligopeptide Ligand-Mediated Therapeutic Gene Nanocomplex for Liver Cancer-Targeted Therapy. *Biomaterials* **2012**, *33*, 2240–2250.
- (568) Jiang, Q.; Lai, L.; Shen, J.; Wang, Q.; Xu, F.; Tang, G. Gene Delivery to Tumor Cells by Cationic Polymeric Nanovectors Coupled to Folic Acid and the Cell-Penetrating Peptide Octaarginine. *Biomaterials* **2011**, *32*, 7253–7262.

- (569) Ow, Y.-L. P.; Green, D. R.; Hao, Z.; Mak, T. W. Cytochrome *c*: Functions beyond Respiration. *Nat. Rev. Mol. Cell Biol.* **2008**, *9*, 532–542.
- (570) Hoye, A. T.; Davoren, J. E.; Wipf, P.; Fink, M. P.; Kagan, V. E. Targeting Mitochondria. *Acc. Chem. Res.* **2008**, *41*, 87–97.
- (571) Dickinson, B. C.; Srikanth, D.; Chang, C. J. Mitochondrial-Targeted Fluorescent Probes for Reactive Oxygen Species. *Curr. Opin. Chem. Biol.* **2010**, *14*, 50–56.
- (572) Dickinson, B. C.; Chang, C. J. A Targetable Fluorescent Probe for Imaging Hydrogen Peroxide in the Mitochondria of Living Cells. *J. Am. Chem. Soc.* **2008**, *130*, 9638–9639.
- (573) Gardner, A.; Boles, R. G. Is a "Mitochondrial Psychiatry" in the Future? A Review. *Curr. Psychiatry Rev.* **2005**, *1*, 255–271.
- (574) Lesniewsky, E. J.; Moghaddas, S.; Tandler, B.; Kerner, B.; Hoppel, C. L. Mitochondrial Dysfunction in Cardiac Disease: Ischemia-Reperfusion, Aging, and Heart Failure. *J. Mol. Cell. Cardiol.* **2001**, *33*, 1065–1089.
- (575) Karbowski, M.; Youle, R. J. Dynamics of Mitochondrial Morphology in Healthy Cells and during Apoptosis. *Cell Death Differ.* **2003**, *10*, 870–880.
- (576) Masanta, G.; Heo, C. H.; Lim, C. S.; Bae, S. K.; Cho, B. R.; Kim, H. M. A Mitochondria-Localized Two-photon Fluorescent Probe for Ratiometric Imaging of Hydrogen Peroxide in Live Tissue. *Chem. Commun.* **2012**, *48*, 3518–3520.
- (577) Gandre-Babbe, S.; van der Bliek, A. M. The Novel Tail-anchored Membrane Protein Mff Controls Mitochondrial and Peroxisomal Fission in Mammalian Cells. *Mol. Biol. Cell* **2008**, *19*, 2402–2412.
- (578) Neto, B. A. D.; Carvalho, P. H. P. R.; Santos, D. C. B. D.; Gatto, C. C.; Ramos, L. M.; Vasconcelos, N. M. D.; Corrêa, J. R.; Costa, M. B.; de Oliveira, H. C. B.; Silva, R. G. Synthesis, Properties and Highly Selective Mitochondria Staining with Novel, Stable and Superior Benzothiadiazole Fluorescent Probes. *RSC Adv.* **2012**, *2*, 1524–1532.
- (579) Chen, W.-d.; Zhang, D.-w.; Gong, W.-t.; Lin, Y.; Ning, G.-l. Aggregation-Induced Emission of a Novel Conjugated Phosphonium Salt and Its Application in Mitochondrial Imaging. *Spectrochim. Acta, Part A* **2013**, *110*, 471–473.
- (580) Leung, C. W. T.; Hong, Y.; Chen, S.; Zhao, E.; Lam, J. W. Y.; Tang, B. Z. A Photostable AIE Luminogen for Specific Mitochondrial Imaging and Tracking. *J. Am. Chem. Soc.* **2013**, *135*, 62–65.
- (581) Gao, M.; Sim, C. K.; Leung, C. W. T.; Hu, Q.; Feng, G.; Xu, F.; Tang, B. Z.; Liu, B. A Fluorescent Light-Up Probe with AIE Characteristics for Specific Mitochondrial Imaging to Identify Differentiating Brown Adipose Cells. *Chem. Commun.* **2014**, *50*, 8312–8315.
- (582) Lee, P.; Swarbrick, M. M.; Ho, K. K. Y. Brown Adipose Tissue in Adult Humans: A Metabolic Renaissance. *Endocr. Rev.* **2013**, *34*, 413–438.
- (583) Bartelt, A.; Heeren, J. Adipose Tissue Browning and Metabolic Health. *Nat. Rev. Endocrinol.* **2014**, *10*, 24–36.
- (584) Settembre, C.; Fraldi, A.; Medina, D. L.; Ballabio, A. Signals from the Lysosome: A Control Centre for Cellular Clearance and Energy Metabolism. *Nat. Rev. Mol. Cell Biol.* **2013**, *14*, 283–296.
- (585) Warren, C. D.; Alroy, J. Morphological, Biochemical and Molecular Biology Approaches for the Diagnosis of Lysosomal Storage Diseases. *J. Vet. Diagn. Investig.* **2000**, *12*, 483–496.
- (586) Martin, S.; Parton, R. G. Opinion: Lipid Droplets: A Unified View of a Dynamic Organelle. *Nat. Rev. Mol. Cell Biol.* **2006**, *7*, 373–378.
- (587) Murphy, D. J. The Biogenesis and Functions of Lipid Bodies in Animals, Plants and Microorganisms. *Prog. Lipid Res.* **2001**, *40*, 325–438.
- (588) Zehmer, J. K.; Huang, Y.; Peng, G.; Pu, J.; Anderson, R. G.; Liu, P. A Role for Lipid Droplets in Inter-Membrane Lipid Traffic. *Proteomics* **2009**, *9*, 914–921.
- (589) Zhang, H.; Wang, Y.; Li, J.; Yu, J.; Pu, J.; Li, L.; Zhang, H.; Zhang, S.; Peng, G.; Yang, F.; et al. Proteome of Skeletal Muscle Lipid Droplet Reveals Association with Mitochondria and Apolipoprotein A-I. *J. Proteome Res.* **2011**, *10*, 4757–4768.
- (590) Athenstaedt, K.; Zweyck, D.; Jandrositz, A.; Kohlwein, S. D.; Daum, G. Identification and Characterization of Major Lipid Particle Proteins of the Yeast *Saccharomyces Cerevisiae*. *J. Bacteriol.* **1999**, *181*, 6441–6448.
- (591) Blanchette-Mackie, E. J.; Dwyer, N. K.; Barber, T.; Coxey, R. A.; Takeda, T.; Rondinone, C. M.; Theodorakis, J. L.; Greenberg, A. S.; Londos, C. Perilipin is Located on the Surface Layer of Intracellular Lipid Droplets in Adipocytes. *J. Lipid Res.* **1995**, *36*, 1211–1226.
- (592) Cohen, A. W.; Razani, B.; Schubert, W.; Williams, T. M.; Wang, X. B.; Lyengar, P.; Brasaemle, D. L.; Scherer, P. E.; Lisanti, M. P. Role of Caveolin-1 in the Modulation of Lipolysis and Lipid Droplet Formation. *Diabetes* **2004**, *53*, 1261–1270.
- (593) Bascom, R. A.; Chan, H.; Rachubinski, R. A. Peroxisome Biogenesis Occurs in an Unsynchronized Manner in Close Association with the Endoplasmic Reticulum in Temperature-Sensitive *Yarrowia lipolytica* Pex3p Mutants. *Mol. Biol. Cell* **2003**, *14*, 939–957.
- (594) Alberti, K. G. M. M.; Zimmet, P.; Shaw, J. The Metabolic Syndrome—A New Worldwide Definition. *Lancet* **2005**, *366*, 1059–1062.
- (595) Wijffels, R. H.; Barbosa, M. J. An Outlook on Microalgal Biofuels. *Science* **2010**, *329*, 796–799.
- (596) Greenspan, P.; Mayer, E. P.; Fowler, S. D. Nile Red: A Selective Fluorescent Stain for Intracellular Lipid Droplets. *J. Cell Biol.* **1985**, *100*, 965–973.
- (597) Kim, E.; Lee, S.; Park, S. B. A Seoul-Fluor-Based Bioprobe for Lipid Droplets and Its Application in Image-Based High Throughput Screening. *Chem. Commun.* **2012**, *48*, 2331–2333.
- (598) Lee, Y.; Na, S.; Lee, S.; Jeon, N. L.; Park, S. B. Optimization of Seoul-Fluor-Based Lipid Droplet Bioprobes and Their Application in Microalgae for Bio-Fuel Study. *Mol. Biosyst.* **2013**, *9*, 952–956.
- (599) Lee, S.; Kim, E.; Park, S. B. Discovery of Autophagy Modulators through the Construction of a High-content Screening Platform via Monitoring of Lipid Droplets. *Chem. Sci.* **2013**, *4*, 3282–3287.
- (600) Wang, E.; Zhao, E.; Hong, Y.; Lam, J. W. Y.; Tang, B. Z. A Highly Selective AIE Fluorogen for Lipid Droplet Imaging in Live Cells and Green Algae. *J. Mater. Chem. B* **2014**, *2*, 2013–2019.
- (601) *Essential Cell Biology*, 3rd ed.; Albers, B., Bray, D., Hopkin, K., Johnson, A., Lewis, J., Raff, M., Roberts, K., Walter, P., Eds.; Garland Science: New York, 2009.
- (602) Casey, J. R.; Grinstein, S.; Orlowski, J. Sensors and Regulators of Intracellular pH. *Nat. Rev. Mol. Cell Biol.* **2010**, *11*, 50–61.
- (603) Chen, S.; Liu, J.; Liu, Y.; Su, H.; Hong, Y.; Jim, C. K. W.; Kwok, R. T. K.; Zhao, N.; Qin, W.; Lam, J. W. Y.; et al. An AIE-Active Hemicyanine Fluorogen with Stimuli-Responsive Red/Blue Emission: Extending the pH Sensing Range by "Switch + Knob" Effect. *Chem. Sci.* **2012**, *3*, 1804–1809.
- (604) Chen, S.; Hong, Y.; Liu, Y.; Liu, J.; Leung, C. W. T.; Li, M.; Kwok, R. T. K.; Zhao, E.; Lam, J. W. Y.; Yu, Y.; et al. Full-Range Intracellular pH Sensing by an Aggregation-Induced Emission-Active Two-Channel Ratiometric Fluorogen. *J. Am. Chem. Soc.* **2013**, *135*, 4926–4929.
- (605) Burd, C.; Sorrentino, J.; Clark, K.; Darr, D.; Krishnamurthy, J.; Deal, A.; Bardeesy, N.; Castrillon, D.; Beach, D.; Sharpless, N. Monitoring Tumorigenesis and Senescence *in vivo* with A p16-(INK4a)-Luciferase Model. *Cell* **2013**, *152*, 340–351.
- (606) Yu, Z.; Schmaltz, R. M.; Bozeman, T. C.; Paul, R.; Rishel, M. J.; Tsosie, K. S.; Hecht, S. M. Selective Tumor Cell Targeting by the Disaccharide Moiety of Bleomycin. *J. Am. Chem. Soc.* **2013**, *135*, 2883–2886.
- (607) Palaniappan, K. K.; Ramirez, R. M.; Bajaj, V. S.; Wemmer, D. E.; Pines, A.; Francis, M. B. Molecular Imaging of Cancer Cells Using a Bacteriophage-Based <sup>129</sup>Xe NMR Biosensor. *Angew. Chem.* **2013**, *125*, 4949–4953.
- (608) Yu, G.; Tang, G.; Huang, F. Supramolecular Enhancement of Aggregation-Induced Emission and Its Application in Cancer Cell Imaging. *J. Mater. Chem. C* **2014**, *2*, 6609–6617.
- (609) Huang, Y.; Hu, F.; Zhao, R.; Zhang, G.; Yang, H.; Zhang, D. Tetraphenylethylene Conjugated with a Specific Peptide as a Fluorescence Turn-On Bioprobe for the Highly Specific Detection and Tracing of Tumor Markers in Live Cancer Cells. *Chem. - Eur. J.* **2014**, *20*, 158–164.

- (610) Huang, Y.; Zhao, R.; Fu, Y.; Zhang, Q.; Xiong, S.; Li, L.; Zhou, R.; Liu, G.; Chen, Y. Highly Specific Targeting and Imaging of Live Cancer Cells by Using a Peptide Probe Developed from Rationally Designed Peptides. *ChemBioChem* **2011**, *12*, 1209–1215.
- (611) Shao, G.; Zhou, R.; Zhang, Q.; Zhang, Y.; Liu, J. J.; Rui, J.; Wei, X.; Ye, D. Molecular Cloning and Characterization of LAPTM4B, A Novel Gene Upregulated in Hepatocellular Carcinoma. *Oncogene* **2003**, *22*, 5060–5069.
- (612) Li, Y.; Zou, L.; Li, Q.; Haibe-Kains, B.; Tian, R.; Li, Y.; Desmedt, C.; Sotiriou, C.; Szallasi, Z.; Iglesias, J. D.; et al. Amplification of LAPTM4B and YWHAZ Contributes to Chemotherapy Resistance and Recurrence of Breast Cancer. *Nat. Med.* **2010**, *16*, 214–218.
- (613) Li, Y.; Zhang, Q.; Tian, R.; Wang, Q.; Zhao, J. J.; Iglesias, J. D.; Wang, Z. C.; Richardson, A. L. Lysosomal Transmembrane Protein LAPTM4B Promotes Autophagy and Tolerance to Metabolic Stress in Cancer Cells. *Cancer Res.* **2011**, *71*, 7481–7489.
- (614) Wang, S.; Zhang, Q.; Zhou, R. Relationship between LAPTM4B Gene Polymorphism and Susceptibility of Primary Liver Cancer. *Ann. Oncol.* **2012**, *23*, 1864–1869.
- (615) Fukumura, D.; Xu, L.; Chen, Y.; Gohongi, T.; Seed, B.; Jain, R. K. Hypoxia and Acidosis Independently Up-Regulate Vascular Endothelial Growth Factor Transcription in Brain Tumors *in vivo*. *Cancer Res.* **2001**, *61*, 6020–6024.
- (616) Weerakkody, D.; Moshnikova, A.; Thakur, M. S.; Moshnikova, V.; Daniels, J.; Engelmann, D. M.; Andreev, O. A.; Reshetnyak, Y. K. Family of pH (Low) Insertion Peptides for Tumor Targeting. *Proc. Natl. Acad. Sci. U. S. A.* **2013**, *110*, 5834–5839.
- (617) Yao, L.; Daniels, J.; Moshnikova, A.; Kuznetsov, S.; Ahmed, A.; Engelmann, D. M.; Reshetnyak, Y. K.; Andreev, O. A. pH-LIP Peptide Targets Nanogold Particles to Tumors. *Proc. Natl. Acad. Sci. U. S. A.* **2013**, *110*, 465–470.
- (618) Vaux, D. L.; Korsmeyer, S. J. Cell Death in Development. *Cell* **1999**, *96*, 245–254.
- (619) Grüter, M. G. Caspases: Key Players in Programmed Cell Death. *Curr. Opin. Struct. Biol.* **2000**, *10*, 649–655.
- (620) Okada, H.; Mak, T. Pathways of Apoptotic and Non-apoptotic Death in Tumour Cells. *Nat. Rev. Cancer* **2004**, *4*, 592–603.
- (621) Fischer, U.; Schulze-Osthoff, K. New Approaches and Therapeutics Targeting Apoptosis in Disease. *Pharm. Rev.* **2005**, *57*, 187–215.
- (622) Ouakine, F.; Quirino, J. P.; Garrelly, L.; Romestand, B.; Zou, T.; Cottet, H. Simultaneous Electrokinetic and Hydrodynamic Injection for High Sensitivity Bacteria Analysis in Capillary Electrophoresis. *Anal. Chem.* **2011**, *83*, 4949–4954.
- (623) Cheng, M. S.; Lau, S. H.; Chow, V. T.; Toh, C.-S. Membrane-Based Electrochemical Nanobiosensor for Escherichia Coli Detection and Analysis of Cells Viability. *Environ. Sci. Technol.* **2011**, *45*, 6453–6459.
- (624) Miyanaga, L.; Takano, S.; Morono, Y.; Hori, K.; Unno, H.; Tanji, Y. Optimization of Distinction between Viable and Dead Cells by Fluorescent Staining Method and Its Application to Bacterial Consortia. *Biochem. Eng. J.* **2007**, *37*, 56–61.
- (625) (a) Zhao, E.; Chen, Y.; Chen, S.; Deng, H.; Gui, C.; Leung, C. W. T.; Hong, Y.; Lam, J. W. Y.; Tang, B. Z. A Luminogen with Aggregation-Induced Emission Characteristic for Wash-Free Bacterial Imaging, High-Throughput Antibiotics Screening and Bacterial Susceptibility Evaluation. *Adv. Mater.* **2015**, DOI: 10.1002/adma.201501972. (b) Zhao, E.; Chen, Y.; Wang, H.; Chen, S.; Lam, J. W. Y.; Leung, C. W. T.; Hong, Y.; Tang, B. Z. Light-Enhanced Bacterial Killing and Wash-Free Imaging Based on AIE Fluorogen. *ACS Appl. Mater. Interfaces* **2015**, *7*, 7180–7188.
- (626) Li, Y.; Hu, X.; Tian, S.; Li, Y.; Zhang, G.; Zhang, G.; Liu, S. Polyion Complex Micellar Nanoparticles for Integrated Fluorometric Detection and Bacteria Inhibition in Aqueous Media. *Biomaterials* **2014**, *35*, 1618–1626.
- (627) Zhang, X.; Zhang, X.; Tao, L.; Chi, Z.; Xu, J.; Wei, Y. Aggregation Induced Emission-Based Fluorescent Nanoparticles: Fabrication Methodologies and Biomedical Applications. *J. Mater. Chem. B* **2014**, *2*, 4398–4414.
- (628) Li, K.; Liu, B. Polymer-Encapsulated Organic Nanoparticles for Fluorescence and Photoacoustic Imaging. *Chem. Soc. Rev.* **2014**, *43*, 6570–6597.
- (629) Zhang, X.; Zhang, X.; Yang, B.; Liu, M.; Liu, W.; Chen, Y.; Wei, Y. Facile Fabrication and Cell Imaging Applications of Aggregation-Induced Emission Dye-Based Fluorescent Organic Nanoparticles. *Polym. Chem.* **2013**, *4*, 4317–4321.
- (630) Lim, C. K.; Kim, S.; Kwon, I. C.; Ahn, C. H.; Park, S. Y. Dye-Condensed Biopolymeric Hybrids: Chromophoric Aggregation and Self-Assembly toward Fluorescent Bionanoparticles for Near Infrared Bioimaging. *Chem. Mater.* **2009**, *21*, 5819–5825.
- (631) Huang, M.; Ma, Z. S.; Khor, E.; Lim, L. Y. Uptake of FITC-Chitosan Nanoparticles by A<sub>549</sub> Cells. *Pharm. Res.* **2002**, *19*, 1488–1494.
- (632) Jia, X. Y.; Chen, X.; Xu, Y. L.; Han, X. Y.; Xu, Z. R. Tracing Transport of Chitosan Nanoparticles and Molecules in Caco-2 Cells by Fluorescent Labeling. *Carbohydr. Polym.* **2009**, *78*, 323–329.
- (633) Zhang, Y.; Chen, Y.; Li, X.; Zhang, J.; Chen, J.; Xu, B.; Fu, X.; Tian, W. Folic Acid-Functionalized AIE Pdots Based on Amphiphilic PCL-b-PEG for Targeted Cell Imaging. *Polym. Chem.* **2014**, *5*, 3824–3830.
- (634) Zhang, X.; Zhang, X.; Yang, B.; Liu, M.; Liu, W.; Chen, Y.; Wei, Y. Fabrication of Aggregation Induced Emission Dye-Based Fluorescent Organic Nanoparticles via Emulsion Polymerization and Their Cell Imaging Applications. *Polym. Chem.* **2014**, *5*, 399–404.
- (635) Zhang, X.; Zhang, X.; Yang, B.; Liu, M.; Liu, W.; Chen, Y.; Wei, Y. Polymerizable Aggregation-Induced Emission Dye-Based Fluorescent Nanoparticles for Cell Imaging Applications. *Polym. Chem.* **2014**, *5*, 356–360.
- (636) Li, H.; Zhang, X.; Zhang, X.; Yang, B.; Yang, Y.; Wei, Y. Stable Cross-Linked Fluorescent Polymeric Nanoparticles for Cell Imaging. *Macromol. Rapid Commun.* **2014**, *35*, 1661–1667.
- (637) Zhang, X.; Zhang, X.; Yang, B.; Hui, J.; Liu, M.; Chi, Z.; Liu, S.; Xu, J.; Wei, Y. A Novel Method for Preparing AIE Dye Based Cross-Linked Fluorescent Polymeric Nanoparticles for Cell Imaging. *Polym. Chem.* **2014**, *5*, 683–688.
- (638) Zhang, X.; Zhang, X.; Yang, B.; Hui, J.; Liu, M.; Chi, Z.; Liu, S.; Xu, J.; Wei, Y. Facile Preparation and Cell Imaging Applications of Fluorescent Organic Nanoparticles That Combine AIE Dye and Ring-Opening Polymerization. *Polym. Chem.* **2014**, *5*, 318–322.
- (639) Zhang, X.; Zhang, X.; Yang, B.; Hui, J.; Liu, M.; Liu, W.; Chen, Y.; Wei, Y. PEGylation and Cell Imaging Applications of AIE Based Fluorescent Organic Nanoparticles via Ring-Opening Reaction. *Polym. Chem.* **2014**, *5*, 689–693.
- (640) Zhang, X.; Zhang, X.; Yang, B.; Yang, Y.; Wei, Y. Renewable Itaconic Acid Based Cross-Linked Fluorescent Polymeric Nanoparticles for Cell Imaging. *Polym. Chem.* **2014**, *5*, 5885–5889.
- (641) Zhang, X.; Zhang, X.; Yang, B.; Hui, J.; Liu, M.; Wei, Y. Facile Fabrication of AIE-Based Stable Cross-Linked Fluorescent Organic Nanoparticles for Cell Imaging. *Colloids Surf., B* **2014**, *116*, 739–744.
- (642) Liu, M.; Zhang, X.; Yang, B.; Liu, L.; Deng, F.; Zhang, X.; Wei, Y. Polylysine Crosslinked AIE Dye Based Fluorescent Organic Nanoparticles for Biological Imaging Applications. *Macromol. Biosci.* **2014**, *14*, 1260–1267.
- (643) Zhang, X.; Zhang, X.; Yang, B.; Hui, J.; Liu, M.; Chi, Z.; Liu, S.; Xu, J.; Wei, Y. Novel Biocompatible Cross-Linked Fluorescent Polymeric Nanoparticles Based on an AIE Monomer. *J. Mater. Chem. C* **2014**, *2*, 816–820.
- (644) Lu, H.; Sum, F.; Mei, Q.; Tian, Y.; Tian, W.; Johnson, R. H.; Meldrum, D. R. Using Fluorine-Containing Amphiphilic Random Copolymers to Manipulate the Quantum Yields of Aggregation-Induced Emission Fluorophores in Aqueous Solutions and the Use of These Polymers for Fluorescent Bioimaging. *J. Mater. Chem.* **2012**, *22*, 9890–9900.
- (645) Feng, G.; Tay, C. Y.; Chui, Q. X.; Liu, R.; Tomczak, N.; Liu, J.; Tang, B. Z.; Leong, D. T.; Liu, B. Ultrabright Organic Dots with Aggregation-Induced Emission Characteristics for Cell Tracking. *Biomaterials* **2014**, *35*, 8669–8677.
- (646) Li, K.; Zhu, Z.; Cai, P.; Liu, R.; Tomczak, N.; Ding, D.; Liu, J.; Qin, W.; Zhao, Z.; Hu, Y.; et al. Organic Dots with Aggregation-Induced

- Emission (AIE Dots) Characteristics for Dual-Color Cell Tracing. *Chem. Mater.* **2013**, *25*, 4181–4187.
- (647) Qin, W.; Li, K.; Feng, G.; Li, M.; Yang, Z.; Liu, B.; Tang, B. Z. Bright and Photostable Organic Fluorescent Dots with Aggregation-Induced Emission Characteristics for Noninvasive Long-Term Cell Imaging. *Adv. Funct. Mater.* **2014**, *24*, 635–643.
- (648) Wang, D.; Qian, J.; He, S.; Park, J. S.; Lee, K.-S.; Han, S.; Mu, Y. Aggregation-Enhanced Fluorescence in PEGylated Phospholipid Nanomicelles for *in vivo* Imaging. *Biomaterials* **2011**, *32*, 5880–5888.
- (649) Ding, D.; Li, K.; Zhu, Z.; Pu, K. Y.; Hu, Y.; Jiang, X.; Liu, B. Conjugated Polyelectrolyte–Cisplatin Complex Nanoparticles for Simultaneous *in vivo* Imaging and Drug Tracking. *Nanoscale* **2011**, *3*, 1997–2002.
- (650) Ding, D.; Mao, D.; Li, K.; Wang, X.; Qin, W.; Liu, R.; Chiam, D. S.; Tomczak, N.; Yang, Z.; Tang, B. Z.; et al. Precise and Long-Term Tracking of Adipose-Derived Stem Cells and Their Regenerative Capacity via Superb Bright and Stable Organic Nanodots. *ACS Nano* **2014**, *8*, 12620–12631.
- (651) Gimble, J. M.; Katz, A. J.; Bunnell, B. A. Adipose-Derived Stem Cells for Regenerative Medicine. *Circ. Res.* **2007**, *100*, 1249–1260.
- (652) Miranville, A.; Heeschen, C.; Sengenès, C.; Curat, C. A.; Busse, R.; Bouloumié, A. Improvement of Postnatal Neovascularization by Human Adipose Tissue-Derived Stem Cells. *Circulation* **2004**, *110*, 349–355.
- (653) Low, P. S.; Antony, A. C. Folate Receptor-Targeted Drugs for Cancer and Inflammatory Diseases. *Adv. Drug Delivery Rev.* **2004**, *56*, 1055–1058.
- (654) Li, K.; Jiang, Y.; Ding, D.; Zhang, X.; Liu, Y.; Hua, J.; Feng, S. S.; Liu, B. Folic Acid-Functionalized Two-photon Absorbing Nanoparticles for Targeted MCF-7 Cancer Cell Imaging. *Chem. Commun.* **2011**, *47*, 7323–7325.
- (655) Geng, J.; Li, K.; Ding, D.; Zhang, X.; Qin, W.; Liu, J.; Tang, B. Z.; Liu, B. Lipid-PEG-Folate Encapsulated Nanoparticles with Aggregation Induced Emission Characteristics: Cellular Uptake Mechanism and Two-Photon Fluorescence Imaging. *Small* **2012**, *8*, 3655–3663.
- (656) Qin, W.; Ding, D.; Liu, J.; Yuan, W. Z.; Hu, Y.; Liu, B.; Tang, B. Z. Biocompatible Nanoparticles with Aggregation-Induced Emission Characteristics as Far-Red/Near-Infrared Fluorescent Bioprobes for *in vitro* and *in vivo* Imaging Applications. *Adv. Funct. Mater.* **2012**, *22*, 771–779.
- (657) Wang, D.; Qian, J.; Qin, W.; Qin, A.; Tang, B. Z.; He, S. Biocompatible and Photostable AIE Dots with Red Emission for *in vivo* Two-Photon Bioimaging. *Sci. Rep.* **2014**, *4*, 4279.
- (658) Larson, D. R.; Zipfel, W. R.; Williams, R. M.; Clark, S. W.; Bruchez, M. P.; Wise, F. W.; Webb, W. W. Water-Soluble Quantum Dots for Multiphoton Fluorescence Imaging *in vivo*. *Science* **2003**, *300*, 1434–1436.
- (659) Schenke-Layland, K.; Riemann, I.; Damour, O.; Stock, U. A.; König, K. Two-Photon Microscopes and *in vivo* Multiphoton Tomographs—Powerful Diagnostic Tools for Tissue Engineering and Drug Delivery. *Adv. Drug Delivery Rev.* **2006**, *58*, 878–896.
- (660) Frangioni, J. V. *In vivo* Near-infrared Fluorescence Imaging. *Curr. Opin. Chem. Biol.* **2003**, *7*, 626–634.
- (661) Helmchen, F.; Denk, W. Deep Tissue Two-Photon Microscopy. *Nat. Methods* **2005**, *2*, 932–940.
- (662) He, G. S.; Tan, L.-S.; Zheng, Q.; Prasad, P. N. Multiphoton Absorbing Materials: Molecular Designs, Characterizations, and Applications. *Chem. Rev.* **2008**, *108*, 1245–1330.
- (663) Ding, D.; Li, K.; Qin, W.; Zhan, R.; Hu, Y.; Liu, J.; Tang, B. Z.; Liu, B. Conjugated Polymer Amplified Far-Red/Near-Infrared Fluorescence from Nanoparticles with Aggregation-Induced Emission Characteristics for Targeted *in vivo* Imaging. *Adv. Healthcare Mater.* **2013**, *2*, 500–507.
- (664) Geng, J.; Li, K.; Qin, W.; Ma, L.; Gurzadyan, G. G.; Tang, B. Z.; Liu, B. Eccentric Loading of Fluorogen with Aggregation-Induced Emission in PLGA Matrix Increases Nanoparticle Fluorescence Quantum Yield for Targeted Cellular Imaging. *Small* **2013**, *9*, 2012–2019.
- (665) Zhang, X.; Zhang, X.; Yang, B.; Zhang, Y.; Liu, M.; Liu, W.; Chen, Y.; Wei, Y. Fabrication of Water-Dispersible and Biocompatible Red Fluorescent Organic Nanoparticles via PEGylation of Aggregate Induced Emission Enhancement Dye and Their Cell Imaging Applications. *Colloids Surf., B* **2014**, *113*, 435–441.
- (666) Yang, Y.; An, F.; Liu, Z.; Zhang, X.; Zhou, M.; Li, W.; Hao, X.; Lee, C.-S.; Zhang, X. Ultrabright and Ultrastable Near-Infrared Dye Nanoparticles for *in vitro* and *in vivo* Bioimaging. *Biomaterials* **2012**, *33*, 7803–7809.
- (667) Wu, W.-C.; Chen, C.-Y.; Tian, Y.; Jang, S.-H.; Hong, Y.; Liu, Y.; Hu, R.; Tang, B. Z.; Lee, Y.-T.; Chen, C.-T.; et al. Enhancement of Aggregation-Induced Emission in Dye-Encapsulating Polymeric Micelles for Bioimaging. *Adv. Funct. Mater.* **2010**, *20*, 1413–1423.
- (668) *Chemiluminescence in Analytical Chemistry*; Garcia-Campana, A. M., Baeyens, W. R. G., Eds.; Marcel Dekker: New York, 2001.
- (669) Roda, A.; Guardigli, M.; Pasini, P.; Mirasoli, M.; Michelini, E.; Musiani, M. Bio- and Chemiluminescence Imaging in Analytical Chemistry. *Anal. Chim. Acta* **2005**, *541*, 25–35.
- (670) Lee, Y.-D.; Lim, C.-K.; Singh, A.; Koh, J.; Kim, J.; Kwon, I. C.; Kim, S. Dye/Peroxalate Aggregated Nanoparticles with Enhanced and Tunable Chemiluminescence for Biomedical Imaging of Hydrogen Peroxide. *ACS Nano* **2012**, *6*, 6759–6766.
- (671) Mahtab, F.; Hong, Y. N.; Liu, J. Z.; Yu, Y.; Lam, J. W. Y.; Qin, A. J.; Lu, P.; Tang, B. Z. Fabrication of Fluorescent Silica Nanoparticles Hybridized with AIE Luminogens and Exploration of Their Applications as Nanobiosensors in Intracellular Imaging. *Chem. - Eur. J.* **2010**, *16*, 4266–4272.
- (672) Mahtab, F.; Yu, Y.; Lam, J. W. Y.; Liu, J.; Zhang, B.; Lu, P.; Zhang, X.; Tang, B. Z. Fabrication of Silica Nanoparticles with Both Efficient Fluorescence and Strong Magnetization and Exploration of Their Biological Applications. *Adv. Funct. Mater.* **2011**, *21*, 1733–1740.
- (673) Li, M.; Lam, J. W. Y.; Mahtab, F.; Chen, S.; Zhang, W.; Hong, Y.; Xiong, J.; Zheng, Q.; Tang, B. Z. Biotin-Decorated Fluorescent Silica Nanoparticles with Aggregation-Induced Emission Characteristics: Fabrication, Cytotoxicity and Biological Applications. *J. Mater. Chem. B* **2013**, *1*, 676–684.
- (674) Mahtab, F.; Lam, J. W. Y.; Yu, Y.; Liu, J.; Yuan, W.; Lu, P.; Tang, B. Z. Covalent Immobilization of Aggregation-Induced Emission Luminogens in Silica Nanoparticles through Click Reaction. *Small* **2011**, *7*, 1448–1455.
- (675) Zhang, X.; Zhang, X.; Yang, B.; Liu, L.; Hui, J.; Liu, M.; Chen, Y.; Wei, Y. Aggregation-Induced Emission Dye Based Luminescent Silica Nanoparticles: Facile Preparation, Biocompatibility Evaluation and Cell Imaging Applications. *RSC Adv.* **2014**, *4*, 10060–10066.
- (676) Zhang, X.; Zhang, X.; Wang, S.; Liu, M.; Zhang, Y.; Tao, L.; Wei, Y. Facile Incorporation of Aggregation-Induced Emission Materials into Mesoporous Silica Nanoparticles for Intracellular Imaging and Cancer Therapy. *ACS Appl. Mater. Interfaces* **2013**, *5*, 1943–1947.
- (677) Cheng, H.; Qin, W.; Zhu, Z. F.; Qian, J.; Qin, A. J.; Tang, B. Z.; He, S. L. Nanoparticles with Aggregation-Induced Emission for Monitoring Long Time Cell Membrane Interactions. *Prog. Electromagn. Res.* **2013**, *140*, 313–325.
- (678) Mulder, W. J. M.; Griffioen, A. W.; Strijkers, G. J.; Cormode, D. P.; Nicolay, K.; Fayad, Z. A. Magnetic and Fluorescent Nanoparticles for Multimodality Imaging. *Nanomedicine* **2007**, *2*, 307–324.
- (679) Chambers, A. F.; Groom, A. C.; MacDonald, I. C. Metastasis: Dissemination and Growth of Cancer Cells in Metastatic Sites. *Nat. Rev. Cancer* **2002**, *2*, 563–572.
- (680) Bhirde, A.; Xie, J.; Swierczewska, M.; Chen, X. Nanoparticles for Cell Labeling. *Nanoscale* **2011**, *3*, 142–153.
- (681) Choi, J.-S.; Park, J. C.; Nah, H.; Woo, S.; Oh, J.; Kim, K. M.; Cheon, G. J.; Chang, Y.; Yoo, J.; Cheon, J. A Hybrid Nanoparticle Probe for Dual-Modality Positron Emission Tomography and Magnetic Resonance Imaging. *Angew. Chem., Int. Ed.* **2008**, *47*, 6259–6262.
- (682) Li, K.; Ding, D.; Huo, D.; Pu, K. Y.; Thao, N. N. P.; Hu, Y.; Li, Z.; Liu, B. Conjugated Polymer Based Nanoparticles as Dual-Modal Probes for Targeted *in vivo* Fluorescence and Magnetic Resonance Imaging. *Adv. Funct. Mater.* **2012**, *22*, 3107–3115.

- (683) Lee, H.-Y.; Li, Z.; Chen, K.; Hsu, A. R.; Xu, C.; Xie, J.; Sun, S.; Chen, X. PET/MRI Dual-Modality Tumor Imaging Using Arginine-Glycine-Aspartic (RGD)-Conjugated Radiolabeled Iron Oxide Nanoparticles. *J. Nucl. Med.* **2008**, *49*, 1371–1379.
- (684) Li, K.; Ding, D.; Prashant, C.; Qin, W.; Yang, C. T.; Tang, B. Z.; Liu, B. Gadolinium-Functionalized Aggregation-Induced Emission Dots as Dual-Modality Probes for Cancer Metastasis Study. *Adv. Healthcare Mater.* **2013**, *2*, 1600–1605.
- (685) Chen, Y.; Li, M.; Hong, Y.; Lam, J. W. Y.; Zheng, Q.; Tang, B. Z. Dual-Modal MRI Contrast Agent with Aggregation-Induced Emission Characteristic for Liver Specific Imaging with Long Circulation Lifetime. *ACS Appl. Mater. Interfaces* **2014**, *6*, 10783–10791.
- (686) Xue, X.; Zhao, Y.; Dai, L.; Zhang, X.; Hao, X.; Zhang, C.; Huo, S.; Liu, J.; Liu, C.; Kumar, A.; et al. Spatiotemporal Drug Release Visualized through a Drug Delivery System with Tunable Aggregation-Induced Emission. *Adv. Mater.* **2014**, *26*, 712–717.
- (687) Zhang, C.; Jin, S.; Li, S.; Xue, X.; Liu, J.; Huang, Y.; Jiang, Y.; Chen, W.-Q.; Zou, G.; Liang, X.-J. Imaging Intracellular Anticancer Drug Delivery by Self-Assembly Micelles with Aggregation-Induced Emission (AIE Micelles). *ACS Appl. Mater. Interfaces* **2014**, *6*, 5212–5220.
- (688) Chen, J.-I.; Wu, W.-C. Fluorescent Polymeric Micelles with Aggregation-Induced Emission Properties for Monitoring the Encapsulation of Doxorubicin. *Macromol. Biosci.* **2013**, *13*, 623–632.
- (689) Yuan, Y.; Chen, Y.; Tang, B. Z.; Liu, B. A Targeted Theranostic Platinum(IV) Prodrug Containing a Luminogen with Aggregation-Induced Emission (AIE) Characteristics for *in situ* Monitoring of Drug Activation. *Chem. Commun.* **2014**, *50*, 3868–3870.
- (690) Yuan, Y.; Kwok, R. T. K.; Tang, B. Z.; Liu, B. Targeted Theranostic Platinum(IV) Prodrug with a Built-In Aggregation-Induced Emission Light-Up Apoptosis Sensor for Noninvasive Early Evaluation of Its Therapeutic Responses *in Situ*. *J. Am. Chem. Soc.* **2014**, *136*, 2546–2554.
- (691) Yuan, Y.; Kwok, R. T. K.; Zhang, R.; Tang, B. Z.; Liu, B. Targeted Theranostic Prodrugs Based on an Aggregation-Induced Emission (AIE) Luminogen for Real-time Dual-Drug Tracking. *Chem. Commun.* **2014**, *50*, 11465–11468.
- (692) Pinzani, V.; Bressolle, F.; Haug, I. J.; Galtier, M.; Blayac, J. P.; Balmès, P. Cisplatin-Induced Renal Toxicity and Toxicity-Modulating Strategies: A Review. *Cancer Chemother. Pharmacol.* **1994**, *35*, 1–9.
- (693) Wang, X. Y.; Guo, Z. J. Targeting and Delivery of Platinum-Based Anticancer Drugs. *Chem. Soc. Rev.* **2013**, *42*, 202–224.
- (694) Graf, N.; Lippard, S. J. Redox Activation of Metal-Based Prodrugs as a Strategy for Drug Delivery. *Adv. Drug Delivery Rev.* **2012**, *64*, 993–1004.
- (695) Hickman, J. A. Apoptosis Induced by Anticancer Drugs. *Cancer Metastasis Rev.* **1992**, *11*, 121–139.
- (696) Thigpen, J. T. Phase III Trial of Doxorubicin with or without Cisplatin in Advanced Endometrial Carcinoma: A Gynecologic Oncology Group Study. *J. Clin. Oncol.* **2004**, *22*, 3902–3908.
- (697) Allison, R. R.; Downie, G. H.; Guenca, R.; Hu, X.-H.; Childs, C. J. H.; Sibata, C. H. Photosensitizers in Clinical PDT. *Photodiagn. Photodyn. Ther.* **2004**, *1*, 27–42.
- (698) Wilson, B. C.; Patterson, M. S. The Physics, Biophysics and Technology of Photodynamic Therapy. *Phys. Med. Biol.* **2008**, *53*, R61–R109.
- (699) Celli, J.; Spring, B.; Rizvi, I.; Evans, C.; Samkoe, K.; Verma, S.; Pogue, B.; Hasan, T. Imaging and Photodynamic Therapy: Mechanisms, Monitoring, and Optimization. *Chem. Rev.* **2010**, *110*, 2795–2838.
- (700) Lovell, J. F.; Liu, T. W. B.; Chen, J.; Zheng, G. Activatable Photosensitizers for Imaging and Therapy. *Chem. Rev.* **2010**, *110*, 2839–2857.
- (701) Hu, F.; Huang, Y.; Zhang, G.; Zhao, R.; Yang, H.; Zhang, D. Targeted Bioimaging and Photodynamic Therapy of Cancer Cells with an Activatable Red Fluorescent Bioprobe. *Anal. Chem.* **2014**, *86*, 7987–7995.
- (702) He, H. R.; Mortellaro, M. A.; Leiner, M. J. P.; Fraatz, R. J.; Tusa, J. K. A Fluorescent Sensor with High Selectivity and Sensitivity for Potassium in Water. *J. Am. Chem. Soc.* **2003**, *125*, 1468–1469.
- (703) Kim, J.; McQuade, D. T.; McHugh, S. K.; Swager, T. M. Ion-Specific Aggregation in Conjugated Polymers: Highly Sensitive and Selective Fluorescent Ion Chemosensors. *Angew. Chem., Int. Ed.* **2000**, *39*, 3868–3872.
- (704) Schuweiler, N.; Klok, H.-A. A Potassium-Selective Quartz Crystal Microbalance Sensor Based on Crown-Ether Functionalized Polymer Brushes. *Adv. Mater.* **2010**, *22*, 3251–3255.
- (705) Xia, W.-S.; Schmehl, R. H.; Li, C.-J. A Highly Selective Fluorescent Chemosensor for K<sup>+</sup> from a Bis-15-Crown-5 Derivative. *J. Am. Chem. Soc.* **1999**, *121*, 5599–5600.
- (706) Wang, X.; Hu, J.; Liu, T.; Zhang, G.; Liu, S. Highly Sensitive and Selective Fluorometric Off-On K<sup>+</sup> Probe Constructed via Host–Guest Molecular Recognition and Aggregation-Induced Emission. *J. Mater. Chem.* **2012**, *22*, 8622–8628.
- (707) Ratte, H. T. Bioaccumulation and Toxicity of Silver Compounds: A Review. *Environ. Toxicol. Chem.* **1999**, *18*, 89–108.
- (708) Kazuyuki, M.; Nobuo, H.; Takatoshi, K.; Yuriko, K.; Osamu, H.; Yoshihisa, I.; Kiyoko, S. Sensitive Method for Detection and Semiquantification of Bence Jones Protein by Cellulose Acetate Membrane Electrophoresis Using Colloidal Silver Staining. *Clin. Chem.* **2001**, *47*, 763–766.
- (709) Wan, A. T.; Conyers, R. A.; Coombs, C. J.; Masterton, J. P. Determination of Silver in Blood, Urine, and Tissues of Volunteers and Burn Patients. *Clin. Chem.* **1991**, *37*, 1683–1687.
- (710) Liu, L.; Zhang, G.; Xiang, J.; Zhang, D.; Zhu, D. Fluorescence “Turn On” Chemosensors for Ag<sup>+</sup> and Hg<sup>2+</sup> Based on Tetraphenylethylene Motif Featuring Adenine and Thymine Moieties. *Org. Lett.* **2008**, *10*, 4581–4584.
- (711) Robinson, N. J.; Winge, D. R. Copper Metallochaperones. *Annu. Rev. Biochem.* **2010**, *79*, 537–562.
- (712) Bruijn, L. I.; Miller, T. M.; Cleveland, D. W. Unraveling the Mechanism Involved in Motor Neuron Degeneration in ALS. *Annu. Rev. Neurosci.* **2004**, *27*, 723–749.
- (713) Feng, H.-T.; Song, S.; Chen, Y.-C.; Shen, C.-H.; Zheng, Y.-S. Self-Assembled Tetraphenylethylene Macrocycle Nanofibrous Materials for the Visual Detection of Copper(II) in Water. *J. Mater. Chem. C* **2014**, *2*, 2353–2359.
- (714) Cui, K.; Lu, X.; Cui, W.; Wu, J.; Chen, X.; Lu, Q. Fluorescent Nanoparticles Assembled from a Poly(ionic liquid) for Selective Sensing of Copper Ions. *Chem. Commun.* **2011**, *47*, 920–922.
- (715) Song, P.; Xiang, Y.; Wei, R. R.; Tong, A. A Fluorescent Chemosensor for Cu<sup>2+</sup> Detection in Solution Based on Aggregation-Induced Emission and Its Application in Fabricating Cu<sup>2+</sup> Test Papers. *J. Lumin.* **2014**, *153*, 215–220.
- (716) Khandare, D. G.; Kumar, V.; Chattopadhyay, A.; Banerjee, M.; Chatterjee, A. An Aggregation-Induced Emission Based “Turn-on” Fluorescent Chemodosimeter for the Selective Detection of Ascorbate Ions. *RSC Adv.* **2013**, *3*, 16981–16985.
- (717) Sanji, T.; Nakamura, M.; Tanaka, M. Fluorescence ‘Turn-on’ Detection of Cu<sup>2+</sup> Ions with Aggregation-Induced Emission-Active Tetraphenylethene Based on Click Chemistry. *Tetrahedron Lett.* **2011**, *S2*, 3283–3286.
- (718) Zhang, S.; Yan, J. M.; Qin, A. J.; Sun, J. Z.; Tang, B. Z. The Specific Detection of Cu(II) Using an AIE-active Alanine Ester. *Chin. Chem. Lett.* **2013**, *24*, 668–672.
- (719) Mertz, W. The Essential Trace Elements. *Science* **1981**, *213*, 1332–1338.
- (720) Lieberman, R. L.; Rosenzweig, A. C. Crystal Structure of a Membrane-Bound Metalloenzyme That Catalyses the Biological Oxidation of Methane. *Nature* **2005**, *434*, 177–182.
- (721) Cuenoud, B.; Szostak, J. W. A DNA Metalloenzyme with DNA Ligase Activity. *Nature* **1995**, *375*, 611–614.
- (722) Kim, E. E.; Wyckoff, H. W. Reaction Mechanism of Alkaline Phosphatase Based on Crystal Structures. Two-Metal Ion Catalysis. *J. Mol. Biol.* **1991**, *218*, 449–464.
- (723) Que, E. L.; Domaille, D. W.; Chang, C. J. Metals in Neurobiology: Probing Their Chemistry and Biology with Molecular Imaging. *Chem. Rev.* **2008**, *108*, 1517–1549.

- (724) Xu, Z.; Yoon, J.; Spring, D. R. Fluorescent Chemosensors for  $Zn^{2+}$ . *Chem. Soc. Rev.* **2010**, *39*, 1996–2006.
- (725) Hong, Y.; Chen, S.; Leung, C. W. T.; Lam, J. W. Y.; Liu, J.; Tseng, N.-W.; Kwok, R. T. K.; Yu, Y.; Wang, Z.; Tang, B. Z. Fluorogenic  $Zn(II)$  and Chromogenic  $Fe(II)$  Sensors Based on Terpyridine-Substituted Tetraphenylethenes with Aggregation-Induced Emission Characteristics. *ACS Appl. Mater. Interfaces* **2011**, *3*, 3411–3418.
- (726) Yin, S.; Zhang, J.; Feng, H.; Zhao, Z.; Xu, L.; Qiu, H.; Tang, B.  $Zn^{2+}$ -Selective Fluorescent Turn-On Chemosensor Based on Terpyridine-Substituted Siloles. *Dyes Pigm.* **2012**, *95*, 174–179.
- (727) Sun, F.; Zhang, G.; Zhang, D.; Xue, L.; Jiang, H. Aqueous Fluorescence Turn-On Sensor for  $Zn^{2+}$  with a Tetraphenylethylene Compound. *Org. Lett.* **2011**, *13*, 6378–6381.
- (728) Xie, D.-X.; Ran, Z.-J.; Jin, Z.; Zhang, X.-B.; An, D.-L. A Simple Fluorescent Probe for  $Zn(II)$  Based on the Aggregation-Induced Emission. *Dyes Pigm.* **2013**, *96*, 495–499.
- (729) Järup, L. Hazards of Heavy Metal Contamination. *Br. Med. Bull.* **2003**, *68*, 167–182.
- (730) Zhang, H.; Qu, Y.; Gao, Y.; Hua, J.; Li, J.; Li, B. A Red Fluorescent ‘Turn-On’ Chemosensor for  $Hg^{2+}$  Based on Triphenylamine-Triazines Derivatives with Aggregation-Induced Emission Characteristics. *Tetrahedron Lett.* **2013**, *S4*, 909–912.
- (731) Ma, K.; Li, X.; Xu, B.; Tian, W. A Sensitive and Selective ‘Turn-On’ Fluorescent Probe for  $Hg^{2+}$  Based on Thymine– $Hg^{2+}$ –Thymine Complex with an Aggregation-Induced Emission Feature. *Anal. Methods* **2014**, *6*, 2338–2342.
- (732) Sun, X.; Shi, W.; Ma, F.; Hui, Y.; Xu, L.; Mi, H.; Tian, Y.; Xie, Z. Thymine-Covalently Decorated, AIEE-Type Conjugated Polymer as Fluorescence Turn-On Probe for Aqueous  $Hg^{2+}$ . *Sens. Actuators, B* **2014**, *198*, 395–401.
- (733) Pramanik, S.; Bhalla, V.; Kumar, M. Mercury Assisted Fluorescent Supramolecular Assembly of Hexaphenylbenzene Derivative for Femtogram Detection of Picric Acid. *Anal. Chim. Acta* **2013**, *793*, 99–106.
- (734) Ozturk, S.; Atilgan, S. A Tetraphenylethene Based Polarity Dependent Turn-On Fluorescence Strategy for Selective and Sensitive Detection of  $Hg^{2+}$  in Aqueous Medium and in Living Cells. *Tetrahedron Lett.* **2014**, *55*, 70–73.
- (735) Yan, Y.; Che, Z.; Yu, X.; Zhi, X.; Wang, J.; Xu, H. Fluorescence ‘On-Off-On’ Chemosensor for Sequential Recognition of  $Fe^{3+}$  and  $Hg^{2+}$  in Water Based on Tetraphenylethylene Motif. *Bioorg. Med. Chem.* **2013**, *21*, 508–513.
- (736) Zhang, Y. Q.; Li, X. D.; Gao, L. J.; Qiu, J. H.; Heng, L. P.; Tang, B. Z.; Jiang, L. Silole-Infiltrated Photonic Crystal Films as Effective Fluorescence Sensor for  $Fe^{3+}$  and  $Hg^{2+}$ . *ChemPhysChem* **2014**, *15*, 507–513.
- (737) Chen, J.; Liu, W.; Wang, Y.; Zhang, H.; Wu, J.; Xu, H.; Ju, W.; Wang, P. Turn-On Fluorescence Sensor Based on the Aggregation of Pyrazolo[3,4-b]pyridine-Based Coumarin Chromophores Induced by  $Hg^{2+}$ . *Tetrahedron Lett.* **2013**, *S4*, 6447–6449.
- (738) Zhang, G.; Ding, A.; Zhang, Y.; Yang, L.; Kong, L.; Zhang, X.; Tao, X.; Tian, Y.; Yang, J. Schiff Base Modified  $\alpha$ -Cyanostilbene Derivative with Aggregation-Induced Emission Enhancement Characteristics for  $Hg^{2+}$  Detection. *Sens. Actuators, B* **2014**, *202*, 209–216.
- (739) Rifai, N.; Cohen, G.; Wolf, M.; Cohen, L.; Faser, C.; Savory, J.; DePalma, L. Incidence of Lead Poisoning in Young Children from Inner-City, Suburban, and Rural Communities. *Ther. Drug Monit.* **1993**, *15*, 71–74.
- (740) Zuch, C. L.; O’Mara, D. J.; Cory-Slechta, D. A. Low-Level Lead Exposure Selectively Enhances Dopamine Overflow in Nucleus Accumbens: An *in vivo* Electrochemistry Time Course Assessment. *Toxicol. Appl. Pharmacol.* **1998**, *150*, 174–185.
- (741) Godwin, H. A. The Biological Chemistry of Lead. *Curr. Opin. Chem. Biol.* **2001**, *5*, 223–227.
- (742) Ernhart, C. B. A Critical Review of Low-Level Prenatal Lead Exposure in the Human: 2. Effects on the Developing Child. *Reprod. Toxicol.* **1992**, *6*, 21–40.
- (743) Jedrychowski, W.; Perera, F.; Jankowski, J.; Rauh, V.; Flak, E.; Caldwell, K. L.; Jones, R. L.; Pac, A.; Lisowska-Miszczyn, I. Prenatal Low-Level Lead Exposure and Developmental Delay of Infants at Age 6 Months (Krakow Inner City Study). *Int. J. Hyg. Environ. Health* **2008**, *211*, 345–351.
- (744) Panich, S.; Wilson, K. A.; Nuttall, P.; Wood, C. K.; Albrecht, T.; Edel, J. B. Label-Free  $Pb(II)$  Whispering Gallery Mode Sensing Using Self-Assembled Glutathione-Modified Gold Nanoparticles on an Optical Microcavity. *Anal. Chem.* **2014**, *86*, 6299–6306.
- (745) Khandare, D. G.; Joshi, H.; Banerjee, M.; Majik, M. S.; Chatterjee, A. An Aggregation-Induced Emission Based ‘Turn-On’ Fluorescent Chemodosimeter for the Selective Detection of  $Pb^{2+}$  Ions. *RSC Adv.* **2014**, *4*, 47076–47080.
- (746) Crapper, D. R.; Krishnan, S. S.; Dalton, A. J. Brain Aluminum Distribution in Alzheimer’s Disease and Experimental Neurofibrillary Degeneration. *Science* **1973**, *180*, 511–513.
- (747) Perl, D. P.; Brody, A. R. Alzheimer’s Disease: X-Ray Spectrometric Evidence of Aluminum Accumulation in Neurofibrillary Tangle-bearing Neurons. *Science* **1980**, *208*, 297–299.
- (748) Perl, D. P.; Gajdusek, D. C.; Garruto, R. M.; Yanagihara, R. T.; Gibbs, C. J. Intraneuronal Aluminum Accumulation in Amyotrophic Lateral Sclerosis and Parkinsonism-Dementia of Guam. *Science* **1982**, *217*, 1053–1055.
- (749) House, E.; Collingwood, J.; Khan, A.; Korczakina, O.; Berthon, G.; Exley, C. Aluminium, Iron, Zinc and Copper Influence the *in vitro* Formation of Amyloid Fibrils of Abeta42 in a Manner Which May Have Consequences for Metal Chelation Therapy in Alzheimer’s Disease. *J. Alzheimers Dis.* **2004**, *6*, 291–301.
- (750) Flaten, T. P. Aluminium as A Risk Factor in Alzheimer’s Disease, with Emphasis on Drinking Water. *Brain Res. Bull.* **2001**, *55*, 187–196.
- (751) Exley, C. Aluminium and Iron, But Neither Copper Nor Zinc, Are Key to The Precipitation of Beta-Sheets of Abeta<sub>{42}</sub> in Senile Plaque Cores in Alzheimer’s Disease. *J. Alzheimers Dis.* **2006**, *10*, 173–177.
- (752) Han, T.; Feng, X.; Tong, B.; Shi, J.; Chen, L.; Zhi, J.; Dong, Y. A Novel ‘Turn-On’ Fluorescent Chemosensor for the Selective Detection of  $Al^{3+}$  Based on Aggregation-Induced Emission. *Chem. Commun.* **2012**, *48*, 416–418.
- (753) Shi, X.; Wang, H.; Han, T.; Feng, X.; Tong, B.; Shi, J.; Zhi, J.; Dong, Y. A Highly Sensitive, Single Selective, Real-Time and ‘Turn-On’ Fluorescent Sensor for  $Al^{3+}$  Detection in Aqueous Media. *J. Mater. Chem.* **2012**, *22*, 19296–19302.
- (754) Na, N.; Wang, F.; Huang, J.; Niu, C.; Yang, C.; Shang, Z.; Han, F.; Ouyang, J. An Aggregation-Induced Emission-Based Fluorescent Chemosensor of Aluminium Ions. *RSC Adv.* **2014**, *4*, 35459–35462.
- (755) Samanta, S.; Goswami, S.; Hoque, M. N.; Ramesh, A.; Das, G. An Aggregation-Induced Emission (AIE) Active Probe Renders  $Al(III)$  Sensing and Tracking of Subsequent Interaction with DNA. *Chem. Commun.* **2014**, *50*, 11833–11836.
- (756) Guo, Z.; Nam, S. W.; Park, S.; Yoon, J. A Highly Selective Ratiometric Near-Infrared Fluorescent Cyanine Sensor for Cysteine with Remarkable Shift and Its Application in Bioimaging. *Chem. Sci.* **2012**, *3*, 2760–2765.
- (757) Lu, Y.; Berry, S. M.; Pfister, T. D. Engineering Novel Metalloproteins: Design of Metal-Binding Sites into Native Protein Scaffolds. *Chem. Rev.* **2001**, *101*, 3047–3080.
- (758) Theil, E. C.; Goss, D. J. Living with Iron (and Oxygen): Questions and Answers about Iron Homeostasis. *Chem. Rev.* **2009**, *109*, 4568–4579.
- (759) Ye, J.-H.; Liu, J.; Wang, Z.; Bai, Y.; Zhang, W.; He, W. A New  $Fe^{3+}$  Fluorescent Chemosensor Based on Aggregation-Induced Emission. *Tetrahedron Lett.* **2014**, *55*, 3688–3692.
- (760) Bian, N.; Chen, Q.; Qiu, X.-L.; Qi, A.-D.; Han, B.-H. Imidazole-Bearing Tetraphenylethylene: Fluorescent Probe for Metal Ions Based on AIE Feature. *New J. Chem.* **2011**, *35*, 1667–1671.
- (761) Chen, X.; Shen, X. Y.; Guan, E.; Liu, Y.; Qin, A.; Sun, J. Z.; Tang, B. Z. A Pyridinyl-Functionalized Tetraphenylethylene Fluorogen for Specific Sensing of Trivalent Cations. *Chem. Commun.* **2013**, *49*, 1503–1505.
- (762) Chan, C. Y. K.; Zhao, Z.; Lam, J. W. Y.; Liu, J.; Chen, S.; Lu, P.; Mahtab, F.; Chen, X.; Sung, H. H. Y.; Kwok, H. S.; et al. Efficient Light

- Emitters in the Solid State: Synthesis, Aggregation-Induced Emission, Electroluminescence, and Sensory Properties of Luminogens with Benzene Cores and Multiple Triarylvinyli Peripherals. *Adv. Funct. Mater.* **2012**, *22*, 378–389.
- (763) Chan, C. Y. K.; Lam, J. W. Y.; Jim, C. K. W.; Sung, H. H. Y.; Williams, I. D.; Tang, B. Z. Polycyclotrimerization of Dinitriles: A New Polymerization Route for the Construction of Soluble Nitrogen-Rich Polytriazines with Hyperbranched Structures and Functional Properties. *Macromolecules* **2013**, *46*, 9494–9506.
- (764) Macfarlane, A. M. The Overlooked Back End of the Nuclear Fuel Cycle. *Science* **2011**, *333*, 1225–1226.
- (765) Chen, X.; He, L.; Wang, Y.; Liu, B.; Tang, Y. Trace Analysis of Uranyl Ion ( $\text{UO}_2^{2+}$ ) in Aqueous Solution by Fluorescence Turn-On Detection via Aggregation Induced Emission Enhancement Effect. *Anal. Chim. Acta* **2014**, *847*, 55–60.
- (766) Toal, S. J.; Jones, K. A.; Magde, D.; Troglar, W. C. Luminescent Silole Nanoparticles as Chemosselective Sensors for Cr(VI). *J. Am. Chem. Soc.* **2005**, *127*, 11661–11665.
- (767) Yang, X.; Jiang, Y.; Shen, B.; Chen, Y.; Dong, F.; Yu, K.; Yang, B.; Lin, Q. Thermo-Responsive Photoluminescent Polymer Brushes Device as a Platform for Selective Detection of Cr(VI). *Polym. Chem.* **2013**, *4*, 5591–5596.
- (768) Peng, L. H.; Wang, M.; Zhang, G. X.; Zhang, D. Q.; Zhu, D. B. A Fluorescence Turn-On Detection of Cyanide in Aqueous Solution Based on the Aggregation-Induced Emission. *Org. Lett.* **2009**, *11*, 1943–1946.
- (769) Duan, Y.-L.; Zheng, Y.-S. A New Sensitive and Selective Fluorescence Probe for Detection of Cyanide. *Talanta* **2013**, *107*, 332–337.
- (770) Pramanik, S.; Bhalla, V.; Kumar, M. Hexaphenylbenzene-Based Fluorescent Aggregates for Ratiometric Detection of Cyanide Ions at Nanomolar Level: Set–Reset Memorized Sequential Logic Device. *ACS Appl. Mater. Interfaces* **2014**, *6*, 5930–5939.
- (771) Zhang, Y.; Li, D.; Li, Y.; Yu, J. Solvatochromic AIE Luminogens as Supersensitive Water Detectors in Organic Solvents and Highly Efficient Cyanide Chemosensors in Water. *Chem. Sci.* **2014**, *5*, 2710–2716.
- (772) Huang, X.; Gu, X.; Zhang, G.; Zhang, D. A Highly Selective Fluorescence Turn-On Detection of Cyanide Based on the Aggregation of Tetraphenylethylene Molecules Induced by Chemical Reaction. *Chem. Commun.* **2012**, *48*, 12195–12197.
- (773) Park, C.; Hong, J. I. A New Fluorescent Sensor for the Detection of Pyrophosphate Based on a Tetraphenylethylene Moiety. *Tetrahedron Lett.* **2010**, *51*, 1960–1962.
- (774) Kassl, C. J.; Christopher Pigge, F. Anion Detection by Aggregation-Induced Enhanced Emission (AIEE) of Urea-Functionalized Tetraphenylethylenes. *Tetrahedron Lett.* **2014**, *55*, 4810–4813.
- (775) Turan, I. S.; Cakmak, F. P.; Sozmen, F. Highly Selective Fluoride Sensing via Chromogenic Aggregation of a Silyloxy-Functionalized Tetraphenylethylene (TPE) Derivative. *Tetrahedron Lett.* **2014**, *55*, 456–459.
- (776) *Cyanide in Biology*; Vennesland, B., Comm, E. E., Knownles, C. J., Westly, J., Wissing, F., Eds.; Academic Press: London, 1981.
- (777) Ishii, A.; Seno, H.; Watanabe-Suzuki, K.; Suzuki, O.; Kumazawa, T. Determination of Cyanide in Whole Blood by Capillary Gas Chromatography with Cryogenic Oven Trapping. *Anal. Chem.* **1998**, *70*, 4873–4876.
- (778) Moriya, F.; Hashimoto, Y. Potential for Error When Assessing Blood Cyanide Concentrations in Fire Victims. *J. Forensic Sci.* **2001**, *46*, 1421–1425.
- (779) *Guidelines for Drinking-Water Quality*; World Health Organization: Geneva, Switzerland, 1996.
- (780) Li, Z.; Dong, Y. Q.; Lam, J. W. Y.; Sun, J. X.; Qin, A. J.; Haeussler, M.; Dong, Y. P.; Sung, H. H. Y.; Williams, I. D.; Kwok, H. S.; et al. Functionalized Siloles: Versatile Synthesis, Aggregation-Induced Emission, and Sensory and Device Applications. *Adv. Funct. Mater.* **2009**, *19*, 905–917.
- (781) Yang, Z.; Qin, W.; Lam, J. W. Y.; Chen, S.; Sung, H. H. Y.; Williams, I. D.; Tang, B. Z. Fluorescent pH Sensor Constructed from A Heteroatom-Containing Luminogen with Tunable AIE and ICT Characteristics. *Chem. Sci.* **2013**, *4*, 3725–3730.
- (782) Song, P.; Chen, X.; Xiang, Y.; Huang, L.; Zhou, Z.; Wei, R.; Tong, A. A Ratiometric Fluorescent pH Probe Based on Aggregation-Induced Emission Enhancement and Its Application in Live-cell Imaging. *J. Mater. Chem.* **2011**, *21*, 13470–13475.
- (783) Liu, Y.; Tang, Y. H.; Barashkov, N. N.; Irgibaeva, I. S.; Lam, J. W. Y.; Hu, R. R.; Birimhanova, D.; Yu, Y.; Tang, B. Z. Fluorescent Chemosensor for Detection and Quantitation of Carbon Dioxide Gas. *J. Am. Chem. Soc.* **2010**, *132*, 13951–13953.
- (784) Tian, T.; Chen, X.; Li, H.; Wang, Y.; Guo, L.; Jiang, L. Amidine-Based Fluorescent Chemosensor with High Applicability for Detection of  $\text{CO}_2$ : A Facile Way to “See”  $\text{CO}_2$ . *Analyst* **2013**, *138*, 991–994.
- (785) Landete, J. M.; de las Rivas, B.; Marcabal, A.; Munoz, R. Molecular Methods for the Detection of Biogenic Amine-Producing Bacteria on Foods. *Int. J. Food Microbiol.* **2007**, *117*, 258–269.
- (786) Aneja, V. P.; Roelle, P. A.; Murray, G. C.; Scutherland, J.; Erisman, J. W.; Falter, D.; Asman, W. A. H.; Patni, N. Atmospheric Nitrogen Compounds II: Emissions, Transport, Transformation, Deposition and Assessment. *Atmos. Environ.* **2001**, *35*, 1903–1911.
- (787) Lee, B.; Scopelliti, R.; Severin, K. A Molecular Probe for the Optical Detection of Biogenic Amines. *Chem. Commun.* **2011**, *47*, 9639–9641.
- (788) Han, T.; Lam, J. W. Y.; Zhao, N.; Gao, M.; Yang, Z.; Zhao, E.; Dong, Y.; Tang, B. Z. A Fluorescence-Switchable Luminogen in the Solid State: A Sensitive and Selective Sensor for the Fast “Turn-On” Detection of Primary Amine Gas. *Chem. Commun.* **2013**, *49*, 4848–4850.
- (789) Szabó, C. Hydrogen Sulphide and Its Therapeutic Potential. *Nat. Rev. Drug Discovery* **2007**, *6*, 917–935.
- (790) Li, L.; Rose, P.; Moore, P. K. Hydrogen Sulfide and Cell Signaling. *Annu. Rev. Pharmacol. Toxicol.* **2011**, *51*, 169–187.
- (791) Baskar, R.; Bian, J. Hydrogen Sulfide Gas Has Cell Growth Regulatory Role. *Eur. J. Pharmacol.* **2011**, *656*, 5–9.
- (792) Papapetropoulos, A.; Pyriochou, A.; Altaany, Z.; Yang, G.; Marazioti, A.; Zhou, Z.; Jeschke, M. G.; Branski, L. K.; Herndon, D. N.; Wang, R.; et al. Hydrogen Sulfide Is an Endogenous Stimulator of Angiogenesis. *Proc. Natl. Acad. Sci. U. S. A.* **2009**, *106*, 21972–21977.
- (793) Lefer, D. J. A New Gaseous Signaling Molecule Emerges: Cardioprotective Role of Hydrogen Sulfide. *Proc. Natl. Acad. Sci. U. S. A.* **2007**, *104*, 17907–17908.
- (794) Blackstone, E.; Morrison, M.; Roth, M. B.  $\text{H}_2\text{S}$  Induces a Suspended Animation-Like State in Mice. *Science* **2005**, *308*, 518–518.
- (795) Gadalla, M. M.; Snyder, S. H. Hydrogen Sulfide as a Gasotransmitter. *J. Neurochem.* **2010**, *113*, 14–26.
- (796) Eto, K.; Asada, T.; Arima, K.; Makifuchi, T.; Kimura, H. Brain Hydrogen Sulfide Is Severely Decreased in Alzheimer’s Disease. *Biochem. Biophys. Res. Commun.* **2002**, *293*, 1485–1488.
- (797) Yang, W.; Yang, G.; Jia, X.; Wu, L.; Wang, R. Activation of KATP Channels by  $\text{H}_2\text{S}$  in Rat Insulin-Secreting Cells and the Underlying Mechanisms. *J. Physiol.* **2005**, *569*, 519–531.
- (798) Cai, Y.; Li, L.; Wang, Z.; Sun, J. Z.; Qin, A.; Tang, B. Z. A Sensitivity Tuneable Tetraphenylethene-Based Fluorescent Probe for Directly Indicating the Concentration of Hydrogen Sulfide. *Chem. Commun.* **2014**, *50*, 8892–8895.
- (799) Luo, W.; Zhu, Y.; Zhang, J.; He, J.; Chi, Z.; Miller, P. W.; Chen, L.; Su, C.-Y. A Dynamic Covalent Imine Gel as a Luminescent Sensor. *Chem. Commun.* **2014**, *50*, 11942–11945.
- (800) Feng, H.-T.; Zheng, Y.-S. Highly Sensitive and Selective Detection of Nitrophenolic Explosives by Using Nanospheres of a Tetraphenylethylene Macrocyclic Displaying Aggregation-Induced Emission. *Chem. - Eur. J.* **2014**, *20*, 195–201.
- (801) Wang, J.-H.; Feng, H.-T.; Zheng, Y.-S. Synthesis of Tetraphenylethylene Pillar[6]arenes and the Selective Fast Quenching of Their AIE Fluorescence by TNT. *Chem. Commun.* **2014**, *50*, 11407–11410.
- (802) Kumar, M.; Vij, V.; Bhalla, V. Vapor-Phase Detection of Trinitrotoluene by AIEE-Active Hetero-Oligophenylene-Based Carbazole Derivatives. *Langmuir* **2012**, *28*, 12417–12421.

- (803) Zhao, Z.; Liu, J.; Yip Lam, J. W.; Chan, C. Y. K.; Qiu, H.; Tang, B. Z. Luminescent Aggregates of a Starburst Silole-Triphenylamine Adduct for Sensitive Explosive Detection. *Dyes Pigm.* **2011**, *91*, 258–263.
- (804) Bejoymohandas, K. S.; George, T. M.; Bhattacharya, S.; Natarajan, S.; Reddy, M. L. P. AIEP-Active Green Phosphorescent Iridium(III) Complex Impregnated Test Strips for The Vapor-Phase Detection of 2,4,6-Trinitrotoluene (TNT). *J. Mater. Chem. C* **2014**, *2*, 515–523.
- (805) Qin, A. J.; Lam, J. W. Y.; Tang, L.; Jim, C. K. W.; Zhao, H.; Sun, J. Z.; Tang, B. Z. Polytriazoles with Aggregation-Induced Emission Characteristics: Synthesis by Click Polymerization and Application as Explosive Chemosensors. *Macromolecules* **2009**, *42*, 1421–1424.
- (806) Li, J.; Liu, J.; Lam, J. W. Y.; Tang, B. Z. Poly(arylene ynynylene) with an Aggregation-Enhanced Emission Characteristic: A Fluorescent Sensor for Both Hydrazine and Explosive Detection. *RSC Adv.* **2013**, *3*, 8193–8196.
- (807) Gao, M.; Lam, J. W. Y.; Liu, Y.; Li, J.; Tang, B. Z. A New Route to Functional Polymers: Atom-Economical Synthesis of Poly(pyrazolylnaphthalene)s by Rhodium-Catalyzed Oxidative Polycoupling of Phenylpyrazole and Internal Diynes. *Polym. Chem.* **2013**, *4*, 2841–2849.
- (808) Zhou, H.; Li, J.; Chua, M. H.; Yan, H.; Tang, B. Z.; Xu, J. Poly(acrylate) with a Tetraphenylethene Pendant with Aggregation-Induced Emission (AIE) Characteristics: Highly Stable AIE-Active Polymer Nanoparticles for Effective Detection of Nitro Compounds. *Polym. Chem.* **2014**, *5*, 5628–5637.
- (809) Liang, G.; Weng, L.-T.; Lam, J. W. Y.; Qin, W.; Tang, B. Z. Crystallization-Induced Hybrid Nano-Sheets of Fluorescent Polymers with Aggregation-Induced Emission Characteristics for Sensitive Explosive Detection. *ACS Macro Lett.* **2014**, *3*, 21–25.
- (810) Gao, M.; Lam, J. W. Y.; Li, J.; Chan, C. Y. K.; Chen, Y.; Zhao, N.; Han, T.; Tang, B. Z. Stoichiometric Imbalance-Promoted Synthesis of Polymers Containing Highly Substituted Naphthalenes: Rhodium-Catalyzed Oxidative Polycoupling of Arylboronic Acids and Internal Diynes. *Polym. Chem.* **2013**, *4*, 1372–1380.
- (811) Lu, P.; Lam, J. W. Y.; Liu, J.; Jim, C. K. W.; Yuan, W.; Chan, C. Y. K.; Xie, N.; Hu, Q.; Cheuk, K. K. L.; Tang, B. Z. Regioselective Alkyne Polyhydrosilylation: Synthesis and Photonic Properties of Poly(silylenevinylene)s. *Macromolecules* **2011**, *44*, 5977–5986.
- (812) Li, H.; Wang, J.; Sun, J. Z.; Hu, R.; Qin, A.; Tang, B. Z. Metal-Free Click Polymerization of Propiolates and Azides: Facile Synthesis of Functional Poly(aroxycarbonyltriazole)s. *Polym. Chem.* **2012**, *3*, 1075–1083.
- (813) Qin, A. J.; Tang, L.; Lam, J. W. Y.; Jim, C. K. W.; Yu, Y.; Zhao, H.; Sun, J. Z.; Tang, B. Z. Metal-Free Click Polymerization: Synthesis and Photonic Properties of Poly(aroyltriazole)s. *Adv. Funct. Mater.* **2009**, *19*, 1891–1900.
- (814) Hu, R.; Lam, J. W. Y.; Yu, Y.; Sung, H. H. Y.; Williams, I. D.; Yuen, M. M. F.; Tang, B. Z. Facile Synthesis of Soluble Nonlinear Polymers with Glycogen-Like Structures and Functional Properties from “Simple” Acrylic Monomers. *Polym. Chem.* **2013**, *4*, 95–105.
- (815) Hu, R.; Lam, J. W. Y.; Li, M.; Deng, H.; Li, J.; Tang, B. Z. Homopolycyclotrimerization of A<sub>4</sub>-Type Tetrayne: A New Approach for the Creation of a Soluble Hyperbranched Poly(tetraphenylethene) with Multifunctionalities. *J. Polym. Sci., Part A: Polym. Chem.* **2013**, *51*, 4752–4764.
- (816) Li, H.; Wu, H.; Zhao, E.; Li, J.; Sun, J. Z.; Qin, A.; Tang, B. Z. Hyperbranched Poly(aroxycarbonyltriazole)s: Metal-Free Click Polymerization, Light Refraction, Aggregation-Induced Emission, Explosive Detection, and Fluorescent Patterning. *Macromolecules* **2013**, *46*, 3907–3914.
- (817) Zhao, Z.; Guo, Y.; Jiang, T.; Chang, Z.; Lam, J. W. Y.; Xu, L.; Qiu, H.; Tang, B. Z. A Fully Substituted 3-Silolene Functions as Promising Building Block for Hyperbranched Poly(Silylenevinylene). *Macromol. Rapid Commun.* **2012**, *33*, 1074–1079.
- (818) Yuan, W. Z.; Hu, R.; Lam, J. W. Y.; Xie, N.; Jim, C. K. W.; Tang, B. Z. Conjugated Hyperbranched Poly(aryleneethynylene)s: Synthesis, Photophysical Properties, Superquenching by Explosive, Photopatternability, and Tunable High Refractive Indices. *Chem. - Eur. J.* **2012**, *18*, 2847–2856.
- (819) Wu, W.; Ye, S.; Yu, G.; Liu, Y.; Qin, J.; Li, Z. Novel Functional Conjugative Hyperbranched Polymers with Aggregation-Induced Emission: Synthesis through One-Pot “A<sub>2</sub>+B<sub>4</sub>” Polymerization and Application as Explosive Chemosensors and PLEDs. *Macromol. Rapid Commun.* **2012**, *33*, 164–171.
- (820) He, G.; Peng, H.; Liu, T.; Yang, M.; Zhang, Y.; Fang, Y. A Novel Picric Acid Film Sensor via Combination of the Surface Enrichment Effect of Chitosan Films and the Aggregation-Induced Emission Effect of Siloles. *J. Mater. Chem.* **2009**, *19*, 7347–7353.
- (821) Li, D.; Liu, J.; Kwok, R. T. K.; Liang, Z.; Tang, B. Z.; Yu, J. Supersensitive Detection of Explosives by Recyclable AIE Luminogen-Functionalized Mesoporous Materials. *Chem. Commun.* **2012**, *48*, 7167–7169.
- (822) Miao, C.; Li, D.; Zhang, Y.; Yu, J.; Xu, R. AIE Luminogen Functionalized Mesoporous Silica Nanoparticles as Efficient Fluorescent Sensor for Explosives Detection in Water. *Microporous Mesoporous Mater.* **2014**, *196*, 46–50.
- (823) Liao, Y.-X.; Li, K.; Wu, M.-Y.; Wu, T.; Yu, X.-Q. A Selenium-Contained Aggregation-Induced “Turn-On” Fluorescent Probe for Hydrogen Peroxide. *Org. Biomol. Chem.* **2014**, *12*, 3004–3008.
- (824) Li, G.; Zhu, D.; Liu, Q.; Xue, L.; Jiang, H. Rapid Detection of Hydrogen Peroxide Based on Aggregation Induced Ratiometric Fluorescence Change. *Org. Lett.* **2013**, *15*, 924–927.
- (825) Sanji, T.; Nakamura, M.; Kawamata, S.; Tanaka, M.; Itagaki, S.; Gunji, T. Fluorescence “Turn-On” Detection of Melamine with Aggregation-Induced-Emission-Active Tetraphenylethene. *Chem. - Eur. J.* **2012**, *18*, 15254–15257.
- (826) Liu, Z.; Xue, W.; Cai, Z.; Zhang, G.; Zhang, D. A Facile and Convenient Fluorescence Detection of Gamma-Ray Radiation Based on the Aggregation-Induced Emission. *J. Mater. Chem.* **2011**, *21*, 14487–14491.
- (827) *Criminalistics: An Introduction to Forensic Science*, 9th ed.; Saferstein, R., Ed.; Prentice Hall, Inc.: Upper Saddle River, NJ, 2006.
- (828) Wilshire, B. Advances in Fingerprint Detection. *Endeavour* **1996**, *20*, 12–15.
- (829) Xu, L.; Li, Y.; Li, S.; Hu, R.; Qin, A.; Tang, B. Z.; Su, B. Enhancing the Visualization of Latent Fingerprints by Aggregation Induced Emission of Siloles. *Analyst* **2014**, *139*, 2332–2335.
- (830) Pu, L. Fluorescence of Organic Molecules in Chiral Recognition. *Chem. Rev.* **2004**, *104*, 1687–1716.
- (831) Hembury, G. A.; Borovkov, V. V.; Inoue, Y. Chirality-Sensing Supramolecular Systems. *Chem. Rev.* **2008**, *108*, 1–73.
- (832) Zehnacker, A.; Suhm, M. A. Chirality Recognition between Neutral Molecules in the Gas Phase. *Angew. Chem., Int. Ed.* **2008**, *47*, 6970–6992.
- (833) Zheng, Y. S.; Hu, Y. J. Chiral Recognition Based on Enantioselectively Aggregation-Induced Emission. *J. Org. Chem.* **2009**, *74*, 5660–5663.
- (834) Li, D.-M.; Zheng, Y.-S. Single-Hole Hollow Nanospheres from Enantioselective Self-Assembly of Chiral AIE Carboxylic Acid and Amine. *J. Org. Chem.* **2011**, *76*, 1100–1108.
- (835) Zheng, Y. S.; Hu, Y. J.; Li, D. M.; Chen, Y. C. Enantiomer Analysis of Chiral Carboxylic Acids by AIE Molecules Bearing Optically Pure Aminol Groups. *Talanta* **2010**, *80*, 1470–1474.
- (836) Li, D.-M.; Zheng, Y.-S. Highly Enantioselective Recognition of A Wide Range of Carboxylic Acids Based on Enantioselectively Aggregation-Induced Emission. *Chem. Commun.* **2011**, *47*, 10139–10141.
- (837) Liu, N.-N.; Song, S.; Li, D.-M.; Zheng, Y.-S. Highly Sensitive Determination of Enantiomeric Composition of Chiral Acids Based on Aggregation-Induced Emission. *Chem. Commun.* **2012**, *48*, 4908–4910.
- (838) Li, D.-M.; Wang, H.; Zheng, Y.-S. Light-Emitting Property of Simple AIE Compounds in Gel, Suspension and Precipitates, and Application to Quantitative Determination of Enantiomer Composition. *Chem. Commun.* **2012**, *48*, 3176–3178.
- (839) Scalise, R. E.; Caradonna, P. A.; Tracy, H. J.; Mullin, J. L.; Keirstead, A. E. 1,1-Dimethyl-2,3,4,5-tetraphenylsilole as a Molecular

- Rotor Probe to Investigate the Microviscosity of Imidazolium Ionic Liquids. *J. Inorg. Organomet. Polym. Mater.* **2014**, *24*, 431–441.
- (840) Li, J.; Zhang, Y.; Mei, J.; Lam, J. W. Y.; Hao, J.; Tang, B. Z. Aggregation-Induced Emission Rotors: Rational Design and Tunable Stimuli Response. *Chem. - Eur. J.* **2015**, *21*, 907–914.
- (841) Tang, L.; Jin, J. K.; Qin, A.; Yuan, W. Z.; Mao, Y.; Mei, J.; Sun, J. Z.; Tang, B. Z. A Fluorescent Thermometer Operating in Aggregation-Induced Emission Mechanism: Probing Thermal Transitions of PNIPAM in Water. *Chem. Commun.* **2009**, 4974–4976.
- (842) Yin, X.; Meng, F.; Wang, L. Thermosensitivity and Luminescent Properties of New Tetraphenylethylene Derivatives Bearing Peripheral Oligo(ethylene glycol) Chains. *J. Mater. Chem. C* **2013**, *1*, 6767–6773.
- (843) Lai, C.-T.; Chien, R.-H.; Kuo, S.-W.; Hong, J.-L. Tetraphenylthiophene-Functionalized Poly(*N*-isopropylacrylamide): Probing LCST with Aggregation-Induced Emission. *Macromolecules* **2011**, *44*, 6546–6556.
- (844) Yang, C.-M.; Lai, Y.-W.; Kuo, S.-W.; Hong, J.-L. Complexation of Fluorescent Tetraphenylthiophene-Derived Ammonium Chloride to Poly(*N*-isopropylacrylamide) with Sulfonate Terminal: Aggregation-Induced Emission, Critical Micelle Concentration, and Lower Critical Solution Temperature. *Langmuir* **2012**, *28*, 15725–15735.
- (845) Li, S.-T.; Lin, Y.-C.; Kuo, S.-W.; Chuang, W.-T.; Hong, J.-L. Aggregation Induced Emission Enhancement in Relation to the Secondary Structures of Poly( $\gamma$ -benzyl-L-glutamate) Containing A Fluorescent Tetraphenylthiophene Moiety. *Polym. Chem.* **2012**, *3*, 2393–2402.
- (846) Shih, K.-Y.; Hsiao, T.-S.; Deng, S.-L.; Hong, J.-L. Water-Soluble Poly( $\gamma$ -propargyl-L-glutamate) Containing Pendant Sulfonate Ions and Terminal Fluorophore: Aggregation-Enhanced Emission and Secondary Structure. *Macromolecules* **2014**, *47*, 4037–4047.
- (847) Zhang, S.; Yan, J.; Qin, A.; Sun, J.; Tang, B. Z. Probing the pH-Dependent Chain Dynamics of Poly(acrylic acid) in Concentrated Solution by Using a Cationic AIE Fluorophore. *Sci. China: Chem.* **2013**, *56*, 1253–1257.
- (848) Tang, L.; Jin, J. K.; Zhang, S.; Mao, Y.; Sun, J. Z.; Yuan, W. Z.; Zhao, H.; Xu, H. P.; Qin, A. J.; Tang, B. Z. Detection of the Critical Micelle Concentration of Cationic and Anionic Surfactants Based on Aggregation-Induced Emission Property of Hexaphenylsilole Derivatives. *Sci. China, Ser. B: Chem.* **2009**, *52*, 755–759.
- (849) Zhu, C.; Pang, S.; Xu, J.; Jia, L.; Xu, F.; Mei, J.; Qin, A.; Sun, J.; Ji, J.; Tang, B. Z. Aggregation-Induced Emission of Tetraphenylethene Derivative as a Fluorescence Method for Probing the Assembling/Disassembling of Amphiphilic Molecules. *Analyst* **2011**, *136*, 3343–3348.
- (850) Zhu, Q.; Huang, L.; Su, J.; Liu, S. A Sensitive and Visible Fluorescence-Turn-On Probe for the CMC Determination of Ionic Surfactants. *Chem. Commun.* **2014**, *50*, 1107–1109.
- (851) Jin, J.-K.; Sun, J.-Z.; Dong, Y.-Q.; Xu, H.-P.; Yuan, W.-Z.; Tang, B. Z. Aggregation-Induced Emission of an Aminated Silole: A Fluorescence Probe for Monitoring Layer-by-Layer Self-Assembling Processes of Polyelectrolytes. *J. Lumin.* **2009**, *129*, 19–23.
- (852) Jia, J.; Wang, Z.; Lu, W.; Yang, L.; Wu, Q.; Qin, W.; Hu, Q.; Tang, B. Z. Monitoring Layer-by-Layer Self-Assembly Process of Natural Polyelectrolytes by Fluorescent Bioconjugate with Aggregation-Induced Emission Characteristic. *J. Mater. Chem. B* **2014**, *2*, 8406–8411.
- (853) Guan, W.; Lu, J.; Zhou, W.; Lu, C. Aggregation-Induced Emission Molecules in Layered Matrices for Two-Color Luminescence Films. *Chem. Commun.* **2014**, *50*, 11895–11898.
- (854) Zhang, C.; Liu, C.; Xue, X.; Zhang, X.; Huo, S.; Jiang, Y.; Chen, W.-Q.; Zou, G.; Liang, X.-J. Salt-Responsive Self-Assembly of Luminescent Hydrogel with Intrinsic Gelation-Enhanced Emission. *ACS Appl. Mater. Interfaces* **2014**, *6*, 757–762.
- (855) Li, J.; Li, Y.; Chan, C. Y. K.; Kwok, R. T. K.; Li, H.; Zrazhevskiy, P.; Gao, X.; Sun, J. Z.; Qin, A.; Tang, B. Z. An Aggregation-Induced-Emission Platform for Direct Visualization of Interfacial Dynamic Self-Assembly. *Angew. Chem., Int. Ed.* **2014**, *53*, 13518–13522.
- (856) Wu, J.; Sun, S.; Feng, X.; Shi, J.; Hu, X.-Y.; Wang, L. Controllable Aggregation-Induced Emission Based on a Tetraphenylethylene-Functionalized Pillar[5]arene via Host–Guest Recognition. *Chem. Commun.* **2014**, *50*, 9122–9125.
- (857) Pucci, A.; Iasilli, G.; Tantussi, F.; Fuso, F.; Ruggeri, G. Aggregation Induced Emission as a New Tool for Polymer Traceability. *AIP Conf. Proc.* **2012**, *1459*, 89–91.
- (858) Iasilli, G.; Battisti, A.; Tantussi, F.; Fuso, F.; Allegrini, M.; Ruggeri, G.; Pucci, A. Aggregation-Induced Emission of Tetraphenylethylene in Styrene-Based Polymers. *Macromol. Chem. Phys.* **2014**, *215*, 499–506.
- (859) Taniguchi, R.; Yamada, T.; Sada, K.; Kokado, K. Stimuli-Responsive Fluorescence of AIE Elastomer Based on PDMS and Tetraphenylethene. *Macromolecules* **2014**, *47*, 6382–6388.
- (860) Kokado, K.; Nagai, A.; Chujo, Y. Poly( $\gamma$ -glutamic acid) Hydrogels with Water-Sensitive Luminescence Derived from Aggregation-Induced Emission of *o*-Carborane. *Macromolecules* **2010**, *43*, 6463–6468.
- (861) Wu, Y.; Hu, J. L.; Huang, H. H.; Li, J.; Zhu, Y.; Tang, B. Z.; Han, J. P.; Li, L. B. Memory Chromic Polyurethane with Tetraphenylethylene. *J. Polym. Sci., Part B: Polym. Phys.* **2014**, *52*, 104–110.
- (862) Baldo, M. A.; Thompson, M. E.; Forrest, S. R. High-Efficiency Fluorescent Organic Light-Emitting Devices Using a Phosphorescent Sensitizer. *Nature* **2000**, *403*, 750–753.
- (863) Wu, K. C.; Ku, P. J.; Lin, C. S.; Shih, H. T.; Wu, F. I.; Huang, M. J.; Lin, J. J.; Chen, I. C.; Cheng, C. H. The Photophysical Properties of Dipyrrenylbenzenes and Their Application as Exceedingly Efficient Blue Emitters for Electroluminescent Devices. *Adv. Funct. Mater.* **2008**, *18*, 67–75.
- (864) Park, H.; Lee, J.; Kang, I.; Chu, H. Y.; Lee, J. I.; Kwon, S. K.; Kim, Y. H. Highly Rigid and Twisted Anthracene Derivatives: A Strategy for Deep Blue OLED Materials with Theoretical Limit Efficiency. *J. Mater. Chem.* **2012**, *22*, 2695–2700.
- (865) Kim, Y.-H.; Jeong, H.-C.; Kim, S.-H.; Yang, K.; Kwon, S.-K. High-Purity-Blue and High-Efficiency Electroluminescent Devices Based on Anthracene. *Adv. Funct. Mater.* **2005**, *15*, 1799–1805.
- (866) Lee, M.-T.; Liao, C.-H.; Tsai, C.-H.; Chen, C. H. Highly Efficient, Deep-Blue Doped Organic Light-Emitting Devices. *Adv. Mater.* **2005**, *17*, 2493–2497.
- (867) Wu, C.-C.; Lin, Y.-T.; Wong, K.-T.; Chen, R.-T.; Chien, Y.-Y. Efficient Organic Blue-Light-Emitting Devices with Double Confinement on Terphorennes with Ambipolar Carrier Transport Properties. *Adv. Mater.* **2004**, *16*, 61–65.
- (868) Zhou, J.; He, B. R.; Chen, B.; Lu, P.; Sung, H. H. Y.; Williams, I. D.; Qin, A. J.; Qiu, H. Y.; Zhao, Z. J.; Tang, B. Z. Deep Blue Fluorescent 2,5-Bis(phenylsilyl)-substituted 3,4'-diphenylsiloles: Synthesis, Structure and Aggregation-Induced Emission. *Dyes Pigm.* **2013**, *99*, 520–525.
- (869) Zhao, Z. J.; Chen, S. M.; Shen, X. Y.; Mahtab, F.; Yu, Y.; Lu, P.; Lam, J. W. Y.; Kwok, H. S.; Tang, B. Z. Aggregation-Induced Emission, Self-Assembly, and Electroluminescence of 4,4'-Bis(1,2,2-triphenylvinyl)biphenyl. *Chem. Commun.* **2010**, *46*, 686–688.
- (870) Huang, J.; Sun, N.; Dong, Y.; Tang, R.; Lu, P.; Cai, P.; Li, Q.; Ma, D.; Qin, J.; Li, Z. Similar or Totally Different: The Control of Conjugation Degree through Minor Structural Modifications, and Deep-Blue Aggregation-Induced Emission Luminogens for Non-Doped OLEDs. *Adv. Funct. Mater.* **2013**, *23*, 2329–2337.
- (871) Huang, J.; Sun, N.; Chen, P.; Tang, R.; Li, Q.; Ma, D.; Li, Z. Largely Blue-Shifted Emission Through Minor Structural Modifications: Molecular Design, Synthesis, Aggregation-Induced Emission and Deep-Blue OLED Application. *Chem. Commun.* **2014**, *50*, 2136–2138.
- (872) Zhao, Z. J.; Chen, S. M.; Lam, J. W. Y.; Chan, C. Y. K.; Jim, C. K. W.; Wang, Z. M.; Wang, C. L.; Lu, P.; Kwok, H. S.; Ma, Y. G.; et al. Luminescent Tetraphenylethene-Substituted Silanes. *Pure Appl. Chem.* **2010**, *82*, 863–870.
- (873) Tang, X.; Yao, L.; Liu, H.; Shen, F.; Zhang, S.; Zhang, H.; Lu, P.; Ma, Y. An Efficient AIE-Active Blue-Emitting Molecule by Incorporating Multifunctional Groups into Tetraphenylsilane. *Chem. - Eur. J.* **2014**, *20*, 7589–7592.
- (874) Moorthy, J. N.; Venkatakrishnan, P.; Natarajan, P.; Lin, Z. H.; Chow, T. J. Nondoped Pure-Blue OLEDs Based on Amorphous

- Phenylenevinylene-Functionalized Twisted Bimesitylenes. *J. Org. Chem.* **2010**, *75*, 2599–2609.
- (875) Huang, J.; Jiang, Y. B.; Yang, J.; Tang, R. L.; Xie, N.; Li, Q.; Kwok, H. S.; Tang, B. Z.; Li, Z. Construction of Efficient Blue AIE Emitters with Triphenylamine and TPE Moieties for Non-Doped OLEDs. *J. Mater. Chem. C* **2014**, *2*, 2028–2036.
- (876) Huang, J.; Sun, N.; Yang, J.; Tang, R.; Li, Q.; Ma, D.; Li, Z. Blue Aggregation-Induced Emission Luminogens: High External Quantum Efficiencies Up to 3.99% in LED Device, and Restriction of the Conjugation Length through Rational Molecular Design. *Adv. Funct. Mater.* **2014**, *24*, 7645–7654.
- (877) Huang, J.; Tang, R.; Zhang, T.; Li, Q.; Yu, G.; Xie, S.; Liu, Y.; Ye, S.; Qin, J.; Li, Z. A New Approach to Prepare Efficient Blue AIE Emitters for Undoped OLEDs. *Chem. - Eur. J.* **2014**, *20*, 5317–5326.
- (878) Zhao, Z.; Chen, S.; Deng, C.; Lam, J. W. Y.; Chan, C. Y. K.; Lu, P.; Wang, Z.; Hu, B.; Chen, X.; Lu, P.; et al. Construction of Efficient Solid Emitters with Conventional and AIE Luminogens for Blue Organic Light-emitting Diodes. *J. Mater. Chem.* **2011**, *21*, 10949–10956.
- (879) He, B.; Chang, Z.; Jiang, Y.; Xu, X.; Lu, P.; Kwok, H. S.; Zhou, J.; Qiu, H.; Zhao, Z.; Tang, B. Z. Piezochromic Luminescent and Electroluminescent Materials Comprised of Tetraphenylethene Plus Spirofluorene or 9,9-Diphenylfluoren. *Dyes Pigm.* **2014**, *106*, 87–93.
- (880) Zhao, Z.; Deng, C.; Chen, S.; Lam, J. W. Y.; Qin, W.; Lu, P.; Wang, Z.; Kwok, H. S.; Ma, Y.; Qiu, H.; Tang, B. Z. Full Emission Color Tuning in Luminogens Constructed from Tetraphenylethene, Benzo-2,1,3-thiadiazole and Thiophene Building Blocks. *Chem. Commun.* **2011**, *47*, 8847–8849.
- (881) Zhao, Z. J.; Chen, S. M.; Lam, J. W. Y.; Jim, C. K. W.; Chan, C. Y. K.; Wang, Z. M.; Lu, P.; Deng, C. M.; Kwok, H. S.; Ma, Y. G.; et al. Steric Hindrance, Electronic Communication, and Energy Transfer in the Photo- and Electroluminescence Processes of Aggregation-Induced Emission Luminogens. *J. Phys. Chem. C* **2010**, *114*, 7963–7972.
- (882) Chen, B.; Jiang, Y.; He, B.; Zhou, J.; Sung, H. H. Y.; Williams, I. D.; Lu, P.; Kwok, H. S.; Qiu, H.; Zhao, Z.; et al. Synthesis, Structure, Photoluminescence, and Electroluminescence of Siloles that Contain Planar Fluorescent Chromophores. *Chem. - Asian J.* **2014**, *9*, 2937–2945.
- (883) Gong, Y.; Zhang, Y.; Yuan, W. Z.; Sun, J. Z.; Zhang, Y. D.–A Solid Emitter with Crowded and Remarkably Twisted Conformations Exhibiting Multifunctionality and Multicolor Mechanochromism. *J. Phys. Chem. C* **2014**, *118*, 10998–11005.
- (884) Zhao, Z.; Geng, J.; Chang, Z.; Chen, S.; Deng, C.; Jiang, T.; Qin, W.; Lam, J. W. Y.; Kwok, H. S.; Qiu, H.; et al. A Tetraphenylethene-Based Red Luminophor for an Efficient Non-Doped Electroluminescence Device and Cellular Imaging. *J. Mater. Chem.* **2012**, *22*, 11018–11021.
- (885) Li, H.; Chi, Z.; Zhang, X.; Xu, B.; Liu, S.; Zhang, Y.; Xu, J. New Thermally Stable Aggregation-Induced Emission Enhancement Compounds for Non-Doped Red Organic Light-Emitting Diodes. *Chem. Commun.* **2011**, *47*, 11273–11275.
- (886) Du, X.; Qi, J.; Zhang, Z.; Ma, D.; Wang, Z. Y. Efficient Non-Doped Near Infrared Organic Light-Emitting Devices Based on Fluorophores with Aggregation-Induced Emission Enhancement. *Chem. Mater.* **2012**, *24*, 2178–2185.
- (887) Yue, Z. N.; Cheung, Y. F.; Choi, H. W.; Zhao, Z. J.; Tang, B. Z.; Wong, K. S. Hybrid GaN/Organic White Light Emitters with Aggregation Induced Emission Organic Molecule. *Opt. Mater. Express* **2013**, *3*, 1906–1911.
- (888) Liu, S. J.; Li, F.; Diao, Q.; Ma, Y. G. Aggregation-Induced Enhanced Emission Materials for Efficient White Organic Light-Emitting Devices. *Org. Electron.* **2010**, *11*, 613–617.
- (889) Zhao, Z.; Lam, J. W. Y.; Tang, B. Z. Aggregation-Induced Emission of Tetraarylethene Luminogens. *Curr. Org. Chem.* **2010**, *14*, 2109–2132.
- (890) Chen, S. M.; Zhao, Z. J.; Tang, B. Z.; Kwok, H. S. Non-Doped White Organic Light-Emitting Diodes Based on Aggregation-Induced Emission. *J. Phys. D: Appl. Phys.* **2010**, *43*, 095101.
- (891) Liu, Y.; Chen, S.; Lam, J. W. Y.; Mahtab, F.; Kwok, H. S.; Tang, B. Z. Tuning the Electronic Nature of Aggregation-Induced Emission Chromophores with Enhanced Electron-Transporting Properties. *J. Mater. Chem.* **2012**, *22*, 5184–5189.
- (892) Yuan, W. Z.; Chen, S.; Lam, J. W. Y.; Deng, C.; Lu, P.; Sung, H. H. Y.; Williams, I. D.; Kwok, H. S.; Zhang, Y.; Tang, B. Z. Towards High Efficiency Solid Emitters with Aggregation-Induced Emission and Electron-Transport Characteristics. *Chem. Commun.* **2011**, *47*, 11216–11218.
- (893) Zhao, Z.; Liu, D.; Mahtab, F.; Xin, L.; Shen, Z.; Yu, Y.; Chan, C. Y. K.; Lu, P.; Lam, J. W. Y.; Sung, H. H. Y.; et al. Synthesis, Structure, Aggregation-Induced Emission, Self-Assembly, and Electron Mobility of 2,5-Bis(triphenylsilylethynyl)-3,4-diphenylsiloles. *Chem. - Eur. J.* **2011**, *17*, 5998–6008.
- (894) Son, H.-J.; Han, W.-S.; Wee, K. R.; Lee, S.-H.; Hwang, A.-R.; Kwon, S.; Cho, D. W.; Suh, I.-H.; Kang, S. O. Intermolecular Peripheral 2,5-Bipyridyl Interactions by Cyclization of 1,1'-Silanylene Unit of 2,3,4,5-Aryl Substituted Siloles: Enhanced Thermal Stability, High Charge Carrier Mobility, and Their Application to Electron Transporting Layers for OLEDs. *J. Mater. Chem.* **2009**, *19*, 8964–8973.
- (895) Chen, L.; Jiang, Y.; Nie, H.; Lu, P.; Sung, H. H. Y.; Williams, I. D.; Kwok, H. S.; Huang, F.; Qin, A.; Zhao, Z.; et al. Creation of Bifunctional Materials: Improve Electron-Transporting Ability of Light Emitters Based on AIE-Active 2,3,4,5-Tetraphenylsiloles. *Adv. Funct. Mater.* **2014**, *24*, 3621–3630.
- (896) Mu, G.; Zhang, W.; Xu, P.; Wang, H.; Wang, Y.; Wang, L.; Zhuang, S.; Zhu, X. Constructing New n-Type, Ambipolar, and p-Type Aggregation-Induced Blue Luminogens by Gradually Tuning the Proportion of Tetraphenylethene and Diphenylphosphine Oxide. *J. Phys. Chem. C* **2014**, *118*, 8610–8616.
- (897) Zhao, Z.; Lam, J. W. Y.; Chan, C. Y. K.; Chen, S.; Liu, J.; Lu, P.; Rodriguez, M.; Maldonado, J.-L.; Ramos-Ortiz, G.; Sung, H. H. Y.; et al. Stereoselective Synthesis, Efficient Light Emission, and High Bipolar Charge Mobility of Chiasmatic Luminogens. *Adv. Mater.* **2011**, *23*, 5430–5435.
- (898) Lin, S.-L.; Chan, L.-H.; Lee, R.-H.; Yen, M.-Y.; Kuo, W.-J.; Chen, C.-T.; Jeng, R.-J. Highly Efficient Carbazole- $\pi$ -Dimesitylboration Bipolar Fluorophores for Nondoped Blue Organic Light-Emitting Diodes. *Adv. Mater.* **2008**, *20*, 3947–3952.
- (899) Chen, P.; Lalancette, R. A.; Jäkle, F. Applying the Oligomer Approach to Luminescent Conjugated Organoboranes. *J. Am. Chem. Soc.* **2011**, *133*, 8802–8805.
- (900) Entwistle, C. D.; Marder, T. B. Boron Chemistry Lights the Way: Optical Properties of Molecular and Polymeric Systems. *Angew. Chem., Int. Ed.* **2002**, *41*, 2927–2931.
- (901) Murata, H.; Malliaras, G. G.; Uchida, M.; Shen, Y.; Kafafi, Z. H. Non-Dispersive and Air-Stable Electron Transport in An Amorphous Organic Semiconductor. *Chem. Phys. Lett.* **2001**, *339*, 161–166.
- (902) Mäkinen, A. J.; Uchida, M.; Kafafi, Z. H. Electronic Structure of a Silole Derivative-Magnesium Thin Film Interface. *J. Appl. Phys.* **2004**, *95*, 2832–2838.
- (903) Yu, G.; Yin, S.; Liu, Y.; Chen, J.; Xu, X.; Sun, X.; Ma, D.; Zhan, X.; Peng, Q.; Shuai, Z.; et al. Structures, Electronic States, Photoluminescence, and Carrier Transport Properties of 1,1-Disubstituted 2,3,4,5-Tetraphenylsiloles. *J. Am. Chem. Soc.* **2005**, *127*, 6335–6346.
- (904) Ma, D. G.; Wang, G.; Hu, Y. F.; Zhang, Y. G.; Wang, L. X.; Jing, X. B.; Wang, F. S.; Lee, C. S.; Lee, S. T. A Dinuclear Aluminum 8-Hydroxyquinoline Complex with High Electron Mobility for Organic Light-Emitting Diodes. *Appl. Phys. Lett.* **2003**, *82*, 1296–1298.
- (905) Liu, Z.; Hu, S.; Zhang, L.; Chen, J.; Peng, J.; Cao, Y. Electroluminescence Performances of 1,1-Bis(4-(*N,N*-dimethylamino)-phenyl)-2,3,4,5-tetraphenylsilole Based Polymers in Three Cathode Architectures. *Sci. China: Chem.* **2013**, *56*, 1129–1136.
- (906) Hu, R.; Lam, J. W. Y.; Deng, H.; Song, Z.; Zheng, C.; Tang, B. Z. Fluorescent Self-Assembled Nanowires of AIE Fluorogens. *J. Mater. Chem. C* **2014**, *2*, 6326–6332.
- (907) Wang, E.; Lam, J. W. Y.; Hu, R.; Zhang, C.; Zhao, Y. S.; Tang, B. Z. Twisted Intramolecular Charge Transfer, Aggregation-Induced Emission, Supramolecular Self-Assembly and the Optical Waveguide of Barbituric Acid-Functionalized Tetraphenylethene. *J. Mater. Chem. C* **2014**, *2*, 1801–1807.

- (908) Yuan, W. Z.; Mahtab, F.; Gong, Y.; Yu, Z.-Q.; Lu, P.; Tang, Y.; Lam, J. W. Y.; Zhu, C.; Tang, B. Z. Synthesis and Self-Assembly of Tetraphenylethene and Biphenyl Based AIE-Active Triazoles. *J. Mater. Chem.* **2012**, *22*, 10472–10479.
- (909) Shen, X. Y.; Wang, Y. J.; Zhao, E.; Yuan, W. Z.; Liu, Y.; Lu, P.; Qin, A.; Ma, Y.; Sun, J. Z.; Tang, B. Z. Effects of Substitution with Donor–Acceptor Groups on the Properties of Tetraphenylethene Trimer: Aggregation-Induced Emission, Solvatochromism, and Mechanochromism. *J. Phys. Chem. C* **2013**, *117*, 7334–7347.
- (910) Zhang, Y.; Liang, C.; Shang, H.; Ma, Y.; Jiang, S. Supramolecular Organogels and Nanowires Based on a V-Shaped Cyanostilbene Amide Derivative with Aggregation-Induced Emission (AIE) Properties. *J. Mater. Chem. C* **2013**, *1*, 4472–4480.
- (911) Chung, J. W.; Yang, H.; Singh, B.; Moon, H.; An, B.-k.; Lee, S. Y.; Park, S. Y. Single-Crystalline Organic Nanowires with Large Mobility and Strong Fluorescence Emission: A Conductive-AFM and Space-Charge-Limited-Current Study. *J. Mater. Chem.* **2009**, *19*, 5920–5925.
- (912) Shi, C.; Guo, Z.; Yan, Y.; Zhu, S.; Xie, Y.; Zhao, Y. S.; Zhu, W.; Tian, H. Self-Assembly Solid-State Enhanced Red Emission of Quinolinemalononitrile: Optical Waveguides and Stimuli Response. *ACS Appl. Mater. Interfaces* **2013**, *5*, 192–198.
- (913) Tian, B. Z.; Liu, J.; Dvir, T.; Jin, L. H.; Tsui, J. H.; Qing, Q.; Suo, Z. G.; Langer, R.; Kohane, D. S.; Lieber, C. M. Macroporous Nanowire Nanoelectronic Scaffolds for Synthetic Tissues. *Nat. Mater.* **2012**, *11*, 986–994.
- (914) Patolsky, F.; Zheng, G. F.; Lieber, C. M. Nanowire Sensors for Medicine and the Life Sciences. *Nanomedicine* **2006**, *1*, 51–65.
- (915) Dimitrakopoulos, C. D.; Malenfant, P. R. L. Organic Thin Film Transistors for Large Area Electronics. *Adv. Mater.* **2002**, *14*, 99–117.
- (916) Reese, C.; Roberts, M.; Ling, M.-M.; Bao, Z. Organic Thin Film Transistors. *Mater. Today* **2004**, *7*, 20–27.
- (917) Yamashita, Y. Organic Semiconductors for Organic Field-Effect Transistors. *Sci. Technol. Adv. Mater.* **2009**, *10*, 024313.
- (918) Zhao, Z.; Li, Z.; Lam, J. W. Y.; Maldonado, J.-L.; Ramos-Ortiz, G.; Liu, Y.; Yuan, W.; Xu, J.; Miao, Q.; Tang, B. Z. High Hole Mobility of 1,2-Bis[4’-(diphenylamino)biphenyl-4-yl]-1,2-diphenylethene in Field Effect Transistor. *Chem. Commun.* **2011**, *47*, 6924–6926.
- (919) Aldred, M. P.; Zhang, G.-F.; Li, C.; Chen, G.; Chen, T.; Zhu, M.-Q. Optical Properties and Red to Near Infrared Piezo-Responsive Fluorescence of a Tetraphenylethene–Perylenebisimide–Tetraphenylethene Triad. *J. Mater. Chem. C* **2013**, *1*, 6709–6718.
- (920) Heng, L.; Wang, X.; Tian, D.; Zhai, J.; Tang, B. Z.; Jiang, L. Optical Waveguides Based on Single-Crystalline Organic Micro-Tiles. *Adv. Mater.* **2010**, *22*, 4716–4720.
- (921) Gu, X.; Yao, J.; Zhang, G.; Yan, Y.; Zhang, C.; Peng, Q.; Liao, Q.; Wu, Y.; Xu, Z.; Zhao, Y.; et al. Polymorphism-Dependent Emission for Di(p-methoxyphenyl)dibenzofulvene and Analogues: Optical Waveguide/Amplified Spontaneous Emission Behaviors. *Adv. Funct. Mater.* **2012**, *22*, 4862–4872.
- (922) Zhao, N.; Zhang, C.; Lam, J. W. Y.; Zhao, Y. S.; Tang, B. Z. An Aggregation-Induced Emission Luminogen with Efficient Luminescent Mechanochromism and Optical Waveguiding Properties. *Asian J. Org. Chem.* **2014**, *3*, 118–121.
- (923) Gu, X.; Yao, J.; Zhang, G.; Zhang, C.; Yan, Y.; Zhao, Y.; Zhang, D. New Electron-Donor/Acceptor-Substituted Tetraphenylethylenes: Aggregation-Induced Emission with Tunable Emission Color and Optical-Waveguide Behavior. *Chem. - Asian J.* **2013**, *8*, 2362–2369.
- (924) Ribierre, J. C.; Tsiminis, G.; Richardson, S.; Turnbull, G. A.; Samuel, I. D. W.; Barcena, H. S.; Burn, P. L. Amplified Spontaneous Emission and Lasing Properties of Bisfluorene-Cored Dendrimers. *Appl. Phys. Lett.* **2007**, *91*, 081108.
- (925) Richardson, F. S.; Riehl, J. P. Circularly Polarized Luminescence Spectroscopy. *Chem. Rev.* **1977**, *77*, 773–792.
- (926) Riehl, J. P.; Richardson, F. S. Circularly Polarized Luminescence Spectroscopy. *Chem. Rev.* **1986**, *86*, 1–16.
- (927) Spano, F. C.; Meskers, S. C. J.; Hennebicq, E.; Beljonne, D. Probing Excitation Delocalization in Supramolecular Chiral Stacks by Means of Circularly Polarized Light: Experiment and Modeling. *J. Am. Chem. Soc.* **2007**, *129*, 7044–7054.
- (928) Ng, J. C. Y.; Li, H.; Yuan, Q.; Liu, J.; Liu, C.; Fan, X.; Li, B. S.; Tang, B. Z. Valine-Containing Silole: Synthesis, Aggregation-Induced Chirality, Luminescence Enhancement, Chiral-Polarized Luminescence and Self-Assembled Structures. *J. Mater. Chem. C* **2014**, *2*, 4615–4621.
- (929) Li, H.; Cheng, J.; Zhao, Y.; Lam, J. W. Y.; Wong, K. S.; Wu, H.; Li, B. S.; Tang, B. Z. L-Valine Methyl Ester-Containing Tetraphenylethene: Aggregation-Induced Emission, Aggregation-Induced Circular Dichroism, Circularly Polarized Luminescence, and Helical Self-Assembly. *Mater. Horiz.* **2014**, *1*, 518–521.
- (930) Liu, X.; Jiao, J.; Jiang, X.; Li, J.; Cheng, Y.; Zhu, C. A Tetraphenylethene-Based Chiral Polymer: An AIE Luminogen with High and Tunable CPL Dissymmetry Factor. *J. Mater. Chem. C* **2013**, *1*, 4713–4719.
- (931) Ng, J. C. Y.; Liu, J.; Su, H.; Hong, Y.; Li, H.; Lam, J. W. Y.; Wong, K. S.; Tang, B. Z. Complexation-Induced Circular Dichroism and Circularly Polarised Luminescence of an Aggregation-Induced Emission Luminogen. *J. Mater. Chem. C* **2014**, *2*, 78–83.
- (932) Bertolotti, M.; Sansoni, G.; Scudieri, F. Dye Laser Emission in Liquid Crystal Hosts. *Appl. Opt.* **1979**, *18*, 528–531.
- (933) Grell, M.; Bradley, D. D. C. Polarized Luminescence from Oriented Molecular Materials. *Adv. Mater.* **1999**, *11*, 895–905.
- (934) Sergeyev, S.; Pisula, W.; Geerts, Y. H. Discotic Liquid Crystals: A New Generation of Organic Semiconductors. *Chem. Soc. Rev.* **2007**, *36*, 1902–1929.
- (935) O'Neill, M.; Kelly, S. M. Liquid Crystals for Charge Transport, Luminescence, and Photonics. *Adv. Mater.* **2003**, *15*, 1135–1146.
- (936) Binnemans, K.; Görller-Walrand, C. Lanthanide-Containing Liquid Crystals and Surfactants. *Chem. Rev.* **2002**, *102*, 2303–2346.
- (937) Chen, S. H.; Shi, H.; Conger, B. M.; Mastrangelo, J. C.; Tsutsui, T. Novel Vitrifiable Liquid Crystals as Optical Materials. *Adv. Mater.* **1996**, *8*, 998–1001.
- (938) Sentman, A. C.; Gin, D. L. Fluorescent Trimeric Liquid Crystals: Modular Design of Emissive Mesogens. *Adv. Mater.* **2001**, *13*, 1398–1401.
- (939) Luo, M.; Zhou, X.; Chi, Z.; Liu, S.; Zhang, Y.; Xu, J. Fluorescence-Enhanced Organogelators with Mesomorphic and Piezofluorochromic Properties Based on Tetraphenylethylene and Gallic Acid Derivatives. *Dyes Pigm.* **2014**, *101*, 74–84.
- (940) Wan, J. H.; Mao, L. Y.; Li, Y. B.; Li, Z. F.; Qiu, H. Y.; Wang, C.; Lai, G. Q. Self-Assembly of Novel Fluorescent Silole Derivatives into Different Supramolecular Aggregates: Fibre, Liquid Crystal and Monolayer. *Soft Matter* **2010**, *6*, 3195–3201.
- (941) Yoon, S.-J.; Kim, J. H.; Kim, K. S.; Chung, J. W.; Heinrich, B.; Mathevet, F.; Kim, P.; Donnio, B.; Attias, A.-J.; Kim, D.; et al. Mesomorphic Organization and Thermochromic Luminescence of Dicyanodistyrylbenzene-Based Phasmidic Molecular Disks: Uniaxially Aligned Hexagonal Columnar Liquid Crystals at Room Temperature with Enhanced Fluorescence Emission and Semiconductivity. *Adv. Funct. Mater.* **2012**, *22*, 61–66.
- (942) Ren, Y.; Kan, W. H.; Henderson, M. A.; Bomben, P. G.; Berlinguette, C. P.; Thangadurai, V.; Baumgartner, T. External-Stimuli Responsive Photophysics and Liquid Crystal Properties of Self-Assembled “Phosphole-Lipids”. *J. Am. Chem. Soc.* **2011**, *133*, 17014–17026.
- (943) Kim, J.; Cho, S.; Cho, B.-K. An Unusual Stacking Transformation in Liquid-Crystalline Columnar Assemblies of Clicked Molecular Propellers with Tunable Light Emissions. *Chem. - Eur. J.* **2014**, *20*, 12734–12739.
- (944) Tanabe, K.; Suzui, Y.; Hasegawa, M.; Kato, T. Full-Color Tunable Photoluminescent Ionic Liquid Crystals Based on Tripodal Pyridinium, Pyrimidinium, and Quinolinium Salts. *J. Am. Chem. Soc.* **2012**, *134*, 5652–5661.
- (945) Mao, W. G.; Chen, K.; Ouyang, M.; Sun, J. W.; Zhou, Y. B.; Song, Q. B.; Zhang, C. Synthesis and Characterization of New Cyanostilbene-Based Compound Exhibiting Reversible Mechanochromism. *Huaxue Xuebao* **2013**, *71*, 613–618.
- (946) Lu, H.; Qiu, L.; Zhang, G.; Ding, A.; Xu, W.; Zhang, G.; Wang, X.; Kong, L.; Tian, Y.; Yang, J. Electrically Switchable Photoluminescence of Fluorescent-Molecule-Dispersed Liquid Crystals

- Prepared via Photoisomerization-Induced Phase Separation. *J. Mater. Chem. C* **2014**, *2*, 1386–1389.
- (947) Park, J. W.; Nagano, S.; Yoon, S.-J.; Dohi, T.; Seo, J.; Seki, T.; Park, S. Y. High Contrast Fluorescence Patterning in Cyanostilbene-Based Crystalline Thin Films: Crystallization-Induced Mass Flow via a Photo-Triggered Phase Transition. *Adv. Mater.* **2014**, *26*, 1354–1359.
- (948) Yuan, W. Z.; Yu, Z.-Q.; Lu, P.; Deng, C.; Lam, J. W. Y.; Wang, Z.; Chen, E.-Q.; Ma, Y.; Tang, B. Z. High Efficiency Luminescent Liquid Crystal: Aggregation-Induced Emission Strategy and Biaxially Oriented Mesomorphic Structure. *J. Mater. Chem.* **2012**, *22*, 3323–3326.
- (949) Yuan, W. Z.; Yu, Z.-Q.; Tang, Y.; Lam, J. W. Y.; Xie, N.; Lu, P.; Chen, E.-Q.; Tang, B. Z. High Solid-State Efficiency Fluorescent Main Chain Liquid Crystalline Polytriazoles with Aggregation-Induced Emission Characteristics. *Macromolecules* **2011**, *44*, 9618–9628.
- (950) Mi, B.; Dong, Y.; Li, Z.; Lam, J. W. Y.; Haussler, M.; Sung, H. H.; Kwok, H. S.; Dong, Y.; Williams, I. D.; Liu, Y.; et al. Making Silole Photovoltaically Active by Attaching Carbazolyl Donor Groups to the Silolyl Acceptor Core. *Chem. Commun.* **2005**, 3583–3585.
- (951) Li, Y.; Li, Z.; Wang, Y.; Compaan, A.; Ren, T.; Dong, W.-J. Increasing the Power Output of a CdTe Solar Cell via Luminescent Down Shifting Molecules with Intramolecular Charge Transfer and Aggregation-Induced Emission Characteristics. *Energy Environ. Sci.* **2013**, *6*, 2907–2911.
- (952) *Handbook of Photovoltaic Science and Engineering*; Luque, A., Hegedus, S., Eds.; John Wiley & Sons, Ltd: Hoboken, NJ, 2003.
- (953) Rose, D. H.; Hasoon, F. S.; Dhore, R. G.; Albin, D. S.; Ribelin, R. M.; Li, X. S.; Mahathongdy, Y.; Gessert, T. A.; Sheldon, P. Fabrication Procedures and Process Sensitivities for CdS/CdTe Solar Cells. *Prog. Photovoltaics* **1999**, *7*, 331–340.
- (954) Ferrini, R.; Nicolet, O.; Huber, S.; Zuppiroli, L.; Chappellet, S.; Lovey, C.; Perrenoud, J.; Pauchard, M. Fluorescent Nanopigments: Quantitative Assessment of Their Quantum Yield. *J. Appl. Phys.* **2010**, *107*, 114323–114329.
- (955) Richards, B. S.; McIntosh, K. R. Overcoming the Poor Short Wavelength Spectral Response of CdS/CdTe Photovoltaic Modules via Luminescence Down-shifting: Ray-Tracing Simulations. *Prog. Photovoltaics* **2007**, *15*, 27–34.
- (956) Yuan, H.; Wang, K.; Yang, K.; Liu, B.; Zou, B. Luminescence Properties of Compressed Tetraphenylethene: The Role of Intermolecular Interactions. *J. Phys. Chem. Lett.* **2014**, *5*, 2968–2973.
- (957) Li, C.; Luo, X.; Zhao, W.; Li, C.; Liu, Z.; Bo, Z.; Dong, Y.; Dong, Y. Q.; Tang, B. Z. Switching the Emission of Tetrakis(4-methoxyphenyl)ethylene among Three Colors in the Solid State. *New J. Chem.* **2013**, *37*, 1696–1699.
- (958) Luo, X.; Zhao, W.; Shi, J.; Li, C.; Liu, Z.; Bo, Z.; Dong, Y. Q.; Tang, B. Z. Reversible Switching Emissions of Tetraphenylethene Derivatives among Multiple Colors with Solvent Vapor, Mechanical, and Thermal Stimuli. *J. Phys. Chem. C* **2012**, *116*, 21967–21972.
- (959) Wang, J.; Mei, J.; Hu, R.; Sun, J. Z.; Qin, A.; Tang, B. Z. Click Synthesis, Aggregation-Induced Emission, *E/Z* Isomerization, Self-Organization, and Multiple Chromisms of Pure Stereoisomers of a Tetraphenylethene-Cored Luminogen. *J. Am. Chem. Soc.* **2012**, *134*, 9956–9966.
- (960) Shi, J. Q.; Zhao, W. J.; Li, C. H.; Liu, Z. P.; Bo, Z. S.; Dong, Y. P.; Dong, Y. Q.; Tang, B. Z. Switching Emissions of Two Tetraphenylethene Derivatives with Solvent Vapor, Mechanical, and Thermal Stimuli. *Chin. Sci. Bull.* **2013**, *58*, 2723–2727.
- (961) Zhang, G.-F.; Wang, H.; Aldred, M. P.; Chen, T.; Chen, Z.-Q.; Meng, X.; Zhu, M.-Q. General Synthetic Approach toward Geminal-Substituted Tetraarylethene Fluorophores with Tunable Emission Properties: X-ray Crystallography, Aggregation-Induced Emission and Piezofluorochromism. *Chem. Mater.* **2014**, *26*, 4433–4446.
- (962) Xu, B.; Chi, Z.; Zhang, J.; Zhang, X.; Li, H.; Li, X.; Liu, S.; Zhang, Y.; Xu, J. Piezofluorochromic and Aggregation-Induced-Emission Compounds Containing Triphenylethylene and Tetraphenylethylene Moieties. *Chem. - Asian J.* **2011**, *6*, 1470–1478.
- (963) Xu, B.; Xie, M.; He, J.; Xu, B.; Chi, Z.; Tian, W.; Jiang, L.; Zhao, F.; Liu, S.; Zhang, Y.; et al. An Aggregation-Induced Emission Luminophore with Multi-Stimuli Single- and Two-Photon Fluorescence Switching and Large Two-Photon Absorption Cross Section. *Chem. Commun.* **2013**, *49*, 273–275.
- (964) Misra, R.; Jadhav, T.; Dhokane, B.; Mobin, S. M. Reversible Mechanochromism and Enhanced AIE in Tetraphenylethene Substituted Phenanthroimidazoles. *Chem. Commun.* **2014**, *50*, 9076–9078.
- (965) Zhou, X.; Li, H.; Chi, Z.; Zhang, X.; Zhang, J.; Xu, B.; Zhang, Y.; Liu, S.; Xu, J. Piezofluorochromism and Morphology of a New Aggregation-Induced Emission Compound Derived from Tetraphenylethylene and Carbazole. *New J. Chem.* **2012**, *36*, 685–693.
- (966) Zhao, N.; Yang, Z.; Lam, J. W. Y.; Sung, H. H. Y.; Xie, N.; Chen, S.; Su, H.; Gao, M.; Williams, I. D.; Wong, K. S.; et al. Benzothiazolium-Functionalized Tetraphenylethene: An AIE Luminogen with Tunable Solid-State Emission. *Chem. Commun.* **2012**, *48*, 8637–8639.
- (967) Mei, J.; Wang, J.; Qin, A.; Zhao, H.; Yuan, W.; Zhao, Z.; Sung, H. H. Y.; Deng, C.; Zhang, S.; Williams, I. D.; et al. Construction of Soft Porous Crystal with Silole Derivative: Strategy of Framework Design, Multiple Structural Transformability and Mechanofluorochromism. *J. Mater. Chem.* **2012**, *22*, 4290–4292.
- (968) Li, C.; Luo, X.; Zhao, W.; Huang, Z.; Liu, Z.; Tong, B.; Dong, Y. Switching the Emission of Di(4-ethoxyphenyl)dibenzofulvene among Multiple Colors in the Solid State. *Sci. China: Chem.* **2013**, *56*, 1173–1177.
- (969) Luo, X.; Li, J.; Li, C.; Heng, L.; Dong, Y. Q.; Liu, Z.; Bo, Z.; Tang, B. Z. Reversible Switching of the Emission of Diphenyldibenzofulvenes by Thermal and Mechanical Stimuli. *Adv. Mater.* **2011**, *23*, 3261–3265.
- (970) Zhang, X.; Chi, Z.; Li, H.; Xu, B.; Li, X.; Zhou, W.; Liu, S.; Zhang, Y.; Xu, J. Piezofluorochromism of an Aggregation-Induced Emission Compound Derived from Tetraphenylethylene. *Chem. - Asian J.* **2011**, *6*, 808–811.
- (971) Lin, Y.; Chen, G.; Zhao, L.; Yuan, W.; Zhang, Y.; Tang, B. Z. Diethylamino Functionalized Tetraphenylethenes: Structural and Electronic Modulation of Photophysical Properties, Implication for the CIE Mechanism and Application to Cell Imaging. *J. Mater. Chem. C* **2015**, *3*, 112–120.
- (972) Qi, Q.; Zhang, J.; Xu, B.; Li, B.; Zhang, S. X.-A.; Tian, W. Mechanochromism and Polymorphism-Dependent Emission of Tetrakis(4-(dimethylamino)phenyl)ethylene. *J. Phys. Chem. C* **2013**, *117*, 24997–25003.
- (973) Lv, Y.; Liu, Y.; Guo, D.; Ye, X.; Liu, G.; Tao, X. Mechanochromic Luminescence of Fluorenol-Substituted Ethylenes. *Chem. - Asian J.* **2014**, *9*, 2885–2890.
- (974) Gong, Y.; Liu, J.; Zhang, Y.; He, G.; Lu, Y.; Fan, W. B.; Yuan, W. Z.; Sun, J. Z.; Zhang, Y. AIE-Active, Highly Thermally and Morphologically Stable, Mechanochromic and Efficient Solid Emitters for Low Color Temperature OLEDs. *J. Mater. Chem. C* **2014**, *2*, 7552–7560.
- (975) Bu, L.; Sun, M.; Zhang, D.; Liu, W.; Wang, Y.; Zheng, M.; Xue, S.; Yang, W. Solid-State Fluorescence Properties and Reversible Piezochromic Luminescence of Aggregation-Induced Emission-Active 9,10-Bis[(9,9-dialkylfluorene-2-yl)vinyl]anthracenes. *J. Mater. Chem. C* **2013**, *1*, 2028–2035.
- (976) Zhang, X.; Chi, Z.; Zhang, J.; Li, H.; Xu, B.; Li, X.; Liu, S.; Zhang, Y.; Xu, J. Piezofluorochromic Properties and Mechanism of an Aggregation-Induced Emission Enhancement Compound Containing N-Hexyl-phenoxyazine and Anthracene Moieties. *J. Phys. Chem. B* **2011**, *115*, 7606–7611.
- (977) Li, H.; Zhang, X.; Chi, Z.; Xu, B.; Zhou, W.; Liu, S.; Zhang, Y.; Xu, J. New Thermally Stable Piezofluorochromic Aggregation-Induced Emission Compounds. *Org. Lett.* **2011**, *13*, 556–559.
- (978) Zheng, M.; Zhang, D. T.; Sun, M. X.; Li, Y. P.; Liu, T. L.; Xue, S. F.; Yang, W. J. Cruciform 9,10-Distyryl-2,6-bis(p-dialkylamino-styryl)-anthracene Homologues Exhibiting Alkyl Length-Tunable Piezochromic Luminescence and Heat-Recovery Temperature of Ground States. *J. Mater. Chem. C* **2014**, *2*, 1913–1920.
- (979) Zhang, P.; Dou, W.; Ju, Z.; Tang, X.; Liu, W.; Chen, C.; Wang, B.; Liu, W. Modularity Analysis of Tunable Solid-State Emission Based on a Twisted Conjugated Molecule Containing 9,9'-Bianthracene Group. *Adv. Mater.* **2013**, *25*, 6112–6116.

- (980) Yoon, S.-J.; Chung, J. W.; Gierschner, J.; Kim, K. S.; Choi, M.-G.; Kim, D.; Park, S. Y. Multistimuli Two-Color Luminescence Switching via Different Slip-Stacking of Highly Fluorescent Molecular Sheets. *J. Am. Chem. Soc.* **2010**, *132*, 13675–13683.
- (981) Yoon, S.-J.; Park, S. Polymorphic and Mechanochromic Luminescence Modulation in the Highly Emissive Dicyanodistyrylbenzene Crystal: Secondary Bonding Interaction in Molecular Stacking Assembly. *J. Mater. Chem.* **2011**, *21*, 8338–8346.
- (982) Xu, B.; Chi, Z.; Zhang, X.; Li, H.; Chen, C.; Liu, S.; Zhang, Y.; Xu, J. A New Ligand and Its Complex with Multi-Stimuli-Responsive and Aggregation-Induced Emission Effects. *Chem. Commun.* **2011**, *47*, 11080–11082.
- (983) Sun, J.; Lv, X.; Wang, P.; Zhang, Y.; Dai, Y.; Wu, Q.; Ouyang, M.; Zhang, C. A Donor–Acceptor Cruciform  $\pi$ -System: High Contrast Mechanochromic Properties and Multicolour Electrochromic Behavior. *J. Mater. Chem. C* **2014**, *2*, 5365–5371.
- (984) Zhang, Y.; Sun, J.; Bian, G.; Chen, Y.; Ouyang, M.; Hua, B.; Zhang, C. Cyanostilben-Based Derivatives: Mechanical Stimuli-Responsive Luminophors with Aggregation-Induced Emission Enhancement. *Photochem. Photobiol. Sci.* **2012**, *11*, 1414–1421.
- (985) Song, N.; Chen, D.-X.; Qiu, Y.-C.; Yang, X.-Y.; Xu, B.; Tian, W.; Yang, Y.-W. Stimuli-Responsive Blue Fluorescent Supramolecular Polymers Based on a Pillar[5]arene Tetramer. *Chem. Commun.* **2014**, *50*, 8231–8234.
- (986) Zheng, H.; Li, C.; He, C.; Dong, Y. Q.; Liu, Q.; Qin, P.; Zeng, C.; Wang, H. Luminescent Hydrogels Based on Di(4-propoxyphenyl)-dibenzofulvene Exhibiting Four Emission Colours and Organic Solvents/Thermal Dual-Responsive Properties. *J. Mater. Chem. C* **2014**, *2*, 5829–5835.
- (987) Zang, L.; Shang, H.; Wei, D.; Jiang, S. A Multi-Stimuli-Responsive Organogel Based on Salicylidene Schiff Base. *Sens. Actuators, B* **2013**, *185*, 389–397.
- (988) Xu, Y.; Xue, P. C.; Xu, D. F.; Zhang, X. F.; Liu, X. L.; Zhou, H. P.; Jia, J. H.; Yang, X. C.; Wang, F. Y.; Lu, R. Multicolor Fluorescent Switches in Gel Systems Controlled by Alkoxy Chain and Solvent. *Org. Biomol. Chem.* **2010**, *8*, 4289–4296.
- (989) Chen, Q.; Zhang, D. Q.; Zhang, G. X.; Yang, X. Y.; Feng, Y.; Fan, Q. H.; Zhu, D. B. Multicolor Tunable Emission from Organogels Containing Tetraphenylethene, Perylenediimide, and Spiropyran Derivatives. *Adv. Funct. Mater.* **2010**, *20*, 3244–3251.
- (990) Han, T.; Feng, X.; Shi, J.; Tong, B.; Dong, Y.; Lam, J. W. Y.; Dong, Y.; Tang, B. Z. DMF-Induced Emission of an Aryl-Substituted Pyrrole Derivative: a Solid Thermo-Responsive Material to Detect Temperature in a Specific Range. *J. Mater. Chem. C* **2013**, *1*, 7534–7539.
- (991) Yao, X.; Ma, X.; Tian, H. Aggregation-Induced Emission Encoding Supramolecular Polymers Based on Controllable Sulfonato-calixarene Recognition in Aqueous Solution. *J. Mater. Chem. C* **2014**, *2*, S155–S160.
- (992) Hu, J.; He, Z.; Wang, Z.; Li, X.; You, J.; Gao, G. A Simple Approach to Aggregation Induced Emission in Difluoroboron Dibenzoylelmethane Derivatives. *Tetrahedron Lett.* **2013**, *54*, 4167–4170.
- (993) Cheng, X.; Zhang, Z.; Zhang, H.; Han, S.; Ye, K.; Wang, L.; Zhang, H.; Wang, Y. CEE-Active Red/Near-Infrared Fluorophores with Triple-Channel Solid-State “ON/OFF” Fluorescence Switching. *J. Mater. Chem. C* **2014**, *2*, 7385–7391.
- (994) Wang, S.; Xiao, S.; Chen, X.; Zhang, R.; Cao, Q.; Zou, K. Crystalline Solid Responsive to Mechanical and Acidic Stimuli: Boroneflourine Derivative with TICT Characteristic. *Dyes Pigm.* **2013**, *99*, 543–547.
- (995) Peterson, J. J.; Davis, A. R.; Werre, M.; Coughlin, E. B.; Carter, K. R. Carborane-Containing Poly(fluorene): Response to Solvent Vapors and Amines. *ACS Appl. Mater. Interfaces* **2011**, *3*, 1796–1799.
- (996) Schmidbaur, H.; Schier, A. A Briefing on Auophilicity. *Chem. Soc. Rev.* **2008**, *37*, 1931–1951.
- (997) Meinershagen, J. L.; Bein, T. J. Optical Sensing in Nanopores. Encapsulation of the Solvatochromic Dye Nile Red in Zeolites. *J. Am. Chem. Soc.* **1999**, *121*, 448–449.
- (998) Vickery, J. C.; Olmstead, M. M.; Fung, E. Y.; Balch, A. L. Solvent-Stimulated Luminescence from the Supramolecular Aggregation of a Trinuclear Gold(I) Complex that Displays Extensive Intermolecular Au···Au Interactions. *Angew. Chem., Int. Ed. Engl.* **1997**, *36*, 1179–1181.
- (999) Mansour, M. A.; Connick, W. B.; Lachicotte, R. J.; Gysling, H. J.; Eisenberg, R. Linear Chain Au(I) Dimer Compounds as Environmental Sensors: A Luminescent Switch for the Detection of Volatile Organic Compounds. *J. Am. Chem. Soc.* **1998**, *120*, 1329–1330.
- (1000) Pang, J.; Marcotte, E. J.-P.; Seward, C.; Brown, R. S.; Wang, S. A Blue Luminescent Star-Shaped Zn(II) Complex that Can Detect Benzene. *Angew. Chem., Int. Ed.* **2001**, *40*, 4042–4045.
- (1001) Kui, S. C. F.; Chui, S. S.-Y.; Che, C.-M.; Zhu, N. Structures, Photoluminescence, and Reversible Vapoluminescence Properties of Neutral Platinum(II) Complexes Containing Extended  $\pi$ -Conjugated Cyclometalated Ligands. *J. Am. Chem. Soc.* **2006**, *128*, 8297–8309.
- (1002) Baldauff, E. A.; Buriak, J. M. Optical Sensing of Amine Vapors with a Series of Tin Compounds. *Chem. Commun.* **2004**, 2028–2029.
- (1003) Ni, J.; Zhang, L.-Y.; Wen, H.-M.; Chen, Z.-N. Luminescence Vapochromic Properties of a Platinum(II) Complex with S,S-Bis(trimethylsilylethynyl)-2,2-bipyridine. *Chem. Commun.* **2009**, 3801–3803.
- (1004) Maini, L.; Braga, D.; Mazzeo, P. P.; Ventura, B. Polymorph and Isomer Conversion of Complexes Based on CuI and PPh<sub>3</sub> Easily Observed via Luminescence. *Dalton Trans.* **2012**, *41*, 531–539.
- (1005) Mizukami, S.; Houjou, H.; Sugaya, K.; Koyama, E.; Tokuhisa, H.; Sasano, T.; Kaneko, M. Fluorescence Color Modulation by Intramolecular and Intermolecular  $\pi$ – $\pi$  Interactions in a Helical Zinc(II) Complex. *Chem. Mater.* **2005**, *17*, 50–56.
- (1006) Fernández, E. J.; López-de-Luzuriaga, J. M.; Monge, M.; Montiel, M.; Olmos, M. E.; Pérez, J. A Detailed Study of the Vapochromic Behavior of {Tl[Au(C<sub>6</sub>Cl<sub>5</sub>)<sub>2</sub>]}<sub>n</sub>. *Inorg. Chem.* **2004**, *43*, 3573–3581.
- (1007) Rawashdeh-Omary, M. A.; Rashdan, M. D.; Dharanipathi, S.; Elbjeirami, O.; Ramesh, P.; Dias, H. V. R. On/Off Luminescence Vapochromic Selective Sensing of Benzene and Its Methylated Derivatives by a Trinuclear Silver(I) Pyrazolate Sensor. *Chem. Commun.* **2011**, *47*, 1160–1162.
- (1008) Beauvais, L. G.; Shores, M. P.; Long, J. R. Cyano-Bridged Re<sub>6</sub>Q<sub>8</sub> (Q = S, Se) Cluster-Cobalt(II) Framework Materials: Versatile Solid Chemical Sensors. *J. Am. Chem. Soc.* **2000**, *122*, 2763–2772.
- (1009) Ma, C.; Xu, B.; Xie, G.; He, J.; Zhou, X.; Peng, B.; Jiang, L.; Xu, B.; Tian, W.; Chi, Z.; et al. An AIE-Active Luminophore with Tunable and Remarkable Fluorescence Switching Based on the Piezo and Protonation–Deprotonation Control. *Chem. Commun.* **2014**, *50*, 7374–7377.
- (1010) Qi, Q.; Fang, X.; Liu, Y.; Zhou, P.; Zhang, Y.; Yang, B.; Tian, W.; Zhang, S. X.-A. A TPE-Oxazoline Molecular Switch with Tunable Multi-Emission in Both Solution and Solid State. *RSC Adv.* **2013**, *3*, 16986–16989.
- (1011) Xie, N. *Development, Mechanistic Study and Electro-, Chemi- and Mechanoluminescence of Aggregation-Induced Emission Materials*. Ph.D. Dissertation, HKUST, Hong Kong, 2013 (<http://ibezone.ust.hk/bib/b1255225>).
- (1012) Zhang, Z.; Miao, Y.; Zhang, Q.; Lian, L.; Yan, G. Selective Room Temperature Phosphorescence Detection of Heparin Based on Manganese-Doped Zinc Sulfide Quantum Dots/Polybrene Self-Assembled Nanosensor. *Biosens. Bioelectron.* **2015**, *68*, 556–562.
- (1013) Yang, J.; Li, J.; Hao, P.; Qiu, F.; Liu, M.; Zhang, Q.; Shi, D. Synthesis, Optical Properties of Multi Donor-Acceptor Substituted AIE Pyridine Derivatives Dyes and Application for Au<sup>3+</sup> Detection in Aqueous Solution. *Dyes Pigm.* **2015**, *116*, 97–105.
- (1014) Yan, X. Z.; Cook, T. R.; Wang, P.; Huang, F. H.; Stang, P. J. Highly Emissive Platinum(II) Metallacages. *Nat. Chem.* **2015**, *7*, 342–348.
- (1015) Guo, K.; Gao, Z.; Cheng, J.; Shao, Y.; Lu, X.; Wang, H. Linear Thiophene-Containing  $\pi$ -Conjugated Aldehydes with Aggregation-Induced Emission for Building Solid Red Luminophors. *Dyes Pigm.* **2015**, *115*, 166–171.
- (1016) Hu, F.; Zhang, G.; Zhan, C.; Zhang, W.; Yan, Y.; Zhao, Y.; Fu, H.; Zhang, D. Highly Solid-State Emissive Pyridinium-Substituted Tetraphenylethylene Salts: Emission Color-Tuning with Counter

- Anions and Application for Optical Waveguides. *Small* **2015**, *11*, 1335–1344.
- (1017) Xue, P.; Sun, J.; Yao, B.; Gong, P.; Zhang, Z.; Qian, C.; Zhang, Y.; Lu, R. Strong Emissive Nanofibers of Organogels for the Detection of Volatile Acid Vapors. *Chem. - Eur. J.* **2015**, *21*, 4712–4720.
- (1018) Tasso, T. T.; Furuyama, T.; Kobayashi, N. Dinitriles Bearing AIE-Active Moieties: Synthesis, *E/Z* Isomerization, and Fluorescence Properties. *Chem. - Eur. J.* **2015**, *21*, 4817–4824.
- (1019) Li, Y.; Yu, H.; Shao, G.; Gan, F. A Tetraphenylethylene-Based “Turn On” Fluorescent Sensor for the Rapid Detection of  $\text{Ag}^+$  Ions with High Selectivity. *J. Photochem. Photobiol., A* **2015**, *301*, 14–19.
- (1020) Hang, Y.; He, X.; Yang, L.; Hua, J. Probing Sugar-Lectin Recognitions in the Near-Infrared Region Using Glyco-Diketopyrrolo-pyrrole with Aggregation-Induced-Emission. *Biosens. Bioelectron.* **2015**, *65*, 420–426.
- (1021) Roy, B.; Noguchi, T.; Tsuchiya, Y.; Yoshihara, D.; Yamamoto, T.; Shinkai, S. Molecular Recognition Directed Supramolecular Control over Perylene-bisimide Aggregation Resulting in Aggregation Induced Enhanced Emission (AIEE) and Induced Chiral Amplification. *J. Mater. Chem. C* **2015**, *3*, 2310–2318.
- (1022) Zhao, L.; Chen, Y.; Yuan, J.; Chen, M.; Zhang, H.; Li, X. Electrospun Fibrous Mats with Conjugated Tetraphenylethylene and Mannose for Sensitive Turn-On Fluorescent Sensing of *Escherichia Coli*. *ACS Appl. Mater. Interfaces* **2015**, *7*, 5177–5186.
- (1023) Peng, L.; Zheng, Y.; Wang, X.; Tong, A.; Xiang, Y. Photoactivatable Aggregation-Induced Emission Fluorophores with Multiple-Color Fluorescence and Wavelength-Selective Activation. *Chem. - Eur. J.* **2015**, *21*, 4326–4332.
- (1024) Raju, M. V. R.; Lin, H.-C. Self-Assembly of Tetraphenylethene-Based [2]Catenane Driven by Acid-Base-Controllable Molecular Switching and Its Enabled Aggregation-Induced Emission. *Org. Lett.* **2014**, *16*, 5564–5567.
- (1025) Zhang, T.; Ma, H.; Niu, Y.; Li, W.; Wang, D.; Peng, Q.; Shuai, Z.; Liang, W. Spectroscopic Signature of the Aggregation-Induced Emission Phenomena Caused by Restricted Nonradiative Decay: A Theoretical Proposal. *J. Phys. Chem. C* **2015**, *119*, 5040–5047.
- (1026) Xue, X.; Jin, S.; Zhang, C.; Yang, K.; Huo, S.; Chen, F.; Zou, G.; Liang, X.-J. Probe-Inspired Nano-Prodrug with Dual-Color Fluorogenic Property Reveals Spatiotemporal Drug Release in Living Cells. *ACS Nano* **2015**, *9*, 2729–2739.
- (1027) Ma, K.; Wang, H.; Li, X.; Xu, B.; Tian, W. Turn-On Sensing for  $\text{Ag}^+$  Based on AIE-Active Fluorescent Probe and Cytosine-Rich DNA. *Anal. Bioanal. Chem.* **2015**, *407*, 2625–2630.
- (1028) Dong, L.; Wang, W.; Lin, T.; Diller, K.; Barth, J. V.; Liu, J.; Tang, B. Z.; Klappenberger, F.; Lin, N. Two-Dimensional Hierarchical Supramolecular Assembly of a Silole Derivative and Surface-Assisted Chemical Transformations. *J. Phys. Chem. C* **2015**, *119*, 3857–3863.
- (1029) Wang, Z.; Yong, T.-Y.; Wan, J.; Li, Z.-H.; Zhao, H.; Zhao, Y.; Gan, L.; Yang, X.-L.; Xu, H.-B.; Zhang, C. Temperature-Sensitive Fluorescent Organic Nanoparticles with Aggregation-Induced Emission for Long-Term Cellular Tracing. *ACS Appl. Mater. Interfaces* **2015**, *7*, 3420–3425.
- (1030) Ezhumalai, Y.; Wang, T.-H.; Hsu, H.-F. Regioselective Synthesis of Tetraphenyl-1,3-butadienes with Aggregation-Induced Emission. *Org. Lett.* **2015**, *17*, 536–539.
- (1031) Yuan, Y.; Zhang, C.-J.; Gao, M.; Zhang, R.; Tang, B. Z.; Liu, B. Specific Light-Up Bioprobe with Aggregation-induced Emission and Activatable Photoactivity for the Targeted and Image-Guided Photodynamic Ablation of Cancer Cells. *Angew. Chem., Int. Ed.* **2015**, *54*, 1780–1786.
- (1032) Wang, K.; Zhang, X.; Zhang, X.; Yang, B.; Li, Z.; Zhang, Q.; Huang, Z.; Wei, Y. One-Pot Preparation of Cross-Linked Amphiphilic Fluorescent Polymer Based on Aggregation Induced Emission Dyes. *Colloids Surf., B* **2015**, *126*, 273–279.
- (1033) Zhu, S.; Song, Y.; Zhao, X.; Shao, J.; Zhang, J.; Yang, B. The Photoluminescence Mechanism in Carbon Dots (Graphene Quantum Dots, Carbon Nanodots, and Polymer Dots): Current State and Future Perspective. *Nano Res.* **2015**, *8*, 355–381.
- (1034) Zhang, J.; Li, C.; Zhang, X.; Huo, S.; Jin, S.; An, F.-F.; Wang, X.; Xue, X.; Okeke, C. I.; Duan, G.; et al. In vivo Tumor-targeted Dual-modal Fluorescence/CT Imaging Using a Nanoprobe Co-Loaded with an Aggregation-Induced Emission Dye and Gold nanoparticles. *Biomaterials* **2015**, *42*, 103–111.
- (1035) Zhang, D.; Gao, Y.; Dong, J.; Sun, Q.; Liu, W.; Xue, S.; Yang, W. Two-Photon Absorption and Piezofluorochromism of Aggregation-Enhanced Emission 2,6-Bis(p-dibutylaminostyryl)-9,10-bis(4-pyridyl-vinyl-2)anthracene. *Dyes Pigm.* **2015**, *113*, 307–311.
- (1036) Cao, H.-T.; Shan, G.-G.; Yin, Y.-M.; Sun, H.-Z.; Wu, Y.; Xie, W.-F.; Su, Z.-M. Manipulating Efficiencies through Modification of *N*-Heterocyclic Phenyltriazole Ligands for Blue Iridium(III) Complexes. *Dyes Pigm.* **2015**, *113*, 655–663.
- (1037) Singh, A.; Singh, R.; Shellaiah, M.; Prakash, E. C.; Chang, H.-C.; Raghunath, P.; Lin, M.-C.; Lin, H.-C. A New Pyrene-Based Aggregation Induced Ratiometric Emission Probe for Selective Detections of Trivalent Metal Ions and Its Living Cell Application. *Sens. Actuators, B* **2015**, *207*, 338–345.
- (1038) Geng, J.; Liao, L.-D.; Qin, W.; Tang, B. Z.; Thakor, N.; Liu, B. Fluorogens with Aggregation Induced Emission: Ideal Photoacoustic Contrast Reagents Due to Intramolecular Rotation. *J. Nanosci. Nanotechnol.* **2015**, *15*, 1864–1868.
- (1039) Kizaki, K.; Imoto, H.; Kato, T.; Naka, K. Facile Construction of *N*-Alkyl Arylaminomaleimide Derivatives as Intensively Emissive Aggregation Induced Emission Dyes. *Tetrahedron* **2015**, *71*, 643–647.
- (1040) Zhang, L.; He, N.; Lu, C. Aggregation-Induced Emission: A Simple Strategy to Improve Chemiluminescence Resonance Energy Transfer. *Anal. Chem.* **2015**, *87*, 1351–1357.
- (1041) Wang, A.; Yang, Y.; Yu, F.; Xue, L.; Hu, B.; Fan, W.; Dong, Y. A Highly Selective and Sensitive Fluorescent Probe for Quantitative Detection of  $\text{Hg}^{2+}$  Based on Aggregation-Induced Emission Features. *Talanta* **2015**, *132*, 864–870.
- (1042) Okazawa, Y.; Kondo, K.; Akita, M.; Yoshizawa, M. Polyaromatic Nanocapsules Displaying Aggregation-Induced Enhanced Emissions in Water. *J. Am. Chem. Soc.* **2015**, *137*, 98–101.
- (1043) Xu, S.; Liu, T.; Mu, Y.; Wang, Y.-F.; Chi, Z.; Lo, C.-C.; Liu, S.; Zhang, Y.; Lien, A.; Xu, J. An Organic Molecule with Asymmetric Structure Exhibiting Aggregation-Induced Emission, Delayed Fluorescence, and Mechanoluminescence. *Angew. Chem., Int. Ed.* **2015**, *54*, 874–878.
- (1044) Qi, Q.; Qian, J.; Ma, S. Q.; Xu, B.; Zhang, S. X.-A.; Tian, W. Reversible Multistimuli-Response Fluorescent Switch Based on Tetraphenylethene–Spiropyran Molecules. *Chem. - Eur. J.* **2015**, *21*, 1149–1155.
- (1045) Cai, Y.; Samedov, K.; Dolinar, B. S.; Song, Z.; Tang, B. Z.; Zhang, C.; West, R. Synthesis and High Solid-State Fluorescence of Cyclic Silole Derivatives. *Organometallics* **2015**, *34*, 78–85.
- (1046) Chen, D.; Zhan, J.; Zhang, M.; Zhang, J.; Tao, J.; Tang, D.; Shen, A.; Qiu, H.; Yin, S. A Fluorescent Supramolecular Polymer with Aggregation Induced Emission (AIE) Properties Formed by Crown Ether-Based Host–Guest Interactions. *Polym. Chem.* **2015**, *6*, 25–29.
- (1047) Zhang, Y.; Chen, G.; Lin, Y.; Zhao, L.; Yuan, W.; Lu, P.; Jim, C. K. W.; Zhang, Y.; Tang, B. Z. Thiol–Bromo Click Polymerization for Multifunctional Polymers: Synthesis, Light Refraction, Aggregation-Induced Emission and Explosive Detection. *Polym. Chem.* **2015**, *6*, 97–105.
- (1048) Li, D.; Li, B.; Yang, S. I. A Selective Fluorescence Turn-On Sensing System for Evaluation of  $\text{Cu}^{2+}$  Polluted Water Based on Ultra-Fast Formation of Fluorescent Copper Nanoclusters. *Anal. Methods* **2015**, *7*, 2278–2282.
- (1049) Wang, A.; Yang, Y.; Yu, F.; Xue, L.; Hu, B.; Dong, Y.; Fan, W. Switching the Recognition Preference of Thiourea Derivative by Replacing  $\text{Cu}^{2+}$ : Spectroscopic Characteristic of Sggregation-Induced Emission and the Mechanism Studies for Recognition of  $\text{Hg}(\text{II})$  in Aqueous Solution. *Anal. Methods* **2015**, *7*, 2839–2847.
- (1050) Zhang, Y.; Wang, J.-H.; Zheng, J.; Li, D. A Br-Substituted Phenanthroimidazole Derivative with Aggregation Induced Emission from Intermolecular Halogen–Hydrogen Interactions. *Chem. Commun.* **2015**, *51*, 6350–6353.

- (1051) Alam, P.; Kaur, G.; Chakraborty, S.; Choudhury, A. R.; Laskar, I. R. Aggregation Induced Phosphorescence Active "Rollover" Iridium(III) Complex as a Multi-Stimuli-Responsive Luminescence Material. *Dalton Trans.* **2015**, *44*, 6581–6592.
- (1052) Zhang, Y.; Song, Q.; Wang, K.; Mao, W.; Cao, F.; Sun, J.; Zhan, L.; Lv, Y.; Ma, Y.; Zou, B.; Zhang, C. Polymorphic Crystals and Their Luminescence Switching of Triphenylacrylonitrile Derivatives upon Solvent Vapour, Mechanical, and Thermal Stimuli. *J. Mater. Chem. C* **2015**, *3*, 3049–3054.
- (1053) Sun, J.; Dai, Y.; Mi, O.; Zhang, Y.; Zhan, L.; Zhang, C. Unique Torsional Cruciform-Architectures Composed of Donor and Acceptor Axes Exhibiting Mechanochromic and Electrochromic Properties. *J. Mater. Chem. C* **2015**, *3*, 3356–3363.
- (1054) Liu, J.; Meng, L.; Zhu, W.; Zhang, C.; Zhang, H.; Yao, Y.; Wang, Z.; He, P.; Zhang, X.; Wang, Y.; et al. A Cross-Dipole Stacking Molecule of an Anthracene Derivative: Integrating Optical and Electrical Properties. *J. Mater. Chem. C* **2015**, *3*, 3068–3071.
- (1055) Liu, G.; Wu, D.; Liang, J.; Han, X.; Liu, S. H.; Yin, J. Tetraphenylethene Modified [n]Rotaxanes: Synthesis, Characterization and Aggregation-Induced Emission Behavior. *Org. Biomol. Chem.* **2015**, *13*, 4090–4100.
- (1056) Watt, M. M.; Engle, J. M.; Fairley, K. C.; Robitshek, T. E.; Haley, M. M.; Johnson, D. W. "Off-On" Aggregation-Based Fluorescent Sensor for the Detection of Chloride in Water. *Org. Biomol. Chem.* **2015**, *13*, 4266–4270.
- (1057) Zhang, R.; Kwok, R. T. K.; Tang, B. Z.; Liu, B. Hybridization Induced Fluorescence Turn-on of AIEgen-Oligonucleotide Conjugates for Specific DNA Detection. *RSC Adv.* **2015**, *5*, 28332–28337.
- (1058) Fu, Y.; Qiu, F.; Zhang, F.; Mai, Y.; Wang, Y.; Fu, S.; Tang, R.; Zhuang, X.; Feng, X. A Dual-Boron-Cored Luminogen Capable of Sensing and Imaging. *Chem. Commun.* **2015**, *51*, 5298–5301.
- (1059) He, G.; Wiltshire, B. D.; Choi, P.; Savin, A.; Sun, S.; Mohammadpour, A.; Ferguson, M. J.; McDonald, R.; Farsinezhad, S.; Brown, A.; et al. Phosphorescence within Benzotellurophenes and Color Tunable Tellurophenes under Ambient Conditions. *Chem. Commun.* **2015**, *51*, 5444–5447.
- (1060) Song, N.; Chen, D.-X.; Xia, M.-C.; Qiu, X.-L.; Ma, K.; Xu, B.; Tian, W.; Yang, Y.-W. Supramolecular Assembly-Induced Yellow Emission of 9,10-Distyrylanthracene Bridged Bis(pillar[5]arene)s. *Chem. Commun.* **2015**, *51*, 5526–5529.
- (1061) Yang, J.; Sun, N.; Huang, J.; Li, Q.; Peng, Q.; Tang, X.; Dong, Y.; Ma, D.; Li, Z. New AIEgens Containing Tetraphenylethene and Silole Moieties: Tunable Intramolecular Conjugation, Aggregation-Induced Emission Characteristics and Good Device Performance. *J. Mater. Chem. C* **2015**, *3*, 2624–2631.
- (1062) Lin, Y.; Li, C.; Song, G.; He, C.; Dong, Y.; Wang, H. Freezing-Induced Multi-Colour Emissions of AIE Luminogen Di(4-propoxypyphenyl) Dibenzofulvene. *J. Mater. Chem. C* **2015**, *3*, 2677–2685.
- (1063) Zhang, G.; Sun, J.; Xue, P.; Zhang, Z.; Gong, P.; Peng, J.; Lu, R. Phenothiazine Modified Triphenylacrylonitrile Derivates: AIE and Mechanochromism Tuned by Molecular Conformation. *J. Mater. Chem. C* **2015**, *3*, 2925–2932.
- (1064) Liu, Q.; Wang, X.; Yan, H.; Wu, Y.; Li, Z.; Gong, S.; Liu, P.; Liu, Z. Benzothiazole-Enamide-Based BF<sub>2</sub> Complexes: Luminophores Exhibiting Aggregation-Induced Emission, Tunable Emission and Highly Efficient Solid-State Emission. *J. Mater. Chem. C* **2015**, *3*, 2953–2959.
- (1065) Hsiao, T.-S.; Huang, P.-C.; Lin, L.-Y.; Yang, D.-J.; Hong, J.-L. Crystallization-Promoted Emission Enhancement of Poly(L-lactide) Containing a Fluorescent Salicylideneazine Center with Aggregation-Enhanced Emission Properties. *Polym. Chem.* **2015**, *6*, 2264–2273.
- (1066) Kaur, S.; Kumar, M.; Bhalla, V. AIEE Active Perylene Bisimide Supported Mercury Nanoparticles for Synthesis of Amides via Aldoximes/Ketoximes Rearrangement. *Chem. Commun.* **2015**, *51*, 4085–4088.
- (1067) Zhang, C.; Li, Y.; Xue, X.; Chu, P.; Liu, C.; Yang, K.; Jiang, Y.; Chen, W.-Q.; Zou, G.; Liang, X.-J. A Smart pH-Switchable Luminescent Hydrogel. *Chem. Commun.* **2015**, *51*, 4168–4171.
- (1068) Zhang, L.; Hu, W.; Yu, L.; Wang, Y. Click Synthesis of A Novel Triazole Bridged AIE Active Cyclodextrin Probe for Specific Detection of Cd<sup>2+</sup>. *Chem. Commun.* **2015**, *51*, 4298–4301.
- (1069) Dong, X.; Hu, F.; Liu, Z.; Zhang, G.; Zhang, D. A Fluorescent Turn-On Low Dose Detection of Gamma-Radiation Based on Aggregation-Induced Emission. *Chem. Commun.* **2015**, *51*, 3892–3895.
- (1070) Huang, W.; Sun, L.; Zheng, Z.; Su, J.; Tian, H. Colour-Tunable Fluorescence of Single Molecules Based on the Vibration Induced Emission of Phenazine. *Chem. Commun.* **2015**, *51*, 4462–4464.
- (1071) Gao, Z.; Chen, Y. Two-Photon Pumped Emission of Polymeric Thin Film Doped with Dicyanopyranone Derivative. *RSC Adv.* **2015**, *5*, 20712–20715.
- (1072) Preis, E.; Dong, W.; Brunklaus, G.; Scherf, U. Microporous, Tetraarylethylene-Based Polymer Networks Generated in a Reductive Polyolefination Process. *J. Mater. Chem. C* **2015**, *3*, 1582–1587.
- (1073) Yang, M.; Zhang, Y.; Zhu, W.; Wang, H.; Huang, J.; Cheng, L. H.; Zhou, H. P.; Wu, J.; Tian, Y. Difunctional Chemosensor for Cu(II) and Zn(II) Based on Schiff Base Modified Anthryl Derivative with Aggregation-Induced Emission Enhancement and Piezochromic Characteristics. *J. Mater. Chem. C* **2015**, *3*, 1994–2002.
- (1074) Lu, Q.; Li, X.; Li, J.; Yang, Z. Y.; Xu, B.; Chi, Z.; Xu, J.; Zhang, Y. Influence of Cyano Groups on the Properties of Piezofluorochromic Aggregation-Induced Emission Enhancement Compounds Derived from Tetraphenylvinyl-Capped Ethane. *J. Mater. Chem. C* **2015**, *3*, 1225–1234.
- (1075) Chen, M.; Li, L.; Nie, H.; Tong, J.; Yan, L.; Xu, B.; Sun, J. Z.; Tian, W.; Zhao, Z.; Qin, A.; et al. Tetraphenylpyrazine-Based AIEgens: Facile Preparation and Tunable Light Emission. *Chem. Sci.* **2015**, *6*, 1932–1937.
- (1076) Liao, C.-W.; Rao, M. R.; Sun, S.-S. Structural Diversity of New Solid-State Luminophores Based on Quinoxaline- $\beta$ -Ketoiminate Boron Difluoride Complexes with Remarkable Fluorescence Switching Properties. *Chem. Commun.* **2015**, *51*, 2656–2659.
- (1077) Chen, Z.; Han, X.; Zhang, J.; Wu, D.; Yu, G.-A.; Yin, J.; Liu, S. H. Fluorene-Based Novel Gold(I) Complexes with Aggregation-Induced Emission (AIE) or Aggregate Fluorescence Change Characteristics: From Green to White Emission. *RSC Adv.* **2015**, *5*, 15341–15349.
- (1078) Hu, Z.; Huang, G.; Lustig, W. P.; Wang, F.; Wang, H.; Teat, S. J.; Banerjee, D.; Zhang, D.; Li, J. Achieving Exceptionally High Luminescence Quantum Efficiency by Immobilizing An AIE Molecular Chromophore into a Metal–Organic Framework. *Chem. Commun.* **2015**, *51*, 3045–3048.
- (1079) Butler, T.; Morris, W. A.; Samonina-Kosicka, J.; Fraser, C. L. Mechanochromic Luminescence and Aggregation Induced Emission for a Metal-Free  $\beta$ -Diketone. *Chem. Commun.* **2015**, *51*, 3359–3362.
- (1080) Yang, C.; Trinh, Q. T.; Wang, X.; Tang, Y.; Wang, K.; Huang, S.; Chen, X.; Mushrif, S. H.; Wang, M. Crystallization-Induced Red Emission of a Facilely Synthesized Biodegradable Indigo Derivative. *Chem. Commun.* **2015**, *51*, 3375–3378.
- (1081) Kim, B. S. I.; Jin, Y.-J.; Lee, W.-E.; Byun, D. J.; Yu, R.; Park, S.-J.; Kim, H.; Song, K.-H.; Jang, S.-Y.; Kwak, G. Highly Fluorescent, Photostable, Conjugated Polymer Dots with Amorphous, Glassy-State, Coarsened Structure for Bioimaging. *Adv. Opt. Mater.* **2015**, *3*, 78–86.
- (1082) Niu, Y.; Zhang, F.; Bai, Z.; Dong, Y.; Yang, J.; Liu, R.; Zou, B.; Li, J.; Zhong, H. Aggregation-Induced Emission Features of Organometal Halide Perovskites and Their Fluorescence Probe Applications. *Adv. Opt. Mater.* **2015**, *3*, 112–119.
- (1083) Mailty, A.; Ali, F.; Agarwalla, H.; Anothumakkool, B.; Das, A. Tuning of Multiple Luminescence Outputs and White-Light Emission from a Single Gelator Molecule through an ESIPT Coupled AIEE Process. *Chem. Commun.* **2015**, *51*, 2130–2133.
- (1084) Liu, X.-G.; Wang, H.; Chen, B.; Zou, Y.; Gu, Z.-G.; Zhao, Z.; Shen, L. A Luminescent Metal–Organic Framework Constructed Using a Tetraphenylethene-Based Ligand for Sensing Volatile Organic Compounds. *Chem. Commun.* **2015**, *51*, 1677–1680.
- (1085) Ding, D.; Kwok, R. T. K.; Yuan, Y.; Feng, G.; Tang, B. Z.; Liu, B. A Fluorescent Light-Up Nanoparticle Probe with Aggregation-Induced Emission Characteristics and Tumor-Acidity Responsiveness for

- Targeted Imaging and Selective Suppression of Cancer Cells. *Mater. Horiz.* **2015**, *2*, 100–105.
- (1086) Shen, Z.; Wang, T.; Liu, M. Macroscopic Chirality of Supramolecular Gels Formed from Achiral Tris(ethyl cinnamate) Benzene-1,3,5-tricarboxamides. *Angew. Chem., Int. Ed.* **2014**, *53*, 13424–13428.
- (1087) Hu, Q.; Gao, M.; Feng, G.; Liu, B. Mitochondria-Targeted Cancer Therapy Using a Light-Up Probe with Aggregation-Induced-Emission Characteristics. *Angew. Chem., Int. Ed.* **2014**, *53*, 14225–14229.
- (1088) Yoshii, R.; Hirose, A.; Tanaka, R.; Chujo, Y. Functionalization of Boron Diiminates with Unique Optical Properties: Multicolor Tuning of Crystallization-Induced Emission and Introduction into the Main Chain of Conjugated Polymers. *J. Am. Chem. Soc.* **2014**, *136*, 18131–18139.
- (1089) Raj, T.; Saluja, P.; Singh, N. A New Class of Pyrene Based Multifunctional Chemosensors for Differential Sensing of Metals in Different Media: Selective Recognition of  $Zn^{2+}$  in Organic and  $Fe^{3+}$  in Aqueous Medium. *Sens. Actuators, B* **2015**, *206*, 98–106.
- (1090) Chen, W.; Li, Q.; Zheng, W.; Hu, F.; Zhang, G.; Wang, Z.; Zhang, D.; Jiang, X. Identification of Bacteria in Water by a Fluorescent Array. *Angew. Chem., Int. Ed.* **2014**, *53*, 13734–13739.
- (1091) Wang, X.; Wu, Y.; Liu, Q.; Li, Z.; Yan, H.; Ji, C.; Duan, J.; Liu, Z. Aggregation-Induced Emission (AIE) of Pyridyl-Enamido-Based Organoboron Luminophores. *Chem. Commun.* **2015**, *51*, 784–787.
- (1092) Guo, Y.; Tong, X.; Ji, L.; Wang, Z.; Wang, H.; Hu, J.; Pei, R. Visual Detection of  $Ca^{2+}$  Based on Aggregation-Induced Emission of Au(I)-Cys Complexes with Superb Selectivity. *Chem. Commun.* **2015**, *51*, 596–598.
- (1093) Chen, Z.; Zhang, J.; Song, M.; Yin, J.; Yu, G.; Liu, S. H. A Novel Fluorene-Based Aggregation-Induced Emission (AIE)-Active Gold(I) Complex with Crystallization-Induced Emission Enhancement (CIEE) and Reversible Mechanochromism Characteristics. *Chem. Commun.* **2015**, *51*, 326–329.
- (1094) Liu, H.; Wei, R.; Xiang, Y.; Tong, A. Fluorescence Turn-On Detection of Pyrophosphate Based on Aggregation-Induced Emission Property of 5-Chlorosalicylaldehyde Azine. *Anal. Methods* **2015**, *7*, 753–758.
- (1095) Mazumdar, P.; Das, D.; Sahoo, G. P.; Salgado-Morán, G.; Misra, A. Aggregation Induced Emission Enhancement of 4,4'-Bis(diethylamino)benzophenone with an Exceptionally Large Blue Shift and Its Potential Use as Glucose Sensor. *Phys. Chem. Chem. Phys.* **2015**, *17*, 3343–3354.
- (1096) Tu, Z.; Liu, M.; Qian, Y.; Yang, G.; Cai, M.; Wang, L.; Huang, W. Easily Fixed Simple Small ESIPT Molecule with Aggregation Induced Emission for Fast and Photostable “Turn-On” Bioimaging. *RSC Adv.* **2015**, *5*, 7789–7793.
- (1097) Wang, Y.; Chen, Y.; Wang, H.; Cheng, Y.; Zhao, X. Specific Turn-On Fluorescent Probe with Aggregation-Induced Emission Characteristics for SIRT1Modulator Screening and Living-Cell Imaging. *Anal. Chem.* **2015**, *87*, 5046–5049.
- (1098) Minei, P.; Koenig, M.; Battisti, A.; Ahmad, M.; Barone, V.; Torres, T.; Guldi, D. M.; Brancato, G.; Bottari, G.; Pucci, A. Reversible Vapochromic Response of Polymer Films Doped with a Highly Emissive Molecular Rotor. *J. Mater. Chem. C* **2014**, *2*, 9224–9232.
- (1099) Zhang, Y.; Li, J.; Tang, B. Z.; Wong, K. S. Aggregation Enhancement on Two-Photon Optical Properties of AIE-Active D-TPE-A Molecules. *J. Phys. Chem. C* **2014**, *118*, 26981–26986.
- (1100) Alam, P.; Kaur, G.; Climent, C.; Pasha, S.; Casanova, D.; Alemany, P.; Choudhury, A. R.; Laskar, I. R. New ‘Aggregation Induced Emission (AIE)’ Active Cyclometalated Iridium(III) Based Phosphorescent Sensors: High Sensitivity for Mercury(II) Ions. *Dalton Trans.* **2014**, *43*, 16431–16440.
- (1101) Honda, H.; Kuwabara, J.; Kanbara, T. Aggregation-Induced Emission Behavior of a Pincer Platinum(II) Complex Bearing a Poly(ethylene oxide) Chain in Aqueous Solution. *J. Organomet. Chem.* **2014**, *772*, 139–142.
- (1102) Gao, Y.; Feng, G.; Jiang, T.; Goh, C.; Ng, L.; Liu, B.; Li, B.; Yang, L.; Hua, J.; Tian, H. Biocompatible Nanoparticles Based on Diketo-Pyrrolo-Pyrrole (DPP) with Aggregation-Induced Red/NIR Emission for in vivo Two-Photon Fluorescence Imaging. *Adv. Funct. Mater.* **2015**, *25*, 2857–2866.
- (1103) Mallet, C.; Moussalem, C.; Faurie, A.; Allain, M.; Gohier, F.; Skene, W. G.; Frère, P. Rational Topological Design for Fluorescence Enhancement upon Aggregation of Distyrylfuran Derivatives. *Chem. - Eur. J.* **2015**, *21*, 7944–7953.
- (1104) Chang, Z.-F.; Jing, L.-M.; Wei, C.; Dong, Y.-P.; Ye, Y.-C.; Zhao, Y. S.; Wang, J.-L. Hexaphenylbenzene-Based,  $\pi$ -Conjugated Snowflake-Shaped Luminophores: Tunable Aggregation-Induced Emission Effect and Piezofluorochromism. *Chem. - Eur. J.* **2015**, *21*, 8504–8510.
- (1105) Zhang, H.; Li, H.; Wang, J.; Sun, J.; Qin, A.; Tang, B. Z. Axial Chiral Aggregation-Induced Emission Luminogens with Aggregation-Annihilated Circular Dichroism Effect. *J. Mater. Chem. C* **2015**, *3*, 5162–5166.
- (1106) Singh, R. S.; Gupta, R. K.; Paitandi, R. P.; Dubey, M.; Sharma, G.; Koch, B.; Pandey, D. S. Morphological Tuning via Structural Modulations in AIE Luminogens with the Minimum Number of Possible Variables and Their Use in Live Cell Imaging. *Chem. Commun.* **2015**, *51*, 9125–9128.
- (1107) Zhang, W.; Kwok, R. T. K.; Chen, Y.; Chen, S.; Zhao, E.; Yu, C. Y.; Lam, J. W. Y.; Zheng, Q.; Tang, B. Z. Real-Time Monitoring of the Mitophagy Process by a Photostable Fluorescent Mitochondrion-Specific Bioprobe with AIE Characteristics. *Chem. Commun.* **2015**, *51*, 9022–9025.
- (1108) Oueslati, I. Building Functional Materials via Self-Assembly of Calixazacrowns. *Mater. Today: Proceedings* **2015**, *2*, 57–62.
- (1109) Shao, A.; Xie, Y.; Zhu, S.; Guo, Z.; Zhu, S.; Guo, J.; Shi, P.; James, T. D.; Tian, H.; Zhu, W.-H. Far-Red and Near-IR AIE-Active Fluorescent Organic Nanoprobes with Enhanced Tumor-Targeting Efficacy: Shape-Specific Effects. *Angew. Chem., Int. Ed.* **2015**, *54*, 7275–7280.
- (1110) Zhao, Y.; Yu, C. Y. Y.; Kwok, R. T. K.; Chen, Y.; Chen, S.; Lam, J. W. Y.; Tang, B. Z. Photostable AIE Fluorogens for Accurate and Sensitive Detection of S-Phase DNA Synthesis and Cell Proliferation. *J. Mater. Chem. B* **2015**, *3*, 4993–4996.
- (1111) Li, C.; Tang, X.; Zhang, L.; Li, C.; Liu, Z.; Bo, Z.; Dong, Y. Q.; Tian, Y.-H.; Dong, Y.; Tang, B. Z. Reversible Luminescence Switching of an Organic Solid: Controllable On–Off Persistent Room Temperature Phosphorescence and Stimulated Multiple Fluorescence Conversion. *Adv. Opt. Mater.* **2015**, DOI: [10.1002/adom.201500115](https://doi.org/10.1002/adom.201500115).
- (1112) Chen, S.; Hong, Y.; Zeng, Y.; Sun, Q.; Liu, Y.; Zhao, E.; Bai, G.; Qu, J.; Hao, J.; Tang, B. Z. Mapping Live Cell Viscosity with an Aggregation-Induced Emission Fluorogen by Means of Two-Photon Fluorescence Lifetime Imaging. *Chem. - Eur. J.* **2015**, *21*, 4315–4320.
- (1113) Li, J.; Jiang, Y.; Cheng, J.; Zhang, Y.; Su, H.; Lam, J. W. Y.; Sung, H. H.; Wong, K. S.; Kwok, H. S.; Tang, B. Z. Tuning the Singlet-Triplet Energy Gap of AIE Luminogens: Crystallization-Induced Room Temperature Phosphorescence and Delay Fluorescence, Tunable Temperature Response, Highly Efficient Non-Doped Organic Light-Emitting Diodes. *Phys. Chem. Chem. Phys.* **2015**, *17*, 1134–1141.
- (1114) Gong, Y.; Zhao, L.; Peng, Q.; Fan, D.; Yuan, W. Z.; Zhang, Y.; Tang, B. Z. Crystallization-Induced Dual Emission from Metal- and Heavy Atom-Free Aromatic Acids and Esters. *Chem. Sci.* **2015**, *6*, 4438–4444.
- (1115) Zhao, Z.; He, B.; Tang, B. Z. Aggregation-Induced Emission of Siloles. *Chem. Sci.* **2015**, *6*, DOI: [10.1039/c5sc01946j](https://doi.org/10.1039/c5sc01946j).